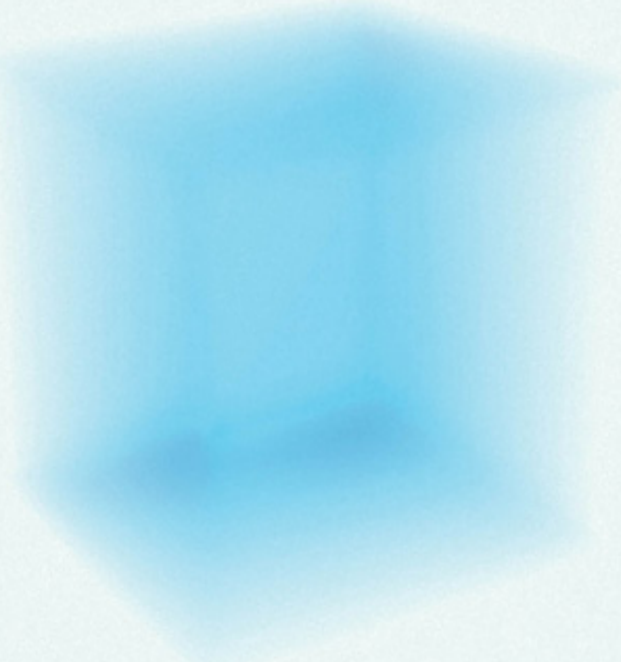
AEROGELS FOR ENERGY SAVING AND STORAGE



EDITED BY MELDIN MATHEW, HANNA J. MARIA, ANGE NZIHOU, AND SABU THOMAS

WILEY

Aerogels for Energy Saving and Storage

Aerogels for Energy Saving and Storage

Edited by

Meldin Mathew
Mahatma Gandhi University
Kottayam, India

Hanna J. Maria
Mahatma Gandhi University
Kottayam, India

Ange Nzihou
CNRS-IMT Mines Albi
Occitanie, France

Sabu Thomas
Mahatma Gandhi University
Kottayam, India

WILEY

Copyright © 2024 by John Wiley & Sons, Inc. All rights reserved, including rights for text and data mining and training of artificial technologies or similar technologies.

Published by John Wiley & Sons, Inc., Hoboken, New Jersey
Published simultaneously in Canada

No part of this publication may be reproduced, stored in a retrieval system, or transmitted in any form or by any means, electronic, mechanical, photocopying, recording, scanning, or otherwise, except as permitted under Section 107 or 108 of the 1976 United States Copyright Act, without either the prior written permission of the Publisher, or authorization through payment of the appropriate per-copy fee to the Copyright Clearance Center, 222 Rosewood Drive, Danvers, MA 01923, (978) 750-8400, fax (978) 646-8600, or on the web at www.copyright.com. Requests to the Publisher for permission should be addressed to the Permissions Department, John Wiley & Sons, Inc., 111 River Street, Hoboken, NJ 07030, (201) 748-6011, fax (201) 748-6008, or online at www.wiley.com/go/permissions.

Trademarks: Wiley and the Wiley logo are trademarks or registered trademarks of John Wiley & Sons, Inc. and/or its affiliates in the United States and other countries and may not be used without written permission. All other trademarks are the property of their respective owners. John Wiley & Sons, Inc. is not associated with any product or vendor mentioned in this book.

Limit of Liability/Disclaimer of Warranty: While the publisher and author have used their best efforts in preparing this book, they make no representations or warranties with respect to the accuracy or completeness of the contents of this book and specifically disclaim any implied warranties of merchantability or fitness for a particular purpose. No warranty may be created or extended by sales representatives or written sales materials. The advice and strategies contained herein may not be suitable for your situation. You should consult with a professional where appropriate. Further, readers should be aware that websites listed in this work may have changed or disappeared between when this work was written and when it is read. Neither the publisher nor authors shall be liable for any loss of profit or any other commercial damages, including but not limited to special, incidental, consequential, or other damages.

For general information on our other products and services or for technical support, please contact our Customer Care Department within the United States at (800) 762-2974, outside the United States at (317) 572-3993 or fax (317) 572-4002.

Wiley also publishes its books in a variety of electronic formats. Some content that appears in print may not be available in electronic formats. For more information about Wiley products, visit our web site at www.wiley.com.

Library of Congress Cataloging-in-Publication Data
Names: Mathew, Meldin, editor. | Maria, Hanna J., editor. | Nzihou, Ange, editor. | Thomas, Sabu, editor.
Title: Aerogels for energy saving and storage / edited by Meldin Mathew, Mahatma Gandhi University, Kottayam, India, Hanna J. Maria, Mahatma Gandhi University Kottayam, India, Ange Nzihou, CNRS-IMT Mines Albi, Occitanie, France, Sabu Thomas, Mahatma Gandhi University, Kottayam, India.
Description: Hoboken, New Jersey : John Wiley & Sons, Inc., [2023] | Includes index.
Identifiers: LCCN 2023024508 (print) | LCCN 2023024509 (ebook) | ISBN 9781119717638 (hardback) | ISBN 9781119717621 (adobe pdf) | ISBN 9781119717652 (epub)
Subjects: LCSH: Energy storage–Equipment and supplies. | Insulation (Heat)–Materials. | Aerogels.
Classification: LCC TK2945.A37 A38 2023 (print) | LCC TK2945.A37 (ebook) | DDC 621.402/4–dc23/eng/20240118
LC record available at https://lccn.loc.gov/2023024508
LC ebook record available at https://lccn.loc.gov/2023024509

Cover Design: Wiley
Cover Image: © dandesign86/Shutterstock

Set in 9.5/12.5pt STIXTwoText by Straive, Pondicherry, India

Contents

List of Contributors *xv*
Preface *xix*

1 The History, Physical Properties, and Energy-Related Applications of Aerogels *1*
Ai Du and Chengbin Wu
1.1 Definition and History of the Aerogels *1*
1.1.1 Basic Characteristics and Definition of Aerogels *1*
1.1.2 Brief History and Evolution of the Aerogel Science *4*
1.2 The Physics Properties of the Aerogels *5*
1.2.1 Mechanical Properties *7*
1.2.2 Thermal Properties *11*
1.2.2.1 Solid Conductivity *11*
1.2.2.2 Gaseous Conductivity *12*
1.2.2.3 Radiative Heat Transfer *12*
1.2.3 Optical Properties *13*
1.2.4 Electrical Properties *14*
1.2.4.1 Dielectric Properties *14*
1.2.4.2 Electrical Conductivity *15*
1.2.4.3 Negative Permittivity and Negative Permeability *15*
1.2.5 Acoustic Properties *15*
1.3 Energy-Related Aerogel Applications *16*
1.3.1 Applications in Energy Saving *16*
1.3.2 Applications in Energy Conversion *18*
1.3.3 Applications in Energy Storage *18*
1.4 Prospects *19*
1.4.1 Fundamental Science of the Aerogels *19*
1.4.2 Novel Aerogels *20*
1.4.3 Novel Application and Industrialization Technology of the Aerogels *20*
References *21*

2 Aerogels and Their Composites in Energy Generation and Conversion Devices *38*
Juno A. Rose, Aruchamy Kanakaraj, and Nataraj Sanna Kotrappanavar
2.1 Introduction to Aerogels *38*
2.2 Strategies for Development of Aerogel Materials *40*
2.2.1 Oxide-based Aerogel *40*
2.2.2 Organic Aerogel *42*

2.2.3 Carbon-based Aerogel *42*
2.2.4 Chalcogenide Aerogel *43*
2.2.5 Inorganic Gels *44*
2.3 Chemistry and Mechanisms of Aerogels Formation *44*
2.3.1 Mechanism of Network Formation in Aerogels *45*
2.3.1.1 Sol-Gel Method *45*
2.3.1.2 Self-Assembly Method *45*
2.3.1.3 Emulsion Method *46*
2.3.1.4 3-D Printing *46*
2.4 Drying Techniques *46*
2.4.1 Supercritical Drying *46*
2.4.2 Freeze Drying *47*
2.4.3 Ambient Pressure Drying *47*
2.4.4 Organic Solvent Sublimation Drying *47*
2.5 Properties and Characterization *48*
2.5.1 Aerogel Characterization *48*
2.5.2 Optical and IR Properties *48*
2.5.3 Thermal Properties *48*
2.5.4 Mechanical and Acoustic Properties *48*
2.6 Applications of Aerogel in Energy Storage and Energy Saving *48*
2.6.1 Batteries *49*
2.6.1.1 Li–ion Battery *49*
2.6.1.2 Li-S Battery *49*
2.6.1.3 Li-air Battery *51*
2.6.1.4 Zn-ion Battery *52*
2.6.1.5 Zn-air Battery *52*
2.6.1.6 Na-ion Battery *53*
2.6.2 Supercapacitors *53*
2.6.2.1 Electric Double Layer Capacitors *53*
2.6.2.2 Pseudo-capacitors *54*
2.6.2.3 Hybrid Capacitors *54*
2.6.3 Fuel Cells *54*
2.6.4 Electrocatalytic Hydrogen Evolution *55*
2.6.5 Electrocatalytic Oxygen Reduction *56*
2.7 Summary and Future Prospects *57*
Acknowledgments *57*
References *58*

3 Metal Aerogels for Energy Storage and Conversion *61*
Ran Du
3.1 Introduction of Metal Aerogels *61*
3.2 Characterizations *63*
3.2.1 Densities and Pore Structures *63*
3.2.2 Morphologies *64*
3.2.3 Element Distribution *64*
3.2.4 Crystalline Structure *64*
3.2.5 Mechanical Properties *64*

3.2.6 Time-Lapse Techniques *64*
3.3 Synthesis Methodologies *65*
3.3.1 Mechanistic Insights *65*
3.3.2 Two-Step Gelation *67*
3.3.2.1 Precursors *67*
3.3.2.2 Reductants *69*
3.3.2.3 Initiation *69*
3.3.3 One-Step Gelation *73*
3.3.4 Acceleration *75*
3.3.5 Postsynthesis *75*
3.3.6 Drying of Wet Gels *75*
3.3.7 Freezing-Based Method *76*
3.3.7.1 Freeze-Casting *76*
3.3.7.2 Freeze-Thawing *77*
3.3.7.3 3D Printing *77*
3.4 Energy-Related Applications *77*
3.4.1 Electrocatalysis in Fuel Cells *78*
3.4.1.1 Fuel Oxidation Reactions *78*
3.4.1.2 Oxygen Reduction Reactions *79*
3.4.2 Electrocatalysis in Water Splitting *81*
3.4.2.1 Oxygen Evolution Reactions *81*
3.4.2.2 Hydrogen Evolution Reactions *81*
3.4.3 Electrocatalytic CO_2 Reduction *82*
3.4.4 Photoelectrocatalysis for Alcohol Oxidation *82*
3.4.4.1 Energy Storage and Conversion *83*
3.4.4.2 Electrochemical Energy Storage *84*
3.4.4.3 Hydrogen Storage *84*
3.4.4.4 Self-Propulsion Devices *84*
3.5 Conclusions *86*
References *86*

4 Aerogels Using Polymer Composites *90*
Wei Fan, Jin Tian, and Tianxi Liu
4.1 Introduction *90*
4.2 Preparation of Polymer-Based Aerogels *92*
4.2.1 The Sol-Gel Process *93*
4.2.2 Aging *94*
4.2.3 Gel–Aerogel Transition (Drying) *94*
4.2.3.1 Supercritical Drying *94*
4.2.3.2 Ambient Pressure Drying *94*
4.2.3.3 Freeze Drying *95*
4.2.3.4 Other Drying Methods *95*
4.2.4 Combination of a Polymer Aerogel with Another Component *96*
4.3 Several Common Polymer Aerogels and Their Composites *98*
4.3.1 Polyimide-Based Aerogels *98*
4.3.1.1 Polyimide-Based Aerogels Combined with Carbon Materials *100*
4.3.1.2 Cellulose/Polyimide Composite Aerogels *102*

4.3.1.3 Polyimide-Based Aerogels Combined with Inorganic Materials *102*
4.3.2 Poly(Vinyl Alcohol)-Based Aerogels *104*
4.3.2.1 PVA-Based Aerogels Combined with Carbon Materials *105*
4.3.2.2 Cellulose/PVA Composite Aerogels *105*
4.3.2.3 PVA-Based Aerogels Combined with Inorganic Materials *106*
4.3.2.4 PVA-Based Aerogels Combined with Hybrid Materials *106*
4.3.3 Phenolic Resin-Based Aerogels *106*
4.3.3.1 Phenolic Resin-Based Aerogel Composites *108*
4.4 Applications of Polymer Aerogel Composites *108*
4.4.1 Absorption *108*
4.4.2 Thermal Insulation *110*
4.4.3 Flame Retardant Materials *111*
4.4.4 Sensing *112*
4.4.5 Electromagnetic Interference Shielding *116*
4.5 Conclusions and Outlook *119*
References *120*

5 Epoxide Related Aerogels; Sol-Gel Synthesis, Property Studies and Energy Applications *128*
Mahmoud Khalil and Houssam El-Rassy
5.1 Overview of Epoxide Aerogels *128*
5.1.1 History of Aerogels *128*
5.1.2 Advantages of Epoxide-Assisted Approach *129*
5.2 Synthesis and Drying Technique *130*
5.2.1 Metal Salt Precursors for Aerogels *130*
5.2.1.1 Selection of Precursors *130*
5.2.1.2 Choice of Solvents *130*
5.2.2 Hydrolysis *130*
5.2.2.1 Hydrolysis in Aqueous Media: Formation of Hydroxo/Oxo Ligands *131*
5.2.2.2 Hydrolysis in Organic Solvents *133*
5.2.3 Epoxide-Assisted Gelation and Condensation *134*
5.2.3.1 Olation Condensation *134*
5.2.3.2 Oxolation Condensation *134*
5.2.4 Gel Drying *135*
5.2.4.1 Supercritical Drying (SCD) *137*
5.2.4.2 Freeze Drying *138*
5.2.4.3 Ambient Pressure Drying *139*
5.3 Epoxide-assisted Aerogels *139*
5.3.1 Metal Oxides *139*
5.3.1.1 Alumina Aerogels *140*
5.3.1.2 Titania Aerogels *140*
5.3.1.3 Vanadia Aerogels *141*
5.3.1.4 Zirconia Aerogels *141*
5.3.1.5 Other Oxide Aerogels *141*
5.3.2 Composites Aerogels *142*
5.3.2.1 Inorganic-inorganic Composites *142*
5.3.2.2 Inorganic-Organic Composites *144*

5.4 Aerogels Properties and Characterization *145*
5.4.1 Structural Characterization *145*
5.4.1.1 X-ray Diffraction *145*
5.4.1.2 Electron Microscopy *149*
5.4.1.3 Infrared Spectroscopy *152*
5.4.2 Mechanical Characterization *157*
5.5 Some Applications and Examples *158*
5.5.1 Catalysis *158*
5.5.2 Solid Fuel Cell *159*
5.5.3 Water Treatment *160*
5.5.4 Biodiesel Production *160*
5.5.5 Energy Conversion and Storage Applications *161*
5.6 Summary *161*
References *161*

6 CNT-Based Aerogels and Their Applications *169*
Zili Li and Zhiqun Lin
6.1 Introduction *169*
6.2 The Fundamental Principle of Preparing CNT-based Aerogels *170*
6.3 Strategies for Preparation of CNT-based Aerogels *171*
6.3.1 Preparation of CNT-based Aerogels via CVD *171*
6.3.1.1 Isotropic CNT Aerogels *172*
6.3.1.2 3D Vertical CNT Arrays *172*
6.3.1.3 Template-assisted CNT-based Aerogels *172*
6.3.2 Surface-modified CNT-based Aerogels *173*
6.3.2.1 Preparation of Aerogels with Noncovalent Modified CNTs *173*
6.3.2.2 Preparation of Aerogels with Covalent Modified CNTs *174*
6.3.3 CNT Doping in 3D Aerogels *175*
6.3.4 CNT/Inorganic Nanocrystal Composite Aerogels *179*
6.4 Applications *180*
6.4.1 Water Treatment *180*
6.4.2 Energy Storage and Conversion *183*
6.4.3 Catalysts *186*
6.5 Conclusions and Perspectives *189*
References *189*

7 Silica-Based Aerogels for Building Transparent Components *197*
Cinzia Buratti, Elisa Belloni, Francesca Merli, Costanza Vittoria Fiorini, Piergiovanni Domenighini, and Michele Zinzi
7.1 Introduction *197*
7.2 Silica Aerogels Production *197*
7.2.1 Preparation Steps *198*
7.2.1.1 Precursors *199*
7.2.1.2 Gel Preparation *200*
7.2.1.3 Aging *200*
7.2.1.4 Drying *201*
7.2.2 Rapid Extraction Methods *203*

7.3 Silica Aerogel Properties *204*
7.3.1 Mechanical Properties *204*
7.3.2 Thermal Properties *207*
7.3.3 Optical Properties *209*
7.3.4 Acoustic Properties *214*
7.4 Energy Performance of Silica Aerogels in Buildings *216*
7.4.1 Energy Performance of Monolithic Aerogel Glazing Systems *216*
7.4.2 Energy Performance of Granular Aerogel Glazing Systems *218*
7.5 Applications *226*
7.6 Conclusions *228*
7.7 Outlook *229*
References *230*

8 Inorganic Aerogels and Their Composites for Thermal Insulation in White Goods *237*
Özge Payanda Konuk, Orçun Yücel, and Can Erkey
8.1 Introduction *237*
8.1.1 Energy Consumption in White Goods *238*
8.1.2 Aerogels *240*
8.1.2.1 Synthesis of Aerogels *240*
8.1.2.2 Classification of Aerogels *240*
8.1.2.3 Forms of Aerogels *243*
8.2 Heat Transfer Mechanisms in Aerogels *245*
8.2.1 Solid Thermal Conductivity *245*
8.2.2 Gaseous Thermal Conductivity *248*
8.2.3 Radiative Thermal Conductivity *251*
8.2.3.1 Approximations Neglecting Some Physical Process *252*
8.2.3.2 Optically Thin Approximation Optically *252*
8.2.3.3 Optically Thick Approximation *252*
8.2.3.4 Two Flux Method *253*
8.2.3.5 Discrete Ordinate Method *253*
8.3 Inorganic Aerogels and Their Composites in White Goods *254*
8.3.1 Refrigerators *254*
8.3.1.1 Thermal Insulation in Refrigerators *254*
8.3.1.2 Aerogels for Vacuum Insulation Panels *255*
8.3.1.3 Aerogel Blankets for Refrigerators *256*
8.3.1.4 Monolithic Aerogels for Refrigerators *257*
8.3.1.5 Aerogel Polyurethane Composites *258*
8.3.2 Ovens *259*
8.3.2.1 Thermal Insulation in Ovens *259*
8.3.2.2 Aerogel Blankets for Ovens *259*
8.3.2.3 Monolithic Aerogel Panels *260*
8.4 Conclusions *261*
References *261*

9 Natural Polymer-Based Aerogels for Filtration Applications *267*
Mahaveer A. Halakarni, M. Manohara Halanur, and Sanna Kotrappanavar Nataraj
9.1 Introduction *267*
9.2 Material Option for the Preparation of Aerogel *269*

9.2.1 Synthetic Polymers *269*
9.2.2 Biopolymers-Based Aerogels *270*
9.3 Application of Aerogels in Water Purification *271*
9.3.1 Organic Molecule Separation *271*
9.3.2 Organic Solvent Separation *274*
9.3.3 Oil–Water Separation *275*
9.3.4 Solar-Driven Water Evaporation *276*
9.3.5 Heavy Metal Ions Separation *279*
9.3.6 Factors Affecting Adsorption of Heavy Metal Ions *281*
9.4 Conclusion and Future Prospect *282*
Acknowledgments *282*
References *282*

10 Organic and Carbon Aerogels *291*
Marina Schwan and Barbara Milow
10.1 Introduction *291*
10.2 Overview on Organic Aerogels *293*
10.2.1 Synthesis and Properties of Resorcinol-Formaldehyde Aerogels *293*
10.2.1.1 Synthesis of Resorcinol-Formaldehyde Aerogels *293*
10.2.1.2 Gelation, Aging, and Drying of Resorcinol-Formaldehyde Aerogels *295*
10.2.1.3 Influence of the Final Structure through Different Synthesis Parameters *297*
10.2.2 Synthesis and Properties of Melamine-based Aerogels *299*
10.2.2.1 Melamine-Formaldehyde Aerogels *299*
10.2.2.2 Melamine-Resorcinol-Formaldehyde Xerogels *300*
10.2.3 Synthesis and Properties of Tannin-Formaldehyde Aerogels *302*
10.2.4 Synthesis and Properties of Other Organic Aerogels Crosslinked by Formaldehyde or Furfural *304*
10.3 Application of Organic Aerogels for Energy Saving *305*
10.4 Overview on Organic-based Carbon Aerogels *308*
10.4.1 Carbonization Process *308*
10.4.2 Properties and Microstructure of Carbon Aerogels *312*
10.5 Applications of Organic-Based Carbon Aerogels for Energy Saving and Storage *313*
10.5.1 Applications in Supercapacitors *313*
10.5.2 Applications in Battery Technologies *314*
10.5.3 Other Relevant Applications of Carbon Aerogels *317*
10.5.3.1 Foundry Application *317*
10.5.3.2 Hydrogen Storage *317*
10.5.3.3 Thermal Insulation *318*
10.5.3.4 Adsorption Material *318*
10.5.3.5 Microwave Adsorption *319*
10.6 Summary and Outlook *319*
References *319*

11 Carbonaceous Aerogels for Fuel Cells and Supercapacitors *331*
Meryem Samancı and Ayşe Bayrakçeken Yurtcan
11.1 Introduction *331*
11.2 Carbonaceous Materials *332*
11.3 Carbonaceous Aerogels *335*

11.3.1 What Are Aerogels? *335*
11.3.2 Carbon Aerogels *339*
11.3.3 CNT-Based Aerogels *340*
11.3.4 Graphene Aerogels *340*
11.3.5 Activated Carbon Aerogels *341*
11.3.6 Biomass-Derived Aerogels *342*
11.4 Fuel Cells *342*
11.4.1 Fuel Cell Components *344*
11.4.2 Carbonaceous Aerogels for Fuel Cells *350*
11.5 Supercapacitors *351*
11.5.1 Supercapacitor Materials *359*
11.5.2 Carbonaceous Aerogels for Supercapacitors *363*
11.6 Conclusions *373*
References *374*

12 Aerogels for Electrocatalytic Hydrogen Production *386*
Arun Prasad Murthy
12.1 Introduction *386*
12.1.1 Energy Crisis *386*
12.1.2 Electrocatalytic Water Splitting *387*
12.1.3 Electrocatalysts for HER and OER *387*
12.1.4 Application of Aerogels as Electrocatalyst Materials for HER and OER *388*
12.1.5 Basics of Electroanalysis of Water Splitting *388*
12.2 Application of Aerogels in Hydrogen Evolution Reaction *389*
12.3 Application of Aerogels in Oxygen Evolution Reaction *395*
12.4 Application of Aerogels for Overall Water Splitting *399*
12.5 Concluding Remarks *402*
References *403*

13 Clay-Based Aerogel Composites *407*
Basim Abu-Jdayil, Bilkis Ajiwokewu, Safa Ahmed, and Saheed Busura
13.1 Introduction *407*
13.1.1 Aerogels *407*
13.1.2 Clay Aerogels Composites *408*
13.1.3 Clays Used in Aerogels Development *409*
13.2 Synthesis Techniques of Clay Aerogels Composites *410*
13.3 Properties of Clay Aerogels *411*
13.3.1 Clay Aerogels Microstructure *411*
13.3.2 Mechanical Properties *414*
13.3.3 Thermal Conductivity *415*
13.3.4 Fire/Combustion Behavior *417*
13.3.5 Hydrophobicity/Hydrophilicity Behavior *418*
13.4 Enhancement Techniques of Clay Aerogels *418*
13.4.1 Natural Polymers Enhanced Clay Aerogels *419*
13.4.2 Synthetic Polymers Enhanced Clay Aerogels *421*
13.4.3 Natural Fibers Enhanced Clay-Polymer Aerogels *422*
13.4.4 Carbon Nanotubes Enhanced Clay-Polymer Aerogels *423*

13.4.5 Modified Organoclay Enhanced Clay Aerogel *423*
13.4.6 Enhancing Clay Aerogels with Polymer Coating *423*
13.5 Applications and Integration Techniques of Clay Aerogel Composites *424*
13.6 Economy and Limitations of Clay Aerogel and Composites *424*
13.7 Future Direction of Research *425*
13.8 Conclusions *426*
References *426*

14 Hybrid Aerogels for Energy Saving Applications *430*
Nilay Gizli and Selay Sert Çok
14.1 Introduction *430*
14.2 Silica-Based Hybrid Aerogels *431*
14.2.1 Polymer-Crosslinked Silica Aerogels *431*
14.2.1.1 Crosslinking by Posttreatment Methods *431*
14.2.1.2 Crosslinking by One-Pot Synthesis *432*
14.2.1.3 Double Crosslinking with Radical Polymerization *432*
14.2.2 Hybrids Based on Organically Modified Polysiloxanes by Co-gelation Approach *433*
14.2.2.1 Co-gelation Approach with Di/Tri Functional Organosilanes *433*
14.2.2.2 Co-gelation with Bridged Bis-Silane Precursors (Bridging Chain Approach) *434*
14.2.3 Fiber Reinforcement *435*
14.3 Thermal Properties of Hybrid Aerogels *437*
14.4 Hybrid Aerogels in Energy Saving Applications *440*
14.5 Conclusion and Future Perspective *440*
References *441*

15 Porous Graphene-Based Aerogels for Batteries *447*
Maryam Hasanpour and Mohammad Hatami
Graphic Abstract *447*
15.1 Introduction *448*
15.2 Preparation and Synthesized Method for Graphene-Based Aerogel *448*
15.3 Application of Graphene-Based Aerogels (GBAs) for Energy Storage Devices *449*
15.3.1 Recent Advances in Porous Graphene-Based Aerogels for Batteries *451*
15.3.1.1 Lithium-Ion Batteries (LIBs) *451*
15.3.1.2 Sodium-Ion Batteries (SIBs) *455*
15.3.1.3 Lithium-Sulfur Batteries (LSBs) *457*
15.3.1.4 Other Batteries *461*
15.4 Conclusions *466*
References *466*

16 Theoretical Modeling of the Thermal and Mechanical Structure-Property Relationships in Aerogels *473*
Ameya Rege and Barbara Milow
16.1 Introduction *473*
16.2 Modeling the Thermal Structure-Property Relationships of Aerogels *474*
16.2.1 Radiative Thermal Conductivity *476*
16.2.2 Gaseous Thermal Conductivity *477*
16.2.3 Solid Thermal Conductivity *478*

16.2.4 Modeling the Thermal Conductivity of Aerogel Composites and Some Applications *480*
16.3 Modeling the Mechanical Structure-Property Relationships of Aerogels *481*
16.3.1 All-Atom Simulations *482*
16.3.2 Coarse-Grained Modeling *484*
16.3.3 Micro-Mechanical Modeling *487*
16.4 Outlook *490*
References *491*

17 Aerogels in Energy: State of Art and New Challenges *497*
Golnoosh Abdeali and Ahmad Reza Bahramian
17.1 Introduction *497*
17.2 Aerogel in Thermal and Electrical Energy *497*
17.2.1 Thermal Energy *497*
17.2.2 Electrical Energy *498*
17.2.3 Design and Manufacture *499*
17.2.3.1 Carbonization Process *501*
17.2.3.2 Carbothermal Reduction *502*
17.2.3.3 Aerogel Modification Using Carbon-Based Additives *502*
17.2.4 Opportunities and Challenges *506*
17.3 Methodology for Energy Performance Analysis *509*
17.3.1 Thermal Conductivity *509*
17.3.2 Time-Temperature History *510*
17.3.3 Electrical Performance *511*
17.3.4 Potential Applications from an Energy Perspective *511*
17.3.4.1 Potential Applications for Electrical Energy Storage *511*
17.3.4.2 Potential Applications for Thermal Energy Storage *512*
17.4 Conclusions *513*
Acknowledgments *513*
References *514*

Index *517*

List of Contributors

Golnoosh Abdeali
Polymer Engineering Department
Faculty of Chemical Engineering
Tarbiat Modares University
Tehran, Iran

Basim Abu-Jdayil
Chemical and Petroleum Engineering Department
UAE University
Al Ain, UAE

Safa Ahmed
Chemical and Petroleum Engineering Department
UAE University
Al Ain, UAE

Bilkis Ajiwokewu
Chemical and Petroleum Engineering Department
UAE University
Al Ain, UAE

Ayşe Bayrakçeken Yurtcan
Department of Chemical Engineering
Atatürk University
Erzurum, Turkey
and
Department of Nanoscience and Nanoengineering
Atatürk University
Erzurum, Turkey

Elisa Belloni
Department of Engineering
University of Perugia
Perugia, Italy

Cinzia Buratti
Department of Engineering
University of Perugia
Perugia, Italy

Saheed Busura
Chemical and Petroleum Engineering Department
UAE University
Al Ain, UAE

Ai Du
Shanghai Key Laboratory of Special Artificial Microstructure Materials and Technology
Tongji University
Shanghai, China
and
School of Physics Science and Engineering
Tongji University
Shanghai, China

Ran Du
School of Materials Science and Engineering
Beijing Institute of Technology
Beijing, PR China

Piergiovanni Domenighini
Department of Engineering
University of Perugia
Perugia, Italy

Can Erkey
Materials Science and Engineering
Koç University
Istanbul, Turkey
and
Chemical and Biological Engineering
Koç University
Istanbul, Turkey
and
Tüpraş Energy Center (KUTEM)
Koç University
Istanbul, Turkey

Houssam El-Rassy
Department of Chemistry
American University of Beirut
Beirut, Lebanon

Wei Fan
Key Laboratory of Synthetic and Biological Colloids, Ministry of Education
School of Chemical and Material Engineering
Jiangnan University
Wuxi, PR China
and
State Key Laboratory for Modification of Chemical Fibers and Polymer Materials
College of Materials Science and Engineering
Donghua University
Shanghai, PR China

Nilay Gizli
Chemical Engineering Department
Ege University, İzmir, Turkey

Mahaveer A. Halakarni
Centre for Nano and Material Science
Jain University
Bangalore, India

M. Manohara Halanur
Centre for Nano and Material Science
Jain University
Bangalore, India

Maryam Hasanpour
Department of Chemical Engineering
University of Bojnord
Bojnord, Iran
and
Department of Mechanical Engineering
Esfarayen University of Technology
Esfarayen, Iran

Mohammad Hatami
Department of Mechanical Engineering
Esfarayen University of Technology
Esfarayen, Iran

Aruchamy Kanakaraj
Center for Nano and Material Sciences
Jain University
Bangalore, India

Mahmoud Khalil
Department of Chemistry
American University of Beirut
Beirut, Lebanon

Sanna Kotrappanavar Nataraj
Centre for Nano and Material Science
Jain University
Bangalore, India
and
Polymer Science and Engineering
Chonnam National University
Gwangju, South Korea

Zili Li
School of Information Science and Technology
Fudan University
Shanghai, China
and
School of Materials Science and Engineering
Georgia Institute of Technology
Atlanta, USA

Zhiqun Lin
School of Materials Science and Engineering
Georgia Institute of Technology
Atlanta, USA

Tianxi Liu
Key Laboratory of Synthetic and Biological Colloids, Ministry of Education
School of Chemical and Material Engineering
Jiangnan University
Wuxi, PR China
and
State Key Laboratory for Modification of Chemical Fibers and Polymer Materials
College of Materials Science and Engineering
Donghua University
Shanghai, PR China

Francesca Merli
Department of Engineering
University of Perugia
Perugia, Italy

Barbara Milow
German Aerospace Center
Linder Hoehe
Cologne, Germany
and
Department of Aerogels and Aerogel Composites
Institute of Materials Research, German Aerospace Center
Cologne, Germany

Özge Payanda Konuk
Materials Science and Engineering
Koç University
Istanbul, Turkey

Arun Prasad Murthy
Department of Chemistry
School of Advanced Sciences
Vellore Institute of Technology
Vellore, Tamil Nadu, India

Ameya Rege
Department of Aerogels and Aerogel Composites
Institute of Materials Research, German Aerospace Center
Cologne, Germany

Ahmad Reza Bahramian
Polymer Engineering Department
Faculty of Chemical Engineering
Tarbiat Modares University
Tehran, Iran

Juno A. Rose
Center for Nano and Material Sciences
Jain University
Bangalore, India

Meryem Samancı
Department of Chemical Engineering
Atatürk University
Erzurum, Turkey

Nataraj Sanna Kotrappanavar
Center for Nano and Material Sciences
Jain University
Bangalore, India
and
Polymer Science and Engineering
Chonnam National University
Gwangju, South Korea

Marina Schwan
German Aerospace Center
Linder Hoehe
Cologne, Germany

Selay Sert Çok
Chemical Engineering Department
Ege University, İzmir, Turkey

Jin Tian
State Key Laboratory for Modification of Chemical Fibers and Polymer Materials
College of Materials Science and Engineering
Donghua University
Shanghai, PR China

Costanza Vittoria Fiorini
DIAEE Department of Astronautical, Electrical, and Energy Engineering
"Sapienza" University of Rome
Rome, Italy

Chengbin Wu
Shanghai Key Laboratory of Special Artificial Microstructure Materials and Technology
Tongji University
Shanghai, China
and
School of Physics Science and Engineering
Tongji University
Shanghai, China

Orçun Yücel
Material Technologies Department
Arçelik A.Ş., Central R&D
Istanbul, Turkey

Michele Zinzi
ENEA, Centro Ricerche Casaccia
Via Anguillarese
Rome, Italy

Preface

Increasing population and high energy consumption per capita in many countries have steadily increased the global demand for energy. This follows several issues related to energy production, storage, and consumption. Recently, many industries have started to promote aerogel energy for purposeful applications, including thermal insulators, catalysis, energy storage devices, sensors, electrodes, and super capacitors. The specialties involved in aerogel technology have many possibilities to influence the scientific society by helping in research, industrial access, commercialization, and social development. Aerogels have attained worldwide attention from many research and industrial areas due to their fascinating properties – high porosity, low density, high specific surface area, and low dielectric permittivity, as well as extraordinarily low thermal conductivity. All of these special properties of aerogel are capable of promoting sustainable and successful development.

Aerogels for Energy Saving and Storage has huge relevance due to the efficient properties of aerogels that will satisfy multiple purposes in the future energy saving technology. The upcoming energy still exists as a question because of the progressing consumption of energy due to large population growth over the world. The energy storage, storage system, and energy consumption rate have much influence in these aspects. Aerogels offer several attractive properties for overcoming energy-related challenges.

This book discusses current and promising applications for energy-based aerogels. Chapter 1 illustrates the history and properties of aerogels in a detailed manner. The next chapter gives information about the overall outlook of aerogel in different conversion devices. Other chapters deal with aerogels based on materials such as metal, inorganic and organic materials, polymer, graphene, clay, silica, and so on. Moreover, hybrid, graphene, and CNT-based aerogels, including their applications, are detailed in other chapters. Theoretical modeling on thermal-mechanical structure and property is portrayed in Chapter 16. The book culminates with the future state of art and new challenges in aerogel research and study progression.

This is the first time such a comprehensive analysis using energy studies has been undertaken to understand the diverse applications possible with aerogels. Therefore, a reference book of this type is invaluable for recognizing the hidden possibilities of future energy and the storage in aerogel. Many industries, researchers, and students will benefit from this book because of the science-based perspective that we are offering on aerogel in future energy and storage.

Aerogel experts have been willing to share their knowledge through this book, which is of significant benefit to scientists and researchers around the world. It brings attention to new discoveries for researchers and students in the field of energy and environmental sustainability.

Of significant value, this book reviews the scientific literature published so far in order to study the energy of aerogel from the various branches of science. We cover all the advances developed from aerogels and the specialties relating their morphology, properties, processability, applications, and future perspectives.

We express our sincere thanks to the team at Wiley for their extreme support and encouragement throughout this journey. We also express our sincere thanks to the contributors who have put their maximum efforts and cooperation into the progression.

We would like to thank our parental institutions Mahatma Gandhi University, Kottayam, Kerala, India, and Institute of Mines Telecome, Albi-Carmaux, France. Moreover, we acknowledge all the reviewers and advisory experts who were involved in the successful completion of these chapters. We would like to thank our family members and motivators who stood with us and supported us. All above, we thank our Lord for his great kindness and blessings.

1

The History, Physical Properties, and Energy-Related Applications of Aerogels

Ai Du[1,2] *and Chengbin Wu*[1,2]

[1] *Shanghai Key Laboratory of Special Artificial Microstructure Materials and Technology, Tongji University, Shanghai, 200092, China*
[2] *School of Physics Science and Engineering, Tongji University, Shanghai, 200092, China*

Chinese physicist Prof. Kun Huang mentioned in his course "Solid State Physics" before 1964 that "here we only discuss the crystal, not because non-crystalline solids are unimportant but because they are over-complicated" (translated) [1]. Aerogels, normally nanoporous noncrystalline solids, exhibit numerous unique properties but are not fully understood. Among them, their physical properties are fundamental to aerogel science, which strongly affects the noncrystalline theory and related applications. The aerogel science has been booming recently. Plenty of aerogels with novel compositions, structures, properties, and applications have joined the community. Research papers and patents related to aerogels have increased sharply. A symposium mainly referring to aerogel was added to the 2017 MRS Spring Meeting & Exhibit, and two series of international conferences (International Seminar on Aerogels, and International Conference on Aerogel-Inspired Materials) and one series of regional conferences (Sino-International Symposium on Aerogels) has been held biennially. Many new findings and concepts have come to the fore but lack timely updates about the definition and theory.

Thus, in this chapter, we will briefly introduce the history, physical properties, and applications, especially for the energy-related applications. The definition of aerogels, mechanisms, and prospects will also be discussed. We hope the audience can learn something and perhaps come up with novel ideas based on the historical progress, developing theory, smart design for specific applications, and selected works in this chapter. We hope more researchers join us and paint a bright future for the aerogel science.

1.1 Definition and History of the Aerogels

1.1.1 Basic Characteristics and Definition of Aerogels

The aerogel is a very special solid whose physics properties could be much different from its solid and gas components. One of the most notable samples is the sonic velocity in aerogels. As we know, the sound velocity through silica aerogels could be as low as $100\,m\,s^{-1}$, which is much lower than that in the dense silica ($>5000\,m\,s^{-1}$) and the air ($\sim 340\,m\,s^{-1}$) included. Therefore, in our

Aerogels for Energy Saving and Storage, First Edition. Edited by Meldin Mathew, Hanna J. Maria, Ange Nzihou, and Sabu Thomas.
© 2024 John Wiley & Sons, Inc. Published 2024 by John Wiley & Sons, Inc.

previous review, we suggested that aerogel is not only a novel material but also a new state of matter due to its unique position in the phase diagram and the diverse compositions [2].

There is no uniform definition of the term *aerogel* since the concept is still developing. Traditional academicians think that aerogel is a supercritical fluid-dried gel, while the gels with freeze drying, air drying, and ambient drying without large shrinkage are regarded as cryogel, xerogel and ambigel, respectively. The public may think the classifications are complex and prefer simple and identifiable definitions. Thus, the aerogel is defined as "a light, highly porous solid formed by replacement of liquid in a gel with a gas so that the resulting solid is the same size as the original" and "a solid material of extremely low density, produced by removing the liquid component from a conventional gel" by Merriam-Webster Dictionaries and Oxford Dictionaries, respectively. These definitions indicate a wet process the aerogel has undergone and a distinctive feature of ultralight. Similarly in the *Aerogel Handbook,* Pierre applied the initial idea of Kistler to define it as the "gels in which the liquid has been replaced by air, with very moderate shrinkage of the solid network" [3]. A longer definition in Hüsing's review (also in Ullmann's Encyclopedia of Industrial Chemistry) designates the aerogel as the "materials in which the typical structure of the pores and the network is largely maintained . . . while the pore liquid of a gel is replaced by air."

Recently, several studies have used the term *aerogel* to refer to the solid formed from a gel by nonsupercritical drying [4]. Thus, the academic community of aerogel science tends to approve the definition of the aerogels identified by the specific structure but not the preparation or drying method. IUPAC (international union of pure and applied chemistry) gave aerogel a definition of "gel comprised of a microporous solid in which the dispersed phase is a gas," seeming not to mention the forming or drying method [5]. However, the word *gel* refers to a wet sol-gel process. Indeed, most aerogels reported are derived from the wet gel via a sol-gel process. Some are not, however, For example, Gao's group developed a "sol-cryo" method to construct ultra-flyweight carbon aerogels by direct cryodesiccation of the aqueous, fluid solutions of carbon nanotubes (CNTs) and graphene oxide(GO) without undergoing the gelation process. That means the aerogel is not necessarily derived from a gel [6]. The other representative sample is that Aliev et al. developed a dry method (catalytic chemical vapor deposition) to prepare straight sidewalls of multi-walled nanotube forests and corresponding transparent carbon nanotube aerogel. The wet sol-gel process is not necessary to form an aerogel as well. Thus, in a broad sense, aerogel-related porous materials classified originally as xerogel or cryogel are gradually accepted as aerogels. Nowadays, aerogel is increasingly recognized as a matter with gel-like structure and unique characteristics, without considering the preparation or drying method.

Here, the definition of an aerogel in a broad sense should be regarded as *a state of matter whose structure is similar to the solid networks of a gel with gas or vacuum in-between* [2]. This definition ensures the aerogel in a high-vacuum environment could be still called "aerogel." Moreover, this definition does not emphasize the wet sol-gel process but focuses on the gel-like structure. According to IUPAC, *gel* means a "non-fluid colloidal network or polymer network that is expanded throughout its whole volume by a fluid." To induce the concept of gel-like structure could further avoid discussing the preparation process.

But it is not easy to describe the gel structure due to its complexity. In our opinion, as shown in Figure 1.1, a typical gel-like structure should have the following characteristics: (i) highly dispersed, coherent, and randomly distributed networks and pores that are expanded throughout its whole volume; (ii) hierarchical structure ranging from nanoscale primary structure (building blocks and pores) to its monolithic appearance; (iii) fractals in-between different hierarchies; (iv) normally composed of noncrystalline or nanocrystalline matter. Normal nanoporous powders with porosity could not be identified as the aerogel since they cannot be monolithic.

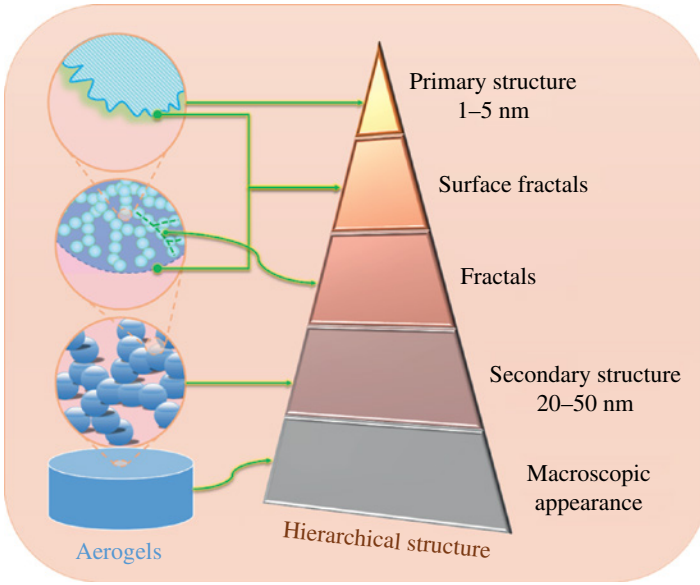


Figure 1.1 Typical gel-like structure of aerogels.

Traditional foams or cellular solids, even though their density is ultralow, cannot be recognized as aerogels probably due to the closed pores or large primary structure. Biology-derived porous materials with fine and hierarchical structure (like woods) could not be regarded as aerogels because of their relatively ordered structure and lack of microscopic fractal features. It is worth noting that fractals are emphasized because they are usually derived from multi-body random movements of the building blocks normally limited by diffusion or reaction. The forming process, named self-organized criticality by Bak, leads to a significantly complex structure, which may be extremely important for the unique properties or special behavior of the aerogel [7].

The gel-like structure leads to some property characteristics of aerogels, such as ultralow density, ultralow thermal conductivity, ultralow modulus, ultralow refractive index, ultralow dielectric constant, ultralow sound speed, high specific surface area and ultrawide adjustable ranges of physical properties. As one frequently mentioned characteristic, apparent density of the aerogel could be lower than air density. However, ultralow density is not a necessary feature, since many kinds of aerogels show relatively high density. Also, the aerogel could be, but not necessarily, formed as a monolith. The common forms of the aerogel include thin film, granule, powder, and sheet, for example.

The gel-like structure could be characterized by using different characterizations, among which nitrogen adsorption/desorption and small-angle X-ray scattering (SAXS) analysis are the most powerful tools in our opinion. By using BET (Brunner–Emmet–Teller), BJH (Barrett-Joyner-Halenda), DFT (Density Functional Theory), or FHH (Frenkel–Halsey–Hill) method to treat nitrogen adsorption/desorption results, we could statistically analyze the pore structure, getting abundant information including specific surface area, pore volume, average pore size, surface interaction, pore size distribution, micropore size distribution, surface fractal dimension, and so on [8]. The fractal types and fractal dimensions in different sizes, and characteristic lengths of hierarchical structure could be statistically obtained by analyzing the intensity-wave vector relationship of SAXS results [9–12].

1.1.2 Brief History and Evolution of the Aerogel Science

The history of the aerogel science was introduced in detail in our previous review [2]. Here we just make a brief introduction and update. As we know, aerogel was invented and named by Kistler in 1931. The roots of "aerogel" include *aero* and *gel,* which means the wet gel replaces the liquid inside with the air without damaging its solid microstructure [13]. Although a series of different aerogels were prepared, and some fascinating properties were shown, the following research was limited before the 1970s, probably because of complex and time-consumption preparation processes [14]. After that, in the period of the 1970s and 1980s, organic precursors developed by Teichner's group in 1968 and Russo et al. in 1986 simplified the preparation, leading to a fast development of aerogel science [15, 16]. At the same period, novel sol-gel methods and carbon dioxide supercritical fluid drying also promoted the development significantly [17]. The first and second international symposiums on aerogels (ISA) were held in 1985 and 1988, respectively. In the 1990s, the birth of organic and carbon aerogel and surface-modified ambient drying aroused broad interest from both academic and industrial communities [3, 18–20]. The third to sixth ISA continued to promote aerogel research, generating various ideas for potential applications that are still developing now. From the early twenty-first century to the present, many great achievements in aerogel science were realized. Numerous novel advances – including versatile sol-gel methods for preparing oxide aerogels, complex gradient aerogels, and ingeniously designed composite aerogels – have been developed and successfully applied in the fields of energy, environment, architecture, medicine, and aerospace [21–42]. Moreover, Brock et al. first prepared the chalcogenide aerogel via reverse micelle synthesis and supercritical fluid drying, arousing a broad interest in developing the single-component aerogels with novel composition [43–45]. After that, a series of novel aerogels, including CNT aerogel, graphene aerogel, carbide aerogel, diamond aerogel, single-element aerogels, hybrid aerogels, biomass aerogels, polymeric aerogels, and bio-inspired aerogels were added into the aerogel communities in succession [6, 41, 46–99]. In addition, the properties, applications, industrialization, and commercialization of the aerogel were widely developed in this period. Several series of academic conferences mainly concerning aerogels were held recently and produced many novel ideas.

As shown in Figure 1.2, there are 20,354 papers recorded in Science Citation Index (SCI, Web of Science WOS Core Collection) from 1975 to 2020, searching with the keyword "aerogel" or "aerogels" as the topic on October 14, 2020. The number of papers published increased sharply from 1975 to 2020. The one-year record in 2019 is 2459, higher than the total papers published during 1975–2001 (2287 in total for 27 years), showing that aerogel science has become a relatively hot topic.

Also, aerogel science becomes more and more interdisciplinary, affecting fundamental science to applied science. As shown in Figure 1.3, in the early period of 1975–1984, the top five fields include physics, instruments, nuclear science, chemistry, and electrochemistry. More than 70% of the papers belong to physics-related areas. But during 1985–1994, the proportion of physics-related areas decrease to less than one-half. Materials science and chemistry increases significantly, according to the data in Figure 1.3b. After that, the proportion of physics-related areas tends to decrease continuously, and the proportion of chemistry and materials science reaches about 50%. At the same time, engineering researches increase obviously to about one-fifth of the top five fields. To further analyze the interdisciplinarity, the "interdisciplinary index" is introduced by calculating the quotient of the total number of research areas divided by the article counts. As shown in Figure 1.4, the interdisciplinary index increased significantly from 2.18 in 1985–1994 to 4.33 from 2015 to 2020, which means that on average, each article covered 4.33 research areas during 2015–2020.

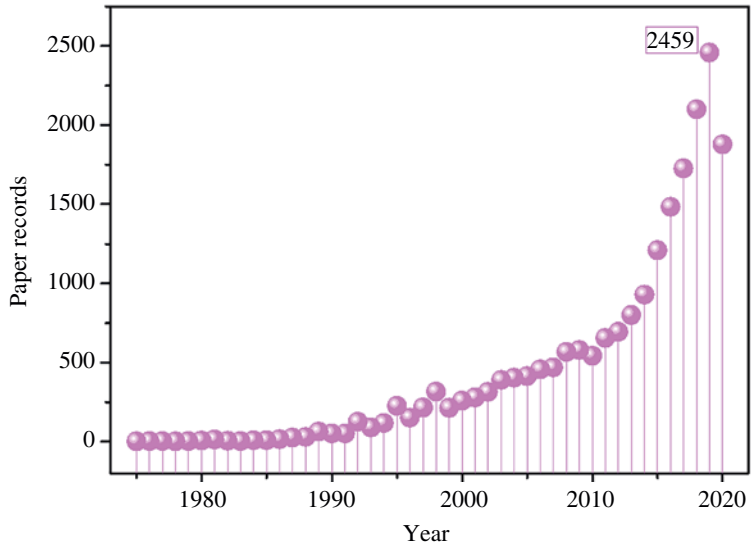


Figure 1.2 Papers recorded in Web of Science Core Collection from 1975 to 2020.

The *Journal of Non-Crystalline Solids, ACS Applied Materials & Interfaces, Journal of Sol-Gel Science and Technology, RSC Advances, Journal of Materials Chemistry A, Carbon, Chemical Engineering Journal, Nuclear Instruments Methods in Physics Research Section A, Microporous and Mesoporous Materials,* and *Chemistry of Materials* are the top 10 journals published aerogel-related articles. Interestingly, in the early period of 1985–1994, the top 5 journals include *Journal of Non-Crystalline Solids, Journal de Physique, Physical Review Letters, Physical Review B,* and *Journal of Sol-Gel Science and Technology,* in which the physics-related researches dominate. However, from 2018 to 2020, the top 5 journals changed to *ACS Applied Materials & Interfaces, Chemical Engineering Journal, Journal of Materials Chemistry A, Carbon and Carbohydrate Polymers,* in which the chemistry-related researches dominate. *Journal of Non-Crystalline Solids* ranks over 30 during 2018–2020, indicating a dramatic change in aerogel science. The average number of citations per paper is 26.6, according to the data from WOS core collection. High average citations and wide distribution of frequent journals indicate that aerogel research has gotten broad attention. More and more scientists, engineers, businesspeople, investors, government officers, and the public pay close attention to the aerogel field, which ensures a bright future of aerogel science.

1.2 The Physics Properties of the Aerogels

One of the most fascinating things of aerogels lies in their unique properties. According to incomplete statistics, there are more than 10 property records held by silica aerogels among solid state matter, including lowest reflective index, lowest sound speed, lowest modulus, lowest dielectric constant, and broadest adjustable range of several kinds of properties. Today the records may be refreshed by other materials, but most of them are other kinds of aerogels. Thus, aerogels are truly interesting materials, worth being regarded as a new state of matter [2].

Here we will briefly update the physics properties of the aerogels, including the mechanical, thermal, optical, electrical, and acoustic properties. We will focus on the discussion about why the

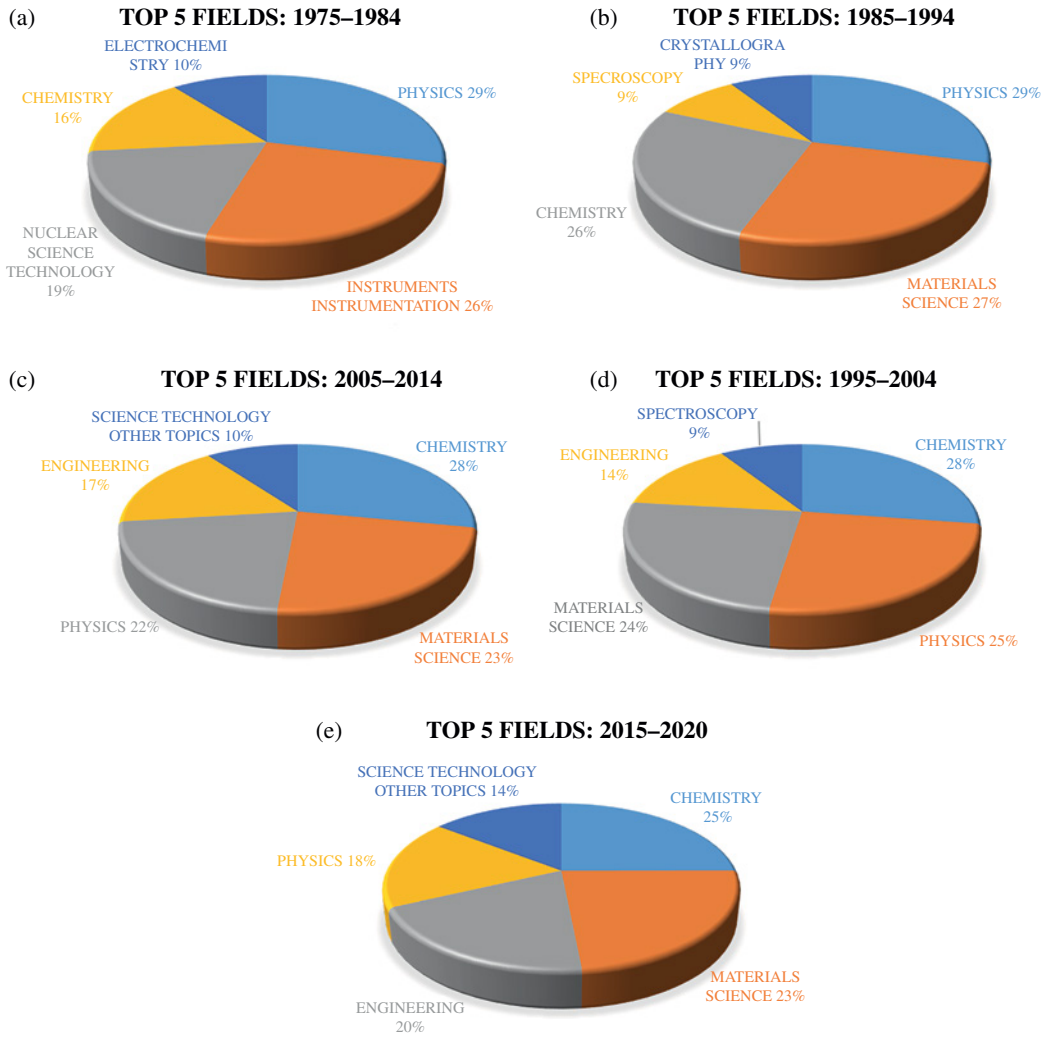


Figure 1.3 Top five field distributions during (a) 1975–1984, (b) 1985–1994, (c) 1995–2004, (d) 2005–2014, and (e) 2015–2020.

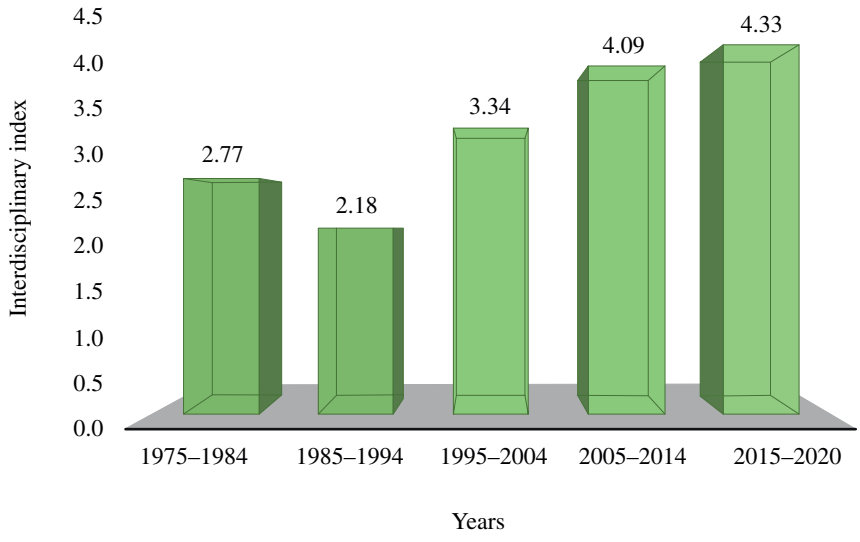


Figure 1.4 Interdisciplinary index of aerogel science during different periods.

different kinds of aerogels exhibit unique properties and attempt to clarify the relationship between the microstructure and properties. Since there are far too many studies about the different properties, only the most relevant works will be chosen for this chapter. Most of them relate to aerogels with a single component but not composites in order to give a simple physical picture and possible mechanism.

1.2.1 Mechanical Properties

Nanoporous structure is one of the characteristics of aerogels [3], and porosity over 90% gives the aerogel many unique characteristics. The first one is the extremely low density. The apparent density of silica aerogel can be as low as 1–3 $mg\,cm^{-3}$, which is close to the density of air [100]. It is possible to prepare aerogels with even lower density. Mecklenburg et al. prepared an aerogel-like materials called aerographite by depositing carbon on an adjustable ZnO template [101]. The metal Zn reduced by hydrogen gas evaporates and leaves an ultralight aerographite with the lowest density of 0.18 $mg\,cm^{-3}$. Gao's group even developed an all-carbon aerogel with the lowest density of 0.16 $mg\,cm^{-3}$ by directly freeze-drying aqueous solutions of CNTs and giant graphene oxide sheets [6]. The aerogel is currently the lowest-density solid, and its density can be normally determined by the ratio of reagents and the shrinkage ratio. The adjustable range of density and relative properties are quite broad, which could be designed in the ingenious gradient density aerogel [102]. Aerogels also have the properties of large specific surface area, good macroscopic uniformity, and strong doping adsorption capacity mainly due to its nanoscale structure and ultralow density.

However, the ultralow density leads to some characteristics, among which mechanical properties are unique. Normally, the aerogels are ultra-soft (low modulus) and extremely fragile, which may limit their applications. Thus, the mechanical properties of aerogels are of great concern. The mechanical performance could be evaluated from different aspects, such as tensile strength, bending strength, impact strength, and hardness. It is not hard to understand that these mechanical properties are closely related to the density of the aerogel. Due to the brittleness of the nanoporous structure and framework particles, the aerogel has low rigidity, high brittleness, and low tensile and compressive strength, and these mechanical properties are highly dependent on density. Studies have shown that there is a power function relationship between mechanical parameters such as Young's modulus, hardness, and the elastic parameters (EP) of silica aerogels, and density [103]. In one study, silica gels were produced by hydrolysis and polycondensation of tetramethoxysilane (TMOS) diluted in acetone in a one-step synthesis mode, and dried by supercritical drying method. Figure 1.5 shows that the low-density aerogels are more elastic, while the high-density aerogels are more rigid [104, 105]. In lower densities, within a range of 80–150 $kg\,m^{-3}$, the silica aerogels can withstand up to 70% of the compressive strain and restore to the original volume; at higher densities, they tend to break under small strains and exhibit glass-like behavior [106]. To understand the viscoelastic behavior of the aerogels, DMA/DMTA (dynamic mechanical analysis or dynamic mechanical thermal analysis) is one of the most commonly used methods. DMA/DMTA can be used to measure the storage modulus, loss modulus, and loss factor, which are three important factors of dynamic mechanical properties [107]. Tensile or compressive testing is another widely used method, by which the Young's modulus, tensile strength, and elongation at break can be measured.

There is a well-known scaling law between the modulus and density of silica aerogels. The exponent could be larger than 3, which means the modulus of the aerogels could be much lower than that of other porous materials or cellular solids [108, 109]. Brinker et al. mentioned that the ultrahigh modulus-density scaling exponents (~3.6) of the silica aerogels may be due to dangling

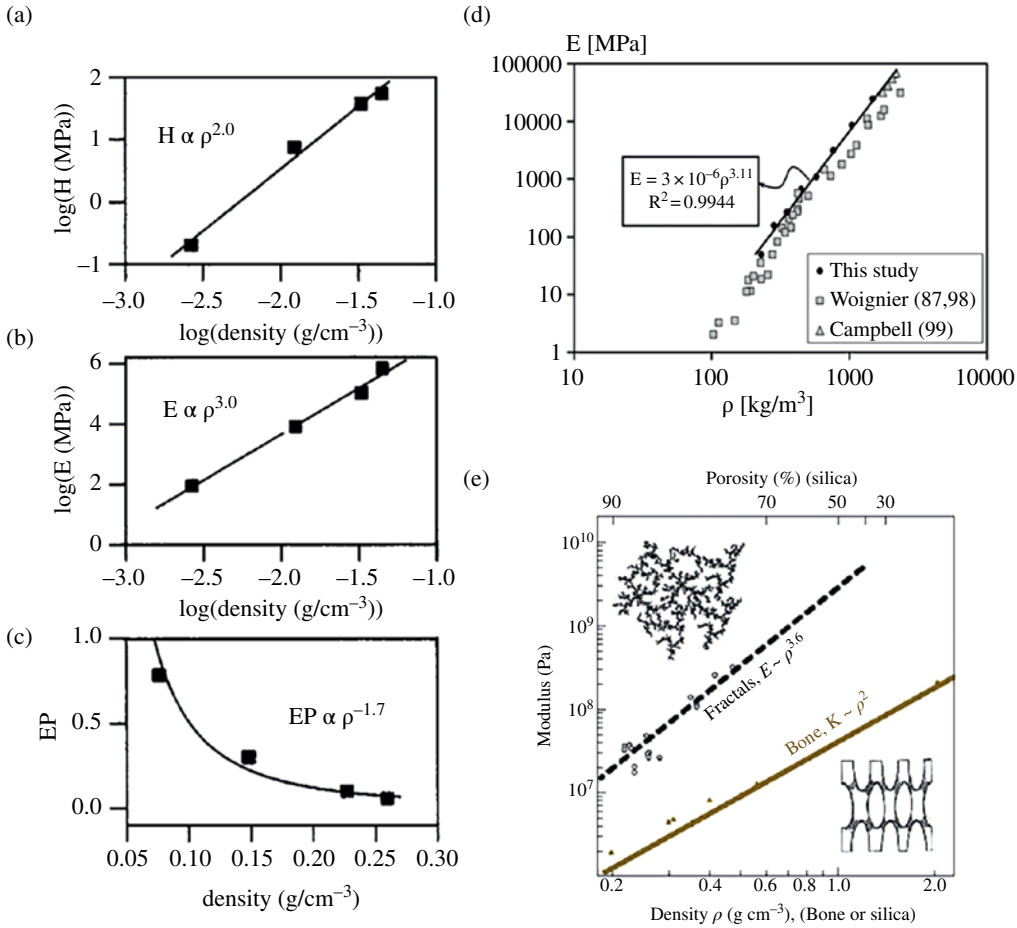


Figure 1.5 (a) Hardness, (b) Young's modulus, and (c) elastic parameters of the aerogel with different density [103] / with permission of AIP Publishing; (d) simulated elastic modulus vs. density for silica aerogels [106] / with permission of Elsevier; (e) modulus-density scaling relationships of highly porous gels and human bone [107] / With permission of Springer Nature.

skeletons without load bearing [105]. This explanation may be the best understanding about the ultralow modulus of the silica aerogel and ultralow sound speed from the statics. However, there must be a special mechanism of the scaling law, but not the other forms like linear or just positively related. Murillo et al. simulated the density-modulus relationship of the modeled silica aerogels and obtained the exponent larger than 3 (3.11) [104]. It was nice data, which approximately coincided with the experimental results. However, the study lacks enough evidence for structural similarity between the silica aerogels and the model samples formed through 3000 K thermal treatment and cooling down of β-cristobalite. There is still no study considering the microscopic mechanism of the scaling law.

Researchers have done fruitful works in enhancing the mechanical properties of aerogels. One commonly adopted method is to design fiber-enhanced doped aerogel composites [110]. The brittleness of the silica aerogel can be traced to the weak interparticle connecting zones. Therefore, it is reasonable to enhance the interparticle connection to improve the toughness of aerogels. In this respect, to bridge the nanoparticles could improve the mechanical properties and behaviors of

silica aerogels [111]. At present, the methods commonly used to enhance the mechanical properties of silica aerogels mainly include nano-additives enhancement and organics-inorganics hybrid enhancement.

For the first method, nano-scale fibers or fillers such as polymer nanofibers [112–115], nanocellulose [116–119], nanotubes [120, 121], inorganic nanofibers [122–124], graphene, and graphene oxide [125, 126] can significantly reinforce silica aerogels. The basic mechanism is shown in Figure 1.6. Representatively, Li et al. [113] prepared polyethylene oxide/polyurethane (PEO/PU) nanofiber reinforced polydimethylsiloxane/ethyl orthosilicate (PDMS/TEOS) hybrid silicon aerogel through electrospinning technology. The experimental results prove that the addition of an appropriate amount of PEO/PU nanofibers significantly improves the flexibility and toughness of the gel matrix, leading to a bendable composites aerogel film.

For the second method, in recent years, researchers have tried to introduce organic components into the inorganic framework of silica aerogels to form an inorganic-organic hybrid network, thereby improving the mechanical properties of aerogels substantially, as shown in Figure 1.7. Leventis et al. [127–129] used the surface reactive groups of silica aerogels to crosslink organic polymers. Native silica aerogels or amino-functionalized silica aerogels derived from aminopropyltriethoxysilane (APTES) are cross-linked with di-isocyanates, epoxies, or styrenes, leading to the enhanced mechanical properties (the compression modulus of the hybrid aerogels could be as

Figure 1.6 Schematic diagram of nanoadditives enhancement.

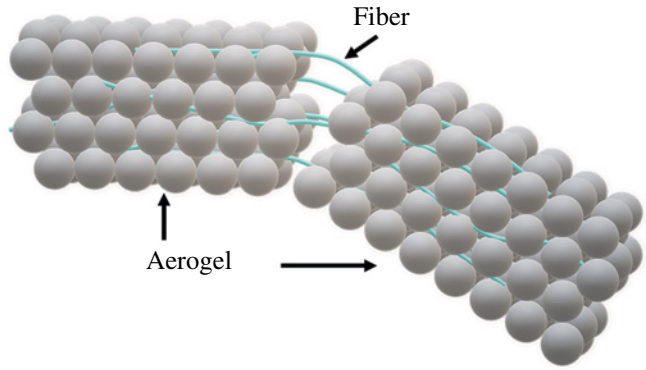
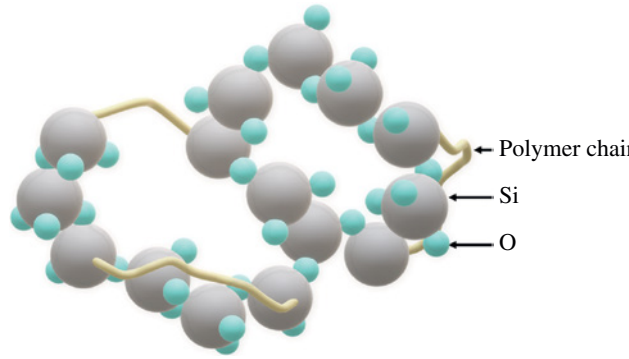


Figure 1.7 Schematic diagram of organics-inorganics hybrid enhancement.



Organics-inorganics hybrid enhancement

high as 129 MPa). Considering high-temperature stability, our group [130] prepared polyimide cross-linked silica aerogels by using polyamide acid and methyltrimethoxysilane (MTMS)-derived networks as the skeleton, and bis(trimethoxysilylpropyl) amine (BTMSPA) as the cross-linker. The hybrid aerogel presents relatively low density (lower than 180 mg cm^{-3}), high specific area (450–600 m^2 g^{-1}), and low shrinkage ratio (up to 20%). The other representative method is to use organotrialkoxysilanes or bis (trialkoxysilyl)-organometallic compounds, mainly developed by Nakanishi and Kanamori's group. In 2004, Kanamori et al. [131] used MTMS as the silicon source and methanol or ethanol as the solvent to prepare an elastic aerogel. And Kanamori et al. [132, 133] prepared elastic transparent aerogels by using MTMS as the silicon source, changing to water as the solvent, using the ammonia water produced by the slow decomposition of urea under heating as the alkaline catalyst, and using CO_2 supercritical drying. By this method, the aerogels show a drastic linear strain as large as 80% and subsequent almost perfect "spring-back." Similarly, Zu et al. [134] further prepared a transparent bulk aerogel by the acid-base two-step method and alcohol supercritical drying, which can return to 78% of the original after 60% compression, and rebound to 94% after heat treatment. Our group developed the method to prepare monolithic MTMS-derived aerogels with low density of 38 and 48 mg cm^{-3} via ethanol supercritical fluid drying and ambient drying, respectively [135, 136]. Interestingly, the ultralight aerogels showed excellent mechanical stability in the temperature of −150 to 300 °C and high transparency (81.3% at 550 nm). The group of Kanamori and Nakanishi further developed a series of novel methods including mixed organic silica resources and inorganic-organic (polymerization) hybrid to improve or adjust the mechanical properties [52, 131, 132].

In addition, polymeric coating layer on aerogels surface could improve the mechanical properties of aerogel. Leventis's group developed a route to polymer-crosslinked silica aerogel monoliths by introducing polymers like polyurethane or polystyrene into silica-based networks. The mechanical properties (modulus, breaking strength, etc.) of the reinforced aerogels could increase by up to several orders of magnitude [127, 129, 137]. Our group further found that the pore distribution of silica-based aerogel and "polymer-crosslinked" aerogel was similar, indicating that the polymer is likely to be coated thinly and homogeneously on the silica-based networks [138]. Smirnova's group [139] prepared spherical silica aerogel particles, and coated aerogel particles with different polymeric materials in a slit-shaped spouted fluidized bed with two horizontal gas inlets and adjustable gas supply. This technology provides a specific release mechanism of pharmaceuticals.

Although it is difficult for oxide-based aerogels to achieve good rigidity and toughness, carbon-based aerogels – including graphene-based aerogels (GAs) – exhibit good overall mechanical properties [140–144], due to their high-strength σ bonds [145]. For example, in the field of organic solvent adsorption, the high compression resilience of GAs can ensure that GAs have better impact resistance, and have better performance and regeneration capabilities when repeatedly squeezed to achieve recycling [142, 146]. When adsorbing gaseous pollutants, it can ensure the structural integrity of the material after repeated desorption and recovery.

In recent years, the research on enhancing the mechanical properties of GA has attracted widespread attention [147]. At present, Han [148], Severin [149], Guan [150] and others have studied the enhancement effect of polydimethylsiloxane (PDMS), boronic acids (SBS), and silane coupling agent (SCAs) on the mechanical properties of GAs. PDMS can coat the GAs framework with a layer of polymer to enhance the strength of the pore walls, and at the same time, it can produce chemical crosslinks between graphene sheets. The maximum stress can be increased to 7.7 kPa; Boric acid can form C–O–B covalent bonds between graphene sheets to strengthen the framework of GAs. The prepared aerogel has ultra-high elasticity (99%) and adjustable Poisson's ratio ($-0.30 < \nu < 0.46$), and the maximum stress is increased to 10 kPa. Different types of SCAs

can introduce different functional groups into the framework of GAs to functionalize them. The hydrolyzed SCAs can react with graphene oxide sheets to form C–O–Si covalent bonds to improve the connection strength between graphene sheets. In addition, some new methods for preparing GAs have appeared in recent years, and the prepared GAs have good mechanical properties. Zhu et al. [80] used 3D printing technology to prepare periodic graphene aerogel microlattices, and its Young's modulus has been improved by orders of magnitude. Jin et al. [151] innovatively proposed "liquid sodium-water interface reaction self-assembly" to prepare GAs. The resulting aerogel has vertical trihedral and other polyhedral pores, making it super elastic and thermally stable.

1.2.2 Thermal Properties

Scientists and engineers recognized early that this diaphanous substance, the aerogel, is a promising thermal insulation material [152]. In 1992, Fricke et al. [153] successfully prepared SiO_2 aerogel with a density of 120 kg m^{-3} and a thermal conductivity of 0.013 W m^{-1} K^{-1} at 300 K, and systematically studied its internal heat transfer mechanism by changing the density of SiO_2 aerogel and the concentration of doped infrared opacifiers.

Research on the thermal properties of aerogels has made considerable progress. The thermal property generally regarded as the most significant is their ultralow thermal conductivity, which is the reason that aerogel can play an important role in the field of heat insulation.

Fricke's group has made great contribution to understand the thermal conductivity of different aerogels. In most cases, the ultralow thermal conduction of aerogels is mainly contributed by heat conduction by solid, heat transfer within the gaseous phase, and radiative heat transfer. Aerogel is composed of nanoscale pores and particles, resulting in its extremely low thermal conductivity. The particles that can form the heat conduction path have very little connection, which greatly limits heat transfer. Similarly, because the pore size of the aerogel could be smaller than the mean free path of gas molecules colliding, its nanoporous structure inhibits gas heat conduction and convection. Also, the radiant heat conduction of aerogel near ambient temperature could be very low, probably due to its high scattering in the mid-infrared region (8–25 μm), while the extinction and ultimately the radiant heat conduction in the near infrared and mid infrared region could be easily increased by the addition of opacifiers with strong absorption or scattering [153].

1.2.2.1 Solid Conductivity

Solid conductivity is primarily reliant on the backbone structure and its chemical composition. The heat transfer process can be regarded as the propagation of phonons throughout the aerogel skeleton, which can be described in terms of the phonon diffusion model by Debye [154, 155]:

$$\lambda_0(T) = \frac{1}{3}\rho_0 C_V(T) l_{ph}(T) v_0(T) \tag{1.1}$$

In the formula: λ_0 represents the thermal conductivity of the aerogel skeleton, ρ_0 represents the skeleton density, C_V represents the specific heat capacity at constant volume, l_{ph} represents the mean free path of phonons, and v_0 represents the average velocity of elastic waves within the backbone. When the temperature is above 100 K, it is necessary to consider the influence of the aerogel morphology on its solid-state heat conduction, and introduce a geometric factor $G(\rho)$ [156] that depends on the skeleton density but is independent of temperature:

$$\lambda_s(T) = G(\rho)\lambda_0(T) \tag{1.2}$$

For porous systems such as aerogels, based on the phonon diffusion model, the geometric factor G can usually be obtained by measuring the apparent density and sound velocity of the aerogel material [157, 158], so Eq. (1.2) can be expressed as:

$$\lambda_s(T) = \lambda_0(T)\frac{\rho}{\rho_0}\cdot\frac{v}{v_0} \tag{1.3}$$

where ρ is the density of the porous media, ρ_0 is the density of the backbone material, v is the sound velocity of the porous media, v_0 is the sound velocity in the corresponding nonporous (backbone) material. For a specific system, $\lambda_0/(\rho_0 \cdot v_0)$ is a constant, and v is strongly related to the density of the skeleton [159]. Therefore, by reducing the density of the aerogel material, the solid phase heat transfer of the material can be well weakened, and the aerogel has ultrahigh porosity, which results in the heat transfer via solid backbone accounts for a small proportion. Furthermore, although lowering the density can reduce the heat transfer by the solid, it will also decrease the strength of the aerogel skeleton. Therefore, it is necessary to select the appropriate density and balance between the solid heat conduction and the strength of the skeleton.

1.2.2.2 Gaseous Conductivity

The gaseous conductivity in aerogel mainly includes gas-phase heat conduction and gas-phase heat convection.

The gaseous conductivity (λ_g) in aerogels is [155, 160]:

$$\lambda_g(p,T) = \frac{\Pi \cdot \lambda_{g,0}(T)}{1 + 2\cdot\alpha(T)\cdot Kn(T)} \tag{1.4}$$

where Π is the porosity of the aerogel, $\lambda_{g,0}(T)$ is the thermal conductivity of the non-convecting free gas, $\alpha(T)$ is a coefficient, related to the gas type and temperature, $Kn(T)$ is Knudsen number, which is the ratio of the mean free path of the gas molecules l_g and the effective pore dimension D [161]

$$Kn(T) = \frac{l_g}{D} \tag{1.5}$$

Equations (1.4) and (1.5) show that the pore size, through the effect of the Knudsen number, is a significant factor in reducing the gaseous contribution to conductivity. Small average pore sizes increase the Knudsen number and decrease the gaseous thermal conductivity. Low porosity also decreases the gaseous thermal conductivity. By controlling the formation and size of the interconnected particles or chains that make up the solid matrix, it is feasible to control the pore sizes and porosity [162]. However, small average pore sizes and low porosity will also increase the solid heat conduction. Therefore, reducing the pressure of the gas in the pores and reducing the probability of collisions between molecules is the more effective way to reduce the gaseous heat transfer of aerogels.

1.2.2.3 Radiative Heat Transfer

Radiation is a noncontact heat transfer method. It does not require any medium for propagation in aerogel materials and can be regarded as the interaction of photons and aerogel materials. The radiative part of the thermal conductivity in porous materials as given in Eq. (1.6) by Caps and Fricke [163] is:

$$\lambda_r(T) = \frac{16\cdot\sigma\cdot n^2\cdot T_r^3}{3\cdot e(T)\cdot(\rho'/\rho_s)} \tag{1.6}$$

where σ is the Stefan-Boltzmann constant ($\sigma = 5.67 \cdot 10^{-8}\,\mathrm{W \cdot m^{-2} \cdot K^{-4}}$), n is the index of refraction (which is in the case of the low-density aerogel close to 1), $e(T)$ is average extinction coefficient, and ρ' and ρ_s are the respective densities of the aerogel and the solid from which the aerogel is made.

The equation shows that the radiative heat transfer is proportional to the cube of the temperature, so the radiant heat transfer of the aerogel material will dominate in the high-temperature stage, and it will increase rapidly at the speed of the cube. The most common way to reduce the radiation heat transfer of aerogel materials is to introduce some opacifiers to increase the extinction coefficient of the system to reduce the radiation heat transfer. Such opacifiers mainly include carbon, silicon carbide, and titanium dioxide [164–166]. The introduction of opacifiers is mainly to increase the extinction coefficient of the material by increasing the absorption and re-scattering effects of the infrared radiation of the system. However, while increasing the extinction coefficient, the introduced infrared opacifiers may destroy the original three-dimensional nano-network structure of the material. As a result, the heat transfer between the solid phase and the gas phase increases. Therefore, in actual use, the type and content of doped sunscreen should be selected according to the actual use, to achieve the purpose of effectively improving the radiation heat transfer of the material.

1.2.3 Optical Properties

The optical properties of the aerogels depend on their compositions first. The aerogels composed of dielectrics without strong visible absorption (e.g. SiO_2-based aerogels) are normally transparent, while those with weak visible absorption (e.g. other oxide or resorcinol-formaldehyde [RF] aerogels) remain their original color. When the aerogels are composed of strong visible absorption like carbon, they are black. The microstructure strongly affects the optical properties, and even the interaction with the electromagnetic wave. In this section, we mainly discuss the optical properties of silica aerogels and carbon-based aerogels, representing for the typical aerogels without or with strong visible absorption, respectively.

The optical properties of silica aerogels vary with their preparation conditions, usually between transparent and translucent. The transparency and translucency appearances of aerogels are primarily due to Rayleigh scattering [167]. When light passes through the aerogel, the pores and silica particles will have a scattering effect. Compared with the wavelength of the visible spectra, the size of a single particle and pores is smaller, which meets the condition of Rayleigh scattering. Rayleigh scattering is inversely proportional to the fourth power of the wavelength, that is, the shorter the wavelength of the light, the more it scatters. Therefore, an aerogel appears light blue when placed against a dark background, and demonstrates yellowish when exposed to bright surroundings [168, 169]. Total scattering also includes surface scattering, which is due to scratch and crack in the surface [170]. On the other hand, the scattering efficiency is a function of the size of the scattering center. Therefore, different wavelengths will be scattered with different amplitudes [170]. And when the size of the scattering center becomes close to the wavelength of the incident light, an increase in scattering can be observed [171].

The transparency and reflectance can be measured by UV/VIS/NIR spectrometry or by means of an integration sphere [172, 173]. By solving the inverse problem of the 1-D Radiative Transfer Equation and measured transmittance and reflectance spectra (from 250 to 2500 nm), Zhao et al. evaluated the radiative properties of silica aerogels. The obtained radiative properties were found to be derived from the aerogel's microstructure, and can be used to predict the hemispherical transmittance and reflectance of silica aerogels [174].

Danilyuk et al. [175] found that monolithic aerogels prepared by a two-step sol-gel method are more transparent than those synthesized by a one-step method. Venkateswara Rao and Pajonk produced a monolithic durable hydrophobic silica aerogel with high direct light transmittance and low light diffusion by adding methyltrimethoxysilane (MTMS) as a co-precursor [176]. Woignier et al. [177] studied the function of TEOS consistency and adjunction of ammonia as a base catalysis on light transmission in the visible spectrum. When ammonia is added to the aerogel process, the transmittance in the visible light range will be greatly improved. Recently, in 2020, Du et al. [178] report a reaction spinning toward highly porous silica aerogel fibers, and the aggregation degree of the primary particles can be precisely controlled by pH-dependent hydrolyzation, and thus, the light transmittance of aerogel fiber can be controlled from 20% to 92%.

Although the measurement and adjustment of the optical properties of silica aerogels are frequently studied, the microscopic mechanism is rarely discussed. Which is the main scatterer of the Rayleigh scattering, primary particle or secondary particle (or pores)? Is the scattering coherent? What is the quantitative or semiquantitative relationship between the microstructure and optical properties? In one of our works, we found a way to continuously adjust the fractal dimension of silica aerogels and demonstrate that the visual light scattering is derived from incoherent Rayleigh scattering of secondary particles, while the size of primary particles and fractal dimension determine the refractive index of secondary particles [11]. Our group found that CA has super low visible light reflectance, and proved the black-body behavior was mainly a result of its randomly abundant subwavelength structures, which affect the electrons' behavior of CA when the electrons couple with the electromagnetic resonance of incident light and forcedly vibrate. And by adjusting the nanostructure of CAs, the reflectance could be decreased to approximately 0.19% [179].

The ultra-low refractive index is another significant optical property of silica aerogel, which makes it an important application in Cherenkov detector, which necessitates a medium with a refractive index close to one [180]. Glancing-angle-deposited nanowires, sponge-like block copolymers, and porous silica have been used to develop low-refractive index thin films. But in ultralow refractive index materials, the aerogels are currently the lowest [132].

1.2.4 Electrical Properties

The electrical properties are significant factors in application of aerogels for electronic devices and capacitors. Similar to the optical properties, the electrical properties mainly depend on the composition (dielectric properties) of the aerogels.

1.2.4.1 Dielectric Properties

Ultra-low dielectric constant is a significant property of silica aerogels, which is mainly due to their high porosity. The dielectric properties are dominated by the large fraction of gas trapped within aerogels, and it has been found that the dielectric properties of aerogels are linearly related to the density [181]. As the relative dielectric constants of air is 1.000585 at room temperature and pressure, the silica aerogels with greater than 99% porosity and density of $8\,g\,cm^{-3}$ have relative dielectric constants as low as 1.0008 [182]. And also, the organic aerogels have similar dielectric properties but have better performance in mechanical properties [183].

The low dielectric constants and loss tangents of aerogels, along with their controllable thermal expansion properties, make them promising materials as thin films in electronic devices, especially in integrated-circuit. And researchers have done much work to study the dielectric properties of aerogels. For example, Othman et al. [184] made porous polyimides by incorporation of tetraethyl orthosilicate into the polymer matrix and then acid etching. The relative dielectric constant

decreased with increasing porosity, and it was further reduced by the incorporation of hexafluoroisopropylidene groups in the polyimide backbone. Other studies [185, 186] also showed that the use of fluorinated monomers in a polyimide backbone can reduce the dielectric properties of aerogels. And Meador et al. [183] revealed that the change in dielectric due to density is the same with and without fluorine substitution. Meador et al. also developed the application of low dielectric polyimide aerogels as substrates for lightweight patch antennas [57].

1.2.4.2 Electrical Conductivity

Organic aerogels can be pyrolyzed in an inert atmosphere to give carbon aerogels in the form of monoliths, powders, microspheres, or thin film composites [19]. And the electrical properties of carbon aerogels are very different form silica aerogels and organic aerogels. Carbon aerogel is attractive as electrodes in capacitors due to its monolithic structure, high surface area, and electrical conductivity [187, 188]. The electrical conductivity of carbon aerogels is about $50\,S\,cm^{-1}$ and varied from the pyrolysis condition, and it was found that post heat-treatment of carbon aerogels in air atmosphere was very effective for improving the electrochemical properties of electrodes [189].

Another excellent property of carbon aerogels as electrodes is the high specific capacitance, and it can be well improved by hybrid. For example, Zhou et al. [190] prepared a hierarchical porous carbon aerogel composited with polymer polypyrrole (PPy), which shows a high specific capacitance of $387.6\,F\,g^{-1}$ ($0.5\,A\,g^{-1}$ in $1.0\,M\ H_2SO_4$).

Our group found a novel intrinsic negative TCR (temperature coefficient of resistance) of superblack carbon aerogel films. The negative TCR is derived from the surface oxygen-contained groups on the carbon networks, which exhibit an ultrabroad band response from UV to microwave [191].

1.2.4.3 Negative Permittivity and Negative Permeability

Recently, our group found an interesting behavior of carbon aerogels with negative permittivity and permeability in the radio frequency (about 600–1000 MHz) [192]. This is the first report about the double negative property of artificial random materials with single component. We believe that there should be structure similarity (like the split ring resonator in metamaterials) and size uniformity in the aerogels to some extent, although they have a random position and distribution. Thus, the basic nanoscale units could resonate in the same frequency, leading to a macroscopic resonance and a double negative property near the resonant frequency. In order to further avoid the influence of the different microstructure, the same original RF aerogels were carbonized partially into partly carbonized RF aerogels, carbon aerogels and partly graphitized carbon aerogels sequentially. Negative permittivity (epsilon-negative) property was achieved in carbon aerogels, and its value was adjusted continuously by changing the composition of carbon aerogels but keeping their microstructure unchanged [193]. These studies may provide fundamental materials and design for novel metamaterials.

1.2.5 Acoustic Properties

Aerogels present interesting acoustic properties. Monolithic silica aerogels are well known for their dramatically low sound velocity, down to $90\,m\,s^{-1}$ overhearing frequencies and even lower than $20\,m\,s^{-1}$ at the ultrasonic ranges [159, 194], when it is compared with the sound velocities of normal solid materials, for example, quartz glass ($5000\,m\,s^{-1}$) [195]. Gross et al. [194] noted that the lowest sound velocity could achieve to be $80\,m\,s^{-1}$ for nonevacuated silica aerogels with a density of approximately $20\,kg\,m^{-3}$. It was determined that variation of density follows a simple scaling law. Forest et al. [196] revealed that smaller granules of $80\,\mu m$ have a sound velocity of approximately 40–70 m s^{-1} in the frequency range of 500–2500 Hz.

The sound velocity is directly related to the density, elasticity, air pressure, temperature, and pore sizes. For aerogels with densities above 100 kg m^{-3}, sound propagation is mainly influenced by the elastic properties of the skeleton, which is influenced by density, temperature, and microstructure. It is the main parameter representing the sound velocity. While for the low-density aerogels with $\rho = 50\,\mathrm{kg\,m^{-3}}$, the trapped air becomes the main issue [197].

Aerogels also present good sound absorption and attenuation, which have a consistent dependence on pore size [198]. The attenuation increased linearly with frequency between 10 and 200 kHz in monolithic and granular silica aerogels [199]. And a remarkable absorption in difficult low frequency range (1–3 kHz) was found for granular silica aerogels [200]. In addition, aerogels have the lowest impedance of all solid materials because the product of density and sound velocity is the acoustic impedance, and both are very low. With these interesting acoustic properties, aerogels have found great use as acoustic insulators and have had applications in acoustic wave generation [130, 159, 201–203].

Since the aerogel has a deep-subwavelength nanoscale structure (very weak Rayleigh scattering) and ultralow solid content, it is of great interests to understand microscopically why the sound wave could slow down significantly. Brinker's group mentioned that the "not completely mechanically connected . . . dangling arms" inside the silica aerogels may lead to a low modulus compared with the other foams with the same density, and ultimately a slow sound propagation speed according to the Newton-Laplace equation for the sound speed [105]. Murillo et al. further demonstrated the ultralow modulus and ultra-high modulus-density scaling exponents (over 3) of the structure similar to the silica aerogels via molecular dynamics simulation [104]. We have found the ultraslow sound behavior in a nonresonant hybrid Cu-PAA (polyacrylic acid) meta-aerogel [204]. The lowest sound velocity reaches about 62 m s^{-1}, according to a physics model of hierarchical spring vibrator chains. The model has been deduced by static mechanics, equivalent circuit, analytical method, and simulation, showing a versality for microscopically understanding the slow sound behavior of different aerogels. Also, we have done a work to explain the low-speed behavior of silica aerogel by numerical simulation, and proposed a hybrid skeleton model with dangling branches, which exchanges the acoustic energy and induces the delay [205]. This work may help to understand the other slow wave behaviors and promote the application of aerogels in the area of meta-materials or metasurfaces.

1.3 Energy-Related Aerogel Applications

Energy-related aerogel uses are very hot topics. Lots of papers and reviews (also in the following chapters of this book) have explored potential applications. Thus, here we only briefly introduce the direction these studies are moving. Figure 1.8 shows representative energy-related applications of aerogels.

1.3.1 Applications in Energy Saving

The loss of the primary energy in producing low-temperature thermal energy for building heating, domestic water, and industrial process heat is a significant proportion in total energy consumption [206]. Therefore, thermal insulation is a vital part of energy saving. The nanoporous network structure of aerogel gives it extremely low thermal conductivity, and it has the best thermal insulation property among all solid materials. It can be widely used for thermal insulation of spacecrafts, skyscrapers, automobiles, electronic devices, clothing, submarine, petroleum transportation, metallurgy, chemical industry, and household appliances [35, 153, 207, 208].

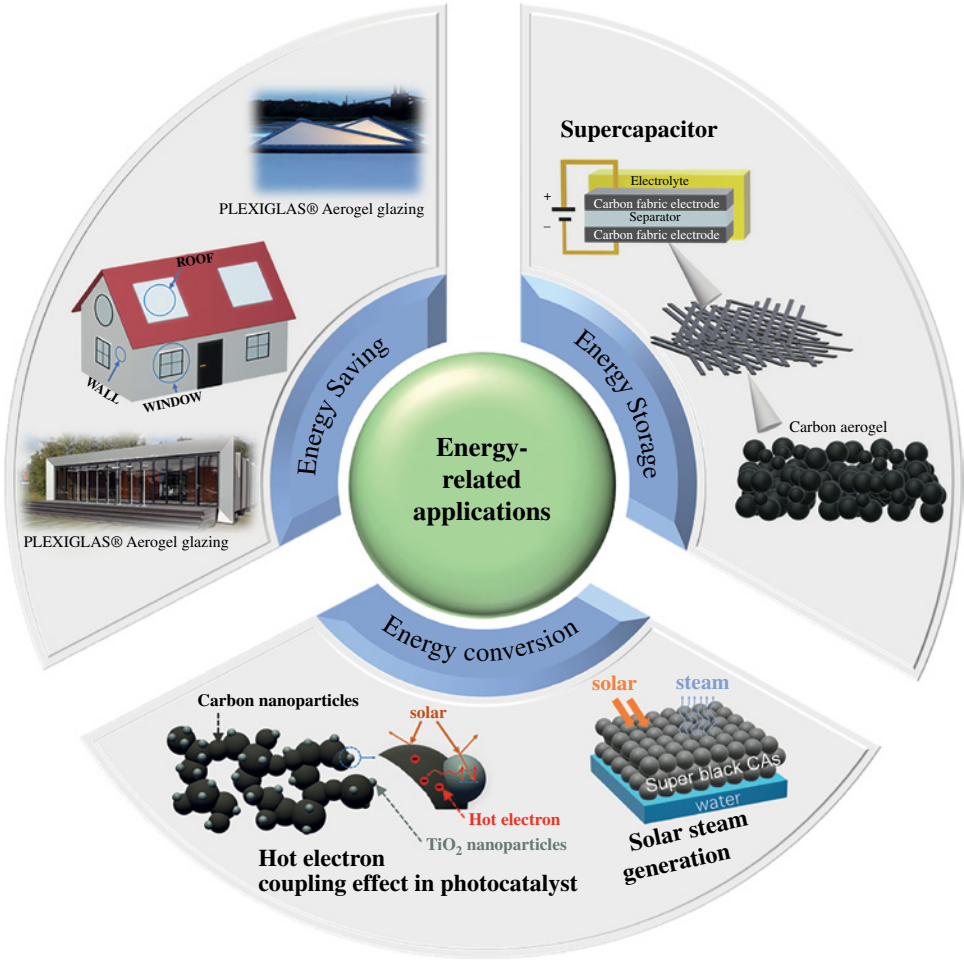


Figure 1.8 The energy-related applications.

SiO_2 aerogel and its composite materials are the earliest and relatively mature aerogels in the field of heat insulation. Kuhn et al. [209] studied the influence of the absorption and scattering properties of several opacifiers (TiO_2, ilmenite, Fe_3O_4, B_4C, Al_2O_3) on the extinction spectra of silica aerogel for different amounts of the opacifier in 1995, and demonstrated that doped SiO_2 aerogels are efficient high-temperature insulating materials. Zeng et al. [210] and Lu et al. [211] have investigated the efficiency of the opacification of silica aerogels with carbon blacks. In 1998, our group reported the preparation of the ceramic fiber-reinforced silica aerogel composites, which is regarded as the fundamental design of modern aerogel insulating materials [110]. And carbide aerogel is also a promising thermal insulation material due to its oxidation resistance. Currently, the most researched carbide aerogels mainly include titanium carbide, molybdenum carbide, and silicon carbide, concentrated for the most part on nanopowder [212, 213], nanowires [214], and porous ceramics [215]. Our group developed a low-temperature (all lower than 800 °C) conversion method to prepare various carbide-based aerogels (including SiC, TiC, NbC, et al.) [64, 92, 216].

One of the applications is aerogel felt, which has been commercialized to some extent. The aerogel felt has been applied in some important areas, such as architecture, spaceflight, and pipeline.

Vacuum insulation panel is one of the applications of aerogel felt, which could remarkably extend the service life [217]. And the aerogels' hydrophobicity allows the vacuum insolation panel with aerogel felt to be used for building insulation in humid areas [218].

Aerogels with high transparency and low thermal conductivity are very promising in the field of solar energy utilization. For example, Jesen et al. [219] injected silicon aerogel between the double-layer glass as transparent insulation, and the heat loss coefficient at the center was less than $0.7\,W\,m^2\,K^{-1}$, and the solar light transmittance was 76%.

1.3.2 Applications in Energy Conversion

Solar energy is one of the cleanest energy, with its abundant reserves and nonpollution [220]. Therefore, solar energy conversion technology has attracted unprecedented attention. Solar energy can be conserved and stored in different ways. Photo-thermal conversion is one popular method, with highest energy efficiency of solar–thermal conversion compared with other solar utilizations like photovoltaics and photocatalysis [221, 222]. And phase change materials (PCMs) have been recognized as ideal media [223].

The porous carbon-based aerogel as supporting material of PCM has attracted great attention, because it has high energy storage density and stable shape by using the porous carbon-based aerogels composite PCM, and the thermal conductivity of the composite PCM was low. For example, Fang et al. [224] prepared a form-stable PCM with graphene-based carbon aerogel (CA) for thermal energy storage. The results showed a thermal conductivity enhancement of 107.9% and 29.5% along the *x-y* and *z* directions, respectively, for a CA loading of nearly 2 wt%. In addition, the PCM had great form stability and a satisfactory latent heat capacity ($220\,kJ\,kg^{-1}$).

Solar steam generation through heat localization is a new approach to efficiently utilize solar energy, and nanocomposites with noble metals and other porous materials have been employed to generate solar vapor at a high light intensity. But now, ultra-black carbon aerogels with ultra-low reflection, ultra-high absorption, and no transmission have potential to take place them. For instance, inspired by pinecones, our group has designed ultra-black pinecone with multibranched, arterially porous, and hierarchical structures, which shows excellent solar steam generation performance under omnidirectional illumination [225].

Also, ultra-black CAs could markedly improve the photocatalysis efficiency of photocatalyst because of the strong hot electron coupling effect and high light absorption [226–228].

1.3.3 Applications in Energy Storage

Supercapacitors are also called electric double-layer capacitors or pseudocapacitors, in which energy is stored via separation of charges across a polarized electrode/electrolyte interface [229]. Compared with batteries and traditional capacitors, supercapacitors have higher capacitance, charging and discharging speed, and cycle life, which make them play an important role in meeting the demands of new energy storage devices and systems both now and in the future [230]. They are currently the research hotspots of new energy materials and devices. The energy storage method of a capacitor relies on a static method rather than a chemical reaction. It can be charged by providing a gradually changing voltage on the positive and negative electrodes.

Electrode material preparation is one of the key technologies for the development of supercapacitors. Among them, carbon materials are the earliest and most mature technology. They mainly include carbon aerogels, activated carbon powder, activated carbon fiber, carbon nanotubes, and so on. Carbon aerogel is one of the ideal materials as electrodes for supercapacitors due to their interconnected microstructure, high specific surface area, and high electrical conductivity [231, 232].

1.4 Prospects

As mentioned previously, aerogel science is booming. Many novel aerogels have entered the aerogel community and new smart designs for different applications have been developed. The scale production, industrialization, and commercialization of the aerogels bring them into our daily life. We think that the future of aerogel science may lie in the development of fundamental science, novel materials, new developing applications, and industrialization technology.

1.4.1 Fundamental Science of the Aerogels

Aerogel science is the foundation for the design, preparation, and application of the aerogels with advanced performances. Although understanding the interactions between aerogels and other matters has been promoted, many theoretical problems have not yet been fully solved.

In the aspect of mechanics and acoustics, Brinker et al. mentioned that the ultrahigh modulus-density scaling exponents (~3.6) of silica aerogels may be due to dangling skeletons without load bearing [105]. This explanation may be the best understanding about the ultralow modulus of the silica aerogel and ultralow sound speed from the statics. However, there must be a special mechanism of the scaling law, but not the other forms like linear or just positively related. Murillo et al. simulated the density-modulus relationship of the modeled silica aerogels and obtained an exponent larger than 3 [104]. It was a nice data, which approximately coincided with the experimental results. However, the study lacks enough evidence for structural similarity between the silica aerogels and the model samples formed through 3000 K thermal treatment and cooling down of β-cristobalite. Moreover, there is no study considering the microscopic mechanism. We think further study could focus on the forming method of simulated sample, the statistics of dangling skeleton proportion, and quantitative analysis of microscopic mechanics. This may provide an answer to the questions of why the modulus-density scaling exponents are very high and why the modulus of the silica aerogel is ultralow (ultra-soft) by comparison with the other kind of porous silica with the same density. Quantitative mechanism and the application for acoustic manipulation (like acoustic metamaterials or metasurfaces) would be studied in the near future.

Interestingly, traditional aerogels like silica aerogel are ultra-soft but fragile when bearing slightly uneven load. Unbelievably, these ultra-soft materials exhibit extremely good performance when they interact with hypervelocity particles. As mentioned previously, although the high-efficiency capturing performance is known as the combined contribution of fracture energy, inelastic collision, shock dissipation, and thermal loss, their affecting proportions and mechanism have not been quantitatively studied. Recently we have developed a method to deduce the impact processes of different hypervelocity particles and found a novel type of track (A-β) and its corresponding analysis method [233, 234]. Further quantitative researches are needed to determine why the aerogels could capture the hypervelocity particles efficiently. And aerogels with low thermal effect and low damage could be designed and used for high-efficiency capture of cosmic particles or even demonstrating the origins of water, organics, and life of Earth.

In the aspect of thermology, Fricke's group systematically studied the solid thermal conductivity of the aerogels and found an interesting puzzle that "if corrected for full density" the solid conductivity of the silica aerogels "are still more than one magnitude smaller than for massive silica glass" [235]. Fricke et al. considered that "this puzzle may be explained by the small sound velocity" according to the phonon diffusion model. Here we can see the importance of microscopically understanding the ultraslow sound propagation in the aerogels (it may even affect the thermal conductivity significantly).

In the aspect of optics, we know that the UV-Vis-NIR spectral could be explained by the incoherent Rayleigh scattering of secondary particles [11]. The primary particle size and mass fraction determine the refractive index of secondary particles. The superblack behavior of carbon-based aerogels may be derived from the small-size conductor effect (the electron–electron mean free path of a small-size conductor decreases sharply) via an indirect interaction among electromagnetic wave, electrons and conductor [179]. Many other interesting behaviors could be derived from this hypothesis [191, 226, 227, 236–238].

In the aspect of electrics, negative permittivity and negative permeability of the carbon aerogels are of great interest, as they may provide novel substrate or design for metamaterials [192]. The continuous adjustment of electromagnetic parameters is very important [193]. Thus, the microscopic mechanism and the interaction should be studied to clear the relationship between the microstructure (e.g. the shape and size of the resonant unit) and properties (including parameters and resonant frequency).

Thus, in our opinion, development of aerogel science mainly depends on the continuous control of the microstructure, as well as quantitative description of the complex microstructure and microscopic mechanism of the interactions.

1.4.2 Novel Aerogels

Aerogels with novel chemical composition or microstructure are always the most fascinating studies. That means a new category could join the constantly expanding aerogel community. Numerous aerogels with novel chemical composition include novel chalcogenide aerogels (Brock's group) [43–45, 239–241], carbon-based aerogels (Worsley's group and Gao's group) [6, 81, 88, 89, 242–245], metal aerogels (Eychmüller's group) [67, 69, 71, 72, 246–251], polymer-based aerogels (Leventis's group, Meador's group and Zhang's group) [11, 56, 57, 75, 183, 252–284], and hybrid polyorganosiloxanes aerogels (Nakanishi and Kanamori's group) [46, 48, 49, 52–54, 133, 203, 285–292]. Our group also developed the high-performance Al_2O_3-based aerogels [293, 294], single-element aerogels (Si, Ta, and Ti via a low-temperature magnesiothermic or alcohothermal reaction) [87, 91, 295, 296], and carbide aerogels (SiC, TiC and NbC) [64, 92, 216].

The novel design of the aerogel structure is important for high-performance or multifunctional applications. On one hand, 3D printing, especially for direct ink writing (DIW), is a facile way to design macroscopic structure. Worsley, Zhao, and Zhang et al. developed novel 3D-printed graphene-based or silica-based aerogels [79, 80, 297–300]. On the other hand, bio-inspired structure or function of various animals or plants is promoting the fast development of the modern materials science [99, 301–343]. Recently, our group developed several kinds of bioinspired (including polar bear hair, pinecone, monstera leaf, and viper scale) aerogel-related materials to advance the overall performance of the aerogels and the efficiency of the solar steam generation [63, 225, 237]. More kinds of 3D-printed and bio-inspired aerogels will further facilitate the development of aerogel science.

1.4.3 Novel Application and Industrialization Technology of the Aerogels

In the 1990s, many aerogel scientists proposed developing different insulation applications (including outer wall and daylighting) of the silica-based aerogels and electrical or electrochemical applications (including supercapacitor, lithium-ion battery, and seawater desalination) of carbon-based aerogels, which have a profound influence on the modern aerogel industry. Thus, the novel applications are of great importance to the future of aerogels. In our opinion, multifunctionalization

and functional conversion may be the route to new ideas [63, 191, 344]. Novel design of the aerogels could bring new insight into the application in health, energy, or environment [75, 225, 236, 237, 283, 345, 346].

Industrial applications benefit human beings directly. Smirnova (Hamburg University of Technology), Koeble (Swiss Federal Laboratories for Materials Science and Technology, EMPA), Steiner (Aerogel Technologies, LLC), and Shen's (Tongji University) groups are devoted to promoting the industrialization of the aerogels. Many companies – including Aspen, Cabot, Aerogel Technology, Nano High-Tech, BASF, Guangdong Alison Hi-Tech, Active Aerogels, Enersens, Jios Aerogel Corporation, IBIH New Materials, Guizhou Aerospace, UGOO Tech, Green Earth Aerogel Technologies – are exploring the insulation materials market. Many new scenarios have been developed, including power battery packages in electric vehicles, industry insulation, building insulation, and LNG (liquefied natural gas) tank insulation. We believe that the development of aerogel science and technology will create a bright future for our life.

References

1 Huang, K. (2014). *Solid State Physics: Rearranged Version*, 2e. Beijing: Peking University Press.
2 Du, A., Zhou, B., Zhang, Z.H., and Shen, J. (2013). A special material or a new state of matter: a review and reconsideration of the aerogel. *Materials* 6: 941–968.
3 Aegerter, M.A., Leventis, N., and Koebel, M.M. (2011). *Aerogels Handbook*. Springer Science & Business Media.
4 Vareda, J.P., Lamy-Mendes, A., and Duraes, L. (2018). A reconsideration on the definition of the term aerogel based on current drying trends. *Micropor. Mesopor. Mater.* 258: 211–216.
5 McNaught, A.D. and Wilkinson, A. (1997). *Compendium of Chemical Terminology*, vol. 1669. Blackwell Science Oxford.
6 Sun, H.Y., Xu, Z., and Gao, C. (2013). Multifunctional, ultra-flyweight, synergistically assembled carbon aerogels. *Adv. Mater.* 25: 2554–2560.
7 Bak, P. (2013). *How Nature Works: The Science of Self-Organized Criticality*. Springer Science & Business Media.
8 Du, A., Zhou, B., Xu, W. et al. (2013). Reaction-induced microsyneresis in oxide-based gels: the assembly of hierarchical microsphere networks. *Langmuir* 29: 11208–11216.
9 Fu, J.Y., Jiao, J.Q., Hao, S. et al. (2020). Fractal-in-a-sphere: confined self-assembly of fractal silica nanoparticles. *Chem. Mater.* 32: 341–347.
10 Wang, Y.X. et al. (2019). Diffusion of resveratrol in silica alcogels. *Molecules* 24.
11 Li, T.M., Du, A., Zhang, T. et al. (2018). Continuous adjustment of fractal dimension of silica aerogels. *J. Non-Cryst. Solids* 499: 159–166.
12 Li, T.M., Zhou, B., Du, A. et al. (2017). Microstructure control of the silica aerogels via pinhole drying. *J. Sol-Gel Sci. Technol.* 84: 96–103.
13 Kistler, S.S. (1931). Coherent expanded aerogels and jellies. *Nature* 127: 741–741.
14 Kistler, S.S. (2002). Coherent expanded-aerogels. *J. Phys. Chem.* 36: 52–64.
15 Russo, R.E. and Hunt, A.J. (1986). Comparison of ethyl versus methyl sol gels for silica aerogels using polar nephelometry. *J. Non-Cryst. Solids* 86: 219–230.
16 Nicolaon, G. and Teichner, S. (1968). On a new process of preparation of silica xerogels and aerogels and their textural properties. *Bull. Soc. Chim. Fr.* 5: 1900.
17 Tewari, P.H., Hunt, A.J., and Lofftus, K.D. (1985). Ambient-temperature supercritical drying of transparent silica aerogels. *Mater. Lett.* 3: 363–367.

18 Smith, D.M., Deshpande, R., and Brinke, C.J. (1992). Preparation of low-density aerogels at ambient pressure. *MRS Online Proc. Library Arch.* 271: 567–572.

19 Pekala, R.W. (1989). Organic aerogels from the polycondensation of resorcinol with formaldehyde. *J. Mater. Sci.* 24: 3221–3227.

20 Pekala, R.W. ((1989). *Low Density, Resorcinol-Formaldehyde Aerogels*. Livermore, CA: Lawrence Livermore National Lab (LLNL) No. US 4873218.

21 Chervin, C.N., Clapsaddle, B.J., Chiu, H.W. et al. (2005). Aerogel synthesis of yttria-stabilized zirconia by a non-alkoxide sol-gel route. *Chem. Mater.* 17: 3345–3351.

22 Gash, A.E., Satcher, J.H., and Simpson, R.L. (2003). Strong akaganeite aerogel monoliths using epoxides: synthesis and characterization. *Chem. Mater.* 15: 3268–3275.

23 Gash, A.E., Tillotson, T.M., Satcher, J.H. et al. (2001). New sol-gel synthetic route to transition and main-group metal oxide aerogels using inorganic salt precursors. *J. Non-Cryst. Solids* 285: 22–28.

24 Gash, A.E., Tillotson, T.M., Sather, J.H. Jr. et al. (2001). Use of epoxides in the sol-gel synthesis of porous iron(III) oxide monoliths from Fe(III) salts. *Chem. Mater.* 13: 999–1007.

25 Du, A., Zhou, B., Shen, J. et al. (2009). Monolithic copper oxide aerogel via dispersed inorganic sol-gel method. *J. Non-Cryst. Solids* 355: 175–181.

26 Du, A., Zhou, B., Zhong, Y.H. et al. (2011). Hierarchical microstructure and formative mechanism of low-density molybdena-based aerogel derived from $MoCl_5$. *J. Sol-Gel Sci. Technol.* 58: 225–231.

27 Gui, J.Y., Zhou, B., Zhong, Y.H. et al. (2011). Fabrication of gradient density SiO_2 aerogel. *J. Sol-Gel Sci. Technol.* 58: 470–475.

28 Shen, Y., Du, A., Li, X.G. et al. (2016). Preparation and optimization of aerogel flyer-plates with graded density. *Mater. Des.* 110: 225–232.

29 Du, A., Zhou, B., Shen, J. et al. (2011). A versatile sol-gel route to monolithic oxidic gels via polyacrylic acid template. *New J. Chem.* 35: 1096–1102.

30 Horz, F., Bastien, R., Borg, J. et al. (2006). Impact features on stardust: implications for comet 81P/wild 2 dust. *Science* 314: 1716–1719.

31 Tabata, M., Kawai, H., Yano, H. et al. (2016). Ultralow-density double-layer silica aerogel fabrication for the intact capture of cosmic dust in low-Earth orbits. *J. Sol-Gel Sci. Technol.* 77: 325–334.

32 Tsou, P. (1995). Silica aerogel captures cosmic dust intact. *J. Non-Cryst. Solids* 186: 415–427.

33 Baetens, R., Jelle, B.P., and Gustavsen, A. (2011). Aerogel insulation for building applications: a state-of-the-art review. *Energy Build.* 43: 761–769.

34 Barrios, E., Fox, D., Sip, Y.Y.L. et al. (2019). Nanomaterials in advanced, high-performance aerogel composites: a review. *Polymers-Basel* 11 (4): 726.

35 Cuce, E., Cuce, P.M., Wood, C.J., and Riffat, S.B. (2014). Toward aerogel based thermal superinsulation in buildings: a comprehensive review. *Renew. Sustain. Energy Rev.* 34: 273–299.

36 Cui, Y.Q. and Riffat, S. (2011). Review of latest developments in microporous aerogel for building applications. *Appl. Mech. Mater.* 71–78: 1967–1970.

37 Esquivel-Castro, T.A., Ibarra-Alonso, M.C., Oliva, J., and Martinez-Luevanos, A. (2019). Porous aerogel and core/shell nanoparticles for controlled drug delivery: a review. *Mater. Sci. Eng. C-Mater.* 96: 915–940.

38 Hu, L., He, R.J., Lei, H.S., and Fang, D.N. (2019). Carbon aerogel for insulation applications: a review. *Int. J. Thermophys.* 40: 1–25.

39 Karamikamkar, S., Naguib, H.E., and Park, C.B. (2020). Advances in precursor system for silica-based aerogel production toward improved mechanical properties, customized morphology, and multifunctionality: a review. *Adv. Colloid Interface* 276: 102101.

40 Lamy-Mendes, A., Silva, R.F., and Duraes, L. (2018). Advances in carbon nanostructure-silica aerogel composites: a review. *J. Mater. Chem. A* 6: 1340–1369.

41 Stergar, J. and Maver, U. (2016). Review of aerogel-based materials in biomedical applications. *J. Sol-Gel Sci. Technol.* 77: 738–752.

42 Wan, W.C., Zhang, R.Y., Ma, M.Z., and Zhou, Y. (2018). Monolithic aerogel photocatalysts: a review. *J. Mater. Chem. A* 6: 754–775.

43 Arachchige, I.U. and Brock, S.L. (2006). Sol-gel assembly of CdSe nanoparticles to form porous aerogel networks. *J. Am. Chem. Soc.* 128: 7964–7971.

44 Mohanan, J.L. and Brock, S.L. (2004). A new addition to the aerogel community: unsupported US aerogels with tunable optical properties. *J. Non-Cryst. Solids* 350: 1–8.

45 Mohanan, J.L., Arachchige, I.U., and Brock, S.L. (2005). Porous semiconductor chalcogenide aerogels. *Science* 307: 397–400.

46 Zu, G.Q., Kanamori, K., Wang, X.D. et al. (2020). Superelastic triple-network polyorganosiloxane-based aerogels as transparent thermal superinsulators and efficient separators. *Chem. Mater.* 32: 1595–1604.

47 Zu, G.Q., Kanamori, K., Nakanishi, K., and Huang, J. (2019). Superhydrophobic ultraflexible triple-network graphene/polyorganosiloxane aerogels for a high-performance multifunctional temperature/strain/pressure sensing array. *Chem. Mater.* 31: 6276–6285.

48 Zu, G.Q., Kanamori, K., Maeno, A. et al. (2018). Superflexible multifunctional polyvinylpolydimethylsiloxane-based aerogels as efficient absorbents, thermal superinsulators, and strain sensors. *Angew. Chem. Int. Ed.* 57: 9722–9727.

49 Shimizu, T., Kanamori, K., Maeno, A. et al. (2017). Transparent ethenylene-bridged polymethylsiloxane aerogels: mechanical flexibility and strength and availability for addition reaction. *Langmuir* 33: 4543–4550.

50 Nakanishi, Y., Hara, Y., Sakuma, W. et al. (2020). Colorless transparent melamine-formaldehyde aerogels for thermal insulation. *ACS Appl. Nano Mater.* 3: 49–54.

51 Kanamori, K., Ueoka, R., Kakegawa, T. et al. (2019). Hybrid silicone aerogels toward unusual flexibility, functionality, and extended applications. *J. Sol-Gel Sci. Technol.* 89: 166–175.

52 Kanamori, K. and Nakanishi, K. (2011). Controlled pore formation in organotrialkoxysilane-derived hybrids: from aerogels to hierarchically porous monoliths. *Chem. Soc. Rev.* 40: 754–770.

53 Kanamori, K., Aizawa, M., Nakanishi, K., and Hanada, T. (2007). New transparent methylsilsesquioxane aerogels and xerogels with improved mechanical properties. *Adv. Mater.* 19: 1589.

54 Aoki, Y., Shimizu, T., Kanamori, K. et al. (2017). Low-density, transparent aerogels and xerogels based on hexylene-bridged polysilsesquioxane with bendability. *J. Sol-Gel Sci. Technol.* 81: 42–51.

55 Guo, H.Q., Meador, M.A.B., McCorkle, L. et al. (2011). Polyimide aerogels cross-linked through amine functionalized polyoligomeric silsesquioxane. *ACS Appl. Mater. Interface* 3: 546–552.

56 Meador, M.A.B., Malow, E.J., Silva, R. et al. (2012). Mechanically strong, flexible polyimide aerogels cross-linked with aromatic triamine. *ACS Appl. Mater. Inter.* 4: 536–544.

57 Meador, M.A.B., Wright, S., Sandberg, A. et al. (2012). Low dielectric polyimide aerogels as substrates for lightweight patch antennas. *ACS Appl. Mater. Interface* 4: 6346–6353.

58 Druel, L., Bardl, R., Vorwerg, W., and Budtova, T. (2017). Starch aerogels: a member of the family of thermal superinsulating materials. *Biomacromolecules* 18: 4232–4239.

59 Garcia-Gonzalez, C.A., Jin, M., Gerth, J. et al. (2015). Polysaccharide-based aerogel microspheres for oral drug delivery. *Carbohydr. Polym.* 117: 797–806.

60 Ricci, A., Bernardi, L., Gioia, C. et al. (2010). Chitosan aerogel: a recyclable, heterogeneous organocatalyst for the asymmetric direct aldol reaction in water. *Chem. Commun.* 46: 6288–6290.

61 Nguyen, S.T., Feng, J., Le, N.T. et al. (2013). Cellulose aerogel from paper waste for crude oil spill cleaning. *Ind. Eng. Chem. Res.* 52: 18386–18391.

62 Jin, H., Nishiyama, Y., Wada, M., and Kuga, S. (2004). Nanofibrillar cellulose aerogels. *Colloid Surf. A* 240: 63–67.

63 Du, A., Wang, H.Q., Zhou, B. et al. (2018). Multifunctional silica nanotube aerogels inspired by polar bear hair for light management and thermal insulation. *Chem. Mater.* 30: 6849–6857.

64 Chen, K., Huang, X.W., Zhang, Z.X. et al. (2015). Low temperature pseudomorphic synthesis of nanocrystalline carbide aerogels for electrocatalysis. *J. Mater. Chem. A* 3: 11745–11749.

65 Li, G.Y., Zhu, M.Y., Gong, W.B. et al. (2019). Boron nitride aerogels with super-flexibility ranging from liquid nitrogen temperature to 1000 degrees C. *Adv. Funct. Mater.* 29: 1900188.

66 Fan, X.L., Zerebecki, S., Du, R. et al. (2020). Promoting the electrocatalytic performance of noble metal aerogels by ligand-directed modulation. *Angew. Chem. Int. Ed.* 132 (14): 5755–5760.

67 Jiang, B., Wan, Z., Kang, Y.Q. et al. (2021). Auto-programmed synthesis of metallic aerogels: Core-shell Cu@ Fe@ Ni aerogels for efficient oxygen evolution reaction. *Nano Energy.* 81: 105644.

68 Fan, X.L., Cai, B., Du, R. et al. (2019). Ligand-exchange-mediated fabrication of gold aerogels containing. Different Au(I) content with peroxidase-like behavior. *Chem. Mater.* 31: 10094–10099.

69 Du, R., Wang, J.Y., Wang, Y. et al. (2020). Unveiling reductant chemistry in fabricating noble metal aerogels for superior oxygen evolution and ethanol oxidation. *Nat. Commun.* 11: 1590.

70 Du, R., Joswing, J.O., Hübner, R. et al. (2020). Freeze-thaw-promoted fabrication of clean and hierarchically structured noble-metal aerogels for electrocatalysis and photoelectrocatalysis. *Angew. Chem. Int. Ed.* 59: 8370–8377.

71 Du, R., Hu, Y., Hübner, R. et al. (2019). Specific ion effects directed noble metal aerogels: versatile manipulation for electrocatalysis and beyond. *Sci. Adv.* 5.

72 Du, R., Fan, X.L., Jin, X.Y. et al. (2019). Emerging noble metal aerogels: state of the art and a look forward. *Matter* 1: 39–56.

73 Zhang, X.T., Sui, Z.Y., Xu, B. et al. (2011). Mechanically strong and highly conductive graphene aerogel and its use as electrodes for electrochemical power sources. *J. Mater. Chem.* 21: 6494–6497.

74 Meng, Q.H., Jin, Q., Wang, X.Y. et al. (2020). 3D Ti3C2Tx aerogel-modified separators for high-performance Li-S batteries. *J. Alloy Compd.* 816.

75 Lyu, J., Liu, Z.W., Wu, X.H. et al. (2019). Nanofibrous Kevlar aerogel films and their phase-change composites for highly efficient infrared stealth. *ACS Nano* 13: 2236–2245.

76 Liu, Z.W., Lyu, J., Fang, D., and Zhang, X.T. (2019). Nanofibrous Kevlar aerogel threads for thermal insulation in harsh environments. *ACS Nano* 13: 5703–5711.

77 Li, L., Zhang, M.Y., Zhang, X.T., and Zhang, Z.G. (2017). New Ti_3C_2 aerogel as promising negative electrode materials for asymmetric supercapacitors. *J. Power Sources* 364: 234–241.

78 Li, G.Y., Hong, G., Dong, D.P. et al. (2018). Multiresponsive graphene-aerogel-directed phase-change smart fibers. *Adv. Mater.* 30.

79 Cheng, Q.Q., Liu, Y., Lyu, J. et al. (2020). 3D printing-directed auxetic Kevlar aerogel architectures with multiple functionalization options. *J. Mater. Chem. A* 8: 14243–14253.

80 Zhu, C., Han, T.Y.J., Duoss, E.B. et al. (2015). Highly compressible 3D periodic graphene aerogel microlattices. *Nat. Commun.* 6.

81 Worsley, M.A., Pauzauskie, P.J., Olson, T.Y. et al. (2010). Synthesis of graphene aerogel with high electrical conductivity. *J. Am. Chem. Soc.* 132: 14067–14069.

82 Pauzauskie, P.J., Crowhurst, J.C., Worsley, M.A. et al. (2011). Synthesis and characterization of a nanocrystalline diamond aerogel. *Proc. Natl. Acad. Sci. U.S.A.* 108: 8550–8553.

83 Harley-Trochimczyk, A., Pham, T., Chang, J.Y. et al. (2016). Platinum nanoparticle loading of boron nitride aerogel and its use as a novel material for low-power catalytic gas sensing. *Adv. Funct. Mater.* 26: 433–439.

84 Chandrasekaran, S., Campbell, P.G., Baumann, T.F., and Worsley, M.A. (2017). Carbon aerogel evolution: allotrope, graphene-inspired, and 3D-printed aerogels. *J. Mater. Res.* 32: 4166–4185.

85 Liu, H.Z., Geng, B.Y., Chen, Y.F., and Wang, H.Y. (2017). Review on the aerogel-type oil sorbents derived from nanocellulose. *ACS Sustain. Chem. Eng.* 5: 49–66.

86 Ganesan, K., Budtova, T., Ratke, L. et al. (2018). Review on the production of polysaccharide aerogel particles. *Materials* 11.

87 Xu, W.W., Du, A., Xiong, J. et al. (2016). Freestanding titanium metallic aerogel. *Mater. Des.* 97: 93–97.

88 Xu, Z., Zhang, Y., Li, P.G., and Gao, C. (2012). Strong, conductive, lightweight, neat graphene aerogel fibers with aligned pores. *ACS Nano* 6: 7103–7113.

89 Xu, Z., Sun, H.Y., and Gao, C. (2013). Perspective: graphene aerogel goes to superelasticity and ultraflyweight. *Appl. Mater.* 1.

90 Aliev, A.E., Oh, J.Y., Kuznetsov, M.E. et al. (2009). Giant-stroke, superelastic carbon nanotube aerogel muscles. *Science* 323: 1575–1578.

91 Chen, K., Bao, Z.H., Shen, J. et al. (2012). Freestanding monolithic silicon aerogels. *J. Mater. Chem.* 22: 16196–16200.

92 Chen, K., Bao, Z.H., Du, A. et al. (2012). Synthesis of resorcinol-formaldehyde/silica composite aerogels and their low-temperature conversion to mesoporous silicon carbide. *Micropor. Mesopor. Mater.* 149: 16–24.

93 Zhan, H.J., Wu, K.J., Hu, Y.L. et al. (2019). Biomimetic carbon tube aerogel enables super-elasticity and thermal insulation. *Chem-US* 5: 1871–1882.

94 Zhan, H.J., Chen, J.F., Zhao, H.Y. et al. (2020). Biomimetic difunctional carbon-nanotube-based aerogels for efficient steam generation. *ACS Appl. Nano Mater.* 3: 4690–4698.

95 Zeng, X.L., Ye, L., Yu, S.H. et al. (2015). Facile preparation of superelastic and ultra low dielectric boron nitride nanosheet aerogels via freeze-casting process. *Chem. Mater.* 27: 5849–5855.

96 Wu, Z.Y., Liang, H.W., Hu, B.C., and Yu, S.H. (2018). Emerging carbon-nanofiber aerogels: chemosynthesis versus biosynthesis. *Angew. Chem. Int. Ed.* 57: 15646–15662.

97 Wu, Z.Y., Li, C., Liang, H.W. et al. (2013). Ultralight, flexible, and fire-resistant carbon nanofiber aerogels from bacterial cellulose. *Angew. Chem. Int. Ed.* 52: 2925–2929.

98 Li, S.C., Hu, B.C., Ding, Y.W. et al. (2018). Wood-derived ultrathin carbon nanofiber Aerogels. *Angew. Chem. Int. Ed.* 57: 7085–7090.

99 Zhao, N., Wang, Z., Cai, C. et al. (2014). Bioinspired materials: from low to high dimensional structure. *Adv. Mater.* 26: 6994–7017.

100 Kocon, L., Despetis, F., and Phalippou, J. (1998). Ultralow density silica aerogels by alcohol supercritical drying. *J. Non-Cryst. Solids* 225: 96–100.

101 Mecklenburg, M., Schuchardt, A., Mishra, Y.K. et al. (2012). Aerographite: ultra lightweight, flexible nanowall, carbon microtube material with outstanding mechanical performance. *Adv. Mater.* 24: 3486–3490.

102 Jones, S.M. (2007). A method for producing gradient density aerogel. *J. Sol-Gel Sci. Technol.* 44: 255–258.

103 Moner-Girona, M., Roig, A., Molins, E. et al. (1999). Micromechanical properties of silica aerogels. *Appl. Phys. Lett.* 75: 653–655.

104 Murillo, J.S.R., Bachlechner, M.E., Campo, F.A., and Barbero, E.J. (2010). Structure and mechanical properties of silica aerogels and xerogels modeled by molecular dynamics simulation. *J. Non-Cryst. Solids* 356: 1325–1331.

105 Fan, H.Y., Hartshorn, C., Tallant, T. et al. (2007). Modulus-density scaling behaviour and framework architecture of nanoporous self-assembled silicas. *Nat. Mater.* 6: 418–423.

106 Linhares, T., de Amorim, M.T.P., and Duraes, L. (2019). Silica aerogel composites with embedded fibres: a review on their preparation, properties and applications. *J. Mater. Chem. A* 7: 22768–22802.

107 Salimian, S., Zadhoush, A., Naeimirad, M. et al. (2018). A review on aerogel: 3D nanoporous structured fillers in polymer-based nanocomposites. *Polym. Compos.* 39: 3383–3408.

108 Woignier, T. and Phalippou, J. (1989). Scaling law variation of the mechanical-properties of silica aerogels. *J. Phys.-Paris* 50: C4179–C4184.

109 Gibson, L.J. and Ashby, M.F. (1999). *Cellular Solids: Structure and Properties*. Cambridge University Press.

110 Deng, Z.S., Wang, J., Wu, A.M. et al. (1998). High strength SiO_2 aerogel insulation. *J. Non-Cryst. Solids* 225: 101–104.

111 Nicholas, L. (2007). Three-dimensional core-shell superstructures: mechanically strong aerogels. *Acc. Chem. Res.* 40 (9): 874–884.

112 Chen, Q., Chen, Y., Wu, H.J., and Zhou, X.Q. (2015). Preparation and characterisation of aerogel composites reinforced with electrospun nanofibre. *Mater. Res. Innovations* 19 (sup2): S2–S185.

113 Li, L., Yalcin, B., Nguyen, B.N. et al. (2009). Flexible nanofiber-reinforced aerogel (xerogel) synthesis, manufacture, and characterization. *ACS Appl. Mater. Interface* 1: 2491.

114 Wu, H., Chen, Y., Chen, Q. et al. (2013). Synthesis of flexible aerogel composites reinforced with electrospun nanofibers and microparticles for thermal insulation. *Journal of Nanomaterials* 2013: 10.

115 Wu, H.J., Liao, Y.D., Ding, Y.F. et al. (2014). Engineering thermal and mechanical properties of multilayer aligned fiber-reinforced aerogel composites. *Heat Transfer Engineering* 35: 11–12.

116 Li, M., Jiang, H., Xu, D., and Yang, Y. (2017). A facile method to prepare cellulose whiskers–silica aerogel composites. *J. Sol-Gel Sci. Technol.* 83: 72–80.

117 Kim, C.Y., Lee, J.K., and Kim, B.I. (2008). Synthesis and pore analysis of aerogel–glass fiber composites by ambient drying method. *Colloids Surf. A Physicochem. Eng. Aspects* 313: 179–182.

118 Wong, J.C.H., Kaymak, H., Tingaut, H. et al. (2015). Mechanical and thermal properties of nanofibrillated cellulose reinforced silica aerogel composites. *Micropor. Mesopor. Mater.* 217: 150–158.

119 A.D., G.R., A.R., and T.B. (2014). Cellulose-silica composite aerogels from "one-pot" synthesis. *Cellulose* 21: 2625–2636.

120 A.S., Bar, G., Goldbart, O. et al. (2015). Reinforcing silica aerogels with tungsten disulfide nanotubes. *J. Supercrit. Fluids* 106: 9–15.

121 Liu, H., Chu, P., Li, H. et al. (2016). Novel three-dimensional halloysite nanotubes/silica composite aerogels with enhanced mechanical strength and low thermal conductivity prepared at ambient pressure. *J. Sol Gel Sci. Technol.* 80: 651–659.

122 losarczyk, A. (2017). Synthesis and characterization of silica aerogel-based nanocomposites with carbon fibers and carbon nanotubes in hybrid system. *Journal of Sol Gel Part. Sci. Technol.* 84: 16–22.

123 Wei, T.Y., Lu, S.Y., and Chang, Y.C. (2009). A new class of opacified monolithic aerogels of ultralow high-temperature thermal conductivities. *J. Phys. Chem. C* 113: 7424–7428.

124 Tang, X., Sun, A.H., Chu, C.Y. et al. (2017). A novel silica nanowire-silica composite aerogels dried at ambient pressure. *Mater. Des.* 115: 415–421.

125 Zhang, H., Fang, W., Li, Z., and Tao, W. (2015). The influence of gaseous heat conduction to the effective thermal conductivity of nano-porous materials. *Int. Commun. Heat Mass Transfer* 68: 158–161.

126 Lei, Y., Hu, Z., Cao, B. et al. (2016). Enhancements of thermal insulation and mechanical property of silica aerogel monoliths by mixing graphere oxide. *Mater. Chem. Phys.* 187: 183–190.

127 Ilhan, F., Fabrizio, E.F., McCorkle, L. et al. (2006). Hydrophobic monolithic aerogels by nanocasting polystyrene on amine-modified silica. *J. Mater. Chem.* 16: 3046–3054.

128 Meador, M., Fabrizio, E., llhan, F. et al. (2005). Cross-linking Amine-Modified Silica Aerogels with Epoxies: Mechanically Strong Lightweight Porous Materials. *Chem. Mater.* 17 (5): 1085–1098.

129 Leventis, N., Sotiriou-Leventis, C., Zhang, G., and Rawashdeh, A.-M.M. (2002). Nanoengineering strong silica aerogels. *Nano Lett.* 2: 957–960.

130 Yan, P., Zhou, B., and Du, A. (2014). Synthesis of polyimide cross-linked silica aerogels with good acoustic performance. *RSC Adv.* 4: 58252–58259.

131 Kanamori, K., Yonezawa, H., Nakanishi, K. et al. (2004). Structural formation of hybrid siloxane-based polymer monolith in confined spaces. *J. Sep. Sci.* 27: 874–886.

132 Kanamori, K., Aizawa, M., Nakanishi, K., and Hanada, T. (2007). New transparent methylsilsesquioxane aerogels and xerogels with improved mechanical properties. *Adv. Mater.* 19: 1589–1593.

133 Kanamori, K., Aizawa, M., Nakanishi, K., and Hanada, T. (2008). Elastic organic–inorganic hybrid aerogels and xerogels. *J. Sol-Gel Sci. Technol.* 48: 172–181.

134 Zhu, G.Q., Shen, J., Zhou, L.P. et al. (2014). Preparation of elastic airgel and its mechanical and thermal properties. *Journal of Inorganic Material* 29 (4): 417–422.

135 Li, T.M., Du, A., Zhang, T. et al. (2018). Efficient preparation of crack-free, low-density and transparent polymethylsilsesquioxane aerogels via ambient pressure drying and surface modification. *RSC Adv.* 8: 17967–17975.

136 Li, Y.N., Du, A., Shen, J. et al. (2018). Temperature dependence of dynamic mechanical behaviors in low density MTMS-derived silica aerogel. *J. Porous Mater.* 25: 1229–1235.

137 Zhang, G.H., Dass, A., Rawashdeh, A.M. et al. (2004). Isocyanate-crosslinked silica aerogel monoliths: preparation and characterization. *J. Non-Cryst. Solids* 350: 152–164.

138 Peng, Y., Zhou, B., Du, A., and Li, C.H. (2014). Isocyanate-crosslinked silica aerogel monoliths: preparation and characterization. *Atomic Energy Science and Technology* 48 (6): 1100–1105.

139 Alnaief, M., Antonyuk, S., Hentzschel, C.M. et al. (2012). A novel process for coating of silica aerogel microspheres for controlled drug release applications. *Micropor. Mesopor. Mater.* 160: 167–173.

140 Li, C.W., Qiu, L., Zhang, B.Q. et al. (2016). Robust vacuum−/air-dried graphene aerogels and fast recoverable shape-memory hybrid foams. *Adv. Mater.* 28: 1510–1516.

141 Lu, H., Li, C.W., Zhang, B.Q. et al. (2016). Toward highly compressible graphene aerogels of enhanced mechanical performance with polymer. *RSC Adv.* 6: 43007–43015.

142 Worsley, M.A., Kucheyev, S.O., Mason, H.E. et al. (2012). Mechanically robust 3D graphene macroassembly with high surface area. *Chem. Commun.* 48: 8428–8430.

143 Han, Z., Tang, Z.H., Shen, S.L. et al. (2014). Strengthening of graphene aerogels with tunable density and high adsorption capacity towards Pb^{2+}. *Sci. Rep.-UK* 4.

144 Wu, Y.P., Yi, N.B., Huang, L. et al. (2015). Three-dimensionally bonded spongy graphene material with super compressive elasticity and near-zero Poisson's ratio. *Nat. Commun.* 6.

145 Frank, I.W., Tanenbaum, D.M., Van der Zande, A.M., and McEuen, P.L. (2007). Mechanical properties of suspended graphene sheets. *J. Vac. Sci. Technol., B* 25: 2558–2561.

146 Ye, S.B., Feng, J.C., and Wu, P.Y. (2013). Highly elastic graphene oxide-epoxy composite aerogels via simple freeze-drying and subsequent routine curing. *J. Mater. Chem. A* 1: 3495–3502.

147 Qiu, L., Liu, D.Y., Wang, Y.F. et al. (2014). Mechanically robust, electrically conductive and stimuli-responsive binary network hydrogels enabled by superelastic graphene aerogels. *Adv. Mater.* 26: 3333-+.

148 Hu, H., Zhao, Z.B., Wan, W.B. et al. (2014). Polymer/graphene hybrid aerogel with high compressibility, conductivity, and "sticky" superhydrophobicity. *ACS Appl. Mater. Interface* 6: 3242–3249.

149 Severin, K. (2009). Boronic acids as building blocks for molecular nanostructures and polymeric materials. *Dalton Trans.* 5254–5264.

150 Guan, L.Z., Gao, J.F., Pei, Y.B. et al. (2016). Silane bonded graphene aerogels with tunable functionality and reversible compressibility. *Carbon* 107: 573–582.

151 Jin, H.L., Bu, Y.F., Li, J. et al. (2018). Strong graphene 3D assemblies with high elastic recovery and hardness. *Adv. Mater.* 30.

152 White, J. (1939). Silica aerogel effect of variables on its thermal conductivity. *Ind. Eng. Chem.* 31: 827–831.

153 Fricke, J., Lu, X., Wang, P. et al. (1992). Optimization of monolithic silica aerogel insulants. *Int. J. Heat Mass Transfer* 35: 2305–2309.

154 Planck, M. (1914). Vorträge über die kinetische theorie der materie und der elektrizität, gehalten in Göttingen auf einladung der Kommission der Wolfskehlstiftung. In: *Mathematische vorlesungen an der Universität Göttingen*, iv. Leipzig, Berlin: B.G. Teubner, 196 p.

155 Ebert, H.-P. (2011). *Aerogels Handbook*, 537–564. Springer.

156 Scheuerpflug, P., Morper, H.J., Neubert, G., and Fricke, J. (1991). Low-temperature thermal transport in silica aerogels. *J. Phys. D: Appl. Phys.* 24: 1395–1403.

157 Nilsson, O., Rueschenpoehler, G., Gross, J., and Fricke, J. (1989). Correlation between thermal conductivity and elasto-mechanical properties of compressed porous media. *High Temp. High Press.* 21: 267–274.

158 Lee, O.J., Lee, K.H., Yim, T.J. et al. (2002). Determination of mesopore size of aerogels from thermal conductivity measurements. *J. Non-Cryst. Solids* 298: 287–292.

159 Gross, J. and Fricke, J. (1992). Ultrasonic velocity measurements in silica, carbon and organic aerogels. *J. Non-Cryst. Solids* 145: 217–222.

160 Kaganer, M.G. (1969). Thermal Insulation in Cryogenic Engineering. Israel program for scientific translations.

161 Kaviany, M. (2012). *Principles of Heat Transfer in Porous Media*. Springer Science & Business Media.

162 Tillotson, T. and Hrubesh, L. (1992). Transparent ultralow-density silica aerogels prepared by a two-step sol-gel process. *J. Non-Cryst. Solids* 145: 44–50.

163 Caps, R. and Fricke, J. (1986). Infrared radiative heat transfer in highly transparent silica aerogel. *Sol. Energy* 36: 361–364.

164 Lee, D., Stevens, P.C., Zeng, S.Q., and Hunt, A.J. (1995). Thermal characterization of carbon-opacified silica aerogels. *J. Non-Cryst. Solids* 186: 285–290.

165 Zhang, H.-X., He, X.-D., and He, F. (2009). Microstructural characterization and properties of ambient-dried SiO_2 matrix aerogel doped with opacified TiO_2 powder. *J. Alloy Compd.* 469: 366–369.

166 Jinpeng, F. (2009). Nano silica porous thermal insulating material with SiC as infrared opacifier. *Aerosp. Mater. Technol.* 39: 38–41.

167 Fricke, J. and Tillotson, T. (1997). Aerogels: production, characterization, and applications. *Thin Solid Films* 297: 212–223.

168 Cao, W. and Hunt, A.J. (1994). Improving the visible transparency of silica aerogels. *J. Non-Cryst. Solids* 176: 18–25.

169 Wang, P., Körner, W., Emmerling, A. et al. (1992). Optical investigations of silica aerogels. *J. Non-Cryst. Solids* 145: 141–145.

170 Emmerling, A., Petricevic, R., Beck, A. et al. (1995). Relationship between optical transparency and nanostructural features of silica aerogels. *J. Non-Cryst. Solids* 185: 240–248.

171 Reim, M., Reichenauer, G., Körner, W. et al. (2004). Silica-aerogel granulate–structural, optical and thermal properties. *J. Non-Cryst. Solids* 350: 358–363.

172 Zhu, Q., Li, Y., and Qiu, Z. (2007). *Research Progress on Aerogels as Transparent Insulation Materials*. Berlin Heidelberg: Springer.

173 Zhu, Q., Duan, R., and Li, Y. (2007). *ASME/JSME Thermal Engineering Heat Transfer Summer Conference Collocated with the ASME Interpack Conference*. Vancouver, British Columbia, Canada: ASME.

174 Zhao, L., Yang, S., Bhatia, B. et al. (2016). Modeling silica aerogel optical performance by determining its radiative properties. *AIP Adv.* 6: 025123.

175 Danilyuk, A., Kravchenko, E., Okunev, A. et al. (1999). Synthesis of aerogel tiles with high light scattering length. *Nucl. Instrum. Methods Phys. Res., Sect. A* 433: 406–407.

176 Rao, A.V. and Pajonk, G. (2001). Effect of methyltrimethoxysilane as a co-precursor on the optical properties of silica aerogels. *J. Non-Cryst. Solids* 285: 202–209.

177 Woignier, T., Duffours, L., Colombel, P., and Durin, C. (2013). Aerogels materials as space debris collectors. *Adv. Mater. Sci. Eng.* 2013.

178 Du, Y., Zhang, X.H., Wang, J. et al. (2020). Reaction-spun transparent silica aerogel fibers. *ACS Nano* 14: 11919–11928.

179 Sun, W., Du, A., Feng, Y. et al. (2016). Super black material from low-density carbon aerogels with subwavelength structures. *ACS Nano* 10: 9123–9128.

180 Sumiyoshi, T., Adachi, I., Enomoto, R. et al. (1998). Silica aerogels in high energy physics. *J. Non-Cryst. Solids* 225: 369–374.

181 Hrubesh, L.W. and Pekala, R.W. (1994). *Sol-Gel Processing and Applications* (ed. Y.A. Attia), 363–367. Boston, MA: Springer US.

182 Hrubesh, L.W., Keene, L.E., and Latorre, V.R. (1993). Dielectric properties of aerogels. *J. Mater. Res.* 8: 1736–1741.

183 Meador, M.A.B., McMillon, E., Sandberg, A. et al. (2014). Dielectric and other properties of polyimide aerogels containing fluorinated blocks. *ACS Appl. Mater. Interface* 6: 6062–6068.

184 Othman, M.B.H., Ming, N.A.S., Akil, H.M., and Ahmad, Z. (2011). Dependence of the dielectric constant on the fluorine content and porosity of polyimides. *J. Appl. Polym. Sci.* 121: 3192–3200.

185 Ronova, I.A., Bruma, M., and Schmidt, H.-W. (2012). Conformational rigidity and dielectric properties of polyimides. *Struct. Chem.* 23: 219–226.

186 Simpson, J.O. and St, A.K. (1997). Clair, fundamental insight on developing low dielectric constant polyimides. *Thin Solid Films* 308–309: 480–485.

187 Takamura, T. (1995). Materials for electrochemical energy storage and conversion – batteries, capacitors, and fuel cells. Symposium held April 17–19, San Francisco, CA. *Mat. Res. Soc. Symp. Proc* (393).

188 Farmer, J.C., Fix, D.V., Mack, G.V. et al. (1996). Capacitive deionization of NH_4ClO_4 solutions with carbon aerogel electrodes. *J. Appl. Electrochem.* 26: 1007–1018.

189 Kim, S.J., Hwang, S.W., and Hyun, S.H. (2005). Preparation of carbon aerogel electrodes for supercapacitor and their electrochemical characteristics. *J. Mater. Sci.* 40: 725–731.

190 Zhuo, H., Hu, Y., Chen, Z., and Zhong, L. (2019). Cellulose carbon aerogel/PPy composites for high-performance supercapacitor. *Carbohydr. Polym.* 215: 322–329.

191 Ji, X.J., Wang, H.Q., Chen, T.Z. et al. (2020). Intrinsic negative TCR of superblack carbon aerogel films and their ultrabroad band response from UV to microwave. *Carbon* 161: 590–598.

192 Xie, P.T., Sun, W., Liu, Y. et al. (2018). Carbon aerogels towards new candidates for double negative metamaterials of low density. *Carbon* 129: 598–606.
193 Xie, P.T., Sun, W., Du, A. et al. (2020). Epsilon-negative carbon aerogels with the state transition from dielectric to degenerate semiconductor. *Adv. Electron. Mater.* 7 (3): 2000877.
194 Gross, J., Fricke, J., and Hrubesh, L. (1992). Sound propagation in SiO_2 aerogels. *J. Acoust. Soc. Am.* 91: 2004–2006.
195 Fricke, J. and Emmerling, A. (1992). *Chemistry, Spectroscopy and Applications of Sol-Gel Glasses*, 37–87. Springer.
196 Forest, L., Gibiat, V., and Hooley, A. (2001). Impedance matching and acoustic absorption in granular layers of silica aerogels. *J. Non-Cryst. Solids* 285: 230–235.
197 Gross, J., Reichenauer, G., and Fricke, J. (1988). Mechanical properties of SiO_2 aerogels. *J. Phys. D: Appl. Phys.* 21: 1447.
198 Zimmermann, A., Gross, J., and Fricke, J. (1995). Constant-Q acoustic attenuation in silica aerogels. *J. Non-Cryst. Solids* 186: 238–243.
199 Schmidt, M. and Schwertfeger, F. (1998). Applications for silica aerogel products. *J. Non-Cryst. Solids* 225: 364–368.
200 Jichao, W., Shen, J., Ni, X.Y. et al. (2010). Acoustic properties of nanoporous silica aerogel. *Rare Met. Mater. Eng.* 39: 14–17.
201 Yang, T., Xiong, X.M., Venkataraman, M. et al. (2019). Investigation on sound absorption properties of aerogel/polymer nonwovens. *J. Text. Inst.* 110: 196–201.
202 Xie, Y. and Beamish, J. (1998). Ultrasonic properties of silica aerogels at low temperatures. *Phys. Rev. B* 57: 3406.
203 G. Hayase, Kanamori, K., and Nakanishi, K. (2011). New flexible aerogels and xerogels derived from methyltrimethoxysilane/dimethyldimethoxysilane co-precursors. *J. Mater. Chem.* 21: 17077–17079.
204 Du, A., Xie, Y.H., Li, Y. et al. (2020). Ultra-slow sound in non-resonant meta-aerogel. *arXiv* 09059.
205 Xie, Y.H., Zhou, B., and Du, A. (2021). Slow-sound propagation in aerogel-inspired hybrid structure with backbone and dangling branch. *Adv. Compos. Hybrid Mater.* 4: 248–256.
206 Wittwer, V. (1992). Development of aerogel windows. *J. Non-Cryst. Solids* 145: 233–236.
207 Fricke, J. (1986). *Aerogels*, 2–19. Springer.
208 Herrmann, G., Iden, R., Mielke, M. et al. (1995). On the way to commercial production of silica aerogel. *J. Non-Cryst. Solids* 186: 380–387.
209 Kuhn, J., Gleissner, T., Arduini-Schuster, M.C. et al. (1995). Integration of mineral powders into SiO_2 aerogels. *J. Non-Cryst. Solids* 186: 291–295.
210 Zeng, S., Hunt, A., and Greif, R. (1995). Theoretical modeling of carbon content to minimize heat transfer in silica aerogel. *J. Non-Cryst. Solids* 186: 271–277.
211 Lu, X., Wang, P., Arduini-Schuster, M.C. et al. (1992). Thermal transport in organic and opacified silica monolithic aerogels. *J. Non-Cryst. Solids* 145: 207–210.
212 Won, J.Y., Kim, S.R., Lee, Y.J. et al. (2013). Effect of temperature and carbon contents on the synthesis of β-SiC powder. *J. Nano Res.* 21: 83–87.
213 Dyjak, S., Norek, M., Polański, M. et al. (2013). A simple method of synthesis and surface purification of titanium carbide powder. *Int. J. Refract. Met. Hard Mater.* 38: 87–91.
214 Li, X.T., Chen, X.H., and Song, H.H. (2011). Preparation of silicon carbide nanowires via a rapid heating process. *Mater. Sci. Eng. B* 176 (1): 87–91.
215 Ebrahimpour, O., Dubois, C., and Chaouki, J. (2014). Fabrication of mullite-bonded porous SiC ceramics via a sol–gel assisted in situ reaction bonding. *J. Eur. Ceram. Soc.* 34: 237–247.

216 Niu, T.T., Zhou, B., Zhang, Z.H. et al. (2020). Low-temperature synthesis of monolithic titanium carbide/carbon composite aerogel. *Nanomaterials* 10: 2527.

217 Liang, Y., Wu, H., Huang, G. et al. (2017). Thermal performance and service life of vacuum insulation panels with aerogel composite cores. *Energy Build.* 154: 606–617.

218 Liu, Y., Wu, H., Zhang, Y. et al. (2020). Structure characteristics and hygrothermal performance of silica aerogel composites for building thermal insulation in humid areas. *Energy Build.* 228: 110452.

219 Jensen, K.I., Schultz, J.M., and Kristiansen, F.H. (2004). Development of windows based on highly insulating aerogel glazings. *J. Non-Cryst. Solids* 350: 351–357.

220 Lewis, N.S. (2007). Toward cost-effective solar energy use. *Science* 315: 798–801.

221 Grätzel, M. (2011). *Materials for Sustainable Energy: A Collection of Peer-Reviewed Research and Review Articles from Nature Publishing Group*, 26–32. World Scientific.

222 Mu, B. and Li, M. (2019). Synthesis of novel form-stable composite phase change materials with modified graphene aerogel for solar energy conversion and storage. *Sol. Energy Mater. Sol. Cells* 191: 466–475.

223 Sahan, N. and Paksoy, H.O. (2014). Thermal enhancement of paraffin as a phase change material with nanomagnetite. *Sol. Energy Mater. Sol. Cells* 126: 56–61.

224 Fang, X., Xin, P., Song, B. et al. (2017). Form-stable phase change material embedded with chitosan-derived carbon aerogel. *Mater. Lett.* 195: 79–81.

225 Wang, H.Q., Zhang, C., Zhou, B. et al. (2021). Ultra-black pinecone for efficient solar steam generation under omnidirectional illumination. *Adv. Sustain. Syst.* 5: 2000244.

226 Wang, H., He, X., Zhou, B. et al. (2018). Hot electrons coupling-enhanced photocatalysis of super black carbon aerogels/titanium oxide composite. *MRS Commun.* 8: 521–526.

227 Wang, H., Du, A., Zhang, Z. et al. (2017). An optical dustbin made by the subwavelength-induced super-black carbon aerogels. *J. Mater. Res.* 32: 3524–3531.

228 Meier, S.R., Korwin, M.L., and Merzbacher, C.I. (2000). Carbon aerogel: a new nonreflective material for the infrared. *Appl. Opt.* 39: 3940–3944.

229 Zheng, J.P., Huang, J., and Jow, T. (1997). The limitations of energy density for electrochemical capacitors. *J. Electrochem. Soc.* 144: 2026.

230 Burke, A. (2000). Ultracapacitors: why, how, and where is the technology. *J. Power Sources* 91: 37–50.

231 Mayer, S.T., Pekala, R.W., and Kaschmitter, J.L. (1993). The aerocapacitor: an electrochemical double-layer energy-storage device. *J. Electrochem. Soc.* 140: 446–451.

232 Lu, X., Caps, R., Fricke, J. et al. (1995). Correlation between structure and thermal conductivity of organic aerogels. *J. Non-Cryst. Solids* 188: 226–234.

233 Liu, M.F., Du, A., Li, T.M. et al. (2019). Simple deceleration mechanism confirmed in the terminal hypervelocity impacted tracks in SiO_2 aerogel. *Icarus* 317: 365–372.

234 Du, A., Ma, Y., Liu, M.F. et al. (2021). Morphology analysis of tracks in the aerogels impacted by hypervelocity irregular particles. *High Power Laser Sci. Eng.* 9: e14.

235 Fricke, J. (1988). Aerogels – highly tenuous solids with fascinating properties. *J. Non-Cryst. Solids* 100: 169–173.

236 Wang, H.Q., Du, A., Ji, X.J. et al. (2019). Enhanced photothermal conversion by hot-electron effect in ultrablack carbon aerogel for solar steam generation. *ACS Appl. Mater. Interface* 11: 42057–42065.

237 Wang, H.Q., Zhang, C., Zhang, Z.H. et al. (2020). Artificial trees inspired by Monsterafor highly efficient solar steam generation in both normal and weak light environments. *Adv. Funct. Mater.* 30.

238 Wang, H.Q., Zhang, C., Zhou, B. et al. (2019). Ultra-black carbon@silica core-shell aerogels with controllable electrical conductivities. *Adv. Compos. Hybrid Mater.* 2: 743–752.

239 Ganguly, S., Zhou, C., Morelli, D. et al. (2012). Synthesis and characterization of telluride aerogels: effect of gelation on thermoelectric performance of Bi_2Te_3 and $Bi_{2-x}Sb_xTe_3$ nanostructures. *J. Phys. Chem. C* 116: 17431–17439.

240 Kalebaila, K.K., Georgiev, D.G., and Brock, S.L. (2006). Synthesis and characterization of germanium sulfide aerogels. *J. Non-Cryst. Solids* 352: 232–240.

241 Yu, H.T. and Brock, S.L. (2008). Effects of nanoparticle shape on the morphology and properties of porous CdSe assemblies (aerogels). *ACS Nano* 2: 1563–1570.

242 Steiner, S.A., Baumann, T.F., Bayer, B.C. et al. (2009). Nanoscale zirconia as a nonmetallic catalyst for graphitization of carbon and growth of single- and multiwall carbon nanotubes. *J. Am. Chem. Soc.* 131: 12144–12154.

243 Worsley, M.A., Kuntz, J.D., Cervantes, O. et al. (2009). Route to high surface area TiO_2/C and TiCN/C composites. *J. Mater. Chem.* 19: 7146–7150.

244 Worsley, M.A., Pham, T.T., Yan, A. et al. (2014). Synthesis and characterization of highly crystalline graphene aerogels. *ACS Nano* 8: 11013–11022.

245 Worsley, M.A., Shin, S.J., Merrill, M.D. et al. (2015). Ultra low density, monolithic WS_2, MoS_2, and MoS_2/graphene aerogels. *ACS Nano* 9: 4698–4705.

246 Herrmann, A.K., Formanek, P., Borchardt, L. et al. (2014). Multimetallic aerogels by template-free self-assembly of Au, Ag, Pt, and Pd nanoparticles. *Chem. Mater.* 26: 1074–1083.

247 Cai, B., Wen, D., Liu, W. et al. (2015). Function-led design of aerogels: self-assembly of alloyed PdNi hollow nanospheres for efficient electrocatalysis. *Angew. Chem. Int. Ed.* 54: 13101–13105.

248 Wen, D., Liu, W., Haubold, D. et al. (2016). Gold aerogels: three-dimensional assembly of nanoparticles and their use as electrocatalytic interfaces. *ACS Nano* 10: 2559–2567.

249 Henning, S., Ishikawa, H., Kühn, L. et al. (2017). Unsupported Pt-Ni aerogels with enhanced high current performance and durability in fuel cell cathodes. *Angew. Chem. Int. Ed.* 56: 10707–10710.

250 Du, R., Joswig, J.O., Fan, X. et al. (2020). Disturbance-promoted unconventional and rapid fabrication of self-healable noble metal gels for (photo-)electrocatalysis. *Matter* 2: 908–920.

251 Du, R., Joswig, J.O., Hübner, R. et al. (2020). Freeze-thaw-promoted fabrication of clean and hierarchically structured noble-metal aerogels for electrocatalysis and photoelectrocatalysis. *Angew. Chem. Int. Ed.* 59: 8293–8300.

252 Leventis, N., Sotiriou-Leventis, C., Chandrasekaran, N. et al. (2010). Multifunctional polyurea aerogels from isocyanates and water. A structure-property case study. *Chem. Mater.* 22: 6692–6710.

253 Leventis, N., Chidambareswarapattar, C., Molite, D.P. et al. (2011). Multifunctional porous aramids (aerogels) by efficient reaction of carboxylic acids and isocyanates. *J. Mater. Chem.* 21: 11981–11986.

254 Leventis, N., Sotiriou-Leventis, C., Mohite, D.P. et al. (2011). Polyimide aerogels by Ring-Opening Metathesis Polymerization (ROMP). *Chem. Mater.* 23: 2250–2261.

255 Chidambareswarapattar, C., Mohite, D.P., Larimore, Z.J. et al. (2012). One pot synthesis of multifunctional aramid aerogels. *Mater. Res. Soc. Symp. P* 1403: 29–34.

256 Rubenstein, D.A., Lu, H.B., Mahadik, S.S. et al. (2012). Characterization of the physical properties and biocompatibility of polybenzoxazine-based aerogels for use as a novel hard-tissue scaffold. *J. Biomater. Sci. Polym. E* 23: 1171–1184.

257 Sadekar, A.G., Mahadik, S.S., Bang, A.N. et al. (2012). From 'Green' aerogels to porous graphite by emulsion gelation of acrylonitrile. *Chem. Mater.* 24: 26–47.

258 Chidambareswarapattar, C., McCarver, P.M., Luo, H.Y. et al. (2013). Fractal multiscale nanoporous polyurethanes: flexible to extremely rigid aerogels from multifunctional small molecules. *Chem. Mater.* 25: 3205–3224.

259 Mohite, D.P., Mahadik-Khanolkar, S., Luo, H.Y. et al. (2013). Polydicyclopentadiene aerogels grafted with PMMA: I. Molecular and interparticle crosslinking. *Soft Matter* 9: 1516–1530.

260 Bang, A., Buback, C., Sotiriou-Leventis, C., and Leventis, N. (2014). Flexible aerogels from hyperbranched polyurethanes: probing the role of molecular rigidity with poly(urethane acrylates) versus poly(urethane norbornenes). *Chem. Mater.* 26: 6979–6993.

261 Leventis, N., Chidambareswarapattar, C., Bang, A., and Sotiriou-Leventis, C. (2014). Cocoon-in-web-like superhydrophobic aerogels from hydrophilic polyurea and use in environmental remediation. *ACS Appl. Mater. Interface* 6: 6872–6882.

262 Mahadik-Khanolkar, S., Donthula, S., Sotiriou-Leventis, C., and Leventis, N. (2014). Polybenzoxazine aerogels. 1. High-yield room-temperature acid-catalyzed synthesis of robust monoliths, oxidative aromatization, and conversion to microporous carbons. *Chem. Mater.* 26: 1303–1317.

263 Donthula, S., Mandal, C., Leventis, T. et al. (2017). Shape memory superelastic poly (isocyanurate-urethane) aerogels (PIR-PUR) for deployable panels and biomimetic applications. *Chem. Mater.* 29: 4461–4477.

264 Malakooti, S., Churu, H.G., Lee, A. et al. (2017). Sound insulation properties in low-density, mechanically strong and ductile nanoporous polyurea aerogels. *J. Non-Cryst. Solids* 476: 36–45.

265 Donthula, S., Mandal, C., Schisler, J. et al. (2018). Nanostructure-dependent Marcus-type correlation of the shape recovery rate and the Young's modulus in shape memory polymer aerogels. *ACS Appl. Mater. Interface* 10: 23321–23334.

266 Malakooti, S., Churu, H.G., Lee, A. et al. (2018). Sound transmission loss enhancement in an inorganic-organic laminated wall panel using multifunctional low-density nanoporous polyurea aerogels: experiment and modeling. *Adv. Eng. Mater.* 20.

267 Malakooti, S., Rostami, S., Churu, H.G. et al. (2018). Scalable, hydrophobic and highly-stretchable poly(isocyanurate-urethane) aerogels. *RSC Adv.* 8: 21214–21223.

268 Malakooti, S., Qin, G.Q., Mandal, C. et al. (2019). Low-cost, ambient-dried, superhydrophobic, high strength, thermally insulating, and thermally resilient polybenzoxazine aerogels. *ACS Appl. Polym. Mater.* 1: 2322–2333.

269 Rewatkar, P.M., Saeed, A.M., Far, H.M. et al. (2019). Polyurethane aerogels based on cyclodextrins: high-capacity desiccants regenerated at room temperature by reducing the relative humidity of the environment. *ACS Appl. Mater. Interface* 11: 34292–34304.

270 Guo, H.Q., Meador, M.A.B., McCorkle, L. et al. (2012). Tailoring properties of cross-linked polyimide aerogels for better moisture resistance, flexibility, and strength. *ACS Appl. Mater. Interface* 4: 5422–5429.

271 Meador, M.A. (2015). Taking nanotechnology to new heights: the potential impact on future aerospace vehicles. *MRS Bull.* 40: 815–821.

272 Guo, H.Q., Meador, M.A.B., McCorkle, L. et al. (2016). Poly(maleic anhydride) cross-linked polyimide aerogels: synthesis and properties. *RSC Adv.* 6: 26055–26065.

273 Meador, M.A.B., Agnello, M., McCorkle, L. et al. (2016). Moisture-resistant polyimide aerogels containing propylene oxide links in the backbone. *ACS Appl. Mater. Interface* 8: 29073–29079.

274 Michal, B.T., Brenn, W.A., Nguyen, B.N. et al. (2016). Thermoresponsive shape-memory aerogels from thiol-ene networks. *Chem. Mater.* 28: 2341–2347.

275 Nguyen, B.N., Meador, M.A.B., Scheiman, D., and McCorkle, L. (2017). Polyimide aerogels using triisocyanate as cross-linker. *ACS Appl. Mater. Interface* 9: 27313–27321.

276 Guo, H.Q., Dewey, O.S., McCorkle, L.S. et al. (2019). Polyimide aerogels as lightweight dielectric insulators for carbon nanotube cables. *ACS Appl. Polym. Mater.* 1: 1680–1688.
277 Talley, S.J., Vivod, S.L., Nguyen, B.A. et al. (2019). Hierarchical morphology of poly(ether ether ketone) aerogels. *ACS Appl. Mater. Interface* 11: 31508–31519.
278 Guo, H.Q., Meador, M.A.B., Cashman, J.L. et al. (2020). Flexible polyimide aerogels with dodecane links in the backbone structure. *ACS Appl. Mater. Interface* 12: 33288–33296.
279 Vivod, S.L., Meador, M.A.B., Pugh, C. et al. (2020). Toward improved optical transparency of polyimide aerogels. *ACS Appl. Mater. Interface* 12: 8622–8633.
280 Li, Q.X., Wang, J., Ye, L. et al. (2019). Recyclable nanoporous materials with ordered tunnels self-assembled from alpha- and gamma-cyclodextrins. *Chem. Tech.* 5: 838–846.
281 Lu, Y., He, W.N., Cao, T. et al. (2014). Elastic, conductive, polymeric hydrogels and sponges. *Sci. Rep.-UK* 4.
282 Wang, J., Du, R., and Zhang, X.T. (2018). Thermoresponsive polyrotaxane aerogels: converting molecular necklaces into tough porous monoliths. *ACS Appl. Mater. Interface* 10: 1468–1473.
283 Wang, J., Wang, X.C., and Zhang, X.T. (2017). Cyclic molecule aerogels: a robust cyclodextrin monolith with hierarchically porous structures for removal of micropollutants from water. *J. Mater. Chem. A* 5: 4308–4313.
284 Zhang, X.T., Chang, D.W., Liu, J.R., and Luo, Y.J. (2010). Conducting polymer aerogels from supercritical CO_2 drying PEDOT-PSS hydrogels. *J. Mater. Chem.* 20: 5080–5085.
285 Kanamori, K., Kodera, Y., Hayase, G. et al. (2011). Transition from transparent aerogels to hierarchically porous monoliths in polymethylsilsesquioxane sol-gel system. *J. Colloid Interface Sci.* 357: 336–344.
286 Kanamori, K. (2013). Liquid-phase synthesis and application of monolithic porous materials based on organic-inorganic hybrid methylsiloxanes, crosslinked polymers and carbons. *J. Sol-Gel Sci. Technol.* 65: 12–22.
287 Hayase, G., Kanamori, K., Maeno, A. et al. (2016). Dynamic spring-back behavior in evaporative drying of polymethylsilsesquioxane monolithic gels for low-density transparent thermal superinsulators. *J. Non-Cryst. Solids* 434: 115–119.
288 Shimizu, T., Kanamori, K., Maeno, A. et al. (2016). Transparent, highly insulating polyethyl- and polyvinylsilsesquioxane aerogels: mechanical improvements by vulcanization for ambient pressure drying. *Chem. Mater.* 28: 6860–6868.
289 Shimizu, T., Kanamori, K., Maeno, A. et al. (2016). Transparent ethylene-bridged polymethylsiloxane aerogels and xerogels with improved bending flexibility. *Langmuir* 32: 13427–13434.
290 Shimizu, T., Kanamori, K., and Nakanishi, K. (2017). Silicone-based organic-inorganic hybrid aerogels and xerogels. *Chem. Eur. J.* 23: 5176–5187.
291 Zu, G.Q., Kanamori, K., Shimizu, T. et al. (2018). Versatile double-cross-linking approach to transparent, machinable, supercompressible, highly bendable aerogel thermal superinsulators. *Chem. Mater.* 30: 2759–2770.
292 Zu, G.Q., Shimizu, T., Kanamori, K. et al. (2018). Transparent, superflexible doubly cross-linked polyvinylpolymethylsiloxane aerogel superinsulators via ambient pressure drying. *ACS Nano* 12: 521–532.
293 Zu, G.Q., Shen, J., Zou, L.P. et al. (2013). Nanoengineering super heat-resistant, strong alumina aerogels. *Chem. Mater.* 25: 4757–4764.
294 Zu, G.Q., Shen, J., Wang, W.Q. et al. (2014). Robust, highly thermally stable, core-shell nanostructured metal oxide aerogels as high-temperature thermal superinsulators, adsorbents, and catalysts. *Chem. Mater.* 26: 5761–5772.

295 Chen, K., Xu, W., Du, A. et al. (2014). Template confined synthetic strategy for three-dimensional free-standing hierarchical porous nanocrystalline tantalum. *Mater. Lett.* 116: 31–34.

296 Xu, W.W., Du, A., Tang, J. et al. (2014). Template confined synthesis of Cu- or Cu_2O-doped SiO_2 aerogels from Cu(II)-containing composites by in situ alcohothermal reduction. *RSC Adv.* 4: 49541–49546.

297 Chandrasekaran, S., Yao, B., Liu, T. et al. (2018). Direct ink writing of organic and carbon aerogels. *Mater. Horiz.* 5: 1166–1175.

298 Qi, Z., Ye, J.C., Chen, W. et al. (2018). 3D-Printed, superelastic polypyrrole-graphene electrodes with ultrahigh areal capacitance for electrochemical energy storage. *Adv. Mater. Technol.-US* 3.

299 Yao, B., Chandrasekaran, S., Zhang, H. et al. (2020). 3D-Printed structure boosts the kinetics and intrinsic capacitance of pseudocapacitive graphene aerogels. *Adv. Mater.* 32.

300 Zhu, C., Liu, T.Y., Qian, F. et al. (2016). Supercapacitors based on three-dimensional hierarchical graphene aerogels with periodic macropores. *Nano Lett.* 16: 3448–3456.

301 Du, G.L., Mao, A.R., Yu, J.H. et al. (2019). Nacre-mimetic composite with intrinsic self-healing and shape-programming capability. *Nat. Commun.* 10.

302 Wang, H., Wu, J.J., Cai, C. et al. (2014). Mussel inspired modification of polypropylene separators by catechol/polyamine for Li-ion batteries. *ACS Appl. Mater. Interface* 6: 5602–5608.

303 Wang, Z.H., Liu, J.M., Li, C.Y. et al. (2019). Bacterial biofilm bioinspired persistent luminescence nanoparticles with gut-oriented drug delivery for colorectal cancer imaging and chemotherapy. *ACS Appl. Mater. Interface* 11: 36409–36419.

304 Wu, J.J., Zhang, L., Wang, Y.X. et al. (2011). Mussel-inspired chemistry for robust and surface-modifiable multilayer films. *Langmuir* 27: 13684–13691.

305 Yang, M., Zou, W.Z., Gou, J. et al. (2020). Bioinspired "Skin" with cooperative thermo-optical effect for daytime radiative cooling. *ACS Appl. Mater. Interface* 12: 25286–25293.

306 Zhao, N.F., Li, M., Gong, H.X., and Bai, H. (2020). Controlling ice formation on gradient wettability surface for high-performance bioinspired materials. *Sci. Adv.* 6.

307 Cai, Y., Lin, L., Xue, Z.X. et al. (2014). Filefish-inspired surface design for anisotropic underwater oleophobicity. *Adv. Funct. Mater.* 24: 809–816.

308 Cai, Y., Lu, Q.H., Guo, X.L. et al. (2015). Salt-tolerant superoleophobicity on alginate gel surfaces inspired by seaweed (Saccharina japonica). *Adv. Mater.* 27: 4162–4168.

309 Chen, Y., He, J., Wang, L. et al. (2014). Excellent bead-on-string silkworm silk with drop capturing abilities. *J. Mater. Chem. A* 2: 1230–1234.

310 Chen, Z., Wang, J., Pan, D. et al. (2018). Mimicking a dog's nose: scrolling graphene nanosheets. *ACS Nano* 12: 2521–2530.

311 Chen, Z.P., Lin, Y.Y., Lee, W. et al. (2018). Additive manufacturing of honeybee-inspired microneedle for easy skin insertion and difficult removal. *ACS Appl. Mater. Interface* 10: 29338–29346.

312 Cheng, Q.F., Duan, J.L., Zhang, Q., and Jiang, L. (2015). Learning from nature: constructing integrated graphene-based artificial nacre. *ACS Nano* 9: 2231–2234.

313 Dou, X.Q., Zhang, D., Feng, C.L., and Jiang, L. (2015). Bioinspired hierarchical surface structures with tunable wettability for regulating bacteria adhesion. *ACS Nano* 9: 10664–10672.

314 Dou, Y.H., Tian, D.L., Sun, Z.Q. et al. (2017). Fish gill inspired crossflow for efficient and continuous collection of spilled oil. *ACS Nano* 11: 2477–2485.

315 Duan, J.L., Gong, S.S., Gao, Y. et al. (2016). Bioinspired ternary artificial nacre nanocomposites based on reduced graphene oxide and nanofibrillar cellulose. *ACS Appl. Mater. Interface* 8: 10545–10550.

316 Feng, Y.P., Zhu, W.W., Guo, W., and Jiang, L. (2017). Bioinspired energy conversion in nanofluidics: a paradigm of material evolution. *Adv. Mater.* 29.

317 Gong, S.S., Ni, H., Jiang, L., and Cheng, Q.F. (2017). Learning from nature: constructing high performance graphene-based nanocomposites. *Mater. Today* 20: 210–219.
318 Gong, X.J., Gao, X.F., and Jiang, L. (2017). Recent progress in bionic condensate microdrop self-propelling surfaces. *Adv. Mater.* 29.
319 Guo, T.Q., Heng, L.P., Wang, M.M. et al. (2016). Robust underwater oil-repellent material inspired by columnar nacre. *Adv. Mater.* 28: 8505–8510.
320 Hou, X., Yang, F., Li, L. et al. (2010). A biomimetic asymmetric responsive single nanochannel. *J. Am. Chem. Soc.* 132: 11736–11742.
321 Ju, J., Yao, X., Yang, S. et al. (2014). Cactus stem inspired cone-arrayed surfaces for efficient fog collection. *Adv. Funct. Mater.* 24: 6933–6938.
322 Peng, J.S., Huang, C.J., Cao, C. et al. (2020). Inverse nacre-like epoxy-graphene layered nanocomposites with integration of high toughness and self-monitoring. *Matter* 2: 220–232.
323 Si, Y.F., Dong, Z.C., and Jiang, L. (2018). Bioinspired designs of superhydrophobic and superhydrophilic materials. *ACS Central Sci.* 4: 1102–1112.
324 Su, B., Tian, Y., and Jiang, L. (2016). Bioinspired interfaces with superwettability: from materials to chemistry. *J. Am. Chem. Soc.* 138: 1727–1748.
325 Wang, S.T., Liu, K.S., Yao, X., and Jiang, L. (2015). Bioinspired surfaces with superwettability: new insight on theory, design, and applications. *Chem. Rev.* 115: 8230–8293.
326 Wu, M.X., Shuai, H., Cheng, Q.F., and Jiang, L. (2014). Bioinspired green composite lotus fibers. *Angew. Chem. Int. Ed.* 53: 3358–3361.
327 Zhang, Z., Wen, L.P., and Jiang, L. (2018). Bioinspired smart asymmetric nanochannel membranes. *Chem. Soc. Rev.* 47: 322–356.
328 Li, C.X., Dai, H.Y., Cao, C. et al. (2019). Bioinspired inner microstructured tube controlled capillary rise. *Proc. Natl. Acad. Sci. U.S.A.* 116: 12704–12709.
329 Chen, H.W., Zhang, P.F., Zhang, L.W. et al. (2016). Continuous directional water transport on the peristome surface of Nepenthes alata. *Nature* 532: 85.
330 Gao, X.F. and Jiang, L. (2004). Water-repellent legs of water striders. *Nature* 432: 36–36.
331 Zheng, Y.M., Bai, H., Huang, Z.B. et al. (2010). Directional water collection on wetted spider silk. *Nature* 463: 640–643.
332 Chen, H.W., Ran, T., Gan, Y. et al. (2018). Ultrafast water harvesting and transport in hierarchical microchannels. *Nat. Mater.* 17: 935.
333 Tian, Y. and Jiang, L. (2013). WETTING intrinsically robust hydrophobicity. *Nat. Mater.* 12: 291–292.
334 Bai, H., Chen, Y., Delattre, B. et al. (2015). Bioinspired large-scale aligned porous materials assembled with dual temperature gradients. *Sci. Adv.* 1.
335 Bai, H., Ju, J., Zheng, Y.M., and Jiang, L. (2012). Functional fibers with unique wettability inspired by spider silks. *Adv. Mater.* 24: 2786–2791.
336 Bai, H., Tian, X.L., Zhang, Y.M. et al. (2010). Direction controlled driving of tiny water drops on bioinspired artificial spider silks. *Adv. Mater.* 22: 5521–5525.
337 Bai, H., Wang, L., Lu, J. et al. (2014). Efficient water collection on integrative bioinspired surfaces with star-shaped wettability patterns. *Adv. Mater.* 26: 5025–5030.
338 Xu, Z.P., Wu, M.R., Gao, W.W. et al. (2020). Skin-inspired composite film with outstanding tear resistance based on flat silk cocoon. *Adv. Mater.* 32.
339 Bai, H., Ju, J., Sun, R. et al. (2011). Controlled fabrication and water collection ability of bioinspired artificial spider silks. *Adv. Mater.* 23: 3708.
340 Li, D.W., Bu, X.C., Xu, Z.P. et al. (2020). Bioinspired multifunctional cellular plastics with a negative Poisson's ratio for high-energy dissipation. *Adv. Mater.* 32.

341 Tian, X.L., Chen, Y., Zheng, Y.M. et al. (2011). Controlling water capture of bioinspired fibers with hump structures. *Adv. Mater.* 23: 5486.

342 Wegst, U.G.K., Bai, H., Saiz, E. et al. (2015). Bioinspired structural materials. *Nat. Mater.* 14: 23–36.

343 Osotsi, M.I., Zhang, W., Zada, I. et al. (2020). Butterfly wing architectures inspire sensor and energy applications. *Natl. Sci. Rev.* 8 (3): nwaa107.

344 Zhang, Y.F., Wu, L., Wang, X.F. et al. (2020). Super hygroscopic nanofibrous membrane-based moisture pump for solar-driven indoor dehumidification. *Nat. Commun.* 11.

345 Wang, B., Li, G., Xu, L. et al. (2020). Nanoporous boron nitride aerogel film and its smart composite with phase change materials. *ACS Nano* 14 (12): 16590–16599.

346 Wang, H.Q., Zhang, C., Zhou, B. et al. (2020). Hydrophobic silica nanorod arrays vertically grown on melamine foams for oil/water separation. *ACS Appl. Nano Mater.* 3: 1479.

2

Aerogels and Their Composites in Energy Generation and Conversion Devices

Juno A. Rose[1], Aruchamy Kanakaraj[1], and Nataraj Sanna Kotrappanavar[1,2]

[1] *Center for Nano and Material Sciences, Jain University, Jain Global Campus, Bangalore, 562112, India*
[2] *Polymer Science and Engineering, Chonnam National University, 77 Yongbong-ro, Buk-gu, Gwangju, South Korea*

2.1 Introduction to Aerogels

Aerogels are a diverse class of ultraporous, solid gel materials in which the liquid part is completely replaced with gas, inducing a stable solid network structure. Therefore, aerogels are known for their extremely low densities (0.0011 to ~0.5 g cm^{-3}). Due to this ultra-low density solid network having only very little solid material left overall, a solid foam structure consists primarily of air (up to 99.8%); hence aerogels are frequently referred to as *frozen smoke*.

Due to their porous and flexible nature, aerogels can be prepared in different shapes and forms. Initially, aerogels were prepared using silica-based precursor; however, discovery proceeded with different precursor due to their potential applications in different fields. Therefore, researcher and innovators in recent times have prepared aerogel with precursors like carbaneous materials, metal oxides, polymer-based aerogels, aerogels of semiconductor nanostructures, and metal-based aerogels (gold and copper) to meet various applications [1, 2].

Aerogel is the term used to cover all materials with a specific physical and geometrical structure as it consists of extremely porous, interconnected solid network with interconnected branches from a few nanometers to a few microns across. Externally, it looks like a solid foam. As per IUPAC, aerogels are defined as gels that contain a micro-porous solid in which the dispersed phase is in the gaseous state (gas in solid).

The term *aerogels* was first introduced by S. Kistler in the 1930s when pore liquid of wet gels were extracted to attain air-filled solid materials having similar dimensions as the original wet gels using supercritical drying approach. In this approach, the supercritical fluid is formed by evacuating the liquid, which has been saturated with the gels. The continuous exploration in this field of study helped to prepare alumina-based aerogels to ferric, tungstic, and nickel tartrate-based solid foams. Lately, several other precursors have been converted to aerogels, including biopolymers like chitosan, gelatin, agar, nitrocellulose, and cellulose. Initially, silica-based aerogels were successfully prepared in large scale for potential application in aerospace, catalysis, insulating materials, water repellents, and thickening agents. Sodium silicate (water glass, Na_2SiO_3) was the precursor used for synthesizing silica aerogels, and water is used to disperse the gel to a powder near aqueous

Aerogels for Energy Saving and Storage, First Edition. Edited by Meldin Mathew, Hanna J. Maria, Ange Nzihou, and Sabu Thomas.
© 2024 John Wiley & Sons, Inc. Published 2024 by John Wiley & Sons, Inc.

medium critical point. The wet gels were subjected to dialysis for the replacement of water with ethanol, which helped initiate supercritical drying using ethanol [3, 4].

Later, Teichner et al. explored the preparation of aerogels using various simple and binary oxides. Initially, the cations from oxide gels (metallic salts) were treated as precursors; however, lately sol-gel method has been used for aerogel preparation via hydrolysis of organic component in which a slow proton scavenger was added. Alkoxides $M(OR)_n$, which used to synthesize silica xerogels, are now the most recommended precursors. Here, *R* represents the alkyl group and *OR* designates alkoxide group [5]. These alkoxides are readily available in the parent solution (alcohol), which directly dry these gels using supercritical drying methods. Oxy alkoxides are another category of precursors now available, $[O_xM(OR)_y$ and $XSi(OR)_3]$, in which *X* stands for an organic group. The remaining part is the ligand, which shows fascinating characteristic properties like hydrophobicity and possibility polymerization.

Polymer-based aerogel preparation proceeds with the decant of swelling agent or solvent from the crosslinked polymer 3D network. This removal leads to no change in the volume and densification in the polymer network. This leads to the replacement of liquid phase with air using either supercritical CO_2 or freeze-drying techniques. Selection of drying techniques were identified and applied, depending on the type and mechanical stability of the gels. Generally, the network structure of gels would crumble by eliminating the capillary forces during simple evaporative drying method [6]. But this effect can be achieved by the freeze-drying method; this is only applicable if the gel structure has the ability to withstand capillary forces of ice-crystal growth. Occasionally, modified surface structure of gels displays a spring-back, which allows for evaporative drying method without major pore collapse. Supercritical CO_2 drying method conserves the original structure of aerogel and produces a larger surface area. Therefore, the highly porous and three-dimensional network structure of aerogels can be effectively prepared via sol-gel method with proper drying technology.

Aerogels differ in their exterior and internal-structure compared to all other ultra-low density solid materials like foam, down, fiber mats, feathers, and insulating foams due to their microporosity and their distribution. Aerogels possess fascinating 3D interconnected, bi-continuous network-structures, containing mesoporous voids, which can induce numerous physical and chemical properties in a single solid framework. With this, dispersed phase attains uniquely arranged ultra-high porosity (around 99.9%), large pore volume, excellent adsorption capacity, ultra-low density and relative density, high refractive index, ultra-low dielectric constant, refractive index and thermal conductivity, high insulation performance, and super large surface area [7]. With these properties, aerogels has become ideal material for thermal insulation due to thermal conductivity [4]. Also, aerogels are finding their way into many applications due to their extremely light-weight and transparent with inorganic precursors, channeled microporosity with polymer precursors, bicontinuous voids in metallic, as well as uniquely different in composite precursors as shown in Figure 2.1.

Based on several criteria required for end use, aerogel have been classified as follows:

1) On the basis of preparation methods, they are classified into hydrogel, xerogel, and cryogel.
2) Based on their physical state, they can be monoliths, fibers, films or powders and their related various microstructures.
3) Based on chemical structure and precursor, they are categorized as polymers, mixed oxides, composites, and hybrid aerogels. [4]
4) Based on the micro structures, this includes mesoporous, microporous, and mixed porous aerogel.

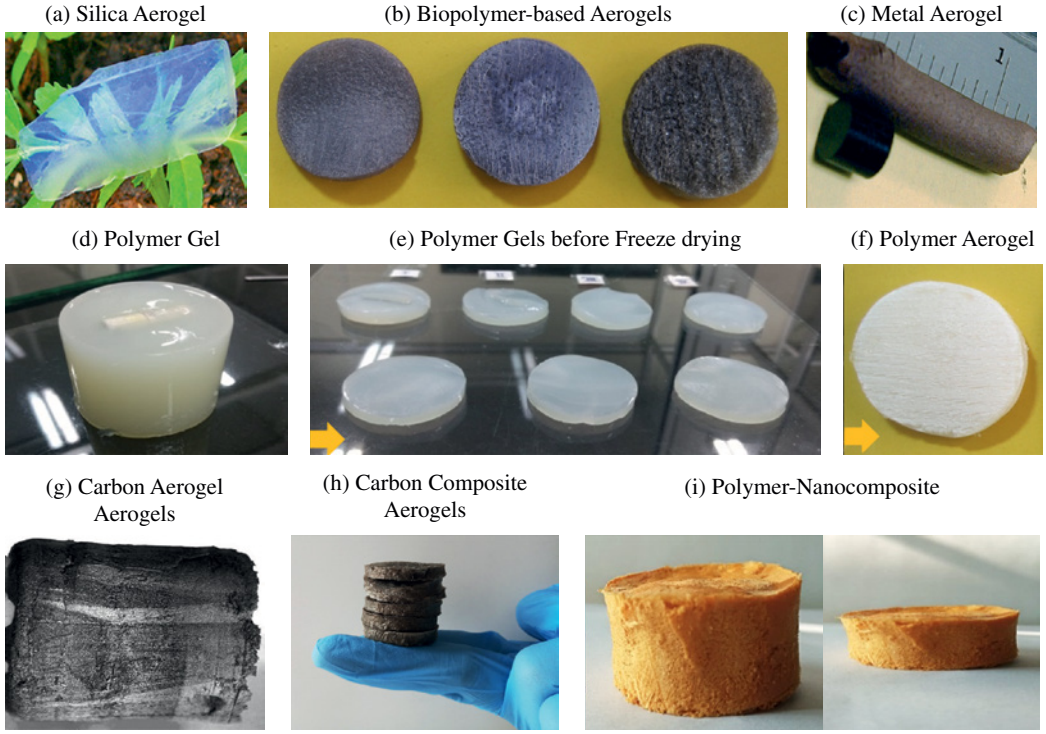


Figure 2.1 Photographs of aerogels made from different precursors with typical look and microstructure for different applications from (a) silica, (b) biopolymer-based, (c) metal aerogel, (d–f) polymer aerogel journey from polymer gel to aerogel, (g) carbon-based aerogel, (h) carbon composite aerogel and (i) polymer-nanocomposite aerogels.

5) The final and most often used type is based on composition, namely, organic such as resin and cellulose based, carbonaceous aerogels, single component aerogel, which comprises oxide, chalcogenide, and hybrid or composite aerogel.

2.2 Strategies for Development of Aerogel Materials

2.2.1 Oxide-based Aerogel

Oxide-based aerogels are a class of aerogels studied earliest and applied most widely, which finds many applications in energy saving and storage field. Because metal-oxide-based aerogels have metal and oxygen-rich flexible for electrochemical transformation during energy-saving and storage application, they are an abundant and fascinating class of aerogels. Among metal-oxide systems there are three versatile methods to synthesis oxide-based aerogels namely sol-gel originated. In this method, conversion of liquid to gel goes through two major reactions: hydrolysis and condensation reactions [8]. First, hydrolysis occurs when metal alkoxide reacts with water to form hydroxyl groups. Simultaneous condensation reaction follows as the alkoxide gets hydrolyzed. Interestingly, during condensation various metal atoms get bridged by an oxygen atom through dealcoholization between an alkoxy and a hydroxyl group or dehydration reaction of two different hydroxyl groups as shown in a schematic representation in Figure 2.2.

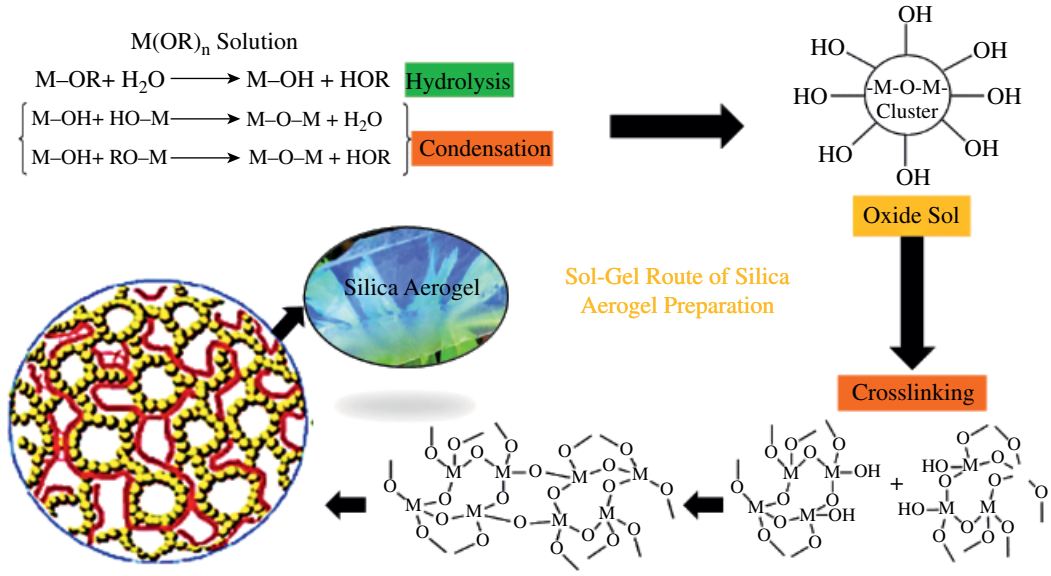


Figure 2.2 General schematics of silica aerogel preparation following sol-gel method.

Similarly, several metal-oxide precursors have been used via sol-gel method for preparing different aerogels such as titania, alumina, and silica aerogels. In 2001, researchers used an epoxide addition method with inorganic salts and epoxides as precursor and catalyst, respectively. The advantage of this method is that, at important stages, both hydrolysis and condensation reactions can be easily controlled. This method proceeds with hydration, hydrolysis, and condensation [9].

First the existence of metal salt in water-contained solution is in the hydrated ion form, as shown in Eq. (2.1),

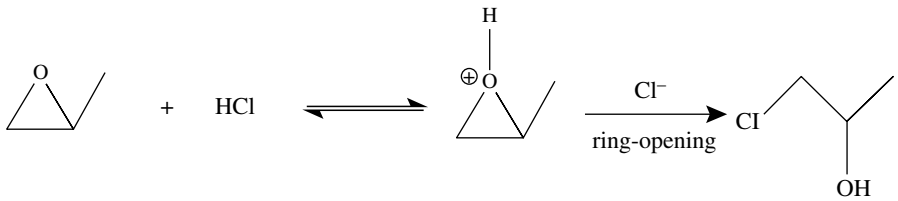
$$M^{n+} + xH_2O \rightarrow \left[M\left(H_2O\right)_x\right]^{n+} \tag{2.1}$$

Following, hydrolysis reactions of hydrated ions occur spontaneously in multistages and produce hydrogen ions by making the solution partially acidic. Given in Eqs. (2.2) and (2.3),

$$\left[M\left(H_2O\right)_x\right]^{n+} \rightleftharpoons \left[M\left(H_2O\right)_{x-1}\left(OH\right)\right]^{(n-1)+} + H^+ \tag{2.2}$$

$$\left[M\left(H_2O\right)_{x-y}\left(OH\right)_y\right]^{(n-y)+} \rightleftharpoons \left[M\left(H_2O\right)_{x-y-1}\left(OH\right)_{y+1}\right]^{(n-y-1)+} + H^+ \tag{2.3}$$

Finally, the epoxides consume hydrogen through ring-opening nucleophilic addition reactions but they fail to increase the pH value as quickly as alkali. Here, in this reaction, propylene oxide with hydrochloric acid is taken as an example. Here, the dehydration and condensation take via hydroxylated ions, similar to M-O-M bond and rapid process,



(2.4)

2.2.2 Organic Aerogel

Organic aerogels are synthesized by sol-gel polymerization followed by supercritical drying [4]. Generally, polymers, resins, and blends of polymer moieties can be used to prepare organic aerogels. In this category, cellulose-based aerogels are the oldest and the first organic aerogels, reported along with silica aerogel. Usually, cellulose gel is formed by diffusion and regeneration of cellulose in organic solvent in the presence of water. The physical and mechanical stabilities in 3D cellulosic network can be achieved via crosslinking of polymer chain in gel. Similarly, resin-based aerogels are formed by treating them in an aqueous solution of Na_2CO_3 (base) catalyzed to lead polycondensation of resorcinol with formaldehyde (RF gel) [10]. The preparation of RF gel formation proceeds with homogeneous polymerization of resorcinol and formaldehyde in copious amount of water. In this, formation of hydroxymethyl resorcinol monomers by the addition reaction of resorcinol and formaldehyde followed by bridging between monomers, which produces water and formaldehyde as products. Finally, with continued polymerization results in RF clusters followed by Na_2CO_3 catalyzed gel and aerogels formation as depicted in Figure 2.3.

2.2.3 Carbon-based Aerogel

Currently, carbonaceous materials are widely being used as electrodes for energy generation, conversion, and storage in fuel cells, batteries, and supercapacitors. Recent research trends are showing growing influence of aerogels in energy application due to their high micro/meso-pore structure and retaining conductivity in the skeletal structure. Carbonaceous materials like graphene, graphene oxide, and carbon nanotubes (CNTs) have been widely used as precursors for preparation of aerogels [11]. The first carbon aerogel was reported by Pekala in 1989 by carbonization of RF aerogel. One of the main advantages of this type of aerogel is that it can be synthesized from various organic gels through pyrolysis. Further, the high temperature (800–1200 °C)

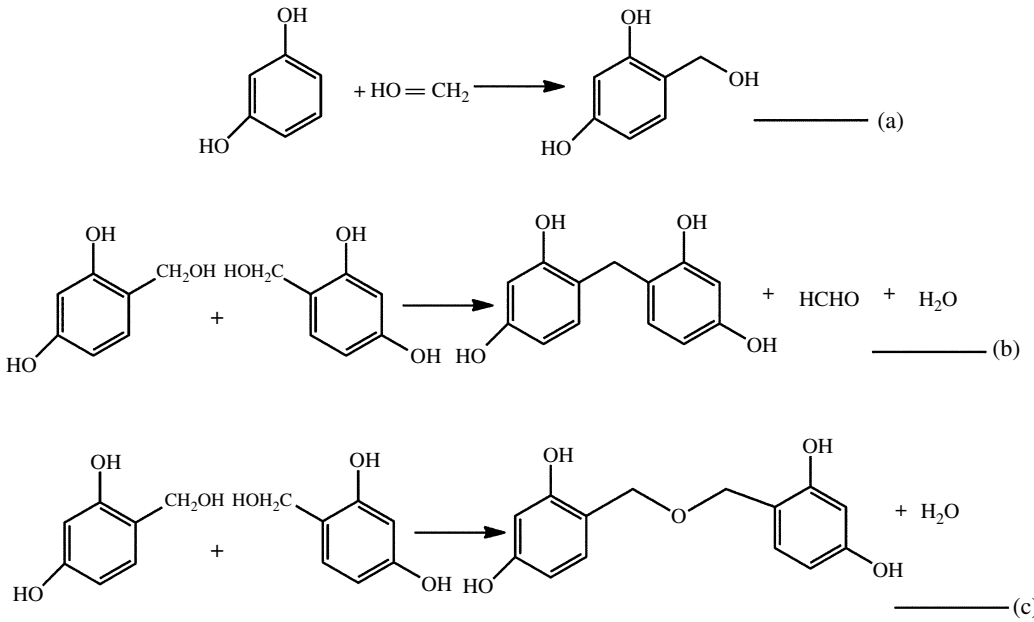


Figure 2.3 Reaction schematics of the preparation of RF gel formation.

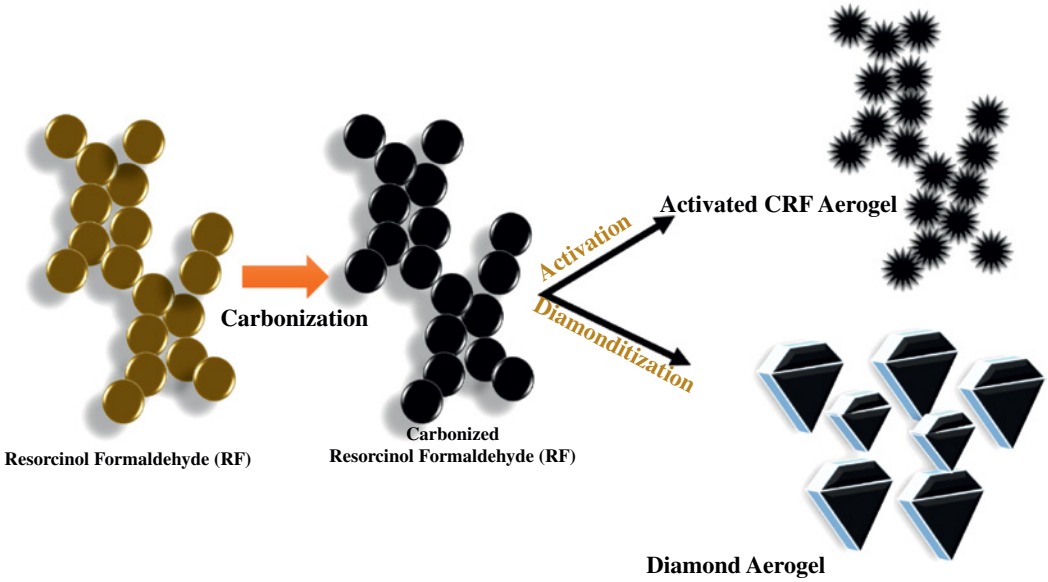


Figure 2.4 Conversion of crystallized amorphous CRF aerogel into diamond aerogel.

treatment of RF aerogel leading to carbonization results in high carbon content in carbonized RF aerogel (CRF) end product under inert atmosphere. However, RF aerogels are usually end up as an amorphous-graphite based and high-porous network. In another study, a simple method has been used to activate CRF to make ultra-high surface area CRF aerogel by activating the carbon skeletons with carbon dioxide. Furthermore, this method was slightly modified to achieve crystalized carbon under high temperatures and pressure to yield CRF aerogel into diamond aerogel with the help of laser-heated diamond anvil cell, as shown in Figure 2.4.

Graphene-based aerogels were first reported in 2009 by Wang et al. following conversion of graphene oxide solution into gel followed by aerogel via ultrasonic-induced gelation, drying, and thermal reduction. In 2010, Worsley et al. simplified CRF aerogel preparation by carbonizing the mixture of RF cross linked graphene oxide aerogel. Later, Zhang et al., used L-ascorbic acid as a reducing agent to produce pure graphene aerogel from graphene oxide in the wet gel followed by drying of the wet gel without heat treatment. Recently, CNTs have been widely used to prepare highly conductive and high surface area carbonaceous aerogels. One such study used surfactant and polyvinyl alcohol to prepare solution containing CNTs using sonication. Further, sonicated polymer composite was crosslinked and stabilized as gel. Upon drying, highly porous CNTs-based aerogel was obtained. Likewise, there have been several aerogels produced using biowaste and biomass, following simple, green, and economically viable approaches. One such aerogel was from the pear waste peel, which was hydrothermally converted to yield highly porous 3D graphene aerogel (GA), as shown in Figure 2.5. This was further used as electrode materials in asymmetric supercapacitor in combination with ionic liquid and organic electrolytes as ion transportation media.

2.2.4 Chalcogenide Aerogel

Yet another class of fascinating electroactive materials is chalcogenide, first converted into aerogel in 2004 by Brock et al., following capping and crosslinking methods at low temperatures. This led

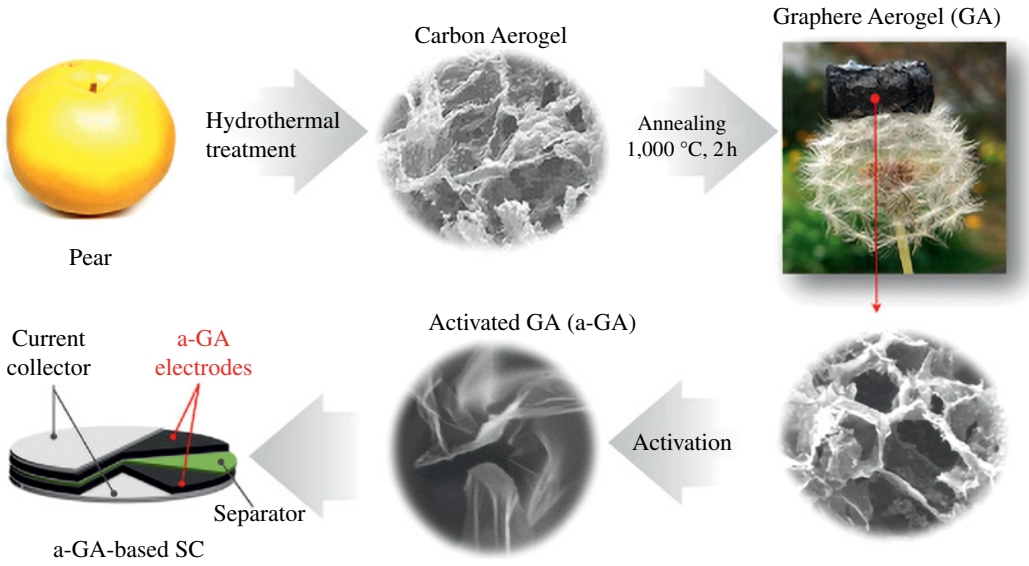


Figure 2.5 Preparation of highly porous graphene aerogel from biomass waste via hydrothermal carbonization, gelation and drying. Myung, Y., et al., 2019 / With permission of American Chemical Society.

to the preparation of different metal-based chalcogenide (Pt, Hg) cluster aerogels with tunable band gap that helped in electrochemical performances. The conversion of chalcogenide in the form of gel subsequent aerogel is governed by the crosslinking step. It is important to control the agglomeration of nanoparticles in the colloidal state before gelation. To achieve this nanoparticle capping is used, following crosslinking of nanoparticles, which leads to gel formation.

2.2.5 Inorganic Gels

The accidental discovery of silica gel led Ebelmen in 1846 to try several other combinations of inorganic gels with mixed end results. Ever since many combinations of inorganic precursors have been tried and tested for stable aerogel formation including alkoxides and metal oxides such as Alumina (Al_2O_3) from aluminum sec-butylate, Silica (SiO_2) from tetramethoxysilane (TMSO), Titania (TiO_2) from tetraisopropoxy titanate, Zirconia (ZrO_2) from zirconium isopropoxide, so on. In all cases, due to the stability and reproducibility in controlling hydrolysis and condensation parameters, researchers extensively used sol-gel method for inorganic aerogel preparation method. Inorganic aerogels yield extreme properties like ultra-low density (~0.003 g cm^{-3}), microporosity (>99.8%), and high surface area (500–1200 m^2 g^{-1}). In all cases, 3D network structure can be controlled during hydrolysis, condensation, and even during wet gel drying step.

2.3 Chemistry and Mechanisms of Aerogels Formation

There are several steps and ways to control ultra-high porosity in 3D network of aerogels. Overall chemistry of aerogel is directly governed by the use of precursors, and the physical properties can be controlled during gelation and drying process. The gel formation initiates via the formation of

primary nanoparticles by means of hydrolysis followed by the condensation of the building block, as shown schematically in Figure 2.5. Gelation stabilizes the network structure and extent of inflation, which finally leads to the removal of liquid phase without agitating the network structure. With external stimuli like temperature and stirring, the hydrolysis and condensation step can be altered. However, due to randomness and competition between these two phenomena, attention needs to be paid to control the particle growth and termination. Finally, methods, time, temperature, and ambience used for drying gel define the porosity and network formation.

2.3.1 Mechanism of Network Formation in Aerogels

2.3.1.1 Sol-Gel Method

The network formation of aerogels involves two primary steps. In the first, the alkoxide precursor undergoes nucleophilic substitution by hydroxyl groups during hydrolysis followed by a crosslinking reactions takes place between M-OH and MI-OR groups. The second step eliminates alcohol or water from M-OH groups during condensation. The crosslinking consumes every possible monomers/nanoparticles available and continuous crosslinking until mechanically stable network structure of aerogel developed. There are two possible mechanisms involved that lead to stable aerogel, as predicted in the following steps:

Step 1: Hydrolysis reaction proceeds following, M-OR + R-OH or $H_2O \rightarrow$ M-OH + R-OH
Step 2: Condensation of two M-OH groups, M-OH + HO-M $\rightarrow$ M-O-M + H_2O
or
Step 2: Condensation M-OH and M-OR groups, M-OR + HO-M $\rightarrow$ M-O-M + R-OH

In the sol-gel method, the rate at which hydrolysis and the condensation takes place is very fast which affects the final aerogel structure; however, it is the critical step to control. A simple way to control the hydrolysis and condensation is to use epoxides to initiate controlled gelation, which in the first step gets pronated followed by ring opening. At this point, the solution's pH may alter depending on the nature of precursor; however, with time condensation rate decreases, which can be used for tailoring the properties of aerogel network. However, in some cases, depending on the end use, aerogels prepared via the sol-gel method may require further calcination to achieve crystallinity, which may affect the collapse of network structures or uniqueness of the aerogel.

2.3.1.2 Self-Assembly Method

Self-assembly method is generally used for the preparation of a large-scale complex network structure originated from molecular level precursors. Precursor that undergoes easy self-assembly such as 1D and 2D nanomaterials can be converted to stable aerogels. The aerogels of metal chalcogenides like PbS, CdS, ZnS, and CdSe, in pristine, blend and composite form can be easily converted using self-assembly method without the help of crosslinking agents. However, this method requires nanoparticle capping to initiate the gelation such as thiolate capping followed by supercritical drying. This method is generally suitable to tune the photo-physical properties in quantum confined building blocks and carbonitrides used in solar cell, photovoltaic and other energy generation and conversion devices. The main advantage of self-assembly method over sol-gel synthetic route is that crystalline aerogels can be directly obtained without following additional heat treatment step. This method can also be easily used to prepare aerogel with abundant functional groups, which find several potential applications in energy conversion and storage applications.

2.3.1.3 Emulsion Method

Emulsion method follows sol-gel procedure where preparation of dispersed phase via sol-gel method tailed by emulsification in a continuous phase. The dispersed phase then proceeds with crosslinking to result in stable microspheres. Aerogels of microspherical nanostructures in the network formation can be achieved by this method. This method can be applied where the monolithic aerogel structure properties are desired and the microspherical nanostructures precursor's properties can be retained. Generally, in the emulsion method the crosslinking medium is oil–water emulsion.

2.3.1.4 3-D Printing

The most advanced and fascinating of all is three-dimensional (3D) printing technology, which is leaving its footprint in every aspect of life. State-of-the-art 3D printing can be used to fabricate extremely lightweight and structure-specific 3D nanostructure end products. 3D printing can be applied to convert a variety of nanomaterials in to stable 3D nanostructure network with size and shape specific dimensions. 3D printing can also be used to multi-layered hetero nanostructure building to impart application specific properties via layer-by-layer coating. With the support of virtual designs and application specific dimensions, 3D printing can be used for porous nanostructure printing of polymeric aerogels, polymer-inorganic composite aerogels, graphene composites, chalcogenide, and their composite printing, which finds huge potential in energy conversion and storage applications. In addition to porous sheets, pyramids, octet, cubes, and honeycomb structures can be directly 3D printed and used for preparation of energy conversion and storage devices.

2.4 Drying Techniques

The most important step in controlling aerogel network structure and their stability during preparation is gel drying. Choice of drying techniques depends on the precursors and the process followed to prepare wet-gels. The drying process defines end structure and becomes an important defining step as primary or parent nano-phase must be conserved and prevented from contraction in gel after the process of drying. The critical step is the formation of liquid–vapor meniscus inside the gel, which makes it challenging to remove the preoccupied pore liquid without affecting the gel-network. During drying, abrupt or uncontrolled elimination of liquid/solvents, which flow out of the surface from interior part of gel, results in the deformation, collapse, or shrinkage of the gel network. The hydroxyl groups at the gel's surface will likely become vulnerable to the contraction, leading to a series of compression loss [12]. As it is generally observed in room temperature, dying of gels leads to complete shrinkage of gel, whereas temperature-assisted drying leads to xerogel. In order to retain predetermined shape, size, microporosity, and properties, wet-gels need to be subjected to special and commercially viable drying techniques such as supercritical drying using affordable conditions (e.g. lyophilization or freeze drying, pressure drying, and organic sublimation with greener and sustainable parameters, which retain desired properties in product aerogel).

2.4.1 Supercritical Drying

Supercritical drying involves removal of preoccupied liquid in the pore or solvent from the crosslinked gel via exchange of solvent above its critical point. To avoid the contraction of porous network structure during drying as a result of capillary forces developed by the surface tension of the pore liquid, it is important to minimize the surface tension effect of occupied solvent. This can

be achieved by converting the pore liquid into a fluid, which minimizes the surface tension to zero. Since the surface tension of the liquid is directly proportional to capillary forces exerting on crosslinked phase, by controlling surface tension, the effect of capillary forces can be easily minimized. With this, capillary forces acting on the pore wall also becomes zero; however, during supercritical drying, both pressure and temperature need to be optimized depending on the liquid in the pore [12]. However, possibly at higher pressure and temperature, dispersed phase rearrangement reactions may constantly take place in the gel, which leads to inducing undesired properties to aerogels. In order to abandon these recombination forces, low-temperature supercritical drying is necessary with the help of liquid carbon dioxide. As liquid carbon dioxide has relatively low critical point compared to other solvents, supercritical drying becomes feasible for stable aerogel production. However, the variation in the solvent miscibility factors associated with the CO_2, the solvent exchange from pore liquid becomes a time-consuming process.

2.4.2 Freeze Drying

On the laboratory scale, freeze drying or lyophilization is generally used to prepare aerogels with controlled porous network. The process of freeze drying or lyophilization involves two steps. First, the liquid in the pores are frozen to solid, followed by removal of solidified liquid via sublimation in vacuum retaining stabilized 3D pore walls. Porous network is prepared via the freeze drying route generally known as cryogel, and this method yields relatively less surface area in comparison to aerogels.

2.4.3 Ambient Pressure Drying

Ambient pressure drying is a relatively economical and reliable method of producing aerogels compared to cost-intensive supercritical drying and freeze-drying techniques. Unlike previously discussed techniques, which are unpredictable in reproducing similar parameters at a large scale aerogel production, ambient pressure drying is simple and low risk [13]. This technique uses simple instrumentation with different approaches to adopt and implement for removal of pore liquid under ambient conditions without altering the crosslinked network. These surfactants have been widely used to reduce capillary forces exerted on the pore walls. With this, the contact angle between the pore wall and the pre-occupied pore liquid prevents the network from collapsing.

2.4.4 Organic Solvent Sublimation Drying

Among recent advancements, the organic solvent sublimation method (OSSD) is an innovative and simple technique. However, this method is suitable for solvents like tert-butanol and acetonitrile having high freezing point and low surface tension and readily undergoes sublimation. This method involves the formation of M–O–M bridges through the surface hydroxyl groups, which preserves the structural integrity of the network in a certain elastic range under the influence of applied vacuum [12]. This proceeds with the increased vacuum that contributes to drying and evaporation of outer surface solvent molecules. This again influences drastic decrease in the bulk temperature of the network structure, which leads to solidification of solvent. Further, continued process reduces surface tension by avoiding solvent crystallization inside pores. This method is suitable for the preparation of crack-free and stable metal-oxide aerogels like Al_2O_3, NiO, Fe_2O_3, and SiO_2 [8]. Therefore, this is an extremely simple and appropriate method for preparing metal-oxide aerogels useful for energy generation, conversion, and storage applications without the use of high pressure and temperature.

2.5 Properties and Characterization

2.5.1 Aerogel Characterization

Depending on the end use aerogel precursors, preparation methods and the desired properties are tuned. During and upon preparation of wet gels and aerogels, various properties are monitored with the help of series of characterization techniques. Physical parameters like porosity, surface area and pore characteristics are measured with nitrogen adsorption measurements in Bruner Emmet Teller (BET) analysis. In some cases, mercury porosimetry is adopted to measure accurate pore size and their distribution. Recent studies have also used nuclear magnetic resonance (NMR) spectroscopy in scattering mode to predict structural features. In this technique, the monoenergetic photons or particles is irradiated on sample specimen, which in turn scatters due to irregularities in the sample. With this, scattered patterns will be evaluated again the structural irregularities of the sample such as cross sectional length, morphology of aerogel and the particle clusters in case composite aerogels [8].

2.5.2 Optical and IR Properties

The optical and IR properties like Rayleigh scattering is widely used for aerogels, which gives confirmative test results toward the blue and ultraviolet spectral region. In the infrared, metal-oxide aerogels show the strong adsorption bands typical for oxide region [12]. These optical and IR characteristics help in deciding aerogel's end applications for example silica aerogels block thermal IR radiation and transmit solar light and thus, such aerogels can be recommended for transparent insulation materials [13].

2.5.3 Thermal Properties

Aerogels are generally characterized for their ultra-low thermal conductivity. Most of the metal-oxide aerogels possess 10–100 times smaller than that of full density metal oxides. Heat transportation in aerogel occurs through solid conduction, gaseous conduction, and infrared radiative transfer. However, highly porous aerogel with large gaseous conduction channels suppress the heat transfer.

2.5.4 Mechanical and Acoustic Properties

Aerogels attain a variety of mechanical properties from brittle, rigidity, and spongy based on their precursors and extent of crosslinking in the network structure. Generally, polymer aerogels are soft and flexible, metal-oxide aerogels are rigid, carbon-based aerogels are spongy in nature. On the other hand, the tortuosity and the elasticity of the air within the pores of the aerogel makes a significant contribution to the sound propagation.

2.6 Applications of Aerogel in Energy Storage and Energy Saving

Aerogels have gained prominence as energy materials in recent years. Since their discovery, aerogels have been especially regarded as good insulating materials for both heat and electricity. Low refractive indices make them favorable in aerospace application. In recent times, due to the

advancements in nanotechnology, aerogels have been used as energy materials directly and indirectly for the preparation of energy conversion and storage devices. Currently, aerogels prepared using polymeric, metal-oxide, carbaneous, and nanocomposite precursors are showing significant potential as electrodes in water splitting, fuel cells, solar cells, supercapacitors, and batteries applications [14]. For energy-related applications, materials should possess tunable pore size, and their distribution along with ion absorption and mobility characteristics. The open porous structure and high surface area in the aerogels would be responsible for furthering electrolytic diffusion, which leads to the molecular adsorption at the solid-liquid interface. These properties make aerogel a suitable choice for the fabrication of high-performance energy storage and conversion devices [15]. The ultra-high surface area in the aerogels would provide large space for dye molecules adsorption on the semiconductor surface, which leads to the diffusion of the electrolyte at the interface. This make dye-sensitized solar cells work efficiently. Similarly, Li-ion and other metal-ion adsorption and propagation in batteries and supercapacitors make aerogels invaluable during device fabrication [16].

2.6.1 Batteries

2.6.1.1 Li–ion Battery

Advancement in the miniature gadgets and flexible devices has greatly increased the need for flexible and ultra-lightweight energy storage devices. Currently, Li-ion battery is ruling the world of electronic gadgets. Therefore, it is essential to fabricate energy storage devices that are lightweight and easy for usage and transport [17]. Currently, commercial lithium ion batteries use porous and hard carbon as anode material such as carbon imparts great cyclic stability and flat intercalation potential of lithium ions to the device at low cost. Extensively used anode material for lithium ion batteries is graphite because of high columbic efficiency, low discharge profile, and outstanding cycle life. However, due to slow lithium ion diffusivity, these carbon anodes suffer poor rate performance.

On the contrary, performance of device can be achieved by decreasing the travel distance of lithium ions inside the carbon matrix using a combination of CNTs and carbon having mesoporous nature. Tunable pore structure and surface area of the aerogel electrodes induce two important features related to charge storage mechanism in Li-ion batteries. This highly porous structure and high surface area of electrodes are the properties that are useful to lower the resistance toward diffusion of ions and the huge number of active sites for lithium-ion intercalation. During the process of charging, in lithium-ion batteries, electrons from cathode move toward anode through an external circuit and lithium ions get diffused from cathode to anode via electrolyte. The redox reaction that happens at charge/discharge steps is responsible for intercalation of lithium ions in the electrodes. Therefore, in this condition carbon-based aerogel, which is prepared from graphene, graphene nanocomposites, and CNTs play important role as anode material in Li-ion batteries. Also, for low-cost device preparation, naturally biomass-based carbon composite would be suitable choice [18].

2.6.1.2 Li-S Battery

Ever since its discovery and commercialization in 1991, the Li-ion battery has been the leading player the energy storage device sector. Thinking beyond Li-ion battery has always been a challenging task for researchers. In recent times, this challenge was overcome by the development of Li-air (or Li-O_2 as O_2 is the fuel) and Li-sulfur (Li-S) batteries. Both the batteries use the same anode material but different active cathode material (S and O_2), which differ in their states of operation

and performance. Theoretically, Li-S batteries have shown superior storage performance as they carry more energy (density three to five times higher) than the Li-ion batteries as they have higher energy density of 2600 Wh kg^{-1} and specific capacity of 1672 mA h g^{-1} [19]. Currently, Li-S are evaluated to be one of the best energy-storage devices because of their ultra-high energy density and high theoretical capacity of sulfur. Natural abundance, low price, and nontoxicity of sulfur are the other important features that makes these batteries more advantageous. Among all other transition metal sulfides, molybdenum disulfide (MoS_2) has a layered structure and high theoretical specific capacity (669 mA h g^{-1}) making it quite functional. The atoms present in MoS_2 are bonded covalently to produce 2D layers, which are assembled together with weak van der Waals forces. These properties make MoS_2 a suitable candidate for intercalation in lithium ions as well as accommodation of large charges. Nowadays, graphene-based aerogels are being adopted as electrodes due to their high porosity, light weight, and electrolytic wettability. These aerogels also help in forming freestanding and self-supporting structures that facilitate the synthesis of binder-free cathodes, which increases the energy density practically. These fascinating graphene-based aerogels can be easily surface modified using nanomaterials and can be adopted for designing stable sulfur cathode. Low cycle performance and rate capability are the major reasons that affect the application of Li-S batteries in various gadgets. These two reasons are mainly due to the dissolution of intermediate, insulation of sulfur, and occurrence of unwanted reactions between lithium anode and polysulfides. In this condition, good candidates to accumulate and immobilize sulfur in a binder-free electrode assembly are graphene-based aerogels due to their mesoporous nature. These mesopores help in increasing the encapsulation of sulfur by allowing the high loading of sulfur. Macropores may interfere in the migration of polysulfides via an increase in the infiltration of electrolyte, but highly porous aerogels play important role in Li-S batteries. Therefore, graphene-based aerogels can be a potential choice for the construction of sulfur cathodes.

In this direction, Li_2S/doped graphene aerogel (GA) cathodes has been prepared and tested for stable cycling performance with initial specific capacities of the cathodes of 720 and 801 mA h g^{-1}, respectively, which are much higher than those of the Li_2S/rGO and the commercial Li_2S-rGO hybrid. The preparation composite was initiated using LiS_2 solution coating on GA, as depicted in first part of Figure 2.6. After careful evaluation (>100 cycles, seen in the second part of Figure 2.6), Li_2S coated N- and B-doped GA cathodes retained ~100% Coulombic efficiency. The presence of B or N causes the decrease in the particle size of Li_2S and thereby a decrease in the energy barrier of Li-S system (Figure 2.7). This enhances the interaction between graphene and lithium polysulfides [20].

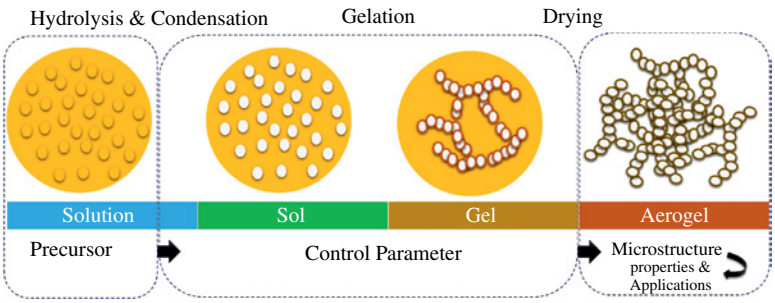


Figure 2.6 Schematic representation for the synthesis of aerogels using sol-gel method with process parameter highlighted.

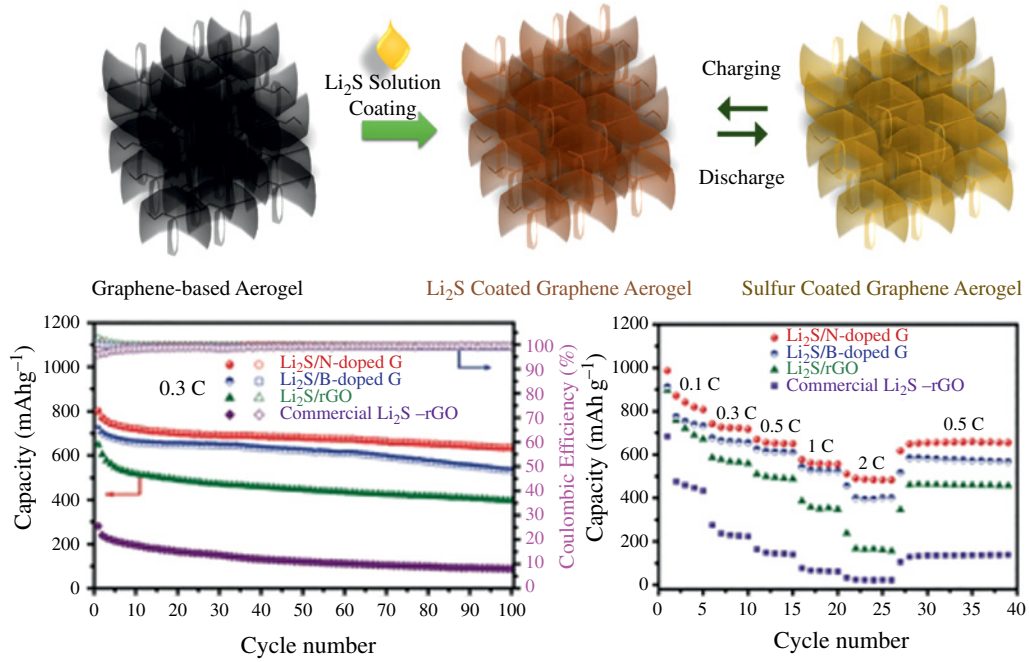


Figure 2.7 Schematic representation of conversion of graphene-based aerogel to sulfur coated graphene aerogel and graphs depicting cycle number vs. capacity (cyclic stability). (Zeitschrift für Physikalische Chemie 232.9-11 (2018): 1647-1674.)

2.6.1.3 Li-air Battery

Li-air batteries, also known as Li-oxygen (Li-O_2) batteries are being regarded as future leaders among all energy storage devices [21]. Currently, there are four variants of Li-air batteries in the developmental stage, among which three of them uses liquid electrolytes namely aqueous electrolyte, fully aprotic liquid electrolyte and a hybrid system, which involves an aprotic electrolyte immersed in the anode and an aqueous electrolyte immersed in the cathode. The fourth chemical architecture in Li-air batteries involves the use of a solid state electrolyte. The chemistry of Li-air battery mainly depends on the electrolyte. However, major attention need to be paid to develop efficient air transportation media through which air enters to act as cathode. For overall device, porous cathode is an air-breathing system that passes O_2 and at the same time keeps the environmental contaminants like CO_2, H_2O, and N_2 out. With this, cathode should provide safe substrate environment toward nucleophilic attack caused by O^{2-} and O_2^{2-} over operating voltage of 2.0–4.0 V. Therefore, cathode should possess adequate electronic conductivity, provide enough space to ionic species, nontoxicity, and light weight at low cost. Therefore, carbon-based cathodes materials have been extensively used in Li-air batteries, but advancement in the designing ultraporous, lightweight aerogels meet several property requirements in addition to conventional carbon electrode provided. Conventional carbon cathode charging above 3.0 V decomposes during the oxidation of Li_2O_2, which further leads to the breakdown of the electrolyte. Carbon-based aerogels are robust and resistant to chemical, thermal, and mechanical instabilities in the cell. In addition to this, graphene aerogels and their composites possess numerous conductive interconnecting points facilitating both ionic migration (intercalation and deintercalation), catalytic active site, storage, and long cyclic stability, which makes them ideal for various energy systems [22].

Further, composite graphene aerogel having electroactive metal/metal oxides such as Ru and RuO_2 helps to improve the cyclic stability and reduce the charge potential [23]. In another study, environmentally benign manganese oxide (MnO_2,) has been incorporated into graphene aerogel to utilize its abundance, high intrinsic activity and low cost with exceptional catholic activity [24]. Also, 2D MnO_2 sheets in aerogel having open channel for oxygen transportation can greatly increase the reaction kinetics and ultrathin substrate, and metal oxide sheets can shorten ion migration path length. These properties make metal-oxides in aerogel composite a better choice in comparison to their bulk materials.

2.6.1.4 Zn-ion Battery

Zinc-ion batteries come close to Li-ion and are still considered to be a promising alternative, having several advantages. The major advantage is low cost of Zn (70 ppm) due to its abundance compared to Li (18 ppm) in the Earth's crust with its small ionic radius (0.74 Å) [25]. Furthermore, low reactivity of zinc with air and water makes it much safer in comparison to Li. On the other hand, manganese oxide has been widely used as cathode material in Zn-ion battery due to its abundance and a high theoretical capacity (308 mA h g^{-1}). However, MnO_2 suffers from inferior cycling sustainability, poor rate performance and low electrical conductivity. In order to reverse the performance of bulk MnO_2, Zinc-ion batteries have been fabricate using polyaniline (PANI)-coated composite aerogel of MnO_2 and rGO (MnO_2/rGO/PANI). Interestingly, the MnO_2 coated by rGO and PANI inhibits the dissolution of manganese, which improves both the cycling stability. In addition to this, presence of dense skeleton in interconnected graphene nanosheets have effectively improved the ion conductivity and their migration [26].

2.6.1.5 Zn-air Battery

Parallel to the Li-air batteries, Zn-air batteries have been successfully applied for commercial use. However, unlike Li-air batteries, Zn-air systems need to go a long way to achieve reliable rechargeability. This is due to Zn-air suffering from large over potentials and low oxygen reversibility. To avoid this, noble-metal-based electrocatalyst like Pt, Ru, and Ir have been used in Zn-air batteries for better electrocatalytic oxygen performance. But noble-metal based electrocatalysts are expensive to adopt commercially. To replace noble-metals, several nonprecious metal have been also tried to catalyze oxygen such as nitrides [27], perovskites [28], metal oxides/sulfides [29], carbons [30], and spinel/mixed oxides [31].

Among all tested, heteroatom-doped carbon materials have shown great potential in fast electron-transfer capacity and tunability for surface chemistry. Nevertheless, lately aerogels of different precursor origin both in pristine carbaneous and composite form have been gaining prominence as electrode material in Zn-air batteries. Also, precisely structure controlled covalent organic framework building blocks synthesized with light elements like N, O, H, P, S, C, and B have attracted significant attention either in foam or aerogel form [32, 33].

In this direction, hierarchical 3D sulfur-modulated porous C_2N aerogels were prepared using a template-free method of creating highly porous network via polymerization of chloroanilic acid. This composite aerogel showed improved mass transport and oxygen release properties maintaining exceptional structural stability in Zn-air batteries [34]. Likewise, composite aerogel of CNTs/cobalt (II/III) oxide/nitrogen-doped CNT (Co_3O_4/N-CNT) was prepared by anchoring bifunctional catalysts inside of an interconnected, conductive CNT aerogel film. As prepared, structurally stable aerogel electrode was used an air electrode in zinc–air batteries. The Zn-air battery with composite aerogel exhibited high charging/discharging stability and low electrical resistance. Additionally, the thin-flexible and controllability of composite aerogel electrode make them ideal candidates for wearable devices/gadgets [35].

2.6.1.6 Na-ion Battery

Advancement in the Li-ion batteries over the years have exploited the maximum theoretical capacity possible in the device form. Now, focus is shifting toward sodium-ion batteries (SIBs), on account of their lower cost and substantially good electrochemical performance. However, SIBs face the challenge of insufficient contact with the current collector or conductive agent and anisotropic expansion of volume that results in the pulverization of active electrode material. This is speculated due to the radius of Na^+ (1.06 Å) is about 1.4 times larger than that of Li^+ (0.76 Å). However, the redox potential of sodium is higher that than of Li, which poses a drawback for Na-ion batteries. Finding a suitable host material having large-sized tunnel structure and fast ion diffusion pathway is a primary concern; Sn- based materials like SnO_2 have been explored due to their high theoretical capacities. In addition, the average working potential of SnO_2 (~0.5 V vs. Li/Li^+) electrodes provide a safe working environment, making it a promising anode for Na-ion batteries. However, intrinsic electrical conductivity of SnO_2 is very poor with a band gap of ~3.6 eV, which makes it very cumbersome to be used as an electrode material in device form. Therefore, great effort has been made to improve both structural stability and electrical conductivity of SnO_2-based electrode material by growing SnO_2 on grapheme, carbon nano fibers, CNTs, and doping of Sb [36, 37].

Further, graphite was earlier considered to be an ideal anode material for Li-ion batteries, but it has proven to be ineffective for Na ions. Some studies have also used red phosphorous as an anode for Na-ion batteries due to their ultra-high theoretical specific capacity of 2595 mAh g^{-1} because of the three-electron transfer mechanism [38]. However, the practical implementation of red phosphorus has hindered due to its tremendous volumetric change of >300% during cycling leading to structural degradation, low electrical conductivity, and unstable solid electrolyte interface. Recent efforts are revealing the use of these aforementioned electroactive agents in aerogel form to improve the electronic conductivity and ionic mobility in Na-ion batteries.

2.6.2 Supercapacitors

2.6.2.1 Electric Double Layer Capacitors

Electric double-layer capacitors (EDLCs) are electrical storage devices that are capable of cycling millions of times, offer higher power density than traditional batteries, and can store significantly high amounts of energy. These devices often use a redox-pseudo-capacitive material of high surface area. The EDLC phenomenon is generally a physical adsorption of charges with minimum interference of redox activity. EDLCs have potential applications in equipment that require high power and fast charging capabilities such as electric vehicles. In the initial years of supercapacitor device making, the use of conducting polymers and metal oxides was common. Later, focus shifted to carbon–carbon and carbon–carbon/composite supercapacitors, which are inexpensive to adopt. Recent trends are showing extensive use of carbon-based aerogels as EDLC materials due to their high charge storage capabilities. Also, aerogels provide tunable porosity (appropriate combination of meso and microporosity), pore structure, high usable surface area for EDL formation, and high electrical conductivity, making them highly desirable electrode for both in symmetric and asymmetric approach. Aerogel can provide improved electrode wettability with suitable combination of nanomaterial, which is missing in conventional carbon electrode where the necessity of wetting agent like surfactant (sodium oleate) and vinyl trimethoxy silane (Vtmos) functional groups have been reported [39–41]. Nowadays, graphene-based aerogels are regarded as an exceptional material for the fabrication of supercapacitors, as they possess high electrical conductivity ($>2\times10^3$ S cm^{-1}), and stable thermal, chemical, and mechanical properties with high theoretical

surface area ($>3000\,m^2\ g^{-1}$). In addition, graphene-based aerogels in combination with nanocomposites can induce high specific capacitance. This makes graphene-based aerogels a superior material for supercapacitor application.

2.6.2.2 Pseudo-capacitors

Pseudo-capacitors are another class of electrical capacitors that undergo Faradaic reactions at the surface of redox-active materials. The redox-active materials used to store charges are redox polymers or transition metal oxides or carbon/metal oxides and/or aerogel/metal oxides. Although Faradaic reactions occur at a slower rate than charge adsorption-desorption that occurs in EDLCs, the pseudo-capacitors' gravimetric capacitance greatly exceeds that of EDLCs. Pseudo-capacitor electrodes are generally constructed by depositing electrically conducting high surface area porous scaffolds. Most pseudo-capacitors utilize transition metal oxides on account of their high intrinsic gravimetric capacitance. Among all oxides, MnO_2 has been extensively studied due to its low cost and environmentally friendly nature and achieved total and gravimetric capacitances up to 600 and $1380\,F\,g^{-1}$, respectively [42]. The composite of single walled carbon nanotube (SWCNT) aerogels with MnO_2 electrodes have been used for the fabrication of super elastic supercapacitors to avoid performance compression [43]. These have shown stable volumetric and gravimetric capacitances across broad scan rates in addition to a long lifetime even under 0% compression [44]. SWCNT aerogels that are coated with graphene recover fully with degradation of electrical conductivity even after compressions of greater than 90%. A study conducted by depositing polypyrrole (PPY) into a highly compressible graphene aerogel was carried out, resulting in significant enhancement in the specific capacitance of graphene aerogel due to the presence of PPY. Therefore, presence of PPY caused the mechanical strength of the graphene cell walls to increase, which led to super elasticity of graphene aerogel [45].

2.6.2.3 Hybrid Capacitors

Hybrid capacitors are capacitors that combine the features of both electrolytic and electrochemical capacitors. Activated carbon or high surface area carbon is widely used in EDLC type devices. Efforts have been made to advance hybrid capacitors by combining the best features of the pseudo-capacitors and EDLC to improve energy density, actuation, and voltages. With the use of various nanomaterial combinations and tailormade material combinations, the energy density of the hybrid capacitors can be improved. However, hybrid supercapacitor still undergoing rigorous test condition to overcome nonlinear parameters. Currently, hybrid supercapacitor has been under investigation to optimize their charge/discharge behaviors, contact resistance problems, and issues associated with current collector and an electrode. However, there have been encouraging results emerging from the use of aerogel base electrodes, which try to resolve the issues discussed earlier such as use of monolith type aerogel, which does not require use of any current collector. In addition to this, hybrid supercapacitors have been tested using transition metal oxide aerogel anode and carbon aerogel cathode along with an electrolyte and a separator. These may help in increasing the overall cell potential, power density, and energy of an energy storage system.

2.6.3 Fuel Cells

Lately, fuel cells are regaining their importance after years of negligence. Researchers are now realizing the importance of fuel cells over batteries, as they can be used in plug-n-use mode. Fuel cells are also getting prominence as many reports are emerging with the details of self-discharging

effect in various types of batteries, which make them unreliable both from an economic and environmental point of view. Among all fuel cells, proton exchange membrane fuel cells (PEMFC) directly convert chemical energy to electrical energy via chemical reactions using hydrogen as fuel at low operating temperatures. The power density of PEMFC is quite high and is superior to existing internal combustion engines. Commercialization of PEMFCs have seen limited success owing to their high production cost. Cost reduction in PEMFCs can be achieved by the use of efficient, low cost, and reliable, supported, or unsupported catalyst. At present, fuel cells use noble-metal based catalysts like Pt, and cost reduction for fuel cell device will only begin with the use of low-cost nonprecious metal electrocatalyst. In order to achieve good metal dispersion, it is desired for the carbon supported material to have a high surface area and a mesoporous structure for enabling the diffusion of products and reactants. For this purpose, numerous allotropic carbon materials have been explored as supports such as graphene, CNT, carbon aerogels, and carbon black. Carbon black is the most widely used support material, as it has a low cost and is easily available. However, it has a large number of micropores that limit diffusion of products and reactants, which results in potential loss affecting the overall cell performance. To overcome this limitation, the use of aerogels as support in PEMFC catalyst has been adopted. Further, studies have shown that the use of pure SnO_2 as a support enhances the durability of PEMFC owing to their corrosion resistance properties [46]. In another study, use of niobium and antimony-doped SnO_2 in composition with aerogel as catalysts support for PEMFC improved electronic conductivity and surface area [47].

On the other hand, direct methanol fuel cells (DMFCs) has attracted great interest among the scientific community over PEMFC due to their advantages of reduced system weight, high energy efficiency, low emissions, compactness, complexity, easy transportation, and storage of fuels. However, DMFC too have several drawback that hinder their commercialization. These factors include high costs of noble metal catalysts, low electrocatalytic activity of catalysts for methanol oxidation, lack of suitable proton-exchange membrane, fuel loss, and susceptibility of the catalysts for methanol oxidation reaction. In DMFCs, Pt and Pb have been widely used electrocatalysts due to the unique electrocatalytic activity toward methanol oxidation reaction. However, Pt is costly and have poor poison tolerance when used in DMFCs and these two factors hinders the commercialization of DMFCs. There have been attempts to replace Pt-based catalysts of which Rhodium (Rh) nanocrystals has attracted great interest due to its greater resistance to byproducts (mainly CO) in alkaline medium with exceptional methanol oxidation activity [48]. Recently, use of aerogels in combination with different electroactive coating are in progress to reduce the cost of electrocatalysts.

2.6.4 Electrocatalytic Hydrogen Evolution

Hydrogen production in large scale is overdue; this attempt is waiting for radical breakthrough. In this direction, hydrogen evolution reaction (HER) is an important step in the electrolysis of water where hydrogen is generated by the electrocatalytic reduction of hydrogen ions. The use of efficient HER catalysts is essential as they accelerate the reaction rate and improve energy conversion efficiency. Studies in HER catalyst are essential because they help to accelerate the reaction rate and improve the energy conversion efficiency. In this field also platinum (Pt), its alloys, and other noble metals have been widely used for HER. This is because noble metal enjoys low overpotential and high energy conversion ability. However, noble metals are expensive, which hinders their large-scale industrial applications.

Transition metals are abundantly available and also cheap. Some of their chemical compounds have structural properties similar to that of platinum. Due to this, transition metals have been considered as a viable substitute of Pt in the HER process. Recent studies showed that 2D transition metal chalcogenides such as MoS_2, $MoSe_2$, WS_2, and WSe_2 exhibit excellent electrocatalytic performance for HER [49]. For example, the characteristic edge sulfur atoms in MoS_2 was utilized for HER, which poses similar catalytic activities to that of the enzymatic centers [50]. The activity of MoSe strongly depended on is active selenium edge sites which can be activated by converting MoSe in to the nanoscale through which maximum active site can be utilized. In addition to these activities, MoSe can be enhanced by the formation of composite with carbon materials such as carbon, CNTs, carbon nanofibers (CNFs), activated carbon, graphene, carbon aerogels (CAs), and carbon fiber cloth, which impart certain unique physico-chemical properties and are considered to be ideal substrates for several non-noble metal oxides and sulfides such as $MOSe_2$ [51].

2.6.5 Electrocatalytic Oxygen Reduction

Fuel cells, owing to their high fuel efficiency and zero emissions at the point of operation, represent one of the most promising energy conversion technologies. For widespread commercialization of PEMFCs and DMFCs, the most important challenge is to reduce electrocatalyst cost by replacing noble-metal-based efficient oxygen reduction reaction (ORR) catalysts at the cathode. Therefore, searching for efficient and less expensive nonplatinum catalysts (NPC) on suitable substrate such as graphene have attracted great interest. The efficient ORR catalyst is a long-awaited task for researchers, and it requires consideration of greener and sustainable options. Among several reported carbon-based electrocatalysts, nitrogen-doped graphene materials show promising ORR performance in alkaline electrolyte but suffer from relatively low activity in acid medium, making them less competitive than commercial Pt/C catalyst. The introduction of transition metals such as Fe, Co etc., into the graphene matrix results in metal−nitrogen−carbon (M−N−C)-based NPC, which showed promising ORR activity in acid media. Based on the above considerations, high ORR performance materials have been considered with Co−N moieties decorated graphene aerogel (Co−N−GA), which has unique hierarchical pores, large surface area, and an abundant of potential Co−N active sites [52].

In a recent study, PANI has been used as pore-forming agent to aid in the self-assembly of graphene oxide (GO) species into a highly porous hydrogel structure, which was further converted to aerogel with unique chemical structure [53]. The fabricated graphene aerogel was used as a catalyst to achieve several merits, including (i) to maximize the Co−N active sites density useful for fuel utilization and ionic mobility, (ii) to maximize the utilization of active sites to increase the energy and power density, and (iii) to facilitate good transfer of reactant and product that affect overall performance. With this, the composite Aerogel (Co−N−GA) exhibited impressive electrochemical performance in acid medium. Owing to aerogels uniqueness, tunable properties, and ability to host numerous electroactive site of different metal-origins, serious efforts and time has been devoted to searching for suitable combination of systems in the form of aerogels. Already, several core-shell materials have been constructed using metallic cores such as Co, Fe, Fe_3C nanoparticles, and carbon shells have been considered to be promising substitutes for noble metals [54]. Recent advancements also show the use of aerogels-based electrocatalysts in microfluidic fuel cell (MFC) with N-doped ionothermal carbon as host aerogel cathode for efficient ORRs, as shown in Figure 2.8 [55, 56].

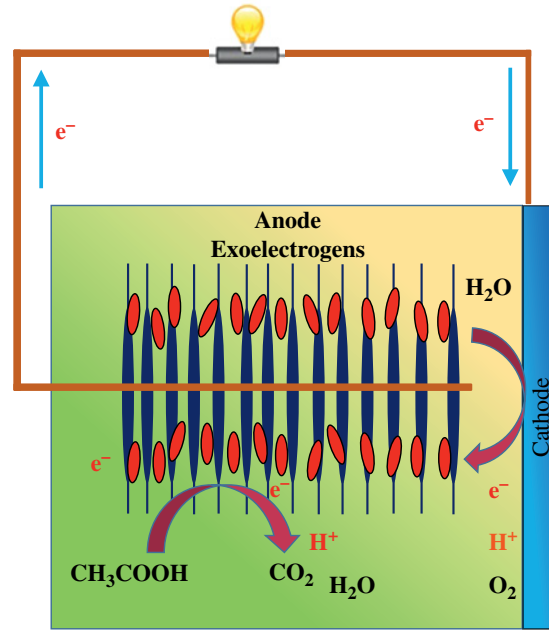


Figure 2.8 N-doped ionothermal carbon aerogel used as cathode for efficient oxygen reduction reactions in microfluidic fuel cell (MFC).

2.7 Summary and Future Prospects

In summary, aerogels are gaining prominence as efficient energy material playing different role as substrate, support, host, and active material itself. Recent understanding and evaluation reports on several aspect of energy generation, conversion, and storage devices reveal new insights into the workings of electrocatalysts. Researchers are gaining more details on the working mechanisms of devices, such as effect of operating voltage, long cycle life, no memory effect, low self-discharge, and high power or energy densities in various electrochemical devices. As there is a huge demand for energy storage/conversion devices in the ever-increasing market from flexible watches, to mobile phone, and personal laptops, which require high energy density, up to the heavy electrical vehicles that are waiting for high-power density output in the same set of devices, demand for high-performance energy material is ever growing. In this changing time, owing to their adoptability and tunability, aerogels will keep growing as potential and ideal energy material stock.

Acknowledgments

SKN greatly acknowledge Jain University Management Research Project Grant (JU/MRP/CNMS/18/2022), the Ministry of Science and Technology, NANOMISSION GRANT (SR/NM/NT-1073/2016), DST INSPIRE faculty grant (IFA12-CH-84) and DST-Technology Mission Division (DST/TMD/HFC/2K18/124G) Government of India for financial support. Talent Attraction Program was funded by the Community of Madrid Spain (2017-T1/AMB5610) for financial support.

References

1 Pierre, A.C. (2011). History of aerogels. In: *Aerogels Handbook*, 3–18. New York: Springer.
2 Ziegler, C., Wolf, A., Liu, W. et al. (2017). Modern inorganic aerogels. *Angew. Chem. Int. Ed.* 56: 13200–13221.
3 Du, A., Zhou, B., Zhang, Z., and Shen, J. (2013). A special material or a new state of matter: a review and reconsideration of the aerogel. *Materials* 6 (3): 941–968.
4 Tao, Y., Endo, M., and Kaneko, K. (2008). A review of synthesis and nanopore structures of organic polymer aerogels and carbon aerogels. *Recent Patents Chem. Eng.* 1: 192–200.
5 Brock, S.L. and Yu, H. (2011). Chalcogenide aerogels. In: *Aerogels Handbook*, 367–384. New York, NY: Springer.
6 Sultanov, F.R., Pei, S.S.S., Auyelkhankyzy, M. et al. (2014). Aerogels based on graphene oxide with addition of carbon nanotubes: synthesis and properties. *Euras. Chem. Technol. J.* 16: 265–269.
7 Sam, D.K., Sam, E.K., Durairaj, A. et al. (2020). Synthesis of biomass-based carbon aerogels in energy and sustainability. *Carbohydr. Res.* 491: 107986.
8 Pierre, A.C. and Pajonk, G.M. (2002). Chemistry of aerogels and their applications. *Chem. Rev.* 102: 11.
9 Fricke, J. (1992). Aerogels and their applications. *J. Non-Cryst. Solids* 356–362.
10 Torikai, D., Suzuki, C.K., Shimizu, H. et al. (1994). Comparison of high-purity H_2/O_2 and LPG/O_2 flame-fused silica glasses from sol-gel silica powder. *J. Non-Cryst. Solids* 179: 328–334.
11 Fricke, J. and Tillotson, T. (1997). Aerogels: production, characterization, and applications. *Thin Solid Films* 297: 212–223.
12 Hüsing, N. and Schubert, U. (1998). Aerogels–airy materials: chemistry, structure, and properties. *Angew. Chem. Int. Ed.* 37: 22–45.
13 Burger, T., Emmerling, A., Fricke, J., and Weth, M. (1997). Aerogels – production, properties and applications. *KONA* 15: 32–42.
14 Xu, X., Zhou, J., Nagaraju, D.H. et al. (2015). Flexible, highly graphitized carbon aerogels based on bacterial cellulose/lignin: catalyst-free synthesis and its application in energy storage devices. *Adv. Funct. Mater.* 1–10.
15 Alwin, S. and Sahaya Shajan, X. (2020). Aerogels: promising nanostructured materials for energy conversion and storage applications. *Mater. Renew. Sustain. Energy* 7–27.
16 Karaaslan, M.A., Kadla, J.F., and Ko, F.K. (2016). Lignin-based aerogels. *Lignin Polym. Compos.* 67–93.
17 Mirzaeian, M. and Hall, P.J. (2009). Preparation of controlled porosity carbon aerogels for energy storage in rechargeable lithium oxygen batteries. *Electrochim. Acta* 54: 7444–7451.
18 Biener, J., Stadermann, M., Suss, M. et al. (2011). Advanced carbon aerogels for energy applications. *Energy Environ. Sci.* 4: 656.
19 Li, P., Deng, J., Li, J. et al. (2019). Hollow graphene spheres coated separator as an efficient trap for soluble polysulfides in Li-S battery. *Ceram. Int.* 45 (10): 13219–13224.
20 Wang, C., Fu, Q., and Wen, D. (2018). Functionalization of graphene aerogels and their applications in energy storage and conversion. *Z. Phys. Chem.* 232: 1647–1674.
21 Christensen, J., Albertus, P., Sanchez-Carrera, R.S. et al. (2012, 2012). A critical review of Li/air batteries. *J. Electrochem. Soc.* 159 (2): R1–R30.
22 Mao, J., Iocozzia, J., Huang, J. et al. (2013). Graphene aerogels for efficient energy storage and conversion. *Energy Environ. Sci.* 11 (4): 1–3.
23 Jiang, J., He, P., Tong, S. et al. (2016). Ruthenium functionalized graphene aerogels with hierarchical and three-dimensional porosity as a free-standing cathode for rechargeable lithium-oxygen batteries. *NPG Asia Mater.* 8 (1): 1–7.

24 Chen, S., Liu, G., Yadegari, H. et al. (2012). Three-dimensional MnO_2 ultrathin nanosheet aerogel for high-performance Li-O_2 batteries. *J. Mater. Chem. A* 00: 1–3.

25 Cang, R., Ye, K., Zhu, K. et al. (2020). Organic 3D interconnected graphene aerogel as cathode materials for high-performance aqueous zinc ion battery. *J. Energy Chem.* 45: 52–58.

26 Mao, J., Wu, F.F., Shi, W.H. et al. (2019). Preparation of polyaniline-coated composite aerogel of MnO_2 and reduced graphene oxide for high-performance zinc-ion battery. *Chin. J. Polym. Sci.* 1–8.

27 Meng, F., Zhong, H., Bao, D. et al. (2016). In situ coupling of strung Co_4N and intertwined N—C fibers toward free-standing bifunctional cathode for robust, efficient, and flexible Zn-air batteries. *J. Am. Chem. Soc.* 138: 10226–10231.

28 Petrie, J.R., Cooper, V.R., Freeland, J.W. et al. (2016). Enhanced bifunctional oxygen catalysis in strained $LaNiO_3$ perovskites. *J. Am. Chem. Soc.* 138: 2488–2491.

29 Li, G., Wang, X., Fu, J. et al. (2016). Pomegranate-inspired design of highly active and durable bifunctional electrocatalysts for rechargeable metal-air batteries. *Angew. Chem. Int. Ed.* 55: 4977–4982.

30 Zhang, J., Zhao, Z., Xia, Z., and Dai, L. (2015). A metal-free bifunctional electrocatalyst for oxygen reduction and oxygen evolution reactions. *Nat. Nanotechnol.* 10: 444–452.

31 Jung, J.I., Risch, M., Park, S. et al. (2016). Optimizing nanoparticle perovskite for bifunctional oxygen electrocatalysis. *Energy Environ. Sci.* 9: 176–183.

32 Sakaushi, K. and Antonietti, M. (2015). Carbon- and nitrogen-based organic frameworks. *Acc. Chem. Res.* 48: 1591–1600.

33 Xu, Y., Jin, S., Xu, H. et al. (2013). Conjugated microporous polymers: design, synthesis and application. *Chem. Soc. Rev.* 42: 8012–8031.

34 Shinde, S.S., Lee, C.H., Yu, J.Y. et al. (2018). Hierarchically designed 3D holey C_2N aerogels as bifunctional oxygen electrodes for flexible and rechargeable Zn-Air batteries. *ACS Nano* 12 (1): 596–608.

35 Zeng, S., Chen, H., Wang, H. et al. (2017). Crosslinked carbon nanotube aerogel films decorated with cobalt oxides for flexible rechargeable Zn–air batteries. *Small* 13 (29): 1700518.

36 Zhang, B., Zheng, Q.B., Huang, Z.D. et al. (2011). SnO_2-graphene-carbon nanotube mixture for anode material with improved rate capacities. *Carbon* 49: 4524–4534.

37 Tanjew, M. and Haase, M. (2000). Wet-chemical synthesis of doped nanoparticles: optical properties of oxygen-deficient and antimony-doped colloidal SnO_2. *J. Phys. Chem. B* 104: 8430–8437.

38 Liu, S., Feng, J., Bian, X. et al. (2017). A controlled red phosphorus@ Ni–P core@ shell nanostructure as an ultralong cycle-life and superior high-rate anode for sodium-ion batteries. *Energy Environ. Sci.* 10: 1222–1233.

39 Fang, B., Wei, Y.Z., Suzuki, K., and Kumagai, M. (2005). Surface modification of carbonaceous materials for EDLCs application. *Electrochim. Acta* 50: 3616–3621.

40 Wei, Y.Z., Fang, B., Iwasa, S., and Kumagai, M. (2005). A novel electrode material for electric double-layer capacitors. *J. Power Sources* 141: 386–391.

41 Fang, B. and Binder, L. (2006). A modified activated carbon aerogel for high-energy storage in electric double layer capacitors. *J. Power Sources* 163: 616–622.

42 Zhang, L.L. and Zhao, X.S. (2009). Carbon-based materials as supercapacitor electrodes. *Chem. Soc. Rev.* 38: 2520–2531.

43 Cheng, X., Gui, X., Lin, Z. et al. (2015). Three-dimensional alpha-Fe_2O_3/carbon nanotube sponges as flexible supercapacitor electrodes. *J. Mater. Chem. A* 3: 20927–20934.

44 Bryning, M.B., Milkie, D.E., Islam, M.F. et al. (2007). Carbon nanotube aerogels. *Adv. Mater.* 19: 661–664.

45 Peng, L. (2018). Highly compressible graphene/polypyrrole aerogel for superelastic pseudocapacitors. *Fullerenes, Nanotubes Carbon Nanostruct.* 26: 23–29.

46 Takabatake, Y., Noda, Z., Lyth, S.M. et al. (2014). Cycle durability of metal oxide supports for PEFC electrocatalysts. *Int. J. Hydrogen Energy* 39: 5074–5082.

47 Ozouf, G. and Beauger, C. (2016). Niobium-and antimony-doped tin dioxide aerogels as new catalyst supports for PEM fuel cells. *J. Mater. Sci.* 51: 5305–5320.

48 Li, M., Jiang, Q., Yan, M. et al. (2018). Three-dimensional boron-and nitrogen-codoped graphene aerogel-supported Pt nanoparticles as highly active electrocatalysts for methanol oxidation reaction. *ACS Sustain. Chem. Eng.* 6: 6644–6653.

49 Liao, L., Zhu, J., Bian, X. et al. (2013). MoS_2 formed on mesoporous graphene as a highly active catalyst for hydrogen evolution. *Adv. Funct. Mater.* 23: 5326–5333.

50 Zhou, W., Jia, J., Lu, J. et al. (2016). Recent developments of carbon-based electrocatalysts for hydrogen evolution reaction. *Nano Energy* 28: 29–43.

51 Mao, S., Wen, Z., Ci, S. et al. (2015). Perpendicularly oriented $MoSe_2$/graphene nanosheets as advanced electrocatalysts for hydrogen evolution. *Small* 11: 414–419.

52 Fu, X., Choi, J.Y., Zamani, P. et al. (2016). Co–N decorated hierarchically porous graphene aerogel for efficient oxygen reduction reaction in acid. *ACS Appl. Mater. Interfaces* 8: 6488–6495.

53 Wu, G., Johnston, C.M., Mack, N.H. et al. (2011). Synthesis – structure–performance correlation for polyaniline – Me–C non-precious metal cathode catalysts for oxygen reduction in fuel cells. *J. Mater. Chem.* 21: 11392–11405.

54 Deng, D., Yu, L., Chen, X. et al. (2013). Iron encapsulated within pod-like carbon nanotubes for oxygen reduction reaction. *Angew. Chem.* 125: 389–393.

55 Shaari, N. and Kamarudin, S.K. (2019). Current status, opportunities, and challenges in fuel cell catalytic application of aerogels. *Int. J. Energy Res.* 43: 2447–2467.

56 Schneider, M. and Baiker, A. (2006). Aerogels in catalysis. *Catal. Rev. Sci. Eng.* 37 (4): 515–556.

3

Metal Aerogels for Energy Storage and Conversion

Ran Du

School of Materials Science & Engineering, Beijing Institute of Technology, No. 5, South Street, Zhongguancun, Haidian District, Beijing, 100081, PR China

3.1 Introduction of Metal Aerogels

Metal aerogels are derived from their wet-gel counterparts by critical-point drying (CPD) or freeze-drying (FD), where a post-treatment may be required. Featuring merits of the aerogels (e.g. large specific surface areas [SSAs], porous networks, and monolithic structures) and the metals (e.g. excellent catalytic activity, high electrical conductivity, and adjustable plasmonic properties), MAs have emerged as a new class of porous materials in the last decade [1–3]. Nanoporous metals (e.g. nanoporous gold) or metal foams (e.g. commercial copper foams and nickel foams), which may also feature a self-supported and porous structure similar to aerogels, have been studied for more than half a century ago. However, due to the lack of a wet-gel state during synthesis, they are not regarded as metal aerogels according to the definition from IUPAC, where an aerogel is defined as "gel comprised of a microporous solid in which the dispersed phase is a gas" [4]. Therefore, in this context, only the materials produced from the wet gels or directly from the corresponding solutions (i.e. the freeze-casting method) will be discussed. Readers may refer to several reviews for nanoporous metals and/or metal foams [5–7].

Over the last decade, a wide range of metals has been engineered into the aerogel form (Figure 3.1) [3]. The first metal aerogel was claimed in 2009 by Leventis et al. from Missouri University of Science and Technology [8], where an iron (Fe) aerogel was obtained through pyrolysis of a resorcinol-formaldehyde (RF) and iron oxide (FeO_x) composite aerogel in argon based on a smelting process (i.e. $Fe_2O_3 + C \rightarrow Fe + CO_2$). This method has further been extended to the cobalt (Co), nickel (Ni), tin (Sn), and copper (Cu) by the same group [9]. Further expanding the carbothermal reaction to the magnesiothermic reaction (i.e. magnesium [Mg]-assisted reduction), aerogels made up of tantalum (Ta), titanium (Ti), and silicon (Si) were also acquired accordingly [10–12]. However, the reaction proceeding at a high temperature can seriously affect the porous structure of original aerogels and induce fusion of small-size metals, retarding delicate structure design and manipulation. Additionally, inert metals – which do not easily form metal oxides – are unlikely to be converted into aerogels in this way.

In 2009, Eychmüller's group in Technische Universität Dresden reported the direct assembly of several noble metal nanoparticles (NPs) into hydrogels, thus deriving the corresponding aerogels

Aerogels for Energy Saving and Storage, First Edition. Edited by Meldin Mathew, Hanna J. Maria, Ange Nzihou, and Sabu Thomas.
© 2024 John Wiley & Sons, Inc. Published 2024 by John Wiley & Sons, Inc.

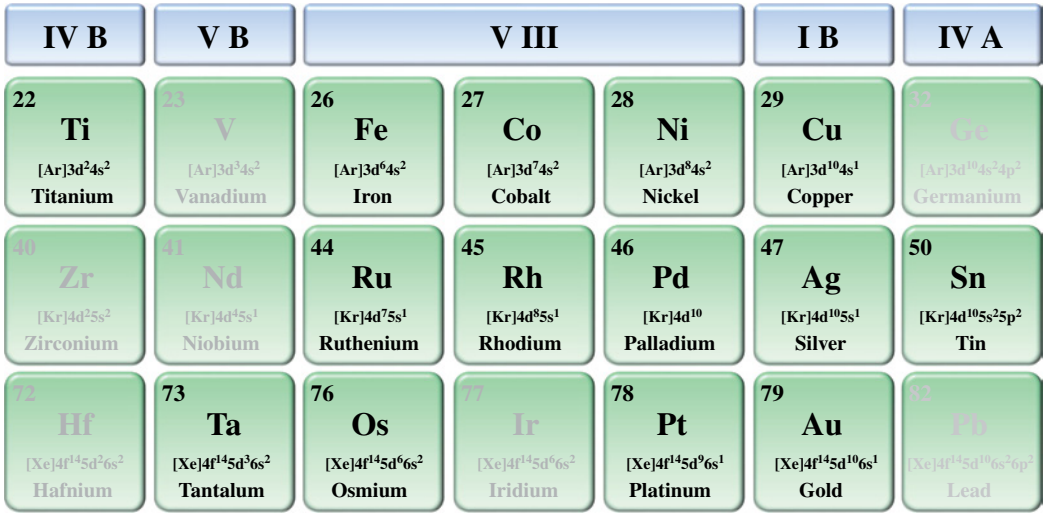


Figure 3.1 Currently available elements for single-component metal aerogels (the black ones).

based on gold (Au), silver (Ag), and platinum (Pt) after following CPD [13]. These milestone studies pioneers the solution-based fabrication of metal aerogels similar to the conventional sol-gel process in other systems, opening up a new direction of the on-target design of a broad spectrum of MAs with adjustable nanostructures. Instead of using pre-fabricated metal NPs, it is also feasible to directly convert metal salts into gels by controlling the number of reductants [14, 15]. Following these pioneering works, a series of MAs based on palladium (Pd), ruthenium (Ru), rhodium (Rh), osmium (Os), Ni, and their combinations have been extensively explored by various research groups, developing a promising category of materials holding unprecedented potential in electrocatalysis and beyond [1, 7].

A few years later, as initiated by Yu's group, highly concentrated aqueous solutions of metal nanowires (NWs) and metal NPs were directly converted into the corresponding MAs by freeze-casting strategy [16, 17]. This approach combines the gelation and drying process in one step, facilitating preparation procedures. Particularly, aerogels assembled from metal NWs can usually retain a regular shape and a better mechanical strength compared to the MAs produced by previous strategies, enabling them to explore new application space.

The aforementioned three-type strategies constitute the main fabrication methods, while the latter two have received more attention. Particularly, the mild reaction conditions and highly tunable reaction parameters featured by the second-class method endow great versatility for material design, which is beneficial for tailoring desirable applications. In this regard, the following discussions are restricted to MAs derived from wet gels and metal precursor solutions, where the former is emphasized.

Despite the bright prospect of metal aerogels, the current research is far from mature. Suffering from the ambiguous understanding of the gel formation mechanisms, which considerably deviate from that for conventional gel systems, big challenges remain for precise controlling, tailoring, as well as expanding chemical compositions and multiscale structures of MAs for task-specific applications. This chapter strives to summarize typical characterization techniques, synthesis methodologies, and energy-related applications of MAs so as to depict a landscape for this young yet promising field and direct its development.

3.2 Characterizations

Metal aerogels can be characterized with properties common to other aerogels. To avoid duplication, the focus will be centered on the pitfalls and misunderstandings of typical characterizations and special techniques that are dominantly applied for MAs.

3.2.1 Densities and Pore Structures

In comparison with conventional materials, aerogels are known for their lower densities and highly porous structures. Regarding MAs, their mechanical fragileness and the high plasticity necessitate special attention for characterizations.

Generally, with respect to other aerogels, MAs usually hold much larger densities (several tens to several hundred $cm^3\ g^{-1}$), which is attributed to the high densities of bulk metals (e.g. $19.32\times10^3\,kg\,m^{-3}$ for gold vs. ~$2.2\times10^3\,kg\,m^{-3}$ for carbon). Because of the mechanical fragileness and the irregular shape of most MAs, a precise density is hard to obtain due to the difficulty in operation. Certain works determine the volume by inserting aerogel pieces into regular-shaped vials [18]. However, an overcompression may lead to aerogels' severe deformation because of their high plasticity [19]. Simultaneously, less compression may leave significant unoccupied space between those aerogel pieces, both of which can lead to a large deviation. Therefore, it is recommended to estimate the density by performing with self-supported MAs of sufficiently large volume, and the final results should be averaged from several samples.

The porous structure of aerogels is usually determined by the gas sorption test, particularly with nitrogen as the probe. As for MAs, the much larger atomic weights of metals compared to other elements usually lead to much lower SSAs and specific pore volumes (undetectable to several tens of $m^2\ g^{-1}$ in general for SSAs and $<1\,cm^3\ g^{-1}$ for pore volumes). From the operation aspect, during the degas step, a low temperature (e.g. 323 K) is required to avoid the fusion of metal nanostructures. Additionally, for low-surface-area MAs, the nitrogen can be replaced by krypton (Kr) to acquire a more accurate SSA because of the lower saturation pressure of Kr (≈2.63 Torr for supercooled liquid krypton at 77 K) compared to that of N_2 (≈760 Torr at 77 K) [6]. From the data analysis aspect, some works normalized the surface area by the moles (i.e. molar surface area) to eliminate the difference of atomic weights between metals and other elements, yielding values of 100–20 000 $m^2\ mol^{-1}$ [19, 20]. However, to make a comparison with other aerogels, the surface area normalized by the mass (i.e. SSA) must also be reported. Regarding pore analysis, density-functional theory (DFT) is frequently used for estimating the pore size distribution (PSD) at the micro- and mesopore regions, and the single-point pore volume (e.g. at p/p_0 of 0.99) is usually applied for acquiring the total pore volume. However, we must note that the "total pore volume" obtained from the gas sorption test cannot reflect the contribution of all large pores. Instead, the specific pore volume contributed from all-size pores can be deduced from the following equation [7]

$$V_{tot} = 1/\rho_a - 1/\rho_b \tag{3.1}$$

where ρ_a and ρ_b represent the apparent density of the aerogel and the density of the bulk material, respectively. Then the porosity (ϕ) can be derived accordingly by [21]

$$\phi = \left(1 - \rho_a/\rho_b\right)\times100\% \tag{3.2}$$

3.2.2 Morphologies

The characterization of morphologies by scanning electron microscopy (SEM) and transmission electron microscopy (TEM) is quite mature, which can reveal microscale structures of broad aerogels. As for MAs, optical imaging has been developed recently [19, 22], which allows gels to rapidly image in real time in a large dimension. Therefore, by combining SEM, TEM, and optical imaging, it is feasible to reveal the gel structure at all length scales.

3.2.3 Element Distribution

Although the large atomic weight of metals renders a low SSA and specific volume for MAs, it allows to accurately discern different elements with respect to aerogels made of light elements (e.g. boron and nitrogen). To examine the alloy state or special structures, energy-dispersive X-ray spectroscopy (EDXS) or electron energy-loss spectroscopy (EELS) performed in high-angle annular dark-field scanning transmission electron microscopy (HAADF-STEM) is usually adopted [23, 24]. In this way, it is possible to unveil the spatially resolved chemical composition down to a nanometer scale.

3.2.4 Crystalline Structure

To characterize the crystalline structures of MAs, powder X-ray diffraction (PXRD) is frequently applied. It can determine the element or alloying state from the peak position as well as the peak shape, reflect the crystalline degree from the peak intensity, and estimate the domain size of crystals from the full width at half maximum (FWHM) of peaks [19]. Besides, performing the selected-area electron diffraction (SAED) in TEM provides crystalline information at the microscale. Recently, extended X-ray-absorption fine structure (EXAFS) spectroscopy has also been explored to probe short-range structures of MAs, capable of providing information down to sub-nanometers [25].

3.2.5 Mechanical Properties

Because of the fragileness of most reported MAs, mechanical properties are difficult to determine by routine characterization techniques. Limited examples are shown with freeze-casting-prepared MAs, where Young's moduli are determined to be a few kilopascals, and large, irreversible deformation is frequently observed [26, 27]. This is further qualitatively verified by a recent work, where the compression of several noble metals can cause large, irreversible deformation (>98%) and induce a dark-to-shining transition owing to the regained "mirror surfaces" [19]. In a recent study, the mechanical properties of an Au-Ag aerogel were explored by piezo-rheology and colloidal-probe atomic force microscope (AFM), respectively [28]. A shear storage modulus of around 1–3 kPa was obtained with a homemade piezo-rheology, while an elastic modulus of 7–10 kPa was acquired with colloidal-probe AFM based on a 20 μm silica bead. However, the two techniques are rarely used in the gel system; hence both the equipment cost and the data reliability need further attention.

3.2.6 Time-Lapse Techniques

Developing time-lapse characterization methods – particularly in situ techniques – is also essential to disclose metal gels' formation mechanisms. Previously, the time-lapse technique was mainly based on TEM observation. The reaction system is sampled at a different stage [29]. However, the ex-situ characterization cannot reflect the real state of the sample during synthesis. Recently,

several in situ techniques including ultraviolet-visible (UV-vis) spectra, dynamic light scattering (DLS), and optical microscopy have been developed, strongly facilitating the mechanistic study of the gelation process that will be described in the next section [19, 30].

3.3 Synthesis Methodologies

Amongst more than 90 metals in the periodic table, only around 10% have been converted to aerogels and most of which are based on noble metals, presumably due to their higher stability compared to other metals. The key challenges remain in the unconventional formation behavior of metal gels and the lack of effective synthesis strategies, retarding the composition and the structure control. Because the gelation step is the core process for the aerogel manipulation; hence, this section will mainly focus on the gelation process. To facilitate understanding, the current opinions for the gelation mechanisms will be outlined before introducing respective synthesis strategies.

3.3.1 Mechanistic Insights

The formation of metal gels is largely associated with the assembly process of the corresponding metal NPs. An early study has explored the formation process of gold aggregates, where the assembly mode of spherical gold NPs was claimed to be mainly determined by the ratio of electrostatic potential (V_{elec}) and the van der Waals potential (V_{vdw}) according to the Derjaguin-Landau-Vervey-Overbeek (DLVO) theory [31]. As shown in Figure 3.2a, the long-range V_{elec} suppresses the aggregation of NPs while the short-range V_{vdw} promotes the approaching of NPs. After the formation of a dimer, the symmetry of the NP reduces, thus leading to an anisotropic electrostatic repulsion force (F_{elec}) and an isotropic repulsion force (F_{vdw}) experience by the third NP. Therefore, the dimension of the resulted aggregates will be increased from 1D, 2D, to 3D with an increasing fraction of isotropic F_{vdw}. Although this study can guide the design of gold aggregates, there is still a large gap between small aggregates and macroscopic gels.

Recently, the gelation mechanism of metal gels has been studied in depth [19]. As seen in Figure 3.2b,c, a gold gel was induced by the addition of ammonium fluoride. In sharp contrast with the conventional gelation process, where the resulting gel holds a similar volume compared to the original solution, a precipitation-like phenomenon was observed for the formation of gold gels. Combining with the in situ time-lapse optical imaging and DLS (Figure 3.2d,e), the gelation process can be described as a gravity-driven sediment process, as shown in Figure 3.2c. Upon addition of salts, metal NPs are quickly transformed into aggregates, followed by the gravity-driven sediment due to the high density of bulk metals. Along with the continuous concentrating of aggregates at the bottom, the concentration reaches the gelation threshold, and eventually, a monolithic gel film is yielded. Because of such an unconventional gelation behavior, gels can form under an initial precursor concentration of only 0.002–0.04 mg ml^{-1}, much less than that required for other gels (e.g. typically 1–10 mg ml^{-1} for nano carbons). Moreover, by examining various salts, the assembly mechanism at the microscope has been proposed (Figure 3.2f). Salt cations strip the negative-charged ligands on the NPs (i.e. sodium citrate), and salt anions replace the position of original ligands (i.e. through a ligand exchange process), jointly producing naked NPs and inducing the fusion of those high-surface-energy NPs to form gel networks. By controlling the kinds of applied salts, F_{elec} and F_{vdw} can be tuned, thus enabling to control of the growth direction and to adjust the ligament size of gold aerogels across a wide-scale range (ca. 6.9–113.7 nm). However, the observed phenomenon is not pronounced for other metal systems, presumably due to the different

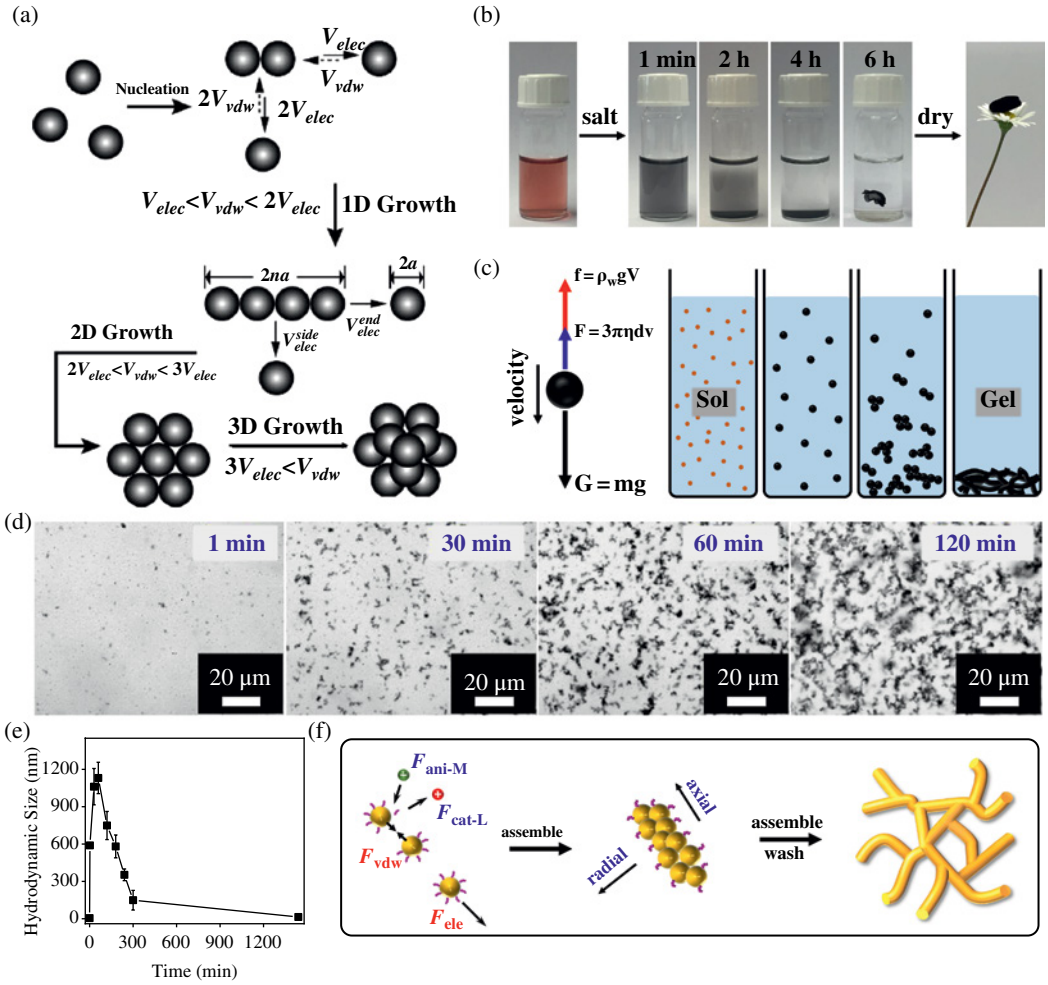


Figure 3.2 Analysis of the gelation process for metal gels. (a) The DLVO theory analysis of the gold NP assembly [31] / With permission of John Wiley & Sons. (b–e) Experimental analysis of the gelation process. (b–c) Photographs and the proposed model for the gelation process of gold hydrogels. (d–f) Time-lapse in situ (d) optical microscopy and (e) dynamic light scattering characterizations of the gelation of gold hydrogels. (f) Proposed microscale assembly mechanisms of gold hydrogels [19] / American Association for the Advancement of Science / Licensed under CC BY 4.0.

thermodynamic and kinetic parameters of different metals. In addition, because of the extremely complicated environment in the gel system, the proposed mechanism needs to be further verified.

After having an impression of the gelation process, the respective synthesis methods will be introduced. Current strategies are summarized in Figure 3.3a, i.e. (i) two-step gelation (from metal salts to NPs, and to wet gels) plus drying, (ii) one-step gelation (from metal salts to wet gels) plus drying, and (iii) freeze casting (from metal NPs to aerogels). Sometimes, a post-synthesis process is also included for constructing complex-structured aerogels. During synthesis, it is essential to separately engineer important gradients during fabrication, including precursors, reductants, initiators, ligands, solvents, and external fields, so as to accelerate the fabrication process and acquire MAs with desirable chemistry and structures (Figure 3.3b) [2]. All these ideas will be discussed in the following sections.

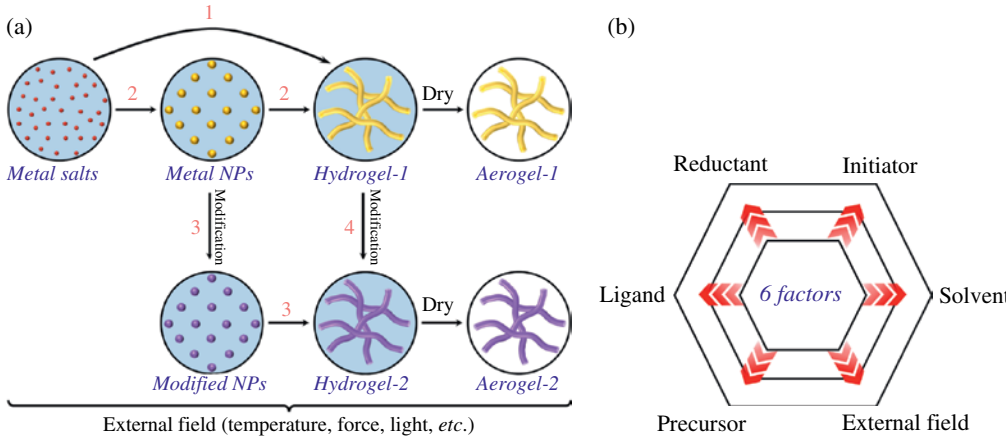


Figure 3.3 (a) Summarized strategies for synthesizing metal aerogels and (b) important factors involved in the metal aerogel fabrication [2] / With permission of Elsevier.

3.3.2 Two-Step Gelation

The gelation step is the core process for deriving metal aerogels, which will be comprehensively discussed in Sections 3.3.2–3.3.4. The two-step gelation, i.e. the sequential formation of the metal NPs and the wet gels, is the earliest and the most adopted strategy. In this method, the NPs and the wet-gel formation are decoupled, which allows to separately engineer NPs and modulate their assembly modes by bottom-up design. In this section, the design of precursors, reductants, and the initiation process will be sequentially introduced.

3.3.2.1 Precursors

At the very beginning, common capping-agent-stabilized spherical metal NPs with an average size of several nanometers are prepared in aqueous solutions as precursors for assembling the corresponding wet gels [13, 32]. However, only fused nanowire-like networks were produced, and undesirable organic ligands are difficult to be fully eliminated, failing to generate clean metal gels with desirable structures.

The cleanliness issue has been addressed by two approaches. On the one hand, by using metal salts as precursors, they are directly converted into wet gels by using specific amounts of inorganic reductants (e.g. $NaBH_4$) without involving organic ligands [14, 15]. On the other hand, assisted by sequential laser ablation and fragmentation, the produced gold and palladium NPs can be stabilized by a trace amount of inorganic salts (e.g. 1 mM NaOH) and thus serve as precursors for preparing surface-clean metal aerogels [33].

To control the nanoscale structure or design multiscale structures, it is natural to come up with the idea of predesigning metal NPs. This endeavor was attempted in 2013, where metal hydrogels were assembled from pre-synthesized Au–Ag, Pd–Ag, and Pt–Ag alloy nanoshells induced by sodium chloride (Figure 3.4a) [34]. Later on, by performing a galvanic replacement reaction (GRR) on as-obtained nickel NPs, the obtained hollow Pd-Ni nanospheres (average size of ~30 nm) were used for the following assembly (Figure 3.4b,c) [35]. In another study, highly concentrated Pt nanocubes and nanospheres were produced in organic phase stabilized by oleylamine and oleic acid (the concentration of the metal salt $c_M > 150$ mM, which is much higher than $c_M < 1$ mM for water-phase synthesis), allowing to form gels with specific microstructures [18].

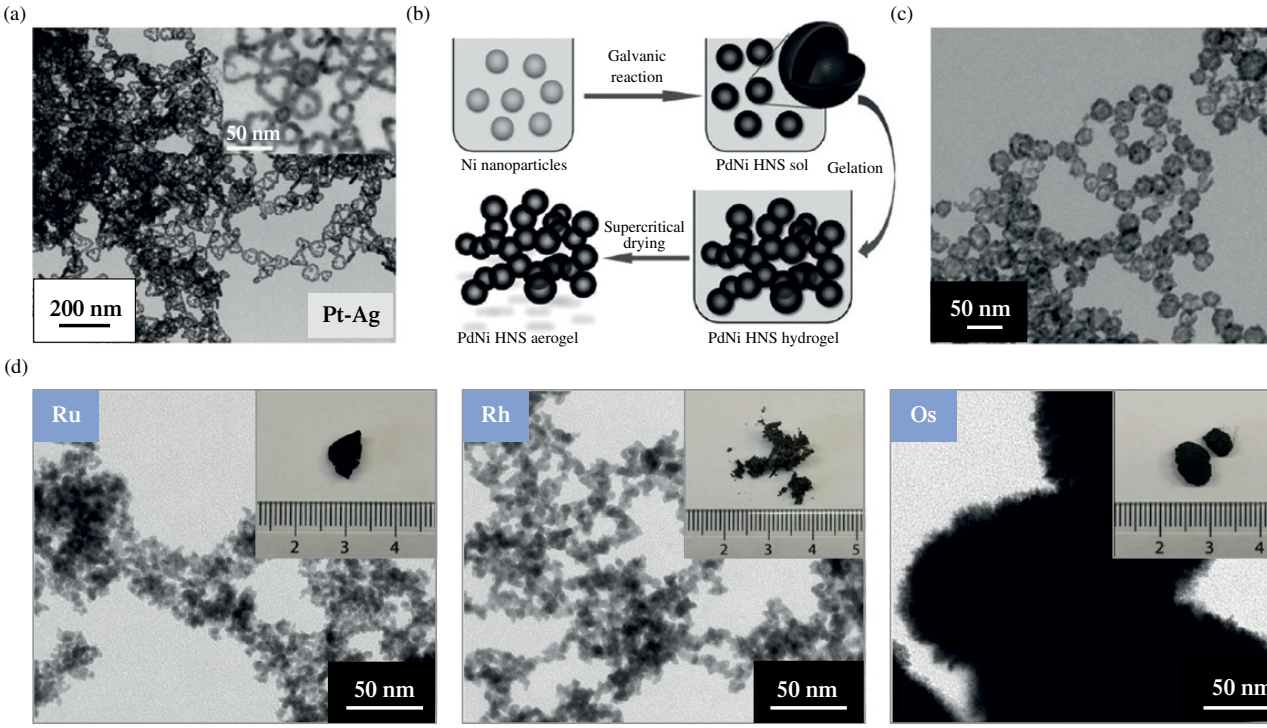


Figure 3.4 Engineering precursors. (a) TEM image of the Pt/Ag aerogels assembled from the corresponding individual nanoshells (the inset) [34] / With permission of John Wiley & Sons. (b–c) Schematic illustration for preparing Pd-Ni aerogels based on Pd-Ni hollow nanospheres [35] / With permission o John Wiley & Sons. (d) TEM images and photographs (insets) of Ru, Rh, and Os aerogels. The photograph of the Rh shows the product after the spontaneou combustion of Rh aerogels in the air [15] / Springer Nature.

3.3.2.2 Reductants

To produce pure metallic metal gels from metal salts, a reducing process is a prerequisite. Sodium borohydride and an array of other reductants (e.g. carbon monoxide (CO) [36, 37], hydrazine [18], dimethylamine borane [38], and Na_2HPO_2 [39]) have been explored, while the mechanisms of those reductants were not comprehensively revealed until very recently. This section will highlight multiple functions of reductants and discuss the underlying mechanisms, so as to offer a comprehensive understanding of the roles played by reductants in metal gel fabrication.

Most gel fabrication processes proceed solely in a liquid phase, where $NaBH_4$ is dominantly adopted as a reductant. In the beginning, $NaBH_4$ was only used as a reducing agent to convert metal salts into NPs (the ratio of $NaBH_4$ to metal salts [R/M] was around 4) [13]. Interestingly, Liu et al. discovered that a small amount of $NaBH_4$ (R/M = 1.5) can trigger the formation of Pd gels (c_M = 0.2 mM) without extra initiators [14]. However, the long gelation time (3–17 days) is problematic. Several follow-up works have explored different reductants (e.g. hydrazine, dimethylamine borane, and Na_2HPO_2) and reaction conditions (e.g. c_M or temperature) for inducing gelation with sole reductants [18, 38, 39] while the underlying gelation mechanisms remain unclear.

Very recently, the roles played by reductants have been deciphered [15]. Experimental results and theoretical calculations suggest that the functions of reductants are highly dependent on R/M, where reducing, stabilizing, and destabilizing functions sequentially appear with increasing R/M. Particularly, a large R/M by using $NaBH_4$ as reductant showed an unprecedented destabilization ability, enabling to produce several new kinds of metal aerogels based on ruthenium (Ru), rhodium (Rh), and osmium (Os) (Figure 3.4d). Details can be found in Section 3.3.3.

In addition to common reductants, gas-phase reductants have also been explored in recent years. By bubbling CO into an acetic acid solution of palladium acetylacetonate ($Pd(acac)_2$) and trioctylphosphine oxide (i.e. the ligand) followed by aging at 313 K, monolithic Pd gels were obtained [36]. Intriguingly, the resulting gel is structured from 2D nanosheets, which can be ascribed to the coordination function of either CO or the acetic acid solvents [36, 37].

3.3.2.3 Initiation

Initiation is the most critical process for gel fabrication. During this process, various factors, including initiators, ligands, solvents, and feeding process, can affect the gelation behavior as well as the structures/properties of the obtained MAs.

3.3.2.3.1 Initiators In the last decade, a wide range of initiating tactics have been developed. Confining the pH of Au NP solution within 11.9–12.4 in the presence of D-glucose is the first reported method to induce gelation [32]. Afterward, H_2O_2 has been proposed as initiators to oxidize the surface ligands capped on metal NPs, yielding hydrogels in 1–4 weeks [13]. Another efficient oxidant (tetranitromethane, $C[NO_2]_4$) has also been adopted, capable of producing silver-shell-based hydrogels with tunable optical features in 4–12 hours (Figure 3.5a) and giving rise to an SSA of up to 160 $m^2\ g^{-1}$ [20]. Aside from oxidants, a poor solvent (e.g. ethanol), which is miscible with water, can also induce the assembly of metal NPs [13], which is similar to the recrystallization process. However, a highly concentrated metal NP solution (c_M of ca. 10 mM) usually prepared by an expensive ultracentrifugation process is required for the above initiation methods, largely raising the production cost. Additionally, the destabilization power of the aforementioned initiators seems moderate, only working well with weakly stabilized NPs (e.g. with sodium citrate as stabilizers) and limited metal systems (only demonstrated for Au, Ag, Pd, and Pt).

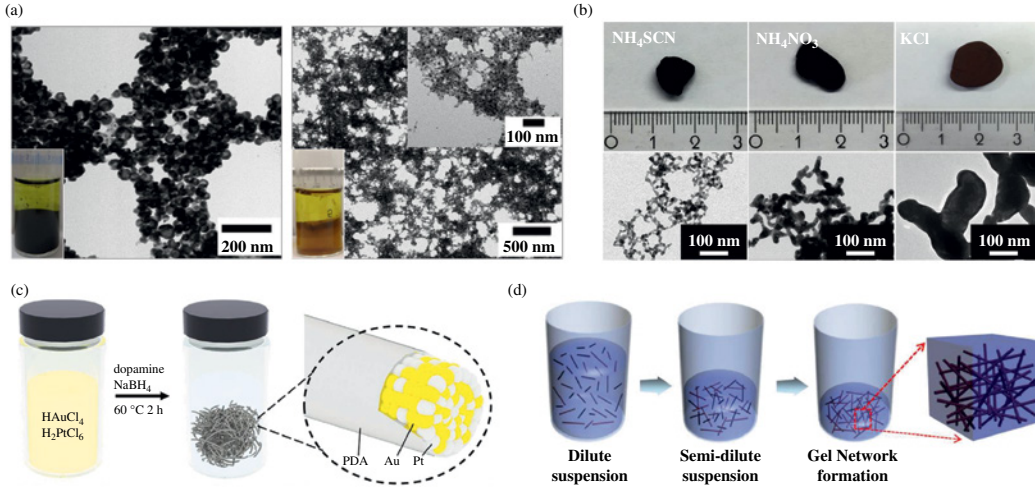


Figure 3.5 Designing initiation methods. (a) Opaque and transparent Ag hydrogels synthesized by using different amounts of $C(NO_2)_4$ (oxidant/thiolate is 2.2 for the opaque one and 7.7 for the transparent one) [20]. (b) Typical photographs and TEM images of Au gels with different ligament sizes as fabricated by the indicated salts [19]. (c) Schematic illustration of the gel formation by the dopamine-induced assembly [40]. (d) Schematic illustration of the gel formation by controlled evaporation [42].

Salts contribute to another category of initiators. Initiated in 2013, Arachchige's group synthesized various bimetallic alloy gels (Au/Ag, Pd/Ag, Pt/Ag) by rotatory evaporation or adding sodium chloride (8–250 mmol l^{-1}), both of which can considerably increase the ionic strength and thus destabilize the metal NP colloidal solutions [34]. In another study, by employing a trace amount of Ca^{2+} (10^{-3} to 10^{-6} M) as initiators, ultracentrifugation-derived citrate-stabilized Pd NPs ($c_M = 10$ mM) have been converted into the corresponding gels [41]. As elaborated in Section 3.3.1, by tuning the interactions between metal NPs and ions with different salts, gold gels featuring adjustable ligament size were obtained (Figure 3.5b), realizing broad manipulation of diverse gel parameters (e.g. ligament sizes, pore volumes, SSAs, and mechanical strength) [19].

Dopamine-initiated destabilization, although the mechanism is not clear, can efficiently gelate metal NPs. Particularly, gold gels with a ligament size of as small as 5–6 nm can be obtained in 6–72 hours from dilute Au NP solutions ($c_M = 0.2$ mM), giving rise to a SSA of as high as 50.1 m^2 g^{-1} [29]. However, the involved initiator (i.e. dopamine) cannot be completely removed (Figure 3.5c) [40].

Apart from introducing additives, modulating the temperature field can also induce gelation. Mild evaporation at 313 K has been demonstrated to gelate 1D metal colloids due to the promoted physical crosslinking between anisotropic building blocks (Figure 3.5d) [42]. The resulting silver NW aerogels exhibited an SSA of 5.5 m^2 g^{-1} and a very high electrical conductivity of 3×10^{-6} S m^{-1}. The inclusion of a Cu NW synthesis step can further extend the method to produce Cu NW gels directly from copper salt precursors [44]. The obtained aerogels held a density as low as 3.79 mg cm^{-3} and electrical conductivity of up to $>1 \times 10^6$ S m^{-1}. Besides elevating the temperature, a low-temperature field can also cause gel formation, which will be elaborated in Section 3.3.7.

3.3.2.3.2 Ligands Specific ligands are known to strongly interact with metals. Thus, during the initiation process, the introduction of appropriate ligands can modify the gelation behavior and dictate diverse gel parameters (e.g. ligament size, dimension, and facet).

However, a critical challenge is that "efficient" ligands can shield the metal surfaces and retard the connection of building blocks, discouraging the formation of metal gels. This issue has been solved in a recent work, where an excessive amount of $NaBH_4$ was found to efficiently destabilize various ligand-capped gold NPs (e.g. with polyvinylpyrrolidone (PVP), hexadecyltrimethylammonium bromide (CTAB), and sodium deoxycholate (NaDC) as ligands) [15]. Attributed to the ligand-promoted anisotropic growth, the ligament size of gold gels can be modulated across 4.8–27.9 nm and a record-high SSA of 59.8 m^2 g^{-1} was achieved. Recently, Xue et al. found that by applying a appropriate common ligands (sodium citrates) to Pt-Bi binary systems can efficiently tuning the dimension of nano-building blocks (0D nanospheres, 1D nanowires, 2D nanosheets, and 3D microspheres) [43]. However, the molecular-level mechanism is under investigation.

Aside from structure manipulation, ligands may also serve as active sites to promote the assembly of metal building blocks. As illustrated in Figure 3.6a, after the exchange with thiol-group-functionalized glutamic acid derivatives, surface-functionalized Pt NWs assembled to a supramolecular metal gel in several organic solvents driven by the strong hydrogen-bonding between capping ligands [45].

3.3.2.3.3 Solvents The functions of solvents are beyond solvation during the gel formation process. On the one hand, the introduction of a poor solvent (e.g. ethanol) in concentrated aqueous solutions of metal NPs can induce the gelation, although it takes a long synthesis period of more than 1 week [13]. On the other hand, solvents can also function as ligands. A recent study

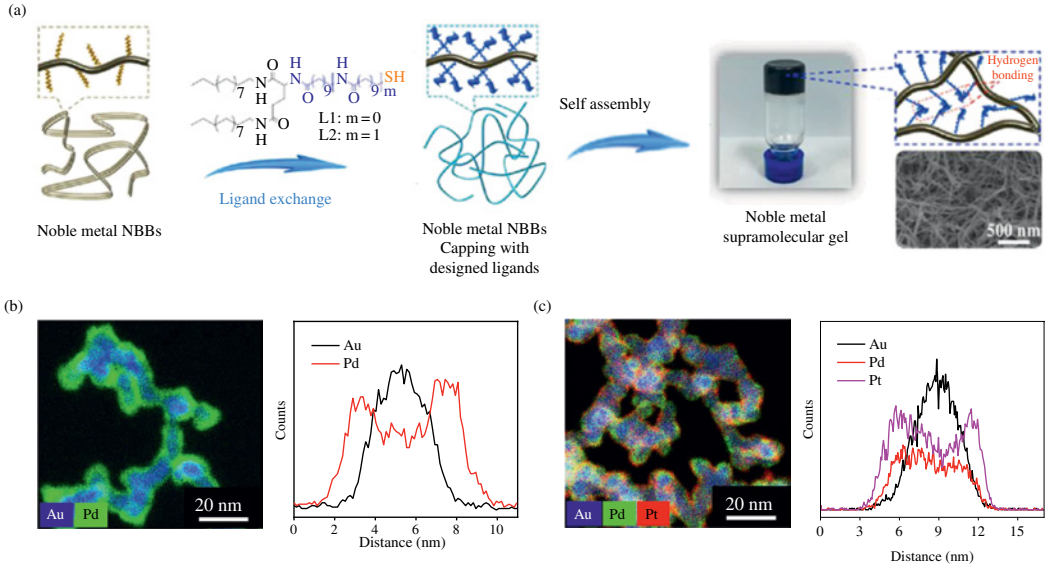


Figure 3.6 Designing ligands and the feeding order of the reactants. (a) Fabrication of noble metal supramolecular gels based on Pt NWs by the self-assembly of capping ligands [45] / With permission of American Chemical Society. (b–c) Core-shell structured Au-Pd and Au-Pd-Pt aerogels. Element mappings and the corresponding line scans [19] / American Association for the Advancement of Science / Licensed under CC BY 4.0.

showed that carboxylic-acid-based solvents with different-length alkyl groups show different affinities to palladium, thus influencing the morphologies of the resulting Pd gels [37]. Particularly, Pd gels assembled from micrometer-sized 2D sheets can be acquired in acetic acid or propionic acid.

3.3.2.3.4 Feeding Process Instead of tediously adjusting reaction parameters, the design of the feeding process can serve as a simple and efficient way to alter the initiation process as well as the gel parameters. One of the most impressive examples is the so-called "dynamic shelling approach (DSA)" proposed recently [19, 22]. Conventionally, multi-metallic gels were prepared by either destabilizing mixed metal NPs [13, 46] or by one-step reducing mixed metal salts [14, 15], while often the element distribution is random. To control the distribution, the feeding process was changed to adding the second (and/or third) metal salts immediately after initiating the gelation of the first metal. In this way, the second metal (the shell) can nucleate and conformally grow on the semi-network of the first metal (the core) due to the reduced energy cost, thereby dynamically forming the core-shell-structured multi-metallic gels with tunable shell thickness (Figure 3.6b,c). The DSA strategy obtained great success for various Au-cored multi-metallic gels. It mostly saved the time/cost compared to other methods. At the same time, the feasibility of broad systems needs further tests. Nevertheless, it points out a new direction to facilely prepare specifically structured metal aerogels in a dynamic process.

3.3.3 One-Step Gelation

To avoid the tedious procedures required for two-step methods and to reduce the introduction of impurities, one-step gelation has been developed in 2013 [14], where metal salts are directly transformed into gels triggered by a specific amount of reductants. Briefly, Pd-Pt gels were facilely prepared from the dilute metal salt solution ($c_M = 0.2$ mM) at room temperature by adding 1.5 equiv. of $NaBH_4$. Although the underlying mechanisms were not deeply explored, this extremely simple method has been adopted by a series of following works, yielding diverse metal aerogels based on Au, Pd, Pt, M-Cu (M = Ir, Pd, Pt, and Au), Bi-doped Ni, etc. [24, 47, 48].

To promote the understanding of the gelation process, a recent work unveiled the roles of reductants experimentally and theoretically [15]. Taking an Au NP sol as an example, it was found that electrolyte-type reductants sequentially exhibited the reducing function, stabilization function, and destabilization function with increasing R/M (Figure 3.7a). At a low R/M, all reductants are consumed during reducing gold salts to Au NPs, where the formed bare Au NPs tend to aggregate driven by their high surface energy; at a medium R/M, extra unreacted reductant anions can stabilize the as-formed Au NPs and thus produce stable NP sols; at a high R/M, a large number of left reductant ions will induce enhanced salting-out effect and trigger the assembly of NPs into a gel.

Particularly, an excess amount of $NaBH_4$ (e.g. R/M = 100) displayed an unprecedented destabilization ability, capable of gelating diverse metals (Au, Ag, Pd, Pt, Ru, Rh, Os, and diverse alloys) and various-ligands-stabilized gold NPs (ligands: PVP, CTAB, NaDC, trisodium citrates, etc.). To explain this phenomenon, the underlying chemistry was deciphered. As shown in Figure 3.7b, (i) BH_4^- anions replace citrates capped on Au NPs due to their high binding energy with Au; (ii) BH_4^- anions are catalytically decomposed by Au NPs, forming BO_2^- anions and hydrogen gas; (iii) the loosely bonded BO_2^- anions easily detach the gold surface and generate bare NPs, while H_2 bubbles promote the collisions between NPs, which jointly promote the formation of gels.

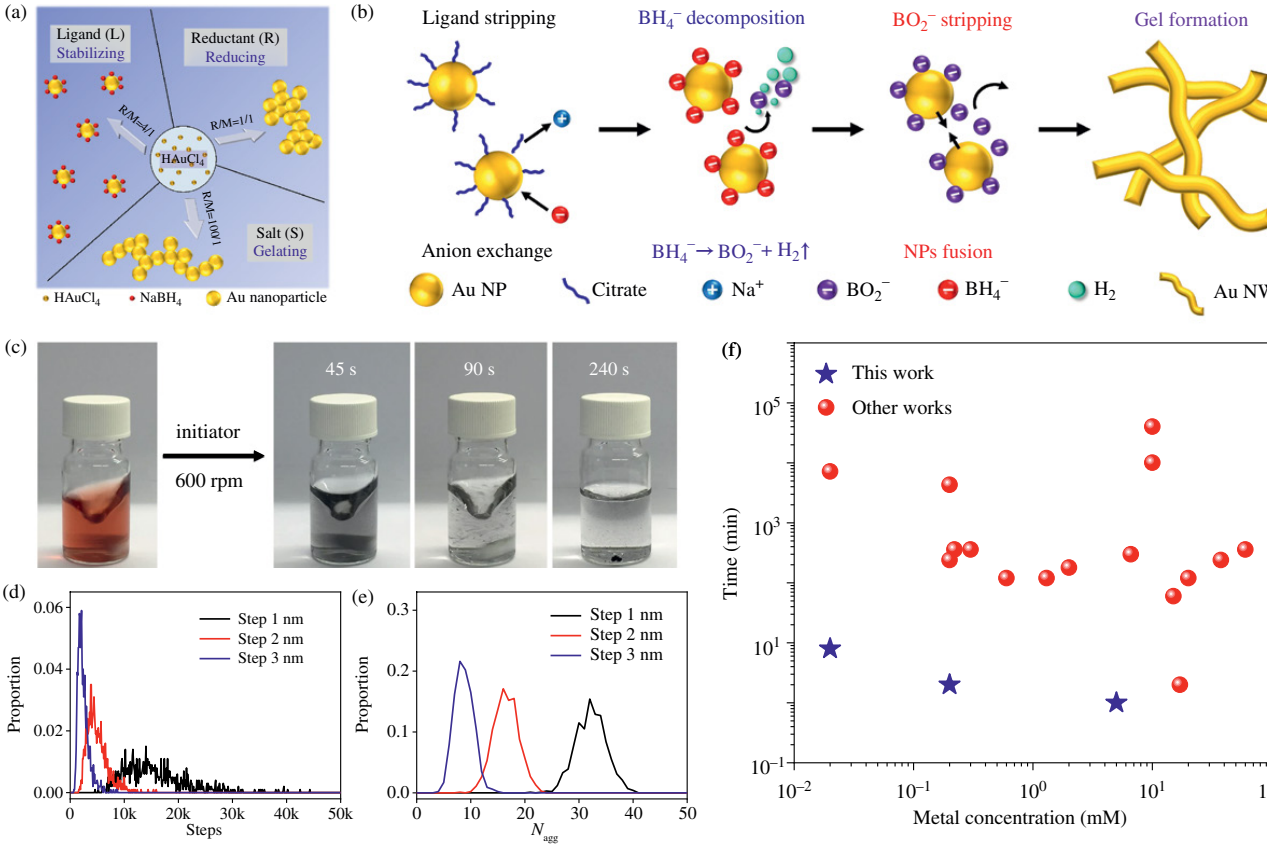


Figure 3.7 Designing reductants and the force field. (a–b) The R/M-dependent function evolution of the reductants and proposed mechanisms for the excessive-$NaBH_4$-directed gelation [15] / Springer Nature / Licensed under CC BY 4.0. (c–f) Disturbance-directed ultrafast gelation. (c) Gelation process of a gold NP solution under stirring. (d–e) Monte Carlo (MC) simulation under different disturbing conditions (maximum step lengths, x = 1, 2, and 3 nm). (d) The number of left aggregates after 5000 MC step and (e) the required steps to form a single aggregate. (f) Plots of metal precursor concentration and the gelati time obtained by conventional routes and by disturbance-assisted gelation method [22] / with permission of Elsevier.

Aside from liquid-phase reduction, one-step gelation has also been achieved in a liquid-gas phase. By bubbling CO into the acetic acid solution of Pd salts, gels made of 2D Pd nanosheets were obtained after aging [36, 37]. However, the underlying formation mechanisms have not been clearly revealed.

3.3.4 Acceleration

The gelation of metals from a dilute solution (e.g. $c_M < 0.5$ mM) usually takes from several days to weeks at ambient temperature. The low reaction kinetics can considerably affect the practical production and applications. Various solutions have been proposed to address this issue, mostly focused on raising the reaction temperature (313–348 K) [39, 46, 47] and the reactant concentration (e.g. >5 mM) [38, 41]. For example, starting from a dilute solution ($c_M = 0.3$ mM), Zhu et al. prepared Au-Cu, Pd-Cu, and Pt-Cu hydrogels in a few hours at 333 K [47], which is much faster than the gelation time for Pd-Pt gels obtained at room temperature (3–17 days) [13]. However, these tactics may either affect microstructures of gels, require a costly procedure to obtain highly concentrated NP precursors, or suffer from a still relatively long reaction time (e.g. several hours).

In fact, the core issue accounting for the low gelation kinetics is the high mass transfer barrier incurred by the still gelation condition. However, conventional wisdom would note that a disturbed condition can destroy the gel network and thus discourage gel formation. Occasionally, it was found that inorganic metal hydrogels exhibit a unique self-healing behavior [19]. In this light, an unconventional disturbance-directed ultrafast gelation method was accordingly proposed, as shown in Figure 3.7c [22]. The reaction system was disturbed to break the mass transfer barrier, shortening the reaction to a few minutes. Then the external disturbance was removed, allowing the as-formed metal aggregates (or gel pieces) to connect with each other, eventually yielding a monolithic gel triggered by the self-healing properties. The effect of mass transfer was modeled by Monto Carlo (MC) simulations by using different step lengths, where enhanced mass transfer (i.e. a large step length) can considerably reduce the number of left aggregates after a certain number of MC steps and lead to a fewer number of MC steps for assembling all particles into a single aggregate (Figure 3.7d,e). For this reason, diverse monolithic metal hydrogels can be acquired in a few minutes, which is ca. two to four orders of magnitude faster than that for conventional methods (Figure 3.7f).

3.3.5 Postsynthesis

To create complicated structures, a postsynthesis process performed on as-obtained metal gels is frequently used. For example, by conducting a GRR on a silver hydrogel by using H_2PtCl_6, a part of silver was replaced by Pt due to the higher redox potential of Pt than Ag [49]. In this way, a Pt-Ag gel with a two-level structure (i.e. nanotubes [diameter of several tens of nanometers] assembled from thin NWs [diameter of ~2.6 nm]) was yielded (Figure 3.8a), largely boosting the SSA from 10.0 to 83.4 $m^2\ g^{-1}$. In another work, starting from a Pd–Au hydrogel, sequential underpotential copper deposition and galvanic replacement of Cu by Pt endowed a continuous thin Pt outer shell on the core hydrogel, resulting in a superior electrocatalyst for oxygen reduction [25]. However, these methods usually suffer from tedious steps, and sometimes the integrity of gels cannot maintain during operation.

3.3.6 Drying of Wet Gels

After acquiring wet gels, a suitable drying process is needed to yield the corresponding aerogels. To avoid large capillary forces developed around the gel network during drying, CPD and freeze-drying (FD) are usually adopted. Because of the fragileness of most metal aerogels, CPD is

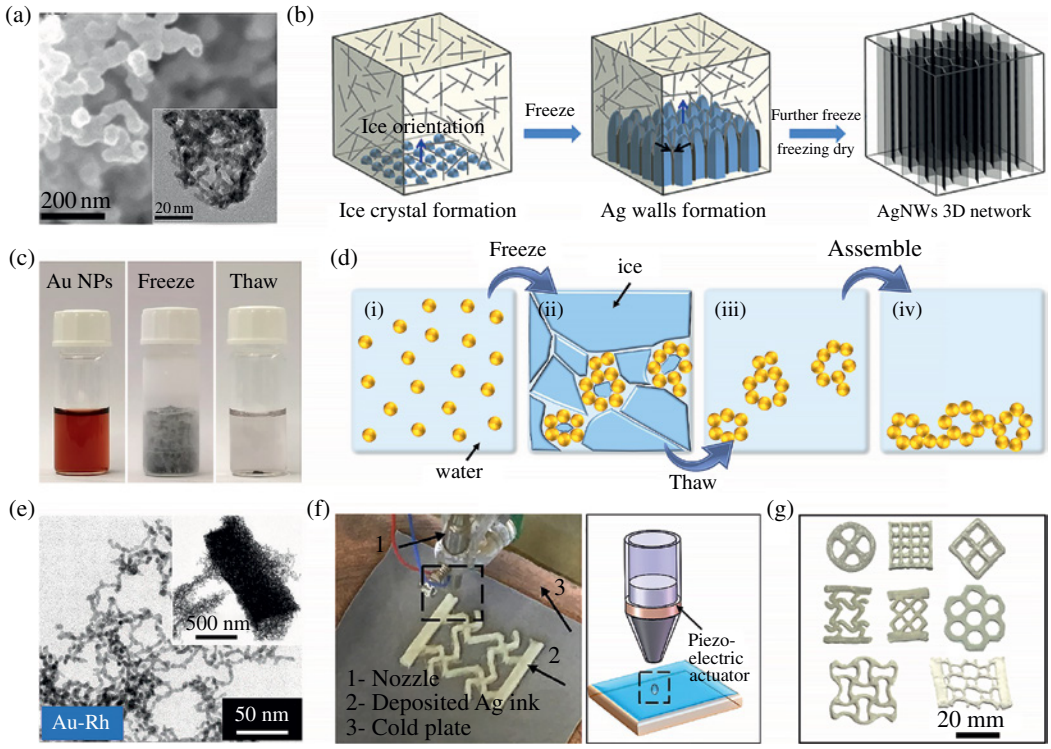


Figure 3.8 Fabrication of metal gels by postsynthesis, freezing, and 3D printing. (a) Hierarchical Pt-Ag nanotubular aerogels prepared by performing GRR on silver aerogels [49]. (b) Schematic demonstration for synthesizing silver aerogels by unidirectional freeze casting [16] / with permission of John Wiley & Sons. (c–e) Freeze-thaw-directed fabrication. (c) Photographs and (d) proposed mechanisms of the fabrication process. (e) TEM image of an Au-Rh aerogel [30] / John Wiley & Sons. (f–g) 3D printing of silver nanowire aerogels. (f) A 3D freeze assembling printing technique integrated with drop-on-demand inkjet. (g) Diverse 3D printed aerogel architectures [52] / with permission of John Wiley & Sons.

dominantly used to minimize structural damage. However, CPD requires a solvent exchange process with ethanol or acetone and expensive high-pressure equipment, which is not feasible for broad use. In comparison, FD – which only requires freezing following by a vacuum drying process – has also been adopted recently [15, 19]. Although the structure damage incurred by FD can be alleviated by replacing water with other organic solvents (e.g. tert-butanol) [2], the formation of crystals during the freezing process can still result in an adverse effect on the mechanical properties of MAs.

3.3.7 Freezing-Based Method

3.3.7.1 Freeze-Casting

The freeze-casting method combines the gelation and drying process in one step, allowing for yielding aerogels directly from the aqueous solutions of metal NPs by sequentially freezing and vacuum drying. Upon freezing, phase separation occurs, and NPs are pushed to aggregate at the boundaries between ice crystals. If the NP concentration is sufficiently high, a continuous network following the ice surface can be formed. Therefore, a monolithic aerogel can be obtained after ice sublimation by vacuum drying.

The majority of metal aerogels prepared in this way adopt metal NWs as precursors (e.g. Cu NWs [26], Ag NWs [16, 50], Pd NWs [51], and Au NWs [27]), resulting in MAs with regular shape, reasonable mechanical strength, and ultralight density of as low as $<10\,mg\,cm^{-3}$. Particularly, directional freezing can produce aerogels with ordered structures (Figure 3.8b), further facilitating specific applications [16]. Aside from using NWs, common spherical metal NPs (e.g. Au, Ag, Pd, and Pt) can also be engineered into aerogels by freeze-casting [17]. However, presumably due to the smaller fraction of linkages with strong metal bonds, the obtained MAs are quite fragile. Note that the freeze-casting method requires a stable precursor solution with a very high concentration ($c_M > 10\,mM$), hence a tedious concentrating process is usually inevitable. Additionally, because the freezing and drying are coupled together, the impurities (e.g. stabilizers) will remain in the final products and may affect the evaluation of the intrinsic properties of MAs. Moreover, the freeze-casting method always produces aerogels with quite a large feature size (typically several tens to more than a hundred nanometers), which considerably reduces the SSA.

3.3.7.2 Freeze-Thawing

To overcome the aforementioned issues in freeze-casting, a freeze–thaw approach was recently reported [30]. Taking advantage of the self-healing properties of metal hydrogels, as mentioned in Section 3.3.4, clean metal hydrogels can be produced by freezing dilute metal NP solutions ($c_M < 0.5\,mM$) followed by thawing. As shown in Figure 3.8c,d, separate metal aggregates form first upon freezing; after thawing, these aggregates sediment driven by gravity and assemble into a monolithic gel at the bottom of vials due to their self-healing properties. Before drying, impurities in the as-formed gels can be removed by solvent cleaning, overcoming the issue that remained in freeze-casting. Particularly, due to the templating effect of ices, hierarchically structured MAs were yielded, and an SSA of up to $83.6\,m^2\,g^{-1}$ was acquired (Figure 3.8e).

3.3.7.3 3D Printing

As a rising technique to create 3D objects with desirable shapes, 3D printing has been applied for fabricating MAs in conjunction with the freeze-casting method. As illustrated in Figure 3.8f,g, by printing Ag NW solution with a drop-on-demand inkjet on a cold plate, desirable shapes can be fixed. Afterward, the frozen matter was converted to monolithic aerogels by sublimation, giving rise to materials with versatile architectures [52].

3.4 Energy-Related Applications

Driven by the concerns for the energy crisis, many efforts have been put into energy storage and energy conversion in the last few decades. Featuring conductive, interconnected, and highly catalytically active networks, metal aerogels can simultaneously offer fast electron/mass transfer channels, countless reaction sites, and robust structures resisting aggregation/collapse [66]. These attributes endow MAs with great potential in energy storage and conversion, including the application as (photo)electrocatalysts for batteries, as electrode materials and current collectors for batteries/supercapacitors, as hosts for hydrogen storage, and as self-propulsion devices.

Among the aforementioned applications, electrolysis with MAs is the earliest [14] and dominantly studied field. Combining highly active metal sites with the structural merits of aerogels, MAs can serve as additive-free electrocatalysts, considerably outperforming other metal or nonmetal materials. However, the exploration of underlying structure-performance correlations and

performance optimization needs to be strengthened so as to release the full potential of MAs and fulfill practical requirements. On the other hand, most other energy-related applications have also been sporadically explored recently [19, 51, 53], calling for further efforts to verify their practical values. In this section, the emphasis will be focused on the MAs for electrocatalysis use, while other applications will also be briefed.

3.4.1 Electrocatalysis in Fuel Cells

Fuel cells can efficiently convert chemical energy to electrical energy by controlled oxidation of fuels with oxygen. During operation, accompanied by the redox reaction where electrons transfer from fuels to oxygen, the energy stored in fuels is transformed into electricity. In the cell, the anode reaction (i.e. the fuel oxidation) and the cathode reaction (i.e. the oxygen reduction) occur at different places, thus allowing for separately engineering electrocatalysts for respective reactions. Both electrode reactions, particularly for the oxygen reduction reaction (ORR) at the cathode, often suffer from sluggish kinetics and/or poor stability, requiring the advancement of efficient and robust electrocatalysts. Here, MAs as electrocatalysts for fuel oxidation and oxygen reduction will be sequentially discussed, highlighting the design principles with modulating chemical compositions and microstructures.

3.4.1.1 Fuel Oxidation Reactions

For electrocatalytic fuel oxidation, Pd-based metal aerogels are dominantly explored due to the intrinsically high catalytic activity of palladium. For evaluation, the forward current density (If) is often used as an indicator to characterize the electrocatalytic activity, and the commercial palladium (palladium/carbon or palladium black) is usually used as a reference. According to the fuels employed, an array of fuel oxidation reactions, including alcohol oxidation reaction (AOR), hydrogen oxidation reaction (HOR), formic acid/formate oxidation reaction (FOR), and glucose oxidation reaction (GOR), have been studied. Presumably, due to the operational easiness and the low cost, AOR has received the most attention. This section will introduce the research of MAs as electrocatalysts for respective fuel oxidation.

3.4.1.1.1 Alcohol Oxidation Reactions At the very beginning, single-metallic Pd-nanowire-fused aerogels were applied for ethanol oxidation reaction (EOR), displaying a slightly higher forward current density (1.2–2.3 times) than that for commercial Pd/C [54]. Afterward, composition and structure design have been explored to further boost catalysis performance.

From the composition perspective, imparting additional metals may enhance the electrical conductivity and activate the synergistic effects. For instance, Pd-Cu aerogels were fabricated, showing an I_f of two to three times higher than for Pd/C for EOR [47]. By using ternary Au-Pd-Pt aerogels, I_f was further boosted to 6.1 times [19]. The comparative experiments indicated that the introduction of highly conductive gold can increase the current density, while the enrollment of Pt can promote more complete alcohol oxidation during the forward scanning. Recently, a bismuth-doped nickel aerogel ($Ni_{97}Bi_3$) delivered outstanding stability for the methanol oxidation reaction [46]. Compared to the previously reported MA-based electrocatalysts (typically <30% retention within 1 hour), the $Ni_{97}Bi_3$ aerogel manifested a substantially enhanced stability with 78% current retention after a 12-hour operation.

Besides altering the kinds of metals, decorating MAs with specific ligands was proved to be another way to modulate the electronic structure of catalysts and thus promote EOR performance [15, 33]. It was found that the surface metal valence of Au-Pd aerogels can be modulated

by decorating with specific ligands, where the EOR performance can be accordingly adjusted [33]. As shown in Figure 3.9a, I_f was proportional to the surface metal valence of both gold and palladium. For example, decoration with polyvinylpyrrolidone (PVP) can induce the electron transfer from the metal to the ligand, thus generating partially positively charged metal surfaces and facilitating the oxidation process of ethanol (Figure 3.9b). In this light, an I_f of 5.3 times higher than that for Pd/C was realized.

From the perspective of structure design, specific multiscale structures can facilitate mass transfer, enrich active sites, and create highly active catalytic sites, thereby boosting the performance. Engineering the building blocks into 2D architecture, Pd nanosheet structured aerogels displayed a mass activity of 5.8 times to Pd/C [36]. By assembling presynthesized Pd-Ni hollow nanospheres, the resulting aerogels held abundant catalytic sites and mass transfer channels, thus gaining an I_f of up to 5.6 times higher than that for Pd/C [35]. In another study, a hierarchically structured Au-Pd gel was produced by a freeze-thaw process [30]. The freezing-induced meso- and macro structures allow the fast mass transfer, enabling a mass activity of 4.7 times higher than that for Pd/C. Recently, by anchoring ultrafine Pd ensembles (<1 nm) on Au-Cu aerogels, an outstanding I_f of up to 11.6 times compared to Pd black was achieved, which was attributed to the combined ligand effect and geometric effect incurred by this unique architecture [23].

3.4.1.1.2 Formic Acid/Formate Oxidation Reactions Formic acid/formate is another kind of fuel that has been widely studied. A Pd-Cu aerogel featured a mass activity of ca. two times compared to Pd/C toward formic acid oxidation, while the morphology was less controlled [55]. By constructing Pt-Ag nanotubular aerogels with multiscale structure, a catalytic current density of up to 19.0 times higher than for Pt black was achieved for formic acid oxidation, highlighting the importance of enhancing mass transfer and increasing SSA [49]. Recently, it was found that surface restructuring of Ag-Pd-Pt aerogels occurred by cycling at high voltage, thus promoting the electrocatalytic HCOOK oxidation (Figure 3.9c,d) [55]. In brief, cycling as-prepared ternary aerogel from −0.1 to 1.3 V drove an outward diffusion of silver, promoting the oxidation of the exposed silver and forming amorphous Ag_2O-coupled Pd-Pt-enriched metal surfaces. Such structure change led to a downshift of the d-band center, thus weakening chemisorption of H_{ad} intermediates and dramatically enhancing the mass activity (five times higher compared to Pd/C).

3.4.1.1.3 Other Fuel Oxidation Reactions Aside from alcohols and formic acid/formate, other fuels have also been studied. As a carbon-neutral fuel, hydrogen has been employed for hydrogen-oxygen fuel cells. Recently, lamellar Pt-Rh aerogels have been applied for the hydrogen oxidation reaction (HOR), showing the specific activity and mass activity of 5.5 and 2.6 times higher than that for commercial Pt/C, respectively [56]. Besides, GOR has also been demonstrated. On the one side, Pd aerogels have been adopted as conductive and large-SSA hosts to accommodate catalytically active glucose oxidase, promoting the catalytic current by more than 50-fold [43]. On the other hand, Au aerogels were directly applied as active electrocatalysts for GOR, where the β-CD modification substantially boosted the GOR sensitivity (332.9 $\mu A\,mM^{-1}$) due to its large electrochemical active surface area (18.2 $m^2\,g^{-1}$) [29].

3.4.1.2 Oxygen Reduction Reactions

The sluggish oxygen reduction process has posed a great challenge for achieving high-efficient fuel cells, thus drawing tremendous attention. In 2013, Liu et al. [14] pioneered introducing

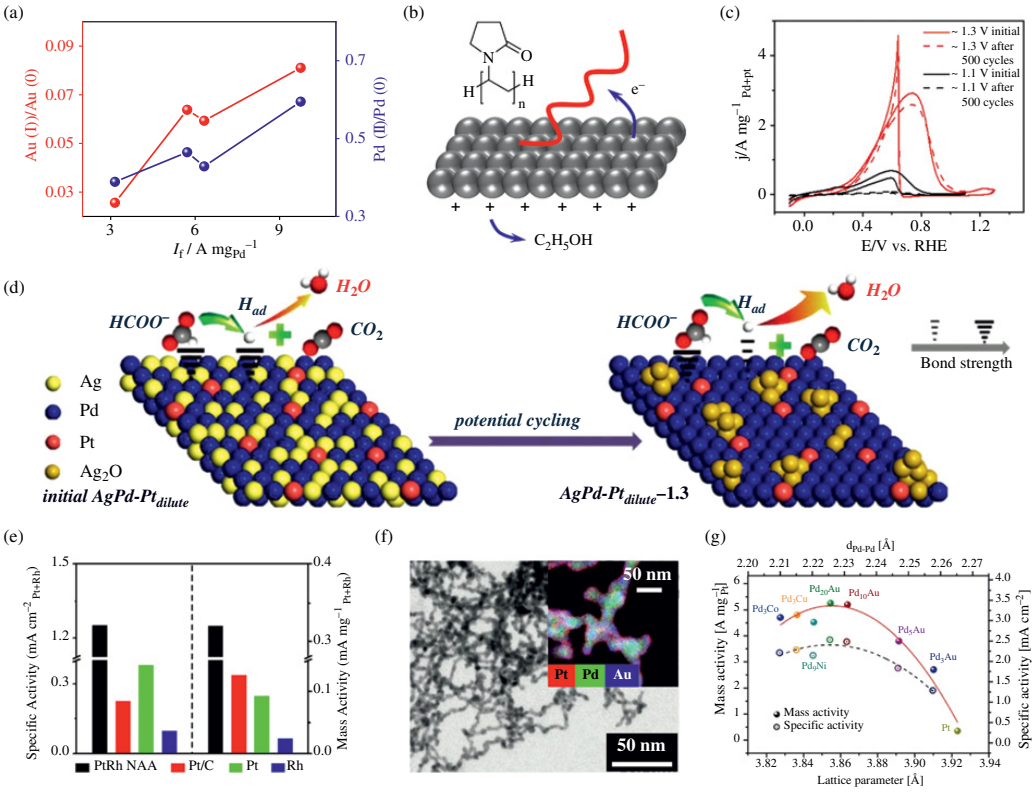


Figure 3.9 MAs for electrocatalytic processes in fuel cells. (a–b) Ligand-directed modulation for enhanced EOR. (a) Correlation between I_f and the valence states of gold and palladium. (b) Proposed mechanism of PVP-enhanced ethanol oxidation [33] / John Wiley & Sons. (c–d) High-potential-driven surface restructuring for enhanced HCOOK oxidation. (c) CV curves before and after successive scans of 500 cycles within different potential windows. (d) Schemati illustration of the transformation from pristine AgPd–Pt to surface-restructured AgPd–Pt–1.3 by potential cycling. Reproduced from Wang et al. [55], with permission. (e) Electrocatalytic performance of HOR. Specific activities and mass activities at an overpotential of 50 mV [37] / with permission of Elsevier. (Electrocatalytic performance of ORR. (f) TEM image and element mapping of a PdAu-Pt core-shell aerogel. (g) MAs and SAs of Pd_xM-Pt core-shell aerogels (M = Au, Ni, Co, Cu) as a function of the lattice parameter and the Pd–Pd interatomic distance (d_{Pd-Pd}) of the Pd_xM core aerogels [25] / with permission of Jo Wiley & Sons.

MAs for ORR. By incorporating Pd to modify the d-band center of the Pt aerogel, the optimized aerogel (i.e. Pd_{20}-Pt_{80} aerogel) displayed a catalytic current of more than five times higher than that of Pt/C in 0.1 M $HClO_4$ solution. In the following, PdAu–Pt core–shell-structured aerogels have been demonstrated. Owing to the strain induced by the lattice mismatch between the Pt shell and the Pd-Au core network (Figure 3.9f,g), they manifested an extraordinary mass activity of as high as 18.7 times compared to Pt/C [25]. Recently, by using Au and Pt to respectively provide electrical conductivity and catalytic activity, an Au-Pt aerogel was demonstrated, outperforming Pt/C in both acidic and alkaline environments (specific activity >3 times compared to Pt/C) [57].

3.4.2 Electrocatalysis in Water Splitting

Electrochemical water splitting can efficiently yield hydrogen – a clean energy source – from abundant water, which is critical for energy applications. This process consists of the anodic oxygen evolution reaction (OER) and the cathodic hydrogen evolution reaction (HER), where usually the former is catalyzed by Ru- and Ir-based catalysts while the latter is catalyzed by the Pt-based catalysts.

3.4.2.1 Oxygen Evolution Reactions

The large overpotential of OER (usually >300 mV) often restricts the overall efficiency of electrochemical water splitting. Although ruthenium and iridium (or their oxides) are known for high catalytic activity toward OER, it is difficult to engineer them into aerogels due to the difficulty for gelation or the instability in air [15].

Recently, the electrocatalytic OER by using MAs was pioneered by Lin's group. It is possible to fabricate the Ir-Cu aerogel with a nanovoid structure by utilizing the difference of redox potential between iridium and copper (Figure 3.10a) [25]. By balancing the binding energies of the adsorbed oxygen species toward gels, the optimized Ir_3-Cu aerogel displayed the smallest overpotential of 298 mV and the best specific activity (~3.5 times higher compared to the IrO_2 NPs, see Figure 3.10b). In another work, an OER overpotential of 245 mV (at 10 mA cm^2 in 1.0 M KOH aqueous solution) was obtained with an Au-Ir core-shell-structured aerogel (Figure 3.10c) [15]. This was attributed to the synergy between conductive gold and catalytically active iridium.

3.4.2.2 Hydrogen Evolution Reactions

As the cathodic reaction in water splitting, HER has also been explored by using MA-based electrocatalysts. A lamellar Pt-Rh aerogel has been acquired for HER in 1.0 M KOH solution, showing an overpotential of 55 mV at 10 mA cm^{-2} and 2.3-fold higher mass activity compared to commercial Pt/C (Figure 3.10d,e) [56]. In a recent study, an Au-Rh aerogel was fabricated as a pH-universal HER electrocatalyst [57], which displayed small overpotentials (18–22 mV at 10 mA cm^{-2}) and Tafel slopes (29–47 mV) in 1 M KOH, 1 M PBS, and 0.5 M H2SO4 solutions. Particularly, an electrolyzer assembled from Au-Rh aerogels and commercial RuO_2 delivered a smaller operation voltage than that for the Pt/C || RuO_2 electrolyzer across a wide range of current densities in different pH values (Figure 3.10d–f).

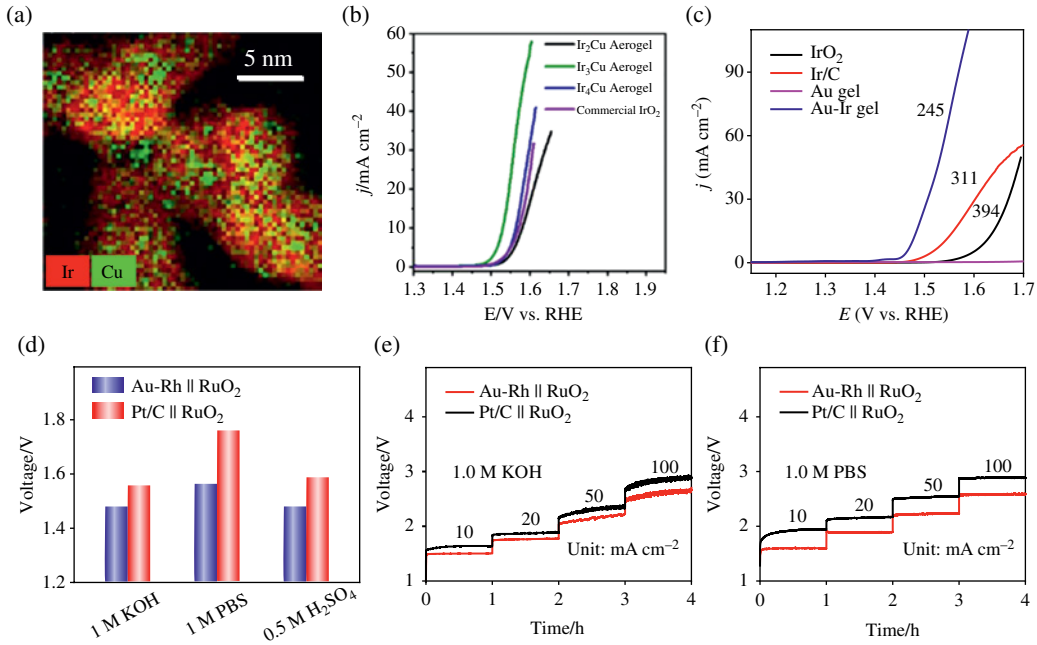


Figure 3.10 MAs for electrocatalytic processes in water splitting. (a) Element mapping of an Ir-Cu aerogel. (b) Electrocatalytic performance of OER [24] / with permission of American Chemical Society. (c) Polarization curves of an Au-Ir aerogel and reference electrocatalysts performed in an N_2-saturated 1.0 M KOH aqueous solution [15] / Springer Nature / Licensed under CC BY 4.0. MAs for electrocatalytic processes in water splitting. (d) SEM and TEM images of lamellar Pt-Rh aerogels [56] / with permission of Elsevier. (e) Electrocatalytic performance of HER. (f) Water splitting performance of an Au -Rh-aerogel || RuO_2 electrolyzer and a Pt/C || RuO_2 electrolyzer in various pH environments [57] / John Wiley & Sons.

3.4.3 Electrocatalytic CO_2 Reduction

The electrochemical carbon dioxide reduction (COR) has received wide attention in the last few years, which is triggered by both environmental concerns (i.e. the greenhouse effect) and the emerging metal-CO2 batteries [59]. However, this field has rarely been explored using MAs. A recent work studied bimetallic Pd–Cu aerogels for COR in an aqueous solution of 1-butyl-3-methylimidazolium tetrafluoroborate (Figure 3.11a,b) [60]. Optimizing the valence states of metals by adjusting the ratio of two metals, a CH_3OH selectivity of up to 80.0% was realized in the $Pd_{83}Cu_{17}$ aerogel. XPS analysis suggested that a high proportion of low-valence-state metal species may account for the high selectivity. A recent study suggests that a core-shell-structured Au-Pd aerogel can selectively promote CO_2 activation while suppressing H_2 activation evolution, and thereby realizing an impressive Faradaic efficiency (98%) at $\eta = 390$ mV over a period of 12 hours [61].

3.4.4 Photoelectrocatalysis for Alcohol Oxidation

Nanostructured metals are not only known for their high catalytic activity but also feature unique optical properties such as plasmonic absorption in the visible-light range. While holding both

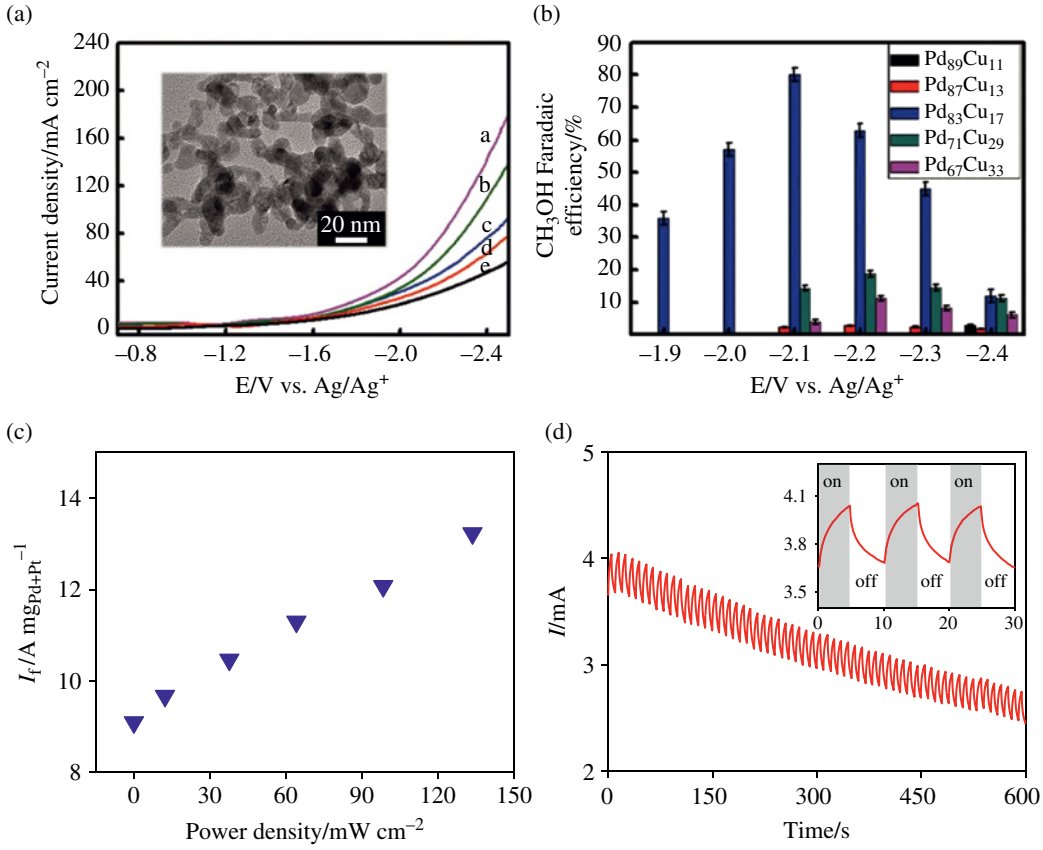


Figure 3.11 (a, b) Electrochemical CO_2 reduction catalyzed by Pd-Cu aerogels. (a) LSV curves for Pd_xCu_y aerogels: (a) $Pd_{67}Cu_{33}$, (b) $Pd_{71}Cu_{29}$, (c) $Pd_{83}Cu_{17}$, (d) $Pd_{87}Cu_{13}$, (e) $Pd_{89}Cu_{11}$. (b) Faradaic efficiency for CH_3OH over Pd_xCu_y aerogels. All tests were performed in CO_2-saturated [Bmim]BF_4 aqueous solution with 25 mol% [Bmim]BF_4 and 75 mol% water [60]. (c–d) Photoelectrocatalytic oxidation of ethanol with an Au-Pd-Pt aerogel. (c) The dependency of the I_f versus the input light power density. (d) The photoelectrochemical response during a chronoamperometry test. All tests were performed in N_2-saturated 1.0 M KOH + 1.0 M ethanol solution [22] / with permission of Elsevier.

impressive optical and catalytic attributes, the photoelectrocatalytic (PEC) properties of MAs have only been demonstrated recently [22, 30]. Exposing under a white-light LED source, the catalytic current density of an Au-Pd-Pt aerogel can be stepwise rising from 9.1 to 13.2 A mg_{Pd+Pt}^{-1} with light power density increasing from 0 to 133 mW cm^{-2} (Figure 3.11c), reaching 7.3 times higher than that for Pd/C. Since the wavelength of the used LED crosses a wide region of 350–800 nm, the enhancement mechanisms were attributed to a combination of plasmonic enhancement [62] and nonplasmonic thermal effects. Interestingly, such PEC property can be further utilized to construct a light-responsive device with a sensitivity of >40.2 mA mW^{-1} (Figure 3.11d).

3.4.4.1 Energy Storage and Conversion

In recent years, the application space of MAs has been extended to various energy storage (chemical and electrical energy) and conversion fields. In this section, the use of MAs for hydrogen storage, electrochemical energy storage, and self-propulsion devices will be introduced.

3.4.4.2 Electrochemical Energy Storage

Holding high electrical conductivity and large SSAs, the potential of MAs in electrochemical energy storage has been revealed recently. The supercapacitor application – by using Au, Pd, and Pt aerogels [38] – is not successful (specific capacitance $<10\,F\,g^{-1}$). In addition to the high cost, the chemical inertness and the large atomic weights of the employed noble metals are unsolved issues.

In comparison, MAs have obtained certain success as electrode materials for batteries. Recently, a Si-containing Sn-Ni gel was fabricated by reducing a Si@Sn-Ni hybrid cyanogel (Figure 3.12a) [63]. The embedding of high-capacity Si particles in the conductive Sn-Ni porous network not only enabled a substantial capacity compared to the Sn-Ni network but also afforded remarkable capacity retention and rate performance compared to naked Si particles (Figure 3.12b). In another study, a silver NW aerogel has been applied as the anode host for lithium-ion batteries (LIBs) [53]. The combination of the high conductivity of silver and the high-SSA of aerogels enabled a uniform Li plating due to the small overpotential and the reduced local current density, substantially alleviating the growth of Li dendrites (Figure 3.12c). This is particularly important for high-rate operation. As shown in Figure 3.12d, the assembled Li–Ag aerogel//lithium iron phosphate (LFP) cell showed a much higher capacity than that for Li//LFP cells at a charge/discharge rate of 4.0 C.

3.4.4.3 Hydrogen Storage

The storage of hydrogen – an important clean energy – has received wide attention. Among various hosts, palladium is advantageous in reversibly storing hydrogen at ambient temperature and pressure, where the α- and β-phase hydrides formed at lower and higher hydrogen concentrations, respectively.

In comparison with bulk Pd, nanostructured Pd can considerably enhance the absorption kinetics with quick gas uptake at low hydrogen pressure [64]. In this consideration, the hydrogen storage behavior of Pd aerogels was studied [51]. As shown in Figure 3.12e,f, compared to Pd micropowders, aerogels assembled from as-prepared Pd nanowires (diameter of ~200 nm) displayed a quicker hydrogen absorption kinetics yet a reduced amount of the total H_2 uptake (>20%). However, further exploration of the hydrogen storage with MAs remains to be conducted.

3.4.4.4 Self-Propulsion Devices

By utilizing specific chemical reactions, self-propulsion devices allow converting chemical energy into mechanical energy. Although self-propulsion devices, particularly based on Pt-containing materials, have been widely explored [65], programming desirable self-propulsion behavior is still a vital challenge.

Recently, it was found that metal aerogels can display impressive compressibility due to the malleability of metals as well as the empty space in aerogels. Interestingly, even two different metal aerogels can be welded together upon compression. In this regard, a gold and a silver aerogel were integrated by compression [19]. Because the silver is catalytically active while the gold is inactive toward H_2O_2 decomposition, the resulting macroscopically hetero-structured aerogel showed an interesting rotation behavior in an H_2O_2 solution driven by the generated bubbles at the silver part. In comparison, the single silver aerogel can only walk randomly due to the uncontrolled propulsion behavior.

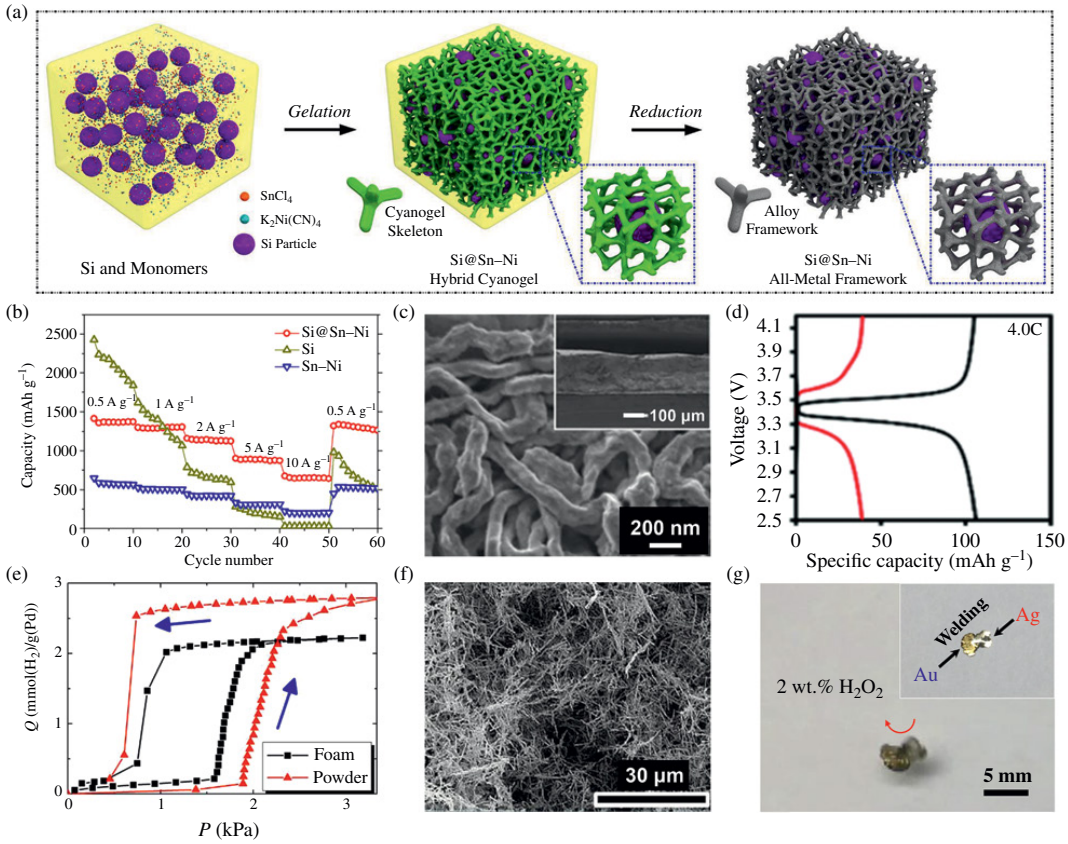


Figure 3.12 (a–d) MAs for lithium-ion batteries. (a–b) Synthesis of a Si@Sn–Ni all-metal framework and its rate performance for lithium storage [63]. (c) S images of an Ag NW aerogel (AgNWA) after 20 Li plating/stripping cycles and (d) the charge-discharge profiles of a Li//LFP and Li–AgNWA//LFP full cell [53 with permission of Royal Society of Chemistry. (e, f) Hydrogen storage by using palladium aerogels. (e) Hydrogen absorption/desorption isotherms of aeroge and nanoparticles, and (f) the SEM image of palladium aerogels [49] / with permission of Royal Society of Chemistry. (g) Self-propulsion of a compressed gold-silver aerogel in an H_2O_2 solution [19].

3.5 Conclusions

The unique physicochemical properties and the widely tunable compositions of metals motivate the exploration of metal aerogels. As one of the youngest members of the aerogel family, MAs have stimulated broad interest in the last decade. This chapter introduces the state-of-the-art development of MAs from both the synthesis methodology and the practical application aspects.

Thanks to the unremitted efforts in the last few years, the unconventional formation mechanisms of metal gels have been partially clarified, largely advancing the fundamental research such as on-target manipulating composition and structure. Additionally, diverse synthesis strategies in view of engineering precursors, initiators, reductants, ligands, solvents, and external fields have been developed, laying a solid material basis. The aforementioned achievements further facilitate the target-specific design of MAs for a library of applications, particularly in energy-related fields, including serving as electrocatalysts for important electrochemical process in cells/batteries, as electrode materials for supercapacitors/batteries, as host materials for clean energy (e.g. hydrogen), and as self-propulsion devices for controllable energy conversion.

In spite of the aforementioned achievements, quite a few issues still challenge the development of this field. From the synthesis side, an unambiguous physical picture for the gelation process that adapts to various gelation methods is needed so as to fully unveil the underlying mechanisms for material design and the expansion of the available composition. To address it, a combination of fundamental experimental and theoretical efforts is needed. From the application side, efforts should be focused on disclosing structure-performance correlation to direct material design. Moreover, the application scope needs to be broadened, and disruptive uses of MAs beyond electrocatalysis must be explored.

Currently, although the research of MAs only accounts for a small part of the entire aerogel family (~5%), we believe that progress in the synthesis methodology development, as well as their vast application potential, will inevitably draw the attention of more scientists.

References

1 Du, R., Fan, X., Jin, X. et al. (2019). Emerging noble metal aerogels: state of the art and a look forward. *Matter* 1 (1): 39–56.

2 Jiang, X., Du, R., Hübner, R. et al. (2021). A roadmap for 3D metal aerogels: materials design and application attempts. *Matter* 4 (1): 54–94.

3 Wang, N., Li, Y., Cui, Q. et al. (2023). Metal Aerogels: Controlled synthesis and applications. *Acta Phys. -Chim. Sin.* 39 (9): 2212014.

4 Alemán, J., Chadwick, A.V., He, J. et al. (2007). Definitions of terms relating to the structure and processing of sols, gels, networks, and inorganic-organic hybrid materials (IUPAC recommendations 2007). *Pure Appl. Chem.* 79 (10): 1801–1829.

5 Ashby, M.F. and Lu, T. (2003). Metal foams: a survey. *Sci. China, Ser. B Chem.* 46 (6): 521–532.

6 Tappan, B.C., Steiner, S.A., and Luther, E.P. (2010). Nanoporous metal foams. *Angew. Chem. Int. Ed.* 49 (27): 4544–4565.

7 Du, R., Jin, X., Hübner, R. et al. (2020). Engineering self-supported noble metal foams toward electrocatalysis and beyond. *Adv. Energy Mater.* 10 (11): 1901945.

8 Leventis, N., Chandrasekaran, N., Sotiriou-Leventis, C., and Mumtaz, A. (2009). Smelting in the age of nano: iron aerogels. *J. Mater. Chem.* 19 (1): 63–65.

9 Leventis, N., Chandrasekaran, N., Sadekar, A.G. et al. (2009). One-pot synthesis of interpenetrating inorganic/organic networks of CuO/resorcinol-formaldehyde aerogels: nanostructured energetic materials. *J. Am. Chem. Soc.* 131 (13): 4576–4577.

10 Chen, K., Bao, Z., Shen, J. et al. (2012). Freestanding monolithic silicon aerogels. *J. Mater. Chem.* 22 (32): 16196–16200.

11 Xu, W., Du, A., Xiong, J. et al. (2016). Freestanding titanium metallic aerogel. *Mater. Des.* 97: 93–97.

12 Chen, K., Xu, W., Du, A. et al. (2014). Template confined synthetic strategy for three-dimensional free-standing hierarchical porous nanocrystalline tantalum. *Mater. Lett.* 116: 31–34.

13 Bigall, N.C., Herrmann, A.K., Vogel, M. et al. (2009). Hydrogels and aerogels from noble metal nanoparticles. *Angew. Chem. Int. Ed.* 48 (51): 9731–9734.

14 Liu, W., Rodriguez, P., Borchardt, L. et al. (2013). Bimetallic aerogels: high-performance electrocatalysts for the oxygen reduction reaction. *Angew. Chem. Int. Ed.* 52 (37): 9849–9852.

15 Du, R., Wang, J., Wang, Y. et al. (2020). Unveiling reductant chemistry in fabricating noble metal aerogels for superior oxygen evolution and ethanol oxidation. *Nat. Commun.* 11 (1): 1590.

16 Gao, H.L., Xu, L., Long, F. et al. (2014). Macroscopic free-standing hierarchical 3D architectures assembled from silver nanowires by ice templating. *Angew. Chem. Int. Ed.* 53 (18): 4561–4566.

17 Freytag, A., Sánchez-Paradinas, S., Naskar, S. et al. (2016). Versatile aerogel fabrication by freezing and subsequent freeze-drying of colloidal nanoparticle solutions. *Angew. Chem. Int. Ed.* 55 (3): 1200–1203.

18 Naskar, S., Freytag, A., Deutsch, J. et al. (2017). Porous aerogels from shape-controlled metal nanoparticles directly from nonpolar colloidal solution. *Chem. Mater.* 29 (21): 9208–9217.

19 Du, R., Hu, Y., Hübner, R. et al. (2019). Specific ion effects directed noble metal aerogels: versatile manipulation for electrocatalysis and beyond. *Sci. Adv.* 5: eaaw4590.

20 Gao, X., Esteves, R.J., Luong, T.T.H. et al. (2014). Oxidation-induced self-assembly of Ag nanoshells into transparent and opaque Ag hydrogels and aerogels. *J. Am. Chem. Soc.* 136 (22): 7993–8002.

21 Du, R., Zhao, Q., Zhang, N., and Zhang, J. (2015). Macroscopic carbon nanotube-based 3D monoliths. *Small* 11 (27): 3263–3289.

22 Du, R., Joswig, J.-O., Fan, X. et al. (2020). Disturbance-promoted unconventional and rapid fabrication of self-healable noble metal gels for (photo-)electrocatalysis. *Matter* 2 (4): 908–920.

23 Shi, Q., Zhu, C., Tian, M. et al. (2018). Ultrafine Pd ensembles anchored-Au_2Cu aerogels boost ethanol electrooxidation. *Nano Energy* 53: 206–212.

24 Shi, Q., Zhu, C., Zhong, H. et al. (2018). Nanovoid incorporated Irx Cu metallic aerogels for oxygen evolution reaction catalysis. *ACS Energy Lett.* 3 (9): 2038–2044.

25 Cai, B., Hübner, R., Sasaki, K. et al. (2018). Core–shell structuring of pure metallic aerogels towards highly efficient platinum utilization for the oxygen reduction reaction. *Angew. Chem. Int. Ed.* 57 (11): 2963–2966.

26 Tang, Y., Yeo, K.L., Chen, Y. et al. (2013). Ultralow-density copper nanowire aerogel monoliths with tunable mechanical and electrical properties. *J. Mater. Chem. A* 1 (23): 6723–6726.

27 Qian, F., Troksa, A., Fears, T.M. et al. (2020). Gold aerogel monoliths with tunable ultralow densities. *Nano Lett.* 20 (1): 131–135.

28 Schneider, K., Melnyk, I., Hiekel, K. et al. (2019). Mechanical characterization of self-supported noble metal gel monoliths. *J. Phys. Chem. C* 123 (45): 27651–27658.

29 Wen, D., Liu, W., Haubold, D. et al. (2016). Gold aerogels: three-dimensional assembly of nanoparticles and their use as electrocatalytic interfaces. *ACS Nano* 10 (2): 2559–2567.

30 Du, R., Joswig, J.-O., Hübner, R. et al. (2020). Freeze-thaw-promoted fabrication of clean and hierarchically structured noble metal aerogels for electrocatalysis and photoelectrocatalysis. *Angew. Chem. Int. Ed.* 59 (21): 8293–8300.

31 Zhang, H. and Wang, D. (2008). Controlling the growth of charged-nanoparticle chains through interparticle electrostatic repulsion. *Angew. Chem. Int. Ed.* 47 (21): 3984–3987.

32 Qin, G.W., Liu, J., Balaji, T. et al. (2008). A facile and template-free method to prepare mesoporous gold sponge and its pore size control. *J. Phys. Chem. C* 112 (28): 10352–10358.

33 Fan, X., Zerebecki, S., Du, R. et al. (2020). Promoting the electrocatalytic performance of noble metal aerogels by ligand-directed modulation. *Angew. Chem. Int. Ed.* 59 (14): 5706–5711.

34 Ranmohotti, K.G., Gao, X., and Arachchige, I.U. (2013). Salt-mediated self-assembly of metal nanoshells into monolithic aerogel frameworks. *Chem. Mater.* 25 (17): 3528–3534.

35 Cai, B., Wen, D., Liu, W. et al. (2015). Function-led design of aerogels: self-assembly of alloyed PdNi hollow nanospheres for efficient electrocatalysis. *Angew. Chem. Int. Ed.* 54 (44): 13101–13105.

36 Yazdan-Abad, M.Z., Noroozifar, M., Alam, A.R.M., and Saravani, H. (2017). Palladium aerogel as a high-performance electrocatalyst for ethanol electro-oxidation in alkaline media. *J. Mater. Chem. A* 5 (21): 10244–10249.

37 Zareie Yazdan-Abad, M., Noroozifar, M., Douk, A.S. et al. (2019). Shape engineering of palladium aerogels assembled by nanosheets to achieve a high performance electrocatalyst. *Appl. Catal., B-Environ.* 250: 242–249.

38 Burpo, F.J., Nagelli, E.A., Morris, L.A. et al. (2017). Direct solution-based reduction synthesis of Au, Pd, and Pt aerogels. *J. Mater. Res.* 32 (22): 4153–4165.

39 Zhu, C., Shi, Q., Fu, S. et al. (2018). Core–shell PdPb@ Pd aerogels with multiply-twinned intermetallic nanostructures: facile synthesis with accelerated gelation kinetics and their enhanced electrocatalytic properties. *J. Mater. Chem. A* 6 (17): 7517–7521.

40 Wu, Y., Jiao, L., Xu, W. et al. (2019). Polydopamine-capped bimetallic AuPt hydrogels enable robust biosensor for organophosphorus pesticide detection. *Small* 15 (17): 1900632.

41 Wen, D., Herrmann, A.-K., Borchardt, L. et al. (2014). Controlling the growth of palladium aerogels with high-performance toward bioelectrocatalytic oxidation of glucose. *J. Am. Chem. Soc.* 136 (7): 2727–2730.

42 Jung, S.M., Jung, H.Y., Dresselhaus, M.S. et al. (2012). A facile route for 3D aerogels from nanostructured 1D and 2D materials. *Sci. Rep.* 2: 849.

43 Xue, G., Li, Y., Du, R. et al. Leveraging ligand and composition effects: Morphology-tailorable Pt–Bi bimetallic aerogels for enhanced (photo-)electrocatalysis. *Wiley Online Library* 2301288. https://doi.org/10.1002/smll.202301288.

44 Jung, S.M., Preston, D.J., Jung, H.Y. et al. (2016). Porous Cu nanowire aerosponges from one-step assembly and their applications in heat dissipation. *Adv. Mater.* 28 (7): 1413–1419.

45 Zheng, Y., Li, N., Mukherjee, S. et al. (2019). A versatile strategy for tailoring noble metal supramolecular gels/aerogels and their application in hydrogen evolution. *ACS Appl. Nano Mater.* 2 (5): 3012–3020.

46 Herrmann, A.-K., Formanek, P., Borchardt, L. et al. (2013). Multimetallic aerogels by template-free self-assembly of Au, Ag, Pt, and Pd nanoparticles. *Chem. Mater.* 26 (2): 1074–1083.

47 Zhu, C., Shi, Q., Fu, S. et al. (2016). Efficient synthesis of MCu (M = Pd, Pt, and Au) aerogels with accelerated gelation kinetics and their high electrocatalytic activity. *Adv. Mater.* 28 (39): 8779–8783.

48 Dubale, A.A., Zheng, Y., Wang, H. et al. (2020). High-performance bismuth-doped nickel aerogel electrocatalyst for the methanol oxidation reaction. *Angew. Chem. Int. Ed.* 59 (33): 13891–13899.

49 Liu, W., Haubold, D., Rutkowski, B. et al. (2016). Self-supporting hierarchical porous PtAg alloy nanotubular aerogels as highly active and durable electrocatalysts. *Chem. Mater.* 28 (18): 6477–6483.

50 Qian, F., Lan, P.C., Freyman, M.C. et al. (2017). Ultralight conductive silver nanowire aerogels. *Nano Lett.* 17 (12): 7171–7176.

51 Gilbert, D.A., Burks, E.C., Ushakov, S.V. et al. (2017). Tunable low density palladium nanowire foams. *Chem. Mater.* 29 (22): 9814–9818.

52 Yan, P., Brown, E., Su, Q. et al. (2017). 3D printing hierarchical silver nanowire aerogel with highly compressive resilience and tensile elongation through tunable poisson's ratio. *Small* 13 (38): 1701756.

53 Phattharasupakun, N., Wutthiprom, J., Duangdangchote, S., and Sawangphruk, M. (2019). A 3D free-standing lithiophilic silver nanowire aerogel for lithium metal batteries without lithium dendrites and volume expansion: in operando X-ray diffraction. *Chem. Commun.* 55 (40): 5689–5692.

54 Liu, W., Herrmann, A.K., Geiger, D. et al. (2012). High-performance electrocatalysis on palladium aerogels. *Angew. Chem. Int. Ed.* 51 (23): 5743–5747.

55 Wang, J., Chen, F., Jin, Y. et al. (2019). In situ high-potential-driven surface restructuring of ternary AgPd–Pt dilute aerogels with record-high performance improvement for formate oxidation electrocatalysis. *Nanoscale* 11 (30): 14174–14185.

56 Jin, Y., Chen, F., Wang, J. et al. (2019). Lamellar platinum–rhodium aerogels with superior electrocatalytic performance for both hydrogen oxidation and evolution reaction in alkaline environment. *J. Power Sources* 435: 226798.

57 Du, R., Jin, W., Hübner, R. et al. (2020). Engineering multimetallic aerogels for pH-universal HER and ORR electrocatalysis. *Adv. Energy Mater.* 10 (12): 1903857.

58 Douk, A.S., Farsadrooh, M., Damanigol, F. et al. (2018). Porous three-dimensional network of Pd–Cu aerogel toward formic acid oxidation. *RSC Adv.* 8 (42): 23539–23545.

59 Ahmadiparidari, A., Warburton, R.E., Majidi, L. et al. (2019). A long-cycle-life lithium–CO_2 battery with carbon neutrality. *Adv. Mater.* 31 (40): 1902518.

60 Lu, L., Sun, X., Ma, J. et al. (2018). Highly efficient electroreduction of CO_2 to methanol on palladium–copper bimetallic aerogels. *Angew. Chem. Int. Ed.* 57 (43): 14149–14153.

61 Du, R., Jin, W., Wu, H. et al. (2021). Rapid synthesis of gold–palladium core–shell aerogels for selective and robust electrochemical CO_2 reduction. *J. Mater. Chem A* 9 (32): 17189–17197.

62 Zhang, Z., Zhang, C., Zheng, H., and Xu, H. (2019). Plasmon-driven catalysis on molecules and nanomaterials. *Acc. Chem. Res.* 52 (9): 2506–2515.

63 Zhang, A., Fang, Z., Tang, Y. et al. (2019). Inorganic gel-derived metallic frameworks enabling high-performance silicon anodes. *Nano Lett.* 19 (9): 6292–6298.

64 Yamauchi, M., Kobayashi, H., and Kitagawa, H. (2009). Hydrogen storage mediated by Pd and Pt nanoparticles. *ChemPhysChem* 10 (15): 2566–2576.

65 Sanchez, S. and Pumera, M. (2009). Nanorobots: the ultimate wireless self-propelled sensing and actuating devices. *Chem. Asian J.* 4 (9): 1402–1410.

66 Li, W., Weng, B., Sun, X. et al. (2023). A Decade of Electrocatalysis with Metal Aerogels: A Perspective. *Catalysts* 13 (1): 167.

4

Aerogels Using Polymer Composites

Wei Fan[1,2], *Jin Tian*[2], *and Tianxi Liu*[1,2]

[1] *Key Laboratory of Synthetic and Biological Colloids, Ministry of Education, School of Chemical and Material Engineering, Jiangnan University, 1800 Lihu Avenue, Wuxi 214122, PR China*
[2] *State Key Laboratory for Modification of Chemical Fibers and Polymer Materials, College of Materials Science and Engineering, Donghua University, 2999 North Renmin Road, Shanghai 201620, PR China*

4.1 Introduction

Aerogels can be divided into two broad categories including inorganic and organic (polymer) aerogels, each category being further divided according to the nature of the materials used in the design of the gel structure [1]. The development of aerogels initiated from inorganic aerogels. The first aerogel was fabricated via supercritical fluid drying by Kistler in 1931. Kistler preserved the network structure of the silica hydrogel after drying by taking the pore-filling solvent above its critical point and venting it off as a gas. Since there is no gas-liquid interface formed in the gel and no surface tension is exerted on the silica skeleton, which maintains its shape and size, and the resulting low-density solid is practically the similar size as the original wet gel [2]. Although ambient pressure drying has been tried, surface tension forces on the skeletal framework cause excessive shrinkage even the collapse of structure, as the fragile connections between silica particles fail to resist the pressure the drying capillary pressures [3]. Owing to the high manufacturing cost, tedious and time-consuming procedures during the synthesis process, after Kistler, aerogels were "forgotten" for almost 25 years. Despite these limitations, a research effort in the development of aerogels was rapidly registered due to their special characteristics only after a few decades, when the evolution of the sol-gel method was combined with the supercritical extraction technology [4], such as ultralow thermal conductivity, sonic velocity and dielectric constant, high specific surface area, as well as ultra-wide adjustable density and refractive index [5, 6]. Therefore, it is an attractive material for applications in chemical sensors, thermal insulators, chemical adsorbents, catalysts or catalytic carriers, and space explorations [7–9]. During the following decades, the researches on aerogels were just limited to silica and several inorganic compositions [10, 11]. Nevertheless, despite that great potential, the lack of large-scale commercial aerogel applications is also immediately apparent. The wide disparity between the real and the realizable applications is reconciled in terms of poor mechanical properties (silica aerogels are fragile materials), hydrophilicity (leading to environmental instability), and the need for drying from a supercritical fluid (posing cost and safety issues as supercritical drying is a high-pressure process) [5].

Aerogels for Energy Saving and Storage, First Edition. Edited by Meldin Mathew, Hanna J. Maria, Ange Nzihou, and Sabu Thomas.
© 2024 John Wiley & Sons, Inc. Published 2024 by John Wiley & Sons, Inc.

These issues were not alleviated until the appearance of polymer aerogels. At the end of the 1980s, a new type of aerogel was invented by Pekala through the usage of an organic polymer, resorcinol-formaldehyde (RF), during the sol-gel process to develop organic and carbon aerogels [12]. Indeed, it was the right beginning of organic or polymer aerogels. Afterward, the chemical composition of organic aerogels progressively diversified and the family of organic aerogels steadily increased. Various polymer aerogels have been fabricated, including polyimide (PI)-based aerogels [13], poly(vinyl alcohol) (PVA)-based aerogels [14], polyurethane (PU)-based aerogels, and so on [15]. Additionally, aerogels derived from supramolecular gels, which are formed by the self-assembly of low molecular weight organic gelators, pave the way for their developments in high-tech materials [16]. At the same time, it was found that the polymer that makes up an organic aerogel can be dehydrated after heating to certain temperatures in an inert atmosphere (such as nitrogen or argon), leaving behind the carbon aerogel. The use of aerogels developed slowly and the species is relatively single before the1990s. After entering the twenty-first century, however, research on aerogels exploded with a variety of aerogels possessing excellent properties [17].

Besides single-component aerogels, aerogels with multi-components were also fabricated to meet the ever-increasing desire for high performance and multi-functions. For example, polyimide/silica aerogels combine the excellent mechanical properties of polyimide and the flame resistance of silica aerogels [18]. Functional carbon nanomaterials (i.e. graphene oxide (GO), carbon fibers, and carbon nanotubes (CNTs), etc.) [19–22], inorganic non-carbon materials such as silica and clay (i.e. one-dimensional halloysite, two-dimensional montmorillonite [MMT], etc.) [23, 24], cellulose nanomaterials (such as bacterial cellulose nanofibers, cellulose nanocrystals, etc.) [25, 26], or hybrid nanomaterials have been introduced for the formation of the strong interaction (i.e. chemical bond, hydrogen bond [Figure 4.1], van der Waals force, etc.) with polymer matrix to form a three-dimensional network structure [27, 28].

As fillers of polymer-based aerogels, carbon nanomaterials with unique low dimensional structure, high mechanical strength and good thermal stability, and clay with excellent thermal stability, flame retardant can not only adjust the pore structure of polymer matrix but also improve performance and expand applications of aerogels. This will provide the possibility for the design and development of high-performance and multifunctional polymer-based nanocomposite aerogel materials. In addition, interestingly, some of the strengthening phases are not used as functional fillers, but instead form three-dimensional network in the skeleton of polymer aerogel in several researches, the binary-network aerogel avoids the problem that the fillers cannot homogeneously dispersed in the polymer matrix, resulting in a more robust network structure [29]. Compared to the well-studied graphene, the newly emerged 2D early transition metal carbides and nitrides (MXenes) integrating superb electrical conductivity began to be introduced into polymer aerogels as functional materials, and the obtained composite aerogel with excellent electrical conductivity and electromagnetic interference (EMI) shielding performance has attracted more interest recently [30, 31]. The reinforcement phases in polymer-based aerogel composites are summarized in Figure 4.1.

Even though silica aerogels are the most widely studied, potential applications of silica aerogels in aerospace, industry, and daily life have been restricted because of their poor mechanical properties and hygroscopic nature. On the other hand, polymer aerogels including PVA-based, resin-based, and PI-based aerogels exhibit diverse structures and properties, which widely broaden the application of aerogels. Furthermore, aerogel composites with multi-components show enhanced performance and multi-functions, which are attracting more and more interest recently. Therefore, in this chapter, recent advances in the field of polymer aerogels and aerogels using polymer composites will be discussed, with particular emphasis placed on their fabrication/synthesis methods, structures, properties, and applications.

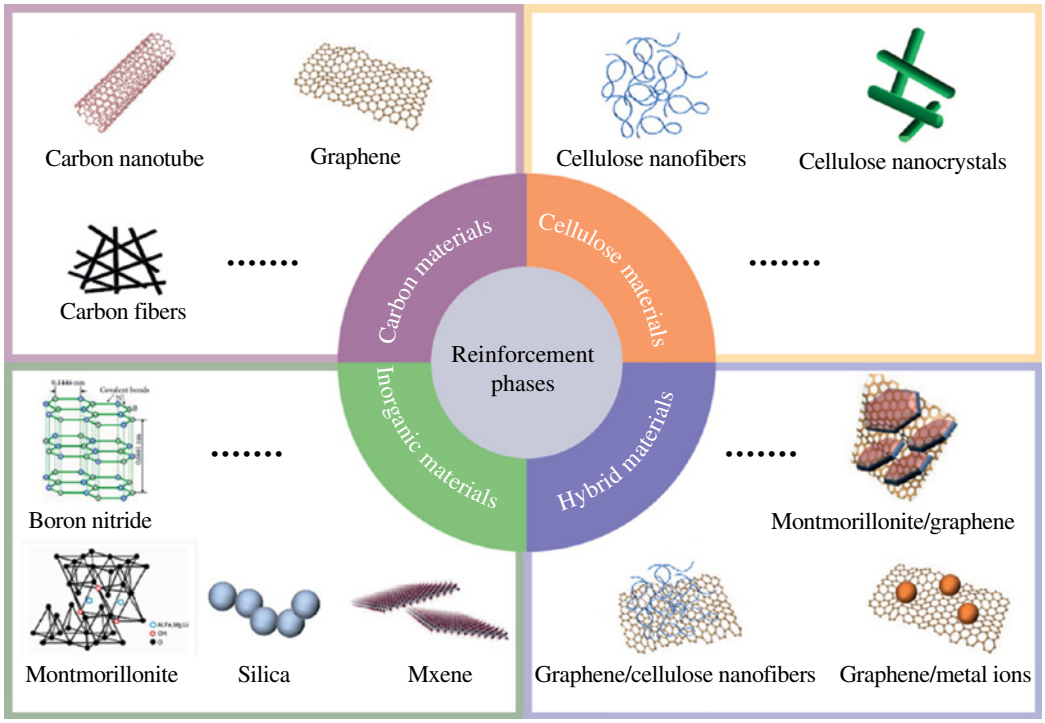


Figure 4.1 The reinforcement phases in polymer-based aerogel composites.

4.2 Preparation of Polymer-Based Aerogels

The potential application of an aerogel depends on its properties, which are strongly based on the microstructure. Therefore, it is very important to realize the microstructure control during the preparation process. Normally, the preparation process of the aerogel includes following three steps (Figure 4.2) [17]:

i) Sol-gel transition (gelation): Nanoscale sol particles are crosslinked and hierarchically assembled into a wet-gel spontaneously or catalyzed by catalysts via hydrolysis or condensation reactions.
ii) Network perfection (aging): Mechanically reinforce the tenuous solid skeleton generated during the sol-gel process.

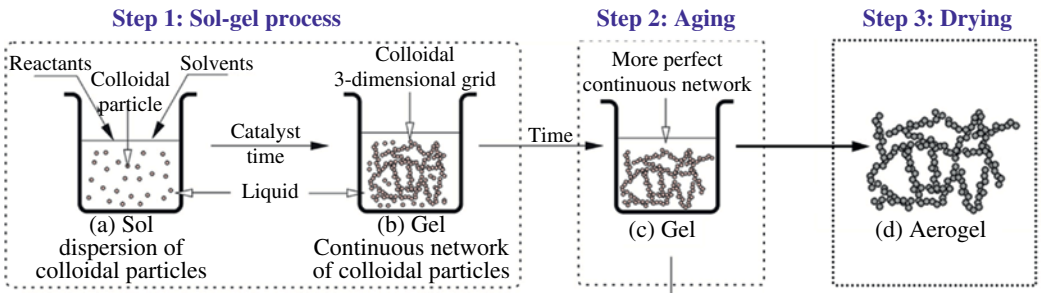


Figure 4.2 General preparation process of polymer aerogels. *Source:* [17] / MDPI / Licensed under CC BY 4.0.

iii) Gel-aerogel transition (drying): The solvent inside the wet gel is replaced by air without serious microstructure damage.

All three steps could determine the microstructure of the aerogels and affect their properties and applications. In the following sections, the basic preparation procedure of aerogels – including the sol-gel process, aging, and drying methods – will be introduced in details.

4.2.1 The Sol-Gel Process

The sol-gel process designates the transition of a colloidal solution into a disordered, branched, and continuous network linked by colloidal particles, which is interpenetrated by a liquid at low temperature (typically $T < 100\,°C$). This gelation process can take place by the aggregation of colloidal particles via destabilizing the sol, or by hydrolysis and polycondensation of precursors, or by polycondensation of water-glass. The second route is used most frequently for the preparation of aerogels, which allows the most convenient variation of reaction parameters. Using this route, aerogels of main group oxides, transition and semimetal oxides, as well as organic compounds, can be produced.

Typically, there are two steps in the sol-gel process [32]. The first step is the dissolution of monomers in a solvent. Then, independent solid colloidal particles with the size of approximately 2–10 nm are formed as a result of the polymerization process, which involves the establishment of chemical bonds between the monomers. Thus, a colloidal suspension, also termed a *sol,* is obtained with the solid colloidal particles stably dispersed in the solvent. Sol can be prepared by two techniques, condensation and dispersion of particles. Condensation proceeds by nucleation growth of particles to the appropriate size, whereas dispersion involves the reduction of large particles down to the colloidal dimensions. The size and properties of the resulting particles depend on the relative rates of these two processes. Sol formation is favored when the rate of nucleation is high and the rate of crystal growth is low. Depending on the degree of crosslinking and the growth process by which they are formed, the inorganic clusters can be either colloidal or polymeric in nature and can range from 10 to 200 Å in diameter. Several factors, such as polarity of the solvent, ionic strength of the reaction medium, and temperature, can be used to manipulate the formation of the sol.

In the second step, these colloidal particles are made to link with each other as the polymerization process continues or crosslinked by additional crosslinkers in the solvent, so as to build a three-dimensional (3D) open grid, which is termed a gel. Sol particles and small clusters in the solution attach to the spanning cluster and extend the gel network as time goes on. Commonly, the gels transformed from a sol by the gelation process are termed colloidal gels. For preparation of aerogels, the gelation is most conveniently induced through a change in the pH of the reaction solution. The mechanical state of the gel depends very much on the number of cross-links in the network. It is obvious that the greater the degree of cross-linking, the more rigid the structure formed. On the other hand, it is also possible to form some gels directly from linear polymers instead of a precursor solution, without the intermediate occurrence of individual particles. In this condition, the gels are termed polymeric gels [32].

It is obvious that the sol-gel process allows us to tailor nanostructured materials by choosing appropriate reaction parameters. In addition, the sol-gel process provides the possibility of doping gels with molecular compounds. This can be performed either chemically by using suitable alkoxide derivates or physically by introducing additives in the porous network. For example, the integration of hydrophobic hydrolyzed methyltrimethoxysilane (MTMS) can improve the water resistance of aerogels, and the inclusion of MMT can endow aerogels with flame retardant [33, 34].

4.2.2 Aging

When a gel is maintained in its liquid form, its structure and properties continue to change long after the gel point. This process is termed aging. Generally, the aim of such an aging step is to mechanically reinforce the tenuous solid skeleton generated during the sol-gel process [5, 35].

During aging, four processes can take place singly or simultaneously, including polycondensation, syneresis, coarsening, and phase transformation. Polycondensation reactions continue to occur within the gel network as long as the neighboring sol particles are close enough to react, which effectively increases the connectivity of the network and its fractal dimension. Syneresis is the spontaneous shrinkage of the gel, resulting from the expulsion of liquid from the pores. This process is generally attributed to the formation of new bonds during polycondensation reactions, which increases the bridging bonds and causes contraction of the gel network. As a result, larger particles grow at the expense of smaller ones and necks between the particles are filled up, thus leading to a narrow particle size distribution with larger mean particle diameter and decreased specific surface area but without shrinkage. This phenomenon can be further enhanced by increasing pH, temperature or pressure, resulting in coarsening of the gel structure.

4.2.3 Gel–Aerogel Transition (Drying)

For aerogels, the drying procedure is a very important step in order to preserve the highly porous structure. The gel, still embedded in the solvent, which consists mainly of alcohol with some water and catalyst, is called an alcogel or hydrogel. To remove the liquid, several extraction methods, such as supercritical drying (using CO_2, acetone, or ethanol) [12, 36], ambient pressure drying [37, 38], freeze drying [21, 25, 31], microwave drying [39], and vacuum drying [40, 41], can be employed. Normal drying at ambient conditions leads to capillary tensions as the vapor/liquid interface retreats into the porous structure. The resulting shrinkage or even cracking of the gel network proceeds until the densified structure is able to withstand these forces. Depending on the aging, the structure of the dry aerogels consists of a more or less densely packed arrangement of gel particles or network chains with the remaining porosity amounting to about 50%. Shrinkage can be reduced by prolonged aging, by aging with additional catalyst, or by using chemical additives.

4.2.3.1 Supercritical Drying

Compared to other drying methods, supercritical drying is a more effective method for preventing the shrinkage or collapse of pores. This type of drying prevents the formation of a liquid-vapor meniscus, which recedes during the emptying of the pores in the wet gels. Practically, supercritical drying consists of heating the wet gel in a closed container, so that the pressure and temperature exceeds the critical temperature (Tc), and critical pressure (Pc), of the solvent entrapped in the pores inside the gel. As in a supercritical fluid, liquid and vapor phase become indistinguishable, and no capillary forces occur. Critical conditions are very different depending on the fluid that impregnates the wet gel, and the most commonly used is CO_2 [42]. For example, PI aerogels with an intrinsically hydrophobic nature and little shrinkage by a supercritical CO_2 drying procedure [43].

4.2.3.2 Ambient Pressure Drying

Ambient pressure drying is known as a promising technique that can be applied on large scale for industrial purposes. This method relies on a passivation of the pore surface inside the gel, so as to impede further formation of new chemical bonds after condensation reactions when

the gel network is compressed under the drying stresses. At the end of the solvent evaporation process, an aerogel monolith is no longer submitted to capillary stresses so that it can resume its wet size by a spring-back effect. For example, Schwan et al. prepared RF organic aerogels via a sol-gel process in sodium carbonate solution, followed by solvent exchange with acetone and then dried under ambient pressure condition [41]. Though ambient pressure drying is a simple and energy-saving way to prepare aerogels, simple evaporation of solvent from the hydrogels under ambient conditions may cause significant shrinkage or even form solid bulk essentially without porosity.

4.2.3.3 Freeze Drying

In general, freeze drying is a simple, more economic and environmentally friendly process to obtain aerogels with good porous structures. In this method, liquid in the wet gel is first frozen and thereafter dried by sublimation under low pressures. These freeze-dried aerogels show a porosity of 80% at maximum and only half the inner surface of a comparable aerogel. Special precautions for freeze drying are long aging periods to stabilize the gel body, a solvent exchange to provide a low expansion coefficient and high sublimation pressure, and the addition of salts to achieve low freezing rates and freezing temperatures. Compared to aerogels prepared with supercritical CO_2 drying, freeze-dried aerogels show more macroporous structures with larger shrinkage and Brunauer-Emmett-Teller (BET) value. In contrast, compared to aerogels synthesized by ambient pressure drying or vacuum-drying, freeze-dried aerogels show smaller shrinkage, narrower pore size distribution (PSD), and smaller BET value [44]. Practically, compared with silica aerogels, freeze drying is more common for polymer aerogels because it is easier and faster to obtain the whole aerogels due to their stronger skeleton structure.

4.2.3.4 Other Drying Methods

Other techniques such as microwave drying and vacuum drying have also been applied to obtain aerogels with high surface area and porosity [39–41]. Microwave drying is a time-saving method to prepare mesoporous and 3D interconnected macroporous aerogels. Aerogels prepared by this method show similar structures to those prepared by freeze drying, but with more small-sized macropores. Vacuum drying is an energy-conserving process in which materials are dried under a reduced pressure, which needs less heat for rapid drying. For example, microporous PI aerogels were prepared with BET surface area up to 1454 $m^2\ g^{-1}$ and a narrow PSD in the range from 5 to 6 Å via vacuum drying [45].

Among various drying methods, supercritical drying technique is the most effective method to prevent the drying shrinkage or collapse of mesopores and obtain well-defined structures. However, the long-time solvent exchange, the involvement of massive organic solvent, high temperature, and pressure used in the drying process make it a time-consuming and high-cost method, which severely limits their practical applications. On the contrary, freeze drying is a much easier, more economic, and more environmentally friendly method. Although direct freeze drying is simple, it is heavily dependent on freezing rate and concentration of precursors in the wet gel. Ordered porous aerogels can only be obtained by elaborately controlling the freeze-drying process. Ambient pressure drying is designed to dry the wet gel at ambient pressure, which can be applied in large-scale industrial production, whereas it may result in environment pollution for the evaporation of solvents. Microwave drying and vacuum drying usually produce large pores or even induce the collapse of materials. Therefore, the drying methods have a great influence on the structure, surface area, porosity, and pore volume of aerogels, and proper drying methods should be considered according to practical requirements.

4.2.4 Combination of a Polymer Aerogel with Another Component

The polymer-based aerogel composites are materials in which polymer network are combined with one or more other components; hence, the formed final materials consist of an aerogel matrix and one or more additional components [46]. The aerogel composites can be prepared in two different ways. The first method is based on incorporation of a target additive in the liquid precursor or the sol before gelation, while the second includes additional preparation step, another component usually grows in situ inside the pores of aerogels by immersing the pre-synthesized aerogel in the precursor solution [47, 48]. In the first method, soluble organic or inorganic compounds, insoluble powders, nanofibers, and biomaterials are just examples with proven successful incorporation [49–53]. All additional components must be resistant to the same conditions as the matrix material. It is simpler and more flexible than the second, since a versatile range of different additional compounds can be added into the solution prior to gelation. On the other hand, this approach is not without drawbacks. These are related to the fact that not all additives can be homogeneously dispersed in the matrix network due to the weak interfacial interactions with the matrix and to a possible altered internal aerogel structure. This can lead also to a more brittle final material [51, 54]. To overcome this problem, Yu et al. designed a novel phenol-formaldehyde-resin (PFR)/SiO_2 composite aerogel with a 3D binary network by a direct co-polymerization and nanoscale phase-separation strategy, using phenol and formaldehyde as monomers and tetraethyl orthosilicate (TEOS) as an inorganic precursor. Negative charged PFR and SiO_2 oligomers were adsorbed onto the surface of the positively charged chitosan molecular chains by electrostatic interaction. As the polymerization progresses, phase-separation of PFR and SiO_2 at the nanoscale results in the formation of an interpenetrating binary network (Figure 4.3a,b). In the PFR/SiO_2 aerogel obtained, the PFR and the inorganic SiO_2 constituents formed interpenetrating binary network structures with domain sizes below 20 nm (Figure 4.3c) [29].

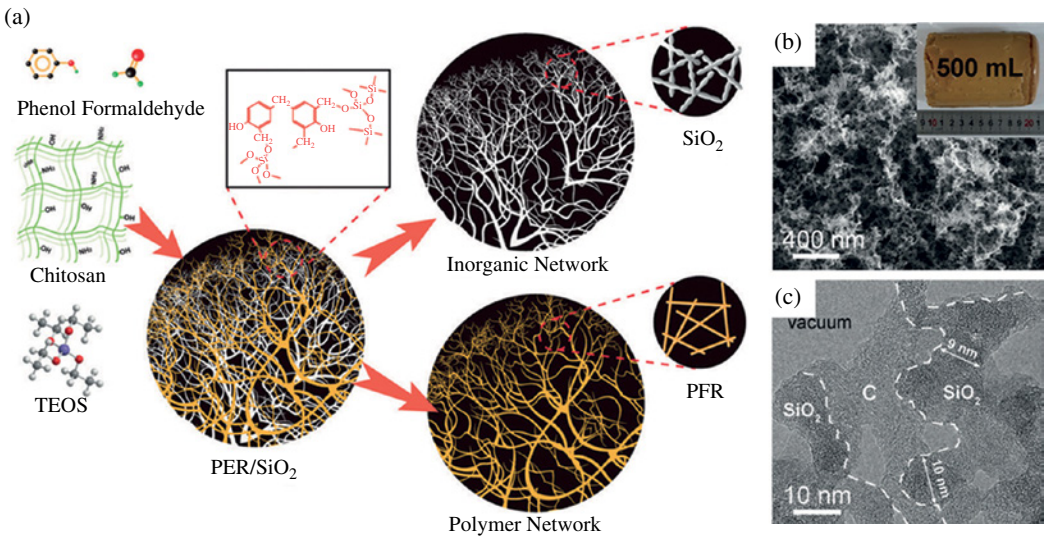


Figure 4.3 (a) Schematic illustration of the synthesis and structural composition of PFR/SiO_2 composite aerogel with interpenetrating binary network. (b) SEM image of PFR/SiO_2 composite aerogel. (c) HRTEM image of a thin and carbonized slice of the aerogel supported by a copper micro grid highlights the distribution of the PFR and silica constituents at the nanoscale. *Source:* [29] / Reproduced with permission of John Wiley & Sons.

The second method presents a post-processing step and implies the incorporation of the additives into the aerogel matrix from the liquid or gaseous phase. Yao et al. designed polyaniline/phenolic (PANI/RF) composite aerogels by putting RF aerogel into aniline solution [48]. With the addition of ammonium persulfate, polyaniline network was found growing on the interface of the micro-pore skeleton of RF aerogel, and the –OH bond of RF aerogel is linked with $–NH_2$ or –NH– bond of PANI under hydrogen-bond interaction (Figure 4.4a). Thus, the obtained PANI/RF aerogel will form an interpenetrating structure with nanopores inside (Figure 4.4b,c). However, using the loading approach with the liquid phase, the bottleneck corresponds to the diffusion (and diffusion coefficient) of the target component in and through the aerogel pores. Since use of incompatible solvents with the aerogel matrix (solvents that dissolve the matrix) can lead to the collapse of the aerogel structure, this step must be thoroughly thought through prior to incorporation. Using the loading by gaseous phase improves the target compound diffusion through the porous aerogel structure but is often limited by the additives low solubility in the gaseous phase.

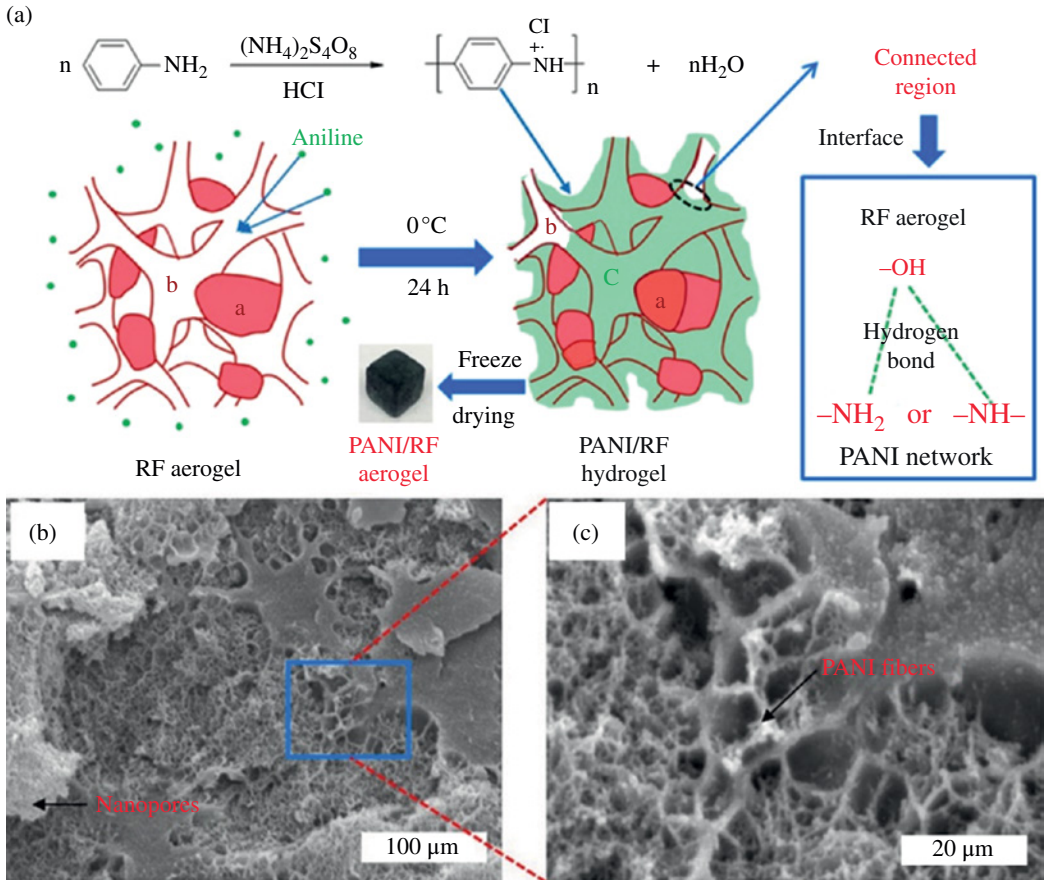


Figure 4.4 (a) Simulated diagram of the reaction and microstructure of PANI/RF aerogels. (b, c) The SEM images of PANI/RF aerogels. *Source:* (a–c) Reproduced with permission [48]. Copyright 2018, Springer-Verlag.

4.3 Several Common Polymer Aerogels and Their Composites

4.3.1 Polyimide-Based Aerogels

Polyimide (PI) represents a class of high-performance polymers with inherent attributes that include high thermal stability, high mechanical strength, chemical resistance, low permitivity, and low refractive indices [55–57]. PI materials are often found in aeronautics and aerospace, optoelectronics, and composite applications because of their ability to retain their physical and mechanical properties in thermally and chemically demanding conditions. PI is typically formed by two-stage, step-growth condensation polymerization of diamines and di-anhydrides forming soluble poly(amic acid) (PAA), which is thermally or chemically imidized. The resulting highly stable, rigid polymer backbone can be tailored by varying the monomer composition to exhibit a wide range of desirable properties. For example, a fully aromatic PI has high thermal and mechanical stability because of the imide rings and high interchain interaction [58, 59]. Therefore, it would be ideal to design PI aerogels for use as highly porous, lightweight, and high-temperature stable materials. Since 1965, when the first porous PI material was prepared by DuPont, PI aerogels have been developed considerably [42]. The materials overcome the issues of the brittleness of inorganic aerogels and the flammability of polymer-based aerogels. However, there is a high technical difficulty in the preparation of PI aerogels because the research covers organic chemistry, polymer chemistry, chemical engineering, chemical machinery, nanotechnology and other disciplines. Several key technologies for the preparation of PI aerogels have been broken through in recent years. Nowadays, PI aerogels with high-temperature resistance, flame retardant, thermal insulation, low dielectric property and good flexibility have been developed successfully [13, 60–64].

The PI aerogels exhibit a rich variety of nanoporous structures, such as crisp fragments [42], loose or close clusters of polymer fibers in the range of tens of nanometers to several micrometers [61–63, 65]. It was found that the morphologies are highly dependent on the solvent interactions during polymerization, as well as the chain rigidity and chain length of monomers and crosslinkers. One merit of PI aerogels is their excellent mechanical properties, which meets the high standard for applications in aerospace. PI aerogels can be produced with very little shrinkage during the processing and have high compressive modulus ranging from 1 to 5 MPa, much higher modulus than typical polymer reinforced silica aerogels with similar density exhibiting compressive modulus ranging from 0.1 to 2 MPa. Additionally, PI aerogels are light yellow to orange yellow in appearance, which can be tailored into different shapes. Thin films (nominally 0.5 mm) of the aerogels from certain formulations are flexible to be rolled or folded backward and completely recover with no evidence of cracking or flaking. Thicker parts such as the $6.5 \times 6.5 \times 1.3$ cm rectangular prism are rigid and strong, even able to support the weight of a car [61].

PI aerogels are typically created by the same two-stage process as conventional nonporous polyimides. However, polymerization is carried out in dilute solution in order to self-assemble the porous framework to form a gel. The gel is then subjected to solvent removal, typically supercritical fluid extraction, without collapsing the pores. The first polyimide aerogels were made as linear, uncross-linked polymers using stoichiometric amounts of pyromellitic dianhydride (PMDA) and 4,4′-oxydianiline (ODA) in N-methyl-2-pyrrolidone (NMP) to first form a PAA precursor which was converted to imide. Later, Leventis et al. used a similar approach to fabricate aerogels from linear polyimides prepared using stoichiometric amounts of PMDA and 4,4′-methylene dianiline or 4,4′-methylene di-isocyanate. In both studies, the gels were heated to 200 °C to complete the imidization, resulting in high shrinkage during the processing [62]. More recently, polyimide aerogels have been fabricated by forming anhydride capped oligomers in solution and cross-linking

them with 1,3,5-tris(4-aminophenyl)benzene or 1,3,5-triaminophenoxybenzene (TAB). Gelation occurred when dehydrating agent (acetic anhydride) and catalyst (pyridine) was added for 30 minutes in glass molds. Depending on the solvent used, the aerogels were produced with very little shrinkage and up to 90% porosity after supercritical fluid extraction. Thus, crosslinking the oligomers within the polyimide aerogel appear to achieve better structural integrity and gelation/imidization with less shrinkage [60, 66].

Imidization is essential for the formation of PI aerogels during gelation, which can be induced either chemically or thermally. The aerogels prepared by thermal imidization exhibited very little shrinkage with a porosity of up to 90%. However, the gels tended to redissolve during thermal imidization and reform upon cooling, obviating the need to keep the gels in molds. This is not conducive to fabrication of free-standing films using roll-to-roll processing, and also suggests that part of the amic acid hydrolyzes during thermal imidization, which breaks up the network structure [42, 61]. On the other hand, PI aerogels prepared by chemical imidization exhibit various structures and properties, which is strongly related to the choice of crosslinking agents. A series of octa(aminophenyl)-silsesquioxane (OAPS) crosslinked PI aerogels were prepared by Guo and co-workers [63]. The morphology of as-prepared PI aerogels resembles bundles of polymer fibers tangled together with fiber diameters in the range of 15–50 nm. The aerogels can be produced with very little shrinkage during the processing and have thermal conductivity comparable to silica aerogels with similar density (only $14\,mW\,m^{-1}K^{-1}$ for aerogels with density of $0.1\,g\,cm^{-3}$) but are much stronger with compressive modulus ranging from 1 to 5 MPa. Most notably, these aerogels can be fabricated as thin films that are flexible and foldable, being stable up to 400 °C for short term exposure as well. PI aerogels using 1,3,5-triaminophenoxybenzene (TAB) as the crosslinker were also reported. The as-prepared PI aerogels show a low dielectric constant value at 1.08 and high compressive moduli of 4–8 MPa (40 times higher than silica aerogels at the same density). In comparison to PI aerogels crosslinked using OAPS, the one crosslinked with TAB has a density about 26% higher, but modulus increases by a factor of 4 and surface areas are also significantly higher for these TAB crosslinked aerogels [60].

Supercritical-drying is a necessary process to conventional fabrication of PI aerogels. But this drying technology requires expensive equipment; dangerous and complicated treatment steps make it hard to be applied in laboratory or industries extensively. Recent years' study shows that the aerogels by freeze drying have even better properties than those by supercritical-drying [31, 67–69]. For the freeze-drying process, the precursor of PI aerogel must form water solution of PAA before aerogel generation [70]. Thus, this drying technology is an environment-friendly and low-cost process receiving more and more attention.

The property of PI aerogels could be affected by the backbone structures; thus, aerogels with different combinations of diamine and dianhydride are examined [61]. A series of TAB crosslinked aerogels derived from three different diamines (i.e. p-phenylene diamine (PPDA), 2,2′-dimethylbenzidine (DMBZ), and 4,4′-oxydianiline (ODA)) and two different dianhydrides (i.e. benzophenone-3,3′,4,4′-tetracarboxylic dianhydride (BTDA) and biphenyl-3,3′,4,4′-tetracarboxylic dianhydride (BPDA)) were prepared and studied. BPDA, PPDA, and DMBZ produces a rigid backbone in the main chain of PI, leading to higher glass transition temperatures, whereas ODA and BTDA provide flexible linking groups between phenyl rings, thus resulting in less rigid structures. Interestingly, the pore structures observed by scanning electron microscopy (SEM) images shown in Figure 4.5 for the aerogels produced using different diamines and dianhydrides are quite dissimilar. Aerogels derived from BPDA (Figure 4.5a–c) all appear as collections of polymer strands ranging from 30 to 50 nm in thickness. The combination of BTDA and ODA (Figure 4.5d) produces aerogels that are the most like silica aerogels with clusters of 50–100 nm particles loosely connected. The aerogels composed of BTDA

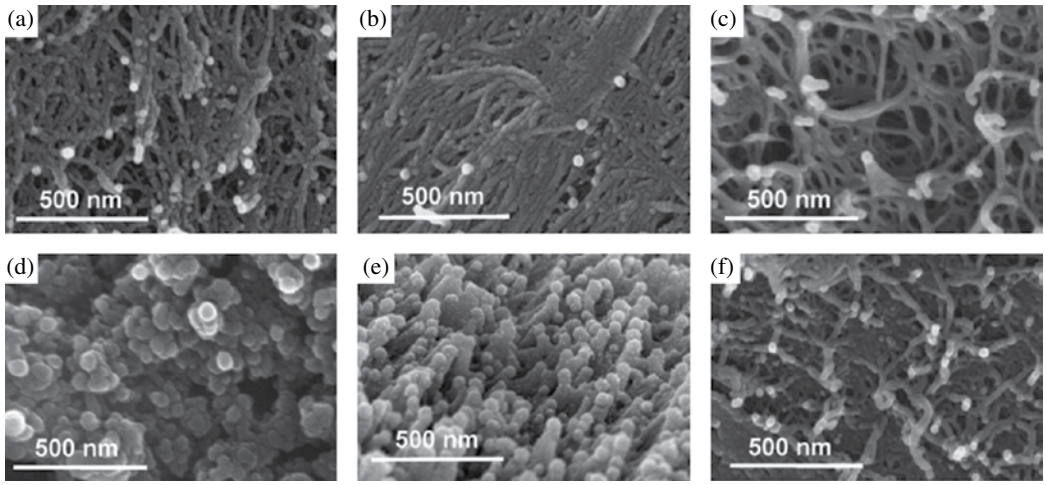


Figure 4.5 SEM images of PI aerogels synthesized from (a) ODA/BPDA, (b) PPDA/BPDA, (c) DMBZ/BPDA, (d) ODA/BTDA, (e) DMBZ/BTDA, and (f) PPDA/BTDA. *Source:* (a–f) Reproduced with permission from ref. [61], ©2012 / American Chemical Society

and DMBZ (Figure 4.5e) also appear as clusters of nanoparticles with more uniform and smaller size (~50 nm). Physical and mechanical properties of TAB crosslinked aerogels polymerized from different dianhydrides and diamines also vary a lot. It was found that aerogel properties, such as density and mechanical properties, were highly dependent on the shrinking degree during gelation. Aerogels made using a combination of BPDA and DMBZ shrank the least and therefore had the lowest density, whereas using BTDA and ODA led to greater shrinkage and higher densities. Aerogels made using ODA also tended to be less brittle, whereas DMBZ-based aerogels tended to decompose at lower temperatures. The PI aerogels have a high onset decomposition temperature over 600 °C using PPDA as the backbone diamine with excellent tensile strengths ranging from 4 to 9 MPa, which can support the weight of a car. Furthermore, it was found that using mixtures of diamines led to combinations of improved properties. For example, 100% ODA gives flexible aerogels that are hydrophilic while 100% DMBZ gives more hydrophobic aerogels that are brittle. A mixture of 50% ODA and 50% DMBZ used in conjunction with BPDA gives polyimide aerogels with better moisture resistance and flexibility.

4.3.1.1 Polyimide-Based Aerogels Combined with Carbon Materials

CNTs are typical nanofillers that have been widely applied for reinforcing the polymer matrix. Non-functionalized CNTs, however, cannot be stably and finely dispersed in polymer matrices because their strong physical interaction will result in heavy aggregations. A common technique to incorporate CNTs into such polymers is through chemical functionalization of the CNTs, which is used to enhance the nanotube-polymer interfacial interactions [46]. Generally, the preparation of polyimide/CNT aerogels consists of three steps: the functionalized CNTs were blended with PAA precursor to construct PI/CNT aerogels via a sol-gel process followed by freeze drying and thermal imidization process [69]. In a study by Fan et al., the increase of interfacial binding between CNTs and the PI aerogel will improve the interfacial strength and enhance crosslinking density, with the goal of improving the macroscopic structure integrity and mechanical properties of the polymer aerogels. Besides, the CNTs could also serve as nanoscale soft building blocks for aerogel materials, further inhibiting the shrinkage and reinforcing the dimensional stability of the composite aerogels. It is

worth mentioning that PI/CNT composite aerogel exhibits high modulus of 33.5 ± 1.8 MPa, showing 74% improvement as compared with that of neat PI aerogel. The type of functional groups on CNTs will influence the properties of composite aerogels as well. Zhu et al. took the ODA-modified CNTs as chemical cross-linking agents of PI chains, which provide rigid cross-linking sites via strong covalent bonding with polymer chains and acts as aerogels skeleton to suppress the collapse and shrinkage. Homogeneous mesoporous obtained by supercritical drying and strong covalent bonding with PAA provided by CNTs resulted in a great improvement in modulus (~46.5 MPa) drastically, which shows a 19-fold increase in Young's modulus [71].

Graphene has drawn a great deal of attention as reinforcement nanofillers in polymer composites due to its low cost, unique two-dimensional honeycomb layered structure, and excellent mechanical properties (fracture stress ~63 GPa) [72, 73]. Compared with CNTs, nanoplatelets have a geometry which can offer isotropic reinforcement in more than one direction, and exhibit more effective reinforcement in polymer composites. Moreover, with numerous oxygen functional groups on the surfaces, graphene oxide can be readily dispersed in water to form a stable colloidal suspension and also form strong interfacial bondings with the polymer matrix [74]. As a consequence, GO can act as the "super gelator" in aqueous solution with a critical gelation concentration (<0.5 wt%), thus obviously accelerating the gelation process to reduce both the drying shrinkage and aerogel density [75]. To generate a graphene structure which can be easily dispersed in solvents without rapid aggregation, oxygen functional groups are generated on edges and planes of graphene sheets, producing graphene oxide. Functional groups, such as epoxy, hydroxyl, carbonyl, and carboxylic groups, dramatically increase the aqueous solubility of graphene and promote the interaction with polymers. Similar to the fabrication of PI/CNT aerogels, the water-soluble PI precursor solution is mixed with a certain amount of GO aqueous dispersion, freeze drying of the mixture and heat treatment in an inert atmosphere (including imidization and reduction of GO) (Figure 4.6a). The oxygen-containing groups on GO sheets and the functional groups on PAA chains can form hydrogen bonds and chemical bonds, which promote the formation of stable crosslinking points. The PI/graphene aerogel prepared by this method reveals a low density (4.51 mg cm^{-3}), which could rest on the top of a dandelion easily (Figure 4.6b) [76]. Qin et al. reported that the skeletons of PI/rGO nanocomposite contributed to the efficient load-transfer between rGO sheets and PI building blocks under mechanical deformation and led to an enhancement of mechanical properties. The synergistic effect between rGO and PI could make the aerogel recover from the deformations of compression, bending, stretching, and torsion [77]. As a reinforcement phase, GO can also be used as a pore modulator and crosslinking agent. In addition, the effects of graphene with different degrees of functionalization on composite aerogels were reported

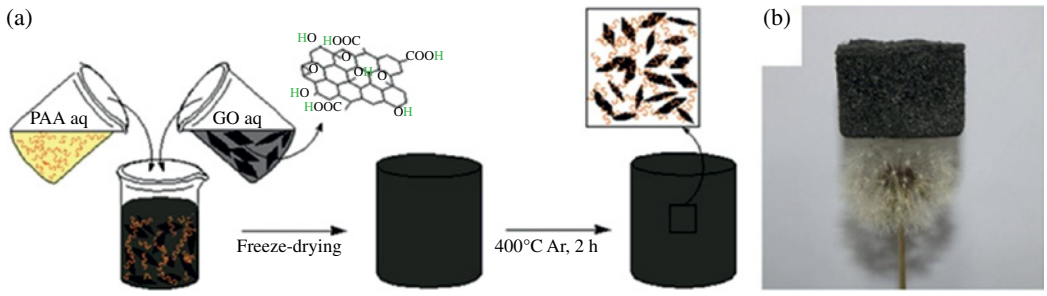


Figure 4.6 (a) Schematic diagram for the synthesis of the PI/graphene nanocomposite. (b) PI/graphene nanocomposite resting on a dandelion. *Source:* [76] / Reproduced with permission of Springer Nature.

by Fan and co-worker. Increasing amounts of functional groups on graphene can form more crosslinking points with PAA chains, contributing to the effective decrease of pore sizes, further resulting in improved compression modulus and thermal-insulating performance [27]. Moreover, GO and CNTs can form a conductive network in the polyimide matrix because of their excellent conductivity, which opened up a new route to explore widespread applications in multifunctional strain sensors [77, 78].

4.3.1.2 Cellulose/Polyimide Composite Aerogels

Cellulose is one of the most abundant renewable polymer materials stored in nature. It can be extracted from cotton, wood, hemp, bamboo, and crop straw. Cellulose is considered to be the main raw material in the energy and chemical fields in the future due to its wide source, renewable property, high specific surface area, low cost, complete biodegradation, and easy physical or chemical modification. The shape ability and mechanical flexibility of cellulose aerogels rely on their cross-linking, pore structure, intrinsic toughness, and dimensionality [79, 80]. Cellulose has moderate diameter and offers the opportunity of producing a fibrous porous matrix, which can be combined with polyimides to produce novel aerogel composites. This combination approach can effectively address the challenge to improve the shrinkage and mechanical properties of polyimides. Nguyen et al. proved that the increase in the amount of carboxylic acid-functionalized cellulose nanocrystals led to slightly lower shrinkage, lower density, and higher porosity in the polyimide composite aerogels. It is worth noting that the addition of t-CNC–COOH allows access to lower-density aerogels with the same mechanical strength, indicating that the filler was providing reinforcement to the aerogel structure [26].

The composite aerogels were prepared by mixing PAA solution and cellulose suspension using a sol-gel process, followed by freeze drying. Polyimide/bacterial cellulose aerogels and polyimide/cellulose nanocrystal composite aerogels were fabricated successfully in this way. When presynthesized PAA and celluloses were mixed together, cellulose might be wrapped by PAA matrix. It might be attributed to the hydrogen bonding between cellulose and the PAA molecular chain, thus improving the compatibility between them. Nanoscale folds on the pore walls and nanofibers between the pore walls suggest that cellulose could enter and support the skeleton of PAA aerogels, thus strengthened the lamellar structures effectively, resulting in the decrease of volume shrinkage [25].

4.3.1.3 Polyimide-Based Aerogels Combined with Inorganic Materials

Attapulgite clay (AT) is a typical porous silicate fibrillar mineral containing ribbons. In addition to its natural and unique fibrillary structure and low production cost, these rod-like nanofillers can be efficiently blended with the polymer matrix. Abundant silanol moieties (Si–OH) on the surface of AT nanorods provide active sites for forming the hydrogen-bonding interaction with the polymer matrix. Recently, AT nanorods were illustrated to have an obvious reinforcement in a wide range of polymer matrix, including epoxy, polyurethane, polyamide, chitosan/poly (vinyl alcohol), and so on [81–84]. Accordingly, the one-dimensional AT nanorods with an ideal geometric structure (length in the micrometer and diameter in only a few nanometers) were always regarded as ideal candidates for nano-building blocks to construct macroscopic structures. Wu et al. added AT in sol-gel process and then obtained PI/AT aerogels by the supercritical CO_2 extraction. As shown in Figure 4.7a–c, the AT nanorods stands out randomly (marked as red arrows) throughout the aerogel while the PI nanofibers were intimately wrapped around these AT nanorods. The Fourier transform infrared (FTIR) results verified that the presence of Si–OH units on the surface of AT allowed the formation of hydrogen-bonding interaction with the polar carbonyl units within

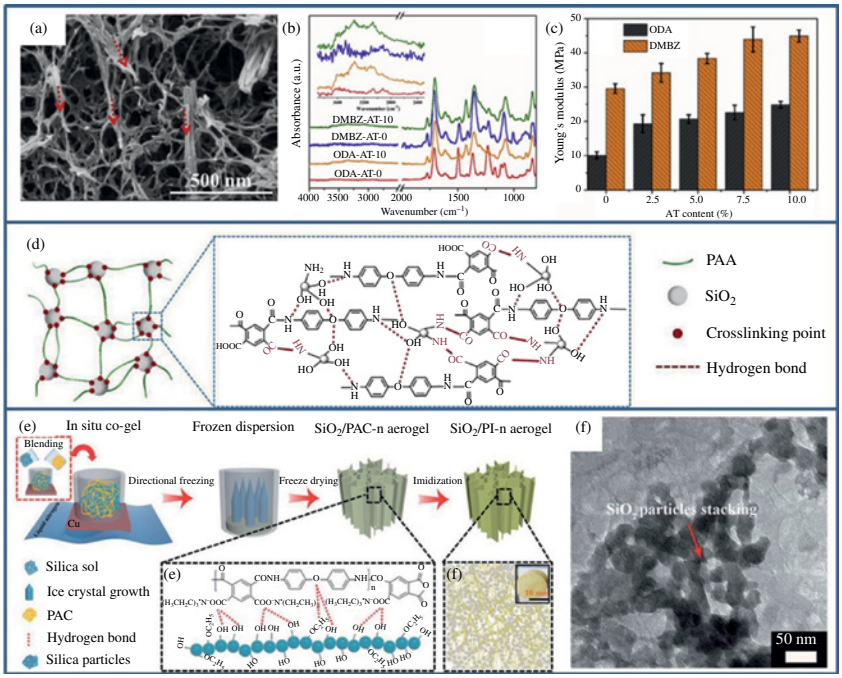


Figure 4.7 (a) SEM micrographs of the fracture surface, (b) FTIR spectra and (c) Young's modulus of PI/AT aerogels. *Source:* (a–c) Reproduced with permission from ref. [85], © 2019 / ELSEVIER (d) Schematic illustration for porous structure of aerogel and interaction between PI chains and functionalized SiO_2 nanoparticles. *Source:* Reproduced with permission from ref. [51]. Copyright 2019, Elsevier Ltd. (e) Schematic illustration of preparation of PI/SiO_2 nanocomposite aerogels using in situ co-gel method. (f) TEM image of the PI/SiO_2 aerogel. *Source:* (e–f) Reproduced with permission [18]. Copyright 2020, The Royal Society of Chemistry.

polyimide because the –OH shifted to lower wavenumbers. The strong interfacial adhesion between the aerogel matrix and AT nanorods made the two phases combine tightly, which likely favored efficient stress transfer from the polymer matrix to the AT nanorods and thus enhanced mechanical properties of the nanocomposites, reflected in the great increase of compressive stress and modulus as the AT content increased [85].

Among different types of nanoporous silica materials, silica aerogels are considered as appropriate candidates for the varieties of applications because of their attractive properties such as high surface area, narrow PSD, flexible processability, low density, as well as thermal conductivity. The introduction of silica into the polymer matrix can reduce the thermal conductivity without sacrificing the mechanical properties. In silica/polyimide composite aerogels, silica usually exists as particles or as three-dimensional continuous networks [18, 51]. Amino functionalized SiO_2 nanoparticles as crosslinkers (Figure 4.7d) could effectively inhibit shrinkage (<20%) and maintain high porosity (>95%) of aerogels, resulting in PI/SiO_2 composite aerogels with good structure stability and excellent thermal insulation properties. However, the uniformity of nanoparticle distribution in the matrix needs to be improved, which may lead to limitation in the improvement of mechanical properties [51]. A "co-gel" strategy (as shown in Figure 4.7e,f) proposed by Zhang et al., as a simple and effect method, improved the homogeneity of the nanocomposite material effectively. In short, TEOS was used as the SiO_2 precursor and poly(amide acid) (PAA) neutralized with trimethylamine was used as the PI precursor. The hydrogen bonds between the PAA chains and silica sol resulted in the excellent dispersion of the mixture [18].

2D transition metal carbides and nitrides (MXenes) have gained extensive attention recently due to their versatile surface chemistry, layered structure, and intriguing properties. By introducing MXene into polymer aerogels, it is hopeful to obtain highly conductive and ultralight composite aerogels for potential applications in energy storage, composites, electronic devices, sensors, electromagnetic radiation protection [86–88]. The assembly of MXene sheets into macroscopic architectures is an important approach to harness their extraordinary properties. However, it is difficult to construct a freestanding, mechanically flexible, and 3D framework of MXene sheets owing to their weak intersheet interactions. An interfacial enhancement strategy to construct multifunctional, superelastic, and lightweight 3D MXene architectures by bridging individual MXene sheets with polyimide macromolecules was developed by Liu and co-workers [89]. The strong interaction between the hydrosoluble PAA molecules and the hydrophilic MXene sheets was crucial for forming a robust 3D architecture. The obtained MXene/PI aerogel exhibited a mechanically strong and interconnected architecture even at an ultralow density of $8.9\,mg\,cm^{-3}$. The synergistic effect between MXene and PI also endowed the aerogel remarkable flexibility to bear deformations of 80% compression, torsion, and even 180° bending, indicating an excellent mechanical stability of the MXene/PI aerogel. Furthermore, the deliberately enhanced interfaces between MXene sheets render the MXene/PI aerogel multifunctional properties, including high electrical conductivity ($4.0\,S\,m^{-1}$), exceptional broadband microwave absorption performance (5.1 GHz, <−10 dB) with a maximum reflection loss of −45.4 dB (9.59 GHz), low thermal conductivity ($0.032\,W\,m^{-1}K^{-1}$) and flame resistance.

4.3.2 Poly(Vinyl Alcohol)-Based Aerogels

Poly(vinyl alcohol) (PVA) is a highly hydrophilic and water-soluble polymer, synthesized by partial or complete hydrolysis of poly(vinyl acetate). The low toxicity, high water content, good mechanical properties, and biocompatibility of PVA hydrogels make them widely used in various fields,

such as drug delivery, contact lenses, wound bandages, tissue engineering, and cell immobilization [17]. The preparation of PVA aerogel is usually simple and not diversified. Typically, an appropriate amount of PVA is dissolved in deionized water at 70–80 °C under vigorous stirring until the polymer is completely dissolved. Then, PVA hydrogels can be fabricated via different techniques, such as the freeze-thaw inducement of crystallization, acid-catalyzed dehydration, irradiation, radical production, and chemical crosslinking. Subsequently, the hydrogels are usually freeze-dried to form aerogels. The obtained aerogels have hierarchical microstructures. Apart from the pores measuring in the dozens of micrometers, many smaller pores are observed on the wall of the aerogels. These unique structural characteristics endow PVA aerogels with high specific surface area (~28 $m^2\ g^{-1}$) and low apparent density (~53 $mg\ cm^{-3}$) [90]. In general, low-density PVA aerogels tend to adsorb water vapor in air, which may cause the collapse of porous structure and the shrinkage of the aerogels. Thus, the functional materials are usually introduced into PVA aerogels to broaden their practical application. Fortunately, the rich hydroxyl groups on the molecular chain are beneficial to the effective combination of polyvinyl alcohol matrix with other functional materials (i.e. GO, cellulose nanofibrils, hydroxyapatite) through hydrogen bonding [91–93].

4.3.2.1 PVA-Based Aerogels Combined with Carbon Materials

In general, graphene is introduced into PVA aerogels to reduce shrinkage and enhance their mechanical properties. The gelation behavior of aqueous dispersions composed of GO and PVA was investigated through rheological study [94]. Strikingly, it has been found that small amplitude oscillatory shear (SAOS) can induce the gelation of graphene dispersions and the rheological properties measured after the completion of SAOS-induced gelation is highly related with the density and the electrical conductivity of graphene aerogels. The as-prepared ultra-light aerogel exhibits low density of 4.0 $mg\ cm^{-3}$, low surface resistivity of 6.6 U $sq.^{-1}$, high specific area of 1069 $m^2\ g^{-1}$, and high recoverable strain of 94% in compression. The structures and properties of PVA/graphene aerogels were investigated by Xiao and co-workers [91]. It was noticed that the pore sizes were very nonuniform and cell walls are pretty thick in PVA aerogels due to the serious shrinkage of them. However, the PVA/graphene aerogels demonstrated a well-defined porous structure with pore size of 20–50 μm, being smaller and ordered than pure PVA and graphene aerogels. On the one hand, the introduction of graphene facilitated the formation of a stable skeleton structure to inhibit shrinkage; on the other hand, the PVA chains prevented the GO sheets from stacking and led to a more orderly architecture, yielding aerogel composites of low densities (5.7–14.4 $mg\ cm{-}^{3}$) and high porosities (>99%). The PVA/graphene aerogels combined the flexibility of PVA aerogels and stiffness of graphene aerogels, owning a modulus of 55.0 KPa and demonstrating a good compressional recovery behavior.

4.3.2.2 Cellulose/PVA Composite Aerogels

Due to the high surface area and aspect ratio, cellulose nanofibrils (CNFs) can easily form an entangled web-like structure to be used in a wide range of applications, such as antibacterial agents, thermal insulation and oil absorbents [95]. Bring CNFs into PVA aerogels also could lower the density (<15 $mg\ cm^{-3}$) and increase the porosity (>98%) of the aerogels. These PVA/CNF aerogels also demonstrated excellent elasticity and high mechanical durability [92]. The improved stability of the aerogel structures could be attributed to the formation of a highly cross-linked network between PVA molecular and cellulose through strong hydrogen bond in the aerogel. More interestingly, the PVA/CNF aerogel became superhydrophobic and superoleophilic after being treated with methyltrichlorosilane [34]. This method avoided the structural shrinkage due to hydroscopicity of PVA/CNF aerogels. The silane-treated, cross-linked PVA/CNF aerogels

exhibited excellent absorption performance for various types of oils, organic solvents and heavy metal ions (e.g. Pb^{2+}, Hg^{2+}). Furthermore, these silane-treated PVA-CNF aerogels demonstrated excellent elasticity and mechanical durability. Additionally, Shen et al. fabricated cellulose/PVA aerogels functionalized with Fe_3O_4 nanoparticles. After in-situ loading Fe_3O_4 nanoparticles on the cellulose/PVA matrix, the mechanical strength could be further enhanced and the composite aerogels exhibited better adsorption capacity of organic dye [96].

4.3.2.3 PVA-Based Aerogels Combined with Inorganic Materials

A series of PVA/clay aerogel composites were investigated by Chen and co-workers, they selected lamellar, disklike, particulate, and fibrous reinforcement (MMT, laponite, silica, and halloysite, respectively) to be the fillers [97, 98]. All four composites exhibited higher modulus than pure PVA aerogels, consistent with the strong affinity of clay with PVA chains. Although the PVA/clay aerogel composites exhibited better mechanical properties and flammability than the corresponding polymer-only materials, two areas could potentially be improved: (i) the compressive strengths of PVA/MMT aerogels were still relatively low for specific applications, and (ii) the flammability of these aerogels was only slightly improved compared with that of pure polymer systems (for example, the limiting-oxygen-index value of a PVA/clay aerogel increases from 21% to 24% with the incorporation of 50 wt% clay in a PVA-based aerogel) [98]. To solve the first problem, chemical crosslinking agent or irradiation-induced cross-linking were adopted by the same group. Furthermore, they indicated that crosslinking could increase the compressive modulus of aerogels and the strengthened PVA/clay aerogels possessed very low flammability [97]. Later, Wang et al. proved that gelatine could be used as crosslinking agent and flame retardant in PVA/clay aerogels. With abundant hydroxyl and amino groups on the chains, gelatin could be compatible with PVA (interacting via hydrogen bonding) and the high nitrogen content from the amino acids in gelatin raised the possibility of low-flammability [99].

4.3.2.4 PVA-Based Aerogels Combined with Hybrid Materials

However, the properties of PVA-based aerogels enhanced by the introduction of one component are not as expected. For example, the combination of laponite clay/graphene hybrid nanofillers brings about a significant enhancement of mechanical and thermal properties of PVA aerogels [100]. A ternary hybrid aerogel containing PVA, CNF, and multi-walled carbon nanotube (MWCNT) was prepared Zheng et al., which showed low density ($<0.031\,g\,cm^{-3}$), high surface area ($160–200\,m^2\,g^{-1}$), and very low thermal conductivity ($<0.031\,W\,m^{-1}K^{-1}$) [95]. The PVA, CNFs, and OH-functionalized MWCNTs were chemically crosslinked via the hydroxyl groups present on these components by using glutaraldehyde, thus the highly interconnected 3D cellular networks were constructed, which might be responsible for their outstanding mechanical properties (Figure 4.8).

4.3.3 Phenolic Resin-Based Aerogels

RF-based aerogels were first described by Pekala through the polycondensation of resorcinol (R) with formaldehyde (F) in an aqueous environment using Na_2CO_3 as a catalyst [12]. The polymerization reaction consists of two steps: (i) addition reaction between R and F to form hydroxymethyl resorcinol monomers; (ii) $–CH_2–$ or $–CH_2OCH_2–$ bridging polymerization between monomers, producing water/formaldehyde or water. Continuous polymerization will produce RF clusters which further crosslink throughout the whole colloid system to gelate. The as-prepared RF aerogels consist of interconnected colloidal-like particles with diameters of approximately 10 nm and form the surface functionalized polymer "clusters" with a low density below $0.1\,g\,cm^{-3}$. The Na_2CO_3-catalyzed RF aerogels

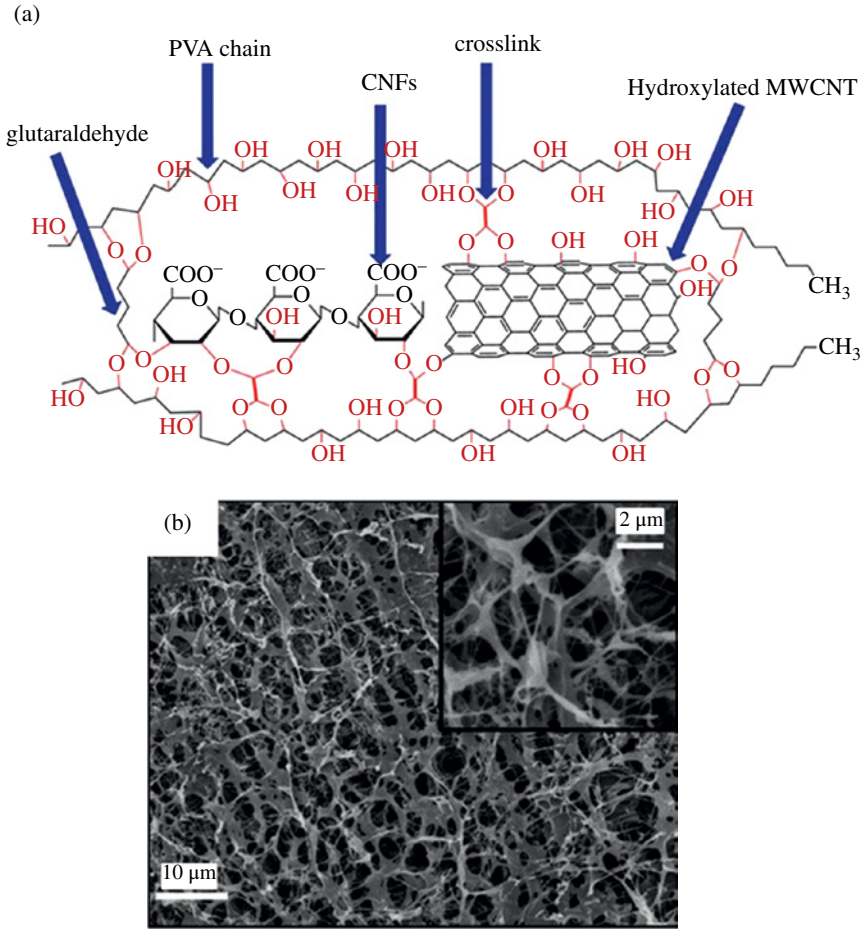


Figure 4.8 (a) The crosslinking mechanism and (b) SEM images of PVA/CNF/MWCNT aerogel. *Source:* (a–b) Reproduced with permission [95]. Copyright 2013, The Royal Society of Chemistry.

and corresponding sol-gel process have been most widely adopted until now, because of the good formability, easy microstructure-controllability, and adjustable properties [101, 102].

However, the rate of these reactions is very slow at room temperature. Normally, a multiple-stage heating process is used to accelerate the gelation process. Besides, catalysts were also applied to accelerate the polycondensation process. The acid-catalyzed route (e.g. acetic acid, hydrochloric acid (HCl), oxalic acid or para-toluenesulfonic acid) was reported for the preparation of RF aerogels [103–107]. Compared with the typical base-catalyzed RF aerogels, acid-catalyzed processes are more time-efficient. The usage of HCl as catalyst for the preparation of RF aerogels leads to organic aerogels in very short gelation times, varying from a few seconds to minutes [108]. The obtained RF aerogels have a 3D network that consists of approximately monodispersed spherical-like particles in the range of 700–1500 nm. On the other hand, the RF aerogels prepared by base-catalyzation show a narrow PSD with the maximum position located at 10–20 nm, while the pores of RF synthesized by acid-catalyzed route are 10 times larger with a broader PSD [109]. Wu et al. prepared phenol-furfural aerogels by dividing the sol-gel polymerization into two steps, i.e. the formation of gel precursors by pre-polymerizing phenol and furfural with NaOH as the catalyst

and subsequently the gelation of the precursors with HCl as the catalyst [110]. It was found that the crosslinking density of the gel precursors, controlled by the catalytic time of NaOH, exerts a great influence on the yield, drying shrinkage, bulk density, and texture of the aerogels obtained. An appropriate increase in the crosslinking density of the gel precursors helps to increase the yield and mesoporosity, leading to an increase of the bulk density. However, the organic aerogels obtained with NaOH-catalyzed pre-polymerization process experience a larger drying shrinkage than those without NaOH-catalysts. In addition, the application of ammonium carbonate as catalyst for the preparation of RF-aerogels leads to organic aerogels without metallic impurities in contrast to the conventional catalysts like sodium carbonate. The particle size and density of the synthesized RF aerogels are 0.15–4 μm and 0.37–0.42 g cm^{-3}, respectively [111].

4.3.3.1 Phenolic Resin-Based Aerogel Composites

In order to broaden the applications of RF aerogels in flame retardant, inorganic materials such as SiO_2, glass fibers and carbon fibers are often introduced to reduce their flammability and improve their ablation performance [21, 112, 113]. However, phase separation commonly prohibits the formation of homogeneous hybrid or composite aerogels in which all the constituents are evenly dispersed at the nanoscale. Therefore, most RF-based hybrid aerogels usually exhibit relatively high density(>270 mg cm^{-3}) and mechanical brittleness. With the exception of RF/SiO_2 composite aerogel with interpenetrating and homogeneous binary network structure fabricated by Yu et al., which endows the composites with low density (25–70 mg cm^{-3}), robust structures, and outstanding fire-retardant properties [29].

Introducing carbon materials into RF aerogels can improve the electrical or thermal conductivity of them. Multi-walled carbon nanotubes (MWCNT)/RF composite aerogels were prepared by sol-gel polymerization of RF monomers in an aqueous suspension of CNTs, followed by supercritical CO_2 drying. MWCNT can form a homogeneous uniform dispersion in aerogels at low concentrations, leading to a homogeneous material at the nanometer scale. The relative thermal conductivity increased slightly with the increasing MWCNT loading. The thermal conductivity of the composite gel exhibited 27% higher than that of the corresponding pure RF gel by incorporation of 1.04 vol% MWCNT [114]. Guo et al. prepared RF composite aerogels by a simple sol–gel polymerization method using graphene oxide as an anti-shrinkage additive. Morphological studies showed that GO can be well dispersed in the RF matrix owing to the good compatibility between the two elements, which effectively strengthen the RF skeleton. The linear shrinkage decreases progressively from 28.3% to 2.0% with GO loadings increasing from 0 to 2 wt%, while the density decreases from 50.6 to 195 mg cm^{-3} simultaneously [115].

4.4 Applications of Polymer Aerogel Composites

The applications of polymer-based aerogels in absorption, thermal insulation, flame retardant, sensing, and EMI shielding will be discussed in detail in this section.

4.4.1 Absorption

Industrial liquid wastes always contain a certain concentration of hazardous heavy metal ions and organics, which pollute the water and environment and endanger human health. Therefore, it is urgent to eliminate hazardous substances from industrial wastewater. In addition, some contaminated fresh water sources are in urgent need of decontamination to reclaim clean fresh water resources [116–118].

Due to their high hydrophobicity, carbon materials are often introduced into polymer aerogels for removal of pollutants and separation of oil from water. For practical applications, the recyclability of the absorbent was great key parameter for the removal of oil spills. Furthermore, compared to the absorption-combustion method [119], the absorption-squeezing method made the reutilization of absorbed oils and organic solvents. The unique porous structures of aerogels and outstanding mechanical properties of polymer matrixes endow these composites with high absorption capacity and excellent compressibility, which is indispensable for the recycling of materials. PI/graphene aerogels fabricated by Ren et al. showed remarkable absorption abilities toward a wide range of oils and organic solvents and the absorption capacity of the composites ranged from 22.94 to 37.44 g g^{-1}. The oil absorption capacity of them still remained stable ($\geq$34 g g^{-1}) during the repeated absorption-squeezing cycles as well [76]. Zhang et al. prepared anisotropic aerogels by freeze-casting PVA/CNF suspensions, together with hydrolyzed methyltrimethoxysilane (MTMS) sols (Figure 4.9a). The MTMS-modified PVA/CNF aerogels combined advantages of ultralightweight,

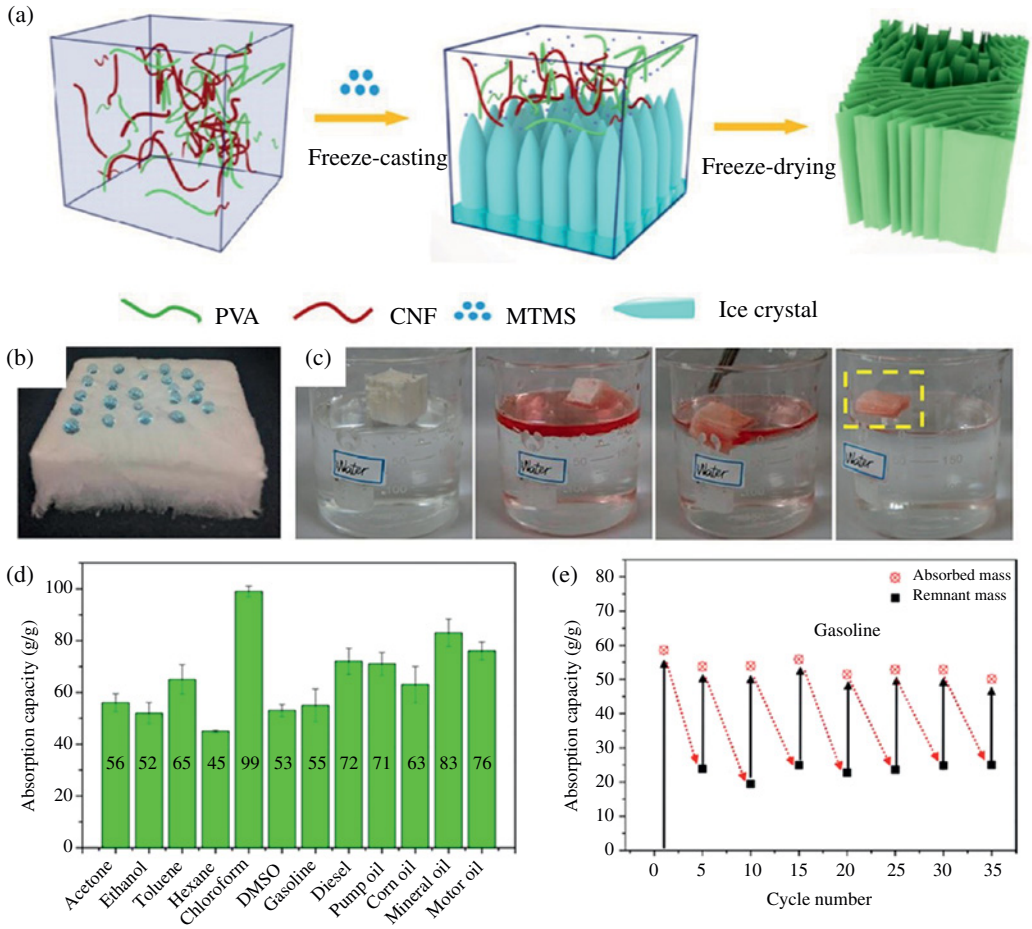


Figure 4.9 (a) Mechanism scheme for the synthesis of modified PVA/CNF aerogels. (b) Hydrophobicity of the modified aerogel. (c) Images showing the selective removal of gasoline from the water surface. (d) Absorption capacities of various oils and solvents. (e) Reusability for absorption of gasoline with a compression-squeezing method. *Source:* (a–e) Reproduced with permission from ref. [34], © 2018 / American Chemical Society.

hydrophobicity, and compression recovery properties. The aerogel could selectively remove the floating gasoline by dipping it into a mixture of oil/solvent and water (Figure 4.9b,c). The composite aerogels exhibited more excellent absorption capacities (45–99 $g\,g^{-1}$) and outstanding reusability with oil sorption retention of over 84% after 35 cycles of absorption-squeezing tests (Figure 4.9d), which was attributed to excellent flexibility and elasticity associated with the aligned porous structure of aerogels via the freeze-casting technique [34].

Superhydrophobic and superoleophilic PVA/CNF hybrid aerogels were reported after being treated with methyltrichlorosilane via a simple thermal chemical vapor deposition process [120]. The silane-treated PVA/CNF aerogels not only exhibited excellent absorption performance for various types of oils (i.e. crude oil) or organic solvents but also showed a remarkable scavenging capability for several types of heavy metal ions. The scavenging capacities of the PVA/CNF aerogels for Hg^{2+}, Pb^{2+}, Cu^{2+}, and Ag^{+} were 157.5, 110.6, 151.3, and 114.3 $mg\,g^{-1}$, respectively, which are greatly improved compared to pure PVA aerogels. It is believed that metal ion scavenging in aqueous solutions by porous materials such as aerogels is mainly driven by electrostatic interaction and complexation between the metal ions and the carboxyl groups present in the porous materials. The remarkable scavenging heavy metal ions capability exhibited by PVA/CNF aerogels makes them versatile absorbents for various potential applications, including water purification.

In brief, the preparation of mechanically robust and hydrophobic aerogel materials that can withstand multiple squeezing-absorption cycles remains a challenge.

4.4.2 Thermal Insulation

The energy needed to maintain a pleasant interior atmosphere accounts for more than 10% of the gross global energy consumption [121]. Thermal insulation plays a major role in controlling the energy efficiency of buildings or aerospace, and it is needed to substantially reduce thermal conductivity (λ) values below those of currently used insulation materials such as expanded polystyrene (EPS; λ = 30–40 $mW\,m^{-1}\,K^{-1}$), polyurethane (λ = 20–30 $mW\,m^{-1}\,K^{-1}$), glass fiber (λ = 33–44 $mW\,m^{-1}\,K^{-1}$) and mineral wool (λ = 30–40 $mW\,m^{-1}\,K^{-1}$). In fact, significantly reducing λ below the value for air (25 $mW\,m^{-1}\,K^{-1}$) is desirable to minimize the required space and materials without severely compromising the architectural design [122]. Approaches to obtain super-insulating materials include the replacement of air with another gas or vacuum or by reducing the pore size below the mean free path of air. However, it is challenging to maintain a special gas or vacuum inside insulating panels for an extended time, which can result in a loss of the initially low thermal conductivity with time. Therefore, nanoporous aerogels are ideal candidates for both ambient and high temperature insulation applications owing to their unique nanostructure, high porosity and light weight. Generally, heat is transferred by radiation, conduction, or convection. Due to the small pore sizes of aerogels (1–100 nm), the convective and gas conduction pathways are virtually eliminated. Hence, what remains is primarily radiative heat transfer and conduction through the aerogel network [123].

Silica aerogels can be used under ambient conditions and still maintain a low λ of ~17–21 $mW\,m^{-1}\,K^{-1}$, but they are brittle and difficult to prepare in large sizes. PI aerogels are ideal candidate for thermal insulation materials, especially in aerospace applications when much higher use temperatures are needed, such as insulation for launch vehicles or for planetary entry, descent, and landing systems. Leventis et al. synthesized PI aerogels by ring-opening metathesis polymerization of a norbornene end-capped diimide [65]. The new materials combine facile one-step

synthesis with heat resistance up to 200 °C, high mechanical compressive strength and specific energy absorption (168 MPa and 50 J g^{-1}, respectively, at 0.39 g cm^{-3} and 88% ultimate strain), low speed of sound (351 m s^{-1} at 0.39 g cm^{-3}) and styrofoam-like thermal conductivity (0.031 W m^{-1} K^{-1} at 25 °C). Therefore, they are reasonable multifunctional candidate materials for further exploration as thermal/acoustic insulation at elevated temperatures. Apart from thermal conductivity, decomposition temperature of aerogels as well as its dependency on external conditions are usually discussed for different classes of thermal insulation aerogels. It is reported that the onset decomposition temperature of crosslinked aromatic PI aerogels can reach up to 525–625 °C [62, 63, 65]. Consequently, PI aerogels can be used for aircraft engine applications because of their high temperature stability, low density and low thermal conductivity. Several studies have shown that introducing inorganic fillers (such as SiO_2 nanoparticles, graphene sheets) or cellulose materials into polyimide aerogels can improve thermal insulation properties [25, 51, 124], which can be explained in two aspects: composite aerogel exhibits a higher porosity and a smaller pore size than pure polyimide aerogel, which contributes to numerous solid-air interfaces, thus leading to tortuous photon conduction and multiple scattering at interfaces, resulting in enhanced thermal insulation behavior. In addition, the incorporation of nano-sized components leads to interfacial thermal resistance, the so-called Kapitza resistance, resulting reduction of the solid conduction of the walls [125]. For example, the PI/rGO/Co aerogel showed a lower thermal conductivity (0.040 W m^{-1} K^{-1} at 25 °C; 0.046 W m^{-1} K^{-1} at 100 °C) than that of the PI aerogel. This difference was due to the low content amount of rGO sheets and the combined effect of interdigitated cellular structures of the PI/rGO/Co aerogel. The smaller and interdigitated cellular structures of the PI/rGO/Co aerogel created more obstacles for air convection and the interfacial thermal resistance produced by rGO sheets and Co ions, resulting in reduction of the solid conduction [126].

In summary, polymer-based aerogel composites have a similar thermal conductivity to that of silica aerogels but are much stiffer and stronger than silica aerogels. Therefore, polymer-based aerogel composites have potential applications as thermal insulation materials with improved thermal stability and mechanical properties, which can meet the requirement in aerospace.

4.4.3 Flame Retardant Materials

Even though polymer aerogels are excellent thermal insulation materials, their applications in flame retardant materials are limited by their poor fire resistance. Therefore, modifications are required to decrease their flammability through the addition of flame retardant compounds. Environmental regulation has restricted the use of some halogenated flame retardant additives, initiating a search for alternative flame retardant additives. Recent work has shown that nanoparticle fillers, such as clays, graphene, and CNTs, are highly attractive for this purpose, since they can simultaneously improve both the mechanical properties and flammability of the polymer aerogels [97–100].

Schiraldi and co-workers prepared a series of PVA hybrid aerogels by using different nanofillers, (e.g. silica, halloysite, MMT and laponite through freeze drying) [99]. The aerogels with layered structures have lower flammability than those nonlayered aerogels and the heat release values of aerogels are much lower than those for commercial EPS foam. This is because the silicate layers with high aspect ratio served as heat and mass transport barriers with a high concentration of clay, which would largely decrease the burning rate. Furthermore, ceramic transformation of high concentration of clay particles helps to form stable structure of sample, and inhibit the flame spread.

Based on these results, they further prepared PVA/MMT aerogels followed by radiation crosslinking to increase the mechanical properties of aerogels [97]. The cross-linked PVA/MMT aerogels possessed very low flammability and high compressive modulus. For the mechanism of flammability, they indicated that with increasing clay content, the heat and mass transport barriers were developed, simultaneously low levels of thermal conductivity were maintained during burning. Furthermore, a facile preparation of PVA/MMT hybrid aerogels was introduced by using water as solvent and divinylsulfone as crosslinking agent. The compressive modulus of PVA/MMT aerogels could increase 29-fold upon crosslinking, which showed a low flammability and a great potential for applications in flame retarded materials [127].

PI aerogels not only have the typical characteristics of ordinary polymer aerogels but also show good heat resistance. As a result, PI could be used to strengthen clay-based aerogels while retaining the good thermal stability of these materials. However, almost all PIs cannot be dissolved in water, which restricts the direct introduction of PI into clay aerogels. In order to solve this problem, Wu et al. used PAA ammonium salt as a water-soluble precursor to produce PI/MMT hybrid aerogels [66]. The resulted PI/MMT aerogels show a "layer-strut" bracing structure, which can improve the mechanical performance and heat resistance of aerogels. Besides, the onset decomposition temperature of the aerogels reached up to 410 °C. The combination of PI and MMT raises the possibility that these modified hybrid aerogels could be used as high-temperature insulation and flame-retarded materials.

However, it is challenging to fabricate homogeneous hybrid or composite aerogels in which all the constituents are evenly dispersed at the nanoscale. Poor compatibility between the inorganic fillers and the polymer matrix can also result in the removal of inorganic fillers even catastrophic disintegration under prolonged high temperature thermal shock [128, 129]. Yu et al. designed a novel PFR/SiO_2 composite aerogel by a direct co-polymerization and nanoscale phase separation approach [29]. The composite aerogel is highly homogeneous and the PFR and SiO_2 constituents form an interpenetrating binary network with a characteristic domain size below 20 nm. Thanks to the special structure, the PFR/SiO_2 composite aerogel with a silica content of 70% can resist approximately 1300 °C flame without disintegration and prevents the temperature on the unexposed side to increase above 350 °C, which suggests that the material could provide extended protection against fire-induced collapse of reinforced concrete structures (Figure 4.10). This composite aerogel can be integrated with architectural materials and have potential for architectural, aerospace, and transport applications.

4.4.4 Sensing

Wearable pressure sensors have attracted considerable attention due to their potential applications in the fields of electronic skin, human-machine interaction, sports-motion detection, and human health monitoring [130–133]. Pressure sensors are generally divided into piezoresistive, piezoelectric, triboelectric, and capacitive types according to the differences of the working mechanism. Among these, due to the superior sensing properties of simple readout and sensitivity to various deformations (torsion, bending, compression, etc.) of piezoresistive pressure sensors, they have received considerable academic interest. Generally, excellent flexibility, biocompatibility, and comfortability are highly desired features for wearable pressure sensors. Hence, the traditional metal and inorganic semiconductor-based piezoresistive pressure sensors are severely constrained because of their rigid nature [134, 135]. Meanwhile, wide sensing range, high sensitivity, and ultralow detection limit are key issues that need to be considered for the fabrication of ideal wearable pressure sensors with full-scale pressure detection.

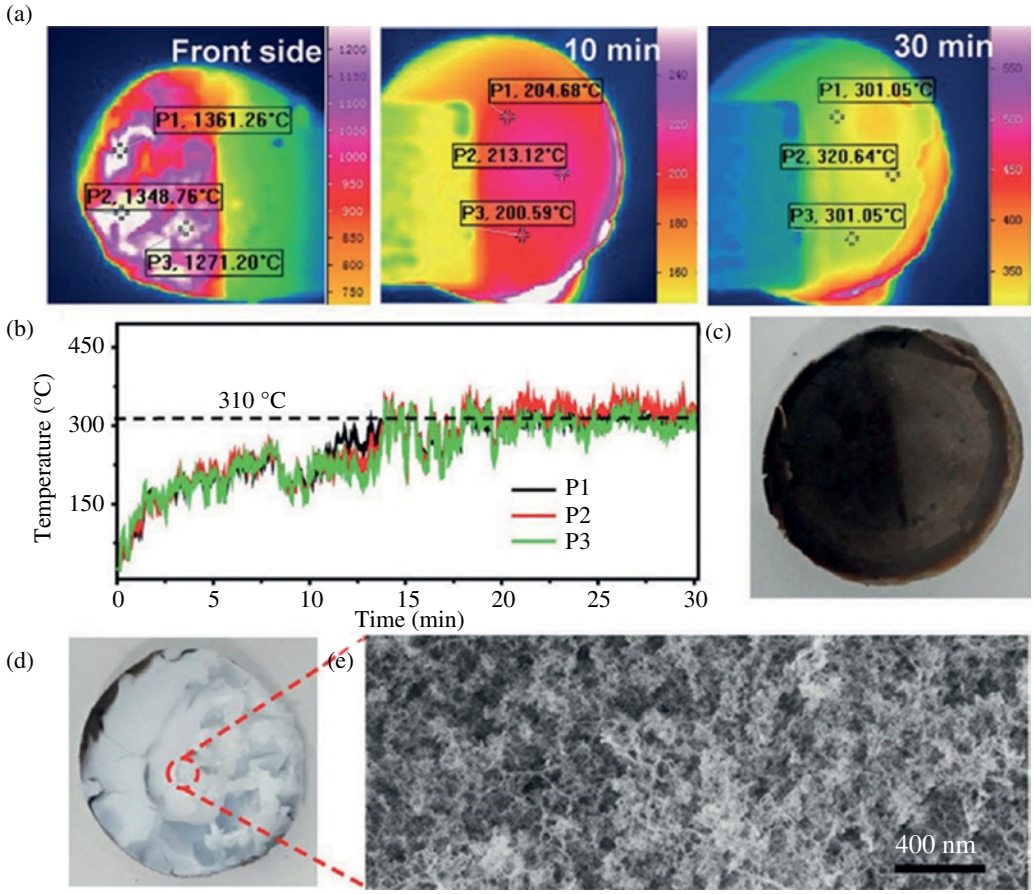


Figure 4.10 (a) Thermal images of the front and back side of the 2 cm thick RF/SiO_2 aerogel at different times from 0 to 30 minutes during extended heating at 1300 °C. (b) The time dependent temperature profile of the three reference points on the back side. Photography of (c) the back side and (d) the front side after the fire resistance test. (e) SEM image of the remaining SiO_2 network on the front side. *Source:* [29] / Reproduced with permission of John Wiley & Sons.

Hence, elastic polymers, including polyorganosiloxane, thermoplastic polyurethane (TPU), and polyimide (PI), were widely intergraded with conductive nanofillers (i.e. CNT, graphene, MXene) for the fabrication of composite foams or aerogels, which are also verified to be excellent candidates of ideal pressure sensors [19, 78, 136]. For example, CNT/TPU foams and graphene/TPU foams have been successfully prepared by the thermal-induced phase separation technique were reported by Chen et al., demonstrating good compressibility up to 90% and outstanding piezoresistive recoverability and reproducibility [137, 138]. Afterward, to develop high-performance wearable pressure sensors, they chose PI as the polymer matrix because of its features of high−/low-temperature tolerance, excellent mechanical properties, chemical and radiation resistance, and good flexibility [78]. The strong chemical interaction between PI and CNT were beneficial for the construction of a robust porous framework in PI/CNT composite aerogel. Based on the contact of adjacent cell walls, the PI/CNT composite aerogel showed high electrical conductivity of 0.445 S m^{-1} and excellent sensing performance upon external pressure, including wide sensing

range (80% strain, 61 kPa), ultrahigh sensitivity (11.28 kPa^{-1}), ultralow detection limit (0.1% strain, <10 Pa), fast response time (50 ms) and recovery time (70 ms), remarkable long-term stability (1000 cycles), and exceptional multiaxial force detection (normal, distortion, and bending). These outstanding sensing properties enabled the PI/CNT composite aerogel to detect various human motions (including airflow, pulse, vocal cord vibration, and human movement). The PI/MXene composite aerogel prepared by Liu and co-workers showed a higher electrical conductivity (4.0 $S\,m^{-1}$) than PI/CNT aerogel [89]. The unique combination of high conductivity and hydrophilicity of MXene sheets enabled the construction of a highly conductive network in polymer matrix even at the extremely low MXene content. The multifunctional MXene/PI aerogel could be used as a wearable sensors monitoring subtle movements, which displayed the rapid and repeatable response of the flexible aerogel sensor to the cyclic bending movement of a finger, and the high sensitivity enabled the aerogel to distinguish the scale and frequency of compression movements. Furthermore, under cyclic bending and release deformations, the aerogel showed outstanding long-term stability in sensitivity and its resistance variation ratio remains almost unchanged even after 1000 cycles (Figure 4.11a–e).

Zu et al. prepared the rGO/polyorganosiloxane aerogels by using modified rGO nanosheets to crosslink with polyorganosiloxane via copolycondensation [139]. The resulting nanocomposite aerogels exhibited a triple-network structure consisting of rGO nanosheets, polyvinyl-poly-(methylsiloxane) and poly(vinylmethylsiloxane) that are cross-linked with each other (Figure 4.11f). More interestingly, the graphene/polyorganosiloxane aerogel with triple-network structure achieved the combination of superhydrophobicity (water contact angle up to 167°), high compressibility, high bendability, superelasticity (reversible 90% compressive strain), excellent machinability. The resulting aerogels were electrically conductive because of the intercross-linked conductive rGO nanosheets in aerogels. It should be noted that the electrical resistance of the aerogel decreases linearly with increasing temperature (Figure 4.11g), because high temperature probably promoted thermally activated charge hopping through the rGO nanosheet junction, increasing the electrical conductance of rGO, which decreased the resistance of the rGO/polyorganosiloxane aerogels. Meanwhile, it also showed fast responses to diverse pressures and the corresponding compressive strains (Figure 4.11h). More contacts among rGO nanosheets could be produced upon compression, which increased the conduction paths and thus decreased the electrical resistance. The rGO/polyorganosiloxane aerogels exhibited high sensitivity and high durability in sensing strain, pressure, and temperature, allowing it to be promising in the practical applications of temperature/strain/pressure sensors and multifunctional wearable electronics (Figure 4.11i).

However, the introduction of reinforcing phase usually results in stress concentration during compression due to its uneven distribution in polymer matrix. Therefore, the large plastic deformation occurs under a high compression strain is the main limit for aerogel-based strain and pressure sensors, which will lead to a permanent deformation and thus an inferior long-term stability of the sensor. This makes the structural design of composite aerogels an important development direction for aerogel-based sensors. Moreover, the multifunctional sensors have attracted more and more attentions and shown great potential for the wearable devices. Because the flexible structure and compound design can be easily realized for the composite aerogels, it is possible to integrate the multiproperties into one aerogel and thus endow the resultant aerogel-based sensors with multifunction. Consequently, the preparation of highly integrated sensors with multifunction will be one of the directions for the aerogel-based sensors.

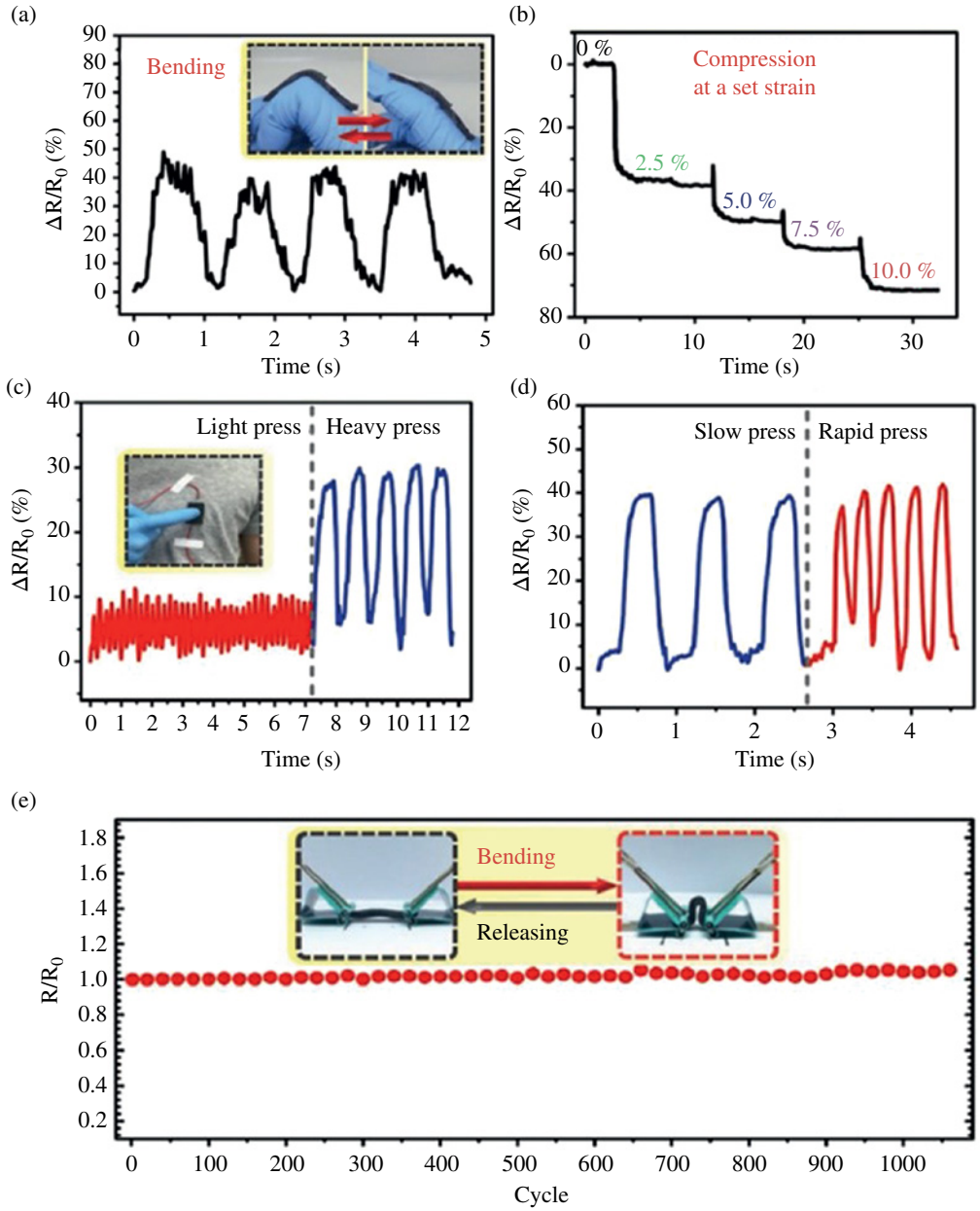


Figure 4.11 (a) Response of the MXene/PI aerogel strain sensor to the motion of finger bending. (b) Relative resistance of the strain sensor at different static strain states. (c, d) Relative resistances of the strain sensor under different compressing conditions. (e) Long-term resistant stability of MXene/PI aerogel with bending for more than 1000 times. *Source:* [89] / Reproduced with permission of John Wiley & Sons. (f) Schematic illustration for triple-network structure of graphene/polyorganosiloxane aerogel. (g) Normalized electrical resistance vs. temperature. (h) Responses to diverse pressures and the corresponding compressive strains. (i) Schematic of the mechanism of temperature, strain, and pressure sensing. *Source:* (f–i) Reproduced with permission [139]. Copyright 2019, American Chemical Society.

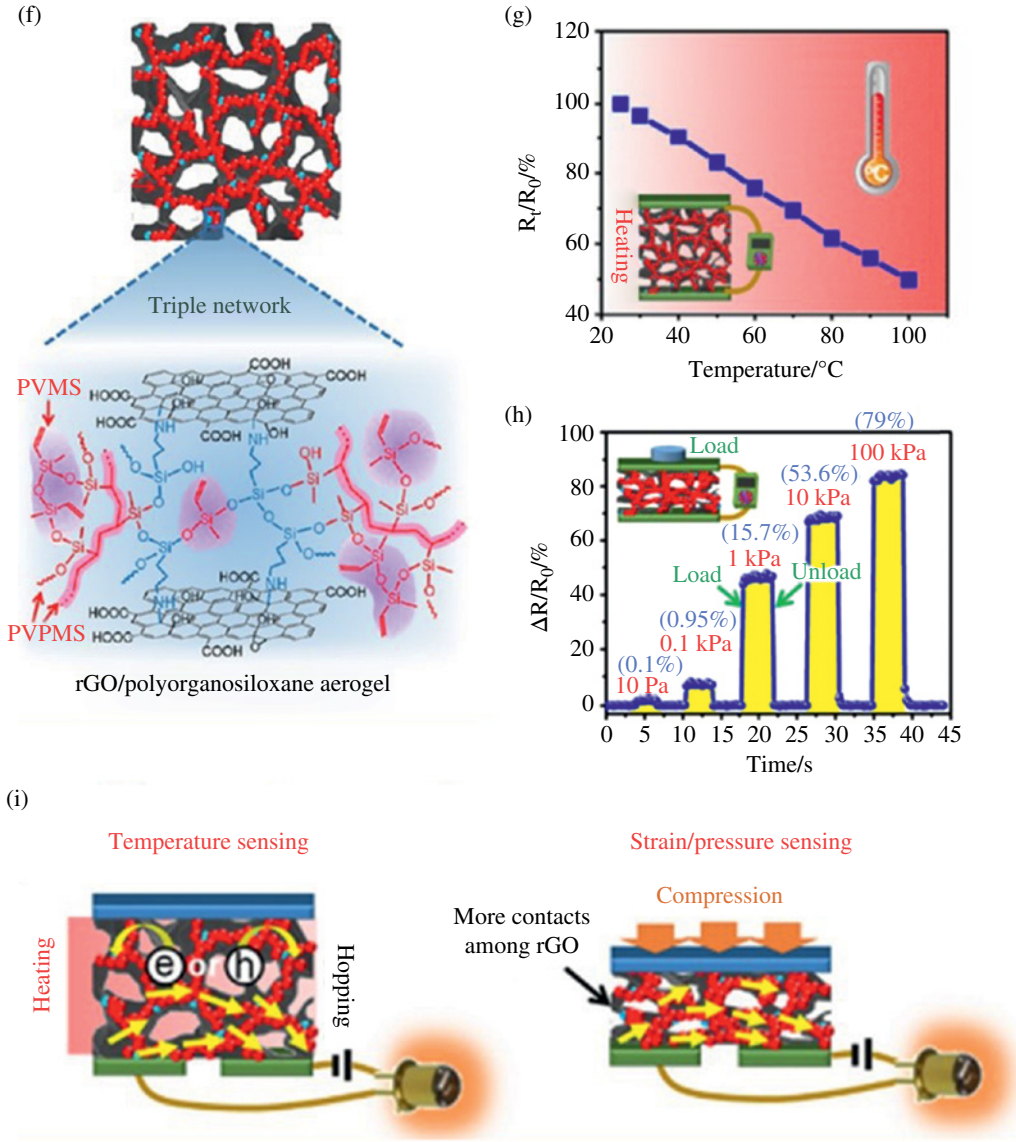


Figure 4.11 (Continued)

4.4.5 Electromagnetic Interference Shielding

In recent years, various electronics and communication devices have developed rapidly. They generate a lot of electromagnetic waves and cause serious electromagnetic pollution, which not only causes EMI to precision electronic equipment but also affects body health [140, 141]. Therefore, the materials with high EMI shielding performance are of great prospect. The traditional EMI shielding materials are mainly conductive metal or ferromagnetic materials.

Yet these materials possess the disadvantages of high density, poor processability and easy corrosion, etc., and the composite shielding materials with metal plating layer have the disadvantages of poor wear and scratch resistance [142]. Conductive polymer composites (CPCs) are increasingly concerned by researchers because of their low density, excellent processing properties, high wear and corrosion resistance [143, 144]. The conductive fillers form conductive network in the matrix of the CPC materials, which improves the electrical conductivity and thus obtains the shielding performance. Composite aerogels are ideal candidate for EMI materials due to their porous structures and adjustable components. The micropores in aerogels could reduce the density of EMI shielding materials, as well as weaken the reflecting and scattering of incident electromagnetic waves between the pore walls and nano-graphene sheets. The electromagnetic waves are hard to get away from the materials; they would be absorbed and converted into heat energy [145]. This could significantly improve the EMI shielding performance of materials and decrease the reflection of electromagnetic waves. Hence, the assembly of CNTs, graphene, MXene, and other ingredients into aerogels with proper composition and structure could be an effective strategy to develop EMI shielding materials [146–149].

Yu et al. successfully fabricated the anisotropic PI/graphene composite aerogels with PAA/graphene suspension through unidirectional freezing, freeze drying, and thermal imidization (Figure 4.12a) [150]. The ice crystals grew along one way during the freezing process, which endowed the composite aerogels with highly aligned tube-like pores (Figure 4.12b,c), and further endowed PI/graphene composite aerogels with anisotropic electrical conductivity, EMI shielding, heat transfer, and compression performance. Their conductivity and EMI shielding effectiveness (SE) in the direction perpendicular to the aligned tube-like pores was higher than those in the orientation direction of tube-like pores (Figure 4.12d,e). This could be attributed to the anisotropic tube-like pores in the composite aerogels. When the electromagnetic waves entered the aerogels from the direction perpendicular to the aligned tube-like pores (horizontal direction), they would be reflected and scattered back and forth by the walls of the aligned tube-like pores, so the electromagnetic waves were gradually dissipated as heat. The composite aerogels thus showed better EMI shielding performance in the direction perpendicular to the aligned tube-like pores. If the electromagnetic waves entered the aerogels from the orientation direction of tube-like pores (parallel to freezing direction), they would easily penetrate, so the electromagnetic dissipation was less. The composites exhibited superior EMI SE in X band (EMI SE: 26.1–28.8 dB), and the specific EMI SE value achieved 1373–1518 dB cm^2 g^{-1} when graphene content was 13 wt%. This work provided a feasible method to make lightweight PI-based EMI shielding materials, especially with anisotropic EMI shielding performance. Further, MXene based composition showed excellent electrical conductivity compared to the graphene. This is because of the functional group present in the MXene gave rise to a better arrangement in the polymer matrix, which promoted a good electron flow path. The PI/MXene aerogel composites fabricated by assembling PI aerogel with 2D Mxene sheets with an interfacial reinforcement strategy exhibited exceptional broadband microwave absorption performance (5.1 GHz, <-10 dB) with a maximum reflection loss of -45.4 dB (9.59 GHz). However, the weak self-gelation capability of MXene hinders the formation of robust and 3D networks, making the development of high-performance polymer/MXene composite aerogels more difficult [89].

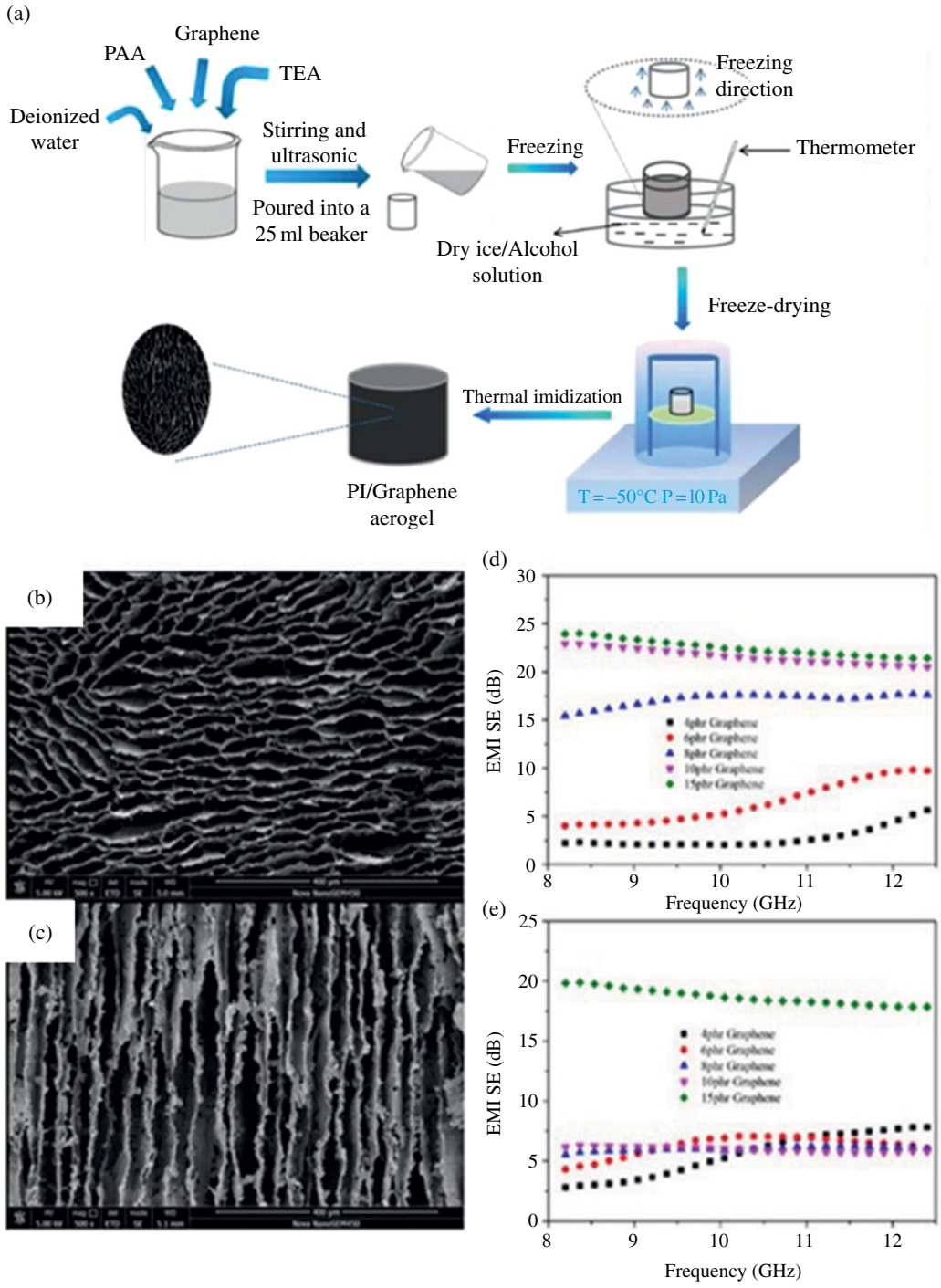


Figure 4.12 (a) Preparation of PI/graphene composite aerogels. SEM micrographs viewed (b) along the freezing direction and (c) perpendicular to the freezing direction of the PI/graphene composite aerogels. EMI SE of the composite aerogels (d) in the direction perpendicular to the aligned tubelike pores (horizontal direction) and (e) in the orientation direction of tubelike pores (vertical direction). *Source:* (a–e) Reproduced with permission from ref. [150], © 2020 / American Chemical Society.

4.5 Conclusions and Outlook

Polymer aerogels and their derivative aerogel composites have been used to bridge the nanoscale porous structures of aerogel materials to practical macro-scale applications, due to their unique structures and properties such as 3D porous networks, high specific surface area, low density, low dielectric constant, and high mechanical properties. This chapter introduced the most recent progress in preparation, structures, and properties of polymer-based aerogels as well as their potential applications in various fields including adsorption, thermal insulation, flame retardancy, and sensing. With successful implementation, these highly porous aerogel structures offer a larger range of applicability and often enhanced performance compared to their primitive polymer precursors.

In the aspect of potential applications, the unique structures and properties of polymer-based aerogels make them promising candidates in many practical areas. Due to their light weight, low thermal conductivity, and low speed of sound, aerogels are hopeful thermal and acoustic insulation materials, which can be applied in building construction, vehicles, automobiles, or spacesuits. The high surface area, high porosity, and low density derived from the 3D porous network of aerogels ensure their practical applications in the fields of sensors, adsorption, and thermal insulation. More importantly, unlike traditional silica aerogels, polymer-based aerogels with enhanced mechanical properties can meet the demands of industry and even aerospace. Finally, the feasibility of fabricating polymer-based aerogels by incorporating nanofillers can endow the aerogels with multiple functions. Therefore, polymer aerogels and their derived composite aerogels with diversified structures and properties significantly extend the practical applications of aerogel-based materials.

However, there are still some challenges to be addressed. The cost and large-scale preparation of the high-quality aerogels is yet to be solved. This problem has accompanied aerogels since their birth. Many efforts have been made to simplify the preparation process, especially the drying process, to reduce the cost and to scale up. Although modified supercritical drying, freeze drying, and even ambient drying were proposed, it is not easy to totally maintain the microstructure of the gel during the drying, and the structure collapse and damage often happen. Moreover, the surface modification employed for ambient drying unavoidably negatively affects the properties of the resultant aerogels. Therefore, it is vital to develop low-cost and large-scale preparation of high-quality aerogels.

At present, composite aerogels are mainly prepared by mixing in sol-gel, followed by aging, drying, and after treatment. However, this method will inevitably lead to ununiform distribution of the reinforcement phase in the aerogel matrix. The reported works have demonstrated that by regulating the structure/morphology and surface/interface properties of different building blocks, efficient assembly and collaborative dispersion of fillers in polymer matrix can be achieved. Therefore, understanding how to regulate and optimize the interface interaction between functional fillers and polymer matrix through efficient preparation method is the key to obtaining high-performance polymer matrix composite aerogel materials. Furthermore, it remains challenging to make functional fillers form a 3D continuous network in the composite aerogel. The excellent enhancement effects on mechanical or conductive properties of this continuous network have been proved in many works. The construction of binary or ternary network is possible to integrate the multiproperties into one aerogel and thus endow the resultant aerogel composite with multifunctions. So finding simple and effective methods to construct multiple networks will be one important direction for aerogel composites.

The precise structure control of composite aerogels, including the pore structure and the morphology, size, composition, defect, and doping of the aerogel's backbone, is of great importance on their properties –including mechanical performance and thermal insulation properties; however, it is still challenging. Composite aerogels often show enhanced performance when compared with single-compound aerogels, but the compositional uniformity of composite aerogels' backbone at molecule level has not been achieved. For the defect and doping control, the reported work studied the influence of doping and defect types on the properties of aerogels. If the precise structure control of the composite aerogel can be realized, the optimized performance can be easily obtained, and the studies on the mechanism of multicomponent synergy can also move forward.

References

1 Du, A., Zhou, B., Zhang, Z., and Shen, J. (2013). A special material or a new state of matter: a review and reconsideration of the aerogel. *Dent. Mater.* 6: 941.
2 Kistler, S.S. (1931). Coherent expanded aerogels and jellies. *Nature* 127: 741.
3 Linhares, T., Pessoa De Amorim, M.T., and Durães, L. (2019). Silica aerogel composites with embedded fibres: a review on their preparation, properties and applications. *J. Mater. Chem. A* 7: 22282.
4 Tewari, P.H., Hunt, A.J., and Lofftus, K.D. (1985). Ambient-temperature supercritical drying of transparent silica aerogels. *Mater. Lett.* 3: 363.
5 Michel, A.A., Nicholas, L., and Matthias, M.K. (2011). *Aerogels Handbook*. New York: Springer.
6 Koebel, M., Rigacci, A., and Achard, P. (2012). Aerogel-based thermal superinsulation: an overview. *J. Sol-Gel Sci. Technol.* 63: 315.
7 Baetens, R., Jelle, B.P., and Gustavsen, A. (2011). Aerogel insulation for building applications: A state-of-the-art review. *Energy Build.* 43: 761.
8 Bheekhun, N., Abu Talib, A.R., and Hassan, M.R. (2013). Aerogels in aerospace: An overview. *Adv. Mater. Sci. Eng.* 2013: 1.
9 Fricke, J. and Emmerling, A. (1998). Aerogels—Recent progress in production techniques and novel applications. *J. Sol-Gel Sci. Technol.* 13: 299.
10 Walrafen, G.E., Hokmabadi, M.S., Holmes, N.C. et al. (1985). Raman spectrum and structure of silica aerogel. *J. Chem. Phys.* 82: 2472.
11 Russo, R.E. and Hunt, A.J. (1986). Comparison of ethyl versus methyl sol-gels for silica aerogels using polar nephelometry. *J. Non-Cryst. Solids* 86: 219.
12 Pekala, R.W. (1989). Organic aerogels from the polycondensation of resorcinol with formaldehyde. *J. Mater. Sci.* 24: 3221.
13 Meador, M.A.B., McMillon, E., Sandberg, A. et al. (2014). Dielectric and other properties of polyimide aerogels containing fluorinated blocks. *ACS Appl. Mater. Interfaces* 6: 6062.
14 Shen, P., Zhao, H., Huang, W., and Chen, H. (1989). Poly(vinyl alcohol)/clay aerogel composites with enhanced flame retardancy. *RSC Adv.* 2016: 6.
15 Biesmans, G., Mertens, A., Duffours, L. et al. (1998). Polyurethane based organic aerogels and their transformation into carbon aerogels. *J. Non-Cryst. Solids* 225: 64.
16 Banerjee, S., Das, R.K., Terech, P. et al. (2013). Hybrid organogels and aerogels from co-assembly of structurally different low molecular weight gelators. *J. Mater. Chem. C* 1: 3305.
17 Zuo, L., Zhang, Y., Zhang, L. et al. (2015). Polymer/carbon-based hybrid aerogels: preparation, properties and applications. *Dent. Mater.* 8: 6806.
18 Zhang, X., Ni, X., Li, C. et al. (2020). Co-gel strategy for preparing hierarchically porous silica/polyimide nanocomposite aerogel with thermal insulation and flame retardancy. *J. Mater. Chem. A* 8: 9701.

19 Wang, F., Zhang, S., Wang, L. et al. (2018). An ultrahighly sensitive and repeatable flexible pressure sensor based on PVDF/PU/MWCNT hierarchical framework-structured aerogels for monitoring human activities. *J. Mater. Chem. C* 6: 12575.

20 Han, Q., Li, W., Zhou, Z. et al. (2019). Graphene Oxide/Polyacrylic acid-based double network skeleton for enhanced cationic dye adsorption. *Polym.-Plast. Technol. Mater.* 58: 1638.

21 Cheng, H., Xue, H., Hong, C., and Zhang, X. (2017). Preparation, mechanical, thermal and ablative properties of lightweight needled carbon fibre felt/phenolic resin aerogel composite with a bird's nest structure. *Compos. Sci. Technol.* 140: 63.

22 Kim, H.M., Noh, Y.J., Yu, J. et al. (2015). Silica aerogel/polyvinyl alcohol (PVA) insulation composites with preserved aerogel pores using interfaces between the superhydrophobic aerogel and hydrophilic PVA solution. *Compos. Part A Appl. Sci. Manuf.* 75: 39.

23 Liang, W., Wang, R., Wang, C. et al. (2019). Facile preparation of attapulgite-based aerogels with excellent flame retardancy and better thermal insulation properties. *J. Appl. Polym. Sci.* 136: 47849.

24 He, L., Jiao, Y., Dou, Y. et al. (2020). Preparation and loads transfer behaviour of graphene/halloysite organic–inorganic hybrid aerogel. *Micro Nano Lett.* 15: 503.

25 Zhang, X., Zhao, X., Xue, T. et al. (2020). Bidirectional anisotropic polyimide/bacterial cellulose aerogels by freeze-drying for super-thermal insulation. *Chem. Eng. J.* 385: 123963.

26 Nguyen, B.N., Cudjoe, E., Douglas, A. et al. (2016). Polyimide cellulose nanocrystal composite aerogels. *Macromolecules* 49: 1692.

27 Zuo, L., Fan, W., Zhang, Y. et al. (2017). Graphene/montmorillonite hybrid synergistically reinforced polyimide composite aerogels with enhanced flame-retardant performance. *Compos. Sci. Technol.* 139: 57.

28 Liu, A., Medina, L., and Berglund, L.A. (2017). High-strength nanocomposite aerogels of ternary composition: poly(vinyl alcohol), clay, and cellulose nanofibrils. *ACS Appl. Mater. Interfaces* 9: 6453.

29 Yu, Z., Yang, N., Apostolopoulou-Kalkavoura, V. et al. (2018). Fire-retardant and thermally insulating phenolic-silica aerogels. *Angew. Chem., Int. Ed.* 57: 4538.

30 Raagulan, K., Kim, B.M., and Chai, K.Y. (2020). Recent advancement of electromagnetic interference (emi) shielding of two dimensional (2D) MXene and graphene aerogel composites. *Nanomaterials* 10: 702.

31 Wang, N., Wang, H., Wang, Y. et al. (2019). Robust, lightweight, hydrophobic, and fire-retarded polyimide/MXene aerogels for effective oil/water separation. *ACS Appl. Mater. Interfaces* 11: 40512.

32 Hench, L.L. and West, J.K. (1990). The sol-gel process. *Chem. Rev.* 90: 32.

33 Shang, K., Ye, D., Kang, A. et al. (2017). Robust and fire-retardant borate-crosslinked poly (vinyl alcohol)/montmorillonite aerogel via melt-crosslink. *Polymer* 131: 111.

34 Zhang, X., Wang, H., Cai, Z. et al. (2018). Highly compressible and hydrophobic anisotropic aerogels for selective oil/organic solvent absorption. *ACS Sustain. Chem. Eng.* 7: 332.

35 Einarsrud, M.A., Nilsen, E., Rigacci, A. et al. (2001). Strengthening of silica gels and aerogels by washing and aging processes. *J. Non-Cryst. Solids* 285: 1.

36 Qin, G., Wei, W., and Guo, S. (2003). Semi-continuous drying of RF gels with supercritical acetone. *Carbon* 41: 851.

37 Cheng, H., Xue, H., Hong, C., and Zhang, X. (2016). Characterization, thermal and mechanical properties and hydrophobicity of resorcinol-furfural/silicone hybrid aerogels synthesized by ambient-pressure drying. *RSC Adv.* 6: 75793.

38 Fidalgo, A., Farinha, J.P.S., Martinho, J.M.G. et al. (2007). Hybrid silica/polymer aerogels dried at ambient pressure. *Chem. Mater.* 19: 2603.

39 Tonanon, N., Wareenin, Y., Siyasukh, A. et al. (2006). Preparation of resorcinol formaldehyde (RF) carbon gels: Use of ultrasonic irradiation followed by microwave drying. *J. Non-Cryst. Solids* 352: 5683.

40 Yang, J., Li, S., Yan, L. et al. (2010). Compressive behaviors and morphological changes of resorcinol–formaldehyde aerogel at high strain rates. *Micropor. Mesopor. Mater.* 133: 134.

41 Schwan, M. and Ratke, L. (2013). Flexibilisation of resorcinol–formaldehyde aerogels. *J. Mater. Chem. A* 1: 13462.

42 Kawagishi, K., Saito, H., Furukawa, H., and Horie, K. (2007). Superior nanoporous polyimides via supercritical CO_2 Drying of Jungle-Gym-Type Polyimide Gels. *Macromol. Rapid Commun.* 28: 96.

43 Shen, D., Liu, J., Yang, H., and Yang, S. (2013). Intrinsically highly hydrophobic semi-alicyclic fluorinated polyimide aerogel with ultralow dielectric constants. *Chem. Lett.* 42: 1230.

44 Kalinin, S.V., Kheifets, L.I., Mamchik, A.I. et al. (1999). Influence of the drying technique on the structure of silica gels. *J. Sol-Gel Sci. Technol.* 15: 31.

45 Li, G. and Wang, Z. (2013). Microporous polyimides with uniform pores for adsorption and separation of CO_2 gas and organic vapors. *Macromolecules* 46: 3058.

46 Barrios, E., Fox, D., Li Sip, Y.Y. et al. (2019). Nanomaterials in advanced, high-performance aerogel composites: a review. *Polymers-Basel* 11: 726.

47 Zhang, J., Cheng, Y., Tebyetekerwa, M. et al. (2019). "Stiff–soft" binary synergistic aerogels with superflexibility and high thermal insulation performance. *Adv. Funct. Mater.* 29: 1806407.

48 Yao, R., Yao, Z., and Zhou, J. (2018). Microstructure, thermal and electrical properties of polyaniline/phenolic composite aerogel. *J. Porous Mater.* 25: 495.

49 Zhang, Z., Wang, X., Zu, G. et al. (2020). Effect of different chemical liquid deposition methods on the microstructure and properties of polyimide-polyvinylpolymethylsiloxane composite aerogels. *J. Supercrit. Fluids* 160: 104811.

50 Hou, X., Zhang, R., and Fang, D. (2020). Flexible, fatigue resistant, and heat-insulated nanofiber-assembled polyimide aerogels with multifunctionality. *Polym. Test.* 81: 106246.

51 Fan, W., Zhang, X., Zhang, Y. et al. (2019). Lightweight, strong, and super-thermal insulating polyimide composite aerogels under high temperature. *Compos. Sci. Technol.* 173: 47.

52 Wu, C., Chen, Z., Wang, F. et al. (2019). Preparation and characterization of ultralight glass fiber wool/phenolic resin aerogels with a spring-like structure. *Compos. Sci. Technol.* 179: 125.

53 Peng, H., Wu, J., Wang, Y. et al. (2016). A facile approach for preparation of underwater superoleophobicity cellulose/chitosan composite aerogel for oil/water separation. *Appl. Phys. A* 122.

54 Wan, B., Li, H., Xiao, Y. et al. (2021). Improved breakdown strength and energy density of polyimide composites by interface engineering between BN and BaTiO3 fibers. *J. Mater. Sci. Technol.* 74: 1.

55 Gouzman, I., Grossman, E., Verker, R. et al. (2019). Advances in polyimide-based materials for space applications. *Adv. Mater.* 31: 1807738.

56 Liaw, D., Wang, K., Huang, Y. et al. (2012). Advanced polyimide materials: Syntheses, physical properties and applications. *Prog. Polym. Sci.* 37: 907.

57 Xiao, Y., Low, B.T., Hosseini, S.S. et al. (2009). The strategies of molecular architecture and modification of polyimide-based membranes for CO_2 removal from natural gas—A review. *Prog. Polym. Sci.* 34: 561.

58 Yue, Z., Cai, Y., and Xu, S. (2014). Facile synthesis of a symmetrical diamine containing bis-benzimidazole ring and its thermally stable polyimides. *J. Polym. Res.* 21: 463.

59 Yu, X., Liang, W., Cao, J., and Wu, D. (2017). Mixed rigid and flexible component design for high-performance polyimide films. *Polymers-Basel* 9: 451.

60 Meador, M.A.B., Wright, S., Sandberg, A. et al. (2012). Low dielectric polyimide aerogels as substrates for lightweight patch antennas. *ACS Appl. Mater. Interfaces* 4: 6346.

61 Meador, M.A.B., Malow, E.J., Silva, R. et al. (2012). Mechanically strong, flexible polyimide aerogels cross-linked with aromatic triamine. *ACS Appl. Mater. Interfaces* 4: 536.

62 Chidambareswarapattar, C., Larimore, Z., Sotiriou-Leventis, C. et al. (2010). One-step room-temperature synthesis of fibrous polyimide aerogels from anhydrides and *isocyanates* and conversion to isomorphic carbons. *J. Mater. Chem.* 20: 9666.

63 Guo, H., Meador, M.A.B., McCorkle, L. et al. (2011). Polyimide aerogels cross-linked through amine functionalized polyoligomeric silsesquioxane. *ACS Appl. Mater. Interfaces* 3: 546.

64 Kim, S.Y., Noh, Y.J., Lim, J., and You, N. (2014). Silica aerogel/polyimide composites with preserved aerogel pores using multi-step curing. *Macromol. Res.* 22: 108.

65 Leventis, N., Sotiriou-Leventis, C., Mohite, D.P. et al. (2011). Polyimide aerogels by ring-opening metathesis polymerization (ROMP). *Chem. Mater.* 23: 2250.

66 Wu, T., Dong, J., Gan, F. et al. (2018). Low dielectric constant and moisture-resistant polyimide aerogels containing trifluoromethyl pendent groups. *Appl. Surf. Sci.* 440: 595.

67 Xu, G., Li, M., Wu, T., and Teng, C. (2020). Highly compressible and anisotropic polyimide aerogels containing aramid nanofibers. *React. Funct. Polym.* 154: 104672.

68 Shen, Y., Wang, L., Liu, F. et al. (2020). Solvent vapor strengthened polyimide nanofiber-based aerogels with high resilience and controllable porous structure. *ACS Appl. Mater. Interfaces* 12: 53104.

69 Fan, W., Zuo, L., Zhang, Y. et al. (2018). Mechanically strong polyimide/carbon nanotube composite aerogels with controllable porous structure. *Compos. Sci. Technol.* 156: 186.

70 Zhang, Y., Fan, W., Lu, H., and Liu, T. (2018). Highly porous polyimide-derived carbon aerogel as advanced three-dimensional framework of electrode materials for high-performance supercapacitors. *Electrochim. Acta* 283: 1763.

71 Zhu, Z., Yao, H., Dong, J. et al. (2019). High-mechanical-strength polyimide aerogels crosslinked with 4, 4′-oxydianiline-functionalized carbon nanotubes. *Carbon* 144: 24.

72 Novoselov, K.S., Geim, A.K., Morozov, S.V. et al. (2004). Electric field effect in atomically thin carbon films. *Science* 306: 666.

73 Geim, A.K. and Novoselov, K.S. (2007). The rise of graphene. *Nat mater.* 6: 183.

74 Stankovich, S., Dikin, D.A., Piner, R.D. et al. (2007). Synthesis of graphene-based nanosheets via chemical reduction of exfoliated graphite oxide. *Carbon* 45: 1558.

75 Bai, H., Li, C., Wang, X., and Shi, G. (2010). A pH-sensitive graphene oxide composite hydrogel. *Chem. Commun.* 46: 2376.

76 Ren, R., Wang, Z., Ren, J., and Lv, Y. (2019). Highly compressible polyimide/graphene aerogel for efficient oil/water separation. *J. Mater. Sci.* 54: 5918.

77 Qin, Y., Peng, Q., Ding, Y. et al. (2015). Lightweight, superelastic, and mechanically flexible graphene/polyimide nanocomposite foam for strain sensor application. *ACS Nano* 9: 8933.

78 Chen, X., Liu, H., Zheng, Y. et al. (2019). Highly compressible and robust polyimide/carbon nanotube composite aerogel for high-performance wearable pressure sensor. *ACS Appl. Mater. Interfaces* 11: 42594.

79 Long, L., Weng, Y., and Wang, Y. (2018). Cellulose aerogels: synthesis, applications, and prospects. *Polymers-Basel* 10: 623.

80 Wan, C., Jiao, Y., Wei, S. et al. (2019). Functional nanocomposites from sustainable regenerated cellulose aerogels: a review. *Chem. Eng. J.* 359: 459.

81 Huang, D., Wang, W., Xu, J., and Wang, A. (2012). Mechanical and water resistance properties of chitosan/poly(vinyl alcohol) films reinforced with attapulgite dispersed by high-pressure homogenization. *Chem. Eng. J.* 210: 166.

82 Niu, X., Huo, L., Cai, C. et al. (2014). Rod-like attapulgite modified by bifunctional acrylic resin as reinforcement for epoxy composites. *Ind. Eng. Chem. Res.* 53: 16359.

83 Shen, L., Lin, Y., Du, Q., and Zhong, W. (2006). Studies on structure–property relationship of polyamide-6/attapulgite nanocomposites. *Compos. Sci. Technol.* 66: 2242.

84 Peng, L., Zhou, L., Li, Y. et al. (2011). Synthesis and properties of waterborne polyurethane/attapulgite nanocomposites. *Compos. Sci. Technol.* 71: 1280.

85 Wu, T., Dong, J., Xu, G. et al. (2019). Attapulgite-reinforced polyimide hybrid aerogels with high dimensional stability and excellent thermal insulation property. *Polymer* 176: 196.

86 Ma, Y., Yue, Y., Zhang, H. et al. (2018). 3D synergistical MXene/reduced graphene oxide aerogel for a piezoresistive sensor. *ACS Nano* 12: 3209.

87 Jiang, Y., Xie, X., Chen, Y. et al. (2018). Hierarchically structured cellulose aerogels with interconnected MXene networks and their enhanced microwave absorption properties. *J. Mater. Chem. C* 6: 8679.

88 Yue, Y., Liu, N., Ma, Y. et al. (2018). Highly self-healable 3D microsupercapacitor with MXene-graphene composite aerogel. *ACS Nano* 12: 4224.

89 Liu, J., Zhang, H., Xie, X. et al. (2018). Multifunctional, superelastic, and lightweight MXene/polyimide aerogels. *Small* 14: 1802479.

90 Yang, L., Yang, J., Tang, L. et al. (2020). Hierarchically porous PVA aerogel for leakage-proof phase change materials with superior energy storage capacity. *Energy Fuels* 34: 2471.

91 Xiao, J., Zhang, J., Lv, W. et al. (2017). Multifunctional graphene/poly(vinyl alcohol) aerogels: *In situ* hydrothermal preparation and applications in broad-spectrum adsorption for dyes and oils. *Carbon* 123: 354.

92 Zheng, Q., Cai, Z., and Gong, S. (2014). Green synthesis of polyvinyl alcohol (PVA)–cellulose nanofibril (CNF) hybrid aerogels and their use as superabsorbents. *J. Mater. Chem. A* 2: 3110.

93 Guo, W., Liu, J., Zhang, P. et al. (2018). Multi-functional hydroxyapatite/polyvinyl alcohol composite aerogels with self-cleaning, superior fire resistance and low thermal conductivity. *Compos. Sci. Technol.* 158: 128.

94 Kim, J.E. and Lee, H.S. (2014). Oscillatory shear induced gelation of graphene–poly(vinyl alcohol) composite hydrogels and rheological premonitor of ultra-light aerogels. *Polymer* 55: 287.

95 Zheng, Q., Javadi, A., Sabo, R. et al. (2013). Polyvinyl alcohol (PVA)–cellulose nanofibril (CNF)–multiwalled carbon nanotube (MWCNT) hybrid organic aerogels with superior mechanical properties. *RSC Adv.* 3: 20816.

96 Shen, D., Liu, J., Gan, L. et al. (2018). Green synthesis of Fe_3O_4/cellulose/polyvinyl alcohol hybride aerogel and its application for dye removal. *J. Polym. Environ.* 26: 2234.

97 Chen, H., Liu, B., Huang, W. et al. (2014). Fabrication and properties of irradiation-cross-linked poly(vinyl alcohol)/clay aerogel composites. *ACS Appl. Mater. Interfaces* 6: 16227.

98 Chen, H., Wang, Y., and Schiraldi, D.A. (2014). Preparation and flammability of poly(vinyl alcohol) composite aerogels. *ACS Appl. Mater. Interfaces* 6: 6790.

99 Wang, Y., Zhao, H., Degracia, K. et al. (2017). Green approach to improving the strength and flame retardancy of poly(vinyl alcohol)/clay aerogels: incorporating biobased gelatin. *ACS Appl. Mater. Interfaces* 9: 42258.

100 Alhwaige, A.A., Herbert, M.M., Alhassan, S.M. et al. (2016). Laponite/multigraphene hybrid-reinforced poly(vinyl alcohol) aerogels. *Polymer* 91: 180.

101 Tian, H.Y., Buckley, C.E., Paskevicius, M., and Wang, S.B. (2011). Carbon aerogels from acetic acid catalysed resorcinol–furfural using supercritical drying for hydrogen storage. *J. Supercrit. Fluids* 55: 1115.

102 Chen, K., Bao, Z., Du, A. et al. (2012). One-pot synthesis, characterization and properties of acid-catalyzed resorcinol/formaldehyde cross-linked silica aerogels and their conversion to hierarchical porous carbon monoliths. *J. Sol-Gel Sci. Technol.* 62: 294.

103 Wu, D. and Fu, R. (2005). Fabrication and physical properties of organic and carbon aerogel derived from phenol and furfural. *J. Porous Mater.* 12: 311.

104 Mayes, R.T., Tsouris, C., Kiggans, J.O. Jr. et al. (2010). Hierarchical ordered mesoporous carbon from phloroglucinol-glyoxal and its application in capacitive deionization of brackish water. *J. Mater. Chem.* 20: 8674.

105 Conceição, F.L., Carrott, P.J.M., and Ribeiro Carrott, M.M.L. (2009). New carbon materials with high porosity in the 1–7 nm range obtained by chemical activation with phosphoric acid of resorcinol–formaldehyde aerogels. *Carbon* 47: 1874.

106 Fairén-Jiménez, D., Carrasco-Marín, F., and Moreno-Castilla, C. (2006). Porosity and surface area of monolithic carbon aerogels prepared using alkaline carbonates and organic acids as polymerization catalysts. *Carbon* 44: 2301.

107 Mulik, S., Sotiriou-Leventis, C., and Leventis, N. (2007). Time-efficient acid-catalyzed synthesis of resorcinol–formaldehyde aerogels. *Chem. Mater.* 19: 6138.

108 Reuß, M. and Ratke, L. (2008). Subcritically dried RF-aerogels catalysed by hydrochloric acid. *J. Sol-Gel Sci. Technol.* 47: 74.

109 Barbieri, O., Ehrburger-Dolle, F., Rieker, T.P. et al. (2001). Small-angle X-ray scattering of a new series of organic aerogels. *J. Non-Cryst. Solids* 285: 109.

110 Wu, D. and Fu, R. (2006). Synthesis of organic and carbon aerogels from phenol–furfural by two-step polymerization. *Micropor. Mesopor. Mater.* 96: 115.

111 Reuß, M. and Ratke, L. (2010). RF-aerogels catalysed by ammonium carbonate. *J. Sol-Gel Sci. Technol.* 53: 85.

112 Wang, C., Cheng, H., Hong, C. et al. (2018). Lightweight chopped carbon fibre reinforced silica-phenolic resin aerogel nanocomposite: Facile preparation, properties and application to thermal protection. *Compos. Part A Appl. Sci. Manuf.* 112: 81.

113 Yin, R., Cheng, H., Hong, C., and Zhang, X. (2017). Synthesis and characterization of novel phenolic resin/silicone hybrid aerogel composites with enhanced thermal, mechanical and ablative properties. *Compos. Part A Appl. Sci. Manuf.* 101: 500.

114 Haghgoo, M., Yousefi, A.A., Zohouriaan Mehr, M.J. et al. (2014). Characterization of multi-walled carbon nanotube dispersion in resorcinol–formaldehyde aerogels. *Micropor. Mesopor. Dent. Mater.* 184: 97.

115 Guo, K., Song, H., Chen, X. et al. (2014). Graphene oxide as an anti-shrinkage additive for resorcinol–formaldehyde composite aerogels. *Phys. Chem. Chem. Phys.* 16: 11603.

116 Wang, H., Yang, J., Liu, X. et al. (2019). A robust 3D superhydrophobic sponge for in situ continuous oil removing. *J. Mater. Sci.* 54: 1255.

117 Wang, E., Wang, H., Liu, Z. et al. (2015). One-step fabrication of a nickel foam-based superhydrophobic and superoleophilic box for continuous oil–water separation. *J. Mater. Sci.* 50: 4707.

118 Huang, H., Liu, M., Li, Y. et al. (2018). Polyphenylene sulfide microfiber membrane with superhydrophobicity and superoleophilicity for oil/water separation. *J. Mater. Sci.* 53: 13243.

119 Bi, H., Yin, Z., Cao, X. et al. (2013). Carbon fiber aerogel made from raw cotton: a novel, efficient and recyclable sorbent for oils and organic solvents. *Adv. Mater.* 25: 5916.

120 Zhai, T., Zheng, Q., Cai, Z. et al. (2016). Synthesis of polyvinyl alcohol/cellulose nanofibril hybrid aerogel microspheres and their use as oil/solvent superabsorbents. *Carbohydr. Polym.* 148: 300.

121 Sadineni, S.B., Madala, S., and Boehm, R.F. (2011). Passive building energy savings: A review of building envelope components. *Renew. Sustain. Energy Rev.* 15: 3617.

122 Jelle, B.P. (2011). Traditional, state-of-the-art and future thermal building insulation materials and solutions – Properties, requirements and possibilities. *Energy Build.* 43: 2549.

123 Hu, F., Wu, S., and Sun, Y. (2018). Hollow-structured materials for thermal insulation. *Adv. Mater.* 31: 1801001.

124 Xue, T., Fan, W., Zhang, X. et al. (2021). Layered double hydroxide/graphene oxide synergistically enhanced polyimide aerogels for thermal insulation and fire-retardancy. *Compos. Part B* 219: 108963.

125 Ruan, K., Shi, X., Guo, Y., and Gu, J. (2020). Interfacial thermal resistance in thermally conductive polymer composites: A review. *Compos. Commun.* 22: 100518.

126 Zhang, X., Li, W., Song, P. et al. (2020). Double-cross-linking strategy for preparing flexible, robust, and multifunctional polyimide aerogel. *Chem. Eng. J.* 381: 122784.

127 Wu, N., Niu, F., Lang, W., and Xia, M. (2019). Highly efficient flame-retardant and low-smoke-toxicity poly(vinyl alcohol)/alginate/montmorillonite composite aerogels by two-step crosslinking strategy. *Carbohydr. Polym.* 221: 221.

128 Yang, X., Zhong, X., Zhang, J., and Gu, J. (2021). Intrinsic high thermal conductive liquid crystal epoxy film simultaneously combining with excellent intrinsic self-healing performance. *J. Mater. Sci. Technol.* 68: 209.

129 Nie, S., Mo, J., Zhang, Y. et al. (2020). Ultra-high thermal-conductive, reduced graphene oxide welded cellulose nanofibrils network for efficient thermal management. *Carbohydr. Polym.* 250: 116971.

130 Guo, Y., Guo, Z., Zhong, M. et al. (2018). A flexible wearable pressure sensor with bioinspired microcrack and interlocking for full-range human–machine interfacing. *Small* 14: 1803018.

131 Zhong, W., Liu, Q., Wu, Y. et al. (2016). A nanofiber based artificial electronic skin with high pressure sensitivity and 3D conformability. *Nanoscale* 8: 12105.

132 Park, Y.J., Sharma, B.K., Shinde, S.M. et al. (2019). All MoS_2-based large area, skin-attachable active-matrix tactile sensor. *ACS Nano* 13: 3023.

133 Zhou, Y., Zhan, P., Ren, M. et al. (2019). Significant stretchability enhancement of a crack-based strain sensor combined with high sensitivity and superior durability for motion monitoring. *ACS Appl. Mater. Interfaces* 11: 7405.

134 Chen, L.Y., Tee, B.C.K., Chortos, A.L. et al. (2014). Continuous wireless pressure monitoring and mapping with ultra-small passive sensors for health monitoring and critical care. *Nat. Commun.* 5.

135 Farcau, C., Moreira, H., Viallet, B. et al. (2011). Monolayered wires of gold colloidal nanoparticles for high-sensitivity strain sensing. *J. Phys. Chem. C* 115: 14494.

136 Teymouri, M., Kokabi, M., and Alamdarnejad, G. (2019). Conductive shape-memory polyurethane/multiwall carbon nanotube nanocomposite aerogels. *J. Appl. Polym. Sci.* 137: 48602.

137 Liu, H., Dong, M., Huang, W. et al. (2017). Lightweight conductive graphene/thermoplastic polyurethane foams with ultrahigh compressibility for piezoresistive sensing. *J. Mater. Chem. C* 5: 73.

138 Liu, H., Huang, W., Gao, J. et al. (2016). Piezoresistive behavior of porous carbon nanotube-thermoplastic polyurethane conductive nanocomposites with ultrahigh compressibility. *Appl. Phys. Lett.* 108: 11904.

139 Zu, G., Kanamori, K., Nakanishi, K., and Huang, J. (2019). Superhydrophobic ultraflexible triple-network graphene/polyorganosiloxane aerogels for a high-performance multifunctional temperature/strain/pressure sensing array. *Chem. Mater.* 31: 6276.

140 Al-Saleh, M.H. and Sundararaj, U. (2009). Electromagnetic interference shielding mechanisms of CNT/polymer composites. *Carbon* 47: 1738.

141 Song, W., Guan, X., Fan, L. et al. (2015). Magnetic and conductive graphene papers toward thin layers of effective electromagnetic shielding. *J. Mater. Chem. A* 3: 2097.

142 El-Tantawy, F., Al-Ghamdi, A.A., and Aal, N.A. (2010). New PTCR thermistors, switching current, and electromagnetic shielding effectiveness from nanosized vanadium sesquioxides ceramic reinforced epoxy resin nanocomposites. *J. Appl. Polym. Sci.* 115: 817.

143 Chung, D.D.L. (2012). Carbon materials for structural self-sensing, electromagnetic shielding and thermal interfacing. *Carbon* 50: 3342.

144 Kar, G.P., Biswas, S., Rohini, R., and Bose, S. (2015). Tailoring the dispersion of multiwall carbon nanotubes in co-continuous PVDF/ABS blends to design materials with enhanced electromagnetic interference shielding. *J. Mater. Chem. A* 3: 7974.

145 Shen, B., Zhai, W., Tao, M. et al. (2013). Lightweight, multifunctional polyetherimide/graphene@Fe_3O_4 composite foams for shielding of electromagnetic pollution. *ACS Appl. Mater. Interfaces* 5: 11383.

146 Huangfu, Y., Ruan, K., Qiu, H. et al. (2019). Fabrication and investigation on the PANI/MWCNT/thermally annealed graphene aerogel/epoxy electromagnetic interference shielding nanocomposites. *Compos. Part A Appl. Sci. Manuf.* 121: 265.

147 Lu, Z., Jia, F., Zhuo, L. et al. (2021). Micro-porous MXene/Aramid nanofibers hybrid aerogel with reversible compression and efficient EMI shielding performance. *Compos. Part A Appl. Sci. Manuf.* 217: 108853.

148 Liang, C., Qiu, H., Song, P. et al. (2020). Ultra-light MXene aerogel/wood-derived porous carbon composites with wall-like "mortar/brick" structures for electromagnetic interference shielding. *Sci. Bull.* 65: 616.

149 Sambyal, P., Iqbal, A., Hong, J. et al. (2019). Ultralight and mechanically robust Ti_3C_2Tx hybrid aerogel reinforced by carbon nanotubes for electromagnetic interference shielding. *ACS Appl. Mater. Interfaces* 11: 38046.

150 Yu, Z., Dai, T., Yuan, S. et al. (2020). Electromagnetic interference shielding performance of anisotropic polyimide/graphene composite aerogels. *ACS Appl. Mater. Interfaces* 12: 30990.

5

Epoxide Related Aerogels; Sol-Gel Synthesis, Property Studies and Energy Applications

Mahmoud Khalil and Houssam El-Rassy

Department of Chemistry, American University of Beirut, P.O. Box 11-0236, Riad El-Solh, 1107 2020, Beirut, Lebanon

5.1 Overview of Epoxide Aerogels

5.1.1 History of Aerogels

An aerogel is a solid material characterized by its extreme low density (0.0011–0.5 g cm^{-3}) and classified as a porous material since its total volume is typically of 95–99% air. Aerogels were synthesized for the first time by the US scientist Samuel Stephens Kistler in 1931 [1]. The term *aerogel* indicates that the liquid inside the gel is replaced by a gas without altering the gel solid network (i.e. shrinking, collapsing). This was initially achieved by a supercritical drying (SCD) of the formed gel, where the liquid is heated above its fluid thermodynamic critical point resulting in its transformation into a supercritical fluid. The fluid is then evacuated while kept above the critical temperature. The obtained material consists of a porous gel solid network. Over the years, different techniques have been implemented in order to obtain aerogels.

Recent years witnessed a revival in aerogels due to their interesting applications in different fields such as thermal insulation, energy related technologies, and many more. The synthesis and ease of use of these materials can also be advantageous since the aerogels can be made from various precursors leading to both inorganic (SiO_2, Al_2O_3, WO_3, Fe_2O_3, SnO_2, NiO, etc.) and organic (gelatin, agarose, albumin egg white protein, rubber, etc.) final products.

The first aerogel produced on an industrial scale was a powdered silica aerogel under the name of "Santocel," manufactured by Monsanto Chemical Company in 1940s. This aerogel had many applications such as thickening agent, cigarette filters, and freezer insulation. Later on, silica aerogels have been used as additives in vermin control products [2, 3]. Monsanto abandoned the production of aerogels in the 1970s due to manufacturing cost and the rise of competitors capable of producing silica aerogels at a lower cost. This latter was made possible due to a major breakthrough discovery by Nicholson and Teichner [4] who synthesized the silica aerogels using a relatively easy method. They found that using alkoxide-based precursors, such as tetramethylorthosilicate (TMOS) instead of sodium silicate that Kistler used, leads to the formation of high-quality monolithic aerogel blocks [5]. In 1985, Tewari et al. prepared silica aerogels by ambient temperature SCD from supercritical CO_2 [6]. In 1993, the first commercial polyurethane aerogel was reported [7]. However, aerogels were not widely successful until the early 2000s, when two major companies,

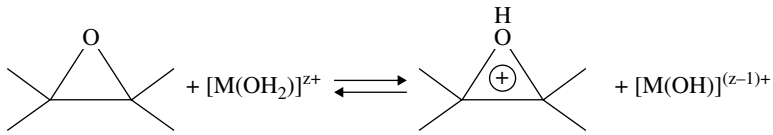
Aerogels for Energy Saving and Storage, First Edition. Edited by Meldin Mathew, Hanna J. Maria, Ange Nzihou, and Sabu Thomas.
© 2024 John Wiley & Sons, Inc. Published 2024 by John Wiley & Sons, Inc.

Aspen and Cabot, launched their new products: blanket and granular silica aerogels. This revitalized the interest in aerogels and sparked a revolution in this domain.

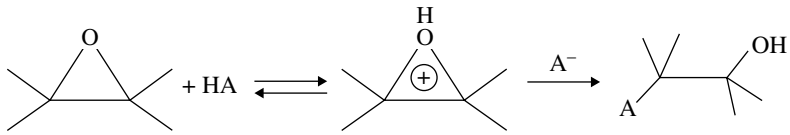
5.1.2 Advantages of Epoxide-Assisted Approach

The epoxide-assisted sol-gel approach was proposed long ago; however, it was revived and further developed by Gash et al. [8]. This approach is a highly versatile technique that allows the preparation of a wide range of metal aerogels from their respective metal salts with excellent quality and reproducibility. The success of this approach led to its expansion to include in addition to metal oxides, transition metal oxides [9]. Nowadays, it is widely used in the synthesis of single and multimetal oxide aerogels as well as for organic-inorganic composites.

The gel formation occurs when an organic epoxide reagent (ethylene oxide, propylene oxide, or epichlorohydrin) is used as an initiator. This compound acts as a proton scavenger and is consumed stoichiometrically in the chemical reaction. When dissolved in water, the cation of the metal salt tends to be solvated by water molecules, thus leading to water ligands coordinated with metal cation. Due to the high acidic character of these ligands, they spontaneously release a proton (H^+) that protonates the epoxide (proton scavenger) according to the following reaction:



Once protonated, the epoxide undergoes a nucleophilic attack by the metal salt's counterion (conjugated base A−) leading to an irreversible ring opening reaction that produces an alcohol as per the following reaction:



Subsequently, the metal hydroxide ions start their polycondensation to form oxo-bridged M-O-M bonds. These olation and oxolation processes lead to a three-dimensional network of colloid and eventually gelation.

The epoxide-assisted gelation approach is very flexible since it can be performed in aqueous or alcoholic solutions. Furthermore, it allows solvent exchange and surface modification, which can alter the properties of the formed materials. This approach is also a versatile technique for the preparation of a wide variety of metal oxides (main and transition), with the most prominent being alumina [10, 11] and iron oxide gels [9].

In addition to being an easy method to synthesize single component oxides, this approach has been used to prepare multi-metallic oxides such as calcium alumina aerogels [12], nickel alumina aerogels [13], strontium-doped lanthanum manganite gels (LSM) [14], yttria-stabilized zirconia gels (YSZ) [15], and cobalt ferrite aerogels [16]. This is another advantage of this approach where mixed binary, ternary, and multicomponent oxide gels can be synthesized. In the future, we expect an increase of usage of this approach especially in hybrid composites due to its high versatility and simplicity.

5.2 Synthesis and Drying Technique

5.2.1 Metal Salt Precursors for Aerogels

5.2.1.1 Selection of Precursors

By using the sol-gel technique, several materials can be prepared either in acidic, neutral, or basic media. The most common ones are metal oxides such as silicon, aluminum, iron, zinc, nickel, and lanthanides oxides. The precursors are typically dissolved in alcoholic solvents (i.e. methanol, ethanol) since these latter allow for a greater solubility of the metal salts, to which propylene oxide is usually added as polymerization reagent. Alumina aerogels can be prepared by using aluminum salts such as aluminum chloride hexahydrate ($AlCl_3.6H_2O$) [11, 17–19] or aluminum nitrate nonahydrate ($Al(NO_3)_3.9H_2O$) [11]. Nickel oxide aerogels can be prepared using nickel(II) chloride hexahydrate ($NiCl_2.6H_2O$) as precursor; however, when using nickel(II) nitrate hexahydrate ($Ni(NO_3)_2.6H_2O$) a green precipitate appears after the addition of propylene oxide thus preventing the formation of the three-dimensional monolithic gel [20]. Zinc(II) nitrate hexahydrate ($Zn(NO_3)_2.6H_2O$) is commonly used in the synthesis of zinc oxide aerogels where different solvents have been used such as ethanol, isopropanol, and acetone [21].

The nature of the solvent turned out to influence the gelation time. For instance, when using ethanol, the gelation has been observed within five to seven hours whereas the use of isopropanol made the gelation to occur within three hours. As for the preparation of iron oxide aerogels, iron(III) nitrate nonahydrate ($Fe(NO_3)_3.9H_2O$) [9] and iron(III) chloride hexahydrate ($FeCl_3.6H_2O$) [9, 22] can also be used as precursors. In the latter case, water can replace the ethanol as solvent, but the gelation time will be longer. Another precursor for the preparation of iron oxide aerogels is the anhydrous iron chloride ($FeCl_3$) [9]; however, the use of an ethanol/water binary solvent is required to make the gelation happen. The presence of water is necessary since it is a required reagent for the chemical reaction to occur; on the contrary, the hydrated salts bring their own water with them in the crystalline form. Chromium oxide aerogels were also synthesized using chromium salts ($Cr(NO_3)_3.9H_2O$ and $CrCl_3.6H_2O$) via the epoxide-assisted route using propylene oxide as a gelation agent [8]. Lanthanide oxide aerogels have been prepared using different lanthanide chloride and nitrate precursors [23]. These aerogels have been characterized by their colors that depend on the metal. Using the respective chlorides, the following colors were obtained Pr (Light yellow), Nd (purple), Sm (yellow), Ho (dark pink), and Er (light pink). Epichlorohydrin has been used as polymerization reagent for these aerogels instead of propylene oxide.

5.2.1.2 Choice of Solvents

The materials synthesized by sol-gel technique require that the precursors be solvated by either aqueous or nonaqueous solvents. Water was widely used as solvent since it plays a major role in binding the oxygen atoms to the metallic cations during condensation. Acids, bases, and complexing agents have also been used as solvents in such preparation.

The organic solvents were used when metal alkoxides were involved in the synthesis because they can help control the hydrolysis of the precursor in addition to sharing the same properties as the products of the reaction. This will result in flexibility and versatility in the final material.

5.2.2 Hydrolysis

During the preparation of aerogels, metal salts (MX) are used as precursors for the sol-gel process. These salts, when put in an aqueous medium, dissolve into their main components M^{n+} and

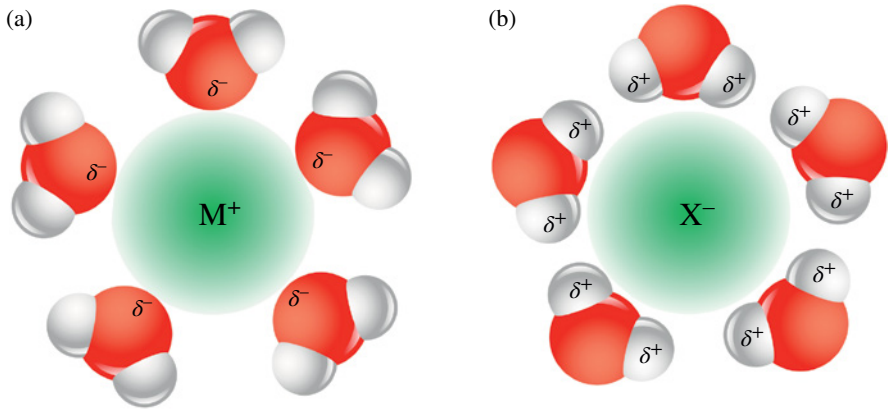


Figure 5.1 Solvation of the cation (a) and anion (b) in aqueous medium.

X^{n-} that are solvated by water molecules (Figure 5.1) due to the strong electrostatic interactions between the polar water molecules and the cations/anions.

In a typical solution, the total absolute formal charge is equal to zero due to the balance between the positive charges of the cations and the negative charges of the anions. Normally, anions are not eliminated since they might have an important factor in the chemical reaction during the sol-gel process; however, they are considered impurities so it is necessary to filter the anions out if pure ceramic oxides are required.

5.2.2.1 Hydrolysis in Aqueous Media: Formation of Hydroxo/Oxo Ligands

The hydrolysis starts with the solvation of the precursor's salt in water. In general, the oxygen atom of the water molecule having a negative partial charge, is drawn to the metallic cation while the hydrogen atoms will be attracted by the anion of the metal salt. Upon solvation of the cation, a cage-like structure is formed where the metal cation will be surrounded by a number of water molecules, as shown in Figure 5.1. This is the first solvation shell, which is tightly bonded to the metallic cation M^{n+} and leads to the formation of $[M(H_2O)_N]^{n+}$ complex with the H_2O ligand, called *aquo*. Each type of metal has a specific number of solvating water molecules, which normally ranges between 4 and 8 with an average of 6 for most metals, i.e. $[Al(H_2O)_6]^{3+}$. A second solvation shell is produced around the first shell where the oxygen atom of the former is oriented toward the hydrogens of the latter. However, this shell has no significance as it is less rigid and does not get involved in the sol-gel processing.

Once solvated, the specie undergoes a hydrolysis/deprotonation reaction that consists of the loss of one or several protons of the solvating water molecules [24]. This deprotonation transforms the "aquo" ligand into a hydroxo ligand (OH−) or an oxo ligand (O^{2-}). This happens when one or two protons leave the metallic complex, respectively [25].

A general equation that represents this hydrolysis reaction can be written as followed:

$$\left[M\left(OH_2\right)_N\right]^{n+} + xH_2O \qquad \left[M\left(OH\right)_x\left(OH_2\right)_{N-x}\right]^{(n-x)+} + xH_3O^+$$

where $[M(OH_2)_N]^{n+}$ and $[M(OH)_x(OH_2)_{N-x}]^{(n-x)+}$ are the most acidic and basic species, respectively. The latter can also be called an *aquo-hydroxo* complex since it contains the two ligands.

The deprotonation of an acidic oxide occurs by the addition of a base, which initiated the hydrolysis. The reaction is similar to the previous one and can be written as followed:

$$\left[M\left(OH_2\right)_N\right]^{n+} + OH^- \qquad \left[M\left(OH\right)\left(OH_2\right)_{N-1}\right]^{(n-1)+} + H_2O$$

Figure 5.2 shows the mechanism of this hydrolysis, which was developed by [26, 27].

As one can see, a nucleophilic attack occurs by OH– on a partial positively charged hydrogen of the complex. This results in the formation of a water molecule that leaves the complex once the electron transfer is over and the partial charge of the water molecule is zero.

For a basic oxide, the formation of the hydroxo ligand can still happen. However, first we have the formation of the oxo ligand (O^{2-}), which is the characteristic of basic oxides. A free H^+ attacks a nucleophilic oxygen of the oxo ligand [24, 26] expressed by the following reaction:

$$\left[MO\left(OH_2\right)_{N-1}\right]^{(n-2)+} + H^+;OH^- \qquad \left[M\left(OH\right)O^+\left(OH_2\right)_{N-1}\right]^{(n-1)+} + OH^-$$

where H_2O acts as an acid in the above reaction. The complex can also react with an acid in a similar reaction:

$$\left[MO\left(OH_2\right)_{N-1}\right]^{(n-2)+} + H_3O^+ \qquad \left[M\left(OH\right)O^+\left(OH_2\right)_{N-1}\right]^{(n-1)+} + H_2O$$

Figure 5.3 transcribes this hydrolysis mechanism.

The formation of oxo ligands occurs when a deprotonation of a hydroxo ligand in the metallic complex takes place according to the below reaction [27]. This results in a O^{2-} ligand attached to the metal.

$$\left[M\left(OH\right)\left(OH_2\right)_{N-1}\right]^{(n-1)+} + H_2O \qquad \left[MO\left(OH_2\right)_{N-1}\right]^{(n-2)+} + H_3O^+$$

A complex containing both water and oxo ligands is known by "oxo-aquo" complex. "Oxo-hydroxo" and "oxo-hydroxo-aquo" ligands can also be found in complexes that have a general

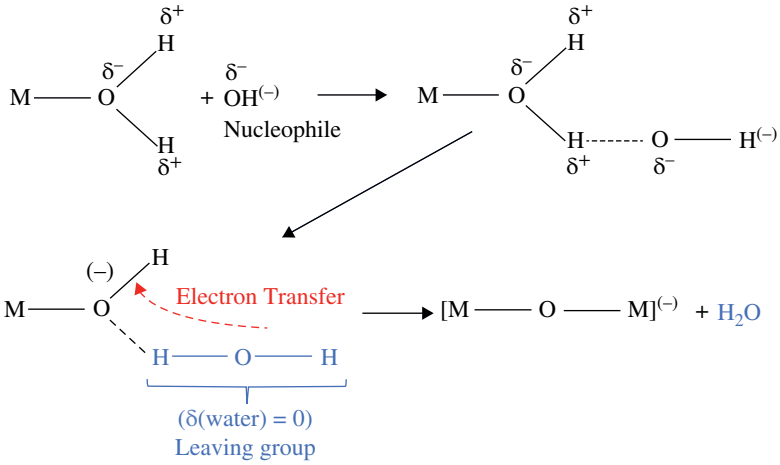


Figure 5.2 Hydrolysis of metal salts in the presence of hydroxyl ion (OH^-) and formation of M-O-M bridges.

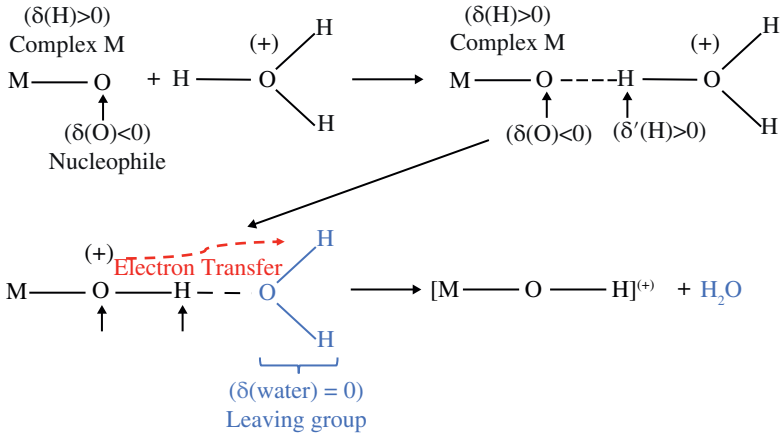


Figure 5.3 Hydrolysis of metal salts in the presence of hydronium ion (H_3O^+) and formation of M-O-M bridges.

formula $[MO_x(OH)_y(OH_2)_{N-x-y}]^{(n-y-2x)+}$. An example of such a complex has been prepared by Jovilet et al. [26] as form of a vanadium complex $[VO(OH)_2(OH_2)_3]^+$.

5.2.2.2 Hydrolysis in Organic Solvents

Metal salts can be hydrolyzed in organic solvents where an epoxide molecule is added to prepare the gel [8]. The epoxide, in this case, acts as a slow proton scavenger where a nucleophilic attack by the counterion of the metal cation (i.e. Cl^- which is a strong Lewis base) on the epoxide occurs. This will result in an increase of the negative partial charge of the epoxide oxygen, leading to the deprotonation of one water ligand leaving a hydroxo ligand attached to the metal. Figure 5.4 depicts the reaction mechanism. The hydrolysis by deprotonation during this reaction is slow and heavily dependents on the nature of the anion.

This technique can be used to prepare different types of monolithic gels and aerogels. Cr, Fe, Al, Zr, and Y salts are considered as main precursors to prepare the respective oxides. In addition, other oxides were synthesized using the same technique such as Y_2O_3 [28], SnO_2 [29], chromia aerogels [8], Y_2O_3-stabilized ZrO_2 aerogels [15], aerogel thermites with dispersed Al nanoparticles [30],

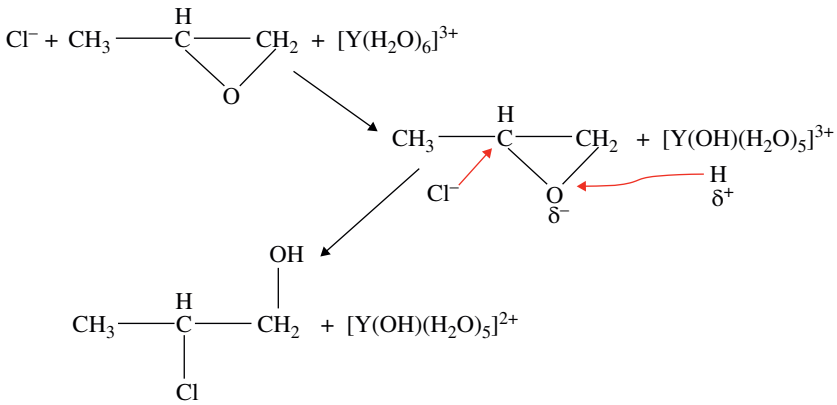


Figure 5.4 Hydrolysis of metal salts in the presence an epoxide molecule.

SiO_2 aerogels with dispersed metal nanoparticles [31], or with CdS nanoparticles grown by lithography inside the aerogel [32]. NiO/Al_2O_3 [13], CaO/Al_2O_3 [12], and $CoFe_2O_4$ [16] aerogels were also prepared using this approach.

5.2.3 Epoxide-Assisted Gelation and Condensation

When two monomers come together, they react and collide into a binuclear complex by a polymerization reaction. This is the condensation that can keep on proceeding, forming bigger polynuclear species given that the conditions allow its continuation.

The polymerization occurs in this type of reaction when a hydroxo ligand (OH) is found in either an aquo-hydroxo $[M(OH)(OH_2)_{N-1}]^{(n-1)+}$ or oxo-hydroxo $[M(OH)(O)_{N-1}]^{(n-2N+1)+}$ complex. Adding a base to acidic oxides or an acid to basic oxides allows the formation of the hydroxo ligand (OH) and therefore initiates the polymerization. Following the polymerization step, a condensation reaction occurs, resulting in the formation of two types of bridges between the metal cations: ol and oxo bridges.

5.2.3.1 Olation Condensation

The formation of an "ol" bridge between two metal cations is the first step of any condensation reaction [26]. For low-charge cations, this is done in two steps with a dissociative S_N1 mechanism being involved:

$$\left[M\left(H_2O\right)_6\right]^{3+} \qquad \left[M\left(H_2O\right)_5OH\right]^{2+} + H^+$$

Followed by

$$\left[M\left(H_2O\right)_5OH\right]^{2+} + \left[M\left(H_2O\right)_6\right]^{3+} \qquad \left[M\left(H_2O\right)_5\left(\mu-OH\right)M\left(H_2O\right)_5\right]^{5+} + H_2O$$

Note that a nucleophilic addition reaction (NA) can take place when the coordination number of the metal cation increases (i.e. $[Al(OH)_4]^-$). On the other hand, an associative S_N2 mechanism occurs for transition metal elements and is shown in Figure 5.5.

The condensation process is the driving force of this reaction. Once the condensation cannot further continue or a solid is formed due to the unlimited polymerization, the process comes to a halt. Table 5.1 shows the different types of ol bridges known to exist for a few cations.

5.2.3.2 Oxolation Condensation

The first step in an oxolation condensation is the formation of ol bridges between two metal cations (Figure 5.6). This step is then followed by a proton transfer and the formation of an oxo bridge and a leaving H_2O group by a S_N2 mechanism. Acids and bases can catalyze this condensation, as shown in Figures 5.7 and 5.8, respectively.

During the acid catalysis, a proton H^+ attacks the oxygen atom of the hydroxo ligand of another metal complex, forming an H_2O ligand that is partially positively charged. An intermediate leaving group H_3O^+ is then formed when the H_2O ligand interacts with another OH ligand leading to the formation of an "oxo" bridge.

On the other hand, a nucleophilic attack occurs by the OH^- on the partially charged hydrogen atom ($H\delta^+$) during basic catalysis (Figure 5.8). This results in an increase of the negative partial charge on the oxygen, allowing it to bind to another solvated hydroxyl group. This gives three leaving groups: two water molecules and OH^- anion. Upon separation from the complex, an "oxo" bridge is formed.

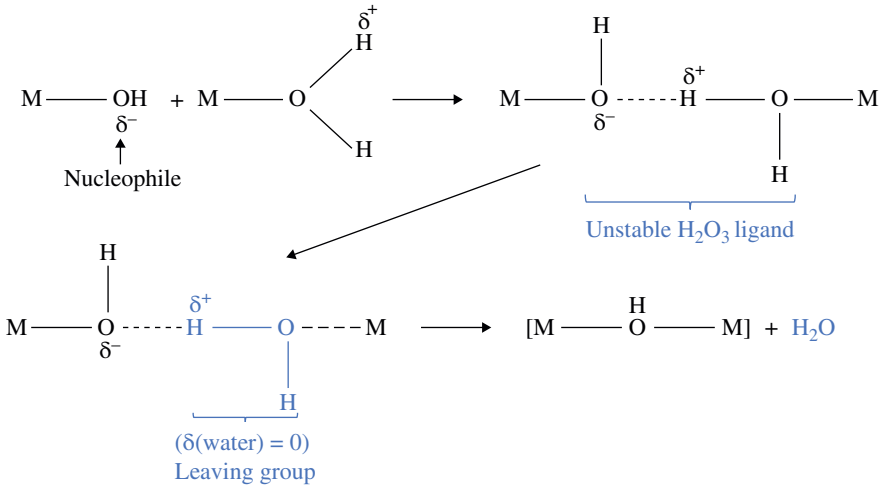
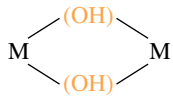
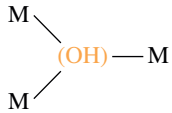
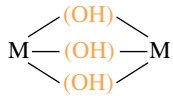


Figure 5.5 Associative olation condensation S_N2 mechanism for transition metals.

Table 5.1 Different types of "ol" bridges that can form during condensation.

Type of "ol" bridges	General formula	Examples
μ_2–OH	M–(OH)–M	$[M_2(OH)(OH_2)_X$ with M^{2+} = Be, Mn, Co, Ni, Zn, Cd, or Pb
$2\mu_2$–OH		$[Zr_4(OH)_8(OH_2)_{16}]^{8+}$
		$[A1_{13}O_4(OH)_{24}(OH_2)_{12}]^{7+}$
		$[M4(OH)_6(NH_3)_{12}]^{6+}$ with $M^{3+} = Cr^{3+}$, Co^{3+}
μ_3–OH		$[M_4(OH)_4(OH_2)]^{4+}$ with M^{2+} = Pb, Co, Ni, Cd
		$[Pb_60(OH)_6(OH_2)]^{4+}$
		$[M_3(OH)_4(OH_2)_N]^{2+}$ with $M^{2+} = Sn^{2+}$, Pb^{2+} with $M^{3+} = Sc^{3+}$, Y^{3+}, La^{3+}, Ce^{3+}
$3\mu_2$–OH		$[Co_2(OH)_3(NH_3)_6]^{3+}$

Source: From Ref. [33].

5.2.4 Gel Drying

Several techniques exist to dry a wet gel, and each has its own effect on the gel and its shrinking during the drying process. However, the simplicity on how to use these techniques is not the same – some of them are more complex than others. In this section, we will discuss three common techniques: supercritical drying or SCD, ambient pressure drying, and freeze drying. Note that other techniques exist, such as the evaporation where the gel is left to dry in air by itself under the capillary mechanism [34, 35], the SCD where it is done at conditions slightly below the critical pressure and temperature of the solvent [36, 37], and the liquid–liquid extraction drying, which is based on water extraction by osmosis.

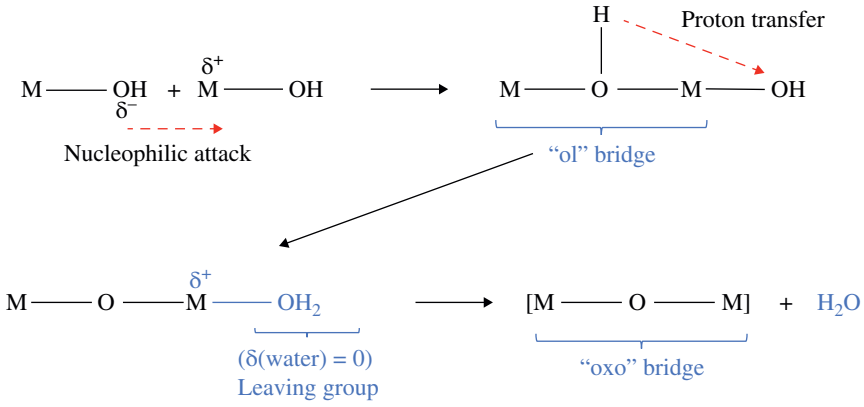


Figure 5.6 Oxolation condensation S_N2 mechanism for transition metals.

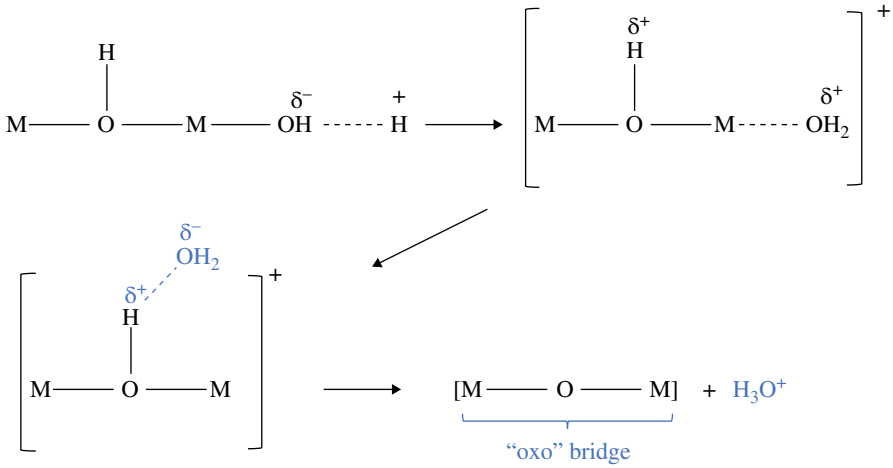


Figure 5.7 Acid-catalyzed Oxolation mechanism.

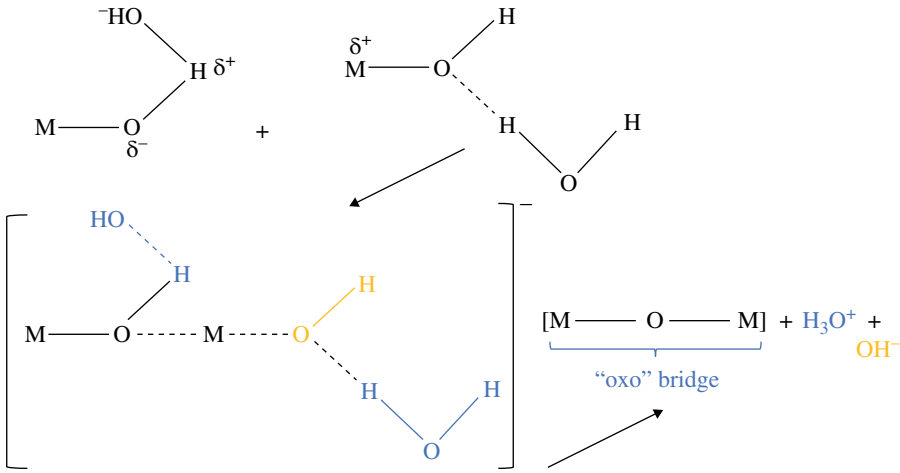


Figure 5.8 Base-catalyzed Oxolation mechanism.

5.2.4.1 Supercritical Drying (SCD)

This technique applies an extreme case of the drying laws where the surface tension of the liquid cancels out. All pores are emptied altogether with a very moderate contraction leading to the final product having high porosity. In some cases, an exchange with an intermediate solvent that has a high miscibility with the supercritical fluid is needed in order to ensure an optimal drying of the gel. For instance, acetone is used an intermediate solvent during the drying of alcogels using supercritical carbon dioxide. The obtained gels using this technique are called aerogels.

Silica aerogels were the first materials synthesized by SCD [1]. In order to obtain a monolithic aerogel, Kistler performed an exchange with ethanol to substitute the water since he used water in the synthesis process. Then, he supercritically dried the gels in ethanol.

This technique consists of bringing, upon heating, the gel above the critical point of the solvent it contains (temperature and pressure) and leaving it under these conditions for a certain time to insure a complete transformation of the fluid inside the pores to the supercritical state. After that, the fluid is slowly evacuated by either flushing the apparatus with dry argon or depressurization.

Figure 5.9 shows the apparatus and the pathway for the SCD technique. Different solvents can be used for this drying technique. Table 5.2 regroups the critical conditions of some of them.

As one can see, using water as solvent is not advantageous due to the high critical pressure and temperature. For this reason, scientists tend to use methanol, ethanol, or liquid CO_2 since the drying is a more feasible and easier [38]. In addition, when using methanol or ethanol as solvent, we are talking about high-temperature SCD (Hot SCD), which is distinguished from low-temperature SCD (Cold SCD) with liquid CO_2. This distinction is due to the relatively high difference of the critical pressure and temperature of the mentioned solvents.

The main disadvantage of Cold SCD is that the liquid CO_2 does not dissolve water and its solubility is relatively low in methanol and ethanol. However, it is completely miscible with acetone. Therefore, it is necessary to perform an exchange with acetone for gels prepared in aqueous solutions before submitting them to cold SCD. Exchanging the alcohol for CO_2 in a normal liquid state will result in a moderate shrinkage [39]. On the other hand, the interdiffusion of CO_2 with methanol or ethanol is highly accelerated when the CO_2 is in its supercritical state [40, 41]. Therefore, it is much easier to exchange the alcohol for CO_2 in these conditions [42].

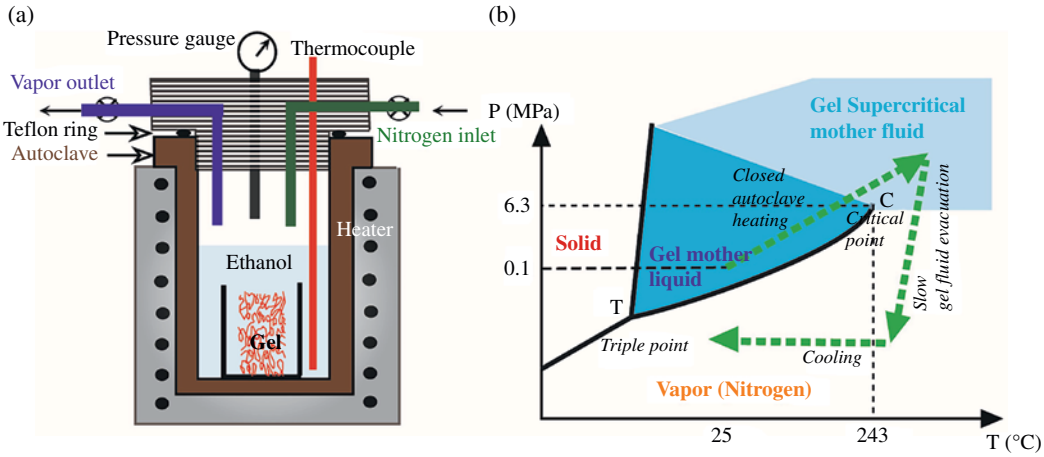


Figure 5.9 Illustration of the type of autoclave used in a HOT SCD process (ethanol- or methanol-impregnated gel) (a) and schematic temperature and pressure pathway (b). *Source:* From Ref. [33].

Table 5.2 Critical point parameters of common fluids.

Fluid	Formula	T_C (°C)	P_c (MPa)
Water	H_2O	374.1	22.04
Carbon dioxide	CO_2	31.0	7.37
Freon® 23	CHF_3	25.9	4.82
Freon® 116	CF_3-CF_3	19.7	2.97
Ammonia	NH_3	132.5	11.27
Acetone	$(CH_3)_2O$	235.0	4.66
Benzene	C_6H_6	288.9	4.89
Nitrous oxide	N_2O	36.4	7.24
Methanol	CH_3OH	239.4	8.09
Ethanol	C_2H_5OH	243.0	6.38
1-Propanol	C_3H_7OH	263.5	5.17
1-Butanol	C_4H_9OH	289.7	4.39

Source: From Ref. [33].

If the CO_2 washing and chamber depressurization steps were slow, a low-gel permeability is obtained [43, 44]. To speed up the CO_2 washing, forced convection is applied in order to assist the molecular diffusion process. This can be done by integrating a series of compression–decompression cycles [45]. On the other hand, some experiments require a high depressurization rate. In this case, gels must be strengthened before drying in order to avoid the formation of cracks [46]. Controlling these parameters minimizes the differential stresses inside the gels during the drying process, which improves the quality of the aerogels [47]. Moreover, the nature of the solvent showed an effect on the textural characteristics of the final dried aerogel. Overall, silica aerogel monoliths with relatively high porosity (84–91%) and a large specific area (up to 800 $m^2 g^{-1}$) can be obtained by cold SCD [48]. However, fluid exchange difficulties where the solvent should be exchanged for the standard supercritical CO_2 route remains a major drawback. For this, different routes are being investigated such as the direct synthesis of the silica gel in supercritical CO_2 by a water-free process [49–51]. In addition, a new rapid supercritical extraction (RSCE) method was also investigated in order to accelerate the drying process [52–56]. This technique consists of bringing the sol-gel precursors to a supercritical state inside a pressurized mold under Hot SCD conditions. The obtained products were crack-free silica aerogel monoliths with a low density and a relatively small size. However, this was not the case when large samples were synthesized as the obtained aerogels were cracked.

SCD can be applied to SiO_2 as well as to Al_2O_3 and TiO_2 [57], to binary systems (SiO_2–B_2O_3; SiO_2–P_2O_5, NiO–Al_2O_3, Fe_2O_3–Al_2O_3) and ternary systems (SiO_2–B_2O_3–P_2O_5) [58].

SCD remains the easiest, most frequent technique to use in order to obtain aerogels. However, being a slow process is considered as the only drawback that this technique presents.

5.2.4.2 Freeze Drying

Different research groups used this technique in order to obtain aerogels [59, 60]. By bypassing the triple point of the gel liquid matrix, aerogels, often called *cryogels,* are obtained by sublimation under vacuum of the frozen wet-gel liquid with the main constituents are either the gels

themselves or a solution of their precursors. Cryogels usually show 80% maximum porosity. When comparing the surface area values, it was found that cryogels only show half the values to those obtained by either supercritical or ambient pressure drying [61, 62]; thus, showcasing the disadvantage of this technique. The gel network is often destroyed or distorted to a certain limit due to the nucleation and growth rate of the solvent crystals to produce large pores [63]. Gels obtained by freeze-drying are cracked or have a powder-like texture [64]. In order to solve this problem, the drying should be carried out in solvents that have low expansion coefficient and high sublimation pressure. In addition, another technique called *flash freezing* can be used. It is a rapid freezing in liquid nitrogen at a cooling rate of $10\,K\,s^{-1}$ allowing the formation of many nucleation crystals sites while preventing the separate crystallization of the various components [65].

Freeze-drying is a simple, fast technique for obtaining cryogel materials with a morphology similar to that of aerogels (SiO_2 and Al_2O_3 powders) [62]. This technique also presents another advantage where unstable materials or hydrogels particularly used for medical applications can be dried [66–69]. These materials (i.e. cellulose, PI, polyvinyl alcohol (PVA), pectin) usually cannot withstand hot SCD conditions therefore it is necessary to utilize another technique.

5.2.4.3 Ambient Pressure Drying

Ambient pressure drying is a technique that requires the modification on the surface area of the gels to make them more hydrophobic. This step greatly reduces the capillary stresses found in the gels in ambient temperature and pressure. Gels obtained by this technique are often referred to *ambigels* [70]. Silica aerogels was first synthesized using this technique by Prakash et al. [71, 72]. Later on, it was applied for organic and organic coated aerogels [73–76]. In general, ambient pressure drying technique is a fast and cheap technique that makes it suitable for industrial aerogels production [61, 76]. Aerogels synthesized from sodium silicate were also obtained using this technique [77].

Drying control chemical additives (DCCA) are organic compounds that are usually added to the gelation solvent. Among DCCA, we have glycerol, formamide, dimethylformamide, oxalic acid, tetramethylammonium hydroxide, polyethylene glycol (PEG), PVA [78–84]. The role of these additives is to decrease the capillary drying stresses that appear inside the gels and to help control the pore size and volume as well as their size distribution depending on their polar/apolar and protic/aprotic characteristics. This is due to their interference with the hydrolysis mechanism of the SiO_2 precursors. Uncracked dry monoliths with a high relative pore volume (97.4%) were obtained using DCCA [85].

Ambient pressure drying is considered to be the most promising manufacturing technique for SiO_2 aerogels. The synthesis of SiO_2 aerogels showed a great success using alkoxides [70, 86, 87] and water glass [88, 89].

5.3 Epoxide-assisted Aerogels

5.3.1 Metal Oxides

A variety of metal oxide aerogels has been prepared with the assistance of epoxide. In this section, we will focus on alumina, titania, vanadia, and zirconia aerogels. First, we have to differentiate between colloidal aerogels and polymeric aerogels. In colloidal aerogels, the tridimensional network formed by the solid particles can be observed. These aerogels can differ by the size, shape, and crystallographic structure, depending on the type of the colloidal solid particles, the connectivity, and the bonding between the particles. For example, a fiber gel may be composed of

spherical particles linked in a very linear fashion. On the other hand, the colloidal particles cannot be observed in the case of polymeric gels.

5.3.1.1 Alumina Aerogels

Alumina aerogels are considered as one of the most studied aerogel type materials synthesized by epoxide-assisted technique. Aluminum chloride or aluminum nitrate are used as precursors. Hund et al. [17] prepared alumina aerogels in a 50% vol/vol mixture solution of water and ethanol using different concentrations of aluminum chloride hexahydrate as a precursor and propylene oxide as a gelation agent. Drying under N_2 for 24 hours has been performed, followed by ethanol curing for 24 hours where the samples were submerged in the solvent. This step was followed by isopropanol exchange over five days in order to remove the excess of water and any unreacted precursors. Finally, the gels were supercritically dried by CO_2. The surface area of the obtained aerogels was $330\,m^2\,g^{-1}$.

Tokudome et al. [18] synthesized alumina aerogels and xerogels using a mixture of aluminum chloride hexahydrate and poly(ethylene oxide) dissolved in an aqueous solution of ethanol. Poly(ethylene oxide) was used to induce phase separation. After complete dissolution, propylene oxide was added to the mixture as a gelation initiator. The gels were kept at 40 °C under closed conditions and then aged at the same temperature for 24 hours. These materials were then subjected to solvent exchange with isopropanol at 60 °C. Supercritically drying the gels under CO_2 resulted in alumina aerogels while xerogels were obtained by evaporative drying at 40 °C. The measured surface area of the synthesized materials was around $200\,m^2\,g^{-1}$.

Alumina aerogels have been also prepared from hydrated aluminum chloride dissolved in different solvents (methanol, ethanol and isopropanol) [19]. Propylene oxide was then added to the mixture and gels were obtained within three minutes. The formed gels were left for aging for 24 hours. Several solvent exchange steps were performed using absolute ethanol before subjecting the gels to RSCE. The obtained aerogels had a high surface area (~$800\,m^2\,g^{-1}$) and a low density (~$0.05\,g\,ml^{-1}$).

In another investigation, alumina monoliths with low-density and high surface areas ($600–700\,m^2\,g^{-1}$) were synthesized using aluminum salts ($AlCl_3.6H_2O$ and $Al(NO_3)_3.9H_2O$) dissolved in aqueous and ethanolic solutions using the epoxide-assisted technique with the addition of propylene oxide. The gels were later subjected to SCD with CO_2 [11].

5.3.1.2 Titania Aerogels

Titanium chloride was used as precursor for the preparation of titania aerogels in aqueous mixture of absolute ethanol and water [90]. The gelation occurred after five to six minutes of adding propylene epoxide (PO) drop-by-drop at room temperature. The obtained translucent monoliths were left to age for 12 hours at room temperature. After the aging process, alcogels were subjected to a solvent exchange in anhydrous ethanol for three days in order to remove any water excess. Using CO_2 SCD, aerogels were obtained while xerogel powder was obtained by direct drying of alcogel where it was exposed to ambient conditions for 24 hours followed by air-drying at 80 °C for two more days. The specific surface area and pore volume of these gels were reported to be $464\,m^2\,g^{-1}$ and $2.06\,cm^3\,g^{-1}$, respectively.

In another study [91], titanium chloride ($TiCl_4$) was used as precursor in a mixed solution of ethanol and isopropanol at 0 °C in order to prepare titania aerogels with propylene oxide being the gelation reagent. The obtained gels were left at room temperature for aging for 12 hours followed by ethanol exchange and n-hexane exchange. Each exchange was done three times in 36 hours. After aging, the surface of the gels was modified from hydrophilic to hydrophobic and the solids

were then dried in a specific way using aluminum foil at different temperatures. Titania aerogels were obtained after cooling. The BET surface area and average pore size are 497.56 $m^2\ g^{-1}$ and 3.2 nm, respectively.

5.3.1.3 Vanadia Aerogels

$VOCl_3$ and epichlorohydrin were used to synthesize vanadium oxide (vanadia) aerogels [92]. These gels showed similar characteristics to those synthesized by vanadium oxytripropoxide hydrolysis. However, the low cost of the epoxide-assisted technique is very advantageous for the preparation of vanadia aerogels. The obtained aerogels showed a microporous nano-worm morphology with a relatively low density (0.103 $g\,cm^{-3}$), high porosity (96.9%), and a specific surface area of 102 $m^2\ g^{-1}$.

5.3.1.4 Zirconia Aerogels

Zirconia aerogels were prepared using zirconium oxychloride octahydrate ($ZrOCl_2.8H_2O$) as a precursor and propylene oxide as a gelation reagent [93]. The alcogels underwent a solvent exchange using ethanol followed by SCD in ethanol to obtain aerogels. In addition, the effect of water and nitric acid contents on the behavior of the gel formation and properties of the aerogels was studied [93]. The aerogels showed a translucent well-developed mesoporous structure with a specific surface area 454 $m^2\ g^{-1}$ and pore volume 1.8 $cm^3\ g^{-1}$. Moreover, they noticed that upon calcination, zirconia aerogels underwent a phase transition from the amorphous phase into the tetragonal phase.

Li et al. [94] studied the effect of propylene oxide on the microstructure of zirconia aerogel. Zirconium n-butoxide was used as a precursor for the aerogel in presence of an ethanolic solution and nitric acid. Propylene oxide was used as a gelation reagent with different molar ratio ranging from 0 to 2.5. The study showed that increasing PO content would lead to an increase in the pH of the solution from 1.2 to 2 while decreasing the gelation time from 40 to 10 minutes, respectively. However, this trend is not observed for the pore radius and pore volume. Upon increasing the PO/Zr molar ratio, the average pore radius increased from 6.6 to 15.1 nm then dropped to 8.5 nm, while the pore volume increased from 1.2 to 1.87 $cm^3\ g^{-1}$ and then decreased to 1.44 $cm^3\ g^{-1}$. This can be explained by the fast gelation time leading to a denser structure and larger particles.

Zirconia aerogels and cryogels were also prepared using the epoxide-assisted method [95]. In an ethanolic solution, zirconium oxynitrate salt was dissolved and subsequently different concentration of cetyltrimethylammonium bromide (CTAB) was added while stirring until the sol was formed. Propylene oxide was used as a gelation reagent. Alcogels were obtained after several ethanol exchange. In order to obtain aerogels, the alcogels were subjected to CO_2 SCD while cryogels were obtained by freeze-drying. The addition of CTAB changed the morphology of the aerogels from small primary particles agglomerates to an interconnected three-dimensional network. In case of cryogels, water molecules were trapped inside the pores when the solvent was freeze-dried allowing the formation of a liquid-vapor interface inside the pores leading to the collapse of the three-dimensional structure. The zirconia aerogel/CTAB showed a specific surface area of 378.6 $m^2\ g^{-1}$ and a pore volume of 1.44 $cm^3\ g^{-1}$, while the addition of CTAB in the cryogels increased the specific surface area from 1.97 to 2.52 $m^2\ g^{-1}$ and the pore volume from 7.31×10^{-3} to 0.01 $cm^3\ g^{-1}$.

5.3.1.5 Other Oxide Aerogels

As mentioned previously, the epoxide-initiated technique can be used to synthesize aerogels for trivalent or tetravalent oxides [8, 29, 96]. In addition to the aerogels mentioned in the previous section, this technique was also applied to the synthesis of tin oxide aerogels [29]. Propylene oxide

was used as an initiator reagent to an aqueous solution of $SnCl_4.5H_2O$. The obtained materials have high surface areas and consist of an interconnected network of crystalline SnO_2 nanoparticles. They appeared interesting for sensor design applications. Gallium and indium oxide aerogels were also prepared by epoxide-assisted method using $GaCl_3.6H_2O$ and $InCl_3.6H_2O$ precursors [8].

Another type of these aerogels can be synthesized using transition metals. The most common prepared aerogel is iron(III) oxide. The advantage of this type of aerogels is the versatility and flexibility it offers. By controlling the structure and properties via the synthetic parameters, iron(III) oxide aerogels can be used in a variety of applications such as energetic materials [97, 98], magnetic nanostructures [99–102], and catalysis [103, 104]. Amorphous chromia aerogels are obtained by adding an epoxide to an ethanolic solution of Cr^{3+} salts [8]. Ruthenium oxide aerogels with high surface area showed an interest in energy storage applications and are prepared via the addition of an epoxide (propylene oxide or 1,2-epoxybutane) to the respective hydrated salt [105]. The synthesis of zirconium, hafnium, niobium, tantalum and tungsten oxide aerogels have also been reported using the respective chloride salts [8].

Lanthanide and actinide oxide aerogels were also prepared using this approach. Adding propylene oxide to a solution of Ce(III) salt resulted in the synthesis of cerium oxide aerogels [106]. The obtained aerogels have high surface electronic conductivities making them an interesting choice as catalysts in solid oxide fuel cells. The synthesis of other lanthanide oxides aerogels has also been reported [107, 108]. Moreover, actinide oxides such as thorium and uranium oxide aerogels have been prepared using the epoxide-assisted technique [109, 110]. By adding propylene oxide to an ethanolic solution of uranyl nitrate $[UO_2(NO_3)_2.6H_2O]$, low-density uranium oxide (UO_3) aerogels can be synthesized. These aerogels gained interest for their use in the production of nuclear fuel materials.

5.3.2 Composites Aerogels

5.3.2.1 Inorganic-inorganic Composites

Aerogels synthesized via the epoxide-assisted route show several advantages as mentioned earlier. One of these advantages is that binary and ternary oxides aerogels can be prepared via this technique. Similar to the synthesis of single oxide aerogels, mixed oxide aerogels can be prepared from solutions containing several salts. Moreover, during the synthesis of these materials, the hydrolysis and condensation reactions can lead to different network architecture. For example, one can find interpenetrating networks of two metal oxides in a binary aerogel: M1-O-M1, M2-O-M2, and M1-O-M2 [96]. In addition, the primary oxide structure can act as a support while the second oxide can have its own entity (i.e. nanoparticles). Several inorganic-inorganic aerogel composites have been synthesized via the epoxide-assisted route such as Co ferrite/ZrO_2 [111], Yttria-stabilized zirconia [15, 112], Strontium-doped lanthanum manganite [14], $ZnFe_2O_4$ [113, 114], $CoAl_2O_4$, $CoCr_2O_4$, $CuCr_2O_4$ [114], ZnO-CuO [115], Cu/Zn/Al xerogels and aerogels [116], iron oxide and silicon dioxide composites [117–119].

Several binary mixed oxides systems were synthesized by the epoxide-assisted route with alumina being the support phase. Hybrid CaO/Al_2O_3 [12] and NiO/Al_2O_3 [13] were prepared from the respective salts dissolved in absolute ethanol followed by the addition of propylene oxide as a gelation agent. Once the gels were formed, aging occurred for 24 hours at RT followed by soaking in acetone for another 24 hours. Aerogels were obtained via CO_2 SCD. In the case of CaO/Al_2O_3 aerogels, it was found that increasing the calcium content resulted in a decrease of the surface area from $369\,m^2\,g^{-1}$ for pure alumina aerogels to $14\,m^2\,g^{-1}$ for CaO/Al_2O_3 (6 : 1 M ratio). The same trend was observed for the pore volume as it decreased from $0.41\,cm^3\,g^{-1}$ for pure alumina to

0.05 $cm^3\ g^{-1}$ for the same hybrid aerogels. As for the NiO/Al_2O_3 hybrid aerogels, the surface area did not show a specific trend upon varying the Ni content. Surface areas between 650 and 188 $m^2\ g^{-1}$ were reported for alumina and nickel oxide-alumina aerogels with an increase in the specific area as the nickel content increases. On the other hand, the pore volume showed a decrease upon increasing the Ni content from 4.46 (pure alumina) to 0.88 $cm^3\ g^{-1}$ (for the highest Ni/Al molar ratio aerogel).

Cobalt ferrite hybrid aerogels were also prepared via this technique. $CoCl_2.6H_2O$ and $FeCl_3.6H_2O$ were completely dissolved in methanol [16]. Propylene oxide was then added where the gelation was observed after 20–25 minutes. The aging period was 24 hours, and acetone solvent exchange was performed for another 24 hours. The final aerogels were obtained by CO_2 SCD. The as-synthesized Co/Fe_2O_4 aerogels showed a high surface area of 576 $m^2\ g^{-1}$ and a pore volume of 1.31 $cm^3\ g^{-1}$. However, upon calcination, these values showed a decreasing trend reaching 13 $m^2\ g^{-1}$ and 0.03 $cm^3\ g^{-1}$ for the surface area and pore volume, respectively, for aerogels calcined at 800 °C.

Co ferrite/ZrO_2 [111] have been prepared using their respective precursors. Once the salts are completely dissolved, propylene oxide is added dropwise. Aging occurred overnight followed by leaving the materials at 100 °C for two hours. An annealing was then performed at different temperatures ranging between 600 and 1000 °C in air for one–five hours. The annealing time had an effect on both specific surface area and pore volume. As the time increases, the specific surface area and pore volume decrease from 10 to 7.5 $m^2\ g^{-1}$ and from 1.52×10^{-3} to 1.03×10^{-3} $cm^3\ g^{-1}$, respectively, when the time increased from one to five hours.

Yttria-stabilized zirconia (YSZ) aerogel, prepared by the addition of propylene oxide to a completely dissolved mixed solution of anhydrous $ZrCl_4$ and $YCl_3.6H_2O$, is another example of a hybrid aerogel [15, 112]. Once the gelation has occurred, the gels were left to age for 24 hours with ethanol exchange for three days. The aerogels were then placed in a supercritical dryer where the ethanol is exchanged with liquid CO_2 for two to three days before drying. Porous YSZ aerogels with surface area of 406 $m^2\ g^{-1}$ were obtained via this method. The dried aerogels were then calcinated at 550 and 1000 °C in air for one hour. At 550 °C, the aerogels retained a relatively high surface area of 159 $m^2\ g^{-1}$. This was not the case when the calcination occurred at 1000 °C which resulted in the destruction of the pores and a surface area of 26 $m^2\ g^{-1}$.

Zinc ferrite aerogels were also synthesized via epoxide addition [113]. Two gels were prepared using nitrate or chloride-based salts. The gels derived from nitrate salts were synthesized by dissolving $Zn(NO_3)_2.6H_2O$ and $Fe(NO_3)_3.9H_2O$ in isopropanol. After complete dissolution, propylene oxide was added, and gelation occurred within minutes. The procedure to prepare chloride-based gels is the same with the addition of water to the solution. The gels were then aged for two to three days. Acetone exchange was performed for two months after the aging period. Aerogels were obtained via SCD in CO_2 with a three-day exchange period in order for the CO_2 to replace all the acetone inside the pores. The aerogels were then calcinated at different temperatures ranging between 150 °C and 450 °C with a dwell time of six hours. Nitrate and chloride aerogels showed surface areas of 371 and 349 $m^2\ g^{-1}$, respectively. Nitrate aerogels showed an average pore radius of 15.8 Å and pore volume of 1.66 $cm^3\ g^{-1}$ with comparable values for the chloride aerogels (15.9 Å and 1.75 $cm^3\ g^{-1}$). As expected, a decrease in the surface area and pore volume but an increase in the average pore diameter was recorded upon calcination.

ZnO-CuO composites aerogels were also prepared using propylene oxide [115]. For the preparation of this composite, a specific procedure was used. First, copper(II) chloride dihydrate ($CuCl_2.2H_2O$) was dissolved in isopropanol then the required amount of propylene oxide was added. The solution was rapidly stirred until a brownish solution was obtained. Gel formation

occurred in 1.5 hours. Zn solution was prepared by dissolving $Zn(NO_3)_2.6H_2O$ in methanol. Propylene oxide was then added. The solution was rapidly stirred and immediately added to the gelling copper solution. This resulted in a change of color from brown to blue. The gel was left to age for three to four days. The aerogels were then washed by acetone over the period of 10 days to allow a complete acetone exchange. The next step was supercritically drying the aerogels where the acetone was exchange with liquid CO_2 over the course of three to five days. The obtained ZnO-CuO composites were then calcinated at different temperatures with a dwell time of two hours resulting in a color change.

Epoxide-assisted route, using propylene oxide as a gelation reagent, was also used in the preparation of ternary metal oxides aerogels and xerogels (Cu/Zn/Al) starting from their respective precursors' salts [116]. In this investigation, shrinkage was only observed when drying in air to obtain xerogels. The obtained aerogels and xerogels had low densities with a surface area of 175 and 57 $m^2\ g^{-1}$, respectively.

The synthesis of Fe-Si mixed oxides aerogels [117] was conducted by dissolving $FeCl_3.6H_2O$ in absolute ethanol (solution A). Once the salt is completely dissolved, propylene oxide is added, and a change of color occurred from yellow-brown to dark-red brown. In a separate vial, TMOS or TEOS is mixed with ethanol (solution B) and then it is added to solution A with the addition of a second dose of propylene oxide. Once the gels were formed, they were left to age for 24 hours followed by ethanol washing for three to five days. Aerogels were obtained by supercritically drying in CO_2 preceded by CO_2 exchange for three to four days at 12 °C. In order to obtain xerogels, drying under fume hood for 15–30 days and heat treatment at 50° for 24 hours were performed. High surface areas between 350 and 450 $m^2\ g^{-1}$, pore volume 1.6–4.85 $ml\ g^{-1}$, and average pore diameters of 15–35 nm were reported for Fe-Si mixed oxides aerogels.

5.3.2.2 Inorganic-Organic Composites

Inorganic-organic composites have been investigated as aerogels, mostly carbon-based such as SiO_2-C, Nb_2O_5-C, and TiO_2-C hybrid aerogels for catalytic, electrochemical, and energetic applications [120–122]. Another type of inorganic-organic hybrid material is Al_2O_3-C that is prepared from furfural, resorcinol, aluminum nitrate, and propylene oxide [123]. Aluminum precursor and resorcinol were dissolved in ethanol at RT and placed in an ice-water bath to reach thermal equilibrium. Furfural is added dropwise to the solution followed by the addition of propylene oxide. The final solution was aged in water at 70 °C for five days. Ethanol exchange was then performed, and hybrid aerogels were obtained by SCD in n-hexane at 240 °C and 6 MPa for one hour followed by carbonization at 800 °C for three hours under nitrogen. These aerogels showed a high surface area reaching up to 520 $m^2\ g^{-1}$, an average pore size of 12–18 nm, and their mesopores volume between 1.08 and 2.3 $cm^3\ g^{-1}$.

ZrCO composite aerogel was also reported [124]. Zirconium oxychloride was dissolved in a mixture of water, ethanol, and formamide until complete hydrolysis. ZrO_2 sol was obtained. In another container, resorcinol, formaldehyde, and water were mixed in order to prepare the resorcinol-formaldehyde sol. Then, both sols were mixed together at RT followed by the addition of a desired amount of propylene oxide until gels were obtained. Subsequently, gels were left to age at 50 °C for one day followed by ethanol exchange over the period of five days. ZrO_2/RF aerogels were obtained by CO_2 SCD. Carbothermal reduction in argon for three hours transformed ZrO_2/RF into ZrCO. Finally, ZrCO aerogels were heat-treated in air at 650 °C for three hours. BET analysis showed that these aerogels have a specific surface area of 637.4 $m^2\ g^{-1}$ for R:Zr ratio of 2. Moreover, the thermal conductivity at RT was relatively low with a value of 0.057 $W\ mK^{-1}$.

5.4 Aerogels Properties and Characterization

5.4.1 Structural Characterization

5.4.1.1 X-ray Diffraction

The X-ray diffraction (XRD) technique has been used to characterize the aerogels prepared using the epoxide-assisted approach. The XRD patterns of alumina aerogels and xerogels obtained via this method showed, in general, broad lines corresponding to pseudoboehmite. This latter is a gelatinous poorly crystallized form of boehmite that contains excess water. The absence of aluminum oxyhydroxide, AlO(OH), or aluminum hydroxide, $Al(OH)_3$ peaks indicates the amorphous nature of the alumina aerogels prepared using aluminum nitrate nonahydrate in absolute ethanol. However, when aluminum chloride is used as a precursor, broad diffraction lines appeared corresponding to pseudoboehmite, AlO(OH) (Figure 5.10a). Upon heat treatment at 800 °C, the pseudoboehmite layers start to collapse allowing the formation of the face-centered cubic structure of γ-Al_2O_3 indicated by the increased intensity of [400, 440] lines in the XRD pattern (Figure 5.10b).

The nature of the hydrolyzed Al(III) polycations and the salt anions affect the particle morphology and crystallinity of the alumina aerogels. For example, when using chloride-based salts, the formation of the gelatinous pseudoboehmite phase is favored in either aqueous or ethanolic solutions. This is due to the "noncomplexing" nature of the chloride anions. In case of "weakly complexing" ions, such as nitrate anions, aerogels show a long or intermediate range organization.

In another study, XRD patterns showed Bragg diffraction peaks at 31°, 59°, and 77°, as well as broad diffraction peaks located approximately at 46° and 85° corresponding to the XRD pattern of the pseudoboehmite structure [11, 125, 126]. An additional peak at $2\theta = 9°$, characteristic of an alkoxyalumoxane prepared using ethanol, can be seen [126, 127]. Alkyl groups present between the alkoxyalumoxane structure layers, result in a similar XRD pattern to pseudoboehmite but with larger interlayer spacing [126, 127]. The formation of a characteristic peak below $2\theta = 10°$ is based on the length of the alkyl chain, which affects the peak shift and the expansion of the interlayer spacing [127]. Heating up to 400 °C resulted in the disappearance of the alkoxyalumoxane characteristic peak. At 500 °C, amorphous alumina phase starts to form until a phase transformation

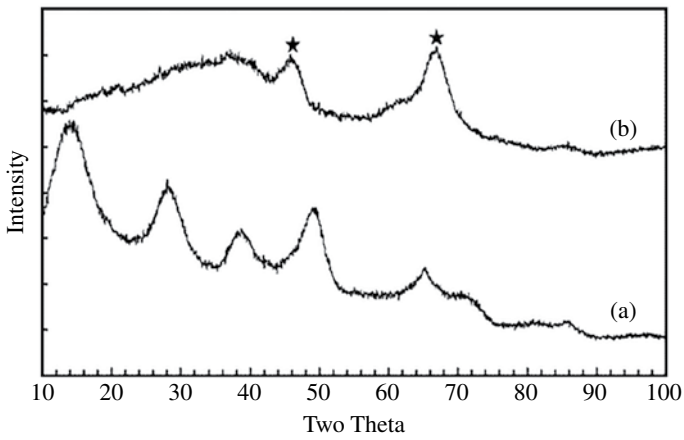


Figure 5.10 Powder X-ray diffraction patterns for alumina aerogels before (a) and after (b) heat treatment with the peaks at 46° and 67° marked with an asterisk to denote the [400, 440] peaks of γ-Al_2O_3.
Source: From Ref. [11].

occurs upon further heating, which turns the amorphous alumina into θ-alumina structure [128]. This is in agreement with the literature [129, 130], where they suggested that gelatinous boehmite can transition to θ-alumina between 800 [129] and 1100 °C [130].

Chen et al. [90] investigated the crystal structure of both titania aerogels and xerogels. They showed that the as-synthesized products are amorphous (Figure 5.11); however, the anatase phase started to appear after calcination in air at 400 °C for four hours where the characteristic peaks can be seen in Figure 5.11b. One can see that the peaks are broadened, an indication of the nanocrystalline nature of the materials. Calcination at 400–600 °C resulted in the enhancement of the degree of crystallinity of both aerogels and xerogels as it is shown from the peaks sharpening. In addition, a phase transformation can be seen at a calcination temperature of 650 °C (Figure 5.11e) where additional peaks start to appear corresponding to the rutile phase of titania. Upon further calcination above 650 °C, a complete phase transformation is observed where both aerogels and xerogels possess the rutile phase. By comparing the XRD pattern of both aerogels and xerogels, one can find that the former has much broader and lower peaks, suggesting that titania aerogels have a smaller anatase crystallite size.

The previous result is in contradiction with the work of Wei et al. [91], who found that the rutile phase was obtained for the prepared aerogels (Figure 5.12). This is probably due to the nature of the titania precursors along with the synthesis, aging, and drying steps.

The XRD pattern of synthesized vanadia aerogels [92] is shown in Figure 5.13. Peaks are in agreement with several known VO_x materials. However, the peaks broadening and their low intensity is an indication of the amorphous nature of the vanadia aerogels.

The crystal structure of zirconia aerogels was investigated by Zhong et al. [93] and is reported in Figure 5.14. As one can see, the raw sample before calcination shows a low-intensity diffraction

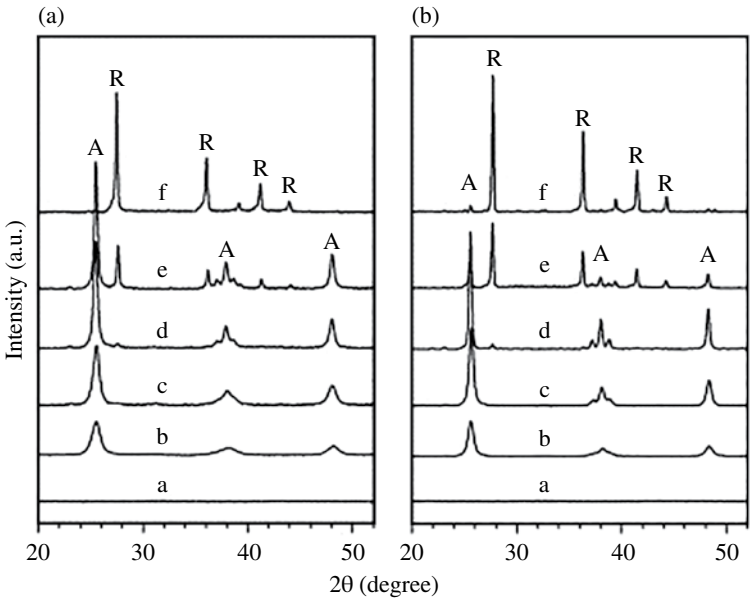


Figure 5.11 XRD patterns of the TiO_2 aerogel (A) and xerogel (B) samples calcined at various temperatures: (a) as-prepared; (b) 400 °C; (c) 500 °C; (d) 600 °C; (e) 650 °C; (f) 700 °C. The peaks marked A and R represent the anatase and rutile phase, respectively. *Source:* From Ref. [90] with permission of ELSEVIER.

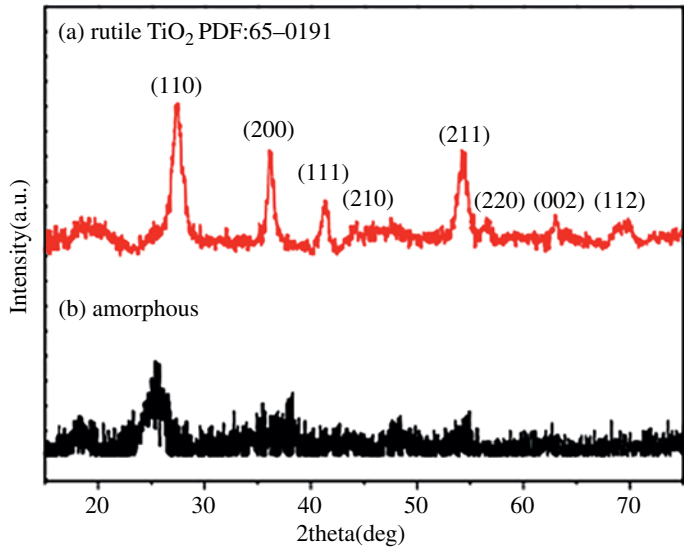


Figure 5.12 XRD patterns of titania aerogels; (a) rutile phase, (b) amorphous phase. *Source:* From Ref. [91].

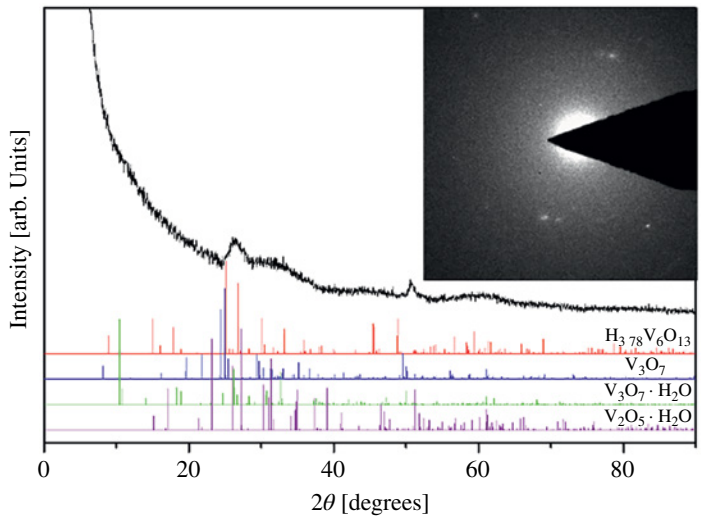


Figure 5.13 X-ray (Cu-Kα) diffraction pattern of a ground vanadia aerogel monolith. Stick patterns for a series of potential $VO_x{\cdot}nH_2O$ species are included for comparison: $V_2O_5{\cdot}H_2O$ (PDF# 01-074-3093), $V_3O_7{\cdot}H_2O$ (01-085-2401), V_3O_7 (01-71-0454), $H_{3.78}V_6O_{13}$ (01-088-1753 38-8). Electron diffraction pattern inset. *Source:* From Ref. [92].

peak at 30° indicating that the aerogel is amorphous. To be noted that a small crystalline peak appears at 50°. This is probably due to the crystallization that occurred during the SCD while preparing the gels. The calcination at high temperature sharpens the peaks indicating that the degree of crystallinity is increasing. At 750 °C, additional peaks start to appear, which are in agreement with the XRD pattern of tetragonal zirconia phase. However, as one can see in Figure 5.14b, the XRD patterns of both tetragonal and cubic zirconia phases are similar making difficult to

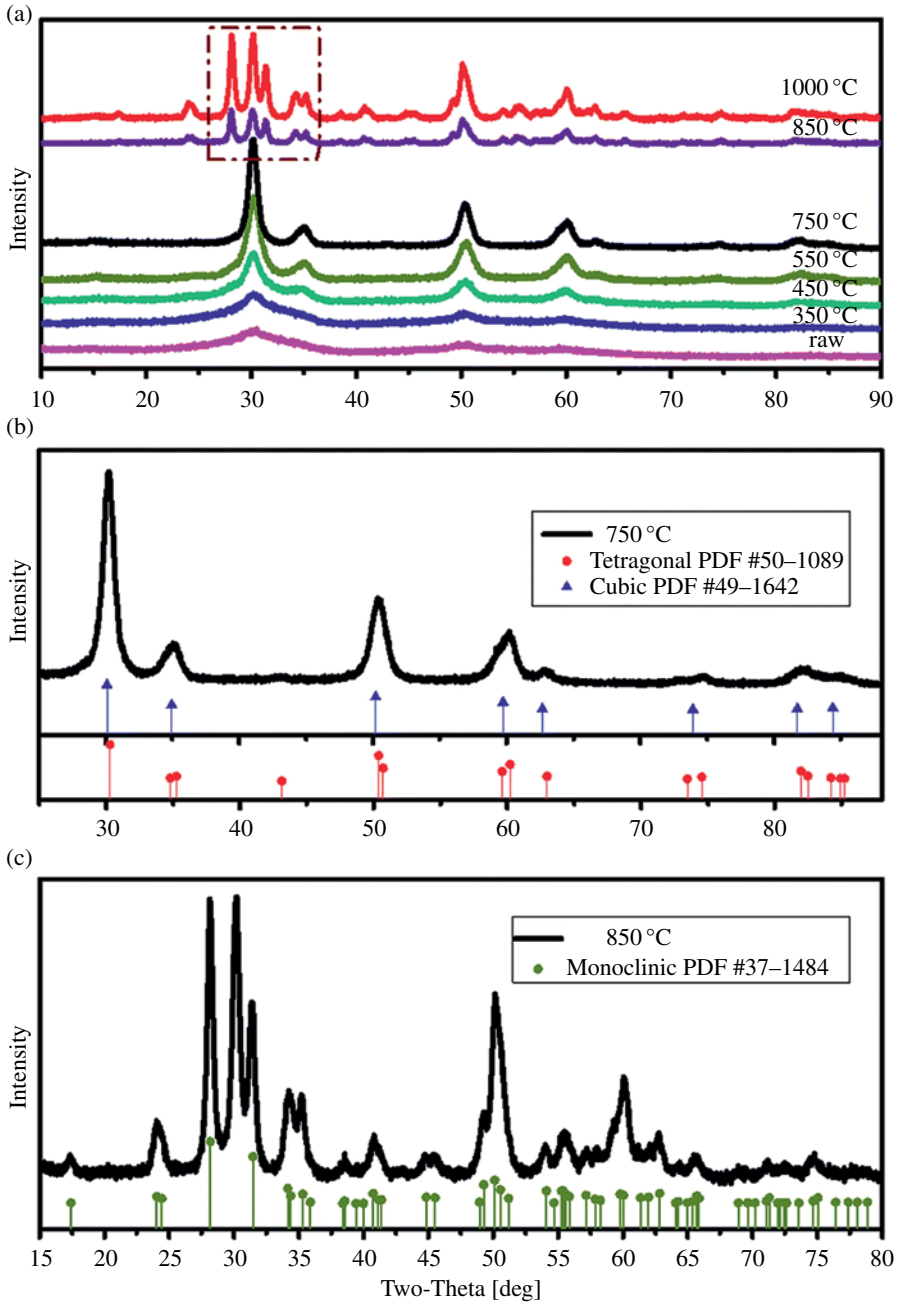


Figure 5.14 XRD patterns of aerogel $N_{1.0}$ calcinated at different temperature: (a) calcinated at 350–1000 °C, respectively; (b) aerogel $N_{1.0}$ calcinated at 750 °C. The XRD pattern for standard cubic and tetragonal ZrO_2 are shown as lines and points with different colors; (c) aerogel $N_{1.0}$ calcinated at 850 °C. The XRD pattern for standard monoclinic ZrO_2 is also shown as lines and points. *Source:* From Ref. [93].

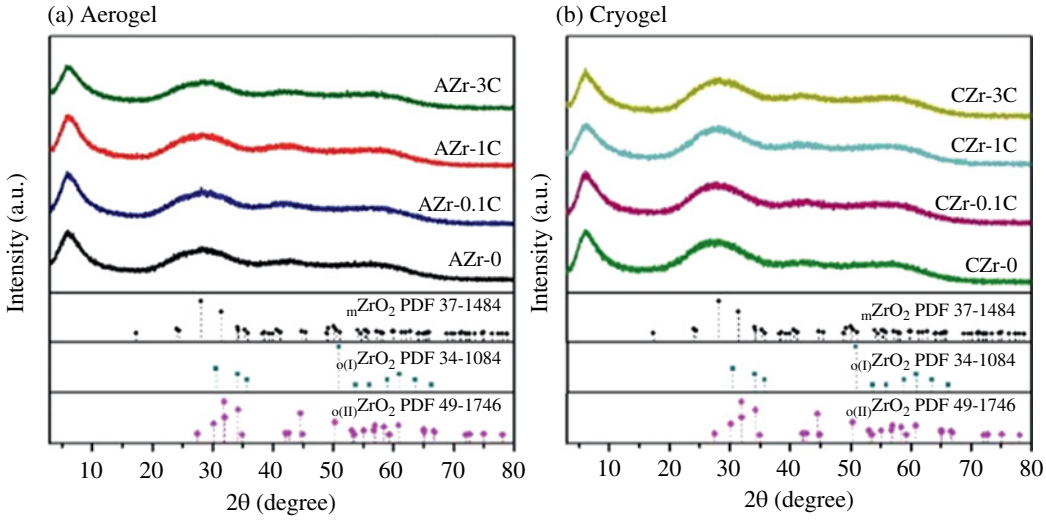


Figure 5.15 XRD spectra of the aerogels (a) and zirconia cryogels; (b) at different CTAB concentration. *Source:* From Ref. [95].

determine which phase is present after calcination based on XRD data solely. Figure 5.14c represents the XRD pattern of zirconia aerogels calcined at 850 °C where a mixture of both monoclinic and tetragonal zirconia phases can be observed.

Zirconia aerogels and cryogels obtained via the assisted-epoxide route using CTAB [95] possess a semi-crystalline structure according to their XRD patterns (Figure 5.15). This can be explained by the peaks broadening. Peaks at 20–35° and 37–46° are very broad, which suggests that both monoclinic and orthorhombic II phases can coexist. Another broad peak can be seen at 50–62° where the three phases of zirconia (monoclinic, orthorhombic I, and orthorhombic II) can be present. The peak at $2\theta = 6°$ is an indication of the nanostructured nature of both aerogels and cryogels where the particles are around 5–10 nm. However, it is not attributed to either of the known zirconia phases.

5.4.1.2 Electron Microscopy

Electron microscopy has been used to investigate the morphology of aerogels prepared using the epoxide-assisted technique. The morphology of alumina aerogels prepared via this route is shown in Juhl et al. [19]. One can notice an interconnected fibrous microstructure for all samples that have been treated differently. This morphology is in agreement with the literature [11]. The elemental composition of the aerogels was also investigated by EDX and revealed an even distribution of oxygen and aluminum atoms through the sample with small traces of carbon and chlorine.

The morphology of alumina aerogels prepared via epoxide assisted method with addition of PEO at different concentrations and dried at various conditions was investigated by Tokudome et al. [18]. It was found that xerogels have a smaller domain size when compared to the aerogels. This is due to the fact that during the drying process, xerogels exhibit considerable shrinkage. The macroporous structure collapses due the capillary force which leads to the disappearance of the micrometer regime during the early stage of phase separation. Upon the secondary phase separation, aerogels show a nest-like structure. This characteristic is missing from the xerogels samples.

Particle size and morphology of TiO_2 aerogels and xerogels were investigated via transmission electron microscopy [90]. Titania aerogels (Figure 5.16a) show an airy sponge-like morphology while the morphology of the titania xerogels (Figure 5.16e) is a highly contracted porous network. A partial retention of the aerogels extended network can be obtained upon calcination at 400 °C and loosely aggregated spherical nanoparticles with the similar particle size around 8–10 nm appeared (Figure 5.16b). Further calcination at 650 °C resulted in grain agglomeration with larger particles (20–30 nm), and big lumps were observed. Xerogels were found to be less thermally stable upon calcination (Figure 5.16e,d,f) where larger particles and severe agglomeration can be seen.

Figure 5.17a shows the TEM image of TiO_2 aerogel after calcination. One can see a mesoporous structure composed of well-connected TiO_2 nanocrystals. HRTEM image (Figure 5.17b) shows that the aerogel backbone is constructed from chemically bonded, well-connected nanocrystals.

The SEM performed on vanadia aerogels shows that these have a macroporous structure morphology (Figure 5.18a). In addition, they possess the same nanoworm micromorphology that can be occasionally seen in gels synthesized via alkoxide hydrolysis [132, 133]. Moreover, the TEM images of vanadia aerogels (Figure 5.18b) show that they consist of small crystalline domains dispersed in an amorphous matrix.

The SEM images of zirconia aerogels prepared by epoxide assisted method show that the amount of propylene used has an effect of the morphology of the final product. One can notice that upon increasing this amount, the particle size and connectivity of the network increase. However, when no PO is used, the aerogels appeared to be in a collection of clusters containing smaller mesopores and a weakly uniform microstructure (Figure 5.19a). Increasing the PO content resulted in an increase of the pH, and therefore an interconnected network of sphere particle aerogels can now be seen (Figure 5.19b,c). For PO/ZrO_2 molar ratio of 2.5, larger particles and denser structure are reported for the zirconia aerogels (Figure 5.19d).

The content of nitric acid and water while preparing zirconia aerogels is found to affect the degree of network and cluster size of these aerogels as shown in the TEM image (Figure 5.20a–c) [93]. When prepared under fast reaction conditions, zirconia aerogels show less network and larger clusters (Figure 5.20a). However, when the reaction conditions are slow, the formed clusters are smaller with a better degree of network (Figure 5.20b). This is probably because nitric acid can suppress the presence of localized condensation resulting in small clusters and a fine skeleton formation (Figure 5.20f). HRTEM images (Figure 5.20e,d) illustrate a fine representation of the size, shape, and connectivity of the clusters. Zirconia aerogels appear to have relatively spherical particles with a diameter ranging between 5 and 10 nm. Moreover, the particles connect to each other to form larger clusters, which are the backbone of the aerogels network.

The effect of CTAB on the morphology of zirconia aerogels was also investigated [95]. SEM images show that when zirconia aerogels are prepared without the use of CTAB, the morphology consists of agglomerates made up of smaller primary particles (Figure 5.21a). Upon adding CTAB, agglomerates merge together and become larger resulting in macropores (>50 nm) – 0.1 mM of CTAB leads to the formation of a 3-D network when nanopores can be observed (Figure 5.21b). Increasing CTAB concentration to 1 mM, the agglomerates become more uniformly distributed, thereby forming the interconnected 3-D network (Figure 5.21c). Similar morphology of the agglomerates was found when 3 mM of CTAB has been used (Figure 5.21d).

In the case of cryogels, it was found that the 3-D network collapsed due to the formation of liquid-vapor interface formed inside the pores. This can be clearly seen from the SEM images (Figure 5.21e–h) where the surface of the sample is composed of smaller particles (<100 nm) and micropores.

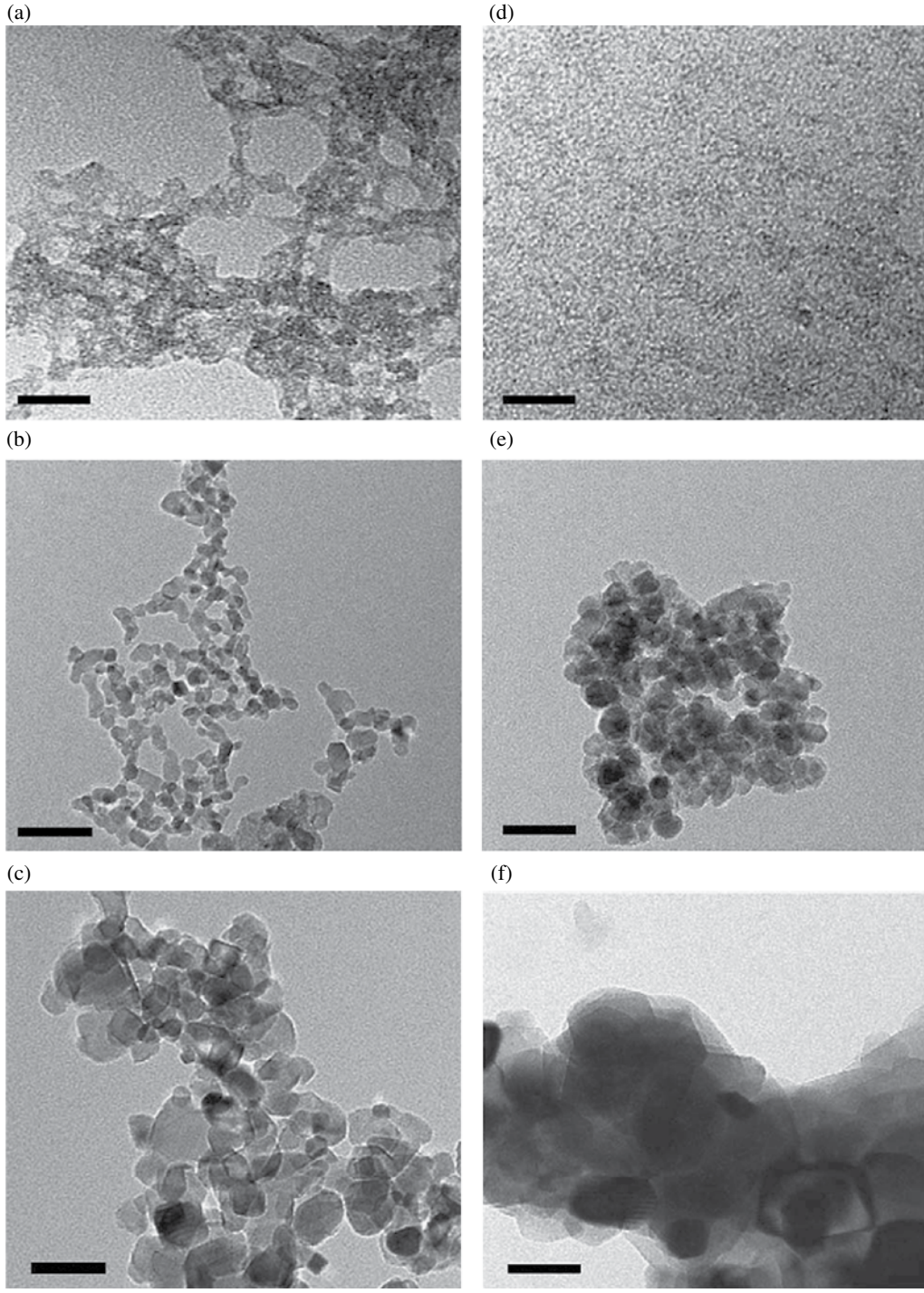


Figure 5.16 TEM images of aerogel (a–c) and xerogel (d–f) TiO_2 samples: as-prepared (a and d) and calcined at 400 °C (b and e) and 650 °C (c and f). Scale bar: 50 nm. *Source:* From Ref. [90].

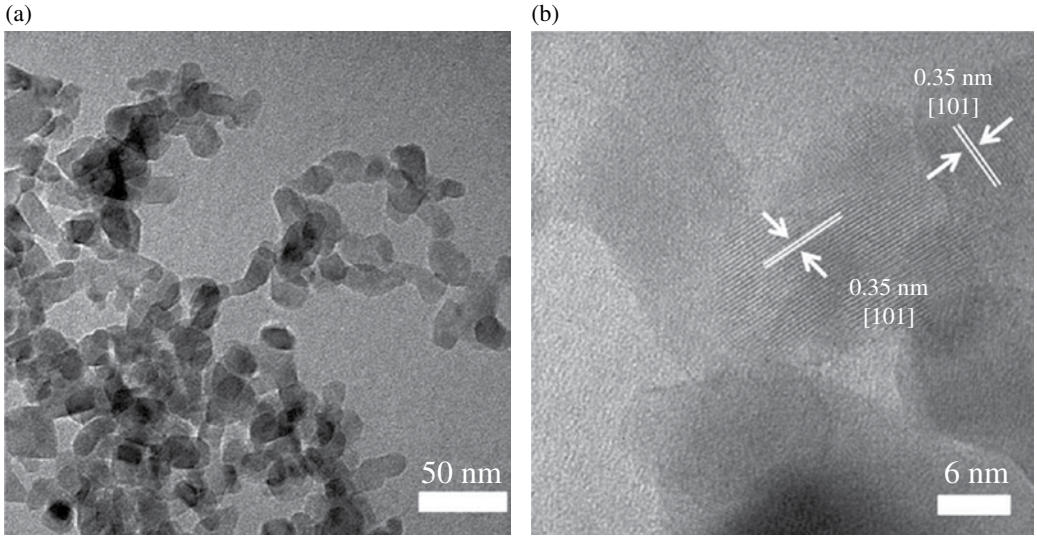


Figure 5.17 TEM image (a) and HRTEM (b) images of TiO_2 aerogels. *Source:* from Ref. [131].

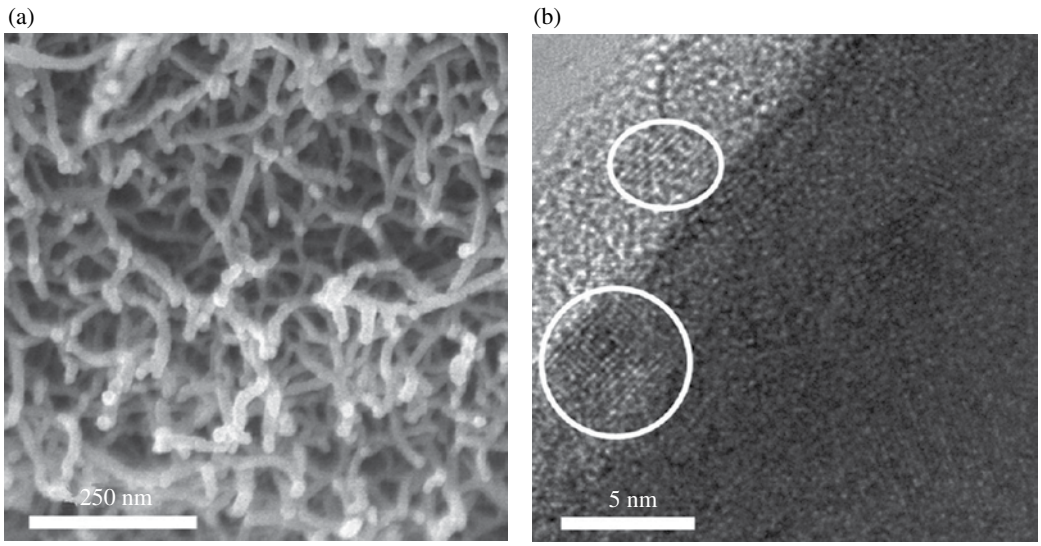


Figure 5.18 Representative SEM (a) and TEM (b) images of VOx aerogels. Several crystalline domains are circled in the TEM image. *Source:* From Ref. [92].

5.4.1.3 Infrared Spectroscopy

Infrared spectroscopy has been widely used to characterize aerogels. A typical IR spectrum of alumina aerogels is presented in Figure 5.22 [19] showing three samples of alumina aerogels with different treatments. After one-time solvent exchange, the sample shows peaks at 3319 and 3082 cm^{-1} (Figure 5.22a) characteristic of the asymmetrical and symmetrical stretching of AlO-H bond in the boehmite structure [125, 134, 135]. The deformation interlayer of AlO-H can be observed at 1164, 1072, 868, and 772 cm^{-1}. The peak at 608 cm^{-1} is attributed to the octahedral Al-O stretching [125, 136] while overlapping peaks can be identified at 465 cm^{-1} corresponding to

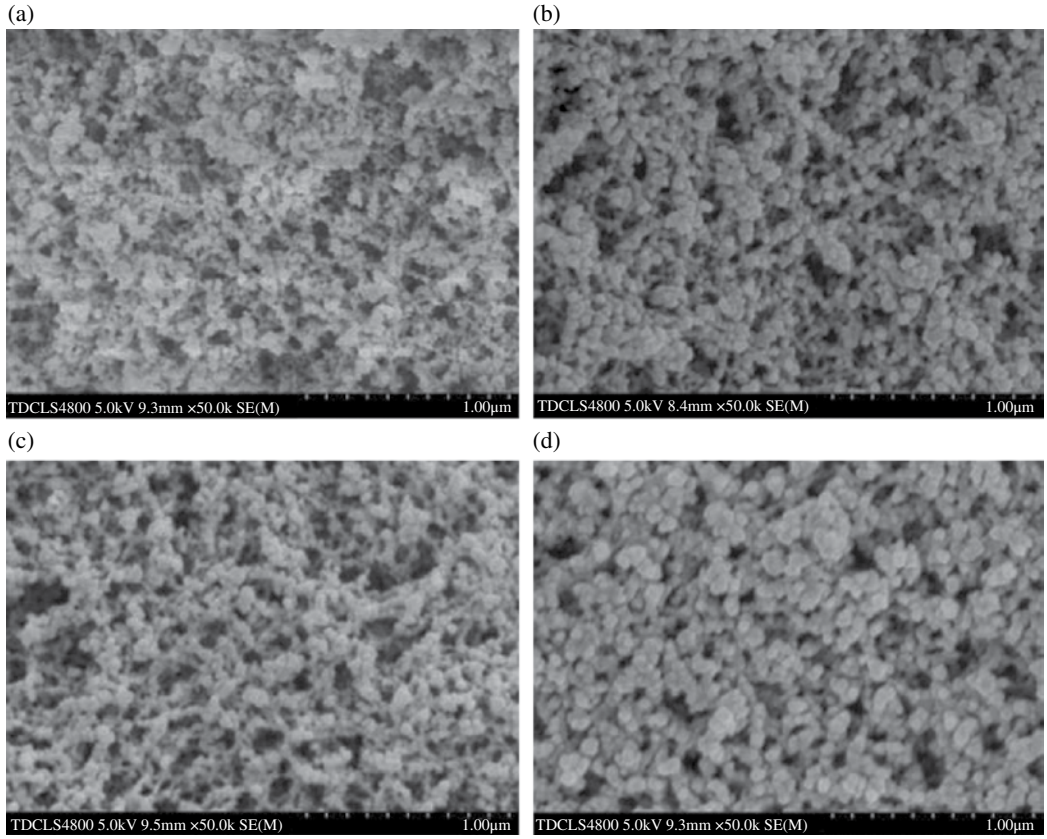


Figure 5.19 SEM of varied X. (a) ZrO_2–0P (b) ZrO_2–1.5P (c) ZrO_2–2P (d) ZrO_2–2.5P. *Source:* From Ref. [94].

the skeletal modes of Al-O layers [125]. No C-H bond stretches are observed in the previous samples, however, after three times solvent exchange, these peaks can be clearly seen in Figure 5.22b. The mentioned characteristic peaks of AlO-H in boehmite are not observed which is probably due to the overlapping with the solvent O-H absorption [125, 134, 135]. Dried aerogels infrared spectrum (Figure 5.22c) shows that the O-H absorption peak disappeared due to the degassing overnight under vacuum at 200 °C. However, the absence of interlayer AlO-H deformation peaks came as a surprise. This is probably an indication that alkyl groups lie within the space between the layers inhibiting AlO-H interlayer interaction. Moreover, peaks at 2972 and 1114 cm^{-1}, the characteristic peaks of C-H stretching and bending, respectively, can be observed. Upon desorption, two additional peaks (3465 and 868–850 cm^{-1}) appeared corresponding to hydroxyl groups that can be found at the surface of alumina [134].

The surface properties of different TiO_2 aerogels and xerogels, synthesized via the epoxide-assisted route, was investigated by the Diffuse Reflectance FTIR spectroscopy. All spectra show broad bands at 3300 and 1625 cm^{-1} corresponding to the surface adsorbed water and hydroxyl groups [137]. The surface vibrational peaks of Ti-O bonds range between 400 and 900 cm^{-1} [138] while the peak at 1385 cm^{-1} in the calcined aerogel and xerogel samples is attributed to Ti-OH bonds. In addition, annealing the samples led to the loss of surface-adsorbed water and hydroxyl groups, in addition to the organic species remaining on the surface (2931, 1400, and 1063 cm^{-1}) as expected. Calcination at 400 °C resulted in decreasing the intensity of the peak at 3000 cm^{-1}

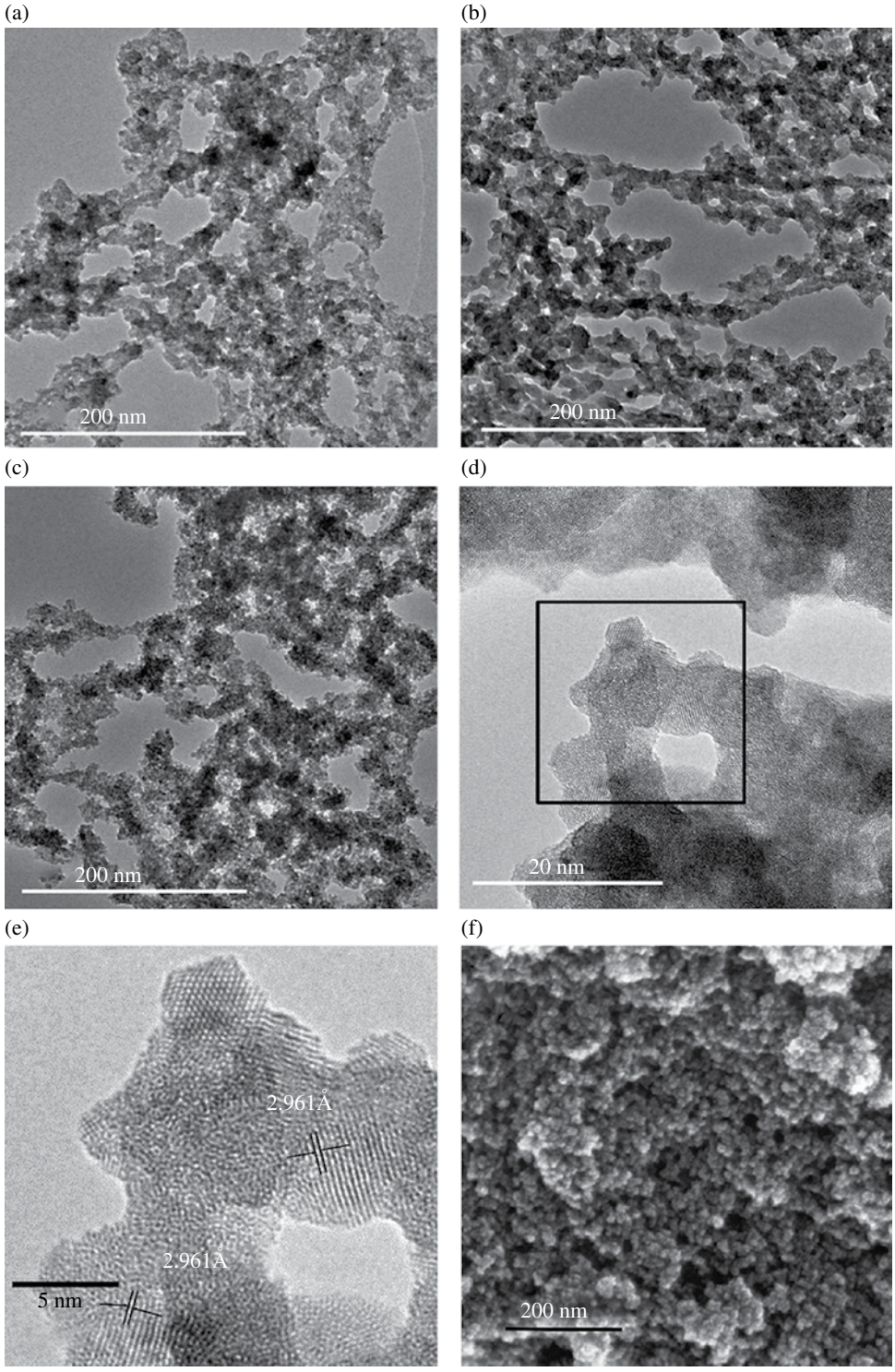


Figure 5.20 TEM images of zirconia aerogels: (a) $N_{0.6}$, (b) $N_{1.0}$, (c) H_2, (d) HRTEM of $N_{1.0}$ and (e) enlarged HRTEM image of the selected area marked by a box in (d); (f) the SEM image of $N_{1.0}$. *Source:* From Ref. [93].

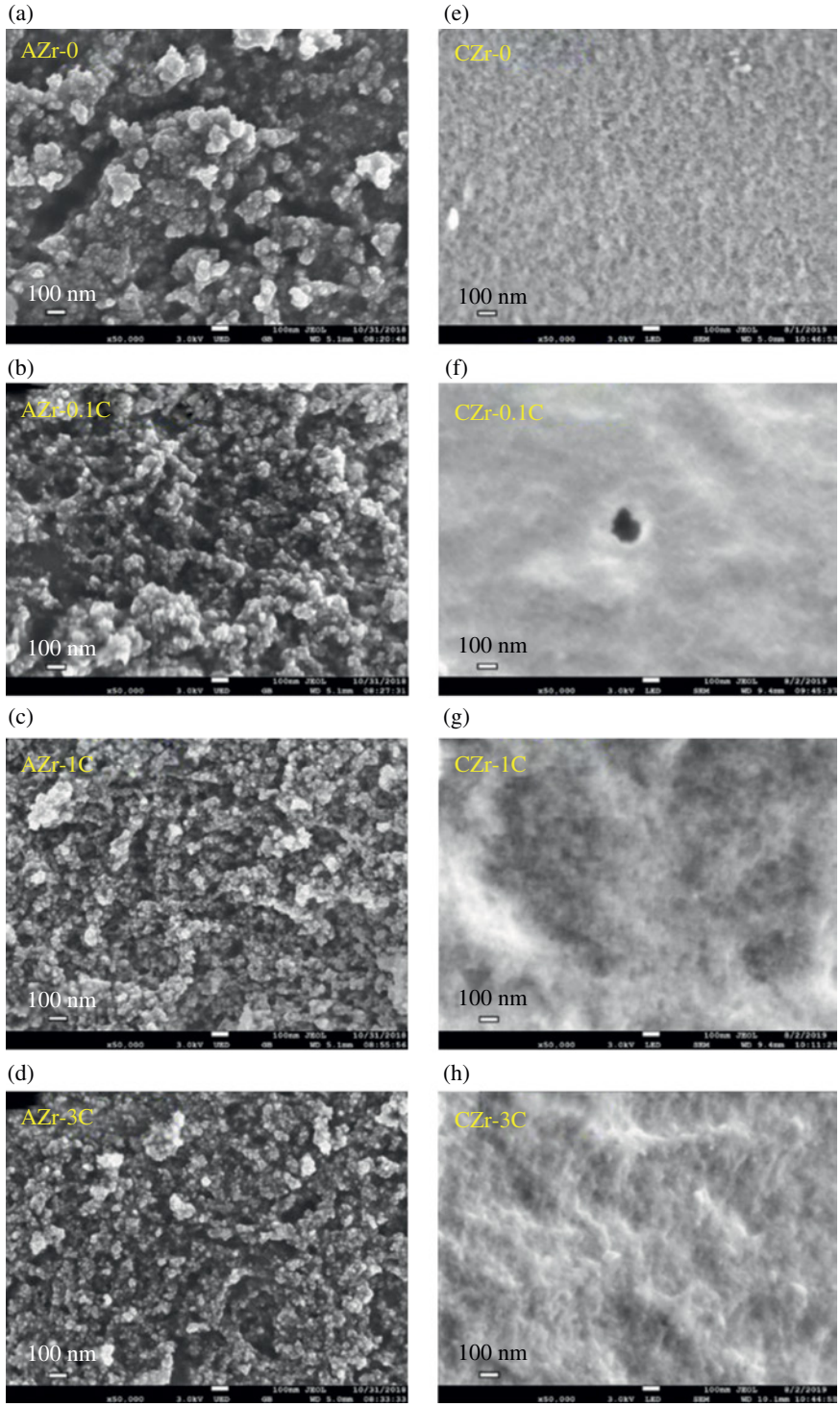


Figure 5.21 SEM images of ZrO_2 aerogels at 0, 0.1, 1, and 3 mM of CTAB concentration (a, b, c, and d, respectively) and ZrO_2 cryogels at 0, 0.1, 1, and 3 mM of CTAB concentration (e, f, g, and h, respectively). *Source:* From Ref. [95].

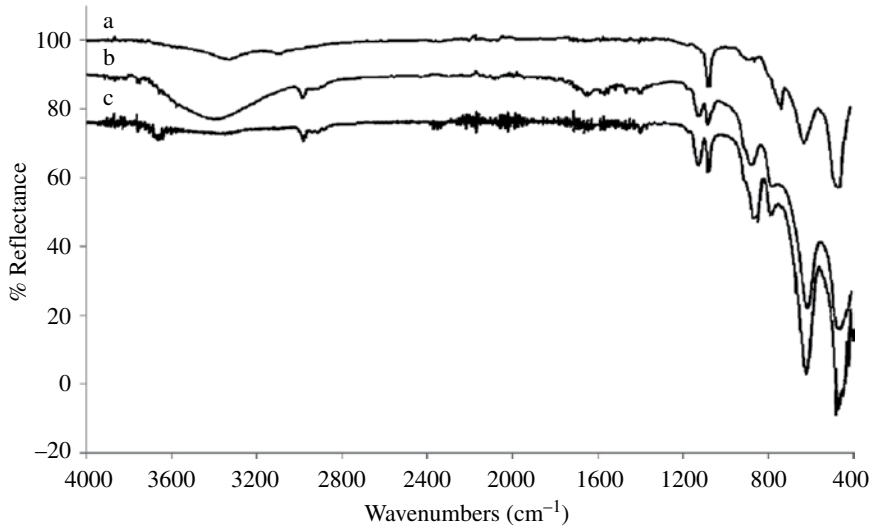


Figure 5.22 FTIR attenuated total reflectance spectra of alumina aerogels prepared with (a) one solvent exchange; (b) three solvent exchanges; (c) three solvent exchanges and subsequent drying to remove adsorbed solvent. Spectra (b) and (c) are offset on the *y*-axis. *Source:* From Ref. [90] with permission of ELSEVIER.

suggested that only traces carbonaceous species are presented. Upon further calcination at 500 °C for four hours, peaks at 2931 and 1400 cm^{-1} disappeared.

FTIR spectroscopy was performed on zirconia aerogels and cryogels, both shown in Figure 5.23a,b, respectively, with different concentrations of CTAB [95]. In both materials, the broad peak at 3420 cm^{-1} is attributed to the stretching of OH bonds of the water molecule with it being more apparent in the aerogels. The deformation band of OH, which is another characteristic peak of water, also appeared at 1550 cm^{-1}. Peaks at 2980 and 2930 cm^{-1} correspond to the asymmetric

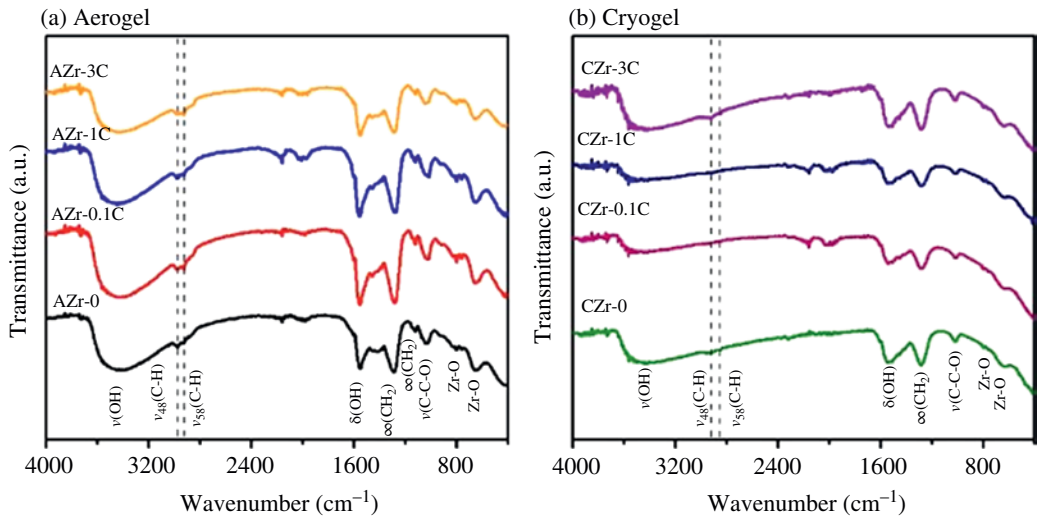


Figure 5.23 Effect of the drying on morphology and texture of aerogels (a) and zirconia cryogels (b). *Source:* From Ref. [95].

stretch of methyl-methylene of propylene oxide while peaks at 1294, 1127, and 1036 cm^{-1} are attributed to the wagging vibration of CH_2 bond due to the deformation of the alcohol, deformation of the epoxide and the C-C-O stretching, respectively. Zr-O-Zr stretching is located at energy band of 800 cm^{-1} and the characteristic peaks of the Zr-O network vibrations in the monoclinic phase are located at 763 and 652 cm^{-1} [139].

5.4.2 Mechanical Characterization

Baumann et al. [11] studied the mechanical properties of different alumina samples. They found that aerogels prepared using a mixture of water and ethanol were much stiffer and more robust when compared to aerogels synthesized via other techniques. The elastic modulus of aerogels can be calculated using a sound velocity measurement technique. A 60 $kg\,m^{-3}$ density aerogel has an elastic modulus of 3.2 MPa. In comparison, an aerogel prepared from alkoxide precursors was found to have an elastic modulus of 0.55 MPa for a density of 40 $kg\,m^{-3}$. This is promising since the prepared aerogel in this study has a higher elastic modulus than those of SiO_2 and Al_2O_3 aerogels of similar density [140].

Vanadia aerogels prepared by epoxide-assisted route are sturdier and exhibit less optical scattering when compared to their alkoxide counterparts [92]. Moreover, X-VO_x aerogels in this study show similar mechanical properties to those prepared by alkoxides route. However, mechanical failure occurred at a lower strain (inset Figure 5.24). This is probably due to the existence of internal voids when prepared via epoxide-assisted route. Aerogels prepared via the hydrolysis of vanadium oxytripropoxide do not possess these voids.

The mechanical properties of different metal oxide aerogels prepared via the epoxide route were investigated [141]. The data, represented in Figure 5.25a, shows that iron oxide and zirconia have a hard texture with high Young's moduli of 8.1 and 10.7 MPa respectively. However, these aerogels were brittle and break at a strain of 6%. In contrast, gallia aerogels have the lowest Young's

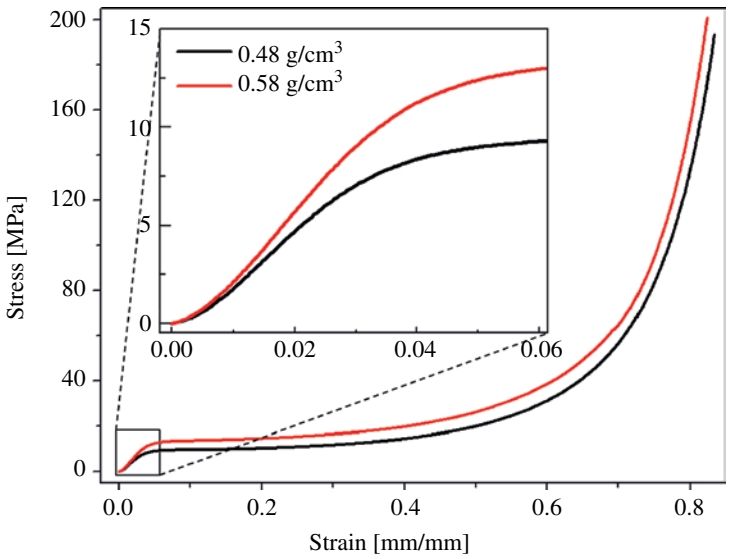


Figure 5.24 Representative quasi-static compression tests of X-VO_x aerogels with different densities, as controlled by isocyanate concentration in crosslinking solutions. Elastic region expanded in inset.
Source: From Ref. [92].

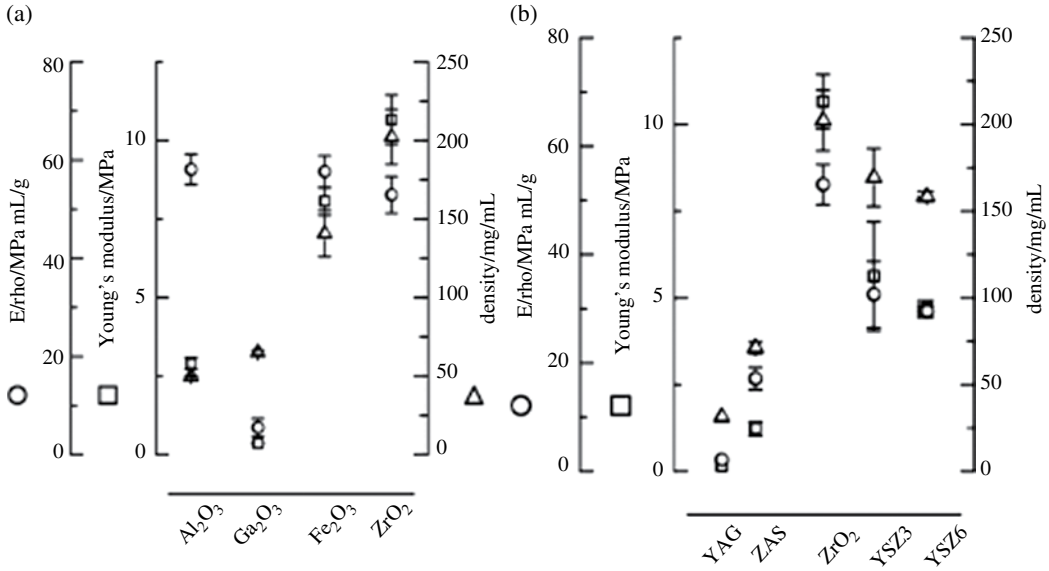


Figure 5.25 Young's modulus of different mono metal oxides aerogels (a) and composite aerogels; (b). *Source:* From Ref. [141].

modulus 0.36 MPa. The low density of the prepared alumina aerogels (50 mg ml^{-1}) resulted in a Young's modulus of 2.9 MPa and a value for the specific modulus of 58.1 MPa ml g^{-1}.

In addition, mixed metal oxides (yttrium stabilized zirconia – YSZ; zinc aluminum spinel – ZAS and yttrium alumina garnet – YAG) aerogels were synthesized and the mechanical properties were investigated (Figure 5.25b). One can notice that when yttrium content increases, the Young's modulus decreases, leading to a loss of stability. However, YSZ remained brittle similar to pure zirconia. ZAS had a moderate Young's modulus of 1.2 MPa and became brittle at a strain of 6%. On the other hand, YAG showed a compressible behavior with a relatively low Young's modulus of 0.07 MPa.

5.5 Some Applications and Examples

In recent years, aerogels have found a wide variety of applications. They have been used in catalysis, thermal insulation, sorption, energy storage, biodiesel production, and water treatment. Moreover, the composition and structure of the aerogels can be tailored for the as-mentioned applications.

5.5.1 Catalysis

Alumina aerogels can be used in catalysis, adsorption, support, thermal insulation, and separation [96]. The interest in these materials appeared since alumina is one of the most widely used solids as support for catalytically active metals and metal oxides.

Iron oxide aerogels are extensively used as catalysts in different reactions. Bali et al. [104] synthesized iron aerogels and xerogels and used them in Fisher-Tropsch reaction. The percent conversion of CO was 7%, 14%, and 35% after 35 hours of reaction time for K-doped iron oxide xerogels, iron aerogels, and K-doped iron oxide aerogels, respectively. The K-doped iron

oxide aerogels conversion rate can be comparable to that of 20%wt Fe supported on SBA-15, which makes it a suitable candidate as catalyst for Fischer-Tropsch reaction.

In addition, iron oxide aerogels have been used as catalyst for water gas shift (WGS) reactions [103]. Pd-doped iron oxide aerogels (1% and 2%) showed higher activity when compared to the undoped aerogels with a conversion value of 0.34 g CO g^{-1} catalyst hours and 0.51 g CO g^{-1} catalyst hours at 350 °C for the uncalcined doped aerogels, respectively. The undoped iron oxides did not show any activity at this temperature. The increase in the catalytic activity can be explained by two factors: Fe_2O_3 phase transforms into the catalytically active phase Fe_3O_4 in reduced atmosphere under WGS conditions, and the fact that the formation of Fe-Pd system results in an enhanced WGS conditions since it allows a thermodynamic driving force leading to the reduction of Fe_2O_3.

Titania aerogels gained an interest in heterogenous photocatalysis in order to limit and reduce the global atmospheric pollution and the purification of polluted water. Titania aerogels synthesized by the epoxide-assisted route [90] showed a superior photocatalytic activity when compared to a commercially titania photocatalyst. This is probably due to the specific area, crystallite size, and phase structure of the aerogel. The catalyst with the highest specific activity for the photodegradation of phenol was the aerogel calcined at 650 °C with a phase composition of 72% anatase and 28% rutile, a relatively low surface area of 36 $m^2 g^{-1}$, and a pore volume of 0.25 $cm^3 g^{-1}$.

$CoFe_2O_4$ aerogels were used in the hydrolysis of 4-nitrophenyl phosphate reaction [16]. The as-synthesized aerogels as well as aerogels calcined at 200 °C showed a high catalytic activity exceeding 50% after 24 hours reaction time (55% and 65%, respectively). This is due to the existence of residual -OH groups that did not condensate. It was also found that increasing the calcination temperature above 200 °C resulted in a decrease of the catalytic activity until a complete inactivity above 600 °C. Therefore, cobalt ferrite aerogel prepared via the epoxide-assisted technique and calcinated at 200 °C is a suitable catalyst for the hydrolysis of 4-nitrophenyl phosphate into 4-nitrophenol showing high conversion rate (65%) and high selectivity (100%).

In addition, ZnO/Al_2O_3, CuO/Al_2O_3, and $CuO/ZnO/Al_2O_3$ are used extensively in the industrial synthesis of methanol, methanol reforming, and water-gas shift reaction [116]. It was found that the higher Cu content and the presence of ZnO in the material lead to a higher catalytic activity which is increased from 4% for CuO/Al_2O_3 (1 : 1) to 22% for $Cu/ZnO/Al_2O_3$ aerogel (1 : 1 : 1).

5.5.2 Solid Fuel Cell

Ceria aerogels are considered as promising candidates for solid-oxides fuel cells (SOFCs) because Ce(IV) present in these materials can be easily transformed into Ce(III), especially at high temperatures (>500 °C). Ceria aerogels and ambigels, prepared via the epoxide-assisted route [106], showed the desired properties of a great SOFC catalyst candidate such as high specific area and interconnected porous bonded network of CeO_2 crystallites. The electrical response and behavior of different ceria-based materials were investigated (aerogels, ambigels, and commercial powder). It was found that the electrical response of ceria aerogels is similar to that of the ambigels. Moreover, ceria ambigels had an electrical conductivity five times greater in oxygen atmosphere when compared to the commercial powder with both materials showing an increased conductivity in Ar atmosphere. The activation energy (E_a) of CeO_2 aerogels was found to be 0.6–0.7 eV in the low-temperature region (<600 °C). This resulted in an increase of the catalytic activity of ceria ambigels in SOFCs.

Another material that can be used as SOFCs catalyst is Yttria-stabilized Zirconia (YSZ) with common operating temperatures between 800 and 1000 °C. YSZ aerogels with 9% mol Y_2O_3 doping were prepared via the epoxide-assisted route [15]. The activation energy (E_a) of these aerogels exhibited a decrease at higher temperatures from 1.12 to 0.95 eV upon heating above 550 °C. Moreover, the ionic conductivity increased with temperature – 0.036 and 0.13 Ω^{-1} cm^{-1} at 800 and 1000 °C, respectively. These properties are favorable for YSZ to be considered as a suitable candidate for SOFCs applications.

Doped lanthanum manganite ($LaMnO_3$) can also be used as a SOFCs catalyst and is considered as the most promising candidate as a standard cathode for high-temperature applications due to its p-type intrinsic conductivity nature. The electrical properties of $LaMnO_3$ aerogels, prepared by epoxide-assisted technique, were investigated and reported [14]. The activation energies of the as-synthesized samples as well as the commercial sample ranged between 0.13 and 0.15 eV. To be noted that the samples prepared with a binder showed a similar electrical conductivity (~120 and 127 Ω^{-1} cm^{-1} at 800 and 1000 °C, respectively) while the electrical conductivity of the sample without a binder was 70 Ω^{-1} cm^{-1} at both temperatures. This can be explained by the fact that the sample without a binder had a larger porosity resulting in a decrease of the electrical conductivity.

On the other hand, spinel aerogels materials that have the chemical composition AB_2O_4 such as $CoAl_2O_4$, $CoCr_2O_4$, $ZnFe_2O_4$, and $CuC_{r2}O_4$ have been widely used as catalysts for cathode materials and heat-resistant pigments [102].

5.5.3 Water Treatment

Ni-based materials are known for their surface properties and their low production cost. However, NiO/Al_2O_3 aerogels were never used as adsorbent materials. In a recent study, this type of material was investigated for the removal for azo-dyes from aqueous media [13]. Although alumina-based adsorbents were reported for this application, it was found that the addition of Ni increased the surface reactivity and the adsorption capacity of the aerogel. The highest adsorption capacity was reported for 40% Ni-alumina aerogels for different dyes, 900, 1484, and 1660 mg g^{-1} for Methyl Orange, Orange II, and Congo Red, respectively, making this adsorbent exceptionally good candidate for dye removal.

Another type of material that can used for water treatment and dye removal is the $ZnFe_2O_4$, which have been also used in the removal of sulfur from coal gas and the degradation of dyes [113]. However, no study investigated the activity of these materials when prepared via the epoxide-assisted route, which might be interesting for future works to investigate this type of application.

5.5.4 Biodiesel Production

CaO/Al_2O_3 hybrid aerogel, an environmentally friendly material, was used as a catalyst for biodiesel production from waste cooking oil (WCO) [12]. Different Ca:Al molar ratios have been used to prepare these aerogels via the epoxide-assisted route. It was found that the use of 1% wt CaO/Al_2O_3 (3 : 1) as catalyst for this reaction yields the highest conversion rate and purity of the formed methyl ester (89.9% and 98%, respectively). This indicates that hybrid CaO/Al_2O_3 aerogels are very advantageous in transesterification reactions due to their high yield as well as their low production cost.

5.5.5 Energy Conversion and Storage Applications

Ruthenium oxides are used as high-energy storage electrode due to their high capacitance and low resistance. Ruthenium oxide aerogels were prepared by the addition of an epoxide to a hydrated solution [105]. These aerogels showed a high capacitive behavior, as expected, with the uncalcined aerogels having the highest specific capacitance of $595\,F\,g^{-1}$. It was found that upon calcination at 250 °C, the specific capacitance decreased significantly ($179\,F\,g^{-1}$), which can be explained by the phase transformation into crystalline rutile anhydrous RuO_2. The lowest specific capacitance value of $71\,F\,g^{-1}$ was obtained after calcination at 500 °C. Therefore, in order to obtain a promising candidate for high-energy storage application, RuO_2 aerogels should be in the form of amorphous hydrous oxides. This can be tailored by controlling the heat treatment conditions which might lead to higher specific capacitance.

Cobalt oxides can also be used as high energy storage materials due to their high specific surface area and high porosity. The epoxide-assisted route enhances these properties where the highest specific capacitance among the cobalt oxides family was reported [142] ($>600\,F\,g^{-1}$) at a high mass loading ($1\,mg\,cm^{-2}$). These aerogels also showed high onset frequencies, excellent reversibility, and cycle stability. These characteristics make cobalt oxide aerogels synthesized via the epoxide-assisted route very promising candidates for supercapacitive applications.

Other metals oxides aerogels have found application in energy domains such as tin oxide aerogels for optic, electronic, and electrochemical applications [29], iron oxide aerogels have a variety of applications including energetic materials [9, 97], magnetic nanostructures [99–102], while thorium and uranium aerogels are used for the production of nuclear fuel materials [109, 110].

5.6 Summary

The aerogels have shown over the years that they are versatile materials that have many applications in different domains. Epoxide-assisted route is a very promising technique for the synthesis of aerogels, xerogels, and nanocomposites, notably metal oxides systems. This is due to the ease of use, simplicity, and rapidity of this technique. This approach consists of using organic epoxides as initiators for the hydrolysis and condensation of hydrated metal species and it is the main component for the formation of bridges leading to the gelation. Moreover, this technique is versatile where the structural characteristics of aerogels can be tailored, depending on the nature of the epoxide, metal salt precursors, and the reaction solvent. Tailoring these properties affects the bulk properties of the final aerogel products leading to a variety of applications for a single type of aerogels. For example, alumina aerogels can be used in catalysis, adsorption, support, and separation as mentioned earlier. In addition, aerogels prepared using the epoxide-assisted route have found applications in energy storage, optics, electronics, and many more. Mixed metal oxide aerogels, organic-inorganic sol-gel composites, as well as nanostructures and microstructures can be synthesized via epoxide-initiated method, giving it an advantage over the traditional sol-gel techniques.

References

1 Kistler, S.S. (1931). Coherent expanded aerogels and jellies. *Nature* 127: 741–741.
2 Cotton, R.T. and Frankenfeld, J.C. (1949). Silica aerogel for protecting stored seed or milled cereal products from insects. *J. Econ. Entomol.* 42: 553–553.

3 Tarshis, I.B. (1964). The use of the silica aerogel insecticides, DRI-DIE 67 and Drione, in new existing structures for the prevention and control of cockroaches. *Lab Anim. Care* 14: 167–184.

4 Nicolaon, G.A. and Teichner, S. (1968). Preparation of silica aerogels from methyl orthosilicate in alcoholic medium, and their properties. *Bull. Soc. Chim. Fr.* 1900: 1906.

5 Fricke, J. and Henning, S. (1986). Largescale production of airglass. In: *Aerogels* (ed. J. Fricke). Berlin: Springer.

6 Tewari, P.H., Hunt, A.J., and Lofftus, K.D. (1985). Ambient-temperature supercritical drying of transparent silica aerogels. *Mater. Lett.* 3: 363–367.

7 G.L.J.G. Biesmans, R. De Vos, Organic Aerogels, U.S. Patent 5,484,818, USA, 1996.

8 Gash, A.E., Tillotson, T.M., Satcher, J.H. Jr. et al. (2001). New sol–gel synthetic route to transition and main-group metal oxide aerogels using inorganic salt precursors. *J. Non-Cryst. Solids* 285: 22–28.

9 Gash, A.E., Tillotson, T.M., Satcher, J.H. et al. (2001). Use of epoxides in the sol–gel synthesis of porous iron(III) oxide monoliths from Fe(III) salts. *Chem. Mater.* 13: 999–1007.

10 Gan, L., Xu, Z., Feng, Y., and Chen, L. (2005). Synthesis of alumina aerogels by ambient drying method and control of their structures. *J. Porous Mater.* 12: 317–321.

11 Baumann, T.F., Gash, A.E., Chinn, S.C. et al. (2005). Synthesis of high-surface-area alumina aerogels without the use of alkoxide precursors. *Chem. Mater.* 17: 395–401.

12 Kesserwan, F., Ahmad, M.N., Khalil, M., and El-Rassy, H. (2020). Hybrid CaO/Al_2O_3 aerogel as heterogeneous catalyst for biodiesel production. *Chem. Eng. J.* 385: 123834.

13 Chaaban, M. and El-Rassy, H. (2020). Nickel–aluminum oxide aerogels: super-adsorbents for azo dyes for water remediation. *ACS Omega* 5: 27401–27412.

14 Chervin, C.N., Clapsaddle, B.J., Chiu, H.W. et al. (2006). A non-alkoxide sol–gel method for the preparation of homogeneous nanocrystalline powders of $La_{0.85}Sr_{0.15}MnO_3$. *Chem. Mater.* 18: 1928–1937.

15 Chervin, C.N., Clapsaddle, B.J., Chiu, H.W. et al. (2005). Aerogel synthesis of yttria-stabilized zirconia by a non-alkoxide sol–gel route. *Chem. Mater.* 17: 3345–3351.

16 Akl, J., Ghaddar, T., Ghanem, A., and El-Rassy, H. (2009). Cobalt ferrite aerogels by epoxide sol–gel addition: efficient catalysts for the hydrolysis of 4-nitrophenyl phosphate. *J. Mol. Catal. A: Chem.* 312: 18–22.

17 Hund, J.F., McElfresh, J., Frederick, C.A. et al. (2007). Fabrication and characterization of aluminum oxide aerogel backlighter targets. *Fusion Sci. Technol.* 51: 701–704.

18 Tokudome, Y., Nakanishi, K., Kanamori, K. et al. (2009). Structural characterization of hierarchically porous alumina aerogel and xerogel monoliths. *J. Colloid Interface Sci.* 338: 506–513.

19 Juhl, S.J., Dunn, N.J.H., Carroll, M.K. et al. (2015). Epoxide-assisted alumina aerogels by rapid supercritical extraction. *J. Non-Cryst. Solids* 426: 141–149.

20 Gash, A.E., Satcher, J.H., and Simpson, R.L. (2004). Monolithic nickel(II)-based aerogels using an organic epoxide: the importance of the counterion. *J. Non-Cryst. Solids* 350: 145–151.

21 Gao, Y.P., Sisk, C.N., and Hope-Weeks, L.J. (2007). A sol–gel route to synthesize monolithic zinc oxide aerogels. *Chem. Mater.* 19: 6007–6011.

22 Gash, A.E., Satcher, J.H., and Simpson, R.L. (2003). Strong akaganeite aerogel monoliths using epoxides: synthesis and characterization. *Chem. Mater.* 15: 3268–3275.

23 Clapsaddle, B.J., Neumann, B., Wittstock, A. et al. (2012). A sol–gel methodology for the preparation of lanthanide-oxide aerogels: preparation and characterization. *J. Sol-Gel Sci. Technol.* 64: 381–389.

24 Baes, C.F. and Mesmer, R.E. (1976). The hydrolysis of cations. In: . New York: John Wiley & Sons.

25 Schimdt, H., Kaiser, A., Rudolph, M., and Lentz, A. (1986). Contribution to the kinetics of glass formation from solutions. In: *Science of Ceramic Chemical Processing* (ed. L.L.H.D.R. Ulrich), 87–93. New York: John Wiley & Sons.

26 Joliver, J.P., Henry, M., and Livage, J. (1994). *De la solution à l'oxyde. Chimie aqueuse des cations métalliques - Synthèse de nanostructures*. Paris: InterEditions/CNRS Editions.

27 Livage, J., Henry, M., and Sanchez, C. (1988). Sol-gel chemistry of transition metal oxides. *Prog. Solid State Chem.* 18: 259–341.

28 Eid, J., Pierre, A.C., and Baret, G. (2005). Preparation and characterization of transparent Eu doped Y_2O_3 aerogel monoliths, for application in luminescence. *J. Non-Cryst. Solids* 351: 218–227.

29 Baumann, T.F., Kucheyev, S.O., Gash, A.E., and Satcher, J.H. Jr. (2005). Facile synthesis of a crystalline, high-surface-area SnO_2 aerogel. *Adv. Mater.* 17: 1546–1548.

30 Gash, A., Pantoya, M., Satcher, J., and Simpson, R. (2008). Nanostructured energetic materials: aerogel thermite composites. *Polym. Prepr. (Am. Chem. Soc., Div. Polym. Chem.)* 49: 558–559.

31 Hund, J.F., Bertino, M.F., Zhang, G. et al. (2004). Synthesis of homogeneous alloy metal nanoparticles in silica aerogels. *J. Non-Cryst. Solids* 350: 9–13.

32 Bertino, M.F., Gadipalli, R.R., Story, J.G. et al. (2004). Laser writing of semiconductor nanoparticles and quantum dots. *Appl. Phys. Lett.* 85: 6007–6009.

33 Pierre, A.C. (2020). *Introduction to Sol-Gel Processing*, 2e. Cham: Springer.

34 Pierre, A.C. and Uhlmann, D.R. (1987). Gelation of aluminum hydroxide sols. *J. Am. Ceram. Soc.* 70: 28–32.

35 Ford, R.W. (1964). *Drying*. London: MacLaren and Sons.

36 Maleki, H. (2016). Recent advances in aerogels for environmental remediation applications: a review. *Chem. Eng. J.* 300: 98–118.

37 Hæreid, S., Nilsen, E., and Einarsrud, M.-A. (1996). Subcritical drying of silica gels. *J. Porous Mater.* 2: 315–324.

38 Tewari, P.H., Hunt, A.J., and Lofftus, K.D. (1986). Advances in production of transparent silica aerogels for window glazings. In: *Aerogels* (ed. J. Fricke), 31–37. Heidelberg: Springer.

39 Wagh, P.B., Begag, R., Pajonk, G.M. et al. (1999). Comparison of some physical properties of silica aerogel monoliths synthesized by different precursors. *Mater. Chem. Phys.* 57: 214–218.

40 Wawrzyniak, P., Rogacki, G., Pruba, J., and Bartczak, Z. (2001). Effective diffusion coefficient in the low temperature process of silica aerogel production. *J. Non-Cryst. Solids* 285: 50–56.

41 Novak, Z., Knez, Z., and Hadolin, M. (1999). Drying of silica aerogel with liquid and supercritical CO_2. *Recent Prog. Génie Proc.* 13.

42 van Bommel, M.J. and de Haan, A.B. (1995). Drying of silica aerogel with supercritical carbon dioxide. *J. Non-Cryst. Solids* 186.

43 Woignier, T., Scherer, G.W., and Alaoui, A. (1994). Stress in aerogel during depressurization of autoclave: II. Silica gels. *J. Sol-Gel Sci. Technol.* 3: 141–150.

44 Scherer, G.W. (1994). Stress in aerogel during depressurization of autoclave: I. Theory. *J. Sol-Gel Sci. Technol.* 3: 127–139.

45 Lee, K.P., Begag, R., Altiparmakov, Z. (2003). Rapid Aerogel Production Process, U.S. Patent 6,670,402, Aspen Aerogels Inc., USA.

46 Pierre, A.C. and Rigacci, A. (2011). SiO_2 aerogels. In: *Aerogels Handbook* (ed. M.A. Aegerter, N. Leventis, and M.M. Koebel), 21–45. New York: Springer.

47 Pajonk, G.M. (1994). A short history of the preparation of aerogels and carbogels. In: *Sol-Gel Processing and Applications* (ed. Y.J. Attia), 201–209. New York: Plenum Press.

48 Fricke, J. (1988). Aerogels – highly tenuous solids with fascinating properties. *J. Non-Cryst. Solids* 100: 169–173.

49 Sharp, K.G. (1994). A two-component, non-aqueous route to silica gel. *J. Sol-Gel Sci. Technol.* 2: 35–41.

50 Loy, D.A., Russick, E.M., Yamanaka, S.A. et al. (1997). Direct formation of aerogels by sol–gel polymerizations of alkoxysilanes in supercritical carbon dioxide. *Chem. Mater.* 9: 2264–2268.

51 Moner-Girona, M., Roig, A., Molins, E., and Llibre, J. (2003). Sol-gel route to direct formation of silica aerogel microparticles using supercritical solvents. *J. Sol-Gel Sci. Technol.* 26: 645–649.

52 Roth, T.B., Anderson, A.M., and Carroll, M.K. (2008). Analysis of a rapid supercritical extraction aerogel fabrication process: prediction of thermodynamic conditions during processing. *J. Non-Cryst. Solids* 354: 3685–3693.

53 Gauthier, B.M., Bakrania, S.D., Anderson, A.M., and Carroll, M.K. (2004). A fast supercritical extraction technique for aerogel fabrication. *J. Non-Cryst. Solids* 350: 238–243.

54 Scherer, G.W., Gross, J., Hrubesh, L.W., and Coronado, P.R. (2002). Optimization of the rapid supercritical extraction process for aerogels. *J. Non-Cryst. Solids* 311: 259–272.

55 Gross, J., Coronado, P.R., and Hrubesh, L.W. (1998). Elastic properties of silica aerogels from a new rapid supercritical extraction process. *J. Non-Cryst. Solids* 225: 282–286.

56 Poco, J.F., Coronado, P.R., Pekala, R.W., and Hrubesh, L.W. (1996). A rapid supercritical extraction process for the production of silica aerogels. *MRS Proc.* 431: 297.

57 Teichner, S.J., Nicolaon, G.A., Vicarini, M.A., and Gardes, G.E.E. (1976). Inorganic oxide aerogels. *Adv. Colloid Interface Sci.* 5: 245–273.

58 Woignier, T., Phalippou, J., and Zarzycki, J. (1984). Monolithic aerogels in the systems SiO_2-B_2O_3, SiO_2-P_2O_5, SiO_2-B_2O_3-P_2O_5. *J. Non-Cryst. Solids* 63: 117–130.

59 Adachi, I., Tabata, M., Kawai, H., and Sumiyoshi, T. (2011). Study of transparent silica aerogel with high refractive index. *Nucl. Instrum. Methods Phys. Res., Sect. A* 639: 222–224.

60 Tabata, M., Adachi, I., Ishii, Y. et al. (2010). Development of transparent silica aerogel over a wide range of densities. *Nucl. Instrum. Methods Phys. Res., Sect. A* 623: 339–341.

61 Zuo, L., Zhang, Y., Zhang, L. et al. (2015). Polymer/carbon-based hybrid aerogels: preparation, properties and applications. *Dent. Mater.* 8.

62 Pajonk, G.M., Repellin-Lacroix, M., Abouarnadasse, S. et al. (1990). From sol-gel to aerogels and cryogels. *J. Non-Cryst. Solids* 121: 66–67.

63 Kocklenberg, R., Mathieu, B., Blacher, S. et al. (1998). Texture control of freeze-dried resorcinol–formaldehyde gels. *J. Non-Cryst. Solids* 225: 8–13.

64 Egeber, E.D. and Engel, J. (1989). Freeze-drying of silica gels prepared from siliciumethoxide. *Rev. Phys. Appl.* 24: 23–28.

65 Shlyakhtin, O.A. and Tretyakov, Y.D. (1999). Recent progress in cryochemical synthesis of oxide materials. *J. Mater. Chem.* 9.

66 Wicklein, B., Kocjan, D., Carosio, F. et al. (2016). Tuning the nanocellulose–borate interaction to achieve highly flame retardant hybrid materials. *Chem. Mater.* 28: 1985–1989.

67 Chen, H.-B., Hollinger, E., Wang, Y.-Z., and Schiraldi, D.A. (2014). Facile fabrication of poly(vinyl alcohol) gels and derivative aerogels. *Polymer* 55: 380–384.

68 Chen, H.-B., Liu, B., Huang, W. et al. (2014). Fabrication and properties of irradiation-cross-linked poly(vinyl alcohol)/clay aerogel composites. *ACS Appl. Mater. Interfaces* 6: 16227–16236.

69 Chen, H.-B., Chiou, B.-S., Wang, Y.-Z., and Schiraldi, D.A. (2013). Biodegradable pectin/clay aerogels. *ACS Appl. Mater. Interfaces* 5: 1715–1721.

70 Land, V.D., Harris, T.M., and Teeters, D.C. (2001). Processing of low-density silica gel by critical point drying or ambient pressure drying. *J. Non-Cryst. Solids* 283: 11–17.

71 Prakash, S.S., Brinker, C.J., and Hurd, A.J. (1995). Silica aerogel films at ambient pressure. *J. Non-Cryst. Solids* 190: 264–275.

72 Prakash, S.S., Brinker, C.J., Hurd, A.J., and Rao, S.M. (1995). Silica aerogel films prepared at ambient pressure by using surface derivatization to induce reversible drying shrinkage. *Nature* 374: 439–443.

73 Schwan, M. and Ratke, L. (2013). Flexibilisation of resorcinol–formaldehyde aerogels. *J. Mater. Chem. A* 1: 13462–13468.

74 Durães, L., Matias, T., Patrício, R., and Portugal, A. (2013). Silica based aerogel-like materials obtained by quick microwave drying. *Materialwiss. Werkstofftech.* 44: 380–385.

75 Leventis, N., Palczer, A., McCorkle, L. et al. (2005). Nanoengineered silica-polymer composite aerogels with no need for supercritical fluid drying. *J. Sol-Gel Sci. Technol.* 35: 99–105.

76 Maleki, H., Durães, L., and Portugal, A. (2015). Development of mechanically strong ambient pressure dried silica aerogels with optimized properties. *J. Phys. Chem. C* 119: 7689–7703.

77 Bangi, U.K.H., Parvathy Rao, A., Hirashima, H., and Venkateswara Rao, A. (2009). Physico-chemical properties of ambiently dried sodium silicate based aerogels catalyzed with various acids. *J. Sol-Gel Sci. Technol.* 50: 87–97.

78 Martin, J., Hosticka, B., Lattimer, C., and Norris, P.M. (2001). Mechanical and acoustical properties as a function of PEG concentration in macroporous silica gels. *J. Non-Cryst. Solids* 285: 222–229.

79 Rao, A.V. and Kulkarni, M.M. (2003). Effect of glycerol additive on physical properties of hydrophobic silica aerogels. *Mater. Chem. Phys.* 77: 819–825.

80 Pierre, M., Buisson, P., Fache, F., and Pierre, A. (2000). Influence of the drying technique of silica gels on the enzymatic activity of encapsulated lipase. *Biocatal. Biotransform.* 18: 237–251.

81 Nakanishi, K., Minakuchi, H., Soga, N., and Tanaka, N. (1998). Structure design of double-pore silica and its application to HPLC. *J. Sol-Gel Sci. Technol.* 13: 163–169.

82 Anderson, M.T., Sawyer, P.S., and Rieker, T. (1998). Surfactant-templated silica aerogels. *Micropor. Mesopor. Mater.* 20: 53–65.

83 Reetz, M.T., Zonta, A., and Simpelkamp, J. (1996). Efficient immobilization of lipases by entrapment in hydrophobic sol-gel materials. *Biotechnol. Bioeng.* 49: 527–534.

84 Zarzycki, J., Prassas, M., and Phalippou, J. (1982). Synthesis of glasses from gels: the problem of monolithic gels. *J. Mater. Sci.* 17: 3371–3379.

85 Hench, L.L. (1986). Use of dying control chemical additives (DCCAs) in controlling sol-gel processing. In: *Science of Ceramic Chemical Processing* (ed. L.L. Hench). New York: John Wiley & Sons.

86 Parvathy, A., Pajonk, G.M., and Rao, A.V. (2005). Effect of preparation conditions on the physical and hydrophobic properties of two step processed ambient pressure dried silica aerogels. *J. Mater. Sci.* 40.

87 Deshpande, R., Hua, D.-W., Smith, D.M., and Brinker, C.J. (1992). Pore structure evolution in silica gel during aging/drying. III. Effects of surface tension. *J. Non-Cryst. Solids* 144: 32–44.

88 Venkateswara Rao, A., Parvathy Rao, A., and Kulkarni, M.M. (2004). Influence of gel aging and Na_2SiO_3/H_2O molar ratio on monolithicity and physical properties of water–glass-based aerogels dried at atmospheric pressure. *J. Non-Cryst. Solids* 350: 224–229.

89 Schwertfeger, F., Frank, D., and Schmidt, M. (1998). Hydrophobic waterglass based aerogels without solvent exchange or supercritical drying. *J. Non-Cryst. Solids* 225: 24–29.

90 Chen, L., Zhu, J., Liu, Y.-M. et al. (2006). Photocatalytic activity of epoxide sol–gel derived titania transformed into nanocrystalline aerogel powders by supercritical drying. *J. Mol. Catal. A: Chem.* 255: 260–268.

91 Wei, W., Xie, J., Wu, Y. et al. (2013). UV-resistant hydrophobic rutile titania aerogels synthesized through a nonalkoxide ambient pressure drying process. *J. Mater. Res.* 28: 378–384.

92 Fears, T.M., Sotiriou-Leventis, C., Winiarz, J.G., and Leventis, N. (2016). Economical synthesis of vanadia aerogels via epoxide-assisted gelation of $VOCl_3$. *J. Sol-Gel Sci. Technol.* 77: 244–256.

93 Zhong, L., Chen, X., Song, H. et al. (2014). Synthesis of monolithic zirconia aerogel via a nitric acid assisted epoxide addition method. *RSC Adv.* 4: 31666–31671.

94 Li, X., Jiao, Y., Ji, H., and Sun, X. (2013). The effect of propylene oxide on microstructure of zirconia monolithic aerogel. *Integr. Ferroelectr.* 146: 122–126.

95 Esquivel-Castro, T.A., Martínez-Luévanos, A., García-Cerda, L.A. et al. (2019). Effect of the drying on morphology and texture of aerogels and zirconia cryogels. *MRS Adv.* 4: 3513–3521.

96 Baumann, T.F., Gash, A.E., and Satcher, J.H. Jr. (2011). A robust approach to inorganic aerogels: the use of epoxides in sol–gel synthesis. In: *Aerogels Handbook* (ed. M.A. Aegerter, N. Leventis, and M.M. Koebe). Springer.

97 Prakash, A., McCormick, A.V., and Zachariah, M.R. (2004). Aero-sol−gel synthesis of nanoporous iron-oxide particles: a potential oxidizer for nanoenergetic materials. *Chem. Mater.* 16: 1466–1471.

98 Tillotson, T.M., Gash, A.E., Simpson, R.L. et al. (2001). Nanostructured energetic materials using sol–gel methodologies. *J. Non-Cryst. Solids* 285: 338–345.

99 Long, J.W., Logan, M.S., Rhodes, C.P. et al. (2004). Nanocrystalline iron oxide aerogels as mesoporous magnetic architectures. *J. Am. Chem. Soc.* 126: 16879–16889.

100 Park, C.-D., Magana, D., and Stiegman, A.E. (2007). High-quality Fe and γ-Fe_2O_3 magnetic thin films from an epoxide-catalyzed sol−gel process. *Chem. Mater.* 19: 677–683.

101 Carpenter, E.E., Long, J.W., Rolison, D.R. et al. (2006). Magnetic and Mössbauer spectroscopy studies of nanocrystalline iron oxide aerogels. *J. Appl. Phys.* 99: 08N711.

102 Cui, H. and Ren, W. (2008). Low temperature and size controlled synthesis of monodispersed γ-Fe_2O_3 nanoparticles by an epoxide assisted sol–gel route. *J. Sol-Gel Sci. Technol.* 47: 81–84.

103 Bali, S., Turpin, G.C., Ernst, R.D. et al. (2008). Water gas shift catalysis using iron aerogels doped with palladium by the gas-phase incorporation method. *Energy Fuels* 22: 1439–1443.

104 Bali, S., Huggins, F.E., Huffman, G.P. et al. (2009). Iron aerogel and Xerogel catalysts for Fischer–Tropsch synthesis of diesel fuel. *Energy Fuels* 23: 14–18.

105 Suh, D.J., Park, T.-J., Kim, W.-I., and Hong, I.-K. (2003). Synthesis of high-surface-area ruthenium oxide aerogels by non-alkoxide sol–gel route. *J. Power Sources* 117: 1–6.

106 Laberty-Robert, C., Long, J.W., Lucas, E.M. et al. (2006). Sol−gel-derived ceria nanoarchitectures: synthesis, characterization, and electrical properties. *Chem. Mater.* 18: 50–58.

107 Tillotson, T.M., Sunderland, W.E., Thomas, I.M., and Hrubesh, L.W. (1994). Synthesis of lanthanide and lanthanide-silicate aerogels. *J. Sol-Gel Sci. Technol.* 1: 241–249.

108 Zhang, H.D., Li, B., Zheng, Q.X. et al. (2008). Synthesis and characterization of monolithic Gd_2O_3 aerogels. *J. Non-Cryst. Solids* 354: 4089–4093.

109 Reibold, R.A., Poco, J.F., Baumann, T.F. et al. (2003). Synthesis and characterization of a low-density urania (UO_3) aerogel. *J. Non-Cryst. Solids* 319: 241–246.

110 Reibold, R.A., Poco, J.F., Baumann, T.F. et al. (2004). Synthesis and characterization of a nanocrystalline thoria aerogel. *J. Non-Cryst. Solids* 341: 35–39.

111 Bhosale, R.R. (2018). Synthesis and characterization of nanocrystalline $CoFe_2O_4$-zirconia via propylene oxide aided sol-gel method. *Ceram. Int.* 44: 8679–8683.

112 Chervin, C.N., Clapsaddle, B.J., Chiu, H.W. et al. (2006). Role of cyclic ether and solvent in a non-alkoxide sol−gel synthesis of yttria-stabilized zirconia nanoparticles. *Chem. Mater.* 18: 4865–4874.

113 Brown, P. and Hope-Weeks, L.J. (2009). The synthesis and characterization of zinc ferrite aerogels prepared by epoxide addition. *J. Sol-Gel Sci. Technol.* 51: 238–243.

114 Cui, H., Zayat, M., and Levy, D. (2005). Sol-gel synthesis of nanoscaled Spinels using propylene oxide as a gelation agent. *J. Sol-Gel Sci. Technol.* 35: 175–181.

115 Allaf, R.M. and Hope-Weeks, L.J. (2014). Synthesis of ZnO-CuO nanocomposite aerogels by the sol-gel route. *J. Nanomater.* 2014: 491817.

116 Guo, Y., Meyer-Zaika, W., Muhler, M. et al. (2006). Cu/Zn/Al xerogels and aerogels prepared by a sol–gel reaction as catalysts for methanol synthesis. *Eur. J. Inorg. Chem.* 2006: 4774–4781.

117 Clapsaddle, B.J., Gash, A.E., Satcher, J.H., and Simpson, R.L. (2003). Silicon oxide in an iron(III) oxide matrix: the sol–gel synthesis and characterization of Fe–Si mixed oxide nanocomposites that contain iron oxide as the major phase. *J. Non-Cryst. Solids* 331: 190–201.

118 Clapsaddle, B.J., Sprehn, D.W., Gash, A.E. et al. (2004). A versatile sol–gel synthesis route to metal–silicon mixed oxide nanocomposites that contain metal oxides as the major phase. *J. Non-Cryst. Solids* 350: 173–181.

119 Zhao, L., Clapsaddle, B.J., Satcher, J.H. et al. (2005). Integrated chemical systems: the simultaneous formation of hybrid nanocomposites of iron oxide and organo silsesquioxanes. *Chem. Mater.* 17: 1358–1366.

120 Shao, X., Lu, W., Zhang, R., and Pan, F. (2013). Enhanced photocatalytic activity of TiO_2-C hybrid aerogels for methylene blue degradation. *Sci. Rep.* 3: 3018.

121 Zhou, B., Zhang, R., Guo, Q.-g. et al. (2011). Preparation of low density and high mesoporosity carbon aerogels by an organic/inorganic hybrid method. *Carbon* 49: 3706.

122 Anasori, B., Beidaghi, M., and Gogotsi, Y. (2014). Hybrid structures for energy storage. *Mater. Today* 17.

123 Zhang, R., Jiang, N., Duan, X.-j. et al. (2017). Synthesis and characterization of Al_2O_3-C hybrid aerogels by a one-pot sol-gel method. *New Carbon Mater.* 32: 258–264.

124 Cui, S., Suo, H., Jing, F. et al. (2018). Facile preparation of ZrCO composite aerogel with high specific surface area and low thermal conductivity. *J. Sol-Gel Sci. Technol.* 86: 383–390.

125 Zhu, Y., Jiang, Z., Zhang, L. et al. (2012). Sol–gel derived boehmite as an efficient and robust carrier for enzyme encapsulation. *Ind. Eng. Chem. Res.* 51: 255–261.

126 Corrias, A., Casula, M.F., Falqui, A., and Paschina, G. (2004). Evolution of the structure and magnetic properties of FeCo nanoparticles in an alumina aerogel matrix. *Chem. Mater.* 16: 3130–3138.

127 Inoue, M., Kimura, M., and Inui, T. (2000). Alkoxyalumoxanes. *Chem. Mater.* 12: 55–61.

128 Keysar, S., Shter, G.E., de Hazan, Y. et al. (1997). Heat treatment of alumina aerogels. *Chem. Mater.* 9: 2464–2467.

129 Paglia, G. (2004). *Determination of the Structure of γ-Alumina Using Empirical and First Principles Calculations Combined with Supporting Experiments*. Australia: Department of Applied Physics and Department of Applied Chemistry, Curtin University of Technology.

130 Wefers, K. and Misra, C. (1987). Oxides and hydroxides of aluminum. In: (ed. A. Laboratories).

131 Chiang, Y.-C., Cheng, W.-Y., and Lu, S.-Y. (2012). Titania aerogels as a superior mesoporous structure for photoanodes of dye-sensitized solar cells. *Int. J. Electrochem. Sci.* 7: 6910–6919.

132 Luo, H., Churu, G., Fabrizio, E.F. et al. (2008). Synthesis and characterization of the physical, chemical and mechanical properties of isocyanate-crosslinked vanadia aerogels. *J. Sol-Gel Sci. Technol.* 48: 113–134.

133 Leventis, N., Sotiriou-Leventis, C., Mulik, S. et al. (2008). Polymer nanoencapsulated mesoporous vanadia with unusual ductility at cryogenic temperatures. *J. Mater. Chem.* 18: 2475–2482.

134 Dickie, S.A. and McQuillan, A.J. (2004). In-situ infrared spectroscopic studies of adsorption processes on boehmite particle films: exchange of surface hydroxyl groups observed upon chelation by acetylacetone. *Langmuir* 20: 11630–11636.

135 Fripiat, J.J., Bosmans, H.J., and Rouxhet, P.G. (1967). Proton mobility in solids. I. Hydrogenic vibration modes and proton delocalization in boehmite. *J. Phys. Chem.* 71: 1097–1111.

136 Tarte, P. (1967). Infra-red spectra of inorganic aluminates and characteristic vibrational frequencies of AlO_4 tetrahedra and AlO_6 octahedra. *Spectrochim. Acta Part A: Mol. Spectrosc.* 23: 2127–2143.

137 Zhu, Z., Tsung, L.Y., and Tomkiewicz, M. (1995). Morphology of TiO_2 aerogels. 1. Electron microscopy. *J. Phys. Chem.* 99: 15945–15949.

138 Kolen'ko, Y.V., Garshev, A.V., Churagulov, B.R. et al. (2005). Photocatalytic activity of sol–gel derived titania converted into nanocrystalline powders by supercritical drying. *J. Photochem. Photobiol., A* 172: 19–26.

139 Gorban, O., Synyakina, S., Volkova, G. et al. (2015). Formation of metastable tetragonal zirconia nanoparticles: competitive influence of the dopants and surface state. *J. Solid State Chem.* 232: 249–255.

140 Poco, J.F., Satcher, J.H., and Hrubesh, L.W. (2001). Synthesis of high porosity, monolithic alumina aerogels. *J. Non-Cryst. Solids* 285: 57–63.

141 Benad, A., Jürries, F., Vetter, B. et al. (2018). Mechanical properties of metal oxide aerogels. *Chem. Mater.* 30: 145–152.

142 Wei, T.-Y., Chen, C.-H., Chang, K.-H. et al. (2009). Cobalt oxide aerogels of ideal supercapacitive properties prepared with an epoxide synthetic route. *Chem. Mater.* 21: 3228–3233.

6

CNT-Based Aerogels and Their Applications

Zili Li[1,2] *and Zhiqun Lin*[2]

[1] *School of Information Science and Technology, Fudan University, Shanghai, 200433, China*
[2] *School of Materials Science and Engineering, Georgia Institute of Technology, Atlanta, GA, 30332, USA*

6.1 Introduction

Aerogels are intriguing microporous materials that have been widely used in an array of practical applications such as biological fields [1], catalytic supports [2], energy storage and conversion [3], and separation [4] due to their high porosity, controlled pore size and distribution, large surface area, ultra-low density, and tunable surface functionalities. Aerogels can maintain three-dimensional (3D) and highly porous network structures without shape shrinkage. In addition, 90–99% of the entire volume of the porous structure is occupied by gas in the synthetic aerogels [5]. These unique characteristics render aerogels with particular performances. However, the pores, unfortunately, introduce internal resistance, the conductivity of resulting aerogels is relatively low. Furthermore, most of the skeletons of the 3D structure are connected by crosslinked organic molecules, thereby the aerogels have weak mechanical performances. Both these drawbacks limit their potential applications. Therefore, the development of aerogels with high mechanical strength and controllable electrical conductivity is highly desired.

Carbon nanotubes (CNTs) are the most studied carbon materials in the past decades, CNTs possess exceptional mechanical strength (e.g. tensile strength 10–500 GPa and elastic modulus 0.3–1 TPa), thermal conductivity ($3500\,W\,m^{-1}\,K^{-1}$), and electronic properties (e.g. electron mobility [$100\,000\,cm^2\,V^{-1}\,s^{-1}$] and electrical conductivity [$10^4\,S\,cm^{-1}$]) because of their one-dimensional (1D) cylindrical shapes consisting of rapped single or multilayer graphene sheets [6, 7]. The nested structure of tubes inside tubes (i.e. multiwalled nanotubes, MWNTs) has a significant influence on determining their mechanical properties [8]. Thereby, CNTs have been touted as ideal reinforcements in composite materials due to their excellent mechanical properties and high aspect ratio that leads to anisotropic geometry. Incorporation of CNTs into polymeric materials has been extensively explored and the resulting composites exhibit significantly improved properties (e.g. electrical and thermal conductive properties as well as mechanical performances) [9, 10].

In this context, CNT-based aerogels can inherit the characteristics of their constituent parts (i.e. CNT and aerogels). Generally, CNT-based aerogels are fabricated through direct chemical vapor deposition (CVD) and wet gel followed by drying methods. CNT-based aerogels have 3D network structures connected with polymers or CNTs, in which their microporous structural

Aerogels for Energy Saving and Storage, First Edition. Edited by Meldin Mathew, Hanna J. Maria, Ange Nzihou, and Sabu Thomas.
© 2024 John Wiley & Sons, Inc. Published 2024 by John Wiley & Sons, Inc.

properties are related to the intra-particle framework, controlling the specific surface areas. In addition, the conductivity of the CNT-based aerogels can promote electron transfer in the network, making them preferable for energy saving and storage. Furthermore, they have high chemical and mechanical stability, thus enabling long-term stability in applications. Herein we summarize the recent progress on CNT-based aerogels and their applications in energy saving and storage. In the first section, fundamental principles to fabricate CNT-based aerogels are briefly introduced. The second section focuses on the strategies toward CNT-based aerogels with different compositions and structures. Then the applications of CNT-based aerogels in energy saving and storage are presented in the third section. After the summary, an outlook for the prospective studies on CNT-based aerogels is presented to conclude the chapter.

6.2 The Fundamental Principle of Preparing CNT-based Aerogels

To construct 3D networks in CNT-based aerogels, two strategies have been adopted, i.e. direct growth by CVD or wet chemistry methods. CVD method can fabricate mechanically flexible and highly conductive CNT aerogels containing high-quality and long individual CNTs at elevated temperatures [11]. The wet chemistry method is based on sol-gel processing consisting of three main steps [12]:

1) *Solution-sol transition*. CNTs disperse in solution to form a colloidal suspension (either "macrodispersions" of CNT bundles or "nanodispersions" of individual CNTs) in which the amount of CNTs is low. When the interactions among the CNTs are sufficient, they form the sol phase.
2) *Sol-gel transition*. In this step, gelation occurs via physical or chemical crosslinking, in which the free dispersed sol is converted into a 3D network filled with solvent.
3) *Gel-aerogel transition*. The crosslinked monolith is dried via supercritical drying or freeze-drying to remove the solvent within the gel without causing damage to the microstructure.

The microstructures of the aerogels are highly dependent on the processing conditions during the fabrication. Therefore, the microstructures of aerogels are different in each batch. The phase transition from the wet gels to the dry gels can be achieved via three different strategies (i.e. supercritical-drying, freeze-drying, and vacuum-drying), as shown in Figure 6.1. Only supercritical-drying or freeze-drying techniques can circumambulate the liquid-gas phase line of the solvent to maintain the integrality of the 3D network structures, yielding aerogels without large shrinkage [11]. Whereas the vacuum-drying will cause severe structural shrinkage, thus limits its application in the preparation of aerogels [13]. It is worth noting that the wet chemistry approach can be operated under mild conditions compared with CVD methods. It is favorable to prepare aerogels with a large scale and high controllability.

Freeze drying is the most commonly used method to dry wet hydrogels [14], in which the frozen solvent sublimes directly from the host to form a gas phase under vacuum and removes. The freezing rate and precursor concentration play a crucial role in controlling the porous structure. Rapid freezing induces small ice crystals, which will generate small pores and a large specific surface area. High precursor concentration suppresses the growth of ice crystals, leading to low pore structure [13]. Supercritical drying is a process that the liquid in a substance transforms into gas in the absence of surface tension and capillary stress in the supercritical state, in which the liquid and vapor phases are indistinguishable. This technique can produce a highly porous and uniform microstructure. Nonetheless, this process is complicated, time-consuming, and chemical-wasting compared with other methods [15].

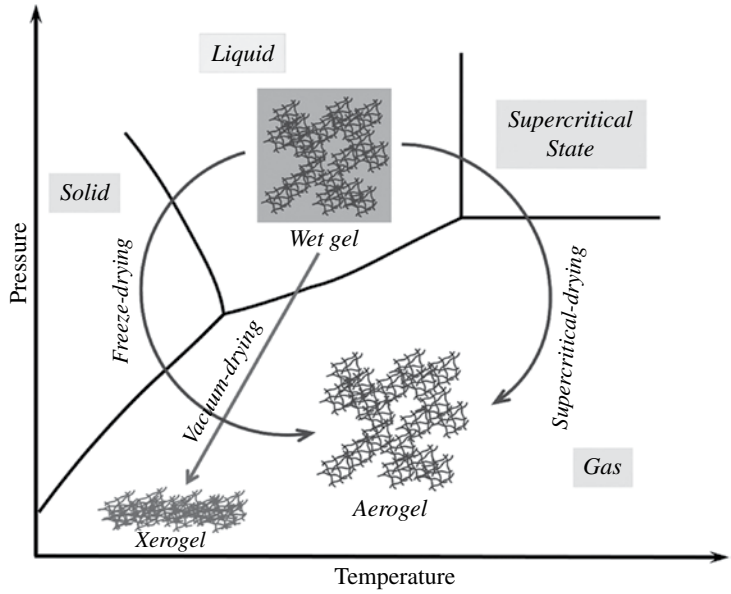


Figure 6.1 The phase transition from wet gels to dry gels via various strategies [11]. *Source:* Copyright 2015. Reproduced with permission from the Royal Society of Chemistry.

6.3 Strategies for Preparation of CNT-based Aerogels

6.3.1 Preparation of CNT-based Aerogels via CVD

CVD techniques are frequently used for CNT preparation, and they have also been exploited to fabricate macroscopic 3D sponges due to their tunable precursors and repeated growth [16, 17]. During the CVD process, the carbon sources will be decomposed on the substrate surfaces (e.g. solid silicon wafer or metal foam) at elevated temperature, and CNT will grow from the substrate; thus, vertically aligned CNT arrays or isotropic CNT sponges can be easily obtained based on the catalyst's formation and reaction conditions (Figure 6.2). However, this method suffers from high temperature, high cost, and difficulty in removing catalysts after the preparation process [18].

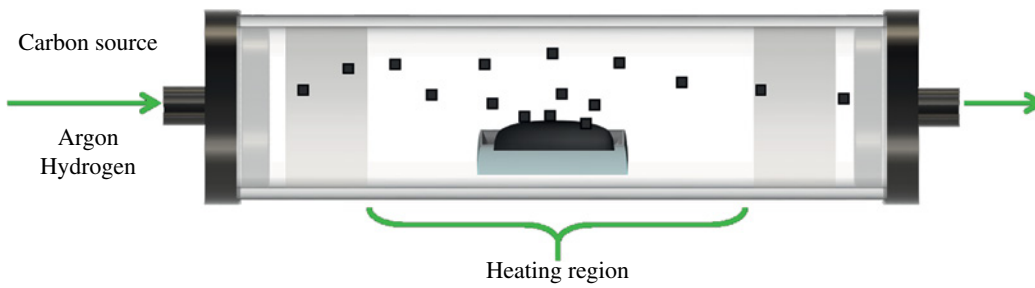


Figure 6.2 3D CNT aerogels prepared by the CVD method.

6.3.1.1 Isotropic CNT Aerogels

3D isotropic CNT aerogels are produced via the floating catalytic chemical vapor deposition (FCCVD) method followed by deposition on a substrate. Generally, an ethanol solution of ferrocene and thiophene was injected into the furnace with a mixture of argon and hydrogen as carrier gases, in which ethanol was used as carbon source, ferrocene was used as catalyst, and thiophene was used as promoter [19]. Thereafter, CNT sponges with a porosity of >99% are prepared via the CVD method using dichlorobenzene as the carbon source, which can disturb the alignment of CNTs growth and form randomly interconnected porous structures [20]. The CNT sponges can be considered as consecutive stacking and penetration of numerous CNT "piles" into high-porosity materials with a thickness of up to 1 cm. The CNT aerogels exhibit excellent structural flexibility, resist structural fatigue under cyclic stress conditions, and have high oil absorption capacity [20]. It has been reported that the ratios of C/Fe/S and the choice of carbon sources (e.g. oxygen-containing alcohol, oxygen-free aromatic carbon, and saturated hydrocarbon) play a significant role in controlling aerogel purity [21]. In addition, bulk CNT aerogel formation occurs near the exit of the reactor, no matter what kind of carbon sources (e.g. CH_4, toluene, or ethanol) [21, 22]. Furthermore, heteroatoms (e.g. N, B, P, and S atoms) have been introduced into CNTs via CVD techniques, thereby, nitrogen-doped CNT-based carbon sponges were synthesized via CVD by incorporating external benzylamine in the common recipe [23].

6.3.1.2 3D Vertical CNT Arrays

Well-established vertically aligned CNTs grown from substrate have been achieved by flowing carbon sources over the catalysts film on a substrate [24, 25]. Vertically aligned CNT arrays grown on Si substrate have been produced via CVD with ferrocene and xylene as the precursors. The peeled CNT films exhibited foam-like structures with a porosity of 87% [26]. However, CNT aerogels were generally grown on nonconducting substrates [17], and multistage processes or post-growth metallization techniques were required to transfer CNT arrays to metal substrates. Direct growth of aligned CNT on Inconel was achieved via CVD with Inconel as both catalyst and substrate [27]. These previously reported methods could not completely control the alignment of CNTs; that is, CNT arrays are aligned or nonaligned. Thereafter, intense efforts have been conducted to fabricate the controllable alignment of CNT arrays via post-treatment methods such as dispersion [28] and mechanical densification [29]. Nonetheless, owing to the strong van der Waals interaction among the long CNTs, they are easy to aggregate and entangle to form nonalignment. Hata and coworkers used Si substrates coated with a thin metal layer of Al_2O_3 (~40 nm)/Fe (~1.6 nm) to grow ideally aligned CNT arrays via water assist, and their alignment could be readily tailored by tuning the density of active catalysts at the catalyst formation stage [24]. With high CNT density, the lateral confinement (i.e. crowding effect) increases, thereby the CNTs could primarily grow in the vertical direction. Herman's Orientation Factor (HOF) is applied to describe the alignment and the catalyst spacing significantly affects the HOF [24].

6.3.1.3 Template-assisted CNT-based Aerogels

The porosity of CNT aerogels is also an important characteristic for their applications. It is difficult to control the porous size and distribution via general CVD techniques. Preparation of 3D CNT aerogels with porous templates can be an alternative and effective method, in which the porous characteristics are pre-made and dominated by the templates. In addition, the 3D interconnect skeleton can suppress the aggregation of CNTs during growth. Notably, the templates can be readily removed after preparation, yielding freestanding 3D porous CNT aerogels. Moreover, the unique

preparation process, size, morphology, and properties of the templates significantly affect the performances of the obtained aerogels [30].

3D hybrid graphene-CNT aerogels have been reported via a two-step CVD technique with nickel foam as the growth substrate. First, the 3D graphene network was grown on nickel foam via CVD techniques, but the surfaces of the porous do not exhibit superhydrophobic. Second, the dense CNT mesh grows coaxially and uniformly on graphene skeletons. Therefore, the resulting CNT-based aerogels are superhydrophobic and superoleophilic [31]. Thereafter, a one-step ambient pressure chemical vapor deposition (APCVD) process was employed to prepare 3D high-quality CNT/graphene aerogels with arbitrary thickness. The intermediate graphene layer can serve as the low-resistance interface to facilitate an electrical connection between the CNT and the nickel foam framework [32]. However, all the reports are based on nickel foam templates to prepare aerogels. This severely limits the potential applications. Furthermore, pure CNTs are rarely used to grow on the template because of the relatively weak π-π stacking between CNTs, which may break the structural integrity during removing the template [11]. Recently, Magnetospirillum magneticum (AMB-1) bacteria were used as a bio-template to fabricate a hierarchical 3D-CNT structure with interconnected porosity [33]. This can broaden the scope of templates used for the preparation of CNT-based aerogels with CVD techniques.

6.3.2 Surface-modified CNT-based Aerogels

CNTs are hydrophobic nanomaterials, and they are easy to form bundles that consist of many single nanotubes. The bundles intertwine, thus making them have poor dispersibility in both organic solvents and aqueous solutions. Sometimes, sonication is employed to facilitate the solubility in some solvents. However, the stability of the dispersion is poor and they will aggregate and precipitate from the solvent when external mechanical force is interrupted [34]. Therefore, surface modifications of CNTs are highly desired to improve their solubility. The main approaches to modify CNTs can be categorized into covalent chemical and noncovalent physical modifications. The former approach is based on the covalent interaction of functional groups on the conjugated skeleton of CNTs [35–37], while the latter is achieved via adsorption or wrapping with functional molecules [38, 39]. With the surface modification of CNTs, it is possible to obtain homogeneous CNT-based wet gels, which can be used for the preparation of CNT-based aerogels.

6.3.2.1 Preparation of Aerogels with Noncovalent Modified CNTs

Noncovalent modification of CNTs is particularly attractive due to the decoration without damaging their intrinsic characteristics. Surfactants (e.g. small molecules and polymers) have amphiphilic characteristics, which have been widely used to help CNTs disperse in the aqueous solution. During the assembly process, the hydrophobic end will assemble around the CNTs and the hydrophilic charged end will locate outside toward the aqueous phase [38]. When the concentration above the critical micelle concentration (CMC), the surfactant will form a gel phase because of the van der Waals interactions among the dispersed CNTs that act as crosslinking points [40]. For instance, sodium dodecylbenzene sulfonate (SDBS) was used to stabilize CNTs and the mixture exhibited gel-like behavior at a volume fraction of 0.26% [41]. Thereafter, freestanding aerogels can be created by using SDBS-assisted hydrogels and sequential removal of solvent. In addition, the surfactants can be readily washed away with acid without inducing significant shrinkage of hydrogels [42, 43]. The lightweight aerogels exhibit a large specific surface area and high porosity, resulting in high mechanical strength and enhanced heat transfer. It should be noted that the pore of the

aerogels can be tuned by the mass density of CNTs [42]. An alternative method to control the porous structure of aerogels is bubbling during the freezing step. Sodium dodecyl sulphate (SDS) is another ionic surfactant that is used to stabilize CNTs to obtain homogeneous dispersion, sometimes van der Waals attractions are inefficient to form a gel phase and a second co-surfactant is applied [44]. Except for the commonly used surfactants, other molecules such as carboxymethyl cellulose (CMC) sodium [45], Tergitol [44], dextrose and citric acid [46], cellulose [47], polyvinyl alcohol (PVA) [48, 49], and synthetic polymers [50, 51] are used to stabilize CNTs. Polymer surfactants have abundant functional groups in one polymer chain, thus they can serve as multifunctional crosslinkers to enhance the mechanical performances of the aerogels. For instance, ferrocene-grafted poly(p-phenyleneethynylene) (Fc-PPE) was used as a gelator to functionalize CNTs to form a 3D nanotube network in organic solvents, in which ferrocenyl moieties show strong noncovalent interaction with the CNT surfaces, acting as anchoring points. After CO_2 supercritical drying of the wet gel, aerogels with excellent electrical conductivity and high mechanical strength were developed [50].

6.3.2.2 Preparation of Aerogels with Covalent Modified CNTs

As mentioned, CNTs are hydrophobic nanomaterials, it is impossible to prepare CNT aerogels without surfactants. Generally, CNTs are treated with an oxidizing medium (i.e. sulfuric acid/potassium permanganate) to enhance the dispersibility in aqueous solutions [52]. The surface functional groups not only increase the hydrophilicity of CNTs but also act as crosslinking moieties because of the hydrogen bonding among them. The acid-treated CNTs could form sludge-like mixture in methanol under sonication, which was then filled into the syringe housing and compressed to CNT columns with various shapes. The resulting CNT aerogels with hyperboloid geometries exhibited high-compressibility and fast expansion rates [53]. To further improve the performances of CNT-based aerogels, external structural binders such as polyvinyl alcohol (PVA) [48, 49, 52] were added into the system to facilitate the fabrication. For example, acid-treated CNT was mixed with PVA to form a homogeneous aqueous suspension, and a cyclic freezing-thawing process was applied to prepare CNT/PVA hydrogels [52]. Subsequent free-drying resulted in the formation of CNT-based aerogels with excellent thermal and catalytic performances as well as high absorption capacity of polynuclear aromatic substances. It is worth noting that the CNTs loading significantly affects the specific surface area as well as the thermal behavior of the CNT-based aerogels. The aerogels exhibited thermal incandescence at temperatures below 200 °C when the CNTs loading was 50 wt% [52].

The surface functional groups (such as –COOH, -OH, and epoxy group) and double bonds can be used as anchor points to graft other polymer chains via various reactions. CNT functionalized with an imidazolium-type ionic liquid polymer was synthesized by in situ radical polymerization with AIBN as initiator [37], with an appropriate concentration of CNTs varied from 0.5 to 1.5 wt%, it will form hydrogels in situ due to the electrostatic interactions [54]. Noncovalent interactions have weak strength between the CNT and surface molecules, thus leading to low mechanical performances. Introducing strong interactions between the CNTs provides an alternative solution to induce the gelation of CNTs and can significantly increase the mechanical properties. Notably, introducing covalent interactions among CNTs can significantly decrease the percolation threshold of gelation with ultralow CNT concentrations [55, 56]. For instance, diblock copolymer, poly(3-hexylthiophene)-*b*-poly(3-(trimethoxysilyl) propyl methacrylate) (P3HT-*b*-PTMSPMA) was synthesized via reversible addition-fragmentation chain transfer (RAFT) polymerization of 3-(trimethoxysilyl) propyl methacrylate using P3HT-based RAFT agent as macromolecular initiator, which was then used to disperse CNTs via π-π interactions

between P3HT and CNT [55]. The PTMSPMA not only serves as a stabilizer for CNT in solutions but also introduces permanent covalent polysilsesquioxane bonds to crosslink the CNTs via hydrolysis and condensation. After removal of the solvent, the resulting freestanding CNT aerogels have a density of $4\,mg\,cm^{-1}$ [3] and ordered macroporous honeycomb structure with straight and parallel voids. Moreover, the aerogels exhibit excellent compression recoverable properties [55].

Thereafter, (3-glycidyloxypropyl) trimethoxysilane was covalently grafted onto oxidized CNTs via the ring-opening reaction of epoxy groups with acid groups [57], followed by hydrolysis of trimethoxysilane anchored on CNTs and tetraethyl orthosilicate (TEOS) to form silicon oxide network [56], yielding covalently crosslinked CNT-based aerogels [56, 57]. In addition, polymeric amines have also been widely used to chemically crosslink the CNTs via amide reaction, forming a 3D macroscopic network [58]. Recently, Suzuki cross-coupling reaction between aryl halide on CNTs and boronic acid derivatives, i.e. 1,4-phenyldiboronic acid [59] and reductive coupling chemistry [60] were employed to crosslink the CNTs, the obtained CNT aerogels after freeze drying demonstrated various network morphologies with higher porosity [59].

6.3.3 CNT Doping in 3D Aerogels

CNTs can serve as binders to crosslink the network, they can also be added as filler into 3D network gels to improve the mechanical and electrical performances of the aerogels. Percolation of CNTs into aqueous gels followed by freeze-drying or supercritical-drying is another important route to prepare aerogels. This goal can be achieved through the sol-gel process of silica-based materials with the presence of CNTs in the system. CNTs exhibit excellent electrical and mechanical properties, which is an ideal candidate for the fabrication of 3D network. Alkoxysilanes are commonly used precursors to form the silica aerogel network, which can be fabricated via hydrolysis and condensation processes [61–64]. The pH of the reaction medium dominates the microstructure of the aerogels. In acid conditions, the condensation step is slower than the hydrolysis step, thus the system will form a more extended network. Whereas at base conditions, the condensation step is predominantly in the system, thereby the highly branched species promote the formation of condensed 3D structure [56]. In addition, other conditions such as temperature, concentration, and water content also play a key role in controlling the porous structure.

Generally, CNTs disperse in alkoxysilanes precursors (e.g. tetramethyl orthosilicate, (TMOS) [61], and TEOS [62, 65]) solution to form a homogeneous suspension, then silica sol derived from hydrolysis of precursors to construct 3D network. Subsequently, crosslinked dispersion was frozen and freeze-dried, yielding CNT-based aerogels with silica gel as the matrix [66]. However, the resulting CNT-based aerogels have low stretchability due to the intrinsic high crosslinking density. Polydimethylsiloxane (PDMS) is an important elastomeric material due to its low glass transition temperature, high gas permeability, low dielectric constant, and excellent biocompatibility [67–69]. With the excellent flexibility and high strength of PDMS, it is favorable to prepare stretchable CNT aerogels. In this strategy, pure CNT aerogels with various shapes and sizes are fabricated, subsequently, silicone gel (i.e. Sylgard 184) with a curing agent are backfilled into the CNT aerogel via vacuum suction. Finally, CNT/PDMS aerogels are obtained after curing at 70 °C [63]. Thereafter, the CNTs in the CNT/PDMS aerogels can be unzipped to form graphene nanoribbon aerogels (Figure 6.3). During the process, the $KMnO_4/H_2SO_4$ solution under sonication was employed to induce intercalation of the nanotube walls from the defects and in-situ unzip the CNT [64]. After the unzipping, GNR aerogels were obtained via supercritical-drying. The crosslinked PDMS not only maintains the

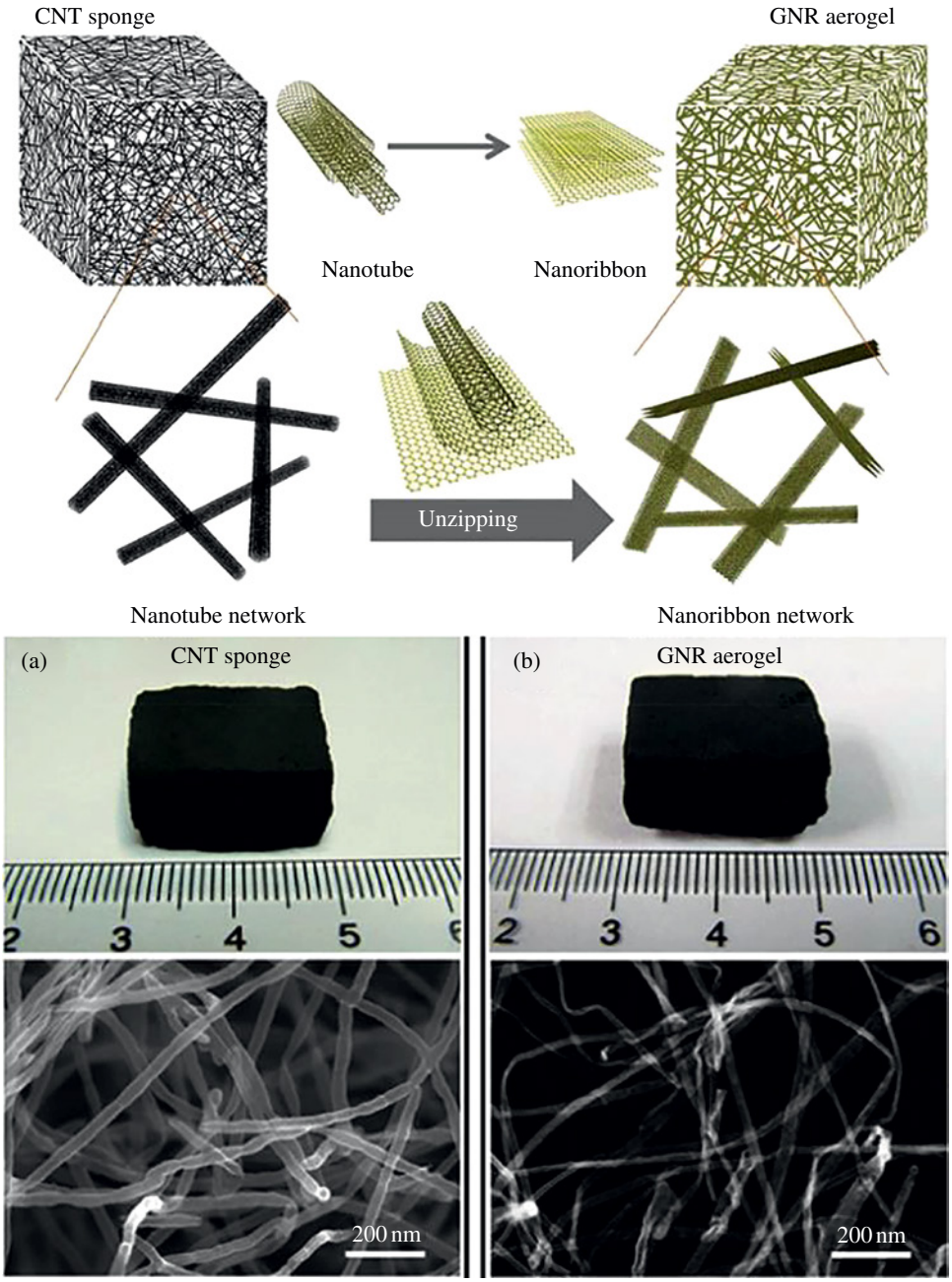


Figure 6.3 Illustration of the process in which a CNT sponge is directly converted into a GNR aerogel by unzipping multi-walled nanotubes into multilayer graphene nanoribbons and the corresponding photographs of (a) CNT and (b) GNR sponges as well as SEM images of internal nanotubes and nanoribbons [64]. *Source:* Copyright 2014. Adapted with permission from John Wiley and Sons Inc.

original 3D network without breaking the interconnection of CNTs but also endows the aerogels with high toughness (a large strain of >300% and tensile stress of 10 MPa). This was attributed to the uniform dispersion of the CNTs or GNRs and the effective load transfer between the nanoscale filler and matrix that can block or deviate the crack from propagating in the PDMS matrix [64].

Other crosslinked matrixes have also been used to support the CNT aerogels. Epoxy resins are important thermosetting materials that have been widely used in many fields because of their excellent mechanical and chemical properties [70]. The intriguing feature of surface functional groups on CNTs is favorable for preparing CNT/epoxy aerogels because the functional groups can react with the epoxy groups, forming another crosslinking network with the epoxy resin network. For example, the CNT aerogel was impregnated in a mixture of epoxy resin and curing agent, followed by the curing process to obtain CNT/epoxy aerogels with a flexural modulus of 3.85 GPa [71]. Thereafter, the acid-treated CNTs were modified with the silane coupling agent to increase the anchoring points for crosslinking, epoxy resin was then mixed and curved to form hybrid gels. The resulting aerogels exhibited higher thermal properties [72]. It should be noted that phenolic resin has also been used to prepare CNT-based aerogels via the sol-gel process. Similarly, CNTs dispersed in resorcinol and formaldehyde aqueous solution with sodium carbonate as the catalyst. The CNT-based aerogels could be obtained with curving at 85 °C, followed by freeze drying [73, 74]. The surfactant significantly affects the density and pore texture of the aerogel materials [73].

With the increase of carbon emissions and deterioration of the petroleum crisis, natural biomass resource materials have been widely used as matrixes for preparing CNT-based aerogels. Among the various natural sources, cellulose is the most abundant polysaccharide biomass resource in nature and has been widely used as a versatile green platform for energy applications [75, 76]. Cellulose exhibits fascinating 1D morphology due to its rigid backbone [77]. In addition, cellulose-based hydrogels have shown significant superiority compared with synthetic polymer-based hydrogels [78]. Therefore, cellulose-based aerogels exhibit intriguing performances due to their biocompatibility, biodegradability, and thermal and chemical stability [79]. When CNTs were incorporated into the system, the resulting composites will inherit the merits of individual counterparts.

There are two strategies to prepare CNT/cellulose aerogels [80–83]. The first method is introducing acid-treated CNT suspension into the pre-formed cellulose hydrogels, followed by freeze-drying the hybrid hydrogels in a mold to obtain aerogels. For example, nanofibrillated cellulose (NFC) was used to prepare hydrogels via combined refining, enzymatic treatment, and high-pressure homogenization; subsequently, functionalized few-walled carbon nanotubes (FWCNT; which can maintain intact inner layers after chemical modifications) were added into the hydrogels. Finally, various freeze-drying methods were employed to remove the solvent, yielding CNT/NFC aerogels with different morphologies (Figure 6.4a) [80]. With slow cooling from liquid nitrogen, the formed large ice crystals facilitated the aggregation of nanofibrils into sheets, which interconnected the aerogel skeleton. Rapid cooling with liquid propane induced the formation of fibrillar aggregates, which served as the skeleton of the aerogels. Moreover, the extensive amount of hydroxyl groups of NFCs and acid groups on CNTs formed hydrogen bonding, leading to the formation of aerogels with excellent compressive performances [80]. Nonetheless, this two-step process is tedious and time-consuming.

The second strategy is the in-situ formation of CNT/cellulose hydrogels, followed by freeze-drying. Generally, acid-treated or surfactant-assisted CNTs dispersed in aqueous solution, while cellulose

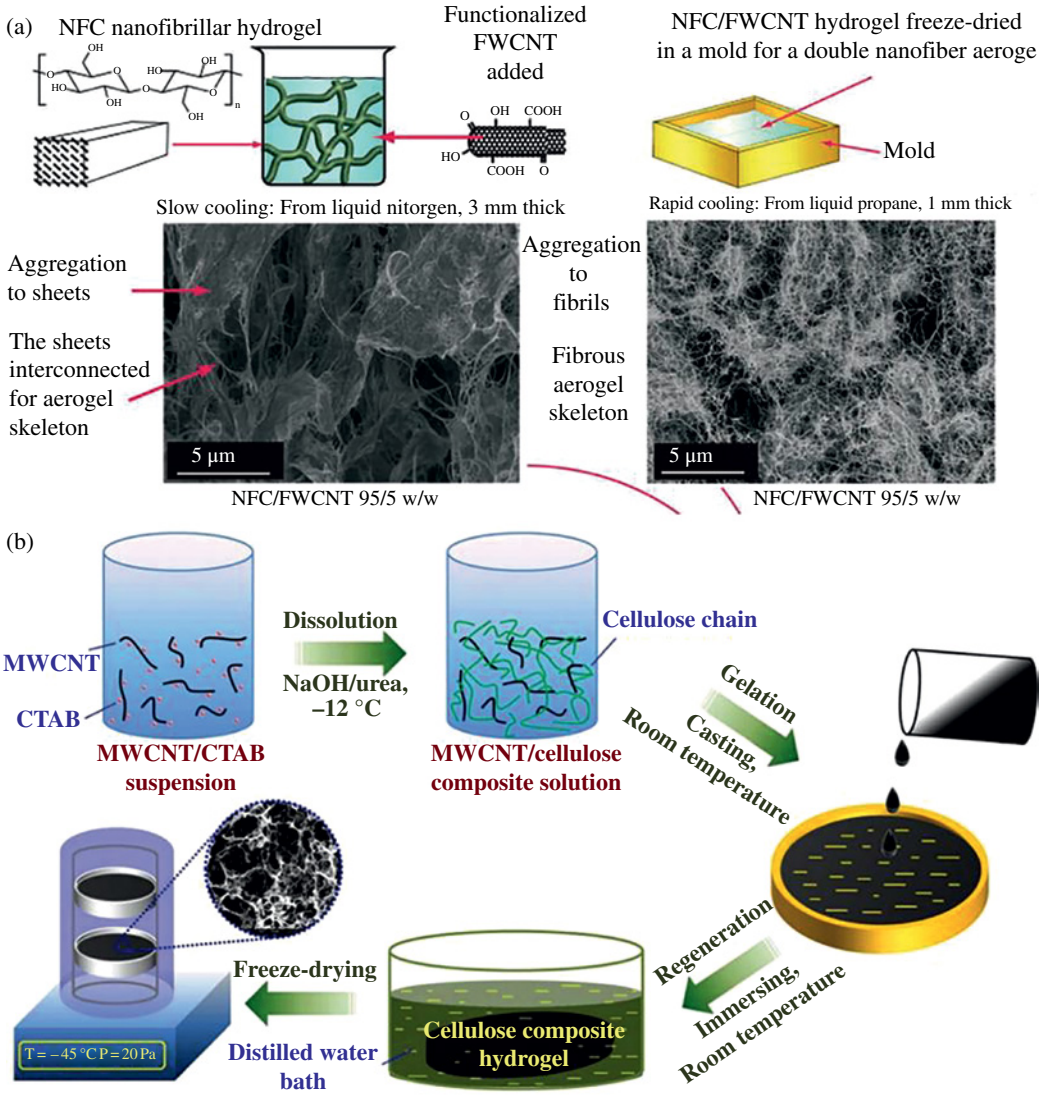


Figure 6.4 (a) Schematic illustration of the two-step process fabrication of CNT/cellulose composite aerogels [80]. *Source:* Copyright 2013. Adapted with permission from John Wiley and Sons Inc. and (b) Schematic illustration of the in-situ fabrication of CNT/cellulose composite aerogels [81]. *Source:* Copyright 2015. Reproduced with permission from the Royal Society of Chemistry.

dissolved in NaOH/urea aqueous solution, which was a nontoxic and environmentally friendly solvent. Then the two solutions were mixed to form a homogeneous solution and poured into the mold for gelation. Subsequently, the hydrogels were immersed in water to remove the base and urea or surfactants. Finally, freeze drying was employed to obtain CNT/cellulose aerogels (Figure 6.4b) [81–83]. The resulting conductive aerogels exhibited excellent electromagnetic interference shielding [81], good thermal stability, and enhanced mechanical properties [82]. Furthermore, chitosan (CS) is

another natural polysaccharide, which has many $-NH_2$ and –OH groups on the backbone. For instance, CNT/CS aerogels have been prepared via the in-situ process that is similar to the preparation of CNT/cellulose aerogels [84, 85]. The amino groups of chitosan can form hydrogen bonding with the oxygen-containing functional groups on the oxidized CNTs. In addition, the positively charged chitosan can interact with negatively charged CNTs via electrostatic interactions. The synergetic effect of hydrogen bonding and electrostatic interactions results in strong interfacial interactions between CNTs and chitosan. Therefore, it forms a strong carbon layer after annealing at 800 °C, which can withstand high compression strain and exhibit excellent conductivity [85].

6.3.4 CNT/Inorganic Nanocrystal Composite Aerogels

To further integrate active materials into the mechanically robust and electrically conductive 3D CNT scaffold, it is highly urgent to eliminate the nonactive materials and increase the energy density of the system. Notably, the porous microstructure and the synergistic effect among organic and inorganic counterparts in the aerogels endow them with intriguing multifunctions. For instance, metal oxides (e.g. SiO_2, SnO_2, TiO_2, and Fe_3O_4) have been deposited on the porous surfaces of CNT aerogels via the sol-gel strategy [86–88]. The metal oxides are deposited as conformal overlayers on the primary skeleton of aerogels, which can preserve the open porosity within the monolith. Therefore, hybrid CNT-based aerogels show great potential in catalysis and energy storage [86]. Fe_3O_4 nanoparticles show significant microwave-absorbing capability via conversion to heat energy because of their magnetic features, high Curie temperature, and low cost [89]. When combined with conductive CNT aerogels, the resulting composite aerogels exhibit excellent microwave absorption properties with extremely strong reflection loss of −59.85 dB [87].

Except for the inorganic nanoparticles, two-dimensional (2D) nanomaterials have garnered much attention due to their low density, good ductility, and exceptional properties [14, 90, 91]. Graphene is the most studied 2D material due to its extraordinary electronic, thermal, and mechanical properties [91]. Though both CNTs and graphene have good toughness and high strength, neat graphene and CNT aerogels have weak elasticity. The combination of CNTs and graphene to prepare 3D composite aerogels show super recyclable compressibility [92, 93]. For instance, CNT/graphene hybrid aerogels have been constructed via supercritical-drying of their hydrogel precursors (Figure 6.5). Acid-treated CNTs or pristine CNTs were mixed with pre-dispersed GO nanosheets and sonicated to form homogeneous complexes. Subsequently, vitamin C (VC) and a catalytic amount of hydrochloric acid were added to the mixture to promote the reaction between GO and VC and thus shortening the gelation time of the mixtures without stirring. It is worth noting that the VC was also served as a reducing agent for the reduction of GO to graphene [93]. The resulting hybrid aerogels after supercritical-drying exhibited high binding capacities to heavy metal ions [93] and diverse organic solvents [94].

As an emerging 2D material, MXene represents a large family of 2D transition metal carbides, nitrides, and carbonitrides. Benefiting from the high electronic conductivity, large specific surface area, and structural stability of MXenes, they have shown a promising opportunity for designing energy storage devices [95]. The $Ti_3C_2T_x$/CNT hybrid aerogels were synthesized by using bidirectional freeze-drying of CNT and MXene mixture [96, 97]. The CNTs were inserted into layers of MXene as fillers and binders to improve the mechanical and electrical properties. The hybrid aerogels exhibited uniform and aligned 3D porous cellular architecture with CNTs distributed over the MXene nanosheet [96].

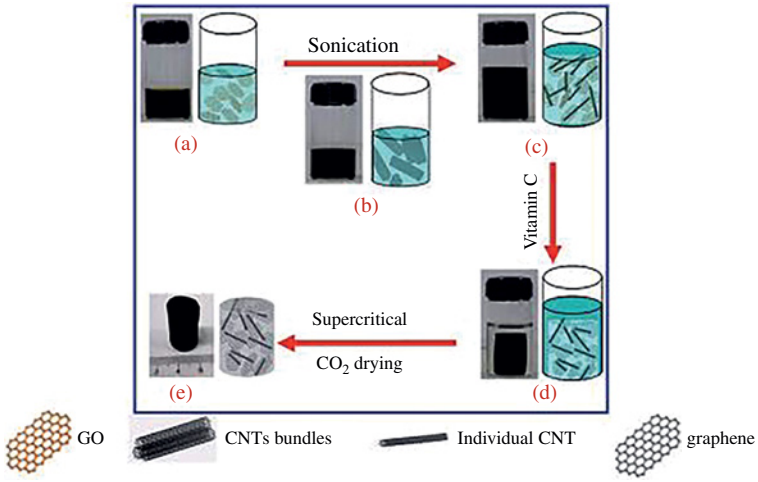


Figure 6.5 Schematic diagram for green synthesis of the CNT/graphene hybrid aerogels: (a) predispersed GO solution, (b) predispersed CNT suspension; (c) the mixture of GO and CNT after sonication; (d) the CNT/graphene hybrid hydrogel, and (e) the CNT/graphene hybrid aerogel [93]. *Source:* Copyright 2012. Reproduced with permission from the Royal Society of Chemistry.

6.4 Applications

The CNT-based aerogels have high porosity, low density, large specific surface areas, and excellent mechanical and electrical properties. Thus, they are promising candidates for developing functional nanocomposites, high-performance energy devices, and environmental materials. In addition, the microstructure and pore engineering dominate the mechanical and electrical properties of aerogels. The 3D CNT networks not only promote charge carrier transport because of the highly conductive paths but also provide anchoring points for doping or coating diverse organic or inorganic active materials. Therefore, CNT-based aerogels have been widely used in an array of applications, including water treatment, battery, supercapacitors, and catalysis.

6.4.1 Water Treatment

With the contamination of water, one-third of the world's population suffers from the lack of freshwater. To solve this global crisis, the emerging solar desalination technology is considered one of the most promising strategies to ensure sufficient water supply due to its low cost, easy operation, potential industrial production, and minimum environmental impact [98]. An ideal solar energy-driven water evaporator should have high efficient sunlight absorption and energy conversion, good thermal management capability, hydrophilic feature, and a high rate of water evaporation [99]. The typical seawater desalination process involves water transportation, light absorption, and evaporation (Figure 6.6) [62].

CNTs have broadband solar light absorption and high chemical stability. In addition, they possess a particular photothermal effect, which can partially or completely converse solar energy to thermal energy due to the photoexcitation of electrons [62, 100, 101]. Therefore, CNT-based aerogels are promising candidates for solar-energy-driven water evaporation. For instance, bilayer-structured aerogels composed of two types of nanofibers (e.g. CNF and CNT [101] or hydroxyapatite

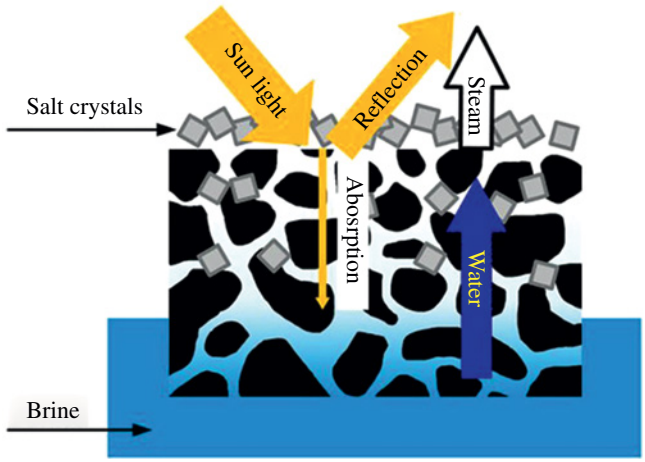


Figure 6.6 Schematic description of water transportation, light absorption, evaporation, and salt crystallization in conventional solar evaporators [62]. *Source:* Copyright 2020. Reproduced with permission from John Wiley and Sons Inc.

(HAP) and CNT [100]) have been fabricated and used for seawater desalination and wastewater purification. In this evaporator, the substrate aerogels were prepared by using ultralong HAP nanowire slurry, followed by freeze-drying. Then the CNT suspension in acetone was deposited on the top of HAP aerogel by spray coating three times to obtain the HAP/CNT bilayer aerogels [100].

The hydrophilic and highly porous HAP aerogel with a low thermal conductivity enables excellent thermal management and high water-evaporation rate, while the CNT coating layer ensures highly efficient solar light absorption and energy conversion. The resulting aerogels exhibit a high water evaporation rate of $1.34\,kg\,m^{-2}\,h^{-1}$ and high water evaporation efficiency of 89.4% under solar light irradiation at a power density of $1\,kW\,m^{-2}$ [100]. Similarly, sustainable and biodegradable CNF was used as the substrate building block to prepare bilayer-structured aerogels for efficient solar steam generation with an efficiency of 81.4% [101].

However, the surface salinity will increase with the evaporation during the practical seawater desalination because of the randomly distributed pores in the aerogels, which block the transport of salt into the bulk water, resulting in salt crystallization [62]. An alternative strategy is preparing aerogels with cellular architecture composed of vertically aligned vessels and porous vessel walls. For example, CNTs@SiO_2 nanofibrous aerogels (CNFAs) were constructed via a three-step process including freeze-drying, calcination, and deposition (Figure 6.7) [62]. First, silica sol was poured into the SiO_2 nanofibers and polyacrylamide (PAM) suspension, followed by the freeze-shaping method. Second, the obtained pre-SNFAs were calcinated at 800 °C to obtain the SNFAs. Third, the SNFAs were immersed into CNT suspensions with various concentrations, followed by freeze-drying to obtain CNFAs. The nanofibers assembled into interconnected cellular architecture with vertically aligned vessels, which were mechanically robust and chemically stable to maintain the network structure (Figure 6.7b–d). In addition, the vertically aligned vessels promoted the transportation of salt and water, avoiding salt crystallization. CNT networks deposited on the vessel walls via π-π stacking ensured the high efficient light absorption. The aerogels exhibited excellent mechanical properties and superior salt-resistance without any salt crystals on the surface of aerogels even in 20 wt% brine and under 6-sun irradiation [62].

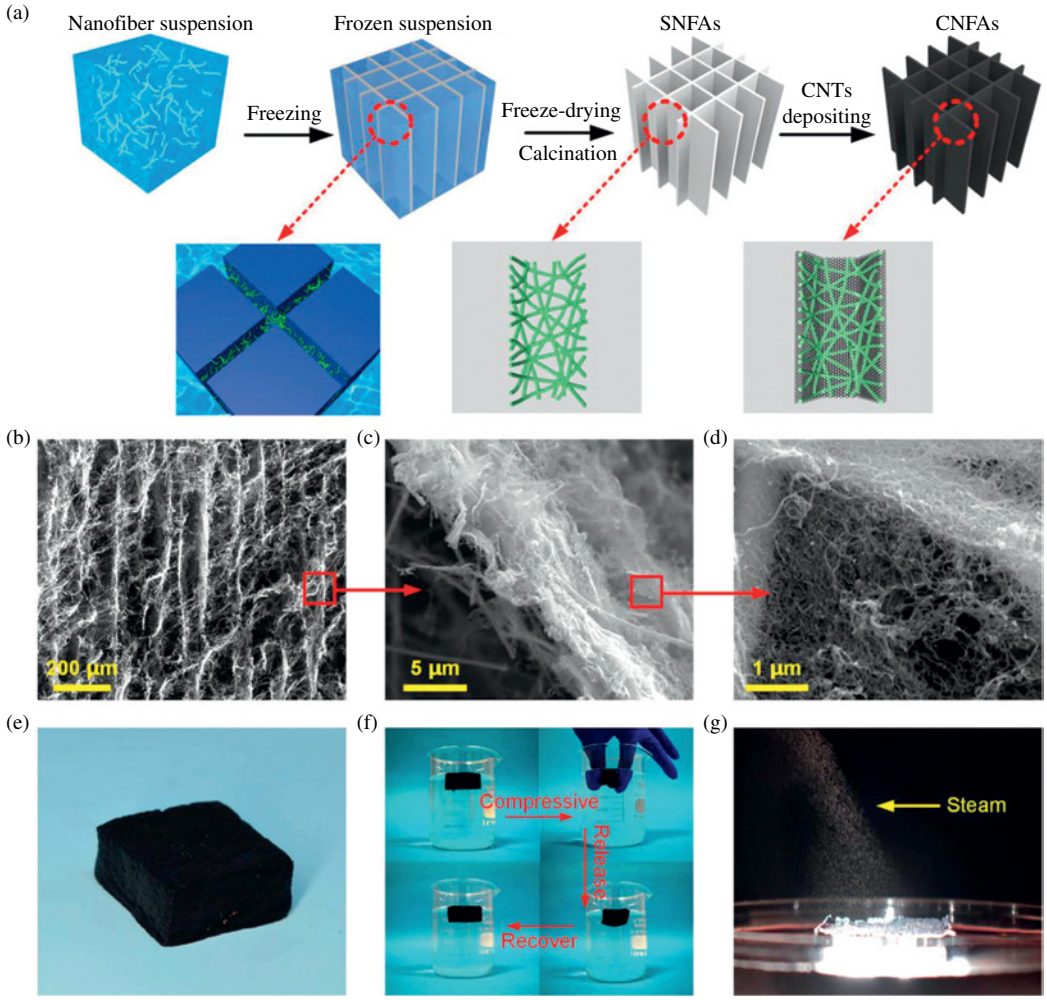


Figure 6.7 (a) Schematic diagram showing the fabrication and architectures of the CNFAs. (b–d) Microscopic cellular architectures of the CNFAs at different magnifications. Digital photos showing (e) the high light absorbance CNFAs, (f) the compressive and recovery of the CNFAs in water, and (g) vapor generated from the CNFAs surface [62]. *Source:* Copyright 2020. Adapted with permission from John Wiley and Sons Inc.

Another strategy for water treatment is how to remove the contaminants such as organic dyestuffs, heavy metal ions, and light metal salts. In addition, the oil spill has caused immeasurable loss to our living environment and economic development. Porous carbon-based aerogels are of significant interest for the separation of pollutants from water due to the facile, rapid, selective, and recyclable process [102]. CNT aerogels exhibit high porosity and hydrophobicity, improving the efficiency and selectivity of water pollutant separation, the CNT aerogels exhibited high oil adsorption up to $107\,g\,g^{-1}$ and good reusability of up to four adsorption-burning cycles [103]. However, the CNT aerogels based on CVD methods are difficult to scale up. Moreover, the

controllability of pore size and affinity of CNT aerogels for adsorbates are still a great challenge. Incorporating a second component can not only tune the porosity but also tailor the surface functional groups and heteroatom doping [65, 94, 104, 105]. For instance, the CNT/graphene aerogels prepared via the "sol-cryo" method exhibited adsorption capacity to crude oil that can reach as high as $290\,g\,g^{-1}$ [92]. Nevertheless, harmful virulent hydrazine was applied in this protocol. Thereafter, the environmentally friendly reducing agent VC was used to prepare CNT/graphene aerogels, which exhibited extremely high desalination capacity ($633.3\,mg\,g^{-1}$) with NaCl and high binding capacities to heavy metals [93]. Ferrous ions as the green reducing agent in combination with the hydrothermal condition were also employed to fabricate CNT/graphene aerogels and the deposited Fe nanoparticles could increase the spacer between graphene nanosheets. The prepared aerogels exhibited outstanding adsorption performances for the removal of petroleum products, fats, and organic solvents [104].

6.4.2 Energy Storage and Conversion

With the fast consumption of fossil fuels and related environmental issues of climate change, extensive efforts have been devoted to developing new techniques toward energy storage and conversion as well as clean energy such as lithium-ion batteries and supercapacitors [3]. Supercapacitor consists of two nonreactive porous plates, or electrodes immersed in an electrolyte and separated by a porous membrane that allows migration of electrolyte ions and electrically isolates the two electrodes. Based on the mechanism of energy storage, supercapacitors can be categorized into electrochemical double-layer capacitors (EDLCs) and pseudocapacitors [106, 107]. EDLCs achieve energy storage via reversible adsorption of anions and cations at the electrode-electrolyte interface (Figure 6.8), and the specific surface areas of electrodes dominate their capacitances. Whereas, the pseudocapacitors store energy through fast surface redox reactions of the electrode material with the electrolyte. These two mechanisms can be easily distinguished from the cyclic voltammetry (CV) curves. Pseudocapacitors usually have obvious redox peaks in the CV curves because of

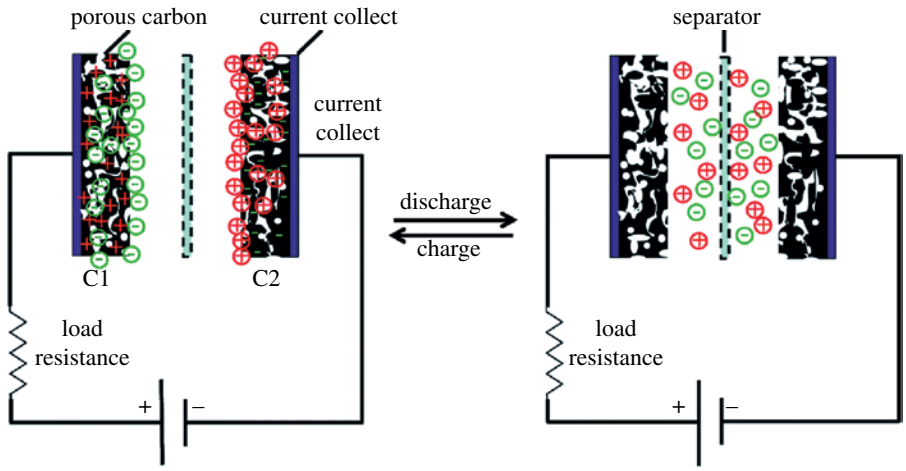


Figure 6.8 Schematic diagram of the charge and discharge processes of EDLCs [3]. *Source:* Copyright 2013. Reproduced with permission from the Royal Society of Chemistry.

faradic processes-redox reactions, while EDLCs show rectangular-shaped CV curves. In some cases, the CV curves of pseudocapacitors (e.g. MnO_2 and RuO_2) also exhibit a rectangular shape, because the redox reactions are confined to the surface or the near-surface volume of the materials [106].

For EDLCs, anions transport to the surface of the positive electrode, and cations transport to the negative electrode during the charging process, forming electrical double layers at the interface. While the adsorbed electrolyte ions release into the solution during the discharge process. Carbon-based materials are widely used in commercial EDLCs [108]. In addition, the capacitance of EDLCs is mainly dominated by the conductivity, surface area, and pore size distribution of electrode materials [3]. Therefore, CNT-based aerogels are suitable for electronic materials, due to structural controllability and remarkable electrical conductivity [13]. Recently, CNT aerogels were prepared by using CNT fibers via electrochemical activation and freeze-drying, which possessed high mechanical strength and excellent electrical conductivity [109]. Then CNT aerogel fiber electrodes were immersed in P(VDF-HFP)/$EMIMBF_4$ ionogel electrolyte, followed by twisting together two electrodes, yielding fiber-shaped supercapacitor. The fibrous CNT aerogel electrode possessed high mechanical strength as well as high specific capacitance and long cycling stability [109]. However, CNT aerogels have low capacitance because of their low specific surface areas and the aggregation tendency of CNTs. To further improve the porosity, graphene sheets were introduced into the system, which can assemble with CNTs to form hierarchical 3D network structure [107, 110–112]. Sometimes, nickel foam was used as the substrate for loading the CNT and graphene, forming hierarchical structure hybrid aerogels. Nevertheless, a single type of pore in the CNT-based aerogels is not good enough for the transportation of electrolyte ions. The presence of all the micropores, mesoporous, and macropores with appropriate pore size is more significant for achieving high specific capacitance than achieving high surface area [3]. Furthermore, doping with metallic compounds is an efficient approach for enhancing the capacitance of CNT-based aerogels [110, 111]. For instance, 3D graphene aerogels (3DGA) doped with nickel particles were obtained by hydrothermal treatment of the mixture of graphene oxide and nickel precursors, followed by freeze-drying (Figure 6.9a). Then the growth of the CNTs on 3DGAs was achieved via CVD, yielding CNTs@3DGA hybrid aerogels. Finally, MnO_2-doped CNTs@3DGA were obtained via hydrothermal reaction [111]. The covalent connection between CNTs and graphene results in superior properties, while maintaining inherited properties in the planar and axial directions. The CNTs@3DGA exhibited a well-interconnected network structure with randomly oriented, entangled CNT forests covered on 3DGA (Figure 6.9b). The CV curves of MnO_2-doped CNTs@3DGA with various MnO_2 loadings exhibited symmetric rectangular shape and the near linear and symmetric charge and discharge curves, suggesting a good pseudocapacitive behavior for the all-solid-state asymmetric supercapacitors (AASCs) devices (Figure 6.9d,e). More importantly, the AASCs exhibited superior long-term cycle stability with 84.6% retention after 20 000 cycles (Figure 6.9f) [111].

CNT-based aerogels have high porosity, conductive network, and good mechanical stability, thus making them promising as 3D porous electrodes for Li-ion batteries (LIBs), however, the theoretical capacity of carbon electrodes in LIBs is still too low for commercialization. While conventional anode materials (e.g. SnO_2 [113] and metal sulfides [114]) possess high theoretical capacities compared with carbon materials. The intrinsic electrical conductivity of SnO_2 is extremely poor with a wide bandgap of ~3.6 eV, making it difficult to be directly used as the electrode material [115]. To address these issues, high-energy density and chemical-activity materials have been proposed to combine with conductive CNT-based aerogels, preparing composite

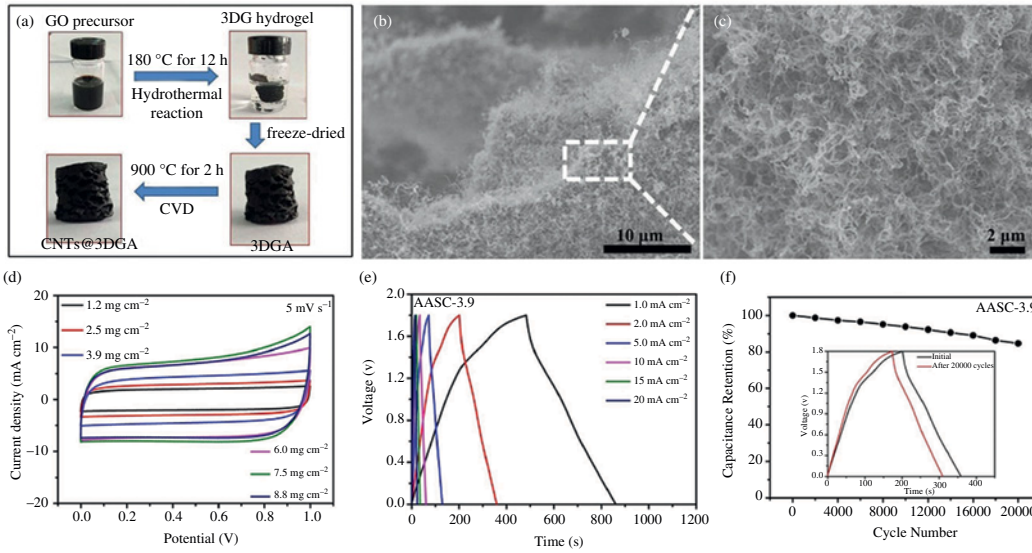


Figure 6.9 (a) Illustration of the growth procedure and (b–c) SEM images of CNTs@3DGA aerogels. (d) CV curves of MnO_2@CNTs@3DGA electrodes with different mass loadings of MnO_2 at the scan rate of 5 mV s^{-1}. (e) Galvanostatic charge-discharge curves and (f) long-term cycle stability of AASC-3.9 [111]. *Source:* Copyright 2017. Adapted with permission from John Wiley and Sons Inc.

electrodes with excellent battery performances [11, 114–117]. It is difficult to simultaneously achieve both enhanced cyclic stability and rate capability through hybridizations. Doping is an alternative method to effectively enhance the electrochemical performance of SnO_2/CNT aerogels. For example, Sb-doped SnO_2 nanoparticle has been grown on CNT/graphene aerogels via hydrothermal self-assembly, and composite electrodes delivered an outstanding rate capability and high capacity retention [115].

Silicon has been an anode material because of its large theoretical capacity; however, rapid performance degradation usually occurred during charge-discharge cycles of Si electrode because of the large volume change. Depositing active nanomaterials on the CNT sponge via CVD has been used to prepare CNT-based aerogels with coaxial core-shell structure CNT hybrid as the LIB anode with improved electrochemical capacity [118, 119]. The embedded CNTs facilitate electron transfer by forming 3D conductive network and act as a stable skeleton for grafting active materials. The resulting coaxial anode exhibited higher charge and discharge capacities with a cutoff voltage of 0.05–1.0 V [118]. It is worth noting that the coating materials must have good compatibility with the CNT to ensure the tight bond between CNT and coating layer. In addition, the thickness of the nonconductive coating layer should be suitable, otherwise, the densely compacted layer will lower the conductivity of CNT-based aerogels, resulting in an unsatisfactory capacity.

Recently, reticulate dual-nanowire aerogel (rDNWA) based on two tightly intertwined nanowires (NWs) has also been used to fabricate freestanding anode for LIB. An rDNWA (FeS_2 nanowire and CNT) was constructed with CNT sponge as the matrix through the in-situ synthesis of FeS_2 nanowire via solvothermal reaction (Figure 6.10) [120]. Washing and annealing treatments were employed to remove the residuals. The FeS_2 nanowires with similar diametral widths were embedded in the CNT aerogel. The aerogel electrode exhibited a strong reduction peak at 1.2 V because of Fe and Li_2S, and the peak at 0.6 V is from the solid electrolyte interface (SEI) film formation in the first discharge cycle. During the charging process, the peaks at 1.98 and 2.5 V corresponded to a two-step conversion reaction to form $Li_{2-x}FeS_2$ and then FeS_y, S, and metallic Li. While the formation of Li_2FeS_2 and Fe, as well as Li_2S produced two peaks at 1.4 and 2.0 V, respectively. An irreversible capacity loss was observed in the discharge-charge curves due to the SEI formation and the formation of S and Li_2S. More importantly, the aerogel electrode exhibited high specific mass capacity and maintain 89% retention to 729 mA h g^{-1} [120].

6.4.3 Catalysts

Inorganic nanomaterials are usually used as catalysts, however, they are easy to aggregate because of their large specific surface area, leading to the deterioration of the catalytic performances. To address this issue, using catalytically active nanomaterials as support can avoid the aggregation of nanocrystals and provide more active sites [13, 121]. CNT-aerogels have large surface areas and macroscopic morphologies, enabling them as ideal candidates for the uniform immobilization of active materials on the substrates. First, the hierarchical porous network promotes the loading of catalysts without blocking the porous structure. Second, the conductive CNT network is favorable to improving the reaction kinetics. Third, the skeleton can dope heteroatoms, preparing multifunctional catalysts. Finally, the mechanical and chemical stabilities are helpful to fabricate catalysts with long-term stability.

Heteroatom doping aims to tailor and adjust the bulk and/or surface properties of carbons to further optimize their catalytic performances [122]. N-doping is the most applied method to improve the catalytic properties of carbon materials [123–125]. Recently, an in-situ doping strategy

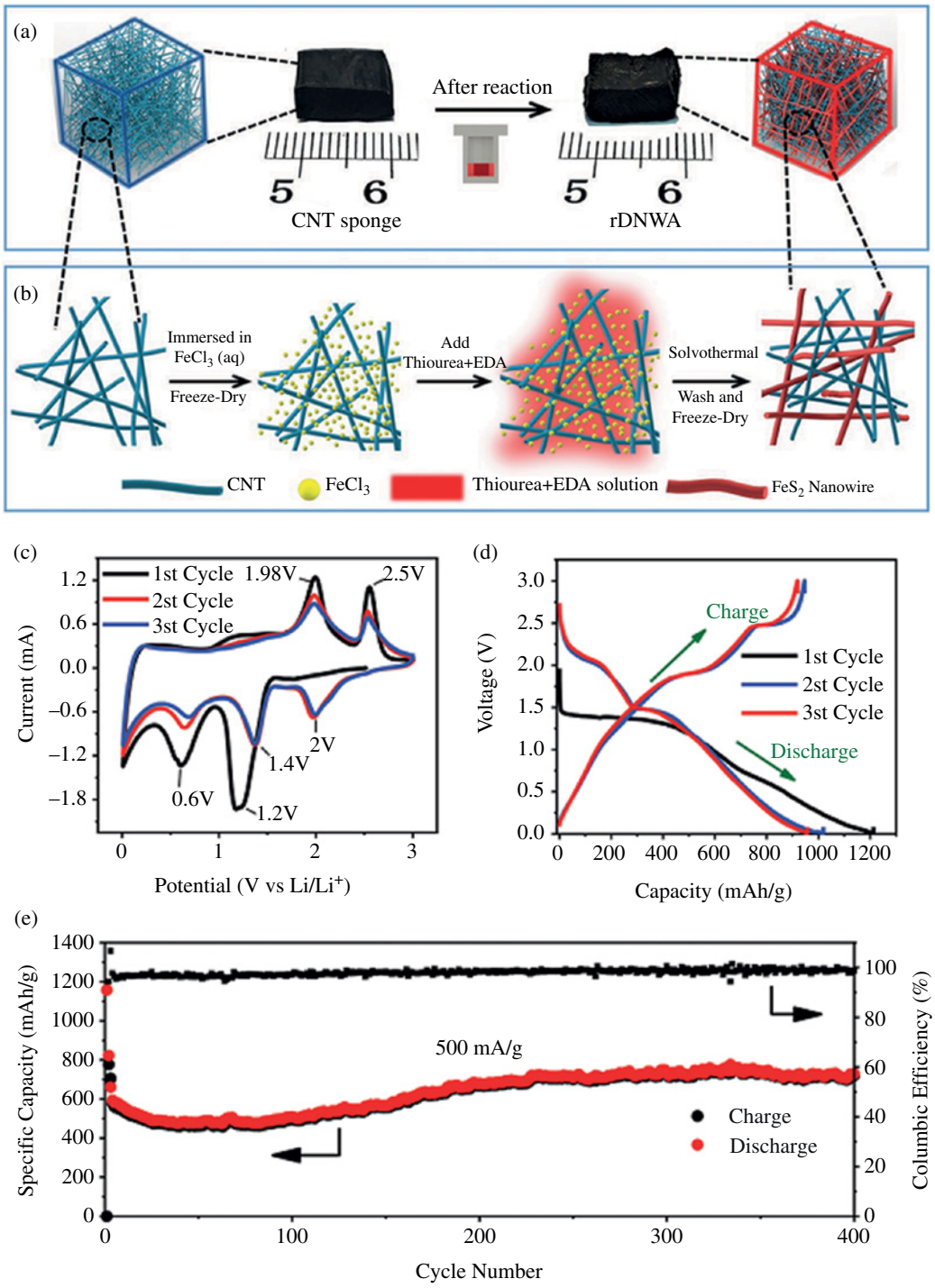


Figure 6.10 Fabrication of rDNWA. (a) Schematic and actual samples of the original bulk CNT sponge and rDNWA. (b) An illustration of the solvothermal process where the precursors are added in a two-step technique and the growth of the FeS_2 nanowires inside the CNT sponge. (c) CV curves of the initial three cycles at a scan rate of 0.3 mVs^{-1}. (d) Discharge/charge voltage profiles of the first three cycles at a current density of 100 mAg^{-1}. (e) Cycling performance of DNWA-70 at a current density of 500 mAg^{-1} after 400 cycles [120]. *Source:* Copyright 2019. Adapted with permission from John Wiley and Sons, Inc.

was developed to prepare the 3D N-doped CNT aerogels by pyrolysis of the presynthesized PPy aerogels [125], in which the methyl orange and ammonium peroxysulfate (MO-APS) acted as templates to direct polypyrrole growth, followed by freeze-drying and carbonization to obtain CNT aerogels. The N-doped CNT aerogels exhibit excellent oxygen reduction reaction (ORR) activity, but also superior stability in the acid conditions [125].

Given the low content of N-doping and single function in CNT aerogels, people have been searching for loading nanocrystals in N-doped aerogels with multifunctional performances [126]. For instance, freestanding cobalt (II/III) oxide/nitrogen-doped CNT (Co_3O_4/N-CNT) aerogels were produced via two-step CVD methods, in which raw 3D CNT aerogels were prepared by FCCVD, followed by electrochemical activation and coating of cobalt oxide catalyst (Figure 6.11). The electrochemical oxidation of the CNT aerogels introduced abundant hydroxide and carboxyl groups, making the film hydrophilic and facilitating the coating of cobalt oxide catalyst particles.

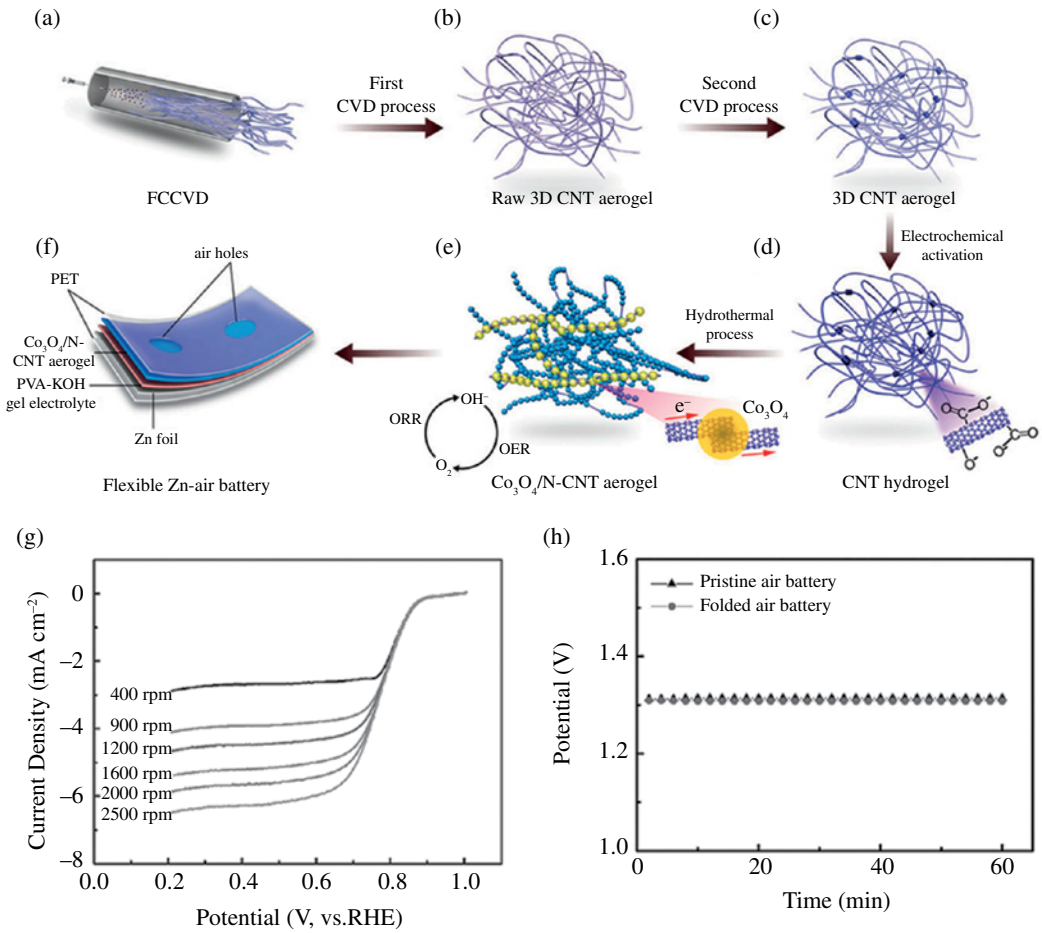


Figure 6.11 (a–f) Schematic showing the preparation of Co_3O_4/N-CNT composite aerogel films utilized for free-standing electrodes of zinc-air batteries. (g) LSV curves for ORR with different rotation speeds for the Co_3O_4/N-CNT electrode. (h) Open-circuit potential versus time curves for pristine and folded air battery, showing no obvious decrease in the potential under folded conditions [126]. *Source:* Copyright 2017. Adapted with permission from John Wiley and Sons, Inc.

The resulting catalyst-supporting scaffolds exhibit excellent ORR performances with the four-electron transfer process, and oxygen evolution reaction (OER) with a potential of 1.7 V (vs. RHE) at 10 mA cm^{-2}, indicating they could serve as efficient bifunctional oxygen catalyst. Finally, Co_3O_4/N-CNT aerogels were used to assemble flexible solid-state zinc-air batteries, which exhibited long-term stable open-circuit potential that is almost the same as the battery before folding [126].

6.5 Conclusions and Perspectives

CNT-based aerogels have attracted significant interest in the past decades because of their intriguing characteristics such as tailorable structural and chemical properties, high porosity, low density, and high conductivity. In this chapter, we first introduced the fundamental principle of preparing CNT-based aerogels. Second, we systematically summarized the strategies to prepare CNT-based aerogels with different compositions and structures such as pure CNT aerogels via CVD, surface-functionalized CNT-base aerogels, and CNT/inorganic nanocrystal composite aerogels. Finally, we summarized the development of CNT-based aerogels in energy-related fields including oil/water separation, seawater desalination, lithium-ion batteries, supercapacitors, and catalysis.

Though CNT-based aerogels have achieved great advances in energy saving and storage. However, the realization of industrial applications is still difficult mainly due to their low efficiency (e.g. oil/water separation, desalination, and energy conversion) and scalability issues. Therefore, many efforts are needed to improve the efficiency of CNT-based aerogels in energy saving and storage. In addition, the capacity and stability of batteries and supercapacitors are also needed to improve for future applications. Furthermore, bifunctional catalysts with excellent performances for zinc-air batteries or water splitting, or event multifunctional catalysts for zinc-air batteries and water splitting are essential in future research.

References

1 Zheng, L., Zhang, S., Ying, Z. et al. (2020). Engineering of aerogel-based biomaterials for biomedical applications. *Int. J. Nanomed.* 15: 2363.

2 Du, R., Zhang, N., Zhu, J. et al. (2015). Nitrogen-doped carbon nanotube aerogels for high-performance ORR catalysts. *Small* 11 (32): 3903–3908.

3 Wu, X.-L. and Xu, A.-W. (2014). Carbonaceous hydrogels and aerogels for supercapacitors. *J. Mater. Chem. A* 2 (14): 4852–4864.

4 Zhang, Y.-G., Zhu, Y.-J., Xiong, Z.-C. et al. (2018). Bioinspired ultralight inorganic aerogel for highly efficient air filtration and oil-water separation. *ACS Appl. Mater. Interfaces* 10 (15): 13019–13027.

5 Guo, F., Jiang, Y., Xu, Z. et al. (2018). Highly stretchable carbon aerogels. *Nat. Commun.* 9 (1): 1–9.

6 Saha, A., Jiang, C., and Martí, A.A. (2014). Carbon nanotube networks on different platforms. *Carbon* 79: 1–18.

7 Sahoo, N.G., Rana, S., Cho, J.W. et al. (2010). Polymer nanocomposites based on functionalized carbon nanotubes. *Prog. Polym. Sci.* 35 (7): 837–867.

8 Takakura, A., Beppu, K., Nishihara, T. et al. (2019). Strength of carbon nanotubes depends on their chemical structures. *Nat. Commun.* 10 (1): 1–7.

9 Liu, Y. and Kumar, S. (2014). Polymer/carbon nanotube nanocomposite fibers – a review. *ACS Appl. Mater. Interfaces* 6 (9): 6069–6087.

10 Kinloch, I.A., Suhr, J., Lou, J. et al. (2018). Composites with carbon nanotubes and graphene: an outlook. *Science* 362 (6414): 547–553.

11 Du, R., Zhao, Q., Zhang, N., and Zhang, J. (2015). Macroscopic carbon nanotube-based 3D monoliths. *Small* 11 (27): 3263–3289.

12 Salimian, S., Zadhoush, A., Naeimirad, M. et al. (2018). A review on aerogel: 3D nanoporous structured fillers in polymer-based nanocomposites. *Polym. Compos.* 39 (10): 3383–3408.

13 Lee, J.-H. and Park, S.-J. (2020). Recent advances in preparations and applications of carbon aerogels: a review. *Carbon*.

14 Li, Z., Tang, M., Dai, J. et al. (2017). Preparation of covalent pseudo-two-dimensional polymers in water by free radical polymerization. *Macromolecules* 50 (11): 4292–4299.

15 García-González, C., Camino-Rey, M., Alnaief, M. et al. (2012). Supercritical drying of aerogels using CO_2: effect of extraction time on the end material textural properties. *J. Supercrit. Fluids* 66: 297–306.

16 Chen, Y. and Zhang, J. (2014). Chemical vapor deposition growth of single-walled carbon nanotubes with controlled structures for nanodevice applications. *Acc. Chem. Res.* 47 (8): 2273–2281.

17 Ozden, S., Tiwary, C.S., Hart, A.H. et al. (2015). Density variant carbon nanotube interconnected solids. *Adv. Mater.* 27 (11): 1842–1850.

18 Kukkar, D., Rani, A., Kumar, V. et al. (2020). Recent advances in carbon nanotube sponge–based sorption technologies for mitigation of marine oil spills. *J. Colloid Interface Sci.*.

19 Li, Y.-L., Kinloch, I.A., and Windle, A.H. (2004). Direct spinning of carbon nanotube fibers from chemical vapor deposition synthesis. *Science* 304 (5668): 276–278.

20 Gui, X., Wei, J., Wang, K. et al. (2010). Carbon nanotube sponges. *Adv. Mater.* 22 (5): 617–621.

21 Hoecker, C., Smail, F., Pick, M., and Boies, A. (2017). The influence of carbon source and catalyst nanoparticles on CVD synthesis of CNT aerogel. *Chem. Eng. J.* 314: 388–395.

22 Hoecker, C., Smail, F., Bajada, M. et al. (2016). Catalyst nanoparticle growth dynamics and their influence on product morphology in a CVD process for continuous carbon nanotube synthesis. *Carbon* 96: 116–124.

23 Muñoz-Sandoval, E., Cortes-López, A.J., Flores-Gómez, B. et al. (2017). Carbon sponge-type nanostructures based on coaxial nitrogen-doped multiwalled carbon nanotubes grown by CVD using benzylamine as precursor. *Carbon* 115: 409–421.

24 Xu, M., Futaba, D.N., Yumura, M., and Hata, K. (2012). Alignment control of carbon nanotube forest from random to nearly perfectly aligned by utilizing the crowding effect. *ACS Nano* 6 (7): 5837–5844.

25 Im, H., Kim, T., Song, H. et al. (2016). High-efficiency electrochemical thermal energy harvester using carbon nanotube aerogel sheet electrodes. *Nat. Commun.* 7 (1): 1–9.

26 Cao, A., Dickrell, P.L., Sawyer, W.G. et al. (2005). Super-compressible foamlike carbon nanotube films. *Science* 310 (5752): 1307–1310.

27 Talapatra, S., Kar, S., Pal, S. et al. (2006). Direct growth of aligned carbon nanotubes on bulk metals. *Nat. Nanotechnol.* 1 (2): 112–116.

28 Futaba, D.N., Hata, K., Yamada, T. et al. (2006). Shape-engineerable and highly densely packed single-walled carbon nanotubes and their application as super-capacitor electrodes. *Nat. Mater.* 5 (12): 987–994.

29 Duggal, R., Hussain, F., and Pasquali, M. (2006). Self-assembly of single-walled carbon nanotubes into a sheet by drop drying. *Adv. Mater.* 18 (1): 29–34.

30 Song, Y., Li, B., Yang, S. et al. (2015). Ultralight boron nitride aerogels via template-assisted chemical vapor deposition. *Sci. Rep.* 5: 10337.

31 Dong, X., Chen, J., Ma, Y. et al. (2012). Superhydrophobic and superoleophilic hybrid foam of graphene and carbon nanotube for selective removal of oils or organic solvents from the surface of water. *Chem. Commun.* 48 (86): 10660–10662.

32 Wang, W., Guo, S., Penchev, M. et al. (2013). Three dimensional few layer graphene and carbon nanotube foam architectures for high fidelity supercapacitors. *Nano Energy* 2 (2): 294–303.

33 Ozden, S., Macwan, I.G., Owuor, P.S. et al. (2017). Bacteria as bio-template for 3D carbon nanotube architectures. *Sci. Rep.* 7 (1): 1–8.

34 Wu, H.-C., Chang, X., Liu, L. et al. (2010). Chemistry of carbon nanotubes in biomedical applications. *J. Mater. Chem.* 20 (6): 1036–1052.

35 Li, Z., Tang, M., Dai, J. et al. (2016). Effect of multiwalled carbon nanotube-grafted polymer brushes on the mechanical and swelling properties of polyacrylamide composite hydrogels. *Polymer* 85: 67–76.

36 Li, G., Wang, H., Zheng, H., and Bai, R. (2010). A facile approach for the fabrication of highly stable superhydrophobic cotton fabric with multi-walled carbon nanotubes-azide polymer composites. *Langmuir* 26 (10): 7529–7534.

37 Li, Q., Liu, L., Liang, S. et al. (2013). Preparation and characterization of composite membranes with ionic liquid polymer-functionalized multiwalled carbon nanotubes for alkaline fuel cells. *RSC Adv.* 3 (32): 13477–13485.

38 Li, Z., Tang, M., Bai, W., and Bai, R. (2017). Preparation of hydrophilic encapsulated carbon nanotubes with polymer brushes and its application in composite hydrogels. *Langmuir* 33 (24): 6092–6101.

39 Samanta, S.K., Fritsch, M., Scherf, U. et al. (2014). Conjugated polymer-assisted dispersion of single-wall carbon nanotubes: the power of polymer wrapping. *Acc. Chem. Res.* 47 (8): 2446–2456.

40 Doe, C., Choi, S.M., Kline, S.R. et al. (2008). Charged rod-like nanoparticles assisting single-walled carbon nanotube dispersion in water. *Adv. Funct. Mater.* 18 (18): 2685–2691.

41 Hough, L., Islam, M., Janmey, P., and Yodh, A. (2004). Viscoelasticity of single wall carbon nanotube suspensions. *Phys. Rev. Lett.* 93 (16): 168102.

42 Kim, K.H., Oh, Y., and Islam, M.F. (2013). Mechanical and thermal management characteristics of ultrahigh surface area single-walled carbon nanotube aerogels. *Adv. Funct. Mater.* 23 (3): 377–383.

43 Schiffres, S.N., Kim, K.H., Hu, L. et al. (2012). Gas diffusion, energy transport, and thermal accommodation in single-walled carbon nanotube aerogels. *Adv. Funct. Mater.* 22 (24): 5251–5258.

44 Leroy, C., Cam, F., Backov, R. et al. (2007). Multiwalled-carbon-nanotube-based carbon foams. *Carbon (New York, NY)* 45 (11): 2317–2320.

45 Thongprachan, N., Nakagawa, K., Sano, N. et al. (2008). Preparation of macroporous solid foam from multi-walled carbon nanotubes by freeze-drying technique. *Mater. Chem. Phys.* 112 (1): 262–269.

46 Liu, Y., Ba, H., Nguyen, D.-L. et al. (2013). Synthesis of porous carbon nanotubes foam composites with a high accessible surface area and tunable porosity. *J. Mater. Chem. A* 1 (33): 9508–9516.

47 Qi, H., Liu, J., Pionteck, J. et al. (2015). Carbon nanotube-cellulose composite aerogels for vapour sensing. *Sens. Actuators, B* 213: 20–26.

48 Gnanaseelan, M., Chen, Y., Luo, J. et al. (2018). Cellulose-carbon nanotube composite aerogels as novel thermoelectric materials. *Compos. Sci. Technol.* 163: 133–140.

49 Park, O.-K. and Lee, J.H. (2018). Carbon nanotube-poly(vinyl alcohol) hybrid aerogels: improvements in the surface area and structural stability by internal morphology control. *Compos. Part B: Eng.* 144: 229–236.

50 Kohlmeyer, R.R., Lor, M., Deng, J. et al. (2011). Preparation of stable carbon nanotube aerogels with high electrical conductivity and porosity. *Carbon* 49 (7): 2352–2361.

51 Hu, P., Lyu, J., Fu, C. et al. (2019). Multifunctional aramid nanofiber/carbon nanotube hybrid aerogel films. *ACS Nano* 14 (1): 688–697.

52 Skaltsas, T., Avgouropoulos, G., and Tasis, D. (2011). Impact of the fabrication method on the physicochemical properties of carbon nanotube-based aerogels. *Micropor. Mesopor. Mater.* 143 (2–3): 451–457.

53 Whitby, R.L., Mikhalovsky, S.V., and Gun'ko, V.M. (2010). Mechanical performance of highly compressible multi-walled carbon nanotube columns with hyperboloid geometries. *Carbon* 48 (1): 145–152.

54 Hong, S.H., Tung, T.T., Kim, T.Y., and Suh, K.S. (2010). Preparation of single-walled carbon nanotube (SWNT) gel composites using poly (ionic liquids). *Colloid. Polym. Sci.* 288 (9): 1013–1018.

55 Zou, J., Liu, J., Karakoti, A.S. et al. (2010). Ultralight multiwalled carbon nanotube aerogel. *ACS Nano* 4 (12): 7293–7302.

56 Noparvar-Qarebagh, A., Roghani-Mamaqani, H., and Salami-Kalajahi, M. (2016). Organic–inorganic nanohybrids of novolac phenolic resin and carbon nanotube: high carbon yields by using carbon nanotube aerogel and resin incorporation into aerogel network. *Micropor. Mesopor. Mater.* 224: 58–67.

57 Zhang, Y., Shen, Y., Han, D. et al. (2006). Reinforcement of silica with single-walled carbon nanotubes through covalent functionalization. *J. Mater. Chem.* 16 (47): 4592–4597.

58 Zhang, Y., Broekhuis, A.A., Stuart, M.C. et al. (2008). Cross-linking of multiwalled carbon nanotubes with polymeric amines. *Macromolecules* 41 (16): 6141–6146.

59 Ozden, S., Narayanan, T.N., Tiwary, C.S. et al. (2015). 3D macroporous solids from chemically cross-linked carbon nanotubes. *Small* 11 (6): 688–693.

60 De Marco, M., Markoulidis, F., Menzel, R. et al. (2016). Cross-linked single-walled carbon nanotube aerogel electrodes via reductive coupling chemistry. *J. Mater. Chem. A* 4 (15): 5385–5389.

61 Duque, J.G., Hamilton, C.E., Gupta, G. et al. (2011). Fluorescent single-walled carbon nanotube aerogels in surfactant-free environments. *ACS Nano* 5 (8): 6686–6694.

62 Dong, X., Cao, L., Si, Y. et al. (2020). Cellular structured CNTs@SiO_2 nanofibrous aerogels with vertically aligned vessels for salt-resistant solar desalination. *Adv. Mater.* 32 (34): 1908269.

63 Kim, K.H., Vural, M., and Islam, M.F. (2011). Single-walled carbon nanotube aerogel-based elastic conductors. *Adv. Mater.* 23 (25): 2865–2869.

64 Peng, Q., Li, Y., He, X. et al. (2014). Graphene nanoribbon aerogels unzipped from carbon nanotube sponges. *Adv. Mater.* 26 (20): 3241–3247.

65 Parmar, K.R., Dora, D., Pant, K., and Roy, S. (2019). An ultra-light flexible aerogel-based on methane derived CNTs as a reinforcing agent in silica-CMC matrix for efficient oil adsorption. *J. Hazard. Mater.* 375: 206–215.

66 Lamy-Mendes, A., Silva, R.F., and Durães, L. (2018). Advances in carbon nanostructure-silica aerogel composites: a review. *J. Mater. Chem. A* 6 (4): 1340–1369.

67 Tang, M., Wang, W., Xu, D., and Wang, Z. (2016). Synthesis of structure-controlled polyborosiloxanes and investigation on their viscoelastic response to molecular mass of polydimethylsiloxane triggered by both chemical and physical interactions. *Ind. Eng. Chem. Res.* 55 (49): 12582–12589.

68 Tang, M., Zheng, P., Wang, K. et al. (2019). Autonomous self-healing, self-adhesive, highly conductive composites based on a silver-filled polyborosiloxane/polydimethylsiloxane double-network elastomer. *J. Mater. Chem. A* 7 (48): 27278–27288.

69 Tang, M., Wu, J., Wang, K. et al. (2020). Preparation of autonomously self-healing electrode based on double network supramolecular elastomer. *2020 IEEE 70th Electronic Components and Technology Conference (ECTC)*, 2247–2251. IEEE.

70 Liu, S., Chevali, V.S., Xu, Z. et al. (2018). A review of extending performance of epoxy resins using carbon nanomaterials. *Composites Part B* 136: 197–214.

71 Li, Y., Dong, L., Zhang, X. et al. (2015). Preparation of carbon nanotubes/epoxy composites using novel aerogel substrates. *Mater. Lett.* 160: 432–435.

72 Najafi-Shoa, S., Roghani-Mamaqani, H., Salami-Kalajahi, M. et al. (2016). Incorporation of epoxy resin and carbon nanotube into silica/siloxane network for improving thermal properties. *J. Mater. Sci.* 51 (19): 9057–9073.

73 Haghgoo, M., Yousefi, A.A., Mehr, M.J.Z. et al. (2015). Correlation between morphology and electrical conductivity of dried and carbonized multi-walled carbon nanotube/resorcinol-formaldehyde xerogel composites. *J. Mater. Sci.* 50 (18): 6007–6020.

74 Worsley, M.A., Pauzauskie, P.J., Kucheyev, S.O. et al. (2009). Properties of single-walled carbon nanotube-based aerogels as a function of nanotube loading. *Acta Mater.* 57 (17): 5131–5136.

75 Kim, J.H., Lee, D., Lee, Y.H. et al. (2019). Nanocellulose for energy storage systems: beyond the limits of synthetic materials. *Adv. Mater.* 31 (20): 1804826.

76 Jiang, B., He, Y., Li, B. et al. (2017). Polymer-templated formation of polydopamine-coated SnO_2 nanocrystals: anodes for cyclable lithium–ion batteries. *Angew. Chem. Int. Ed.* 56 (7): 1869–1872.

77 Pang, X., He, Y., Jung, J., and Lin, Z. (2016). 1D nanocrystals with precisely controlled dimensions, compositions, and architectures. *Science* 353 (6305): 1268–1272.

78 Fu, L.-H., Qi, C., Ma, M.-G., and Wan, P. (2019). Multifunctional cellulose-based hydrogels for biomedical applications. *J. Mater. Chem. B* 7 (10): 1541–1562.

79 Abdul Khalil, H., Adnan, A., Yahya, E.B. et al. (2020). A review on plant cellulose nanofibre-based aerogels for biomedical applications. *Polymers* 12 (8): 1759.

80 Wang, M., Anoshkin, I.V., Nasibulin, A.G. et al. (2013). Modifying native nanocellulose aerogels with carbon nanotubes for mechanoresponsive conductivity and pressure sensing. *Adv. Mater.* 25 (17): 2428–2432.

81 Huang, H.-D., Liu, C.-Y., Zhou, D. et al. (2015). Cellulose composite aerogel for highly efficient electromagnetic interference shielding. *J. Mater. Chem. A* 3 (9): 4983–4991.

82 Qi, H., Mäder, E., and Liu, J. (2013). Electrically conductive aerogels composed of cellulose and carbon nanotubes. *J. Mater. Chem. A* 1 (34): 9714–9720.

83 Du, X., Qiu, J., Deng, S. et al. (2020). Alkylated nanofibrillated cellulose/carbon nanotubes aerogels supported form-stable phase change composites with improved n-alkanes loading capacity and thermal conductivity. *ACS Appl. Mater. Interfaces* 12 (5): 5695–5703.

84 Cheng, P., Gao, H., Chen, X. et al. (2020). Flexible monolithic phase change material based on carbon nanotubes/chitosan/poly (vinyl alcohol). *Chem. Eng. J.* 397 (6): 125330.

85 Luo, Q., Zheng, H., Hu, Y. et al. (2019). Carbon nanotube/chitosan-based elastic carbon aerogel for pressure sensing. *Ind. Eng. Chem. Res.* 58 (38): 17768–17775.

86 Worsley, M.A., Kucheyev, S.O., Kuntz, J.D. et al. (2011). Carbon scaffolds for stiff and highly conductive monolithic oxide–carbon nanotube composites. *Chem. Mater.* 23 (12): 3054–3061.

87 Li, Y., Liu, X., Nie, X. et al. (2019). Multifunctional organic-inorganic hybrid aerogel for self-cleaning, heat-insulating, and highly efficient microwave absorbing material. *Adv. Funct. Mater.* 29 (10): 1807624.

88 Jia, X., Wang, J., Zhu, X. et al. (2017). Synthesis of lightweight and flexible composite aerogel of mesoporous iron oxide threaded by carbon nanotubes for microwave absorption. *J. Alloys Compd.* 697: 138–146.

89 Adebayo, L.L., Soleimani, H., Yahya, N. et al. (2020). Recent advances in the development of Fe_3O_4-based microwave absorbing materials. *Ceram. Int.* 46 (2): 1249–1268.

90 Li, Z., Tang, M., Jiang, C. et al. (2018). Photoinduced reversible morphological transformation of azobenzene-containing pseudo-2D polymers. *Macromol. Rapid Commun.* 39 (11): 1700880.

91 Ferrari, A.C., Bonaccorso, F., Fal'Ko, V. et al. (2015). Science and technology roadmap for graphene, related two-dimensional crystals, and hybrid systems. *Nanoscale* 7 (11): 4598–4810.

92 Sun, H., Xu, Z., and Gao, C. (2013). Multifunctional, ultra-flyweight, synergistically assembled carbon aerogels. *Adv. Mater.* 25 (18): 2554–2560.

93 Sui, Z., Meng, Q., Zhang, X. et al. (2012). Green synthesis of carbon nanotube-graphene hybrid aerogels and their use as versatile agents for water purification. *J. Mater. Chem.* 22 (18): 8767–8771.

94 Tan, D., Zhao, J., Gao, C. et al. (2017). Carbon nanoparticle hybrid aerogels: 3d double-interconnected network porous microstructure, thermoelectric, and solvent-removal functions. *ACS Appl. Mater. Interfaces* 9 (26): 21820–21828.

95 Fu, Z., Wang, N., Legut, D. et al. (2019). Rational design of flexible two-dimensional MXenes with multiple functionalities. *Chem. Rev.* 119 (23): 11980–12031.

96 Sambyal, P., Iqbal, A., Hong, J. et al. (2019). Ultralight and mechanically robust Ti3C2T×hybrid aerogel reinforced by carbon nanotubes for electromagnetic interference shielding. *ACS Appl. Mater. Interfaces* 11 (41): 38046–38054.

97 Wang, J., Zhang, Z., Yan, X. et al. (2020). Rational design of porous N-Ti_3C_2 MXene@CNT microspheres for high cycling stability in Li-S battery. *Nano-Micro Lett.* 12 (1): 4.

98 Chandrashekara, M. and Yadav, A. (2017). Water desalination system using solar heat: a review. *Renew. Sustain. Energy Rev.* 67: 1308–1330.

99 Zhao, F., Zhou, X., Shi, Y. et al. (2018). Highly efficient solar vapour generation via hierarchically nanostructured gels. *Nat. Nanotechnol.* 13 (6): 489–495.

100 Qin, D.-D., Zhu, Y.-J., Chen, F.-F. et al. (2019). Self-floating aerogel composed of carbon nanotubes and ultralong hydroxyapatite nanowires for highly efficient solar energy-assisted water purification. *Carbon* 150: 233–243.

101 Jiang, F., Liu, H., Li, Y. et al. (2018). Lightweight, mesoporous, and highly absorptive all-nanofiber aerogel for efficient solar steam generation. *ACS Appl. Mater. Interfaces* 10 (1): 1104–1112.

102 Gupta, S. and Tai, N.-H. (2016). Carbon materials as oil sorbents: a review on the synthesis and performance. *J. Mater. Chem. A* 4 (5): 1550–1565.

103 Khoshnevis, H., Mint, S.M., Yedinak, E. et al. (2018). Super high-rate fabrication of high-purity carbon nanotube aerogels from floating catalyst method for oil spill cleaning. *Chem. Phys. Lett.* 693: 146–151.

104 Kabiri, S., Tran, D.N., Altalhi, T., and Losic, D. (2014). Outstanding adsorption performance of graphene–carbon nanotube aerogels for continuous oil removal. *Carbon* 80: 523–533.

105 Wan, W., Zhang, R., Li, W. et al. (2016). Graphene-carbon nanotube aerogel as an ultra-light, compressible and recyclable highly efficient absorbent for oil and dyes. *Environ. Sci.: Nano* 3 (1): 107–113.

106 Simon, P. and Gogotsi, Y. (2020). Perspectives for electrochemical capacitors and related devices. *Nat. Mater.* 19 (11): 1151–1163.

107 Ye, S., Feng, J., and Wu, P. (2013). Deposition of three-dimensional graphene aerogel on nickel foam as a binder-free supercapacitor electrode. *ACS Appl. Mater. Interfaces* 5 (15): 7122–7129.

108 González, A., Goikolea, E., Barrena, J.A., and Mysyk, R. (2016). Review on supercapacitors: technologies and materials. *Renew. Sustain. Energy Rev.* 58: 1189–1206.

109 Li, Y., Kang, Z., Yan, X. et al. (2018). A three-dimensional reticulate CNT-aerogel for a high mechanical flexibility fiber supercapacitor. *Nanoscale* 10 (19): 9360–9368.

110 Fan, W., Shi, Y., Gao, W. et al. (2018). Graphene-carbon nanotube aerogel with a scroll-interconnected-sheet structure as an advanced framework for a high-performance asymmetric supercapacitor electrode. *ACS Appl. Nano Mater.* 1 (9): 4435–4441.

111 Pan, Z., Liu, M., Yang, J. et al. (2017). High electroactive material loading on a carbon nanotube@3D graphene aerogel for high-performance flexible all-solid-state asymmetric supercapacitors. *Adv. Funct. Mater.* 27 (27): 1701122.

112 Zheng, Q., Cai, Z., Ma, Z., and Gong, S. (2015). Cellulose nanofibril/reduced graphene oxide/carbon nanotube hybrid aerogels for highly flexible and all-solid-state supercapacitors. *ACS Appl. Mater. Interfaces* 7 (5): 3263–3271.

113 Zhao, S., Sewell, C.D., Liu, R. et al. (2020). SnO_2 as advanced anode of alkali-ion batteries: inhibiting Sn coarsening by crafting robust physical barriers, void boundaries, and heterophase interfaces for superior electrochemical reaction reversibility. *Adv. Energy Mater.* 10 (6): 1902657.

114 Wang, Y., Kong, D., Shi, W. et al. (2016). Ice templated free-standing hierarchically WS_2/CNT-rGO aerogel for high-performance rechargeable lithium and sodium ion batteries. *Adv. Energy Mater.* 6 (21): 1601057.

115 Cui, J., Yao, S., Huang, J.-Q. et al. (2017). Sb-doped SnO_2/graphene-CNT aerogels for high performance Li-ion and Na-ion battery anodes. *Energy Storage Mater.* 9: 85–95.

116 He, J., Chen, Y., Lv, W. et al. (2016). Three-dimensional CNT/graphene-Li_2S aerogel as freestanding cathode for high-performance Li-S batteries. *ACS Energy Lett.* 1 (4): 820–826.

117 Chen, Y., Liu, S., Yuan, X. et al. (2020). rGO-CNT aerogel embedding iron phosphide nanocubes for high-performance Li-polysulfide batteries. *Carbon* 167 (15): 446–454.

118 Hu, L., Wu, H., Gao, Y. et al. (2011). Silicon-carbon nanotube coaxial sponge as Li-ion anodes with high areal capacity. *Adv. Energy Mater.* 1 (4): 523–527.

119 Wang, Y., Ma, Z., Chen, Y. et al. (2016). Controlled synthesis of core-shell carbon@MoS_2 nanotube sponges as high-performance battery electrodes. *Adv. Mater.* 28 (46): 10175–10181.

120 Wang, Z., Wang, Y., Chen, Y. et al. (2019). Reticulate dual-nanowire aerogel for multifunctional applications: a high-performance strain sensor and a high areal capacity rechargeable anode. *Adv. Funct. Mater.* 29 (11): 1807467.

121 Cai, B. and Eychmüller, A. (2019). Promoting electrocatalysis upon aerogels. *Adv. Mater.* 31 (31): 1804881.

122 Wang, H., Shao, Y., Mei, S. et al. (2020). Polymer-derived heteroatom-doped porous carbon materials. *Chem. Rev.* 120 (17): 9363–9419.

123 Cui, X., Gao, L., Lei, S. et al. (2020). Simultaneously crafting single-atomic Fe sites and graphitic layer-wrapped Fe_3C nanoparticles encapsulated within mesoporous carbon tubes for oxygen reduction. *Adv. Funct. Mater.* 2009197.

124 Ni, D., Sun, W., Wang, Z. et al. (2019). Heteroatom-doped mesoporous hollow carbon spheres for fast sodium storage with an ultralong cycle life. *Adv. Energy Mater.* 9 (19): 1900036.

125 Zhang, C., Ma, B., and Zhou, Y. (2019). Three-dimensional polypyrrole derived N-doped carbon nanotube aerogel as a high-performance metal-free catalyst for oxygen reduction reaction. *ChemCatChem* 11 (22): 5495–5504.

126 Zeng, S., Chen, H., Wang, H. et al. (2017). Crosslinked carbon nanotube aerogel films decorated with cobalt oxides for flexible rechargeable Zn-air batteries. *Small* 13 (29): 1700518.

7

Silica-Based Aerogels for Building Transparent Components

Cinzia Buratti[1], Elisa Belloni[1], Francesca Merli[1], Costanza Vittoria Fiorini[2], Piergiovanni Domenighini[1], and Michele Zinzi[3]

[1] *Department of Engineering – University of Perugia, Via G. Duranti 67, 06125, Perugia, Italy*
[2] *DIAEE Department of Astronautical, Electrical, and Energy Engineering, "Sapienza" University of Rome, Via Eudossiana 18, 00184, Rome, Italy*
[3] *ENEA, Centro Ricerche Casaccia, Via Anguillarese, 301, 00123, Rome, Italy*

7.1 Introduction

Silica aerogels are widely studied in the literature, especially as transparent/translucent solutions. They are available in two forms: granular and monolithic. The former is translucent and it is present on the market in different granule sizes, with different applications. The latter is transparent and therefore more suitable for applications as insulating material in buildings' glazing systems, but it is no longer available as a commercial product.

This chapter provides an overview of transparent/translucent silica aerogels both in granular and monolithic form is presented, starting from the description of the production process and highlighting the difference between the different forms. Then a synthesis of the main physical properties is reported: mechanical, thermal, optical, and acoustic characteristics. Finally, energy performance of aerogels incorporated in building glazing systems is described and an overview of the main applications is provided.

7.2 Silica Aerogels Production

Less than 100 years ago, on April 8, 1931, Kistler published on *Nature* [1] a paper titled "Coherent Expanded Aerogels and Jellies," the first one about a new material: aerogel. The challenge was to replace with a gas the liquid present in a jelly, trying to avoid shrinkage. In this first paper he briefly described the fabrication process: A jelly is first formed and then the liquid in the jelly is replaced by another one, completely miscible and characterized by a low critical temperature that avoids dissolving the structure of the gel. In an autoclave with excess of liquid, the jelly is heated above the critical temperature and at or above the vapor pressure of the liquid. In this way, gel collapse is avoided because evaporation does not occur and capillary forces at its surface are not generated, also avoiding contraction. The liquid directly becomes a gas, which fills the gel without

Aerogels for Energy Saving and Storage, First Edition. Edited by Meldin Mathew, Hanna J. Maria, Ange Nzihou, and Sabu Thomas.
© 2024 John Wiley & Sons, Inc. Published 2024 by John Wiley & Sons, Inc.

compressive forces, resulting in "aerogel," a porous solid material with approximately the same volume of the gel [1, 2].

The liquid extraction process brought the first great scission on this kind of materials. A large-scale shrinkage of the network structure defines xerogels, and they have been definitely distinguished from aerogels [3]. Kristler supposed and experimented different kinds of aerogel, even very exotic (tungstenic, ferric or nickel tartrate) [4]. Replacing water with ethanol, Kristler initiated the maintenance of the monolithical character of the gel and monolithic silica aerogel born. Kristler's final efforts were to create aerogel with mechanical-rubber-behavior [5]. Then more efficient precursors were selected: alkoxides were preferable to metallic salts because they are often available in solution in their parent alcohol, making possible the direct drying process. From 1986, the goal of transparency intensified the research and led to important improvements on the material synthesis: tetraethylorthosilicate (TEOS) replaced the tetramethylorthosilicate (TMOS) and acidic catalysts (HF and HCl) were used instead the basic one (mainly NH_2OH). In fact, researchers discovered that HCl addition in the sol-gel step made the aerogel transparent [6].

A few years later, Tewari [7] improved the supercritical drying (SCD) process by replacing CO_2 in alcohols for its lower critical temperature (31 °C) and its chemical inertial behavior. Later studies confirmed the supremacy of TEOS precursors due to their homogeneity in particle and pore size. Although these were important improvements, a revolution occurred in 1992 when a two-step aerogel synthesis was formulated and tested [8]. Researchers introduced a room-temperature reaction in presence of ammonia base of a condensed silica mixture. This allowed a better control of hydrolysis and polymerization. The created two-step silica showed a fine-filaments chain-like microstructure, with average diameter of 2 nm and a 20 nm length. A few years later, TEOS precursor was involved in a new CO_2 and organic dried monolithic aerogels, with sulfuric acid at the first step and fluoric acid at the second step. This new aerogel showed significant improvements in transparency in the whole light spectrum [9]. The last part of the decade was characterized by the confirm of the negative effect of the sodium and potassium ion. A new challenge galvanized researchers from the first years of the new millennium: hydrophobicity. Although improvements were carried out thanks to different conditions of post-heating processes to arise hydrophobicity maintaining transparency [10, 11], this is still a challenging field of study. Besides this property, more recent developments involve different aspects of aerogels like the gel preparation (new supercritical extraction process in pressurize conditions [12] or slow deportation Gash's technique [13]), new hybrid organic-inorganic aerogels, and even their luminescent and magnetic properties [14, 15], leading to new functions and new future developments in an always wider range of applications.

7.2.1 Preparation Steps

Despite the several progresses made since 1930s, the main steps of the aerogels production process are the same [2]: gel preparation, aging, and drying, as shown in Figure 7.1:

1) Gel preparation, in which the solid nanoparticles precursors are dispersed into a liquid; there an agglomeration process led to form a three-dimensional network extending throughout the liquid.
2) Aging, in which acts a homogenous nucleation process of the gel in its previous solution; the aim is to transport material to the neck region of the network and to dissolve small particles into larger ones. This represents a necessary step for preventing shrinkage during the drying phase.

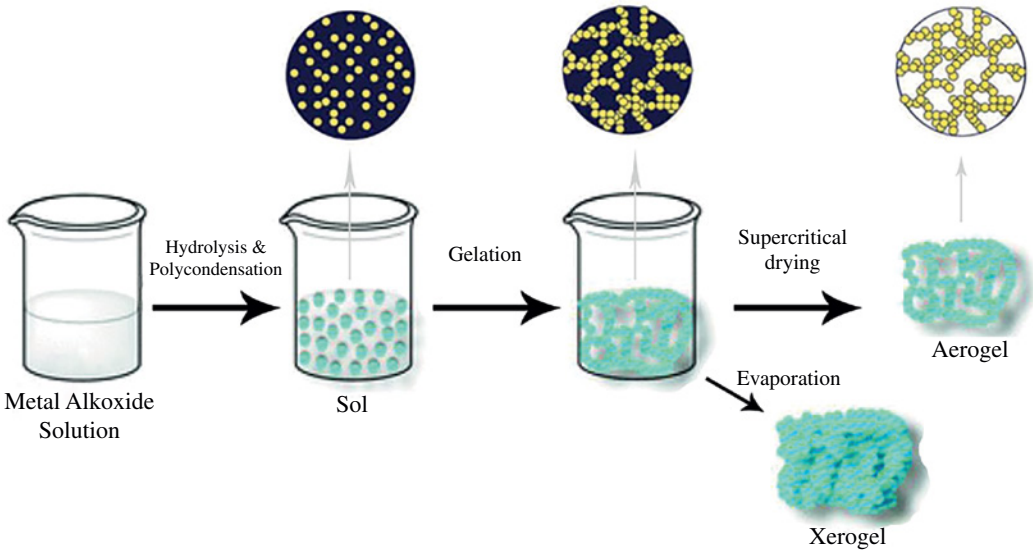


Figure 7.1 General creation steps for aerogels. After gelation process, supercritical drying determines aerogels, uncontrolled evaporation determines lattice fractures that characterize Xerogels.

3) Drying, the most critical step, in which the liquid is replaced by air; in order to avoid shrinkage and collapse of the solid structure. It occurs at supercritical conditions; otherwise, if the drying process occurs at ambient pressure (evaporation), it results in a xerogel [16], which generally cracks and shrinks during drying (Figure 7.1).

By drying at ambient pressure, it is possible to obtain aerogel granulate and powder, a semi-product that is transformed into granular translucent silica aerogel after a few more preparation steps [5]. It is important to highlight that granular silica aerogel is different from xerogel: granular aerogel has a shrinkage less than 15%, while xerogel has a shrinkage higher than 90% [17].

The synthesis of silica aerogel is reviewed in [17] by Dorcheh and Abbasi; the following sections briefly describe the main steps of the process [18–21].

7.2.1.1 Precursors

Many precursors have been used from the discovery of aerogel until today and the material's properties are affected by the nature of these precursors [22]. They are comprised of inorganic and organic matter and there are a wide variety of silicon-containing precursors that can be employed for the fabrication of silica aerogels. The most used, for both monolithic and granular forms, are silicon alkoxides: tetramethyl orthosilicate (TMOS) or tetraethyl orthosilicate (TEOS), in general base-catalyzed with ammonia [5, 23–25]; polyethoxydisiloxane (PEDS-Px) [26] is also often used as a precursor, which can be obtained from TEOS reacting with water in an acidic alcoholic medium. In order to obtain hydrophobic aerogels, TMOS can be replaced with a mixture of TMOS and one organosilane co-precursor, such as methytrimethoxysilane (MTMS), ethyltrimethoxysilane (ETMS), or propyltrimeth-oxysilane (PTMS), resulting in more hydrophobic and less transparent aerogels when the amount of co-precursor is increased, without affecting thermal conductivity [27]. When using methyltriethoxysilane (MTES) as co-precursor with different MTES/TEOS molar ratios, the volume shrinkage can be controlled, affecting transparency and

hydrophobicity; in particular, low contents of MTES result in high transparency and negligible shrinkage, but low hydrophobicity [28]. Silica aerogels were also obtained from rice husk ash [29].

The last generation of aerogels aims to improve the mechanical robustness and to make flexible aerogels, by adding polymeric substances. In particular, the polymeric network could be crosslinked with organosilica precursors (especially ethylene-bridged precursors) and various flexible polymeric networks, including melamine-formaldehyde and resorcinol-formaldehyde. By adding various cellulose derivatives and cellulose nanofibers, highly transparent and flexible composite aerogels can be obtained, featuring enhanced mechanical robustness, tunable optical anisotropy, and low thermal conductivity, with also a reduction in production costs [30]. Thin superflexible aerogels can also be obtained starting from polyvinylpolydimethylsiloxane (PVPDMS) networks, VPDMS/polyvinylpolymethylsiloxane (PVPMS) copolymer networks, and PVPDMS/P VPMS/graphene nanocomposites. Aerogels result in a doubly crosslinked organic–inorganic network structure, consisting of flexible polydimethylsiloxanes and hydrocarbon chains, with tunable cross-linking density, pore size, and bulk density, characterized by high hydrophobicity and superflexibility, selective absorption, and low thermal conductivity [31]. As silica aerogels are very brittle, in a recent study [32] a polymer was applied over their skeletal framework (TMOS +3-aminopropyltriethoxysilane [APTES] + triisocyanate) allowing researchers to obtain samples strong enough to be machined with conventional tools, such as band saws or diamond cutters.

7.2.1.2 Gel Preparation

The hydrolysis of the silicon-containing precursor is the first stage in the formation of the sol-gel matrix from a silicon alkoxide. It is performed with a catalyst and, due to the insolubility of silicon alkoxides in water, precursor recipes include an alcohol (in general methanol or ethanol) able to enhance solubility, and an acid or base to catalyze the hydrolysis reaction. Depending on how many catalysts are used, the sol-gel method can be a one-step or a two-step process [25]: in the one-step process, either aqueous acidic or basic catalyst is added, whereas in the two-step process, both acidic and basic catalysts are used in different stages. After the hydrolysis of some of the alkoxy groups, condensation reactions occur in multiple directions. Clusters of silica form, resulting in a colloidal solution (sol), which becomes a gel when the solid nanoparticles dispersed in it stick together to form a porous, amorphous network polymer (gel). The process needs the collision in the liquid of the nanoparticles with each other; it is facilitated if nanoparticles contain reactive surface groups, which make them stick together by bonding or electrostatic forces, whereas, in absence, an additive could be necessary. Acid hydrolysis and condensation result in weakly branched chains, with long gelation times, whereas in base catalysis uniform particles are easily formed, leading to a broader distribution of larger pores, but less favorable for thermal insulation materials (TIMs).

Alkoxides are expensive precursors, prohibiting silica aerogels mass production and widespread application as construction materials at large scale; the use of water glass or sodium silicate Na_2SiO_3 as raw material can reduce production costs. Another way for production cost reduction is the use of polyethoxydisiloxane (PEDS) as precursor, which requires only the addition of a base catalyst to form an alcogel, which can be directly dried into a transparent aerogel [33].

7.2.1.3 Aging

During hydrolysis and condensation, the gel still contains a significant number of unreacted alkoxide groups, so more time is necessary for the strengthening of the silica network. During this aging phase of the process, material is transported to the neck region and small particles are dissolved into larger ones. pH, sol concentration, and water content should be controlled, affecting aging

time (in the TEOS/ethanol solution time, decreases by increasing pH prior to aging) and the properties of the final aerogels. After aging, water is still present within the pores of the gel and will not be removed during the drying step; therefore, washing with ethanol and/or heptane is necessary, in order to avoid obtaining an opaque and dense aerogel as the final product. When using n-heptane as solvent, lower shrinkage than with acetone and ethanol is obtained in the following drying stage, due to the lower surface tension of n-heptane with respect to the two other solvents. Ethanol–siloxane mixtures allow to add new monomers to the solid silica network and to increase the degree of cross-linking, resulting in a higher stiffness and strength of the gel [16, 18]. Washing and aging significantly improve permeability and mechanical properties of the wet gels, although the process scale-up induces severe cracks during SCD, due to the pore-size distribution gradient between the surface and the bulk of the gel. Less-concentrated polyethoxydisiloxane solutions result in gels with a more homogeneous pore-size distribution and large aerogels monoliths crack-free, light, and transparent [34].

7.2.1.4 Drying

A critical step is to maintain the original structure of the wet sol-gel solution during the liquid replacement by the air, and it represents a fundamental step to the aim of aerogel obtaining from sol-gel solution. Therefore, the solvent mixture must be removed without structural collapse during the final and most critical step of the process: the drying phase. The increased surface tension makes this step particularly critical because shrinking and fractures can occur in this stage. We report the main drying techniques: ambient pressure drying (APD), freeze drying (FD), and SCD (Figure 7.2) [20, 21, 35].

7.2.1.4.1 Ambient Pressure Drying (APD) In this method, the surface of the wet gel is chemically modified by substituting hydrophobic functional groups; H is replaced by hydroxyl groups and drying is performed by evaporation at ambient pressure, crossing the liquid-vapor phase line (see Figure 7.2, dashed line). In order to reduce the effects of surface tension, a solvent exchange with a chemical (i.e. hexane) and a treatment with a silylating agent (i.e. trimethylchlorosilane (TMCS), hexamethyldisiloxane (HMDSO) or hexamethyldisilazane (HMDZ)) occur, promoting reversible

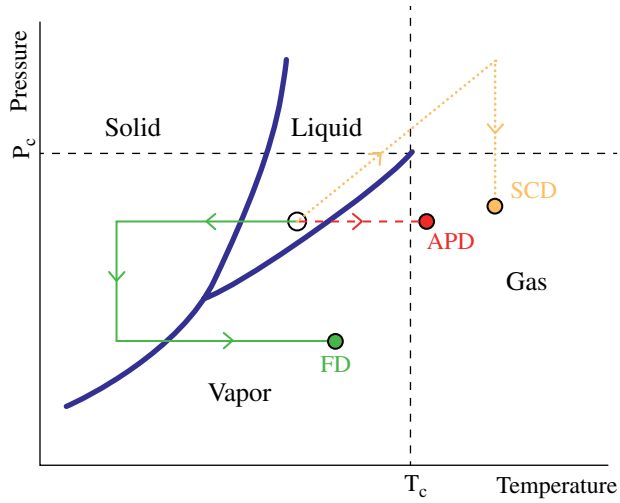


Figure 7.2 State diagram of polyethoxydisiloxane solution and the three possible way to extract the solution: by ambient pressure drying (APD, dashed line), by freeze drying (FD, dark gray line) and by supercritical drying (SCD, dotted line).

shrinkage. The APD protocol imposes on the weak fresh gel a strain that does not allow it to survive; this is why the involved shrinkage process led to a small aggregation of silica particles into granulates or powder.

APD is a low-cost and safe drying process, not requiring expensive and high-pressure, high-temperature equipment. However, multiple processing steps with solvent exchange are necessary and process time is long. APD technique was used for the synthesis of silica–titania mixed oxide aerogels, amorphous and with surface areas and mesopore volumes ideal for catalytic applications [36]. In [37] it was demonstrated that monoliths could be obtained over the entire range of pressure, from atmospheric to supercritical conditions; furthermore, a threshold subcritical pressure above which gels will undergo minimal shrinkage was found.

7.2.1.4.2 Freeze Drying (FD) The pore liquid is frozen and then sublimed in vacuum, so that the liquid-vapor phase line is not crossed (Figure 7.2, dotted lines), but a long aging period is necessary in order to stabilize the gel network; a solvent with lower expansion coefficient and higher sublimation pressure must replace the liquid. The wet gel is frozen and placed in an environment at subambient pressure, then it is heated to room temperature and the solvent is removed from the pores through sublimation. In general, freeze drying resulted in the fabrication of powders, but recently also monoliths were obtained (cellulose-based monolithic aerogels or by the addition of gelatin and chitosan), but they are not translucent.

7.2.1.4.3 Supercritical Drying (SCD) SCD is the drying method used by Kistler in 1931 and it is also the first historically used [1, 2]; thanks to its efficiency, it is also the most used nowadays. This method allows to avoid crossing the liquid-vapor phase line, such as in the freeze drying, but in this case, in order to eliminate surface tension effects, the solvent in the wet-gel pores is brought at supercritical conditions. This is why SCD is the main way in order to obtain monolithic silica aerogel rather than granular silica aerogel. The drying process consists in three steps: the wet gel is heated and pressurized to supercritical conditions, then the supercritical fluid is released when the fluid is depressurized at constant temperature, until the pressure reaches atmospheric value, and finally the solid is cooled to ambient temperature (Figure 7.2, dark gray lines).

Depending on the solvent used in the process, SCD can occur at low temperature or at high temperature, affecting the chemical composition and structure of aerogels [38]:

- Low-temperature CO_2 supercritical extraction (CSCE). CO_2 is used as solvent; it has a supercritical pressure similar to the one of the typical solvents used in aerogel fabrication, but a much lower supercritical temperature, close to ambient temperature (31 °C). Nevertheless, it requires a series of solvent exchanges to replace the solvent in the pores of the wet gel with liquid CO_2 prior to extraction. The preparation of the wet gel must be followed by an aging period and must be soaked in various nonpolar solvents to remove the water and alcohol by-products of the polymerization reaction, for facilitating exchange with CO_2. The main advantage of CO_2 drying is the low critical temperature and nonflammability, resulting in a safer step; it results in high-quality, transparent silica aerogel monoliths. On the other hand, it takes a long time for the solvent-exchange steps and a significant amount of solvent and CO_2 waste are generated.
- High-temperature alcohol supercritical extraction (ASCE). An alcohol is used as solvent, most frequently methanol. This method is characterized by a relatively fast processing time, going directly from wet gel to aerogel without solvent exchange, despite high-temperature release of relatively large quantities of a flammable chemical occurs, which can lead to explosions; it has been found the most appropriate method to minimize the shrinkage of the gel.

7.2.2 Rapid Extraction Methods

Aerogel synthesis is a time-consuming process. In fact, as highlighted by Bertino in a complete review of the different rapid extraction methods [39], the solvent replacement by air in a nanoscale porous material is reasonably very slow because the high tortuosity of the paths the extracted liquid has to follow.

Fortunately, efforts were made in order to accelerate the solvent exchanges; besides the initial proposal to reduce the number of exchanges, the best discovered solution was to use alcohols (like methanol, ethanol, acetone, and acetonitrile) as supercritical dry solvent due to their more advantageous characteristics: a critical temperature above 250 °C and a critical pressure of 60 atm. These conditions are relatively easy to be reached. In general, a confined configuration of the mold during both heating and cooling steps is used, then the precursors are poured and mixed. Thanks to a hydraulic hot press, alcohol is high-temperature extracted in a pressure vessel.

Rapid methods similar to the ASCE one proposed in [40–43] are, a confined mold houses the wet gel in the pressure vessel, with a faster processing, but with excess of solvent. In other cases [44–46] (m)ethanol is used in the drying dip, also without solvent exchange but in order to avoid monolith cracking heating and venting speeds need to be carefully controlled.

There also exists the possibility to reach the supercritical state without an excess of solvent; these rapid methods are safer than the ASCE methods and they were developed at Lawrence Livermore National Laboratory (LLNL, CA, USA) [40, 46] and at Union College (NY, USA, Figure 7.3) [47–52].

At LLNL a Rapid Supercritical Extraction (RSCE) process was developed at the end of the 1990s. In order to prepare silica aerogels in hours rather than days; silica aerogels with improved mechanical properties and slightly lower surface areas than the conventionally dried ones were obtained,

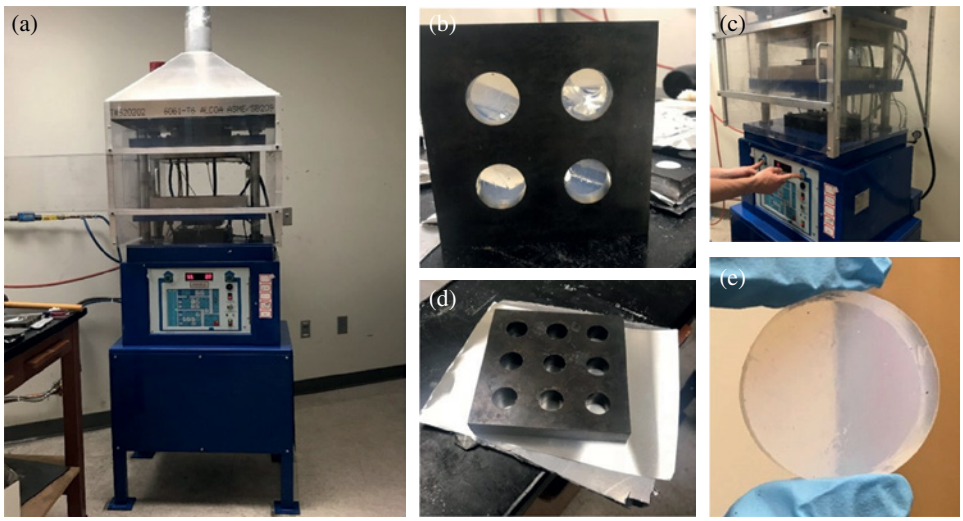


Figure 7.3 The laboratory instrumentation and synthesis's steps for aerogel at Union College. (a) Supercritical extraction machine; (b) silica aerogel mold with an aluminum and graphene sheets; (c) mold preparation and supercritical extraction machine configuration; (d) silica aerogel mold after the extraction; (e) monolithic silica aerogel. *Source:* Original pictures taken by F. Merli.

without compromising optical and thermal performance [40]. In the process, TMOS was used as precursor and ammonia as base catalyst. The liquid sol was poured in a stainless-steel mold placed in an evacuated chamber, with a pressure relief valve; it was immediately heated to supercritical conditions and gelation and aging occur during heating, with high reaction rates due to high temperatures. The gel completely filled the container, enabling relatively fast venting of the supercritical fluid, by providing a constraint for swelling and failure of the gel monolith. The whole process lasted less than an hour [46].

The Union College RSCE aerogel fabrication method was developed since 2004 [47] and patented in 2008 [48]. It is an alcohol high-temperature supercritical extraction technique and allows the fabrication of aerogel monoliths in hours rather than days to weeks required by other methods. Chemical precursors are mixed and poured directly into a metal mold of different dimensions and shapes; the mold is placed between the platens of a hydraulic hot press. After closing the hot press, in order to seal the mixture, a compressive restraining force is provided. Then the mold and the mixture are brought above the supercritical temperature of the alcohol (typically methanol) at a specified rate. During the heating process, the chemicals react and form a gel, which strengthens and ages. When the hot press force is decreased, the supercritical fluid is released and the aerogel is formed inside the mold which, together with the aerogel inside, is cooled to ambient temperature. At the end of the process, the press opens and monolithic aerogels are removed from the mold. This RSCE method is not very time demanding, typically requiring 15–20 minutes preparation time followed by 3–8 hours processing time. Relatively little solvent waste is generated during the process, thanks to the absence of solvent exchanges. Automation and scale-up of the method are possible because hydraulic hot presses are available in many sizes, from benchtop systems to production line equipment; the Union RSCE method typically uses TEOS instead of TMOS as precursor, which is less expensive, despite the process being only 1 hour longer [49, 51]. When compared to CO_2 extraction processes, it requires an investment in equipment not typically found in chemistry-intensive laboratory settings and safety considerations due to the presence of alcohol at high temperature. Nevertheless, it is safer than other high-temperature alcohol-based SCE processes, not requiring excess solvent and being the hot press able to contain supercritical gases and to release as needed. In 2016 [52], the Union RSCE method was scaled up for preparation of larger, highly translucent monolithic silica aerogels for fenestration applications. In order to further shorten aerogel fabrication times, White et al. used an ethanol-water azeotrope, both as gelation and drying solvent, and fabrication time was about 6 hours. Mahadik et al. [42] developed a rapid supercritical extraction process (lasting 4 hours), consisting in rapid heating of the sol in a confined mold under a 50 bar initial pressure supplied by dry N_2 gas in an autoclave; the starting pre-pressure value of N_2 gas and base catalyst concentration dictated whether aerogels or xerogels are formed. The same group mixed poly(methyl methacrylate) (PMMA) in an optimized TEOS sol, obtaining an aerogel with enhanced hydrophobicity, but with lowered transparency and relatively low thermal conductivity (about $0.072\,W\,m^{-1}K^{-1}$) [43].

7.3 Silica Aerogel Properties

7.3.1 Mechanical Properties

Among the functional properties of aerogels, brittleness and lack of cohesion are some of the weaknesses.

A huge amount of mesopores inside aggregates and agglomerates, combined with mesopores and macropores in between macroscopic aerogel grains, induces local stress concentration at contact points. Some grains are in the elastic domain, while others are already plasticized [1].

Experimental mechanical measurements associated with numerical methods allow measurement of Young modulus [MPa], compressive strength [MPa], flexural strength [MPa], and compressibility [MPa], but conducting tests under tension, torsion, or multiaxial stresses are difficult owing to the brittleness of specimens.

Given a common scientific agreement that aerogel can be considered as a cubic lattice structure, with some post missing due to the high porosity, it was shown that its mechanical properties are mainly related to [5, 53, 54]: form [55], texture and roughness of particles, aggregates and agglomerates [56–59], surface roughness, particle dimension, network connectivity, density, and compaction [60, 61]. Synthesis chemistry of the gel, environment, and storage history [62] also play a fundamental role.

In terms of Young modulus, the best values found in the literature belong to the granular aerogel, with variable values depending on the measurement while loading ($1.1 \pm 1\,\mathrm{N\,mm^{-2}}$) or while unloading ($13.0 \pm 1\,\mathrm{N\,mm^{-2}}$) [21].

As open-cell foams, silica aerogels exhibit a tension/compression asymmetry [63]: Young's modulus value (11.5 MPa) in compression is significantly lower than the one in tension (15.9 MPa). By using the unloading branch of the compression curve, the elastic modulus is 15.5 MPa, still lower but much closer to the elastic modulus in tension. The origin of the yield tension-compression asymmetry is related to the significant surface stress that nanoligaments experience (Table 7.1).

For granular aerogels initial height of the sample has a major effect (i.e. mass used) on oedometer modulus and on the derived Young modulus: it decreases linearly with height. Decreasing grain size from 1 mm to below 100 μm decreases modulus standard deviation, without modification of the mean computed value [1]. Experimental conditions also affect Young modulus.

For monolithic aerogels it was observed that an increase in elastic modulus is associated with densification of bulk material [33, 77]. Measurements carried out in [33] by uniaxial compression showed that the logarithm of the elastic modulus is proportional to the logarithm of the density (slope of 3.62 ± 0.05): the values vary from 0.04 to 70 MPa for densities in the 50–350 $\mathrm{kg\,m^{-3}}$ range. These results imply that the mechanical properties of aerogel can be optimized by exploiting the inherent nonbrittle and elastic behavior of low-density silica aerogels to create relatively robust aerogels.

Young's modulus of aerogels decreases with decreasing density much faster than those of open-cell foams [61]. Particles arrangement (exfoliated or stacked) drastically affect the mechanical behavior and Afshar [55] showed that particle form decreases the modulus.

In terms of compressive strength and compressibility, the best values are for monolithic form (Table 7.1).

The failure mode of the aerogels was observed to be density dependent, as well as increasing density a transition from ductile compaction to elastic deformation to brittle fracture takes place.

Aerogels with densities greater than 200 $\mathrm{kg\,m^{-3}}$ are very brittle and shatter abruptly into fine powder, while those with densities lower than 100 $\mathrm{kg\,m^{-3}}$ appear ductile and compress into flattened disks under loading [33]. Aerogels with intermediate densities exhibit elastic properties and appear to recover their original dimensions after being compressed by as much as 40%; the compressive strength (measured within the density range where elastic behavior is observed), is roughly one order of magnitude higher than would be expected from brittle materials, due to their ability to absorb energy.

Table 7.1 Synthesis of the main mechanical properties of monolithic, granular aerogel and aerogel based composite for superinsulation.

	Mechanical property							
							Strain	
Type of aerogel and particle size (mm)	**Density ($kg\,m^{-3}$)**	**Young modulus (MPa)**	**Compressive strength (MPa)**	**Flexural strength (kPa)**	**Tensile strength (MPa)**	**Compressibility (MPa)**	**Elastic**	**Plastic**
Granular	—	1–10	0.06	—	—	0.4–1	—	—
Monolithic	50–300	0.5–4	1–10	20–110	0.011–0.3	0.7–2	37	29
Composites (non-structural)	—	0.8–2.5	0.06–2	20–205	0.0008	—	0.06	
Composites (structural)	—	—	0.36–20	—	—	—	0.06	
References	[61]	[33, 63–66]	[33, 67–73]	[61, 67, 68, 74–76]	[33, 68]	[53, 77–80]	[21]	

Downloaded from https://onlinelibrary.wiley.com/doi/ by ibrahim ragab - Universita Di Firenze Sistema , Wiley Online Library on [21/07/2024]. See the Terms and Conditions (https://onlinelibrary.wiley.com/terms-and-conditions) on Wiley Online Library for rules of use; OA articles are governed by the applicable Creative Commons License

As the material properties pass from the brittle to the ductile regime, an increase in the compressive strength is observed, due to the deformation and densification of the porous materials. In the high-density region (greater than $0.2\,g\,cm^{-3}$), the compressive strength of the brittle aerogels decreases significantly with density (from 4.2 MPa for an aerogel with a density of $0.34\,g\,cm^{-3}$ to just 640 kPa for an aerogel with a density of $0.15\,g\,cm^{-3}$). The scaling of compressive strength as a function of density is interrupted in the density region where the aerogels appear to be highly elastic (density in the 0.1–$0.2\,g\,cm^{-3}$ range). The significant increase in compressive strength is attributed to the considerable degree of deformation due to bending of the aerogel ligaments that the materials could withstand before fracture and the increase in elastic modulus associated with densification of the bulk material [77].

Granular aerogels are affected by size matter: tiny particles plasticize under loading while larger ones are indented. Voivret [81] confirmed by 2D simulation that polydispersity creates clusters of floating small grains, not supporting any loads, while large ones are submitted to indentation and compression.

As the degree of compaction increases, the fraction of smaller granules increases. This is expected since higher degrees of compaction require a greater amount of force to achieve, and higher probability of larger granules becoming broken down into smaller ones. Taking into account the possibility of pulverization, cyclic compression was carried out for different specimens for several times [61]. The reside distribution suggests a negligible effect of the number of compressive cycles (up to 10) on the aerogel distribution up to 50% compression.

Monolithic aerogels with porosities greater than 95% have been tested under the three-point bending mode and were found to have a maximum flexural strength close to 0.02 MPa at a mass density of $100\,kg\,m^{-3}$, giving a specific flexural strength of $200\,Nm\,kg^{-1}$ [74]. Strength of aerogels decrease with decreasing density.

With regard to tensile strength, monolithic aerogels tend to perform poorly: the tensile strengths were found to be 10–100 times lower than their strengths under compression, but it still depends on density. Indeed, the tensile strengths measured in [33] ranged from 12 kPa for aerogels with densities of $80\,kg\,m^{-3}$ to 315 kPa for aerogels with densities of $313\,kg\,m^{-3}$. A clear dependence between tensile strength and sample volume is uncovered in [63].

Many synthetic routes are investigated with the goal of strengthening silica aerogels: the most popular approaches are hybridization and aging [82]. With age, the elastic modulus and the compressive strength increases while the strain at fracture decreases.

The influence of additives, such as fumed silica and carbon nanotubes, on mechanical properties of the composites was also investigated [83]. Packed aerogel grains with low volume fraction binders [67] combined optimal properties, similar to the monolith or blanket solutions [33, 68].

For composites, the modulus value is governed by the aerogel texture at the nanoscale-exponent [64, 77].

The addition of fibers [68] gives the materials a global cohesion and a macro flexibility, which are necessary when handling or installing the insulation products: fibers can increase 10-fold the flexural strength and 20-fold the compressive stress (10% deformation) of the native silica aerogel. An increase of elastic modulus by 85% and strength by 26% was achieved by introducing silica fibers in silica aerogel (10% weight for weight fiber introduced) [62]. Although mechanical properties were greatly improved, the tensile strength remains too low to respect the building standards.

7.3.2 Thermal Properties

Aerogel has a quite low thermal conductivity λ (less than $0.026\,W\,m^{-1}K^{-1}$ of air), and for its high light transmission and low g-value (solar heat gain coefficient), it seems a good candidate in the TIMs context.

The microstructure of aerogels is responsible for their extremely low thermal conductivities; therefore, thermal properties are quite different when considering the granular and the monolithic forms. Monolithic silica aerogels have a thermal conductivity of 0.015 $W m^{-1}K^{-1}$ [5]; their low relative density (less than 5%) reduces conduction through the solid, and the small pore size, on the order of the mean free path of air (<100 nm), reduces conduction through air as well as convection and radiation. Because of their brittleness, for commercial use they are more common in granular form, with an increase in thermal conductivity due to the air between the granules. For an aerogel with density equal to 100 $kg m^{-3}$ at room temperature, λ is 0.020 $W m^{-1}K^{-1}$ [84]. Lower values could be obtained by replacing air within the pores with a lower conductivity gas (such as argon) or by making void the system (thermal conductivity of under vacuum SiO_2 aerogel at 300 K equal to 0.010 $W m^{-1}K^{-1}$). When the pressure becomes lower than 10 mbar, λ-values for granular form are very similar to those of monolithic form; they become different above 100 mbar.

In granular aerogel, thermal conductivity is influenced by particle size: λ goes from 0.020 $W m^{-1}K^{-1}$ for granules of 0.01–1.20 mm, to 0.024 $W m^{-1}K^{-1}$ for granules of 1.20–4.00 mm at 23 °C; it decreases to 0.019 ÷ 0.022 $W m^{-1}K^{-1}$ as the temperature falls to 10° [85, 86] (Figure 7.4).

Also the preparation method can strongly influence thermal performance: Wei et al. [87] prepared monoliths by APD, with surface modification processes in order to improve the mechanical properties of the samples. Multiple surface modification allowed us to obtain λ equal to 0.036 $W m^{-1}K^{-1}$, whereas λ was 0.079 $W m^{-1}K^{-1}$ for single surface modification; data are not very performant, but they are related to relatively old investigations (2007).

A typical application of transparent silica aerogel is in buildings' fenestration, where transparent systems incorporating aerogel (both glazing units and polycarbonates) were proposed in the literature.

As expected, thermal transmittance decreases with increasing the aerogel layer thickness. A significant influence was observed in [88] by varying the aerogel layer thickness between 20 and 30 mm: thermal transmittance U-value was in the 1.0–1.1 $W m^{-2}K^{-1}$ range and it decreased to

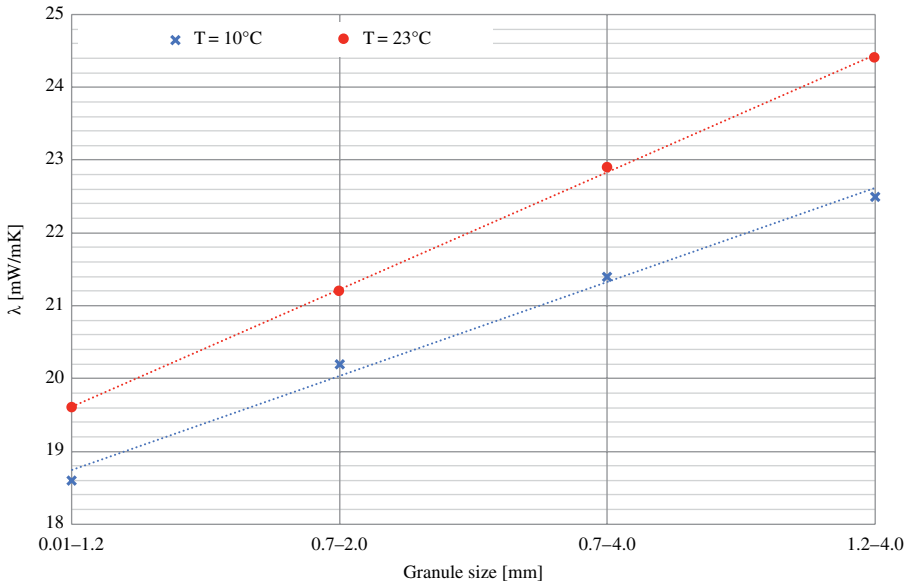


Figure 7.4 Thermal conductivity of granular aerogel vs. granule size at 10 and 23 °C Adapted from [85, 86].

0.6–0.7 $W m^{-2}K^{-1}$, respectively. Also in polycarbonate panels filled with translucent granular aerogel [89, 90], U-value decreases from 1.30 $W m^{-2}K^{-1}$ for 16 mm-thick aerogel layer to 0.60 $W m^{-2}K^{-1}$ when the thickness increases up to 40 mm, in the 40–46% range when compared to thermal performance of air-filled PC systems.

The best result (U-value equal to 0.29 $W m^{-2}K^{-1}$) was obtained in [91] for a 72 mm-thick sample with 60 mm of granular aerogel, confirmed by a U-value of 0.3 $W m^{-1}K^{-1}$ measured in [92, 93] for a glazing system with an aerogel layer of the same thick (60 mm) with granules in the 0.5–3 mm range.

Another important general finding is that convection in the cavity does not affect the thermal performance of aerogel granulate glazing systems, with similar U-values obtained upon tilting the aerogel granulate glazings [89–91]. An experimental campaign carried out in a Hot-Box system, by varying the tilt of the window [91], gave for the system filled with 60 mm of granular aerogel of a center-of-glass U-value of 0.29 $W m^{-2}K^{-1}$ in vertical position and 0.21 $W m^{-2}K^{-1}$ in the horizontal one. The total U-value of the window was 0.63 and 0.66 $W m^{-2}K^{-1}$ respectively, and the corresponding thermal conductivity of the aerogel layer was 0.017 and 0.019 $W m^{-1}K^{-1}$, assuming the thermal conductivity of glass as 1 $W m^{-1}K^{-1}$. The reduction of the center-of-glass U-value was by ~89% when compared to a vertical cavity with air.

The thermal transmittance reduction as a function of the thickness is more significant for monolithic solutions than for granular ones [24, 52, 94–96]. Tests in [24] confirmed U-values in the 0.41–0.47 $W m^{-2}K^{-1}$ range, and a very high solar and visible transmittance (g-value equal to 0.79), making their development very desirable.

Another promising improvement consists of under-vacuum aerogel windows. Prototypes with 12.7 mm-thick layer of aerogel, fabricated with a rapid supercritical extraction (RSCE) process, yielded thermal resistance R-values as high as 1.55 $m^2 K W^{-1}$ at about 6 KPa and of 1.21 $m^2 K W^{-1}$ at 30.5 KPa. They represented an improvement in R-values of about 73% and 35% when compared to the same nonevacuated window (R-value equal to 0.86 $m^2 K W^{-1}$) [52].

Considering a thermal conductivity of 0.010 $W m^{-1}K^{-1}$ for a 15-mm aerogel pane, aerogel glazing prototypes made under vacuum conditions have a center-of-glass U-value equal to 0.66 $W m^{-2}K^{-1}$, the same as the best triple glazing systems filled with gases in the gaps, whereas the solar transmittance is higher than 75% [95]. A window $1.2 \times 1.2\,m^2$ composed of those prototype tiles provided an overall U-value of $0.72 \pm 0.04\,W m^{-2}K^{-1}$ [97], that compared to the center-of-glass U-value of 0.66 $W m^{-2}K^{-1}$ confirmed the very small thermal bridge effect of the developed seal solution.

7.3.3 Optical Properties

Optical properties play a key role in the transparent aerogel applications, due to their ability to allow the light transmission, which makes aerogel a good candidate in buildings fenestration. In the literature they were often proposed as transparent envelope solutions, characterized by high thermal insulation properties, although applications at real scale are currently limited to granular form.

The studies on the optical behavior of aerogel were focused for many years on basic material properties, such as refraction index, transparency, and scattering. Granular aerogel is translucent and it diffuses light due to the scattering behavior of multiple reflections among granules; its application is desirable when, although a high level of natural lighting is needed, the vision through is not required. It is the case of skylights or, in large scale, in buildings intended for visual tasks requiring a high light contribution: diffuse indoor illuminance significantly reduces energy requirements for lighting and prevents glare discomfort.

In the monolithic form, aerogel is instead transparent; for this reason it is suitable for all architectural applications, increasingly designed to make glass surfaces and visual permeability the central features of the design. From haze-value (the ratio of diffuse transmittance on the hemispherical transmittance) the analogy of the behavior of the monolithic aerogel with that of the float glass can be deduced. The main optical properties worthy of investigation are visible transmittance τ_v, solar transmittance τ_e, and solar factor g.

Table 7.2 summarizes the main data available. Data are related to the pure material in monolithic and granular form and to glazing systems assembled with aerogel in the gap.

The visible transmittance of monolithic aerogel is in the 0.60–0.98 range, whereas the solar transmittance is in the 0.80–0.86 range when the thickness varies from 2.5 to 17 mm.

Granular aerogel shows different τ_v and τ_e values, depending on the granule size and on the layer thickness. Typical values of τ_v increase from 0.15 to 0.50 when the granule size increases from 0.5 to 4.0 mm, for a standard gap thickness of about 14–16 mm; the corresponding τ_e values are in the 0.14–0.47 range, whereas the g-value is about 0.27–0.57.

Given the silica aerogel transparency to the solar radiation, the quality of the vision is strongly affected by the production process in terms of visual sharpness and color rendering [22, 100]. Furthermore the experimental apparatus strongly affects the measurements. Conventional spectrophotometers are critical due to monolithic aerogel scattering and granular aerogel substantial diffusing behaviors; the problem is significant especially for the latter and increases with the aerogel layer thickness, when the size of the usual sized integrating spheres does not allow collection of all the transmitted/reflected radiation. This underestimation leads to an absorptance overestimation, which deeply affects the response of the building in terms of energy performance (g-value and solar gains) and thermal comfort (surface temperatures of the glazing components and operative temperature).

Scattering is a radiation transfer mode taking place in aerogels. First studies were related to light scattering, observed as soon as the material was first produced, and it is responsible for the color shift of the material.

Early research carried out at the beginning of the twentieth century by Kistler highlighted that silica aerogels appear yellowish-orange against a bright background and bluish against a dark background, complying with the Rayleigh theory. Scattering mainly affects the shorter wavelengths of the solar spectrum. It is applicable to structure-forming units smaller than the wavelength of the visible light; thus, it is suitable for primary skeletal silica particles, owing to their small size (lower than 10 nm), and pores falling in the medium-to-low part of the mesopore range (2–50 nm), that have been also proposed as primary scatterers [2, 24, 108–110].

Later it was observed that discontinuities of a large order significantly increase the scattering of the transmitted light, first referred to the surface, and in accordance with the wavelength independent Mie scattering [32, 103, 110, 111]. As the density decreases, the size of secondary particles increases and Mie scattering also affects the bulk. In [103] Beck et al. described the close relation between the scattering behavior of aerogel granules and their bulk and surface configuration. Scattering distribution analysis at 633 nm showed that scattered intensity at angles above 20° is predominantly due to bulk scattering, while at larger angles the surface scattering becomes predominant. The elimination of the large structural imperfections on the surface of the granule produces a slight improvement (2–3%) of the hemispheric transmission, whereas it is possible to observe a noticeable (60–65%) increase in transmission if bulk inhomogeneities decrease. The main potential in producing advanced aerogel lies therefore in the optimization of the nanostructured network [103].

Table 7.2 Synthesis of the main optical properties of monolithic, granular aerogel and aerogel glazing systems available in the literature.

	Type of aerogel and particle size (mm)	Description	Aerogel layer thickness (mm)	τ_v (–)[a]	τ_e (–)[a]	g	Experimental apparatus	References
Pure Material	Monolithic	Aerogel monolith	14	0.78[b]	0.80	—	Small sphere (75 mm)	[93]
	Monolithic	Aerogel monolith	17	0.6	—	—	Small sphere (150–160 mm)	[47]
		Aerogel monolith	7–12	0.92–0.84[b]	0.92–0.86	—		[24]
		Aerogel monolith	1.4–3.5	0.97–0.91[b]	—	—		[98]
		Aerogel monolith	2.5–5.3	0.98–0.94[b]	—	—		[99]
		Aerogel monolith	10	0.64–0.92[c]	—	—		[100]
	2.7	Granules layer	7.5	0.31	—	—		[101]
		Granules layer	10	0.22	—	—		
	0.93	Granules layer	7.5	0.30	—	—		
		Granules layer	10	0.21	—	—		
	0.64	Granules layer	7.5	0.26	—	—		
		Granules layer	10	0.16	—	—		
	0.41	Granules layer	7.5	0.23	—	—		
		Granules layer	10	0.13	—	—		
	4.00	Granules layer	14	0.50	0.47	0.57		[102]
	0.50	Granules layer	14	0.15	0.14	0.27		
	4.70	Granules layer	10	0.75	—	—	Large sphere	[88]
		Granules layer	20	0.67	—	—		

(*Continued*)

Downloaded from https://onlinelibrary.wiley.com/doi/ by ibrahim ragab - Universita Di Firenze Sistema , Wiley Online Library on [21/07/2024]. See the Terms and Conditions (https://onlinelibrary.wiley.com/terms-and-conditions) on Wiley Online Library for rules of use; OA articles are governed by the applicable Creative Commons License

Table 7.2 (Continued)

Type of aerogel and particle size (mm)	Description	Aerogel layer thickness (mm)	τ_v (–)[a]	τ_e (–)[a]	g	Experimental apparatus	References
	Granules layer	35	0.52	—	—		
2.70	Granules layer	10	0.71	—	—		
	Granules layer	20	0.60	—	—		
	Granules layer	35	0.45	—	—		
0.60	Granules layer	10	0.64	—	—		
	Granules layer	20	0.54	—	—		
	Granules layer	35	0.41	—	—		
3.5	Granules layer	20	0.58 ± 0.04	—	—	—	[103]
Granular translucent fragments	Granules layer	16	0.74 ± 0.04	0.71 ± 0.04	—	Large sphere (350 mm)	[104]
Granular translucent fragments	Granules layer	10	0.85 ± 0.04[b]	0.88 ± 0.04	—	Large sphere (350 mm)	[105]
Granular semi-translucent fragments	Granules layer	10	0.65 ± 0.04[b]	0.65 ± 0.04	—		
Granular semi-translucent spheres	Granules layer	10	0.43 ± 0.03[b]	0.43 ± 0.04	—		

Downloaded from https://onlinelibrary.wiley.com/doi/ by ibrahim ragab - Universita Di Firenze Sistema , Wiley Online Library on [21/07/2024]. See the Terms and Conditions (https://onlinelibrary.wiley.com/terms-and-conditions) on Wiley Online Library for rules of use; OA articles are governed by the applicable Creative Commons License

Glazing systems	Monolithic	4 hardened pane/15 aerogel/4 hardened pane	20	0.72	0.75	0.79	Small sphere	[24]
	Monolithic	4.7 borosilicate pane/15 aerogel/4.7 borosilicate pane	15	0.69	0.62	—	Large sphere	[106]
	Monolithic	4 pane/14 aerogel/4 pane	14	0.60	0.51	—	Small sphere (75 mm)	[92]
	Monolithic	4 pane/14 aerogel/6/7 acoustic pane	14	0.58	0.46	—		
	Monolithic	4 pane/14 aerogel/6/7 low-e pane	14	0.57	0.35	—		
	Monolithic	10/11 acoustic pane/14 aerogel/6/7 acoustic pane	14	0.55	0.37	—		
	Monolithic	4 pane/14 aerogel/4 pane	14	0.62	0.55	—	Small sphere (75 mm)	[93]
	Monolithic	4 pane/14 aerogel/4 low-e pane	14	0.56	0.49	—		
	Monolithic	4 pane/14 aerogel/4 pane	14	0.58	0.51	—	Small sphere (75 mm)	[107]
	Monolithic	5 pane/14 aerogel/5 pane	14	0.59	0.51	—		
	Monolithic	6 pane/14 aerogel/6 pane	14	0.57	0.46	—		
	Monolithic	5 pane/14 aerogel/4 low-e pane	14	0.48	0.39	—		
	Granular semi-translucent spheres	4 low-e pane ($\varepsilon = 0.08$)/12 (80% Kr and 20% air)/16 aerogel/12 (80% Kr and 20% air)/4 low-e pane ($\varepsilon = 0.08$)	16	0.26 ± 0.03	0.22 ± 0.02	0.31 ± 0.03	—	[104, 105]
	Granular semi-translucent fragments	4 low-e pane ($\varepsilon = 0.03$)/12 (60% Kr and 40% air)/16 aerogel/12 (60% Kr and 40% air)/4 low-e pane ($\varepsilon = 0.03$)	16	0.27 ± 0.03	0.13 ± 0.02	0.20 ± 0.02	—	[104, 105]

[a] Values are referred to aerogel layers sandwiched between two glasses with standard thickness (4–6 mm).
[b] Only aerogel without glasses.
[c] Depending on the precursor, catalyst and solvent.

Downloaded from https://onlinelibrary.wiley.com/doi/ by ibrahim ragab - Universita Di Firenze Sistema , Wiley Online Library on [21/07/2024]. See the Terms and Conditions (https://onlinelibrary.wiley.com/terms-and-conditions) on Wiley Online Library for rules of use; OA articles are governed by the applicable Creative Commons License

When considering glazing systems composed of monolithic aerogel panes in the interspace [106] and granular aerogel filled windows [88], the former has light and solar transmittance 0.06–0.07 greater than the latter.

Light and solar transmittance peak values for the assembly of 15-mm thick monolithic aerogel tiles, embedded between two 4.7 mm borosilicate glass sheets, are 0.69 and 0.62, respectively [106]. Angular measurements at 45° and 60° highlights 10% and 24% reduction in transmittance, respectively, when compared to normal incidence values. Light and solar reflectance values are 0.25 and 0.19.

A systematic characterization of double-glazing systems (DGU) with aerogel in gap was carried out in [92, 93, 107], where transmittance and reflectance measurements were performed with a spectrophotometer equipped with a 75-mm integrating sphere; light transmittance was in the 0.55–0.60 range, where the lowest values belong to acoustic and low-e glasses.

Tests conducted in a building façade with granular aerogel [105] showed that daylighting system combine good light transmittance (0.24–0.54) and high g-value (0.33–0.45). Results obtained in [102] confirm the impact of the granule size on g-value, providing higher values for large sized granules (4 mm) with respect to that of small sized (lower than 0.5 mm) (0.57 and 0.27, respectively).

7.3.4 Acoustic Properties

The first studies on acoustic properties of aerogels were about sound propagation and they were carried out both for monolithic and granular forms [109, 112, 113]. Monolithic aerogels showed rather low longitudinal acoustic velocity, on the order of $100\,m\,s^{-1}$ (values down to $40\,m\,s^{-1}$ were also measured) [18, 23, 110, 112, 114, 115]. The low velocity of sound, combined with the low density, allows rather low acoustic impedance, the minimum value among solid and liquid substances.

Starting from 2014, a systematic investigation on the influence of granule size on acoustic performance of aerogels has been carried out [85, 116, 117].

Sound absorption and noise insulation measurements of building materials are in general performed by measuring noise reduction index and absorption coefficient at laboratory scale, in reverberating rooms at diffused incidence [118, 119]. This type of experimentations requires large surfaces (some square meters), in general not available for aerogels, therefore most of the studies are carried out by using the impedance tube (Kundt's tube) at normal incidence [85, 116, 117, 120–123]; absorption coefficient and transmission loss are measured.

In order to compare the sound absorption behavior of the materials, the noise reduction coefficient (NRC), calculated as the average of the absorption coefficient values in the one-octave band at 250, 500, 1000, and 2000 Hz, is in general considered. Data available in the literature for monolithic and granular aerogel are summarized in Figure 7.5; average values at different frequencies (800–1600 Hz) are also reported. The NRCs increase with increasing thickness: the best absorption properties are related to small granule samples (NRC ranging from 0.27 to 0.58 for thicknesses in the 15–40 mm range). For large granules, NRC values vary in the 0.13 – 0.47 range with the same thickness variation. The monolithic form has a worst behavior in terms of acoustic absorption α and the NRC are about the same when considering different thicknesses (0.20 – 0.22) [106]. In [117], α-values only at 800 and 1600 Hz are available; the average are reported in Figure 7.5, and also in this case the mean absorption coefficient α_{mean} values increase when increase the thickness (the best behavior is for the small granules, as expected).

Considering the insulation properties, in general, transmission loss (TL) increases when increasing the frequency [109]; in Figure 7.6 the average value in the 100–1600 Hz frequency range of aerogel panes and granule layers of different thickness and size is reported. It can be

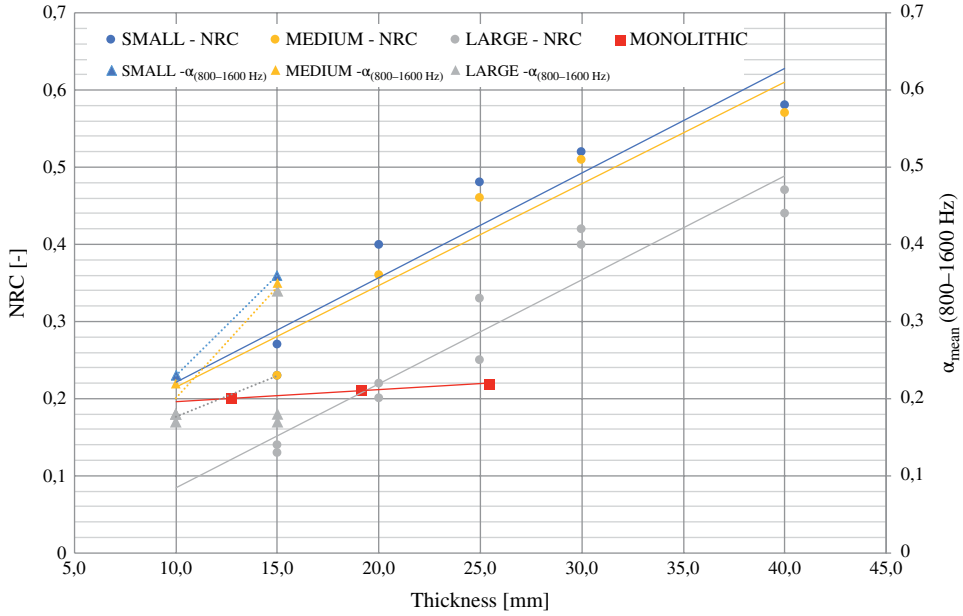


Figure 7.5 Noise reduction coefficient NRC (average value of the absorption coefficients calculated at the frequencies of 250, 500, 1000, and 2000 Hz) and α_{mean} (800–1600 Hz) of aerogel panes and granule layers for different thickness and size.

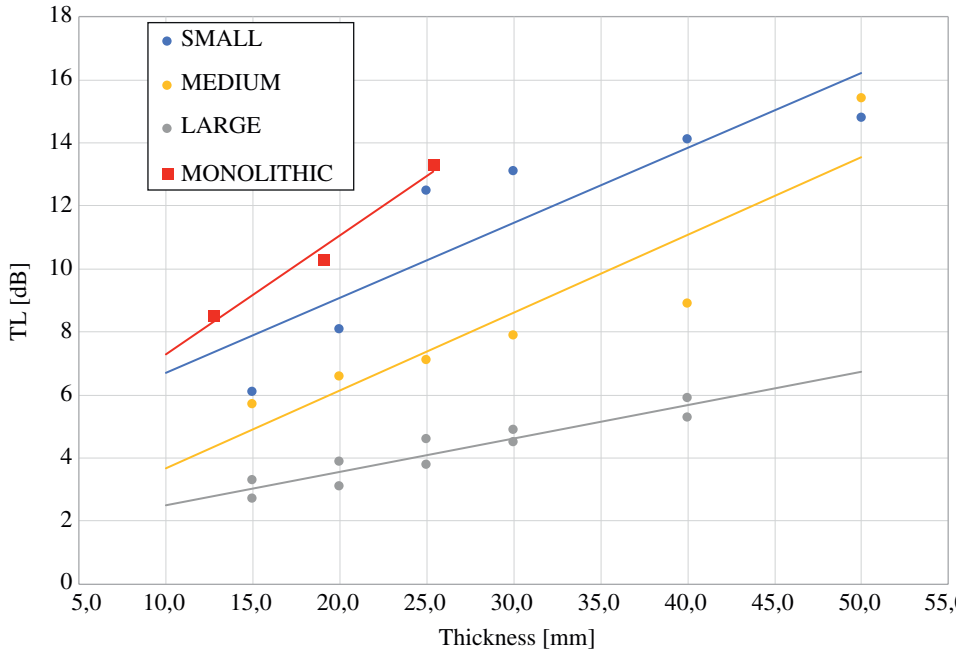


Figure 7.6 Average value of the transmission loss in the 100–1600 Hz frequency range of aerogel panes and granule layers for different thickness and size.

observed that TL increases with layer thickness increasing and granule size decreasing: as expected and in compliance with the Mass law, the acoustic insulation is better for higher thicknesses and higher densities (small granules) [85]. The monolithic form presents the best behavior in terms of acoustic insulation (TL values variable in the 8–14 dB range, for thicknesses from 12.7 to 25.4 mm) [121].

When assembled in glazing systems, aerogel can improve the acoustic performance in the central frequency range, with an overall effect corresponding to about 3 dB. It is confirmed on real-scale window prototypes, with laboratory tests [92], according to EN ISO 10140-2 [118], or on the façade acoustic insulation index measured in situ, according to ISO 140-5 [124]. Weighted sound insulation index R_w of 37 and 34 dB were obtained for two aluminum-frame windows, one with granular aerogel gap and the other one with air gap, respectively, showing an increasing performance of 3 dB due to the presence of aerogel [92]. The same increasing was found in situ [124], in a test room at real scale with two wooden windows, one with granular aerogel gap and the other one with air gap. The façade acoustic insulation index $D_{2m,nTw}$ was 31 and 28 dB, respectively, confirming the 3 dB improvement.

Same results were obtained in an impedance tube [121]: 12.7-mm monolithic panes were assembled within two glass layers and results were compared with two double glazing samples with air and with granular aerogel in the gap, respectively. The aerogel samples showed an increase in noise insulation performance of 3 dB for the monolithic sample and of about 1–2 dB for the granular one when compared to the sample with air.

7.4 Energy Performance of Silica Aerogels in Buildings

The application of innovative materials both in new buildings and refurbishment interventions is the main focus in order to improve energy performance, especially when considering the transparent elements, in which the most heat losses and gains occur. In a well-insulated building, windows represent the weakest part of the envelope in terms of energy consumptions. The influence of glazing systems with monolithic and granular aerogel fillings with respect to traditional double and triple glazing solutions were widely studied in the literature in terms of heating and cooling energy demand. Moreover, some authors investigated the impact on indoor daylighting comfort. Results are highly influenced by several factors, such as the geometry and exposure of the considered building, the glazing configurations, the climate areas, the simulation software, and the hypothesis. The following section discusses the energy performance of monolithic and granular solutions.

7.4.1 Energy Performance of Monolithic Aerogel Glazing Systems

Monolithic aerogel windows were considered as a solution able to reduce energy demand in heating-dominant climates due to high solar and light transmittance, high solar factor, and low thermal conductivity, comparable with the one of a conventional triple glazing. The combination of these parameters achieves a net energy gain during the heating seasons. Within the financed European projects HILIT and HILIT +, aerogel panes were fabricated at large scale improving thermal and optical properties and drying, duration, safety process parameters [97]. The influence of 15-mm thick silica aerogel pane in an under vacuum superinsulating glazing in a well-insulated frame on the heating energy consumption was evaluated in northern European climate [94]. Thermal transmittance and total solar energy transmittance of the system were 0.5 $W m^{-2}K^{-1}$ and

0.75, respectively. The impact on the heating energy consumption was evaluated through annual energy simulations, taking into account two different case studies: a typical single-family house in a Danish climate (insulated according to the Danish building Standard) and a building insulated to under a passive house standard (space heating demand lower than 15 kWh m^{-2} $year^{-1}$). In the comparison, also argon-filled triple glazing with two low-e coatings (U-value of 0.6 W $m^{-2}K^{-1}$ and g equal to 0.46) was considered. An energy saving of 19% was achieved in the traditional building with the aerogel solution with respect to triple glazing (space heating demand equal to 5040 kWh $year^{-1}$ for aerogel and 6220 kWh $year^{-1}$ for triple glazing). When considering the low-energy house, the energy saving increases (−34%, corresponding to about 700 kWh $year^{-1}$).

Similar results were obtained for a passive house residential building (Myhrerenga Borettslag) with 24 apartments located near Oslo (Norway) [125]. The influence in the building energy use for heating of three different window-to-wall ratios (0.24, 0.33, and 0.50) was investigated using EnergyPlus software. Monolithic aerogel of 14-mm thickness in the gap of two 4-mm float clear layers (U of about 0.65 W $m^{-2}K^{-1}$, g equal to 0.74) involves a reduction of 20% in the heating energy demand, namely 6% of the total building amount, with respect to an argon triple glazing (28-mm thick, U 0.79 W $m^{-2}K^{-1}$, g equal to 0.46). With monolithic panes, the heating energy consumptions are in the 16–20 kWh m^{-2} $year^{-1}$ range for 0.24 and 0.50 window-to-wall ratio, respectively, instead of 18–26 kWh m^{-2} $year^{-1}$ of the triple conventional solution. Furthermore, 14-mm monolithic aerogel window represents a valuable solution in the retrofitting project of an educational building at Worcester Polytechnic Institute, located in the cold area of Massachusetts (US), built in the 1960s [126]. A detailed energy audit was conducted between January and July 2014, in order to measure several indoor environmental parameters, envelope transmittance, and the building air-tightness and to create an accurate energy model in EnergyPlus code. The annual energy demand for the building is 285 kWh m^{-2} $year^{-1}$, 74% due to the heating. The simulations were carried out by considering a low-e glazing window with 12-mm air in the gap (U of 1.5 W $m^{-2}K^{-1}$) and four different configurations: 40% (U equal to 1.2 W $m^{-2}K^{-1}$), 60% (U equal to 0.9 W $m^{-2}K^{-1}$), 80% (U equal to 0.7 W $m^{-2}K^{-1}$), and 100% (U equal to 0.6 W $m^{-2}K^{-1}$) of the whole area of the windows incorporating aerogel panes. When increasing the aerogel surface percentage, the heating consumption decreases linearly up to about 28 kWh m^{-2} $year^{-1}$ (100% aerogel) with respect to the solution without aerogel. However, a small increase (about 3–4 kWh m^{-2} $year^{-1}$) was obtained in cooling energy demand, and it was almost stable when aerogel percentage area was higher than 60% (U- and g-values decrease). Moreover, the Useful Daylight Index (UDI) was calculated in order to quantify the percentage of time in which the daylight illuminance level is sufficient and useful for occupants (illuminance in the 100–2000 lux range). A nonlinear relationship between the amount of aerogel and UDI was found. Taking into account 100% aerogel surface area, a UDI reduction of only 1% (rooms with mostly facing east) and 10% (rooms with mostly facing west) was found. 40% aerogel area represented a good solution in order to reduce the energy consumption without too penalizing daylighting. The simulations were repeated for different climate conditions and also in cooling-dominant cities such as Miami (Florida) the aerogel window resulted in a valid solution for reducing energy demand without shading systems.

Different results were obtained for a typical nonresidential building with large eastern and western strip windows [96]. It was modeled considering two different window-to-wall-ratios (50% and 100%). The impact of the innovative solution with monolithic aerogel pane (15-mm thick) sandwiched between two clear float glasses (4.7-mm thick) was simulated taking into account hot, moderate, and cold climate conditions, and it was compared with double and triple low-e commercial glazing systems. A screen was considered as external shading device, due to

the large window area. Aerogel glazing involves an energy demand reduction for space heating of about 10% with respect to double glazing units in all the climate conditions, especially in moderate ones. The benefits increase to 15% when increasing the window-to-wall ratio. However, the cooling energy demand increases of about 11% in moderate climates, due to the high solar factor. The annual energy demand is comparable with the one of a low-e triple glazing unit with argon ($U = 0.7\,W\,m^{-2}K^{-1}$, $g = 0.44$), but it is characterized by a higher thickness (36 mm instead of about 24 mm) and weight. The good light transmission of the monolith systems contributes to maintain quite similar energy demand for artificial lighting with respect to the conventional glazing.

A moderate increase in cooling energy consumptions was also obtained for a prototype of an Evolutive House designed by two important architects, Renzo Piano and Peter Rice, built in 1978 near to Perugia (Italy) [127]. It was characterized by a changeability of the internal spaces due to the movable glazing façade, able to run along a rail, and by two large glass walls in the east and west exposures (U equal to $2.3\,W\,m^{-2}K^{-1}$). In-situ experimental campaigns (measurements of thermal transmittance of the external wall, inside and outside air temperatures and relative humidity, temperature of the ground floor) were carried out and a weather file representative of the real climatic conditions was implemented, in order to validate the dynamic simulation models. The simulations were performed using both EnergyPlus (Direct Root Finding method) and TRNSYS (State-Space method) software and the influence of a double glazing with monolithic aerogel (14-mm) was investigated. A significant reduction in energy consumptions during the heating period was achieved with the innovative transparent solution (about −65%). Despite the high solar factor (0.75) of the monolithic window involves an increasing in summer energy consumptions, the annual ideal energy demand varies from $980\,kWh\,m^{-2}$ (Energy Plus) – $882\,kWh\,m^{-2}$ (TRNSYS) with the existing glazing system to an average value of $259\,kWh\,m^{-2}$ (Energy Plus) – $342\,kWh\,m^{-2}$ (TRNSYS) with the innovative transparent solution, resulting in a considerable benefit.

Monolithic aerogel represents the best solution in winter for different climatic zones (Rome, London, Moscow, Helsinki, Ottawa, and Beijing) also when considering south exposure windows in a multifunctional building (thermal transmittance $0.5\,W\,m^{-2}K^{-1}$, solar factor 0.75) [128]. Despite the innovative double-glazing unit with monolithic pane (20-mm thick) allows a heating energy demand reduction of about 25%, the cooling energy demand increases, due to the high solar factor, especially in temperate areas. Overall, this system is the best for all cities except for Rome (higher global solar radiation), allowing a maximum annual energy savings of about 29% for Ottawa with respect to standard double glazing with air.

Synthesis of the main simulation results, the main features of the glazing systems, and the annual heating and cooling energy savings in comparison with conventional double and triple glazing systems is provided in Table 7.3.

7.4.2 Energy Performance of Granular Aerogel Glazing Systems

An investigation in six cities in different climate zones (Rome, London, Moscow, Helsinki, Ottawa, and Beijing) showed that granular aerogel used in a multifunctional building allows an annual energy demand reduction of about 10–20% with respect to standard double-glazing systems [128]. The granular solution makes the most in cold climates, even better than the monolithic one, despite not being transparent. In this way, having a lower solar factor, it can archive a higher energy saving for cooling than monolithic solution in temperate climates. Glazing systems with granular aerogel are characterized by a lower thermal transmittance than standard double-glazing

Table 7.3 Influence of monolithic aerogel glazing systems in heating and cooling energy consumptions in different climatic conditions.

Case study	Glazing solutions	Climate area	Annual heating and cooling savings [%]	References
• Danish building code insulated house	Triple low-e argon-filled ($U = 0.6\,W\,m^{-2}K^{-1}$; g = 0.46)	Denmark	19	[94]
• Passive house standard	15-mm evacuated aerogel ($U = 0.5\,W\,m^{-2}K^{-1}$; g = 0.75)		34	
Myhrerenga Borettslag – residential building	Triple low-e argon-filled (4 low-e – 8 argon – 4 low-e – 8 argon – 4 low-e) (28-mm; $U = 0.79\,W\,m^{-2}K^{-1}$; g = 0.46) 14-mm evacuated aerogel (4 clear – 14 monolithic – 4 clear) ($U = 0.65\,W\,m^{-2}K^{-1}$; g = 0.74)	Oslo	11 (WWR 0.24) – 21 (WWR 0.5)	[125]
Educational building at Worcester Polytechnic Institute	Double low-e air filled (4 clear – 12 air – 4 low-e) ($U = 1.5\,W\,m^{-2}K^{-1}$) 14-mm aerogel (4 clear – 14 monolithic – 4 clear) Percentage aerogel area: 40% ($U = 1.2\,W\,m^{-2}K^{-1}$) 60% ($U = 0.9\,W\,m^{-2}K^{-1}$) 80% ($U = 0.7\,W\,m^{-2}K^{-1}$) 100% ($U = 0.6\,W\,m^{-2}K^{-1}$)	Massachusetts	8 (40%) – 22 (100%)	[126]

(*Continued*)

Downloaded from https://onlinelibrary.wiley.com/doi/ by ibrahim ragab - Universita Di Firenze Sistema , Wiley Online Library on [21/07/2024]. See the Terms and Conditions (https://onlinelibrary.wiley.com/terms-and-conditions) on Wiley Online Library for rules of use; OA articles are governed by the applicable Creative Commons License

Table 7.3 (Continued)

Case study	Glazing solutions	Climate area	Annual heating and cooling savings [%]	References
Non-residential buildings with WWR 50% and with WWR 100%	Double low-e argon filled (6 clear – 16 argon – 4 low-e) ($U = 1.1\,W\,m^{-2}K^{-1}$; g = 0.55)	Helsinky Turin	5 (WWR 50) – 7 (WWR 100) 4 (WWR 50) – 6 (WWR 100)	[96]
	15-mm aerogel (4.7 clear – 15 monolithic – 4.7 clear) ($U = 1.0\,W\,m^{-2}K^{-1}$; g = 0.7)	Paris Rome	6 (WWR 50) – 8 (WWR 100) 0.5 (WWR 50) – -2 (WWR 100)	
Prototype of Evolutive house	Triple air filled (3 clear – 6 air – 3 clear – 7 air – 3 clear) ($U = 2.3\,W\,m^{-2}K^{-1}$; g = 0.75)	Perugia	13	[127]
	14-mm aerogel (4 clear – 14 monolithic – 4 clear) ($U = 0.63\,W\,m^{-2}K^{-1}$; g = 0.75)			
Multifunctional building	Double air filled (4 clear – 15 air – 6 clear) ($U = 2.7\,W\,m^{-2}K^{-1}$; g = 0.77)	Ottawa London Helsinki	29 27 23	[128]
	20-mm aerogel (4 clear – 20 monolithic – 4 clear) ($U = 0.5\,W\,m^{-2}K^{-1}$; g = 0.75)	Beijing Moscow Rome	22 24 3	

Downloaded from https://onlinelibrary.wiley.com/doi/ by ibrahim ragab - Universita Di Firenze Sistema , Wiley Online Library on [21/07/2024]. See the Terms and Conditions (https://onlinelibrary.wiley.com/terms-and-conditions) on Wiley Online Library for rules of use; OA articles are governed by the applicable Creative Commons License

units (0.54 $W m^{-2}K^{-1}$ vs. 2.7 $W m^{-2}K^{-1}$), reducing energy needed for cooling in various amounts, depending on the geographical location. In cold climates like Helsinki, both heating (10 $kWh m^{-2}$) and cooling (4 $kWh m^{-2}$) energy demand decrease; obviously, the colder the climate, the higher is the energy saved for cooling. The greatest amount of annual energy reduction is recorded in Canada (−15.4%), Helsinki (−18.3%), and Moscow (−17.6%), but in hotter places like China or Italy, the value becomes much lower (5 and 8 $W m^{-2}K^{-1}$). Due to its broad range of climates, China is an interesting experimental field to test and demonstrate how different annual climate conditions constrain the efficiency of the granular aerogel. On a giant 40-story office building with 49,000 m^2, the greatest energy demand reduction is obtained in the coldest region (Harbin, 20%), whereas the lowest reduction is obtained in the hottest and wettest ones (Shanghai, 9%) [129]. The simulation included two different kinds of comparison: a standard low-e insulating glass system (U of about 1.9 $W m^{-2}K^{-1}$) with two different kind of granular silica aerogel (both equal to 0.72 $W m^{-2}K^{-1}$). In Harbin, the annual energy saving for heating and cooling was 300 MWh and in Shanghai it was 50 MWh. It is important to highlight that the real positive impact of granular systems is recorded during the winter period, when monthly building heating load saving can reach 180 MWh in Harbin and decrease even to zero in July. Changing the geographical area and going in temperate regions like Canada, it was demonstrated that transparent envelope of an historical building with large windows (Ryerson University in Toronto's downtown), with a 20-mm thick granular aerogel glazing system, allowed an annual energy saving of 29.8 $kWh m^{-2}$ (with respect to 266 $kWh m^{-2}y^{-1}$ of the actual solution) and an annual energy saving of 73.08 MWh [130]. Nevertheless, the high costs (even 620,000 Canadian dollar (C$)) of a large-scale retrofit process results in a very long payback period (more than 50 years with 9500 C$/year saving). Combinations between granular aerogel and conventional glazing units could be a good solution in humid subtropical cooling-dominant climates [131]. A reduction of cooling load (even 8 $kWh m^{-2}$ $year^{-1}$ in the most favorable conditions) was obtained considering 15-mm granules in the interspace of glazing units set upping large east-west strip windows, in a typical 1990s office building in different climate conditions [86]. A system with two conventional clear float layers (4-mm) and 15-mm of granular aerogel ($U = 1.0\ W m^{-2}K^{-1}$) is compared with a glass with low-e and solar control coating on the external surface (4-mm) and a clear float glass (4-mm) on the internal surface ($U = 1.6\ W m^{-2}K^{-1}$), with a gap of 15 mm filled with different types of granules ($U = 1.1\ W m^{-2}K^{-1}$). Reference unit is a standard double-glazing system with a 15-mm air-filled gap ($U = 2.7\ W m^{-2}K^{-1}$). Results highlight a reduction for heating demand in all climate conditions and a reduction of cooling energy demand, although in a smaller magnitude. A combination between granular aerogel and low-e glass seems to be the best performer solution (reduction of transmittance about 31% compared with the low-e glass system). However, the benefits of the translucent material on the energy demand for cooling in low-e case are negligible. The artificial lighting energy demand is quite similar for all the considered solutions. Another possible solution is to couple a nanogel glazing with a nano-vacuum insulation panel (VIP) [132]. Choosing a very extreme hot climate like the Dhahran region of Saudi Arabia, Ecotec energy simulations with three different commercial building configurations were performed: without thermal insulation (U = 1.61 $W m^{-2}K^{-1}$), with conventional wall and roof insulation (0.48–0.52 $W m^{-2}K^{-1}$) and double-glazing window (2.71 $W m^{-2}K^{-1}$), and with nanogel glazing and nano VIP for wall and roof (0.06 $W m^{-2}K^{-1}$). Although it should be expected that the biggest advantage with the more complex VIP solution, vacuum-layer equipped systems archived a performance improvement of only the 0.8% in the reduction of annual energy consumption (less than 20 MWh). The widest difference is archived replacing conventional glazing units with nanogel ones and keeping polystyrene foam in walls and roof (annual energy consumption reduction 14%, more than 300 MWh). Nanogel glazing units

should be a valid solution when applied to the skylight of the building, due to its low thermal transmittance (0.45 $W m^{-2}K^{-1}$) and the possibility to reduce the lighting energy consumption. Ecotec simulation was used to investigate the influence of glazing systems with 0.25–0.5 mm particles in 7.5-mm thick gap installed at different positions on a large atrium building under cooling-dominant climate in Guangzhou, China. Atrium represented the 30% of the total building cooling load (52–58 $kWh m^{-2}$), and it was observed that indoor air temperature fell about 4 °C. The envelope heat gain decreases of 31% when compared to a single glass and an indoor natural illuminance of 1500 lx is obtained (required value 300 lx) [133]. Other innovative solutions such as polycarbonate multisheet panels were filled with aerogel granules; polycarbonates have gained market presence since 2000 due their high transparency, reduced weight, and competitive costs. This representing a very advantageous solution, especially for nonresidential buildings. Three panels, different in geometry and thickness of the gap (16, 25, and 40 mm) with the presence of granules (0.7–4.0 mm) (thermal transmittance from 1.4 to 0.6 $W m^{-2}K^{-1}$), were considered as transparent solutions in a typical industrial building [89]. Despite the great decrease of the thermal transmittance of the aerogel filled panels with respect to air-filled ones (even 1.6 $W m^{-2}K^{-1}$ with a reduction of the 73% of the total value), a moderate reduction of heating from 7% to 12% was observed, depending climate condition (hot-Rome, moderate-London, and cold-Helsinki climates) and on the aerogel thickness is achieved. Nowadays, one of the most performer glazing units available on the market is the triple glass window, able to achieve high thermal insulation maintaining with significant transparency, but its high weight represents a great disadvantage and can even force architectural solutions to allow structural security. In this context, comparison between triple unit and granular silica aerogel ones is interesting. Modeling a typical office building with an aerogel glazing and a solar control triple glazing or a building in Germany, a clear advantage of the aerogel solution was demonstrated (U equal to 0.4 $W m^{-2}K^{-1}$, g of 0.3 over U equal to 0.8 $W m^{-2}K^{-1}$, g equal to 0.6) [104]. In summer conditions, overheating is not allowed by aerogel layer on the southern east/west façades. This behavior is showed in a quite different entity using triple glazing. In fact, the comparison results in a better transmittance of the aerogel versus the triple-glazing even of 15 $kWh m^{-2}$ during July. However, during winter aerogel solution reach near-zero or even negative values of the flux with a consequently bad influence on the annual energy balance. Anyway, the best aerogel layer performance is archived on the north-facing façade of the test building with a heating periods yields of 10 $kWh m^{-2}$.

When considering the House designed by Renzo Piano and Peter Rice described in Section 4.1 [127], a granular solution was also proposed (U = 0.91 $W m^{-2}K^{-1}$), archiving an energy saving of (7 $kWh m^{-2}$ in January and 0.2 $kWh m^{-2}$ in June), with a significant reduction in energy consumption only during the heating period (in the 64–70% range).

A simulation analysis with 3–5 mm aerogel particles into the cavity of a double-glazing unit with clear glass (U = 1.19 $W m^{-2}K^{-1}$) in a building located in Oslo (Norway) showed a reduction in heat loss of 58%, resulting in a total reduction of even 21% in energy consumption for heating, cooling, and lighting (30 $kWh m^{-2}$ $year^{-1}$) a standard solution with air [134].

When considering the Oslo study reported in Section 4.1, also granular aerogel was taken into account and similar results were found (U equal to 0.44 $W m^{-2}K^{-1}$): depending on the thickness of the granular aerogel glazing system, it was possible to move from a 10 to 13 $kWh m^{-2}$ $year^{-1}$ of energy saved [125].

In Table 7.4 a synthesis of the main simulation results available in the literature is reported, highlighting the windows technologies, the annual energy savings and the related climate area.

Table 7.4 Influence of granular aerogel glazing systems in heating and cooling energy consumption in different climate areas.

Case study	Glazing solutions	Climatic area	Annual heating and cooling savings [%]	References
Multifunctional building	Double air filled (4 clear – 15 air – 6 clear) ($U = 2.7\,W\,m^{-2}K^{-1}$; g = 0.77) (C1) PC panels with granular aerogel (25 mm) (g = 0.53, $U = 0.91\,W\,m^{-2}K^{-1}$) (C2) PC panels with granular aerogel (40 mm) (g = 0.25, $U = 0.54\,W\,m^{-2}K^{-1}$)	Ottawa London Helsinki Beijing Moscow Rome	15.4 (C1)–11.6 (C2) 19 (C1)–21.6 (C2) 18.3 (C1)–21 (C2) 15 (C1)–10 (C2) 17.6 (C1)–17.6 (C2) 19 (C1)–23.5 (C2)	[128]
A story office building model	Standard insulation glass (6 clear – 12 air – 6 mm clear) (C1) 15-mm aerogel (4 low iron glass outer – 15 aerogel – 4 clear inner) (C2) 15-mm aerogel (4 clear – 15 aerogel – 4 mm clear inner)	Harbin Beijing Shanghai Guangzhou Kunming 	2.6 (C1) 13.3 (C2) −2 (C1) 10 (C2) 3 (C1) 6.66 (C2) −2 (C1) 7.5 (C2) −6 (C1) 5 (C2)	[129]
Monetary Times building	Double glazed Nanogel system (10 mm) ($U = 1.38\,W\,m^{-2}K^{-1}$) Double glazed Nanogel system (20 mm) ($U = 0.78\,W\,m^{-2}K^{-1}$) Double glazed Nanogel system (40 mm) ($U = 0.42\,W\,m^{-2}K^{-1}$) Double-glazed Nano gel system (70 mm) ($U = 0.25\,W\,m^{-2}K^{-1}$) Double glazed Okagel system (4/30/6) ($U = 0.6\,W\,m^{-2}K^{-1}$) Double-glazed Okagel system (4/60/6) ($U = 0.3\,W\,m^{-2}K^{-1}$) Double-glazed Nanogel+Solera system (76.2 mm) ($U = 0.31\,W\,m^{-2}K^{-1}$)	Toronto	11.20	[130]

(*Continued*)

Downloaded from https://onlinelibrary.wiley.com/doi/ by ibrahim ragab - Universita Di Firenze Sistema | Wiley Online Library on [21/07/2024]. See the Terms and Conditions (https://onlinelibrary.wiley.com/terms-and-conditions) on Wiley Online Library for rules of use; OA articles are governed by the applicable Creative Commons License

Table 7.4 (Continued)

Case study	Glazing solutions	Climatic area	Annual heating and cooling savings [%]	References
Commercial building	Standard low-e glass system	Hong Kong	4–8% (for cooling)	[131]
	10-mm aerogel (6 float-10 granular aerogel-6 float)			
Office building	(C1) Standard glazing (4 float-15 air-4 float) ($U = 2.7\,W\,m^{-2}K^{-1}$)	Rome	17 (C1) 3 (C2)	[86]
	15-mm aerogel (4 float −15 granular aerogel A-type-4 float) ($U = 1\,W\,m^{-2}K^{-1}$)	Paris	28 (C1) 8 (C2)	
		Ottawa	15 (C1) 4 (C2)	
	(C2) Standard low-emission glazing (4 solar control+low-e-15 air – 4 float clear) ($U = 1.6\,W\,m^{-2}K^{-1}$)			
	15-mm aerogel (4 low-e-15 granular aerogel B-type-4 low-e) ($U = 1.1\,W\,m^{-2}K^{-1}$)			
Multi/story office building	Double glazed ($g = 0.75$, $U = 2.71\,W\,m^{-2}K^{-1}$)	Dhahran, Saudi Arabia	13.27	[132]
	16-mm aerogel (5 float-12 Argon–16 Granular Aerogel – 12 Argon– 5 float) ($g = 0.35$, $U = 0.45\,W\,m^{-2}K^{-1}$)			
Large atrium building – library	Single glazed system	Guanghou, China	−31	[133]
	Granular aerogel glazing system			
Office building	DGU system (6 float glass – 16 argon 90% – 4 float clear)	Rome	10	[89]
		London	8	
	PC Granular aerogel filled systems (40 mm) ($g = 0.51$)			
		Helsinki	12.7	

Downloaded from https://onlinelibrary.wiley.com/doi/ by ibrahim ragab - Universita Di Firenze Sistema , Wiley Online Library on [21/07/2024]. See the Terms and Conditions (https://onlinelibrary.wiley.com/terms-and-conditions) on Wiley Online Library for rules of use; OA articles are governed by the applicable Creative Commons License

Prototype of Evolutive house	Standard glazing (3 float – 6 air – 3 float – 6 air – 3 float) (g = 0.75, U = 2.3 $W m^{-2}K^{-1}$)	Perugia, Italy	72.3	[127]
	14-mm aerogel (4 float – 14 Granular Aerogel – 4 float) (g = 0.53, U = 0.91 $W m^{-2}K^{-1}$)			
Office building	Standard glazing (4 float – 14 air – 4 float) (g = 0.76, U = 2.86 $W m^{-2}K^{-1}$)	Oslo, Norway	—	[135]
	14-mm aerogel (4 float – 14 granular aerogel – 4 float)			
Myhrerenga Borettslag – residential building	Triple glazing unit-argon (4 Low-e – 8 Argon 90% – 4 Low-e – 8 Argon 90% – 4 Low-e) (g = 0.46, U = 0.79 $W m^{-2}K^{-1}$)	Oslo, Norway	20	[125]
	25-mm aerogel (4 clear – 25 granular aerogel – 4 clear) (g = 0.31, U = 0.44 $W m^{-2}K^{-1}$)			

Downloaded from https://onlinelibrary.wiley.com/doi/ by ibrahim ragab - Universita Di Firenze Sistema , Wiley Online Library on [21/07/2024]. See the Terms and Conditions (https://onlinelibrary.wiley.com/terms-and-conditions) on Wiley Online Library for rules of use; OA articles are governed by the applicable Creative Commons License

7.5 Applications

The high thermal performance of granular silica aerogel is the main reason why companies tried to place this material on the market of building construction materials. Although the material has a decades long history (see Section 2), the first real application in granular form is quite recent. One of first examples is the result of the ISOTEG experiment, in collaboration with R&D Project in 2000 [19]. A PMMA (poly methyl methacrylate) system with granular aerogel (U-value 0.37–0.56 $W m^{-2}K^{-1}$, depending on the configuration) was applied on the façade of the Bayerisches ZAE (Zentrum fur Angewandte Energieforschung) in Wurzburg, Germany [128] (Figure 7.7a).

In 2003, the Scobatherm product by Scobalit allowed the pioneer application of an aerogel glazing system for daylighting in a building: the School *Buchwiesen* in Zurich, Switzerland. The innovative system, made of a glass-dfiber reinforced polyester resin filled with granular aerogel (certified U-value 0.41 $W m^{-2}K^{-1}$) [137] was used by the architects V. and A. Amsler in the project of the roof of the gymnastics and physical education hall of the school [136].

Another important example of the granular aerogel application in education buildings concerns the 2007 project for the cluster campus at the Yale University in Connecticut, USA (Figure 7.7b) [134]. The great-scale project of a campus forecasted a group of buildings with different destinations and with a spatial interaction with the external area. The new art gallery was located in the perimeter

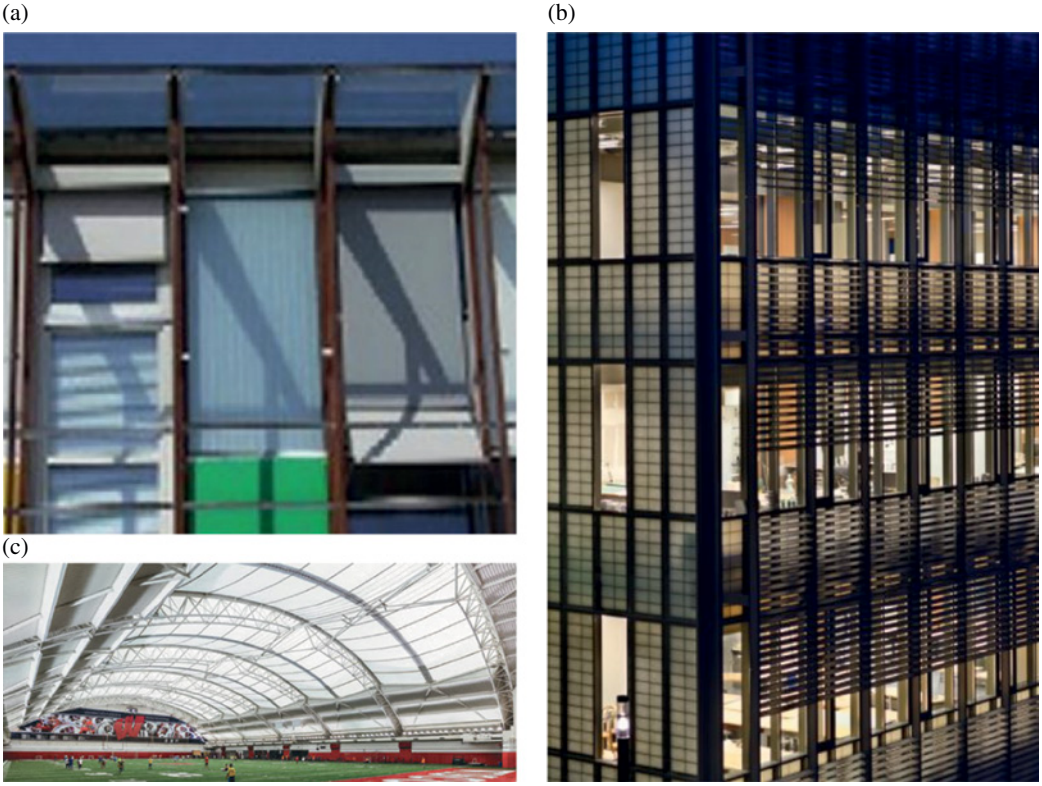


Figure 7.7 Applications of granular aerogel from experimental to large scale public buildings: (a) The façade of the ZAE (Bayerisches Zentrum fur Angewandte Energieforschung), Wurzburg, Germany [128]; (b) Perimetral surface of the Lantern building at Yale University, Connecticut, USA [134]. Cuce et al., 2014/with permission of Elsevier; (c) The Dedmon Athletic Center of Radford University, Virginia, USA [136].

of the main structure, whereas the central building was designed as a lantern that illuminates the complex. A great translucency was therefore required for the perimeter surfaces of the building. A combination of granular silica aerogel and glazing system allowed a light transmitting envelope with even a high thermal performance. This Kieran Timberlake's project archived the platinum LEED certification [138].

In 2008, a new technology involving aerogel allowed to cover the huge 5000 m^2 Dedmon Athletic Center of Radford University in the United States [136] (Figure 7.7c). It was part of the retrofitting process of the complex; a tens structure named Tensotherm system and designed by Birdair covers the field, with a granular aerogel layer between a PTFE sheet and a vapor barrier, for a total thickness of 24 mm and a thermal transmittance of 0.56 $W m^{-2}K^{-1}$ [139]. This solution limited the high heat loss of the standard tens structure.

Granular aerogel was also used in daily and smaller-scale applications: the Tengelmann Climate Market in Muhlheim, Germany [136] (Figure 7.8a), where a roof window Okagel system by Okalux GmbH was used to allow a natural illumination inside the market area, thanks to the alternate disposition of laminate roof elements and *una tantum* aerogel pains maintaining a good thermal insulation (U-value certified 0.3 $W m^{-2}K^{-1}$ certificated by Okalux) [140]. Another interesting example of granular aerogel applications in daily buildings is the roof of a pharmacy in Neuhausen, Switzerland [141]. The Scobatherm product for roof by Scobalit allows the creation of a completely translucent roof for a part of the pharmacy, making a natural illumination effect. Like in the market situation, also the pharmacy's roof has a competitive U-value of 0.41 $W m^{-2}K^{-1}$ [138].

These last examples show that granular aerogel could be an interesting technology for small-scale applications. However, the performance of the material becomes significant when considering great size buildings, possibly industrial or transport connected hangars, because it allows to create great translucent surfaces, leading to important energy savings in terms of both air conditioning and lighting.

(a) (b)

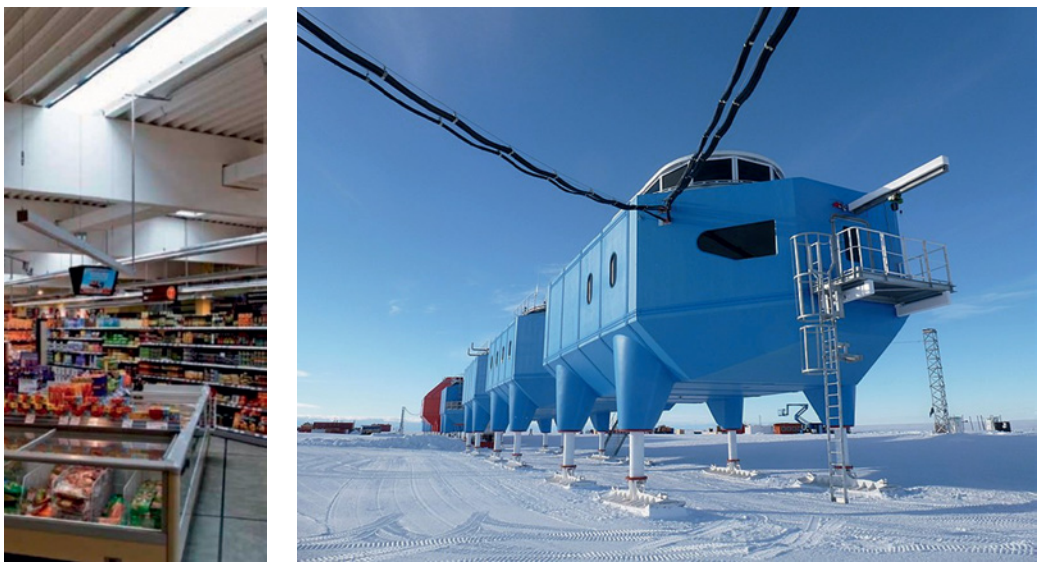


Figure 7.8 Granular aerogel vertical systems applications in buildings: (a) The Tengelmann Climate Market, Muhlheim, Germany [136]; (b) The Halley VI Research Station, Antarctica [136].

In this context, RODA developed a granular aerogel frame system made with Lumira aerogel (Nanogel) by Cabot Corporation; it was used to create the great translucent vertical surfaces of the SNFC Lyon TGV maintenance hall. The granular aerogel filled polycarbonate panels were used also for punctual installation on the roof, ensuring a high level of indoor illuminance. The 25-mm thick polycarbonate with Nanogel pain has a thermal transmittance of $0.91\,W\,m^{-2}K^{-1}$ [142]. Kalwall Corporation developed a similar product, with interesting application cases: in Israel, Ghafari Architects designed the Woodward Aircraft Turbine Systems factory at Rock Campus Loves Park, with the upper level of the main hangar equipped with granular aerogel filled panels [143]. Another example is the AUDI showroom in West London, United Kingdom, where granular aerogel is used to make the great windows of the car exposition [143]. Bigger vehicles require bigger hangars, and the energy requirements for lighting become important. For this reason, Kalwall's system is used also for the top continuous translucent façade of the American Airlines Hangar at the O'Hare Airport in Chicago, USA. The designer is Ghafari Architects and the system ensures an indoor daylight illumination standard even in this large dimension space [143]. Wannemacher Jensen Architects applied the same technology for a church. The "Christ the King" Church located in Christian Ministry Center Largo in Florida (USA) is a quite different space, but it is an efficient example on how it is possible to create modern rose windows as translucent surfaces with a high thermal performance [143]. Exactly this property is the main reason of maybe the most unusual application in an uncommon location: the Halley VI Research Station [121]. This center (Figure 7.8b) is located at Brunt Ice Shelf, Antarctica, and it is the successor of the Halley V research center. Granular aerogel in this extreme climatic condition is ideal for the window termed Okagel by OKalux GmbH. With a thickness of 60 mm, the thermal transmittance is $0.3\,W\,m^{-2}K^{-1}$ [144]. The installation allowed the presence of transparent elements in extreme climatic conditions, without exaggerate thicknesses and then weights. It appears also as an elegant architectural solution for the base.

7.6 Conclusions

Glazing systems with silica aerogel are suitable for building applications, providing a larger thermal insulation without substantial reduction of the light transmission, compared to conventional glazing units.

These solutions are very efficient systems in cold climates due to their low thermal transmittance and high total solar energy transmittance; conversely, the energy demand for cooling might increase, especially in temperate and hot climates.

The properties of transparent aerogel, also when assembled in glazing systems, depend on the production process, on the layer thickness, on the features of the glazing panes, on the geometry of the systems and, finally, on the type of aerogel (granular or monolithic form). Keeping the material layer under pressure could improve thermal performance. In particular, a thermal conductivity of about 0.019 and $0.010\,W\,m^{-1}K^{-1}$ was found for the granules at ambient and 10 mbar pressure, respectively, whereas the monolithic form decreases from 0.015 to $0.008\,W\,m^{-1}K^{-1}$ at ambient pressure and under vacuum, respectively.

The light transmittance of a 10 mm monolithic aerogel pane is comparable to that of a 6-mm clear float glass; the visible transmittance of monolithic aerogel is in the 0.60–0.98 range, whereas the solar transmittance is in the 0.80–0.86 range when the thickness varies in the 2.5–17 mm range. When considering the granular form, optical visual transmittance is significantly affected by the particle size and the vision through the material layer is not allowed; nevertheless, it could be

preferred in some situations, because the light gets very deep in the room, significantly reducing glare problems. On the contrary, monolithic aerogel allows the vision through the window, making it suitable for residential building applications.

Aerogel is also able to reduce the transmitted noise by about 3 dB when compared to standard glazing solutions.

The mechanical strength of aerogels decreases with density: monolithic aerogels poorly perform in terms of tensile strength, 10–100 times lower than the compression strength. Many synthetic routes are investigated with the aim of strengthening silica aerogels. The most important approaches are hybridization and aging.

The influence of glazing systems with monolithic and granular aerogel fillings with respect to traditional double and triple glazing solutions were widely studied by means of energy dynamic simulations. Numerical analyses show that the technology outperforms conventional double- and triple-glazing systems, but some difficulties are related to the lack of standards and consolidated models of the aerogel internal structure. It is important for the calculation of the solar factor of such components, which is critical to determining the solar gains of the façade and the whole energy performance of the building.

The high thermal performance of granular silica aerogel is the main reason companies have tried to place this material on the market of building construction materials since 2000. The composed aerogel-based systems were applied in many buildings, and the effectiveness of the solutions was evaluated by means of in situ measurements. A wide number of applications of daylighting systems with granular aerogels could be found in schools, commercial, public and industrial buildings, airports, etc., especially in USA and in North Europe.

7.7 Outlook

Based on the presented work, daylighting insulating systems with translucent or transparent silica aerogel could have the highest potential in the fenestration market, targeting thermal transmittance values up to $0.3\,W\,m^{-2}K^{-1}$, depending on the thickness and the form. Progress in the production process is needed to manufacture large sheets of monolithic aerogels. Furthermore, problems related to the compaction of granular aerogel windows should be solved. Being a particle aggregation system, the volume of the aerogel granules tends to shrink along with time to reach the highest possible packing density, causing an air gap at the top of the glazing system, which becomes a thermal bridge.

Even though aerogel windows have a lot of excellent properties, they are far from cost-effective, in order to compete with standard solutions. As regards transparent aerogel components, the market is quite unstable, and cost will remain much higher than conventional glazing systems (double- and triple-pane), especially when considering an expected 50% cost reduction for the production process. The cost-effectiveness of aerogel glazings is likely to evolve in the next years, thanks to recent studies focused on improving the quality of the view through the panes by means of the control of hydrophobicities, to shorten the fabrication time, and to reduce costs and waste through alternative fabrication methods such as rapid extraction in supercritical conditions. Strong developments are needed for monolithic aerogel, which may easily penetrate the building market, including the residential sector, thanks to its full transparent aspect; however, the technology is still far from the technological maturity.

Future studies should focus also on the aging effect on the properties of aerogel monoliths and granules, by considering environmental factors such as temperature, moisture, and solar radiation.

References

1 Kistler, S.S. (1931). Coherent expanded aerogels and jellies. *Nature* 127 (3211): 741.
2 Kistler, S.S. (1932). Coherent expanded aerogels. *J. Phys. Chem.* 32: 56.
3 Alemal, J., Chadwick, A.V., He, J. et al. (2007). Definitions of terms relating to the structure and processing of sols, gels, networks, and inorganic–organic hybrid materials (IUPAC recommendations 2007). *Pure Appl. Chem.* 79: 1801–1829.
4 Kistler, S.S. (1932). Coherent expanded aerogels. *J. Phys. Chem.* 36: 52–64.
5 Aegerter, M.A., Leventis, N., and Koebel, M. (2011). *Aerogels Handbook*. New York: Springer.
6 Schmitt, W.J.1982). The preparation and properties of acid-catalyzed silica aerogel. MSc Thesis. University of Wisconsin, Madison.
7 Tewari, P.H., Hunt, A.J., and Lofftus, K.D. (1985). Improving the visible transparency of silica aerogels. *Mater. Lett.* 3: 363.
8 Tillotson, T.M. and Hrubesh, L.W. (1992). Transparent ultralow-density silica aerogels prepared by a two-step sol-gel process. *J. Non-Cryst. Solids* 145: 44.
9 Lee, K.H., Kim, S.Y., and Yoo, K.P. (1995). Preparation and characterization of hydrophobic silica aerogels. *J. Non-Cryst. Solids* 186: 18.
10 Yokagawa, H. and Yokayama, M. (1995). Hydrophobic silica aerogels. *J. Non-Cryst. Solids* 186: 23.
11 Tajiri, K., Igarashi, K., and Nishio, T. (1995). Effects of supercritical drying media on structure and properties of silica aerogel. *J. Non-Cryst. Solids* 186: 83.
12 Roth, T.B., Anderson, A.M., and Carroll, M.K. (2008). Analysis of a rapid supercritical extraction aerogel fabrication process: prediction of thermodynamic conditions during processing. *J. Non-Cryst. Solids* 354: 3685–3693.
13 Baumann, T.F., Kucheyev, S.O., Gash, A.E., and Satcher, J.H. Jr. (2016). Facile synthesis of a crystalline, high-surfacearea SnO_2 aerogel. *Adv. Mater.* 17: 1546–1548.
14 Baudrin, E., Sudant, G., Larcher, D. et al. (2006). Preparation of nanotextured VO2[B] from vanadium oxide aerogels. *Chem. Mater.* 18: 4369–4374.
15 Carpenter, E.E., Long, J.W., Rolison, D.R. et al. (2006). Magnetic and Mossbauer spectroscopy studies of nanocrystalline iron oxide aerogels. *J. Appl. Phys.* 99 (8): 08N711.
16 Hæreid, S., Nilsen, F., and Einarsrud, M.A. (1996). Properties of silica aerogel aged in TEOS. *J. Non-Cryst. Solids* 204: 228–234.
17 Dorcheh, A.S. and Abbasi, M.H. (2008). Silica aerogel; synthesis, properties and characterization. *J. Mater. Process. Technol.* 199: 10–26.
18 Baetens, R., Jelle, B.P., and Gustavsen, A. (2011). Aerogel insulation for building applications: a state-of-the-art review. *Energy Build.* 43: 761–769.
19 Buratti, C. and Moretti, E. (2013). Silica nanogel for energy-efficient windows. In: *Nanotechnology in Eco-Efficient Construction* (ed. F.P. Torgal, M.V. Diamanti, A. Nazari, and C.G. Granqvist), 207–235. Philadelphia: Woodhead Publishing.
20 Cuce, E., Cuce, P.M., Wood, C.J., and Riffat, S.B. (2014). Monolithic aerogel preparation. *Renew. Sustain. Energy Rev.* 34: 273–299.
21 Anderson, A.M. and Carroll, M.K. (2019). Silica nanogel for energy-efficient windows. In: *Translucent Silica Aerogel: Properties, Preparation and Applications* (ed. C. Buratti), 1–30. New York: Novapublishers.
22 Wagh, P.B., Begag, R., Pajonk, G.M. et al. (1999). Comparison of some physical properties of silica aerogel monoliths synthesized by different precursors. *Mater. Chem. Phys.* 57 (3): 214–218.
23 Hüsing, N. and Schubert, U. (1998). Aerogels—airy materials: chemistry, structure, and properties. *Angew. Chem. Int. Ed.* 37: 22–45.

24 Duer, K. and Svendsen, S. (1998). Monolithic silica aerogel in superinsulating glazings. *Sol. Energy* 63 (4): 259–267.

25 Zhu, Q., Li, Y., and Qiu, Z. (2007). Research progress on aerogels as transparent insulation materials. International Conference on Power Engineering-2007, (October 23-27, 2007). In: *Challenges of Power Engineering and Environment* (ed. K. Cen, Y. Chi, and F. Wang). Berlin, Heidelberg: Springer.

26 Chao, X., Shen, J., and Bin, Z. (2009). Ultralow density silica aerogels prepared with PEDS. *J. Non-Cryst. Solids* 355 (8): 492–495.

27 Anderson, A.M., Carroll, M.K., Green, E.C. et al. (2010). Hydrophobic silica aerogels prepared via rapid supercritical extraction. *J. Sol-Gel Sci. Technol.* 53 (2): 199–207.

28 Pisal, A.A. and Rao, A.V. (2017). Development of hydrophobic and optically transparent monolithic silica aerogels for window panel applications. *J. Porous Mater.* 24 (3): 685–695.

29 Halimaton, H. (2007). Silica aerogels. US Patent 2, 007, 027, 605, 1A1.

30 Liu, Q., Frazier, A.H., Zhao, X. et al. (2018). Flexible transparent aerogel as window retrofitting films and optical elements with tunable birefringence. *Nano Energy* 48: 266–274.

31 Zu, G., Kanamori, K., Maeno, A. et al. (2018). Superflexible multifunctional polyvinylpolydimethylsiloxane based aerogels as efficient absorbents, thermal superinsulators, and strain sensors. *Angew. Chem. Int. Ed.* 57 (31): 9722–9727.

32 Mandal, C., Donthula, S., Far, H.M. et al. (2019). Transparent, mechanically strong, thermally insulating cross-linked silica aerogels for energy-efficient windows. *J. Sol-Gel Sci. Technol.* 92: 84–100.

33 Wong, J.C.H., Kaymak, H., Brunner, S., and Koebel, M.M. (2014). Mechanical properties of monolithic silica aerogels made from polyethoxydisiloxanes. *Micropor. Mesopor. Mater.* 183: 23–29.

34 Rigacci, A., Einarsrud, M.A., Nilsen, E. et al. (2004). Improvement of the silica aerogel strengthening process for scaling-up monolithic tile production. *J. Non-Cryst. Solids* 35: 196–201.

35 Bisson, A., Rigacci, A., Lecomte, D. et al. (2003). Drying of silica gels to obtain aerogels: phenomenology and basic techniques. *Drying Technol.* 21 (4): 593–628.

36 Aravind, P.R., Shajesh, P., Mukundan, P., and Warrier, K.G.K. (2009). Silica–titania aerogel monoliths with large pore volume and surface area by ambient pressure drying. *J. Sol-Gel Sci. Technol.* 52 (3): 328–334.

37 Kirkbir, F., Murata, H., Meyers, D., and Chaudhuri, S.R. (1998). Drying of large monolithic aerogels between atmospheric and supercritical pressures. *J. Sol-Gel Sci. Technol.* 13 (1–3): 311–316.

38 Hüsing, N., Schwertfeger, F., Tappert, W., and Schubert, U. (1995). Influence of supercritical drying fluid on structure and properties of organically modified silica aerogels. *J. Non-Cryst. Solids* 18: 37–43.

39 Bertino, M.F. (2018). Rapid fabrication of hybrid aerogels and 3D printed porous materials. *J. Sol-Gel Sci. Technol.* 86 (2): 239–254.

40 Poco, J.F., Coronado, P.R., Pekala, R.W., and Hrubesh, L.W. (1996). A rapid supercritical extraction process for the production of silica aerogels. *MRS Online Proc. Lib. Arch.* 431: 431.

41 Wagh, P.B., Ingale, S.V., and Gupta, S.C. (2011). New technology for rapid processing and moulding of silica aerogel materials in prescribed shapes and sizes and their characterization. *J. Sol-Gel Sci. Technol.* 58 (2): 481–489.

42 Mahadik, D.B., Lee, Y.K., Chavan, N.K. et al. (2016). Monolithic and shrinkage-free hydrophobic silica aerogels via new rapid supercritical extraction process. *J. Supercrit. Fluids* 107: 84–91.

43 Jung, H.N.R., Lee, Y.K., Parale, V.G. et al. (2017). Hydrophobic silica composite aerogels using poly (methyl methacrylate) by rapid supercritical extraction process. *J. Sol-Gel Sci. Technol.* 83 (3): 692–697.

44 Pajonk, G.M., Venkateswara Rao, A., Sawant, B.M., and Parvath, N.N. (1997). Dependence of monolithicity and physical properties of TMOS silica aerogels on gel aging and drying conditions. *J. Non-Cryst. Solids* 209: 40–50.

45 Yoda, S. and Ohshima, S. (1999). Supercritical drying media modification for silica aerogel preparation. *J. Non-Cryst. Solids* 248 (2–3): 224–234.

46 Gross, J., Coronado, P.R., and Hrubesh, L.W. (1998). Elastic properties of silica aerogels from a new rapid supercritical extraction process. *J. Non-Cryst. Solids* 225: 282–286.

47 Gauthier, B.M., Bakrania, S.D., Anderson, A.M., and Carroll, M.K. (2004). A fast supercritical extraction technique for aerogel fabrication. *J. Non-Cryst. Solids* 350: 238–243.

48 Gauthier, B.M., Anderson, A.M., Bakrania, S. et al. (2008). Method and device for fabricating aerogels and aerogel monoliths obtained thereby. US. Patent 7, 384, 988 and 8, 080, 591. Washington, DC: U.S. Patent and Trademark Office.

49 Carroll, M.K., Anderson, A.M., and Gorka, C.A. (2014). Preparing silica aerogel monoliths via a rapid supercritical extraction method. *J. Vis. Exp.: JoVE* 84: e51421.

50 Anderson, A.M., Wattley, C.W., and Carroll, M.K. (2009). Silica aerogels prepared via rapid supercritical extraction: effect of process variables on aerogel properties. *J. Non-Cryst. Solids* 355 (2): 101–108.

51 Estok, S.K., Hughes, T.A., Carroll, M.K., and Anderson, A.M. (2014). Fabrication and characterization of TEOS-based silica aerogels prepared using rapid supercritical extraction. *J. Sol-Gel Sci. Technol.* 70: 371–377.

52 Bhuiya, M.M.H., Anderson, A.M., Carroll, M.K. et al. (2016). Preparation of monolithic silica aerogel for fenestration applications: scaling up, reducing cycle time, and improving performance. *Ind. Eng. Chem.* 55: 6971–6981.

53 Ma, H.S., Roberts, A.P., Prevost, J.H. et al. (2000). Mechanical structure-property relationship of aerogels. *J. Non-Cryst. Solids* 277: 127–141.

54 Woignier, T. and Phalippou, J. (1989). Scaling law variation of the mechanical properties of silica aerogels. *Rev. Phys. Appl.* 24 (C4): 179–184.

55 Afshar, T., Disfani, M.M., Arulrajah, A. et al. (2017). Impact of particle shape on breakage of recycled construction and demolition aggregates. *Powder Technol.* 308 (2017): 1–12.

56 Yao, W., Guangsheng, G., Fei, W., and Jun, W. (2002). Fluidization and agglomerate structure of SiO_2 nanoparticles. *Powder Technol.* 124 (2002): 152–159.

57 Cavarretta, I., Coop, M., and O'Sullivan, C. (2010). The influence of particle characteristics on the behaviour of coarse grained soils. *Géotechnique* 60: 413–423.

58 Quarch, K., Durand, E., Schilde, C. et al. (2010). Mechanical fragmentation of precipitated silica aggregates. *Chem. Eng. Res. Des.* 88: 1639–1647.

59 Huan, H., Guo, Z., Stroeven, P. et al. (2009). Characterization of the packing of aggregate in concrete by a discrete element approach. *Mater. Charact.* 60: 1082–1087.

60 Wang, D. and Pfeffer, R. (2013). Mixing and packing of binary hydrophobic silica aerogels. *Powder Technol.* 235 (2013): 975–982.

61 Neugebauer, A., Chen, K., Tang, A. et al. (2014). Thermal conductivity and characterization of compacted, granular silica aerogel. *Energy Build.* 79: 47–57.

62 Parmenter, K.E. and Milstein, F. (1998). Mechanical properties of silica aerogels. *J. Non-Cryst. Solids* 223: 179–189.

63 Gonçalves, W., Morthomas, J., Chantrenne, P. et al. (2018). Elasticity and strength of silica aerogels: a molecular dynamics study on large volumes. *Acta Mater.* 145.

64 Woignier, T., Primera, J., Alaoui, A.H., and Calas, S. (2015). Mechanical Properties and Brittle Behavior of Silica Aerogels. *Gels.* 1: 256–275.

65 Kucheyev, S.O., Lord, K.A., and Hamza, A.V. (2011). Room-temperature creep of nanoporous silica. *J. Mater. Res.* 26: 781–784.

66 Tillotson, T.M. and Reynolds, J.G. (2003). Structure and characterization of sol–gel and aerogel materials and oxidation products from the reaction of $(CH_3O)_4Si$ and $C_{16}H_{33}Si(OCH_3)_3$. *J. Non-Cryst. Solids* 331: 168–176.

67 Perret, A., Foray, G., Roiban, L. et al. (2014). 3D multiscale characterization of silica aerogels composites. 3DMS 2014. *Proceedings of the 2nd International Congress on 3D Materials Science*.

68 Nocentini, K., Achard, P., and Biwole, P. (2018). Hygro-thermal properties of silica aerogel blankets dried using microwave heating for building thermal insulation. *Energy Build.* 158: 14–22.

69 Achard, P., Rigacci, A., Echantillac, T. et al. (2011). Insulating silica xerogel plaster. W0/2011/083174.

70 Gao, T., Jelle, B.P., Gustavsen, A., and Jacobsen, S. (2014). Aerogel-incorporated concrete: an experimental study. *Constr. Build. Mater.* 52: 130–136.

71 Ng, S., Jelle, B.P., Sandberg, L.I.C. et al. (2015). Experimental investigations of aerogel-incorporated ultra-high performance concrete. *Constr. Build. Mater.* 77: 307–316.

72 Fickler, S., Milow, B., Ratke, L. et al. (2015). Development of high performance aerogel concrete. *Energy Proc.* 78: 406–411.

73 Guptaa, N. and Ricci, W. (2007). Processing and compressive properties of aerogel/epoxy composites. *J. Mater. Process. Technol.* 198: 1–3.

74 Woignier, T. and Phalippou, J. (1988). Mechanical strength of silica aerogels. *J. Non-Cryst. Solids* 100: 404–408.

75 Perret, A. (2015). 3D Characterizations Tools Dedicated to Porous Material for Superinsulation. PhD's thesis, INSA-Lyon, University of Lyon.

76 Yrieix, B., Morel, B., Foray, G. et al. (2014). Aerogel-based material that is super-insulating at athmospheric pressure. US Patent 2014/0361209 A1.

77 Kucheyev, S.O., Stadermann, M., Shin, S.J. et al. (2012). Super-compressibility of ultralow-density nanoporous silica. *Advanced Materials* 24 (6): 776–780.

78 Bisson, A., Rigacci, A., Lecomte, D., and Achard, P. (2004). Effective thermal conductivity of divided silica xerogel beds. *Journal of Non-Crystalline Solids* 350: 379–384.

79 Chal, B., Yrieix, B., Roiban, L., and Masemelli-Varlot, K. (2018). Hygrothermal aging of nanostructured silica, mechanical properties evolution. *RUGC St Etienne*, 35–37. France.

80 Gelb, L.D. (2007). Simulating silica aerogels with a coarse-grained flexible model and langevin dynamics. *J. Phys. Chem. C* 111: 15792–15802.

81 Voivret, C., Radjaï, F., Delenne, J.Y., and El Youssoufi, M.S. (2009). Multiscale force networks in highly polydisperse granular media. *Physical Review Letters* 102: 2–5.

82 Einasrud, M.A., Dahle, M., Lima, S., and Hæreid, S. (1995). Preparation and properties of monolithic silica xerogels from TEOS-based alcogels aged in silane solutions. *Journal of Non-Crystalline Solids* 186: 96–103.

83 Joshi, S.C., Manikandan, P., and Jothi, Y. (2011). Enhancement studies on manufacturing and properties of novel silica aerogel composites. *Gels* 4 (1): 5.

84 Fricke, J. and Emmerling, A. (1992). Aerogels – Preparation, Properties, Applications. *Structure and Bonding* 77: 37–87.

85 Buratti, C., Merli, F., and Moretti, E. (2017). Aerogel-based materials for building applications: Influence of granule sizes on thermal and acoustic performance. *Energy and Buildings* 152: 472–482.

86 Buratti, C., Moretti, E., and Zinzi, M. (2017). High energy-efficient windows with silica aerogel for building refurbishment: Experimental characterization and preliminary simulations in different climate conditions. *Buildings* 7: 1–12.

87 Wei, T.Y., Chang, T.F., Lu, S.Y., and Chang, Y.C. (2007). Preparation of monolithic silica aerogel of low thermal conductivity by ambient pressure drying. *Journal of the American Ceramic Society* 90 (7): 2003–2007.

88 Moretti, E., Belloni, E., Merli, F. et al. (2019). Laboratory and pilot scale characterization of granular aerogel glazing systems. *Energy and Buildings* 202: 109349.

89 Moretti, E., Zinzi, M., Merli, F., and Buratti, C. (2018). Optical, thermal, and energy performance of advanced polycarbonate systems with granular aerogel. *Energy Build.* 166: 407–417.

90 Moretti, E., Zinzi, M., Carnielo, E., and Merli, F. (2017). Advanced Polycarbonate Transparent Systems with Aerogel: Preliminary Characterization of Optical and Thermal Properties. *Energy Proc.* 113: 9–16.

91 Ihara, T., Grynnig, S., Gao, T. et al. (2015). Impact of convection on thermal performance of aerogel granulate glazing systems. *Energy and Buildings* 88: 165–173.

92 Buratti, C. and Moretti, E. (2012). Experimental performance evaluation of aerogel glazing systems. *Applied Energy* 97: 430–437.

93 Buratti, C. and Moretti, E. (2012). Glazing systems with silica aerogel for energy savings in buildings. *Applied Energy* 98: 396–403.

94 Schultz, J.M. and Jensen, K.I. (2008). Evacuated aerogel glazings. *Vacuum* 82 (7): 723–729.

95 Jensen, K.I., Schultz, J.M., and Kristiansen, F.H. (2004). Development of windows based on highly insulating aerogel glazings. *Journal of Non-Crystalline Solids* 350: 351–357.

96 Buratti, C., Moretti, E., Belloni, E., and Zinzi, M. (2019). Experimental and Numerical Energy Assessment of a Monolithic Aerogel Glazing Unit for Building Applications. *Appl. Sci.* 9: 5473.

97 Schultz, J.M., Jensen, K.I., and Kristiansen, F.H. (2005). Super insulating aerogel glazing. *Solar energy materials and solar cells.* 89 (2-3): 275–285.

98 Marszewski, M., King, S.C., Yan, Y. et al. (2019). Thick Transparent Nanoparticle-Based Mesoporous Silica Monolithic Slabs for Thermally Insulating Window Materials. *Appl. Nano Mater.* .

99 Zhao, L., Strobach, E., Bhatia, B. et al. (2019). Theoretical and experimental investigation of haze in transparent aerogels. *Optics Express* 27 (4): A39–A50.

100 Pajonk, G.M., Elaloui, E., Chevalier, B., and Begag, R. (1997). Optical transmission properties of silica aerogels prepared from polyethoxidisiloxanes. *Journal of Non-Crystalline Solids* 210: 224.

101 Lv, Y., Huang, R., Wu, H. et al. (2017). Study on thermal and optical properties and influence factors of aerogel glazing units. *Proc. Eng.* 205: 3228–3234.

102 Gao, T., Jelle, B.P., Ihara, T., and Gustavsen, A. (2014). Insulating glazing units with silica aerogel granules: The impact of particle size. *Applied Energy* 128: 27–34.

103 Beck, A., Korner, W., and Fricke, J. (1994). Optical investigations of granular aerogel fills. *Journal of Physics D: Applied Physics* 27 (1): 13.

104 Reim, M., Beck, A., Körner, W. et al. (2002). Highly insulating aerogel glazing for solar energy usage. *Solar Energy* 72: 21–29.

105 Reim, M., Körner, W., Manara, J. et al. (2005). Silica Aerogel Granulate Material for Highly Thermal Insulation and Daylighting. *Solar Energy* 79: 131–139.

106 Zinzi, M., Rossi, G., Anderson, A.M. et al. (2019). Optical and visual experimental characterization of a glazing system with monolithic silica aerogel. *Solar Energy* 183: 30–39.

107 Buratti, C. and Moretti, E. (2011). Lighting and energetic characteristics of transparent insulating materials: experimental data and calculation. *Indoor Built Environ.* 20: 400–411.

108 Pajonk, G.M. (1998). Transparant silica aerogels. *J. Non-Cryst. Solids* 225: 307–314.

109 Forest, L., Gibiat, V., and Hooley, A. (2001). Impedance matching and acoustic absorption in granular layers of silica aerogels. *J. Non-Cryst. Solids* 285: 230–235.

110 Pierre, A.C. and Pajonk, G.M. (2002). Chemistry of aerogels and their applications. *Chem. Rev.* 102 (11): 4243–4266.

111 Alexander, S. (1989). Vibrations of fractals and scattering of light from aerogels. *Phys. Rev. B* 40: 7953.

112 Gibiat, V., Lefeuvre, O., Woigniert, T. et al. (1995). Acoustic properties and potential applications of silica aerogels. *J. Non-Cryst. Solids* 186: 244–255.

113 Forest, L., Gibiat, V., and Woignier, T. (1998). Biot's theory of acoustic propagation in porous media applied to aerogels and alcogels. *J. Non-Cryst. Solids* 225: 287–292.

114 Conroy, J.F., Hosticka, B., Davis, S.C. et al. (1999). Microscale thermal relaxation during acoustic propagation in aerogel and other porous media. *Microscale Thermophys. Eng.* 3 (3): 199–215.

115 Patel, R.P., Purohit, N.S., and Suthar, A.M. (2009). An overview of silica aerogels. *Int. J. Chem. Tech. Res.* 1 (4): 1052–1057.

116 Moretti, E., Merli, F., Cuce, E., and Buratti, C. (2017). Thermal and acoustic properties of aerogels: preliminary investigation of the influence of granule sizes. *Energy Proc.* 111: 472–480.

117 Sachithanadam, M. and Joschi, S.C. (2016). Effect of granule sizes on acoustic properties of protein-based silica aerogel composites via novel inferential transmission loss method. *Gels* 2: 11.

118 ISO 10140-2: 2010. Acoustics - laboratory measurement of sound insulation of building elements - measurement of airborne sound insulation.

119 ISO 354: 2003. Acoustics - measurement of sound absorption in a reverberation room.

120 Bheekhun, N., Abu Talib, A.R., and Hassan, M.R. (2013). Aerogels in aerospace: an overview. *Adv. Mater. Sci. Eng.* 1–18.

121 Merli, F., Anderson, A.M., Carroll, M.K., and Buratti, C. (2018). Acoustic measurements on monolithic aerogel samples and application of the selected solutions to standard window systems. *Appl. Acoust.* 142: 123–131.

122 Takeshita, S., Akasaka, S., and Yoda, S. (2019). Structural and acoustic properties of transparent chitosan aerogel. *Mater. Lett.* 254: 258–261.

123 ISO 10534-2: 1998. Acoustics – determination of sound absorption coefficient and impedance in impedance tubes – part 2: transfer-function method.

124 ISO 140-5: 1998. Acoustics - measurement of sound insulation in buildings and of building elements - part 5: field measurements of airborne sound insulation of façade elements and façades.

125 Lolli, N. and Andresen, I. (2016). Aerogel vs. argon insulation in windows: a greenhouse gas emissions analysis. *Build. Environ.* 101: 64–76.

126 Berardi, U. (2015). The development of a monolithic aerogel glazed window for an energy retrofitting project. *Appl. Energy* 154: 603–615.

127 Buratti, C., Belloni, E., and Palladino, D. (2014). Evolutive housing system: refurbishment with new technologies and unsteady simulations of energy performance. *Energy Build.* 74: 173–181.

128 Buratti, C. and Moretti, E. (2013). Nanogel windows. In: *Nearly Zero Energy Building Refurbishment, a Multidisciplinary Approach* (ed. F.P. Torgal, M. Mstretta, A. Kaklauskas, et al.), 555–581. London: Springer.

129 Wang, H., Wu, H., Ding, Y. et al. (2014). Feasibility and optimization of aerogel glazing system for building energy efficiency in different climates. *Int. J. Low-Carbon Technol.* 10: 412–419.

130 Berardi, U. (2018). Aerogel-enhanced systems for building energy retrofits: insights from a case study. *Energy Build.* 159: 370–381.

131 Huang, Y. and Niu, J. (2015). Energy and visual performance of the silica aerogel glazing system in commercial buildings of Hong Kong. *Constr. Build. Mater.* 94: 57–72.

132 Mujeebu, M.A., Ashraf, N., and Alsuwayigh, A. (2016). Energy performance and economic viability of nano aerogel glazing and nano vacuum insulation panel in multi-story office building. *Appl. Energy* 113: 949–956.
133 Yang, Y., Wu, H., Yang, L. et al. (2019). Thermal and day-lighting performance of aerogel glazing system in large atrium building under cooling-dominant climates. *Energy Proc.* 158: 6347–6357.
134 Cuce, E., Cuce, P.M., Wood, C.J., and Riffat, S.B. (2014). Toward aerogel based thermal superinsulation in buildings: a comprehensive review. *Renew. Sustain. Energy Rev.* 273–299.
135 Gao, T., Ihara, T., Grynning, S. et al. (2016). Perspective of aerogel glazings in energy efficient buildings. *Build. Environ.* 95: 405–413.
136 Koebel, M., Rigacci, A., and Achard, P. (2012). Aerogel-based thermal superinsulation: an overview. Springer science+business media, LLC. *J. Sol-Gel Sci. Technol.* 63 (2012): 315–339.
137 School *"Buchwiesen"* in Zurich. https://www.scobalit.de/produkte/hohlkammer.html (accessed 15 November 2023).
138 Kieran Timberlake. https://kierantimberlake.com/page/sculpture-building-and-school-of-art-gallery (accessed 15 November 2023).
139 Dedmon Athletic Centre. https://www.birdair.com/birdair-portfolio/mcclain-athletic-facility (accessed 15 November 2023).
140 Okalux products. https://www.okaluxna.com/.
141 Riffat, S.B. and Qiu, G. (2013). A review of state-of-the-art aerogel applications in buildings. *Int. J. Low-Carbon Technol.* 8: 1–6.
142 Lumira aerogel products. https://www.roda.de/wp-content/uploads/2018/03/Lumira_facade_systems.pdf.
143 Kalwall products. https://www.kalwall.com/portfolio (accessed 15 November 2023).
144 The Halley VI Research Station, Antarctica. https://hbarchitects.co.uk/halley-vi-british-antarctic-research-station (accessed 15 November 2023).

8

Inorganic Aerogels and Their Composites for Thermal Insulation in White Goods

Özge Payanda Konuk[1], Orçun Yücel[2], and Can Erkey[1,3,4]

[1] *Materials Science and Engineering, Koç University, Rumelifeneri Yolu 34450 Sarıyer, Istanbul, Turkey*
[2] *Material Technologies Department, Arçelik A.Ş., Central R&D, 34950, Çayırova 34950 Tuzla, Istanbul, Turkey*
[3] *Chemical and Biological Engineering, Koç University, Rumelifeneri Yolu 34450 Sarıyer, Istanbul, Turkey*
[4] *Tüpraş Energy Center (KUTEM), Koç University, Rumelifeneri Yolu 34450 Sarıyer, Istanbul, Turkey*

8.1 Introduction

Worldwide energy production and consumption is increasing. Although the share of energy from renewable sources has been steadily increasing, 84% of the world's energy is still produced from coal, oil, and natural gas sources according to BP's 2020 data [1]. The use of fossil fuels leads to emission of greenhouse gases, which causes environmental pollution, affecting the climate. In addition, it threatens human health, nature, and biodiversity.

Energy saving and sustainability are getting more and more attention in order to protect the environment and natural resources, and for this purpose, more studies are focused on developing products with low energy consumption.

According to IEA, the residential energy consumption in the world accounts for 20% of all energy consumption as shown in Figure 8.1.

The breakdown of residential energy consumption is given in Figure 8.2 and indicates that the residential appliances – refrigerators/freezers, dishwashers, washing machines and dryers, televisions, home entertainment devices, PCs, other information technology devices, and other small home appliances – account for 19% of total residential energy consumption [2].

Therefore, energy saving measures in residential appliances are being enforced by regulations.

EU energy labels have been in use since 1994 and they are important guides for consumers when they are purchasing electrical appliances. The other aim of EU energy labels is to encourage manufacturers to develop products that consume less energy. For this purpose, energy labels were created from A to G, with A being the best category. With improving technology, manufacturers began to develop more energy efficient products. As the energy efficiency of the new products exceeded the efficiency of products with the energy level A, A+, A++, and even A+++ were added to the classification system. In addition, some products with lower categories (E, F, G) have become less preferred or been removed due to eco-design requirements.

In order to raise awareness of consumers and encourage the industry to develop products that consume less energy, it was decided to establish a simpler scale of EU energy labels in which the

Aerogels for Energy Saving and Storage, First Edition. Edited by Meldin Mathew, Hanna J. Maria, Ange Nzihou, and Sabu Thomas.
© 2024 John Wiley & Sons, Inc. Published 2024 by John Wiley & Sons, Inc.

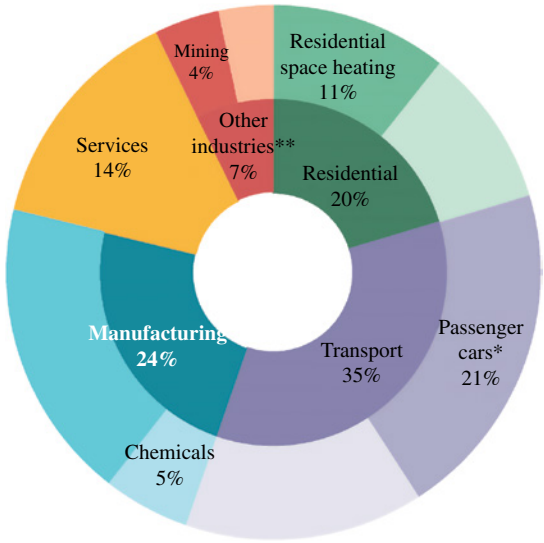


Figure 8.1 Largest end uses by sector [2] / IEA.

* Passenger cars includes cars, sport utility vehicles and personal trucks.

** Other industries includes agriculture, mining and construction.

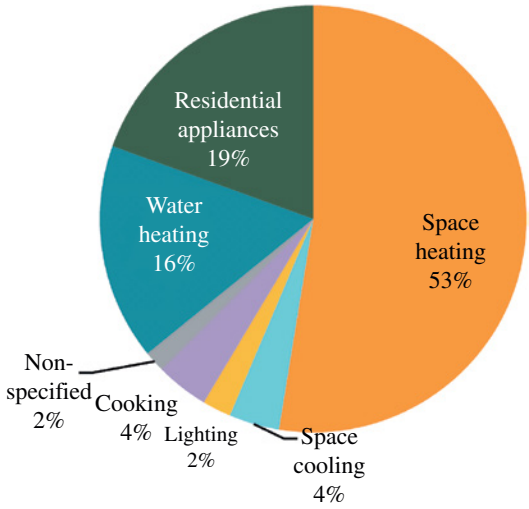


Figure 8.2 Shares of residential energy consumption by end use [2] / IEA.

only the letters A to G are used (Regulation [EU] 2017/1369). The new regulations are also much stricter in terms of energy consumption. For example, according to the new labeling, a refrigerator with a A+++ label in the old system will have a C label, although it is as energy efficient as before. As another example, an A++ dishwasher will have an E label. The European Commission declared that dishwashers, washing machines, refrigerators, and electronic displays with new energy labels will appear in stores starting March 1, 2021. It was expected that there would be no products with an A label and very few products with B and C labels [3].

For this reason, white good companies have been focused on improving the energy efficiencies of their products.

8.1.1 Energy Consumption in White Goods

To reduce energy consumption, several insulation materials are used in white goods such as polyurethane, vacuum insulation panels (VIP), expanded polystyrene (EPS), extruded polystyrene (XPS), glass wool, and rock wool. In addition to conventional insulation materials, aerogels are being studied for potential applications in white goods recently. Aerogels are lightweight porous solid materials which have low density, high porosity, high surface area, and open

structure [4]. These unique properties make them very attractive not only for thermal insulation [5–8], but also for many applications such as acoustic insulation [9], solar systems [10, 11], drug delivery [12], tissue engineering [13], catalysts and supports [14, 15], adsorption processes [14, 16–18], sensors [19], gas storage and separation [14, 17], energy conversion, and storage applications [14, 15, 20].

Liang et al. investigated the thicknesses required to achieve the same insulation performance with different insulation materials [21]. According to the results, aerogels are the materials with the best insulation performance. Indeed, aerogels have been commercially used for thermal insulation of pipelines, buildings, glazings and spacecrafts, due to their low thermal conductivity. The largest company for aerogel production is Aspen Aerogels, which produces fiber reinforced silica based aerogel blankets for industrial and residential thermal insulations (Figure 8.3) [22]. The global leader in the production of aerogel particles is Cabot Corporation. Cabot Corporation produces hydrophobic silica aerogel particles for industrial and residential thermal insulation, architectural daylighting, and performance additives [23]. The third biggest company is Nanotech Inc., which produces aerogel boards, blankets and particles for energy infrastructure, Li-ion battery insulation, high-speed trains, and nuclear energy by using a combination of Sc-drying and ambient pressure drying (APD) [24]. Nanotech Inc. also developed a new kind of paint by the incorporation of aerogel particles into paints [25]. The company researchers claim that this patented material termed Nansulate® [26] could provide a significant thermal insulation performance. This material was prepared by combining highly porous particles with a film-forming resin system comprising at least one film-forming polymer in the presence of a stabilizer [26]. The product is believed to restrain the heat transfer with a thin layer and can be used for insulation purposes in walls, attics, and windows, which do not require complete clarity, plastic or wood blinds, and hot water heaters. The fact that it can be used on prepainted walls or can be painted over with water-based paints could expand the versatility of this invention [25].

The next section provides a comprehensive review on heat transfer mechanisms of aerogels and the use of inorganic aerogels in white goods for thermal insulation applications.

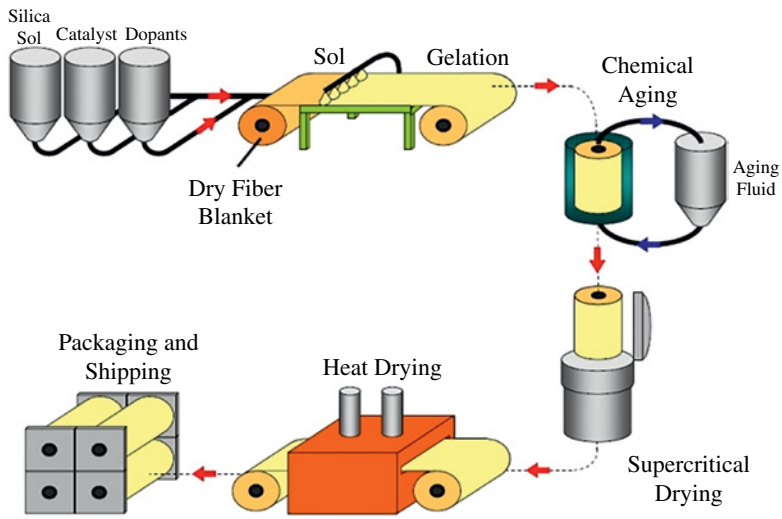


Figure 8.3 Manufacturing process of aerogel blanket [56] / Public domain.

8.1.2 Aerogels

8.1.2.1 Synthesis of Aerogels

Samuel Kistler synthesized various inorganic and organic aerogels for the first time in 1932 [27]. Aerogels are solid, open porous networks, which are formed by replacing the liquid phase in a gel with the gas phase. Gels can be synthesized by sol-gel method or freeze-thaw-induced gelation [28]. In some cases, gels are aged to obtain better mechanical properties. After these processes, the drying step begins, and this is the most critical step since the drying techniques determine the porous structure of aerogels. There are three drying techniques: ambient pressure drying, freeze drying, and supercritical drying.

8.1.2.1.1 Ambient Pressure Drying In APD, liquid phase in the wet gel evaporates at ambient conditions. During the evaporation of the liquid from the pores, a meniscus forms in the vapor-liquid interface. Due to this capillary pressure, gel shrinks and a denser gel called xerogel is formed [29]. There are some studies for silica aerogels showing that it is possible to reduce shrinkage by springback effect, which is the re-expansion of the gel. The patent for this technique was issued in 1996. After the solvent exchange step, the hydroxyl groups on the internal surface of the alcogels were reacted with organic substances of the form R_xMX_y where *R* is usually an organic group such as CH_3, C_2H_5; *M* is Si or Al, and *X* is a halogen, which is usually Cl. The replacement of hydrophilic hydroxyl groups with organic groups resulted in hydrophobic aerogels. This process was actually performed in order to modify the contact angle between the pore liquid and the pore walls during drying to reduce capillary stresses. During APD, a springback effect was observed with the re-expansion of the wet gel since neighboring surface silyl groups were chemically inert and did not interact with each other [12]. In addition to that, the gel structure can be strengthened to withstand the capillary pressure, or solvents with low surface tension can be used [30].

8.1.2.1.2 Freeze Drying In freeze drying, the wet gel is frozen and the liquid inside the pores become solid. Then, pressure is reduced below the sublimation pressure. After the sublimation of the solid in the pores, temperature, and pressure are brought to ambient conditions. The resulting gels are called cryogels. In addition, there are some disadvantages of freeze drying such as bigger pore sizes due to the crystal growth in the pores, cracks in the structure, and long process time [29].

8.1.2.1.3 Supercritical Drying In supercritical drying technique, supercritical fluids are used since these fluids do not have any interfaces at supercritical conditions. Thanks to their density close to liquids and their viscosity close to gases, they can easily replace the solvent in the pores. In general, supercritical CO_2 ($scCO_2$) is used as supercritical fluid as CO_2 has easily accessible critical points (critical temperature 31 °C and critical pressure 73.7 bar) [31]. Moreover, CO_2 is chemically inert, nontoxic, nonflammable, and low cost. In order to extract the solvent in the pores efficiently, the solvent should have high solubility in $scCO_2$. Mostly, water is used during the preparation of sol and has low solubility in $scCO_2$; thus, water in the wet gel is generally replaced with acetone, ethanol, or methanol by solvent exchange. During solvent exchange, it is important to increase the solvent concentration gradually to avoid shrinkage.

Furthermore, in comparison to other drying techniques, it is possible to obtain an aerogel having higher pore volume, higher surface area, and higher porosity [29, 32].

8.1.2.2 Classification of Aerogels

Aerogels can be classified based on their chemical compositions as inorganic, organic, carbon, and hybrid/composite aerogels.

8.1.2.2.1 Inorganic Inorganic aerogels were first synthesized by Kistler by the sol-gel process and supercritical drying of gels of silica, alumina, tungsten oxide, ferric oxide, stannic oxide and nickel tartarate [27]. Since then, various inorganic aerogels have been prepared [33]. Silica aerogels are most extensively studied and use aerogels for thermal insulation due to their very low thermal conductivity. Sol-gel polymerization is commonly used to prepare inorganic aerogels. Metal alkoxides such as tetraethylorthosilicate (TEOS) or tetramethylorthosilicate (TMOS) are the generally used chemical precursors for the synthesis of silica aerogels. First, these precursors are hydrolyzed in a mixture of water and alcohol, where the alkoxide groups of the precursor are replaced with hydroxyl groups, as shown in Eq. (8.1).

$$\mathrm{Si(OR)_4 + 4H_2O \leftrightarrow Si(OH)_4 + 4R - OH} \tag{8.1}$$

The kinetics of hydrolysis reaction can be accelerated by the addition of an acid or a base catalyst. Subsequently, $Si(OH)_4$ molecules go through water (Eq. (8.2)) and alcohol (Eq. (8.3)) condensation reactions forming a silica network. This step can be accelerated by the addition of a base catalyst.

$$\equiv \mathrm{Si - OH + HO - Si} \equiv \rightarrow \equiv \mathrm{Si - O - Si} \equiv + \mathrm{H_2O} \tag{8.2}$$

$$\equiv \mathrm{Si - OR + HO - Si} \equiv \rightarrow \equiv \mathrm{Si - O - Si} \equiv + \mathrm{R - OH} \tag{8.3}$$

The mixture finally forms a gel, which is mostly constituted of SiO_2.

However, some side chains might remain unreacted (Si-OR) or partially reacted (Si-OH) at the end of the condensation reactions. These Si-OH groups render the aerogel hydrophilic and make it susceptible to water adsorption leading to structural collapse. To improve the mechanical strength and to finish hydrolysis and condensation reactions of unreacted precursors in the gels, the wet gels are placed in an aging solution consisting of water and alcohol. This step is necessary to obtain more compact structures, which are more resistant to shrinkage and any damage. Then, the gel is subjected to solvent exchange step during which it is placed in pure solvent, which is generally an alcohol to replace water and to remove any impurities remaining in the pores. The final step is to dry this wet gel, which is also called alcogel without damaging its structure [12].

Other types or inorganic aerogels like titania aerogels are also prepared using the same sol-gel route but with different precursors such as tetrabutyl orthotitanate, titanium n-butoxide, and titanium tetraisopropoxide [12].

8.1.2.2.2 Organic Kistler also synthesized the first organic aerogels from cellulose, nitrocellulose, gelatin, agar, egg albumin, and rubber in 1932 [27]. In 1989, Pekala synthesized an organic aerogel by polycondensation of resorcinol–formaldehyde (RF) in an aqueous solution using Na_2CO_3 as a catalyst. The gelation mechanism was similar to the sol-gel processing of silica, and he used supercritical CO_2 drying to obtain RF aerogel [34]. Since then, several organic aerogels have been prepared from different organic precursors such as melamine-formaldehyde, phenol-furfural, phenol-melamine and polyurethane, polyimide, poly(vinyl alcohol), and poly(vinyl chloride) [35, 36]. The primary step is to form a hydrogel from an aqueous starting solution triggered by a cross-linking promoter, which can have either a chemical nature (chemical cross-linker) or physical nature (pH, temperature) [37]. The subsequent step, which is called the aging/solvent exchange step, involves replacing the water within the porous structure with an appropriate solvent, which is usually an alcohol. The next and final step is to dry the wet gel supercritically with carbon dioxide [12].

Furthermore, in recent years, aerogels from polysaccharides have attracted increasing attention since they are natural, abundant, renewable, biocompatible, biodegradable, and low cost [38].

These polysaccharide aerogels are mostly synthesized from cellulose, cellulose derivatives, alginate, starch, pectin, chitin, and chitosan. As a result of their biocompatibility and biodegradability, polysaccharide aerogels are being investigated for use in tissue engineering, wound-care applications, and drug delivery [12, 37, 39, 40]. Among them, cellulose aerogels are also being investigated for thermal insulation applications [41].

8.1.2.2.3 Carbon Carbon aerogels are prepared by pyrolyzing organic aerogels at elevated temperatures under an inert atmosphere. Carbon aerogel was first synthesized by Pekala by pyrolysis of RF aerogel at 1050 °C under inert atmosphere, and RF is the most widely studied organic precursor [42]. Carbon aerogels can be fabricated by pyrolyzing bio-based aerogels [36, 43]. In addition to these, self-assembled carbon aerogels include graphene aerogels and carbon nanotube aerogels [44].

Carbon aerogels have high specific surface area, high porosity, low density, and significantly high electrical conductivity [36]. The structure of carbon aerogel can be manipulated by tuning the pyrolysis conditions such as temperature, heating rate, pressure, and duration [45]. For instance, between 600 °C and 900 °C, as the pyrolysis temperature increases, surface area, and pore volume of the aerogel reduces. Moreover, aerogels pyrolyzed at 1200 °C are much denser than those pyrolyzed at 600 °C. In addition, high pyrolysis temperature increases electrical conductivity [36, 45].

Carbon aerogels are burned in oxidizing atmospheres; therefore, they should be used in an evacuated system that also suppress the gaseous thermal conductivity in the aerogel. Since carbon aerogels are good IR absorbers, radiative thermal conductivity is also reduced. Besides, solid thermal conductivity of carbon aerogels is low due to high porosity and low density. Thus, overall thermal conductivity of carbon aerogels is very low [45, 46].

8.1.2.2.4 Hybrid Aerogels Hybrid aerogels are attracting increased attention due to their enhanced and multifunctional properties. These kinds of aerogels can be synthesized by polymerization during the sol step or after the gelation step. Hybrid aerogels are comprised of inorganic and organic components and they are either formed by electrostatic forces, van der Waals forces, hydrogen bonding, or covalent bonds [47].

There are several studies of hybrid aerogels such as polymethylmethacrylate-silica aerogels, cellulose-silica aerogels, and chitosan-silica aerogels. According to these studies, it can be deduced that combining inorganic and organic components improve the aerogel properties, such as specific surface area, thermal conductivity, and Young modulus in comparison to individual aerogels [48–50].

8.1.2.2.5 Composite Aerogels There are also various studies on composite aerogels in which clay, SiO_2, carbon nanotube, cellulose nanofibrils, graphene, or graphene oxide are added to strengthen the structure of aerogels. In addition to better mechanical properties, it is possible to give new features to aerogels such as hydrophobicity, lipophilicity, or electrical conductivity [36]. For instance, silica aerogels are rigid and brittle. Also, silica aerogels are transparent and adsorb moisture, which leads to an increase in effective thermal conductivity [51]. To overcome these drawbacks, some nanoparticles or fibers such as SiC and carbon fibers are added to improve both mechanical properties and thermal properties. Moreover, addition of ZrO_2 and TiO_2 as an opacifier increase the thermal resistance of silica aerogels [52]. Inclusion of clays into silica aerogel also enhance the mechanical properties [53, 54]. As another example, due to the brittleness and frailty of carbon aerogels, they are reinforced with carbon fibers, graphene, graphene oxide, or carbon nanotubes [45]. Additionally, carbon aerogels are incorporated with metal oxides, metal hydroxides, and metal sulfides to impart new properties for different applications [36].



Figure 8.4 Aspen Cryogel x201 flexible aerogel blanket [57].

In the last decade, a new class of composite aerogels, metal–organic framework/aerogel composites (MOFACs) was introduced. MOFs also have high surface area, high pore volume, high porosity, and low density. Therefore, integration of MOFs into aerogels leads to hierarchically porous materials with superior properties [28].

Aerogel blankets are also composite materials. The first industrial scale of aerogel blanket was produced by Aspen Aerogel in 2007 [55]. As shown in Figure 8.3, firstly, silica sol is first cast onto a dry fiber blanket. After the gelation process, gel-blanket composite is supercritically dried and a flexible aerogel blanket (Figure 8.4) is obtained.

Cabot Corporation also produced aerogel blankets called ThermalWrap™ under the trade name of Nanogel [58]. Aspen Aerogels declared that aerogel blankets are used for thermal insulation in several application areas due to their lower thermal conductivity than traditional insulation materials [55]. Aerogel blankets are more flexible than monolithic and granular aerogels and are also easy to handle [60].

8.1.2.3 Forms of Aerogels

8.1.2.3.1 Monolithic Aerogels Monolithic aerogels are prepared by performing the gelation process in molds. During gelation, gel takes the form of the mold, and after supercritical drying, aerogel maintains its form [37]. The choice of the material of the mold is equally important in the preparation conditions in order to obtain a crack-free monolithic aerogel. It should be chosen so that the mold will not stick to the alcogel surface, allowing easy release, and also should not interact with the sol before and after the gelation [12].

8.1.2.3.2 Powder and Granulate Aerogels Preparing aerogels in the form of granules or beads increases their usability in various applications, which requires different sizes and shapes. Aerogels in the form of particles can be prepared by different methods such as dripping method [61], emulsion-gelation method [38], and spraying method [29]. Granulate aerogels (Figure 8.5) can be formed by crushing monoliths or by using the spring-back technique [37, 63].

Smith et al. indicated that beds of granulate and powder aerogels have higher thermal conductivity than monolithic aerogels due to the gaseous heat conduction in the interparticular voids. He also added that it is possible to obtain similar thermal conductivities for granulates and monoliths at very low pressures [64]. On the other hand, Ebert stated that solid thermal conductivity of the bed has decreased as contact points of the particles increase the thermal resistances [63].

8.1.2.3.3 Aerogel Fibers Aerogel fibers are fabricated by the wet spinning method. Like other aerogel forms, the gelation and drying processes are applied to produce aerogel fibers. In general, first, the prepared solution is filled into an injection device, which can be a syringe or an extruder. Then the solution is extruded directly into a solvent bath in which the solution is both gelled and regenerated. After that, wet gel is dried supercritically and aerogel fiber is obtained [65–67].

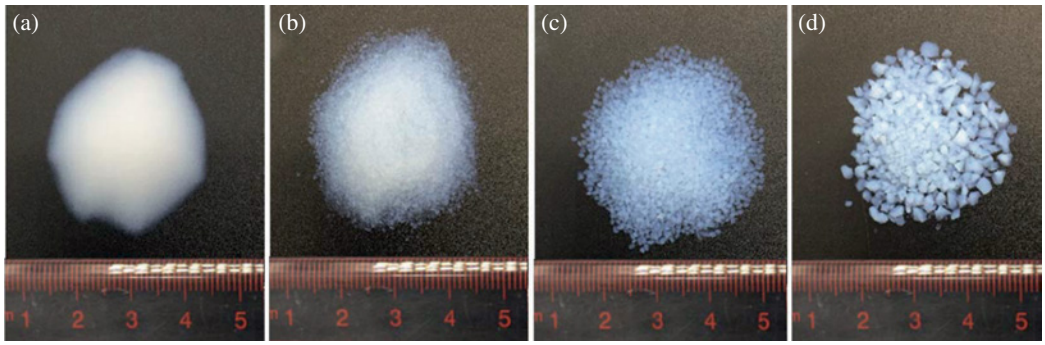


Figure 8.5 Granulate aerogel with different particle size (a) $P_{0.41}$ (b) $P_{0.64}$ (c) $P_{0.93}$ (d) $P_{2.7}$ [110].

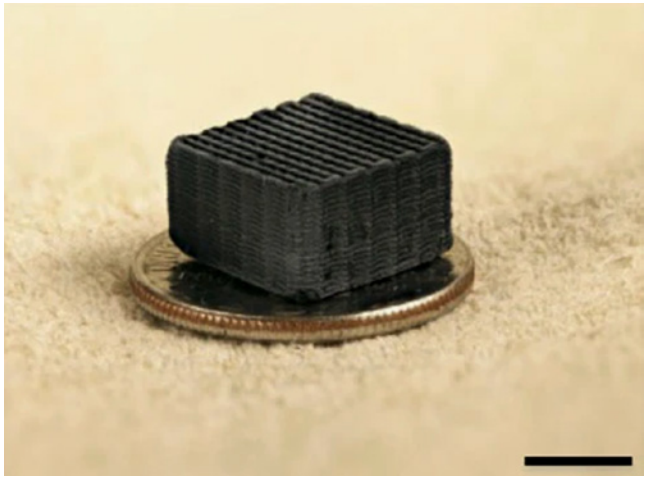


Figure 8.6 3D printed graphene aerogel [68].

8.1.2.3.4 3D Printed Aerogels 3D printing or additive manufacturing is an attractive developing field, since it provides fabricating geometrically complex or customized materials in a shorter time. In recent years, researchers have focused on 3D printing of different kind of aerogels such as cellulose, gold, graphene, graphene oxide, carbon nitride, and resorcinol-formaldehyde aerogels. Moreover, although silica aerogel is a brittle material, Zhao et al. managed to fabricate a silica aerogel [68–70]. An example of a 3D-printed graphene aerogel is given in Figure 8.6.

There are three 3D printing techniques for aerogels: direct ink writing (DIW), inkjet, and room-temperature freeze gelation (RTFG). In DIW technique, ink is extruded through a nozzle that follows the determined toolpath. The important point is that the ink should flow, but after printing it should retain its shape; therefore, ink should be a thixotropic fluid. In inkjet technique, low-viscosity Newtonian ink is 3D printed into a cold sink to freeze the 3D structure instantly. As the melted layer settles on the frozen layer, the ink fills the gap between the layers, thus achieving a more durable structure. In RTFG technique, there is a nozzle for extrusion and it follows the toolpath like DIW technique. Generally, temperature is room temperature or below similar to freeze casting. Ink consists of precursor and solvent with have high vapor pressure which provides sublimation of the solvent at room temperature. This is an important parameter since the solvent

determines the microstructures of the 3D printed aerogel. For all three techniques, after the printing step, gelation, solvent exchange, and drying steps are conducted [68–70].

8.2 Heat Transfer Mechanisms in Aerogels

Heat transfer in a porous media is classified into three mechanisms, which are conduction, convection, and radiation. In Figure 8.7, a schematic representation of the heat transfer mechanisms in a porous media is given.

Conduction heat transfer can be separated into solid and gaseous heat conduction, due to the motions and collisions of phonons and gas molecules, respectively. The gas convection in aerogels is negligible since the mean aerogel pore diameters are in nanoscale. Radiative heat transfer is affected by photon scattering.

According to the three heat transfer modes in aerogel, there are three types of thermal conductivity: solid, gaseous, and radiative thermal conductivity. The overall thermal conductivity is called effective thermal conductivity [52].

8.2.1 Solid Thermal Conductivity

Solid thermal conductivity depends on the phonon transport. Phonons are quantized lattice vibrations, which are the source of many physical properties of the crystals such as heat transfer and heat capacity [71]. Although aerogels are usually amorphous materials, localized vibrations are used for the determination of solid thermal conductivity [52].

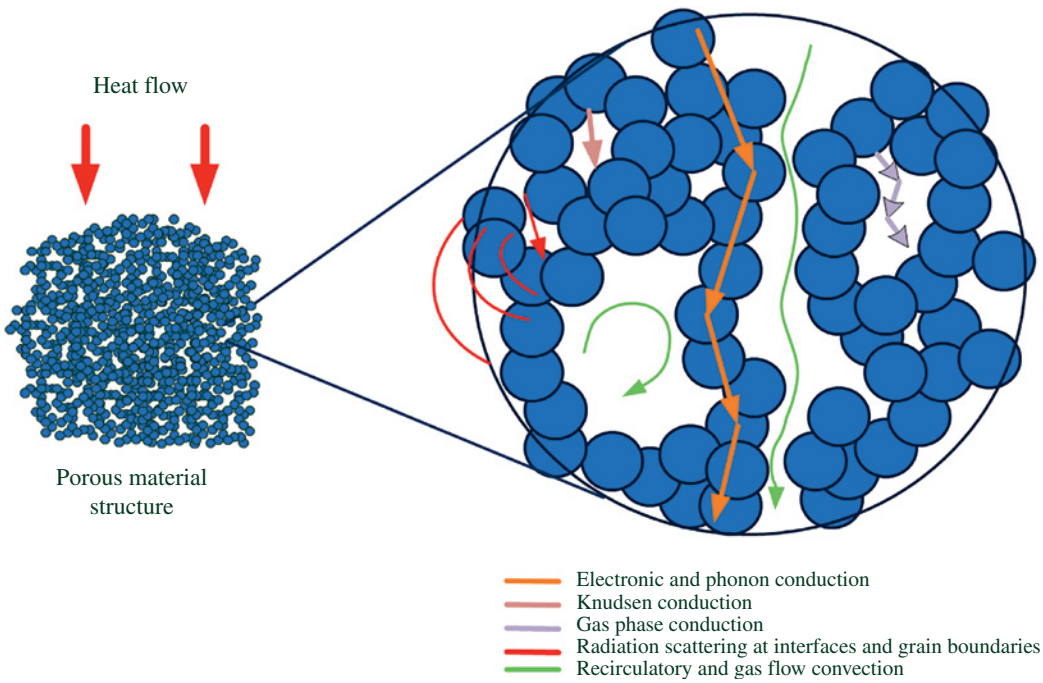


Figure 8.7 Heat transfer mechanisms in a porous media. [25] / Reproduced with permission of Elsevier..

The general equation of solid thermal conductivity based on the kinetic theory is given:

$$\lambda_s = \frac{1}{3} c_v \rho v_{ph} \Lambda_{ph} \tag{8.4}$$

where c_v is specific heat at constant volume, ρ is the density of the solid backbone, v_{ph} is the phonon velocity and Λ_{ph} is the mean free path of a phonon between two consecutive collisions [63, 71]. The specific heat is a function of temperature and it is calculated by Debye theory:

$$\overline{c_v}(T) = 9Nk_B \left(\frac{T}{\Theta_D}\right)^3 \int_0^{x_D} \frac{x^4 e^x}{\left(e^x - 1\right)^2} dx \tag{8.5}$$

where N is the number of atoms, k_B is the Stefan–Boltzmann constant, $x_D = \Theta_D/T$ and Θ_D is the Debye temperature. The specific heat is almost constant at the temperatures that is close to Debye temperature or higher than Debye temperature [72].

The mean free path of phonons is the product of phonon velocity v_{ph} and average relaxation time τ_{ph} [52]. The mean free path of phonons depends on scattering mechanisms which are Umklapp phonon-phonon scattering, phonon-defect scattering, phonon-electron scattering, and phonon-boundary scattering [72]. The average relaxation time of phonons can be calculated by Matthiessen's rule [52]:

$$\frac{1}{\tau_{ph}} = \frac{1}{\tau_U} + \frac{1}{\tau_M} + \frac{1}{\tau_S} + \ldots \tag{8.6}$$

Thus, the mean free path of phonons can be calculated by [52]:

$$\frac{1}{\Lambda_{ph}} = \frac{1}{\Lambda_U} + \frac{1}{\Lambda_M} + \frac{1}{\Lambda_S} + \ldots \tag{8.7}$$

The scattering mechanisms are categorized into three groups: volumetric scattering Λ_V (scattering due to the phonons, defects, impurities and grain boundaries), boundary scattering Λ_S and interfacial scattering Λ_T [52].

$$\frac{1}{\Lambda_{ph}} = \frac{1}{\Lambda_V} + \frac{1}{\Lambda_S} + \frac{1}{\Lambda_T} \tag{8.8}$$

Λ_V is calculated as,

$$\Lambda_V = \Lambda_{\text{bulk}} = \frac{3\lambda_{\text{bulk}}}{c_v \rho v_{ph}} \tag{8.9}$$

where λ_{bulk} is the thermal conductivity of the bulk material and Λ_{bulk} is the mean free path of the bulk material. Also, v_{ph} is the mean sound velocity of the solid backbone [52].

Λ_T is calculated as,

$$\Lambda_T = 3LT_D \tag{8.10}$$

where T_D is the energy transmissivity from one particle to another. If the particles are the same kind of material, the T_D will ve 0.5. In addition, L is the segment length of the solid phase and is calculated by:

$$L = \sqrt{{d_p}^2 - a^2} \tag{8.11}$$

where d_p is the particle diameter and a is the contact diameter of the two adjacent particles [52].

Liu classified the heat flux into two types, which are longitudinal (perpendicular) heat flux and the transverse (parallel) heat flux.

According to that, Λ_s is calculated as,

$$\Lambda_s = \frac{1+p}{1-p}a \tag{8.12}$$

$$\Lambda_s = \frac{1+p}{1-p}d_p \tag{8.13}$$

where p is the boundary specularity. If it is assumed that the boundary is completely diffused, p will be equal to zero [52].

Consequently, the longitudinal $\lambda_{eff,L}$ and transverse $\lambda_{eff,T}$ solid thermal conductivity can be calculated as [52]

$$\lambda_{eff,L} = \frac{\lambda_b}{1+\frac{\Lambda_{bulk}}{a}+\frac{\Lambda_{bulk}}{3LT_D}} \tag{8.14}$$

and

$$\lambda_{eff,T} = \frac{\lambda_b}{1+\frac{\Lambda_{\text{bulk}}}{d_p}} \tag{8.15}$$

Bi et al. declared that the above model is not convenient for aerogels since aerogel backbone have interconnected structure and particle sizes are larger than contact diameters, resulting in interfacial resistance as heat is transferred through the interconnected particles. They also stated that Λ_s depends on both the contact diameter and particle diameter. Therefore, Bi et al. developed a new model for Λ_s including the size effect and the interfacial resistance of the interconnected particles [73]:

$$\Lambda_s = \frac{1}{a}\frac{2A_{\text{inter}}}{A_{\text{eff}}}+\frac{1}{d_p}\frac{A_{\text{sphere}}}{A_{\text{eff}}} \tag{8.16}$$

where A_{inter} and A_{sphere} are the areas of the interface and spherical cap, respectively. A_{eff} is the effective atomic scattering area of a single particle and

$$A_{eff} = 2A_{\text{inter}} + A_{\text{sphere}} \tag{8.17}$$

Based on the cylindrical superlattice nanowire models derived by Dames et al. [74]

$$\Lambda_T = 3LT_D/2 \tag{8.18}$$

and Chen et al. [75]

$$T_D = \frac{C_{V,B}v_B}{C_{V,B}v_B + C_{V,A}v_A} \tag{8.19}$$

(where A and B indicates the two adjacent segments of superlattice nanowire). Bi et al. developed a new model for interfacial scattering Λ_T. They declared that the contact diameter of the interconnected particles a is always smaller than the particle diameter d_p and the energy transmission area is $\pi a^2/4$ instead of $\pi d_p^2/4$. Therefore, Eq. (8.19) is modified as [73],

$$T_D = \frac{C_{V,B}v_B}{C_{V,B}v_B + C_{V,A}v_A}\frac{a^2}{d_p^2} \tag{8.20}$$

where A and B indicates the two adjacent particles of aerogel backbone.

There are several factors that affect the solid thermal conductivity in aerogels. Heat conduction paths in aerogels are longer than the bulk materials due to their complex nanoporous structures. Besides, characteristic lengths of aerogels are equal to or less than phonon mean free path. Therefore, these size effects suppress the solid thermal conductivity in aerogels [52, 53].

Density also has a significant effect on solid thermal conductivity. As the density increases, solid thermal conductivity increases. However, density affects all three types of thermal conductivity. Therefore, in order to obtain the lowest thermal conductivity, an optimum density should be found [76].

Increasing porosity is also another important method to suppress the solid conductivity because it will not only decrease the density but also restrict the motions of phonons in the solid structure [41].

8.2.2 Gaseous Thermal Conductivity

Gaseous heat transfer in porous materials is reduced in comparison to heat transfer in free gas due to the restricted collisions of the gas molecules in the porous structure [77].

The first gaseous thermal conductivity model was based on the kinetic theory and it was developed by Kistler in 1935 [78]:

$$\lambda_g = BC_{V,g}\eta_g \tag{8.21}$$

where B is a constant, $C_{V,g}$ is the specific heat at constant volume and η_g is the viscosity, which can be calculated by [78]:

$$\eta_g = 0.35\rho_g \upsilon_g l_g \tag{8.22}$$

where ρ_g is the density, υ_g is the arithmetical average velocity of the molecules, and l_g is the mean free path of the gas molecules. From the above equations, the gaseous thermal conductivity was finally derived as [78]:

$$\lambda_g = 0.058\alpha\sqrt{\frac{m_g}{T}}C_{V,g}l_0\frac{D^2}{\frac{2Ll_0(1-\alpha)}{p}+\alpha L\left(L+\frac{l_0}{p}\right)} \tag{8.23}$$

where m_g is the molecular weight, T is the temperature, p is the pressure, D is the average pore diameter, L mean free path of a highly attenuated gas within the aerogel, and l_0 is the normal mean free path of the gas molecules. In this equation, α is the accommodation coefficient, which is the fraction of the gas molecules that comes to thermal equilibrium when they collide to the surface, accordingly, $1 - \alpha$ is specularly reflected fraction [78].

In 1969, Kaganer derived Knudsen formula, which describes the gaseous thermal conductivity of free gas between two parallel plates [52]:

$$\lambda_g = \frac{\lambda_g^0}{1+2\beta K_n} \tag{8.24}$$

where λ_g^0 is the thermal conductivity of the gas in free space. β is a coefficient that is calculated as [52]:

$$\beta = \frac{2\gamma}{\gamma+1}\frac{2-\alpha}{\alpha}\frac{1}{P_r} \tag{8.25}$$

where α is the accommodation coefficient, γ is the adiabatic coefficient of the gas, and P_r is the Prandtl number. β is 1.4, 1.8, 1.6, 10.2, and almost 2 for CO_2, Ar, N_2, He, and air, respectively [79, 80].

In Eq. (8.24) K_n is the Knudsen number, which is the ratio of the mean free path of the gas molecules l_g and the mean pore diameter D [81]:

$$K_n = l_g / D \tag{8.26}$$

The mean free path of the gas molecules can be calculated from Eq. (8.27) [81]:

$$l_g = \frac{k_B T}{\sqrt{2}\pi d_g^2 p} \tag{8.27}$$

where k_B is the Boltzmann's constant, T is gas temperature, d_g is the diameter of a gas molecule, and p is the gas pressure inside porous material [81].

If the mean pore diameter is smaller than the mean free path of the gas molecules, K_n will be greater than 1, which means there is molecular heat transfer. In this case, gas molecules mostly collide with the solid backbone and therefore the contribution of the thermal conductivity is proportional to the number of gas molecules. On the contrary, if the mean pore diameter is greater than the mean free path of the gas molecules, K_n will be less than 1, which means there is diffusive heat transfer. In this case, gas molecules mostly collide with each other, and the gaseous thermal conductivity is equal to the thermal conductivity of free gas, which does not depend on gas pressure at ambient and moderate pressures.

After Kaganer's formula, several models are proposed to obtain thermal conductivity more accurately. Kaganer used mean free path of the free space instead of the mean free path of the gas in porous material and it leads to large computational deviations. Consequently, in 1995, Zeng et al. derived the mean free path of gas molecules in silica aerogel and proposed a new analytical model based on gas kinetics [77, 82]:

$$\lambda_g = \frac{\left(2.25\gamma - 1.25\right)0.461\left(\frac{p}{k_B T}\right)\left(\frac{8k_B T}{m_g \pi}\right)^{0.5}}{\frac{0.25S\rho}{\phi} + \sqrt{2}\left(\frac{p}{k_B T}\right)\pi d_g^2}\frac{C_v}{N_A} \tag{8.28}$$

where γ is the adiabatic coefficient of the gas, m_g is the molecular weight, N_A is Avogadro constant, C_v is the specific heat at constant volume, ρ is the density of aerogel, ϕ is the aerogel porosity, and S is the specific surface area of aerogel.

There are still some large errors due to the nonuniform pore size distribution in aerogels. Thus, Reichenauer et al. proposed a new model, assuming that there are two different mean pore diameters (D_1 and D_2) and two different corresponding porosity (ϕ_1 and ϕ_2) and the sum of porosities is unity [53]:

$$\lambda_g = \frac{\lambda_g^0 \phi_1}{1 + \frac{2\beta\Lambda_g}{D_1}} + \frac{\lambda_g^0 \phi_2}{1 + \frac{2\beta\Lambda_g}{D_2}} \tag{8.29}$$

After that, Reichenauer et al. modified the model by assuming that there is a Gaussian distribution function for the pore size distribution:

$$\lambda_g = \frac{1}{N}\int \frac{\lambda_g^0}{1 + \frac{2\beta\Lambda_g}{D'}} e^{-\frac{\left(D'-D\right)^2}{2\sigma^2}} dD' \quad \left(D' > 0\right) \tag{8.30}$$

where D is the mean pore size, D' is the convolution variable, σ is the standard deviation of the Gauss distribution function (the distribution width of the pore-size) and N is a factor that normalizes the integration to provide the correct total porosity. Although Eq. (8.30) is easy to apply, it is not convenient since N must be calculated separately after the integration [81].

In order to make an easier and more convenient computation, Bi et al. developed an approximate equation in which all the pores act as parallel paths [81]:

$$\lambda_g = \sum_{i=1}^{n} \phi_i K\left(D_i\right) \tag{8.31}$$

where n is the number of pores, i is the pore index, ϕ_i is the contribution to the total porosity and $K(D_i)$ is a simplified form of Eq. (8.24). ϕ_i was calculated as:

$$\phi_i = \int_{D_i}^{D_i+\Delta D} \frac{1}{\sqrt{2\pi}\sigma} e^{-\frac{\left(D'-D\right)^2}{2\sigma^2}} dD' \approx \frac{\Delta D}{\sqrt{2\pi}\sigma} e^{-\frac{\left(D_i-D\right)^2}{2\sigma^2}} \quad \left(D_i > 0\right) \tag{8.32}$$

Thus, if n is large enough, the total gaseous thermal conductivity can be written as

$$\lambda_g \approx \sum_{i=1}^{n} \left[\frac{\Delta D}{\sqrt{2\pi}\sigma} e^{-\frac{\left(D_i-D\right)^2}{2\sigma^2}} \right] K\left(D_i\right) \quad \left(D_i > 0\right) \tag{8.33}$$

Bi et al. also derived the total proportion of the pore size distribution when it is in the confidence interval $[D-3\sigma, D+3\sigma]$ as

$$\lim_{n\to\infty} \sum_{i=1}^{n} \phi_i = \int_{D-3\sigma}^{D+3\sigma} \frac{1}{\sqrt{2\pi}\sigma} e^{-\frac{\left(D'-D\right)^2}{2\sigma^2}} dD' \approx 0.9974\left(D-3\sigma > 0\right) \tag{8.34}$$

However, the pore size distributions in aerogels are generally nonuniform. In addition, the contributions of the large pores to the gaseous thermal conductivity are greater than the contributions of the small pores. Based on these considerations, Bi et al. developed an improved model using a double times probability of $[D+\sigma, D+3\sigma]$ and the random and nonuniform pore size distribution function [81]:

$$\phi_i = \begin{cases} \dfrac{\Delta D}{\sqrt{2\pi}\sigma} e^{-\frac{\left(D_i-D\right)^2}{2\sigma^2}}, \; D_i \in \left[D-\sigma, D+\sigma\right] D_i - \sigma > 0 \\ \dfrac{2\Delta D}{\sqrt{2\pi}\sigma} e^{-\frac{\left(D_i-D\right)^2}{2\sigma^2}}, \; D_i \in \left[D+\sigma, D+3\sigma\right] \end{cases} \tag{8.35}$$

Later studies showed that neglecting solid-gas coupling effects can cause an underestimation of the effective thermal conductivity. There are two types of solid gas coupling: the first one is the thermal bridge interaction between adjacent particles and gas in the gap and the second one is the local solid–gas interaction. For that reason, several models were developed by Swimm et al., Zhao et al., and Bi et al. Consequently, Guo et al. proposed a novel and more accurate model, including the effect of solid–gas coupling [83]. The effective thermal conductivity is given as

$$\lambda_{eff} = \lambda_s + \lambda_r + \lambda_{g,e} + \lambda_c \tag{8.36}$$

where λ_s is the solid phase thermal conductivity, λ_r is the radiative thermal conductivity, $\lambda_{g,e}$ is the equivalent gaseous thermal conductivity of bulk aerogels, and λ_c is the solid–gas coupling thermal conductivity [83].

The equivalent gaseous thermal conductivity of bulk aerogels $\lambda_{g,e}$ is calculated as

$$\lambda_{g,e} = \varphi\lambda_g \tag{8.37}$$

where φ is the porosity of the aerogel and λ_g can be obtained from Eqs. (8.24), (8.26), and (8.27). The summation of the equivalent gaseous thermal conductivity $\lambda_{g,e}$ and solid–gas coupling thermal conductivity λ_c was expressed as gas-contributed thermal conductivity, $\lambda_{g,c}$

$$\lambda_{g,c} = \lambda_{g,e} + \lambda_c \tag{8.38}$$

If the effective thermal conductivity under vacuum atmosphere is subtracted from the effective thermal conductivity at given pressure, the gas-contributed thermal conductivity can be acquired,

$$\lambda_{g,c} = \lambda_{\text{eff}} - \lambda_{\text{eff,vacuum}} \tag{8.39}$$

Guo and Tang indicated that the total heat flux in aerogel backbone is divided into two types, which are the heat transfer from the solid backbone to the gas phase $q_{c,\text{cross}}$ and the heat conduction along the particle chains and the gas molecules $q_{c,in}$ [83].

According to this expression, the solid thermal conductivity is derived:

$$\lambda_c = \varphi_{c,in}\lambda_{c,in} + \varphi_{c,\text{cross}}\lambda_{c,\text{cross}} \tag{8.40}$$

where $\varphi_{c,in}$ and $\varphi_{c,\text{cross}}$ are the function parameters of the thermal-bridge and local solid–gas interaction system, respectively. The detailed expressions of these parameters can be found in Ref. [83].

There are various methods to suppress the gaseous heat transfer. Small pore diameters increase the Knudsen effect and therefore gaseous thermal conductivity decreases. Preparing an aerogel with more uniform pore size distribution can decrease the gaseous thermal conductivity [53]. Decreasing porosity reduces the gaseous thermal conductivity, but also increases the solid–gas coupling effect [25, 83]. Therefore, an optimum density and porosity should be found. In addition, vacuum can be applied to aerogels to reduce gaseous thermal conductivity. For this purpose, evacuation to 10 mbar is sufficient [76].

8.2.3 Radiative Thermal Conductivity

The radiative heat transfer occurs from the emissions of electromagnetic radiation from a material surface. Aerogels are participating materials, which means that aerogels absorb, emit, and scatter electromagnetic radiation. In participating materials, radiation exchange occurs between the volume and surface elements, as well as between the surface elements [84].

Radiative transfer equation (RTE) for aerogels is derived as

$$\frac{dI_\lambda(s,\boldsymbol{s})}{ds} = -(\sigma_{a\lambda} + \sigma_{s\lambda})I_\lambda(s,\boldsymbol{s}) + \sigma_{a\lambda}I_{b\lambda}(s) + \frac{\sigma_{s\lambda}}{4\pi}\int_{4\pi} I_\lambda(s,\boldsymbol{s_i})\phi_\lambda(\boldsymbol{s_i},s)d\Omega\Omega_i \tag{8.41}$$

where $I_\lambda(s, \boldsymbol{s})$ is the spectral radiation intensity, s is the spatial location, $\boldsymbol{s}$ is the direction radiation intensity, and λ is the wavelength. $\sigma_{a\lambda}$ and $\sigma_{s\lambda}$ indicate the spectral absorption and scattering coefficient, respectively and the summation of $\sigma_{a\lambda}$ and $\sigma_{s\lambda}$ is the spectral extinction coefficient $\sigma_{e\lambda}$. Moreover, $\phi_\lambda(\boldsymbol{s_i}, s)$ is the phase function [84].

RTE is an integro-diffential and nonlinear equation. In order to solve RTE, some approximations should be applied. These approximations are categorized in two groups: neglecting physical processes owing to the intrinsic characteristics of the material and making mathematical approximations [52].

8.2.3.1 Approximations Neglecting Some Physical Process

If the scattering effect is neglected, then Eq. (8.41) becomes

$$\frac{dI_\lambda\left(s,\boldsymbol{s}\right)}{ds}=-\sigma_{a\lambda}I_\lambda\left(s,\boldsymbol{s}\right)+\sigma_{a\lambda}I_{b\lambda}\left(s\right) \tag{8.42}$$

If the extinction effect (absorption and scattering) is neglected, then Eq. (8.41) becomes,

$$\frac{dI_\lambda\left(s,\boldsymbol{s}\right)}{ds}=\sigma_{a\lambda}I_{b\lambda}\left(s\right) \tag{8.43}$$

8.2.3.2 Optically Thin Approximation Optically

The optical thickness is the product of the extinction coefficient of the material and the thickness of the material. If it is far less than 1, then the material is called an optically thin medium. Due to the absorption and scattering processes in optically thin medium, the radiation is almost not attenuated. Therefore, the incident intensity from the boundary is dominant [52].

Consequently, the diffuse spectral radiative heat fluxes at the boundaries are obtained as

$$q_{\lambda 0,1}=\frac{\varepsilon_{\lambda,1}e_{\lambda b,1}+\varepsilon_{\lambda,2}e_{\lambda b,2}\left(1-\varepsilon_{\lambda,1}\right)}{1-\left(1-\varepsilon_{\lambda,1}\right)\left(1-\varepsilon_{\lambda,2}\right)} \tag{8.44}$$

$$q_{\lambda 0,2}=\frac{\varepsilon_{\lambda,2}e_{\lambda b,2}+\varepsilon_{\lambda,1}e_{\lambda b,1}\left(1-\varepsilon_{\lambda,2}\right)}{1-\left(1-\varepsilon_{\lambda,1}\right)\left(1-\varepsilon_{\lambda,2}\right)} \tag{8.45}$$

8.2.3.3 Optically Thick Approximation

In optically thick mediums, photons can travel a short distance before they are absorbed or scattered. Most of the organic aerogels and carbon aerogels are optically thick materials. Radiative heat transfer is diffusive in optically thick aerogels and radiative thermal conductivity can be derived from Stefan-Boltzmann equation for photons [53]:

$$\lambda_r=\frac{16}{3}\frac{n^2\sigma_B}{\rho E_s\left(T\right)}T^3 \tag{8.46}$$

where n is the refractive index, σ_B is the Stefan-Boltzmann constant, T is the temperature, ρ is the density and E_s is the temperature dependent Rosseland mean extinction coefficient which is calculated from the following equations [53]:

$$\frac{1}{E_s\left(T\right)}=\int_0^\infty\frac{1}{E_s\left(l\right)}\frac{\partial I_b\left(l\right)}{\partial I_b}dl \tag{8.47}$$

with

$$\frac{\partial I_b\left(l\right)}{\partial I_b}=\frac{15}{4\pi^4z^6}\frac{\exp\left(1/z\right)}{\left[\exp\left(1/z\right)-1\right]^2} \tag{8.48}$$

and

$$z = \frac{k_B T}{hc} l \tag{8.49}$$

where $E_s(l)$ is the spectral extinction coefficient, l is the radiation wavelength of photons, $I_b(l)$ is the spectral blackbody flux, I_b is the black-body flux, k_B is the Boltzmann constant, h is the Planck's constant, and c is the speed of light [53].

Two assumptions are made to calculate Rosseland mean extinction coefficient. One of the assumptions is that the radiative heat transfer is far enough from the boundaries, and the other is that the temperature change with respect to the optical thickness is small [63].

The spectral extinction coefficient describes the attenuation of electromagnetic waves by absorption or scattering processes and it depends on the chemical composition and structure of the materials. Tang et al. stated that spectral extinction coefficient cannot be obtained directly, however, it can be obtained by experimental measurements or numerical simulations [53, 85].

8.2.3.4 Two Flux Method

The intensity of the radiation depends on the direction, however, it can be assumed to be constant, to solve the RTE as linear differential equations. This method is called as the two-flux method or the Schuster-Schwarschild approximation. Moreover, the two-flux method is only accurate for the optically thin assumption and isotropic scattering. The radiation intensity is assumed as

$$I(\tau,\mu) = \begin{cases} I^-(\tau), & -1 < \mu < 0 \\ I^+(\tau), & 0 < \mu < 1 \end{cases} \tag{8.50}$$

Substituting Eq. (8.50) into Eq. (8.41) gives

$$\mu \frac{dI(\tau)}{d\tau} = (1-\omega) I_b(\tau) - I(\tau) + \frac{\omega}{2}\left(I^+ + I^-\right) \quad -1 < \mu < 1 \tag{8.51}$$

In order to obtain the differential equations of the positive and negative radiation intensity, Eq. (8.51) is integrated over each hemisphere of solid angles:

$$\frac{1}{2}\frac{dI^+}{d\tau} = (1-\omega) I_b(\tau) - I^+ + \frac{\omega}{2}\left(I^+ + I^-\right) \tag{8.52}$$

$$-\frac{1}{2}\frac{dI^-}{d\tau} = (1-\omega) I_b(\tau) - I^- + \frac{\omega}{2}\left(I^+ + I^-\right) \tag{8.53}$$

The radiative heat fluxes in the positive and negative directions are derived from Eqs. (8.52) and (8.53).

$$\frac{dq_x^+}{dx} = \kappa E_b - (\kappa + \sigma_s) q_x^+ + \frac{\sigma_s}{2}\left(q_x^+ + q_x^-\right) \tag{8.54}$$

$$\frac{dq_x^-}{dx} = -\kappa E_b + (\kappa + \sigma_s) q_x^- - \frac{\sigma_s}{2}\left(q_x^+ + q_x^-\right) \tag{8.55}$$

8.2.3.5 Discrete Ordinate Method

Discrete ordinate method is the extended version of the two-flux method. If discrete ordinate method is applied to Eq. (8.41) in the three-dimensional Cartesian coordinate system, then modified RTE can be obtained as

$$\xi^m \frac{dI_\lambda^m}{dx} + \eta^m \frac{dI_\lambda^m}{dy} + \mu^m \frac{dI_\lambda^m}{dz} = -\left(\sigma_{ek}\right) I_\lambda^m + \sigma_{a\lambda} I_{b\lambda}\left(s\right) + \frac{\sigma_{s\lambda}}{4\pi}\left[\sum_{l=1}^{N\Omega} w^l I_\lambda^l \phi_\lambda^{m,l}\right] \tag{8.56}$$

where the superscripts m and l indicates the m^{th} and l^{th} angular directions. ξ^m, η^m and μ^m denotes the direction cosines of m^{th} direction and w^l is the weighting factor of the l^{th} direction. In addition, N is the total discrete angular direction in 4π space and $\phi_\lambda^{m,l}$ is the phase function.

For an opaque boundary wall, the radiation intensity is derived as

$$I_{\lambda,w}\left(\boldsymbol{s}\right) = \varepsilon_{\lambda,w} I_{b\lambda,w} + \frac{1-\varepsilon_{\lambda,w}}{\pi} \int\limits_{n_w . s_i < 0} I_{\lambda,w}\left(\boldsymbol{s_i}\right) \left|\boldsymbol{n_w} . \boldsymbol{s_i}\right| d\Omega\Omega_i \tag{8.57}$$

where the superscript w indicates the wall surface, $\varepsilon_{\lambda,w}$ is the spectral emissivity of the wall and $\boldsymbol{n}$ is the normal vector of the wall pointing into the material [52].

In comparison to Rosseland diffusion approximation and two-flux methods, the discrete ordinate method leads to more accurate results. However, it is more difficult to solve the discrete ordinate method [52].

Further approximations and numerical methods for RTE such as finite volume method and finite element method can be found in literature [84].

At high temperatures, the radiative thermal conductivity increases and becomes dominant. This increase is greater in transparent and translucent aerogels. In order to suppress the radiative heat transfer, some opacifiers such as SiC, carbon black, carbon fibers, TiO_2 and ZrO_2 can be added to aerogels. Due to their highly porous structure, aerogels are usually fragile. Therefore, opacifiers that are added to reduce radiative thermal conductivity will also improve the mechanical properties of aerogels. However, these doping materials can also increase the solid thermal conductivity of aerogel [52, 53, 63].

8.3 Inorganic Aerogels and Their Composites in White Goods

8.3.1 Refrigerators

8.3.1.1 Thermal Insulation in Refrigerators

The main components of the refrigerators are refrigerant, compressor, condenser, evaporator, capillary tube, and thermostat. Refrigerant is the cooling liquid that is circulated in the system. Compressor is located at the back of the refrigerator and it circulates the refrigerant throughout the system by compressing the refrigerant. During compression, the temperature and the pressure of the refrigerant increases. Then the refrigerant comes to the condenser. Condenser is placed on the back side of the refrigerator and it cools and condenses the refrigerant coming from the compressor. While passing through the condenser, the heat is discharged toward the outer environment. The refrigerant coming from the condenser outlet flows through capillary tubes that reduces the pressure of the refrigerants and arrives to evaporator. Evaporator, the heat exchanger, is placed inside the refrigerator. Inside the evaporator, refrigerant changes phase from liquid to gas by absorbing heat inside the refrigerator. Finally, the refrigerant in the gas phase moves to the compressor and the cycle starts again. In addition, thermostat controls the temperature inside the refrigerator by switching the compressor on and off.

Refrigerators consist of two compartments, which are fresh food and freezer. In fresh food compartment, food and beverages were kept fresh for several days. In freezer compartment, food that need to be kept as frozen are stored. The internal temperatures of the fresh food and freezer

compartments in refrigerators are between (+2) – (+8) and (−25) – (−18) °C, respectively. The difference between the ambient temperature and internal temperature is high, thus, thermal insulation in refrigerators is very important to reduce energy consumption. Refrigerators consist of a metal sheet outer casing and a polystyrene inner liner. Between these, thermal insulation materials are placed. Besides, thermal insulation materials are also placed between the fresh food and freezer compartments. The conventional thermal insulation materials in refrigerators are polyurethane and VIPs and their thermal conductivities are between 20.5–21.5 $mW\,m^{-1}K^{-1}$ and 2–5 $mW\,m^{-1}K^{-1}$ at 23 °C.

8.3.1.2 Aerogels for Vacuum Insulation Panels

Vacuum insulation panels consist of a core material, a barrier film and sometimes a desiccant [25]. VIPs are produced by packing the core material with the barrier film and then vacuuming the package. VIPs have excellent thermal insulation performance due to suppressed gaseous thermal conductivity. The envelope of the VIP has a critical role since it preserves the vacuum in the panel. Mostly used barrier films are aluminum films or polymeric films and they comprise of multiple layers. Since pressure increase leads to an increase in the thermal conductivity, barrier films should have low vapor and gas permeability to prevent pressure increase [85]. In addition, getters and desiccants can be used to adsorb gases and water vapor in the VIPs, respectively [86].

The pore diameter of the core material should be small to suppress the gaseous thermal conductivity and in order to evacuate the gas, the core material must have open cell structure [86, 88]. Aerogels have highly porous open cell structure and pore diameter are in nanoscale. Due to the nanostructure of silica aerogels, the thermal conductivity increase as a function of pressure in silica aerogel VIPs is less than the VIPs with other core materials [87]. Besides, aerogels have larger surface area than the other core materials leading to higher vapor and gas adsorption capacity. These properties make aerogels a good candidate as core materials; therefore, several studies are conducted on silica aerogel VIPs.

In order to improve the mechanical properties, silica surface can be modified by polymers with low thermal conductivity such as polystyrene, isocyanates, and epoxies. However, surface modification increases the aerogel density, which leads to an increase in the thermal conductivity [25]. Furthermore, reinforcing fibers can be added into the silica aerogel. Liang et al. investigated effect of density and fiber felt on the thermal conductivity and service life of silica aerogel VIP. As the density of the core material increases, the effective thermal conductivity of aerogel core and VIP increases and service life of VIP first increases then decreases. Increasing fiber felt first lead to a decrease in the effective thermal conductivity of aerogel core and VIP, then leads to an increase. Liang et al. pointed out that at 1 Pa and 300 K, for minimum thermal conductivity (λ: 4.3 $mW\,m^{-1}K^{-1}$), optimum fiber felt content should be 6.6 vol.% [21]. In their other study, Liang et al. obtained lower thermal conductivity (λ: 3.9 $mW\,m^{-1}K^{-1}$) for silica aerogel VIP and also showed that when pressure increases, the optimum fiber felt content should be decreased to obtain minimum thermal conductivity [89].

VIP envelopes are generally opaque; however, Karayılan produced transparent VIP with silica aerogel (Figure 8.8) and transparent barrier film in his thesis studies [90]. There are some factors that affect the transparency of silica aerogel such as heat treatment after drying, addition of silytating agent and solvent exchange. He pointed out that as the molar ratio of the solvent to precursor in the sol mixture decreases, the transparency of the aerogel increases. In addition, it is indicated that when acetone was used as a co-solvent, the best transparency was obtained. He synthesized large silica aerogel from tetraethyl orthosilicate (TEOS) and the thermal conductivity of the silica aerogel was 16 $mW\,m^{-1}K^{-1}$. The transparent barrier film was produced by deposition of silicon



Figure 8.8 Transparent aerogel VIP [90].

oxide by electron beam evaporation. At Arçelik laboratories, silica aerogel was packed with barrier film and vacuumed immediately. The thermal conductivity of the transparent aerogel VIP was $12\,mW\,m^{-1}K^{-1}$.

According to these studies, aerogel VIPs can be used in refrigerators in several ways. Normally, VIPs are placed inside the polyurethane so, instead of these classical VIPs, aerogel VIPs can be used.

Most people open the refrigerator door and look inside and close it. In such cases, the internal temperature of the refrigerator increases and the compressor works harder to decrease the temperature of the refrigerator to its normal conditions, which leads to extra energy consumption. For this purpose, transparent aerogel VIPs can be used as a small window on the refrigerator door. Alternatively, VIPs can be placed behind the refrigerator door as a single piece so that heat loss is minimized when the refrigerator door is opened.

8.3.1.3 Aerogel Blankets for Refrigerators

Iliş et al. applied aerogel blankets (Aspen Aerogel – Cryogel Z type) to the refrigerators in order to save energy [91]. Thermal conductivity of Cryogel Z aerogel blanket is 17 and $15\,mW\,m^{-1}K^{-1}$ at 23.9 and −73.3 °C, respectively [92]. The experiments were conducted in two-type household refrigerators that were static type with cooler (341 l) and four-door no frost with cooler (292 l) and freezer (110 l). Static refrigerators do not have any ventilation system and natural convection occurs; therefore, the temperature of different parts of the refrigerator is different. In addition, static refrigerators need to be defrosted regularly. On the contrary, no-frost refrigerators have a ventilator that circulates the air and provides even temperature inside the refrigerator. The main aim of no-frost refrigerators is to keep the food fresh for a longer time. In order to cool the food quicker and prevent moisture from forming, cold and dry air is supplied to the refrigerator. Furthermore, no-frost refrigerators consume less energy as they cool the food faster. Therefore, it is more economical in the long term. The tested refrigerators worked with 230 V–50 Hz, and the refrigerant was R600a.

In static refrigerator, aerogel blankets were placed onto the evaporator and the porous structure was in contact with the PU. In no-frost refrigerator, in one test, the porous side of the aerogel blanket was in contact with PU and in the other test, the porous side of the aerogel blanket was at the outer surface of the refrigerator without PU contact.

Tests were conducted according to steady-state Energy Consumption (EC) test and ISO 15502 standard procedures. Tests were conducted in a climate chamber and the temperature of the climate chamber was stable at 25 °C. In order to simulate the foods, M packages having a specific heat capacity similar to the food were loaded into the freezer of the no-frost refrigerator. Since the static refrigerator do not have freezer compartment, M packages were not loaded; however, the same EC test procedures were applied. In addition, T-type thermocouples were used for the determination of the temperature of M packages and different parts of the refrigerator during the tests.

From this study, it was deduced that aerogel blanket application was not suitable for static-type refrigerators. In no-frost type refrigerator, aerogel blanket in contact with PU does not show any improvement. However, when the aerogel blanket was placed on the outer surface, energy consumption decreased 5%. Iliş also stated that aerogel blankets can be used for places where PU cannot fill or they can be used to prevent heat bridges [91].

8.3.1.4 Monolithic Aerogels for Refrigerators

In recent years, instead of conventional window insulations such as air/argon filled double glazing or coated glazing, granular aerogels between polycarbonate or polymethylmethacrylate panels are being studied due to their better insulation properties and shorter payback periods. Garnier et al. investigated the heat transfer coefficient and daylight factor of Cabot's Lumira aerogel and the U-value was $0.3\,W\,m^{-2}\,K^{-1}$, which was lower than conventional glazing. However, due to the granular structure, these glazing are not transparent; they are translucent and the visible quality is not as good as conventional glazing [93, 94]. Gao et al. pointed out that particle size of the aerogel granules in the glazing affects the heat losses and light transmissions. As the particle size decreases, thermal conductivity reduces, but light transmissions and visible quality also reduces [95]. Accordingly, monolithic aerogels can be better candidates for glazing applications.

Schultz et al. developed an evacuated monolithic silica aerogel glazing. To improve the visible quality, they applied anti-reflective treatment and heat treatment to the low iron glass and silica aerogel, respectively. As a result, the solar transmittance was obtained 82% for a 15 mm silica aerogel and 76% for low iron glass. In addition, in order to reduce the thermal conductivity and tensile stress in the aerogel, vacuum below 10 hPa was applied. The thermal conductivity of the evacuated glazing with silica aerogel was approximately calculated as $10\,mW\,m^{-1}K^{-1}$ from the average center U-value and aerogel thickness which are $0.66 \pm 0.03\,W\,m^{-2}K^{-1}$ and 14.8 mm, respectively [96].

In 2017, Strobach et al. developed monolithic silica aerogel, which is optically transparent and thermally insulating, for concentrated solar power systems. Tetramethyl orthosilicate (TMOS) and methyl silicate 51 were used as silica aerogel precursors. Strobach et al. stated that both transparency and insulation properties depend on the porous structure. In order to optimize the porous structure, they applied high temperature annealing method at 400 and 600 °C. Strobach et al. indicated that annealing at 400 °C increased the solar transmittance by 3%; however, it also increased the effective thermal conductivity by 40%. Therefore, it is important to determine the optimum annealing temperature and time. As a result, they obtained monolithic silica aerogel with almost 96% solar transmittance through a 9.5 mm thick sample and with an effective thermal conductivity of $0.055\,W\,m^{-1}\,K^{-1}$ between 400 and 50 °C [10].

AeroShield, produced super-insulating, transparent silica aerogels for windows (Figure 8.9) [98]. In her PhD thesis, Strobach prepared silica aerogels by sol-gel polymerization of tetramethyl orthosilicate (TMOS) or methyl silicate 51 [99]. As a catalyst, ammonia solution was used. She stated that as the catalyst and reactant ratio increases, haze reduces. In addition, TMOS have lower haze than methyl silicate 51 for the same formulation. To obtain more clear transparent silica aerogel, she conducted supercritical drying in a more controlled condition. In addition, as a post process,



Figure 8.9 Aeroshield monolithic silica aerogel [99].

high-temperature annealing was applied to increase the transparency by modifying the pore and/or particle sizes and density. The visible transmittance and visible haze of monolithic silica aerogel was greater than 98% and less than 2%, respectively. The thermal conductivity of the aerogel was approximately 13 $mW\,m^{-1}K^{-1}$ and it was indicated that double windows with AeroShield is more insulating than double-pane with gas and comparable to triple-pane.

In consideration of these studies, monolithic aerogels can also be used as a window for refrigerator door or may be used as a whole refrigerator door. For this application, aerogel should have high transparency.

Furthermore, monolithic silica aerogels may also be used inside PU. The major drawback of VIPs is risk of puncture and thermal bridging effect, which is arisen from the higher thermal conductivity of the barrier films [100]. Although, monolithic silica aerogels have higher thermal conductivity than VIPs and VIPs with aerogel core, instead of VIPs, monolithic silica aerogels can be placed inside the polyurethane in refrigerators to see how thermal bridge effects the overall heat transfer and energy efficiency.

8.3.1.5 Aerogel Polyurethane Composites

Dourbash et al. prepared silica aerogel/polyurethane (PU) composites by dry mixing of granular and powdered silica aerogels (PSAs) with first polyol, chain extender, catalyst and surfactant, and then diisocynate. Granular silica aerogel (GSA) was supplied from Cabot (Lumira). The particle sizes were between 0.7 and 4 mm, average pore diameter was 20 nm and density was between 65 and 85 $g\,l^{-1}$. PSA with particle size of 0.05–1 mm was obtained by grinding the granular aerogel in the laboratory. Three different rigid PU foams were used – E90, E30, and PY. First, silica aerogel was added into polyol part due to easier dispersion and then mixed with polymeric methylene diethyl diisosyanate (PMDI). After that, mixture was casted and polymerized in the mold. The highest amount of silica aerogel that can be added into PU was 4 wt% since the viscosity of the mixture increases with increasing silica aerogel content. Field emission scanning electron microscopy (FE-SEM) images of E30, E90, and PY composites showed that addition of the silica aerogel caused distortion in the cell structure and spherical cells nearly became elliptical and cylindrical [101].

The thermal conductivity of lightweight rigid PU foams (E30 and E90) was increased by the addition of GSAs. However, the thermal conductivity of PY decreased from 53 to 48.4 $mW\,m^{-1}K^{-1}$ with the addition of GSA. Besides, composites with PSA had lower thermal conductivity than composites with GSA, Dourbash et al. stated that the reasons could be the higher contact surface area and better dispersion [101].

Nazeran et al. investigated the impact of different silica aerogel contents (0, 1, 3, and 5 wt.%), different blowing agents (CFC-11, cyclopentane, normal pentane, and normal hexane), and two methods (method 1: mixing silica aerogel with methane diphenyl diisocyanate, method 2: mixing silica aerogel with polyol) on rigid polyurethane foams (RPUFs). Scanning electron microscope showed that addition of silica aerogels into PU matrix decreased the cell sizes. In addition to better thermal insulation properties provided by the smaller cell sizes and more uniform cell structure, silica aerogels also reduced the thermal conductivity by acting like a heat barrier because of their low thermal conductivity. It was showed that for two states and for all kind of blowing agents, increasing silica aerogel content decreased the thermal conductivity of RPUFs. However, mixing silica aerogel with methane diphenyl diisocyanate resulted in better insulation properties. Moreover, increasing silica aerogel content also increased the hydrophobicity of RPUFs. Besides, except from 5 wt.% silica content, the mechanical properties of RPUFs were significantly improved [102].

In light of these studies, silica aerogel – PU composites with better thermal properties or different kind of aerogel – PU composites can be developed and then can be used in refrigerator insulations instead of neat polyurethane.

8.3.2 Ovens

8.3.2.1 Thermal Insulation in Ovens

In electric ovens, generally there are two heating resistors; the heating resistor at the bottom part of the oven is used to cook the food and the heating resistor at the top part is generally used for frying the food. Heating resistors generate heat by the electric current passing through them and the temperature inside the oven is controlled by the thermostat. Moreover, some ovens include a fan, which provides uniform distribution of heat. To prevent heat loss, the oven's cooking zone is wrapped in insulation.

The internal oven temperature can usually reach 400–450 °C, and the areas in contact with the resistance can be 600 °C or more. Since the relative humidity will decrease with the temperature, during heating, the amount of humidity decreases to 20% and below. Glass and rock wool are generally used for thermal insulation in ovens. In higher-end models, ceramic wool is used. The thermal conductivities of these insulation materials are between 30 and 35 $mW\,m^{-1}K^{-1}$ at room temperature. However, the areas where the insulation materials are placed can be 600 °C or more and the effective thermal conductivity increases as the temperature increases, which means thermal conductivity of the insulation material will be higher than 30–35 $mW\,m^{-1}K^{-1}$ [103].

Due to the high operating temperatures, inorganic aerogels are more suitable for oven applications, as organic aerogels decompose at high temperatures.

8.3.2.2 Aerogel Blankets for Ovens

As it can be seen from Table 8.1, commercial aerogel blankets have lower thermal conductivity than glass wool, rock wool and ceramic wool [104–107]. In addition, these aerogel blankets are resistant to high temperatures and are suitable for oven applications.

Table 8.1 Properties of insulation materials Adapted [104–107].

Insulation material	Thermal conductivity ($mW\,m\,K^{-1}$)	Max. use temperature (°C)	Density ($kg\,m^{-3}$)	Specific heat ($J\,kg^{-1}\,K^{-1}$)
Glass wool	31–43 (at 10 °C)	500	32.55	1030
Rock wool	35–40 (at 10 °C)	650	70	800
Ceramic wool	81–82 (at 600 °C)	1650	160	1200
Pyrogel HPS[a]	21 (at 25 °C)	650	200	—
Pyrogel XTE[a]	20.75 (at 25 °C)	650	200	—
Pyrogel XTF[a]	20.75 (at 25 °C)	650	200	—
Pyrogel 6650[a]	13–14 (at 25 °C)	650	110	1046
Slentex[b]	19 (at 25 °C) 84.5 (at 600 °C)	650	190–200	790

[a] Aspen Aerogel.
[b] BASF.

Table 8.1 also shows that densities of aerogel blankets are much higher than conventional insulation materials. Although there is a decrease in heat loss due to the low thermal conductivity, aerogel blankets also offer higher energy storage due to the higher density. Bozgeyik indicated that this energy storage may have negative effect and increase the energy consumption in ovens. Some of the energy used to heat the oven is stored in the insulation material. As the density and specific heat of the insulation material increases, more energy is stored and more energy is needed to heat the oven. For instance, Bozgeyik investigated the effect of using 25 mm ceramic wool instead of 30 mm glass wool. The experiments showed that the energy consumption of the furnace increased by ~6.2% with ceramic wool since it has a higher density ($\rho = 160\,kg\,m^{-3}$) than glass wool ($\rho = 32.55\,kg\,m^{-3}$) [107].

Yücel et al. developed silica aerogel blanket material in order to use as an insulation material in household appliances such as ovens and dryers. They prepared silicate solution from grain pulps and rice husks, described in detail in Ref. [108]. They established two methods for aerogel blanket preparation: immersing glass wool blanket into the silicate solution and casting the solution onto glass wool blankets. After the immersing or casting process, the composite was gelled with sulfuric acid and tetraethylortosilicate and then the composite was dried in atmospheric pressure gradually for 12 hours at 25 °C, for 2 hours at 80 °C, and for 1 hour at 150 °C. It was also added that the aerogel blanket can be used between glass wool blankets as a sandwich form in household appliances. Moreover, Yücel et al. pointed out that the application of aerogel blankets can save 5–10% energy [108].

To overcome this drawback, aerogels with lower density and specific heat can be developed or aerogel blankets can be used together with glass wool and rock wool in the form of sandwiches. For instance, Hsu et al. prepared silica aerogel-mineral wool composites by APD. According to their results, the thermal conductivity of the mineral wool was decreased from 0.071 to $0.055\,W\,m^{-1}K^{-1}$ with the addition of 75 wt% of silica aerogel [109].

8.3.2.3 Monolithic Aerogel Panels

Due to the large difference between the interior temperature of the oven and the ambient temperature, radiative heat transfer becomes important and most of the heat losses are caused by the

glasses on the oven doors. In order to reduce the heat losses from the oven door, several studies were conducted such as reducing the glass surface by using an insulation material, coating the glass surface by a reflective material and increasing the number of glasses.

The studies of Bozgeyik showed that increasing the number of glasses from two to three can decrease the energy consumption from 835 to 809 Wh. However, he also declared that adding a fourth glass, metal frames, or hinges increases the energy consumption since these materials have thermal inertia in proportion to their mass [107].

High-temperature resistant tempered glass is used on the oven doors. In order to provide insulation, the double pane is vacuumed or gases such as air and argon are filled in. The oven door is used not only to load or unload food into the oven, but also to observe the cooking process of the food inside. When purchasing an oven, it is very important for customers to have a clear view of the oven glass. Thus, as an alternative insulation method, transparent monolithic silica aerogel can be used between the glass panes. Since silica aerogel has lower thermal conductivity and lower density than air, silica aerogel is a good candidate for thermal insulation in oven doors.

As another application, monolithic silica aerogels may be used between glass wool and rock wool like a sandwich form. Since the aerogel will not be visible and radiative thermal conductivity is affected by transparency, the thermal conductivity of the silica aerogels can be reduced by adding opacifiers.

8.4 Conclusions

In order to improve the energy efficiency of white goods, strict energy regulations were established. Therefore, white good manufacturers have been working to develop more energy efficient products and thermal insulation materials play an important role in energy saving.

Besides the conventional thermal insulation materials such as VIP and PU, aerogels are great candidates for many applications in refrigerators and ovens due to their low thermal conductivity, low density and high adsorption capacities. Aerogels can be integrated to white goods in the form of VIP core materials, monoliths, granulates, powders, or blankets. The use of aerogels in white goods can be expanded by improving their thermal, physical, and mechanical properties and also by reducing production costs. Thus, more environmentally friendly products with low energy consumption can be obtained.

References

1 BP (2020). Statistical Review of World Energy 2020 [Internet]. https://www.bp.com/en/global/corporate/energy-economics/statistical-review-of-world-energy.html

2 IEA (2020). Energy Efficiency Indicators Highlights 2020. https://www.iea.org/reports/energy-efficiency-indicators

3 In focus: A new generation of EU energy labels [Internet]. (2020). https://ec.europa.eu/info/news/focus-new-generation-eu-energy-labels-2020-aug-13_en

4 Gurav, J.L., Jung, I.K., Park, H.H. et al. (2010). Silica aerogel: synthesis and applications. *J. Nanomater.* 2010: 23.

5 Baetens, R., Jelle, B.P., and Gustavsen, A. (2011). Aerogel insulation for building applications: a state-of-the-art review. *Energy Build.* 43: 761–769.

6 Fesmire, J.E. (2006). Aerogel insulation systems for space launch applications. *Cryogenics* 46 (2–3): 111–117.

7 Jones, S.M. (2006). Aerogel: space exploration applications. *J. Sol-Gel Sci. Technol.* 40: 351–357.

8 Reim, M., Beck, A., Körner, W. et al. (2002). Highly insulating aerogel glazing for solar energy usage. *Sol. Energy* 72 (1): 21–29.

9 Feng, J., Le, D., Nguyen, S.T. et al. (2016). Silica–cellulose hybrid aerogels for thermal and acoustic insulation applications. *Colloids Surf. A Physicochem. Eng. Asp.* 506: 298–305.

10 Strobach, E., Bhatia, B., Yang, S. et al. (2017). High temperature annealing for structural optimization of silica aerogels in solar thermal applications. *J. Non-Cryst. Solids* 462: 72–77.

11 Li, Q., Zhang, Y., Wen, Z.X., and Qiu, Y. (2020). An evacuated receiver partially insulated by a solar transparent aerogel for parabolic trough collector. *Energy Convers. Manag.* 214 (January): 112911.

12 Ulker, Z. and Erkey, C. (2014). An emerging platform for drug delivery: aerogel based systems. *J. Controlled Release* 177 (1): 51–63.

13 Mirtaghavi, A., Luo, J., and Muthuraj, R. (2020). Recent advances in porous 3D cellulose aerogels for tissue engineering applications: a review. *J. Compos. Sci.* 4 (4): 152.

14 Lee, J.H. and Park, S.J. (2020). Recent advances in preparations and applications of carbon aerogels: a review. *Carbon N. Y.* 163: 1–18.

15 Biener, J., Stadermann, M., Suss, M. et al. (2011). Advanced carbon aerogels for energy applications. *Energy Environ. Sci.* 4 (3): 656–667.

16 Venkateswara Rao, A., Hegde, N.D., and Hirashima, H. (2007). Absorption and desorption of organic liquids in elastic superhydrophobic silica aerogels. *J. Colloid Interface Sci.* 305 (1): 124–132.

17 Maleki, H. (2016). Recent advances in aerogels for environmental remediation applications: a review. *Chem. Eng. J.* 300: 98–118.

18 Hasanpour, M. and Hatami, M. (2020). Application of three dimensional porous aerogels as adsorbent for removal of heavy metal ions from water/wastewater: a review study. *Adv. Colloid Interface Sci.* 284: 102247.

19 Yang, J., Li, Y., Zheng, Y. et al. (2019). Versatile aerogels for sensors. *Small* 15: 41.

20 Alwin, S. and Sahaya Shajan, X. (2020). Aerogels: promising nanostructured materials for energy conversion and storage applications. *Mater. Renew. Sustain. Energy* 9 (2).

21 Liang, Y., Wu, H., Huang, G. et al. (2017). Thermal performance and service life of vacuum insulation panels with aerogel composite cores. *Energy Build.* 154: 606–617.

22 About ASPEN AEROGELS https://www.aerogel.com

23 Cabot Corporation [Internet]. https://www.cabotcorp.com

24 Nano Tech Co., Ltd. [Internet]. http://www.nanuo.cn/index.php/English

25 Ülker, Z., Sanli, D., and Erkey, C. (2014). Applications of aerogels and their composites in energy-related technologies. In: *Supercritical Fluid Technology for Energy and Environmental Applications* (ed. V. Anikeev and M. Fan), 157–180. Elsevier B.V.

26 Stuart, G. and Burchill, J.P.W. (2006). Composition for thermal insulating layer.

27 Kistler, S.S. (1896). Coherent expanded aerogels. *J. Phys. Chem.* 1928 (318): 52–64.

28 Inonu, Z., Keskin, S., and Erkey, C. (2018). An emerging family of hybrid nanomaterials: metal-organic framework/aerogel composites. *ACS Appl. Nano Mater.* 1 (11): 5959–5980.

29 Şahin, İ., Özbakır, Y., İnönü, Z. et al. (2017). Kinetics of supercritical drying of gels. *Gels* 4 (1): 3.

30 Maleki, H., Durães, L., and Portugal, A. (2014). An overview on silica aerogels synthesis and different mechanical reinforcing strategies. *J. Non-Cryst. Solids* 385: 55–74.

31 Pierre, A.C. (2011). History of aerogels. In: *Aerogels Handbook Advances in Sol-Gel Derived Materials and Technologies* (ed. M. Aegerter, N. Leventis, and M.M. Koebel), 3–18. New York, NY: Springer.

32 García-González, C.A., Camino-Rey, M.C., Alnaief, M. et al. (2012). Supercritical drying of aerogels using CO_2: effect of extraction time on the end material textural properties. *J. Supercrit. Fluids* 66: 297–306.

33 Stergar, J. and Maver, U. (2016). Review of aerogel-based materials in biomedical applications. *J. Sol-Gel Sci. Technol.* 77 (3): 738–752.

34 Pekala, R.W. (1989). Organic aerogels from the polycondensation of resorcinol with formaldehyde. *J. Mater. Sci.* 24 (9): 3221–3227.

35 Mulik, S. and Sotiriou-Leventis, C. (2011). Resorcinol–formaldehyde aerogels. In: *Aerogels Handbook Advances in Sol-Gel Derived Materials and Technologies* (ed. M. Aegerter, N. Leventis, and M.M. Koebel), 215–234. New York, NY: Springer.

36 Zuo, L., Zhang, Y., Zhang, L. et al. (2015). Polymer/carbon-based hybrid aerogels: preparation, properties and applications. *Materials* 8: 6806–6848.

37 García-González, C.A., Alnaief, M., and Smirnova, I. (2011). Polysaccharide-based aerogels – promising biodegradable carriers for drug delivery systems. *Carbohydr. Polym.* 86 (4): 1425–1438.

38 Alnaief, M., Alzaitoun, M.A., García-González, C.A., and Smirnova, I. (2011). Preparation of biodegradable nanoporous microspherical aerogel based on alginate. *Carbohydr. Polym.* 84 (3): 1011–1018.

39 Rigacci, A. and Achard, P. (2011). Cellulosic and polyurethane aerogels. In: *Aerogels Handbook Advances in Sol-Gel Derived Materials and Technologies* (ed. M. Aegerter, N. Leventis, and M.M. Koebel), 191–214. New York, NY: Springer.

40 Gavillon, R. and Budtova, T. (2008). Aerocellulose: new highly porous cellulose prepared from cellulose-NaOH aqueous solutions. *Biomacromolecules* 9 (1): 269–277.

41 Illera, D., Mesa, J., Gomez, H., and Maury, H. (2018). Cellulose aerogels for thermal insulation in buildings: trends and challenges. *Coatings* 8 (10): 1–13.

42 Pekala, R.W., Alviso, C.T., Kong, F.M., and Hulsey, S.S. (1992). Aerogels derived from multifunctional organic monomers. *J. Non-Cryst. Solids* 145 (C): 90–98.

43 Zhuo, H., Hu, Y., Tong, X. et al. (2016). Sustainable hierarchical porous carbon aerogel from cellulose for high-performance supercapacitor and CO_2 capture. *Ind. Crops Prod.* 87: 229–235.

44 Allahbakhsh, A. and Bahramian, A.R. (2015). Self-assembled and pyrolyzed carbon aerogels: an overview of their preparation mechanisms, properties and applications. *Nanoscale* 7 (34): 14139–14158.

45 Hu, L., He, R., Lei, H., and Fang, D. (2019). Carbon aerogel for insulation applications: a review. *Int. J. Thermophys.* 40 (4): 1–25.

46 Biesmans, G. (1998). Polyurethane based organic aerogels and their transformation into carbon aerogels. *Journal of Non-crystalline Solids* 225: 64–68.

47 Leventis, N. and Lu, H. (2011). Polymer-crosslinked aerogels. In: *Aerogels Handbook Advances in Sol-Gel Derived Materials and Technologies* (ed. M. Aegerter, N. Leventis, and M.M. Koebel), 251–285. New York: Springer.

48 Mackenzie, J.D. and Angeles, L. (2000). Hybrid Organic—Inorganic Materials The Sol—Gel Approach. 226–236.

49 Demilecamps, A., Beauger, C., Hildenbrand, C. et al. (2015). Cellulose-silica aerogels. *Carbohydr. Polym.* 122: 293–300.

50 Yao, C.J., Liu, X., and Risen, W.M. (2011). Biopolymer-containing aerogels: chitosan-silica hybrid aerogels. In: *Aerogels Handbook Advances in Sol-Gel Derived Materials and Technologies* (ed. M. Aegerter, N. Leventis, and M.M. Koebel), 385–401. New York, NY: Springer.

51 Pierre, A.C. and Rigacci, A. (2011). SiO_2 aerogels. In: *Aerogels Handbook Advances in Sol-Gel Derived Materials and Technologies* (ed. M. Aegerter, N. Leventis, and M.M. Koebel), 21–45. New York, NY: Springer.

52 He, Y.L. and Xie, T. (2015). Advances of thermal conductivity models of nanoscale silica aerogel insulation material. *Appl. Therm. Eng.* 81: 28–50.

53 Tang, G.H., Bi, C., Zhao, Y., and Tao, W.Q. (2015). Thermal transport in nano-porous insulation of aerogel: factors, models and outlook. *Energy* 90: 701–721.

54 Zhao, J.J., Duan, Y.Y., Wang, X.D. et al. (2013). Optical and radiative properties of infrared opacifier particles loaded in silica aerogels for high temperature thermal insulation. *Int. J. Therm. Sci.* 70: 54–64.

55 Press Releases. http://news.aerogel.com/press-releases?item=66347

56 Fiber-Reinforced Aerogel Composite Blankets from Aspen Aerogels. http://www.aerogel.org/?p=1058

57 Aspen Cyrogel x201 Flexible Aerogel Blanket, Data Sheet https://www.aerogel.com/products-and-solutions/product-documents

58 Aerogel Blanket. https://www.cabotcorp.com/solutions/products-plus/aerogel/blanket

59 Hoseini, A., McCague, C., Andisheh-Tadbir, M., and Bahrami, M. (2016). Aerogel blankets: from mathematical modeling to material characterization and experimental analysis. *Int. J. Heat Mass Transfer* 93: 1124–1131.

60 Koebel, M.M., Rigacci, A., and Achard, P. (2011). Aerogels for superinsulation: a synoptic view. In: *Aerogels Handbook Advances in Sol-Gel Derived Materials and Technologies* (ed. M. Aegerter, N. Leventis, and M.M. Koebel), 607–633. New York, NY: Springer.

61 Şahin, İ., Uzunlar, E., and Erkey, C. (2018). Investigation of kinetics of supercritical drying of alginate alcogel particles. *J. Supercrit. Fluids* 2019 (146): 78–88.

62 Cabot aerogel: aerogel for insulation, daylighting and additives. (2005). http://www.cabot-corp.com

63 Ebert, H.P. (2011). Thermal properties of aerogels. In: *Aerogels Handbook Advances in Sol-Gel Derived Materials and Technologies* (ed. M. Aegerter, N. Leventis, and M.M. Koebel), 537–564. New York, NY: Springer.

64 Smith, D.M., Maskara, A., and Boes, U. (1998). Aerogel-based thermal insulation. *J. Non-Cryst. Solids* 225 (1–3): 254–259.

65 Aegerter, M.A., and Prassas, M. (2011). *Aerogels Handbook*, New York: Springer-Verlag.

66 Yang, H., Wang, Z., Liu, Z. et al. (2019). Continuous, strong, porous silk firoin-based aerogel fibers toward textile thermal insulation. *Polymers (Basel)* 11 (11): 1–14.

67 Karadagli, I., Schulz, B., Schestakow, M. et al. (2015). Production of porous cellulose aerogel fibers by an extrusion process. *J. Supercrit. Fluids* 106: 105–114.

68 Zhu, C., Han, T.Y.J., Duoss, E.B. et al. (2015). Highly compressible 3D periodic graphene aerogel microlattices. *Nat. Commun.* 6: 1–8.

69 Zhao, S., Siqueira, G., Drdova, S. et al. (2020). Additive manufacturing of silica aerogels. *Nature* 584 (7821): 387–392.

70 Chandrasekaran, S., Campbell, P.G., Baumann, T.F., and Worsley, M.A. (2017). Carbon aerogel evolution: allotrope, graphene-inspired, and 3D-printed aerogels. *J. Mater. Res.* 32 (22): 4166–4185.

71 Razeghi, M. (2009). *Fundamentals of Solid State Engineering*, 3e. New York: Springer.

72 Zhang, Z.M. (2020). *Nano/Microscale Heat Transfer*, 2e, vol. XXVI, 761. Springer International Publishing.

73 Bi, C. and Tang, G.H. (2013). Effective thermal conductivity of the solid backbone of aerogel. *Int. J. Heat Mass Transfer* 64: 452–456.

74 Dames, C. and Chen, G. (2004). Theoretical phonon thermal conductivity of Si/Ge superlattice nanowires. *J. Appl. Phys.* 95 (2): 682–693.

75 Chen, G. (1998). Thermal conductivity and ballistic-phonon transport in the cross-plane direction of superlattices. *Phys. Rev. B* 57 (23): 958–973.

76 Lu, X., Arduini-Schuster, M.C., Kuhn, J. et al. (1992). Thermal conductivity of monolithic organic aerogels. *Science* 255 (5047): 971–972.

77 Zeng, S.Q., Hunt, A., and Greif, R. (1995). Mean free path and apparent thermal conductivity of a gas in a porous medium. *J. Heat Transfer* 117 (3): 758–761.

78 Relation, T.H.E. and Heat, B. (1935). The relation between heat conductivity and structure in silica aerogel. *J. Phys. Chem.* 39 (1): 79–86.

79 Swimm, K., Vidi, S., Reichenauer, G., and Ebert, H.P. (2017). Coupling of gaseous and solid thermal conduction in porous solids. *J. Non-Cryst. Solids* 456: 114–124.

80 Lu, X., Caps, R., Fricke, J. et al. (1995). Correlation between structure and thermal conductivity of organic aerogels. *J. Non-Cryst. Solids* 188 (3): 226–234.

81 Bi, C., Tang, G.H., and Tao, W.Q. (2012). Prediction of the gaseous thermal conductivity in aerogels with non-uniform pore-size distribution. *J. Non-Cryst. Solids* 358 (23): 3124–3128.

82 Zeng, S.Q., Hunt, A., and Greif, R. (1995). Transport properties of gas in silica aerogel. *J. Non-Cryst. Solids* 186: 264–270.

83 Guo, J.F. and Tang, G.H. (2019). A theoretical model for gas-contributed thermal conductivity in nanoporous aerogels. *Int. J. Heat Mass Transfer* 137: 64–73.

84 Howell, J.R., Mengüç, M.P., Daun, K., and Siegel, R. (2020). *Thermal Radiation Heat Transfer*, 7e, 1040. Boca Raton: CRC Press.

85 Zhang, H., Wang, X., and Li, Y. (2017). Measuring radiative properties of silica aerogel composite from FTIR transmittance test using KBr as diluents. *Exp. Therm Fluid Sci.* 2018 (91): 144–154.

86 Baetens, R., Jelle, B.P., Thue, J.V. et al. (2010). Vacuum insulation panels for building applications: a review and beyond. *Energy Build.* 42 (2): 147–172.

87 Reichenauer, G., Heinemann, U., and Ebert, H.P. (2007). Relationship between pore size and the gas pressure dependence of the gaseous thermal conductivity. *Colloids Surf. A Physicochem. Eng. Asp.* 300(1-2 SPEC. ISS: 204–210.

88 Kucukpinar, E., Miesbauer, O., Carmi, Y. et al. (2016). Development of transparent and opaque vacuum insulation panels for energy efficient buildings. *Energy Proc.* 2015 (78): 412–417.

89 Liang, Y., Wu, H., Huang, G. et al. (2017). Prediction and optimization of thermal conductivity of vacuum insulation panels with aerogel composite cores. *Proc. Eng.* 205: 2855–2862.

90 Karayılan, M. (2014). *Investigations of Sol-Gel Parameters, Thermal and Optical Properties of Silica Aerogels for Large Scale Production*. Koç University.

91 Iliş, G.G. (2014). Experimental insulation performance evaluation of aerogel for household refrigerators. *Prog Exergy, Energy, Environ.* 1–1086.

92 Aspen Aerogels. Cryogel Z Datasheet EN. 2019.

93 Abdul Mujeebu, M., Ashraf, N., and Alsuwayigh, A. (2016). Energy performance and economic viability of nano aerogel glazing and nano vacuum insulation panel in multi-story office building. *Energy* 113: 949–956.

94 Garnier, C., Muneer, T., and McCauley, L. (2015). Super insulated aerogel windows: impact on daylighting and thermal performance. *Build. Environ.* 94 (P1): 231–238.

95 Gao, T., Jelle, B.P., Ihara, T., and Gustavsen, A. (2014). Insulating glazing units with silica aerogel granules: the impact of particle size. *Appl. Energy* 128: 27–34.

96 Schultz, J.M., Jensen, K.I., and Kristiansen, F.H. (2005). Super insulating aerogel glazing. *Sol. Energy Mater. Sol Cells* 89 (2–3): 275–285.

97 Schultz, J.M. and Jensen, K.I. (2008). Evacuated aerogel glazings. *Vacuum* 82 (7): 723–729.

98 The AeroShield Material ultra-clear silica aerogel. (2020). https://www.aeroshield.tech/technology

99 Strobach, E. (2020). *Optically Transparent, Thermally Insulating and Soundproofing (OTTIS) Aerogel for High-Efficiency Window Applications*. Massachusetts Institute of Technology.

100 Gangåssæter, H.F., Jelle, B.P., Mofid, S.A., and Gao, T. (2017). Air-filled nanopore based high-performance thermal insulation materials. *Energy Proc.* 132: 231–236.

101 Dourbash, A., Buratti, C., Belloni, E., and Motahari, S. (2017). Preparation and characterization of polyurethane/silica aerogel nanocomposite materials. *J. Appl. Polym. Sci.* 134 (8): 1–13.

102 Nazeran, N. and Moghaddas, J. (2017). Synthesis and characterization of silica aerogel reinforced rigid polyurethane foam for thermal insulation application. *J. Non-Cryst. Solids* 461: 1–11.

103 Wei, G., Liu, Y., Zhang, X. et al. (2011). Thermal conductivities study on silica aerogel and its composite insulation materials. *Int. J. Heat Mass Transfer* 54 (11–12): 2355–2356.

104 Ceramic Fiber Blankets. https://armilcfs.com/wp-content/uploads/2015/07/Ceramic-Fiber-Blankets.pdf

105 Stone Wool. www.izocam.com.tr/images/product/technical-image/stone-wool796.pdf

106 Glass Wool. www.izocam.com.tr/images/product/technical-image/glass-wool949.pdf

107 Bozgeyik, A. (2006). *Elektrikli Fırınların Enerji Tüketimini Azaltmaya Yönelik Yöntemlerin Deneysel Olarak Etkisinin Araştırılması*. Istanbul Technical University.

108 Yücel, O., Sıyın, N., and Yusufoğlu Y. (2019). An aerogel blanket and the household appliance using the same. Patent No. WO2019076630.

109 Hsu, M.W., Chen, Y.S., Chen, Y.S. et al. (2017). To improve the thermal properties of mineral wool by adding aerogel. *Sensors Mater.* 29 (4): 445–452.

110 Lv, Y., Huang, R., Wu, H., Wang, S., and Zhou, X. (2017). Study on Thermal and Optical Properties and Influence Factors of Aerogel Glazing Units. *Procedia Eng.* 205: 3228–34. https://doi.org/10.1016/j.proeng.2017.10.295.

9

Natural Polymer-Based Aerogels for Filtration Applications

Mahaveer A. Halakarni[1], M. Manohara Halanur[1], and Sanna Kotrappanavar Nataraj[1,2]

[1] *Centre for Nano & Material Science, Jain University, Jain Global Campus, Bangalore, 562112, India*
[2] *Polymer Science and Engineering, Chonnam National University, 77 Yongbong-ro, Buk-gu, Gwangju, South Korea*

9.1 Introduction

The combination of increasing population growth, demographic changes, urbanization, climate change and increasing water scarcity is posing numerous challenges for water supply systems [1–3]. Water scarcity is defined as the lack of sufficient available water resources to meet a particular region's water needs [4]. It has been widely reported that more and more consumers around the world are entering an era of severe water shortages and limitations in freshwater supply are already evident where large areas are facing augmented consequences of deteriorating and disappearing water reserves [5]. On the other hand, water systems are polluted by various point and nonpoint sources, which includes untreated municipal wastewater, industrial wastewater as well as pesticides, and fertilizers washing sourced from farm areas into aquatic systems [6–8]. These effects can be immediate or take time to build up in the environment and food chain before the effects are recognized [9]. Methods such as adsorption [10], ion exchange [11], coagulation [12], and membrane-based technologies [13] are proposed to access potable water. However, high-cost, flexibility for diversified pollutants, and low water permeability restrict their large-scale efficacy. Thus, development of a cost-effective protocol for rapid and versatile water purification is of utmost importance.

As is widely discussed, water pollution is a global problem threatening the entire biosphere and affecting the life of millions of people around the world. With the increase in demand for standard quality water, several purification techniques have been adopted. Interestingly, from the past few decades, tremendous advancements have been made to discover and develop low-cost, high-performance polymer-based purification technology to treat contaminated water. In this direction, polymer-based gels, hydrogels, and aerogels are rapidly gaining attention, as these end products can be easily prepared from sustainable precursors due to their unique structure, results in exceptional low density, and high porosity, which provides substantial opportunities for rapid water purification. The aerogel systems are easy to handle and separate from water due to their distinctive properties, and can readily be recycled and reused. Thus, understanding the chemistry of polymer-based gels, hydrogels, and aerogels and their application in water purification is crucial and very helpful. Herein, the book chapter critically discusses the material option, strategies to prepare sustainable aerogels, tuning their properties and lastly the emerging application in water

Aerogels for Energy Saving and Storage, First Edition. Edited by Meldin Mathew, Hanna J. Maria, Ange Nzihou, and Sabu Thomas.
© 2024 John Wiley & Sons, Inc. Published 2024 by John Wiley & Sons, Inc.

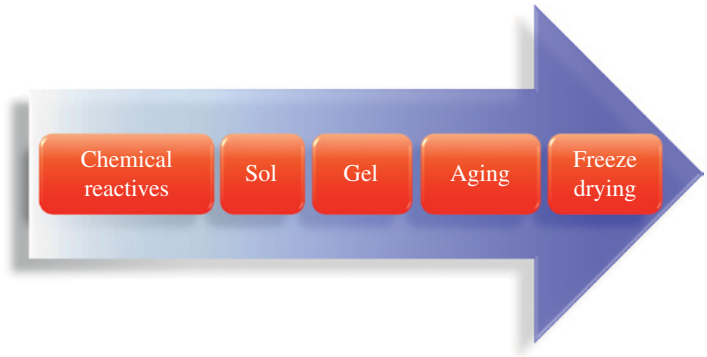


Figure 9.1 Schematics of bottom-up strategy generally followed in preparing aerogel-membranes.

purification such as removal of organic dyes, oil-water emulsion, heavy metal ion separation, and seawater purification.

Toward this endeavor, polymer-based aerogels presenting great potential and showing wider opportunities for rapid water purification with high quality yield [14]. In the recent past, self-assembling micro/nanostructures into three-dimensional (3D) hierarchical architectures such as foams, sponges, aerogels, and xerogels through a "bottom-up" strategy (Figure 9.1) attracted several research groups because of their wide range of applications.

Interestingly, being the lightest synthetic solid on Earth, tremendous growth was observed in polymer-based aerogels research, inspired by sustainability arguments, unique and tunable properties, and ease of functionalization [15, 16]. The temperature of the system increases when a liquid is held under a pressure always greater than the vapor pressure turns in to critical temperature which transforms liquid into a gas without two phases having been present at any time. Using this phenomenon, the synthesis of aerogel became easier.

Aerogels are had been known to researcher close to century now, however practical importance of aerogels were realized in 1980s. The historical account of the progressive development of various kinds of aerogels are shown in Figure 9.2. First aerogel was reported by Kistler in 1932 by

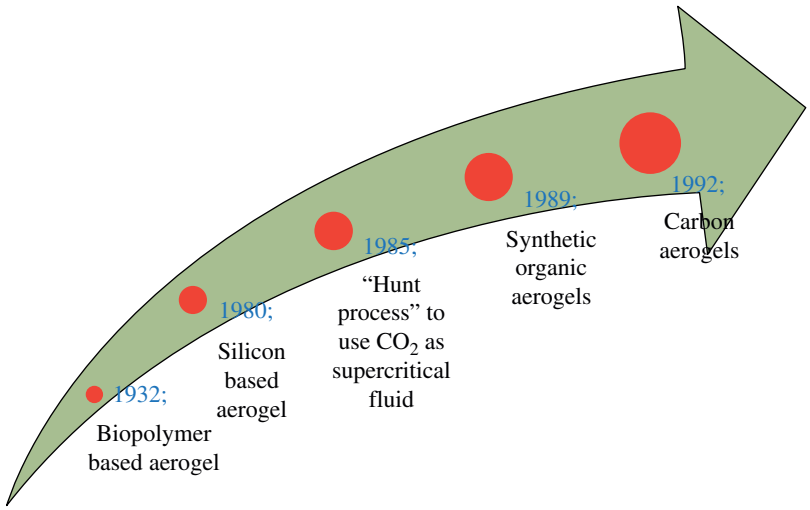


Figure 9.2 Schematics showing evolution of aerogels and their material specifications history.

evaporating organic solvents such as alcohols under high pressure, but this invention was almost forgotten for four decades because of a complicated multistage preparation process [17, 18]. Year 1980 saw the first report of silica-based aerogel followed by in 1985, Hunt introduces simple supercritical drying of aerogels near ambient temperature by substituting liquid CO_2 for the alcohol to prepare transparent silica [19] aerogels. This finding initiates tremendous research in silicon-based aerogel for a wide variety of application [20]. In subsequent research, a large number of inorganic aerogels have also been investigated such as alumina aerogels [21], metal alkoxides-based aerogel [22] and metal oxide aerogels [23]. In 1989, Pekala reported polycondensation of resorcinol with formaldehyde under alkaline conditions results in the first organic aerogels that are processed under supercritical [24] conditions.

In 1992, Pekala et al. demonstrated first ever [25], carbon-based aerogels by pyrolyzing organic aerogels in an inert atmosphere at 1323 K. In the early 1990, organic precursors yielded an interesting new class of monolithic aerogels, prepared by the sol-gel-emulsion techniques such as phenol-formaldehyde based aerogels [26]. Unfortunately, their large-scale production still has been limited by drying problems where supercritical drying involves hazardous high pressures, and is difficult to scale-up. Thereafter, aerogels prepared from synthetic and/or bio-polymers as precursor by supercritical extraction of the solvent from the wet gels through the freeze drying experienced a massive acceleration in terms of published papers. In the process of freeze drying a 3D hybrid network with ultra-porous macrostructures are created after solvent molecule removal [27]. Synthetic polymers such as polyvinyl alcohol (PVA), polyurethane (PU), polypropylene, polyamide, polyvinylidine difluoride (PVDF), and biopolymers like cellulose, alginate, chitosan, pectin, and starch were successfully employed for the preparation of aerogels [28–30]. These polymer-based aerogels attracted researchers because of their unique physical and chemical characteristics such as high mechanical strength, enhanced chemical and thermal stability, and flexibility [31].

From a technical point of view, aerogels are a porous macro material with very low density (range from 0.0011 to ~0.5 g cm^{-3}), high porosity, high surface area, and surface functionality [29]. Their ultra-low density is due to this solid-in-air type solid foam structure consisting of up to 99.8% air, with very little solid material left overall. The unique characteristics help in utilization of aerogels in variety of applications includes thermal insulations, catalysts, sensors, fuel storage, ion exchange, etc. [32,33]. In recent times the emerging application of aerogel is found in various process of contaminated water purification and treatment, which includes organic dye contaminated wastewater treatment, crude oil leakage treatment, organic solvent separation, heavy metal ion separation, and solar driven water evaporation. These wide applications are matched with aerogels properties that show excellent mechanical strength, surface functionality, and tunable hydrophilic properties [29, 34]. Furthermore, polymer-based aerogels possess high reusability that can greatly increase shelf life, promote reusability, and reduce economic losses. Hence, this chapter discusses the material option and trends in the application of polymer-based aerogel system toward emerging water purification.

9.2 Material Option for the Preparation of Aerogel

9.2.1 Synthetic Polymers

Unlike silica-aerogels, which are fragile and hygroscopic, polymer-aerogels usually exhibit better mechanical and environmental stability for a variety of applications. A remarkable growth in polymer-based aerogel research was observed from natural polymers and non-silica inorganic oxides to synthetic organic polymers. Similar to silica aerogel, polymeric aerogel can be obtained

either by polymerizing monomers into cross-linked network, or by transforming the liquid to solid phase via physical phase inversion [33, 35, 36]. The potential application of the aerogel is based on its properties, which strongly rely on the microstructure, surface functionality, and mechanical properties. Synthetic polymer-based materials have an advantage over conventional material due to their low cost, suitability for monolithic large-scale fabrication, and being intrinsically insulating for heat. In early research, organic aerogels were formed by polymerizing reactive organic monomer such as formaldehyde, resorcinol, phenol, and methyl methacrylate using suitable solvent to form gels via simple sol-gel process followed by a supercritical drying process. The organic aerogels can be produced with very little shrinkage during the processing and have thermal conductivity comparable to silica aerogels but are much stronger with compressive modulus of 1–5 MPa [37]. Moreover, structural parameters of organic aerogels include flexibility, pore size, ordering, and even symmetric and/or asymmetric pore shape, apart from endowing them with multiple functional properties. Synthetic polymer-based flexible polymer-based aerogels can be obtained from resorcinol-[38] formaldehyde, poly (vinyl alcohol) [39], and supra molecules [40], and some of them exhibit good absorption of organic solvents/oils. The polymer scaffolds featured by columnar building blocks with 2-D hexagonally ordered mesopores and highly branched truss-like structures acquire high compressive elasticity as well as good flexibility. The porosity of polyimide aerogels can be varied by changing the initial concentration of the solids in the solutions resulting high porosity (91–98%), high specific surface area (473–953 $m^2\ g^{-1}$) and low bulk density [40]. Further, superhydrophobic or superoleophilic, highly porous and light-weight PVDF aerogel can be prepared without using any additives through vapor-induced phase inversion process [41] with unique hierarchical micro-nanostructures. Essentially, the textural property of aerogels is significant for robust performance in water purification.

A series of aerogels have been prepared via polymerization of a new span 80-based W/O gel-emulsion with high water content. Internal structure as well as mechanical strength and thermal conductivity of the monoliths could be facilely adjusted by varying water content in the gel emulsion templates. Under optimized condition, a typical hydrophobic aerogel with density of 0.035 $g\,cm^3$ has been obtained [42]. In another study, an ultra-light and robust 3D nanofiber aerogel or nanofiber sponge with tunable porosity and flexibility was synthesized from short synthetic pullulan or polyvinyl alcohol or polyacrylic acid nanofibers using a freeze-casting process followed by thermal crosslinking [43]. Interestingly various novel hybrid aerogels were investigated by crosslinking with silica [44], graphene oxide (GO), carbon nanotubes (CNTs) [39], and boron nitride nanofibers [45], based on specific application [46–48]. These additives can impart mechanical and chemical strength to the aerogel material as well as provide adsorption sites.

9.2.2 Biopolymers-Based Aerogels

The first-ever series of aerogels were prepared using various natural polymers such as gelatin, cellulose, agar, and albumin [49]. Naturally derived polymers called biopolymers are low cost, biodegradable, biocompatible and nontoxic polymers [50]. During the last decade(s), massive research interest grew toward biopolymer-based aerogel over synthetic polymers due to the high density of surface functional groups and their renewable and sustainable feedstock origin. Biopolymer-aerogels are open-celled, predominantly mesoporous solids of natural and semi-natural polymers typically produced by supercritical drying. Combining the inherent advantages of biopolymers with the three-dimensional unique structures of aerogels has opened up attractive new potential applications in the separation process. Biopolymers consist of monomeric units that are covalently bonded to form larger molecules with enriched functional groups such as hydroxyl and amine

groups. There are three main classes of biopolymers, classified according to monomers units and the structure of the biopolymer formed – namely, polynucleotides, polypeptides, and polysaccharides – out of which polysaccharides such as cellulose, starch, chitosan, and alginate are widely investigated for the preparation of aerogel. Cellulose aerogels are the most popular aerogel among other which accounts half of the biopolymer-based aerogel publications. Cellulose can be divided based on their preparation, processing conditions, density, mechanical properties, and surface area. Further, chitosan is in many ways comparable to cellulose, which has been greatly explored in recent academic research accounting up to 10% of all biopolymers. Due to amino groups in chitosan pKa is 6.5 and easily protonate in acidic solution, with a charge density that depends on the pH. Significantly, this causes chitosan soluble in acidic aqueous solution and bio adhesion property to bind to negatively charged substances [51]. Alginate is another biopolymer appealed research community accounting total of 12% of biopolymer research due to its global negative charge at neutral pH. The formation of gel can be initiated by addition of divalent cations such as Ca^{2+}, Zn^{2+}, Zr^{2+} following an egg-box mechanism. Biopolymer aerogels have also been prepared from agar, pectin, starch, carrageenan, xanthan, guar, and pullulan. All these polysaccharides have specific molecular structures, leading to a variety of gelation mechanisms and gel and aerogel properties.

9.3 Application of Aerogels in Water Purification

Aerogels are among the most versatile materials available for technological applications, where they are used or considered for real end use such as laser experiments, sensors, ultrasonic and gas, nuclear particle detection, thermal insulation, waste management, water purifications including organic molecules separation, solvent separation, oil-water separation, and solar-driven water evaporations.

9.3.1 Organic Molecule Separation

Currently, water contaminations are posing serious environmental problems and main danger to public health all over the world. Due to the rapid development of industries and the growing of population [52] organic contaminants and dyes have major contribution in environmental degradation compared to various other water pollutants. Annually, more than one lakh profitable dyes are consumed by various industrials like paper-board and paper [53], manufacture of rubber, plastic, food processing [54, 55], textile industries [56], leather, tanning [57] etc. These Industrial wastewaters have significant amount of the hazardous materials which causes imbalance to human health (See Table 9.1) and aquatic organisms in the environment [69]. Unluckily, we don't know the exact number of produced dyes in the world. It is estimated that annually over 100 tonnes of dyes are discharged into water resources [70]. Moreover, conventional treatment technologies have various short comings to emerging chemical contaminants, which are not effective in removing approved standards. This also leads to larger threat to natural resources and life cycle. In addition, most of the emerging pollutants are stable at higher temperature, under light exposure and resistant to chemical reactions. So, the segregation of organic dyes from industrial aqueous solution before discharging to water resources is crucial and very important [70]. Throughout the past decades, various treatment methods have been employed in the field to segregation of dyes from water/wastewater such as coagulation, advanced oxidation, adsorption, and membrane separation [71]. Among these various methods, many researchers have been focused on dyes adsorption

Table 9.1 List of emerging organic molecules detected in various wastewaters that are hazardous to human health.

Organic molecule	Effect to human health	Refs.
Benzene	Affect to the central nervous system and hematopoietic system.	[58]
Rhodamine B	RB is causing skin irritation, eye irritation, and respiratory tract irritation. This is also carcinogenic, toxic for nervous, reproductive, and developmental system.	[58]
Acid yellow 17 dye	Even at low concentration, this dye affects skin, gastrointestinal tract, lungs, hemoglobin adducts and disturbance of blood formation.	[59, 60]
Phenolic compounds	High concentration of phenolic compounds is very toxic and mutagenic and absorbed through the skin.	[61]
Congo red	Reasons irritation in eye and skin, causes somnolence (sleepiness or drowsiness), respiratory problems, and carcinogenic in nature.	[62]
Methylene Blue	induces discoloration of skin, etc.	[63]
Crystal violet	Causes bladder cancer, vomiting, nausea, and central nervous system depression at high concentration	[63]
Azo dyes	Makes chromosomal damage and reductive cleavage of azo groups form carcinogenic aromatic amine	[64]
Basic fuchsin (BF)	Causes eye burn and irritation to skin	[65]
DDT	Causes endocrine and reproductive disorders, chronic liver damage, immune suppression, and cytogenic affects	[66]
Endosulfan	Affects kidney, fetus, liver, and reproductive system; mutagenic in nature	[67]
Malathion	Carcinogenic, mutagenic, etc.	[66]
Chlorpyrifos	Causes neurobehavioral disorders like persistent headache, blurred vision, memory, concentration	[66, 67]
Carbofuran	Affect function of nervous system	[67]
Simazine	Causes cancer of testes	[66, 68]

through aerogels and it is well-known adsorption method for removal waste organic dyes [72–74]. Many researchers used various materials like biopolymer, synthetic polymer, and hybrid polymer aerogels to remove the organic molecules. Among these, biopolymers have shown unique properties compared to synthetic and hybrid polymer as discussed in earlier sections. However, biopolymers are unstable in water and to enhance the stability researchers used many crosslinking agents via different mechanism as shown in Figure 9.3.

In the specific field of water remediation, chitosan (CS)-based aerogels are receiving growing attention. CS have amine and hydroxyl groups which are highly effective in binding both anionic pollutants and heavy metal ions. Slazana et al. reported chitosan and graphene oxide-based aerogel for dye removal; they achieved $376.8 \pm 32.3\,mg\,g^{-1}$ adsorption of indigo carmine and up to $168.6 \pm 9.6\,mg\,g^{-1}$ adsorption of methylene blue [76]. Further, Alessandro and the group demonstrated GO doped chitosan-gelatine aerogels where gelatine acts as a crosslinking agent for the separation of micropollutants. They have studied the adsorption capacity of both systems on two organic molecules such as fluoroquinolonic antibiotics ofloxacin and ciprofloxacin; their results show up to 80% adsorption of organic molecules [77]. Biopolymer cellulose mixed with graphene oxide and Fe_3O_4 were used to prepared aerogel through freeze drying, which exhibited ionic adsorption capability for removing

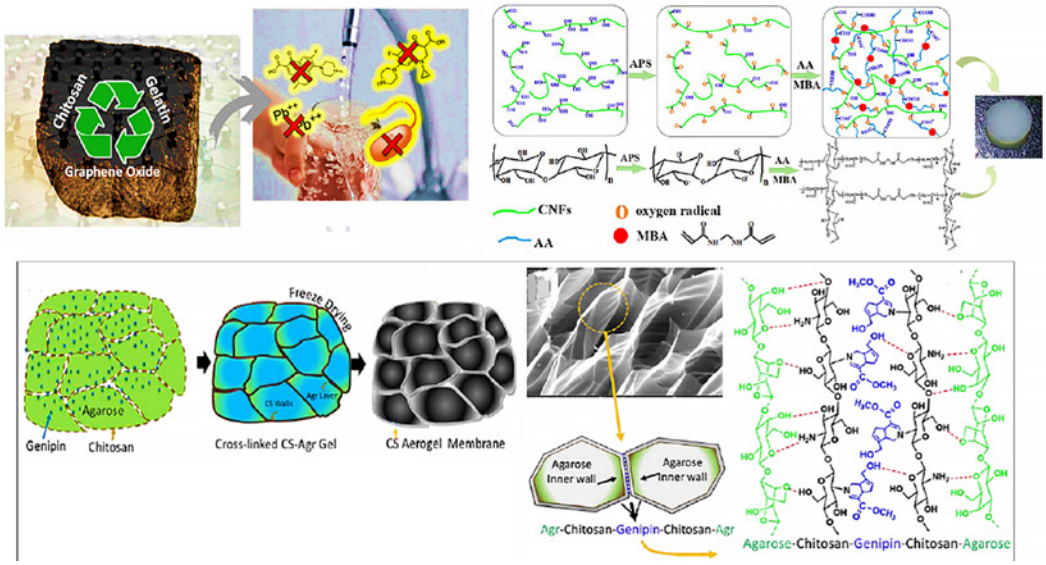


Figure 9.3 Actual images and schematics of various aerogels prepared using crosslinked chitosan and its crosslinking mechanism, respectively [75] / with permission of John Wiley & Sons.

both anionic and cationic contaminants, including dyes. The saturated adsorption capacity for Congo red and methylene blue reaches up 282 and 346 mg g^{-1} [78]. Zhang et al. used chitosan and cellulose mixed aerogels for separation of organic molecules without using crosslinking agent. In this study, researchers achieved methylene blue adsorption capacity up to 505 mg g^{-1} even after five successive adsorption–desorption cycles [79]. Cellulose nanofibril composite aerogels are prepared through a double-cross-linking method and applied as adsorbents to remove Bisphenol-A from water. In the result, within 10 seconds at an adsorption rate of 532.2 mg g^{-1} and their removal efficiency reach 97.0% [80]. Recently, Mezzenga and group demonstrated outstanding capability of amyloid fibrils-based aerogel as sustainable, effective, and cheap solution for organic pollutants removal from water. The adsorption of Bentazone, Bisphenol-A, and Ibuprofen succeed to removal of through amyloid fibrils aerogels, and exhibited 92%, 78%, and 98%, respectively [81].

Many researchers proposed synthetic polymer-based aerogel to remove organic contaminants. One such research group synthesized ultra-light nanofiber sponge with tunable porosity and flexibility from polyvinyl alcohol/polyacrylic acid nanofibers using a freeze casting process followed by thermal crosslinking. The prepared aerogel proved to be promising adsorbents for cationic dyes (383 mg g^{-1}) and their reusability. Regeneration ability and promising stability of the synthesized synthetic aerogel makes them very suitable for industrial applications [43]. Further, another research team developed a new kind of aerogel consisting of GO and synthetic polymer polyvinyl alcohol (PVA), in which PVA exhibited a role to stabilize the 3D porous structure of GO. Aerogels exhibited high absorption selectivity for dyes, especially for the dyes with positive charges, the adsorption efficiency was over 96% and they can completely adsorb Sudan red/cyclohexane from the water within five seconds [46]. A graphene/cysteamine hydrogel was prepared by heating a mixed solution containing cysteamine as a covalent cross-linker to fabricate graphene oxide aerogel and GO. Aerogel was obtained by freeze-drying method. In the result adsorption capacity for common dyes, such as methylene blue with 207.8 mg g^{-1} and methyl orange of 70.2 mg g^{-1} possible interaction of organic molecules and aerogels as shown in Figure 9.4 [83].

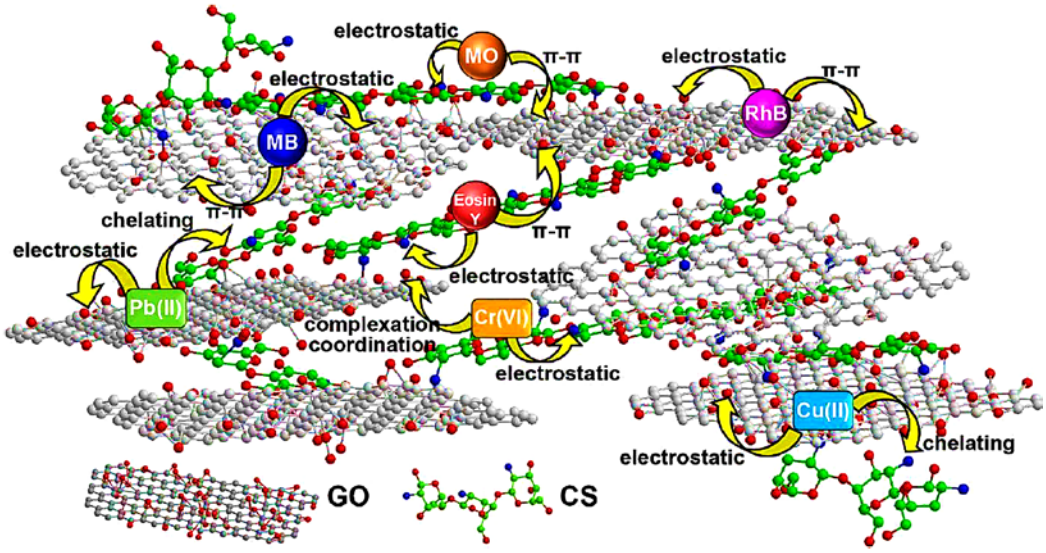


Figure 9.4 Schematic showing possible interaction of organic contaminants and GO-based aerogels [84] / with permission of American Chemical Society.

9.3.2 Organic Solvent Separation

The water crisis is the most frightening and immediate problem looming on the horizon of the twenty-first century. Even though, more than 70% of the Earth's surface is covered by water, but there are still tens of thousands of thirsty humans who rely on limited supplies of freshwater to thriving. Undoubtedly, a string of major chemical accidents in the past few decades had magnified the water scarcity issue, such as organics leak in Songhua River in China, the Gulf of Mexico oil spill, the gold event in Romania, recent crude oil carrier vessel accident in Indian Ocean etc. These events usually have the characteristics of complex situation, long continuance, great perniciousness, and pose prolonged environmental threat. Almost all kinds of living organisms are affected by these water pollutants owing to their inflammability, toxicity, and carcinogenicity, especially some organic solvents, such as aromatic compounds, ester, ketone, gasoline, diesel, and kerosene. Hence, it is crucial to explore effective techniques to remove such organic solvents from water [84, 85]. Researchers have proposed various kinds of methods: chemical methods like dispersion, in-situ burning and solidification; bioremediation involving microorganisms to degrade hydrocarbon in organics; and physical methods using booms and skimmers to hold the oil. However, all these methods suffer from many disadvantages such as energy-intensive steps involved, low separation efficiency, difficulty to handle equipment, high operating costs, and environmental hazards. Inversely, physical adsorption techniques have shown promising results in treating organic contaminants due to their simple design, low cost of operation, ease of handling [86], and tunable surface chemistry in adsorbent plays an important role in the process of adsorption-desorption to regenerate and reuse the substrate. Therefore, it is important to develop the innovative absorbents with excellent absorption capacity, higher hydrophobicity, low price, and recyclability [14]. Also, these physical adsorption methods prove a very efficient way to eliminate organic solvents from the wastewater. Amongst different adsorbents, high surface area, porous materials having micro/meso with narrow pore size, and tunable pore surface chemistry are reported as a well alternative with high adsorbent capacities [87]. With these requirements, aerogels can easily meet the

adsorption necessities and their application in removal of the existing and emerging toxic pollutants [88]. The activated carbon aerogel is reported as a good material to absorb toluene vapors with an excellent possibility of regeneration [88]. The maximum toluene adsorption capacity of carbon aerogels was 1180 mg g^{-1} with a possibility of complete desorption at 400 °C [89]. Silica aerogel was also specified to be a promising sorbent to adsorb benzene vapors with saturation adsorption capacity of 3000 mg g^{-1} while this value was reported only 500 mg g^{-1} in the case of activated carbon powders [90]. Silica monolith aerogels with different degrees of hydrophobicity were prepared by incorporating methyltrimethoxysilane (MTMS) or trimethylethoxysilane (TMES) in standard sol-gel synthesis followed by supercritical drying of gels with carbon dioxide (CO_2) at 40 °C and 100 bar. Prepared aerogel show good surface area, and organic solvent adsorption properties as hydrophobic silica aerogels remain stable even after 20 adsorption/desorption cycles [91]. Cellulose-based aerogel was prepared from waste newspaper without any pretreatment using 1-allyl-3-methyimidazolium chloride as a solvent via regeneration and freeze drying. After being treated with trimethylchlorosilane via a simple thermal chemical vapor deposition process, the resulting aerogel were rendered both hydrophobic and oleophilic. Also, results showed absorption capacity for organic solvents such as chloroform with a representative weight gain ranging from 11 to 22 times of their own dry weight [92].

9.3.3 Oil–Water Separation

Industrial effluent contains large amount of oil, grease, and many other hazardous materials, which poses harmful effect to both living organisms and the environment. The oil spillage accidents happened during production or transportation could leave long-lasting health and environmental impacts [93]. To separate emulsified oil/water waste usually, researchers followed numerous methods such as centrifugation and flotation. On the other hand, these methods have shown some disadvantages like poor separation efficiency, energy loss, and low removal capabilities. On the other hand, pressure-driven membrane filtration was employed to be effective in removing emulsified oil; however, the method consumes a large amount of energy [94]. As such, it would be a highly desirable to develop new materials with strong hydrophobic or oleophilic surface properties that can selectively separate oil from water or rapidly absorb it at low cost, save energy, have easy operation, and reduce spillage [95, 96]. During filtration of oil/water mixture through hydrophobic or oleophilic material, only the oil phase can pass through the material.

Based on these criteria, many materials have been introduced to segregate oil from water – for example, aerogel. Aerogel contributes many unique properties to separate oil from water, such as low density, low thermal conductivity, and high porosity [14]. A decade ago, only limited categories of aerogels were examined – for examples, however recent years have seen many innovative aerogels, such as CNT aerogel [97] and graphene aerogels [98] and nanocomposite aerogels.

Conventional aerogels are usually brittle, preventing them from practical applications. As a result, researchers have been developing polymeric aerogels with good mechanical strength, apart from endowing them with multiple functional properties and the mechanism of adsorption, desorption as shown in Figure 9.5 (a and b). To start with John G.et al. came up with hydrophobic, CF_3– functionalized silica aerogel used for oil/water mixtures separation. Further, oil-absorbing capacity studies of the solid aerogel have shown that the CF_3– functionalized aerogel as a powder has the potential of effectively separating oil from oil/water mixtures up to 14 times the weight of the aerogel [101]. Here, porous poly (vinylidene fluoride) (PVDF) aerogel, which is super hydrophobic and super oleophilic, was prepared through vapor-induced phase inversion. The PVDF aerogel is super hydrophobic and can almost instantaneously absorb oil.

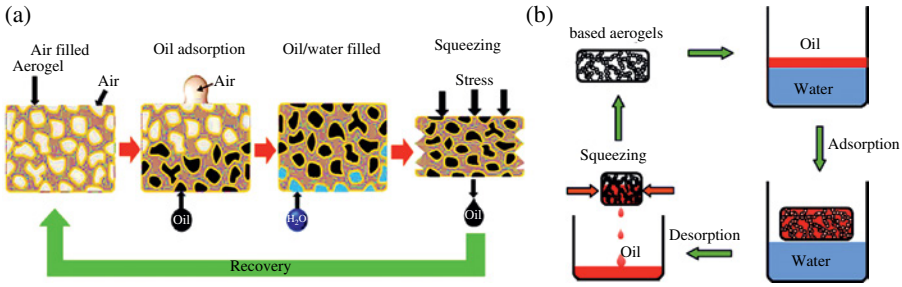


Figure 9.5 Mechanism of oil adsorption, desorption of oil from contaminated water mixture using various types of aerogels [99, 100].

Through PVDF, aerogel oil-in-water emulsion can be effectively separated under gravity with good flux and high filtrate purity up to 99.99% with excellent oil-absorption capacity 3–7 $g\,g^{-1}$ and high uptaking rate for various kind of oils [41].

PVA-supported GO aerogels were prepared through a freeze-drying technique. The surface modification of self-assembled graphene-oxide-induced PVA-aerogel promote stable microporous structure, structure stability, and excellent adsorption ability for different oil/water separation. Further, fluorinated functional groups are introduced into the surface of three-dimensionally macroporous graphene aerogel through a one-step solution immersion method in the result exhibits excellent absorption performance for various types of oils [46, 102]. In another study, reduced graphene oxide/polydopamine composite aerogel is reinforced with chitosan and perfluorodecanethiol (PFDT). Oil/water separation studies showed that nearly 95% of oil was absorbed from the contaminated mixture [103]. Advances in aerogel development have seen extensive use of biopolymers to prepare smart and targeted aerogels such as chitosan-based gel was transformed into highly porous aerogel membrane using bio-origin Genipin as crosslinking agent. Furthermore, oil/water separation studies used as developed chitosan-based aerogels in large scale showed recovery of high-quality water (>99% purity) from real oil spill sample collected from ship breaking yard [104].

9.3.4 Solar-Driven Water Evaporation

Solar energy and water are two of the most plentiful resources on the Earth [105, 106]. Solar evaporation, which combines these resources, is regarded as one of the most attractive and facile operations of solar thermal technology and has been used to generate potable water since ancient times [107, 108]. Steam and clean water generation from either wastewater or seawater is the basic application of the solar evaporation technique, which represents one of the most promising green and sustainable solutions to the pressing global challenge of water shortages [109–112]. Nowadays, an increasing number of applications are being driven by this fundamental photothermal process, including electricity generation [113], steam sterilization [114], and fuel production [115]. However, traditional solar evaporation approaches generally deliver a low photothermal conversion efficiency of 30–45% because of poor solar absorption and large amount of heat losses that result from the placement of light absorbers at the bottom of the water source. This, in turn, greatly hinders the practical application of this technology [116, 117]. On the other hand, the material choice to prepare solar-driven water evaporation processes, photothermal materials as solar absorbers, and thermal-insulating and water-transporting materials are key elements in solar

evaporation devices. The performance of solar evaporation is mainly determined by the properties of solar absorber, insulator, and water-transporting materials. For solar absorber design, high light absorption across the full solar spectrum range of 0.3–2.5 μm and high light-to-heat conversion efficiency are equally important, while for substrate material design, good thermal insulating and water-transport properties are desired.

The past decade has witnessed a fast growth of photothermal and substrate materials, mainly enabled by advances in nanotechnology through either new material development or structural engineering of existing materials. In this section, we will outline recent progress in developing substrate materials. The substrate material is equally important in high-efficiency solar evaporation design. The substrate material generally needs to provide two basic, key functions: water transport/evaporation and thermal insulation. For efficient water transport and evaporation, both good wetting properties and continuous pathways are critical. For improved thermal insulation, low thermal conductivity and porous structures are desirable. It is worth noting that pore structure is a key element for both water transport and thermal insulation. However, the balance between efficient water transport, which generally requires pores to be filled with water and thermal insulation which requires pores to be filled with air must be considered. Researchers have developed materials with specific designs to address this conflict by sorting out the water-transport pathways from the thermal insulation structures via one-dimension or two-dimension water pathway designs. Based on these guidelines, the improved water transport and thermal management has been achieved via hydrophilic, porosity, and/or thermal insulating to make them suitable substrates for solar evaporation. One such material is cellulose foam/aerogel [118], which demonstrates excellent hydrophilicity, low thermal conductivity, and abundant hierarchical porosity, ensuring sufficient water transport/evaporation and good thermal management capabilities for efficient solar evaporation. Natural wood, with the majority of its components being cellulose, possesses good hydrophilicity, well-aligned hierarchical channels, and low thermal conductivity. Therefore, cellulose-based precursors as a substrate material have inspired several solar evaporation structures by using wood itself [119–124]. In addition to this, PU and polystyrene (PS) foams have shown great potential as excellent commercially available thermal insulators in solar evaporation and also beneficial as they enable interfacial solar evaporators to easily float on the surface of water [125–127]. Other efficient substrate materials include GO aerogel [128] air-laid paper [129] and CNT arrays [130]. In general, the rapid development of substrate materials with desirable water transport/evaporation and thermal insulation properties and diverse structural designs have boosted the development of solar evaporation devices and systems. From recent developments it is clear that the ideal absorbers should possess several properties, broadband and efficient solar absorption, reduced thermal conductivity for localized water heating, hydrophilicity for efficient water supply, and porous networks for vapor channels. As alternatives to all these conventional materials, aerogels are emerging as unique substitutes for porous solids [33] with many fascinating properties such as low mass density, high porosity, large surface area, and low thermal conductivity. Besides, graphene oxide-based (GO) aerogels were used for solar steam generation [128], plenty of aerogel-based evaporators, including metal aerogels [131], CNT aerogels [118, 132], and graphene-based aerogels [133, 134], etc. have also been fabricated to harvest solar energy for water desalination or purification.

These aerogels have proven useful for solar desalination because of their well solar-absorbing capacity, high porosity, large surface area, and low thermal conductivity [135]. However, it also should be pointed out that many aerogels share the similar disadvantages of complex preparation process and high capital loss to some extent, limiting their practical applicant. Therefore, it is of great significance to expand the aerogels material-pools for solar declamation.

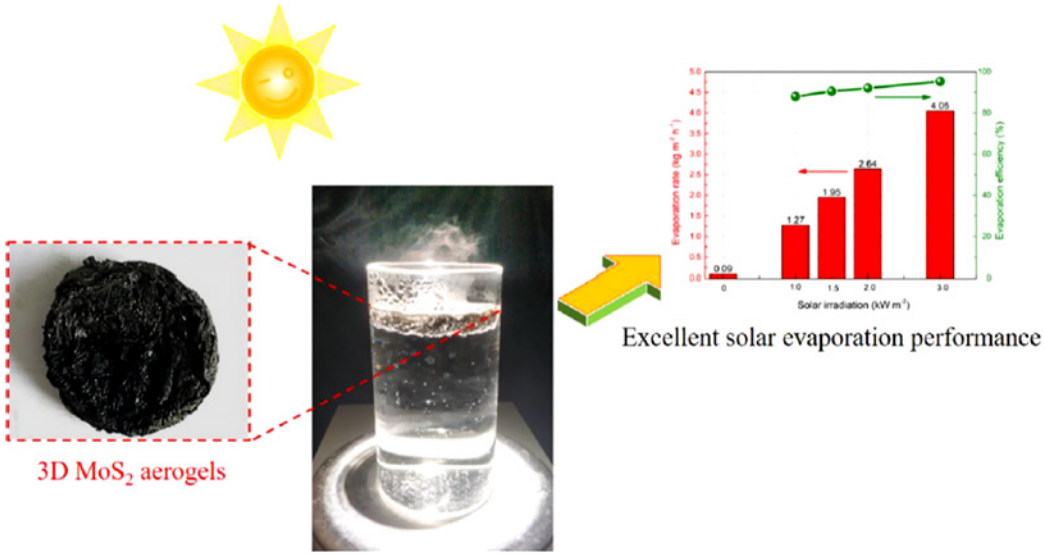


Figure 9.6 Mechanism of solar evaporation using 3D MoS_2-based aerogel [142].

On the other hand, MoS_2 as one of the most attractive advanced materials is gaining importance in the field of electronics, catalysis, biomedical, environmental, and energy related fields [136–138]. The MoS_2 nanosheets are also expected to have new applications in solar desalination. This is because the MoS_2 nanosheets have direct and narrow band gaps of 1.89 eV that reduce the separation and transportation of carriers at the interfaces [139–141] mechanism, as shown in Figure 9.6. Unfortunately, MoS_2 nanosheets fail to be a prominent material like GO or CNTs in terms of fabricating aerogels for advanced applications. Chitosan often serves as the basic framework for various aerogels with the help of cross-linkers [143]; it can also be expected to work as the frameworks in aerogels to prepare MoS_2 aerogels because of its rich hydroxyl and amino groups [144]. The use of MoS_2, polydopamine, and chitosan to prepare cost-effective solar evaporator holds the promising perspective because of their earth-abundant sources. Here, one such group 3D photo-thermal aerogels composed of reduced graphene oxide (RGO) nanosheets, rice-straw-derived cellulose fibers, and sodium alginate (SA) have been prepared for solar-steam generation. The use of rice straw fibers as skeletal support significantly reduces the need for the more expensive RGO by 43.5%, turning the rice straw biomass waste into value-added materials.

The integration of rice straw fibers and RGO significantly enhances the flexibility and mechanical stability of the obtained photothermal RGO–SA–cellulose aerogel. The photothermal aerogel shows a strong broadband light absorption of 96–97%. During solar-steam generation, the 3D photothermal aerogel effectively decreases the radiation and convection energy loss while enhancing energy harvesting from the environment leading to an extremely high evaporation rate of 2.25 $kg\,m^{-2}\,h^{-1}$, corresponding to an energy conversion efficiency of 88.9% under 1.0 sun irradiation. The salinity of clean water collected during the evaporation of real seawater was evaluated and found to be only 0.37 ppm [145].

One more group reported the preparation of a kapok fibers-PPy aerogels with super-wetting porous structure, high light absorption, and high mechanical strength by polypyrrole modification of the Ca^{2+} crosslinked kapok fibers aerogels. The kapok fibers-PPy aerogels show 3D structure with nearly 94% porosity, excellent light absorption (ca. 97%), low thermal conductivity of

0.0241 $W m^{-1} k^{-1}$, and high mechanical strength of 0.12 Mpa under 75% of strain. As solar steam generation device, a high energy conversion efficiency of 82.4% is achieved under 1 $kW m^{-2}$ illumination [146]. In another study, a commercial degreased cotton, photothermal CuS yolk-shell nanocages, and agarose were combined to produce a highly flexible photothermal aerogel, which delivered a high-energy efficiency of 94.9% for solar steam generation under 1.0 sun irradiation, corresponding to a water evaporation rate of 1.63 $kg m^{-2} h^{-1}$.

The preparation of the photothermal aerogel can easily be scaled up due to the simplicity of the applied casting method. The obtained aerogel showed excellent stability for solar steam generation with no degradation in performance after at least 15 cycles. The salinity of the clean water produced during solar-thermal desalination of seawater was only 0.54 ppm [131]. Herein, we develop the solar steam generator based on the defect-abundant graphene sheets for highly efficient production of clean water with high rejection of ions, organic media, and bacteria. The thermal conductivity of defect-abundant graphene aerogel is as low as 0.0075 $W m^{-1} K^{-1}$ with a record surface temperature of up to 90 °C under sun, which thus promotes a high water evaporation rate of 1.78 $kg m^{-2} h^{-1}$. Efficient production of clean water with high rejection of ions, oil, and bacteria was demonstrated [147].

9.3.5 Heavy Metal Ions Separation

Water resources are increasingly polluted by heavy metals through industrial discharges and ineffective treatment methods. Water contamination from heavy metals has become a universal problem and one of the most serious environmental issues in recent decades. Heavy metals have leached into various bodies knowingly and unknowingly for years, posing a serious threat to the environment, which directly leads to a negative impact on public health [148–150]. Some of the serious health issues detected due to the consumption of heavy metal via food chain are listed in Table 9.2.

Industrial activates such as electroplating, automobile accessories, battery production/assembly, staining, stabilizers and metallurgy, chemical industries, mines, oil refineries, electrical industries, and rubber industries impart different toxic metals into the environment [158]. Most industrial wastewater includes one or more toxic heavy metal ions such as such as chromium (Cr), copper (Cu), lead (Pb), mercury (Hg), manganese (Mn), cadmium (Cd), nickel (Ni), zinc (Zn), and iron (Fe) [156]. Therefore, it is vital to remove these heavy metals from the contaminated water sources with a suitable technique before releasing them into the environment. Various approaches such as membrane separation process, precipitation, filtration, ion exchange, adsorption, electrochemical, and biological process have been effectively utilized.

Recently, aerogels have been employed for the removal of heavy metal ions from the waste solutions through different approaches [159–161]. However, due to the several shortcomings such as high energy demand, high operational cost, and complicated operational approaches fail to meet a standard protocol for recovered water. Also, these processes are ineffective for removal of heavy metals at lower concentrations. Therefore, among these approaches aerogel adsorption technique is considered as the most efficient approach regarding an easy implementation and aerogel adsorption mechanisms are mainly based on the physical adsorption to adsorb heavy metal ions and as a result of highly porosity and surface area, aerogels have shown great potential toward heavy metal interaction through which metal ions are captured and removed from the wastewater systems at low price [162]. Also, functionality on aerogel surface, pore size, pore size distribution, specific surface area, and composition chemistry can be utilized to desorb the contaminants post-capturing and aerogels can be easily recycled for further reuse. Several organic, inorganic, hybrid, and nanocomposite aerogels have been proposed for this purpose [74, 163].

Table 9.2 Human health effects related to heavy metals found in wastewater in the food chain.

Metal ions	Human health effects	Refs.
Ag	Causes skin and other body tissues to turn gray or blue-gray, breathing problems, algeria, respiratory damage.	[151, 152]
As	Affects essential cellular processes such as oxidative phosphorylation and ATP synthesis. Causes toxicological lung and throat, skin and vascular diseases, visceral cancer, immunotoxic, genotoxicity through generation of reactive oxygen species and lipid peroxidation. Causes melanosis, keratosis, and hyperpigmentation in humans, irritation, and stomach pains.	[152–154]
Cd	Acute effects in children, carcinogenic, mutagenic, endocrine disruptor, lung damage and fragile bones, affects calcium regulation in biological systems. Causes serious damage to kidneys and bones in humans, emphysema, anemia, renal disorders and damage, bronchitis.	[151, 152]
Cr	Hair losses, headache, diarrhea, nausea, and carcinogenic.	[152, 153, 155]
Cu	Brain and kidney damage, elevated levels result in liver cirrhosis and chronic anemia, stomach and intestine irritation, liver damage, Wilson's disease, and insomnia.	[153, 156]
Hg	Autoimmune diseases, depression, drowsiness, fatigue, hair losses, insomnia, loss of memory, restlessness, disturbance of vision, tremors, temper outbursts, brain damage, lung and kidney failure, rheumatoid arthritis, circulatory and nervous disorders.	[152, 153]
Ni	Allergic skin diseases such as itching, cancer of the lungs, nose, sinuses, throat through continuous inhalation, immunotoxic, neurotoxic, genotoxic, affects fertility, hair loss, dermatitis, chronic asthma, carcinogenic, high phytotoxicity, damaging fauna, eczema of hands; high concentration can cause DNA damage.	[152, 153]
Pb	Excess exposure in children causes impaired development, reduced intelligence, short-term memory losses, and disabilities in learning and coordination problems, risk of cardiovascular disease, cerebral disorders, and renal, circulatory, and nervous disorders.	[153, 157]
Zn	Dizziness, fatigue, depression, lethargy, neurological signs, increased thirst, anemia, phototoxic, abdominal pain, lack of muscular coordination.	[153, 157]

The effective mechanism to remove heavy metals using ionic or functional polymers is via chelation formation. Polymers or polymer-based aerogels would readily chelate with heavy metal via functional groups containing N, O, S, and P as donor atoms, which are capable of forming a coordination complex with different metal ions [164–168]. In another study, the amino-modified silica xerogels were prepared via sol-gel reaction, which provides the possibility of tailoring the surface chemistry with various chelating groups by using a series of organically modified silica precursors. As prepared aerogel by Kłonkowski et al. [14] via anchoring (3-aminopropyl) trimethoxysilane, (3-[2-aminoethyl]aminopropyl) trimethoxysilane to the xerogel surface and interior sections with the high feasibility of chemisorption of Cu (II) ions through making a complex with them. Also, silica gel modified with several aliphatic mono-, di-, tri-, and tetramine-based functionalities possesses an interesting capturing efficiency toward several heavy metal ions [168]. Anchoring the dithiocarbamate moieties into aerogels using a sialylation chemistry was reported to capture trace amounts of metal ions [164].

9.3.6 Factors Affecting Adsorption of Heavy Metal Ions

To develop effective and efficient adsorbent with high capacity of capturing for inorganic pollutants like heavy metal ions from wastewater, precursors and preparation parameters such as pH solution, adsorbent dose, initial heavy metal ions concentration, adsorption time, temperature, and the effect of coexisting ions are major factors. The effect of contaminant pH value on the adsorption capacity toward heavy metals is one of the important parameters that determine sorption process and its kinetics. This important parameter also influences the overall characteristics of adsorbent, the ionization, protonation degree of adsorbent and the surface charge. The effect of pH on the adsorption and tuning materials accessibility to reach contaminant is important aspect of product design which make product highly efficient and effective. The material combination and product design aspects have been recently studied by several researchers in detail. Some results illustrate that heavy metal have different activity and mechanism toward maximum adsorption capacity. It must be mentioned that for in further studies on the effect of pH value on heavy metal ions adsorption, the zeta potentials at different pH values must be measured. By increasing the pH value, a better adsorption capacity was observed due to more negative surface charge, which enhances the electrostatic attraction toward heavy metal ions to promote the adsorption process [169]. Further, the effect of adsorbent dose is one of the key process factors to determine the adsorption capacity at different experimental conditions. Some researchers have shown results demonstrating the percentage removal of heavy metal ions increases quickly with increase in the dosage of the different adsorbents because of the greater accessibility of the surface area or exchangeable sites. Furthermore, the removal percentage of heavy metal ions adsorption on adsorbents are determined by the adsorption capacity of the adsorbent for various heavy metal ions. Similarly, the extreme adsorption capacity might emerge due to the increase in the active sites on adsorbent surfaces [170]. Initial concentration of the inorganic pollutants (heavy metal ions) shows a main role in the adsorption capacity. Usually, the influence of initial heavy metal ions concentration relies on existing active sites on surface of adsorbent and concentration of the heavy metals. Also, several studies reveal that the effect of contaminant concentration on the adsorption capacity on aerogel-based adsorbents [81, 171]. Temperature is another major parameter that influences the adsorption property. On the other hand, the effect of temperature influences the adsorption capacity by affecting the molecular interactions and solubility. In most of these cases, the adsorption capacity of heavy metal ions increases with increasing temperature, which is due to the availability of higher amount of adsorption site on adsorbent surface or the acceleration in the diffusion rate of metal ions. But the adsorption capacity of heavy metal ions possibly decreases by increasing the temperature in some cases. This adsorption capacity declines over a period of time was due to exothermal process of the adsorption of heavy metal ions onto aerogel adsorbent, so water treatment at the lower temperature would thermodynamically favor the adsorption [172, 173]. The actual heavy metal pollutants commonly coexistent with ions such as Cl^{-}, NO^{3-}, SO_4^{2-}, PO_4^{3-} and etc., which might affect the adsorption capacity of target pollutant [174–176]. However, it is precisely the existence of coexisting ions that can cause an inhibition for the adsorption process of heavy metal ions. The results displayed that multivalent ion such as SO_4^{2-}, PO_4^{3-}, etc. have a greater competitive with heavy metal ions compared to monovalent anions such as $NO^{3-}$and Cl^{-}. Also, results showed that the adsorption capacity of heavy metal ions decreases with increasing the effective nuclear charge at cations. This might be because of hydration radius decrease, which increases the effective nuclear charge at cations [177].

9.4 Conclusion and Future Prospect

In conclusion, polymer-based aerogels are gaining importance as efficient filtration or adsorption media playing different role as support, blend material, substrate for several nano/micro particles, and host for surface activation to provide desired functionality. Recent advancements in nanotechnology techniques and material evaluation on several aspect of contaminant adsorption, treatment, separation, and removal devices divulge new insights into the workings of separation and purification materials. Researchers and innovators are looking at material details and designs to suit water filtration standards. On the other hand, issues related to water pollution are widely discussed in view of greener and more sustainable materials and processes. The competition for finding suitable material combinations and techniques is gaining momentum as the discharge of wastewater into natural resources is ever-increasing from industries and domestic sources. In this competition, different classes of aerogels are gaining prominence as a possible option for water treatment. Literature search reveals that the aerogel is effective in removing oils, organic solvents, heavy metal ions, dyes from water, and solar-driven water evaporation efficiently, especially with a high adsorption capacity and reusability. There is growing demand for water-filtration devices that are easy to use, and easy to adopt for individual, community, and at large industrial applications. Therefore, polymer-based aerogels will remain in the attention of researchers and innovators owing to their adoptability and tunability.

Acknowledgments

SKN greatly acknowledge Jain University Management Research Project Grant (JU/MRP/CNMS/18/2022), the Ministry of Science and Technology, NANOMISSION GRANT (SR/NM/NT-1073/2016), DST INSPIRE faculty grant (IFA12-CH-84), and DST-Technology Mission Division (DST/TMD/HFC/2K18/124G), Government of India for financial support. Talent Attraction Program funded by the Community of Madrid Spain (2017-T1/AMB5610) for financial support.

References

1 Mancosu, N., Girma Gonfa et al. (2015). Water scarcity and future challenges for food production. *Water* 7 (3): 975–992.
2 McDonald, R.I., Pamela Green, Deborah Balk. et al. (2011). Urban growth, climate change, and freshwater availability. *Proc. Natl. Acad. Sci.* 108 (15): 6312–6317.
3 du Plessis, A. et al. (2019). Current and future water scarcity and stress. In: *Water as an Inescapable Risk*, 13–25.
4 Jaeger, W.K., Plantinga, A.J., Chang, H. et al. (2013). Toward a formal definition of water scarcity in natural-human systems. *Water Resour. Res.* 49 (7): 4506–4517.
5 L'vovich, M.I. and Raymond L. (1979). *World Water Resources and Their Future*. American Geophysical Union.
6 Hao, J., He Kebin, Duan, Lei. et al. (2007). Air pollution and its control in China. *Front. Environ. Sci. Eng. Chin.* 1 (2): 129–142.
7 Ioannis, K., Dimitra, G., Triantafyllos, A. et al. (2006). The status of pesticide pollution in surface waters (rivers and lakes) of Greece. Part I. Review on occurrence and levels. *Environ. Pollut.* 141: 555–570.

8 Aguilera, E., Luis Lassaletta., Alberto Sanz-Cobena. et al. (2013). The potential of organic fertilizers and water management to reduce N_2O emissions in Mediterranean climate cropping systems. A review. *Agric. Ecosyst. Environ.* 164: 32–52.

9 van Loosdrecht, M.C. et al. (2016). *Experimental Methods in Wastewater Treatment*. IWA Publishing.

10 Singh, N., Nagpal, G., and Agrawal, S. (2018). Water purification by using adsorbents: a review. *Environ. Technol. Innov.* 11: 187–240.

11 Arden, T.V. (2012). *Water Purification by Ion Exchange*. Springer Science & Business Media.

12 Matilainen, A., Vepsäläinen, M., and Sillanpää, M. (2010). Natural organic matter removal by coagulation during drinking water treatment: a review. *Adv. Colloid Interface Sci.* 159 (2): 189–197.

13 Chang, H., Li, T., Liu, B. et al. (2019). Potential and implemented membrane-based technologies for the treatment and reuse of flowback and produced water from shale gas and oil plays: a review. *Desalination* 455: 34–57.

14 Maleki, H. (2016). Recent advances in aerogels for environmental remediation applications: a review. *Chem. Eng. J.* 300: 98–118.

15 Zhao, S., Malfait, W.J., Guerrero-Alburquerque, N. et al. (2018). Biopolymer aerogels and foams: chemistry, properties, and applications. *Angew. Chem. Int. Ed.* 57 (26): 7580–7608.

16 Cao, C., Ren, J., Lv, Y.K. et al. (2020). A functionalized graphene aerogel for efficient water purification. *Green Mater.* 9 (1): 21–28.

17 Fricke, J. and Emmerling, A. (2005). Aerogels—preparation, properties, applications. In: *Chemistry, Spectroscopy and Applications of Sol-Gel Glasses*, 37–87.

18 Foams, S.-B.M. (1931). 53257140007025700D in 1992, 1993, 1994, and 1995 and. *Nature* 127 (741).

19 Gao, G.-M., Miao, L. N., Ji. et al. (2009). Preparation and characterization of silica aerogels from oil shale ash. *Mater. Lett.* 63 (30): 2721–2724.

20 Anderson, A.M. and Carroll, M.K. (2011). Hydrophobic silica aerogels: review of synthesis, properties and applications. In: *Aerogels Handbook*, 47–77.

21 Samokhvalov, A. (2018). Aluminum metal–organic frameworks for sorption in solution: a review. *Coord. Chem. Rev.* 374: 236–253.

22 Schneider, M. and Baiker, A. (1997). Titania-based aerogels. *Catal. Today* 35: 339-365.

23 Pan, L., Shunli, L., Oderinde, O. et al. (2018). Facile fabrication of graphene-based aerogel with rare earth metal oxide for water purification. *Appl. Surf. Sci.* 427: 779–786.

24 Pekala, R. (1989). Organic aerogels from the polycondensation of resorcinol with formaldehyde. *J. Mater. Sci.* 24 (9): 3221–3227.

25 Pekala, R., Alviso, C.T., Kong, F.M. et al. (1992). Aerogels derived from multifunctional organic monomers. *J. Non-Cryst. Solids* 145: 90–98.

26 Pekala, R., Alviso, C., and LeMay, J. (1991). *Organic Aerogels: A New Type of Ultrastructured Polymer*. CA, USA: Lawrence Livermore National Lab.

27 He, Y., Xu, T., Hu, J. et al. (2017). Amine functionalized 3D porous organic polymer as an effective adsorbent for removing organic dyes and solvents. *RSC Adv.* 7 (48): 30500–30505.

28 Paraskevopoulou, P., Chriti, D., Raptopoulos, G. et al. (2019). Synthetic polymer aerogels in particulate form. *Materials* 12 (9): 1543.

29 Aegerter, M.A., Leventis, N., and Koebel, M.M. (2011). *Aerogels Handbook*. Springer Science & Business Media.

30 Pekala, R. and Kong, F.-M. (1989). A synthetic route to organic aerogels-mechanism, structure, and properties. *Le Journal de Physique Colloques* 50 (C4): C4-33–C4-40.

31 Zuo, L., Zhang, Y., Zhang, L. et al. (2015). Polymer/carbon-based hybrid aerogels: preparation, properties and applications. *Materials* 8 (10): 6806–6848.

32 Fricke, J. and Tillotson, T. (1997). Aerogels: production, characterization, and applications. *Thin Solid Films* 297 (1–2): 212–223.

33 Biener, J., Stadermann, M., Suss, M. et al. (2011). Advanced carbon aerogels for energy applications. *Energy Environ. Sci.* 4 (3): 656–667.

34 Akimov, Y.K. (2003). Fields of application of aerogels. *Instrum. Exp. Tech.* 46 (3): 287–299.

35 Kim, S.H., Marcus A. Worsley, Carlos A. Valdez. et al. (2012). Exploration of the versatility of ring opening metathesis polymerization: an approach for gaining access to low density polymeric aerogels. *RSC Adv.* 2 (23): 8672–8680.

36 Gu, S., Li, Z., Miyoshi, T. et al. (2015). Polybenzoxazine aerogels with controllable pore structures. *RSC Adv.* 5 (34): 26801–26805.

37 Meador, M.A.B., Ericka J. Malow, Silva, R. et al. (2012). Mechanically strong, flexible polyimide aerogels cross-linked with aromatic triamine. *ACS Appl. Mater. Interfaces* 4 (2): 536–544.

38 Hasegawa, G., Shimizu, T., Kanamori, K. et al. (2017). Highly flexible hybrid polymer aerogels and xerogels based on resorcinol-formaldehyde with enhanced elastic stiffness and recoverability: insights into the origin of their mechanical properties. *Chem. Mater.* 29 (5): 2122–2134.

39 Ma, C.B., Du, B. et al. (2017). Self-crosslink method for a straightforward synthesis of poly (vinyl alcohol)-based aerogel assisted by carbon nanotube. *Adv. Funct. Mater.* 27 (10): 1604423.

40 Wang, J. and Zhang, X. (2015). Binary crystallized supramolecular aerogels derived from host–guest inclusion complexes. *ACS Nano* 9 (11): 11389–11397.

41 Chen, X., Yen Nan Liang, Xiu-Zhi Tang. et al. (2017). Additive-free poly (vinylidene fluoride) aerogel for oil/water separation and rapid oil absorption. *Chem. Eng. J.* 308: 18–26.

42 Liu, J., Yang, H., Liu, K. et al. (2020). Gel–emulsion-templated polymeric aerogels for water treatment by organic liquid removal and solar vapor generation. *ChemSusChem* 13 (4): 749–755.

43 Mousavi, S., Deuber, F., Petrozzi, S. et al. (2018). Efficient dye adsorption by highly porous nanofiber aerogels. *Colloids Surf., A* 547: 117–125.

44 Kim, H.M., Noh, Y. J., Yu, J. et al. (2015). Silica aerogel/polyvinyl alcohol (PVA) insulation composites with preserved aerogel pores using interfaces between the superhydrophobic aerogel and hydrophilic PVA solution. *Compos. A: Appl. Sci. Manuf.* 75: 39–45.

45 Gao, X., Rui, Li., Long Hu. et al. (2020). Preparation of boron nitride nanofibers/PVA composite foam for environmental remediation. *Colloids Surf., A* 604: 125287.

46 Dai, J., Huang, T., Tian, S.Q. et al. (2016). High structure stability and outstanding adsorption performance of graphene oxide aerogel supported by polyvinyl alcohol for waste water treatment. *Mater. Des.* 107: 187–197.

47 Bentini, R., Pola, A., Giorgia Rizzi, L. et al. (2019). A highly porous solvent free PVDF/expanded graphite foam for oil/water separation. *Chem. Eng. J.* 372: 1174–1182.

48 Tian, Y. and Ma, H. (2020). Solvent-free green preparation of reusable EG-PVDF foam for efficient oil-water separation. *Sep. Purif. Technol.* 253: 117506.

49 Kistler, S.S. (1931). Coherent expanded aerogels and jellies. *Nature* 127 (3211): 741–741.

50 Smidsrød, O., Moe, S., and Moe, S.T. (2008). *Biopolymer Chemistry*. Tapir Academic Press.

51 Goosen, M.F. (1996). *Applications of Chitan and Chitosan*. CRC Press.

52 Zhang, J., Tian, B., Wang, L. et al. (2018). *Photocatalysis: Fundamentals, Materials and Applications*, vol. 100. Springer.

53 Ivanov, K., Gruber, E., Schempp, W. et al. (1996). Possibilities of using zeolite as filler and carrier for dyestuffs in paper. *Papier* 50 (7–8): 456.

54 Wróbel, D., Boguta, A., and Ion, R.M. (2001). Mixtures of synthetic organic dyes in a photoelectrochemical cell. *J. Photochem. Photobiol., A* 138 (1): 7–22.

55 Dawood, S., Sen, T.K., and Phan, C. (2014). Synthesis and characterisation of novel-activated carbon from waste biomass pine cone and its application in the removal of Congo red dye from aqueous solution by adsorption. *Water Air Soil Pollut.* 225 (1): 1818.

56 Sokolowska-Gajda, J., Freeman, H.S., and Reife, A. (1996). Synthetic dyes based on environmental considerations. *Dyes Pigm.* 30: 1–20.

57 Kabdaşli, I., Tünay, O., and Orhon, D. (1999). Wastewater control and management in a leather tanning district. *Water Sci. Technol.* 40 (1): 261–267.

58 Organization, W.H (2003). *Atrazine in Drinking-Water: Background Document for Development of WHO Guidelines for Drinking-Water Quality*. World Health Organization.

59 Ashraf, M.A., Hussain, M., Mahmood, K. et al. (2013). Removal of acid yellow-17 dye from aqueous solution using eco-friendly biosorbent. *Desalin. Water Treat.* 51 (22–24): 4530–4545.

60 Karthikeyan, K. and Jothivenkatachalam, K. (2014). Removal of acid yellow-17 dye from aqueous solution using turmeric industrial waste activated carbon. *J. Environ. Nanotechnol.* 3 (2): 69–80.

61 Liu, Q.-S. et al. (2010). Adsorption isotherm, kinetic and mechanism studies of some substituted phenols on activated carbon fibers. *Chem. Eng. J.* 157 (2–3): 348–356.

62 Ahmad, R. and Kumar, R. (2010). Adsorptive removal of congo red dye from aqueous solution using bael shell carbon. *Appl. Surf. Sci.* 257 (5): 1628–1633.

63 Joseph, C. and Elilarasi, L. (2017). Removal of Methylene Blue Dye from Aqueous Solution Using a Newly Synthesized TiO_2-SiO_2 Photocatalyst in the Presence of Active Chlorine Species. *IOP Conference Series: Materials Science and Engineering*. IOP Publishing.

64 Chung, K.-T. (2016). Azo dyes and human health: a review. *J. Environ. Sci. Health C* 34 (4): 233–261.

65 Khan, T.A. and Khan, E.A. (2015). Removal of basic dyes from aqueous solution by adsorption onto binary iron-manganese oxide coated kaolinite: non-linear isotherm and kinetics modeling. *Appl. Clay Sci.* 107: 70–77.

66 Wauchope, R.D. et al. (1992). The SCS/ARS/CES pesticide properties database for environmental decision-making. In: *Reviews of Environmental Contamination and Toxicology*, 1–155.

67 Howard, P. (2017). *Handbook of Environmental Fate and Exposure Data: For Organic Chemicals, Volume III Pesticides*. Routledge.

68 Ahrens, W.H. (1994). Herbicide Hand Book.

69 Maleki, H. and Hüsing, N. (2018). Current status, opportunities and challenges in catalytic and photocatalytic applications of aerogels: environmental protection aspects. *Appl. Catal., B* 221: 530–555.

70 Gupta, V.K. et al. (2013). Adsorptive removal of dyes from aqueous solution onto carbon nanotubes: a review. *Adv. Colloid Interface Sci.* 193: 24–34.

71 Gupta, V. (2009). Application of low-cost adsorbents for dye removal – a review. *J. Environ. Manage.* 90 (8): 2313–2342.

72 Chen, W. et al. (2014). Comparative study of aerogels obtained from differently prepared nanocellulose fibers. *ChemSusChem* 7 (1): 154–161.

73 Ye, S., Liu, Y., and Feng, J. (2017). Low-density, mechanical compressible, water-induced self-recoverable graphene aerogels for water treatment. *ACS Appl. Mater. Interfaces* 9 (27): 22456–22464.

74 Yagub, M.T., Sen, T.K., Afroze, S. et al. (2014). Dye and its removal from aqueous solution by adsorption: a review. *Adv. Colloid Interface* 209: 172–184.

75 Tian, C. et al. (2018). Reusable and cross-linked cellulose nanofibrils aerogel for the removal of heavy metal ions. *Polym. Compos.* 39 (12): 4442–4451.

76 de Luna, M.S. et al. (2019). Optimization of dye adsorption capacity and mechanical strength of chitosan aerogels through crosslinking strategy and graphene oxide addition. *Carbohydr. Polym.* 211: 195–203.

77 Kovtun, A. et al. (2020). Multifunctional graphene oxide/biopolymer composite aerogels for microcontaminants removal from drinking water. *Chemosphere* 259: 127501.

78 Xiong, J. et al. (2020). Amphiprotic cellulose mediated graphene oxide magnetic aerogels for water remediation. *Chem. Eng. J.* 400, 125890.

79 Zhang, X. et al. (2019). Biohybrid hydrogel and aerogel from self-assembled nanocellulose and nanochitin as a high-efficiency adsorbent for water purification. *ACS Appl. Mater. Interfaces* 11 (50): 46714–46725.

80 Zhao, D. et al. (2019). PAF-1@ cellulose nanofibril composite aerogel for highly-efficient removal of bisphenol A. *J. Mater. Chem. A* 7 (1): 157–164.

81 Peydayesh, M. et al. (2020). Amyloid fibrils aerogel for sustainable removal of organic contaminants from water. *Adv. Mater.* 32 (12): 1907932.

82 Yu, R. et al. (2017). Graphene oxide/chitosan aerogel microspheres with honeycomb-cobweb and radially oriented microchannel structures for broad-spectrum and rapid adsorption of water contaminants. *ACS Appl. Mater. Interfaces* 9 (26): 21809–21819.

83 Chen, C., Zhu, X., and Chen, B. (2018). Covalently cross-linked graphene oxide aerogel with stable structure for high-efficiency water purification. *Chem. Eng. J.* 354: 896–904.

84 Inyang, M. and Dickenson, E. (2015). The potential role of biochar in the removal of organic and microbial contaminants from potable and reuse water: a review. *Chemosphere* 134: 232–240.

85 Ohsedo, Y. (2016). Low-molecular-weight organogelators as functional materials for oil spill remediation. *Polym. Adv. Technol.* 27 (6): 704–711.

86 Bhatnagar, A. and Sillanpää, M. (2017). Removal of natural organic matter (NOM) and its constituents from water by adsorption – a review. *Chemosphere* 166: 497–510.

87 Chen, D., Chang, X., and Jiao, X. (2014). Aerogels in the environment protection. In: *The Role of Colloidal Systems in Environmental Protection*, 573–591.

88 Fairén-Jiménez, D., Carrasco-Marín, F., and Moreno-Castilla, C. (2007). Adsorption of benzene, toluene, and xylenes on monolithic carbon aerogels from dry air flows. *Langmuir* 23 (20): 10095–10101.

89 Maldonado-Hódar, F.J. et al. (2007). Reversible toluene adsorption on monolithic carbon aerogels. *J. Hazard. Mater.* 148 (3): 548–552.

90 Zhihua, Z., et al. (2008). Benzene adsorption properties of silica aerogel-fiber composites. *2008 2nd IEEE International Nanoelectronics Conference*. IEEE.

91 Štandeker, S., Novak, Z., and Knez, Ž. (2007). Adsorption of toxic organic compounds from water with hydrophobic silica aerogels. *J. Colloid Interface Sci.* 310 (2): 362–368.

92 Jin, C. et al. (2015). Fabrication of cellulose-based aerogels from waste newspaper without any pretreatment and their use for absorbents. *Carbohydr. Polym.* 123: 150–156.

93 Wang, Y. et al. (2016). Synthesis and oil absorption of biomorphic MgAl layered double oxide/acrylic ester resin by suspension polymerization. *Chem. Eng. J.* 284: 989–994.

94 Zhang, W. et al. (2013). Superhydrophobic and superoleophilic PVDF membranes for effective separation of water-in-oil emulsions with high flux. *Adv. Mater.* 25 (14): 2071–2076.

95 Zang, D. et al. (2015). Superhydrophobic coating on fiberglass cloth for selective removal of oil from water. *Chem. Eng. J.* 262: 210–216.

96 Obaid, M. et al. (2015). Effective polysulfone-amorphous SiO2 NPs electrospun nanofiber membrane for high flux oil/water separation. *Chem. Eng. J.* 279: 631–638.

97 Aliev, A., Jiyoung, O. et al. (2009). Giant–Stroke, superelastic carbon nanotube aerogel muscles. *Science* 323 (5921): 1575–1578.

98 Worsley, M., Peter, A., Pauzauskie, J. et al. Synthesis of graphene aerogel with high electrical conductivity. *J. Am. Chem. Soc.* 2010, 132: 14067–14069.

99 Huang, J. and Yan, Z. (2018). Adsorption mechanism of oil by resilient graphene aerogels from oil–water emulsion. *Langmuir* 34 (5): 1890–1898.

100 Yu, Y., Wu, X., and Fang, J. (2015). Superhydrophobic and superoleophilic "sponge-like" aerogels for oil/water separation. *J. Mater. Sci.* 50 (15): 5115–5124.

101 Reynolds, J.G., Coronado, P.R., and Hrubesh, L.W. (2001). Hydrophobic aerogels for oil-spill cleanup? Intrinsic absorbing properties. *Energy Sources* 23 (9): 831–843.

102 Hong, J.-Y. et al. (2015). Highly-efficient and recyclable oil absorbing performance of functionalized graphene aerogel. *Chem. Eng. J.* 269: 229–235.

103 Cao, N. et al. (2017). Facile synthesis of fluorinated polydopamine/chitosan/reduced graphene oxide composite aerogel for efficient oil/water separation. *Chem. Eng. J.* 326: 17–28.

104 Chaudhary, J.P. et al. (2015). Chitosan-based aerogel membrane for robust oil-in-water emulsion separation. *ACS Appl. Mater. Interfaces* 7 (44): 24957–24962.

105 Crabtree, G.W. and Lewis, N.S. (2007). Solar energy conversion. *Phys. Today* 60 (3): 37–42.

106 Kabir, E. et al. (2018). Solar energy: potential and future prospects. *Renewable Sustainable Energy Rev.* 82: 894–900.

107 Schwarzenbach, R.P. et al. (2006). The challenge of micropollutants in aquatic systems. *Science* 313 (5790): 1072–1077.

108 Qiblawey, H.M. and Banat, F. (2008). Solar thermal desalination technologies. *Desalination* 220 (1–3): 633–644.

109 Chandrashekara, M. and Yadav, A. (2017). Water desalination system using solar heat: a review. *Renewable Sustainable Energy Rev.* 67: 1308–1330.

110 Shengquan, Y. et al. (2008). Separation of carcinogenic aromatic amines in the food colourants plant wastewater treatment. *Desalination* 222 (1–3): 294–301.

111 Elimelech, M. and Phillip, W.A. (2011). The future of seawater desalination: energy, technology, and the environment. *Science* 2011 (333): 712.

112 Zhou, L. et al. (2016). 3D self-assembly of aluminium nanoparticles for plasmon-enhanced solar desalination. *Nature Photon* 10: 393.

113 Yang, P. et al. (2017). Solar-driven simultaneous steam production and electricity generation from salinity. *Energy Environ. Sci.* 10 (9): 1923–1927.

114 Neumann, O. et al. (2013). Compact solar autoclave based on steam generation using broadband light-harvesting nanoparticles. *Proc. Natl. Acad. Sci.* 110 (29): 11677–11681.

115 Izumi, Y. (2013). Recent advances in the photocatalytic conversion of carbon dioxide to fuels with water and/or hydrogen using solar energy and beyond. *Coord. Chem. Rev.* 257 (1): 171–186.

116 Kaushal, A. (2010). Solar stills: a review. *Renewable Sustainable Energy Rev.* 14 (1): 446–453.

117 Kabeel, A. and El-Agouz, S. (2011). Review of researches and developments on solar stills. *Desalination* 276 (1-3): 1–12.

118 Jiang, F. et al. (2018). Lightweight, mesoporous, and highly absorptive all-nanofiber aerogel for efficient solar steam generation. *ACS Appl. Mater. Interfaces* 10 (1): 1104–1112.

119 Zhu, M. et al. (2017). Tree-inspired design for high-efficiency water extraction. *Adv. Mater.* 29 (44): 1704107.

120 Chen, C. et al. (2017). Highly flexible and efficient solar steam generation device. *Adv. Mater.* 29 (30): 1701756.

121 Li, T. et al. (2018). Scalable and highly efficient mesoporous wood-based solar steam generation device: localized heat, rapid water transport. *Adv. Funct. Mater.* 28 (16): 1707134.

122 Xue, G. et al. (2017). Robust and low-cost flame-treated wood for high-performance solar steam generation. *ACS Appl. Mater. Interfaces* 9 (17): 15052–15057.

123 Liu, H. et al. (2018). High-performance solar steam device with layered channels: artificial tree with a reversed design. *Adv. Energy Mater.* 8 (8): 1701616.

124 Wang, Y., Liu, H., Chen, C. et al. (2019). All natural, high efficient groundwater extraction via solar steam/vapor generation. *Adv. Sustain. Syst.* 3 (1): 1800055.

125 Li, Xiuqiang, Weichao, Xu, Mingyao, Tang. et al. (2016). Graphene oxide-based efficient and scalable solar desalination under one sun with a confined 2D water path. *Proc. Natl. Acad. Sci.* 113 (49): 13953–13958.

126 Awad, F.S. et al. (2018). Plasmonic graphene polyurethane nanocomposites for efficient solar water desalination. *ACS Appl. Energy Mater.* 1 (3): 976–985.

127 Villamizar, M., Ruiz, A., Aschner, P. et al. (2005). Segundo consenso nacional sobre detección, evaluación y tratamiento de las dislipoproteinemias en adultos. *Rev. Colomb. Cardiol.* 11 (2): 407–409.

128 Hu, X., Weichao, Xu, Zhou. L. et al. (2017). Tailoring graphene oxide-based aerogels for efficient solar steam generation under one sun. *Adv. Mater.* 29 (5): 1604031.

129 Liu, Y. et al. (2015). A bioinspired, reusable, paper-based system for high-performance large-scale evaporation. *Adv. Mater.* 27 (17): 2768–2774.

130 Yin, Z. et al. (2017). Extremely black vertically aligned carbon nanotube arrays for solar steam generation. *ACS Appl. Mater. Interfaces* 9 (34): 28596–28603.

131 Wu, X. et al. (2019). A flexible photothermal cotton-CuS nanocage-agarose aerogel towards portable solar steam generation. *Nano Energy* 56: 708–715.

132 Mu, P. et al. (2019). Superwetting monolithic hollow-carbon-nanotubes aerogels with hierarchically nanoporous structure for efficient solar steam generation. *Adv. Energy Mater.* 9 (1): 1802158.

133 Kudo, S. et al. (2017). Production of levoglucosenone and dihydrolevoglucosenone by catalytic reforming of volatiles from cellulose pyrolysis using supported ionic liquid phase. *ACS Sustainable Chem. Eng.* 5 (1): 1132–1140.

134 Iamprasertkun, P., Krittayavathananon, A., and Sawangphruk, M. (2016). N-doped reduced graphene oxide aerogel coated on carboxyl-modified carbon fiber paper for high-performance ionic-liquid supercapacitors. *Carbon* 102: 455–461.

135 McEnaney, Kenneth, Lee Weinstein, L. et al. (2017). Aerogel-based solar thermal receivers. *Nano Energy* 40: 180–186.

136 Voiry, D. et al. (2013). Goki Eda, and Manish Chhowalla. *Nano Lett.* 13: 6222.

137 Liu, C. et al. (2019). Adsorption of heavy metals on molybdenum disulfide in water: a critical review. *J. Mol. Liq.* 292: 111390.

138 Wang, Q. et al. (2018). Removal of Cd (II) from water by using nano-scale molybdenum disulphide sheets as adsorbents. *J. Mol. Liq.* 263: 526–533.

139 Guo, Z. et al. (2018). PEGylated self-growth MoS_2 on a cotton cloth substrate for high-efficiency solar energy utilization. *ACS Appl. Mater. Interfaces* 10 (29): 24583–24589.

140 Wang, Q. et al. (2020). MoS_2@ sponge with double layer structure for high-efficiency solar desalination. *Desalination* 481: 114359.

141 Xu, D. et al. (2020). Insights into the photothermal conversion of 2D MXene nanomaterials: synthesis, mechanism, and applications. *Adv. Funct. Mater.* 30.47, 2000712.

142 Wang, Q. et al. (2020). Facile preparation of three-dimensional MoS_2 aerogels for highly efficient solar desalination. *ACS Appl. Mater. Interfaces* 12 (29): 32673–32680.

143 Takeshita, S. and Yoda, S. (2015). Chitosan aerogels: transparent, flexible thermal insulators. *Chem. Mater.* 27 (22): 7569–7572.

144 Meraz, K.A.S. et al. (2016). Eco-friendly innovation for nejayote coagulation–flocculation process using chitosan: evaluation through zeta potential measurements. *Chem. Eng. J.* 284: 536–542.

145 Storer, D.P. et al. (2020). Graphene and rice-straw-fiber-based 3d photothermal aerogels for highly efficient solar evaporation. *ACS Appl. Mater. Interfaces* 12 (13): 15279–15287.

146 Mu, P. et al. (2019). Conductive hollow kapok fiber-PPy monolithic aerogels with excellent mechanical robustness for efficient solar steam generation. *J. Mater. Chem. A* 7 (16): 9673–9679.

147 Zhang, P. et al. (2018). High throughput of clean water excluding ions, organic media, and bacteria from defect-abundant graphene aerogel under sunlight. *Nano Energy* 46: 415–422.

148 Petrie, B., Barden, R., and Kasprzyk-Hordern, B. (2015). A review on emerging contaminants in wastewaters and the environment: current knowledge, understudied areas and recommendations for future monitoring. *Water Res.* 72: 3–27.

149 Lajeunesse, A., Blais, M., Barbeau, B., et al. (2013). Ozone oxidation of antidepressants in wastewater–treatment evaluation and characterization of new by-products by LC-QToFMS. *Chem. Cent. J.* 7 (1): 15.

150 Amoyaw, P.A., Williams, M., and Bu, X.R. (2009). The fast removal of low concentration of cadmium (II) from aqueous media by chelating polymers with salicylaldehyde units. *J. Hazard. Mater.* 170 (1): 22–26.

151 Wang, S., Ning, H., Hu, N. et al. (2019). Preparation and characterization of graphene oxide/silk fibroin hybrid aerogel for dye and heavy metal adsorption. *Compos. Part B* 163: 716–722.

152 Hiew, B.Y.Z., Lee, L.Y. et al. (2018). Review on synthesis of 3D graphene-based configurations and their adsorption performance for hazardous water pollutants. *Process Saf. Environ. Prot.* 116: 262–286.

153 Liu, L. et al. (2019). Application of nanotechnology in the removal of heavy metal from water. In: *Nanomaterials for the Removal of Pollutants and Resource Reutilization*, 83–147.

154 Ye, S., Jin, W., Huang, Q. et al. (2017). Da-KGM based GO-reinforced FMBO-loaded aerogels for efficient arsenic removal in aqueous solution. *Int. J. Biol. Macromol.* 94: 527–534.

155 Zhitkovich, A. (2011). Chromium in drinking water: sources, metabolism, and cancer risks. *Chem. Res. Toxicol.* 24 (10): 1617–1629.

156 Wang, J. and Chen, C. (2009). Biosorbents for heavy metals removal and their future. *Biotechnol. Adv.* 27 (2): 195–226.

157 Lim, Jihn Yih, Mubarak, N.M. et al. (2018). Recent trends in the synthesis of graphene and graphene oxide based nanomaterials for removal of heavy metals—a review. *J. Ind. Eng. Chem.* 66: 29–44.

158 Netpae, T. and Phalaraksh, C. (2009). Water quality and heavy metal monitoring in water, sediments, and tissues of corbicula sp. from bung Boraphet reservoir, Thailand. *Chiang Mai J. Sci.* 36 (3): 395–402.

159 Namasivayam, C. and Senthilkumar, S. (1998). Removal of arsenic (V) from aqueous solution using industrial solid waste: adsorption rates and equilibrium studies. *Ind. Eng. Chem. Res.* 37 (12): 4816–4822.

160 Namasivayam, C. and Ranganathan, K. (1995). Removal of Pb (II), Cd (II), Ni (II) and mixture of metal ions by adsorption onto 'waste' Fe (III)/Cr (III) hydroxide and fixed bed studies. *Environ. Technol.* 16 (9): 851–860.

161 Hartiger, L. (1991). *hand buch der Abwasser—und Recycling techniques Munchen*. Wien: Carl Hanser Verlag.

162 Li, N., Zhang, Q., Gao, S. et al. (2013). Three-dimensional graphene foam as a biocompatible and conductive scaffold for neural stem cells. *Sci. Rep.* 3 (1): 1–6.

163 Meena, A.K., Mishra, G.K., Rai, P.K. et al. (2005). Removal of heavy metal ions from aqueous solutions using carbon aerogel as an adsorbent. *J. Hazard. Mater.* 122 (1–2): 161–170.

164 Leyden, D.E. and Luttrell, G.H. (1975). Preconcentration of trace metals using chelating groups immobilized via silylation. *Anal. Chem.* 47 (9): 1612–1617.

165 Khatib, I. and Parish, R. (1989). Insoluble ligands and their applications: I. A comparison of silica-immobilized ligands and functionalized polysiloxanes. *J. Organomet. Chem.* 369 (1): 9–16.

166 Parish, R., Habibi, D., and Mohammadi, V. (1989). Insoluble ligands and their applications: II. Polysiloxane-phosphine ligands, their complexes, and hydrogenation catalysts. *J. Organomet. Chem.* 369 (1): 17–28.

167 Walcarius, A. et al. (1999). Electrochemical evaluation of polysiloxane-immobilized amine ligands for the accumulation of copper (II) species. *Electrochim. Acta* 44 (25): 4601–4610.

168 Soliman, E.M. (1997). Synthesis and metal collecting properties of mono, di, tri and tetramine based on silica gel matrix. *Anal. Lett.* 30 (9): 1739–1751.

169 Sehaqui, H. et al. (2014). Enhancing adsorption of heavy metal ions onto biobased nanofibers from waste pulp residues for application in wastewater treatment. *Cellulose* 21 (4): 2831–2844.

170 Yan, M., Huang, W., and Li, Z. (2019). Chitosan cross-linked graphene oxide/lignosulfonate composite aerogel for enhanced adsorption of methylene blue in water. *Int. J. Biol. Macromol.* 136: 927–935.

171 Jiang, L., Wang, Q., Zhou, M. et al. (2020). Role of adsorption and oxidation in porous carbon aerogel/persulfate system for non-radical degradation of organic contaminant. *Chemosphere* 241: 125066.

172 Abramian, L. and El-Rassy, H. (2009). Adsorption kinetics and thermodynamics of azo-dye Orange II onto highly porous titania aerogel. *Chem. Eng. J.* 150 (2–3): 403–410.

173 Goel, J., Kadirvelu, K., Rajagopal, C. et al. (2005). Removal of lead (II) from aqueous solution by adsorption on carbon aerogel using a response surface methodological approach. *Ind. Eng. Chem. Res.* 44 (7): 1987–1994.

174 Da, H.-J., Yang, C.-X., and Yan, X.-P. (2019). Cationic covalent organic nanosheets for rapid and selective capture of perrhenate: an analogue of radioactive pertechnetate from aqueous solution. *Environ. Sci. Technol.* 53 (9): 5212–5220.

175 Purwajanti, S., Yang, J., Huang, X. et al. (2016). Rational design of functional nanoporous materials to confine water pollutant in controlled nano-space. In: *Rational Design of Next-Generation Nanomaterials and Nanodevices for Water Applications*, 37.

176 Kumar, R., Singh, R.K., Kumar, V. et al. (2019). Functionalized nanosize graphene and its derivatives for removal of contaminations and water treatment. In: *A New Generation Material Graphene: Applications in Water Technology*, 133–185.

177 Li, J., Li, J., Meng, H. et al. (2014). Ultra-light, compressible and fire-resistant graphene aerogel as a highly efficient and recyclable absorbent for organic liquids. *J. Mater. Chem. A* 2 (9): 2934–2941.

10

Organic and Carbon Aerogels

Marina Schwan and Barbara Milow

German Aerospace Center, Linder Hoehe, 51147, Cologne, Germany

10.1 Introduction

Aerogels are open-porous solid materials in which the pores are filled with air [1]. Samuel Stephens Kistler succeeded in producing the first aerogels without destroying the filigree gel structure during drying in the 1930s [2–4]. Kistler dried the gels at elevated temperature and pressure in an autoclave instead of drying them by evaporation. In his work, Kistler describes the production of silica-based aerogels, but also of a large number of other aerogels – for example aluminum oxide, tungsten oxide, iron oxide, tin oxide, cellulose, gelatine, and agar aerogels. The first production of synthetic organic aerogels was developed and reported by Richard W. Pekala in 1989 with the synthesis of highly porous resorcinol-formaldehyde (RF) aerogels [5]. The polymerization mechanism and the influence of the reactant concentration on the reaction rate as well as on the properties of the aerogels were investigated by his group. The RF aerogels had densities below $0.1\,g\,cm^{-3}$ and a dark red color. Besides of RF aerogels, the spectrum of organic aerogels is continuously expanded (Figure 10.1): phenol-formaldehyde [6], melamine-formaldehyde [7], cresol-formaldehyde [8], phenol-furfural [9], polyimide [10], and polyurethane aerogels [11] were developed. Due to the outstanding properties of this material (a high porosity of up to 98%, a high specific surface area of up to $1500\,m^2\,g^{-1}$, a low thermal conductivity of $0.012\,W\,m^{-1}\,K^{-1}$ [12–14], and a low density in the range of $0.05–0.30\,g\,cm^{-3}$ [5, 12, 13], organic aerogel research started rapidly growing since the 1990ies. According to ScienceDirect, new types of aerogels, synthetic routes, aerogel composites as well as new characterization methods and areas of applications are described in around 21 680 publications (October 2020).

The properties of organic aerogels determine their areas of application. They are excellent insulating materials, which are nonflammable and nontoxic. Most of the organic aerogels are used as a precursor for the production of carbon aerogels. Carbon aerogels are highly conductive materials with large porosities and surface areas. The unique properties and the related applications in the field of energy saving and storage technologies led to a rising interest within the last decades.

Aerogels for Energy Saving and Storage, First Edition. Edited by Meldin Mathew, Hanna J. Maria, Ange Nzihou, and Sabu Thomas.
© 2024 John Wiley & Sons, Inc. Published 2024 by John Wiley & Sons, Inc.

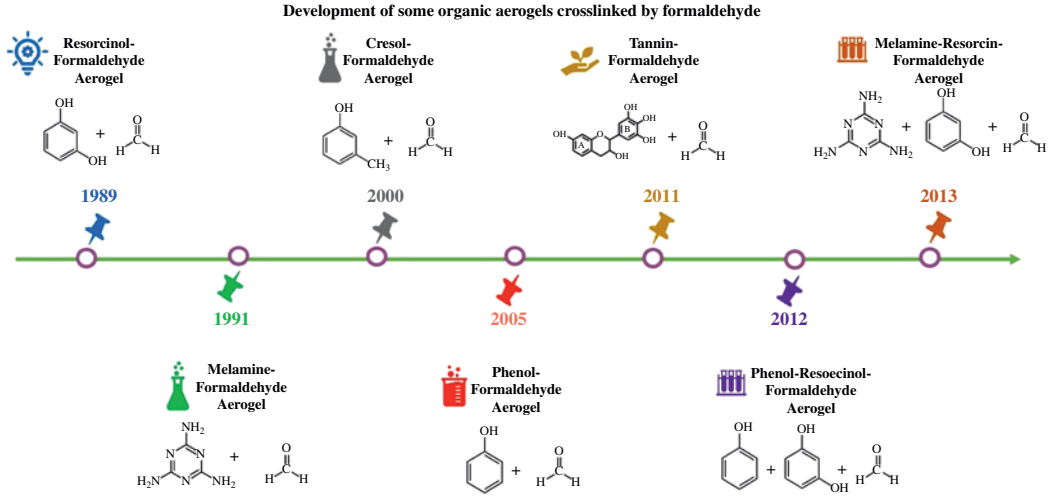


Figure 10.1 Discovery of organic aerogels based on phenols-formaldehyde chemistry.

10.2 Overview on Organic Aerogels

The synthesis of organic aerogels based on phenols crosslinked by formaldehyde is reported in a large number of publications. Generally, the synthesis in aqueous solution contains two main steps: addition and condensation reactions. The pH value amounts and ratio of educts, choice of catalyst, and other synthesis parameters influence the structure of organic aerogels and the corresponding carbon aerogels. Moreover, processing conditions such as aging, solvent exchange, and drying method play a crucial role.

10.2.1 Synthesis and Properties of Resorcinol-Formaldehyde Aerogels

Resorcinol-formaldehyde polymers are thermosets and belong to the class of phenolic resins. The basics of RF aerogel manufacturing were developed by Pekala at the Lawrence Livermore National Laboratory in Livermore, USA, in the 1980s. Within this chapter the three main routines of synthesis depending on the used catalytic conditions belonging to different pH values are described. The process conditions during the sol-gel reaction lead to a certain three-dimensional open porous network structure, which is further influenced during aging and drying.

10.2.1.1 Synthesis of Resorcinol-Formaldehyde Aerogels

The typical reaction mechanism of the RF synthesis is based on the phenolic resin chemistry [15, 16]. For understanding the mechanisms, the tautomerism of the educts play a major role. The benzene ring of the resorcinol molecule has two hydroxyl groups that are placed in *meta*-position (Figure 10.2). The oxygen provides free electron pairs for the mesomerism and thus adds increased electron density to the aromatic ring due to the mesomeric (+M)-effect. The increased electron density at the *ortho*- and *para*-positions increases the reactivity of the molecule toward electrophilic aromatic substitution.

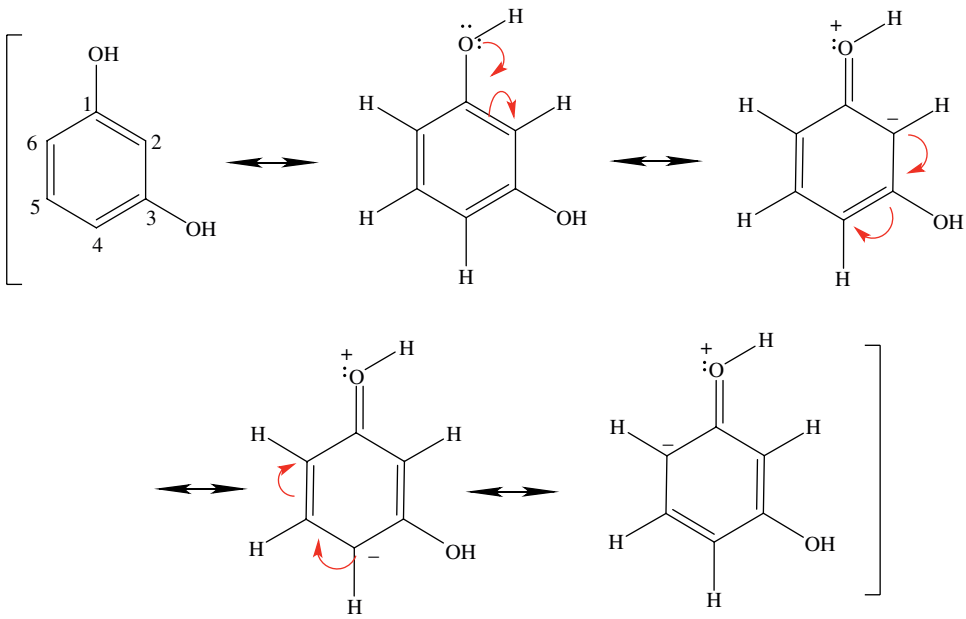


Figure 10.2 Mesomere structures of resorcinol molecule [17].

Because of the steric hindrance at position 2 due to the OH-groups, the reactivity at this location is reduced. In contrast, the *meta*-position (position 5) is not reactive under normal reaction conditions and does not take part in the reaction [18]. Formaldehyde itself can undergo the electrophilic aromatic substitution of resorcinol (at its positions 4 and 6) and its polarized carbonyl group. This reaction can take place at room temperature without any catalyst. However, investigations on the reaction kinetics show that the reaction rate strongly depends on the pH value. The minimum reaction rate is observed in the pH range of 3–4, it increases and reaches maxima at a pH values of 1 and between 6 and 7. Thus, the gelation time can be adjusted by varying the pH value either leading to oxonium ions, increasing the electrophilicity of the formaldehyde, or with hydroxide ions [19].

In a basic environment, deprotonation leads to the formation of resorcinol ions, which are more reactive than uncharged resorcinol due to a stronger (+M)-effect. This is followed by the reaction of the activated benzene ring with the electrophilic molecule formaldehyde to form hydroxymethylresorcinol. Moreover, the reaction rate of the hydroxymethylation can be accelerated by improving the kinetics using a catalyst.[1] In this reaction, carbonates (K_2CO_3, Na_2CO_3, $BaCO_3$, or Li_2CO_3) are usually used as the basic catalysts [20]. In this context the temperature-dependent reaction rate constant k increases with increasing valence of the carbonate cation and its diameter [21], e.g.

$$k_{Li^+} < k_{Na^+} < k_{Ba^{2+}}$$

Under these conditions the hydroxymethylresorcinol reacts with excess formaldehyde to form dihydroxymethylresorcinol, and in the next step, the hydroxymethylresorcinol molecules and their derivatives are linked to one another via methylene or dimethylene ether bridges. That means that both methylene and dimethylene ether bridges are built under basic catalyzed conditions. Such molecular structures are called resols. The term *resol* originates in the phenolic resin chemistry and was adopted to denote aerogel structures. Accordingly, *ortho-ortho* (*o-o*), *ortho-para* (*o-p*), or *para-para* (*p-p*) bridges can be formed between the resorcinol molecules (monomers). In contrast, studies on phenolic resins show that *para*-positions are more reactive than *ortho*-positions, and therefore the formation of *para-para* methylene bridges is preferred [22]. Within further reaction steps, nanometer-sized clusters are formed from dimers, trimers, and oligomers, and the so-called sol particles emerge, which poly-condense to form the typical network.

In 2001, acid-catalyzed synthesis of RF aerogels was explored by Berthon et al. [23] and Barbieri et al. [24]. Both groups used perchloric acid as an acid catalyst. The sol-gel process was carried out in acetone instead of water. The advantage of acid catalysis consists in the higher speed of the reaction. The sol-gel process is fast enough to be carried out at room temperature. Protons favor condensation, and monomers are quickly linked to build a network by causing the elimination of water. Brandt and Fricke studied the synthesis in aqueous medium [25]. The formaldehyde molecules are predominantly present in its hydrated form as methylene glycol and thus, the protonation of formaldehyde under the acidic conditions is supported, which increases its electrophilicity, as shown in Figure 10.3.

In the next step, the protonation of the hydroxy group takes place. An *ortho*-quinone methide is formed as an intermediate product, which further reacts with resorcinol due to its poor stability. In this reaction, the molecules are linked together, building methylene bridges.

1 The term catalyst has been introduced by Pekala and still is used in synthesis descriptions. Although, it is not entirely correct, as the salts used are consumed during reaction.

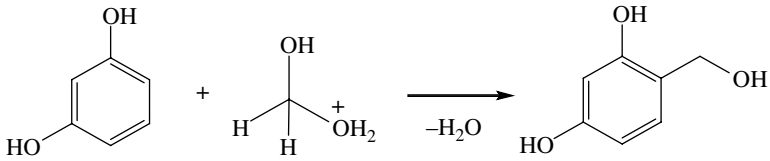


Figure 10.3 Condensation reaction of resorcinol and the protonated methylene glycol [17].

The received RF structures with methylene linkages only are called novolac. Like resol the reaction product obtained under alkaline conditions, the term *novolac* was adopted from phenolic resin chemistry, too. Acid catalysis can take place in aqueous as well as nonaqueous media (e.g. acetonitrile [26]). Hydrochloric acid, citric acid, acetic acid, formic acid, or perchloric acid, among others, are used as catalysts [24, 26–28].

In basic-acid catalysis, both main reactions (i.e. the addition and the condensation reaction) are specifically accelerated. The investigations on resorcinol–formaldehyde aerogels from a base–acid catalyzed synthesis route are discussed in detail by Laskowski et al. [29]. After the base-accelerated hydroxymethylation, hydroxy groups are split off in an acidic environment forced by H^+-ions. The quinone methide is formed and finally reacts with (di)-hydroxymethylresorcinol to build the oligomers and continuously combine to form a network. It is obviously that the point of time adding as well as the concentration of the acid catalyst influence the final structure. If the acid is added early, a high number of monomers is activated and results in the formation of big particles, 2–5 µm in size. Conversely, a later addition of acid (approx. after 3 hours) leads to the formation of much smaller nanometer-sized particles. In addition, the degree of dilution influences the number of bonds between the particles.

10.2.1.2 Gelation, Aging, and Drying of Resorcinol-Formaldehyde Aerogels

During the polymerization process, individual monomers start to form dimers and oligomers and within the degree of polymerization a three-dimensional network is built. In the beginning, nuclei in the solution are formed; they grow to a certain size, and under Brownian motion hit each other and form a three-dimensional network. This process is called *gelation*. A gel is a three dimensionally stable porous material with compact matter and a capillary space – pores filled with the solvent. During gelation a continuous increase of the viscosity can be observed. At the gelation point the viscosity reaches its maximum. The gel body is formed. At this point some monomers, dimers, and oligomers are still presented in the pore fluid, also unreacted educts can be found. Further reactions take place in the pore fluid, but also on the particles' surface, which are already connected to the network.

These reactions strengthen the network and belong to the final step of the sol-gel process called *aging*. The aging of the RF aerogels usually takes place at higher temperatures (e.g. 60–80 °C) in order to accelerate the reaction kinetics. Lambert et al. [30] studied the effect of aging on the degree of crosslinking in RF aerogels. The gels aged less than 20 hours showed swelling during preparation for drying (solvent exchange, see below). Two types of crosslinking during aging were suggested in the literature: intraparticle crosslinking within the nanometer-sized particles and interparticle crosslinking within the gel matrix. Insufficient aged gels swelled in isopropanol due to the weak intraparticle crosslinking. Aging can also be carried out in an aqueous solution. The strengthening was found to be more pronounced under acidic conditions than in water. The improvement is related to accelerated polycondensation reaction rate [31].

After the gel body has aged for several days, it can be dried. Several drying techniques are used for aerogels.

Due to the interfacial tension between the liquid and gas phase, menisci will be formed in the pores during drying. The capillary forces in the pores are inversely proportional to the pore radius and thus increase as the pore diameter decreases. Since a gel network consists of pores of different sizes, stress gradients are formed, which act on the pore walls and can lead to cracking. For this reason, large pores, networks with increased strength, and structures with the narrowest possible pore size distribution are advantageous to prevent crack formation. A further possibility to reduce the capillary forces is lowering the surface tension of the pore liquid. For this reason, the solvent, water from the synthesis with a surface tension of about $71.99\,mN\,m^{-1}$, is usually replaced by acetone ($23.46\,mN\,m^{-1}$), methanol ($22.07\,mN\,m^{-1}$), or ethanol ($21.97\,mN\,m^{-1}$) [32].

Another way to avoid the capillary forces is the supercritical drying proposed by Kistler [3, 4]. By use of supercritical carbon dioxide the interfacial tensions are not arose and the aerogels' structure is protected. Prior supercritical drying the pore liquid will be exchanged for a nonpolar solvent such as acetone, which is solvable in supercritical CO_2. This process is called solvent exchange, and it serves to remove water and unreacted monomers from the pores of the gel and to prepare it for the drying process. During solvent exchange, the wet gels are placed in a proper solvent bath. The solvent is refreshed several times until water is completely exchanged. In a high-pressure vessel, an autoclave, the pore liquid (mostly acetone, ethanol, methanol, or isopropanol) in the gels is dissolved in carbon dioxide, which is in a supercritical state. The pore fluid is then extracted and at least replaced with supercritical CO_2 ($scCO_2$). The solvent is continuously removed in a separator with lower pressure. The extraction process ends as soon as the solvent has been completely removed and replaced by $scCO_2$ in the pores. The pressure in the autoclave is then slowly reduced, and the supercritical carbon dioxide changes its aggregation state into the gas phase and relieved. In the process of supercritical drying, the occurrence of phase boundaries is excluded, if the solvent is mixable with $scCO_2$. As a result, the deformation or shrinkage after supercritical drying is minimized or even avoided entirely.

Nevertheless, there are processes in which RF aerogels can be produced without shrinkage drying under ambient pressure, so called *subcritical drying*. Fischer et al. [33] described a manufacturing method in which the capillary forces were avoided by designing large pore network structures in the micrometer range and by increasing the density (up to $0.3\,g\,cm^{-3}$). A high resorcinol content and a reduced amount of catalyst lead to the formation of those micrometer-sized particles and pores. Drying at ambient pressure is carried out in drying cabinets at 25–90 °C. From the perspective of the IUPAC definition, such materials can be called aerogels as long as they do not shrink during drying.

Furthermore, *freeze drying* can be used [34]. The liquid-gaseous phase boundary is avoided due to sublimation of the solvent (mostly water in the case of RF aerogels) under reduced pressure. Gels that are freeze-dried are called cryogels. Compared to the other drying methods RF cryogels show the lowest shrinkage and have a high specific surface area. Due to the expansion of the water during freezing, the structure of the aerogel can be changed during freeze drying. In addition, when the water freezes, dendrites are created and anisotropic structures are created. The size of the dendrites depends on the cooling rate – the slower, the coarser. In general, dendrites are coarse, so that mostly macroporous structures arise and mesostructures and microstructures are destroyed. Despite the low shrinkage, freeze drying is rarely used for RF aerogels due to fracture of microstructure during drying [35]. Subcritically dried aerogels, on the other hand, shrink very strongly, so that their surface area is reduced by almost 90%. Aerogels that are dried in the autoclave show only slight shrinkage [34]. When choosing the drying method, knowledge about the

microstructure is crucial. The subcritical drying is suitable for stable structures (low catalyst and water content, high solid amount). Filigree structures, which are synthesized with a high catalyst content and low solid content, require gentle drying (supercritical).

10.2.1.3 Influence of the Final Structure through Different Synthesis Parameters

The relationship between the properties of RF aerogels and the synthesis parameters is widely discussed in the aerogel community. As shown in Figure 10.4, the final physical properties of the materials depend strongly on the microstructure, which in turn is related to the manufacturing process.

The pH value strongly influences the final morphology of the aerogel: in general, an increase in the pH value causes an increase in the specific surface area [36, 37]. The structural changes depending on the pH value have been intensively reviewed by Job et al. [38]. The additional reaction supported in a basic environment leads to the formation of many monomers, so many small clusters are formed which later coagulate to form a network. Because of this, this network consists of small particles and small pores. In an acidic environment, on the other hand, polycondensation is favored, which leads to rapid growth of the primary particles formed and to larger clusters. The special characteristic of such a network is that it has large particles and large pores. In addition, the condensation prevented in the basic environment causes the formation of a weakly connected network. The drying of such gels at ambient pressure leads to the collapse and shrinkage of the gel structure and results in dense aerogels [39]. The pH value also has an influence on the gelation time. According to the literature, the maximum speed is at pH <4 [40]. Furthermore, a change in the color of the aerogels can be observed: At pH <6, RF aerogels are yellow-brown and at higher pH values are dark red, which is due to the amount of unreacted *o*-quinone methide, which has a red color; the deeper the red color, the higher the *o*-quinone methide content [41].

Pekala et al. have investigated the effect of the amount of catalyst on the microstructure of aerogels in basic catalysis [5, 42, 43]. The catalyst content is usually expressed by the molar ratio of resorcinol (R) to catalyst (C) or R/C. With increasing catalyst content (e.g. sodium carbonate), small R/C, the specific surface was increased. The reason for this is the change in pH with increasing catalyst content. As already described, high pH values cause the formation of a fine structure

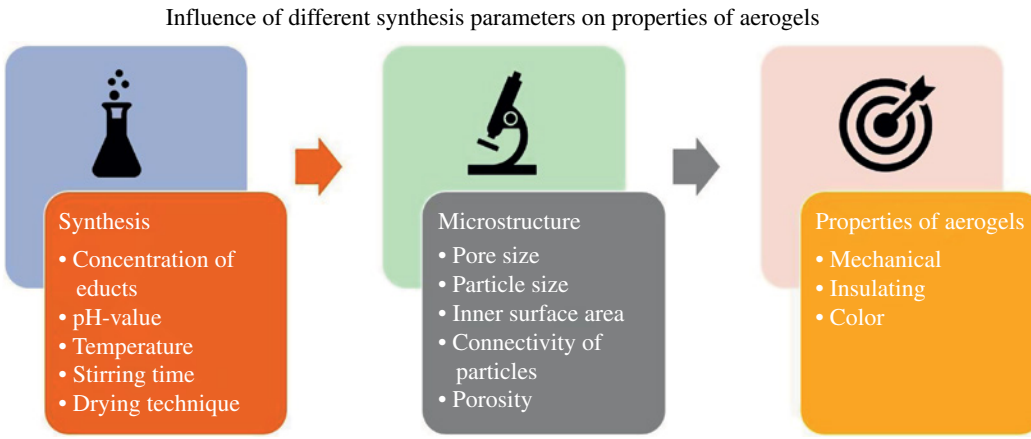


Figure 10.4 The final properties of aerogels are dictated by synthesis parameters. The molar ratios of educts, pH value and other factors are reflected in the structure and properties of aerogels.

with micro (<2 nm) and mesopores (2–50 nm) and small particles, which in turn increases the specific surface. The connectivity of the particles is also influenced by the catalyst content [42, 44]. Low R/C ratio leads to the formation of nanometer-sized particles that are connected to one another by wide necks. In contrast, with a higher R/C ratio, small particles up to 200 nm are connected by narrow necks like pearls on a chain. Such structures are called "polymeric" and "colloidal." Wide necks between the particles ensure an increase in the aerogel density and improved mechanical properties. Colloidal RF aerogels have a three times lower compression modulus, which reflects the influence of the smaller contact area between particles on the mechanical properties. In addition, the gelation time was investigated as a function of the R/C ratio. A rapid formation of a large number of polymers, which is present with a high catalyst content, increases the viscosity and, as a result, shortens the gel formation time [45].

The resorcinol-to-water ratio (R/W) also influences the properties of the RF aerogels. A high resorcinol content leads to a higher thermal conductivity over the solid phase [14], a higher density and a higher modulus of elasticity. At the same time, the specific surface and the pore volume are reduced [36, 46, 47]. In addition, the R/W ratio has an influence on the particle size at high catalyst concentrations. In dilute solutions there are a few molecules that can form nuclei for particle growth. Leading to small particles. The higher the monomer concentration, the larger are the particles, which can be formed [48]. The combination of low R/C (e.g. 50) and very low R/W (e.g. 0.008) molar ratios lead to the formation of gels with small particles and large pores. Such RF aerogel – flexible aerogels – can be deformed to a certain degree and spring back to its initial size [49]. Their flexibility is based on the structural properties, where thin pore walls (marked in red in Figure 10.5) can be deformed without touching neighbor walls. Thus, they do not fracture under uniaxial load, their deformation is reversible. The increase of resorcinol amount by constant catalyst ratio causes growth of particles, inducing a drastic reduction in the flexibility of the network. At $R/W > 0.01$ the network becomes stiff.

The formaldehyde concentration also influences the structure and properties of RF aerogels. The aerogels with R/F molar ratio of 0.4 exhibit higher stiffness compared to aerogels with $R/F = 0.5–0.6$. It was suggested that the degree of crosslinking of network is enhanced at low R/F ratios. At $R/F = 0.6$, resol structures are created that are weakly networked, due to less amount of formaldehyde. When $R/F = 0.5$, i.e. a higher formaldehyde concentration, the degree of crosslinking

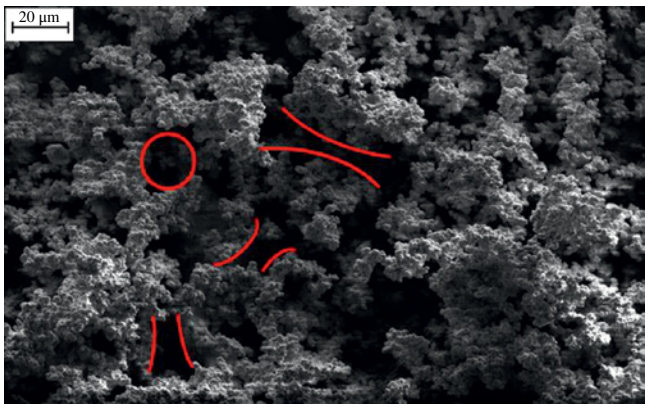


Figure 10.5 SEM image of a network of flexible resorcinol-formaldehyde aerogel. Large pores of about 10–20 µm (in red) provide empty room for reversible deformation of pore walls [17].

increases and the polymer chains become stiffer. R/F = 0.4 leads to the formation of resol structures with a reduced degree of freedom of the carbon atoms. The high formaldehyde content stiffens the polymer chains and the network [17].

10.2.2 Synthesis and Properties of Melamine-based Aerogels

Synthesis and properties of melamine-based aerogels are discussed in this chapter. The synthesis of these aerogels is similar to the synthesis of RF-based aerogels. Moreover, the synthesis parameters such pH-value, concentrations of educts, and the solvent influence crucial the properties of aerogels.

10.2.2.1 Melamine-Formaldehyde Aerogels

The first melamine containing aerogels were reported by Pekala and Alviso [7, 50]. Melamine (M) is mainly used to incorporate nitrogen into RF gels by substituting resorcinol. It is a hexafunctional monomer, where each of amine hydrogens is capable of reactions with formaldehyde. Since, melamine is a crystalline solid with lower water solubility than resorcinol, the solution shall be heated to about 60–75 °C or at room temperature for a prolonged period of time. The formaldehyde can react with melamine under alkaline conditions and form hydroxymethyl groups. In principle, melamine and formaldehyde undergo a reaction similar to resorcinol and formaldehyde. After formation of hydroxymethyl groups, the solution shall be acidified to promote the next step – the condensation. The crosslinking reactions of methylomelamines include the formation of diamino methylene (-NH-CH_2-NH-) or diamino methylene ether (-NH-CH_2-O-CH_2-NH-) bridges between melamine molecules. At low pH (7–8) diamino methylene bridges are favored, while at pH ≥ 9 ether bridges are predominant [51]. The preferable molar ratio of melamine and formaldehyde is about 1 : 3; an excess of formaldehyde would maximize the crosslinking of methylomelamines.

Among other organic aerogels melamine-formaldehyde aerogels have a colorless or translucent appearance, unlike other organic aerogels such as dark red RF aerogels [52], white cellulose [53], or chitosan-based [54] aerogels. The pioneer study of optical and structural properties of melamine–formaldehyde aerogels has been done from Canadian researchers Nguyen and Dao [55]. Different melamine–formaldehyde aerogels were prepared with the concentrations of 10 wt.% and 12 wt.% of poly (melamine-co-formaldehyde) in an aqueous solution. The pH was adjusted to 2.3, 2.0, 1.8, and 1.5. The gels were dried supercritical, unlike samples of R. Pekala. The concentration of precursor solution strongly influenced the optical and structural properties of organic MF aerogels. The best transmittance was obtained at pH = 1.8 for the 12 wt.% and at pH = 2.2 for the 10 wt.% concentration. The average particle radius was calculated with a new approach. It was obtained from the fit of the turbidity spectrum with the following equation:

$$\frac{\tau}{\varphi_s} = 32\frac{\pi^4}{\lambda^4}\left(\frac{n^2-1}{n^2+2}\right)^2 \frac{\int_0^\infty a^6 p(a)\,\mathrm{d}a}{\int_0^\infty a^3 p(a)\,\mathrm{d}a}; \tag{10.1}$$

where τ is turbidity, φ_s porosity, λ the wavelength in the medium, a the correlation length, and $p(a)\,\mathrm{d}a$ is the number fraction of particles with a radius between a and $a + \mathrm{d}a$. The pH was found to affect the particle radius for both concentrations. However, this effect is more pronounced for higher concentration of MF precursors (12 wt.%).

Melamine-formaldehyde aerogels synthesized in aqueous solutions exhibit surface area of about 1016 $m^2\,g^{-1}$ with pores in the region of 5–30 nm [56]. In contrast to MF aerogels prepared in water,

MF aerogels synthesized with dimethyl sulfoxide as a solvent showed very low density of about 0.07 g cm^{-3} and better thermal stability [57].

A drawback of MF aerogels is very slow polymerization and the cross-linkage rate of melamine and formaldehyde. Moreover, their gelation process would not occur under low precursor concentration conditions [58]. At the gelation temperature about 95 °C, whereas the precursor concentration was in the range of 6–10 wt.%, the gelation took about one to seven days to form the gel [7]. The implementation of an additional step in the synthesis with the acceleration of polymerization progress was found to be very successful. Ren et al. [59] optimized the synthesis route by adding of alkali (NaOH) in MF system, which speeds up the cross-linking of oligomers. This improvement leads to the reduction of gelation time and the gelation under lower concentration condition (4–6 wt.%). The density of rapidly synthesized MF aerogels was found to be very similar to previously reported (0.06–0.07 g cm^{-3}). The FTIR spectra of these aerogels showed no significant difference from "slow" and "rapid" methods, which indicated that the addition of the alkali to the MF system only speed up the gelation progress and did not change the reaction mechanism. The gelation time for MF wet gels was reduced to five hours, and the precursor concentration of the MF gel was adjusted to 4%.

Recently, a novel synthetic approach to synthesize pure, transparent MF aerogels in a nonaqueous sol-gel process was developed [60]. To achieve high transparency, Nakanishi et al. used an aprotic solvent with higher affinity to the MF precursor and polymers. This approach leads to suppression of macroscopic phase separation and, thus to transparent MF aerogels. The authors pointed out the importance of the nonaqueous solvent (dimethyl sulfoxide and trifluoroacetic acid) for successful production of transparent MF aerogels. The decrease in transparency is caused by a decrease in compatibility between water-based solvent and organic skeleton. Reported MF aerogels exhibited high mechanical strength, low envelope density and low thermal conductivity.

Generally, the properties of melamine-formaldehyde aerogels are controlled by the same parameters as for RF gels, i.e. molar ratio of monomers, catalyst, time of reaction, temperature, and the pH value [61].

10.2.2.2 Melamine-Resorcinol-Formaldehyde Xerogels

The combining of both synthesis RF and MF to MRF-route was first studied by Zhou et al. [62]. His group has developed facile preparation method of MRF-microspheres under hydrothermal conditions. The reaction of RF and MF can take place without any catalyst when it is performed under hydrothermal conditions. As shown in Figure 10.6 after addition reaction between resorcinol with formaldehyde and melamine with formaldehyde, the hydroxymethyl groups are formed. In the next step – the condensation – hydroxymethylresorcinols react with methylomelamines under formation of both methylene and methylene ether bridges. The molecules can further agglomerate to form small clusters, which then can continuously grow to form microspheres. The particle size was found to be easily tunable by adjusting of melamine to resorcinol ratio. Smaller microspheres could be synthesized at a higher M/R ratio. The molecular weight of polymers increases with increasing M/R ration, which leads to a strong decrease in the compatibility of polymers and solvent. Thus, the duration of growth stage is reduced leading to the formation of small particles.

Based on the work of Zhou et al. [63] first melamine-resorcinol-formaldehyde xerogels were synthesized. The gels were prepared in ethanol and, similar to synthesis of Pekala, first melamine and formaldehyde were heated up to 60 °C. Additionally, an additive F68 (PEO76–PPO29–PEO76) was added to the solution. In the second step, resorcinol was added, the reaction was catalyzed with NaOH. After stirring the sol was placed in an oven at 60 °C for 72 hours. Afterwards, the solvent exchange was carried out with ethanol six times. The drying took place subcritically at

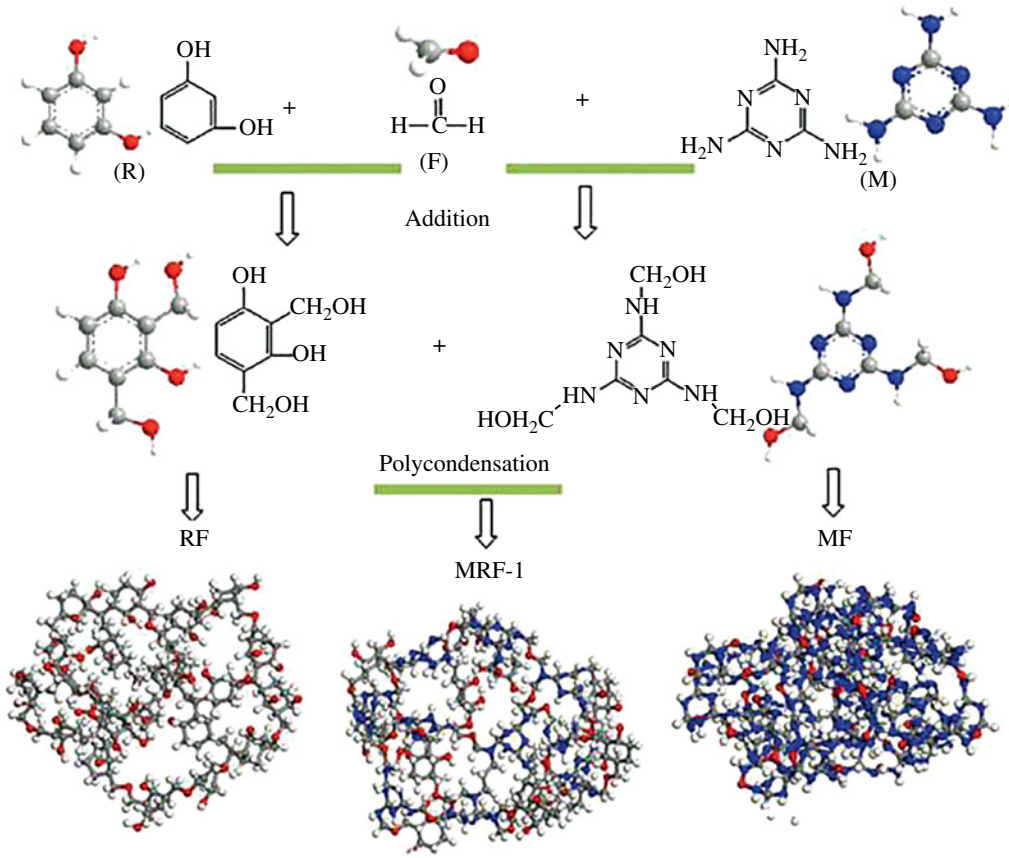


Figure 10.6 Synthesis of MRF network. *Source:* [63] / Reproduced with permission of Royal Society of Chemistry.

ambient pressure and 60 °C. The prepared xerogels showed negligible volume shrinkage and are mechanically stable. The addition of PEO–PPO–PEO micelles was found to contribute to the formation of additional porosity.

The melamine amount used in the synthesis dictates chemical structure of MRF aerogels or xerogels [61]. The nitrogen amount increases linearly with higher melamine content. The FTIR spectroscopy shows more imide functionalities (1697 cm^{-1}) and the reduction of O-H stretching vibrations (3550–3200 cm^{-1}) as a consequence of substitution of resorcinol by melamine in the reaction. The melamine content has an impact on pore sizes, pore volume, and inner surface area of xerogels. The melamine-resorcinol-formaldehyde xerogels exhibit Type IV nitrogen sorption isotherms, and hysteresis loops changes from Type H2 to H1 (IUPAC classification) as melamine content increases. This was found to be related to narrow necked and wide-bodied pores. The mean pore width became larger (from 3 to 10 nm) by increase of melamine amount (from 1 to 40 wt.%) at constant R/C and R/F molar ratios. Nevertheless, this effect is diminished with increasing R/F molar ratio. Principe et al. [61] found that melamine content above 30 wt.% drastically decreases surface area. The authors suggested to use R/C of 50–100, R/F < 0.5 and melamine content between 0 and 20 wt.% in order to obtain xerogels with high nitrogen amount and at the same time material with high surface area. The resorcinol to water molar ratio controls the

mechanical stability of MRF xerogels. Whether the value is increased, the final xerogel structure becomes weaker and, in most cases, gelation fails. The R/F molar ratios of 0.25 and 0.5 result in stable gels, due to improved crosslinking during cluster aggregation. The level of crosslinking, the number of substitutions occurring in the ring is controlled by R/F directly. The density of MRF xerogels depends on melamine amount and increases from 0.47 g cm^{-3} to 0.51 g cm^{-3} at M/R ratio 0.5 and 1.0, respectively [64]. Also, the particle size increased drastically with increased melamine content.

In general, the synthesis of melamine-resorcinol-formaldehyde xerogels is fast, allowing access to rapid manufacturing of MRF- and carbon xerogels. Negligible shrinkage after subcritical drying makes them very attractive. The growing interest in MRF aerogels is due to easy adjustable microstructure, similar to RF aerogels. Another promising property of MRF aerogels is the tunable nitrogen content, coming from an inexpensive and commercially available triazine polymer, which is an important aspect for further applications.

10.2.3 Synthesis and Properties of Tannin-Formaldehyde Aerogels

Resorcinol besides its benefits such as high reactivity and high solubility in water has some drawbacks. The chemical is expensive, environmentally harmful, and comes from the petroleum industry. The rapid depletion of oil sources, as well as the effect of environmental pollution caused by refining, forced scientists to identify alternate precursors. Especially, abundant, cheap, environmentally friendly precursors make the synthesis of aerogels very attractive. In the last decade, aerogels derived from biomass have garnered considerable attention due to their biodegradability and costs efficiency. Among others, tannin belongs to this class of material. Tannins (T) are the most abundant compounds from the biomass after cellulose, hemicellulose, and lignin. They are present in almost every part of plants such as barks, woods, leaves, fruits, roots, and seeds.

The reaction of tannin with formaldehyde is based on polymerization of flavonoids units from condensed tannins with formaldehyde, especially with the flavonoids A-rings through methylene bridge linkages [65]. However, in a more reactive medium (acidic or alkaline), the B-rings are also able to react with formaldehyde [66–69]. As shown in Figure 10.7, the main reactions are the formation of both methylene bridges ($-CH_2-$) and unstable methylene ether bridges ($-CH_2OCH_2-$). The methylene ether bridges are unstable and undergo fast rearrangement to form methylene bridges by releasing formaldehyde [65, 70].

Szczurek et al. [71] pioneered work on synthesis of tannin-formaldehyde aerogels (TF) in 2011. This group developed a synthesis route, where mimosa tannin powder was first dissolved in aqueous solution of methanol. In the second step, aqueous solution of formaldehyde was added. The pH-value was adjusted to both conditions acidic (by acetic acid) and alkaline (by NaOH). At pH = 3 no gelation occurred. From the solutions with pH = 3.3–8.3, gels were obtained after two days. After gelation and curing, a solvent exchange took place. Typically, acetone [71], *tert*-butanol [72] or ethanol with carbon dioxide [73] can be used. The solvents were refreshed every day for three days [71, 73, 74].

The tannin-formaldehyde aerogels can be dried in supercritical carbon dioxide [73] or in supercritical acetone [71]. Both methods are suitable in order to avoid capillary forces in the gel network and result in crack- and shrinkage-free aerogels. However, the drying in organic solvents, such as acetone, requires higher temperatures and pressures (250 °C and 14 MPa). Supercritical drying with carbon dioxide is desirable because CO_2 is chemically inert and a non-flammable fluid. Additionally, carbon dioxide has a low critical temperature and pressure (31 °C and 7.4 MPa). Tannin-formaldehyde xerogels show considerable shrinkage after subcritical drying; thus, the

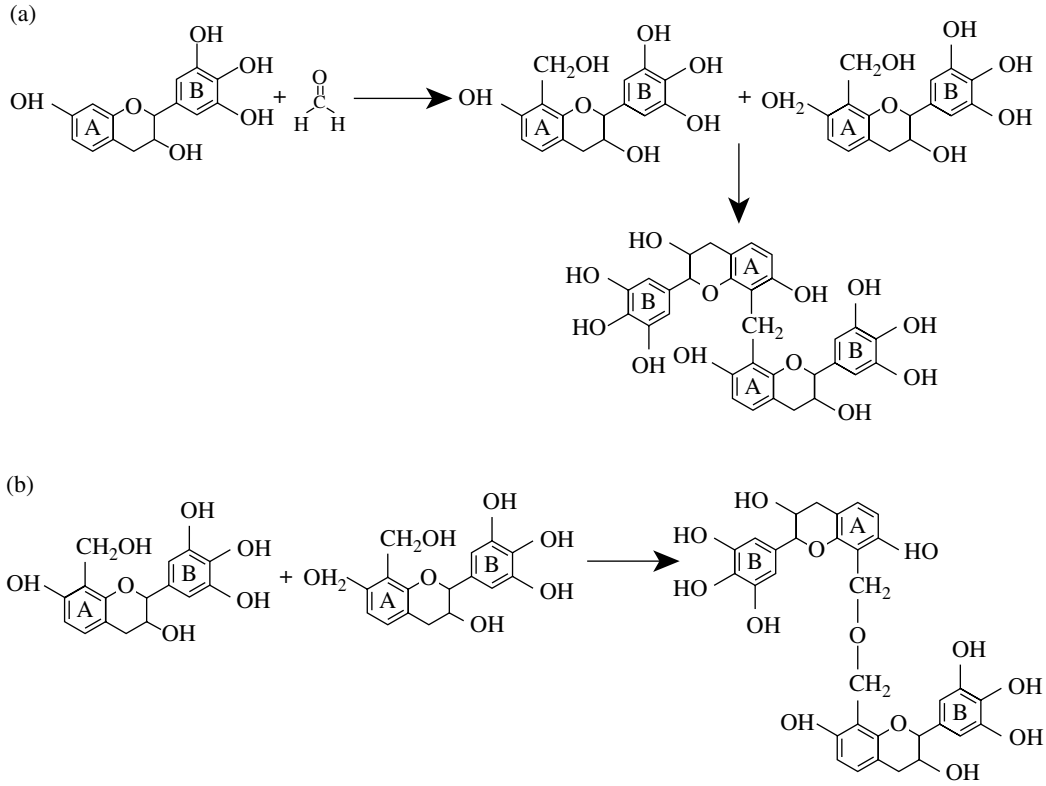


Figure 10.7 Schematic diagram of the reaction of tannin and formaldehyde with formation of (a) methylene and (b) methylene ether bridges [70] / MDPI / Licensed under CC BY 4.0.

porosity is drastically reduced [70]. The TF cryogels show microcracks caused by formation of dendrites and water expansion during freeze drying.

Amaral-Labat et al. [73] performed a systematic study on influence of pH-value on the structure of TF aerogels. Similar to previously discussed organic aerogels, the pH-value was found to be a crucial factor in the synthesis of TF aerogels. The TF aerogels were synthesized at pH = 2–10 and with solid content of 4–40 wt.%. It was pointed out that the transparency and the color are influenced by pH and solid concentration. Through the increase of both pH and concentration, the size of the aerogels' nodules is decreased, leading to a higher transparency of the material. Thus, higher pH and/or higher concentration lead to more transparent gels. The color of TF aerogels varied from red-brown at low pH to orange-red at neutral pH and to dark red in base region. These differences in color were found to be related to the presence of quinones, which are produced by oxidation of phenolic compounds.

Braghiroli et al. [70] investigated the reactivity of phenolic rings A and B at different pH-values. They came to the conclusion that the pH control is extremely important in the reactional system of phenolics. The C8 position on the A-ring (Figure 10.8) is the position with higher reactivity [75]. The C6 position on the A-ring is also very reactive, but less than C8 position due to steric hindrance. In general, these two positions on the A-ring are involve only. The B-ring was found to be particularly unreactive. Nevertheless, the substitution at the 6′ position of the B-ring can occur at pH of about 10. Thus, the reactivity of positions in catechins and phloroglucinol A-ring type

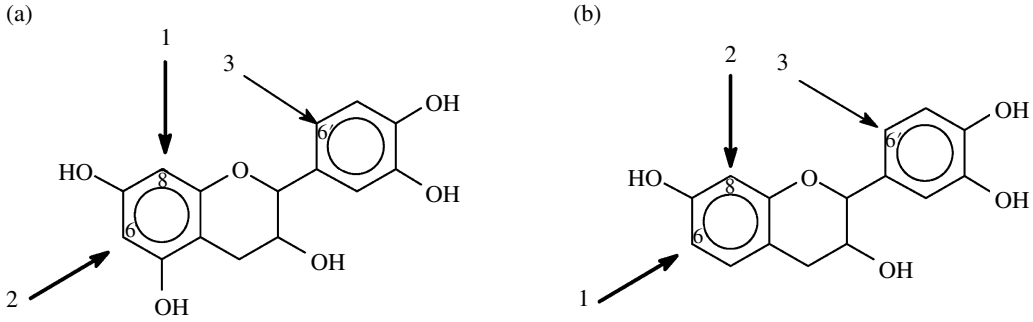


Figure 10.8 The reactivity for (a) catechins and phloroglucinol A-rings type flavonoids is C8 > C6 > C6′ and for (b) robinetinidin and fisetinidin A-rings C6 > C8 > C6′ [70] / MDPI / Licensed under CC BY 4.0.

flavonoids is C8 > C6 > C6′. In contrast, for robinetinidin and fisetinidin A-ring type flavonoids (Figure 10.8), the reactivity sequence was found to be C6 > C8 > C6′. In this kind of rings, the accessibility of C6 position is higher and the steric hindrance lower.

Thus, the kinetics of reaction is faster at pH = 10 and also at pH < 1–2 and very slow at pH around 4. At high pH-values and high solid amount the stiffness of TF aerogels was increased. The compressive modulus was determined in the region of 0.48 and 6.34 MPa for 18% and 40%, respectively. The enveloped density is quite higher compared to other organic aerogels (0.18–0.84 $g\,cm^{-3}$). The TF aerogels exhibit low thermal conductivity of about 0.04 $W\,m^{-1}\,K^{-1}$ with densities lower than 0.2 $g\,cm^{-3}$.

An interesting phenomenon of tannin-formaldehyde aerogels was reported by Amaral-Labat et al. [73]. A formation of physical TF gel at pH = 8 and solid amount 4 wt.%, and at pH = 10 and solid content 6 wt.% was observed. These samples gelled at room temperature after being removed from the oven. The observed gelation was reversible. All other compositions (lower pH-values and higher solid concentrations) gelled irreversible. No other organic gels showed this behavior. Nevertheless, the reversible gelation was found to be very difficult to reproduce [76]. It strongly depends on quality of educts, especially of formaldehyde and tannin.[2] Organic cryogels prepared by sol-gel process of resorcinol and formaldehyde in the presence of tannin were reported from Szczurek et al. [72]. The authors aimed to reduce of the costs of RF aerogels. Thus, they replaced ca. 66% of resorcinol with condensed tannin. The study shows a strong influence of pH-value on the properties of TF cryogels. The highest porosity could be reached at pH = 4–5. TF cryogels with pronounced cross-linking were obtained at acid or alkali conditions with higher amount of formaldehyde. The author confirmed that replacing two-thirds of resorcinol by tannin leads to 30 times cheaper product. Moreover, the freeze drying is also cheaper compared to the supercritical drying.

10.2.4 Synthesis and Properties of Other Organic Aerogels Crosslinked by Formaldehyde or Furfural

After discovery of the first organic aerogel, where phenol molecules are crosslinked with formaldehyde, a large number of other chemicals were used for new type of aerogels. The high interest on this class of material is caused by well-adjustable microstructures by controlling of synthesis parameters. Organic aerogels obtained by polycondensation of phenolics and formaldehyde exhibit

2 From private communication with the authors of reference [73].

suitable properties for specific applications. Among others, new variations in the synthesis aim at the reduction of synthesis costs and the replacement of resorcinol by other, environmentally friendly, cheap, and abundant chemicals. An enhancement of synthesis route was proposed in 1995 [9]. The replacement of resorcinol by phenolic and formaldehyde by furfural allows a non-aqueous synthesis route, thus eliminating solvent exchange step prior to supercritical drying. The new type of aerogels is very similar to RF aerogels, except the shape of the particles. Their appearance reminds flat platelets unlike almost perfect shaped spherical particles of RF aerogels. The thermal conductivity of phenolic-furfural (PFur) aerogels is about 0.015–0.017 $W\,m^{-1}\,K^{-1}$, the specific surface area measured by nitrogen sorption is of about 385 $m^2\,g^{-1}$, the envelope density in the range of 0.1–0.25 $g\,cm^{-3}$. Although, the properties are very similar to RF aerogels, the costs of PF aerogels were found to be considerably lower and made the synthesis faster.

Another approach in order to fasten the synthesis was suggested by Li and Guo from Dalian University of Technology [77]. They discovered low-dense cresol-formaldehyde (CF) aerogels. This aerogel was prepared with almost three times higher solid amount. Nevertheless, the envelope density of CF aerogels is comparable with RF aerogels, 0.09 and 0.075 $g\,cm^{-3}$, respectively. Considerable higher strength and low shrinkage are important feature of these aerogels. Due to high solid content the aging step could me minimalized, thus shortening the synthesis duration. Additionally, cresol is by about factor 4 cheaper than resorcinol [78], which makes CF aerogels very attractive for industrial synthesis. The IR transmittance spectra of CF aerogels show typical adsorption bands of CH_2- and CH_3-stretching vibration at 2921 and 2862 cm^{-1}, respectively. The crosslinking is analogous to RF aerogels; the methylene and dimethylene ether bridges could be detected by IR spectroscopy [8].

Wu et al. followed the approach of Pekala et al. [58] to replace expensive resorcinol by phenolic. However, the use of furfural was found to be difficult due to its self-condensation under acid condition. Thus, formaldehyde was used as a crosslinker. The synthesis of phenol-formaldehyde (PF) aerogels was performed under basic conditions by use of NaOH. After supercritical drying the PF aerogels shrunk around 15–24%, their envelope density is about 0.22–0.37 $g\,cm^{-3}$. Low-price PF aerogels exhibit similar to RF structure with particles about 10–15 nm and pores in mesopore region.

A similar approach can be found by Amaral-Labat et al. [79]. Low-cost phenolic-resorcinol-formaldehyde aerogel was called *blue glue* due to its blue color. The resorcinol amount was halved and phenolic added to the solution. Additionally, urea was used as branching agents in order to increase the reaction kinetics. The gelation time could be reduced up to 10 minutes but the properties of the gels were not satisfactory. Additional amount of furfural was required to obtain well-crosslinked gels. Among others, imide groups could be seen in IR spectra due to urea branching.

The formaldehyde was successfully used as a crosslinker in many others synthesizes of organic aerogels such as lignin-phenol-formaldehyde [80], lignin-resorcinol-formaldehyde [81], 5-methylr esorcinol-formaldehyde [82], or isocyanate-crosslinked RF aerogels [83, 84]. These and other organic aerogels are discussed in other chapters of this book.

10.3 Application of Organic Aerogels for Energy Saving

Thermal, mechanical, and optical properties define the application fields of organic aerogels. Six possible application fields are introduced here:

1) Organic aerogels are mostly used as a precursor for carbon aerogels. Their tunable properties such as porosity, specific surface area, pore and particle sizes, connectivity, and solid content are reflected in carbon aerogels. An overview of organic-based carbon aerogels is given below.

2) Reported thermal conductivity of organic aerogels is about 0.012 $W m^{-1} K^{-1}$) [85] and, thus, is lower than of some inorganic aerogels, and suitable as an insulating material [86]. For several years BuyAerogel.com™ from Aerogel Technologies has sold RF aerogel as an insulating material [87]. Aspen Aerogels, Inc. developed silica aerogel-based insulation called Spaceloft® with thermal conductivity of 0.013 $W m^{-1} K^{-1}$. Another inorganic aerogel-based insulation material is Nanogel® Compression Pack™, discovered by Cabot Aerogel with a thermal conductivity of 0.014 $W m^{-1} K^{-1}$ [88, 89]. Light, superinsulating material for space application based on a benzoxazine organic-inorganic hybrid aerogel blanket with crosslinking between a resorcinol-formaldehyde matrix and a (3-Aminopropyl) triethoxysilane matrix was published. The densities of aerogels is in the range of 0.03 $g cm^{-3}$ and the thermal conductivity as low as 0.019 $W m^{-1} K^{-1}$) in room conditions [90].

   Enhanced flexibility of resorcinol-formaldehyde aerogels improved their handling. Although, the RF aerogels are stiffer than silica aerogels, they are still very brittle. The brittleness complicates the use of RF aerogels in e.g. construction area for buildings insulation. Flexible RF aerogels can be reversibly deformed to a certain degree without break. The thermal conductivity of flexible RF are in the range of 0.041–0.047 $W m^{-1} K^{-1}$ [49].

   Melamine-formaldehyde aerogels are also suggested for thermal insulation application [70]. Transparent MF aerogels with thermal conductivity of about 0.013 $W m^{-1} K^{-1}$ and low density of about 0.18 $g cm^{-3}$ were published recently [60]. Moreover, these aerogels are highly transparent and mechanically strong with a Young's modulus of about 14.9 MPa. Tannin-formaldehyde aerogels were also suggested as a thermal insulating material, with a thermal conductivity of about 0.027 $W m^{-1} K^{-1}$.
3) Highly flexibly resorcinol-formaldehyde aerogels deliver remarkable energy absorption and dissipation performance [91]. The absorbed energy was determined in loading-unloading tests with a maximum strain of 50% or 80% and straining rate of 0.5 s^{-1} (Figure 10.9). A considerable high energy adsorption up to 31 $J g^{-1}$ and energy dissipation up to 24 $J g^{-1}$ was measured. Thus, this material can be used as energy absorptive.

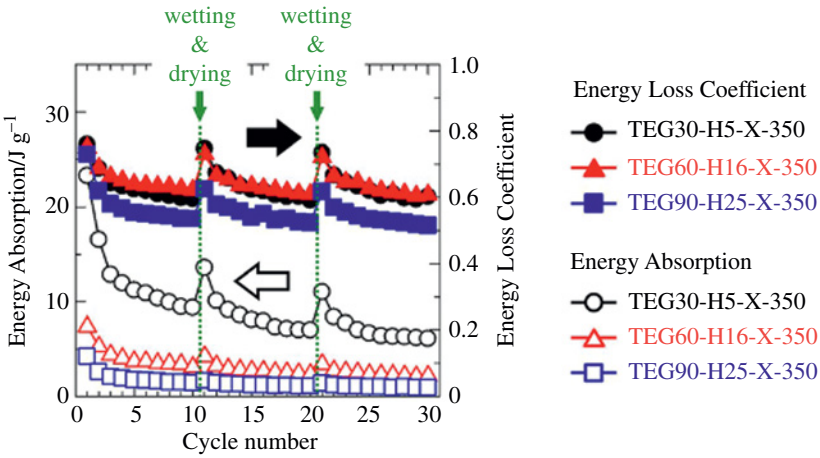


Figure 10.9 Energy absorption capabilities of the heat-treated RF aerogels during the cycling compression to 70%. After the tenth and twentieth cycles, the compressed gels were wetted in 2-propanol and dried in vacuum at 60 °C. *Source:* [91] / Reproduced with permission of American Chemical Society.

4) Superhydrophobic RF reinforced aerogels with a contact angle of about 168° can be an interesting candidate for application in energy-saving and oil- or chemical-cleanup fields. These aerogels are mechanically strong with compression modulus in the range of 4–35 MPa, low density of ca. 0.14–0.26 g cm^{-3}. As a fluid absorption material they were successfully tested with ethanol, liquid paraffin, seed oil, kerosene, cyclohexane, xylene, *n*-hexane, propanol, and methanol [92]. Figure 10.10 shows the results. Remarkable absorption capacity was investigated; aerogel could absorb more than five to six times its own weight in liquid.
5) RF aerogels prepared with Fe, Co, and Ni acetates as catalytic precursors were suggested as a photoactive material [93]. Orellana-Garcia et al. observed the band-gap values <4 eV. Thus, they behaved as photoactive materials in the presence of UV radiation. The authors found that RF-doped aerogels with Fe, Co, and Ni are effective materials for the degradation and removal of the herbicide amitrole in aqueous solution.
6) The trapping of metals such as Cr^{2+}, Cu^{2+}, Pb^{2+}, and Zn^{2+} was investigated by the application of tannin-gel. TF-aerogels exhibit phenolic hydroxyl molecules and thus have a specific affinity to metal ions. They can be applied as adsorbents for the removal of metal contaminants from water at a concentration above the threshold [70].

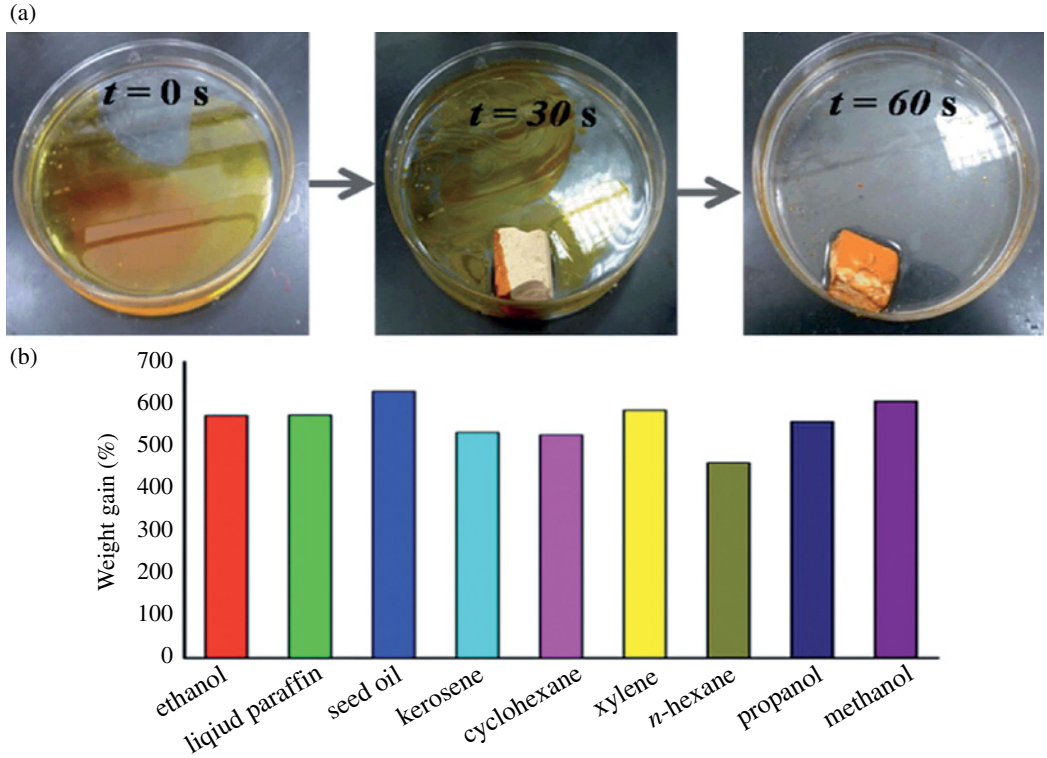


Figure 10.10 (a) Complete absorption of organic liquids by superhydrophobic RF/SiO_2 aerogel within 60 seconds; (b) absorption capacity in wt.% of aerogel for several organic liquids [92] / Reproduced with permission of Royal Society of Chemistry.

Organic aerogels can undoubtedly be used in many other applications. However, until now only few examples have been published. The reason for limited application examples could be insufficient stiffness of organic aerogels, high costs, high production duration, and absence of considerably experiments in upscaling. Merely, only one company is purchasing RF aerogels for $50 for a RF piece of about 1.8 cm × 0.6 cm [94]. Further development of one-pot, fast, and cheap syntheses in large, industrial scale are necessary.

10.4 Overview on Organic-based Carbon Aerogels

Carbon aerogels (Figure 10.11) are highly porous, electrically conductive material with tunable micro- and mesoporosity as well as surface area and envelope density. Their properties are dictated from sol-gel process of their organic precursors and carbonization conditions (Table 10.1). Due to their well-adjustable properties, they became very attractive in many fields, such as CO_2 capture, thermal insulation, catalysis agent, microwave adsorbent, or as electrodes for supercapacitors and batteries.

10.4.1 Carbonization Process

Organic aerogels can be converted into carbon aerogels by carbonization under exclusion of oxygen. Nitrogen, helium, or argon are typically used as inert gases for carbonization. The carbonization is the first stage of pyrolysis and ends at around 1200–1600 °C. The second stage, known as pregraphitization, takes place between 1600 and 2000 °C. The activation energies of the first and the second step are very similar of about 65 kcal mol^{-1} [120]. The third and final step is called graphitization and takes place in the range between 2000 and 3000 °C.

Carbonization is often divided into three stages. During the first carbonization stage (50–100 °C) the desorption of adsorbed water takes place, which often corresponds to a mass loss of about 5–8%

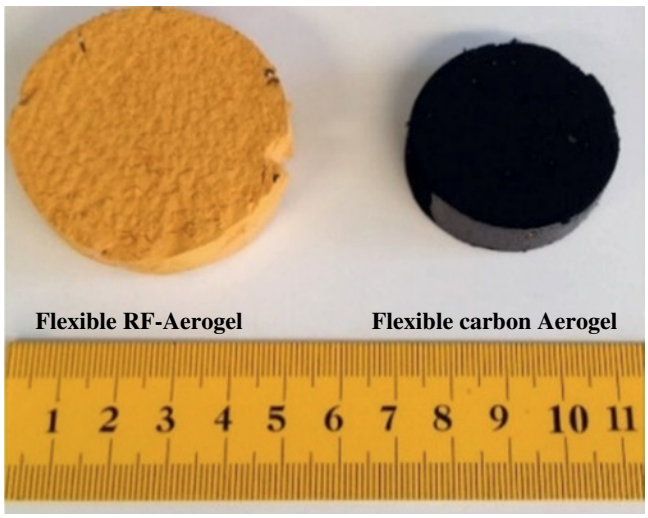


Figure 10.11 Resorcinol-formaldehyde aerogel before (beige) and after (black) carbonization. Carbon aerogel shows about 15–18% of radial shrinkage. Credit : Jiacheng Wang et.al., 2012 / with permission of Royal Society of Chemistry.

Table 10.1 Overview of influence of synthesis and carbonization parameters on the properties of carbon aerogels.

Properties/ Parameter	Phenols: catalyst molar ratio/type of catalyst	Phenols: water molar ratio/ Phenols: Aldehyde molar ratio	pH-value	Drying	Carbonization/Activation
S_{BET}	• Surface area is higher at low R/C ratio [95]. • Base catalyzed CAs exhibit higher SBET than acidic catalyzed [95]	• Increase in R/W molar ratio under alkaline conditions results in a decrease of SBET [95].	• Surface area is higher at pH = 5.4–6.6 and continuously decreases at pH > 6.8 in acid-base synthesis [39]. • TRF-based [72] and TF- based [96] carbon aerogels exhibit higher surface area at increased pH-value.	• Carbon aerogels exhibit higher surface area than carbon xerogels [37].	• CO_2 activation leads to increase of S_{BET} [95]. • Steam activation causes higher surface area [97]. • Higher carbonization temperature causes an increase of S_{BET} till 1000 °C [98] and a decrease up to 1000 °C [99, 100]. • Chemical activation of TF-aerogels with NaOH or KOH induces development of surface area [101].
Pore volume/ Pore size distribution/ porosity	• Pore size distribution is controlled by R/C and catalyst type. The pore size (PS) changes as follow $PS(K_2CO_3; Na_2CO_3) < PS\ (NaHCO_3) < PS(KHCO_3)$ [102]. • At high R/C surface area is dominated by micropores [103].	• At higher R/W the mesoporosity is reduced [95].	• Mesopore volume decreases with raised pH, at pH = 7.0–7.5 it reaches the minimum [39]. • Increase of microporosity of TF-based carbon aerogels can be reached at higher pH-values [96].	• Use of *t*-butanol during solvent exchange allows preparation of mesoporous carbon aerogels [104].	• CO_2 activation develops and widens the micropores [95, 105, 106]. • Higher carbonization temperature leads to decrease of porosity [105, 107, 108]. • High degree of steam activation increases microporosity [97].
Density/ Shrinkage	• CAs prepared using Na_2CO_3 are denser, than those prepared using K_2CO_3 [95]. • Low dense CA can be obtained at higher molar ratio of phenol to NaOH [109] • Increase of catalyst amount (NaOH) of cresol-formaldehyde based carbon aerogels results in decrease of density [77].	• Increase of R/W leads to increase of density [95]. • Higher P/F ratio leads to increase of density [109].	• The envelope density increases in pH-range from 5.45 to 7.35 [98].	• The envelope density of supercritically dried CAs is quite lower than that of corresponded carbon cryogels; density of carbon xerogels compared to cryogels and aerogels is much higher [35]. • Drying in supercritical acetone leads to CA with low density and low shrinkage; drying in supercritical ethanol causes high shrinkage and increase of density (except for R/W ≥ 0.2) [110].	• As the duration of CO_2 activation increases, the skeletal density increases also [105]. • Envelope density decreases with increased carbonization temperature [99].

(*Continued*)

Downloaded from https://onlinelibrary.wiley.com/doi/ by ibrahim ragab - Universita Di Firenze Sistema , Wiley Online Library on [21/07/2024]. See the Terms and Conditions (https://onlinelibrary.wiley.com/terms-and-conditions) on Wiley Online Library for rules of use; OA articles are governed by the applicable Creative Commons License

Table 10.1 (Continued)

Properties/ Parameter	Phenols: catalyst molar ratio/type of catalyst	Phenols: water molar ratio/ Phenols: Aldehyde molar ratio	pH-value	Drying	Carbonization/Activation
Mechanical properties		• Combination of high dilution and high catalyst amount results in flexible carbon aerogels [111].		• Crack formation is often obtained after freeze-drying; stiff aerogel can be produced by subcritical drying with high R/C ratio [35, 112].	
Electrical conductivity/ Thermal conductivity	• Under low R/C (e.g. 50) small particles about 7–9 nm in polymeric structures lead to increase of conductivity. In colloidal structures under high R/C conductivity is reduced due to more non-conductive regions [113]	• Increase of mass ratio of reactants causes more closely packed conductive paths, increase of density, and thus, increase of conductivity [113]. • Electrical conductivity λs scales directly with the density ρs $\lambda_s \propto \rho_s^{\alpha}$, where $\alpha = 1.5 \pm 0.1$ [114].	• Electrical conductivity increases with higher pH and strongly depends on microstructure [98].		• Electrical conductivity increases with annealing temperature and saturates above 2000 °C [99, 115] • Thermal conductivity increases continuously with the heat-treatment temperature [99].
Handling/ Synthesis duration/ Synthesis costs	• Synthesis with high R/C ratio shorten the synthesis duration up to 1 day [116]. • Pulverization of CA synthesized with high R/C can easily be pulverized than CAs with low R/C [117].			• Supercritical drying in acetone reduces the duration and costs of RF aerogels [118]. • Subcritical drying allows reduced production costs and shorten synthesis [119]. • Freeze-dried TRF cryogels result in low-cost carbon aerogels [72].	

Downloaded from https://onlinelibrary.wiley.com/doi/ by ibrahim ragab - Universita Di Firenze Sistema , Wiley Online Library on [21/07/2024]. See the Terms and Conditions (https://onlinelibrary.wiley.com/terms-and-conditions) on Wiley Online Library for rules of use; OA articles are governed by the applicable Creative Commons License

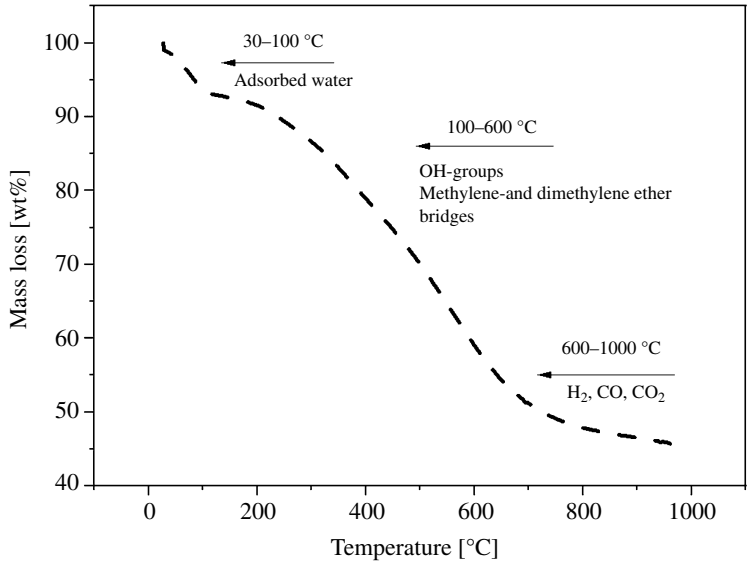


Figure 10.12 TGA-curve of carbonization of RF-aerogel under argon atmosphere with 10 K min^{-1}.

(Figure 10.12). In this stage, due to release of water, two endothermal reactions can be observed between 50 and 100 °C [121].

In the second stage, in the range of 100 to 600 °C polyaromatic planar ring structures are developed. Such structures are randomly distributed within the material. Organic residues such as water, carbon dioxide, and hydrocarbons are released. A flow of bubbles induces stresses in the material and the aromatic molecules tend to align in a direction parallel to the flow. Because the gas release is random, irregular pores in the structure are formed. The walls of pores are formed from molecular stacks; thus, areas of parallel oriented molecules appear. In this stage hydroxyl groups, methylene and dimethylene ether bridges are removed. The resulting water reacts with methylene groups to form CO and H_2. At the same time, the released hydrogen forms methane with methylene groups. Moreover, carbon monoxide is formed when the dimethylene ether bridges decompose. The TGA-FTIR spectra of released gases at 600 °C demonstrated the disappearance of the broad OH-band from OH-groups of resorcinol [121]. A high proportion of oxygen, sulfur, and nitrogen atoms in the bridges causes the formation of small pores. In oxygen-rich materials (e.g. cellulose), very small (≤100 Å) pores can be formed; in hydrogen-rich materials, very large (≥100 μm) pores are formed [120]. The degree of crosslinking between the benzene rings is reduced by the decomposition, which drastically increases the mobility of the aromatics. The reorientation of the aromatic rings causes formation of new, closely linked microstructures, to polyaromatic planar ring structures. The mass loss of second stage is about 40–50 wt.%.

In the third and final stage of carbonization at 600–900 °C, C-H bonds in the aromatic rings are broken. The resulting gases CH_4, H_2, small amount of carbon monoxide, and carbon dioxide are released from the material [122]. In this stage, no significant changes occur, the pore size stays constant, and the stacks do not grow. Far et al. [123] showed that carbon produced by carbonization of phenolic resins at 800 °C always contains fused pyrylium rings, irrespective of the oxidation process.

10.4.2 Properties and Microstructure of Carbon Aerogels

The influence of the sol-gel process, the drying technique, as well as the carbonization parameters are summarized in Table 10.1.

In general, the concentration of educts, the catalyst amount, and the drying method dictate the microstructure of organic aerogels and, in turn, the morphology and properties of carbon aerogels. The variations in the carbonization conditions cause significant changes in the properties of carbon aerogels. A summary of these changes is shown in Table 10.1. Moreover, the process parameters influence the cost and duration of aerogels production. A well-considered selection of precursors and adjusted process parameters can not only reduce the costs but also positively affect the environment and the global CO_2 footprint.

The influence of synthesis parameters is discussed in detail in the previous chapter and summarized in Table 10.1. Among these, carbonization strongly affects the morphology and properties of carbon aerogels. The morphological changes take place during all three stages of carbonization. First, the crosslinks begin to break, thus transporting the solid to the inner surface of the pores. The filling of pores leads to compaction of the material and to a partly closed-porous structure, thus, an increase of the bulk and skeletal densities is observed. The compaction of the material is followed by a reduction of the particle boundary interface area and coarsening of the structure. In the last stage of carbonization at high temperature, due to the evolution of hydrogen, the final structure consists of coalesced rings [122]. During carbonization, the particles became smoother, as if they are covered on their surface. This process was described by Gruber [124], treating quite generally the smoothing of rough surfaces by curvature-driven mass transport. Several investigations show that merging or smoothing can cause a strengthening of the aerogels [111, 125, 126].

Carbonization at temperatures above 1000 °C significantly reduces the micropore surface area due to excessive densification of the aerogel network. In contrast, the external surface area remains almost constant in the temperature region of 800–2500 °C [99]. Whereupon Zhang et al. [127] pointed out 600 °C as a critical temperature to achieve the highest surface area.

In addition, the activation step is used extensively in order to create highly microporous carbon aerogels. When inert gases, such as N_2, Ar, or He, are used to convert the carbonaceous organic aerogel into another more stable and heat resistant carbon aerogel that consists mainly of carbon, non-inert gases, e.g. carbon dioxide, oxygen, are used to carry out the reaction with the carbon. According to the reverse Boudouard reaction $CO_2 + C \leftrightarrow 2\,CO$, at around 800 °C, carbon reacts with CO_2. Thus, the carbon from the solid network is removed and released in the form of gas (CO). This reaction is endothermic with a slow reaction kinetics and it is responsible for the creation of high microporosity over the entire range of burn-off [128].

Several works have indicated that the final structure is affected not only through the activation temperature, but also through the activation time and CO_2 flow rate [105, 129, 130]. Guo et al. [129] have reported that widening of pores and an increase in mesoporosity is favorable at higher activation temperatures (e.g. 950 °C). With increasing activation time from 120 to 240 minutes, ultramicropore (smaller 0.7 nm) volume is decreased, while the volume of supermicropores (0.7–2 nm) is increased. During activation time of 300 minutes, most of the micropores were formed. Further increase of activation time leads to the collapse of pores and thus, decrease of porosity. The flow rate of CO_2 was found to be favorable to the creation of micropores. Nevertheless, the increase of CO_2 flow rate larger than 800 $cm^3\ min^{-1}$ leads to a decrease in microporosity and an increase in mesoporosity.

Besides thermal activation, chemical activation was found to be a very effective tool. Szczurek et al. [101] reported about soaking of tannin-based organic gels with NaOH and KOH prior heat

treatment. The vacuum-dried, impregnated aerogels showed high surface area and micropore volume after carbonization. The activation with water vapor is also very effective, in order to increase the surface area [131]. Generally, activated carbon aerogels exhibit very high surface areas above $1000\,m^2\ g^{-1}$ and high micropore volumes of about $0.3–0.4\,cm^3\ g^{-1}$ [132]. Their skeletal density is about $2.2 \pm 0.04\,g\,cm^{-3}$ [117] and the envelope density is in the range of about $0.05–0.3\,g\,cm^{-3}$ [112]. The mechanical response of carbon aerogels is dictated by their solid content: the higher the solid concentration, the higher the tensile strength. The same is valid for composites of carbon-organic aerogels [133].

The skeletal thermal conductivity λ_s of carbon aerogels is influenced by the envelope density ρ. Lu et al. [114] have published values in the range of $0.03–0.04\,W\,m^{-1}\,K^{-1}$ for aerogels with densities of $0.08–0.14\,g\,cm^{-3}$. The electrical conductivity σ scales also with the density. In the following equation, the scaling exponents *a and t* were both found to be 1.5 ± 0.1.

$$\lambda_s \propto \rho^a; \sigma \propto \rho^t.$$

Thus, carbon aerogels with lower thermal conductivities are less dense and their network consists of smaller pores and smaller particles.

Summing up, controlled carbonization and subsequent activation steps allow for the synthesis of accurately tuned morphologies and properties of carbon aerogels. Thus, knowing the application requirements, suitable materials can be produced to achieve the highest performance for further utilization.

10.5 Applications of Organic-Based Carbon Aerogels for Energy Saving and Storage

Carbon aerogels are suitable materials for a wide spectrum of applications due to their unique structure and excellent properties. The focus of this chapter is on the applications for supercapacitors and batteries. Among others, diverse applications such as catalysis on doped aerogels, hydrogen storage, foundry, and thermal insulation are discussed here.

10.5.1 Applications in Supercapacitors

The development of supercapacitors began in the 1950s with Howard Becker patenting the first "low voltage electrolytic capacitor" [134]. Later, two storage principles in the electric double-layer of electrodes were postulated. To the total capacitance of an electrochemical capacitor contribute the double-layer capacitance and the pseudocapacitance. In the first case, the charge is stored in a Helmholtz double layer, at the interface between an insoluble solid electrode surface and a liquid or solid electrolyte. The pseudocapacitance is based on faradic charge transfer, without chemical reactions with electrodes. Several processes can induce the charge transfer, such as intercalation, electrosorption, or redox process on the surface of the electrodes [135, 136].

The first results on carbon aerogels as an electrode material for supercapacitors were published by Mayer et al. in 1993 [137]. The authors studied the effect of R/C ratio on capacitance. They concluded that the smaller the particle size the higher is the capacitance. Small particles are connected by smaller contact areas; thus, the contact resistivity is low and the performance is enhanced. Later, Fischer et al. [33] investigated the influence of the carbonization temperature T_C on the performance of supercaps. They observed maximum capacity at $T_C = 800\,°C$, where a very high

micropore area was formed at that temperature. It was assumed that the reason for high capacitance is the existence of pseudocapacitance originating from organic groups on the surface. Moreover, micropores are also important because they participate in the charge storage process. Activated carbon aerogels (e.g. in air) exhibit an increased capacity of about 25%, which can be explained by a roughening of the structure and widening of the pathways to the pores in the particles [138]. Mesopores in the aerogels structure strongly influence the performance of supercaps. The best voltammetry characteristics and the highest capacitance values of about 70–150 $F g^{-1}$ were achieved with carbon aerogels having a pore diameter in the range of 3–13 nm [78]. It should be pointed out that with decrease in the pore size, an increasing number of the pores are smaller than the radius of the hydrated ions, and thus are no longer accessible.

The effect of thermal activation has been studied by several authors. The activation with hot air induces a pseudocapacitance effect, which leads to the improvement of specific capacitance [40]. Among others, metal doping leads to distinguished electrochemical performance. Zapata-Benabithe et al. [139] have incorporate copper and silver into carbon aerogels in order to increase the electrochemical performance. High gravimetric (192 $F g^{-1}$) and volumetric (98 $F cm^{-3}$) capacitance was achieved. Whereupon, silver-doped aerogels showed lower values, probably due to lower oxygen content after oxygen activation. Nevertheless, distinguished cycle stability over 2000 cycles was achieved with both materials. A significant improvement of capacitance, high stability of 92.4% after 1500 cycles was achieved by incorporation of MoS_2 into carbon aerogel [140]. Recently, Zhai et al. [141] enhanced the gravimetric capacitance of carbon aerogels by embedding cupper nanoparticles. The new material with homogeneously distributed Cu-particles combined with high surface area showed specific capacitance of 414 $F g^{-1}$ at 0.3 $mV s^{-1}$. A detailed overview on metal-doped carbon aerogels can be found by Morena-Castilla et al. [142]. There, important aspects, such as synthesis methods, microstructural properties, and stability, are discussed in detail.

In the last decade, nitrogen-doping has been proven as an essential technique in order to enhance the electrochemical reactivity of carbon aerogels. The insertion of nitrogen provides more active sites for interface electrochemical reactions. Moreover, by means of nitrogen-doping, large number of surface defects have been introduced that further, e.g. improve lithium intercalation properties in Li-based batteries. Further, Einert et al. [143] postulated that nitrogen bonding configuration, textural structure, and surface area are critically important in the energy-storage applications. Graphitic nitrogen improves the electrical conductivity of N-doped carbons due to the substitution of the carbon atoms with nitrogen ones in the graphene structure. It further can contribute an additional *p*-electron to the delocalized π-electron system without generating any structural defects.

The capacities of several, different supercaps are summarized in Table 10.2.

10.5.2 Applications in Battery Technologies

The increasing energy demands and the need for a greener and cleaner environment force the research on renewable energy and energy storage systems. Lithium has remained the center of attention for battery technology. Thus, lithium-based systems have been extensively studied over the past six decades. Metallic lithium as the anode material can provide high specific capacity of 3861 $mAh g^{-1}$ at a negative potential of −3.04 V vs. standard hydrogen electrode. The cathode material in lithium-ion batteries (LIB) stores the lithium during the discharge process. Conventionally, lithium metal oxides (e.g. $LiCoO_2$, $LiMn_2O_4$, or $LiFePO_4$) are used for this purpose as they trap the lithium ions and release them during charging. Graphite is mostly used as anode material. Unfortunately, lithium metal oxides have several limitations such as high material costs

Table 10.2 Capacitance of supercapacitors based on carbon aerogel as electrode material.

Material	Capacitance	Additional information	References
Carbon aerogel (R/C = 50, T_C = 1050 °C)	26 F cm^{-3}	Current density 4 A cm^{-2}, 4 M KOH as electrolyte Scan rate of 0.5 mV s^{-1}	[137]
Carbon aerogel (R/C = 100, T_C = 800 °C)	46 F cm^{-3}	30 wt.% H_2SO_4 as electrolyte	[33]
Carbon aerogel (R/C = 500, T_C = 1050 °C)	171 F g^{-1}	30 wt.% H_2SO_4 as electrolyte, charging voltage of 1.15 V	[138]
Carbon aerogel (R/C = 500 with 40 wt.% of cresol, T_C = 900 °C)	104 F g^{-3} or 77 F cm^{-1}	1 M H_2SO_4 Scan rate of 5 mV s^{-1}	[78]
Carbon aerogel (R/C = 50, T_C = 1000 °C)	21.8 F g^{-1}	1 M tetraethylammonium tetrafluoroborate (Et_4NBF_4) Scan rates 10–200 mV s^{-1}	[145]
Activated carbon aerogel (R/C = 1000, pH = 5.5, T_C = 800 °C, T_A = 450 °C in hot air)	220 F g^{-1}	6 M H_2SO_4 as electrolyte Scan rate of 1 mV s^{-1}	[40]
MoS_2-doped carbon aerogel	260 F g^{-1}	1 M Na_2SO_4 as electrolyte	[140]
N-doped carbon aerogel	139 F g^{-1}	2 M KOH as electrolyte	[146]
N-doped carbon aerogel	208 F g^{-1}	6 M KOH Scan rate 5–15 mV s^{-1}	[144]
Cu-doped carbon aerogel	192 F g^{-1}	6 M H_2SO_4 as electrolyte	[139]
Cu-doped carbon aerogel	414 F g^{-1}	Scan rate 0.3 mV s^{-1}	[141]

and low theoretical capacity, only a half of Li ions can be extracted without lattice breakdown. Thus, improvements to this system are needed. Carbon-based anode materials are suitable for lithium-based systems [147]. To this end, carbon aerogels with their adjustable microstructure are promising candidates [148]. High mesoporosity combined with high surface area provide large ion accessibility for their storage, as well as enhanced mass transfer capability. Excellent high-rate performance and higher specific capacity of 610 mAh g^{-1} at 0.1 A g^{-1} could be achieved with carbon aerogels activated with H_3PO_4 [149].

One area of significant interest in carbon aerogels is the doping of carbon network. The goal of the incorporation of metal or other elements, such as nitrogen, sulfur, or oxygen, into the aerogel matrix is the modification of the surface in order to increase the conductivity and catalytic activity of carbon aerogels.

Nitrogen-doped carbon aerogels with multiscaled porosity and an average pore size around 2 nm and high surface area of about 2912 m^2 g^{-1} show improved capacity of LIB [63]. Such materials tested at 0.1C showed 645 and 280 mAh g^{-1} at 5C. The authors pointed out that the quaternary-nitrogen being the main chemical state of nitrogen enhances the anode performance in LIB. Due to the improvement of electrochemical reactivity and electrical conductivity, nitrogen-doping of carbonaceous electrodes has been found to improve long-term electrochemical stability in LIB.

Several metal-doped carbon aerogels (e.g. molybdenum [150], platin [151], iron [152–154], zirconium, cerium [155], copper [139, 141, 156, 157], ruthenium [158], silver [159] containing aerogels) have been synthetized and characterized for their catalytic and microstructural properties. According to published studies, carbon aerogels as catalyst exhibit sufficient activity and selectivity. Sarapuu et al. [152] demonstrated electrocatalytic activity of carbon aerogels for oxygen reduction reaction (ORR) in alkaline solution. An enhancement of the ORR activity was achieved with increased nitrogen and iron content. Another example for successful application of metal-doped carbon aerogel was published recently by Wu et al. [154], where they constructed a 3D honeycomb nanostructured FeP/Fe_2O_3@N,P-doped carbon aerogel as bifunctional air electrode by directional freeze-casting. High specific capacity of about 676 mAh g^{-1} and an energy density of 517 Wh kg^{-1} at 5 mA cm^{-2} combined with sufficient cycling stability were achieved in Zn–air battery. Similar excellent electrochemical stability after being tested for 10 000 seconds was achieved by usage of nitrogen doped carbon aerogels coupled with iron-cobalt particles for rechargeable Zn–air batteries [160]. Mahadik et al. [161] investigated the effect of carbon aerogel doping with tin oxide on the performance of LIB. The incorporation of SnO_2 improved the mechanical properties of anode material, which in turn strongly improved the cycling stability. High initial charge capacity of about 1012 mAh g^{-1} could be measured.

Remarkably, higher capacity can be achieved with oxygen as cathode active material in a Li-oxygen battery. The oxygen electrode is a carbon electrode with highly porous structure in which several electrochemical and transport processes occur simultaneously: (i) gas transport in pores for the diffusion of oxygen to the carbon-electrolyte interface; (ii) formation, storage, and electrochemical decomposition of Li_2O_2; (iii) diffusion of electrolyte into the porous structure. Thus, the cell performance strongly depends on the morphology of the carbon material. Using CO_2, thermal activated carbon aerogels for Li-O_2 battery with high pore volume lead to promising results (1290 mAh g^{-1}). The pore volume and pore size of carbon aerogels are the key factors for this application. Mirzaeian et al. [162] found that appropriate pore volume and pore diameter contribute to high capacity. Similar results were published from the group of Zhang et al. [163]: specific capacity of about 1000 mAh g^{-1} in lithium-air cell by application of carbon aerogel with dual pore size distribution. In comparison, commercially available carbon material KB600 exhibits similar capacity of about 1005 mAh g^{-1} and SuperP only 635 mAh g^{-1}.

Among others, lithium-sulfur (Li-S) battery is a promising alternative to LIB. Due to the abundance of sulfur on Earth, the high theoretical specific capacity (1675 mAh g^{-1}) of sulfur cathode, and the high theoretical gravimetric as well as volumetric energy density, Li-S battery is attracting increased attention. Many efforts have been made to improve the performance of Li-S batteries [164]. Introducing porous carbon materials into sulfur cathode was found to be an effective strategy [165–169]. In general, carbon materials contribute to high electronic conductivity and provide accessible porous structure, which adsorbs and immobilizes highly soluble lithium polysulfides as well as contributes to lithium ion pathways, thus improving cyclic stability. The pore size was found to play a crucial role affecting the stability and performance of Li-S batteries [170]. Since the porosity and microstructure of carbon aerogels are tunable, this material was studied by several groups as a cathode.

Li et al. [171] published results with micropore-rich carbon aerogels. Specific capacity of about 900 mAh g^{-1} at 0.5 C could be measured. The authors assume that short lithium polysulfides (e.g. S_2–S_4) can be stored in micropores, preventing their solubility in the electrolyte and leading to enhanced stability. Balakumar et al. [172] pointed out further advantages of carbon aerogels. They showed that the carbon aerogels exhibit the combination of amorphous and graphitic carbon,

offering better mechanical response against volume expansion during charging-discharging and enhanced conductivity. Flexible carbon aerogel shows good cyclability as well, due to its reversible mechanical deformation caused by volume change of cathode [173].

Moreover, doping with different molecules was found to be an effective strategy to suppress the loss of polysulfides. For effective anchoring of polysulfides, MoS_2 decorated carbon aerogels with multi-walled carbon nanotubes were developed by Li et al [174]. Due to the adsorption and anchoring of polysulfides on the surface of MoS_2, the electrochemical performance was effectively improved. The initial capacity amounted to 1343 mAh g^{-1} at 0.2 C and 723 mAh g^{-1} at 5 C [175]. Similar results were achieved by doping with Ce nanoparticles [176], SeS_2 [177], Cd [178], and MoS_3 [179] with 1381 mAh g^{-1} at 0.2 C, 1150 mAh g^{-1} at current density of 50 mA g^{-1}, 1318 mAh g^{-1} at 0.2 C, and 585 mAh g^{-1} at 0.8 A g^{-1}, respectively. Those cathode materials demonstrated impressive long-term stability and high Coulombic efficiency due to immobilization of polysulfides intermediates. Remarkably, doped carbon aerogels could be used in both carbonate- and ether-based electrolytes.

Highly porous carbon aerogels are also successfully used as an electrode material in Li-Se [180], Na-S [181], Li-ion all-solid-state [182], or Na-ion [183, 184] batteries.

10.5.3 Other Relevant Applications of Carbon Aerogels

The unique porous structure of carbon aerogels provides a large pore volume and huge surface area allowing for their application in diverse fields.

10.5.3.1 Foundry Application

Aerogels as additives for foundry application open up a new research and development area. The addition of granulated aerogel to the sand binder system improves both the properties of the lost sand cores as well as the quality of the castings. The positive influence in terms of suppressed emission of casting gases and the core stability leads to a significant increase in quality. Measurements on the casting metal surface show that roughness could be reduced by up to 60%. The improved roughness and easier core removal allow to save processing steps and, thus energy sources and production costs [185, 186].

10.5.3.2 Hydrogen Storage

Another application field for carbon aerogels is safe and efficient hydrogen storage. It is known, that at 77 K the hydrogen bindings energy on carbonaceous sorbent is about 6 kJ mol^{-1} hydrogen. However, the amount of hydrogen varies linearly with surface area: gravimetric uptake is ca. 1 wt.% H_2 per 500 m^2 g^{-1} of inner surface area [187]. Previous studies have highlighted the linear dependence of hydrogen sorption at 77 K and 35 bar pressure [188–190]. High hydrogen uptake of 5.3 wt.% was achieved with surface area of about 3200 m^2 g^{-1}.

The incorporation of nickel or cobalt can enhance the performance of highly porous carbon aerogels. The expected enhancement can be linked to the interaction of hydrogen with accessible metal particles. This behavior is mostly called as "spillover," and is the dissociation of molecular hydrogen at the surface of the metal followed by migration and adsorption on the carbon surface. The adsorption enthalpy of metal-doped carbon aerogels is slightly higher than that of pure carbon materials. It is about 7.0–7.5 kJ mol^{-1}. As shown in Figure 10.13, the hydrogen storage behavior could be enhanced with nickel particles [188].

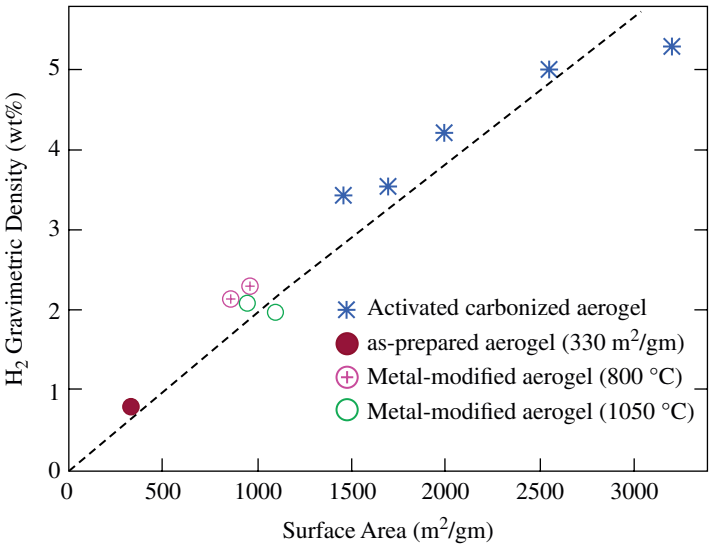


Figure 10.13 Gravimetric density saturation values at 77 K as a function of inner surface area of pure and nickel-doped carbon aerogels. The metal-modified carbon aerogels were carbonized at different temperatures, which are given in brackets [188] / Reproduced with permission of American Chemical Society.

10.5.3.3 Thermal Insulation

Carbon aerogels are promising materials for high temperature thermal insulation. The thermal conductivity was measured in the region of about 0.05–0.4 $W\,m^{-1}\,K^{-1}$ [99]. Later, Feng et al. [191] could achieve low values of about 0.1–0.17 $W\,m^{-1}\,K^{-1}$. Due to the introduction of carbon fibers into the aerogel matrix, the shrinkage during carbonization could be effectively decreased.

Wiener et al. [192] have investigated the thermal conductivity of carbon aerogels at different temperatures in Ar atmosphere at 0.1 MPa, with promising results. For carbon aerogels with density of about 0.2 $g\,cm^{-3}$, thermal conductivity was found to be 0.12 $W\,m^{-1}\,K^{-1}$ at 2000 K, and it increases slightly to 0.16 $W\,m^{-1}\,K^{-1}$ at 2700 K. Recently, a new carbon aerogel for more energy-efficient thermal insulation was published, where the research group at the Bavarian Center for Applied Energy Research together with the industrial partner SGL carbon could save up to 40% of the required process energy with the new thermal insulation material [193].

10.5.3.4 Adsorption Material

With regards to air pollution, the high concentration of industrially produced gaseous wastes and of greenhouse gases affect global warming, thus becoming a high priority crisis. Carbon dioxide and methane, mostly generated by the combustion of fossil fuels, lead to the generation of environmental issues. Therefore, it is of environmental interest to synthesize high performance and cost-effective materials for CO_2 and CH_4 adsorption. Thus, two key factors that influence CO_2 and CH_4 adsorption have been detected: pore structure and chemical surface nature. Narrow micropores in the range of 0.6–0.8 nm exhibit the highest CO_2 adsorption performance. In the micropore, a high volume of gaseous wastes can be captured. On the other hand, the quadrupole moment of carbon dioxide allows for the enhanced adsorption capacity on porous solids by surface interaction with functional groups on the surface [194].

Several groups have investigated CO_2 and CH_4 adsorption on carbon aerogels. Indeed, the highest performance was observed on carbon aerogels either with a high nitrogen amount of about 1.4 wt.% [195], which was introduced into the structure by using urea, or on aerogels with high surface area (1927 $m^2 g^{-1}$) and high micropore volume (0.8 $cm^3 g^{-1}$) [131].

10.5.3.5 Microwave Adsorption

Carbon aerogels can be successfully used as a radar absorbing material. The higher the thickness of aerogel samples, the lower the frequency to reach the maximum reflection coefficient. For example, as the thickness was increased from 2 to 4 mm, for a constant frequency the maximum reflection coefficient decreased from −22 to −32 dB. The bandwidth corresponding to the reflection coefficient below −10 dB is more than 5 GHz. Zhang et al. [196] showed that the maximum reflection coefficient is more sensitive to the thickness in the case of colloidal carbon aerogel than that of polymeric carbon aerogel. Therefore, the reflection coefficient has a close relationship with the microstructure of the carbon aerogel. The absorbing mechanism was described with the hopping of photons from low energy levels to higher ones. Additionally, multiple scattering and interface polarization provide further absorbing mechanisms.

10.6 Summary and Outlook

Organic and carbon aerogels are finding an ever-widening application in many fields. Their simple synthesis, tunable morphology, and low density make them very attractive for e.g. energy storage, thermal insulation, catalysis, and hydrogen storage. However, most of the applied designs are still of an experimental character on the laboratory scale. The mass production and reduction of costs are still important challenges that need to be addressed. Nevertheless, there have been promising studies describing examples and approaches for enabling fast, green, and cheap synthesis routes for large-scale production.

References

1 McNaught, A.D. and Wilkinson, A. (1997). *IUPAC. Compendium of Chemical Terminology*. Blackwell Scientific Publications, Oxford.

2 Kistler, S.S. (1932). Coherent expanded-aerogels. *J. Phys. Chem.* 36: 52. https://doi.org/10.1021/j150331a003.

3 Kistler, S.S. (1932). Coherent expanded aerogels. *Rubber Chem. Technol.* 5: 600. https://doi.org/10.5254/1.3539386.

4 Kistler, S.S. (1931). Coherent expanded aerogels and jellies. *Nature* 127: 741.

5 Pekala, R.W. (1989). Organic aerogels from the polycondensation of resorcinol with formaldehyde. *J. Mater. Sci.* 24: 3221.

6 Mukai, S.R., Tamitsuji, C., Nishihara, H., and Tamon, H. (2005). Preparation of mesoporous carbon gels from an inexpensive combination of phenol and formaldehyde. *Carbon* 43: 2628. https://doi.org/10.1016/j.carbon.2005.05.004.

7 Pekala, R.W. (1992). Melamine-formaldehyde aerogels. US Patent US5081163 A.

8 Li, W.-C., Lu, A.-H., and Guo, S.-C. (2001). Characterization of the microstructures of organic and carbon aerogels based upon mixed cresol–formaldehyde. *Carbon* 39: 1989. https://doi.org/10.1016/S0008-6223(01)00029-X.

9 Pekala, R.W., Alviso, C.T., Lu, X. et al. (1995). New organic aerogels based upon a phenolic-furfural reaction. *J. Non-Cryst. Solids* 188: 34. https://doi.org/10.1016/0022-3093(95)00027-5.

10 Rhine, W., Wang, J., and Begag, R. (2004). Polyimide aerogels, carbon aerogels, and metal carbide aerogels and methods of making same. US Patent US20040132845 A1.

11 Biesmans, G., Mertens, A., Duffours, L. et al. (1998). Polyurethane based organic aerogels and their transformation into carbon aerogels. *J. Non-Cryst. Solids* 225: 64. https://doi.org/10.1016/S0022-3093(98)00010-6.

12 Barral, K. (1998). Low-density organic aerogels by double-catalysed synthesis. *J. Non-Cryst. Solids* 225: 46. https://doi.org/10.1016/S0022-3093(98)00007-6.

13 Fricke, J. and Emmerling, A. (1998). Aerogels—recent progress in production techniques and novel applications. *J. Sol-Gel Sci. Technol.* 13: 299. https://doi.org/10.1023/A:1008663908431.

14 Lu, X., Wang, P., Arduini-Schuster, M.C. et al. (1992). Thermal transport in organic and opacified silica monolithic aerogels. *J. Non-Cryst. Solids* 145: 207. https://doi.org/10.1016/S0022-3093(05)80457-0.

15 Šebenik, A., Osredkar, U., and Vizovišek, I. (1981). Study of the reaction between resorcinol and formaldehyde. *Polymer* 22: 804. https://doi.org/10.1016/0032-3861(81)90019-7.

16 Werstler, D.D. (1986). Quantitative 13C n.m.r. characterization of aqueous formaldehyde resins: 2. Resorcinol-formaldehyde resins. *Polymer* 27: 757. https://doi.org/10.1016/0032-3861(86)90136-9.

17 Schwan, M. (2018). Synthese und Eigenschaften flexibler Resorcin-Formaldehyd- und Kohlenstoffaerogele. PhD Thesis

18 Durairaj, R.B. (2005). Resorcinol structure and physical properties. In: *Resorcinol: Chemistry, Technology and Applications*, 1–9. Berlin Heidelberg, Berlin, Heidelberg: Springer.

19 Durairaj, R.B. (2005). Special compounds. In: *Resorcinol: Chemistry, Technology and Applications*, 117–177. Berlin Heidelberg, Berlin, Heidelberg: Springer.

20 Morales-Torres, S., Maldonado-Hódar, F.J., Pérez-Cadenas, A.F., and Carrasco-Marín, F. (2010). Textural and mechanical characteristics of carbon aerogels synthesized by polymerization of resorcinol and formaldehyde using alkali carbonates as basification agents. *Phys. Chem. Chem. Phys.* 12: 10365. https://doi.org/10.1039/C003396K.

21 Grenier-Loustalot, M.-F., Larroque, S., Grande, D. et al. (1996). Phenolic resins: 2. Influence of catalyst type on reaction mechanisms and kinetics. *Polymer* 37: 1363. https://doi.org/10.1016/0032-3861(96)81133-5.

22 Grenier-Loustalot, M.-F., Larroque, S., Grenier, P., and Bedel, D. (1996). Phenolic resins: 3. Study of the reactivity of the initial monomers towards formaldehyde at constant pH, temperature and catalyst type. *Polymer* 37: 939. https://doi.org/10.1016/0032-3861(96)87276-4.

23 Berthon, S., Barbieri, O., Ehrburger-Dolle, F. et al. (2001). DLS and SAXS investigations of organic gels and aerogels. *J. Non-Cryst. Solids* 285: 154. https://doi.org/10.1016/S0022-3093(01)00447-1.

24 Barbieri, O., Ehrburger-Dolle, F., Rieker, T.P. et al. (2001). Small-angle X-ray scattering of a new series of organic aerogels. *J. Non-Cryst. Solids* 285: 109. https://doi.org/10.1016/S0022-3093(01)00440-9.

25 Brandt, R. and Fricke, J. (2004). Acetic-acid-catalyzed and subcritically dried carbon aerogels with a nanometer-sized structure and a wide density range. *J. Non-Cryst. Solids* 350: 131. https://doi.org/10.1016/j.jnoncrysol.2004.06.039.

26 Mulik, S., Sotiriou-Leventis, C., and Leventis, N. (2007). Time-efficient acid-catalyzed synthesis of resorcinol–formaldehyde aerogels. *Chem. Mater.* 19: 6138. https://doi.org/10.1021/cm071572m.

27 Brandt, R. (2004). Sauer katalysierte, unterkritisch getrocknete Resorcin-Formaldehyd-Aerogele und daraus abgebildete Kohlenstoffaerogele. PhD Thesis

28 Reuß, M. and Ratke, L. (2008). Subcritically dried RF-aerogels catalysed by hydrochloric acid. *J. Sol-Gel Sci. Technol.* 47: 74. https://doi.org/10.1007/s10971-008-1733-0.

29 Laskowski, J., Milow, B., and Ratke, L. (2014). Subcritically dried resorcinol–formaldehyde aerogels from a base–acid catalyzed synthesis route. *Microporous Mesoporous Mater.* 197: 308. https://doi.org/10.1016/j.micromeso.2014.06.031.

30 Lambert, S.M., Overturf, G.E. III, Wilemski, G. et al. (1997). Fabrication of low-density foam shells from resorcinol-formaldehyde aerogel. *J. Appl. Polym. Sci.* 65: 2111. https://doi.org/10.1002/(sici)1097-4628(19970912)65:11<2111::aid-app7>3.0.co;2-k.

31 Despetis, F., Barral, K., Kocon, L., and Phalippou, J. (2000). Effect of aging on mechanical properties of resorcinol-formaldehyde gels. *J. Sol-Gel Sci. Technol.* 19: 829. https://doi.org/10.1023/a:1008732705214.

32 (1974). *CRC Handbook of Chemistry and Physics*. Ohio: CRC Press.

33 Fischer, U., Saliger, R., Bock, V. et al. (1997). Carbon aerogels as electrode material in supercapacitors. *J. Porous Mater.* 4: 281. https://doi.org/10.1023/A:1009629423578.

34 Czakkel, O., Marthi, K., Geissler, E., and László, K. (2005). Influence of drying on the morphology of resorcinol–formaldehyde-based carbon gels. *Microporous Mesoporous Mater.* 86: 124. https://doi.org/10.1016/j.micromeso.2005.07.021.

35 Job, N., Théry, A., Pirard, R. et al. (2005). Carbon aerogels, cryogels and xerogels: influence of the drying method on the textural properties of porous carbon materials. *Carbon* 43: 2481. https://doi.org/10.1016/j.carbon.2005.04.031.

36 Al-Muhtaseb, S.A. and Ritter, J.A. (2003). Preparation and properties of resorcinol–formaldehyde organic and carbon gels. *Adv. Mater.* 15: 101. https://doi.org/10.1002/adma.200390020.

37 Zanto, E.J., Al-Muhtaseb, S.A., and Ritter, J.A. (2002). Sol—gel-derived carbon aerogels and xerogels: design of experiments approach to materials synthesis. *Ind. Eng. Chem. Res.* 41: 3151. https://doi.org/10.1021/ie020048g.

38 Job, N., Panariello, F., Marien, J. et al. (2006). Synthesis optimization of organic xerogels produced from convective air-drying of resorcinol–formaldehyde gels. *J. Non-Cryst. Solids* 352: 24. https://doi.org/10.1016/j.jnoncrysol.2005.11.024.

39 Lin, C. and Ritter, J. (1997). Effect of synthesis pH on the structure of carbon xerogels. *Carbon* 35: 1271.

40 Hwang, S.-W. and Hyun, S.-H. (2004). Capacitance control of carbon aerogel electrodes. *J. Non-Cryst. Solids* 347: 238. https://doi.org/10.1016/j.jnoncrysol.2004.07.075.

41 Mulik, S. and Sotiriou-Leventis, C. (2011). Resorcinol–Formaldehyde aerogels. In: *Aerogels Handbook* (ed. M.A. Aegerter, N. Leventis, and M.M. Koebel), 215–234. New York: Springer.

42 Pekala, R.W. and Alviso, C.T. (1992). *MRS Online Proceedings Library*.

43 Schaefer, D.W., Pekala, R., and Beaucage, G. (1995). Origin of porosity in resorcinol-formaldehyde aerogels. *J. Non-Cryst. Solids* 186: 159. https://doi.org/10.1016/0022-3093(95)00043-7.

44 Lu, X., Caps, R., Fricke, J. et al. (1995). Correlation between structure and thermal conductivity of organic aerogels. *J. Non-Cryst. Solids* 188: 226. https://doi.org/10.1016/0022-3093(95)00191-3.

45 Job, N., Panariello, F., Crine, M. et al. (2007). Rheological determination of the sol–gel transition during the aqueous synthesis of resorcinol-formaldehyde resins. *Colloids Surf. A* 293: 224. https://doi.org/10.1016/j.colsurfa.2006.07.037.

46 Awadallah-F, A., Elkhatat, A.M., and Al-Muhtaseb, S.A. (2011). Impact of synthesis conditions on meso- and macropore structures of resorcinol–formaldehyde xerogels. *J. Mater. Sci.* 46: 7760. https://doi.org/10.1007/s10853-011-5755-6.

47 Petričević, R., Reichenauer, G., Bock, V. et al. (1998). Structure of carbon aerogels near the gelation limit of the resorcinol–formaldehyde precursor. *J. Non-Cryst. Solids* 225: 41. https://doi.org/10.1016/S0022-3093(98)00006-4.

48 Moudrakovski, I.L., Ratcliffe, C.I., Ripmeester, J.A. et al. (2005). Nuclear magnetic resonance studies of resorcinol—formaldehyde aerogels. *J. Phys. Chem. B* 109: 11215. https://doi.org/10.1021/jp050610r.

49 Schwan, M., Tannert, R., and Ratke, L. (2016). New soft and spongy resorcinol–formaldehyde aerogels. *J. Supercrit. Fluids* 107: 201. https://doi.org/10.1016/j.supflu.2015.09.010.

50 Alviso, C. and Pekala, R. (1991). *Lawrence*. CA (USA): Livermore National Lab.

51 Hodgins, T., Hovey, A., Hewett, S. et al. (1941). Melamine-Formaldehyde film-forming compositions. *Ind. Eng. Chem.* 33: 769.

52 Schwan, M., Naikade, M., Raabe, D., and Ratke, L. (2015). From hard to rubber-like: mechanical properties of resorcinol–formaldehyde aerogels. *J. Mater. Sci.* 50: 5482. https://doi.org/10.1007/s10853-015-9094-x.

53 Ganesan, K., Dennstedt, A., Barowski, A., and Ratke, L. (2016). Design of aerogels, cryogels and xerogels of cellulose with hierarchical porous structures. *Mater. Des.* 92: 345. https://doi.org/10.1016/j.matdes.2015.12.041.

54 Ganesan, K., Heyer, M., Ratke, L., and Milow, B. (2018). Facile Preparation of Nanofibrillar Networks of "Ureido-Chitin" Containing Ureido and Amine as Chelating Functional Groups. *Chem. Eur. J.* 24: 19332. https://doi.org/10.1002/chem.201804405.

55 Nguyen, M.H. and Dao, L.H. (1998). Effects of processing variable on melamine–formaldehyde aerogel formation. *J. Non-Cryst. Solids* 225: 51. https://doi.org/10.1016/S0022-3093(98)00008-8.

56 Zhang, Y., Ren, H., Xu, J. et al. (2006). Synthesis and characterization of MF aerogels. *J. High Power Laser Part. Beams* 18: 1841.

57 Shang, C., Hu, W., Ren, H. et al. (2010). Catalyst-free preparation of low density melamine-formaldehyde aerogel. *J. High Power Laser Part. Beams* 22: 2901.

58 Pekala, R.W., Alviso, C.T., Kong, F.M., and Hulsey, S.S. (1992). Aerogels derived from multifunctional organic monomers. *J. Non-Cryst. Solids* 145: 90. https://doi.org/10.1016/S0022-3093(05)80436-3.

59 Ren, H., Zhu, J., Bi, Y. et al. (2018). Rapid fabrication of low density melamine–formaldehyde aerogels. *J. Porous Mater.* 25: 351. https://doi.org/10.1007/s10934-017-0446-6.

60 Nakanishi, Y., Hara, Y., Sakuma, W. et al. (2020). Colorless transparent melamine–formaldehyde aerogels for thermal insulation. *ACS Appl. Nano Mater.* 3: 49. https://doi.org/10.1021/acsanm.9b02275.

61 Principe, I.A. and Fletcher, A.J. (2018). Parametric study of factors affecting melamine-resorcinol-formaldehyde xerogels properties. *Mater. Today Chem.* 7: 5. https://doi.org/10.1016/j.mtchem.2017.11.002.

62 Zhou, H., Xu, S., Su, H. et al. (2013). Facile preparation and ultra-microporous structure of melamine–resorcinol–formaldehyde polymeric microspheres. *Chem. Commun.* 49: 3763. https://doi.org/10.1039/C3CC41109E.

63 Liu, X., Li, S., Mei, J. et al. (2014). From melamine–resorcinol–formaldehyde to nitrogen-doped carbon xerogels with micro- and meso-pores for lithium batteries. *J. Mater. Chem. A* 2: 14429. https://doi.org/10.1039/C4TA02928C.

64 Muehlemann, S.E., Huber, L., Zhao, S. et al. (2018). Facile synthesis of resorcinol-melamine-formaldehyde based carbon xerogel. *Mater. Today: Proc.* 5: 13776. https://doi.org/10.1016/j.matpr.2018.02.018.

65 Pizzi, A. (2003). Natural phenolic adhesives 1: tannin. In: *Handbook of Adhesive Technology* (ed. A. Pizzi and K.L. Mittal), 568–582. New York: Marcel Dekker.

66 Fraser, D.A., Hall, R.W., Jenkins, P.A., and Raum, A.L.J. (1957). Preparation of 'high-ortho' novolak resins. II. The course of the reaction. *J. Appl. Chem.* 7: 689. https://doi.org/10.1002/jctb.5010071208.

67 Fraser, D.A., Hall, R.W., and Raum, A.L.J. (1957). Preparation of 'high-ortho' novolak resins I. Metal ion catalysis and orientation effect. *J. Appl. Chem.* 7: 676. https://doi.org/10.1002/jctb.5010071207.

68 Pizzi, A. (1979). Phenolic and tannin-based adhesive resins by reactions of coordinated metal ligands. I. Phenolic chelates. *J. Appl. Polym. Sci.* 24: 1247. https://doi.org/10.1002/app.1979.070240510.

69 Pizzi, A. (1979). Phenolic and tannin-based adhesive resins by reactions of coordinated metal ligands. II. Tannin adhesive preparation, characteristics, and application. *J. Appl. Polym. Sci.* 24: 1257. https://doi.org/10.1002/app.1979.070240511.

70 Braghiroli, F.L., Amaral-Labat, G., Boss, A.F.N. et al. (2019). Tannin gels and their carbon derivatives: a review. *Biomolecules* 9: https://doi.org/10.3390/biom9100587.

71 Szczurek, A., Amaral-Labat, G., Fierro, V. et al. (2011). The use of tannin to prepare carbon gels. Part I: carbon aerogels. *Carbon* 49: 2773. https://doi.org/10.1016/j.carbon.2011.03.007.

72 Szczurek, A., Amaral-Labat, G., Fierro, V. et al. (2011). The use of tannin to prepare carbon gels. Part II. Carbon cryogels. *Carbon* 49: 2785.

73 Amaral-Labat, G., Szczurek, A., Fierro, V. et al. (2013). Systematic studies of tannin-formaldehyde aerogels: preparation and properties. *Sci. Technol. Adv. Mater.* 14: https://doi.org/10.1088/1468-6996/14/1/015001.

74 Amaral-Labat, G., Szczurek, A., Fierro, V., and Celzard, A. (2015). Unique bimodal carbon xerogels from soft templating of tannin. *Mater. Chem. Phys.* 149: 193. https://doi.org/10.1016/j.matchemphys.2014.10.006.

75 Roux, D.G., Ferreira, D., Hundt, H.K., and Malan, E. (1975). Structure, stereochemistry, and reactivity of natural condensed tannins as basis for their extended industrial application. *Conf.: Appl. Polym. Symp.* 1975: 335.

76 Naaß, D. (2020). Synthese und Entwicklung von Kohlenstoff-Aerogelen auf Basis von Tannin-Formaldehyd hinsichtlich des Einsatzes in Batterie- und Gießereianwendungen. Bachelor Thesis

77 Li, W. and Guo, S. (2000). Preparation of low-density carbon aerogels from a cresol/formaldehyde mixture. *Carbon* 38: 1520. https://doi.org/10.1016/S0008-6223(00)00114-7.

78 Li, W., Reichenauer, G., and Fricke, J. (2002). Carbon aerogels derived from cresol–resorcinol–formaldehyde for supercapacitors. *Carbon* 40: 2955. https://doi.org/10.1016/S0008-6223(02)00243-9.

79 Amaral-Labat, G., Szczurek, A., Fierro, V. et al. (2012). "Blue glue": a new precursor of carbon aerogels. *Microporous Mesoporous Mater.* 158: 272. https://doi.org/10.1016/j.micromeso.2012.03.051.

80 Grishechko, L.I., Amaral-Labat, G., Szczurek, A. et al. (2013). Lignin–phenol–formaldehyde aerogels and cryogels. *Microporous Mesoporous Mater.* 168: 19. https://doi.org/10.1016/j.micromeso.2012.09.024.

81 Castro, C.D. and Quintana, G.C. (2015). Mixture design approach on the physical properties of lignin-resorcinol-formaldehyde xerogels. *Int. J. Polym. Sci.* 2015: 272851. https://doi.org/10.1155/2015/272851.

82 Pérez-Caballero, F., Peikolainen, A.L., Uibu, M. et al. (2008). Preparation of carbon aerogels from 5-methylresorcinol–formaldehyde gels. *Microporous Mesoporous Mater.* 108: 230. https://doi.org/10.1016/j.micromeso.2007.04.006.

83 Aghabararpour, M., Mohsenpour, M., Motahari, S., and Ghahreman, A. (2019). Mechanical and thermal insulation properties of isocyanate crosslinked resorcinol formaldehyde aerogel: effect of isocyanate structure. *J. Appl. Polym. Sci.* 136: 48196. https://doi.org/10.1002/app.48196.

84 Mulik, S., Sotiriou-Leventis, C., and Leventis, N. (2008). Macroporous electrically conducting carbon networks by pyrolysis of isocyanate-cross-linked resorcinol-formaldehyde aerogels. *Chem. Mater.* 20: 6985. https://doi.org/10.1021/cm801428p.

85 Lu, X., Arduini-Schuster, M.C., Kuhn, J. et al. (1992). Thermal conductivity of monolithic organic aerogels. *Science* 255: 971.

86 Rey-Raap, N., Calvo, E.G., Menéndez, J.A., and Arenillas, A. (2017). Exploring the potential of resorcinol-formaldehyde xerogels as thermal insulators. *Microporous Mesoporous Mater.* 244: 50. https://doi.org/10.1016/j.micromeso.2017.02.044.

87 Aerogel Technologies, LLC. (2023). Spaceloft® Blanket. http://www.buyaerogel.com/product/spaceloft/ (accessed 4 December 2020).

88 Baetens, R., Jelle, B.P., and Gustavsen, A. (2011). Aerogel insulation for building applications: a state-of-the-art review. *Energy Build.* 43: 761. https://doi.org/10.1016/j.enbuild.2010.12.012.

89 Berardi, U. (2018). Aerogel-enhanced systems for building energy retrofits: insights from a case study. *Energy Build.* 159: 370. https://doi.org/10.1016/j.enbuild.2017.10.092.

90 Berthon-Fabry, S., Hildenbrand, C., and Ilbizian, P. (2016). Lightweight superinsulating resorcinol-formaldehyde-APTES benzoxazine aerogel blankets for space applications. *Eur. Polym. J.* 78: 25. https://doi.org/10.1016/j.eurpolymj.2016.02.019.

91 Hasegawa, G., Shimizu, T., Kanamori, K. et al. (2017). Highly flexible hybrid polymer aerogels and xerogels based on resorcinol-formaldehyde with enhanced elastic stiffness and recoverability: insights into the origin of their mechanical properties. *Chem. Mater.* 29: 2122. https://doi.org/10.1021/acs.chemmater.6b04706.

92 Yun, S., Luo, H., and Gao, Y. (2014). Ambient-pressure drying synthesis of large resorcinol–formaldehyde-reinforced silica aerogels with enhanced mechanical strength and superhydrophobicity. *J. Mater. Chem. A* 2: 14542.

93 Orellana-García, F., Álvarez, M.A., López-Ramón, M.V. et al. (2016). Photoactivity of organic xerogels and aerogels in the photodegradation of herbicides from waters. *Appl. Catal., B* 181: 94. https://doi.org/10.1016/j.apcatb.2015.07.044.

94 http://www.aerogel.com/products-and-solutions/all-insulation-products. Accessed: 4 December 2020.

95 Fairén-Jiménez, D., Carrasco-Marín, F., and Moreno-Castilla, C. (2006). Porosity and surface area of monolithic carbon aerogels prepared using alkaline carbonates and organic acids as polymerization catalysts. *Carbon* 44: 2301. https://doi.org/10.1016/j.carbon.2006.02.021.

96 Amaral-Labat, G., Szczurek, A., Fierro, V. et al. (2012). Pore structure and electrochemical performances of tannin-based carbon cryogels. *Biomass Bioenergy* 39: 274. https://doi.org/10.1016/j.biombioe.2012.01.019.

97 Zapata-Benabithe, Z., Carrasco-Marin, F., de Vicente, J., and Moreno-Castilla, C. (2013). Carbon xerogel microspheres and monoliths from resorcinol-formaldehyde mixtures with varying dilution ratios: preparation, surface characteristics, and electrochemical double-layer capacitances. *Langmuir* 29: 6166. https://doi.org/10.1021/la4007422.

98 Job, N., Pirard, R., Marien, J., and Pirard, J.-P. (2004). Porous carbon xerogels with texture tailored by pH control during sol–gel process. *Carbon* 42: 619. https://doi.org/10.1016/j.carbon.2003.12.072.

99 Wiener, M., Reichenauer, G., Hemberger, F., and Ebert, H.P. (2006). Thermal conductivity of carbon aerogels as a function of pyrolysis temperature. *Int. J. Thermophys.* 27: 1826. https://doi.org/10.1007/s10765-006-0086-6.

100 Lee, J.-H. and Park, S.-J. (2020). Recent advances in preparations and applications of carbon aerogels: a review. *Carbon* 163: 1. https://doi.org/10.1016/j.carbon.2020.02.073.

101 Szczurek, A., Amaral-Labat, G., Fierro, V. et al. (2014). Chemical activation of tannin-based hydrogels by soaking in KOH and NaOH solutions. *Microporous Mesoporous Mater.* 196: 8. https://doi.org/10.1016/j.micromeso.2014.04.051.

102 Horikawa, T., Hayashi, J., and Muroyama, K. (2004). Controllability of pore characteristics of resorcinol–formaldehyde carbon aerogel. *Carbon* 42: 1625. https://doi.org/10.1016/j.carbon.2004.02.016.

103 Saliger, R., Bock, V., Petricevic, R. et al. (1997). Carbon aerogels from dilute catalysis of resorcinol with formaldehyde. *J. Non-Cryst. Solids* 221: 144.

104 Kraiwattanawong, K., Tamon, H., and Praserthdam, P. (2011). Influence of solvent species used in solvent exchange for preparation of mesoporous carbon xerogels from resorcinol and formaldehyde via subcritical drying. *Microporous Mesoporous Mater.* 138: 8. https://doi.org/10.1016/j.micromeso.2010.10.001.

105 Lin, C. and Ritter, J.A. (2000). Carbonization and activation of sol–gel derived carbon xerogels. *Carbon* 38: 849. https://doi.org/10.1016/S0008-6223(99)00189-X.

106 Tao, Y., Endo, M., and Kaneko, K. (2008). A review of synthesis and Nanopore structures of organic polymer aerogels and carbon aerogels. *Recent Patents Chem. Eng.* 1: 192.

107 Hanzawa, Y., Hatori, H., Yoshizawa, N., and Yamada, Y. (2002). Structural changes in carbon aerogels with high temperature treatment. *Carbon* 40: 575. https://doi.org/10.1016/S0008-6223(01)00150-6.

108 Tamon, H., Ishizaka, H., Araki, T., and Okazaki, M. (1998). Control of mesoporous structure of organic and carbon aerogels. *Carbon* 36: 1257. https://doi.org/10.1016/S0008-6223(97)00202-9.

109 Wu, D., Fu, R., Sun, Z., and Yu, Z. (2005). Low-density organic and carbon aerogels from the sol–gel polymerization of phenol with formaldehyde. *J. Non-Cryst. Solids* 351: 915. https://doi.org/10.1016/j.jnoncrysol.2005.02.008.

110 Szczurek, A., Amaral-Labat, G., Fierro, V. et al. (2011). Porosity of resorcinol-formaldehyde organic and carbon aerogels exchanged and dried with supercritical organic solvents. *Mater. Chem. Phys.* 129: 1221. https://doi.org/10.1016/j.matchemphys.2011.06.021.

111 Schwan, M. and Ratke, L. (2016). Flexible Carbon Aerogels. *C* 2: 22.

112 Rege, A., Schwan, M., Chernova, L. et al. (2020). Microstructural and mechanical characterization of carbon aerogels: an in-situ and digital image correlation-based study. *J. Non-Cryst. Solids* 529: 119568. https://doi.org/10.1016/j.jnoncrysol.2019.119568.

113 Wang, J., Zhang, S.Q., Shen, J. et al. (2001). Electrical transport properties of carbon aerogels. *J. Porous Mater.* 8: 167. https://doi.org/10.1023/a:1009611329483.

114 Lu, X., Nilsson, O., Fricke, J., and Pekala, R.W. (1993). Thermal and electrical conductivity of monolithic carbon aerogels. *J. Appl. Phys.* 73: 581. https://doi.org/10.1063/1.353367.

115 Arenillas, A., Menéndez, J.A., Reichenauer, G. et al. (2019). Properties of carbon aerogels and their organic precursors. In: *Organic and Carbon Gels: From Laboratory Synthesis to Applications*, 87–121. Cham: Springer International Publishing.

116 Wiener, M., Reichenauer, G., Scherb, T., and Fricke, J. (2004). Accelerating the synthesis of carbon aerogel precursors. *J. Non-Cryst. Solids* 350: 126. https://doi.org/10.1016/j.jnoncrysol.2004.06.029.

117 Schwan, M., Schettler, J., Badaczewski, F.M. et al. (2020). The effect of pulverization methods on the microstructure of stiff, ductile, and flexible carbon aerogels. *J. Mater. Sci.* 55: 5861. https://doi.org/10.1007/s10853-020-04397-w.

118 Liang, C., Sha, G., and Guo, S. (2000). Resorcinol–formaldehyde aerogels prepared by supercritical acetone drying. *J. Non-Cryst. Solids* 271: 167. https://doi.org/10.1016/S0022-3093(00)00108-3.

119 Léonard, A., Job, N., Blacher, S. et al. (2005). Suitability of convective air drying for the production of porous resorcinol-formaldehyde and carbon xerogels. *Carbon* 43: 1808.

120 Bonijoly, M., Oberlin, M., and Oberlin, A. (1982). A possible mechanism for natural graphite formation. *Int. J. Coal Geol.* 1: 283. https://doi.org/10.1016/0166-5162(82)90018-0.

121 Kuhn, J., Brandt, R., Mehling, H. et al. (1998). In situ infrared observation of the pyrolysis process of carbon aerogels. *J. Non-Cryst. Solids* 225: 58. https://doi.org/10.1016/S0022-3093(98)00009-X.

122 Trick, K.A. and Saliba, T.E. (1995). Mechanisms of the pyrolysis of phenolic resin in a carbon/phenolic composite. *Carbon* 33: 1509. https://doi.org/10.1016/0008-6223(95)00092-R.

123 Far, H.M., Donthula, S., Taghvaee, T. et al. (2017). Air-oxidation of phenolic resin aerogels: backbone reorganization, formation of ring-fused pyrylium cations, and the effect on microporous carbons with enhanced surface areas. *RSC Adv.* 7: 51104. https://doi.org/10.1039/C7RA10958J.

124 Gruber, E.E. and Mullins, W.W. (1966). Extended analysis of surface scratch smoothing. *Acta Metall.* 14: 397. https://doi.org/10.1016/0001-6160(66)90098-8.

125 Mulik, S., Sotiriou-Leventis, C., Churu, G. et al. (2008). Cross-linking 3D assemblies of nanoparticles into mechanically strong aerogels by surface-initiated free-radical polymerization. *Chem. Mater.* 20: 5035. https://doi.org/10.1021/cm800963h.

126 Yang, J., Li, S., Yan, L. et al. (2010). Compressive behaviors and morphological changes of resorcinol–formaldehyde aerogel at high strain rates. *Microporous Mesoporous Mater.* 133: 134. https://doi.org/10.1016/j.micromeso.2010.04.025.

127 Zhang, S., Wang, J., Shen, J. et al. (1999). The investigation of the adsorption character of carbon aerogels. *Nanostruct. Mater.* 11: 375.

128 Baird, T., Fryer, J.R., and Grant, B. (1974). Carbon formation on iron and nickel foils by hydrocarbon pyrolysis—reactions at 700°C. *Carbon* 12: 591. https://doi.org/10.1016/0008-6223(74)90060-8.

129 Guo, S., Peng, J., Li, W. et al. (2009). Effects of CO_2 activation on porous structures of coconut shell-based activated carbons. *Appl. Surf. Sci.* 255: 8443. https://doi.org/10.1016/j.apsusc.2009.05.150.

130 Shen, J. and Guan, D.Y. (2011). Preparation and application of carbon aerogels. In: *Aerogels Handbook* (ed. A.M. Aegerter, N. Leventis, and M.M. Koebel), 813–831. New York, NY: Springer.

131 Guarín-Romero, J.R., Rodríguez-Estupiñán, P., Giraldo, L., and Moreno-Piraján, J.C. (2019). Study of adsorption of CO_2 and CH_4 on resorcinol–formaldehyde aerogels at high pressures. *J. Chem. Eng. Data* 64: 5263. https://doi.org/10.1021/acs.jced.9b00489.

132 Ahmadpour, A. and Do, D.D. (1995). Characterization of modified activated carbons: equilibria and dynamics studies. *Carbon* 33: 1393. https://doi.org/10.1016/0008-6223(95)00085-R.

133 Chen, W.-J., Shen, M.-Y., Li, Y.-L. et al. (2011). Electrical and mechanical properties of carbon aerogels/phenolic resin for nanocomposites. *Adv. Mater. Res.* 236–238: 1725. https://doi.org/10.4028/www.scientific.net/AMR.236-238.1725.

134 Howard, B. (1954). Low voltage electrolytic capacitor.

135 Simon, P. and Gogotsi, Y. (2008). Materials for electrochemical capacitors. *Nat. Mater.* 7: 845. https://doi.org/10.1038/nmat2297.

136 Zhang, L.L. and Zhao, X.S. (2009). Carbon-based materials as supercapacitor electrodes. *Chem. Soc. Rev.* 38: 2520. https://doi.org/10.1039/B813846J.

137 Mayer, S., Pekala, R., and Kaschmitter, J. (1993). The aerocapacitor: an electrochemical double-layer energy-storage device. *J. Electrochem. Soc.* 140: 446.

138 Saliger, R., Fischer, U., Herta, C., and Fricke, J. (1998). High surface area carbon aerogels for supercapacitors. *J. Non-Cryst. Solids* 225: 81. https://doi.org/10.1016/S0022-3093(98)00104-5.

139 Zapata-Benabithe, Z., Carrasco-Marín, F., and Moreno-Castilla, C. (2013). Electrochemical performance of Cu- and Ag-doped carbon aerogels. *Mater. Chem. Phys.* 138: 870.

140 Huang, K.-J., Wang, L., Zhang, J.-Z., and Xing, K. (2015). Synthesis of molybdenum disulfide/carbon aerogel composites for supercapacitors electrode material application. *J. Electroanal. Chem.* 752: 33. https://doi.org/10.1016/j.jelechem.2015.06.005.

141 Zhai, Z., Ren, B., Xu, Y. et al. (2019). Green and facile fabrication of Cu-doped carbon aerogels from sodium alginate for supercapacitors. *J. Organ. Electron.* 70: 246.

142 Moreno-Castilla, C. and Maldonado-Hódar, F.J. (2005). Carbon aerogels for catalysis applications: an overview. *Carbon* 43: 455. https://doi.org/10.1016/j.carbon.2004.10.022.

143 Einert, M., Wessel, C., Badaczewski, F. et al. (2015). Nitrogen-doped carbon electrodes: influence of microstructure and nitrogen configuration on the electrical conductivity of carbonized polyacrylonitrile and poly(ionic liquid) blends. *Macromol. Chem. Phys.* 216: 1930. https://doi.org/10.1002/macp.201500169.

144 Mirzaeian, M., Abbas, Q., Gibson, D., and Mazur, M. (2019). Effect of nitrogen doping on the electrochemical performance of resorcinol-formaldehyde based carbon aerogels as electrode material for supercapacitor applications. *Energy* 173: 809. https://doi.org/10.1016/j.energy.2019.02.108.

145 Park, D.-W., Cañas, N.A., Schwan, M. et al. (2016). A dual mesopore C-aerogel electrode for a high energy density supercapacitor. *Curr. Appl Phys.* 16: 658. https://doi.org/10.1016/j.cap.2016.03.021.

146 Lu, C., Huang, Y.H., Hong, J.S. et al. (2018). The effects of melamine on the formation of carbon xerogel derived from resorcinol and formaldehyde and its performance for supercapacitor. *J. Colloid Interface Sci.* 524: 209. https://doi.org/10.1016/j.jcis.2018.04.006.

147 Liu, C., Li, F., Ma, L.-P., and Cheng, H.-M. (2010). Advanced materials for energy storage. *Adv. Mater.* 22: E28. https://doi.org/10.1002/adma.200903328.

148 Gao, X.-r., Xing, Z., Li, Z.-j. et al. (2020). A review on recent advances in carbon aerogels: their preparation and use in alkali-metal ion batteries. *New Carbon Mater.* 35: 486. https://doi.org/10.1016/S1872-5805(20)60504-2.

149 Yang, X., Wei, C., and Zhang, G. (2016). Activated carbon aerogels with developed mesoporosity as high-rate anodes in lithium-ion batteries. *J. Mater. Sci.* 51: 5565.

150 Morales-Torres, S., Jirglova, H., Pastrana-Martinez, L.M., and Maldonado-Hodar, F.J. (2020). Influence of electrostatic interactions during the resorcinol-formaldehyde polymerization on the characteristics of Mo-doped carbon gels. *Processes* 8: 16. https://doi.org/10.3390/pr8060746.

151 Saquing, C.D., Cheng, T.-T., Aindow, M., and Erkey, C. (2004). Preparation of platinum/carbon aerogel nanocomposites using a supercritical deposition method. *J. Phys. Chem. B* 108: 7716. https://doi.org/10.1021/jp049535v.

152 Sarapuu, A., Kreek, K., Kisand, K. et al. (2017). Electrocatalysis of oxygen reduction by iron-containing nitrogen-doped carbon aerogels in alkaline solution. *Electrochim. Acta* 230: 81. https://doi.org/10.1016/j.electacta.2017.01.157.

153 Steiner, S.A., Baumann, T.F., Kong, J. et al. (2007). Iron-doped carbon aerogels: novel porous substrates for direct growth of carbon nanotubes. *Langmuir* 23: 5161. https://doi.org/10.1021/la063643m.

154 Wu, K., Zhang, L., Yuan, Y. et al. (2020). An iron-decorated carbon aerogel for rechargeable flow and flexible Zn–air batteries. *Adv. Mater.* 32: 2002292. https://doi.org/10.1002/adma.202002292.

155 Bekyarova, E. and Kaneko, K. (2000). Structure and physical properties of tailor-made Ce,Zr-doped carbon aerogels. *Adv. Mater.* 12: 1625. https://doi.org/10.1002/1521-4095(200011)12:21<1625::AID-ADMA1625>3.0.CO;2-9.

156 Baumann, T.F., Fox, G.A., Satcher, J.H. et al. (2002). Synthesis and characterization of copper-doped carbon aerogels. *Langmuir* 18: 7073.

157 Cotet, L., Gich, M., Roig, A. et al. (2006). Synthesis and structural characteristics of carbon aerogels with a high content of Fe, Co, Ni, Cu, and Pd. *J. Non-Cryst. Solids* 352: 2772.

158 Zhang, Y., Kang, D., Aindow, M., and Erkey, C. (2005). Preparation and characterization of ruthenium/carbon aerogel nanocomposites via a supercritical fluid route. *J. Phys. Chem. B* 109: 2617. https://doi.org/10.1021/jp0467595.

159 Zhang, S., Fu, R., Wu, D. et al. (2004). Preparation and characterization of antibacterial silver-dispersed activated carbon aerogels. *Carbon* 42: 3209. https://doi.org/10.1016/j.carbon.2004.08.004.

160 Fu, G., Liu, Y., Chen, Y. et al. (2018). Robust N-doped carbon aerogels strongly coupled with iron–cobalt particles as efficient bifunctional catalysts for rechargeable Zn–air batteries. *Nanoscale* 10: 19937. https://doi.org/10.1039/C8NR05812A.

161 Mahadik, D.B., Lee, Y.K., Kim, T. et al. (2018). Structural and electrochemical properties of SnO_2-carbon composite aerogels for Li-ion battery anode material. *Solid State Ionics* 327: 76. https://doi.org/10.1016/j.ssi.2018.10.025.

162 Mirzaeian, M. and Hall, P.J. (2009). Preparation of controlled porosity carbon aerogels for energy storage in rechargeable lithium oxygen batteries. *Electrochim. Acta* 54: 7444. https://doi.org/10.1016/j.electacta.2009.07.079.

163 Zhang, Y., Zhang, H., Li, J. et al. (2013). The use of mixed carbon materials with improved oxygen transport in a lithium-air battery. *J. Power Sources* 240: 390. https://doi.org/10.1016/j.jpowsour.2013.04.018.

164 Eftekhari, A. and Kim, D.-W. (2017). Cathode materials for lithium–sulfur batteries: a practical perspective. *J. Mater. Chem. A* 5: 17734. https://doi.org/10.1039/C7TA00799J.

165 Barai, P., Mistry, A., and Mukherjee, P.P. (2016). Poromechanical effect in the lithium–sulfur battery cathode. *Extreme Mech. Lett.* 9: 359. https://doi.org/10.1016/j.eml.2016.05.007.

166 Dörfler, S., Althues, H., Härtel, P. et al. (2020). Challenges and key parameters of lithium-sulfur batteries on pouch cell level. *Joule* 4: 539. https://doi.org/10.1016/j.joule.2020.02.006.

167 Fedorkova, A.S., Kazda, T., Gavalierova, K. et al. (2018). Synthesis and characterization of porous sulfur/MWCNTs composites with improved performance and safety as cathodes for Li-S batteries. *Int. J. Electrochem. Sci.* 13: 551. https://doi.org/10.20964/2018.01.67.

168 Ji, X., Lee, K.T., and Nazar, L.F. (2009). A highly ordered nanostructured carbon–Sulphur cathode for lithium–Sulphur batteries. *Nat. Mater.* 8: 500. https://doi.org/10.1038/nmat2460.

169 Li, G., Sun, J., Hou, W. et al. (2016). Three-dimensional porous carbon composites containing high sulfur nanoparticle content for high-performance lithium–sulfur batteries. *Nat. Commun.* 7: 10601. https://www.nature.com/articles/ncomms10601#supplementary-information.

170 Xin, S., Gu, L., Zhao, N.-H. et al. (2012). Smaller sulfur molecules promise better lithium–sulfur batteries. *J. Am. Chem. Soc.* 134: 18510. https://doi.org/10.1021/ja308170k.

171 Li, Z., Li, X., Liao, Y. et al. (2016). Sulfur loaded in micropore-rich carbon aerogel as cathode of lithium-sulfur battery with improved cyclic stability. *J. Power Sources* 334: 23. https://doi.org/10.1016/j.jpowsour.2016.10.003.

172 Balakumar, K. and Kalaiselvi, N. (2015). High sulfur loaded carbon aerogel cathode for lithium-sulfur batteries. *RSC Adv.* 5: 34008. https://doi.org/10.1039/C5RA01436K.

173 Milow, B., Schwan, M., Wagner, N., and Warth, F. (2018). Elastisch verformbare Kohlenstoffaerogele als Matrixmaterial in Schwefelelektroden. DE102018123285.3

174 Liu, Y., Cui, C., Liu, Y. et al. (2020). Application of MoS_2 in the cathode of lithium sulfur batteries. *RSC Adv.* 10: 7384. https://doi.org/10.1039/C9RA09769D.

175 Li, X., Zhao, K., Zhang, L. et al. (2017). MoS_2-decorated coaxial nanocable carbon aerogel composites as cathode materials for high performance lithium-sulfur batteries. *J. Alloys Compd.* 692: 40. https://doi.org/10.1016/j.jallcom.2016.09.004.

176 Li, X., Pan, L., Wang, Y., and Xu, C. (2016). High efficiency immobilization of sulfur on Ce-doped carbon aerogel for high performance lithium-sulfur batteries. *Electrochim. Acta* 190: 548. https://doi.org/10.1016/j.electacta.2016.01.009.

177 Zhang, Z., Jiang, S., Lai, Y. et al. (2015). Selenium sulfide@mesoporous carbon aerogel composite for rechargeable lithium batteries with good electrochemical performance. *J. Power Sources* 284: 95. https://doi.org/10.1016/j.jpowsour.2015.03.019.

178 Ma, L., Li, X., Gao, W. et al. (2020). The immobilizing polysulfide mechanism of cadmium-doping carbon aerogels via a microtemplate for high performance Li–S batteries. *New J. Chem.* 44: 1001. https://doi.org/10.1039/C9NJ05405G.

179 Ye, H., Ma, L., Zhou, Y. et al. (2017). Amorphous MoS_3 as the sulfur-equivalent cathode material for room-temperature Li–S and Na–S batteries. *Proc. Natl. Acad. Sci.* 114: 13091. https://doi.org/10.1073/pnas.1711917114.

180 Jiang, S., Zhang, Z., Lai, Y. et al. (2014). Selenium encapsulated into 3D interconnected hierarchical porous carbon aerogels for lithium–selenium batteries with high rate performance and cycling stability. *J. Power Sources* 267: 394. https://doi.org/10.1016/j.jpowsour.2014.05.116.

181 Ye, H., Wang, L., Deng, S. et al. (2017). Amorphous MoS_3 infiltrated with carbon nanotubes as an advanced anode material of sodium-ion batteries with large gravimetric, areal, and volumetric capacities. *Adv. Energy. Mater.* 7: 1601602. https://doi.org/10.1002/aenm.201601602.

182 Oudenhoven, J.F.M., Baggetto, L., and Notten, P.H.L. (2011). All-solid-state lithium-ion microbatteries: a review of various three-dimensional concepts. *Adv. Energy Mater.* 1: 10. https://doi.org/10.1002/aenm.201000002.

183 Chen, Y., Zhang, Z., Lai, Y. et al. (2017). Self-assembly of 3D neat porous carbon aerogels with NaCl as template and flux for sodium-ion batteries. *J. Power Sources* 359: 529. https://doi.org/10.1016/j.jpowsour.2017.05.066.

184 Pan, Y., Cheng, X., Gao, M. et al. (2020). Cagelike $CoSe_2$@N-doped carbon aerogels with pseudocapacitive properties as advanced materials for sodium-ion batteries with excellent rate performance and cyclic stability. *ACS Appl. Mater. Interfaces* 12: 33621. https://doi.org/10.1021/acsami.0c06296.

185 Meyer, E., Barowsk, A., Schestakow, M. et al. (2016). Aerogele als Sandkernadditive zur Verbesserung der Gussteilqualität. *Giesserei* 103: 40.

186 Milow, B., Nolte, E., and Lorenz, R (2006). Kernwerkstoff aus Aerogelsand enthaltend Additivsand und dessen Verwendung. DE102006056093B4

187 Biener, J., Stadermann, M., Suss, M. et al. (2011). Advanced carbon aerogels for energy applications. *Energy Environ. Sci.* 4: 656. https://doi.org/10.1039/c0ee00627k.

188 Kabbour, H., Baumann, T.F., Satcher, J.H. et al. (2006). Toward new candidates for hydrogen storage: high-surface-area carbon aerogels. *J. Chem. Mater.* 18: 6085.

189 Tian, H.Y., Buckley, C.E., Wang, S.B., and Zhou, M.F. (2009). Enhanced hydrogen storage capacity in carbon aerogels treated with KOH. *Carbon* 47: 2128. https://doi.org/10.1016/j.carbon.2009.03.063.

190 Yu, S., Song, S., Li, R., and Fang, B. (2020). The lightest solid meets the lightest gas: an overview of carbon aerogels and their composites for hydrogen related applications. *Nanoscale* 12: 19536. https://doi.org/10.1039/D0NR05050D.

191 Feng, J., Zhang, C., and Feng, J. (2012). Carbon fiber reinforced carbon aerogel composites for thermal insulation prepared by soft reinforcement. *Mater. Lett.* 67: 266. https://doi.org/10.1016/j.matlet.2011.09.076.

192 Wiener, M., Reichenauer, G., Braxmeier, S. et al. (2009). Carbon aerogel-based high-temperature thermal insulation. *Int. J. Thermophys.* 30: 1372. https://doi.org/10.1007/s10765-009-0595-1.

193 Federal Ministry for Economic Affairs and Climate Action. (2020). Innovative thermal insulation for high-temperature furnaces. https://www.bmwi-energiewende.de/EWD/Redaktion/EN/Newsletter/2020/09/Meldung/news2.html (accessed 15 December 2020).

194 Gholipour, F. and Mofarahi, M. (2016). Adsorption equilibrium of methane and carbon dioxide on zeolite 13X: experimental and thermodynamic modeling. *J. Supercrit. Fluids* 111: 47. https://doi.org/10.1016/j.supflu.2016.01.008.

195 Ello, A.S., Yapo, J.A., and Trokourey, A. (2013). N-doped carbon aerogels for carbon dioxide (CO_2) capture. *Afr. J. Pure Appl. Chem.* 7: 61.

196 Zhang, S.Q., Huang, C.G., Zhou, Z.Y., and Li, Z. (2002). Investigation of the microwave absorbing properties of carbon aerogels. *Mater. Sci. Eng., B* 90: 38. https://doi.org/10.1016/S0921-5107(01)00750-4.

11

Carbonaceous Aerogels for Fuel Cells and Supercapacitors

Meryem Samancı[1] *and Ayşe Bayrakçeken Yurtcan*[1,2]

[1] *Faculty of Engineering, Department of Chemical Engineering, Atatürk University, Erzurum, 25240, Turkey*
[2] *Department of Nanoscience and Nanoengineering, Atatürk University, Erzurum, 25240, Turkey*

11.1 Introduction

Until the past 50–60 years ago, humanity's basic needs such as heating, transportation and electricity were met by natural energy sources including coal, oil and natural gas, which contain high carbon and hydrocarbons. Currently, the most important part of global electricity generation is also provided by these natural resources. However, energy requirements are increasing rapidly increasing population and the effects of developments in industry and technology. In this case, it causes rapid depletion of fossil fuels. The energy supply is predicted to double by 2050 [1]. This situation has increased the use of renewable energy sources such as wind, tidal, wave, solar, hydrogen, hydraulic (hydroelectric), and biomass energy in the last decade. High efficiency storage and conversion technologies are required to ensure widespread use of renewable energies. In particular, the trend toward work on energy conversion (fuel cells) and storage (supercapacitors) has increased tremendously in the last 20 years due to environmental concerns.

Direct electricity is generated in fuel cells as a result of the reaction of hydrogen fuel (obtained from fossil fuels and other alternative fuels) with oxygen or air. In other words, fuel cells are the energy conversion devices that convert chemical energy directly into electrical energy. The most important barrier in the technological development of the fuel cell is to increase the catalytic activity and mechanical strength of the catalysts. In this context, it was very much work done to improve catalysts in fuel cells. These studies are generally directed at the preparation of the supports to ensure more efficient and homogeneous spread of catalysts along the electrode area. The use of the support material has resulted in improved catalyst activity (high contact surface area of the catalyst and minimizing agglomeration) and less use of the catalyst amount and consequently decrease the fuel cell costs to a minimum [2, 3].

Supercapacitors, also called ultracapacitors and electrochemical capacitors (ECs), have a lot of applications in energy storage technology. Supercapacitors are systems that can store electrical energy physically and chemically. Supercapacitors, as a modern energy storage system with the most fascinating features such as long cycle life, environmental safety, high energy and power density, offer the best solutions for electrical energy needs in our daily life. It is used in electric and hybrid electric vehicles, industrial equipment, warships, power generation plants, uninterrupted

Aerogels for Energy Saving and Storage, First Edition. Edited by Meldin Mathew, Hanna J. Maria, Ange Nzihou, and Sabu Thomas.
© 2024 John Wiley & Sons, Inc. Published 2024 by John Wiley & Sons, Inc.

and backup power supplies and consumer devices (digital cameras). In addition, supercapacitors can be used as circuit elements with fuel cells or batteries found in some energy devices. It is determined by electrodes designed using nano and micro technologies to improve the performance and capacity of a supercapacitor. Choosing a suitable electrolyte can also increase the energy density of the supercapacitor system [4–8]. There is a lot of research on synthesizing advanced electrode materials to improve the performance of fuel cells and supercapacitors [9]. The materials to be used for the electrode must have high durability, specific surface area, porosity, and electronic and ionic conductivity [10].

New carbonaceous materials with superior superficial, morphological, and electrical properties are constantly being investigated and studied as electrode materials in potential supercapacitors and fuel cells. Extensive research has been conducted to produce carbonaceous materials with the desired specific properties for use in fuel cells and supercapacitors. Another important class of nanomaterials are aerogels due to their excellent three-dimensional properties and superior performance. These structures are widely used materials for a variety of energy applications, such as adsorption, catalysis, energy storage and conversion. In this sense, aerogels, in which different carbonaceous materials are used as precursors, draw attention with their specific surface properties. Studies have shown that three-dimensional (3D) carbon aerogel structures attract great attention in many fields of energy (especially fuel cells and supercapacitors) due to their physicochemical, electrochemical, and thermal properties [11]. In addition, such carbonaceous materials and carbonaceous aerogel can provide alternative solutions instead of nonrenewable energy sources.

11.2 Carbonaceous Materials

Until the end of the 1900s, only graphite and diamond were known as the carbonaceous material family. For many years, carbon science was an intriguing one that emerged at the end of the twentieth century, with discoveries of the fullerenes by Kroto et al. in 1985 [12], of the carbon nanotubes by Iijima in 1991 [13], and finally of the graphene by Geim and Novoselov in 2004 (Figure 11.1) [14]. Carbonaceous materials mean to materials composed of and contain carbon. Carbon has a very different place among chemical elements due to its high natural abundance, low specific gravity, and its availability in various solid forms or allotropes. Due to the chemical and thermal sturdiness of different carbon allotropes, it has been used more and more in high performance materials in the last 20 years [15]. In particular, it can be used in a wide variety of fields, such as new energy sources, energy storage, sustainable chemical technology, high performance construction materials, and organic electronic materials [16].

Carbonaceous materials play an essential role in the systems where electrochemical energy is converted and stored. Carbon is used in the composite electrodes of the systems where energy is converted and stored, with the help of porous tubular channels that transmit the charge, to effectively transmit and distribute current. Carbonaceous materials are easily processed, abundant, and environmentally friendly, attracting the attention of researchers.

Graphite is a naturally occurring form of carbon and was discovered in 1564. Graphite atoms consist of layered structures in 2D honeycomb shape, hexagonal, and rhombus forms. Its parallel layers are weakly connected by van der Waals forces, and the distance between the layers is about 0.335 nm. The energy connecting the interlayer graphene layers is about 5.9 kJ mol^{-1}. Later, graphene was discovered and became the new star of the carbon family [14]. Graphene (2D) is defined as the monolayer form of graphite with sp^2 hybridized carbon atom style, arranged in a hexagonal lattice. Three of the four valence electrons in carbon atoms form sp^2 hybrid bonds. It forms a

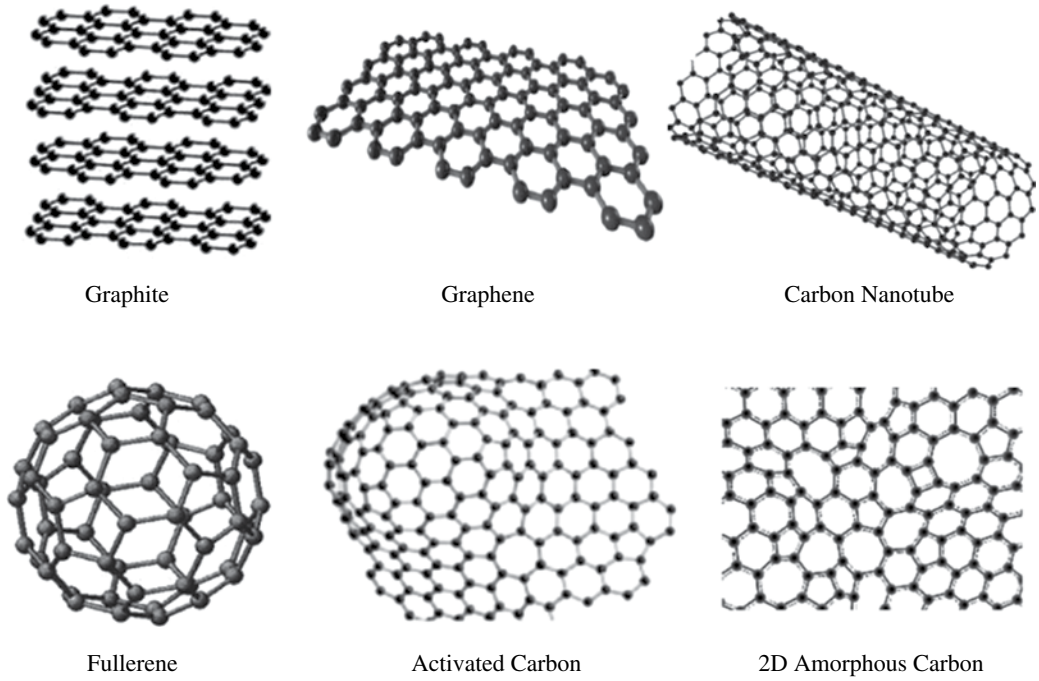


Figure 11.1 Different structures of carbon material.

π bond and these moving π electrons also make graphene a good conductor, which is suitable for energy applications.

Graphene is named according to the number of layers. It is known as two-layer graphene if it has two layers and three-layer graphene if it has three layers. Graphene from 5–10 layers is called few layers-graphene. Graphene up to ~20–30 layers is called multilayer graphene, thick graphene, or nanocrystalline thin graphite. The planar atomic structure of graphene is also used as a precursor material (under the influence of weak interactions) to synthesize other graphitic materials. Two-dimensional (2D) graphene forms three-dimensional (3D) graphite when stacked, one-dimensional (1D) carbon nanotubes when rolled, and zero-dimensional (0D) fullerene when folded [17, 18]. Porous materials made of graphene have some important properties. First, graphene allows to increase the mechanical strength and stability of highly porous structures with an aspect ratio. It also prevents these structures from shrinking or collapsing. Second, graphene's unique thermal and chemical stability prevents these materials from deforming under different operating conditions. Third, tubular paths in these materials are suitable for easy access of electrolytes into the structure. In addition, graphene's superior electrochemical properties serve as an ideal current collector for fast transport of charges within the structure. Fourthly, it is the precursor material for synthesizing graphene derivatives with different physical (more imperfect) and chemical properties (containing functional groups of oxygen) such as graphene oxide (GO) and reduced graphene oxide (RGO). Because these graphene-based materials are more active in structure, different types of chemicals (organic or inorganic types) can be easily bonded. This also makes it easy to make three-dimensional materials such as graphene aerogels. [19]. Graphene is widely used, especially in the energy field, due to its high surface area, unique electronic and thermal conductivity, superior mechanical and electrochemical stability and good transparency [20].

Materials with graphene and graphene substructures (GO, RGO, graphene aerogels) are the most versatile and most promising nanotechnological materials, especially for energy applications. These materials are perfectly suited for storing electrical charge, gas storage and catalytic reactions by combining very good electrical conductivity with specific area to weight ratio [21]. Various energy devices such as batteries [22], supercapacitors [23], H_2 storage tanks [24], fuel cells [25], and photovoltaic (PV) cells [26] can use these materials.

The methods used to prepare the graphene are currently intensively researched. Various physical and chemical methods (bottom-up or top-down methods) are used for the current graphene production. The five most obvious of these are [20, 27, 28]:

1) Exfoliation of the graphene sheet by mechanical or chemical techniques
2) Epitaxial growth of graphene on SiO_2 substrate
3) Chemical vapor deposition (CVD) of monolayers graphene
4) Unrolling of CNTs either through electrochemical, chemical or physical techniques
5) Reduction of GO by many methods such as chemically or thermally (many other organic synthetic protocols)

In 1991, Ijima discovered the CNT structure [13]. CNT, which have very good physical, thermal and electrical properties, can be prepared using many different techniques (generally catalytic decomposition of hydrocarbons (CVD), arc discharge, laser ablation). The surface of the CNT electrodes is mostly mesoporous in relation to the outer surface of the tubes. They usually consist of very narrow and long layers of graphite (graphene) that are rounded in a tubular shape with both ends closed. Both single and multiwall nanotubes are available in several nanometer diameters and 1 mm lengths [17, 29, 30].

In 1985, Kroto and Smalley discovered one of the carbon allotropes, buckminsterfullerene [12], in which each carbon atom is in a corner where two six-membered rings and one five-membered ring come together. The most studied and stable fullerene is the C_{60} (nicknamed "Buckyball"). Other fullerenes having carbon cages with different sizes were also synthesized, for example C_{140}, C_{260}, and C_{960}. Since its discovery, in nature buckminsterfullerene was found to occur occasionally. Fullerenes are part of new carbon materials used in energy applications due to their high electrochemical stability, nanometer size, specific morphology, regular structures, and some special properties (such as high electroconductivity, good thermal conductivity, and special mechanical properties). It is also possible to change the chemical functional groups of the fullerene and control the pore structure [17, 31]. Plasma and pyrolysis techniques are generally used in the production of fullerenes [32]. CVD technique is one of the synthesis methods that can be used easily if much production is to be made [33]. In addition, arc discharge is one of the widely used methods. However, its reaction is difficult to control and many impurities are present in the resulting fullerene structures [34].

Activated carbons (ACs) are the oldest and most common type of porous carbon. The earliest use of AC goes back to Egypt as early as 1550 BCE [35]. AC is an irregular form of carbon with small pores and a high surface area. The specific surface area is usually in the range of 1000–3000 $m^2g{-}^1$. Most of the pores in ACs are in the 0.4–4 nm range. Naturally sourced precursors and synthetic polymers can be used for activated carbon synthesis. The activation process is done using thermal (physical activation: carbonization of a precursor and gasification [thermal decomposition]) and chemical (partial oxidation with a chemical reagent) techniques [7, 36]. ACs have carbon structure with mixed pore size (micropores, mesopores, and macropores) containing small amounts of different heteroatoms such as oxygen and hydrogen. The differences in the chemical properties of ACs determine the differences of these heteroatoms in their structures. The type and amount of

these elements are either derived from the nature of the starting material or added during the activation process [37]. The precursor materials used in AC synthesis can be obtained from coconut shell, fossil fuels, natural renewable sources, or unnatural precursors [38].

Recently, a lot of work was done on the conversion of carbon-rich biological resources into carbonaceous materials as an alternative to fossil fuels. In the light of these studies, recycling of wastes and making innovative material designs with environmentally friendly, low cost and simple methods has attracted great attention. Due to the abundance of biomass resources worldwide, it has facilitated the design and synthesis of high performance sustainable electrode materials in all aspects of energy. Biomass resources are divided into main categories: mushroom-based biomass, bacterial-based biomass, seaweed and plant-based biomass, herbaceous and agricultural biomass, human waste-based biomass, industrial waste or contaminated semi-biomass and animal-based biomass [39]. The conversion of biomass to carbonaceous materials is carried out by various techniques, which are divided into three processes as biological, chemical, and thermochemical. Biomass-derived carbonaceous materials with different properties can be used for environmental and energy applications [40].

Several carbon substructure materials developed for energy applications have attract researchers' attention. Some important information about these carbonaceous materials is given in Table 11.1.

Apart from these materials, there are other carbonaceous materials that are widely used in energy fields. These are carbon-based materials such as carbon nanocoils, mesoporous carbon, carbon black (CB), carbon nanofibers (CNF), carbide-derived carbon, and carbonaceous aerogels.

11.3 Carbonaceous Aerogels

11.3.1 What Are Aerogels?

Recently, highly porous conductive materials have been rapidly developed in the fields of electrochemistry, biochemistry and renewable energies (systems where energy is converted and stored). In this sense, aerogels, in which different carbon materials are used as precursors, draw attention with their specific surface properties. Aerogels are typical nanomaterials first synthesized by Samuel Kistler in 1932 [51]. The physicochemical properties of aerogels depend on different parameters such as the chemical structure of the precursor synthesis material, reactant concentrations (especially catalyst ratio), reaction conditions (pH and gelation temperature), and drying technique [52]. Aerogels are porous materials prepared with sol-gel technique, in which the liquid in its structure is replaced with gas to obtain a durable nanostructure without pore collapse. The conditions of the drying process have a great effect on the aerogel structure. Due to the interconnected skeletal structure of the aerogels (three-dimensional structure 3D), it has attractive physicochemical (high specific surface area, porous structures, low density, low thermal conductivity, mechanical strength, time-dependent stability in working conditions) and electrochemical (very good electrical conductivity, dielectric constant) properties. Aerogels are nanoporous solids with low density (0.003–0.15 kg m^3), large surface area (500–1000 m^2 g^{-1}), thin, open and high porosity (>90% v/v). Recently, it has been widely researched because of its unique properties of aerogels. Therefore, it is an attractive material for aerogels, electrocatalyst (fuel cells) [53], photocatalyst [54], adsorption (CO_2 removal, H_2 storage) [55], optical [56], energy storage (supercapacitors) [57], chemical sensors [58], heat insulations [59], adsorbents [60], catalysts, and applications in space exploration [61, 62]. Aerogels are the lightest solid materials known and produced nowadays at an industrial scale.

Depending on the physical condition, aerogels are classified into three types as monolith, powder and film. They are classified as aerogel, xerogel, cryogel, and hydrogels according to the form

Table 11.1 General remarks about carbonaceous materials.

Carbonaceous materials	Properties	Advantages	Disadvantages	Usage areas	Refs.
Graphene	Hexagonal, 2D monolayer Surface area: 2500–3000 $m^2 g^{-1}$ Electrical conductivity: 103–106 S m^{-1} Thermal conductivity: ~6000 $Wm^{-1} K^{-1}$ Young's modulus: ~1000 Gpa Carrier mobility: ~200 000 $cm^2 V^{-1} s^{-1}$ Transmittance: 97.7% Band gap value: ~0 to 0.25 eV Breaking strength: 42 N m^{-1}	High surface area, Stable electrochemical and thermal properties, Extraordinary magnetic properties, High strength, Flexible structure, Gas adsorption, Favorable light absorption range, Charge-transfer interactions with molecules, Room temperature Hall effect, High Young's modulus, Effective moisture barrier	Tendency for irreversible agglomerates, Graphitization, Challenge of structural modifications,	Absorbents, Catalysis, Sensors, Fuel cells, Solar cells, Supercapacitors, Biomedical applications, Microelectronic or nanoelectronic devices	[27, 41–43]
Carbon nanotube	Cylindrical 1D structure Aspect ratio: >1000 Zigzag, armchair, chiral SWCNTs diameters: ~1 nm, DWCNTs outer diameter: 1.9–5 nm MWCNTs diameter: 4–50 nm Young's modulus: ~1 to 1.8 TPa Thermal conductivity: ~2800–6000 W $m^{-1} K^{-1}$	High crystallinity, High surface area, Smooth surface topology, Perfect surface specificity, Mesoporous structure, High current carrying, conductive. Strong, Flexible	Inert surface, Poor catalytic activity (oxygen reduction reaction in fuel cells-ORR), Poor solubility in biological environments, Difficulty of CNT production with the same features, Difficulty in maintaining minimum impurities,	Fuel cells, Supercapacitors, Catalysis, Hydrogen storage, Field emission devices, Chemical and biological sensors and probes Biomedical applications, Carrier for drug delivery, Antioxidant (to preserve drugs formulations), Superhydrophobic surfaces	[44, 45]

Downloaded from https://onlinelibrary.wiley.com/doi/ by ibrahim ragab - Universita Di Firenze Sistema , Wiley Online Library on [21/07/2024]. See the Terms and Conditions (https://onlinelibrary.wiley.com/terms-and-conditions) on Wiley Online Library for rules of use; OA articles are governed by the applicable Creative Commons License

Fullerene	0D structure Chemically so reactive diameter: 7–10 Å Density: 1.65 g cm^{-3} Carrier mobility: 0.02 cm^2 V^{-1} s^{-1}	High electron affinity, Density of functional groups, The ability to scavenge radicals	Low electrical conductivity, Difficulty and cost of synthesizing at high purity	Organic solar cells, Supercapacitors, Fuel cells, Hydrogen storage, Medicine, Environmental remediation	[46]
Activated carbon	3D structure Pore size distribution: 0.4–4 nm Specific surface area: 1000–3000 m^2 g^{-1} Natural renewable resources, coconuts hells wood, fossil fuels (pitch, coal or coke) Synthetic precursors: polymers	High specific surface area, Wide pore distribution, Unique electrochemical properties, Low costs, Easy and environmentally friendly production	Ion access limited in non-aqueous electrolytes, Precise control over the pore structure, It is difficult to recover, Adsorption capacity decreases over time.	Supercapacitor, Fuel cells, Absorbents, Hydrogen storage, Environmental Remediation, Drinking water treatment, Industrial filters	[7, 36, 38]
Biomass-Derived Porous Carbon	Surface Areas: >1000 m^2 g^{-1} Pore volumes: >1 cm^3 g^{-1} 1D Biomass Carbon: Young's modulus: 138 Gpa Strength: 2–3 GPa Chitosan (chitin [crabs, lobsters, insects, and fungi.]) Lignin (wood pulp, cotton, hemp) Tannin (Roots, barks, leaves, fruits) Biomass waste	A wide range of sizes of porosity, Resistance to different pH, Cheap, Accessibility, Easy recycling, Hydrophobic structure, High porosity, Large contact surface area, Its pore structure facilitates ion transport, Environmentally harmless, Biodegradable, Sustainability, Renewable nature	Their synthesis involves many steps, Low carbon yield and by-products due to the chemical substance used in the synthesis, Pore structures and sizes are difficult to optimize and control, Poor interface interactions between pseudo-capacitive components and carbon materials	Heterogenous catalysis, Supercapacitance, Adsorption Lithium ion batteries, High-temperature insulation materials, Filter materials, Hydrogen storage, Water treatment,	[47–50]

Downloaded from https://onlinelibrary.wiley.com/doi/ by ibrahim ragab - Universita Di Firenze Sistema , Wiley Online Library on [21/07/2024]. See the Terms and Conditions (https://onlinelibrary.wiley.com/terms-and-conditions) on Wiley Online Library for rules of use; OA articles are governed by the applicable Creative Commons License

of preparation (usually with different drying techniques). In addition, aerogels are divided into three main categories according to their precursor materials during synthesis. They are inorganic, organic, and composite aerogels. Inorganic aerogels are aerogels using metal doped precursors. Organic aerogels include carbonaceous and polymeric aerogels prepared from organic precursor materials. Composite aerogels are a type of aerogel prepared with a combination of inorganic and organic precursors. Carbon, CNT, graphene, activated carbon, and biomass derived aerogels are the most prominent among these carbonaceous aerogels. The specific characteristics of different carbonaceous aerogels are given in the Table 11.2.

Table 11.2 Properties of different carbonaceous aerogels.

Carbonaceous aerogels	Precursors	Properties/Characteristics	Refs.
Carbon aerogels	Aromatics and aldehydes Polymers	High purity and structural controllability, Pore size: 2–50 nm, Porosity: 90–99%, Specific surface area: 400–1000 $m^2\ g^{-1}$, Supercapacitor, batteries, catalysis, gas storage, separation, thermal insulation.	[52, 63, 64]
Carbon nanotube based aerogels	SWCNTs, DWCNTs, MWCNTs, Catalysts, Supports, Surfactant	3D porous structure, Low mass densities (7.3–13.1 mg ml^{-1}), Continuous porosities robust mechanical properties, Excellent flexibility, Lightness, High electrical (1 S cm^{-1}) and thermal conductivity, Surface area (1315 $m^2\ g^{-1}$), Microscopic and macroscopic electronic application	[65–67]
Graphene aerogels	Graphene, GO, RGO	Rapid electron/ion transport, Good chemical and physical stability, Good cycle performance, Cheap material Specific surface area (361–763 $m^2\ g^{-1}$) Supercapacitors, batteries, fuel cells and solar cells, sensors, biomedicine, H_2 and thermal energy storage,	[43, 68, 69]
Activated carbon aerogels	Carbon aerogel, Chemical activator: inorganic acids, alkali hydroxides, inorganic salts, Physical activator: H_2O (steam), CO_2, air	Wide variety of porosity and shape, Very high specific surface area The raw materials and long production process are quite expensive, Absorbents, fuel cell, Supercapacitor	[70, 71]
Biomass-derived aerogels	Hydrated biomass, Highly porous biomass, Cellulose, chitosan, lignin, tannin and biomass waste	Low cost, environmentally, abundant electrochemical active surfaces, short ion transport paths (easy accessibility), Difficult morphology control and incomplete activation, Friendly nature drug delivery, catalysis, Supercapacitors, batteries, gas sensor, CO_2 sequestration, biomedical devices, supercapacitors, absorbents	[49, 57, 71]

Many difficulties are encountered during the aerogel synthesis. First of all, during the preparation of aerogels, due to the long and challenging synthesis steps, it is necessary to minimize the cost by developing different synthesis techniques. The most important of these is the reduction of capillary tension during drying. At the end of these applications, aerogels will have a better three-dimensional pore structure with low-cost synthesis techniques [49].

11.3.2 Carbon Aerogels

The most commonly used aerogels are organic aerogels. Pekala and Kong defined and described the first organic aerogels in the late 1980s [72]. Their designs are based on resorcinol-formaldehyde (RF) resins. However, other types of materials of this class began to be used later. Not only resorcinol-formaldehyde resins, but also many chemicals such as phenol-formaldehyde, melamine formaldehyde, cresol-formaldehyde, phenol-furfural as well as polyamides, polyacrylamides, polyacrylonitriles, polyacrylates, polystyrenes, and polyurethanes [73, 74].

The synthesis of carbon aerogels takes place in three stages: polymerization (sol-gel process), drying, and carbonization. The first important process is polymerization. Here, the solution with highly diluted reactants is mixed thoroughly before the reaction begins. This process generally involves two main steps at the molecular level: (i) creation or activation of reactive regions; and (ii) formation of monomer and oligomer clusters by cross-linking reactive regions. At the end of this process, 3D carbon hydrogel (via crosslinking and agglomeration) is formed [71]. The kinetics of the polymerization step is controlled by various parameters, for example, the concentration of reactants, solvent, catalyst used, catalyst concentration (pH value), temperature, and steric effects [62, 75].

The second important process step for synthesizing an aerogel is removing the liquid from the interconnected pores of the gel – that is, drying. Drying conditions are the most important parameter affecting the structure. Different names are given to the synthesized gel products according to their drying techniques – aerogel by supercritical drying, cryogel by freeze drying, and xeogel by drying under ambient conditions. Apart from these, it is available in hydrogels [71, 76].

The most important drying technique is the supercritical drying technique, which is the most important drying technique used in aerogel synthesis. Supercritical drying is the extraction of a fluid in the supercritical state (critical temperature [T_c] and pressure [P_c]) with another fluid in the pores of the material. Supercritical drying yields gels with higher porosity and uniform structures than other drying techniques. The most commonly used supercritical fluid is supercritical carbon dioxide ($SCCO_2$) [71, 77, 78]. Apart from that, supercritical drying has disadvantages such as being costly, dangerous, complex and time consuming [79, 80]. In freeze drying, the temperature is lowered to provide the solidification (crystallization) of the liquid in the hydrogel. Water converted to ice is removed as vapor under reduced pressure without creating a gas-liquid interface (sublimation). Freeze drying is a simple, relatively affordable and environmentally friendly technique [81, 82]. The main advantage of the ambient pressure method is that it does not require low cost and dangerous high pressure equipment. Although it is a promising method, drying in the environment creates serious capillary tension at the solid-liquid vapor interface, which causes structural shrinkage. Solvent replacement in several stages is required to overcome this problem [83, 84]. Apart from these drying methods, microwave [85] and vacuum drying [86] methods are also used.

After drying, the mechanical stability (microporous properties) of an aerogel is improved by pyrolysis in an inert atmosphere (N_2 or Ar) in the temperature range of 773 and 2500 K. During the

carbonization process, hydrogen and oxygen functional groups, excess water, and other liquids move away from the gases in the structure and leave the 3D carbonated aerogel structure behind. The physical (specific surface area) and electrochemical properties (high electrical conductivity) of aerogels subjected to the carbonization process under different conditions change significantly [62, 87].

Studies have been conducted in many areas related to energy, centered on carbon aerogels such as supercapacitors [88], fuel cells [44], lithium ion batteries [89], solar cells [90], sensors [91], and insulation [92].

11.3.3 CNT-Based Aerogels

CNT aerogels are 3D aerogel structures that are synthesized using CNTs as building blocks. CNTs are 1D materials with high aspect ratio (<1000). Three methods are generally used in CNT aerogels synthesis: CVD and drawing, sol-gel transition, and ice-templating methods.

CNT aerogel can be synthesized by depositing it in 3D networks using the CVD method using CNT arrays. Ferrocene was used as a catalyst and thiophene was used as a support in the CNT aerogel made by Abdullah et al. The mixture was dissolved in toluene and injected into tubular quartz tube (Ar-H_2 medium) with the help of a syringe pump. Later, CNT aerogels were deposited on the inner wall of the quartz tube. The CNT aerogel sample was purified from amorphous carbon (400 °C heating) and catalyst particles (reflux in hydrochloric acid environment) for characterization [93].

However, synthesizing CNT aerogels that retain the unique properties of individual tubes is extremely difficult. Generally, CNT aerogel synthesis begins with the dispersion of CNTs in a solution. Since CNT has a hydrophobic structure, a surfactant is required for dispersion in an aqueous environment. Haghgoo et al. used sodium dodecyl benzene sulfonate (NaDBS) as a surfactant in their aerogel synthesis by sol-gel method [94]. They added it to the resorcinol-formaldehyde-catalyst mixture as in the carbon aerogel. Next, gelation is induced by a physical or chemical cross-linking mechanism. CNT hydrogels were subjected to solvent exchange with acetone, and later, by supercritical drying with CO_2, they reached the aerogel structure. In addition, they reached the CNT xerogel structures by drying the same structure under ambient conditions. Apart from the ambient and supercritical drying methods, other methods such as freeze drying or critical point drying (CPD) can be used [95].

The ice templating method is different from the freeze drying method. Kwon et al. dispersed MWCNTs in aqueous silk fibroin hydrogel and flash freeze them with liquid nitrogen. They can then be subjected to freeze drying. Thus, they synthesized CNT aerogel using the templating method. They synthesized a more regular aerogel compared to the sol gel method followed by freeze-drying CNT aerogel [96].

CNT-based aerogels have many advantages, including robust mechanical properties, excellent flexibility, lightness, high conductivity, and high surface area. Other materials with high electrochemical performance can also be easily incorporated into aerogel to form composite materials. The high production cost of CNT-based aerogels still limits their applications in the field of energy [97].

11.3.4 Graphene Aerogels

Graphene has very different electrochemical and physicochemical properties due to the 2D honeycomb arrangement of the carbon atoms. Extensive research has shown the potential of graphene

or graphene-based sheets in systems where energy is stored and converted. Developing 3D aerogel structures with this extraordinary nanomaterial further increases its importance in terms of both the number of applications and the manufacturability of the devices. Graphene aerogel has unique properties including electronic, thermal, mechanical, and chemical properties and potential technical applications as well as its completely 3D structure. Regarding graphene aerogel synthesis, there are four most commonly used methods. These are defined as hydrothermal reduction, sol-gel, templated-directed reduction, and chemical reduction. Generally, GO (modified graphene) is used as a starting material for graphene aerogel synthesis. GO is prepared by several methods. The most commonly used method is the Hummer method [98]. Chemically derived GO-based aerogels are the most widely used 3D graphene structures in the literature due to their easy synthesis routes and allowing control of pore morphology [99].

The hydrothermal reduction method is one of the most widely used graphene aerogel production techniques. In this method, a GO suspension is first prepared using the Hummers method, in which the graphite powder is oxidized using $NaNO_3$, H_2SO_4, and $KMnO_4$. In this method, the GO solution is first subjected to high temperature and high pressure to produce the graphene hydrogel. Supercritical or freeze-drying methods are then used to prepare the graphene aerogel structures [99].

The reduction method for the mold is a very useful method of obtaining porous graphene aerogels since it prevents random interconnection structures by ensuring controllable and homogeneous pore distribution. The reduction method for the mold uses ice crystals, water droplets or colloidal particles as molds for pore formation. It usually requires precise control over the amount of graphene used and subsequent template removal. Chen et al. reported that a macroporous "bubble" graphene film was synthesized by the templated-directed reduction method. Some latex spheres of monodisperse polymethyl methacrylate (PMMA) served as rigid molds in this material. GO hydrosol and a PMMA sphere suspension are mixed, and after filtration, a composite film is extracted and calcined at 800 °C to form the PMMA mold. At the same time, thermally graphene would be reduced to GO [100].

The chemical reduction method is an easy one-step method. Graphene hydrogel is obtained by adding reducing agents to the graphene oxide solution. Then, graphene aerogels are obtained using supercritical drying or freeze drying. Zhang et al. used low-cost and environmentally friendly oxalic acid (OA) and sodium iodine (NaI) instead of the commonly used toxic HI in their studies [101].

Graphene aerogels are also prepared using traditional organic sol-gel chemistry. One of the synthesis pathways is RF sol-gel synthesis. RF acts as a binder that helps to crosslink individual graphene oxide layers with sodium carbonate as a catalyst. The sol-gel mixture is then transferred into glass molds, sealed and held in an oven at specified temperatures and times. The resulting gels are removed from the molds and rinsed with acetone for several days (solvent change) to remove all water from the pores of the gel mesh. The wet gels are then dried with supercritical CO_2 to give aerogels structures. These aerogels are converted into graphene aerogel by pyrolysis at 1050 °C, usually under N_2 atmosphere, over several hours [102].

11.3.5 Activated Carbon Aerogels

In AC aerogel synthesis, usually first, carbon aerogel synthesis is made by sol gel method. Then, by physically mixing with KOH (chemically activated) [103] or CO_2 gas (thermal or physical activated) [104, 105], pyrolysis is performed in N_2 environment and the final form of the aerogel is obtained. In physical activation, besides CO_2, H_2O (steam) and air can also be used as gaseous

reagents. High activation temperature is required for physical activation. It also has disadvantages such as low yield and low porosity. In chemical activation, NaOH can be used as a chemical reagent other than KOH as alkali hydroxide. Other chemical reagents used are inorganic acids (HCl, H_2SO_4, H_3PO_4) and inorganic salts ($ZnCl_2$, K_2CO_3). High activation temperature required. Higher efficiency and higher porosity are observed in chemical activation compared to physical activation. The major disadvantage in chemical activation is maintenance problems caused by corrosive reagents [71]. The physical and chemical properties of the synthesized activated carbon aerogel depend on the type of material prior to activation, the type of activation and the activating material. The activated carbon aerogel exhibits a hierarchically porous structure with high specific surface area.

11.3.6 Biomass-Derived Aerogels

In energy applications, the selection and structure of active material is the most important parameter affecting the performance. These materials used are generally carbonaceous materials. Most of them are sourced from mineral substances and petroleum, which are about to deplete in the near future. High raw material cost, environmental damage of preparation, and complex production greatly limit energy applications. Therefore, the focus has been on using biomass or their derivatives to obtain porous carbon materials for sustainable development. Porous carbons derived from biomass, a new research topic and perspective, are environmentally harmless, biodegradable, abundant precursors, and low cost. Biomass derived aerogels are a large class of gels consisting of 3D solid networks having a lot of open pores [57, 82]. Generally, the synthesis of biomass-derived carbonaceous aerogels is achieved with the direct carbonization of carbohydrate based organic hydrogels or phenolic molecular-based hydrogels [49]. Biomass-derived carbon aerogels have been studied in several parts. There are cellulose-based carbon aerogels, chitosan-based carbon aerogels, lignin-based carbon aerogels, tannin-based carbon aerogels, and biomass-waste based carbon aerogels.

11.4 Fuel Cells

Fuel cells are energy conversion devices, which were frequently researched in recent years to reduce dependence on traditional fossil fuels and increase fuel efficiency. Fuel cells can be defined as devices in which chemical energy entering the system with a fuel and an oxidizer is directly converted into electrical energy. Batteries that can chemically store electrical energy are closed systems. Unlike batteries, fuel cells are open systems that operate as long as fuel is supplied. Unlike batteries in which the electrodes react, the electrodes in fuel cells act as catalysts for the oxidation/reduction reactions of the fuel during the charge/discharge cycles.

Fuel cells are one of the widely used power sources in the field of sustainable energy (mobile and stationary application) with its high efficiency, low operating temperature, low pollutant emission (one of the long-term solutions to reduce greenhouse gases and urban pollution), easy fuel supply and ease of use is used. These systems find wide use in military and civilian areas, including spacecraft, land vehicles, marine vehicles, electricity and heat generation facilities (combined heat and power systems).

Fuel cells were firstly used in the Apollo, Gemini, and Space Shuttle spaceships in NASA's space program in 1958. The first fuel cell studies were done in 1838 by Sir William Grove on hydrogen oxygen cells. Grove, during his studies, realized that constant current and power were produced as

a result of the reverse reaction of the electrolysis of water. In 1893, Friedrich Wilhelm Ostwald investigated the role and effect of each element in the fuel cell on fuel cell operation. In 1896, William W. Jacques laid the foundations of molten electrolyte fuel cells and aimed to generate electricity directly from the electrochemical energy of coal. In 1937, Emil Baur succeeded Nerst's fuel cell project working with solid oxide electrolyte. The study, which brought fuel cells to their current position and later used in the NASA program, was carried out on alkaline fuel cells by Thomas Bacon in 1939. With the use of fuel cells in space studies, interest in this field has increased. NASA first started to use the hydrogen-oxygen battery in spacecraft in 1958. General Electric's Douglas (1960) used a porous electrode to hold the electrolyte instead of using a matrix. Douglas predicted that a molten carbonate fuel cell with free electrolyte and gas diffusion layers could achieve higher current densities as the electrode spacing could be reduced. In the 1980s, fuel cells operating with hydrogen gained importance due to the decrease in fossil fuel reserves and the environmental problems caused by the use of these fuels. Today, studies are underway to reduce the costs of these systems and to make their use widespread [106–108].

A fuel cell basically consists of anode, cathode, and electrolyte in contact with each other. Electrodes are porous structures with high gas permeability. In a typical fuel cell, the fuel is continuously fed to the anode (negative electrode) and the oxidizer (oxygen/air) to the cathode (positive electrode). Electric current is generated while there is an oxidation/reduction reaction between the fuel and oxygen. The membrane (insulator) did not allow the electrons to pass through so it collects through the electrical circuit which creates an electric current and the hydrogen ion (H^+, proton) pass through the membrane from anode to the cathode. Here, protons recombine with oxygen and electrons coming from the anode to the electrical circuit, producing water and heat (Figure 11.2) [109].

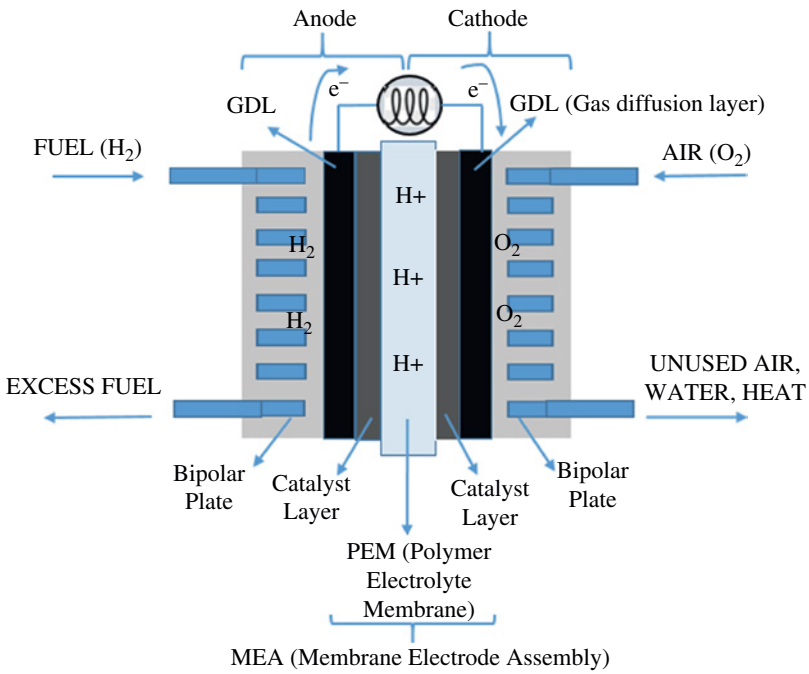


Figure 11.2 Components of the PEM fuel cell.

Different parameters such as reaction type, electrolyte type, and operating temperature are used to classify fuel cells [110]:

- *Reaction type:* In fuel cells, H_2, CH_3OH, CH_4, CO and some inorganic substances can be used as fuel (reducing agent). In fuel cells, pure O_2, air oxygen, H_2O_2, and chlorine can be used as oxidizing agents.
- *Electrolyte type:* In addition to common liquid electrolytes, fuel cells are also generally used solid electrolytes.
- *Operating temperature:* Low-temperature fuel cells (at 120–150 °C), intermediate temperature fuel cells (at 105–250 °C), and high-temperature fuel cells (at above 600 °C) are available.

The main types of fuel cells are (Table 11.3):

- Molten carbonate fuel cells (MCFCs)
- Solid oxide fuel cells (SOFCs)
- Alkaline fuel cells (AFCs)
- Phosphoric acid fuel cells (PAFCs)
- Proton exchange membrane fuel cells (PEMFCs)
- Direct methanol fuel cells (DMFCs)

There are many types of fuel cells other than these fuel cells: direct liquid-fueled fuel cells (direct alcohol fuel cells (DAFCs) (such as dimethyl ether, ethylene glycol, dimethyl oxalate), direct formic acid, and direct borohydride fuel cells), biological fuel cells (microbial fuel cells [MFCs] and enzyme-based fuel cells), membrane-less fuel cells, metal-air cells, single-chamber SOFCs, direct flame SOFCs, and liquid-tin anode SOFCs [111, 112]. Among these, biological fuel cells and micro fuel cells are the most prominent. Biological cells are divided into two: enzymatic fuel cells (enzymes-biocatalysts) and MFCs (microorganisms- electroactive bacteria or proteins). That is, biological fuel cells are low-temperature fuel cells that use biological catalytic reactions instead of metal catalysts in conventional fuel cells to generate electricity from the electrolysis of the fuel and oxidant [115]. Theoretically, biomedical accessories such as pacemakers, neurostimulators, hearing and vision devices, drug pumps, glucose sensors, and bladder control valves can utilize enzymatic fuel cells as a power supply [116]. Generally, it can be used as power generator for MFC application, wastewater treatment unit and recovery system of value added products [117]. Micro fuel cells are compact fuel cell systems in a reduced size (sizes are in millimeter scale). They are used in portable low-power electronic devices. Power densities of micro FCs range from a few tens of microwatts per square centimeter to several hundred milliwatts per square centimeter. Designing micro fuel cells is the hardest part. To install these systems, it is necessary to know and use standard microfabrication techniques very well (for size and cost) [118, 119].

11.4.1 Fuel Cell Components

PEM fuel cells consist of three main components. These are parts membrane electrode assembly (MEA), bipolar plates and heating or cooling plates. The most important is the MEA structure. The MEA consists of a polymer membrane with electrodes (support material and electro-catalyst) and gas diffusion layers. Apart from this, the structure is completed with bipolar plates (fluid plates)

Table 11.3 Types of fuel cells and specific properties [110–114].

Types of FC	Fuel	Electrolyte	Oper. temp. (°C)	Catalyst/ Charge carrier	Cell comp.	Overall effic.	Advantages	Disadvantages	Cell reaction	Applications
MCFCs	Natural gas, Biogas, Coal gas, H_2	Molten-carbonate (Li/K or Li/ Na)-salt	600–800	Nickel/CO_3^{2-}	Stainless based	90%	CO tolerant, Fuel flexible (hydrogen, natural gas, biogas, and clean coal gas), High-quality waste heat, Large stationary power generation, Using metals commonly used in cell design, Inexpensive catalyst,	High operating temperatures, The electrolyte is very corrosive and mobile, Extremely long start-up time, Expensive materials (Materials resistant to high temperatures,), Sulfur tolerance is low	Anode reaction: $H_2 + CO_3^{2-} \rightarrow H_2O + CO_2 + 2e^-$ Cathode reaction: $\frac{1}{2}O_2 + CO_2 + 2e^- \rightarrow CO_3^{2-}$ Overall reaction: $H_2 + \frac{1}{2}O_2 \rightarrow H_2O$	Stationary power, Continuous-power applications
SOFCs	CO, Natural gas, Biogas, Coal gas, H_2	Ceramic Y_2O_2, ZrO_2	600–1000	Perovskites (ceramic)/O^{2-}	Ceramic based	80–85%	High operating efficiency, CO tolerant, Solid ceramic structure reduces the possibility of corrosion, Fuel flexible (hydrogen, natural gas, biogas, and coal gas), High-quality waste heat, Solid electrolyte, Inexpensive catalyst, Large stationary power generation	High operating temperature (cell design problems and slow start capability), Thermal expansions incompatible with high temperature operation, Sealing issues, expensive components, Difficult manufacturing processes due to the selection of heat resistant materials,	Anode reaction: $H_2 + O^{2-} \rightarrow H_2O + 2e^-$ Cathode reaction: $\frac{1}{2}O_2 + 2e^- \rightarrow O^{2-}$ Overall reaction: $H_2 + \frac{1}{2}O_2 \rightarrow H_2O$	Stationary power Continuous-power applications

(*Continued*)

Downloaded from https://onlinelibrary.wiley.com/doi/ by ibrahim ragab - Universita Di Firenze Sistema , Wiley Online Library on [21/07/2024]. See the Terms and Conditions (https://onlinelibrary.wiley.com/terms-and-conditions) on Wiley Online Library for rules of use; OA articles are governed by the applicable Creative Commons License

Table 11.3 (Continued)

Types of FC	Fuel	Electrolyte	Oper. temp. (°C)	Catalyst/ Charge carrier	Cell comp.	Overall effic.	Advantages	Disadvantages	Cell reaction	Applications
AFCs	H_2, O_2	NaOH or KOH	60–250	Platinum/ OH^+	Carbon based	60%	Use of non-precious metals, High performance, Low materials costs, Availability of different electrocatalysts,	CO poisoning in the catalyst, Alkaline electrolyte that absorbs CO_2 (It reduces the electrolyte conductivity.) Needs pure hydrogen and oxygen, Commercial use is expensive (high cost of membrane)	Anode reaction: $H_2 + 2OH^- \rightarrow 2H_2O + 2e^-$ Cathode reaction: $\frac{1}{2}O_2 + 2e^- + H_2O \rightarrow 2OH^-$ Overall reaction: $H_2 + \frac{1}{2}O_2 \rightarrow H_2O$	Space applications
PAFCs	H_2	Concentrated 100% Phosphoric acid	160–220	Platinum/ H^+	Carbon based	70–85%	Tolerates hydrogen impurities, Reliability/ long-term performance, Electrolyte is relatively low cost, Relatively low operating temperature (Suitable for terrestrial applications)	Relatively low efficiency, Bigger and heavier than other fuel cells, Costly, expensive catalyst, Susceptible to CO and S poisoning, Medium-scale power generation	Anode reaction: $H_2 \rightarrow 2H^+ + 2e^-$ Cathode reaction: $\frac{1}{2}O_2 + 2e^- + 2H^+ \rightarrow H_2O$ Overall reaction: $H_2 + \frac{1}{2}O_2 \rightarrow H_2O$	Constant power application, Buses

Downloaded from https://onlinelibrary.wiley.com/doi/ by ibrahim ragab - Universita Di Firenze Sistema | Wiley Online Library on [21/07/2024]. See the Terms and Conditions (https://onlinelibrary.wiley.com/terms-and-conditions) on Wiley Online Library for rules of use; OA articles are governed by the applicable Creative Commons License

PEMFCs	Pure H_2	solid polymer	30–100	Platinum/ H^+	Carbon based	70%	Fast start times, Cold start, Proper power density, High efficiency, compactness, Proper power-to-weight ratio, Suitable for a wide range of applications, Solid electrolyte that resists gas passage	Catalyst and polymer membrane cost, CO poisoning in the catalyst, Heat and water management issues	Anode reaction: $H_2 \rightarrow 2H^+ + 2e^-$ Cathode reaction: $\frac{1}{2}O_2 + 2H^+ + 2e^- \rightarrow H_2O$ Overall reaction: $H_2 + \frac{1}{2}O_2 \rightarrow H_2O$	Passenger cars, buses, vehicle transport, Constant power generation, auxiliary power units, Combined heating and power of dwellings,
DMFCs	Methanol	solid polymer	20–90	Platinum - Pt/Ru/H^+	Carbon based	15–20%	An energy higher than hydrogen per unit volume, Suitable for portable applications, Liquid fuel (Fuel can be easily stored, transported and used)	Low efficiency and power density, Corrosiveness and poisonous nature of fuel, Catalyst poisoning	Anode reaction: $CH_3OH + H_2O \rightarrow CO_2 + 6H^+ + 6e^-$ Cathode reaction: $\frac{3}{2}O_2 + 6H^+ + 6e^- \rightarrow 3H_2O$ Overall reaction: $CH_3OH + \frac{3}{2}O_2 \rightarrow 2H_2O + CO_2$	Promising applications for batteries of cell phones and computers,

Downloaded from https://onlinelibrary.wiley.com/doi/ by ibrahim ragab - Universita Di Firenze Sistema , Wiley Online Library on [21/07/2024]. See the Terms and Conditions (https://onlinelibrary.wiley.com/terms-and-conditions) on Wiley Online Library for rules of use; OA articles are governed by the applicable Creative Commons License

and heating or cooling plates in the flow channels in order to provide a compact structure. Briefly, PEMFC is divided into the following parts (Table 11.4):

- Membrane electrode assembly (MEA)

i) Electrolyte (polymer membrane)
ii) Support material
iii) Electro-catalyst
iv) Gas diffusion layer

- Bipolar plates (fluid plates)
- Heating or cooling plates

Table 11.4 General characteristics of fuel cell components [111, 120–125].

Component	Types	Properties	Duties
Electrolyte	Liquid electrolyte (acid, alkali or fused salt), Solid membrane (a polymer or a ceramic)	Proton conductivity, Chemical and thermal stability, Strength, flexibility, Low gas permeability, Low water drag, Low cost,	An electrolyte medium that conducts ions. It should be both an electronic insulator and ionic conductor. It should be stable under strong oxidizing and strong reducing conditions.
Electro-catalyst	Noble metals: Pt [126, 127], Pd [128], Ir [129], Rh [130], Au [131] and Ru [132] Base metals [133]: Co [134], Cu [135], Ni [136], Fe [137], Ag [138], Cr [139] and Mn [140]	Excellent stability of the anode and cathode electrocatalysts, Electronic/protonic conductivity, Porosity, active reaction area, Catalytic activity	To accelerate kinetically slow reactions and increase the reaction rate.
Support	Carbonaceous materials [44, 141] Metal, Conducting metal oxides Nitrides, carbides, borides Electronically conducting polymers Mesoporous silicas [141, 142]	Surface area improving the dispersion of catalytic metals, Chemical and electrochemical stability, High conductivity, Easy recovery of noble metals in the catalyst used.	Provides more homogeneous distribution of electro catalyst to the electrode surface, Increasing the surface area in contact with reactants, Minimizing catalyst agglomeration
Gas diffusion layer	Carbon cloth or carbon paper [143], Metal (Metal meshes, Sintered metals, Micromachined meshes, metal foams), Silicon-based materials [144]	Electrically conductive, Porous enough A material that does not deform, High thermal conductivity.	Distributes reactant gases or liquids on the surfaces of catalyst particles, Helps to drive water away from the system, Provides electrical connection between plates, Mechanical support

Table 11.4 (Continued)

Component	Types	Properties	Duties
Flow channel	Different geometries: serpentine, parallel, parallel serpentine and discontinuous	Geometries vary depending on the needs and design of each fuel cell	It helps to distribute the reactants homogeneously over the surface of the electrodes.
Bipolar plate	Graphite (or carbon), Carbon/carbon composite (carbon/graphite), Thermoplastic-based graphite composite, Thermoset-based graphite composite [145]	High electrical and thermal conductivity, Good mechanical strength, Chemical stability, Low weight,	Bringing reactive gases to the electrode through flow channels, It helps to distribute the reactants to the surface of the electrodes, It prevents short circuit, Collector for the electric current, Effectively removes water and heat generated in the MEAs, A structural support to the MEAs.
Heating or cooling plates	Materials with high thermal conductivity suitable for the compact structure of the cell	Based on electric and ohmic (resistive) heating	It is used to heat or cool the battery temperature until it provides optimum operating performance.

The membrane in PEM fuel cells is functioning to ensure the connection between the anode and cathode by performing ion transfer. The polymer membrane is designed to facilitate the transport of protons. In addition, the membrane prevents mixing of the two gases (fuel and oxidant) against harsh conditions (active catalysts, temperature fluctuations, strong oxidants and reactive radicals). The membranes used are usually based on perflurosulphonic acid (PFSA), such as Nafion [123].

A wide variety of support materials with different geometries, sizes and porosity are used today. Differences in geometric and chemical properties of support materials can alter the electrocatalytic effect and electrocatalytic centers. One of the most desirable properties of supports for electrochemical systems is their high conductivity. The most prominent support material used in fuel cells is amorphous CB, Vulcan XC-72® (Cabot) [146]. The use of the support material resulted in improved catalyst performance (higher contact surface area of the catalyst, more homogeneous spread on the surface and minimized agglomeration) and reduced amount utilization and hence fuel cell costs to a minimum.

Noble metals such as platinum or one of its alloys are generally used to increase the reaction rate. The rate of an electrochemical reaction is achieved by an electrocatalyst by providing a lower energy pathway with a new mechanism. This catalyst is used on both the anode and the cathode. A noble metal or their alloys are formed into small particles that spread over the surfaces of larger particles of the carbon support. Current studies are generally aimed at reducing the cost of the catalyst used and increasing the mechanical strength of the catalyst by designing suitable support structures. Improving the surface of the support material causes the catalyst to spread more homogeneously on the surface and less agglomerate. Apart from this, recent studies show that the activity of nonprecious metals (especially Fe and Co) can be significantly improved with careful design and optimization of catalytic sites. The electrochemical and physicochemical properties of a

catalyst layer are mainly determined by the method of synthesis and precursor materials and chemical component properties. In recent years, many alternative preparation methods have been investigated in order to investigate the effect of the synthesis method on the catalyst structure and activity, apart from the traditional routes. Alternative deposition methods can be organized into five general types: conventional (impregnation methods), colloidal, molecular precursor, vapor phase, and surface modification [147].

The catalyst particles and the carbon support are bonded to a porous gas diffusion layer made of a carbon-based and electrically conductive material. While the gas diffusion layer distributes reactant gases to the surfaces of the catalyst particles, it allows the water produced at the cathode to move away from the electrolyte membrane. It also acts as the electrical connector between the electrode and the current-conducting bipolar plate [121]. Bipolar plates collect the electrical current that takes place inside the cell. It provides structural support by protecting MEA against external influences. In addition, it ensures that the reactive gases are homogeneously distributed over the electrode surface, and the water and heat generated in the center of the cell are transferred outside the system. Heating or cooling plates can be used to increase or decrease the temperature of the PEMFC until it provides optimum operating performance [120, 122].

11.4.2 Carbonaceous Aerogels for Fuel Cells

Carbonaceous materials are widely used in fuel cell applications to provide mechanical strength and high performance. Because carbon-based materials have unique properties such as high surface area, high electrical conductivity and very good stability in acid and alkali media [21]. In recent years, carbonaceous aerogels are used as gas diffusion layer, membrane and support material in the MEA parts of fuel cell systems. It is widely used especially in support materials. With the improvement of the surface properties of the support materials, the mechanical strength of the electrode against harsh operating conditions (high temperature and pressure) also increases. Apart from this, the most important situation is that the catalyst used by the development of the support material will be distributed homogeneously on the electrode surface without agglomerate and will provide better performance by using less amount of catalyst. One of the problems encountered in nanoscale catalyst-support interaction is the correct adjustment of the size and geometry of both the catalyst and the support. These parameters cause changes in the electronic structure of the electrode. Changes in the electronic structure of the nanoparticle clearly have an effect on the electrochemical properties [148].

Electrical characterization techniques are used to determine three main electrochemical variables (voltage, current, and time) in order to investigate the fuel cell behavior. Electrical characterization techniques are (i) j–V curve measurement, (ii) electrochemical impedance spectroscopy (EIS), (iii) current interrupt, and (iv) cyclic voltammetry (CV) [111]. In the light of these analyzes, the performance parameters used in fuel cells are explained in Table 11.5.

There are many studies in the literature on the use of carbonaceous aerogels as electrode material in fuel cells. The data of some of these studies are summarized in Table 11.6. The content of the important parameters and characterization methods of the studies in Table 11.6 are explained in Table 11.5.

Glora et al. prepared carbon aerogel films to be used as a gas diffusion layer in fuel cells. They added organic fibers to strengthen the structure. The thickness of the films was measured to be about 500 μm or less and have almost 80% porosity. The highest electrical conductivity achieved is about 28 S cm^{-1}. At the same time, this gas diffusion layer, which is synthesized, supports the formation of low resistance electrical contacts between the current collector [174]. Membranes are

Table 11.5 Parameters determining the performance of the fuel cell [113, 149, 150].

Parameter	Analysis	Explanation
Current density	Fuel cell performance is calculated using the polarization (or current-voltage) curve. Electrochemical impedance spectroscopy (EIS) Unit: mA cm^{-2}	Polarization curve data depend on operating conditions such as temperature, pressure, relative humidity, gas flow rates. The EIS spectrum is found by completing it.
Specific power	Specific power is power per unit mass. Unit: kW kg^{-1}	Energy density is the energy stored per unit volume. Power is V·I (voltage. current) and also energy per unit time.
Power density	Cell power density is power per unit volume of the cell. Unit: kW m^{-3} or kW l^{-1}	Current–voltage measurement: Quantitative analysis for performance and power density.
Efficiency	Fuel's chemical energy: Q_{react} Electrical energy: W_e, Thermodynamic efficiency $\eta_{therm} = W_e/Q_{react}$	The ratio between the electrical energy obtained and the energy supplied as fuel (the ratio of electrical energy to chemical energy).
Onset potential	The activity of the catalyst can be measured. High activity will lead to an onset potential (V) at a high peak current.	The activities of different catalysts for the same reaction or the activities of a catalyst for different reactions can be compared.
ECSA	It is the electroactive surface area of the electrode. Unit: m^2g^{-1} catalyst The change in ECSA is the explanation for the durability of the electrode. It is calculated using cyclic voltammetry measurements.	The rapid loss of ECSA indicates low electrode durability. Catalyst particle size affects the degree of ECSA loss.

limiting components in fuel cell operations due to their disadvantages such as their high cost, proton conductivity due to water and humidification requirements for regular operation. For this reason, many polymer electrolyte and composite electrolyte studies with high proton conductivity at high temperatures have been conducted in the last two decades [175]. Xue et al. synthesized the iGO/BuIPBI composite membrane by combining graphite oxide, a carbonaceous material, with polybenzimidazole. They used this synthesized membrane for high temperature PEMFCs. They observed that these highly stable iGO/BuIPBI membranes were able to absorb more acid but undergo only a small amount of swelling. iGO/BuIPBI membranes with high acid content have high proton conductivities at high temperatures (0.027 Scm^{-1} at 140 °C) [176].

11.5 Supercapacitors

Rapid population growth and technological developments in recent years cause the depletion of the energy resources used and the increase of environmental pollution. Therefore, environmental awareness increased with the contribution of environmental organizations, it also pushes

Table 11.6 Some studies on catalysts and carbonaceous aerogels used as support material in fuel cell.

Catalyst/ Support	BET Surface area ($m^2\ g^{-1}$)	ECSA (Elec. chem. surf. area) ($m^2\ g^{-1}$)	Fuel cell type	Onset potential (V)	Media	(I_f) Current density/ Mass current density	I_f/I_b	Power density	Explanation	Refs.
Metal catalysts and, supports made of carbonaceous aerogels and composite aerogels										
Pt/CA	613	73	PEMFC	0.964	0.5 M H_2SO_4	~291 mA $cm^{-2}{}_{Pt}$ 212 mA $mg^{-1}{}_{Pt}$	—	536 mW cm^{-2}	Oxygen reduction reaction activity, catalytic stability and electrical performance were evaluated using platinum catalyst on carbon aerogel support.	[151]
Pt–Ru/ CA1	—	45.2	DMFC	0.56	1 M CH_3OH + 1 M H_2SO_4	—	—	—	Single cell tests of carbon aerogel supported Pt-Ru anode catalyst were investigated.	[152]
Pt/CX	462	55 ($S_{in\ situ}$)	PEMFC	—	—	136 μA $cm^{-2}{}_{Pt}$ 75 mA $mg^{-1}{}_{Pt}$	—	—	Carbon xerogels have also been studied as Pt catalyst supports H_2/O_2 (air) PEMFC.	[153]
PtRu/CX	577	—	DMFC	0.6	2 M CH_3OH + 0.5 M H_2SO_4	—	—	—	The electrocatalyst was prepared with carbon xerogel support and Pt and PtRu nanoparticles and examined for methanol oxidation.	[154]
Pt/ GA(600)	434	102	PEMFC	—	0.1 M $HClO_4$	2.3 μA cm^{-2} 30.6 mA $mg^{-1}{}_{Pt}$	—	—	Oxygen reduction reaction performances of electrocatalyst prepared with Pt catalyst placed on graphene aerogel support were investigated.	[155]
Co/N–rGO-800	83.4	—	FC	0.882	0.1 M KOH	4.99 mA cm^{-2}	—	—	Co/N-rGO-800 carbon aerogel composite was prepared using cobalt alginate and GO hydrogels and oxygen reduction reaction performance was investigated.	[156]

Downloaded from https://onlinelibrary.wiley.com/doi/ by ibrahim ragab - Universita Di Firenze Sistema , Wiley Online Library on [21/07/2024]. See the Terms and Conditions (https://onlinelibrary.wiley.com/terms-and-conditions) on Wiley Online Library for rules of use; OA articles are governed by the applicable Creative Commons License

Pt/BN-GA	369.2	106	DMFC	—	0.5 M H_2SO_4 + 1 M CH_3OH	1.12 mA cm^{-2} 1184.5 mA mg^{-1}	—	—	The 3D Pt/BN-GA catalyst made from ultrafine Pt nanoparticles and graphene aerogel with B and N has been studied for methanol oxidation performance.	[157]
Pt/GA	244.91	—	DFAFC	—	0.5 M H_2SO_4 + 0.5 M HCOOH.	6.78 mA cm^{-2}	—	—	Pt/Graphene aerogel electrocatalysts were synthesized and investigated for formic acid oxidation.	[158]
Pt/NGA	379.71	—	DFAFC	—	0.5 M H_2SO_4 + 0.5 M HCOOH.	4.63 mA cm^{-2}	—	—	The electrocatalyst was synthesized using nitrogen doped graphene aerogel support and Pt catalyst and investigated for formic acid oxidation.	[158]
Pt/BGA	69.92	—	DFAFC	—	0.5 M H_2SO_4 + 0.5 M HCOOH.	5.57 mA cm^{-2}	—	—	The electrocatalyst was synthesized using boron doped graphene aerogel support and Pt catalyst and investigated for formic acid oxidation.	[158]
Pt/GA	244.91	—	DMFC	—	0.5 M H_2SO_4 + 0.5 M CH_3OH.	8.72 mA cm^{-2}	2.02	—	Pt/Graphene aerogel electrocatalysts were synthesized and investigated for methanol oxidation.	[158]
Pt/NGA	379.71	—	DMFC	—	0.5 M H_2SO_4 + 0.5 M CH_3OH.	9.42 mA cm^{-2}	2.03	—	The electrocatalyst was synthesized using nitrogen doped graphene aerogel support and Pt catalyst and investigated for methanol oxidation.	[158]

(*Continued*)

Downloaded from https://onlinelibrary.wiley.com/doi/ by ibrahim ragab - Universita Di Firenze Sistema, Wiley Online Library on [21/07/2024]. See the Terms and Conditions (https://onlinelibrary.wiley.com/terms-and-conditions) on Wiley Online Library for rules of use; OA articles are governed by the applicable Creative Commons License

Table 11.6 (Continued)

Catalyst/ Support	BET Surface area ($m^2\ g^{-1}$)	ECSA (Elec. chem. surf. area) ($m^2\ g^{-1}$)	Fuel cell type	Onset potential (V)	Media	(I_f) Current density/ Mass current density	I_f/I_b	Power density	Explanation	Refs.
Pt/BGA	69.92	—	DMFC	—	0.5 M H_2SO_4 + 0.5 M CH_3OH.	19.28 mA cm^{-2}	1.05	—	The electrocatalyst was synthesized using boron doped graphene aerogel support and Pt catalyst and investigated for methanol oxidation.	[158]
Pd/BNG	170.7	84.6	DFAFC	—	0.5 M HCOOH + 0.5 M H_2SO_4	728.5 mA mg^{-1}	—	—	A 3D hybrid electrocatalyst consisting of Pd nanoparticles and B and N doped graphene aerogel was prepared and examined for formic acid oxidation reaction.	[159]
Pd/BNG	170.7	84.6	DMFC	—	1 M CH_3OH + 0.5 M NaOH	707.5 mA mg^{-1}	—	—	A 3D hybrid electrocatalyst consisting of Pd nanoparticles and B and N doped graphene aerogel was prepared and examined for methanol oxidation reaction.	[159]
Pd/GO aerogel	—	97.43	DEFC	—	1 M KOH + 1 M C_2H_5OH	1300 A g^{-1}	1.96	—	The electrocatalyst was prepared using graphene oxide aerogel support and palladium catalyst, and ethanol was used in the oxidation reaction.	[160]
Ag NW/ rGO-aerogels	80	—	DHPFC	—	0.1 M H_2O_2 + 1 M NaOH	1.15 A g^{-1}	—	56 Wm^{-2} 1.4 Wg^{-1}	Silver nanowire and graphene hybrid aerogel were synthesized and used as electrocatalyst in H_2O_2 reduction reaction.	[161]

Downloaded from https://onlinelibrary.wiley.com/doi/ by ibrahim ragab - Universita Di Firenze Sistema , Wiley Online Library on [21/07/2024]. See the Terms and Conditions (https://onlinelibrary.wiley.com/terms-and-conditions) on Wiley Online Library for rules of use; OA articles are governed by the applicable Creative Commons License

Fe–N–C/AC (Fe(III)/chitosan hydrogel)	760	—	MFC	—	—	16.2 A m^{-2},	—	2.4 ± 0.1 W m^{-2}	Oxygen reduction reaction with Fe-N-C catalyst derived from Fe (III)-chicosan hydrogel was investigated.	[162]
Fe/N--CNFs	584	—	FC	0.88	0.1 M KOH	—	—	—	Oxygen reduction reaction performance was investigated using Fe, N doped carbon nanofibers aerogels.	[163]
Pt/GR-CNT aerogel	138.7	75	DMFC	0.25	0.5 M H_2SO_4 + 1 M CH_3OH	550 mA mg^{-1}	1.53	—	Electrocatalyst was synthesized using Pt catalyst and graphene-carbon nanotube aerogel support and used in methanol oxidation.	[164]
Ni/CA (ANi6)	698	—	FC (ORR)	−0.21	0.1 M KOH	28.1 mA cm^{-2}	—	—	Nickel-added carbon aerogel was prepared. Tested as electrocatalyst for oxygen reduction reaction.	[165]
Co/CA (ACo6)	589	—	FC (ORR)	−0.17	0.1 M KOH	34.9 mA cm^{-2}	—	—	Cobalt-added carbon aerogel was prepared. Tested as electrocatalyst for oxygen reduction reaction.	[165]
Fe/CA (AFe6)	461	—	FC (ORR)	−0.22	0.1 M KOH	26.2 mA cm^{-2}	—	—	Iron-added carbon aerogel was prepared. Tested as electrocatalyst for oxygen reduction reaction.	[165]
Pd/3D rGO aerogel/CFP	248.63	96.26	DEGFC	—	1 M EG + 2 M KOH	267.8 mA cm^{-2}	—	—	Electrocatalytic oxidation of ethylene glycol was tested using 3D reduced graphene oxide aerogel and palladium catalyst.	[166]
Rh/3D-GA	485	79.6	DMFC	—	1 M KOH + 1 M CH_3OH	498.9 mA mg^{-1} 0.63 mA cm^{-2}	—	—	Rhodium doped 3D graphene aerogel networks have been synthesized and used for methanol oxidation.	[167]

(*Continued*)

Downloaded from https://onlinelibrary.wiley.com/doi/ by ibrahim ragab - Universita Di Firenze Sistema , Wiley Online Library on [21/07/2024]. See the Terms and Conditions (https://onlinelibrary.wiley.com/terms-and-conditions) on Wiley Online Library for rules of use; OA articles are governed by the applicable Creative Commons License

Table 11.6 (Continued)

Catalyst/ Support	BET Surface area ($m^2 g^{-1}$)	ECSA (Elec. chem. surf. area) ($m^2 g^{-1}$)	Fuel cell type	Onset potential (V)	Media	(I_f) Current density/ Mass current density	I_f/I_b	Power density	Explanation	Refs.
Pt/GA	265.33	—	PEMFC	—	0.1 M $HClO_4$	—	—	—	Oxygen reduction reaction tests of the electrocatalyst obtained by adding Pt catalyst on the graphene aerogel support were performed.	[168]
Metal-free carbonaceous aerogels and composite aerogels catalysts										
N-doped CA (NCA800)	—	—	MFC	0.82	0.1 M NaOH	12.05 mA cm^{-2}	2.21	1048 ± 47 mWm^{-2}	Nitrogen-doped carbon aerogels have been synthesized and tested for the oxygen reduction reaction.	[169]
B-GA	100.1	—	FC	~ −0.14	0.1 M KOH	—	—	—	Boron-doped graphene aerogel was synthesized and tested as a metal-free catalyst for the oxygen reduction reaction.	[170]
N-GA	141.5	—	FC	~ −0.14	0.1 M KOH	—	—	—	Nitrogen-doped graphene aerogel was synthesized and tested as a metal-free catalyst for the oxygen reduction reaction.	[170]
N,B-GA-1000	545.7	—	FC	~ −0.07	0.1 M KOH	—	—	—	Nitrogen-boron-doped graphene aerogel was synthesized and tested as a metal-free catalyst for the oxygen reduction reaction.	[170]
N-CA (CA-10KOH)	1827	—	MFC	—	—	2.15×10^{-4} A cm^{-2}	—	967 ± 34 mW m^{-2}	Nitrogen-doped carbon aerogel was prepared and activated with KOH for high oxygen reduction reaction activity.	[171]

Downloaded from https://onlinelibrary.wiley.com/doi/ by ibrahim ragab - Universita Di Firenze Sistemi , Wiley Online Library on [21/07/2024]. See the Terms and Conditions (https://onlinelibrary.wiley.com/terms-and-conditions) on Wiley Online Library for rules of use; OA articles are governed by the applicable Creative Commons License

N-graphite foam (NEGF)	—	$61.3 \pm 4.4\,cm^2$	MFC	—	$5\,mM\,K_3[Fe(CN)_6] + 0.1\,M$ KCl	—	—	0.739 $W\,m^{-2}$	Nitrogen-doped 3D expanded graphite foam (NEGF) was prepared and anode and cathode performances were tested.	[172]
Graphene/ active carbon aerogel (GA/AC)	758.19	—	FC (ORR)	0.88	50 mM phosphate buffer sol. (PBS)	4.37×10^{-5} $A\,cm^{-2}$	—	—	Porous graphene/activated carbon aerogel was synthesized and used for the oxygen reduction reaction.	[173]

MFC, Microbial fuel cell.
DEFC, Direct ethanol fuel cell.
DFAFC, Direct formic acid fuel cell.
DEGFC, Direct ethylene glycol fuel cell.
DHPFC, Direct hydrogen peroxide fuel cell.
I_f, Forward current densities.
I_b, Backward current densities.

Downloaded from https://onlinelibrary.wiley.com/doi/ by ibrahim ragab - Universita Di Firenze Sistema , Wiley Online Library on [21/07/2024]. See the Terms and Conditions (https://onlinelibrary.wiley.com/terms-and-conditions) on Wiley Online Library for rules of use; OA articles are governed by the applicable Creative Commons License

scientific circles to work on clean energy systems. The importance of effective, efficient and reliable use of energy is increasing day by day in energy technologies and sustainable energy systems. Over the past decade, very important research efforts have been witnessed to the development of various renewable energy systems such as solar cells and fuel cells. However, there are still some restrictions on alternative energy sources. This situation brings about the use and development of energy storage systems. In order for the electrochemical energy storage to be at maximum levels, importance is given to studies on subject such as higher energy density, lower cost, longer life and improved material sustainability [6].

Batteries and capacitors are used to store energy in industrial applications. Super capacitors, energy storage mechanism is very different than traditional batteries. Supercapacitors are devices that are capable of storing electrical energy converted from various energy sources. Although the production cost of batteries is lower than supercapacitors, energy storage capacity is much more than supercapacitors. But for a few seconds charge times, a supercapacitor can store more energy than a battery. When the charging time decreases, the energy density of the batteries decreases, while the supercapacitors remain almost constant. Since harmful chemicals are used in batteries, materials deteriorate over time. This causes low power density and a shorter lifespan depending on the time. Traditional capacitors have a lower cost than supercapacitors. However, supercapacitors have higher energy density than traditional capacitors. Supercapacitors generally produce high costs due to the use of materials and leading technologies that are expensive to obtain and process. A lot of work is being done in this area to develop supercapacitors and to overcome these difficulties. It is estimated that in the next decade, supercapacitors with high energy and power density will be produced with low production costs and will provide support to the energy field [6, 177, 178]. Supercapacitors are used in various fields for the electrical energy requirements we need in our daily life. For example, many electric vehicle companies use supercapacitors to distribute more power during acceleration. In addition, supercapacitors are used in digital cameras, power backup systems and various electronic devices [5].

The history of supercapacitors dates back approximately 50–60 years. First, in 1957, Howard Becker of General Electric company built electric double-layer charge storage systems. Robert A. Rightmire (1966) and Donald L. Boos (1970) from (SOHIO) produced a new capacitor with a higher capacitance value, now available and widely used. In 1978, Nippon Electric Company (NEC) commercialized supercapacitors under the SOHIO license. After commercialization, supercapacitors were produced with various designs. Nippon made great efforts toward the commercialization of various new series of supercapacitors. Nippon ChemiCon of Japan started mass production of their supercapacitors with higher performance in 1998. Apart from this, Panasonic, Korean company Daewoo and Russian company ESMA produced supercapacitors in different capacitance and designs. Initially, these capacitors were termed as a power backup systems for many consumer electronic devices. Then it continued to be used in different areas [6].

In general, a supercapacitor consists of three main components: electrode, electrolyte, and separator. The designs, performance, and electrochemical properties of supercapacitors depend mainly on the electrode and electrolyte. Choosing a suitable electrolyte can increase the energy density of the supercapacitor system. The cyclic performance of a supercapacitor is determined by the electrode, which can be designed through new nano or microstructured ways to improve load storage capacity. Supercapacitors are examined in three groups according to the electrode material used and energy storage mechanism. Explanations of the classification of supercapacitors are given in Figure 11.3 [178–180].

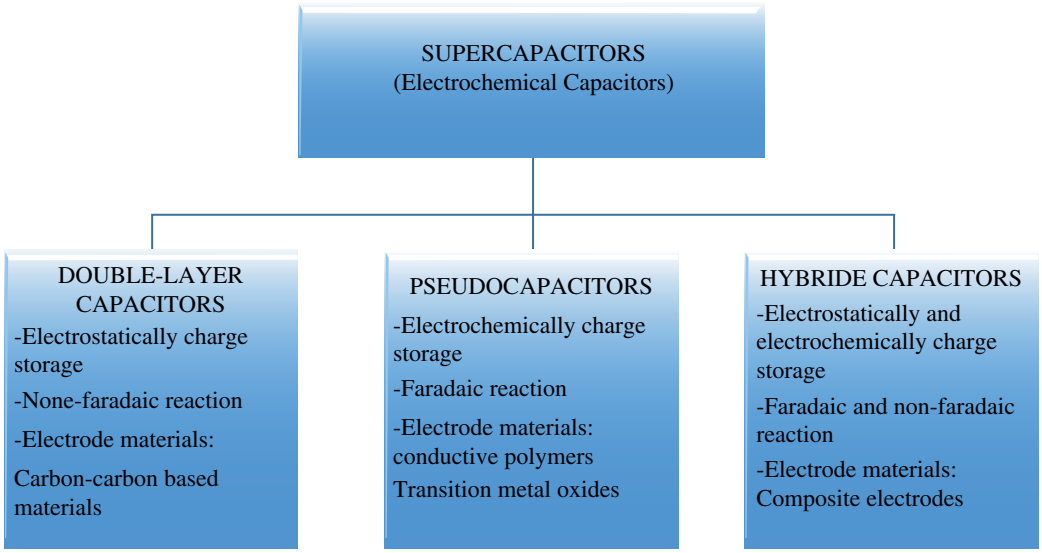


Figure 11.3 Classification of supercapacitors.

11.5.1 Supercapacitor Materials

Supercapacitors, which are used effectively in energy storage, consist of five main components as electrode, electrolyte, current collector, binder and separators (Figure 11.4). It contains two electrodes with an electrolyte solution in the middle, connected to the current collector. Charge spread between electrodes is prevented by a dielectric separator placed between the two electrodes [181].

However, all of its components (active or passive) contribute to the performance of the device. Information about the components used in the design of supercapacitors and their properties are given briefly in the Table 11.7.

Figure 11.4 Components of supercapacitor.

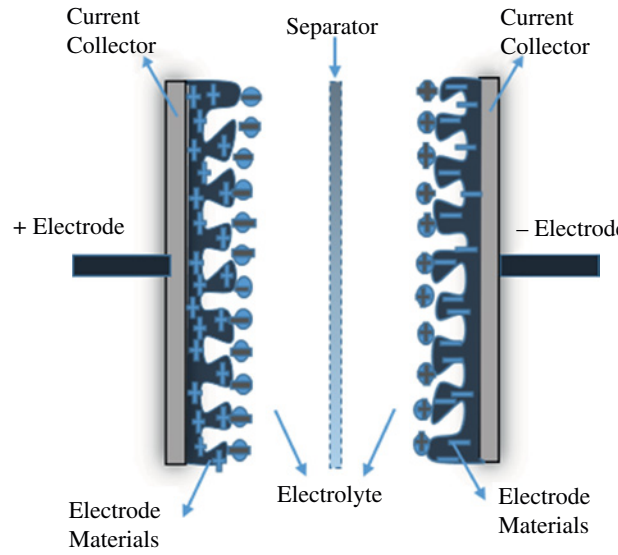


Table 11.7 Components used in the design of supercapacitors [6, 182, 183].

Components	Component type	Materials used	Purpose of use
Electrode material	Active	Carbon based, Conducting polymers (CPs), Transition metal oxide, Metal Nitrides, Composites	The electrode determines the energy storage method and cycle performance of a supercapacitor. All other components used are determined according to the electrode type.
Electrolyte material	Active	Aqueous electrolytes, Organic electrolytes, Ionic liquids	Electrolytes used in supercapacitors both connect two electrodes and carry out load transfer. Ion diffusion of the electrolyte is important in determining the power density.
Current collector	Passive	Metal foil, Ni foam, Carbon-based materials	It increases the durability of the device and thus increases the cell potential. This is important in optimizing and stabilizing the entire system.
Binder	Passive	Fluorinated polymeric materials	Providing the connection between the particle-particle and the particle current collector, Ensuring the connection between the components, The selection of the appropriate binder is effective to reducing the internal resistance.
Separators	Passive	Polypropylene, PVDF, PTFE, cellulose polymer, Glass fiber, Nafion 115 Graphene-based films	Separating electrodes from each other prevents physical contact, Facilitating electron transfer.

Electrode material is a very crucial component of the supercapacitor. Because it determines the specific features of the device. Therefore, electrode materials must meet three major requirements [177]:

1) Electrical conductivity
2) Electrochemical stability
3) Surface area that can be developed with easy methods

Types of electrode materials used in supercapacitors and their advantages and disadvantages are given in the Table 11.8.

Among the various electrode materials, an average of 80–90% of commercial supercapacitors use pure carbonaceous materials as the active electrode material. The cost is very low due to ease of access and abundance of carbon materials [4, 177, 186–188]. A wide range of carbon forms with 0D, 1D, 2D, and 3D (AC, CA, CNF, CNT and graphene) having properties wide specific surface area, porous nature, corrosion resistance, processability, high conductivity and being ecofriendly carbon based supercapacitors have also provided many different electrode designs [1, 189].

Electrode material used is very important in EDLCs, since charge storage is carried out according to non-Faradaic reactions, not according to faradaic reactions. The physicochemical properties

Table 11.8 Electrode materials used in supercapacitors [6, 178, 184, 185].

Electrode materials	Types	Advantages	Disadvantages
Carbon based electrodes	0D-fullerenes, diamond clusters 1D-CNTs, diamond nanorods 2D-graphene sheets, diamond nanoplatelets 3D-carbonaceous aerogel	Ease of access Abundance, Low manufacture and processing cost, Porous nature-High surface area, 0ptimal pore size, Corrosion resistance, Processability, Ecofriendly, Good electrical conductivity, High temperature tolerance	Lower specific energy density, Limited specific capacitance, High contact resistance between carbon particles causing low performance.
Conducting polymers (CPs)	Conducting polymers (PPy, PANI, PEDOT), Their derivatives.	3D porous structure, High capacitance value, Scalable synthesis, Lightweight, Unique electrical conductivity, Large pseudocapacitance, Low cost	Poor cyclic stability, Oxidative degradation of active material, Poor mechanical stability
Transition metal oxide	RuO_2, MnO_2, NiO, CO_3O_4, Bi_2O_3, Some metal oxides	High redox chemistry, Good ion transport kinetics, High electrical conductivity, High capacitive performance, Low resistance, High energy and power density, Excellent structural stability, Variable oxidation states, Cyclic stability, Wide potential window operating range	Too expensive (consumption of the precious metal limited), Only suitable for aqueous electrolytes (rapid breakdown of most metal oxides in acidic solutions [1 V]), Difficulty to control the grain size, It causes environmental problems.
Metal nitrides	Mo_2N, VN, TiN, Li_3N	Enhanced conductivity, High performance among pseudocapacitive materials, High electrical conductivities, Mechanical stability, Improved power density	Causing irreversible oxidation at the aqueous media limits.
Composite materials	Double and triple combination of all electrode materials used (hybrid electrode)	Electrode structure with two different energy storage mechanisms (faradaic and non-faradaic), Higher mechanical strength, Higher energy density, Higher cycle life, The structure that provides ease of movement for the products.	Electrode synthesis time and difficulty, Intense research and optimization

(surface morphology, specific surface area, average pore size distribution) of the electrode material used is an important parameter in increasing the specific capacitance of the EDLCs. The second type of supercapacitor is pseudocapacitors, also called a redox capacitor. In this capacitor type, the load storage mechanism is realized by charge transfer (faradaic reactions) on the electrode surface or near the electrode surface. In such capacitors, conductive polymers or transition metal oxides are used as electrode material. Because electrode materials consisting of conductive polymers and metal oxides are not inert and the charge storage mechanism takes place as a pseudocapacitive effect in the form of physico-chemical adsorption (redox reaction) on the electrode surface [185]. The third type of supercapacitors are hybrid capacitors. In these capacitors, electrode design is made using composite materials. Namely, composites of conductive polymers or metal oxides used in pseudocapacitors with carbon and carbonaceous materials used in EDLCs are synthesized and new electrode design is made. Both Faradaic and non-Faradaic reactions take place on the electrode surface of the hybrid capacitors. This composite electrode design can increase the capacitor's specific capacitance, strength, and mechanical strength.

Electrolytes used in supercapacitors both connect two electrodes and carry out load transfer. In general, electrolytes used in supercapacitors are divided into three different categories: aqueous electrolytes, organic electrolytes and ionic liquids. The choice of electrolytes for supercapacitors depends mainly on the stability and ionic conductivity of the electrolyte in an applied potential window [6]. As a result, different electrolytes were used in different potential window ranges. The stable voltage window used is the potential that all materials in the supercapacitor can be used without deterioration (i.e. irreversible chemical reactions occurring in components, for example, and significant volume changes in the components reduce the electrical performance of the material, etc.). Choosing an ideal electrolyte not only increases energy density values, it also plays an important role in improving cycle life, minimizing internal resistance, increasing specific power output, control over operating temperature, and reducing self-discharge process [185]. Table 11.9 provides general information about the electrolytes used in supercapacitors.

Table 11.9 Properties of electrolytes used in supercapacitors [185, 190].

Electrolytes	Types	Potential windows	Advantages	Disadvantages
Aqueous electrolytes	Acid: H_2SO_4 Alkaline: KOH Neutral: KCl	1.0–1.3 V	It simplifies the manufacturing process of the device with its low cost and easy usage. It contains smaller dissolved ions. It has high dielectric constant. It shows higher conductivity and specific capacitance.	The working voltage is limited (1.2 V-Due to the thermodynamic decomposition of water).
Organic electrolytes	$TEABF_4$/ ACN	2.5–2.7 V	It has improved voltage performance.	Low ionic conductivity High cost Flammability Toxicity
Ionic liquids	(EMIm) (BF4)-ACN	2.5–2.7 V	Energy storage in the temperature range of −30 °C to 60 °C.	Low ionic conductivity at room temperature. High cost

One of the proposed solutions for achieving low resistance in supercapacitors is to place the electrode and electrolyte active ingredients in the current collector, a metallic passive component. The current collector selection plays a crucial role in increasing the durability of a supercapacitor device and thus increasing cell potential. When choosing a current collector, it is necessary to take into account the type of electrolyte and electrode material in the design [185, 191]. Binders are one of the passive components of the supercapacitor. The chemical content, structure and type of binder used greatly affect the performance of the supercapacitor. The binders should provide maximum adhesion, ensuring contact between both the particle-the particle and between the particle-current collector. Interparticle volumes should not be blocked by the binder. Attention should be paid to the concentration of binder used. Fluorinated polymeric materials are often used as binders in the production of supercapacitors. One of the passive components of electrochemical capacitors are separators. Separators prevent physical contact between them by separating the electrodes from each other. It also facilitates electron movement between electrodes. Separators should be as thin as possible, low cost, electrochemically stable, high porosity, high thermal strength, and chemically stable to electrolyte. Separators can be produced from a wide variety of materials, such as synthetic and natural polymers, glass fiber, nafion 115, and graphene oxide films [182].

11.5.2 Carbonaceous Aerogels for Supercapacitors

A supercapacitor consists of five components: electrode, electrolyte, current collector, binder and separator (dielectric membrane). Two of them are active (electrode, electrolyte) and three are passive (current collector, binder and separator) components. The most important of these and the component that determines the performance of the supercapacitor is the electrode. The morphological structure, physicochemical and electrochemical properties of the electrode are the most important parameters determining the performance of the supercapacitor. As electrode materials, carbonaceous materials are at the forefront in terms of different textural properties. In particular, much progress has been made recently in 3D carbon-based nanostructures. Aerogels with 3D nanostructure have many advantages over 2D structures, especially for electrode application in supercapacitors. 3D carbonaceous aerogels not only have large surface areas but also a wide variety of pores and pathways within the structure. Interconnected porous networks reduce ion transport resistance and diffusion distances, while also increasing electrolyte penetration and larger accessible surface areas. Thanks to these structural interconnections, it causes both high mechanical stability and high electrical conductivity as it provides a wider interface between active materials and electrolyte [192]. Interfaces between electrodes and electrolytes store energy and allow supercapacitors to increase their specific capacitance and accordingly provide high power and outstanding cycle life.

Energy density in supercapacitors depends on two factors: specific capacitance and operating voltage. Electrolyte selection is also very important, as high power and high energy density operating voltage is required [178]. There are important parameters and characterization methods in evaluating the performance of the supercapacitor (Table 11.10). CV, galvanostatic charge-discharge (GC-D), and impedance techniques are important characterization techniques usually employed to analyze the properties of supercapacitors. The performance of a supercapacitor depends on the amount of charge stored at voltage change with the specific capacitance parameter, the capacity to store electrical charges (electrons, ions) with the energy density parameter, and the capacity to charge/discharge this energy in the minimum time with the power density parameter [21]. In the light of these parameters, literature studies related to supercapacitor applications of carbon aerogels are summarized in Table 11.11.

Table 11.10 Parameters determining the performance of the supercapacitor [6, 193, 194].

Parameter	Equations	The term analysis	Dependent parameters
Specific capacitance (Cs) Stored charge scale, The properties of the electrode affect the capacitance	Cyclic voltammogram $C = Q/V$ $C = (\int idV)/(V_s\ \Delta V)$ $C_s = C/m$ Galvanostatic charge–discharge $C = (I.\Delta t)/(\Delta V_d.m)$ Equivalent series resistance $C = 1/(m.J.2\pi f.Z'')$	Electrode material; Gravimetric capacitance; $F\,g^{-1}$, Areal capacitance; $F\,cm^{-2}$, Linear capacitance; $F\,cm^{-1}$, Volumetric capacitance; $F\,cm^{-3}$	Mass loading Dimension, Thickness of electrode, Electrode density Types of electrolyte/ separator used
Energy density The amount of electrical energy stored by the device. Energy transfer rate.	$E = (C.\ \Delta V)/2$	Gravimetric energy; $Wh\,kg^{-1}$ Volumetric energy; $Wh\,l^{-1}$	The value of the energy depends on the specific capacitance and potential window range.
Power density The power density shows the degree of how quickly a supercapacitor can be charged.	$P = E/t$	Gravimetric power; $W\,kg^{-1}$ Volumetric power; $W\,l^{-1}$	Cell resistance or reaction polarization System power can be increased by minimizing the causes that increase resistance.
Operating potential window It is the potential window range where all the materials in the device work without deterioration. (safety conditions)	Aqueous electrolyte (1.0–1.3 V), Organic electrolyte (2.5–2.7 V), Ionic liquid (3.5–4.0 V)	Potential is the energy required to move a unit charge across the electrode-electrolyte interface. Voltage and potential; volts (V)	Specific energy and power depend on its value.
İmpedance It reveals both real and complex impedance components. The EIS technique can be used to calculate the ESR value of the supercapacitor.	The ESR value helps to calculate the specific power. $P = V^2/(4ESR)$	With the EIS data, capacitance at any frequency can be measured.	With porous electrodes, capacitance depends on frequency. At high frequencies, the capacitance is low as only the electrode surface is charged. At low frequencies, capacitance is high as the entire surface is charged.

ESR, the effective series resistance.
İ: the voltametric current (A).
*V*s: the potential scan rate (Vs^{-1}).
ΔV: the potential range (V).
M: the mass (g) of the active materials
I: the discharging current (A).
Δt: the discharging time.
ΔV_d: the discharging voltage (V).
Z'', imaginary part; *f*, the frequency.

Table 11.11 Studies on carbonaceous aerogels as electrode materials in supercapacitors.

Sample	BET SSA ($m^2 g^{-1}$)	Test conditions	Electrolyte	Current density/scan rate ($A g^{-1}$/ $mV s^{-1}$)	Energy/Power density ($Wh kg^{-1}$/ $kW kg^{-1}$)	Specific capacitance ($F g^{-1}$)	Explanation	Refs.
Carbon aerogels								
Carbon aerogel (PR–0.1)	1454	GC-D/ three–electrode	6 M KOH	0.5/—	38.4/0.17	174.4	Carbon aerogel microspheres was prepared by sol-gel method using resorcinol, formaldehyde as carbon source and Na_2CO_3 as catalyst.	[195]
Carbon xerogel (CA-2000)	847.3	CV/ two-electrode	1 M TEABF4/ ACN	—/5	—/—	17.6	Carbon aerogels were prepared from the polycondensation of resorcinol and formaldehyde using Na_2CO_3 as the base catalyst.	[196]
Carbon aerogel (CA)	743	GC-D/ three–electrode	6 M KOH	1/—	—/—	189	Carbon aerogels were prepared from the polycondensation of resorcinol and formaldehyde using Na_2CO_3 as the base catalyst.	[197]
Carbon aerogel (CA)	679	CV/ three–electrode	1 M H_2SO_4	1/—	—/—	99	CA was synthesized by polycondensation of resorcinol and formaldehyde. Then it was dried under ambient conditions.	[198]
Carbon aerogel (CA2)	664	CV/ three–electrode	1 M H_2SO_4	—/50	—/—	151	CA was synthesized by polycondensation of resorcinol and formaldehyde. Then it was dried supercritical conditions.	[199]
Carbon xerogel (CAs)	820	GC-D/ three-electrode	6 M KOH	0.5/—	4.09/—	120	Carbon xerogels were prepared from the polycondensation of resorcinol and formaldehyde using Na_2CO_3 as the base catalyst.	[104]
C-aerogel	757.7	GC-D/ two-electrode	1 M Et_4NBF_4/PC	2/—	22.1/2.4	21.8	CA was synthesized by polycondensation of resorcinol and formaldehyde. Then it was dried supercritical conditions.	[200]
Carbon aerogel (CA-SCD)	892	CV/ three–electrode	6 M KOH	—/25	—/—	187	Carbon aerogel is synthesized by pyrolysis of nanocellulose aerogels prepared by dissolving cellulose microcrystalline in NaOH aqueous solutions, gelation, regeneration, and drying with supercritical CO_2.	[201]
Carbon cryogel (CA-FD)	418	CV/ three–electrode	6 M KOH	—/25	—/—	72	Carbon aerogel is synthesized by pyrolysis of nanocellulose aerogels prepared by dissolving cellulose microcrystalline in NaOH aqueous solutions, gelation, regeneration, and freeze drying.	[201]

(*Continued*)

Downloaded from https://onlinelibrary.wiley.com/doi/ by ibrahim ragab - Universita Di Firenze Sistema , Wiley Online Library on [21/07/2024]. See the Terms and Conditions (https://onlinelibrary.wiley.com/terms-and-conditions) on Wiley Online Library for rules of use; OA articles are governed by the applicable Creative Commons License

Table 11.11 (Continued)

Sample	BET SSA ($m^2 g^{-1}$)	Test conditions	Electrolyte	Current density/scan rate ($A g^{-1}$/ $mV s^{-1}$)	Energy/Power density ($Wh kg^{-1}$/ $kW kg^{-1}$)	Specific capacitance ($F g^{-1}$)	Explanation	Refs.
Carbon xerogel (CA-R/C 500)	706	CV/ three–electrode	1 M H_2SO_4	—/5	—/—	197	CA was synthesized by polycondensation of resorcinol and formaldehyde. Then it was dried under ambient conditions.	[84]
Carbon aerogel (POX-900)	519	CV/ three–electrode	1 M H_2SO_4	—/5		142	Aerogel was obtained by polymerization of resorcinol and/or pyrocatechol with formaldehyde and oxalic acid catalyst.	[202]
Carbon nanotube based aerogels								
Carbon nanotube aerogel (CNAG)	1059	CV/—	5 M KOH	—/20	—/—	524	Magnified CNTs were used directly on a microfibrous carbon paper (MFCP) substrate. CAG was then synthesized on CNTs.	[203]
Single-walled carbon nanotube (SWCNT) aerogels	—	GC-D/—	—	6.75/—	—/—	~46	The SWCNTs were suspended in deionized water using sodium dodecylbenzene sulfonate (SDBS) surfactant. SWCNT aerogels were synthesized by drying the wet gel precursors at the critical point.	[204]
CNT-Carbon aerogel	629	GC-D/ two-electrode	6 M KOH	—/—	—/—	326	CA was synthesized by polycondensation of resorcinol and formaldehyde. Also CNT has been added. Then it was dried supercritical conditions.	[88]
Carbon Nanotube Sponges	900–100	CV/ three–electrode	1 M $LiPF_6$	—/1	—/—	28.5	CNT sponge samples were synthesized by CVD. Ferrocene and 1,2-dichlorobenzene were used as the catalyst precursor and carbon source, respectively.	[205]
Binderless carbon nanotubes aerogel (CNAG)	1059	GC-D/ three–electrode	5 M KOH	—/—	—/—	524	Chemical vapor deposition method was used to grow CNAG material, carbon nanotubes on a microfibrous carbon paper substrate. Subsequently, carbon aerogel was synthesized on carbon nanotubes.	[206]

Downloaded from https://onlinelibrary.wiley.com/doi/ by ibrahim ragab - Universita Di Firenze Sistema , Wiley Online Library on [21/07/2024]. See the Terms and Conditions (https://onlinelibrary.wiley.com/terms-and-conditions) on Wiley Online Library for rules of use; OA articles are governed by the applicable Creative Commons License

Binderless carbon nanotubes aerogel (CNAG)	1059	GC-D/ three–electrode	3 M H_2SO_4	—/—	—/—	280	Chemical vapor deposition method was used to grow CNAG material, carbon nanotubes on a microfibrous carbon paper substrate. Subsequently, carbon aerogel was synthesized on carbon nanotubes.	[206]
Carbon nanotubes aerogel (CAG-3%MWNT)	804	GC-D/ three–electrode	3 M H_2SO_4	—/—	—/—	232	Polyacrylonitrile (PAN) and MWNT were dispersed in dimethylformamide (DMF). Then, drying and activation with CO_2 was carried out.	[207]
Graphene based aerogels								
Graphene aerogel (GA)	185	GC-D/ Two-electrode	EMIMBF4	1/—	120/1	216	Aerogel was synthesized using the hydrothermal method with GO. Then freeze-drying process was carried out.	[208]
3D rGO aerogel	—	GC-D/ three-electrode	1 M H_2SO_4	1/—	—/—	214	Aerogels were synthesized by the hydrothermal method. Freeze-drying process has been carried out.	[209]
rGO aerogel	190.4	GC-D/—	—	0.75/—	—/—	182	GOs were synthesized using reduction with L-ascorbic acid followed by drying at ambient pressure.	[210]
Unidirectional graphene aerogel (UGA)	—	GC-D/ three-electrode	1 M H_2SO_4	1/—	—/—	243	The GO dispersion was normally frozen and then freeze dried and thermal reduction was performed to obtain aerogel.	[211]
Graphene aerogel (H-GA)	210	GC-D/ two-electrode	EMIMBF4	1/—	135/1	243	Aerogel was synthesized using the hydrothermal method with H-GO (HCl-containing). Then freeze-drying process was carried out.	[208]
Graphene aerogel (GO)	504	GC-D/ two-electrode	0.5 M H_2SO_4	1/—	45/—	325	Aerogel was obtained from the graphene suspension obtained using the electrochemical exfoliation method. Freeze-drying process has been carried out.	[212]
Graphene aerogel (supercritical CO_2)	512	GC-D/—	6 M KOH	0.05/—	—/—	128	Aerogel was obtained by supercritical drying process with hydrogel precursors synthesized by reducing graphene oxide with L-ascorbic acid.	[213]

(*Continued*)

Downloaded from https://onlinelibrary.wiley.com/doi/ by ibrahim ragab - Universita Di Firenze Sistema , Wiley Online Library on [21/07/2024]. See the Terms and Conditions (https://onlinelibrary.wiley.com/terms-and-conditions) on Wiley Online Library for rules of use; OA articles are governed by the applicable Creative Commons License

Table 11.11 (Continued)

Sample	BET SSA ($m^2 g^{-1}$)	Test conditions	Electrolyte	Current density/scan rate ($A g^{-1}$/ $mV s^{-1}$)	Energy/Power density ($Wh kg^{-1}$/ $kW kg^{-1}$)	Specific capacitance ($F g^{-1}$)	Explanation	Refs.
Graphene aerogel (sol-gel)	793	CV/ three-electrode	0.5 M Na_2SO_4	—/25	—/—	25	GA was synthesized by polycondensation of resorcinol and formaldehyde in GO suspension. Then it was dried supercritical conditions	[214]
Graphene aerogel	504	GC-D/—	1 M $LiPF_6$	1/—	—/—	140	The GO colloidal suspension was slowly evaporated. Afterwards, washing and freeze drying were performed.	[215]
Graphene xerogel	50.9	GC-D/—	1 M $LiPF_6$	1/—	—/—	64	The GO colloidal suspension was slowly evaporated. Afterward, washing and drying process was carried out under ambient conditions.	[215]
Reduced graphene oxide aerogel (RGOA)	830	GC-D/ three electrode	1 M H_2SO_4	0.2/—	—/—	278.6	By using hypophosphorous acid (HPA) and I_2 reducers, aerogel synthesis was done by self-assembly and reduction process.	[216]
Activated carbon aerogels								
Activated carbon aerogels (CO_2 activated)	3431	GC-D/ The single-electrode	1 M Et_4NBF_4-AN	0.3/—	27.5/0 0.171	152	CA was synthesized by polycondensation of resorcinol and formaldehyde. It was then activated with CO_2.	[70]
Activated carbon aerogels (ACA-P/ H_3PO_4 activated)	2477	GC-D/ three electrode	6 M KOH	1/—	—/—	201	CA was synthesized by polycondensation of resorcinol and formaldehyde. It was then activated with H_3PO_4.	[217]
Porous Carbon Aerogel (CR_3-K_2CO_3 activated)	4568.9	GC-D/ three electrode	$EMIMBF_4$	3/—	78.1/2.7	173.6	CA was synthesized by polycondensation of resorcinol and formaldehyde. It was then activated with K_2CO_3. Subsequently, carbonization process was carried out.	[218]

Downloaded from https://onlinelibrary.wiley.com/doi/ by ibrahim ragab - Universita Di Firenze Sistema , Wiley Online Library on [21/07/2024]. See the Terms and Conditions (https://onlinelibrary.wiley.com/terms-and-conditions) on Wiley Online Library for rules of use; OA articles are governed by the applicable Creative Commons License

Activated carbon aerogels (ACA-K_2CO_3 activated)	1384	GC-D/ three electrode	6 M KOH	1/—	—/—	271	RFA was prepared by sol-gel method and then it was prepared by reacting in N_2 environment after activating with K_2CO_3. Subsequently, carbonization process was carried out.	[197]
Activated carbon aerogels (ACA-KOH activated)	1645	GC-D/—	1 M $TEABF_4$/ ACN	1/—	—/—	23.3	CA was synthesized by polycondensation of resorcinol and formaldehyde. It was then activated with KOH.	[103]
Activated carbon aerogels (ACA-CO_2 activated)	1987	CV/ three-electrode	1 M H_2SO_4	—/10	—/—	153	CA prepared by polycondensation of resorcinol and formaldehyde was left in a high temperature CO_2 atmosphere to produce activated carbon aerogel.	[198]
Activated carbon xerogels (GC)	3419	CV/ three-electrode	0.5 M H_2SO_4	—/10	—/—	266.2	CA was synthesized by polycondensation of resorcinol and formaldehyde. Then the surface was activated with CO_2.	[219]
Activated carbon xerogel (ACAs-4)	2119	GC-D/ three-electrode	6 M KOH	0.5/—	8.49/—	250	CA was synthesized by polycondensation of resorcinol and formaldehyde. It was then activated with CO_2 and KOH, respectively.	[104]
Activated carbon aerogels (CO_2 activated)	1268	GC-D/—	6 M KOH	1/—	—/—	94	CA was synthesized by polycondensation of resorcinol and formaldehyde. It was then activated with CO_2.	[220]
Graphene/ activated carbon aerogel	1158	GC-D/ three-electrode	6 M KOH	1/—	—/—	300	Resorcinol-formaldehyde aerogel containing graphene oxide was prepared and activated with K_2CO_3.	[197]
Biomass derived aerogels								
Cellulose aerogel (bagasse)	1892.4	GC-D/ three-electrode	6 M KOH	0.5/2	19.74/0.5	142.1	Cellulose was removed from the dried bagasse. Cellulose aerogel synthesis was done. Freeze drying was carried out. Finally, activation was done with KOH.	[82]

(*Continued*)

Downloaded from https://onlinelibrary.wiley.com/doi/ by ibrahim ragab - Universita Di Firenze Sistema , Wiley Online Library on [21/07/2024]. See the Terms and Conditions (https://onlinelibrary.wiley.com/terms-and-conditions) on Wiley Online Library for rules of use; OA articles are governed by the applicable Creative Commons License

Table 11.11 (Continued)

Sample	BET SSA ($m^2 g^{-1}$)	Test conditions	Electrolyte	Current density/scan rate ($A g^{-1}$/ $mV s^{-1}$)	Energy/Power density ($Wh kg^{-1}$/ $kW kg^{-1}$)	Specific capacitance ($F g^{-1}$)	Explanation	Refs.
Alginate-based aerogel (Sodium alginate)	1811	CV/ two-electrode	6 M KOH	1/—	10.4/—	188	Alginate aerogel was synthesized by making hydrogel from sodium alginate and then freeze drying. After the carbonization process, activation was made with KOH.	[221]
Graphene-like CAs (natural agaric)	2200	CV/ three-electrode	6 M KOH	3/200	~25.5/2	340	The agaric dispersion solution was subjected to hydrothermal treatment. Freeze drying was performed by adding NH_4Cl chemical agent. Then, activation was done with KOH.	[222]
Nanocellulose aerogels	1873	GC-D/ three-electrode	6 M KOH	1/—	—/—	261	Carbon aerogel synthesis via pyrolysis of nanocellulose aerogels prepared by dissolving cellulose microcrystalline in NaOH aqueous solutions, gelation, regeneration, and drying with supercritical CO_2. It is activated using CO_2.	[201]
Biomass derivative/GA (N-C-RGO) (cotton)	728.6	GC-D/ three-electrode	6 M KOH	0.1/—	—/—	320	Carbon networks produced from commercial cotton are hydrothermally transformed into graphene aerogel.	[223]
N-doped carbonaceous aerogels (N–CA-600)	158.3	CV/ three-electrode	6 M KOH	—/5	—/—	281	To obtain a carbonaceous hydrogel, watermelon was made into a monolith by a hydrothermal process. Aerogel structure was obtained by freeze drying. Afterward, N-doped composite materials were synthesized under hydrothermal conditions using polypyrrole source.	[224]
N-doped carbon aerogel (CA27-Aminated tannin)	860	CV/ three-electrode	4 M H_2SO_4	—/2	—/—	362.2	Tannin was dissolved in ammonia solution and subjected to hydrothermal processing. After changing to solvent, supercritical drying was performed.	[225]

Downloaded from https://onlinelibrary.wiley.com/doi/ by ibrahim ragab - Universita Di Firenze Sistema , Wiley Online Library on [21/07/2024]. See the Terms and Conditions (https://onlinelibrary.wiley.com/terms-and-conditions) on Wiley Online Library for rules of use; OA articles are governed by the applicable Creative Commons License

N-doped carbon cryogel (CC27-Aminated tannin)	754	CV/ three-electrode	4 M H_2SO_4	—/2	—/—	387.6	Tannin was dissolved in ammonia solution and subjected to hydrothermal processing. After changing to solvent, freeze drying was performed.	[225]
N-doped carbon xerogel (CX11-Aminated tannin)	552	CV/ three-electrode	4 M H_2SO_4	—/2	—/—	383.3	Tannin was dissolved in ammonia solution and subjected to hydrothermal processing. After changing to solvent, it was dried in a vacuum oven (subcritical conditions).	[225]
Composite aerogels								
Mn-activated carbon aerogel	1166	GC-D/ three-electrode	6 M KOH	1/—	—/—	189	After CA was synthesized by sol gel technique, activation was performed with K_2CO_3. Then, the composite was prepared by using the precursor of Manganese (II) nitrate hexahydrate ($Mn[NO_3]_2.6.H_2O$) and wetness impregnation method.	[226]
Ni- carbon aerogel	584	GC-D/—	6 M KOH	1/—	—/—	126.6	Metal-doped ($Ni[NO_3]_2{\cdot}6H_2O$) carbon aerogels (M-CA) were prepared by an in situ synthesis method.	[227]
RuO_2/ activated carbon aerogel	1748	GC-D/ three-electrode	1 M H_2SO_4	1/—	—/—	326	CA, synthesized by polycondensation of resorcinol and formaldehyde, was activated with K_2CO_3. Ruthenium oxide was impregnated into ACA using microwave assisted polyol method.	[198]
N-doped carbon aerogel (NCG-Cellulose NF)	487	GC-D/ two-electrode	2 M H_2SO_4	0.25/—	31.25/12.9	225	Aerogel, without catalyst, was synthesized by direct pyrolysis of bamboo cellulose nanofiber/melamine/ graphene oxide hybrid aerogel.	[228]
PANI/ graphene–carbon aerogels (AGCA)	2213	CV/ three-electrode	6 M KOH	—/1	—/—	420	Hydrogel by sol-gel method from resorcinol-formaldehyde solution with GO additive, aerogel structure was obtained by freeze drying. PANI was added to the structure by electrochemical polymerization method.	[229]

(*Continued*)

Downloaded from https://onlinelibrary.wiley.com/doi/ by ibrahim ragab - Universita Di Firenze Sistema , Wiley Online Library on [21/07/2024]. See the Terms and Conditions (https://onlinelibrary.wiley.com/terms-and-conditions) on Wiley Online Library for rules of use; OA articles are governed by the applicable Creative Commons License

Table 11.11 (Continued)

Sample	BET SSA ($m^2 g^{-1}$)	Test conditions	Electrolyte	Current density/scan rate ($A g^{-1}$/ $mV s^{-1}$)	Energy/Power density ($Wh kg^{-1}$/ $kW kg^{-1}$)	Specific capacitance ($F g^{-1}$)	Explanation	Refs.
PPy/carbon aerogel (CA1/PPy)	216.5	CV/three-electrode	1 M H_2SO_4	—/50	—/—	231	CA synthesis via polycondensation of resorcinol and formaldehyde. Polypyrrole coating of CA by chemical polymerization method.	[199]
WO_3/carbon aerogel (CA)	710	CV/three-electrode	0.5 M H_2SO_4	—/25	—/—	700	The tungsten oxide single crystal nanoparticles were embedded in the CA structure by an immersion-calcination process.	[230]
MoS_2/graphene aerogel (CMG)	149.3	GC-D/three-electrode	1 M Na_2SO_4	0.5/—	—/—	268	MoS_2 and GO aqueous solutions were mixed. Hydrothermal reduction process has been done. Freeze drying has been carried out.	[231]
3D MnO_2/S--PANI/P-RGO ternary composite aerogel	129.8	GC-D/three-electrode	1 M Na_2SO_4	1/—	—/—	571	$MnSO_4$, $KMnO_4$ and S-PANI were added in certain proportions to the GO solution. Aerogel was obtained by the hydrothermal method. Freeze-drying process has been carried out.	[232]

Downloaded from https://onlinelibrary.wiley.com/doi/ by ibrahim ragab - Universita Di Firenze Sistema , Wiley Online Library on [21/07/2024]. See the Terms and Conditions (https://onlinelibrary.wiley.com/terms-and-conditions) on Wiley Online Library for rules of use; OA articles are governed by the applicable Creative Commons License

Apart from these studies, some studies have been done on other components of the supercapacitor. For example, irreversible collapses due to surface tension can occur at the liquid or liquid/air interface of the membranes. This limits their use in supercapacitor applications. To overcome this, Lee et al., synthesized mechanically robust, electrically conductive, free-standing and transparent hybrid nanomembranes. For this, they used carbon nanotube layers coated with poly (3,4 ethylenedioxythiophene) (PEDOT) and densified using vapor phase polymerization. Hybrid nanomembranes with 66 nm thickness and low area density of $\sim 15\,\mu g\,cm^{-2}$ exhibited high mechanical strength and modulus of 135 MPa and 12.6 GPa, respectively [233]. Li et al., using polydopamine (PDA) as a crosslinker between cellulose and polyacrylamide (PAM), synthesized a flexible double crosslinked hydrogel membrane based on cellulose (C4-DM-40) with hierarchical porosity (maximum 80%). They used this synthesized material as separator in supercapacitors. C4-DM-40 hydrogel exhibited hierarchical porous structure, excellent tensile strength, stimulant-free self-recuperation properties, strong conglutination, and rapid suction [234]. 3D solid polymeric networks (polymeric hydrogels or aerogels) are used as electrolyte materials due to their ability to adsorb and hold water. Choudhury et al., used a natural gel, gelatin hydrogel, as a solid electrolyte for supercapacitors. The synthesized hydrogel has a capacitive performance of $81\,F\,g^{-1}$ [235]. Yamazaki et al., using cellulose and chitin, synthesized new composite hydrogels containing two types of ionic liquids. Hybrid hydrogels soaked in H_2SO_4 aqueous solution were used as electrolyte for supercapacitors. It exhibited an improved capacitive performance of $155\,F\,g^{-1}$ with fast discharge capacity and strength [236]. Park et al., synthesized chemically cross-linked lignin hydrogel electrolytes by integrating them with electrospun lignin/polyacrylonitrile nanofiber electrodes. Cross-linked lignin-based hydrogel electrolyte networks show high ionic conductivity and mechanical integrity. Also, this material provided a maximum energy and power density of $4.49\,Wh\,kg^{-1}$ and $2.63\,kW\,kg^{-1}$ in the supercapacitor, respectively. 3D materials used in binders act as a substrate for the dispersion of electrochemical active materials to form composite electrodes [97]. Choudhury et al., synthesized a new, cost-effective and environmentally friendly electrode binder made of chitosan chemical hydrogel (CCH). It is combined with black pearl carbon as the electrode for use in EDLCs. The data were analyzed and it was found that after the first few hundred charge cycles a decrease in capacitance occurs due to the current loss of active material [237].

11.6 Conclusions

In recent years, due to the rapid progress of scientific and technological developments, studies in the fields of design and controllable materials and devices have increased considerably. In the light of these studies, very different and interesting properties of carbon materials have been discovered. These discoveries have led to the development of devices that enable more efficient use of energy. Today, high performance energy conversion and storage devices have an important place in our daily life due to the increase in the human population and the increasing energy consumption.

Carbonaceous materials play an essential role in systems where electrochemical energy is converted and stored. Carbon has a very different place among chemical elements due to its high natural abundance, low specific gravity, and its availability in various solid forms or allotropes. Among the carbon-based materials, 3D aerogel structures are the most widely used in the energy field. Carbonaceous aerogels are materials that combine the superior properties of both carbonaceous materials and aerogels in their structure. Due to the interconnected skeletal structure of the aerogels, it has attractive physicochemical (high specific surface area, porous structures, low density, low thermal conductivity, mechanical strength, time-dependent stability in working conditions),

and electrochemical (very good electrical conductivity, dielectric constant) properties. The controllability of the synthesis of carbonaceous aerogels facilitates material design with desired properties. Carbonaceous aerogels are constantly being studied and researched in supercapacitors and fuel cells, especially as electrode materials.

Electrode is the most important component that determines device performance, efficiency, stability, and durability in both fuel cells and supercapacitors. Advances in electrode design will reduce the cost and size of fuel cells and supercapacitors further. This situation will increase the usage areas of these devices. In this way, the general problems experienced in the energy field will be avoided.

References

1 Dai, L., Chang, D.W., Baek, J.B., and Lu, W. (2012). Carbon nanomaterials for advanced energy conversion and storage. *Small* 8: 1130–1166.

2 Chang, H., Joo, S.H., and Pak, C. (2007). Synthesis and characterization of mesoporous carbon for fuel cell applications. *J. Mater. Chem.* 17: 3078–3088.

3 Biener, J., Stadermann, M., Suss, M. et al. (2011). Advanced carbon aerogels for energy applications. *Energy Environ. Sci.* 4: 656–667.

4 Simon, P. and Gogotsi, Y. (2010). Materials for electrochemical capacitors, nanoscience and technology: a collection of reviews from nature journals. *World Sci.* 320–329.

5 Hall, P.J., Mirzaeian, M., Fletcher, S.I. et al. (2010). Energy storage in electrochemical capacitors: designing functional materials to improve performance. *Energy Environ. Sci.* 3: 1238–1251.

6 Saravanakumara, B., Muralidharanb, G., Vadivel, S. et al. (2018). Theory, fundamentals and application of supercapacitors. In: *Electrochemical Capacitors: Theory, Materials and Applications*, vol. 26 (ed. M.F.A. Inamuddin, A.M. Asiri, S. Zaidi, and M.R.F. LLC), 1.

7 Gu, W. and Yushin, G. (2014). Review of nanostructured carbon materials for electrochemical capacitor applications: advantages and limitations of activated carbon, carbide-derived carbon, zeolite-templated carbon, carbon aerogels, carbon nanotubes, onion-like carbon, and graphene. *Wiley Interdiscip. Rev.: Energy Environ.* 3: 424–473.

8 Sharma, P. and Bhatti, T. (2010). A review on electrochemical double-layer capacitors. *Energy Convers. Manage.* 51: 2901–2912.

9 Zhu, J., Yang, D., Yin, Z. et al. (2014). Graphene and graphene-based materials for energy storage applications. *Small* 10: 3480–3498.

10 Pottathara, Y.B., Tiyyagura, H.R., Ahmad, Z., and Sadasivuni, K.K. (2020). Graphene-based aerogels: fundamentals and applications as supercapacitors. *J. Energy Storage* 30: 101549.

11 Lai, J., Nsabimana, A., Luque, R., and Xu, G. (2018). 3D porous carbonaceous electrodes for electrocatalytic applications. *Joule* 2: 76–93.

12 Kroto, H.W., Heath, J.R., O'Brien, S.C. et al. (1985). C60: Buckminsterfullerene. *Nature* 318: 162–163.

13 Iijima, S. (1991). Helical microtubules of graphitic carbon. *Nature* 354: 56–58.

14 Novoselov, K.S., Geim, A.K., Morozov, S.V. et al. (2004). Electric field effect in atomically thin carbon films. *science* 306: 666–669.

15 Falcao, E.H. and Wudl, F. (2007). Carbon allotropes: beyond graphite and diamond. *J. Chem. Technol. Biotechnol.* 82: 524–531.

16 Dervishi, E., Li, Z., Xu, Y. et al. (2009). Carbon nanotubes: synthesis, properties, and applications. *Part. Sci. Technol.* 27: 107–125.

17 Dicks, A.L. (2006). The role of carbon in fuel cells. *J. Power Sources* 156: 128–141.

18 Rocha, C., Rümmeli, M., Ibrahim, I. et al. (2011). Tailoring the physical properties of graphene. In: *Graphene: Synthesis and Applications* (ed. W. Choi and J.-W. Lee), 1. Boca Raton, FL: CRC Press.

19 Hou, J., Shao, Y., Ellis, M.W. et al. (2011). Graphene-based electrochemical energy conversion and storage: fuel cells, supercapacitors and lithium ion batteries. *Phys. Chem. Chem. Phys.* 13: 15384–15402.

20 Mandal, M., Maitra, A., Das, T., and Das, C.K. (2015). Graphene and related two-dimensional materials. In: *Graphene Materials: Fundamentals and Emerging Applications* (ed. A. Tiwari and M. Syväjärvi), 1–23. Hoboken, NJ: Wiley.

21 Quesnel, E., Roux, F., Emieux, F. et al. (2015). Graphene-based technologies for energy applications, challenges and perspectives. *2D Mater.* 2: 030204.

22 Liang, M. and Zhi, L. (2009). Graphene-based electrode materials for rechargeable lithium batteries. *J. Mater. Chem.* 19: 5871–5878.

23 Shao, Y., El-Kady, M.F., Wang, L.J. et al. (2015). Graphene-based materials for flexible supercapacitors. *Chem. Soc. Rev.* 44: 3639–3665.

24 Lee, H., Ihm, J., Cohen, M.L., and Louie, S.G. (2010). Calcium-decorated graphene-based nanostructures for hydrogen storage. *Nano Lett.* 10: 793–798.

25 Antolini, E. (2012). Graphene as a new carbon support for low-temperature fuel cell catalysts. *Appl. Catal., B* 123: 52–68.

26 Konios, D., Petridis, C., Kakavelakis, G. et al. (2015). Reduced graphene oxide micromesh electrodes for large area, flexible, organic photovoltaic devices. *Adv. Funct. Mater.* 25: 2213–2221.

27 Brownson, D.A. and Banks, C.E. (2014). *Introduction to Graphene, the Handbook of Graphene Electrochemistry*, 1–22. Springer.

28 Chen, C.-M. (2016). Literature review and research background. In: *Surface Chemistry and Macroscopic Assembly of Graphene for Application in Energy Storage*, 1–49. Springer.

29 González, A., Goikolea, E., Barrena, J.A., and Mysyk, R. (2016). Review on supercapacitors: technologies and materials. *Renewable Sustainable Energy Rev.* 58: 1189–1206.

30 Baddour, C.E. and Briens, C. (2005). Carbon nanotube synthesis: a review. *Int. J. Chem. Reactor Eng.* 3: 1–20.

31 Coro, J., Suárez, M., Silva, L.S. et al. (2016). Fullerene applications in fuel cells: a review. *Int. J. Hydrogen Energy* 41: 17944–17959.

32 Anctil, A., Babbitt, C.W., Raffaelle, R.P., and Landi, B.J. (2011). Material and energy intensity of fullerene production. *Environ. Sci. Technol.* 45: 2353–2359.

33 Kumar, M. and Ando, Y. (2010). Chemical vapor deposition of carbon nanotubes: a review on growth mechanism and mass production. *J. Nanosci. Nanotechnol.* 10: 3739–3758.

34 Churilov, G., Fedorov, A., and Novikov, P. (2003). Influence of electron concentration and temperature on fullerene formation in a carbon plasma. *Carbon* 41: 173–178.

35 Cooney, D.O. (1980). *Activated Charcoal: Antidotal and Other Medical Uses*. Marcel Dekker Incorporated.

36 Kim, M.-H., Kim, K.-B., Park, S.-M., and Roh, K.C. (2016). Hierarchically structured activated carbon for ultracapacitors. *Sci. Rep.* 6: 21182.

37 Chingombe, P., Saha, B., and Wakeman, R. (2005). Surface modification and characterisation of a coal-based activated carbon. *Carbon* 43: 3132–3143.

38 Wei, L. and Yushin, G. (2012). Nanostructured activated carbons from natural precursors for electrical double layer capacitors. *Nano Energy* 1: 552–565.

39 Kaur, P., Verma, G., and Sekhon, S. (2019). Biomass derived hierarchical porous carbon materials as oxygen reduction reaction electrocatalysts in fuel cells. *Prog. Mater Sci.* 102: 1–71.

40 Yang, D.-P., Li, Z., Liu, M. et al. (2019). Biomass-derived carbonaceous materials: recent progress in synthetic approaches, advantages, and applications. *ACS Sustainable Chem. Eng.* 7: 4564–4585.

41 Ma, Y. and Chen, Y. (2015). Three-dimensional graphene networks: synthesis, properties and applications. *Natl. Sci. Rev.* 2: 40–53.

42 Xu, P., Yang, J., Wang, K. et al. (2012). Porous graphene: properties, preparation, and potential applications. *Chin. Sci. Bull.* 57: 2948–2955.

43 Mao, J., Iocozzia, J., Huang, J. et al. (2018). Graphene aerogels for efficient energy storage and conversion. *Energy Environ. Sci.* 11: 772–799.

44 You, P. and Kamarudin, S. (2017). Recent progress of carbonaceous materials in fuel cell applications: an overview. *Chem. Eng. J.* 309: 489–502.

45 Varshney, K. (2014). Carbon nanotubes: a review on synthesis, properties and applications. *Int. J. Eng. Res. Gen. Sci.* 2: 660–677.

46 Yi, H., Zeng, G., Lai, C. et al. (2017). Environment-friendly fullerene separation methods. *Chem. Eng. J.* 330: 134–145.

47 White, R.J., Budarin, V., Luque, R. et al. (2009). Tuneable porous carbonaceous materials from renewable resources. *Chem. Soc. Rev.* 38: 3401–3418.

48 De, S., Balu, A.M., van der Waal, J.C., and Luque, R. (2015). Biomass-derived porous carbon materials: synthesis and catalytic applications. *ChemCatChem* 7: 1608–1629.

49 Sam, D.K., Sam, E.K., Durairaj, A. et al. (2020). Synthesis of biomass-based carbon aerogels in energy and sustainability. *Carbohydr. Res. 491* 491: 107986.

50 Bi, Z., Kong, Q., Cao, Y. et al. (2019). Biomass-derived porous carbon materials with different dimensions for supercapacitor electrodes: a review. *J. Mater. Chem. A* 7: 16028–16045.

51 Kistler, S.S. (1931). Coherent expanded aerogels and jellies. *Nature* 127: 741–741.

52 Aegerter, M.A., Leventis, N., and Koebel, M. (2011). *Advances in Sol-Gel Derived Materials and Technologies*, Aerogels Handbook. New York: Springer.

53 Shaari, N. and Kamarudin, S.K. (2019). Current status, opportunities, and challenges in fuel cell catalytic application of aerogels. *Int. J. Energy Res.* 43: 2447–2467.

54 Zhao, X., Zhang, J., Wang, X. et al. (2019). Polyimide aerogels crosslinked with MWCNT for enhanced visible-light photocatalytic activity. *Appl. Surf. Sci.* 478: 266–274.

55 Singh, S., Bhatnagar, A., Dixit, V. et al. (2016). Synthesis, characterization and hydrogen storage characteristics of ambient pressure dried carbon aerogel. *Int. J. Hydrogen Energy* 41: 3561–3570.

56 Moretti, E., Zinzi, M., Merli, F., and Buratti, C. (2018). Optical, thermal, and energy performance of advanced polycarbonate systems with granular aerogel. *Energy Build.* 166: 407–417.

57 Wu, X.-L., Wen, T., Guo, H.-L. et al. (2013). Biomass-derived sponge-like carbonaceous hydrogels and aerogels for supercapacitors. *ACS Nano* 7: 3589–3597.

58 Dolai, S., Bhunia, S.K., and Jelinek, R. (2017). Carbon-dot-aerogel sensor for aromatic volatile organic compounds. *Sens. Actuators, B* 241: 607–613.

59 Thai, Q.B., Nguyen, S.T., Ho, D.K. et al. (2020). Cellulose-based aerogels from sugarcane bagasse for oil spill-cleaning and heat insulation applications. *Carbohydr. Polym.* 228: 115365.

60 Meena, A.K., Mishra, G., Rai, P. et al. (2005). Removal of heavy metal ions from aqueous solutions using carbon aerogel as an adsorbent. *J. Hazard. Mater.* 122: 161–170.

61 Ülker, Z., Sanli, D., and Erkey, C. (2014). Applications of aerogels and their composites in energy-related technologies. In: *Supercritical Fluid Technology for Energy and Environmental Applications* (ed. V. Anikeev and M. Fan), 157–180. Elsevier.

62 Zuo, L., Zhang, Y., Zhang, L. et al. (2015). Polymer/carbon-based hybrid aerogels: preparation, properties and applications. *Materials* 8: 6806–6848.

63 Li, F., Xie, L., Sun, G. et al. (2019). Resorcinol-formaldehyde based carbon aerogel: preparation, structure and applications in energy storage devices. *Microporous Mesoporous Mater.* 279: 293–315.

64 Yamashita, J., Ojima, T., Shioya, M. et al. (2003). Organic and carbon aerogels derived from poly (vinyl chloride). *Carbon* 41: 285–294.

65 Kim, K.H., Oh, Y., and Islam, M.F. (2013). Mechanical and thermal management characteristics of ultrahigh surface area single-walled carbon nanotube aerogels. *Adv. Funct. Mater.* 23: 377–383.

66 Du, R., Zhao, Q., Zhang, N., and Zhang, J. (2015). Macroscopic carbon nanotube-based 3D monoliths. *Small* 11: 3263–3289.

67 Skaltsas, T., Avgouropoulos, G., and Tasis, D. (2011). Impact of the fabrication method on the physicochemical properties of carbon nanotube-based aerogels. *Microporous Mesoporous Mater.* 143: 451–457.

68 Meng, F., Zhang, X., Xu, B. et al. (2011). Alkali-treated graphene oxide as a solid base catalyst: synthesis and electrochemical capacitance of graphene/carbon composite aerogels. *J. Mater. Chem.* 21: 18537–18539.

69 Gorgolis, G. and Galiotis, C. (2017). Graphene aerogels: a review. *2D Materials* 4: 032001.

70 Liu, N., Shen, J., and Liu, D. (2013). Activated high specific surface area carbon aerogels for EDLCs. *Microporous Mesoporous Mater.* 167: 176–181.

71 Lee, J.-H. and Park, S.-J. (2020). Recent advances in preparations and applications of carbon aerogels: a review. *Carbon* 163: 1–18.

72 Pekala, R. and Kong, F.-M. (1989). A synthetic route to organic aerogels-mechanism, structure, and properties. *Le Journal de Physique Colloques* 50: C4-33–C34-40.

73 Pierre, A.C. and Pajonk, G.M. (2002). Chemistry of aerogels and their applications. *Chem. Rev.* 102: 4243–4266.

74 Araby, S., Qiu, A., Wang, R. et al. (2016). Aerogels based on carbon nanomaterials. *J. Mater. Sci.* 51: 9157–9189.

75 Reichenauer, G. (2000). Aerogels. In: *Kirk-Othmer Encyclopedia of Chemical Technology*, 1–30. Wiley.

76 Smirnova, I. and Gurikov, P. (2017). Aerogels in chemical engineering: strategies toward tailor-made aerogels. *Annu. Rev. Chem. Biomol. Eng.* 8: 307–334.

77 Smirnova, I. and Gurikov, P. (2018). Aerogel production: current status, research directions, and future opportunities. *J. Supercrit. Fluids* 134: 228–233.

78 Barım, Ş.B., Bayrakçeken, A., Bozbağ, S.E. et al. (2017). Control of average particle size of carbon aerogel supported platinum nanoparticles by supercritical deposition. *Microporous Mesoporous Mater.* 245: 94–103.

79 Li, J., Wang, X., Wang, Y. et al. (2008). Structure and electrochemical properties of carbon aerogels synthesized at ambient temperatures as supercapacitors. *J. Non-Cryst. Solids* 354: 19–24.

80 Wang, X., Liu, L., Wang, X. et al. (2011). Preparation and performances of carbon aerogel microspheres for the application of supercapacitor. *J. Solid State Electrochem.* 15: 643–648.

81 Woignier, T., Phalippou, J., Despetis, F., and Calas-Etienne, S. (2018)). *Aerogel Processing*Handbook of Sol-Gel Science and Technology (ed. L. Klein, M. Aparicio, and A. Jitianu), 985–1011. Springer.

82 Hao, P., Zhao, Z., Tian, J. et al. (2014). Hierarchical porous carbon aerogel derived from bagasse for high performance supercapacitor electrode. *Nanoscale* 6: 12120–12129.

83 Li, J., Wang, X., Huang, Q. et al. (2006). Studies on preparation and performances of carbon aerogel electrodes for the application of supercapacitor. *J. Power Sources* 158: 784–788.

84 Lee, Y.J., Jung, J.C., Yi, J. et al. (2010). Preparation of carbon aerogel in ambient conditions for electrical double-layer capacitor. *Curr. Appl Phys.* 10: 682–686.

85 Tonanon, N., Wareenin, Y., Siyasukh, A. et al. (2006). Preparation of resorcinol formaldehyde (RF) carbon gels: use of ultrasonic irradiation followed by microwave drying. *J. Non-Cryst. Solids* 352: 5683–5686.

86 Yang, J., Li, S., Yan, L. et al. (2010). Compressive behaviors and morphological changes of resorcinol–formaldehyde aerogel at high strain rates. *Microporous Mesoporous Mater.* 133: 134–140.

87 Lin, C. and Ritter, J.A. (2000). Carbonization and activation of sol–gel derived carbon xerogels. *Carbon* 38: 849–861.

88 Ciszewski, M., Szatkowska, E., Koszorek, A., and Majka, M. (2017). Carbon aerogels modified with graphene oxide, graphene and CNT as symetric supercapacitor electrodes. *J. Mater. Sci.: Mater. Electron.* 28: 4897–4903.

89 Bakierska, M., Lis, M., Pacek, J. et al. (2019). Bio-derived carbon nanostructures for high-performance lithium-ion batteries. *Carbon* 145: 426–432.

90 Butt, M.T.Z., Preuss, K., Titirici, M.-M. et al. (2018). Biomass-derived nitrogen-doped carbon aerogel counter electrodes for dye sensitized solar cells. *Materials* 11: 1171.

91 Zhuo, H., Hu, Y., Chen, Z. et al. (2019). A carbon aerogel with super mechanical and sensing performances for wearable piezoresistive sensors. *J. Mater. Chem. A* 7: 8092–8100.

92 Hu, L., He, R., Lei, H., and Fang, D. (2019). Carbon aerogel for insulation applications: a review. *Int. J. Thermophys.* 40: 39.

93 Abdullah, H.B., Irmawati, R., Ismail, I., and Yusof, N.A. (2020). Direct synthesis of carbon nanotube aerogel using floating catalyst chemical vapor deposition: effect of gas flow rate. *Chem. Pap.* 74: 1–7.

94 Haghgoo, M., Yousefi, A.A., Mehr, M.J.Z. et al. (2015). Correlation between morphology and electrical conductivity of dried and carbonized multi-walled carbon nanotube/resorcinol–formaldehyde xerogel composites. *J. Mater. Sci.* 50: 6007–6020.

95 Chandrasekaran, S., Campbell, P.G., Baumann, T.F., and Worsley, M.A. (2017). Carbon aerogel evolution: allotrope, graphene-inspired, and 3D-printed aerogels. *J. Mater. Res.* 32: 4166–4185.

96 Kwon, S.-M., Kim, H.-S., and Jin, H.-J. (2009). Multiwalled carbon nanotube cryogels with aligned and non-aligned porous structures. *Polymer* 50: 2786–2792.

97 Wu, X.-L. and Xu, A.-W. (2014). Carbonaceous hydrogels and aerogels for supercapacitors. *J. Mater. Chem. A* 2: 4852–4864.

98 William, S., Hummers, J., and Offeman, R.E. (1958). Preparation of graphitic oxide. *J. Am. Chem. Soc.* 80: 1339–1339.

99 Xu, Y., Sheng, K., Li, C., and Shi, G. (2010). Self-assembled graphene hydrogel via a one-step hydrothermal process. *ACS Nano* 4: 4324–4330.

100 Su, D. (2012). Macroporous 'bubble' graphene film via template-directed ordered-assembly for high rate supercapacitors. *Chem. Commun.* 48: 7149–7151.

101 Zhang, L., Chen, G., Hedhili, M.N. et al. (2012). Three-dimensional assemblies of graphene prepared by a novel chemical reduction-induced self-assembly method. *Nanoscale* 4: 7038–7045.

102 Worsley, M.A., Olson, T.Y., Lee, J.R. et al. (2011). High surface area, sp2-cross-linked three-dimensional graphene monoliths. *J. Phys. Chem. Lett.* 2: 921–925.

103 Kwon, S.H., Lee, E., Kim, B.-S. et al. (2014). Activated carbon aerogel as electrode material for coin-type EDLC cell in organic electrolyte. *Curr. Appl Phys.* 14: 603–607.

104 Liu, D., Shen, J., Liu, N. et al. (2013). Preparation of activated carbon aerogels with hierarchically porous structures for electrical double layer capacitors. *Electrochim. Acta* 89: 571–576.

105 Hanzawa, Y., Kaneko, K., Pekala, R., and Dresselhaus, M. (1996). Activated carbon aerogels. *Langmuir* 12: 6167–6169.

106 Andújar, J.M. and Segura, F. (2009). Fuel cells: history and updating. A walk along two centuries. *Renewable Sustainable Energy Rev.* 13: 2309–2322.

107 Ortiz-Rivera, E.I., Reyes-Hernandez, A.L., and Febo, R.A. (2007). Understanding the history of fuel cells. In: *2007 IEEE Conference on the History of Electric Power*, 117–122. IEEE.

108 Lucia, U. (2014). Overview on fuel cells. *Renewable Sustainable Energy Rev.* 30: 164–169.

109 Carrette, L., Friedrich, K.A., and Stimming, U. (2000). Fuel cells: principles, types, fuels, and applications. *ChemPhysChem* 1: 162–193.

110 Bagotsky, V.S., Skundin, A.M., and Volfkovich, Y.M. (2015). *Electrochemical Power Sources: Batteries, Fuel Cells, and Supercapacitors*. Wiley.

111 O'hayre, R., Cha, S.-W., Colella, W., and Prinz, F.B. (2016). *Fuel Cell Fundamentals*. Wiley.

112 Mench, M.M. (2008). *Fuel Cell Engines*. Wiley.

113 Dicks, A. and Rand, D.A.J. (2018). *Fuel Cell Systems Explained*. Wiley Online Library.

114 Barbir, F. (2012). *PEM Fuel Cells: Theory and Practice*. Academic Press.

115 Leech, D., Kavanagh, P., and Schuhmann, W. (2012). Enzymatic fuel cells: recent progress. *Electrochim. Acta* 84: 223–234.

116 Ivanov, I., Vidaković-Koch, T., and Sundmacher, K. (2010). Recent advances in enzymatic fuel cells: experiments and modeling. *Energies* 3: 803–846.

117 Mohan, S.V., Srikanth, S., Velvizhi, G., and Babu, M.L. (2013). Microbial fuel cells for sustainable bioenergy generation: principles and perspective applications. In: *Biofuel Technologies* (ed. V.K. Gupta and M.G. Tuohy), 335–368. Springer.

118 Pichonat, T. (2009). MEMS-based micro fuel cells as promising power sources for portable electronics. In: *Micro Fuel Cells* (ed. T.S. Zhao), 51–97. Elsevier.

119 Prakash, S., Mustain, W.E., and Kohl, P.A. (2009). Electrolytes for long-life, ultra low-power direct methanol fuel cells. In: *Micro Fuel Cells* (ed. T.S. Zhao), 1–50. Elsevier.

120 Revankar, S.T. and Majumdar, P. (2014). *Fuel Cells: Principles, Design, and Analysis*. CRC Press.

121 Gao, F., Blunier, B., and Miraoui, A. (2013). *Proton Exchange Membrane Fuel Cells Modeling*. Wiley.

122 Gou, B., Na, W., and Diong, B. (2017). *Fuel Cells: Modeling, Control, and Applications*. CRC Press.

123 Yuan, X.-Z. and Wang, H. (2008). *PEM Fuel Cell Fundamentals, PEM Fuel Cell Electrocatalysts and Catalyst Layers*, 1–87. Springer.

124 Zhang, H., Wang, X., Zhang, J., and Zhang, J. (2008). Conventional catalyst ink, catalyst layer and MEA preparation. In: *PEM Fuel Cell Electrocatalysts and Catalyst Layers* (ed. J. Zhang), 889–916. Springer.

125 Jörissen, L. and Garche, J. (2016). Polymer electrolyte membrane fuel cells. In: *Hydrogen and Fuel Cell* (ed. J. Töpler and J. Lehmann), 239–281. Springer.

126 Min, M.-K., Cho, J., Cho, K., and Kim, H. (2000). Particle size and alloying effects of Pt-based alloy catalysts for fuel cell applications. *Electrochim. Acta* 45: 4211–4217.

127 Liu, H., Xia, D., and Zhang, J. (2008). Platinum-based alloy catalysts for PEM fuel cells. In: *PEM Fuel Cell Electrocatalysts and Catalyst Layers* (ed. J. Zhang), 631–654. Springer.

128 Wang, X., Tang, Y., Gao, Y., and Lu, T. (2008). Carbon-supported Pd–Ir catalyst as anodic catalyst in direct formic acid fuel cell. *J. Power Sources* 175: 784–788.

129 Vidal-Iglesias, F., Solla-Gullón, J., Montiel, V. et al. (2007). Screening of electrocatalysts for direct ammonia fuel cell: ammonia oxidation on PtMe (Me: Ir, Rh, Pd, Ru) and preferentially oriented Pt (1 0 0) nanoparticles. *J. Power Sources* 171: 448–456.

130 Choi, J.-H., Park, K.-W., Park, I.-S. et al. (2004). Methanol electro-oxidation and direct methanol fuel cell using Pt/Rh and Pt/Ru/Rh alloy catalysts. *Electrochim. Acta* 50: 787–790.

131 Atwan, M.H., Macdonald, C.L., Northwood, D.O., and Gyenge, E.L. (2006). Colloidal Au and Au-alloy catalysts for direct borohydride fuel cells: electrocatalysis and fuel cell performance. *J. Power Sources* 158: 36–44.

132 Brankovic, S., Wang, J., and Adžić, R. (2001). Pt submonolayers on Ru nanoparticles: a novel low Pt loading, high CO tolerance fuel cell electrocatalyst. *Electrochem. Solid State Lett.* 4: A217.

133 Lee, K., Zhang, L., and Zhang, J. (2008). Non-noble electrocatalysts for the PEM fuel cell oxygen reduction reaction. In: *PEM Fuel Cell Electrocatalysts and Catalyst Layers* (ed. J. Zhang), 715–757. Springer.

134 Tominaka, S., Momma, T., and Osaka, T. (2008). Electrodeposited Pd-Co catalyst for direct methanol fuel cell electrodes: preparation and characterization. *Electrochim. Acta* 53: 4679–4686.

135 Srivastava, R., Mani, P., Hahn, N., and Strasser, P. (2007). Efficient oxygen reduction fuel cell electrocatalysis on voltammetrically dealloyed Pt–Cu–Co nanoparticles. *Angew. Chem. Int. Ed.* 46: 8988–8991.

136 Shobha, T., Aravinda, C., Bera, P. et al. (2003). Characterization of Ni–Pd alloy as anode for methanol oxidative fuel cell. *Mater. Chem. Phys.* 80: 656–661.

137 Li, W., Zhou, W., Li, H. et al. (2004). Nano-stuctured Pt–Fe/C as cathode catalyst in direct methanol fuel cell. *Electrochim. Acta* 49: 1045–1055.

138 Sanlı, E., Çelikkan, H., Uysal, B.Z., and Aksu, M.L. (2006). Anodic behavior of Ag metal electrode in direct borohydride fuel cells. *Int. J. Hydrogen Energy* 31: 1920–1924.

139 Choi, J.-S., Chung, W.S., Ha, H.Y. et al. (2006). Nano-structured Pt–Cr anode catalyst over carbon support, for direct methanol fuel cell. *J. Power Sources* 156: 466–471.

140 Kodali, M., Santoro, C., Serov, A. et al. (2017). Air breathing cathodes for microbial fuel cell using Mn-, Fe-, Co-and Ni-containing platinum group metal-free catalysts. *Electrochim. Acta* 231: 115–124.

141 Samad, S., Loh, K.S., Wong, W.Y. et al. (2018). Carbon and non-carbon support materials for platinum-based catalysts in fuel cells. *Int. J. Hydrogen Energy* 43: 7823–7854.

142 Wang, Y.-J., Wilkinson, D.P., and Zhang, J. (2011). Noncarbon support materials for polymer electrolyte membrane fuel cell electrocatalysts. *Chem. Rev.* 111: 7625–7651.

143 Lee, W.-K., Ho, C.-H., Van Zee, J., and Murthy, M. (1999). The effects of compression and gas diffusion layers on the performance of a PEM fuel cell. *J. Power Sources* 84: 45–51.

144 Blanco, M. and Wilkinson, D.P. (2010). *Diffusion Layers, Proton Exchange Membrane Fuel Cells*, 191. Boca Raton, FL: CRC Press.

145 Cheng, T. (2010). Bipolar plates and plate materials. In: *Proton Exchange Membrane Fuel Cells: Materials Properties and Performance* (ed. D.P. Wilkinson, J. Zhang, R. Hui, et al.), 307–326. CRC Press.

146 Bron, M. and Roth, C. (2015). Carbon materials in low-temperature polymer electrolyte membrane fuel cells. In: *Electrochemistry of Carbon Electrodes* (ed. R.C. Alkire, P.N. Bartlett, and J. Lipkowski), 241–284. Wiley.

147 Thompsett, D. (2009). Recent developments in electrocatalyst activity and stability for proton exchange membrane fuel cells. In: *Proton Exchange Membrane Fuel Cells* (ed. D.P. Wilkinson, J. Zhang, R. Hui, et al.), 1. CRC Press.

148 Ramos-Sanchez, G. and Balbuena, P. (2013). Interactions of platinum clusters with a graphite substrate. *Phys. Chem. Chem. Phys.* 15: 11950–11959.

149 Shah, R. (2007). Introduction to fuel cells. In: *Recent Trends in Fuel Cell Science and Technology* (ed. S. Basu), 1–9. Springer.

150 Zhang, J. and Zhang, J. (2008). Catalyst layer/MEA performance evaluation. In: *PEM Fuel Cell Electrocatalysts and Catalyst Layers* (ed. J. Zhang), 965–1002. Springer.

151 Singh, R., Singh, M., Bhartiya, S. et al. (2017). Facile synthesis of highly conducting and mesoporous carbon aerogel as platinum support for PEM fuel cells. *Int. J. Hydrogen Energy* 42: 11110–11117.

152 Bong, S. and Han, D. (2020). Mesopore-controllable carbon aerogel and their highly loaded PtRu anode electrocatalyst for DMFC applications. *Electroanalysis* 32: 104–111.

153 Liu, B. and Creager, S. (2010). Carbon xerogels as Pt catalyst supports for polymer electrolyte membrane fuel-cell applications. *J. Power Sources* 195: 1812–1820.

154 Alegre, C., Calvillo, L., Moliner, R. et al. (2011). Pt and PtRu electrocatalysts supported on carbon xerogels for direct methanol fuel cells. *J. Power Sources* 196: 4226–4235.

155 Oztuna, F.E.S., Barim, S.B., Bozbag, S.E. et al. (2017). Graphene aerogel supported Pt electrocatalysts for oxygen reduction reaction by supercritical deposition. *Electrochim. Acta* 250: 174–184.

156 Xu, X., Feng, G., and Yuan, F. (2020). Co nanoparticles decorated on N-doped rGO carbon aerogel as a highly efficient electrocatalyst for oxygen reduction. *Funct. Mater. Lett.* 13: 1950090.

157 Li, M., Jiang, Q., Yan, M. et al. (2018). Three-dimensional boron-and nitrogen-codoped graphene aerogel-supported Pt nanoparticles as highly active electrocatalysts for methanol oxidation reaction. *ACS Sustainable Chem. Eng.* 6: 6644–6653.

158 Çögenli, M.S. and Yurtcan, A.B. (2020). Heteroatom doped 3D graphene aerogel supported catalysts for formic acid and methanol oxidation. *Int. J. Hydrogen Energy* 45: 650–666.

159 Yang, Y., Huang, H., Shen, B. et al. (2020). Anchoring nanosized Pd on three-dimensional boron-and nitrogen-codoped graphene aerogels as a highly active multifunctional electrocatalyst for formic acid and methanol oxidation reactions. *Inorg. Chem. Front.* 7: 700–708.

160 Zhang, J., Zhao, Z., Wang, Y. et al. (2020). Ethanol electrooxidation on highly active palladium/graphene oxide aerogel catalysts. *Chem. Phys.* 534: 110753.

161 Yang, Y., Dong, R., Zhu, Y. et al. (2020). High-performance direct hydrogen peroxide fuel cells (DHPFCs) with silver nanowire-graphene hybrid aerogel as highly-conductive mesoporous electrodes. *Chem. Eng. J.* 381: 122749.

162 Yang, W., Wang, X., Rossi, R., and Logan, B.E. (2020). Low-cost Fe–N–C catalyst derived from Fe (III)-chitosan hydrogel to enhance power production in microbial fuel cells. *Chem. Eng. J.* 380: 122522.

163 Song, L.T., Wu, Z.Y., Zhou, F. et al. (2016). Sustainable hydrothermal carbonization synthesis of iron/nitrogen-doped carbon nanofiber aerogels as electrocatalysts for oxygen reduction. *Small* 12: 6398–6406.

164 Zhou, Y., Hu, X., Guo, S. et al. (2018). Multi-functional graphene/carbon nanotube aerogels for its applications in supercapacitor and direct methanol fuel cell. *Electrochim. Acta* 264: 12–19.

165 Abdelwahab, A., Castelo-Quibén, J., Vivo-Vilches, J.F. et al. (2018). Electrodes based on carbon aerogels partially graphitized by doping with transition metals for oxygen reduction reaction. *Nanomaterials* 8: 266.

166 Krittayavathananon, A. and Sawangphruk, M. (2016). Electrocatalytic oxidation of ethylene glycol on palladium coated on 3D reduced graphene oxide aerogel paper in alkali media: effects of carbon supports and hydrodynamic diffusion. *Electrochim. Acta* 212: 237–246.

167 Huang, H., Yang, Y., Song, Y. et al. (2020). Rh-decorated three-dimensional graphene aerogel networks as highly-efficient electrocatalysts for direct methanol fuel cells. *Front. Energy Res.* 8: 60.

168 Öner, E., Öztürk, A., and Yurtcan, A.B. (2020). Utilization of the graphene aerogel as PEM fuel cell catalyst support: effect of polypyrrole (PPy) and polydimethylsiloxane (PDMS) addition. *Int. J. Hydrogen Energy* 45: 34818–34836.

169 Yang, W., Peng, Y., Zhang, Y. et al. (2018). Air cathode catalysts of microbial fuel cell by nitrogen-doped carbon aerogels. *ACS Sustainable Chem. Eng.* 7: 3917–3924.

170 Xu, C., Su, Y., Liu, D., and He, X. (2015). Three-dimensional N, B-doped graphene aerogel as a synergistically enhanced metal-free catalyst for the oxygen reduction reaction. *Phys. Chem. Chem. Phys.* 17: 25440–25448.

171 Tian, X., Zhou, M., Tan, C. et al. (2018). KOH activated N-doped novel carbon aerogel as efficient metal-free oxygen reduction catalyst for microbial fuel cells. *Chem. Eng. J.* 348: 775–785.

172 Guo, W., Chao, S., and Chen, Q. (2020). Improved power generation using nitrogen-doped 3D graphite foam anodes in microbial fuel cells. *Bioprocess. Biosyst. Eng.* 43: 143–151.

173 Yang, Y. and Chang, H. (2018). Multi-scale porous graphene/activated carbon aerogel enables lightweight carbonaceous catalysts for oxygen reduction reaction. *J. Mater. Res.* 33: 1247–1257.

174 Glora, M., Wiener, M., Petričević, R. et al. (2001). Integration of carbon aerogels in PEM fuel cells. *J. Non-Cryst. Solids* 285: 283–287.

175 Su, J., Pu, H., Chang, Z., and Wan, D. (2012). A facile crosslinking method of polybenzimidazole with sulfonyl azide groups for proton conducting membranes. *Polymer* 53: 3587–3593.

176 Xue, C., Zou, J., Sun, Z. et al. (2014). Graphite oxide/functionalized graphene oxide and polybenzimidazole composite membranes for high temperature proton exchange membrane fuel cells. *Int. J. Hydrogen Energy* 39: 7931–7939.

177 Simon, P., Brousse, T., and Favier, F. (2017). *Supercapacitors Based on Carbon or Pseudocapacitive Materials*. Wiley.

178 Zhao, Z., Richardson, G.F., Meng, Q. et al. (2015). PEDOT-based composites as electrode materials for supercapacitors. *Nanotechnology* 27: 042001.

179 Conway, B.E. (1999, 1999). *Electrochemical Supercapacitors. Scientific Fundamentals and Technological Applications*. New York. Electrochemical Supercapacitors, Plenum Publishers, Kluwer Academics: Kluwer Academics/Plenum Publishers.

180 Mombeshora, E.T. and Nyamori, V.O. (2015). A review on the use of carbon nanostructured materials in electrochemical capacitors. *Int. J. Energy Res.* 39: 1955–1980.

181 Moganapriya, C., Kumar, P.S., Pal, S.K. et al. (2018). Electrochemical super capacitors fabricated by the layer-by-layer (LbL) technique. In: *Electrochemical Capacitors: Theory, Materials and Applications*, vol. 26 (ed. Inamuddin, M.F. Ahmer, A.M. Asiri, and S. Zaidi), 236. Materials Research Forum LLC.

182 Jayalekshmi, S. and Puthirath, A. (2014). Supercapacitors: fundamental aspects. In: *Nanostructured Ceramic Oxides for Supercapacitor Applications* (ed. A. Balakrishnan and K.R.V. Subramanian), 41. CRC Press.

183 Kim, B.K., Sy, S., Yu, A., and Zhang, J. (2015). Electrochemical supercapacitors for energy storage and conversion. In: *Handbook of Clean Energy Systems* (ed. L.F. Cabeza, R. Sioshansi, and J. Yan), 1–25. Wiley.

184 Kiamahalleh, M.V. and Zein, S. (2014). Future scope and directions of nanotechnology in creating next-generation supercapacitors. In: *Nanostructured Ceramic Oxides for Supercapacitor Applications* (ed. A. Balakrishnan and K.R.V. Subramanian), 153. CRC Press.

185 Samantara, A.K. and Ratha, S. (2017). *Materials Development for Active/Passive Components of a Supercapacitor: Background, Present Status and Future Perspective*. Springer.

186 Simon, P. and Gogotsi, Y. (2013). Capacitive energy storage in nanostructured carbon–electrolyte systems. *Acc. Chem. Res.* 46: 1094–1103.

187 Zhai, Y., Dou, Y., Zhao, D. et al. (2011). Carbon materials for chemical capacitive energy storage. *Adv. Mater.* 23: 4828–4850.

188 Hao, L., Li, X., and Zhi, L. (2013). Carbonaceous electrode materials for supercapacitors. *Adv. Mater.* 25: 3899–3904.

189 Ghosh, A. and Lee, Y.H. (2012). Carbon-based electrochemical capacitors. *ChemSusChem* 5: 480–499.

190 Zhong, C., Deng, Y., Hu, W. et al. (2015). A review of electrolyte materials and compositions for electrochemical supercapacitors. *Chem. Soc. Rev.* 44: 7484–7539.

191 Azaıs, P. (2013). *Manufacturing of Industrial Supercapacitors* (ed. F. Béguin and E. Frąckowiak). Wiley Online Library.

192 Jiang, H., Lee, P.S., and Li, C. (2013). 3D carbon based nanostructures for advanced supercapacitors. *Energy Environ. Sci.* 6: 41–53.

193 Andreas, H. (2014). Measurement techniques for performance evaluation of supercapacitor materials and systems. In: *Nanostructured Ceramic Oxides for Supercapacitor Applications* (ed. A. Balakrishnan and K.R.V. Subramanian), 71. CRC Press.

194 Ratha, S. and Samantara, A.K. (2018). *Supercapacitor: Instrumentation, Measurement and Performance Evaluation Techniques*. Springer.

195 Li, F., Xie, L., Sun, G. et al. (2018). Structural evolution of carbon aerogel microspheres by thermal treatment for high–power supercapacitors. *J. Energy Chem.* 27: 439–446.

196 Yang, I., Kim, S.-G., Kwon, S.H. et al. (2017). Relationships between pore size and charge transfer resistance of carbon aerogels for organic electric double-layer capacitor electrodes. *Electrochim. Acta* 223: 21–30.

197 Lee, Y.J., Kim, G.-P., Bang, Y. et al. (2014). Activated carbon aerogel containing graphene as electrode material for supercapacitor. *Mater. Res. Bull.* 50: 240–245.

198 Singh, A., Kohli, D., Bhartiya, S. et al. (2017). Ruthenium doped carbon aerogel with CO_2 surface activation for enhanced electrochemical capacitance. *Curr. Appl Phys.* 17: 885–889.

199 Samancı, M., Daş, E., and Bayrakçeken Yurtcan, A. (2021). Carbon aerogel and their polypyrrole composites used as capacitive materials. *Int. J. Energy Res.* 45: 1729–1747.

200 Park, D.-W., Cañas, N.A., Schwan, M. et al. (2016). A dual mesopore C-aerogel electrode for a high energy density supercapacitor. *Curr. Appl Phys.* 16: 658–664.

201 Zu, G., Shen, J., Zou, L. et al. (2016). Nanocellulose-derived highly porous carbon aerogels for supercapacitors. *Carbon* 99: 203–211.

202 Moreno-Castilla, C., Dawidziuk, M.B., Carrasco-Marín, F., and Zapata-Benabithe, Z. (2011). Surface characteristics and electrochemical capacitances of carbon aerogels obtained from resorcinol and pyrocatechol using boric and oxalic acids as polymerization catalysts. *Carbon* 49: 3808–3819.

203 Bordjiba, T., Mohamedi, M., and Dao, L.H. (2008). New class of carbon-nanotube aerogel electrodes for electrochemical power sources. *Adv. Mater.* 20: 815–819.

204 Van Aken, K.L., Pérez, C.R., Oh, Y. et al. (2015). High rate capacitive performance of single-walled carbon nanotube aerogels. *Nano Energy* 15: 662–669.

205 Li, P., Kong, C., Shang, Y. et al. (2013). Highly deformation-tolerant carbon nanotube sponges as supercapacitor electrodes. *Nanoscale* 5: 8472–8479.

206 Bordjiba, T. and Mohamedi, M. (2011). Molding versus dispersion: effect of the preparation procedure on the capacitive and cycle life of carbon nanotubes aerogel composites. *J. Solid State Electrochem.* 15: 765–771.

207 Bordjiba, T., Mohamedi, M., and Dao, L.H. (2007). Charge storage mechanism of binderless nanocomposite electrodes formed by dispersion of CNTs and carbon aerogels. *J. Electrochem. Soc.* 155: A115.

208 Tang, X.-N., Liu, C.-Z., Chen, X.-R. et al. (2019). Graphene aerogel derived by purification-free graphite oxide for high performance supercapacitor electrodes. *Carbon* 146: 147–154.
209 Yang, Y., Xi, Y., Li, J. et al. (2017). Flexible supercapacitors based on polyaniline arrays coated graphene aerogel electrodes. *Nanoscale Res. Lett.* 12: 1–9.
210 Lee, S.P., Ali, G.A., Hegazy, H. et al. (2021). Optimizing reduced graphene oxide aerogel for a supercapacitor. *Energy & Fuels* 35: 4559–4569.
211 Wu, X., Tang, L., Zheng, S. et al. (2018). Hierarchical unidirectional graphene aerogel/polyaniline composite for high performance supercapacitors. *J. Power Sources* 397: 189–195.
212 Jung, S.M., Mafra, D.L., Lin, C.-T. et al. (2015). Controlled porous structures of graphene aerogels and their effect on supercapacitor performance. *Nanoscale* 7: 4386–4393.
213 Zhang, X., Sui, Z., Xu, B. et al. (2011). Mechanically strong and highly conductive graphene aerogel and its use as electrodes for electrochemical power sources. *J. Mater. Chem.* 21: 6494–6497.
214 Wang, C.C., Chen, H.C., and Lu, S.Y. (2014). Manganese oxide/graphene aerogel composites as an outstanding supercapacitor electrode material. *Chem. Eur. J.* 20: 517–523.
215 Jung, S.M., Kim, D.W., and Jung, H.Y. (2019). Which is the most effective pristine graphene electrode for energy storage devices: aerogel or xerogel? *Nanoscale* 11: 17563–17570.
216 Si, W., Wu, X., Zhou, J. et al. (2013). Reduced graphene oxide aerogel with high-rate supercapacitive performance in aqueous electrolytes. *Nanoscale Res. Lett.* 8: 247.
217 Li, C., Yang, X., and Zhang, G. (2015). Mesopore-dominant activated carbon aerogels with high surface area for electric double-layer capacitor application. *Mater. Lett.* 161: 538–541.
218 Li, F., Xie, L., Sun, G. et al. (2017). Boosting the specific surface area of hierarchical porous carbon aerogel through the multiple roles of the catalyst for high-performance supercapacitors. *ChemElectroChem* 4: 3119–3125.
219 Chang, Y.-M., Wu, C.-Y., and Wu, P.-W. (2013). Synthesis of large surface area carbon xerogels for electrochemical double layer capacitors. *J. Power Sources* 223: 147–154.
220 Lee, E.J., Lee, Y.J., Kim, J.K. et al. (2015). Oxygen group-containing activated carbon aerogel as an electrode material for supercapacitor. *Mater. Res. Bull.* 70: 209–214.
221 Wang, B., Li, D., Tang, M. et al. (2018). Alginate-based hierarchical porous carbon aerogel for high-performance supercapacitors. *J. Alloys Compd.* 749: 517–522.
222 Zhang, H., Zhang, Z., Luo, J.D. et al. (2019). A chemical blowing strategy to fabricate biomass-derived carbon-aerogels with graphene-like nanosheet structures for high-performance supercapacitors. *ChemSusChem* 12: 2462–2470.
223 Song, W.-L., Li, X., and Fan, L.-Z. (2016). Biomass derivative/graphene aerogels for binder-free supercapacitors. *Energy Storage Mater.* 3: 113–122.
224 Ren, Y., Zhang, J., Xu, Q. et al. (2014). Biomass-derived three-dimensional porous N-doped carbonaceous aerogel for efficient supercapacitor electrodes. *RSC Adv.* 4: 23412–23419.
225 Braghiroli, F., Fierro, V., Szczurek, A. et al. (2015). Hydrothermally treated aminated tannin as precursor of N-doped carbon gels for supercapacitors. *Carbon* 90: 63–74.
226 Lee, Y.J., Park, H.W., Hong, U.G., and Song, I.K. (2012). Mn-doped activated carbon aerogel as electrode material for pseudo-capacitive supercapacitor: effect of activation agent. *Curr. Appl Phys.* 12: 1074–1080.
227 Wang, S., Xu, Y., Yan, M. et al. (2018). Comparative study of metal-doped carbon aerogel: physical properties and electrochemical performance. *J. Electroanal. Chem.* 809: 111–116.
228 Zhang, X., Zhao, J., He, X. et al. (2018). Mechanically robust and highly compressible electrochemical supercapacitors from nitrogen-doped carbon aerogels. *Carbon* 127: 236–244.

229 Kim, C.H., Zhao, D., Lee, G., and Liu, J. (2016). Strong, machinable carbon aerogels for high performance supercapacitors. *Adv. Funct. Mater.* 26: 4976–4983.

230 Wang, Y.-H., Wang, C.-C., Cheng, W.-Y., and Lu, S.-Y. (2014). Dispersing WO_3 in carbon aerogel makes an outstanding supercapacitor electrode material. *Carbon* 69: 287–293.

231 Yang, M., Jeong, J.-M., Huh, Y.S., and Choi, B.G. (2015). High-performance supercapacitor based on three-dimensional MoS_2/graphene aerogel composites. *Compos. Sci. Technol.* 121: 123–128.

232 Akbar, A.R., Tian, W., Qadir, M.B. et al. (2021). A novel ternary composite aerogel for high-performance supercapacitor. *Colloids Surf., A* 610: 125644.

233 Lee, J.A., Shin, M.K., Kim, S.H. et al. (2012). Hybrid nanomembranes for high power and high energy density supercapacitors and their yarn application. *ACS Nano* 6: 327–334.

234 Li, L., Lu, F., Wang, C. et al. (2018). Flexible double-cross-linked cellulose-based hydrogel and aerogel membrane for supercapacitor separator. *J. Mater. Chem. A* 6: 24468–24478.

235 Choudhury, N.A., Sampath, S., and Shukla, A. (2007). Gelatin hydrogel electrolytes and their application to electrochemical supercapacitors. *J. Electrochem. Soc.* 155: A74.

236 Yamazaki, S., Takegawa, A., Kaneko, Y. et al. (2009). An acidic cellulose–chitin hybrid gel as novel electrolyte for an electric double layer capacitor. *Electrochem. Commun.* 11: 68–70.

237 Choudhury, N.A., Northrop, P.W., Crothers, A.C. et al. (2012). Chitosan hydrogel-based electrode binder and electrolyte membrane for EDLCs: experimental studies and model validation. *J. Appl. Electrochem.* 42: 935–943.

12

Aerogels for Electrocatalytic Hydrogen Production

Arun Prasad Murthy

Department of Chemistry, School of Advanced Sciences, Vellore Institute of Technology, Vellore, Tamil Nadu, 632014, India

12.1 Introduction

12.1.1 Energy Crisis

To meet the world's energy demands, several hundred million barrels of crude oil are used every day [1]. This creates concerns for meeting the energy demands of a rapidly increasing population. Energy security is also a concern of the developed countries in which energy use is very high but the resources are controlled by governments that are at odds with the countries needing them. The energy relationship between the developed countries and oil-rich countries is affected by various global and regional conflicts, which give rise to further impetus to establishing energy independence, including through alternative clean fuels [2]. Environment pollution due to carbon dioxide produced from fossil fuel combustion further complicates the already deteriorating energy crisis. Rise in global temperature, melting of polar ice, rise in sea level, and acid rains are some of the consequences of environment pollution faced by global population [3]. In this context, several countries have issued deadlines to ban vehicles with fossil fuel–based internal combustion engines [4].

Hence, energy demands of the future must be fulfilled from renewable energy sources like solar energy, wind energy, energy derived from biomass, and geothermal energy [1] However, these renewable energy sources are sporadic and intermittent in nature and hence need to be stored in suitable energy carriers. For example, hydrogen, as an energy carrier, can be directly used in (i) fuel cells for producing electricity, (ii) internal hydrogen combustion engines of automobiles and related vehicles, (iii) domestic and industrial heating systems, etc. [2]. Furthermore, hydrogen can be stored in metal hydrides as a solid form.

The term *hydrogen economy* was coined by John Bockris in 1970 for the system that meets the energy demands through hydrogen. In simple terms, the hydrogen economy can be explained as the intermittent energies such as solar and wind in the form of electricity can be stored as chemical energy in hydrogen that has high theoretical mass energy density. The same electricity can be again generated whenever and wherever required through hydrogen fuel cells with water as the only product. It may be noted that multinational aerospace corporation Airbus has announced plans to develop the world's first zero-emission aircrafts ZEROe by 2035. Hydrogen combustion will be used in the ZEROe concept for the future zero emission aircrafts [5].

Aerogels for Energy Saving and Storage, First Edition. Edited by Meldin Mathew, Hanna J. Maria, Ange Nzihou, and Sabu Thomas.
© 2024 John Wiley & Sons, Inc. Published 2024 by John Wiley & Sons, Inc.

Presently, most hydrogen gas is produced from steam reforming of natural gas as follows; $CH_4 + 2H_2O \rightarrow 4H_2 + CO_2$ at refineries and from oil reforming and coal gasification. Carbon dioxide produced as the byproduct in these processes increases the greenhouse effect [6]. In this context, it is imperative to produce hydrogen from water in a pure form through electrochemical water splitting. Naturally, water is the most desirable source of hydrogen that is easily available, abundant, and contains no carbon.

12.1.2 Electrocatalytic Water Splitting

Electrocatalytic water splitting is a simple and well-established green technology for producing hydrogen without carbon dioxide emission. Water and electric energy are the main consumable components of water splitting. During water splitting, electron transfer from anode to cathode results in the simultaneous formation of oxygen and hydrogen at the respective electrodes as follows.

$$2H_2O \xrightarrow{>1.23\,V} 2H_2 + O_2 \tag{12.1}$$

At room temperature, the theoretically required external voltage to drive water splitting is 1.23 V. However, the amount of energy required to achieve reasonable reaction rate is about 286 kJ mol^{-1} [7]. In most cases, highly acidic or basic electrolytes are employed for water splitting in order to enhance the efficiency of the reaction. During water electrolysis, hydrogen is produced at cathode via hydrogen evolution reaction (HER), which occurs as follows:

In acid media $$2H^+ + 2e^- \rightarrow H_2 \tag{12.2}$$

In basic media $$2H_2O + 2e^- \rightarrow H_2 + 2OH^- \tag{12.3}$$

In a similar manner, oxygen is formed at anode via oxygen evolution reaction (OER) and it takes place as follows:

In acid media $$2H_2O \rightarrow O_2 + 4H^+ + 4e^- \tag{12.4}$$

In basic media $$4OH^- \rightarrow O_2 + 2H_2O + 4e^- \tag{12.5}$$

12.1.3 Electrocatalysts for HER and OER

Electrocatalysis is an important part of material science wherein several energy related processes such as HER for hydrogen production, OER for metal-air batteries and water splitting, oxygen reduction reaction for fuel cells are studied [8]. The role of an electrocatalyst is to lower the energy barrier of a reaction and accelerate its reaction rate [9]. HER takes place at platinum at the lowest overpotential; however, large-scale production of hydrogen requires millions of kilograms of Pt, which is not viable since Pt is not available in abundance and is highly expensive. Similarly, in the case of OER, IrO_2 and RuO_2 are the present state-of-the-art electrocatalysts, and they too are scarce and costly for global energy demands [10]. During the past decades, various non-noble metal HER and OER electrocatalysts have been developed as alternatives to expensive noble metals–based electrocatalysts, including chalcogenides, nitrides, carbides, phosphides, alloys, and oxides, for example, and a common feature in these electrocatalysts is transition metal elements. This may be reasoned on the basis of the presence of free d-orbitals and unpaired electrons in transition metals, which can adsorb protons from the solution [11].

12.1.4 Application of Aerogels as Electrocatalyst Materials for HER and OER

Aerogels are a class of porous materials characterized by large specific surface area and ultralow density. These are self-supported architectures that can be structured from a variety of building blocks such as metal oxides, metal chalcogenides, organic-inorganic hybrids, carbons, ceramics, and polymers. Aerogels have attracted wide interest in the research areas of energy storage and conversion, catalysis, adsorption, etc. [8]. Interconnected pores present in aerogels provide open channels for mass transport and the 3D architectures are especially suitable for small molecule reduction/oxidation such as hydrogen, oxygen, methanol, and ethanol [12].

Noble metal aerogels are relatively recent members of aerogel family appeared in 2009 [13] and possess all the desirable properties of aerogels along with excellent catalytic activity, self-supported architectures, and electrical conductivity [14]. Thus, they may fill the gap between macromaterials and nanomaterials. Some metal aerogels showed properties that are superior to those of metal nanoparticles [15]. Noble metal aerogels display higher performance in terms of activity and life in comparison to commercial noble metal catalysts like Pt/C and Pd/C [8]. However, manipulation of parameters such as spatial element distributions and ligaments sizes requires complete understanding of sol-gel process, and structure performance correlations. In a similar manner to metal aerogels, other metallic aerogels have received wide interest regarding electrocatalysis because of their extremely low density, high porosity, and high specific surface area along with metallic conductivity [16].

Carbon aerogels, the lightest solids, are widely employed as electrodes in energy applications. With 3D construction as well as abundant micro and mesoporous network structures, morphology properties of carbon aerogels can be tuned by sol-gel chemistry. Carbon aerogels possess not only low electric resistance but also large Brunauer–Emmett–Teller (BET) surface area of up to 500–600 $m^2\ g^{-1}$. Furthermore, carbon aerogels are also suitable for bio-electrodes with chemical inertness and biocompatibility [17]. Carbon aerogels can be obtained from (i) organic materials, (ii) graphene or carbon nanotubes (CNT), and (iii) biomass. From these materials carbon aerogels are produced through carbonization in inert atmosphere, chemical vapor deposition, self-gelation, drying treatments like freeze drying, for example [18].

Graphene-based aerogels form an important class of aerogels widely employed in catalysis applications. In most cases, graphene aerogels are used for improving structural stability, increasing conductivity, and enhancing active sites [19]. Compared to carbon aerogels, graphene aerogels have better conductivity as well as adjustable pore size distribution and surface area [11]. In addition to good electric conductivity, these aerogels possess more desirable properties such as abundant and highly continuous pores, interconnected structures, and optimized catalytic performance, for example. As support materials, graphene aerogels render stability to the active material and enhance electrical contact to the electrode [20]. Chemical vapor deposition method, direct ink writing, hydrothermal process, and ascorbic acid reduction, are employed to synthesize grapheme-based aerogels [21].

12.1.5 Basics of Electroanalysis of Water Splitting

Evaluation of electro activity of an electrocatalyst for HER/OER or comparison of two or more electrocatalysts involves measuring certain basic parameters. Since these parameters are often mentioned in the discussion of this chapter it will be pertinent to understand these parameters. Generally, routine electrochemical experiments are carried out in a three-electrode cell assembly in a given electrolyte at a relatively lower scan rates. Overpotential (η) to attain a current density (j)

of 10 mA cm^{-2} is denoted simply as η_{10} and is a standard metric for its relevance in solar hydrogen production [22]. However, there are many reports in which η values are reported at other j values as well, such as j = 20, 50, or 100 mA cm^{-2}. In these cases, the overpotentials are denoted as η_x, where x refers to the current density value in mA cm^{-2} unit at which η is mentioned.

Tafel analysis is another important tool to obtain Tafel slope, Tafel constant, and exchange current density values for an electrochemical reaction occurring at the given electrocatalyst. Steady/quasi-steady state j is obtained over a range of η experimentally and converted to logarithmic values (log(j)). Tafel plot is obtained by plotting log(j) vs η and the slope of the linear portion of the plot provides the Tafel slope. Exchange current density of the reaction at the given electrocatalyst and experimental conditions can be obtained from the Tafel plot in conjunction with the Tafel equation through graphical method [23].

Raw polarization data used for Tafel analysis may include Ohmic contributions from bulk solution, external wiring, and substrate, forming series resistance of the electrochemical cell [24]. This limitation of polarization method of Tafel analysis was demonstrated by Vrubel et al. [25] and employed impedance method of Tafel analysis in their study. In impedance method of Tafel analysis, charge transfer resistance R_{ct} is determined at various η values using suitable equivalent circuit models. Finally, $\log(1/R_{ct})$ values are plotted against respective η values to obtain the Tafel plot. Accelerated degradation tests [26], long-term chronoamperometric, or chronopotentiometric tests are generally conducted in the given electrolyte to evaluate the durability of an electrocatalyst. Initial activity of the electrocatalyst is compared to the activity at the end of the durability test, and the loss in activity is determined to evaluate the durability.

12.2 Application of Aerogels in Hydrogen Evolution Reaction

HER is one of the simplest and most well-studied electrochemical reaction occurring through three elementary steps – namely, Volmer, Heyrovsky, and Tafel reactions [3]. Several earlier studies indicated that HER takes place at a rapid rate on the surface that adsorbs hydrogen optimally (i.e. strong enough for the reaction to initiate and weak enough for the adsorbed hydrogen atoms leaving the active sites as hydrogen molecules) [27]. In this context, doped aerogels play a vital role in optimizing binding energy of adsorbed species, thereby enhancing catalytic activity of the electrocatalyst. This section deals with fabrication and HER activities of aerogel-based electrocatalysts.

Douglas et al. [2] fabricated resorcinol (Benzene-1, 3-diol)-formaldehyde carbon aerogels deposited on molybdenum metal and employed it as an efficient HER electrocatalyst in alkaline medium. The principal objective of the authors was to reduce operational cost investment of hydrogen production through enhancing kinetic rate of electrochemical reaction. Resorcinol-formaldehyde (RF) carbon aerogel possessed high surface area of larger than 700 m^2 g^{-1} with nano-pore sizes of 4 nm. RF precursor was used for producing carbon aerogel by sol-gel polymerization of resorcinol and formaldehyde. The carbon aerogel was then deposited thermally on molybdenum metal mesh. It was argued that the hydrogen and oxygen evolutions occurred on the surface of spectator metal-oxo intermediate. Charge transfer resistance of Mo-RF electrode was about 70% lower than that of pure molybdenum electrode. The authors opined that since Mo is 99% less expensive than Pt, replacement of Pt-based electrocatalysts with Mo-based ones in water electrolyzers would reduce capital cost.

Hou et al. [20] employed cost-effective catalysts based on graphene-aerogels for hydrogen production in microbial electrolysis cell from organic wastes. The electrocatalyst was 3D molybdenum disulphide/N-doped graphene aerogel (3D MoS_2/N-GA) produced through hydrothermal method.

In the first step, MoS_2 nanosheets was prepared by liquid exfoliation method and in the next step MoS_2 nanosheets were encapsulated in N-doped grapheme using hydrothermal method. Microbial electrolysis cells are bio-electrochemical electrolysis cells wherein organic materials are oxidized by electrogenic bacteria. The electrons generated are used to reduce protons at the cathode to produce hydrogen. Hence, this technology is considered beneficial for both hydrogen production and wastewater treatment. Electrochemical investigations on HER were conducted in neutral media using 3D MoS_2/N-GA as the working electrode. The electrocatalyst exhibited low onset overpotential of 236 mV and η_{10} of 261 mV. The electrocatalyst showed high stability and Tafel slope of 230 mV dec^{-1}. Bio-electrochemical hydrogen was produced in microbial electrolysis cell using 3D MoS_2/N-GA with peak current density of 0.36 mA cm^{-2} at the applied potential of 0.8 V, which was close to the current density produced by Pt/C (0.40 mA cm^{-2}).

Another application of carbon aerogel in microbial electrolysis cells in the production of hydrogen. In this study, bioanode played the role of supplying electrons to cathode for the reduction of protons. The authors successfully constructed 3D porous carbon aerogel–based bioanode and effected extracellular electron transfer to cathode through bacterial incubation. Initially, organic wet gel was prepared from 1,3-dihydroxy benzene and formaldehyde and subsequently was transformed to carbon aerogel through pyrolysis and activation. The microbial cell consisting of (biocarbon aerogel)||Pt could produce hydrogen at the rate of 0.37 μmol cm^{-2} h^{-1} at bias potential of 0.3 V. The authors ascribed the success of this promising biotechnology to (i) high surface area with abundant micro and mesoporous structures that increased the quantity of incubated bacteria, (ii) good biocompatibility with microbial attachment, (iii) chemical inertness still adsorbing organic species, and (iv) excellent conductivity of the 3D porous carbon aerogel. Other than hydrogen production, the authors suggested employing this technology for pollutant degradation as well.

Unlike nonmetal aerogels, only limited synthetic methods are available for the fabrication of metal aerogels. Kundu et al. [15] reported the synthesis of porous gold aerogel of high surface area on carbon nitride support (Au-aerogel/CN_x) and used it as electrocatalysts for hydrogen evolution and oxygen reduction reactions. It was the first report on the facile synthesis of metal aerogel on a 2D conducting support for catalytic applications. Sodium borohydride was used to reduce $HAuCl_4$ in the presence of CN_x nanosheets, and ultrasonic treatment produced Au-aerogel/CN_x. However, without sodium borohydride as the reducing agent, the authors could produce only gold nanoparticles on carbon nitride nanosheets. The electrocatalyst displayed HER onset overpotential of 30 mV, η_{10} of 185 mV and Tafel slope of 53 mV dec^{-1} in acid electrolyte along with high stability. The authors attributed the high HER performance to the synergistic effect between porous gold aerogel and carbon nitride support.

Another bifunctional electrocatalyst in environment friendly energy-related technologies such as fuel cells and water splitting was reported by Zhu et al. [28] Cobalt embedded nitrogen-doped graphene aerogel (Co/N-GA) was fabricated and employed as electrocatalysts for hydrogen evolution and oxygen reduction reactions. Metal organic framework@GA composite was used for the synthesis of Co/N-GA via hydrothermal anchoring of metal organic framework into GA and pyrolysis. Hierarchical porosity of Co/N-GA consisted of micro, meso and macro pores with large surface area of 466.6 m^2 g^{-1}. In 0.5 M H_2SO_4, the electrocatalyst exhibited very low onset overpotential of 0 mV and Tafel slope of 33 mV dec^{-1} and these values are comparable to those of benchmark Pt electrocatalyst. Furthermore, η_{10} and η_{100} values displayed by the electrocatalyst in the same electrolyte were 46 and 183 mV, respectively. The authors attributed the excellent HER performance and high stability of Co/N-GA to the synergistic effect between Co and N-doped carbon aerogel, large surface area and hierarchical porosity of N-doped graphene aerogels.

Transition metal dichalcogenides have been developed in the recent past as potential alternative catalysts to platinum-based electrocatalysts for HER in acid media. MoS_2 is a typical layered transition metal dichalcogenide having graphene like-structure with high HER activity. Moreover, the properties of edge sulfurs of MoS_2 were similar to those of enzymatic centers. Zhang et al. [29] rationally designed few-layered MoS_2 nanosheets–carbon aerogel hybrid (MoS_2/CA) and employed it as hybrid electrocatalyst for HER. In this study, the authors addressed the key challenge of increasing the electronic conductivity of MoS_2 at the same time maintaining its nanostructure. Carbon aerogel provided active regions for the growth of MoS_2, thereby inhibiting aggregation of MoS_2 nanosheets and also acted as matrix material for the transportation of ions and electrons. MoS_2/CA was obtained through sol-gel, aging, freeze drying followed by carbonization and solvothermal processes. The authors reported onset potential, $\eta_{9.68}$, and Tafel slope values of MoS_2/CA hybrids as 140 mV, 200 mV, and 59 mV dec^{-1}, respectively, in 0.5 M H_2SO_4.

HER activity of unsaturated sulfur atoms at the edges of MoS_2 crystal is well documented. Similarly, HER active species in MoS_x have also been reported. However, aggregation of MoS_x affects its HER activity, thus requiring suitable support/template material for its dispersion. In this context, nanocarbons are suitable materials to serve as templates for the growth of MoS_x and improve the dispersion. Reddy et al. [30] reported preparation of 3D carbon nanotube aerogel/MoS_x and employed it as HER electrocatalyst in 0.5 M H_2SO_4. Solvothermal process was used to synthesis MoS_x/MWCNT aerogel at a relatively low temperature of 200 °C. The reaction was carried out in N,N dimethylformamide using $(NH_4)_2MoS_4$ as a precursor in the presence of multiwalled CNT aerogel. The electrocatalyst exhibited HER onset overpotential, Tafel slope and exchange current density values of 150 mV, 62 mV dec^{-1}, and 6.4 mA cm^{-2} respectively in the acid medium. High stability of the electrocatalyst was determined through long-term 1000 potential cycles. The authors attributed the enhanced performance of the electrocatalyst to synergistic effects between MoS_x and CNT aerogels.

Other issues associated with MoS_2 that are hindering its application in catalysis are inherent semiconductor properties with anisotropic behavior, intrinsic aggregation and stacking. Zhao et al. [31] employed graphene aerogel to construct multidimensional electron transport pathway to MoS_2 for HER electrocatalysis. MoS_2 nanosheets supported on 3D graphene aerogel (GA-MoS_2) were synthesized in two steps. Graphene oxide dispersion was reduced in the first step forming graphene hydrogel. Subsequently, graphene hydrogel, ammonium heptamolybdate and thiourea were subjected to hydrothermal process at 180 °C followed by freeze drying to obtain GA-MoS_2. MoS_2 nanosheets were uniformly deposited on GA-MoS_2, which provided large surface area for growing the nanosheets. The electrocatalyst exhibited onset overpotential and Tafel slope of 100 mV and 41 mV dec^{-1}, respectively, in 0.5 M H_2SO_4. Furthermore, GA-MoS_2 delivered current density of 95 mA cm^{-2} at overpotential of 200 mV, on the other hand, pure MoS_2 displayed only 8 mA cm^{-2} at the same overpotential indicating the beneficial role of graphene aerogel support.

Several reports discussed herein have revealed that carbon materials are promising templates for electrocatalysts. It follows that structure of these materials needs to be carefully designed and engineered in order to bring out the maximum catalytic potential of the active materials through exposure of active sites, enhancement of conductivity and shortening of ion diffusion pathways. Sun et al. [32] used graphene/graphene nanoribbon aerogels to construct high performance HER electrocatalyst (GGNR@MoS_2). The authors immobilized a few layered and highly dispersed MoS_2 nanosheets on the aerogel in which graphene sheets were the building blocks of the aerogel, while graphene nanoribbons bridged different graphene sheets allowing better electrical contacts with MoS_2. Moreover, surface-to-volume ratio of the 3D framework could be tuned through regulating

the amount of graphene nanoribbons. The optimized GGNR@MoS_2 showed HER onset overpotential of 105 mV, η_{10} of 183 mV and Tafel slope of 49 mV dec^{-1} in 0.5 M H_2SO_4.

Another 2D molybdenum dichalcogenide requiring exposure of active edge sites for realizing full catalytic potential for HER is $MoSe_2$. Reducing the size and increasing the exposure of the edge sites could boost the HER activity of $MoSe_2$. Moreover, poor electric conductivity between adjacent $MoSe_2$ layers bonded through van der Waals forces must also be addressed. Zhang et al. [18] fabricated $MoSe_2$/carbon fiber aerogel (CFA) in which active edges of $MoSe_2$ were effectively exposed. A combination of high temperature carbonization and one-pot solvothermal methods was employed to obtain $MoSe_2$/CFA in which CFA was derived from cotton wool. CFA served as the 3D conductive network on the surface of which $MoSe_2$ nanosheets were evenly and perpendicularly decorated. The electrocatalyst exhibited HER onset overpotential, η_{10} and Tafel slope values of 104 mV, 179 mV, and 62 mV dec^{-1}, respectively, in 0.5 M H_2SO_4. The authors ascribed the high performance of the electrocatalyst to the decreased charge transfer resistance between conductive carbon aerogel and active edge sites of $MoSe_2$, decreased aggregation of active nanosheets and increased ion transportation during HER process.

It is clear from the above discussion that ultrathin structures of transition metal dichalcogenides are highly desirable for HER catalysis. Another hierarchically structured carbon aerogel based $MoSe_2$ (GCA-$MoSe_2$) was constructed by Shi et al. [21] and used it as efficient HER electrocatalyst. The carbon structure consisted of graphene carbon nanotube aerogel, which was prepared by freeze drying graphene carbon nanotube dispersion followed by carbonization. The underlying carbon aerogel support rendered stability to $MoSe_2$ and enhanced electrical contact to the electrode. The resultant scroll-sheet architecture possessed unique conjoined structure facilitating transport of electrons. Carbon nanotubes acting as spacers between graphene layers inhibited their restacking. $MoSe_2$ nanostructures were grown perpendicularly on the 3D carbon aerogel by solvothermal method exposing the active edge sites as well as preventing their aggregation. GCA-$MoSe_2$ when used as HER electrocatalyst in acid electrolyte exhibited onset overpotential, η_{10} and Tafel slope of 113 mV, 228 mV and 68 mV dec^{-1} respectively. On the other hand, pure $MoSe_2$ exhibited comparatively lower onset overpotential, η_{10} and Tafel slope values of 198 mV, 297 mV, and 72 mV dec^{-1}, respectively, in the same electrolyte.

Not only does MoS_2 possess active edge sites, species like thiomolybdate ($[Mo_3S_{13}]^{2-}$) exhibits edge sites active for HER. Shang et al. [6] constructed $[Mo_3S_{13}]^{2-}$ nanoclusters anchored on rGO-CNT aerogel (Mo_3S_{13}@rGO-CNT aerogel) and employed it as the electrocatalyst for HER in acid medium. As a strong support material, rGO-CNT aerogel rendered stability and prevented aggregation of $[Mo_3S_{13}]^{2-}$ nanoclusters. It was observed that the elemental distribution of Mo and S were even in the aerogel. $[Mo_3S_{13}]^{2-}$ nanoclusters displayed poor crystallinity and defect-rich nature, which were beneficial to HER activity. Mo_3S_{13}@rGO-CNT aerogels showed HER η_{10} and Tafel slope of 179 mV and 60.2 mV dec^{-1}, respectively, in 0.5 M H_2SO_4. The electrocatalyst exhibited high HER activity even at low mass. The stability of Mo_3S_{13}@rGO-CNT aerogels were assessed through continuous 1000 potential cycles and galvanostatic test at 10 mA cm^{-2}. The electrocatalyst exhibited negligible change in the activity during these tests.

Zhao et al. [11] introduced a facile method to prepare carbon core-shell with cobalt phosphide nanoparticles embedded in graphene aerogels (CoP@C-NPs/GA) through in situ phosphorization method and employed them as HER electrocatalysts in acidic and basic electrolytes. The electrocatalyst exhibited high HER catalytic activity in acid medium with η_{10} and Tafel slope values of 120 mV and 57 mV dec^{-1} respectively. Similarly, in basic medium the η_{10} and Tafel slope values exhibited by the electrocatalyst were 225 mV and 66 mV dec^{-1} respectively. The authors also prepared nickel counterpart of the electrocatalyst i.e. carbon core-shell containing nickel phosphide

embedded in graphene aerogel (Ni_2P@C-NPs/GA) to show the versatility of the synthetic method derived from seaweed biomass. Ni_2P@C-NPs/GA also displayed similar high HER activity in acidic and basic media. The authors attributed the high HER performance of CoP@C-NPs/GA and Ni_2P@C-NPs/GA to 3D graphene aerogel matrix with high electric conductivity, large number of pores along with large surface area facilitating electronic and mass transfer.

Molybdenum disulphide has attracted wide and considerable attention as highly active non-precious metal catalyst. Edge sites of MoS_2 are active while the basal planes are not active for HER. Das et al. [33] synthesized MoS_2 quantum dots with abundant edge sites and embedded them into polyaniline – N, N′-Dibenzoyl-L-cystine hydrogel matrix resulting in conducting hybrid aerogel (DBC-MoS_2-PANI). Quantum dots were prepared by solvent exfoliation method. DBC acted as dopant, gelator, and crosslinker during in situ polymerization of aniline. PANI fabricated in the hybrid was in doped emeraldine salt form.

DBC-MoS_2-PANI aerogel exhibited HER η_{10} of 196 mV and Tafel slope of 58 mV dec^{-1} in 0.5 M H_2SO_4. On the other hand, MoS_2 quantum dots showed much lower HER activity with η_{10} of 262 mV and Tafel slope of 69 mV dec^{-1} when compared to DBC-MoS_2-PANI aerogel. The electrocatalyst delivered high stability with negligible loss in the activity during 1000 potential cycles. The authors attributed the high HER activity of DBC-MoS_2-PANI aerogel to facile electron transfer and large surface area of aerogel framework.

Kong et al. [34] fabricated value-added aerogel composite in the form of sulfur-doped molybdenum carbide anchored on carbon aerogels derived from cellulose nanocrystals (Mo_2C@S-CA). Cellulose nanocrystals possessing sulphate ester groups can be extracted from plant cell wall through acid hydrolysis process. Among several transition metals derived compounds, molybdenum carbide was selected because of its platinum-like characteristics. Mo_2C@S-CA was synthesized using hybrid ammonium molybdate/cellulose nanocrystals as precursors through one-step carbonization process. Mo_2C@S-CA exhibited onset overpotential of 95 mV and η_{10} of 176 mV in 0.5 M H_2SO_4. Tafel slope shown by the electrocatalyst was 66 mV dec^{-1} indicating that HER followed Volmer-Heyrovsky mechanism on the surface of Mo_2C@S-CA. Furthermore, long-term stability was assessed through 10,000 potential cycles and time-dependent current density curves revealing high durability of the electrocatalyst.

Jin et al. [16] reported for the first time a new class of aerogel, platinum-rhodium nano-alloy aerogel (PtRh-nanoalloy aerogel) and employed it as exceptional hydrogen oxidation/evolution electrocatalyst. The authors aimed to fabricate electrocatalysts with improved activity and stability in alkaline electrolytes but having fewer Pt atoms. PtRh-aerogel was prepared through a facile one pot method involving no surfactants at 60 °C. Moreover, with the introduction of oxophilic component Rh into Pt at atomic level, the Pt-Rh alloy would weaken hydrogen binding energy of Pt through modified electronic structure, resulting in improved HER activity. Lamellar architecture, large number of low-coordinated sites, rapid mass transfer and hierarchical pores were the unique features of PtRh-nanoalloy aerogel. The electrocatalyst delivered 5.5 times higher hydrogen oxygen reaction (HORO) activity compared to commercial Pt/C. In the case of hydrogen evolution reaction (HER), the PtRh-aerogel displayed η_{10} and Tafel slope of 55 mV and 45 mV dec^{-1}, respectively, which were lower than those of commercial Pt/C (73 mV and 54 mV dec^{-1} respectively) in 1 M KOH. The nanoalloy aerogel also proved to be highly stable in alkaline medium for HOR and HER even after 5000 potential cycles.

The importance of fabrication of electrocatalysts that are stable in a wide pH range can be understood from the fact that proton exchange membrane based electrolyzers require acid stable electrocatalysts. On the other hand, microbial electrolysis cells require electrocatalysts that are active in neutral pH condition while commercial alkaline electrolyzers need electrocatalysts working in

basic pH media. Unfortunately, most transition metals based electrocatalysts are not pH universal. In this context, Cheng et al. [35] argued that coating metal sulfides with stable conducting carbon materials could render stability to the transition metal sulfides to operate in acidic and basic conditions. The authors initially grew hierarchically layered MoS_2/Co_9S_8 on reduced graphene oxide sheets. Blank graphene oxide and CNTs were introduced to obtain interconnected 3D aerogels (MoS_2/Co_9S_8/rGO-CNT). This binder-free composite aerogel showed promising HER activity with low η_{10} of 90, 176, and 102 mV in 0.5 M H_2SO_4, 1 M PBS and 1 M KOH, respectively. Similarly, the electrocatalyst displayed Tafel slopes of 49, 89, and 61 mV dec^{-1} in 0.5 M H_2SO_4, 1 M PBS and 1 M KOH respectively.

Chen et al. [1] constructed 3D molybdenum disulfide quantum dot aerogel (MoS_2QD-aerogel) through hydrothermal process and demonstrated it as a highly efficient electrocatalyst for HER. MoS_2 thin sheets could be produced through exfoliant assisted liquid phase exfoliation. In this method, attraction between MoS_2 layers was weakened through liquid phase exfoliant followed by sonication/shearing resulting in exfoliated MoS_2 thin sheets. The authors employed the electrocatalyst in acid, neutral, alkaline media, and in seawater. MoS_2QD-aerogel exhibited superior activity in neutral and basic electrolytes compared to benchmark commercial platinum electrocatalyst at high overpotentials. In 0.5 M H_2SO_4, the electrocatalyst exhibited overpotential of 53 mV at 7 mA g^{-1} and Tafel slope of 41 mV dec^{-1}. The electrocatalyst displayed promising electrochemical stability of over 100 hours at 10 mA g^{-1} in 0.5 M H_2SO_4. Furthermore, a stable performance was obtained after 150 scanning cycles in seawater obtained from Pacific Ocean with pH of 8.8. It may be noted that most electrocatalysts would be deactivated and corroded in the seawater.

Magnetic nanomaterials like Fe, Co, and Ni present the possibility of high reusability along with low preparation cost of the catalyst. Shanmugam et al. [36] used naturally occurring cotton and ovalbumin as carbon and nitrogen sources, respectively, to fabricate Ni/N-doped carbonaceous aerogel catalyst (Ni/NCA). Hydrazine hydrate was used in the chemical reduction process to prepare Ni/NCA in which nickel content was varied between 45% and 75%. The composite was employed as a catalyst for HER and the reduction of toxic 4-nitrophenol to less toxic 4-aminophenol. Extensive electrochemical studies revealed that Ni/NCA with 60% Ni content exhibited the highest catalytic performance and recyclability among the investigated electrocatalysts. The optimized electrocatalyst exhibited η_{10} of 170 mV, Tafel slope of 72 mV dec^{-1} and exchange current density of 9.7×10^{-2} mA cm^{-2} in 1 M KOH. The authors computed Tafel slope values from impedance method of Tafel analysis, which is beneficial over voltammetric method [22]. During accelerated durability test, Ni/NCA retained 90% of the initial activity while nickel nanoparticles retained only 75% of the initial activity.

Noble metal aerogels are relatively new members of aerogels that are characterized by porous surface, large specific surface area, self-supported architecture, high electrical conductivity, and excellent catalytic activity. Catalytic reactions on noble metal aerogels with respect to electrochemical energy related processes are restricted owing to limited available compositions. Along with a few reports on oxygen reduction and evolution reactions, electrocatalytic properties of these aerogels were studied mostly on alcohol oxidation. Du et al. [8] fabricated Au-Pt and Au-Rh aerogel electrocatalysts and employed them for hydrogen evolution and oxygen reduction reactions demonstrating remarkable pH-universal activity – even exceeding the activities of commercial Pt/C. The synthetic process generally involves tedious procedures and long fabrication periods. However, the authors developed a salting-out gelation method in which the interactions between metal nanoparticles and salt ions were deliberately regulated based on specific ion effects leading to efficient synthesis of noble metal aerogels with tailored structures. Gelation was triggered by a strong salting-out agent NH_4F as an initiator. The authors especially employed optimized Au-Rh

aerogel for HER and electrochemical water splitting, leading to higher performance over that of commercial Pt/C in a wide pH range. In particular, η_{10} afforded by the electrocatalyst in 1 M KOH, 1 M PBS (pH 7 phosphate-buffered saline) and 0.5 M H_2SO_4 were 22, 18, and 20 mV, respectively, outperforming commercial Pt/C (49, 99, and 24 mV for respective electrolytes). Tafel slopes exhibited by the electrocatalyst were 47, 34, and 29 mV dec^{-1} in 1 M KOH, 1 M PBS, and 0.5 M H_2SO_4, respectively. Furthermore, the long-term activities of the electrocatalyst at various electrolytes evaluated by an accelerated degradation test also showed that Au-Rh aerogel was more stable than commercial Pt/C. In a two-electrode water electrolyzer with Au-Rh aerogel as cathode and RuO_2 as anode (Au-Rh aerogel || RuO_2), cell voltages of 1.48, 1.56, and 1.48 V were obtained in 1 M KOH, 1 M PBS, and 0.5 M H_2SO_4, respectively, at the current density of 10 mA cm^{-2}. It may be noted that these cell voltages were smaller when compared to those of the cell Pt/C || RuO_2 operating at the respective electrolytes. The authors attributed the excellent performance of Au-Rh aerogel to facile electron/mass transfer channels, large surface area, and self-supported architecture of the aerogel.

Deng et al. [37] fabricated a new class of Rh-based aerogels and addressed the need for highly efficient pH universal HER electrocatalysts. Rhodium with partially filled 4d electrons is widely employed in several heterogeneous catalyzes like hydrogenation and oxidation. Moreover, Rh enables optimal adsorption of key reactants like H^+ and H_2O hence possesses great potential as an alternative to Pt-based catalytic materials. The authors employed simple one-pot wet chemical synthesis method to incorporate transition metal M (M = Fe, Co, Ni) and B atoms. In particular, the ternary RhCoB aerogels showed excellent HER activity and stability in a wide pH range. η_{10} exhibited by the electrocatalyst in 1 M KOH, 1 M PBS (pH 7 phosphate-buffered saline) and 0.5 M H_2SO_4 were 43.6, 113, and 12 mV respectively. Similarly, the Tafel slopes showed by RhCoB in 1 M KOH, 1 M PBS, and 0.5 M H_2SO_4 were 40.5, 149.1, and 30.7 mV dec^{-1}, respectively. The high electrocatalytic activities of Rh-based aerogels – especially RhCoB comparable to those of commercial Pt/C in a wide pH range – were attributed to spongy 3D framework of aerogel resulting in high exposure of active sites and synergistic electronic interactions among various elements present in the aerogel.

12.3 Application of Aerogels in Oxygen Evolution Reaction

Anodic reaction of water splitting, OER produces molecular oxygen. OER is a multistep proton coupled electron transfer reaction, which requires active electrocatalyst for overcoming high activation barrier and producing oxygen at low overpotentials. In this context, aerogels are increasingly used, either as active components or supports for active components of the electrocatalysts. In this section, some of the significant recent reports on the synthesis and electrocatalytic evaluation of aerogels based electrocatalysts for OER will be discussed.

OER is the limiting reaction in polymer electrolyte membrane-based water electrolyzers. Iridium oxide is one of the best electrocatalysts for OER; however, it requires suitable support material that is highly conductive and withstands harsh OER conditions. Abbou et al. [38] developed IrO_x nanoparticles supported on appropriately doped SnO_2 aerogels (IrO_x/doped SnO_2) and employed it as highly stable OER electrocatalyst in acid electrolyte. Doped SnO_2 aerogels fulfilled the criteria as supports in oxidative and acidic OER conditions.

These include interconnected structures facilitating water and oxygen transport, large surface area to prevent aggregation of IrO_x nanoparticles, high electrical conductivity, and most importantly corrosion resistance. The authors assessed the corrosion resistance of IrO_x/doped SnO_2 in

acid medium through flow cell attached to inductively coupled mass spectrometer. It was found that the corrosion resistance of the electrocatalyst was controlled by the nature and concentration of the doping element. Under acidic OER conditions, Ta and Nb-doped SnO_2 aerogel supports were stable while Sb-doped SnO_2 dissolved continuously.

Noble metal aerogels possess unique combination of desirable features of large surface areas and high catalytic activities. The report of Du et al. [13] enriched structural and composition diversity of noble metal aerogels and their efficient fabrication for wide applications. The authors developed excessive-reductant-directed gelation strategy enabling integration of ligand chemistry with high specific surface area ($59.8\,m^2\,g^{-1}$) for gold aerogels. In gelation process, initial colloidal solution is destabilized and made into 3D gel and this process is distinct for noble metal systems. Stabilizing, initiating, reducing, and anion effect of reductant were revealed for $NaBH_4$ through theoretical and experimental approaches. The authors employed these aerogels as electrocatalysts for OER and ethanol oxidation reaction and revealed organic-ligand enhancing effect. Especially, core-shell Au-Ir aerogel was employed as high-performance OER electrocatalyst expecting synergy between highly conductive gold core and outer active Ir shell. The electrocatalyst exhibited small overpotential and Tafel slope of 245 mV and $36.9\,mV\,dec^{-1}$, respectively, in 1 M KOH outperforming commercial Ir-based electrocatalyst. Furthermore, Au-Ir aerogels were evaluated as OER electrocatalyst in acid electrolyte as well and the electrocatalyst exhibited better performance in terms of activity and stability compared to commercial Ir-based electrocatalysts.

High electrical conductivity, catalytic activity, and thermal stability make nickel attractive catalyst for OER. It requires a stable, large surface area and conductive support for the dispersion and graphene aerogels are suitable for this purpose. Oztuna et al. [39] fabricated nickel/nickel oxide core-shell nanoparticles decorated on graphene aerogels (Ni/NiO/GA) and evaluated them as OER electrocatalyst. Ni/NiO/GA was prepared through one-pot hydrothermal process and subsequent thermal reduction. The authors demonstrated high control of metal loading on aerogel without compromising the surface area. The aerogel with 40% nickel loading showed high BET surface area of $560\,m^2\,g^{-1}$ because of supercritical CO_2 assisted drying. Increasing nickel loading, i.e. increasing metallicity through regulating Ni^{2+}/GO precursor ratio was directly related to the electrocatalytic activity. In alkaline medium, Ni/NiO/GA exhibited η_{10} of 320 mV, Tafel slope of $61\,mV\,dec^{-1}$, and turn over frequency of $0.11\,s^{-1}$. The above OER evaluation showed that Ni/NiO/GA electrocatalyst outperformed most of the Ni based catalysts reported for OER.

Designing and fabricating active and stable OER electrocatalysts for acid electrolytes that can be employed in proton exchange membrane water electrolyzers are present topic of interest in both academia and industry. Hernandez et al. [40] opined that dispersing IrO_x nanoparticles on high surface area doped SnO_2 aerogels would be a viable strategy for synthesizing low-cost and stable anode electrocatalyst (IrO_x/doped-SnO_2). SnO_2 aerogels doped with Sb and Ta cations were prepared via sol-gel process resulting in highly porous and conducting support. The role of dopants on SnO_2 aerogel was extensively studied through physical and chemical methods and the electrocatalytic activity was assessed through rotating disk electrode. Between aerogel supported IrO_x and unsupported IrO_x, aerogel supported electrocatalyst exhibited 5- and 10-times improvement in OER mass activity at 1.51 and 1.58 V, respectively, in 0.05 M H_2SO_4. Moreover, stability tests conducted using chronopotentiometry at the current density of $1\,mA\,cm^{-2}$ revealed improved lifespan for aerogel supported IrO_x (17 hours) compared to unsupported IrO_x (1 hour).

Enhancing electrocatalytic activity through engineering morphology of the catalyst is steadily gaining attention. Shi et al. [12] reported self-supported Ir_3Cu aerogels with nanovoids incorporated building blocks as high-performance OER electrocatalyst that could be employed in proton exchange membrane water electrolyzers. The self-assembled nanovoid integrated metallic aerogel

was synthesized through one-pot surfactant free method in aqueous environment. The aerogel consisted of macro-sized porous architecture and meso-sized voids resulting in large surface area with abundant active sites. Moreover, the thin-walled hallow nanoparticles could also enhance the efficient usage of precious metals. For high catalytic activity a balance between adsorption and desorption energies is necessary and by alloying with Cu the binding energy of Ir could be optimized. Compared to commercial IrO_2, Ir_3Cu exhibited better OER performance and durability in acid electrolyte. In 0.1 M $HClO_4$, the electrocatalyst showed onset potential of 1.465 V, η_{10} of 298 mV and Tafel slope of 47.4 mV dec^{-1}. The authors attributed the high OER performance of Ir_3Cu aerogel to the 3D porous structure and the synergy present in the alloyed structure.

Compared to oxides, metal sulphides are beneficial in terms of electrical conductivity, selectivity, and redox chemistry, for example, for energy conversion and storage applications. Gao et al. [41] introduced anion exchange method for the first time into sol-gel process and prepared cobalt sulphide aerogel (Co_9S_8) and used it for supercapacitance and OER. In the anion exchange method, the precursor metal oxides, hydroxides, or carbonates are subjected to anion exchange with sulfur sources such as sodium sulphide and thiourea at temperatures below 200 °C without significant modification of the porous microstructure. This can form a general method to prepare metal sulphide aerogels in addition to nanoparticle condensation and metathesis methods. Co_9S_8 aerogel was synthesized by exchanging cobalt citrate in thioacetamide and then drying in supercritical ethanol. Co_9S_8 aerogel possessed large pore volume of 0.87 cm^3 g^{-1} and large surface area of 274.2 m^2 g^{-1}. Co_9S_8 aerogel exhibited OER onset overpotential of 220 mV and Tafel slope of 89 mV dec^{-1} in alkaline medium. On the other hand, Co_3O_4 aerogel showed OER onset overpotential of 270 mV and Tafel slope of 128 mV dec^{-1} under the same conditions.

Recently, transition metal phosphides have been explored as a new class of electrocatalysts for OER and outperforming traditional metal oxide-based electrocatalysts. Especially, iron-doped Ni_2P was a better electrocatalyst in comparison to its oxide counterpart because of the added advantage of better electrical conductivity. Kumar et al. [42] incorporated nickel hexacyanoferrate into graphene aerogel architecture and obtained FeNi-P/graphene aerogel (FeNi-P/GA) by heating with phosphide source. In this preparation method 3D architecture of graphene aerogel was preserved post phosphidation since the aerogel porous structure provided facile pathways to incoming PH_3 and outgoing gaseous products. The authors employed FeNi-P/GA as high-performance OER electrocatalyst in alkaline medium. The OER activity of FeNi-P/GA depended on the iron and nickel precursor concentrations. FeNi-P/GA displayed onset potential of 1.46 V, η_{10} of 280 mV and Tafel slope of 43 mV dec^{-1} in 1 M KOH. Furthermore, long-term durability was evaluated using chronoamperometry at overpotential of 280 mV and the electrocatalyst displayed stable current density of 10 mA cm^{-2} for 8 hours.

Heteroatom-doped nonmetal carbon based electrocatalysts have been increasingly employed in energy storage and conversion devices. Chen et al. [43] fabricated advanced graphene aerogel-based catalyst and employed it as highly efficient oxygen reduction and evolution reaction electrocatalyst. 3D boron and nitrogen co-doped graphene aerogels (BN-GA) were prepared using $NH_4B_5O_8$ precursor through hydrothermal and free-drying methods. In this synthetic method, B and N contents could be modified via controlling synthetic conditions. The electronegativity difference between the dopants and carbon might create unique electronic structure enhancing catalytic activity and number of active sites. BN-GA showed low onset overpotential of 370 mV and its η_{10} value was close to that of benchmark RuO_2. Moreover, OER activity of BN-GA was better than those of singly doped B-GA and N-GA in terms of η_{10} and Tafel slope. The electrocatalyst also exhibited long-term stability with only 2% current loss after 9000 seconds in a durability test. The authors suggested possible OER pathways on BN-GA with the formation and deprotonation of OOH* species to produce molecular oxygen.

Employing supports that are stable in highly oxidizing and corrosive environment is one way of reducing highly active and relatively stable precious metal (for example, Ir) loading at the anode in proton exchange membrane water electrolyzers. It is also desirable to use porous and high surface area supports for the anode catalysts. Wang et al. [44] reported SnO_2-Sb aerogel supported Ir with vanadium additives (Ir/SnO_2:Sb-mod-V) as high performance and stable OER electrocatalyst in acid electrolyte. The authors demonstrated high OER activity of Ir/SnO_2:Sb-mod-V, which was similar to that of unsupported Ir but with more than 70 wt% less metal loading. It was established that vanadium was not playing active catalyst role for OER but helped retain aerogel architecture and lower impurity content. The authors reported mass activities of unsupported IrO_x, Ir/SnO_2:Sb and Ir/SnO_2:Sb-mod-V as 33.2, 94.6, and 121.5 A g^{-1}, respectively, at the overpotential of 280 mV in N_2-saturated 0.05 M H_2SO_4. Furthermore, the above three electrocatalysts exhibited Tafel slopes of 43.7, 41.8, and 40.9 mV dec^{-1}, respectively. Chronopotentiometry was used to assess the stabilities of the above electrocatalysts at a constant current density of 1 mA cm^{-2}. Unsupported IrO_x and Ir/SnO_2:Sb showed increase in potential after 7 and 12 hours, respectively, while Ir/SnO_2:Sb-mod-V exhibited constant potential for 15 hours.

Conventional methods for dispersion of catalyst nanoparticles on high surface area and conducting supports often fail during continuous electrochemical operation due to aggregation, agglomeration, peeling off, and dissolution, resulting in loss of activity. Fu et al. [45] combined nickel and MnO and supported on 3D graphene aerogel (Ni-MnO/rGO aerogel) for use as cost-effective oxygen reduction and evolution electrocatalyst. Ni-MnO/rGO aerogel was prepared through hydrogel route involving formation of graphene oxide crosslinked poly(vinyl alcohol) hydrogel. Metal nanoparticles were anchored into the aerogel network after pyrolysis. The electrocatalyst showed η_{10} of 370 mV, which was comparable to that of RuO_2 (380 mV) and lower than those of MnO/rGO (480 mV) as well as Ni/rGO (430 mV) in 0.1 M KOH. Ni-MnO/rGO aerogel showed lower Tafel slope of 67 mV dec^{-1} compared to RuO_2 (82 mV dec^{-1}), MnO/rGO (97 mV dec^{-1}) and Ni/rGO (132 mV dec^{-1}) in the same electrolyte. The operational stability of the electrocatalyst in alkaline medium was evaluated through chronoamperometry in which a negligible attenuation in current was observed in 10 000 seconds.

Graphene being 2D sheets tends to restack because of van der Waals interactions and π-π stacking. This issue can be prevented by assembling graphene into 3D macroscopic architectures resulting in interconnected frameworks with large surface area and high mechanical strength. Yu et al. [46] employed N-doped graphene aerogel to grow and disperse Co_3O_4 nanocrystals (Co_3O_4/N-GA) and employed it as high-performance oxygen evolution and reduction electrocatalyst. The authors involved 3D porous architecture, nitrogen doping of graphene and transition metal oxide to develop the electrocatalyst. Co_3O_4/N-GA was fabricated through a facile and green process that can be adapted for large-scale production using low-cost precursors. Co_3O_4/N-GA displayed OER η_{10} and Tafel slope of 430 mV and 54 mV dec^{-1}, respectively, in 1 M KOH. Furthermore, the electrocatalyst was subjected to chronoamperometric test for 10 000 seconds showing performance attenuation of less than 2%. The authors ascribed the high activity and stability of Co_3O_4/N-GA to large active surface area, increase in disorder because of Co_3O_4 presence on the surface of N-G aerogel and synergistic interaction between Co_3O_4 and N-G aerogel.

Ma et al. [47] constructed nitrogen, sulfur, and phosphate ternary-doped porous graphene aerogel and Co_9S_8 nanoparticles were homogeneously dispersed on the aerogel (Co_9S_8/NSPG). Graphene is considered as semiconductor with zero bandgap. Pyridinic nitrogen could act as OER active center, S doping could introduce high charge and spin densities while the presence of P could promote synergistic interactions. The authors employed the 3D material as an efficient oxygen evolution and reduction electrocatalyst in alkaline medium. Because of abundant

defects and porous network, Co_9S_8/NSPG displayed high BET surface area of 478 m^2 g^{-1}. The optimized electrocatalyst exhibited low η_{10} of 343 mV, which was similar to that of benchmark RuO_2 in 1 M KOH. During oxidizing potentials cobalt was transformed to OER active $Co(OH)_2$ and CoOOH species under basic condition. A Tafel slope of 82 mV dec^{-1} was obtained for the electrocatalyst, which was close to the value obtained for the benchmark RuO_2. The authors attributed the superior catalytic performance of Co_9S_8/NSPG to high surface area 3D architecture, abundant defects, and active sites as well as strong synergistic interaction between Co_9S_8 and NSPG aerogel.

12.4 Application of Aerogels for Overall Water Splitting

Electrocatalysts for overall water splitting, i.e. bifunctional electrocatalysts for HER and OER, are advanced electrocatalysts since they simultaneously drive both HER and OER of water splitting, making the integration of one electrocatalyst into the device rather than two simpler. Research on bifunctional catalysis has gained momentum since 2015 [48]. Bifunctional electrocatalysts save cost and resources on equipment, precursors, material synthesis, characterization, separation, and purification. Furthermore, employing incompatible electrocatalysts for cathode and anode results in overall loss in the performance because different electrocatalysts perform best in different pH ranges. Compared to the developments on individual HER and OER electrocatalysts in the last decade, progress on bifunctional electrocatalysts is in early stages. In this section, application of aerogels as electrocatalysts or electrocatalyst components for overall water splitting will be discussed.

Active materials for high performance applications in energy conversion and storage require several components to achieve high electric conductivity, large surface area, and mechanical robustness. From recent literature reports, it may be observed that transition metal dichalcogens displayed high activity for HER in acid media whereas transition metal layered double hydroxides showed good performance for OER in basic media. Xu et al. [49] designed and fabricated a ternary hybrid aerogel consisting of three 2D layer components, viz., WSe_2, NiFe-layered double hydroxide nanosheets on nitrogen and sulfur codoped graphene (N,S-rGO/WSe_2/NiFe-LDH). The authors employed the hybrid material as advanced electrodes for overall water splitting and supercapacitor. Initially, hydrothermal method was used to synthesize nitrogen and sulfur codoped graphene and WSe_2 nanosheets-based aerogel. During this stage, graphene oxide was converted to graphene and doped with N and S simultaneously. Then, NiFe-LDH was coupled to the aerogel through electrostatic attraction between the nanosheets of opposite charges. The hybrid aerogel when used as HER electrocatalyst in 1 M KOH exhibited η_1 and Tafel slope of 50 mV and 112 mV dec^{-1}, respectively. In the case of OER in the same electrolyte, the electrocatalyst required 1.48 V to reach 10 mA cm^{-2} and exhibited Tafel slope of 86 mV dec^{-1}. The authors ascribed the excellent bifunctional water-splitting performance of the hybrid material to the synergistic effects among various components. Specifically, high HER performance was attributed to WSe_2 and OER performance to NiFe-LDH.

Transition metal selenides have attracted considerable research attention because of their high HER activity and low cost. The catalytic activity of these selenides toward OER have also been studied and reported, even though the OER active species are surface oxy/hydroxides formed in situ under anodic condition. Xu et al. [50] reported fabrication of penroseite (Ni,Co)Se_2 anchored on graphene aerogel ((Ni,Co)Se_2-GA) and employed it as bifunctional water-splitting electrocatalyst in alkaline media. Initially, graphene oxide nanosheets were used for growing NiCo Prussian blue analogues (PBA). The resulting product was subjected to hydrothermal and freeze drying to

form NiCo PBA-graphene aerogel. Finally, the above product was converted to (Ni,Co)Se_2-GA through thermal selenization at 350 °C. The electrocatalyst exhibited HER η_{10} and Tafel slope values of 128 mV and 79 mV dec^{-1}, respectively. Similarly, the corresponding OER values were 250 mV and 70 mV dec^{-1}, respectively, in 1 M KOH. In a two-electrode alkaline water electrolyzer (Ni,Co)Se_2-GA exhibited cell voltage of 1.6 V at the current density of 10 mA cm^{-2}. The authors attributed the superior performance of hybrid aerogel to the synergy between (Ni,Co)Se_2 and graphene aerogel.

Gu et al. [51] synthesized robust 3D Ni_3FeN/reduced graphene oxide aerogel electrocatalyst (Ni_3FeN/r-GO) and used it as a bifunctional electrocatalyst for HER and OER in alkaline media. The electrocatalyst was prepared using (Ni,Fe)/r-GO alginate hydrogels as precursors via ion exchange method followed by simple one-step nitrogenization using NH_3 at 700 °C. Ni_3FeN/r-GO aerogel showed small HER and OER η_{10} of 94 and 270 mV, respectively, in 1 M KOH. Besides, HER and OER Tafel slopes showed by the electrocatalyst were 90 and 54 mV dec^{-1}. In an alkaline two-electrode water electrolyzer, Ni_3FeN/r-GO aerogel acting as both anode and cathode delivered cell voltage of 1.6 V at the current density of 10 mA cm^{-2} along with high stability of 100 hours. The authors ascribed the good performance of Ni_3FeN/r-GO aerogel to high electrical conductivity of Ni, Fe nitrides, 3D aerogel framework resulting in facile mass transport, and large number of active sites. Furthermore, density functional theory computation revealed covalent interactions of Fe, Ni, and N, resulting in increased electrical conductivity and optimized surface electronic distribution of the nitrides.

Intrinsic catalytic activities of most electrocatalysts are different for HER and OER. For example, bimetallic oxides are highly active for OER in basic media; on the other hand, bimetallic alloys have higher HER activities compared to their oxide counterparts. Zhang et al. [52] demonstrated gas-regulated bimetallic-based HER and OER electrocatalysts and used them for overall water splitting in alkaline media. The authors employed same fabrication procedure and same precursors to prepare two kinds of graphene aerogel-based bimetallic Co, Fe electrocatalysts.

Initially, reduced graphene oxide hydrogel was prepared through hydrothermal treatment of graphene oxide in the presence of required metal ions and thiourea. In the subsequent pyrolysis step, N_2 and NH_3 were used to synthesize $CoFe_2O_4$ encapsulated nitrogen, sulfur-doped reduced graphene oxide aerogel (CoFeO@N/S-rGO), and amorphous bimetallic CoFe encapsulated nitrogen-doped reduced graphene oxide aerogel (CoFe@N-rGO) as OER and HER electrocatalysts, respectively.

Figure 12.1 shows schematic diagram illustrating the synthetic procedures of CoFeO@N/S-rGO and CoFe@N-rGO aerogels and their use in overall water splitting. CoFe@N-rGO aerogel exhibited HER η_{10} and Tafel slope of 116 mV and 78 mV dec^{-1}, respectively, in 1 M KOH. In a similar manner, CoFeO@N/S-rGO showed OER η_{10} and Tafel slope of 248 mV and 40 mV dec^{-1}, respectively, in the same electrolyte. The alkaline water electrolyzer employing CoFeO@N/S-rGO and CoFe@N-rGO aerogels as anode and cathode exhibited cell voltage of 1.63 V at the current density of 10 mA cm^{-2} along with high stability of 100 hours.

Molybdenum sulfides–based materials are potential alternative earth-abundant electrocatalysts for water splitting. Cheng et al. [53] synthesized vertical Mo_xS_y arrays grown on carbon aerogels derived from guar gum (Mo_xS_y@GCA) and employed it as bifunctional electrocatalyst for water splitting. The electrocatalyst consisted of well-assembled architectures of S-edge rich few layered nanoflakes of length ca. 100 nm. The authors employed hydrothermal synthetic method in which thiourea and hexaammonium molybdate served as sulfur and molybdenum precursors, respectively. Guar gum, a polysaccharide, served as a precursor for carbon aerogel, which provided anchoring sites for molybdenum disulfide. Mo_4S_{16}@GCA exhibited low HER η_{10} of 54.13 mV and Tafel slope of 56.24 mV dec^{-1} in 0.5 M H_2SO_4. In 1 M KOH, the same electrocatalyst delivered HER

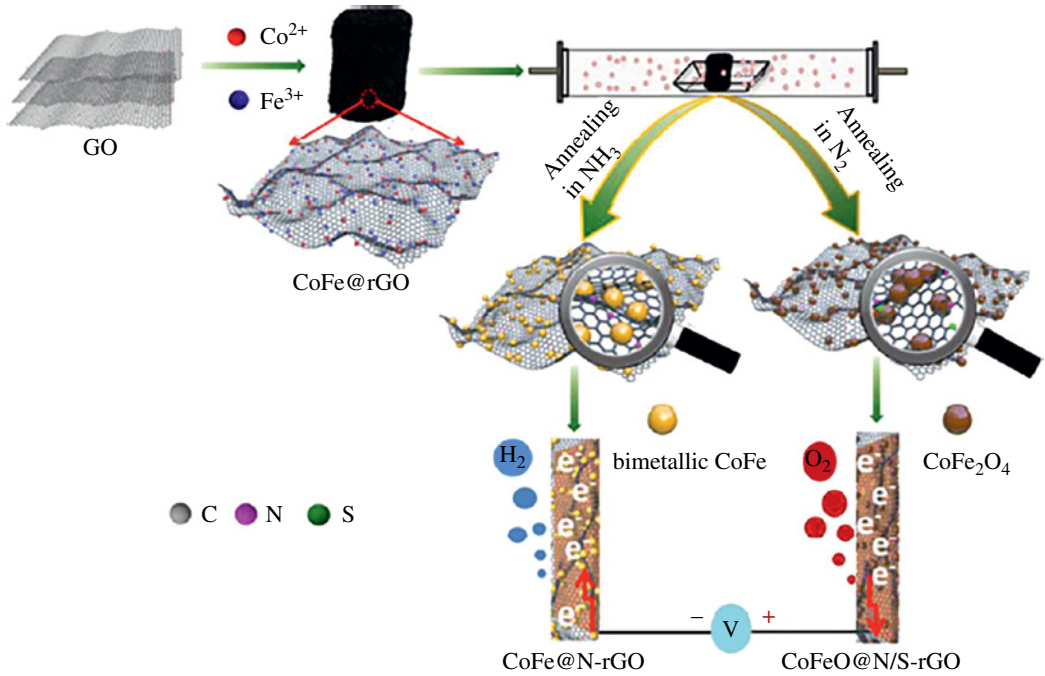


Figure 12.1 Schematic diagram illustrating the synthetic procedures of CoFeO@N/S-rGO and CoFe@N-rGO aerogels and their use in overall water splitting. *Source:* Reprinted with permission from ref. [52], copyright 2018, the Royal Society of Chemistry.

η_{10} of 57.89 mV and Tafel slope of 105.35 mV dec^{-1}. OER experiments were studied in 1 M KOH and Mo_4S_{16}@GCA delivered η_{10} and Tafel slope of 370 mV and 126.78 mV dec^{-1}, respectively. Mo_4S_{16}@GCA, when employed as both anode and cathode in a two-electrode water electrolysis cell, delivered cell voltage of 1.85 V at the current density of 10 mA cm^{-2}.

Zou et al. [9] constructed novel trifunctional highly efficient electrocatalyst via coupling cobalt nitride nanoparticles within 3D N-doped graphene aerogel (CoN_x/NGA) using metal organic framework as a precursor. The authors employed this non-noble multifunctional material as electrocatalysts for HER, oxygen evolution reaction (OER), and oxygen reduction reaction (ORR) and also in a rechargeable Zn-air battery as an air-cathode. It may be noted that HER, OER, and ORR are key electrochemical reactions related to sustainable energy conversion and storage devices, for example, electrochemical water electrolyzers, fuel cells, and rechargeable metal-air batteries. CoN_x/NGA displayed HER η_{10} and Tafel slope of 198 mV and 97.3 mV dec^{-1}, respectively, in 1 M KOH. In the case of OER and in the same electrolyte the η_{10} and Tafel slope values were 295 mV and 82.3 mV dec^{-1}, respectively. CoN_x/NGA acting as bifunctional cathode and anode in a two-electrode alkaline water electrolyzer exhibited cell potential of 1.71 V at the current density of 10 mA cm^{-2}. Integrating CoN_x/NGA-based water electrolyzer with two Zn-air batteries resulted in high oxygen and hydrogen evolutions with respective gas evolution rates of 186 and 372 μmol h^{-1}. The authors ascribed the high activity of the electrocatalyst to (i) prevention of aggregation by N-doped graphene aerogel matrix, (ii) presence of abundant CoN_x and N_xC active sites, and (iii) three-dimensional hierarchical architecture.

Several transition metals–based compounds – such as chalcogenides, nitrides, and borides – have been developed as bifunctional water-splitting electrocatalysts in the past years. However,

these materials suffer from low stability, low electrical conductivity, and low specific surface area. On the other hand, carbon-based materials possess unique advantages such as high tolerance to extreme pH conditions, tunable molecular structures, and high electrical conductivity. Cheng et al. [54] opined that co-doping of carbon nanomaterials, especially 2D nanosheets, with secondary heteroatoms such as N, B, or S would increase the number of active sites thereby facilitating chemisorption/desorption of intermediates through synergistic coupling. B atoms were introduced into the carbon structure through borate cross-linking while N atoms were introduced via cation intercalation stripping with $(NH_4)_6Mo_7O_{24}{\cdot}4H_2O$ of guar gum carbon aerogels. The resulting B, N co-doped carbon nanosheets exhibited comparable HER and OER activities with high performance transition metals-based electrocatalysts. Specifically, the electrocatalyst showed HER and OER onset potentials of 39.12 mV and 1.38 V, respectively, in 0.5 M H_2SO_4. HER η_{10} and Tafel slope values of the electrocatalyst were 51.96 mV and 47 mV dec^{-1}, respectively. In the case of OER, the electrocatalyst exhibited η_{10} and Tafel slope of 170 mV and 67 mV dec^{-1}, respectively, in acid electrolyte. In 1 M KOH, η_{10} and Tafel slope values of the electrocatalyst were found to be 52.34 mV and 43 mV dec^{-1}, respectively. The electrocatalyst also showed promising stability in all pH conditions. In a two-electrode water electrolyzer, B, N co-doped carbon nanosheets employed as bifunctional electrocatalyst showed cell voltage of 1.45 V at the current density of 10 mA cm^{-2} in acid electrolyte; this performance was superior to that of the cell with Pt/C cathode and RuO_2 anode (1.54 V). The authors ascribed the high electrocatalytic performance to synergistic effect of B, N co-doping, and formation of fragmented nanosheets.

Although transition metal phosphides are efficient electrocatalysts, their HER and OER activities need to be promoted by modulating the electronic structure through secondary atom doping. Li et al. [19] constructed 3D (Co, Fe)P nanoframes encapsulated by N, P-codoped graphene aerogel (CFP NFs@NPGA) and employed it as a highly efficient and stable electrocatalyst for HER and OER in alkaline electrolyte. The porous CFP NFs@NPGA was prepared by one-step in situ encapsulation method followed by selective etching and phosphorization. The electrocatalyst displayed low HER and OER η_{10} of 155 and 278 mV respectively in 1 M KOH. Besides, HER and OER Tafel slopes exhibited by the electrocatalyst were 67.2 and 42.2 mV dec^{-1}, respectively. In a two-electrode alkaline water electrolyzer CFP NFs@NPGA as the bifunctional electrocatalyst displayed cell voltage of 1.59 V at the current density of 10 mA cm^{-2} and outstanding stability for 48 hours. The bifunctional performance of CFP NFs@NPGA was close to that of the cell with state-of-the-art Pt/C cathode and RuO_2 anode.

12.5 Concluding Remarks

Large-scale commercialization of water-splitting technology is the need of the hour to convert and store electricity obtained from sustainable and renewable sources into chemical energy, i.e. as molecular hydrogens. Several countries have issued deadlines to discontinue the use of fossil fuels-based automobiles. Multinational corporations are coming forward to replace traditional fuels with hydrogen. In this context, the application of aerogels in electrocatalytic hydrogen production is a relatively new topic. Aerogels possess desirable features as electrocatalyst materials like high porosity, 3D architecture, large specific surface area, electrical conductivity, low density, and good mechanical strength. Hence, aerogels can serve as active component and/or support materials for HER, OER and overall water splitting. As support materials, aerogels provide large surface area for precursors to anchor and grow into nanoparticles; prevent aggregation/agglomeration of active nanocomponents; protect active nanoparticles from corrosion, chemical leaching and dissolution;

facilitate mass transport of reacting species and gaseous products; improve electrical conductivity among nanoparticles; and most importantly, enhance electrocatalytic performance of active components through synergistic effects.

Several types of aerogels, ranging from noble metal aerogels to doped graphene aerogels, have been discussed in this chapter as high-performance materials for electrocatalytic hydrogen production. Aerogels fabricated from biomass-derived sources are environment friendly, sustainable, as well as cost effective. There are many recent reports on facile fabrication methods of aerogel-based electrocatalysts and synthetic methods with control over pore sizes and size distribution. However, large-scale commercial application of aerogel-based electrocatalysts is challenging because of time consuming and energy-intensive synthetic methods, especially the drying techniques used in their fabrication. Besides, more control over pore sizes and pore distribution is highly desired for producing optimized aerogel based electrocatalysts for water-splitting application. Nonetheless, the recent trend in the literature indicates that application of aerogel-based materials in energy conversion and storage techniques appears successful, progressive, and promising.

References

1 Chen, I.W.P., Hsiao, C.-H., Huang, J.-Y. et al. (2019). Highly efficient hydrogen evolution from seawater by biofunctionalized exfoliated MoS_2 quantum dot aerogel electrocatalysts that is superior to Pt. *ACS Appl. Mater. Interfaces* 11: 14159–14165. https://doi.org/10.1021/acsami.9b02582.

2 Douglas, T.G., Cruden, A.J., Infield, D. et al. (2011). Investigation of molybdenum-(resorcinol-formaldehyde) (Mo-RF) electrode for alkaline electrolyser operation. *Int. J. Hydrogen Energy* 36: 7791–7798. https://doi.org/10.1016/j.ijhydene.2011.01.107.

3 Murthy, A.P., Madhavan, J., and Murugan, K. (2018). Recent advances in hydrogen evolution reaction catalysts on carbon/carbon-based supports in acid media. *J. Power Sources* 398: 9–26. https://doi.org/10.1016/j.jpowsour.2018.1007.1040.

4 Cohen, M.J. (2018). Nine countries say they'll ban internal combustion engines. So far, it's just words, Quartz. https://qz.com/1341155/nine-countries-say-they-will-ban-internal-combustion-engines-none-have-a-law-to-do-so (accessed 29 September 2023).

5 ZEROe. Towards the world's first hydrogen-powered commercial aircraft, Airbus, 2023, https://www.airbus.com/en/innovation/low-carbon-aviation/hydrogen/zeroe (accessed 29 September 2023).

6 Shang, Y., Xu, X., Gao, B., and Ren, Z. (2017). Thiomolybdate $[Mo_3S_{13}]^{2-}$ nanoclusters anchored on reduced graphene oxide-carbon nanotube aerogels for efficient electrocatalytic hydrogen evolution. *ACS Sustainable Chem. Eng.* 5: 8908–8917. https://doi.org/10.1021/acssuschemeng.7b01713.

7 Hoa, V.H., Tran, D.T., Le, H.T. et al. (2019). Hierarchically porous nickel–cobalt phosphide nanoneedle arrays loaded micro-carbon spheres as an advanced electrocatalyst for overall water splitting application. *Appl. Catal. B* 253: 235–245. https://doi.org/10.1016/j.apcatb.2019.04.017.

8 Du, R., Jin, W., Huebner, R. et al. (2020). Engineering multimetallic aerogels for pH-universal HER and ORR electrocatalysis. *Adv. Energy Mater.* 10: 1903857. https://doi.org/10.1002/aenm.201903857.

9 Zou, H., Li, G., Duan, L. et al. (2019). In situ coupled amorphous cobalt nitride with nitrogen-doped graphene aerogel as a atrifunctional electrocatalyst towards Zn-air battery deriven full water splitting. *Appl. Catal. B* 259: 118100. https://doi.org/10.1016/j.apcatb.2019.118100.

10 Jayaraman, T., Murthy, A.P., Elakkiya, V. et al. (2018). Recent development on carbon-based heterostructures for their applications in energy and environment: A review. *J. Ind. Eng. Chem.* 64: 16–59.

11 Zhao, W., Lu, X., Selvaraj, M. et al. (2018). M_xP(M = Co/Ni)@carbon core–shell nanoparticles embedded in 3D cross-linked graphene aerogel derived from seaweed biomass for hydrogen evolution reaction. *Nanoscale* 10: 9698–9706. https://doi.org/10.1039/C8NR02852D.

12 Shi, Q., Zhu, C., Zhong, H. et al. (2018). Nanovoid incorporated IrxCu metallic aerogels for oxygen evolution reaction catalysts. *ACS Energy Lett.* 3: 2038–2044. https://doi.org/10.1021/acsenergylett.8b01338.

13 Du, R., Fan, X., Eychmuller, A. et al. (2020). Unveiling reductant chemistry in fabricating nobel metal aerogels for superior oxygen evolution and ethanol oxidation. *Nat. Commun.* 11: 1590. https://doi.org/10.1038/s41467-020-15391-w.

14 Kumar, A., Rana, A., Sharma, G. et al. (2018). Aerogels and metal–organic frameworks for environmental remediation and energy production. *Environ. Chem. Lett.* 16: 797–820. https://doi.org/10.1007/s10311-018-0723-x.

15 Kundu, M.K., Bhowmik, T., and Barman, S. (2015). Gold aerogel supported on graphite carbon nitride: an efficient electrocatalyst for oxygen reduction reaction and hydrogen evolution reaction. *J. Mater. Chem. A* 3: 23120–23135. https://doi.org/10.1039/C5TA06740E.

16 Jin, Y., Chen, F., Wang, J. et al. (2019). Lamellar platinum–rhodium aerogels with superior electrocatalytic performance for both hydrogen oxidation and evolution reaction in alkaline environment. *J. Power Sources* 435: 226798. https://doi.org/10.1016/j.jpowsour.2019.226798.

17 Wang, W.-K., Tang, B., Liu, J. et al. (2019). Self-supported microbial carbon aerogel bioelectrocatalytic anode promoting extracellular electron transfer for efficient hydrogen evolution. *Electrochim. Acta* 303: 268–274. https://doi.org/10.1016/j.electacta.2019.02.099.

18 Zhang, Y., Zuo, L., Zhang, L. et al. (2016). Cotton wool derived carbon fiber aerogel supported few-layered $MoSe_2$ nanosheets as efficient electrocatalysts for hydrogen evolution. *ACS Appl. Mater. Interfaces* 8: 7077–7085. https://doi.org/10.1021/acsami.5b12772.

19 Li, W., Yu, B., Hu, Y. et al. (2020). Encapsulating hollow (Co,Fe)P nanoframes into N,P-codoped graphene aerogel for highly efficient water splitting. *J. Power Sources* 456: 228015. https://doi.org/10.1016/j.jpowsour.2020.228015.

20 Hou, Y., Zhang, B., Wen, Z. et al. (2014). Material development in the past decade for H_2 produciton from microbial electrolysis cells. *J. Mater. Chem. A* 2: 13795–13800. https://doi.org/10.1039/C4TA02254H.

21 Shi, Y., Gao, W., Lu, H. et al. (2017). Carbon-nanotube-incorporated graphene scroll-sheet conjoined aerogels for efficient hydrogen evolution reaction. *ACS Sustainable Chem. Eng.* 5: 6994–7002. https://doi.org/10.1021/acssuschemeng.7b01181.

22 Murthy, A.P., Theerthagiri, J., Madhavan, J., and Murugan, K. (2017). Highly active MoS_2/carbon electrocatalysts for the hydrogen evolution reaction – insight into the effect of the internal resistance and roughness factor on the Tafel slope. *Phys. Chem. Chem. Phys.* 19: 1988–1998. https://doi.org/10.1039/c6cp07416b.

23 Murthy, A.P., Theerthagiri, J., and Madhavan, J. (2018). Insights on Tafel Constant in the analysis of hydrogen evolution reaction. *J. Phys. Chem. C* 122: 23943–23949.

24 Murthy, A.P., Theerthagiri, J., Madhavan, J., and Murugan, K. (2018). Electrodeposited carbon-supported nickel sulfide thin films with enhanced stability in acid medium as hydrogen evolution reaction electrocatalyst. *J. Solid State Electrochem.* 22: 365–374.

25 Vrubel, H., Moehl, T., Gratzel, M., and Hu, X. (2013). Revealing and accelerating slow electron transport in amorphous molybdenum sulphide particles for hydrogen evoltuion reaction. *Chem. Commun.* 49: 8985–8987.

26 Murthy, A. and Manthiram, A. (2012). Application of derivative voltammetry in the analysis of methanol oxidation reaction. *J. Phys. Chem. C* 116: 3827–3832. https://doi.org/10.1021/jp2092829.

27 Theerthagiri, J., Lee, S.J., Murthy, A.P. et al. (2020). Fundamental aspects and recent advances in transition metal nitrides as electrocatalysts for hydrogen evolution reaction: A review. *Curr. Opin. Solid State Mater. Sci.* https://doi.org/10.1016/j.cossms.2020.100805.

28 Zhu, Z., Yang, Y., Guan, Y. et al. (2016). Construction of a cobalt-embedded nitrogen-doped carbon material with the desired porosity derived from the confined growth of MOFs within the graphene aerogels as a superio catalyst towards HER and ORR. *J. Mater. Chem. A* 4: 15536–15545.

29 Zhang, Y., Zuo, L., Huang, Y. et al. (2015). In-situ growth of few-layered MoS_2 nanosheets on highly porous carbon aerogel as advanced electrocatalysts for hydrogen evolution reaction. *ACS Sustainable Chem. Eng.* 3: 3140–3148. https://doi.org/10.1021/acssuschemeng.5b00700.

30 Reddy, S., Du, R., Kang, L. et al. (2016). Three-dimensional CNTs aerogel/MoS_x as an electrocatalyst for hydrogen evolution reaction. *Appl. Catal. B* 194: 16–21. https://doi.org/10.1016/j.apcatb.2016.04.007.

31 Zhao, Y., Xie, X., Zhang, J. et al. (2015). $MoSe_2$ nanosheets supported on 3D graphene aerogel as a highly efficient catalyst for hydrogen evolution. *Chem. Eur. J.* 21: 15908–15913. https://doi.org/10.1002/chem.201501964.

32 Sun, Z., Fan, W., and Liu, T. (2017). Graphene/graphene nanoribbon aerogels as tunable three-dimensional framework for efficient hydrogen evolution reaction. *Electrochim. Acta* 250: 91–98. https://doi.org/10.1016/j.electacta.2017.08.009.

33 Das, S., Ghosh, R., Routh, P. et al. (2018). Conductive MoS_2 quantum dot/polyaniline aerogel for enhanced electroccatalytic hydrogen evolution and photoresponse properties supercapacitors. *ACS Appl. Nano Mater.* 1: 2306–2316. https://doi.org/10.1021/acsanm.8b00373.

34 Kong, X., Chen, S., Zou, Y. et al. (2018). Cellulose nanocrystals (CNC) derived Mo2C@sulfur-doped carbon aerogels for hydrogen evolution. *Int. J. Hydrogen Energy* 43: 13720–13726. https://doi.org/10.1016/j.ijhydene.2018.01.072.

35 Cheng, Y.-S., Ling, M., Jiang, B.-B. et al. (2019). Three-dimensional graphene@carbon nanotube aerogel-supported layered MoS_2/Co_9S_8 compsite as an efficient pH-univeral eletrocatalyst for hydrogen evolution. *ChemElectroChem* 6: 748–756. https://doi.org/10.1002/celc.201801403.

36 Shanmugam, P., Murthy, A.P., Theerthagiri, J. et al. (2019). Orbital-regulated interfacial electronic coupling endows Ni_3N with superior catalytic surface for hydrogen evolution reaction. *Int. J. Hydrogen Energy* 44: 13334–13344.

37 Deng, K., Ren, T., Xu, Y. et al. (2020). Transition metal M (M = Co, Ni, and Fe) and boron co-modulation in Rh-based aerogels for highly efficient and pH-univeral hydrogen evolution electrocatalysis. *J. Mater. Chem. A* 8: 5595–5600. https://doi.org/10.1039/d0ta00398k.

38 Abbou, S., Chattot, R., Martin, V. et al. (2020). Manipulating the corrosion resistance of SnO_2 aerogels through doping for efficient and durable oxygen evolution reaction electrocatalysis in acidic media. *ACS Catal.* 10: 7283–7294. https://doi.org/10.1021/acscatal.0c01084.

39 Sarac Oztuna, F.E., Beyazay, T., and Unal, U. (2019). Facile synthesis of graphene aerogel supported nickel/nickel oxide core–shell nanoparticles: Efficient electrocatalysts for oxygen evolution reactions. *J. Phys. Chem. C* 123: 28131–28141. https://doi.org/10.1021/acs.jpcc.9b07460.

40 Sola-Hernandez, L., Claudel, F., Maillard, F., and Beauger, C. (2019). Doped tin oxide aerogels as oxygen evolution reaction catalyst supports. *Int. J. Hydrogen Energy* 44: 24331–24341. https://doi.org/10.1016/j.ijhydene.2019.07.152.

41 Gao, Q., Shi, Z., Xue, K. et al. (2018). Cobalt sulfide aerogel prepared by anion exchange method with enhanced pseudocapacitive and water oxidation performances. *Nanotechnology* 29: 215601. https://doi.org/10.1088/1361-6528/aab299.

42 Narendra Kumar, A.V., Li, Y., Yu, H. et al. (2018). 3D graphene aerogel supported FeNi-P derived from electroactive nickel. *Electrochim. Acta* 292: 107–114. https://doi.org/10.1016/j.electacta.2018.08.103.

43 Chen, W., Xu, L., Tian, Y. et al. (2018). Boron and nitrogen co-doped graphene aerogels: Facile preparation, tunable doping contents and bifunctional oxygen electrocatalysis. *Carbon* 137: 458–466. https://doi.org/10.1016/j.carbon.2018.05.061.

44 Wang, L., Song, F., Ozouf, G. et al. (2017). Iridium stabilizes ceramic titanium oxynitride support for oxygen evolution reaction. *J. Mater. Chem. A* 5: 3172–3178. https://doi.org/10.1039/C7TA00679A.

45 Fu, G., Yan, X., Chen, Y. et al. (2017). Boosting bifunctional oxygen electrocatalysis with 3D graphene aerogel-supported Ni/MnO particles. *Adv. Mater.* 30: 1704609. https://doi.org/10.1002/adma.201704609.

46 Yu, D., Xu, C., Su, Y. et al. (2017). Nitrogen-doped graphene aerogels-supported cobaltosic oxide nanocrystals as high-performance bi-functional electrocatalysts for oxygen reduction and evolution reactions. *J. Electroanal. Chem.* 787: 46–54. https://doi.org/10.1016/j.jelechem.2017.01.034.

47 Ma, X.-X., Dai, X.-H., and He, X.-Q. (2017). Co_9S_8-modified N, S, and P ternary-doped 3D graphene aerogels as a high-performance electrocatalyst for both the oxygen reduction reaction and oxygen evolution reaction. *ACS Sustainable Chem. Eng.* 5: 9848–9857. https://doi.org/10.1021/acssuschemeng.7b01820.

48 Li, R.-Q., Hu, P., Miao, M. et al. (2018). CoO-modified Co_4N as a heterostructured electrocatalyst for highly efficient overall water splitting in neutral media water splitting. *J. Mater. Chem. A* 6: 24767–24772. https://doi.org/10.1039/c8ta08519f.

49 Xu, X., Chu, H., Zhang, Z. et al. (2017). Integrated energy aerogel of N,S-rGO/WSe_2/NiFe-LDH for both energy conversion and storage. *ACS Appl. Mater. Interfaces* 9: 32756–32766. https://doi.org/10.1021/acsami.7b09866.

50 Xu, X., Liang, H., Ming, F. et al. (2017). Prussian blue analogues derived penroseite (Ni,Co)Se_2 nanocages anchored on 3D graphene aerogel for efficient water splitting. *ACS Catal.* 7: 6394–6399. https://doi.org/10.1021/acscatal.7b02079.

51 Gu, Y., Chen, S., Ren, J. et al. (2018). Electronic structure tuning in Ni3FeN/r-GO aerogel toward bifunctional electrocatalyst for overall water splitting. *ACS Nano* 12: 245–253. https://doi.org/10.1021/acsnano.7b05971.

52 Zhang, B., Wang, H., Zuo, Z. et al. (2018). Tunable CoFe-based active sites on 3D heteroatom doped graphene aerogel electrocatalysts via annealing gas regulation for efficient water splitting. *J. Mater. Chem. A* 6: 15728–15737.

53 Cheng, Y., Yuan, P., Xu, X. et al. (2019). S-edge-rich Mo*x*S*y* arrays vertically grown on carbon aerogels as superior bifunctional HER/OER electrocatalysts. *Nanoscale* 11: 20284–20294. https://doi.org/10.1039/c9nr07277b.

54 Cheng, Y., Pang, K., Xu, X. et al. (2020). Borate crosslinking synthesis of structure tailored carbon-based bifunctional electrocatalysts directly from guar gum hydrogels for efficient overall water splitting. *Carbon* 157: 153–163. https://doi.org/10.1016/j.carbon.2019.10.024.

13

Clay-Based Aerogel Composites

Basim Abu-Jdayil, Bilkis Ajiwokewu, Safa Ahmed, and Saheed Busura

Chemical and Petroleum Engineering Department, UAE University, Al Ain, P.O. Box 15551, UAE

13.1 Introduction

13.1.1 Aerogels

Aerogel is a unique material with remarkable blends of properties of the three states of matter (that is, liquid, gas, and solid) [1]. Aerogels possess three-dimensional open networks that are assembled by coherent NPs or polymer molecules [2]. They differ in bulk properties compared to the other states of matter. Aerogels have ultralow density but maintain a fixed solid volume and shape like the solid state. The density of aerogels is usually in the range of 4–10 $mg\,cm^{-3}$. Air occupies up to 99.98% of its mass, which means they have a highly porous structure [3]. Other unique bulk properties that give significant relevance to aerogels in many industrial applications include high specific surface area (500–1200 $m^2\ g^{-1}$), low thermal conductivity (0.01–0.02 $W\,m^{-1}\,K^{-1}$), ultralow modulus, ultralow dielectric constant, ultralow sound speed, and ultralow refractive index [1, 3]. For example, high specific surface area, porosity, and ultra-hydrophobicity make them excellent chemical adsorbers for cleaning up spills [4]; low thermal conductivity and low-density make them suitable in thermal blankets and insulators [5]. Figure 13.1 illustrates a new insulating brick (filled with aerogel) that would enable walls to conduct heat up to eight times better compared to a wall construction from standard clay and shale bricks.

Aerogels were first introduced in 1931 by Samuel Stephens Kistler when he replaced the liquid inside a wet gel with air without causing any significant shrinkage or damage to the solid microstructure [7]. While some other critical steps are involved in the preparation of aerogels, the replacement of the solvent inside a wet gel is the fundamental attribute of aerogel preparation. According to Du et al. [1], the preparation of aerogel involves three key steps:

1) Preparation of sol particles from precursors using spontaneous or catalyzed hydrolysis and condensation reactions.
2) The solution-sol transition, this is the crosslinking and hierarchically assembling of the sol particles into a wet gel in a coherent network.
3) The gel-aerogel transition, commonly known as the drying stage – this involves the replacement of the solvent inside the wet gel with air without significant damage to the microstructure.

Aerogels for Energy Saving and Storage, First Edition. Edited by Meldin Mathew, Hanna J. Maria, Ange Nzihou, and Sabu Thomas.
© 2024 John Wiley & Sons, Inc. Published 2024 by John Wiley & Sons, Inc.

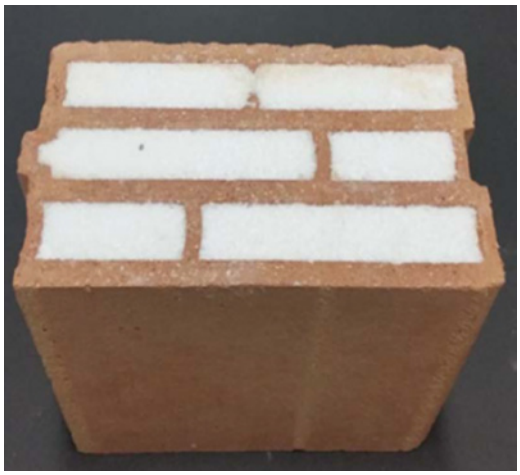


Figure 13.1 Bricks filled with aerogel [6].

The commonly used method of drying is supercritical fluid drying (SCFD), where the liquid initially entrapped in the wet gel is transformed into a supercritical fluid by applying temperature and pressure above the critical point. The silica aerogels are well known for their high-temperature SCFD. SCFD techniques are stymied with high energy requirements, cost, and safety issues in terms of handling high-pressure operations [8]. This calls for other drying alternatives such as natural drying, solvent-replaced ambient drying, surface-modified drying, and freeze drying [1, 7, 9]. The freeze-drying method particularly draws attention in aerogel research because of its environmental and sustainable nature [8, 10–12]. This kind of drying technique is a compatible drying choice for clay-based aerogels composite. The freeze-drying technique causes less damage to the material, rarely causing shrinkage or loss of clay minerals [13].

The properties of aerogel greatly depend on its microstructure and its application [1, 3, 8, 12]. Careful design and control of the resulting microstructure of aerogel is an important aspect of its synthesis and fabrication. Generally, there are two methods of preparing aerogels: single-component and multi-component [1]. The single-component aerogel usually contains one type of component in its preparation. Examples are oxide-based, organic-based (resin-based and cellulose-based aerogel), carbon aerogel, chalcogenide aerogel, and other aerogels from natural materials. The single component is the basis for composite or multicomponent aerogels preparation. Aerogels have a weak skeleton, due to their low Young's modulus and low yield strength, which limits their application. Some form of reinforcement during preparation is usually required to enhance the properties of aerogels [1, 5, 10]. The composite aerogels combine two or more components (metal oxide/silica aerogel, polymer/clay aerogel), or combines two methods (ultrathin graded resorcinol-formaldehyde [RF-based] aerogel), or micro/nanocomposite aerogel.

13.1.2 Clay Aerogels Composites

Clay aerogel is a natural, nontoxic, biodegradable, and biocompatible material [8, 11, 14]. Clay aerogels technology is part of a relatively new family of low-density aerogel materials that create a "house of cards"-like structure by using clay suspension through an environmentally friendly freeze-drying technique called *lyophilization* [5, 13]. Lyophilization technology is commonly used in food and pharmaceutical industries for preservation through a low-temperature dehydration



Figure 13.2 Pectin/clay aerogel composite [12].

process. Clay aerogels developed with this process can exhibit or even exceed favorable properties of foamed aerogels, such as enhanced fire resistance, reduced gas permeability, and increased young modulus [8, 13, 15]. Unlike most silica aerogels, clay aerogels require low temperature in their preparation. This cost reduction and safety measures along with its environmental friendliness make clay aerogels desirable to manufacturers [8].

Clay aerogel by itself should be considered a single-component aerogel but, the potential utilization of clay aerogel is limited by its poor mechanical strength. As a result, robust clay aerogels composites are enhanced clay aerogels containing natural and/or synthetic polymers and fibers in their structure. Many significant works have been done to improve the undesirable properties of bare clay aerogel. The enhancement procedures of clay aerogels involve a balance between improving their low compressive strength and/or reducing their high density [5, 9]. A well-established reinforcement medium is nanomaterials of different components, which have varying effects on the resulting property of the clay aerogel composite. The choice of reinforcement depends on the aerogels' final application. For example, the compressive modulus of clay aerogel composites can reach 22 000 kPa for different reinforced clay aerogels while the single-component clay aerogel is about 10 kPa [8]. This enhanced mechanical property makes clay aerogels composite applicable as packaging and insulation materials [10, 13].

Enhancement materials for the mechanical strength of clay aerogels can be classified by sources: natural polymers, synthetic polymers, natural fibers, carbon nanotubes, and laminating and dip coating [8]. Synthetic polymers for reinforcing clay aerogel are epoxy, polyethyleneimine (PEI), polyimides (PI), and polyvinyl alcohols (PVA). The most successful method of them all is the incorporation of a water-soluble polymer to create a water-based suspension that can withstand the freeze-drying process [8, 10, 14]. Natural polymers used in clay aerogels composites are casein, cellulose, chitin polysaccharide, lignin, natural rubber, and pectin found in the plants' cell wall [5, 10]. Gum Arabic/clay aerogels and pectin/clay aerogels are examples [12, 16], see Figure 13.2.

13.1.3 Clays Used in Aerogels Development

Clay exists in various forms across the world. Scientifically, clay types are often referred to as clay minerals. Clay minerals are hydrated alkaline silicates with very fine particles size [17]. They have

layered structures with silicon as the central atom at the tetrahedral sheet. Aluminum, iron, or magnesium occupies the octahedral site. The silicate layered structures can be 1 : 1, that is, one tetrahedral to one octahedral sheet or 2 : 1- one octahedral sheet sandwiched between two tetrahedral sheets [18]. Kaolinite belongs to the 1 : 1 family while the Smectites group is of the 2 : 1 family. Kaolinite ($Al_2SiO_5(OH)_4$) is electrostatically neutral with a weak hydrogen bond between the layers. Smectite, on the other hand, has a slightly negative charge due to ionic substitutions in the octahedral and tetrahedral sheets. This net charge imbalance is balanced by the interlayer cations. The bond between the layers is also weak but offers an excellent gap between the layers. One special feature of the smectite structure is that the structure expands in the direction normal to the basal plane when water and other polar molecules enter between the unit layers [19]. This property is called swelling-ability [10]. Montmorillonite, saponite, nontronite, and volkonskoite are typical types of Smectite. The montmorillonite is the most common smectite, with its octahedral site occupied by aluminum and partly substituted by iron and magnesium [18].

Several of these layered clay minerals have been studied in aerogel development. Mackenzie and Call studies montmorillonite clay aerogels by freeze drying in the 1950s [10]. Weiss et al. studied several clay-suspension combinations that produced rapid setting and thixotropic gels [10]. Kaolinite and montmorillonite were described as frozen thixotropic clay gels, which demonstrate remarkable high elasticity when sublimed in high vacuum. Montmorillonite interlayer spacings show inverse thixotropic sedimentation when measured by X-ray diffraction. K-Norrish et al. [20] had studied the effect of freezing on the swellings of clay minerals. Montmorillonite clay aerogels were found to retain their shape and partial rigidity when water was removed during freeze drying. The inner crystalline swelling and collapsing were widely reported. Van Olphen [21] studied the effect of incorporating polyelectrolytes into fragile bentonite clay aerogel. Results showed that the structure of bentonite was strengthened by this polyelectrolyte [10]. Bentonite caused significant shrinkage of the gel when incorporated in poly(acrylamide) hydrogel [22]. Of all the types of clay mentioned in the literature, smectite has proven to be the best clay due to its high cation exchange capacity, swelling ability, and high surface area [18]. Smectite clays have high porosity and low density because of the characteristic lamellar structure and interlayer spacing. They have excellent thermal and acoustic properties similar to those of silica aerogels [8].

The clay aerogels composite development is not new in aerogels technology as evident in the reviewed articles herein. It appears that the quest to develop optimal and cost-effective synthesis and reinforcement techniques continues to trend among researchers. This review work aims to critically assess existing literature on clay aerogels and their composites to gain a better understanding of the state-of-the-art and propose possible future direction of research on this emerging aerogel type. In this review work, the clay-based composite aerogels are introduced, followed by their synthesis techniques, enhancement technologies, properties, and industrial application and integration techniques. This survey of current literature hopes to showcase the possible potential of polymer/clay aerogels composite.

13.2 Synthesis Techniques of Clay Aerogels Composites

Clay aerogel composites are preferred over other aerogels because they are cheap to produce compared to other types of aerogel composite. Unlike silica and metal oxide aerogels produced from high temperature and pressure beyond the critical state, clay aerogels are commonly synthesized through the freeze-drying process. Freeze drying is environmentally benign, and it has already been in use in the food and pharmaceutical industry.

Clay aerogel composites are synthesized by incorporating water-soluble dispersive polymers and other various fillers such as montmorillonite clay, halloysite, and inorganic nanofillers to reinforce the poor physical and mechanical strength characteristic of neat clay aerogel [11]. The procedure for synthesizing polymer/clay aerogels composite involves three main processes: (i) the preparation of the composite suspension (or gel); (ii) freezing of the suspension at low temperature to form ice crystals; and (iii) the sublimation of the ice crystals with a high vacuum (low pressure) of about 40 Pa to form the aerogel composite [11].

Preparation of the gel is being targeted toward achieving improved properties such as reduced moisture uptake, enhanced flame retardancy, and/or reduced density of the composite. Polymer/clay composite has specifically gained wide application in the construction industry as insulation materials [5, 9]. The incorporation of polymers into clay aerogels enhances the strength and toughness of the resulting aerogels composite [10, 15].

The environmentally benign dry-freezing process in clay aerogels composite involves dehydrating the polymeric clay mixture at instant low temperature to generate ice crystals, then removing the ice by sublimation at lowered pressure. After the freeze drying, the ice is replaced by air to form different morphological microstructures [8, 10, 13]. At the freezing stage, the microstructure of the aerogel composite is formed. The denser microstructure is the result of lower freezing temperature while retarded ice layer growth is the result of the highly viscous suspension. The high viscosity could be a result of high polymer loading and/or high clay content, which could increase the strength and toughness of the aerogels but can also compromise their density. Hence, critical characterization of the suspension and the microstructure morphology must be carried out at every stage of an aerogel composite preparation. The need for enhancement techniques can only be decided on by detailed characterization results. Table 13.1 shows the summary of studies that have prepared different types of polymer/clay aerogel composites. The preparation technique and component combination were chosen for their application. Where necessary, nanofillers were incorporated for reinforcement of the resulting clay aerogel composite. Figure 13.3 summarizes the preparation steps of a cellulose/montmorillonite composite aerogel [23].

13.3 Properties of Clay Aerogels

13.3.1 Clay Aerogels Microstructure

Aerogels are porous materials of low densities ranging from 0.004 to 0.10 g cm^{-3}. They are made of crosslinked three-dimensional network structures containing air, which occupies not less than 90% of the material structure [1].

Large variations in the layered structures of clay aerogels have been observed, accordingly; the clay materials can be classified into four main groups as illustrated in Table 13.2 [25]. The most utilized structure is the 2 : 1 layer. This type of structure belongs to smectic clays, the most utilized clay type in developing clay-aerogel. The (2 : 1) layer structure is comprised of two tetrahedrally bonded silicon atoms attached to an octahedral sheet of aluminum or magnesium hydroxide through covalent oxygen bonds, as illustrated in (Figure 13.4). The thickness of each layered sheet is 1 nm and its length ranges from tens of nm to more than 1 μm. The van der Waals gap between the platelets is loaded with silicates layers. This gap, which is called interlayer or gallery, is occupied by positive ions (Na^+, Ca^{2+}, etc.), which balance the negative charge of platelets [8, 25].

Table 13.1 Recent advances on preparation of polymer/clay aerogel composites.

Clay aerogel composite	Gel preparation technique	Enhanced property	Setbacks	Possible solution	References
Clay/PVA	2.5 wt.% clay and 2.5 wt.% PVA	• Improved compressive moduli • Hydrophobic • Nontoxic	• Can absorb a high amount of moisture after curing • Highly flammable	• Implementation of water-dispersible repellant agents such as C_6-fluoroalkyl acrylate (WDisRep3) [15] • Addition of cellulose nanofibers as flame retardant [10]	[14]
Natural rubber/clay	2.5 wt.% Xanthan gum and 2.5 wt.% clay	Good elasticity	Flammable	Addition of flame-retardant	[11]
Ammonium alginate/clay	Incorporation of 5 wt.% alginates in pre-freezing suspension	Low flammability	—	—	[11]
Polyimide (PI)/clay	1 wt.% clay and 90 wt.% PI in pre-freezing	—	—	—	[11]
Poly (furfuryl alcohol)/clay	In-situ polymerization of an aqueous solution of 20 wt.% furfuryl alcohol monomer and 5 wt.% clay	Low density	• Flammable when uncured • Thermal instability	Oven curing	[17]
Pectin/clay	5 wt.% pectin added slowly into 5 wt.% clay suspension. [11]	Biodegradable	Microstructural change from lamellar to cellular	—	[12]

PVA, Polyvinyl alcohol.

Downloaded from https://onlinelibrary.wiley.com/doi/ by ibrahim ragab - Universita Di Firenze Sistema , Wiley Online Library on [21/07/2024]. See the Terms and Conditions (https://onlinelibrary.wiley.com/terms-and-conditions) on Wiley Online Library for rules of use; OA articles are governed by the applicable Creative Commons License

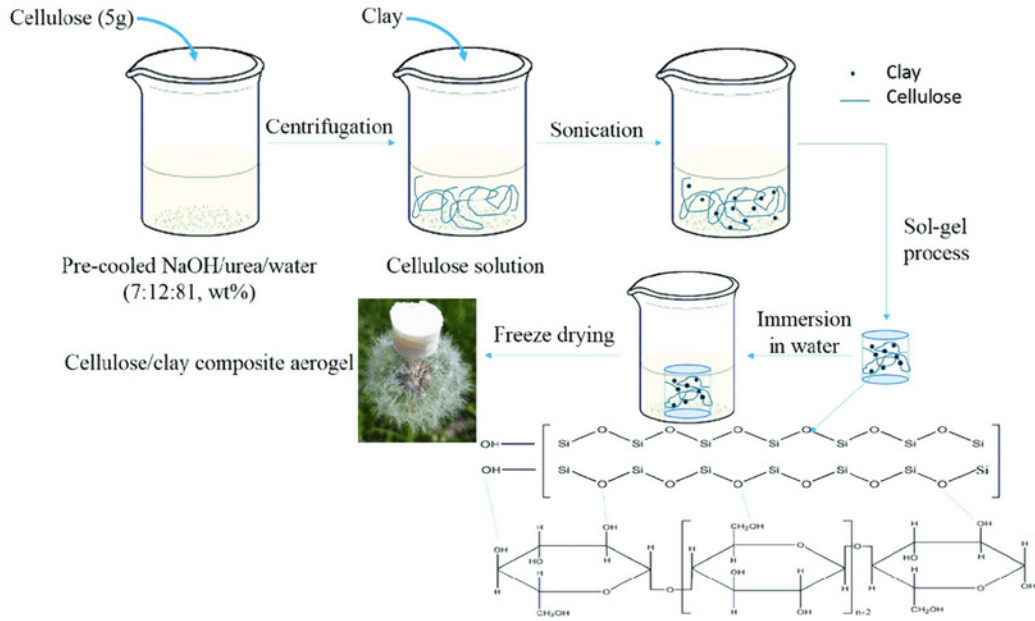


Figure 13.3 Preparation steps of a cellulose/montmorillonite composite aerogel [23] / MDPI / CC BY 4.0.

Table 13.2 Clay types and features Adapted from [24].

Group name	Member mineral	General formula	Layer type	Layer charge
Kaolinite or smectite montmorillonite	Kaolinite, dickite, nacrite Montmorillonite	$Al_2Si_2O_5(OH)_5$	1:1	<0.01
	Talc, pyrophyllite, vermiculite, sauconite, saponite, nontronite	$(Ca,Na,H)(Al,Mg,Fe,Zn)_2(Si,Al)_4O_{10}(OH)_2XH_2O$	2:1	0.5–1.2
Illite	Illite	$(K,H)Al_2(Si,Al)_4O_{10}(OH)_2XH_2O$	2:1	1.4–2.0
Chlorite	(I) amesite	$(Mg,Fe)_4Al_4Si_2O_{10}(OH)_8$	2:1:1	Variable
	(II) chamosite	$(Fe,Mg)_3Fe_3AlSi_3O_{10}(OH)_8$		
	(III) cookeite	$LiAl_5Si_3O_{10}(OH)_8$		
	(IV) nimite	$(Ni,Mg,Fe,Al)_6AlSi_3O_{10}(OH)_8$		

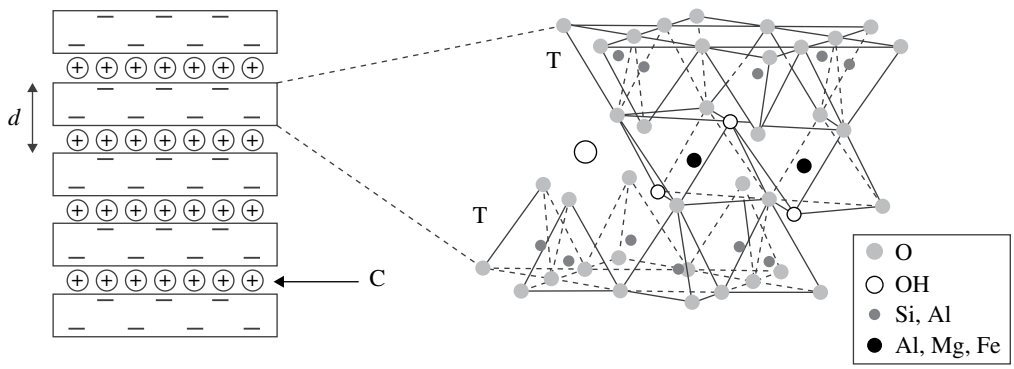


Figure 13.4 2.1 Layered silicate structure (T, tetrahedral sheet; O, octahedral sheet; C, intercalated cations; interlayer distance) Adapted from [26].

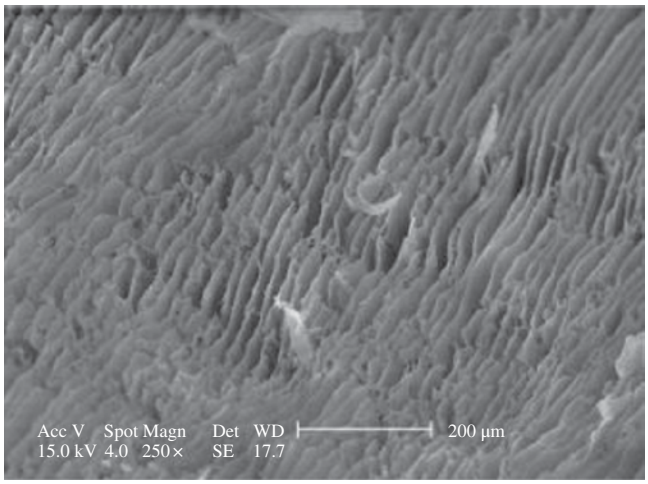


Figure 13.5 Morphology of clay-based aerogel (4 wt.% clay, freeze at −31 °C) [29].

Clay aerogels recently created from clay suspension by freeze drying comprised lamellar "house of cards" structure. The resultant layered structure is of the layer thickness of 1–4 mm and gaps between layers of 20–100 mm, giving ultra-low densities (0.05–0.1 g cm^{-3}) and considerable porosities. Consequently, compared to foamed polymers, the developed clay aerogels showed similar or even superior characteristics with respect to the mechanical properties such as Young's modulus, in addition to less gas permeability and good fire resistivity [24].

An early study conducted by Van Olphen claimed that the interlayers and cations hydration between them is a characteristic of montmorillonite (MMT) clay. This property results in remarkable hydrophilicity capacity [27].

The structure of MMT nanoparticle- aerogels was studied by Van Olphen et al. [28]. It was suggested that MMT nanoparticles are dispersed through the aerogel and interconnected edge-to-face similar to a "house of cards" structure due to the different charges of surface and clay edges.

The impacts of processing conditions (clay concentration and freezing rate) on the structure of clay aerogel were investigated. The change in pore geometry from "polygonal cells to thin lenses" was a consequence of decreasing both clay concentrations and freezing rates [29]. According to the study led by Bandi et al. [29] on sodium montmorillonite (Na^+-MMT) aerogels, the structure of those materials was found to be hierarchically layered, as illustrated in Figure 13.5 in a wide range of clay concentrations and freezing rates.

13.3.2 Mechanical Properties

Clay aerogels are of low mechanical strength unless reinforced with natural or synthetic materials. This is attributed to their layered structure, with large layers spacing resulting in fragile and too-weak materials. Thus, reinforcing the aerogels is essential to enhance their mechanical properties, hence, allow their use for various applications (e.g. insulation and packaging) [27]. The addition of fillers has proved to result in a positive effect on the compressive moduli of the aerogel composites, as it was reported that compressive modulus of different reinforced clay aerogel may reach 22 000 KPa [24].

It was reported, on the other hand, that the density of the aerogels does not always increase significantly by increasing the solid content to enhance the material strength. Hence, it is possible to reinforce the materials while maintaining low density [30]. For instance, while the compressive modulus of unreinforced clay aerogel may not exceed 7 kPa at a density of 0.039 g cm^{-3}, polyimide-reinforced clay aerogels can yield compressive modulus up to 201 kPa at relatively low density (0.075 g cm^{-3}) [26]. That promotes the aerogels as a viable competitor to the foam materials used for building applications [31].

Mechanically strong sodium alginate/clay aerogels were fabricated by adding p-toluene sulfonic acid using a freeze-drying method [32]. The adjusting of pH from 8 (the control) to 6, on the one hand, led to the crosslinking of alginate; on the other hand thickened the clay sol. The compressive modulus of produced aerogel significantly increased from 6.0 MPa (pH = 8) to 17 MPa (pH = 6). The morphological structure characterization showed that the microstructure of aerogels changed from layered to network with decreasing pH value, with cell size ranging from 4 to 8 μm.

In the work of Zhou et al. [33], palygorskite/wood fiber (Pal/WF) composite aerogels with low densities were prepared by an eco-friendly freeze-drying method. In the aerogels, palygorskite contents were up to 80 wt.% while only a small amount of wood fiber was used as reinforced filler. The composite aerogel had an array of porous structure with intertwined palygorskite fibers as pore walls, which resulted in good mechanical strength with the Young's modulus up to 4.7 MPa while the density was lower than 0.08 g/cm^3.

Recently, Rong et al. [34] reported an environmentally friendly and simple liquid nitrogen directional freezing method in which acid-modified montmorillonite was introduced into the cellulose nanofiber (CNF)/chitosan (CS) system to successfully prepare CNF/CS/montmorillonite (MMT) aerogel (CCMA). Compared with other aerogels, CCMA forms a homogeneous three-dimensional directional pore structure, showing excellent mechanical properties, good adsorption performance, and reusability. The results show that the aerogel can withstand heavy objects 1124 times their own weight, while maintaining a stable structure in a strong acid environment. The results might be caused by two aspects: on the one hand, the hydrogen bonding between CNF, CS, and MMT, as well as the existence of intercalation structure, enhances the mechanical properties of aerogels. On the other hand, the directional freezing of liquid nitrogen made the fiber bundles inside the aerogel arranged in an orderly manner to form a regular three-dimensional network structure, which might also enhance the mechanical properties of the material.

Inspired by the tubular structures found in naturally occurring thermal-insulating materials, Sun et al. [35] have recently prepared tubular cellulose aerogels with improved mechanical resistant, thermal insulating and flame-retardant properties from kapok fibers via a facile process. In contrast to fragileness of traditional organic-inorganic composites, an optimized sample exhibited an ultra-high compressive strength of 32 MPa.

The consequence improvements of mechanical properties due to incorporating various modifying materials into clay aerogel's structure have been discussed thoroughly in (clay-aerogels enhancement) section.

13.3.3 Thermal Conductivity

Low thermal conductivity is an essential characteristic of thermal insulation material. The efficiency of the insulators is determined by their ability to minimize the heat flow controlled by the three heat transfer modes: solid conduction, gas conduction, and radiation [3].

Clay aerogels are known for their superior thermal insulation properties. That refers to their lamellar structure, which hinders the heat flow within the material, resulting in low thermal

conductivity in the range between 0.015 and 0.05 $W m^{-1} K^{-1}$ [36]. Heat transfer by solid conduction is limited due to the porous structure of the aerogels. On the other hand, the gas conduction is limited as well because of the three-dimensional network structure, which allows the gas particles to flow through the structure.

At low temperatures, radiation is less important to the total thermal conductivity within an aerogel; comparatively, its contribution can be of significance at high temperatures [37].

The microstructure of aerogels plays a vital role in determining their thermal conductivity [38]. It was proposed that the interconnectivity of the clay platelets through thin struts produces the ideal structure to minimize the heat flow within the materials. The synthesis method and aerogels compositions have a considerable impact on the structure of the material. For instance, PVA/clay aerogels exhibited low thermal conductivity, compared to the thermal conductivity of the sole components [3]. The incorporation PVA into clay aerogels was found to have an influence on the thermal conductivity of the clay aerogels and result in an increase in density from 0.050 to 0.068 g cm^{-3}. It would be expected as with foamed materials that increasing the density above a certain point can sacrifice the porosity and lead to a significant increase in thermal conductivity. However, the thermal conductivity of the clay/PVA aerogel was unexpectedly lower than the specimens without polymer. This may be related to the structure architecture, in which the polymer created small struts between the clay layers resulting in a more complicated path for heat to flow through. Thus, the combination of clay and PVA is able to produce aerogels with a lower conductivity than either of its constituents (e.g. clay and PVA) [3].

A series of low-density, highly porous clay/poly(vinyl alcohol) composite aerogels, incorporating keratin fibers derived from chicken feathers, were fabricated via a convenient and eco-friendly freeze-drying method [39]. The introduction of keratin fibers improved the mechanical performance, as well as decreased thermal conductivities, allowing these materials to have potential utility in thermal insulation. Aerogel samples (5% Clay/2.5% PVOH) frozen at −78 °C exhibited thermal conductivity values as low as 0.075 W ($m^{-1} K^{-1}$), same composition samples frozen in liquid nitrogen has a relatively lower value, 0.070 W ($m^{-1} K^{-1}$), which was attributed to more small-size pores formed in the aerogel. As a well-known nature thermal insulation material, different amount of keratin's introduction improved thermal insulation effect and thermal conductivity values have been decreased to 0.066 W ($m^{-1} K^{-1}$) for 1% fiber reinforced aerogels, and 0.058 W ($m^{-1} K^{-1}$) for 3% fiber reinforced one. Different freezing methods made an impact on thermal conductivity of keratin-reinforced aerogels as well.

In the recent work of Zhou et al. [33], fire-resistant palygorskite/wood fiber composite aerogels with low densities were prepared with palygorskite contents up to 80 wt.% while only a small amount of wood fiber were used as reinforced filler. The composite aerogel had an array of porous structure with intertwined palygorskite fibers as pore walls, which resulted in a low thermal conductivity of 0.033 $W m^{-1} K^{-1}$.

Gupta et al. investigated flame retardancy and thermal insulating properties of sepiolite clay and CNF-based aerogel [40]. Due to the fragile characteristic of sepiolite-based aerogel, CNF has been introduced into the clay to make it a composite aerogel. The prepared hybrid aerogel has been modified with a hydrophobic precursor i.e. Methyltrimethoxysilane (MTMS). The prepared specimens have shown the typical properties of aerogels like low density (11.5–32.5 kg m^{-3}), high porosity (99.2–98.3%) with good dimensional stability. Vertical burning test along with V-0 performance, horizontal burning test, and flame penetration has confirmed its thermal shielding and flame retardancy. Thermal conductivity results also show good thermal insulation properties of prepared composite aerogel. The thermal conductivity is varied in this work between 0.0261 and 0.0396 $W m^{-1} K^{-1}$.

13.3.4 Fire/Combustion Behavior

Aerogels are generally preferred materials in the construction industry. Besides the lightweight and low thermal conductivity, fire retardancy determines the suitability of aerogels application as insulators. The behavior of the aerogels under fire conditions can be tested by a cone calorimeter method. This test is necessary especially when flammable materials are used to mechanically strengthen the aerogels [3].

The type of additives affects the fire behavior of clay aerogels. For example, although utilizing polymers as reinforcing material is beneficial in terms of enhancing the mechanical properties of clay aerogels, they increase the fire risk of the composite materials since they are generally characterized as flammable material. However, synthesis methods of reinforced aerogels also have a significant impact on the flammability of the produced composites. For instance, polymer clay aerogels developed by the freeze-drying method showed less flammability compared to polymer foam materials [11].

To lower the flammability of reinforced clay aerogels, either organic or inorganic fire-retardant agents can be used. It was reported that composites comprising aluminum hydroxide ($Al(OH)_3$) and ammonium polyphosphate (APP) reduced the fire growth rate index, (FIGRA) to 0.5 and 0.4, respectively, compared to 2.0 ($W s^{-1}$) for the original sample [3]. On the other hand, some additives have been proven to improve the fire behavior of clay aerogels. Alginate, a natural polysaccharide used for food applications, is characterized as less-flammable material. Hence, alginate-based aerogels have exhibited slower flame spread. Moreover, it was found that adding clay to alginate aerogel enhances the combustion behavior further, as no flames were reported throughout the entire test [41].

Recently, mechanically strong sodium alginate/clay aerogel were fabricated by addition of p-toluenesulfonic acid using a freeze-drying method [32]. The adjusting of pH from 8 (the control) to 6, on the one hand led to the crosslinking of alginate, on the other hand thickened the clay sol. The combustion tests indicated that all the alginate/clay aerogels possess excellent flame retardancy. The addition of p-toluenesulfonic acid further slightly increased the thermal stability and fire safety of the material. This facile preparation procedure of strengthened polymer/clay aerogel via adjusting pH is promising and can be spread.

CNFs and sepiolite based aerogel have been performed for the horizontal burning test according to UL 94 procedure [40]. The samples are burned at the blue flame of methane gas for 30 seconds to verify the flame retardancy of aerogels. When the pristine CNF aerogel was in contact with flame, flame propagates abruptly within two seconds and the whole aerogel have been burned within five seconds of initial burning. In contrast with pristine CNF aerogel, inorganic-organic hybrid aerogel have shown slow combustion and self-extinguishing behavior according to UL 94 with HF-1 rating. C1S1 (0.2% CNF, 0.2% sepiolite) sample and C1S2 (0.2% CNF, 0.4% sepiolite) sample aerogels have demonstrated that combustion had stopped after 0.5 seconds of flame elimination. The C1S3 (0.2% CNF, 0.6% sepiolite) aerogel, C1S4 (0.2% CNF, 0.8% sepiolite) aerogel, and C1S5 (0.2% CNF, 1.0% sepiolite) aerogels has shown excellent flame retardant behavior. The aerogels were shown self-extinguishing behavior immediately after removal of the flame source. In case of C1S5 aerogel, when the aerogel comes in contact with flame, the flame has not been propagated in the horizontal direction.

In a recent work, tubular cellulose aerogels with improved mechanical resistant, thermal-insulating and flame-retardant properties were prepared from kapok fibers via a facile process [35]. The tubular structure of this material resulted in a 37.4 °C increase in heat preservation compared with that obtained from a pulp aerogel without this morphology. The H_3PO_4 decomposed from

$(NH_4)_2HPO_4$ in the formulation crosslinked the outermost cellulose fibers to generate a clay-reinforced dense carbon layer in conjunction with montmorillonite (MMT), which restricted the movement of flames and the outflow of volatile compounds. The gaseous voids of internal tubular fibers interrupted the heat transport pathways to inhibit thermal transmission and trapped combustible volatiles to reduce the penetration pressure experienced by the dense carbon layer greatly. The combined effects of the carbon layer and tubular structure effectively limited the transfer of heat, oxygen, and volatiles, leading to noncombustion of the optimal sample. Direct flame ignition trials were performed to visually assess the combustion characteristics of the various aerogels. CA (A sample without $(NH_4)_2HPO_4$ or MMT) was highly flammable and began to burn immediately after coming into contact with an ignition source, followed by rapid flame propagation. The flame was extinguished while burning violently over a span of 30 seconds and exhibited smoldering for a long time. In contrast, the CA-MMT-NP0 (sample without $(NH_4)_2HPO_4$) burned and smoldered slowly for 120 seconds and left a loose, dark gray residue. Those samples containing $(NH_4)_2HPO_4$ showed self-extinguishing behavior. The CA-MMT-NP1 produced only a faint flame and exhibited slower spreading of the fire. The flame was observed to die out after burning for 8 seconds and no smoldering occurred. The burning time of the aerogels decreased with increasing of the $(NH_4)_2HPO_4$ content because of the gradually strengthened self-extinguishing effect, such that the CA-MMT-NP3 was difficult to even ignite and showed oxidation rather than combustion with a flame. This process consumed oxygen in conjunction with a very low heat release rate and could be monitored using cone calorimetry.

13.3.5 Hydrophobicity/Hydrophilicity Behavior

Clay aerogels are hydrophilic, which causes their dry composites to be high absorbents of moisture. Consequently, their applications are limited as an insulation material. It was reported that the rise in moisture content by 1%(v/v) may result in a 7% increase in thermal conductivity, in addition to the deterioration in the mechanical properties, which refers to the degradation of the composite structure after long exposure [14]. However, clay aerogels produced with the freeze-drying technique have proved to be effective absorbents of water and ionic solutions, though maintaining the structural integrity after saturation. Such hydrophilic composites can be developed by modifying with water-soluble polymers-enhanced clay aerogels, such as poly (vinyl alcohol) (PVA), poly (ethylene glycol) (PEG), and poly (ethylene oxide) (PEO) [3]. Those composites were reported to be ideal materials for oil/water separation.

In the tubular cellulose aerogels (CA-MMT-NPx) developed by Sun et al. [35] using kapok fibers, montmorillonite (MMT) and different amounts of $(NH_4)_2HPO_4$, CA-MMT-NP3 aerogel sample had an average water contact angle of 120.8°, which illustrates that CA-MMT-NP3 is hydrophobic. However, exploring how to improve the hydrophobicity of clay-based aerogels is the goal of many researchers.

13.4 Enhancement Techniques of Clay Aerogels

Development and improvement of clay aerogels may be pursued in several areas, most importantly, their structure, which leads to brittle clay aerogel of low mechanical strength. Enhancing clay aerogels' properties by incorporating additives, either natural or synthetic, is crucial to allowing their utilization in different applications. Several materials, such as polymers, nanomaterials, and fibers, have been investigated as suitable candidates to improve the mechanical properties of clay aerogels by combining them in the aerogel's framework.

Another targeted improvement is to increase the aerogel's hydrophobicity when considering the materials for certain applications, such as insulation in the construction industry. However, when clay-aerogels are used as absorbents, the water absorption property is favored.

13.4.1 Natural Polymers Enhanced Clay Aerogels

Cellulose is one of the most exploited natural reinforcing agents. It is a natural biopolymer, a polysaccharide formed of β(1 → 4) linked D-glucose units. It is the amplest organic polymer, can be found in the cell wall of green plants, some types of algae, and bacteria. It is also found in cotton, wool, and hemp. Cellulose is widely used in different applications as a reinforcing additive due to its high strength property. Additionally, it is characterized as a hydrophobic, and biodegradable material, which makes it favorable for different uses [42].

There are different forms of cellulose, for instance, whiskers, which is a crystalline nanofiber. This form has been widely utilized and investigated due to the observed improved performance of their composites [3]. Recently, the development of montmorillonite clay aerogel incorporating different forms of cellulose by the freeze-drying process has been explored. It was reported that the addition of cellulose nanofibers to montmorillonite clay/aerogel, rather than increasing the clay content, resulted in the enhanced compressive modulus [24].

On the other hand, it was found that composites of higher density do not always exhibit mechanical strength higher than those of lower density. It was shown that a sample of density (0.031 g cm^{-3}) showed a modulus of 462 kPa, while a sample of 0.069 g cm^{-3} recorded 392 kPa. Hence, the increase in the strength might be attributed to the development of a 3D network by the whiskers, and that results in transferring the stress effectively [43].

Dash et al. [44] studied the effect of the freezing process on the nanofiber cellulose/sodium montmorillonite (MMT) composite aerogels. They found that foam-like, isotropic aerogels were produced by nondirectional freezing, while directional freezing produced anisotropic, honeycomb-like aerogels. The former showed better mechanical strength when stress was applied perpendicularly on the microstructure layers of aerogel. This improved performance is attributed to the effective load resistance offered by the structure of clay sheets. This suggests that not only the increase in solid content will enhance the mechanical properties, since the layered structure may also have an impact on the mechanical properties of the aerogels.

A recent study aimed at developing a cost-effective clay composite with enhanced thermal resistance revealed that adding nanofiber cellulose to starch/clay composite produced thermal insulative aerogel with enhanced mechanical properties. Introducing the NFC decreased the starch content from 4% to 2% without distorting the clay aerogels structure during the freezing process. The resultant material displayed a decrease in the density and thermal conductivity of 0.12 to 0.05 g cm^{-3} and 0.0483 to 0.0415 $W\,m^{-1}\,K^{-1}$, respectively [45].

In the work of Shang et al. [46], cellulose/attapulgite (ATP) composite aerogels were prepared by freeze drying and chemical vapor deposition. ATP is a naturally available 1D natural hydrophilic clay with a diameter of 30 nm and a length range of 0.5–1 μm, which displays the hydrated magnesium aluminum silicate structure with theoretical composition of $Mg(Al)5Si_8O_{20}(OH)_2(OH_2)4{\bullet}4H_2O$. The formation of Si-O-Si and C—H bonds observed according to FTIR and XPS indicated that the methyl groups from methyl trimethoxysilane (MTMS) had been grafted on the composite aerogels. The as-prepared composite aerogels showed high hydrophobicity with water contact angle up to 161.1°. Moreover, the composite aerogels had three-dimensional pore structures and good thermal stability. Compared to the pure microcrystalline cellulose (MCC) aerogel, the maximum compressive strength of composite aerogel with hydroxyethyl cellulose (HEC) and ATP build blocks was able to reach 1.43 MPa.

Another cost-effective supporting material is *Lignin*, which is an amorphous organic polymer that represents the main material in the structure of support tissues of cell walls of most plants. Lignin is known for its rigidity which offers high potentials when incorporating this polymer in polymeric composites as well as aerogels composites. The latter application of the lignin has been explored recently, stimulated by the low cost of this material, which is considered a waste of the pulping process [47].

Viggiano and his collaborators attempted to form a composite of lignin and sodium montmorillonite clay aerogels applying the freeze-drying technique. From this experiment, it was observed that the enhancement of physical and mechanical properties of clay aerogels relied on the functional groups of the lignin alkaline and sodium lignosulfonate [29].

Lignosulfonate acid reinforced clay aerogel exhibited high compressive modulus while maintaining low density. This improvement may be attributed to the water-solubility of lignosulfonic acid (LSA) due to the existence of sulfonic acid groups, which leads to the formation of 3D structures [48]. Furthermore, since LSA is of higher molecular weight than alkali lignin (AL), more hydrogen bonds might form. However, it is generally preferred to have aerogel composites with polymers of moderate molecular weight to avoid a significant increase in composite density [8].

Recently, cellulose nanofibrils (CNF), AL, and montmorillonite (MMT) were used to produce reinforced PVA hydrogels [49]. The effects of MMT and AL contents on the rheological properties of reinforced hydrogel were studied. Compared with PVA/CNF hydrogel, the storage modulus of 40 wt.% MMT-reinforced PVA hydrogel was increased by 41.4%. The rheological properties of MMT-enhanced PVA hydrogel could be adjusted by the variation of MMT loading. Also, as the PVA matrix had a synergistic effect with the embedded MMT and AL, the composite hydrogel demonstrated high efficiency in the removal of methylene blue dye (MB) from wastewater.

Natural rubber, which is an elastic material extracted from latex, has also been used in developing materials composites. NR can elongate and recover its original shape after removing the stress. Another property of NR is the toughness at deformation due to crystallization.

Some types of NR have good potential to produce reinforced polymer-clay aerogels of low gas permeability [29]. For instance, pure vulcanized natural rubber (PNR) has been incorporated into montmorillonite (Naþ-MMT) aerogels [29]. The developed composites have shown increased density in the range 0.36–0.55 g cm^{-3} compared to 0.01–0.10 g cm^{-3} for unreinforced montmorillonite aerogels. This increase in the density is due to an increase in the solid content. However, it is not always related to the enhanced mechanical properties, as the latter might be attributed to the electrostatic interaction between the clay and the rubber, which leads to a strong rubber-clay interface [50].

In a study on clay-NR composite synthesized through freeze point and crosslinked with benzene using the crosslinking agent of sulfur monochloride (S_2Cl_2), the effect of various factors on the clay structure and characteristics were investigated [51]. It was found that increasing (S_2Cl_2) concentration results in a rough structure, consequently, the mechanical properties improve. Yet above 1% (v/v), the density increases without further improvement in mechanical strength. Similarly, increasing crosslinker concentration above a specific degree leads to lower crosslinking efficiency. The optimum conditions to develop the composite were found to be 18 °C for reaction temperature and a 1% (v/v) (S_2C_{l2}), which resulted in the toughness of 13 kPa and compressive modulus of 1800 kPa.

Chitin, another natural reinforcing agent, is a derivative of glucose, found abundantly in cell walls of microorganisms such as fungi, shells of crustaceans and insects, and many other living organisms. Due to its natural strength, chitin has high potential when incorporating with the clay

aerogel composites, as it provides strong aerogel composites. Yet, its application is limited due to its reactivity, since it is only reactive in an acidic environment [8].

The effective dispersion of chitin in aerogel can be achieved when the reaction takes place in an acidic media, due to the formation of ammonium polyelectrolyte. Synthesis of homogenous composites depends on the molecular weight of chitin, as low molecular weight results in homogenous materials, whereas heterogeneous composites are obtained from high molecular weight chitin [52].

It was reported that incorporating some additives in chitin clay-aerogel materials resulted in improved properties. For instance, adding polyacrylic acid enhanced the inorganic nucleation by enhancing the bonding strength, especially in the presence of acidic media, such as carboxylic acid. The resulting composites were of integrated structure and higher moduli. However, due to the high molecular weight of chitosan the density of the composite increased [29].

13.4.2 Synthetic Polymers Enhanced Clay Aerogels

Among the various types of polymers, *PVA* has gained much attention as a reinforcing material. It is a biodegradable water-soluble polymeric material developed by hydrolysis of polyvinyl acetate [8]. PVA is widely used for different industrial and medical applications for providing good toughness and flexibility characteristics as well as gas barrier properties [53, 54].

PVA is a viable cost-effective additive to clay aerogels due to their strong affinity to clays, besides, their good mechanical properties and water solubility. The enhanced mechanical properties of the produced composites refer to the ideal hydrogen bonding between the polymer and clay [8].

The degree of strength of the PVA-clay aerogels strongly depends on the molecular weight of PVA. It was shown that high molecular weight additive provides a random structure, resulting in less stiff materials compared to the composites consist of moderate molecular weight PVA, which gives rigid lamellar structure providing good mechanical strength [55].

Although enhancing PVA materials by adding cross-linking agents such as di- glutaraldehyde and glyoxal have been widely explored, their applications for developing PVA clay aerogels are still limited [32]. However, a study on producing PVA aerogels utilizing the crosslinking agent (divinyl sulfone) through the freeze-drying process reported enhanced mechanical properties by increasing the compressive moduli by 2–30 MPa. The degree of impact of crosslinking on the properties of the produced materials depends on the polymer-clay ratios, as high polymer content increases the crosslinking efficiency [56]. Besides, at lower clay concentrations, enhanced properties were also reported, giving the merit of reinforced low-density materials.

Crosslinking can also be obtained by applying gamma irradiation. It was found to be advantageous compared to chemical cross-linking, as the latter may cause an increase in the materials viscosities hindering obtaining homogenous composites. An experiment has been conducted on the impact of the gamma irradiation on the PVA clay aerogel showed that gamma irradiation resulted in enhanced compressive modulus at low densities, and the optimum dose for synthesis tough composite was recorded as 30 kGy [8].

The improvement in the mechanical performance of poly(vinyl alcohol) (PVOH)/clay aerogel enhanced by a flame retardant (pentaerythritol octa-hydrogen tetraphosphate [PEPA]) was evident by the study carried out by Shen and his collaborators [57]. That was justified by the observed decrease in pores size of the produced composite that enhances the mechanical characteristic. Other parameters, such as thermal stability and flame retardancy, showed improvement as well [58].

Epoxy polymers are preferable reinforcement materials due to their chemical and corrosion resistance, superior mechanical, thermal, and electrical properties [59]. To produce epoxy-clay aerogel, water-soluble crosslinking thermoset agents 1,4-butanediol di-glycidyl ether (BDGE), and triethylenetetramine (TETA) can be used to develop water-soluble epoxy monomers, which are utilized to produce clay-aerogel by freeze drying. It was reported that increasing the polymer content while miniating constant clay load leads to higher density as well as enhanced mechanical properties. The reinforced material showed elastomeric behavior, which enables them to bear high strains. That might be attributed to the structure of (house of cards), as the clay particles are covered with BDGE-TETA polymer, leading to the gained elastomeric behavior [59].

Polyethylene imine (PEI) is a viable candidate to strengthen clay aerogels, as it interacts with smectic clays by developing covalent bonds to form a stable polymer-clay aerogel [60]. It is a water-soluble polymer that is broadly used for membrane synthesis [61]. The PEI-clay aerogels composites were developed by freeze-drying method, and the produced material exhibited excellent initial modulus of 270 kPa, whereas keeping low density (0.075 g cm^{-3}). The solidification method was also considered for producing PEI-clay aerogels applying tetra-methyl-orthosilicate (TMOS). The resultant material structure was found to be rough compared to the laminar form of the unreinforced material. It was reported that the properties of solidified aerogel were sensitive to the relative humidity, since the PEI aerogel composites when treated at humidity of 60% RH, showed an increase in the initial modulus from 270 to 870 KPa. On the other hand, the aerogels treated at 80% RH exhibited an initial modulus of 2.8 MPa, which is a remarkable record compared to the untreated PEI aerogels [8].

A successful attempt to enhance the clay aerogel was achieved by incorporating poly (ethylene imine) polymer into the clay aerogel structure. A further modification was made by biomineralizing the polymer-based clay aerogel with tetramethyl orthosilicate to provide silica encapsulated structures. The resulted materials showed impressive mechanical properties, as the compressive properties increased up to 10-fold compared to unmodified materials, even though, the structure and density have not been affected. Increasing the PEI and orthosilicate enhance the strength further, as producing five layers of silica/PEI improved the mechanical properties up to 20-fold [62].

13.4.3 Natural Fibers Enhanced Clay-Polymer Aerogels

Due to their favorable properties such as low density, low cost, biodegradability, and good mechanical characteristics, natural fibers are targeted as reinforcing materials. There are many limitations for natural fiber application, as their properties differ widely. The factors that affect the characteristics of fiber composites include the type and source of the fiber, in addition to the fabrication method. Although being a sustainable and environmentally friendly material, the use of fibers for reinforcing clay aerogels is still limited [8, 36].

Several studies have been conducted on incorporating different fibers such as silk, hemp, and soy silk into clay aerogels by the freeze-drying method. The resultant composites showed increased compressive modulus up to 8900 kPa while maintaining low density given as 0.012, 0.093, and 0.093 g cm^{-3} for the highest contents of silk, soy silk, and hemp, respectively. The enhanced strength is a consequence of interconnecting the clay platelets by the fibers, by developing long struts, and it might also be attributed to the stiffness of fibers [63].

Arabic gum, a natural fiber comprising the hardened sap of two species of the *acacia* tree, *Acacia senegal* and *Vachellia seyal*, has been explored as a reinforcing material for the clay-aerogels. The composite of Arabic gum and sodium montmorillonite (Na^+-MMT) clay aerogel was developed

through freeze-drying process. Good mechanical properties were obtained, as the specific modulus and the absorbed energy of resultant aerogels increased by 1.6 and 4.2 times respectively at 40% clay content. The power-law model rose from 1.95 to 3.28 because of the resultant anisotropic structures. Furthermore, thermal stability and flame retardancy also showed enhancement, proved by the increase in the initial decomposition temperature by 16 °C approximately [16].

13.4.4 Carbon Nanotubes Enhanced Clay-Polymer Aerogels

Carbon nanotubes are recent materials combining nanotubes and fullerenes. They have gained great attention in respect to nanocomposites development due to their remarkable mechanical, electrical, thermal, and optical characteristics. However, CNTs utilization is limited, due to their difficult processibility, and high cost [64].

There are two forms of CNT: single-walled carbon nanotubes (SWCNT) and multi-walled carbon nanotubes (MWCNT); the latter have been more explored for forming nanocomposites. A study developed nanotubes-clay-polymer composites by incorporating SWCNT aerogels with a gel of Na^+-MMT and poly (acrylic acid) PAA. The produced composites showed enhanced mechanical properties as the modulus increased while maintaining the densities of the composites. Similar to the other aerogels composites, the structure of SWCNT was characterized as lamellar, which indicates that the change in the mechanical properties refers to the properties of the nanotubes, rather than the structure [8, 65].

13.4.5 Modified Organoclay Enhanced Clay Aerogel

Incorporating hydrophobic organically modified clays into clay aerogel composites applying freeze-drying process has resulted in enhanced physical and mechanical properties [58]. A 50% increase in the compressive modulus was reported, which may be attributed to the enhanced interfacial bonding between the additive and clay. The most important improvement obtained by incorporating the organoclay is the remarkable decrease in the moisture adsorption, as it was reduced to 40%, accompanied by a 20% reduction in the thermal conductivity. These achieved properties are highly significant when considering the clay aerogel for insulation applications in the construction industry [66].

13.4.6 Enhancing Clay Aerogels with Polymer Coating

One method to strengthen the clay aerogels is by coating them with rubber using the dip-coating procedure [3]. A significant improvement due to coating application was noticed in the flexural properties, as the flexural modulus increased by 20-fold, and the yield stress increased up to 15-fold. Furthermore, the thermal properties were enhanced by 8% and the hydrophobicity properties enhanced which promotes the modified aerogels as insulating materials [67].

In the work of Jin et al. [68], palygorskite (Pal) based aerogel was successfully fabricated via combining with a very small proportion of alginate to form a distinctive hierarchically meso–microporous structure. By employing ethanol solution (EA) replacement method and freeze-drying process, the resultant aerogel exhibited ultralow density (0.035–0.052 g cm^{-3}), practical mechanical strengths (0.7–2.1 MPa), and low thermal conductivity of 0.0332–0.165 $W m^{-1} K^{-1}$ (25–1000 °C). The hydrophobicity of aerogel was achieved by simple chemical vapor deposition of methyl trimethoxysilane (MTMS). The Pal-based aerogel showed good performance in both fire resistance with high limiting oxygen index up to 90%, and heat resistance with tolerance of flame

up to 1000 °C for 10 minutes. This renewable Pal-based aerogel with a 3D framework is a promising material to be applied in fields of construction and aerospace for thermal insulation and high fire resistance.

13.5 Applications and Integration Techniques of Clay Aerogel Composites

Clay aerogel composites have found great applications in the construction industry as both insulation and adsorbent materials. Lin et al. [69] previously used clay such as bentonite, kaolinite, zeolite, and calcite enhanced with hexadecyltrimethylammonium bromide (HDTMA) and gallic acid as adsorbent material to remove boron from wastewater. The removal was found to be via various surface adsorption mechanisms such as surface complexation and electrostatic physisorption by the calcined hydroxyl groups of calcined layered double hydroxides (CLDHs). The presence of these functional groups on the enhanced clay aerogel surface had a high affinity for the boron to be removed at a moderate temperature of 500 °C via nucleation growth mechanisms with particle size <100 nm.

Gao et al. [70] produced mono-layered nanosheets of Mg-Al- CLDHs(0.7 nm thickness) via ionothermal processes in a deep eutectic solvent with a high specific surface area greater than 200 $m^2 g^{-1}$ based on pseudo-second-order Langmuir adsorption kinetics. A recent study by Madyan et al. [3] revealed that several industrial sectors had made use of clay-based aerogels composites for thermal and acoustic insulation, as well as catalyst support in pharmaceutical and drug industries. In their study, casein-reinforced clay-based aerogels were employed in paper coating, wood adhesives, and food packaging due to their film-forming properties for barrier resistance to nonpolar substances though being weakly water-resistant and high polar group masses.

Epoxy-reinforced clay aerogels have found several applications in automobile industries like natural rubber reinforced clay aerogels due to their elastomeric properties, which give them the ability to sustain large strain while suffering little or no permanent deformation. Polyimide-reinforced clay aerogels are majorly employed in microelectronics owing to their specific electrical, heat, and water-resistant properties at temperatures of up to 300 °C. They can be produced by supercritical CO_2 drying and freeze drying for insoluble and soluble ones, respectively.

Nita et al. [71] submitted as follows in their work:

> *Clay-based aerogels and their composites equally found recent applications in biomaterials community owing to their special properties making them provide advanced cytocompatibility, biocompatibility and biodegradability in tissue engineering, reservoir drug delivery systems, biomedical implantable devices [pacemakers, stents, and artificial heart valves], disease diagnosis and antibacterial materials treatments (wound dressings), biomolecules immobilization, and so on, with detailed methods and procedures.*

13.6 Economy and Limitations of Clay Aerogel and Composites

The basic economic importance of clay-based aerogels includes their low costs, nontoxicity, eco-friendliness, and ease of fabrication, thereby making the regeneration process uneconomic. Hence, the clay-based adsorbent can be easily discarded after a single use.

The notable initial major drawback is their high production costs, along with high operating temperature and pressure involved but this has been circumvented by production via freeze-drying

and CO_2 drying methods as well as other cryogenic conditions entailing the use of safe and harmless inexpensive materials in aqueous clay suspension to yield lamella house of card structural materials based on their constituents. They are capable of transmitting low heat and being fire retardant, making them efficient and economical. Composite clay-based aerogels have recently been designed not to include materials capable of sacrificing their mechanical integrity, thermal/fire retardant, and low conductivity as well as combustibility and density to suit several purposes of using them. The ability to fulfill these uses makes them more profitable and easily employed amidst other materials that can be used for the same purposes. They are equally nontoxic and environmentally friendly by their longer time-to-ignition via production with irradiated cross-linked PVA materials of low combustibility and heat-release rate during combustion.

The incorporation of water-repellant components into clay-based aerogel composites reduces their absorption ability, thereby leading to economic gain. Madyan and Fan [14] asserted that such aerogels maintain low thermal conductivity of $0.038\,W\,m^{-1}\,K^{-1}$.

In pursuance of the above, Chen and Schiraldi [11] opined via experiments that the flame retardant ability of the clay-based aerogel would drastically reduce alloying with polymers. Nevertheless, alloying the aerogels with inorganic materials will improve their fire-retardant properties. Chen and Schiraldi alloyed several polymers such as PVOH, with alginate, halloysite, montmorillonite clay, and laponite. Nanofillers were incorporated to reduce smoke to the barest minimum.

Consequently, the economic value of the clay-based aerogels and their composites can be improved upon by using alginate and incorporating aluminum hydroxide in cellulose-based aerogels as well as silica in conjunction with cellulose whiskers cross-linkers and piperazine. It should be noted that incorporating polymers only benefits the mechanical strengths of the clay-based aerogel at the expense of a drastic reduction in fire-retardant properties.

Most clay-based aerogels are highly hydrophilic, creating an extra-high tendency to absorb water on exposure to water and usages. Hence, this calls for rectification via engineering treatment to make them more useful. Lignin included clay-based aerogel composites had been found with increased compressive modulus with no change in density owing to its high molecular weight that prevented general applications rendering it to specific users. As the molecular mass of the reinforced clay-based aerogels increases in their alloying additive content, their properties change, hindering their effective usages and applications.

13.7 Future Direction of Research

The huge requirement of combining all the properties of clay-based aerogels and composites without sacrificing anyone at the expense of the others has necessitated continuous research into modifications and production of novel clay-based aerogels capable of satisfying this requirement. This effort is required to ensure nonabsorption of water (moisture) by aerogel via various green chemical modifications without losing mechanical strength. It should be noted that hydrophilic aerogel can absorb water vapor in air, thereby reducing the thermal insulation and mechanical properties of the aerogel. Therefore, exploring how to improve the hydrophobicity of clay-based aerogel should be the next research goal of researchers.

The fire-retardant ability and improved mechanical must equally be addressed. Polymer content additives of the alloyed clay-based aerogels always contribute to the undesired change in densities of these aerogels. Efforts should be geared toward discovering and incorporating suitable polymers that will not affect the properties and uses of the aerogels and their composites based on the intended uses.

Since necessity is the mother of invention, it becomes apparent for the researchers to unravel this conundrum to prevent clay-based aerogel from being relegated to the background due to these various limitations. Each of these can be addressed independently and simultaneously by other researchers.

13.8 Conclusions

In this chapter, studies were briefly reviewed to detail the state-of-the-art on the historical discovery and current trend on the existing knowledge as well as future directions in the production, uses, and applicability of the clay-based aerogels. Excellent work was done on the abysmal failure in desirable properties of these aerogels with suggestions to rectify the anomalies and identify the limitations.

It was revealed that smectite clay is the best type of clay to achieve remarkable property modification via the best environmental freeze-drying method, suggesting an optimal clay content addition in the range of 30%. A host of researchers have built on the structural integrity while considering trade-offs between fire retardant property, combustibility, thermal resistance, and water or moisture adsorption resistant with reinforcement now done by incorporation of nanofillers and other additives such as cellulose, lignin, and chitin among others. Characterization of suspensions and microstructure morphology became necessary at every stage due to the timely advantages proffered by having Young's modulus greater than 22 000 kPa as values up to 2.8 MPa modulus have been reported for PEI-based aerogels, less gas permeability as a good fire retardant. This makes them the current best viable foamed material aerogels.

Ideal thermal insulation method was also found to be due to the platelet clay structure with thin struts. The effect of various additives and cross-linkers on the alloyed composites and other clay-based aerogels were also discussed with their limitations, including their merits and demerits based on the tailored applications and uses. It is finally concluded that the tailored application and requirements will always dictate the type and materials of inclusion to satisfy desirable utilities.

References

1 Du, A., Zhou, B., Zhang, Z., and Shen, J. (2013). A special material or a new state of matter: a review and reconsideration of the aerogel. *Materials (Basel)* 6 (3): 941–968.

2 Pierre, A.C. and Pajonk, G.M. (2002). Chemistry of aerogels and their applications. *Chem. Rev.* 102 (11): 4243–4265.

3 Madyan, O.A., Fan, M., Feo, L., and Hui, D. (2016). Physical properties of clay aerogel composites: An overview. *Compos. Part B Eng.* 102: 29–37.

4 Gan, G. et al. (2019). Carbon aerogels for environmental clean-up. *Eur. J. Inorg. Chem.* 2019 (27): 3126–3141.

5 Gurav, J.L., Jung, I.K., Park, H.H. et al. (2010). Silica aerogel: synthesis and applications. *J. Nanomater.* 2010: 1–11.

6 Cowin, L. (2018). These bricks could be a game-changer for insulation. *Rose Law Group Reporter* https://roselawgroupreporter.com/2018/04/these-bricks-could-be-a-game-changer-for-insulation.

7 Aegerter, M.A., Leventis, N., and Koebel, M.M. (2011). *Aerogels Handbook*. Springer Science & Business Media.

8 Madyan, O., Fan, M., Feo, L., and Hui, D. (2016). Enhancing mechanical properties of clay aerogel composites: an overview. *Compos. Part B Eng.* 98: 314–329.

9 Menaa, B., Menaa, F., Aiolfi-Guimaraes, C., and Sharts, O. (2010). Silica-based nanoporous sol-gel glasses: from bioencapsulation to protein folding studies. *Int. J. Nanotechnol.* 7 (1): 1–45.

10 Schiraldi, D.A., Gawyrla, M.D., and Bandi, S.A. (2014). Clay aerogel-based polymer composites, materials, and methods. US patent 20070208124A1, granted 23 December, 2014.

11 Chen, H.-B. and Schiraldi, D.A. (2019). Flammability of polymer/clay aerogel composites: an overview. *Polym. Rev.* 59 (1): 1–24.

12 Chen, H.-B., Chiou, B.-S., Wang, Y.-Z., and Schiraldi, D.A. (2013). Biodegradable pectin/clay aerogels. *ACS Publ.* 5 (5): 1715–1721.

13 P. Fellows, Freeze drying and freeze concentration. *Food Process. Technol*. 4. Woodhead Publ. Ltd., England, pp. 441–451, 2017.

14 Madyan, O.A. and Fan, M. (2018). Hydrophobic clay aerogel composites through the implantation of environmentally friendly water-repellent agents. *Macromolecules* 51 (24): 10113–10120.

15 Mangiacapra, P. and Gorrasi, G. (2006). Biodegradable nanocomposites obtained by ball milling of pectin and montmorillonites. *Carbohydrate Polymers* 64 (14): 516–523.

16 Wang, L., Sánchez-Soto, M., and Abt, T. (2016). Properties of bio-based gum Arabic/clay aerogels. *Ind. Crops Prod.* 91: 15–21.

17 Wang, T., Sun, H., Long, J. et al. (2016). Biobased poly(furfuryl alcohol)/clay aerogel composite prepared by a freeze-drying process. *ACS Sustainable Chem. Eng.* 4 (5): 2601–2605.

18 Madejová, J. (2003). FTIR techniques in clay mineral studies. *Vib. Spectrosc.* 31 (1): 1–10.

19 Grim, R. (1953). *Clay Mineralogy*, 317. New York: McGraw Hill.

20 Norrish, K. and Rausell-Colom, J.A. (1962). Effect of freezing on the swelling of clay minerals. *Clay Miner. Bull.* 5 (27): 9–16.

21 van Olphen, H. (1967). Polyelectrolyte reinforced aerogels of clays—application as chromatographic adsorbents. *Clays Clay Miner.* 15 (1): 423–435.

22 Starodoubtsev, S.G., Churochkina, N.A., and Khokhlov, A.R. (2000). Hydrogel composites of neutral and slightly charged poly(acrylamide) gels with incorporated bentonite. Interaction with salt and ionic surfactants. *Langmuir* 16 (4): 1529–1534.

23 Long, L.Y., Li, F.F., Weng, Y.X., and Wang, Y.Z. (2019). Effects of sodium montmorillonite on the preparation and properties of cellulose aerogels. *Polymers* 11 (3): 415.

24 Wang, Y. (2012). *Processing, Structure and Properties in Layered Films and Clay Aerogel Composites*. Case Western Reserve University School of Graduate Studies.

25 Wang, L. (2015). *Aerogels Based on Biodegradable Polymers and Clay*. Universitat Politècnica de Catalunya.

26 Gawryla, M.D. (2009). *Low Density Materials Through Freeze-Drying: Clay Aerogels and Beyond*. PhD thesis. Case Western Reserve University.

27 Gawryla, M.D., van den Berg, O., Weder, C., and Schiraldi, D.A. (2009). Clay aerogel/cellulose whisker nanocomposites: a nanoscale wattle and daub. *J. Mater. Chem.* 19 (15): 2118–2124.

28 Van Olphen, H. (1977). *An Introduction to Clay Colloid Chemistry: For Clay Technologists, Geologists, and Soil Scientists*. New York: Wiley.

29 Bandi, S., Bell, M., and Schiraldi, D.A. (2005). Temperature-responsive clay aerogel—polymer composites. *Macromolecules* 38 (22): 9216–9220.

30 Viggiano, R.P., Gawryla, M.D., and Schiraldi, D.A. (2014). Foam-like polymer/clay aerogels which incorporate air bubbles. *J. Appl. Polym. Sci.* 131 (3): 1–6.

31 Wu, W., Wang, K., and Zhan, M.-S. (2012). Preparation and performance of polyimide-reinforced clay aerogel composites. *ACS Publ.* 51 (39): 12821–12826.

32 Li, X.-L., Chen, M.-J., and Chen, H.-B. (2019). Facile fabrication of mechanically-strong and flame retardant alginate/clay aerogels. *Compos. Part B Eng.* 164: 18–25.

33 Zhou, X., Jin, H., Xu, T. et al. (2020). Excellent flame retardant and thermal insulated palygorskite/wood fiber composite aerogels with improved mechanical properties. *Appl. Clay Sci.* 184: 105402.

34 Rong, N., Chen, C., Ouyang, K. et al. (2021). Adsorption characteristics of directional cellulose nanofiber/chitosan/montmorillonite biomimetic aerogel as adsorbent for wastewater treatment. *Sep. Purif. Technol.* 274: 119120.

35 Sun, J., Wu, Z., An, B. et al. (2021). Thermal-insulating, flame-retardant and mechanically resistant aerogel based on bio-inspired tubular cellulose. *Compos. Part B* 220: 108997.

36 Arndt, E.M., Gawryla, M.D., and Schiraldi, D.A. (2007). Elastic, low density epoxy/clay aerogel composites. *J. Mater. Chem.* 17 (33): 3525–3529.

37 Ebert, H.-P. (2015). Functional materials for energy-efficient buildings. *EPJ Web Conf.* 98: 8001.

38 Progelhof, R.C., Throne, J.L., and Ruetsch, R.R. (1976). Methods for predicting the thermal conductivity of composite systems: a review. *Polym. Eng. Sci.* 16 (9): 615–625.

39 Sun, M., Sun, H., Hostler, S., and Schiraldi, D.A. (2018). Effects of feather-fiber reinforcement on poly (vinyl alcohol)/clay aerogels: structure, property and applications. *Polymer* 137: 201–208.

40 Gupta, P., Verma, C., and Maji, P.K. (2019). Flame retardant and thermally insulating clay based aerogel facilitated by cellulose nanofibers. *J. Supercrit. Fluids* 152: 104537.

41 Chen, H., Wang, Y., and Sánchez-Soto, M. (2012, 2012). Low flammability, foam-like materials based on ammonium alginate and sodium montmorillonite clay. *Carbohydrate Polymer* 53: 5825–5831.

42 Lu, J., Wang, T., and Drzal, L.T. (2008). Preparation and properties of microfibrillated cellulose polyvinyl alcohol composite materials. *Composites Part A: Applied Science and Manufacturing* 39 (5): 738–746.

43 Wu, Z.-Y., Li, C., Liang, H.-W. et al. (2013). Ultralight, flexible, and fire-resistant carbon nanofiber aerogels from bacterial cellulose. *Angew. Chem.* 125 (10): 2997–3001.

44 Dash, R., Li, Y., and Ragauskas, A.J. (2012). Short communication. *Carbohydr. Polym.* 88 (2): 789–792.

45 Zhao, Y.-W., Tian, M.-Z., and Huang, P. (2021). Starch/clay aerogel reinforced by cellulose nanofibrils for thermal insulation. *Cellulose* 28: 3505–3513.

46 Shang, S., Ye, X., Jiang, X. et al. (2021). Preparation and characterization of cellulose/attapulgite composite aerogels with high strength and hydrophobicity. *J. Non-Cryst. Solids* 569: 120922.

47 Stewart, D. (2008). Lignin as a base material for materials applications: chemistry, application and economics. *Ind. Crops Prod.* 27 (2): 202–207.

48 Chen, Q. et al. (2015). Synthesis of lignin-derived bisphenols catalyzed by Lignosulfonic acid in water for polycarbonate synthesis. *ChemCatChem* 7 (7): 1083–1089.

49 Luo, J., Ma, X., Zhou, X. et al. (2021). Construction of physically crosslinked cellulose nanofibrils/alkali lignin/montmorillonoite/polyvinyl alcohol network hydrogel and its application in methylene blue removal. *Cellulose* 28: 5531–5543.

50 Valadares, L.F., Leite, C.A.P., and Galembeck, F. (2006). Preparation of natural rubber-montmorillonite nanocomposite in aqueous medium: evidence for polymer-platelet adhesion. *Polymer (Guildf)* 47 (2): 672–678.

51 Pojanavaraphan, T., Liu, L., Ceylan, D. et al. (2011). Solution cross-linked natural rubber (NR)/clay aerogel composites. *Macromolecules* 44 (4): 923–931.

52 El Kadib, A. and Bousmina, M. (2012). Chitosan bio-based organic–inorganic hybrid aerogel microspheres. *Chem. – A Eur. J.* 18 (27): 8264–8277.

53 Jang, J. and Lee, D.K. (2003). Plasticizer effect on the melting and crystallization behavior of polyvinyl alcohol. *Polymer (Guildf)* 44 (26): 8139–8146.

54 DeMerlis, C. and Schoneker, D.R. (2003). Review of the oral toxicity of polyvinyl alcohol (PVA). *Food and Chemical Toxicology* 41 (3): 319–326.

55 Lamison, K., Gawryla, M.D., and Schiraldi, D. (2007). The effect of molecular weight on poly (vinyl alcohol)/clay aerogel composite properties. *Polym. Prepr.* 48: 974–975.

56 Gohil, J.M., Bhattacharya, A., and Ray, P. (2006). Studies on the crosslinking of poly (vinyl alcohol). *J. Polym. Res.* 13 (2): 161–169.

57 Shen, P., Zhao, H.B., Huang, W., and Chen, H.B. (2016). Poly (vinyl alcohol)/clay aerogel composites with enhanced flame retardancy. *RSC Adv.* 6 (111): 109809–109814.

58 Wang, L., Sánchez-Soto, M., and Maspoch, M.L. (2013). Polymer/clay aerogel composites with flame retardant agents: mechanical, thermal and fire behavior. *Mater. Des.* 52: 609–614.

59 Azeez, A.A., Rhee, K.Y., Park, S.J., and Hui, D. (2013). Epoxy clay nanocomposites - processing, properties and applications: a review. *Compos. Part B Eng.* 45 (1): 308–320.

60 Wang, S., Hu, Y., Tang, Y. et al. (2003). Preparation of polyethylene–clay nanocomposites directly from Na^+ montmorillonite by a melt intercalation method. *J. Appl. Polym. Sci.* 89 (9): 2583–2585.

61 Chen, Z.A., Deng, M.C., Yong, C. et al. (2004). Preparation and performance of cellulose acetate/polyethyleneimine blend microfiltration membranes and their applications. *J. Membr. Sci.* 235 (1–2): 73–86.

62 Johnson, J.R., Spikowski, J., and Schiraldi, D.A. (2009). Mineralization of clay/polymer aerogels: a bioinspired approach to composite reinforcement. *ACS Appl. Mater. Interfaces* 1 (6): 1305–1309.

63 Finlay, K., Gawryla, M.D., and Schiraldi, D.A. (2008). Biologically based fiber-reinforced/clay aerogel composites. *Ind. Eng. Chem. Res.* 47 (3): 615–619.

64 Popov, V.N. (2004). Carbon nanotubes: properties and application. *Mater. Sci. Eng. R. Rep.* 43 (3): 61–102.

65 Alhassan, S.M., Qutubuddin, S., and Schiraldi, D. (2010). Influence of electrolyte and polymer loadings on mechanical properties of clay aerogels. *Langmuir* 26 (14): 12198–12202.

66 Madyan, O.A., Fan, M., and Huang, Z. (2017). Functional clay aerogel composites through hydrophobic modification and architecture of layered clays. *Appl. Clay Sci.* 141: 64–71.

67 Johnson, J.R. III and Schiraldi, D.A. (2012). Improving the mechanical properties of clay/polymer aerogels by a simple dip-coating procedure. *J. Appl. Polym. Sci.* 126 (6): 2004–2009.

68 Jin, H., Zhou, X., Xu, T. et al. (2020). *ACS Appl. Mater. Interfaces* 12 (10): 11815–11824.

69 Lin, J.-Y., Mahasti, N.N.N., and Huang, Y.-H. (2021). Recent advances in adsorption and coagulation for boron removal from wastewater: a comprehensive review. *J. Hazard. Mater.* 407: 124401.

70 Gao, Z., Xie, S., Zhang, B. et al. (2017). Ultrathin Mg-Al layered double hydroxide prepared by ionothermal synthesis in a deep eutectic solvent for highly effective boron removal. *Chemical Engineering Journal* 319: 108–118.

71 Nita, L.E., Ghilan, A., Rusu, A.G. et al. (2020). New trends in bio-based aerogels. *Pharmaceutics* 12 (5): 449.

14

Hybrid Aerogels for Energy Saving Applications

Nilay Gizli and Selay Sert Çok

Chemical Engineering Department, Ege University, İzmir, Turkey

14.1 Introduction

With the rapid increase of the world's population and the development of technology and industrialization, the world's energy demand is increasing day by day. According to the International Energy Outlook 2018 data, the estimated global energy requirement is 178×10^9 MWh in 2020 and it will increase to 193×10^{10} MWh by the end of 2030 [1]. Since the increasing use of energy and the gradual decrease in fossil fuel resources have become an urgent problem, developing energy saving strategies has a vital importance in today's world. Therefore, effective thermal insulation is an essential requirement in all modern industries in terms of energy. With the development of science and technology, the traditional insulators (e.g. glass wool, rock wool, polyurethane, polystyrene etc.) have begun to be replaced by advanced super insulators in recent years. Silica aerogels are the attractive class of these so-called superinsulators owing to their extraordinary properties such as high specific surface area (500–1200 $m^2 g^{-1}$), high porosity (80–99.8%), low density (0.003–0.5 $g\,cm^{-3}$), high acoustic insulation (low sound velocity of 100 $m\,s^{-1}$), high-temperature resistance (>800 °C), and low thermal conductivity (20–50 $mW\,m^{-1}K^{-1}$) [2]. These unusual characteristics offer great potential for silica aerogels to have a wide range of applications requiring high thermal insulation, fire prevention, light transmittance, and noise reduction; however, their extremely low mechanical strength and intrinsic fragility seriously hinders the potential usage of these materials in such applications.

Silica aerogels possess an open mesoporous structure with a weakly branched silica network comprised of primary and secondary particles. They are usually synthesized via traditional sol-gel method in which a silicon alkoxide (Si-OR_4, most commonly TEOS [tetraethylorthosilicate] or TMOS [tetramethylorthosilicate]) is usually preferred as a sol-precursor. During sol-gel reactions, three-dimensional, nanostructured porous network in the form of siloxane bridges (Si-O-Si) is formed as a result of consequent hydrolysis and condensation reactions of these silicon alkoxides. As the sol-gel transition proceeds, first primary silica particles form and then they aggregate into secondary particles. Eventually they are linked together and cause a pearl-neck-like morphology. Since the secondary silica particles are linked with only few siloxane bonds on the neck region, their usual synthesis ends up with inherently brittle structure with low mechanical strength [3].

Aerogels for Energy Saving and Storage, First Edition. Edited by Meldin Mathew, Hanna J. Maria, Ange Nzihou, and Sabu Thomas.
© 2024 John Wiley & Sons, Inc. Published 2024 by John Wiley & Sons, Inc.

Up to now, different approaches such as (i) preparation of inorganic-organic hybrids by utilizing co-precursor method, (ii) hybridization by polymers, and (iii) incorporation of nanofibers and other additives have been explored in many studies about the mechanical reinforcing of the silica aerogels. In each approach, the intent has been to improve the mechanical properties (e.g. Young's modulus, compressive strength, bending strength) of the silica aerogels by keeping their unique material properties (e.g. low density, high porosity) unchanged.

In this chapter, we provide an extensive insight into hybridization methods of silica aerogels and their use in energy applications. Therefore, in the first section, general hybridization techniques of silica aerogel are overviewed according to recent literature. The next two sections address the thermal characteristics of different hybrid aerogels and their role in energy saving applications. In the last section, general conclusions and future perspectives are briefly discussed.

14.2 Silica-Based Hybrid Aerogels

Hybridization of silica aerogels is without doubt the most popular method, both for strengthening purposes and for exploration of new functionalities of these materials through synergistic combinations of the inorganic and organic moieties [4]. According to the applied method, hybridization of silica aerogels can be divided into three main groups.

14.2.1 Polymer-Crosslinked Silica Aerogels

For the mechanical improvement of silica aerogels, hybridization by cross-linking the solid skeleton through surface silanol groups with polymers is a frequently used method. As already mentioned, in silica aerogels, secondary silica particles were linked to each other via stiff siloxane bonds and incorporation of a polymeric moiety via hybridization leads to the formation of strong C═C covalent bonds between silica particles. Hence, it increases the compressive strength and improves mechanical properties of the silica aerogels [5]. In principle, depending on the chemical interaction between the secondary silica particles and introduced polymer, silica aerogel-polymer hybrid composites can be Class 1 or Class 2 composites.

Class 1 composites are usually obtained from weak interactions such as van der Waals forces, electrostatic forces, or hydrogen bonds between the phases, and embedded polymeric structures are completely independent from silica matrix [6]. In this type of composite, due to weak interactions between the phases, long post-gelation treatments are usually required. Therefore, the conducted studies about the Class 1 silica aerogel hybrid composites are highly restricted [3]. Unlike Class 1 composites, interfacial bonding between the inorganic and organic phases is satisfied via covalent bonding in Class 2 hybrids. Due to the existence of strong chemical bonding, especially around the weak neck regions of the silica matrix, Class 2 hybrids possess very high mechanical strength and rigid form. Up to now, various polymers were investigated, such as epoxies [7, 8], polyamines [9], polystyrenes [10], polyureas [11, 12], and polyacrylates [13], to improve the mechanical characteristics of silica aerogels and crosslinking in this type of composites is accomplished with three different ways.

14.2.1.1 Crosslinking by Posttreatment Methods

This method consists of two basic steps. The first step is based on the functionalization of secondary silica particles by co-gelation of a classically used silicon alkoxide precursors and an organically

modified co-precursor. After the wet gel is obtained, the addition of an organic monomer and induction of polymerization reactions between the functional groups of silica particles and the monomers by various solvent exchange processes constitute the second step of the method. The mechanical improvement of silica aerogels based on this approach has been investigated by many researchers in recent years [5, 10, 14]. However, it has also made it necessary to develop different methods due to disadvantages such as time-consuming solvent exchange steps, slow diffusion kinetics of introduced monomers and the need for a hot environment for faster diffusion kinetics.

14.2.1.2 Crosslinking by One-Pot Synthesis

Meador et al. paved the way for promoting the in-situ synthesis of polymer crosslinked hybrid aerogels by preparing an epoxy-cross linked silica aerogels using a streamlined process in 2010 [15]. Since then, many studies have been carried out following single-pot crosslinking, particularly for its advantage in synthesis time compared to the two-step method [3, 16]. In one-pot synthesis, organic monomers are added to the initial sol with silica precursors and polymerization reactions occurring within the silica network simultaneous with the hydrolysis and condensation reactions. Therefore, diffusion problems are no longer a restricting factor in this method. The difference in these two methods were demonstrated.

Hybridization via polymer crosslinking, in almost all studies, has a significant impact on the mechanical properties of silica aerogel composites. Very high compressive strength values (up to 8 MPa) can be obtained by polymer crosslinking. However, they also usually end up with denser structures ($\approx$0.5–0.8 g cm^{-3}) lower specific surface areas ($\approx$40–600 m^2 g^{-1}) compared to neat silica aerogels [3]. Increasing density also inevitably increases the thermal conductivity of these polymer crosslinked aerogel hybrids and limits their practical application as thermal insulators. Lack of flexibility and bending are other drawbacks for these hybrid materials.

14.2.1.3 Double Crosslinking with Radical Polymerization

Radical polymerization of monomers that contain alkene groups is a new and efficient approach to improve the mechanical characteristics of silica aerogels. Very recently, Zu et al. developed a double-crosslinking approach involves a radical polymerization, followed by hydrolytic polycondensation of from an organoalkoxysilanes with alkene groups [17–20]. In their studies, superflexible polyvinylpolymethylsiloxane (PVPMS)-based hybrid aerogels were prepared by the combination of radical polymerization and hydrolytic polycondensation from a single difunctional silica precursor with one vinyl group and two alkoxy groups, vinylmethyldimethoxysilane (VMDMS) or vinylmethyldiethoxysilane (VMDES), under supercritical or ambient conditions [18].

In this method, an alkoxysilane containing an alken group (precursor) is radically polymerized with an initiator to obtain polyalkenylalkoxysilanes. The degree of polymerization is usually adjusted by reaction time and the initiator concentration. The obtained polyalkenylalkoxysilanes is then subjected to subsequent hydrolysis and condensation with appropriate base catalyst to form polysiloxane network doubly crosslinked with hydrocarbon chains. The transparent, bendable aerogels are then obtained via supercritical drying (SCD) and ambient pressure drying (APD), respectively.

Silica aerogel hybrids prepared by this approach have resulted in a low density (0.16–0.22 g cm^{-3}), uniform pore size (mainly <60 nm), high SSA (900–1000 m^2 g^{-1}), high hydrophobicity (>130° contact angle of water), high transparency (>80% transmittance), excellent machinability, superflexibility in compression (endure 80% compression strain with 500 cycles), superflexibility in bending (endure 100 bending cycles), and superinsulating properties (λ = 15.0–15.4 mW m^{-1} K^{-1});

it has been stated that these superior properties make it quite feasible for these materials to be used as transparent flexible superinsulators in the near future [17].

14.2.2 Hybrids Based on Organically Modified Polysiloxanes by Co-gelation Approach

Among many alternatives, synthesis of polyorganosiloxane-based hybrid networks by co-gelation approach in which a silicon alkoxide precursor is used along with an organically modified co-precursors such as one, two, or trifunctional silanes or organo-bridged alkoxysilanes has attracted much attention for their potential to make flexible, hydrophobic aerogels.

14.2.2.1 Co-gelation Approach with Di/Tri Functional Organosilanes

Incorporating trifunctional silanes ($RSi(OR')_3$) such as methyltrimethoxysilane/methyltriethoxysilane (MTMS/MTES), ethyltrimethoxysilane (ETMS), or vinyltrimethoxysilane (VTMS) and difunctional silanes ($R_1R_2Si(OR')_2$) such as dimethyldimethoxysilane (DMDMS) or dimethyldiethoxysilane (DMDES) as a single or co-precursor has been an efficiently used method in reducing cross-linking degree of the aerogel hybrids and satisfying an elastic/flexible behavior. Compared to neat silica aerogels, these organically modified silica aerogels (ORMOSILs) have one/or two non-hydrolysable radical groups, and as a result of attached organic R groups on the silica chains (Figure 14.1), the interchain bonding within the network can be significantly reduced in this type of aerogels, which yields a highly hydrophobic and elastic silica network [21, 22].

In early studies, both Rao and his co-workers and a research group led by K. Kanamori used MTMS or MTES as a single or a co-precursor for their potential to create superhydrophobic silica hybrid aerogels with high flexibility. Their work has also inspired many others on this issue [23–25].

In their study, Rao et al. investigated both one-pot and two-step synthesis of MTMS-based ORMOSIL aerogels dried under supercritical conditions and stated that the network formation was not continuous due to the incomplete hydrolyzation reaction leading to less flexible aerogels

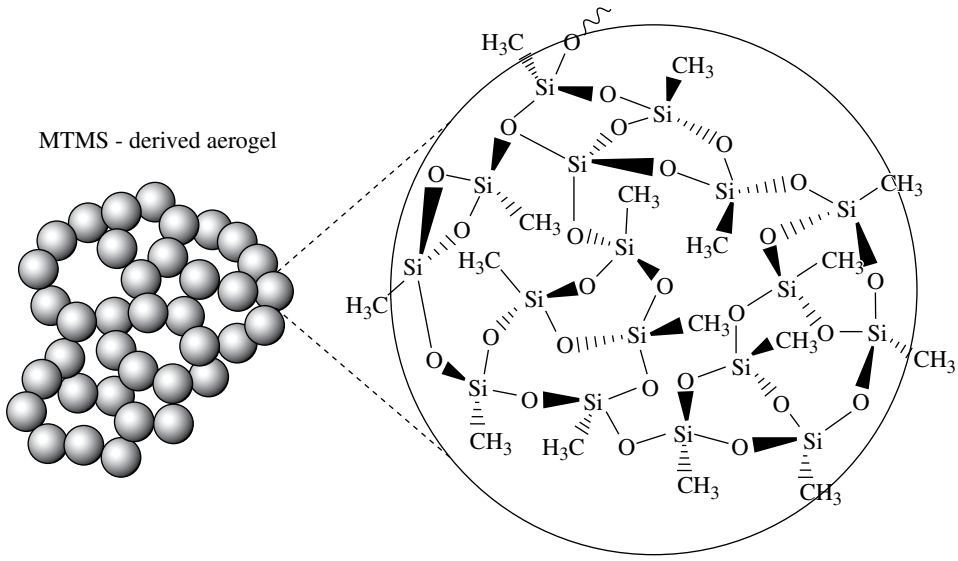


Figure 14.1 Three-dimensional network of the MTMS derived aerogel. *Source:* The picture is adapted from Ref. [3].

(less than 5%, compressible by volume) in one pot method. However, in the two-step method, due to the systematic, complete, and continuous network formation, they obtained highly flexible aerogels with compression as high as around 60% by volume and contact angle value higher than 160°. They also denoted that in a dilute solution (MeOH/MTMS = 35), as the silica chains of the aerogel are well separated from each other and large pores exist in the network, the aerogel undergoes more flexibility when the stress is applied. In lower dilution, however, the degree of polymerization increases and it yields an extensive, more crosslinked network with less flexibility [21].

In another study, Rao and Haranath prepared a monolithic, transparent (~85% to visible light) MTMS-TMOS hybrid aerogel using an MTMS/TMOS molar ratio of 0.7. They also indicated that an increase in the MTMS content decreases the optical transmittance and specific surface area increases the average pore size [23].

Kanamori et al. in 2008 synthesized an organic–inorganic hybrid methylsilsesquioxane aerogel from (MTMS) by a two-step sol-gel method. They first proposed using a suitable surfactant to prevent phase-separation problems during condensation reactions [25].

Since then, extensive studies has been conducted considering both MTMS and MTES as single precursors [26–33], or using co-precursors systems by selecting MTMS/TEOS [34–36], MTES/TEOS [37], MTMS/DMDMS [38], MTMS/VTES [39] as silica sources to produce inorganic-organic polyorganosiloxane-based hybrid aerogels, mostly in ambient conditions. They all indicated a successful improvement in compressibility, and the elasticity of the final material and sum of them has also offered a high potential as thermal insulators with low thermal conductivity values and high thermal stability.

14.2.2.2 Co-gelation with Bridged Bis-Silane Precursors (Bridging Chain Approach)

Another interesting approach to obtain flexible aerogels with improved mechanical properties is to use organo-bridged alkoxysilane precursors with chemical formula of $(R'O)_3Si–R–Si–(OR')_3$, where R is typically alkenyl, alkyl, or aryl (the bridging group) (Figure 14.2). Due to the existence of organic moiety (flexible R groups) that bridges (links) between the secondary silica particles in the network, the silica aerogels containing this type of silanes exhibit higher elasticity and compression strength. Their bending strength is also higher compared to traditionally produced silica aerogel counterparts [41]. The flexible aerogel hybrids synthesized by this approach are called *bridged organosilsesquioxane hybrids*, and the degree of flexibility of such hybrids surely depends on the size of the bridge.

Synthesis of hybrid organic–inorganic aerogels from bridged polysilsesquioxanes, using organic bridges attached to two or more trialkoxysilyl groups via nonhydrolysable carbon–silicon bonds, was originated by Loy and Shea in 1995 [42]. They investigated many precursors to produce bridged silsesquioxanes and indicated that the type and size of the selected bridge has a direct impact on the pore size of the resultant material. They stated that by using a stiffer structure such as an arylene chain, the porosity of the solid matrix can be well controlled and allow for more flexible bridges such as alkyl chains yielding a looser final network [42–44]. As Schaefer et al. denoted, choosing aromatic containing bridges results in stiffer network but can provide excellent control over pore size and distribution on pores [45].

In recent years, various studies have been conducted based on hexylene-bridged polysilsesquioxane [41] and ethylene-bridged/ethenylene-bridged polymethylsiloxane [46, 47], thiourethane bridged polysilsesquioxane aerogels [48]. They all exhibited high compression strength and excellent flexibility. Although they possess bendability due to the presence of organic bridge in their structure, their bending performances are still not so satisfactory for practical thermal insulation applications.

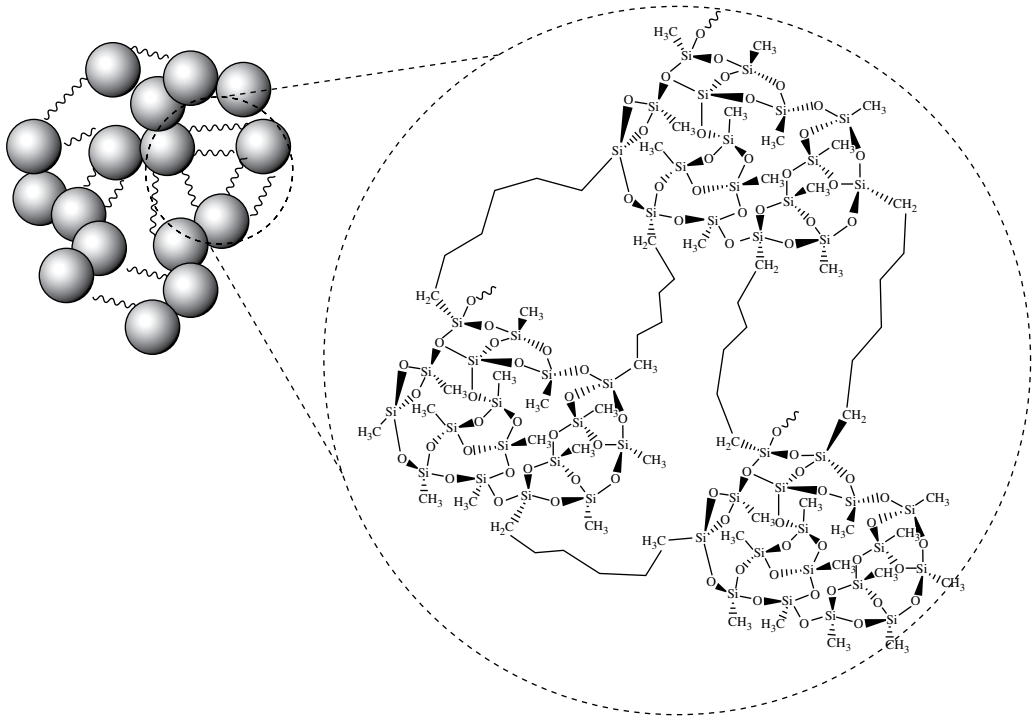


Figure 14.2 ORMOSIL aerogels by bridging chain approach. *Source:* Adapted from Ref. [40].

14.2.3 Fiber Reinforcement

The preparation of silica aerogel hybrids by incorporating various nanofibers in the sol-gels reactions is recognized as an effective technique to broaden the applications of the aerogel composites. It has been observed in many studies that, the embedding of fibers in silica aerogel structure can prevent the shrinkage and network collapse during drying [49–51] and also improve their mechanical strength to a very large extent. However, as Linhares et al. indicated in their study, after the mechanical reinforcement, retaining strict porous morphology of the aerogels and hence, preserving their excellent ability as thermal insulators, still remains as a challenge [52]. Basically, the aerogel-fiber composites can be produced by two different methods, as demonstrated in Figure 14.3. In the first technique, the selected fibers are added to system during sol preparation, and after the dispersion of the fibers are satisfied, the sol mixture is gelated, aged, and dried, respectively (Figure 14.3a). In the second method, web of fibers (or fiber mats) are placed in the molds as one or multiple layers, and then the prepared sol mixture is poured onto molds right before the gelation. After an aging period, the final composite is obtained after drying (Figure 14.3b).

So far, many conventionally available or laboratory developed fibers such as ceramic fibers [53], glass fibers [50, 54–59], carbon nanofibers [60–62], cotton wools [63], polymeric nanofibers [64], cellulose fibers [65–68], and aramid fibers [69, 70] etc. were used as reinforcing agents in the aerogel production. It is a well-known fact that both type and characteristics properties of selected fiber such as length, diameter, density, strength, optical properties, flexibility, and of course their content in the final matrix, play a dominant role, especially on the mechanical and thermal properties of the final composites. For example, due to their low thermal expansion coefficient and high thermal stability, inorganic fibers such as mineral fibers [71], ceramic fibers [53], and glass fibers

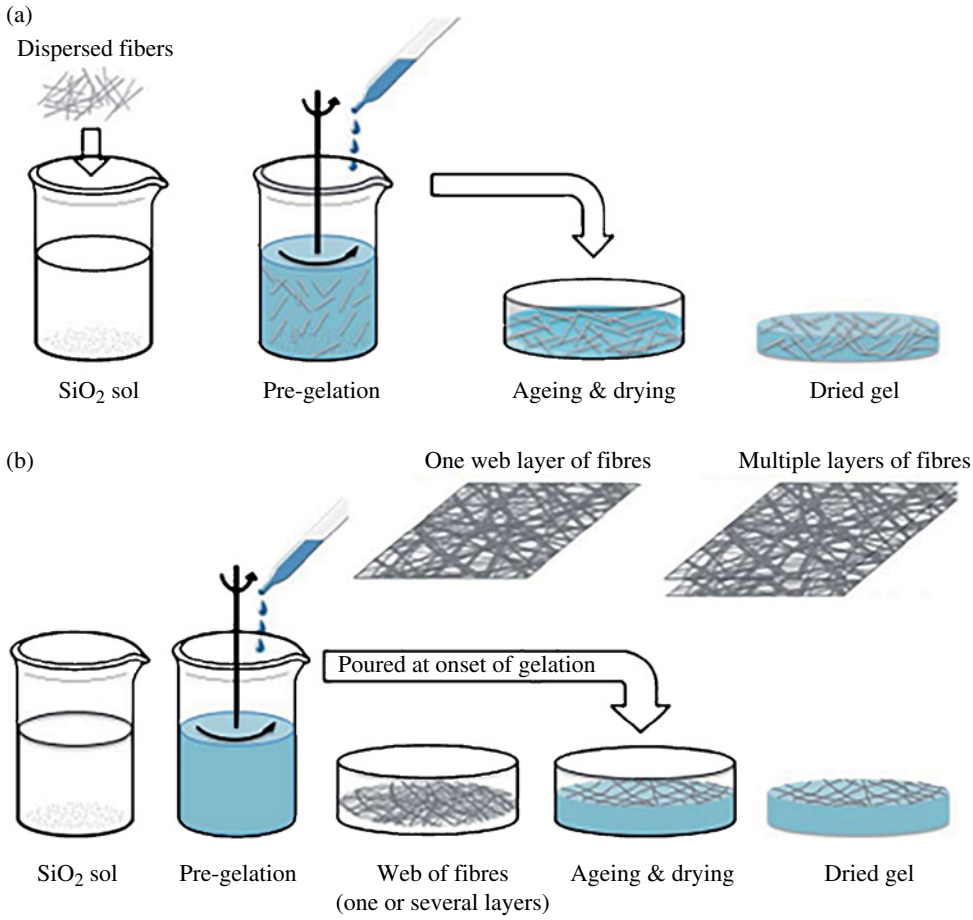


Figure 14.3 Silica aerogel hybrids with embedded fibers (a) one-pot synthesis by dispersing fibers in the sol; (b) synthesis by combining the fibers and sol in the mold before gelation. *Source:* Adapted from Ref. [52].

[55, 57, 58] are often used in thermal insulation systems. Especially for high-temperature applications, with their high thermal resistance, ceramics fibers [53, 72] seem to be the most suitable type of fiber for aerogel composites, whereas carbon-based fibers can be the least popular fibers as they possess a low thermal degradation temperature (~300 °C) [52].

On the other hand, in their study, Li and his co-workers stated that although the addition of inorganic fibers increases the compressive strength with only slight increase in thermal conductivity, such fibers are inefficient in improving the flexibility owing to their brittleness. Therefore, Li et al. proposed using aramid organic fibers (Kevlar by Du Pont) to make silica aerogel composites more flexible, and they produced silica aerogel composites in ambient conditions with low thermal conductivity ($0.0227\,W\,m^{-1}\,K^{-1}$) by adjusting the aramid fiber content (1.5%) [69, 73]. Wu et al. in their study, also emphasized that in terms of silica aerogel hybrids, organic fibers are more flexible than their inorganic counterparts due to their high length-to-diameter ratio.

Apart from inorganic and organic fibers, powders [74], nanotubes [75–77], nanowires [78], nanoparticles [13, 79, 80], oxides [20, 81–83], foams [78], and metal-organic frameworks [84] are

another alternative supporting materials and are frequently investigated for silica aerogel reinforcement and functionality.

14.3 Thermal Properties of Hybrid Aerogels

The heat transfer mechanism of nanoporous silica aerogels is generally associated with three modes (Figure 14.4):

1) Heat transferred through gas molecules (gray particles)
2) Heat transferred through the solid skeleton (orange skeletal structure)
3) Heat transferred through radiation (green wavy arrows)

For porous media, where the pore diameter is lower than 4 mm, heat transfer by the convection could be neglected [85]. Since the pore sizes of aerogels are all nanoscale, the convective heat transfer between gas and solid phases is negligible [86]. Therefore, heat conduction and thermal radiation remain as the two basic heat transfer modes in nanoscale silica aerogels. The total thermal conductivity is described as follows:

$$k_t = k_s + k_g + k_r$$

where k_t (mW/mK) is the total thermal conductivity, k_s and k_g are the solid and gas conduction thermal conductivities, and k_r is the thermal conductivity related with radiation. The structure of aerogel solid phase is complex and usually presents amorphous state, while the thermal conductivity of amorphous solid mostly depends on the localized vibrations of solid atoms/phonons and is limited by the scattering of atoms/phonons at an average collision distance (mean free path). The complex 3-D nanostructure of the aerogels greatly lengthens the path of heat transfer and increases the complexity of heat transfer through solid matrix, which finally yields weak transfer of solid conduction [86]. Gaseous heat conduction in aerogels occurs due to the collision between gas molecules. The pore diameter of aerogel is about 5–100 nm and the mean diameter of pore is about 20–40 nm, while the mean free path of air under the standard temperature and pressure is about 69 nm. The pore diameter of a silica aerogel could be less than or close to the mean free path of the gas molecular. This kind of nanoscaled pores could drastically restrict the free movement of

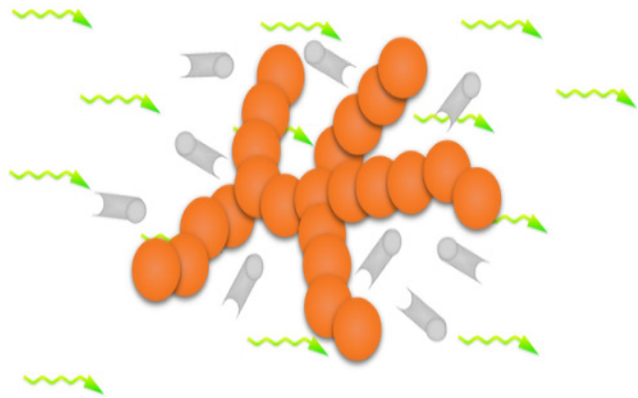


Figure 14.4 Heat transfer modes in silica aerogels.

molecules (Knudsen Effect) and greatly reduce the gaseous heat conduction [85, 87, 88]. The opacity of silica to wavelengths beyond 6 μm is such that no appreciable heat can pass by radiation at ordinary temperatures. However, silica aerogels are almost transparent in the 3–8 μm range of radiation, and when the temperature increases, the insulation performance of the silica aerogel deteriorates due to the rapidly rising thermal radiation, which limits the application area of the aerogels [89]. Zhao et al. indicated that when the temperature rises from 300 to 1000 K, the radiative thermal conductivity can lead to an increase from 8% to 92% of the total conductivity of native silica aerogels [90].

Most of the studies to avoid this disadvantage focused on the addition of opacifiers such as carbon black [91], TiO_2, ZrO_2 to suppress thermal radiation heat transfer [81, 92]. However, these micro-scale opacifiers, which are used to increase the ability of radiation-blocking, have often led to an increase in thermal conductivity of aerogel [91].

The neat aerogels have superior insulating properties (with thermal conductivity values as low as $10\,W\,m^{-1}\,K^{-1}$) due to their low density and high porosity, while their low mechanical strength and brittleness limit the practical use of these materials. Preparation of silica aerogel hybrids with above prescribed techniques surely eliminates the concerns related with its low mechanical strength and long-term stability. However, the trade-off between mechanical reinforcement and preserving good insulation properties should be well considered to achieve the desired overall performance required for their practical applications.

As Li et al. stated, the relationship between thermal conductivity and mechanical strength of aerogel-based thermal insulation materials is determined by the morphology, microstructure, and thermophysical properties of the final composite [2]. For the inorganic and organic hybrids produced by polymerization or co-precursor approach, the final morphological and physicochemical properties greatly depend on the compositions and synthesis parameters, whereas, for the silica aerogel hybrids produced with support phase materials such as fibers, the interaction between the solid matrix and the support materials are also decisive parameters in final characteristics of the hybrid materials. For a specified density, the smaller the pore size, the higher the specific surface area and the better thermal insulation performance.

Among the recent reinforcement techniques (previously summarized in Section 14.2), chemical cross-linking with reactive molecules or polymers yields to superior improvement in their mechanical characteristics, but when increasing the covalent bonds within a system, the total amount of material used for the production of the gel matrix is also increased, and this may cause an unavoidable increase in the solid thermal conductivity of the hybrid aerogel [52].

In the case of ORMOSIL hybrid aerogels, with the aid of organically modified co-precursors, functionalization on the silica backbone is satisfied and this can induce the spring-back effect and flexibility (as a result of loose network with larger pores) of the final hybrids. Thermal conductivity in such hybrids is directly dependent on the average pore size and the nature of the selected precursor, as the existence larger pores and the high molecular weight of the selected precursor can increase both solid and gas phase thermal conductivity and eventually may deteriorate the insulation performance.

In many studies, it has been observed that the addition of supporting materials also increases the mechanical strength of silica aerogels, but mostly, they observed an increase in the bulk density and thermal conductivity of the aerogel hybrids [69].

Table 14.1 summaries the obtained thermal conductivity values according to applied hybridization procedure in detail for comparison purposes. It should be noted that with the appropriate synthesis strategy and component choice, silica aerogel hybrids can have nearly the same thermal characteristics compared to neat aerogels but with excellent mechanical properties.

Table 14.1 Silica aerogel hybrids with synthesis, thermal, and mechanical properties.

Method of hybridization	Sol components	Density (g cm^{-3})	Thermal conductivity (mW m^{-1} K^{-1})	Mechanical strength (MPa)	Remarks	References
Radical polymerization	VMDMS (Precursor) DTBP (Initiator) BzOH, H_2O, IPA, TMAOH	0.13	14.5–16.4	4.7–7.7 (Young's modulus)	Highly bendable and flexible	[18]
Embedding fiber	MTMS (precursor) Acetic acid, H_2O, urea, CTAC, CNF (cellulose nanofiber)	0.097–0.186	16.2–18.8	0.2–1.5 (unaxial compression strength)	Shows bending flexibility	[68]
Co-gelation	Polyrotaxane (consisting of α-CD, PEG, and 1-adamantanamine), TEOS (precursor), IPTS, EtOH, DMF, H_2O.	0.15–0.30	11–19	9.5–15.5 (compression strength)	Transparent and mechanically strong	[93]
Embedding fiber	TEOS, EtOH, H_2O, HCI, NH_4OH, glass fiber	0.226–0.271	17.9–28.3	1.04–1.70 MPa (Elastic modulus)	Dust-free and elastic	[94]
Embedding fiber	TEOS, EtOH, H_2O, HCI, NH_4OH, hexane, aramid fiber	0.14	22	0.14 MPa (Elastic modulus)	Flexible	[73]
Bridging chain approach	VTES (precursor), EDDET (bridging agent), NH_4OH, HCI, EtOH	0.125–0.232	37–43	0.11–1.31 MPa (Young's modulus)	Bendable and flexible	[95]
Co-gelation	VTMS, MTMS, TMOS (precursors), MeOH, $C_2H_2O_4$, NH_4OH	0.089–0.182	40–55	0.012–0.108 MPa Young's modulus	Flexible	[96]

VMDMS: vinylmethyldimethoxysilane, DTBP: ditertbutylperoxide, IPA: isopropylalcohol, BzOH: benzoic acid, TMAOH: Tetramethylammonium hydroxide, CTAC: cetyltrimethylammonium – chloride, α-CD: alpha-cyclodextrin, PEG: polyeythleneglycol, IPTS: triethoxy(3-isocyanatopropyl)silane, DMF: dimethylformamide, VTES: vinyltriethoxysilane, EDDET: 2,2 –(ethylenedioxy)diethanethiol, VTMS: vinyltrimethoxysilane.

Downloaded from https://onlinelibrary.wiley.com/doi/ by ibrahim ragab - Universita Di Firenze Sistema , Wiley Online Library on [21/07/2024]. See the Terms and Conditions (https://onlinelibrary.wiley.com/terms-and-conditions) on Wiley Online Library for rules of use; OA articles are governed by the applicable Creative Commons License

14.4 Hybrid Aerogels in Energy Saving Applications

Thermal insulation is the most popular application area of silica aerogel hybrids. This area has attracted the attention of many researchers in the last decades, and since then, they have proven their potential in a wide range of applications, having already been commercialized. Currently, the aerogel market provides high value-added products, especially in the form of aerogel blankets. All around the world there are companies producing silica aerogel-based products – such as Cabot Corporation, Aspen Aerogel, NanoHigh-Tech Co, BASF SE, and Airglas Inc.

Up to now, studies have indicated that there is a great potential for aerogel composites to be primary insulation resources; however, the following issues should be well addressed for aerogel-based thermal insulators to promote their use in widespread applications:

- Development strategies (such as encouraging APD, one-pot synthesis, reduction in post-gelation treatments) for cost reduction during synthesis.
- Application of different reinforcement methods (apart from the fiber supported silica aerogel hybrids, stimulation of both polymer-crosslinked and ORMOSIL hybrid aerogels for commercialization).
- Satisfying mechanical stability without deteriorating the low thermal conductivity.

Since the final characteristics of aerogels are closely related to the meso-/nanostructure (pore and particle size) and the intrinsic material properties of the system can increase or decrease thermal insulation performance, efforts to synthesize cost-effective aerogels with high surface area and excellent mechanical strength and flexibility should continue.

14.5 Conclusion and Future Perspective

Silica-based aerogels are the most promising advanced materials as thermal superinsulators owing to their ultraporous morphology and very low thermal conductivity. However, their inherently low mechanical characteristics severely hinders their practical applications as insulators. The focus of current research on aerogels as thermal insulators, and the most critical point in the widespread use of these materials in the market, is the ability to develop cost-effective aerogels with excellent mechanical strength and flexibility, as well as high surface area and low thermal conductivity. The most efficient way to achieve this goal is to use silica aerogels as hybrids.

This chapter provided a brief overview about the hybridization techniques (either by co-polymerization with organically functionalized silanes, crosslinking with polymers or embedding nanofibers) of silica aerogels, and their use in energy saving applications. It was noted that, apart from having good mechanical strength, the mechanical properties of the new silica aerogels should be improved in terms of strength against the tensile and shear stress to improve their flexibility in thermal insulation applications. Another great advantage to broaden their large-scale applications would be the shape-control of these materials. With recent developments such as radical polymerization technology, silica aerogel-based hybrids seem to be synthesized in target-specific shapes for special insulation applications. Finally, if the current trade-off between the mechanical strength and thermal insulation properties (low thermal conductivity, transparency, etc.) can be well balanced with the future developments, silica aerogel-based hybrid materials can dominate the thermal insulation market in the near future.

References

1 Alwin, S. and Sahaya Shajan, X. (2020). Aerogels: promising nanostructured materials for energy conversion and storage applications. *Mater. Renew. Sustain. Energy* 9: 1–27. https://doi.org/10.1007/s40243-020-00168-4.

2 Li, C., Chen, Z., Dong, W. et al. (2020). A review of silicon-based aerogel thermal insulation materials: performance optimization through composition and microstructure. *J. Non-Cryst. Solids* 120517. https://doi.org/10.1016/j.jnoncrysol.2020.120517.

3 Maleki, H., Durães, L., and Portugal, A. (2014). An overview on silica aerogels synthesis and different mechanical reinforcing strategies. *J. Non-Cryst. Solids* 385: 55–74. https://doi.org/10.1016/j.jnoncrysol.2013.10.017.

4 Kanamori, K. (2017). *Handbook of Sol-Gel Science and Technology*, 1–22. Springer https://doi.org/10.1007/978-3-319-19454-7.

5 Randall, J.P., Meador, M.A.B., and Jana, S.C. (2011). Tailoring mechanical properties of aerogels for aerospace applications. *ACS Appl. Mater. Interfaces* 3: 613–626. https://doi.org/10.1021/am200007n.

6 Boury, B. and Corriu, R.J.P. (2002). Auto-organisation of hybrid organic – inorganic materials prepared by sol-gel process. *Chemical Communications* 8: 795–802.

7 Meador, M.A.B., Fabrizio, E.F., Ilhan, F. et al. (2005). Cross-linking amine-modified silica aerogels with epoxies: mechanically strong lightweight porous materials. *Chem. Mater.* 17: 1085–1098. https://doi.org/10.1021/cm048063u.

8 Salimian, S., Zadhoush, A., Talebi, Z. et al. (2018). Silica aerogel–epoxy nanocomposites: understanding epoxy reinforcement in terms of aerogel surface chemistry and epoxy–silica interface compatibility. *ACS Appl. Nano Mater.* 1: 4179–4189. https://doi.org/10.1021/acsanm.8b00941.

9 Zou, H., Wu, S., and Shen, J. (2008). Polymer/silica nanocomposites: preparation, characterization, properties, and applications. *Chem. Rev.* 108: 3893–3957. https://doi.org/10.1021/cr068035q.

10 Nguyen, B.N., Meador, M.A.B., Tousley, M.E. et al. (2009). Tailoring elastic properties of silica aerogels cross-linked with polystyrene. *ACS Appl. Mater. Interfaces* 1: 621–630. https://doi.org/10.1021/am8001617.

11 Katti, A., Shimpi, N., Roy, S. et al. (2006). Chemical, physical, and mechanical characterization of isocyanate cross-linked amine-modified silica aerogels. *Chem. Mater.* 18: 285–296. https://doi.org/10.1021/cm0513841.

12 Zhang, G., Dass, A., Rawashdeh, A.M.M. et al. (2004). Isocyanate-crosslinked silica aerogel monoliths: preparation and characterization. *J. Non-Cryst. Solids* 350: 152–164. https://doi.org/10.1016/j.jnoncrysol.2004.06.041.

13 Bauer, F. and Mehnert, R. (2005). UV curable acrylate nanocomposites: properties and applications. *J. Polym. Res.* 12: 483–491. https://doi.org/10.1007/s10965-005-4339-z.

14 Ilhan, F.U., Fabrizio, E.F., McCorkle, L. et al. (2006). Hydrophobic monolithic aerogels by nanocasting polystyrene on amine-modified silica. *J. Mater. Chem.* 16: 3046–3054. https://doi.org/10.1039/b604323b.

15 Meador, M.A.B., Scherzer, C.M., Vivod, S.L. et al. (2010). Epoxy reinforced aerogels made using a streamlined process. *ACS Appl. Mater. Interfaces* 2: 2162–2168. https://doi.org/10.1021/am100422x.

16 Wang, C., Cheng, H., Hong, C. et al. (2018). Lightweight chopped carbon fibre reinforced silica-phenolic resin aerogel nanocomposite: facile preparation, properties and application to thermal protection. *Compos. Part A Appl. Sci. Manuf.* 112: 81–90. https://doi.org/10.1016/j.compositesa.2018.05.026.

17 Zu, G., Shimizu, T., Kanamori, K. et al. (2018). Transparent, superflexible doubly cross-linked polyvinylpolymethylsiloxane aerogel superinsulators via ambient pressure drying. *ACS Nano* 12: 521–532. https://doi.org/10.1021/acsnano.7b07117.

18 Zu, G., Kanamori, K., Shimizu, T. et al. (2018). Versatile double-cross-linking approach to transparent, machinable, supercompressible, highly bendable aerogel thermal superinsulators. *Chem. Mater.* 30: 2759–2770. https://doi.org/10.1021/acs.chemmater.8b00563.

19 Zu, G., Kanamori, K., Maeno, A. et al. (2019). Ambient-dried highly flexible copolymer aerogels and their nanocomposites with polypyrrole for thermal insulation, separation, and pressure sensing. *Polym. Chem.* 10: 4980–4990. https://doi.org/10.1039/c9py00751b.

20 Zu, G., Kanamori, K., Wang, X. et al. (2020). Superelastic triple-network polyorganosiloxane-based aerogels as transparent thermal superinsulators and efficient separators. *Chem. Mater.* 32: 1595–1604. https://doi.org/10.1021/acs.chemmater.9b04877.

21 Venkateswara Rao, A., Bhagat, S.D., Hirashima, H., and Pajonk, G.M. (2006). Synthesis of flexible silica aerogels using methyltrimethoxysilane (MTMS) precursor. *J. Colloid Interface Sci.* 300: 279–285. https://doi.org/10.1016/j.jcis.2006.03.044.

22 Bhagat, S.D., Oh, C.S., Kim, Y.H. et al. (2007). Methyltrimethoxysilane based monolithic silica aerogels via ambient pressure drying. *Microporous Mesoporous Mater.* 100: 350–355. https://doi.org/10.1016/j.micromeso.2006.10.026.

23 Venkateswara Rao, A. and Haranath, D. (1999). Effect of methyltrimethoxysilane as a synthesis component on the hydrophobicity and some physical properties of silica aerogels. *Microporous Mesoporous Mater.* 30: 267–273. https://doi.org/10.1016/S1387-1811(99)00037-2.

24 Rao, A.V., Kulkarni, M.M., Amalnerkar, D.P., and Seth, T. (2003). Superhydrophobic silica aerogels based on methyltrimethoxysilane precursor. *J. Non-Cryst. Solids* 330: 187–195. https://doi.org/10.1016/j.jnoncrysol.2003.08.048.

25 Kanamori, K., Aizawa, M., Nakanishi, K., and Hanada, T. (2008). Elastic organic-inorganic hybrid aerogels and xerogels. *J. Sol-Gel Sci. Technol.* 48: 172–181. https://doi.org/10.1007/s10971-008-1756-6.

26 Cheng, X., Li, C., Shi, X. et al. (2017). Rapid synthesis of ambient pressure dried monolithic silica aerogels using water as the only solvent. *Mater. Lett.* 204: 157–160. https://doi.org/10.1016/j.matlet.2017.05.107.

27 He, S. and Chen, X. (2017). Flexible silica aerogel based on methyltrimethoxysilane with improved mechanical property. *J. Non-Cryst. Solids* 463: 6–11. https://doi.org/10.1016/j.jnoncrysol.2017.02.014.

28 Luo, Y., Li, Z., Zhang, W. et al. (2019). Rapid synthesis and characterization of ambient pressure dried monolithic silica aerogels in ethanol/water co-solvent system. *J. Non-Cryst. Solids* 503–504: 214–223. https://doi.org/10.1016/j.jnoncrysol.2018.09.049.

29 Lei, C., Hu, Z., Zhang, Y. et al. (2018). Tailoring structural and physical properties of polymethylsilsesquioxane aerogels by adjusting $NH_3{\cdot}H_2O$ concentration. *Microporous Mesoporous Mater.* 258: 236–243. https://doi.org/10.1016/j.micromeso.2017.05.009.

30 Lei, C., Li, J., Sun, C. et al. (2018). Transparent, elastic and crack-free polymethylsilsesquioxane aerogels prepared by controllable shrinkage of the hydrogels in the aging process. *Microporous Mesoporous Mater.* 267: 107–114. https://doi.org/10.1016/j.micromeso.2018.02.025.

31 Xu, B., Cai, J.Y., Xie, Z. et al. (2012). An improved method for preparing monolithic aerogels based on methyltrimethoxysilane at ambient pressure part II: microstructure and performance of the aerogels. *Microporous Mesoporous Mater.* 148: 152–158. https://doi.org/10.1016/j.micromeso.2011.08.015.

32 Hayase, G., Kugimiya, K., Ogawa, M. et al. (2014). The thermal conductivity of polymethylsilsesquioxane aerogels and xerogels with varied pore sizes for practical application as thermal superinsulators. *J. Mater. Chem. A* 2: 6525–6531. https://doi.org/10.1039/c3ta15094a.

33 Niu, Z., He, X., Huang, T. et al. (2019). A facile preparation of transparent methyltriethoxysilane based silica xerogel monoliths at ambient pressure drying. *Microporous Mesoporous Mater.* 286: 98–104. https://doi.org/10.1016/j.micromeso.2019.05.036.

34 Li, Z., Cheng, X., He, S. et al. (2016). Tailoring thermal properties of ambient pressure dried MTMS/TEOS co-precursor aerogels. *Mater. Lett.* 171: 91–94. https://doi.org/10.1016/j.matlet.2016.02.025.

35 Li, Z., Cheng, X., He, S. et al. (2014). Preparation of ambient pressure dried MTMS/TEOS co-precursor silica aerogel by adjusting NH_4OH concentration. *Mater. Lett.* 129: 12–15. https://doi.org/10.1016/j.matlet.2014.05.024.

36 Wu, X., Zhong, K., Ding, J. et al. (2020). Facile synthesis of flexible and hydrophobic polymethylsilsesquioxane based silica aerogel via the co-precursor method and ambient pressure drying technique. *J. Non-Cryst. Solids* 530: https://doi.org/10.1016/j.jnoncrysol.2019.119826.

37 Zhang, Y., Xiang, L., Shen, Q. et al. (2020). Rapid synthesis of dual-mesoporous silica aerogel with excellent adsorption capacity and ultra-low thermal conductivity. *J. Non-Cryst. Solids* 120547. https://doi.org/10.1016/j.jnoncrysol.2020.120547.

38 Ding, J., Zhong, K., Liu, S. et al. (2020). Flexible and super hydrophobic polymethylsilsesquioxane based silica aerogel for organic solvent adsorption via ambient pressure drying technique. *Powder Technol.* 373: 716–726. https://doi.org/10.1016/j.powtec.2020.07.024.

39 Yang, Z., Yu, H., Li, X. et al. (2019). Hyperelastic and hydrophobic silica aerogels with enhanced compressive strength by using VTES/MTMS as precursors. *J. Non-Cryst. Solids* 525: 119677. https://doi.org/10.1016/j.jnoncrysol.2019.119677.

40 Karamikamkar, S., Naguib, H.E., and Park, C.B. (2020). Advances in precursor system for silica-based aerogel production toward improved mechanical properties, customized morphology, and multifunctionality: a review. *Adv. Colloid Interface Sci.* 276: 102101. https://doi.org/10.1016/j.cis.2020.102101.

41 Aoki, Y., Shimizu, T., Kanamori, K. et al. (2017). Low-density, transparent aerogels and xerogels based on hexylene-bridged polysilsesquioxane with bendability. *J. Sol-Gel Sci. Technol.* 81: 42–51. https://doi.org/10.1007/s10971-016-4077-1.

42 Loy, D.A. and Shea, K.J. (1995). Bridged polysilsesquioxanes. Highly porous hybrid organic-inorganic materials. *Chem. Rev.* 95: 1431–1442. https://doi.org/10.1021/cr00037a013.

43 Loy, D.A., Jamison, G.M., Baugher, B.M. et al. (1996). Sol-gel synthesis of hybrid organic-inorganic materials. Hexylene- and phenylene-bridged polysiloxanes. *Chem. Mater.* 8: 656–663. https://doi.org/10.1021/cm950067z.

44 Shea, K.J. and Loy, D.A. (2001). Bridged polysilsesquioxanes. Molecular-engineered hybrid organic-inorganic materials. *Chem. Mater.* 13: 3306–3319. https://doi.org/10.1021/cm011074s.

45 Schaefer, D.W., Beaucage, G., Loy, D.A. et al. (2004). Structure of arylene-bridged polysilsesquioxane xerogels and aerogels. *Chem. Mater.* 16: 1402–1410. https://doi.org/10.1021/cm0350683.

46 Shimizu, T., Kanamori, K., Maeno, A. et al. (2016). Transparent ethylene-bridged polymethylsiloxane aerogels and xerogels with improved bending flexibility. *Langmuir* 32: 13427–13434. https://doi.org/10.1021/acs.langmuir.6b03249.

47 Shimizu, T., Kanamori, K., Maeno, A. et al. (2017). Transparent ethenylene-bridged polymethylsiloxane aerogels: mechanical flexibility and strength and availability for addition reaction. *Langmuir* 33: 4543–4550. https://doi.org/10.1021/acs.langmuir.7b00434.

48 Zou, F., Yue, P., Zheng, X. et al. (2016). Robust and superhydrophobic thiourethane bridged polysilsesquioxane aerogels as potential thermal insulation materials. *J. Mater. Chem. A* 4: 10801–10805. https://doi.org/10.1039/c6ta03531k.

49 Torres, R.B., Vareda, J.P., Lamy-Mendes, A., and Durães, L. (2019). Effect of different silylation agents on the properties of ambient pressure dried and supercritically dried vinyl-modified silica aerogels. *J. Supercrit. Fluids* 147: 81–89. https://doi.org/10.1016/j.supflu.2019.02.010.

50 Li, C., Cheng, X., Li, Z. et al. (2017). Mechanical, thermal and flammability properties of glass fiber film/silica aerogel composites. *J. Non-Cryst. Solids* 457: 52–59. https://doi.org/10.1016/j.jnoncrysol.2016.11.017.

51 Gore, P.M. and Kandasubramanian, B. (2018). Functionalized aramid fibers and composites for protective applications: a review. *Ind. Eng. Chem. Res.* 57: 16537–16563. https://doi.org/10.1021/acs.iecr.8b04903.

52 Linhares, T., Pessoa De Amorim, M.T., and Durães, L. (2019). Silica aerogel composites with embedded fibres: a review on their preparation, properties and applications. *J. Mater. Chem. A* 7: 22768–22802. https://doi.org/10.1039/c9ta04811a.

53 Shi, D., Sun, Y., Feng, J. et al. (2013). Experimental investigation on high temperature anisotropic compression properties of ceramic-fiber-reinforced SiO_2 aerogel. *Mater. Sci. Eng., A* 585: 25–31. https://doi.org/10.1016/j.msea.2013.07.029.

54 Nocentini, K., Achard, P., and Biwole, P. (2018). Hygro-thermal properties of silica aerogel blankets dried using microwave heating for building thermal insulation. *Energy Build.* 158: 14–22. https://doi.org/10.1016/j.enbuild.2017.10.024.

55 Ul Haq, E., Zaidi, S.F.A., Zubair, M. et al. (2017). Hydrophobic silica aerogel glass-fibre composite with higher strength and thermal insulation based on methyltrimethoxysilane (MTMS) precursor. *Energy Build.* 151: 494–500. https://doi.org/10.1016/j.enbuild.2017.07.003.

56 Kwon, D.J., Shin, P.S., Kim, J.H. et al. (2017). Interfacial properties and thermal aging of glass fiber/epoxy composites reinforced with SiC and SiO_2 nanoparticles. *Composites, Part B* 130: 46–53. https://doi.org/10.1016/j.compositesb.2017.07.045.

57 Zhou, T., Cheng, X., Pan, Y. et al. (2018). Mechanical performance and thermal stability of glass fiber reinforced silica aerogel composites based on co-precursor method by freeze drying. *Appl. Surf. Sci.* 437: 321–328. https://doi.org/10.1016/j.apsusc.2017.12.146.

58 Kim, C.Y., Lee, J.K., and Kim, B.I. (2008). Synthesis and pore analysis of aerogel-glass fiber composites by ambient drying method. *Colloids Surf. A* 313–314: 179–182. https://doi.org/10.1016/j.colsurfa.2007.04.090.

59 Yuan, B., Ding, S., Wang, D. et al. (2012). Heat insulation properties of silica aerogel/glass fiber composites fabricated by press forming. *Mater. Lett.* 75: 204–206. https://doi.org/10.1016/j.matlet.2012.01.114.

60 Wei, T.Y., Lu, S.Y., and Chang, Y.C. (2009). A new class of opacified monolithic aerogels of ultralow high-temperature thermal conductivities. *J. Phys. Chem. C* 113: 7424–7428. https://doi.org/10.1021/jp900380q.

61 Slosarczyk, A., Wojciech, S., Piotr, Z., and Paulina, J. (2015). Synthesis and characterization of carbon fiber/silica aerogel nanocomposites. *J. Non-Cryst. Solids* 416: 1–3. https://doi.org/10.1016/j.jnoncrysol.2015.02.013.

62 Beach, B., Farkas, G., Hegedus, L. et al. (2010). Powder Tech Note 59 Powder Tech Note 59, Ref. Number ISO. 160, 215–219. http://dx.doi.org/10.1007/s11367-011-0297-3.

63 Guzel Kaya, G. and Deveci, H. (2020). Synergistic effects of silica aerogels/xerogels on properties of polymer composites: a review. *J. Ind. Eng. Chem.* 89: 13–27. https://doi.org/10.1016/j.jiec.2020.05.019.

64 Liu, Q., Chen, J., Mei, T. et al. (2018). A facile route to the production of polymeric nanofibrous aerogels for environmentally sustainable applications. *J. Mater. Chem. A* 6: 3692–3704. https://doi.org/10.1039/c7ta10107d.

65 Liu, Q., Frazier, A.W., Zhao, X. et al. (2018). Flexible transparent aerogels as window retrofitting films and optical elements with tunable birefringence. *Nano Energy* 48: 266–274. https://doi.org/10.1016/j.nanoen.2018.03.029.

66 Zheng, X. and Fu, S. (2019). Reconstructing micro/nano hierarchical structures particle with nanocellulose for superhydrophobic coatings. *Colloids Surf. A* 560: 171–179. https://doi.org/10.1016/j.colsurfa.2018.10.005.

67 Wong, J.C.H., Kaymak, H., Tingaut, P. et al. (2015). Mechanical and thermal properties of nanofibrillated cellulose reinforced silica aerogel composites. *Microporous Mesoporous Mater.* 217: 150–158. https://doi.org/10.1016/j.micromeso.2015.06.025.

68 Hayase, G., Kanamori, K., Abe, K. et al. (2014). Polymethylsilsesquioxane-cellulose nanofiber biocomposite aerogels with high thermal insulation, bendability, and superhydrophobicity. *ACS Appl. Mater. Interfaces* 6: 9466–9471. https://doi.org/10.1021/am501822y.

69 Li, Z., Gong, L., Cheng, X. et al. (2016). Flexible silica aerogel composites strengthened with aramid fibers and their thermal behavior. *Mater. Des.* 99: 349–355. https://doi.org/10.1016/j.matdes.2016.03.063.

70 He, S., Sun, G., Cheng, X. et al. (2017). Nanoporous SiO_2 grafted aramid fibers with low thermal conductivity. *Compos. Sci. Technol.* 146: 91–98. https://doi.org/10.1016/j.compscitech.2017.04.021.

71 Li, X., Wang, Q., Li, H. et al. (2013). Effect of sepiolite fiber on the structure and properties of the sepiolite/silica aerogel composite. *J. Sol-Gel Sci. Technol.* 67: 646–653. https://doi.org/10.1007/s10971-013-3124-4.

72 Yang, X., Sun, Y., Shi, D., and Liu, J. (2011). Experimental investigation on mechanical properties of a fiber-reinforced silica aerogel composite. *Mater. Sci. Eng., A* 528: 4830–4836. https://doi.org/10.1016/j.msea.2011.03.013.

73 Li, Z., Cheng, X., He, S. et al. (2016). Aramid fibers reinforced silica aerogel composites with low thermal conductivity and improved mechanical performance. *Composites, Part A* 84: 316–325. https://doi.org/10.1016/j.compositesa.2016.02.014.

74 Deng, Z., Wang, J., Wu, A. et al. (1998). High strength SiO_2 aerogel insulation. *J. Non-Cryst. Solids* 225: 101–104. https://doi.org/10.1016/S0022-3093(98)00106-9.

75 Lamy-Mendes, A., Girão, A.V., Silva, R.F., and Durães, L. (2019). Polysilsesquioxane-based silica aerogel monoliths with embedded CNTs. *Microporous Mesoporous Mater.* 288: 109575. https://doi.org/10.1016/j.micromeso.2019.109575.

76 Nie, J., Jia, Y., Qu, P., and Shi, Q. (2011). Carbon nanotube/carbon fiber multiscale composite: influence of interfacial strength on mechanical properties. *J. Inorg. Organomet. Polym. Mater.* 21: 937–940. https://doi.org/10.1007/s10904-011-9565-8.

77 Salimian, S., Zadhoush, A., Naeimirad, M. et al. (2018). A review on aerogel: 3D nanoporous structured fillers in polymer-based nanocomposites. *Polym. Compos.* 39: 3383–3408. https://doi.org/10.1002/pc.24412.

78 Dourbash, A., Buratti, C., Belloni, E., and Motahari, S. (2017). Preparation and characterization of polyurethane/silica aerogel nanocomposite materials. *J. Appl. Polym. Sci.* 134: 1–13. https://doi.org/10.1002/app.44521.

79 Liang, M. and Wong, K.L. (2017). Study of mechanical and thermal performances of epoxy resin filled with micro particles and nanoparticles. *Energy Procedia* 110: 156–161. https://doi.org/10.1016/j.egypro.2017.03.121.

80 Börner, M., Noisser, T., and Reichenauer, G. (2013). Cross-linked monolithic xerogels based on silica nanoparticles. *Chem. Mater.* 25: 3648–3653. https://doi.org/10.1021/cm401717q.

81 He, J., Zhao, H., Li, X. et al. (2018). Large-scale and ultra-low thermal conductivity of ZrO_2 fibrofelt/ZrO_2-SiO_2 aerogels composites for thermal insulation. *Ceram. Int.* 44: 8742–8748. https://doi.org/10.1016/j.ceramint.2018.01.089.

82 Haeri, S.Z., Asghari, M., and Ramezanzadeh, B. (2017). Enhancement of the mechanical properties of an epoxy composite through inclusion of graphene oxide nanosheets functionalized with silica nanoparticles through one and two steps sol-gel routes. *Prog. Org. Coat.* 111: 1–12. https://doi.org/10.1016/j.porgcoat.2017.05.003.

83 Kanamori, K. (2011). Organic-inorganic hybrid aerogels with high mechanical properties via organotrialkoxysilane-derived sol-gel process. *J. Ceram. Soc. Jpn.* 119: 16–22. https://doi.org/10.2109/jcersj2.119.16.

84 Wang, L., Xu, H., Gao, J. et al. (2019). Recent progress in metal-organic frameworks-based hydrogels and aerogels and their applications. *Coord. Chem. Rev.* 398: 213016. https://doi.org/10.1016/j.ccr.2019.213016.

85 Hrubesh, L.W. and Pekala, R.W. (1994). Thermal properties of organic and inorganic aerogels. *J. Mater. Res.* 9: 731–738. https://doi.org/10.1557/jmr.1994.0731.

86 He, Y.L. and Xie, T. (2015). Advances of thermal conductivity models of nanoscale silica aerogel insulation material. *Appl. Therm. Eng.* 81: 28–50. https://doi.org/10.1016/j.applthermaleng.2015.02.013.

87 Rabani, R., Heidarinejad, G., Harting, J., and Shirani, E. (2018). Interplay of confinement and density on the heat transfer characteristics of nanoscale-confined gas. *Int. J. Heat Mass Transfer* 126: 331–341. https://doi.org/10.1016/j.ijheatmasstransfer.2018.05.028.

88 Tang, G.H., Tao, W.Q., and He, Y.L. (2005). Lattice Boltzmann method for gaseous microflows using kinetic theory boundary conditions. *Phys. Fluids* 17: 1–4. https://doi.org/10.1063/1.1897010.

89 Xie, T. and He, Y.L. (2016). Heat transfer characteristics of silica aerogel composite materials: structure reconstruction and numerical modeling. *Int. J. Heat Mass Transfer* 95: 621–635. https://doi.org/10.1016/j.ijheatmasstransfer.2015.12.025.

90 Zhao, J.J., Duan, Y.Y., Wang, X.D., and Wang, B.X. (2012). Radiative properties and heat transfer characteristics of fiber-loaded silica aerogel composites for thermal insulation. *Int. J. Heat Mass Transfer* 55: 5196–5204. https://doi.org/10.1016/j.ijheatmasstransfer.2012.05.022.

91 Xie, T., He, Y.L., and Hu, Z.J. (2013). Theoretical study on thermal conductivities of silica aerogel composite insulating material. *Int. J. Heat Mass Transfer* 58: 540–552. https://doi.org/10.1016/j.ijheatmasstransfer.2012.11.016.

92 Ali, N., Ali, F., Khurshid, R. et al. (2020). TiO_2 nanoparticles and epoxy-TiO_2 nanocomposites: a review of synthesis, modification strategies, and photocatalytic potentialities. *J. Inorg. Organomet. Polym. Mater.* 30: 4829–4846. https://doi.org/10.1007/s10904-020-01668-6.

93 Jiang, L., Kato, K., Mayumi, K. et al. (2017). One-pot synthesis and characterization of polyrotaxane-silica hybrid aerogel. *ACS Macro Lett.* 6: 281–286. https://doi.org/10.1021/acsmacrolett.7b00014.

94 Li, S., Ren, H., Zhu, J. et al. (2017). Facile fabrication of superhydrophobic, mechanically strong multifunctional silica-based aerogels at benign temperature. *J. Non-Cryst. Solids* 473: 59–63. https://doi.org/10.1016/j.jnoncrysol.2017.07.032.

95 Yun, S., Luo, H., and Gao, Y. (2015). Low-density, hydrophobic, highly flexible ambient-pressure-dried monolithic bridged silsesquioxane aerogels. *J. Mater. Chem. A* 3: 3390–3398. https://doi.org/10.1039/c4ta05271d.

96 Vareda, J.P., Matias, T., and Durães, L. (2018). Facile preparation of ambient pressure dried aerogel-like monoliths with reduced shrinkage based on vinyl-modified silica networks. *Ceram. Int.* 44: 17453–17458. https://doi.org/10.1016/j.ceramint.2018.06.213.

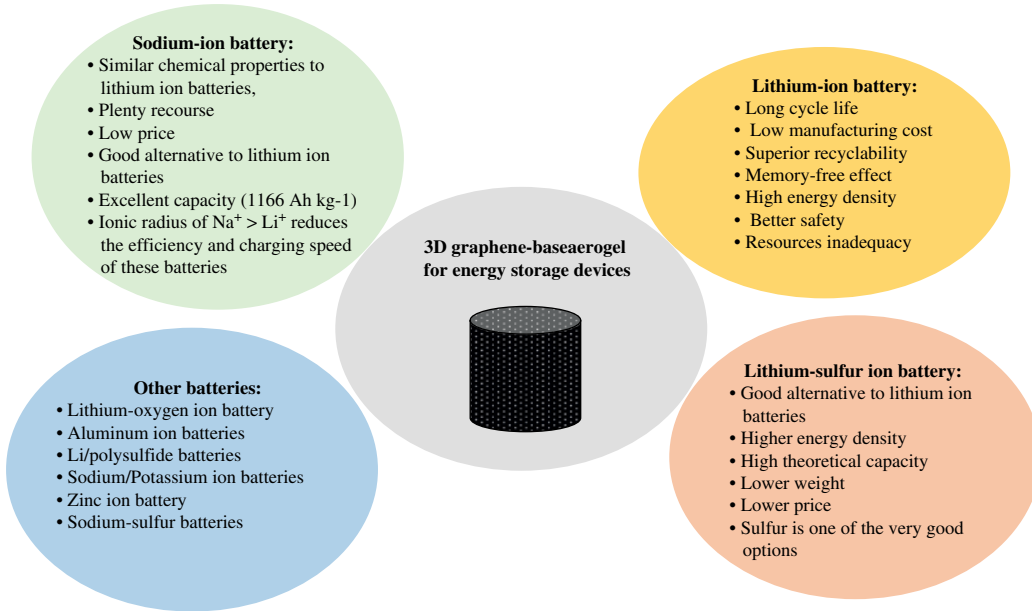
15

Porous Graphene-Based Aerogels for Batteries

Maryam Hasanpour[1,2] *and Mohammad Hatami*[2]

[1] *Department of Chemical Engineering, University of Bojnord, Bojnord, North Khorasan, Iran*
[2] *Department of Mechanical Engineering, Esfarayen University of Technology, Esfarayen, North Khorasan, Iran*

Graphic Abstract



Highlight

- This review describes recent advances in the fields of batteries on graphene-based aerogel.
- 3D graphene-based aerogels are attractive due to good electrical conductivity, low density, high specific surface area, and unique electrochemical performance.
- Graphene-based aerogels are extremely attractive for applications in energy storage systems such as batteries.

Aerogels for Energy Saving and Storage, First Edition. Edited by Meldin Mathew, Hanna J. Maria, Ange Nzihou, and Sabu Thomas.
© 2024 John Wiley & Sons, Inc. Published 2024 by John Wiley & Sons, Inc.

- The hydrothermal method is one of the strongest and most widely used bottom-up methods for producing aerogels.
- The hydrothermal method has received much attention due to its simplicity and cost-effectiveness.

15.1 Introduction

Due to economic growth, industrial development, and a general push for renewable energy resources in consumer electronics and high-performance electrochemical energy storage devices, much study has been devoted to eco-friendly and efficient energy storage systems. Furthermore, electronics industrials and electric vehicles have made great progress [1–3]. Also, providing energy simply and optimally for the development of these devices is an important and undeniable necessity.

Batteries play an important role in everyday life as the heart of electric vehicles and portable electronic equipment. Large automotive companies are spending a lot of money annually on the construction of electric and hybrid vehicles in attempts to reduce air pollution, and one of the most important challenges is how to supply the electricity [4–8]. The best option to solve this problem is to use rechargeable batteries to store electrical energy in these cars. Thus, extensive research in the field of rechargeable batteries has been carried out in world research centers, and this has led to the rapid development of rechargeable batteries in recent decades.

Graphene-based aerogels have attracted great attention due to their unique properties of excellent mechanical flexibility, unique structure, chemical stability, low density, large surface area, high porosity, superior electric, thermal conductivities, and unique electrochemical performance, as documented by numerous researchers for electrochemical energy storage devices [2, 9–11]. There are several review articles and books on 3D graphene-based materials for various applications, such as energy storage devices (supercapacitors, lithium batteries, fuel cells, solar cells, etc.), hydrogen energy production, and environment protection (pollutants detection and environmental remediation) [1, 12].

This chapter focuses on graphene-based aerogels for various energy storage devices such as lithium-ion batteries, lithium-sulfur batteries, sodium batteries, and other batteries.

15.2 Preparation and Synthesized Method for Graphene-Based Aerogel

During the past decade, numerous techniques have been developed and are used to synthesize graphene, including chemical vapor deposition (CVD), epitaxial growth, in situ chemical reduction, hydrothermal [13–15] and solvothermal method [16], and cross-linker induced self-assembly [2, 17]. To improve the efficiency of graphene electrodes, three-dimensional (3D) constructions of graphene (e.g. foam, network, gels, aerogel) have been developed. These 3D graphene-based materials not only retain the intrinsic properties of graphene but also provide a high specific surface area, good mechanical strength, excellent electrical conductivity, and low density [11, 18]. The most common methods to synthesis graphene-based aerogel for storage energy devices are presented in Figure 15.1.

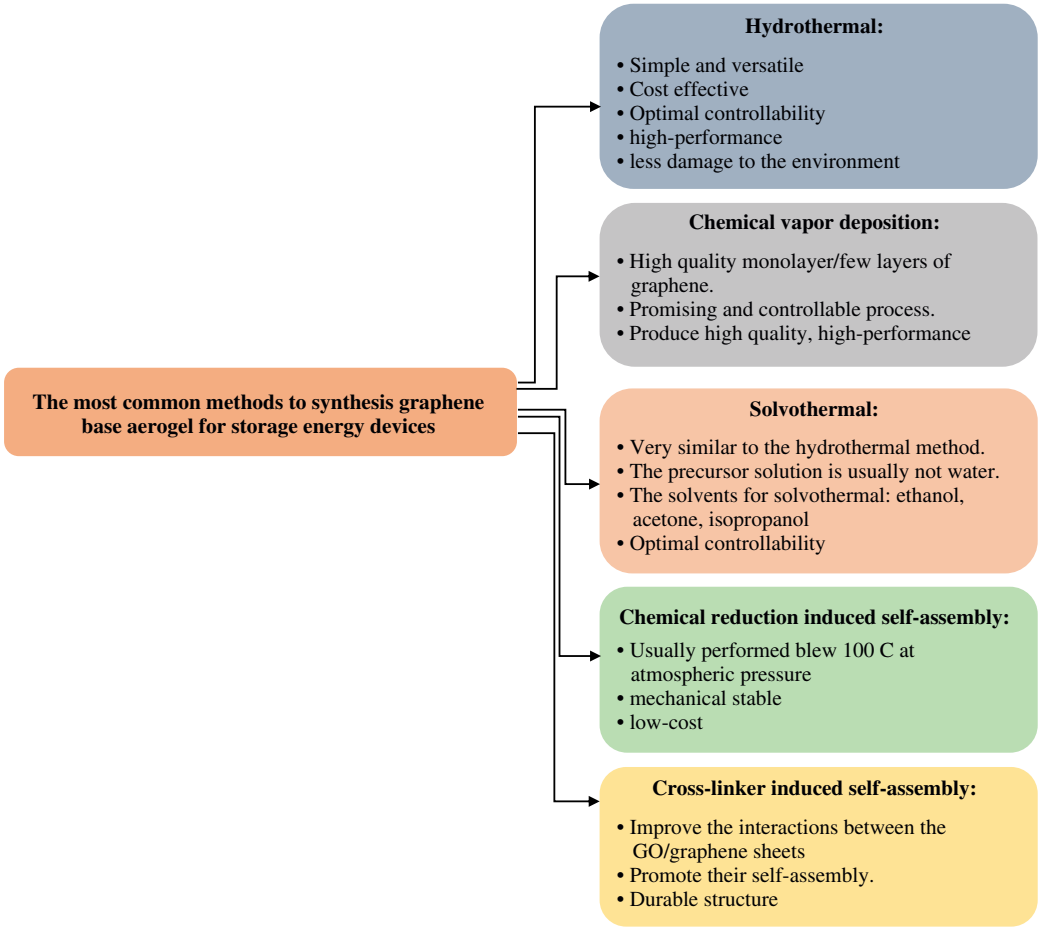


Figure 15.1 The most common method to synthesis graphene-based aerogel for storage energy devices.

Among these methods, the hydrothermal method has attracted a lot of attention. It is one of the strongest and most widely used bottom-up methods and has received much attention from researchers due to its simplicity and cost-effectiveness, [3, 19–24]. The advantages of the hydrothermal technique are high efficiency, optimal controllability, ease of method, production of products with a uniform size distribution, less energy consumption, and less damage to the environment. Table 15.1 summarizes some conventional techniques used to synthesize 3D graphene-based aerogels for energy storage applications.

15.3 Application of Graphene-Based Aerogels (GBAs) for Energy Storage Devices

Graphene-based aerogels have been extremely attracted due to the intrinsic properties such as high porosity, large specific surface area, low density, excellent mechanical properties, and unique electrochemical performance. Advancing from these properties and the distinctive structure, GBAs are

Table 15.1 Conventional techniques to synthesize 3D graphene-based for energy storage applications.

3D graphene-based aerogel	Synthesized method	Devices	As-prepared properties	References
Fe_3O_4/graphene aerogel	Chemical reduction freeze-drying	Lithium-ion batteries	Specific surface area ~96 m^2/g, pore size 2–100 nm, pore volume 0.28 cm^3/g, electrical conductivity ~15 S/cm	[25]
Carbon-coated MoO_2/graphene aerogel	Solvothermal	Lithium-ion batteries	Specific surface area ~82.3 m^2/g, a wide range of pore distribution, including microporous, mesoporous, and macroporous	[16]
SnO_2/graphene aerogel	Hydrothermal	Lithium-ion batteries	Charge transfer resistance in first/Ω ~ 272	[13]
Three-dimensional graphene/NiCo-layered double hydroxide aerogel	Hydrothermal	Lithium-ion batteries	Specific surface area ~56 m^2/g, pore size distribution ~15 to 100 nm	[14]
MnO_2-decorated graphene aerogel	Hydrothermal	Lithium-sulfur battery	—	[8]
Nitrogen-doped graphene nanoribbon aerogels	Hydrothermal	Lithium-sulfur battery	Specific surface area ~ 1380 m^2/g, pore volume values ~ 2.0 cm^3/g, pore size distribution ~ 3.8 nm	[26]
Uniform polypyrrole layer coated sulfur/graphene aerogel	Vapor phase deposition	Lithium-sulfur battery	Surface area ~ 319 m^2/g	[27]
Nitrogen heteroatoms in 3D porous graphene framework	Chemical vapor deposition	Lithium-sulfur battery	Electrical conductivity ~31 S/cm, large surface area ~ 1531 m^2/g, low defect density with a low ID/IG ratio of 1.55.	[28]
Nano-sized lithium sulfide/graphene aerogel	Hydrothermal	Lithium-sulfur battery	—	[29]
Sulfur/3D hierarchically porous titanium monoxide-graphene composite	Traditional emulsion polymerization	Lithium-sulfur battery	Specific surface area pore ~151.85 m^2/g, volume of the porous TiO-G film ~ 0.79 cm^3/g	[30]
Vanadium oxide nanorods embed in porous graphene aerogel	Hydrothermal	Lithium-sulfur battery	—	[31]
3D sulfur/graphene aerogel	Modified two-step hydrothermal reduction	Lithium-sulfur battery	—	[32]
$Li_2S@Li_3PS_4$ nanoparticles incorporated into graphene aerogel	Liquid infiltration-evaporation coating process	Lithium-sulfur battery	Specific surface area ~ 198 m^2/g	[19]

Table 15.1 (Continued)

3D graphene-based aerogel	Synthesized method	Devices	As-prepared properties	References
Graphene aerogel	Self-propagating combustion rapid reduction	Aluminum-ion batteries	Large surface area (513 m^2/g), high electrical conductivity (581 S/cm), dense stacking (0.61 g/cm^3).	[33]
3D MoSx ($1 < x < 2$) nanosheets decorated graphene aerogel	Hydrothermal	Lithium-oxygen (Li-O_2) batteries	specific surface area (280.866 m^2/g),	[34]
3D nitrogen-doped graphene aerogel	Hydrothermal	Li-O_2 batteries	Average pore diameters ~3.82–6.54 nm, pore volume ~ 0.32–0.43 cm^3/g, specific surface area ~ 198–613 m^2/g	[35]
Nitrogen-doped three-dimensional graphene	Hydrothermal	Li-O_2 batteries	Pore size about 120–170 nm, specific surface area ~ 239 m^2/g, pore volume ~ 0.42 cm^3/g	[36]
Nitrogen-doped/3D reduced graphene oxide/carbon nanotube hybrid aerogel	Hydrothermal	Li/polysulfide batteries	Specific surface area ~ 216 m^2/g, density ~ 4 mg/cm^3	[37]
MoS_2/N-doped graphene aerogels	Hydrothermal	Sodium/potassium ion batteries	Pore size ~3.2 nm, specific surface area ~ 114 m^2/g and a total pore volume ~ 0.44 cm^3/g	[38]
3D interconnected graphene aerogel	Solvothermal	Zinc ion battery	—	[39]
Silver-modified porous 3D nitrogen-doped graphene aerogel	Hydrothermal	Zn-air battery	Specific surface area (197 m^2/g), Average pore diameter (14 nm), pore volume (0.77 cm^3/g)	[40]

attractive for a wide range of applications such as energy storage, environmental treatment, and energy conversion [2, 41–45].

15.3.1 Recent Advances in Porous Graphene-Based Aerogels for Batteries

15.3.1.1 Lithium-Ion Batteries (LIBs)

Li-ion batteries (LIBs) are a main class of effective energy storage devices and a type of rechargeable battery in various electrochemical fields that has widely developed to replace lead-acid batteries because of long cycle life, low manufacturing cost, superior recyclability, memory-free effect, high energy density (120–170 Wh/kg), and better safety compared to the traditional batteries [15, 46, 47]. In the past few decades, lithium batteries are extremely regarded by researchers due to their high energy density, long life, and replaceable. One of the significant components of the LIBs is an active substance for the electrode that can impressively affect the electrochemical efficiency of LIBs.

Three-dimensional graphene-based aerogels (3D GBAs) have been compared to other materials used as the electrode materials in energy storage devices, by numerous researchers for using in LIBs [15, 48–50]. Studies show that these materials have excellent properties such as good electrical conductivity, excellent stable cyclability, excellent mechanical property, no-memory effect, and high porosity structure that these properties can increase and improve the performance of the LIBs system [1, 16, 51, 52]. Various transition metal oxides, manganese and metal-organic frameworks, incorporation of some heteroatoms (N, S, O, and F, etc.) such as Fe-Co oxide nanocubes [53], have been commonly used and studied in the as-prepared 3D graphene aerogels due to controllable pore structures, uniform morphology, high adaptabilities, large specific surface areas, improve electrochemical behaviors, their environmental friendliness, natural abundance, and low cost.

Carbon-coated MoO_2 nanoparticles dispersed in 3D graphene aerogel (3D MoO_2@C-GAs hybrids) were prepared through solvothermal technique by Yu Zhou et al. [16]. Their results showed that 3D MoO_2@C-Gas hybrids have a higher specific surface area, conductivity, excellent cyclability and high reversible capacity in contrast to pure MoO_2. In another study on 3D MoO_2@C-GAs hybrids, D. Xie et al. [54] investigated the effect of nitrogen-doped on MoO_2@C-GAs hybrids for high capacity and prolonged stability lithium storage via a hydrothermal-induced self-assembly process. They indicated that the C-MoS_2/N-G electrode, as an anode for lithium-ion batteries, exhibited a high first discharge capacity of 1600 mAh/g and maintains 900 mAh/g after 500 cycles at a current density of 200 mA/g and reversible capacity of 500 mAh/g at a high current density of 4000 mA/g. In another study, Jing Wang et al. [55] investigated the effects of the mass ratio of single-walled carbon nanotube (SWCNT) to graphene on structural and electrochemical properties of SnO_2@Graphene-SWCNT. They showed that the specific capacity of 758 mAh/g for the SnO_2@Graphene-SWCNT with 50% SWCNT in Graphene-SWCNT, as well as a stable specific capacity of 537 mAh/g after 300 cycles was obtained. Linlin Fan et al. [56] synthesized 3D graphene-based aerogels by SnO_2 nanoparticles using a cost-efficient hydrothermal as anodes for lithium-ion batteries. Their electrochemical results displayed that as prepared aerogel, they delivered a discharge capacity of 935 mA/g upon 350 cycles at 100 mA/g. In another study on graphene aerogel, a flexible 3D graphene@CNT@MoS_2 hybrid foam was fabricated via the CVD method and the performance of as-prepared composite as a flexible anode in lithium-ion battery was investigated [48]. The results indicated that 3D graphene@CNT@MoS_2 hybrid exhibited a specific capacity of 935 mA/g at a current density of 0.1 A/g, with high reversible capacity of 606 mAh/g after 200 cycles at 0.2 A/g. A 3D SnS_2/GA nanocomposite was synthesized by a simple and relatively green strategy (Figure 15.2). Their results displayed that the resultant SnS_2/GA composite exhibited a much higher initial reversible capacity (1186 mAh/g), high reversible capacity (1004 mAh/g after 60 cycles), and excellent rate capability (650 mAh/g at a current density of 1000 mA/g) (Figure 15.2) [57].

Ronghua Wang et al. [58] reported that a high capacity of 1121 mAh/g is maintained for 500 cycles for three-dimensional (3D) macroscopic Fe_2O_3 nanocubes/nitrogen-doped graphene (Fe_2O_3-NC/GN) aerogel as anode materials for lithium-ion batteries composite prepared by solvothermal-induced self-assembly approach. Bocheng Qiu et al. [59] synthesized TiO_2/graphene composites aerogel by a simple one-step hydrothermal method and presented a specific capacity of 225 mAh/g at 0.1 A/g after 70 cycles. In another interesting work, Hao Zhang et al. [60] fabricated hybrid aerogel-derived Sn–Ni alloy immobilized within porous carbon/graphene dual matrices as anode for high-performance lithium storage (Figure 15.3a). The composite product showed a high reversible capacity of 503.0 mAh/g (100 cycles at a current density of 100 mA/g) and high average capacities of 326.4 and 260.7 mAh/g at high current densities of 500 mA/g and 1 A/g (shown in Figure 15.3b,c).

In summary, key approaches to synthesize and significant properties from 3D graphene-based aerogels for Li-ion batteries system are presented in Table 15.2.

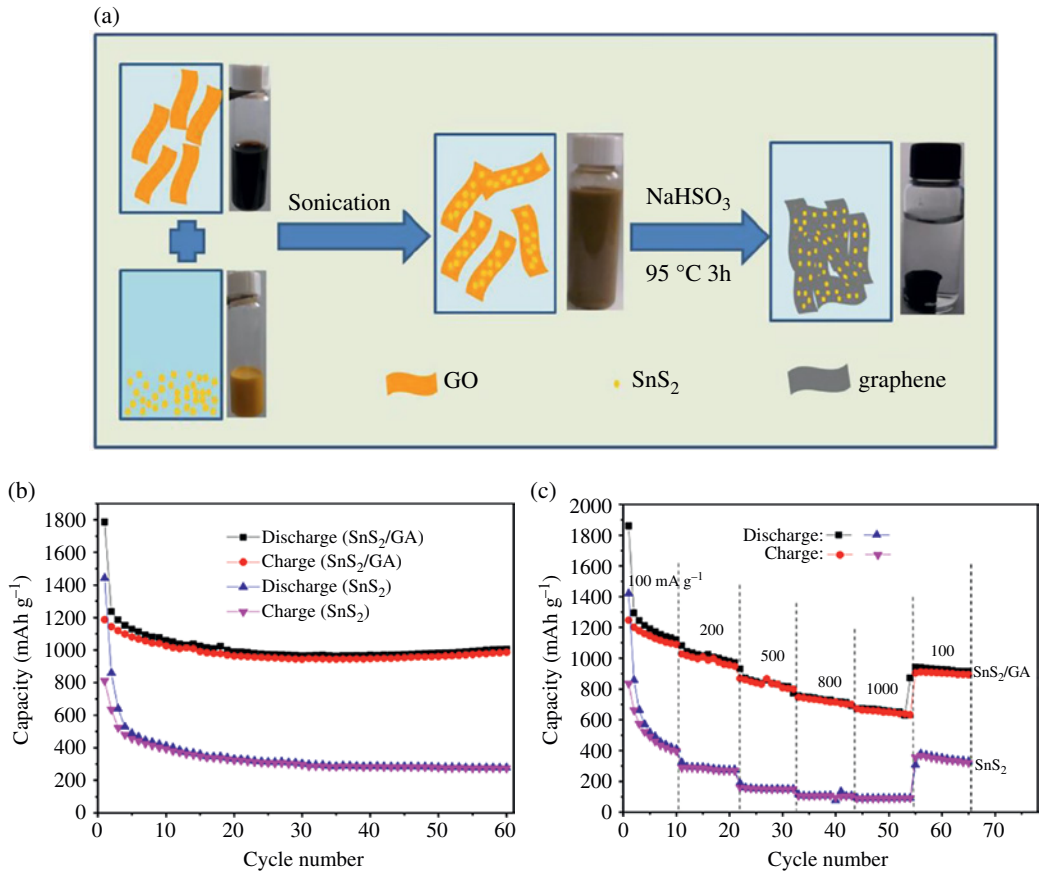


Figure 15.2 (a) Schematic formation process of the as-prepared 3D SnS_2/GA nanocomposite and corresponding digital photos. (b) Cycling stability of SnS_2/GA and SnS_2 electrodes at a current density of 100 mA/g. (c) Rate performances of SnS_2/GA and SnS_2 electrodes at different current densities [57].

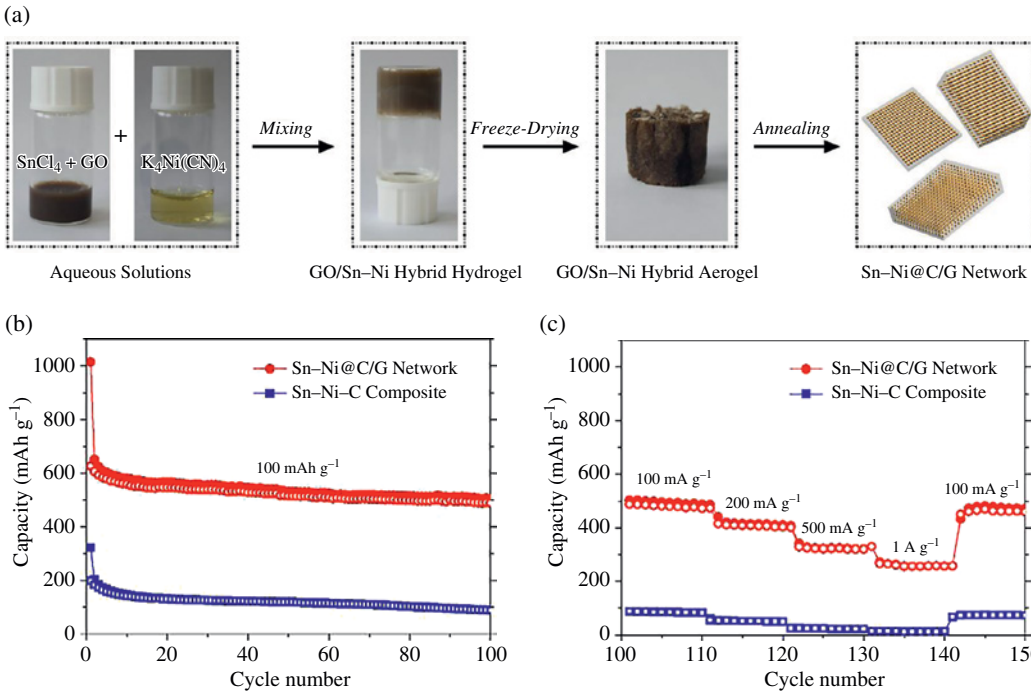


Figure 15.3 (a) Schematic diagram of the synthetic route for the SnANi@C/G network. Lithium-storage performance of the SnANi@C/G network and SnANiAC composite: (b) cycling stability, and (c) rate capability [60].

Table 15.2 Summary of key approaches to synthesize and significant properties from 3D graphene-based aerogels for Li-ion batteries system.

3D graphene-based aerogels	Prepared method	Properties and electrochemical performance	References
Carbon-coated MoO_2/3D graphene aerogel	Solvothermal method	High reversible capacity, high rate of capability with increasing current density and good cycling performance, the discharge capacity of the first cycle 1515 mAh/g, and remaining at 1113 mAh/g over 60 cycles.	[16]
Amorphous SnO_2/graphene aerogel nanocomposites	Hydrothermal approach	Excellent discharge capacity of 700.1 mAh/g in the 80th cycle, high retention capacity (97.6%), and excellent electrochemical performance	[13]
$NiCo_2S_4/Ni_{0.96}$ S/graphene aerogel	Hydrothermal method	High reversible capacity of 965 mAh/g after 200 cycles at 100 mA/g, super-long cycling stability of 620 mAh/g after 800 cycles at 1 A/g, appropriate surface area, and wide pore size distribution	[14]
Sulfur/nitrogen dual-doped porous graphene aerogels	Hydrothermal	High reversible capacity of 1109.8 mAh/g after 400 cycles at a high current density of 800 mA/g.	[61]
Fe_3O_4 nanoparticle/graphene aerogel (Fe_3O_4/GA) composite	One-step liquid phase precipitation method	High reversible capacity of 985 mAh/g at a current density of 0.1 A/g after 100 cycles, good rate capability (434 mAh/g at the current density as high as 2 A/g).	[62]
SnO_2 nanorods anchored on 3D graphene aerogels	Reduction-induced self-assembly method	High initial discharge capacity (1713 mAh/g at 0.1 A/g) and good cycle stability (869 mAh/g at 0.1 A/g) after 50 cycles	[24]
3D porous graphene-encapsulated SnO_2@CNT composite aerogel	Two-step hydrothermal approach	High initial discharge capacity of 1400 mAh/g at 100 mA/g, reversible capacity of 947 mAh/g after 100 cycles at 100 mA/g and increasing the rate capability of 281 mAh/g at 3000 mA/g	[63]
Fe_2O_3 hollow nanoparticles/N-doped graphene aerogels	Sol-gel	High reversible capacity of about 1483 mAh/g at 0.1 A/g up to 100 cycles, high rate capability (550 mAh/g at 5 A/g), and excellent cyclic stability (729 mAh/g at 0.1 A/g for 300 cycles)	[64]
3D Macroscopic SnO_2/nitrogen-doped graphene aerogels	Solvothermal-induced self-assembly process	Large surface area (336 m^2/g), superior rate capability (1126, 855, and 614 mAh/g at 1000, 3000, and 6000 mA/g respectively) and cycling stability at high current densities (905 mAh/g after 1000 cycles at 2000 mA/g)	[65]
3D MoS_2/graphene hybrid aerogels	In-situ thermal decomposition-reduction method	Excellent cycling stability (862.5 mAh/g after 200 cycles at 0.1 A/g with a capacity retention of 109.6%) and good rate capability (622, 563, and 480 mAh/g at 1, 2, and 3 A/g, respectively)	[66]
MnO_2/nitrogen-doped graphene hybrid aerogels	Redox process	Very high discharge capacity of 909 mAh/g after 200 cycles at a current density of 400 mA/g	[50]
Fe_3O_4 quantum dots on 3D-framed graphene aerogel	Hydrothermal	Reversible capacity of 1078 mAh/g after 70 cycles at a current density of 100 mA/g. And the rate capacity remains 536 mAh/g at 1000 mA/g	[67]

Table 15.2 (Continued)

3D graphene-based aerogels	Prepared method	Properties and electrochemical performance	References
3D CuO@nitrogen-graphene aerogel hybrids	Gas-liquid interfacial reaction	Discharge specific capacity of 1442.2 mAh/g at 100 mA/g with a coulombic efficiency of 58.1%, superior cycle stability and excellent rate performance, discharge specific capacity maintains as high as 725.3 mAh/g at 100 mA/g after 100 cycles and 502.4 mAh/g at 1000 mA/g	[46]
SiO_2/nitrogen-doped graphene aerogels	Hydrothermal	Specific capacity of more than 1000 mAh/g at a current density of 100 mA/g after 80 cycles	[68]
Nitrogen-doped graphene aerogels	Hydrothermal	Larger surface area (SBET = 379.1 m^2/g), higher reversible capacity (535.3 mAh/g in the 100th cycle) and more stable cycling performance compared with those of pristine GA	[69]
$ZnFe_2O_4$-graphene aerogels	Two-step method (hydrothermal-calcination)	Specific capacity of 1049 mAh/g at 100 mA/g after 100 cycles	[70]
Fe_3O_4/graphene aerogel	Reduction self-assembly	High reversible capacity of 797 mAh/g at 0.2 A/g, and good rate capacity of 551 mAh/g at 3.2 A/g as well as excellent cycling performance with a stable capacity of ~1138 mAh/g after 100 cycles at 0.2 A/g compared with bare flower-like Fe_3O_4 electrode.	[21]
SnS_2/rGO aerogels	Hydrothermal	Reversible capacity (1682 mAh$/g) with excellent cycle ability (1388.4 mAh/g after 100 cycles at 0.1 A/g) and rate capability (474 mAh/g at the rate of 10 A/g)	[71]
MoS_2 nanosheets/graphene hybrid aerogels on a carbon fiber paper substrate (MoS_2/GS-A)	Hydrothermal or chemical vapor deposition (CVD) methods	Ultra large capacity of 1709 mAh/g at 0.2 A/g and remarkable rate capability of 1384 and 865 mAh/g at current densities of 0.6 and 1.0 A/g, and superior cyclic stability 1526 mAh/g under 0.2 A/g after 100 cycles	[20]
Mo_2C@C core-shell nanocrystals on 3D graphene hybrid aerogel	Hydrothermal	Initial discharge capacity of 1461.4 mAh/g at the current density of 0.1 A/g, and retains a reversible capacity of 1089.8 mAh/g after 100 cycles at a current density of 0.1 A/g	[72]

15.3.1.2 Sodium-Ion Batteries (SIBs)

SIBs are another sort of rechargeable battery in which sodium ions are the key source of current in the circuit. Today, lithium resources are inadequate, their compounds are expensive and toxic, and lithium batteries are serious fire hazards [73, 74]. Therefore, researchers have been looking for a suitable replacement for LIBs.

Sodium metal has similar chemical properties to lithium-ion batteries, and sodium is widely availability and inexpensive. Therefore, sodium-ion batteries can be a good alternative to lithium-ion batteries [3, 75, 76]. Although sodium-ion batteries have an excellent capacity (1166 Ah/kg) of Na^+/Na for the redox reactions, as well as structure and mechanism similar to lithium-ion

batteries, the larger size of sodium (ionic radius of $Na^+ > Li^+$) reduces the efficiency and charging speed of these batteries, which has prevented commercial production of SIB [77–79].

Up to now, numerous materials with various constructions has been considered in the electrochemical efficiency as electrolyte materials for sodium-ion batteries – for instance, carbon fibers, nanowires, carbon nanospheres, reduced graphene oxide, and porous carbon composites [80–83]. Among these materials, graphene is the most attractive electrolyte material for sodium-ion batteries because of its high surface area, remarkable electric conductivity, and significant mechanical flexibility. Specifically, 3D structured graphene with open channels permits free and fast sodium ion intercalation/deintercalation. Furthermore, 3D graphene-based aerogel implemented as free-standing anode material can remove the loss of electrical contact between the electrode material and current collector, ensuring good electron transport [3, 74, 83, 84].

For instance, Yu Wang et al. [85] synthesize a three-dimensional SnO_2 quantum dots/graphene aerogel (SnO_2 QDs/GA) composite via a simplistic and scalable method and used as anode material for sodium-ion batteries. Their results showed that SnO_2 QDs/GA exhibits a better capacity of 319 mAh/g at 50 mA/g after 50 cycles compared to bare SnO_2 electrode. In another work, Yu Zhang et al. [86] prepared Bi_2S_3/GAs composite through a one-step hydrothermal method and freeze-drying process, employed as SIBs anode. Their experimental results displayed that the Bi_2S_3/GAs composite demonstrated a reversible specific capacity of 587 mAh/g at a current density of 100 mA/g, and maintained at 397 mAh/g after 50 cycles while retaining a reversible capacity of 348 mAh/g after 120 cycles at 1 A/g.

Zhou et al. [63] synthesized 3D porous graphene-encapsulated CNT@SnO_2 composite via a facile two-step hydrothermal and investigated it as an anode for both LIBs and SIBs. The resulting CNT@SnO_2@G electrode offers outstanding lithium and sodium storage efficiency with a large specific capacity, significant cycling stability, and excellent rate capability. The results of sodium storage showed that a high discharge capacity of 323 mAh/g after 100 cycles at 25 mA/g was reached. In another study, Gao et al. [23] reported scalable carbon/red phosphorus/graphene aerogel 3D Architecture (C@P/GA) through a localized in situ vapor-redistribution method as anode material for SIBs. They indicated that the as-prepared C@P/GA electrode exhibited a high capacity of 1867 mAh/g after 100 cycles at 0.1 C and demonstrates a major capacity of 1095.5 mAh/g, even at 1 C after 200 cycles (Figure 15.4). In addition, their results showed that the cycling efficiency of the P/GA and C@P/GA electrodes are better than the pure red P and pre-P/GA electrodes.

Another similar work on SIBs using crystalline red phosphorus (CRP), Yan et al. [5] presented a 3D crystalline red P/reduced graphene oxide aerogel architecture anode for sodium-ion batteries. They used CRP as one of the promising anodic materials due to the merits of high theoretical specific capacity and natural abundance in Li- and Na-ion batteries. The results of electrochemical electrode showed that by loading CRP with a mass of 75.9%, the CRP-rGA electrode demonstrated a high initial Na-ion storage capacity of 2427 mAh/g with initial Coulombic efficiency of ~82% at 0.1 A/g and the high capacity can be retained with at higher current densities progressive cycling.

Sn_4P_3 nanoparticles are also promising anode materials for SIBs due to the combination of high electrical conductivity from Sn and high specific capacity from P [87]. Pan et al. [87] prepared Sn_4P_3/graphene aerogel (Sn_4P_3-GA) composite and investigated the electrochemical sodium storage performance of an as-prepared composite. The results showed that Sn_4P_3-GA composite exhibited the high initial discharge capacity of 1180 mAh/g at 0.1 A/g, good cycle stability (657 mAh/g at 0.1 A/g after 100 cycles), and the high-rate capacity of 462 and 403 mAh/g at a current density of 1 and 2 A/g, respectively.

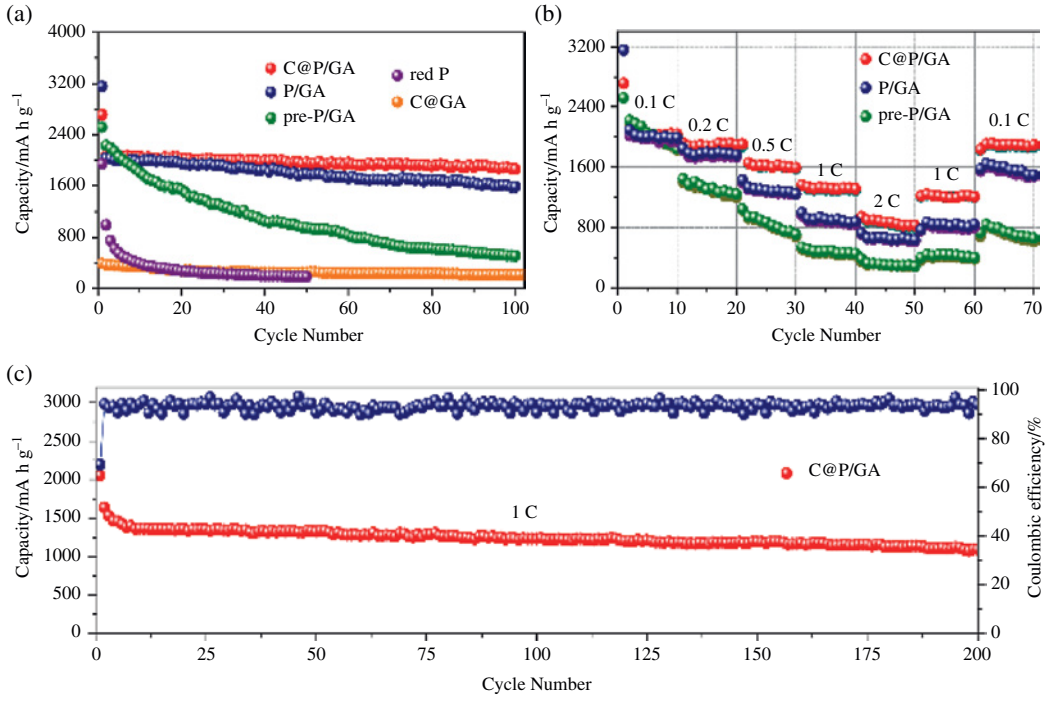


Figure 15.4 (a) Cycling performance of pre-P/GA, P/GA, C@P/GA, red P, and C@GA composites at 0.1 C. (b) Rate performance of pre-P/GA, P/GA, and C@P/GA composites at different current densities. (c) Cycling performance of C@P/GA composite at 1 C (1 C = 2600 mA/g) [23].

Numerous studies have been done on graphene-based aerogels as anode materials for the electrochemical sodium storage performance of SIBs, summarized in Table 15.3.

15.3.1.3 Lithium-Sulfur Batteries (LSBs)

From ancient times, human attention to energy has been very high and has always tried to use the best and most efficient way to produce energy. One of the most challenging issues, however, has always been energy storage. Lithium-sulfur batteries are a type of rechargeable battery that uses a lithium anode and a sulfur cathode to store electricity and are a promising replacement to the usual LIBs. These types of batteries are a good alternative to lithium-ion batteries due to their higher energy density (2500–2600 Wh/kg), high theoretical capacity (1675 mAh/g), lower weight, and lower price [10]. Sulfur is one of the very good options for energy storage in batteries, attracting the attention of many scientists because it is abundant, inexpensive, and nonhazardous.

Beyond the advantages mentioned, however, LSBs are also associated with problems for commercialization. For example, sulfur inside the electrodes decomposes after several charges and discharges, or polysulfide can pass through the cathode and damage the electrolyte [8, 97]. Additionally, sulfur has poor intrinsic electron conductivity and large volume changes, which cause a shuttle effect during charges-discharges. Furthermore, the material selection of the cathode plays a significant role in the electrochemical efficiency of LSBs.

Table 15.3 Electrochemical performance of graphene and graphene-based materials as electrodes for sodium-ion batteries.

Materials	Prepared method	Reversible capacity (mAh/g)	Rate capability	Cycles stability	References
Nitrogen-doped graphene aerogel	Hydrothermal	260.3, 242.9, 215.9, 191.1, and 151.9 mAh/g at the current densities of 1, 2, 3, 4, and 5 A/g, respectively	151.9 mAh/g at a high current density of 5 A/g	287.9 mAh/g after 200 cycles at a current density of 100 mA/g	[3]
SnS_2 nanocrystals decorated on nitrogen and sulfur dual-doped graphene aerogels (SnS_2@N, S-GA)	Hydrothermal	527 mAh/g	340 mAh/g at a current density of 800 mA/g	340 mAh/g after 50 cycles at a current density of 800 mA/g	[4]
SnO_2/graphene aerogels	Hydrothermal	274 mAh/g at 50 mA/g after 100 cycles	274.9 mAh/g	274 mAh/g at 50 mA/g after 100 cycles,	[56]
$Na_{3.12}Fe_{2.44}(P_2O_7)_2$/r-GO aerogels	Seaweed-derived synthesis strategy	116.1 mAh/g	116.1, 106.7, 98.3, 92.8, 86.9, 81.5, and 77.2 mAh/g at the current densities of 0.1, 0.2, 0.5, 1, 2, 5, and 10 C	88.82% capacity retention after 5000 cycles	[6]
Nitrogen and phosphorous dual-doped graphene aerogel	Sol-gel	330 mAh/g at 50 mA/g	218 mAh/g at 1 A/g and 189 mAh/g at 3 A/g	95 mAh/g at 1 A/g after 1000 cycles and 132 mAh/g at 5 A/g after 2000 cycles	[88]
SnO_2 nanorods/graphene aerogel	Reduction-induced self-assembly	208, 173, and 141 mAh/g at a current density of 200, 250, and 500 mA/g	248 mAh/g at 50 mA/g during the first 10 cycles	232 mAh/g at 0.05 A/g after 100	[24]
Sb-doped SnO_2/graphene-CNT aerogels	Hydrothermal	234 mAh/g	124 and 62 mAh/g at 1 and 2 A/g, respectively	74% of its capacity after 500 cycles	[89]
Cobalt disulfide nanoparticles/graphene/carbon nanotubes aerogels	Hydrothermal	360, 230, 165, 108, and 67 mAh/g at current densities of 0.05, 0.1, 0.2, 0.4, and 0.8 A/g	470 mAh/g	258 mAh/g after 100 cycles at 0.05 A/g	[90]

Downloaded from https://onlinelibrary.wiley.com/doi/ by ibrahim ragab - Universita Di Firenze Sistema | Wiley Online Library on [21/07/2024]. See the Terms and Conditions (https://onlinelibrary.wiley.com/terms-and-conditions) on Wiley Online Library for rules of use; OA articles are governed by the applicable Creative Commons License

3D interconnected hollow channel architecture reduced graphene oxide	Electrospinning/ electrospray and carbonization techniques	291.1 mAh/g at 0.1 A/g and 163.9 mAh/g at 2 A/g	229.3 mAh/g.	249.5 mAh/g over 100 cycles at 0.2 A/g and 166.8 mAh/g at 1 A/g	[91]
Polypyrrole modified hierarchical porous CoS_2@ reduced graphene oxide aerogel	Hydrothermal	554 mAh/g at 2.0 A/g	744 mAh/g at the current density of 0.1 A/g	348 mAh/g over a long period of 700 cycles at a high current density of 3 A/g	[92]
Plasma-enabled ternary SnO_2@Sn/nitrogen-doped graphene aerogel	Microwave plasma-based process	975.6 mAh/g	446 mAh/g at a current density of 100 mA/g	54.1, 197.3, and 116.8 mAh/g over a long period of 200 cycles at a high current density of 600, 1000, and 2000 mA/g	[93]
Codoped holey graphene Aerogel	Hydrothermal	343 mAh/g	189 mAh/g at 10 A/g	81.0% capacity retention after 2000 cycles at 5 A/g	[94]
SnO_2/graphene aerogels	Hydrothermal	451 mAh/g at a current density of 20 mA/g	168 mAh/g after 500 cycles at 1000 mA/g	20 mA/g	[95]
Ni_2P@carbon core–shell nanoparticle-arched 3D interconnected graphene aerogel	Solvothermal reaction and in situ phosphorization process	253.6 mAh/g after 100 cycles	460.4 mAh/g	124.5 mAh/g over 2000 cycles at a high current density of 1.0 A/g.	[96]

Downloaded from https://onlinelibrary.wiley.com/doi/ by ibrahim ragab - Universita Di Firenze Sistema , Wiley Online Library on [21/07/2024]. See the Terms and Conditions (https://onlinelibrary.wiley.com/terms-and-conditions) on Wiley Online Library for rules of use; OA articles are governed by the applicable Creative Commons License

As a solution to these problems, various-based compound materials have been suggested (e.g. carbon nanoparticles, multiwall carbon nanotubes, and carbon-based material) to replace pure sulfur in batteries [98]. Among these motioned materials, graphene-based aerogels because of unique features such as high electrical conductivity, excellent electrochemical efficiency, large surface area, superior mechanical flexibility, and good consistency are one of the promising materials and a good candidate to solve these problems in LIBs and LSBs [1, 2, 10, 12]. Currently, numerous studies have been done to develop the electrochemical efficiency of the LSBs, and some of these regarding graphene-based aerogels are presented below.

Zhou et al. [26] prepared the nanostructured porous carbons derived from nitrogen-doped graphene nanoribbon aerogels through a facile physical activation method. The electrochemical lithium storage capacity of as-prepared aerogel showed an initial discharge capacity of 1180 mAh/g at a current density of 0.2 C and a good rate capability of 764 mAh/g in the twentieth cycle. Another work on graphene aerogel, Yan et al. [99] synthesized carbon aerogel/graphene nanosheets (CA/GNS) as cathode for LSBs from in-situ polymerization of resorcinol (R) and formaldehyde (F) in graphene oxide (GO) solution. The resulting material (CA/GNS), as was revealed in Figure 15.5,

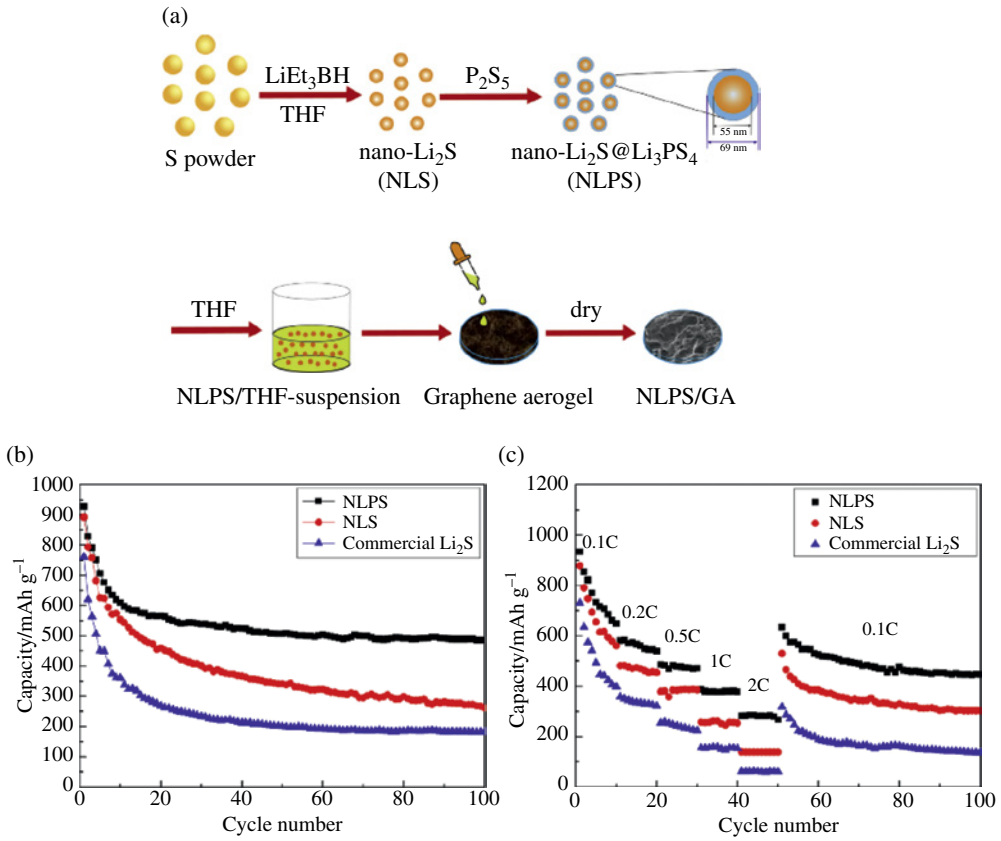


Figure 15.5 (a) Illustration of the formation process of the NLPS/GA composite. (b) Cycle performances. (c) and rate capabilities of commercial Li_2S/GA, NLS/GA and NLPS/GA composites [21].

exhibited, the best electrochemical performances, initial discharging capacity of 1501 mAh/g at 0.1 C, and reversible capacities of 471 mAh/g after 100 cycles and 341 mAh/g after 500 cycles at 1 C [99].

Shi and coworkers [100] investigated the electrochemical performance of 3D graphene/carbon nanotube aerogels as the cathode in LSBs. The G/CNT aerogels display 3D interconnected porous network, large surface area (363 m^2/g), high electrical conductivity (67 S/m), high capacity of 1286 mAh/g at 0.2 C, and long-term cyclability with an extremely low decay rate of 0.06% over 500 cycles at 2 C.

Jiao et al. [19] fabricated a nano-Li_2S@Li_3PS_4/graphene aerogel by a simple liquid infiltration-evaporation coating process and used it directly as a composite cathode without metal substrate for lithium-sulfur batteries (Figure 15.5). Electrochemical tests revealed that the composite exhibited a high discharge capacity of 934.4 mAh/g in the initial cycle and retained 485.5 mAh/g after 100 cycles at 0.1 C rate (Figure 15.5).

Jiang et al. [22] introduced a one-step hydrothermal synthesis of 3D porous graphene aerogels/sulfur nanocrystals to suppress the rapid fading of the sulfur electrode. Their electrochemical tests showed that the as-prepared composite could exhibit a specific capacity of 716.2 mAh/g after 50 cycles at a current density of 100 mA/g and a reversible capacity of 517.9 mAh/g at 1 A/g. In addition, they indicated that the nanometer size of sulfur nanocrystals, a stable open framework of graphene aerogel, intimate contact of the S with graphene conductive matrix, and strong adsorbing ability of functional groups of graphene are the main factors for its outstanding rate capability and cycling efficiency. In another work, Tan and coworkers [7] synthesized the I/N co-doped graphene aerogel (ING) and the MnO_2-decorated graphene aerogel (MG) as the cathode sulfur host and modify the Celgard separator, respectively. Their electrochemical results displayed that the MG@Sep + ING/sulfur demonstrated durable cycle stability (552 mAh/g after 250 cycles), capacity retention (902 mAh/g with Coulombic efficiency over 99%), and all in good condition after 200 cycles. In addition, no shuttled sulfurous species are observed on the anode.

In another study on TiO_2 nanoparticles, Wang et al. [101] successfully prepared sulfur@TiO_2@graphene aerogel (S@TiO_2@GA) through a two-step hydrothermal method as cathode for LSBs. The fabricated S@TiO_2@GA cathode shows excellent electrochemical performance with high discharge capacity (1404 mAh/g at 0.2 C), superior rate capability (>800 mAh/g at 2 C, ~600 mAh/g at 4 C), and durable cycling stability (905 mAh/g during 100 cycles at 0.2 C and 540 mAh/g during 200 cycles at 1 C) as well. A summary of the electrochemical performance of the lithium-sulfur batteries using graphene-based aerogels is presented in Table 15.4.

15.3.1.4 Other Batteries

In addition to the batteries already discussed, 3D GBMs with unique 3D porous structure and excellent intrinsic properties of graphene have been extensively used in other kinds of batteries such as aluminum ion batteries [33], lithium-oxygen batteries [34–36], Li/polysulfide batteries [37], sodium/potassium ion batteries [38], zinc ion battery [39], sodium-sulfur batteries [107], sodium-air batteries [108], magnesium battery [109], and lithium-polysulfide batteries [110]. A summary of the electrochemical performance of the other batteries mentioned in this literature is shown in Table 15.5.

Table 15.4 Electrochemical performance of lithium-sulfur batteries using graphene-based aerogels.

Materials	Prepared method	Initial discharge capacity	Reversible capacities	Rate capacity	Cycle stability	References
MnO_2-decorated graphene aerogel with dual-polymer interpenetrating network	Hydrothermal	1036 mAh/g at 0.2	812 mAh/g at 0.2 C	1492, 1054, 833, 659 mAh/g at 0.1 C, 0.2 C, 0.5 C, 1 C, respectively	755 mAh/g during 250 cycles at 0.2 C and only has 0.06% capacity decay per cycle during 500 cycles at 1 C	[8]
3D porous reduced graphene oxide@ La_2O_3@S (r-GO@ La_2O_3@S) composite	Hydrothermal	1325.5 mAh/g after three activation cycles at 0.05 C	618 mAh/g after 100 cycles	1298, 877, 730, 631, and 515 mAh/g at 0.1 C, 0.2 C, 0.5 C, 1 C, and 2 C, respectively	668.3 mAh/g at 0.2 C after 200 cycles	[102]
3D nitrogen-doped graphene aerogel/sulfur	Hydrothermal	1258 mAh/g at a current rate of 0.1 C	1077 mAh/g after 75 cycles at 0.1 C and 340 mAh/g at 2 C	1258, 987, 631, and 385 mAh/g at 0.1, 0.5, 1, and 2 C respectively	1077 mAh/g after 75 cycles	[103]
Sulfur/graphene aerogel	Two-step hydrothermal reduction	>900 mAh/g at 0.5 C	300 mAh/g during 200 cycles at 0.5 C and 500 mAh/g after 60 cycles at 0.1 C	1120 mAh/g, 690 mAh/g, 600 mAh/g and 390 mAh/g at 0.1 C, 0.2 C, 0.5 C, and 1 C, respectively	300 mAh/g after 200 cycles	[32]
TiO_2/graphene aerogel/ sulfur (TiO_2/GA/S) composites	One-pot hydrothermal	1404 mAh/g at 0.2 C	905 mAh/g at 0.2 C	1400, 1200, 800, and 600 mAh/g at 0.2 C, 0.5 C, 2 C, and 4 C, respectively	553 mAh/g after 500 cycles at 0.2 C	[101]
Graphene aerogel/sulfur (GA/S)		810 mAh/g at 0.2 C	495 mAh/g at 0.2 C	—		
Graphene aerogel-vanadium/carbon black (GA-VOx/CB)	Hydrothermal	1057 mAh/g at 0.05 C	441 mAh/g at 1 C	915, 810, 652, 554, and 442 mAh/g at 0.1 C, 0.2 C, 0.5 C, 1.0 C, and 2.0 C	708 mAh/g after 200 cycles at 0.2 C	[31]
3D hierarchically porous titanium monoxide-graphene composite	Self-assembled	1019 mAh/g at 0.1 C	988 mAh/g at 0.2 C	1350, 1238, 1011, 915, and 831 mAh/g, respectively, at current densities of 0.1 C, 0.2 C, 0.5 C, 1 C, and 2 C, respectively	455 mAh/g after 200 cycles at 2 C	[30]

Downloaded from https://onlinelibrary.wiley.com/doi/ by ibrahim ragab - Universita Di Firenze Sistema , Wiley Online Library on [21/07/2024]. See the Terms and Conditions (https://onlinelibrary.wiley.com/terms-and-conditions) on Wiley Online Library for rules of use; OA articles are governed by the applicable Creative Commons License

Graphene oxide-carbon nanotube-aerogel/sulfur	—	500 mAh/g at 0.1 C	2.2 mAh/cm^2 (500 mAh/g) at 0.1 C	945, 547, 415, 205, and 52 mAh/g at 0.05 C, 0.1 C, 0.2 C, 0.5 C, 1.0 C, respectively	575 mAh/g after 100 cycles at 0.1 C	[104]
MnS decorated N/S co-doped 3D graphene	Hydrothermal	1284 mAh/g at 0.2 C	817 mAh/g at 0.2 C	1353, 1049, 888, 794, 691, and 572 mAh/g at 0.1 C, 0.2 C, 0.5 C, 1.0 C, 2.0 C, respectively	817 mAh/g after 200 cycles. At 0.2 C	[105]
NGF-S	Chemical vapor deposition	959 mAh/g at 1.0 C	530 mAh/g at 1.0 C after 400 cycles	Capacity retention of 51.2% at 5 C	—	[28]
SNG-S		1039 mAh/g at 1.0 C	667 mAh/g at 1.0 C after 400 cycles	58.3% at 5 C	—	
Nitrogen doping of 3D porous graphene	Self-assembly	1185 mAh/g at 0.1 C	730 mAh/g at 1 C	1311, 950, 762, and 580 mAh/g at 0.2 C, 1 C, 2 C, and 3 C respectively	714 mAh/g at 1.5 mA/cm^2 after 400 cycles	[106]
Polypyrrole layer coated sulfur/graphene aerogel composite	Vapor phase deposition	1103 mAh/g after the second cycle at 0.2 C	890 mAh/g after 100 cycles at 0.2 C	1009.1, 918.1, 745.4, 590.9, and 409.1 mAh/g at 0.2 C, 0.5 C, 1 C, 2 C, and 5 C, respectively	698 mAh/g at 0.5 C after 500 cycles	[27]

Downloaded from https://onlinelibrary.wiley.com/doi/ by ibrahim ragab - Universita Di Firenze Sistema , Wiley Online Library on [21/07/2024]. See the Terms and Conditions (https://onlinelibrary.wiley.com/terms-and-conditions) on Wiley Online Library for rules of use; OA articles are governed by the applicable Creative Commons License

Table 15.5 Electrochemical performance of the other batteries mentioned in this literature.

Materials	Prepared method	Type of batteries	Initial discharge capacity	Reversible capacities	Rate capability	Cycle performance	References
Graphene aerogel decorated with MoSx nanosheets (MoSx/HRG)	One-step hydrothermal	Lithium-oxygen ($Li-O_2$) batteries	6678.4 mAh/g at 0.05 mA/cm^2	6400 mAh/g at 0.05 mA/cm^2	6580, 4505, 3403, and 253 mAh/g at 0.05, 0.1, 0.2 and 0.5 mA/cm^2, respectively	500 mAh/g at 0.1 mA/cm^2	[34]
Iron phthalocyanine/N-doped graphene aerogel (FePc/NGA)	One-pot hydrothermal assembly	Lithium-oxygen ($Li-O_2$) batteries	2350 mAh/g at 100 mA/g	2350 mAh/g (98%)	—	500 mAh/g for 40 cycles	[35]
Nitrogen-doped 3D graphene	Hydrothermal and subsequent annealing processes	Lithium-oxygen ($Li-O_2$) batteries	7300 mAh/g at 50 mA/g	—	7300, 5110, and 3900 mAh/g at 50, 100, and 200 mA/g, respectively	—	[36]
Graphene aerogel	Self-propagating combustion rapid reduction	Aluminum ion batteries	113, 100, and 70 mAh/g at 5, 10, and 15 A/g, respectively after 5000 cycles	132 mAh/g	435, 400, 275, 240, 172, 124, 96, and 90 mAh/g at 0.1, 0.2, 0.5, 1, 2, 4, 6, 8, and 10 A/g, respectively	113, 100, and 70 mAh/g at 5, 10, and 15 A/g, respectively after 5000 cycles	[33]
3D nitrogen-doped reduced graphene oxide /carbon nanotube (NrGO/CNT) hybrid aerogel	Hydrothermal	Li/polysulfide batteries	1250 mAh/g at 0.25	881 mAh/g at 0.25 after 100 cycles	1134, 990, 930, and 767 mAh/g at 0.25, 0.5, 1, and 10 C, respectively	610 mAh/g after 400 cycles at 0.5 C	[37]
3D nitrogen-doped reduced graphene oxide (NrGO) aerogel	Hydrothermal	Li/polysulfide batteries	920 mAh/g at 0.25	779 mAh/g at 0.25 after 100 cycles	1010, 890, 200, and 120 mAh/g at 0.25, 0.5 C, 1 C, and 10 C, respectively	—	[37]
3D nitrogen graphene (NG) aerogel	Hydrothermal	Li/polysulfide batteries	910 mAh/g at 0.25	678 mAh/g at 0.25 after 100 cycles	880, 690, 500, and 400 mAh/g at 0.25, 0.5 C, 1 C, and 10 C, respectively	—	[37]

Downloaded from https://onlinelibrary.wiley.com/doi/ by ibrahim ragab - Universita Di Firenze Sistema , Wiley Online Library on [21/07/2024]. See the Terms and Conditions (https://onlinelibrary.wiley.com/terms-and-conditions) on Wiley Online Library for rules of use; OA articles are governed by the applicable Creative Commons License

3D reduced graphene oxide (rGO) aerogel	Hydrothermal	Li/polysulfide batteries	720 mAh/g at 0.25	682 mAh/g at 0.25 after 100 cycles	870, 700, 100, and 20 mAh/g at 0.25, 0.5 C, 1 C, and 10 C, respectively	—	[37]
MoS_2/nitrogen-doped graphene aerogels	Hydrothermal	Sodium/potassium ion batteries	1090 mAh/g	673 mAh/g at a current density of 100 mA/g after 80 cycles	820, 577, 454, 385, and 305 mAh/g at 0.1, 0.2, 0.5, 1, and 2 A/g respectively	305 mAh/g at 2000 mA/g	[38]
Sulfur/carbon-wrapped cobalt nanoparticles on graphene aerogel	Traditional heating process	Sodium-sulfur batteries	572.8 mAh/g at 5 C and 484.9 mAh/g at 0.5 C	349.9 mAh/g at 0.5 C	558, 389, 346.9, 321.4, 304, and 290.5 mAh/g at 0.1 C, 0.2 C, 0.3 C, 0.5 C, and 5 C, respectively	286.5 mAh/g after 1000 cycles at 0.5 C	[107]
Poly 3,4,9,10-perylentetracarboxylic dianhydride (PPTCDA)/ graphene aerogel (GA).	Solvothermal	Zinc ion battery	323 mAh/g at 100 mA/g	281 mAh/g at 100 mA/g	305, 281, 255, 200, 173, and 103 mAh/g at 50, 100, 200, 300, 500, and 1000 mA/g, respectively	102 mAh/g after 300 cycles at 100 mA/g	[39]

Downloaded from https://onlinelibrary.wiley.com/doi/ by ibrahim ragab - Universita Di Firenze Sistema , Wiley Online Library on [21/07/2024]. See the Terms and Conditions (https://onlinelibrary.wiley.com/terms-and-conditions) on Wiley Online Library for rules of use; OA articles are governed by the applicable Creative Commons License

15.4 Conclusions

In response to increasing demand in the electronics and information technology industries, considerable effort has gone into developing efficient and cost-effective energy storage devices, including batteries such as LIBs, SIBs, and LSIs. The most significant factor in preparing a battery is the price for each battery, which is greatly dependent on the abundance of materials used in the battery. Furthermore, whenever the substance used in batteries is more abundant in Earth's crust, batteries can be made more economically. For instance, among the mentioned batteries, sodium-ion batteries are attractive because sodium is dramatically cheaper and much more abundant than lithium.

This chapter presented comprehensive information on the current progress of research and development in energy storage devices such as LIBs, SIBs, and LSIs. Currently, 3D graphene-based aerogels are strongly considered for applications in energy storage to improve the electrochemical performance due to their high mechanical strength, high porosity, excellent electrical conductivity, low density, excellent mechanical properties, unique electrochemical performance, and outstanding thermal and chemical stability. Researchers have explored numerous techniques now in use to synthesize graphene. Among these techniques, the hydrothermal method is more widely used due to its simplicity and versatility, cost-effectiveness, controllability, high-performance, and lower damage to the environment.

References

1 Antink, W.H., Choi, Y., Kim, J.M., and Yuanzhe, P. (2018). Recent progress in porous graphene and reduced graphene oxide-based nanomaterials for electrochemical energy storage devices. *Adv. Mater. Interfaces* 5 (5): 1701212.

2 Wu, Y., Zhu, J., and Huang, L. (2019). A review of three-dimensional graphene-based materials: synthesis and applications to energy conversion/storage and environment. *Carbon* 143: 610–640.

3 Zhang, J., Li, C., Peng, Z. et al. (2017). 3D free-standing nitrogen-doped reduced graphene oxide aerogel as anode material for sodium ion batteries with enhanced sodium storage. *Sci. Rep.* 7 (1): 1–7.

4 Fan, L., Li, X., Song, X. et al. (2018). Promising dual-doped graphene aerogel/SnS_2 nanocrystal building high performance sodium ion batteries. *ACS Appl. Mater. Interfaces* 10 (3): 2637–2648.

5 Yan, Y., Osendi, M.I., Moyano, J.J. et al. (2020). A promising 3D crystalline red P/reduced graphene oxide aerogel architecture anode for sodium-ion batteries. *Chem. Eng. J.* 393: 124788.

6 Liu, B., Zou, Y., Chen, S. et al. (2019). Seaweed-derived synthesis of $Na_3$12$Fe_2$44 (P_2O_7)2/r-GO aerogels as air stable cathode materials for sodium-ion batteries. *Chem. Eng. J.* 365: 325–333.

7 Tan, S., Kan, S., Bu, M. et al. (2020). A combination of MnO_2-decorated graphene aerogel modified separator and I/N codoped graphene aerogel sulfur host to synergistically promote Li–S battery performance. *Electrochim. Acta* 348: 136173.

8 Tan, S., Yang, Z., Yuan, H. et al. (2019). MnO_2-decorated graphene aerogel with dual-polymer interpenetrating network as an efficient hybrid host for Li-S batteries. *J. Alloys Compd.* 791: 483–489.

9 Zhu, J., Yang, Z., Yin, Z. et al. (2014). Graphene and graphene-based materials for energy storage applications. *Small* 10 (17): 3480–3498.

10 Lv, W., Li, Z., Deng, Y. et al. (2016). Graphene-based materials for electrochemical energy storage devices: opportunities and challenges. *Energy Storage Mater.* 2: 107–138.

11 Fan, X., Chen, X., and Dai, L. (2015). 3D graphene based materials for energy storage. *Curr. Opin. Colloid Interface Sci.* 20 (5–6): 429–438.

12 Wang, H., Yuan, X., Zeng, G. et al. (2015). Three dimensional graphene based materials: synthesis and applications from energy storage and conversion to electrochemical sensor and environmental remediation. *Adv. Colloid Interface Sci.* 221: 41–59.

13 Fan, L., Li, X., Yan, B. et al. (2016). Amorphous SnO_2/graphene aerogel nanocomposites harvesting superior anode performance for lithium energy storage. *Appl. Energy* 175: 529–535.

14 Bai, D., Wang, F., Lv, J. et al. (2016). Triple-confined well-dispersed biactive $NiCo_2S_4$/$Ni_{0.96}S$ on graphene aerogel for high-efficiency lithium storage. *ACS Appl. Mater. Interfaces* 8 (48): 32853–32861.

15 Han, S., Wang, J., Li, S. et al. (2014). Graphene aerogel supported $Fe_5 (PO_4)_4 (OH)_3$ $2H_2O$ microspheres as high performance cathode for lithium ion batteries. *J. Mater. Chem. A* 2 (17): 6174–6179.

16 Zhou, Y., Liu, Q., Liu, D. et al. (2015). Carbon-coated MoO_2 dispersed in three-dimensional graphene aerogel for lithium-ion battery. *Electrochim. Acta* 174: 8–14.

17 Fang, Q., Shen, Y., and Chen, B. (2015). Synthesis, decoration and properties of three-dimensional graphene-based macrostructures: a review. *Chem. Eng. J.* 264: 753–771.

18 Olszowska, K., Pang, J., Wrobel, P. et al. (2017). Three-dimensional nanostructured graphene: synthesis and energy, environmental and biomedical applications. *Synth. Met.* 234: 53–85.

19 Jiao, Z., Chen, L., Jian, S. et al. (2017). Core-shell Li_2S@ Li_3PS_4 nanoparticles incorporated into graphene aerogel for lithium-sulfur batteries with low potential barrier and overpotential. *J. Power Sources* 353: 167–175.

20 Yuan, J., Zhu, J., Wang, R. et al. (2020). 3D few-layered MoS_2/graphene hybrid aerogels on carbon fiber papers: a free-standing electrode for high-performance lithium/sodium-ion batteries. *Chem. Eng. J.* 398: 125592.

21 Wang, Y., Jin, Y., Zhao, C. et al. (2018). 3D graphene aerogel wrapped 3D flower-like Fe_3O_4 as a long stable and high rate anode material for lithium ion batteries. *J. Electroanal. Chem.* 830: 106–115.

22 Jiang, Y., Lu, Y., Ling, X. et al. (2015). One-step hydrothermal synthesis of three-dimensional porous graphene aerogels/sulfur nanocrystals for lithium–sulfur batteries. *J. Alloys Compd.* 645: 509–516.

23 Gao, H., Zhou, T., Zheng, Y. et al. (2016). Integrated carbon/red phosphorus/graphene aerogel 3D architecture via advanced vapor-redistribution for high-energy sodium-ion batteries. *Adv. Energy Mater.* 6 (21): 1601037.

24 Wang, Y., Jin, Y., Zhao, C. et al. (2018). 1D ultrafine SnO_2 nanorods anchored on 3D graphene aerogels with hierarchical porous structures for high-performance lithium/sodium storage. *J. Colloid Interface Sci.* 532: 352–362.

25 Chen, W., Li, S., Chen, C. et al. (2011). Self-assembly and embedding of nanoparticles by in situ reduced graphene for preparation of a 3D graphene/nanoparticle aerogel. *Adv. Mater.* 23 (47): 5679–5683.

26 Zhou, H.-Y., Sui, Z.Y., Liu, S. et al. (2019). Nanostructured porous carbons derived from nitrogen-doped graphene nanoribbon aerogels for lithium–sulfur batteries. *J. Colloid Interface Sci.* 541: 204–212.

27 Li, F., Kaiser, M.R., Ma, J. et al. (2020). Uniform polypyrrole layer-coated sulfur/graphene aerogel via the vapor-phase deposition technique as the cathode material for Li–S batteries. *ACS Appl. Mater. Interfaces* 12 (5): 5958–5967.

28 Shi, J.-L., Cheng, T., Huang, J.-Q. et al. (2018). Effective exposure of nitrogen heteroatoms in 3D porous graphene framework for oxygen reduction reaction and lithium–sulfur batteries. *J. Energy Chem.* 27 (1): 167–175.

29 Wang, Z., Chen, L., Xu, C. et al. (2019). In-situ lithiation synthesis of nano-sized lithium sulfide/graphene aerogel with covalent bond interaction for inhibiting the polysulfides shuttle of Li-S batteries. *Electrochim. Acta* 312: 282–290.

30 Chen, Y., Choi, S., Su, D. et al. (2018). Self-standing sulfur cathodes enabled by 3D hierarchically porous titanium monoxide-graphene composite film for high-performance lithium-sulfur batteries. *Nano Energy* 47: 331–339.

31 Zhang, Y., Ge, X., Kang, Q. et al. (2020). Vanadium oxide nanorods embed in porous graphene aerogel as high-efficiency polysulfide-trapping-conversion mediator for high performance lithium-sulfur batteries. *Chem. Eng. J.* 393: 124570.

32 Li, B., Xiao, Q., and Luo, Y. (2018). A modified synthesis process of three-dimensional sulfur/graphene aerogel as binder-free cathode for lithium-sulfur batteries. *Mater. Des.* 153: 9–14.

33 Huang, H., Zhou, F., Shi, X. et al. (2019). Graphene aerogel derived compact films for ultrafast and high-capacity aluminum ion batteries. *Energy Storage Mater.* 23: 664–669.

34 Li, L., Chen, C., Su, J. et al. (2016). Three-dimensional MoS x (1< x< 2) nanosheets decorated graphene aerogel for lithium–oxygen batteries. *J. Mater. Chem. A* 4 (28): 10986–10991.

35 Hsieh, T.-C., Tsou, Y.-H., and Chen, J.-S. (2019). Iron phthalocyanine supported on 3D nitrogen-doped graphene aerogel as an electrocatalyst for non-aqueous Li−O_2 batteries. *Electrochim. Acta* 295: 490–497.

36 He, M., Liu, I., Liu, B. et al. (2016). Hierarchical porous nitrogen doped three-dimensional graphene as a free-standing cathode for rechargeable lithium-oxygen batteries. *Electrochim. Acta* 191: 90–97.

37 Li, X., Pu, X., Han, S. et al. (2016). Enhanced performances of Li/polysulfide batteries with 3D reduced graphene oxide/carbon nanotube hybrid aerogel as the polysulfide host. *Nano Energy* 30: 193–199.

38 Dong, X., Xing, Z., Zheng, G. et al. (2020). MoS_2/N-doped graphene aerogles composite anode for high performance sodium/potassium ion batteries. *Electrochim. Acta* 339: 135932.

39 Cang, R., Ye, K., Zhu, K. et al. (2020). Organic 3D interconnected graphene aerogel as cathode materials for high-performance aqueous zinc ion battery. *J. Energy Chem.* 45: 52–58.

40 Hu, J., Shi, Z., Wang, X. et al. (2019). Silver-modified porous 3D nitrogen-doped graphene aerogel: highly efficient oxygen reduction electrocatalyst for Zn−air battery. *Electrochim. Acta* 302: 216–224.

41 Chen, D., Chang, X., and Jiao, X. (2014). Aerogels in the environment protection. In: *The Role of Colloidal Systems in Environmental Protection* (ed. M. Fanun), 573–591. Elsevier.

42 Hasanpour, M. and Hatami, M. (2020). Photocatalytic performance of aerogels for organic dyes removal from wastewaters: review study. *J. Mol. Liq.* 309: 113094.

43 Villasmil, W., Fischer, L.J., and Worlitschek, J. (2019). A review and evaluation of thermal insulation materials and methods for thermal energy storage systems. *Renewable Sustainable Energy Rev.* 103: 71–84.

44 Cuce, E., Cuce, P.M., Wood, C.J., and Riffat, S.B. (2014). Toward aerogel based thermal superinsulation in buildings: a comprehensive review. *Renewable Sustainable Energy Rev.* 34: 273–299.

45 Singh, N., Nagpal, G., and Agrawal, S. (2018). Water purification by using adsorbents: a review. *Environ. Technol. Innovation* 11: 187–240.

46 Feng, C.-N., Dong, L., Meng, J.-K., and Zheng, X.-C. (2019). 3D CuO@ nitrogen-graphene aerogel hybrids as anodes for lithium-ion batteries: gas-liquid interfacial assembly and superior electrochemical performance. *J. Alloys Compd.* 784: 915–922.

47 Wakihara, M. (2001). Recent developments in lithium ion batteries. *Mater. Sci. Eng.: R: Rep.* 33 (4): 109–134.

48 Ren, J., Ren, R.-P., and Lv, Y.-K. (2018). A flexible 3D graphene@CNT@ MoS_2 hybrid foam anode for high-performance lithium-ion battery. *Chem. Eng. J.* 353: 419–424.

49 Xu, B., Wu, H., Lin, C.X. et al. (2015). Stabilization of silicon nanoparticles in graphene aerogel framework for lithium ion storage. *RSC Adv.* 5 (39): 30624–30630.

50 Sui, Z.-Y., Wang, C., Shu, K. et al. (2015). Manganese dioxide-anchored three-dimensional nitrogen-doped graphene hybrid aerogels as excellent anode materials for lithium ion batteries. *J. Mater. Chem. A* 3 (19): 10403–10412.

51 Han, T., Wei, Y., Jin, X. et al. (2019). Hydrothermal self-assembly of α-Fe_2O_3 nanorings@ graphene aerogel composites for enhanced Li storage performance. *J. Mater. Sci.* 54 (9): 7119–7130.

52 Guo, C., Xie, Y., Pan, K., and Li, L. (2020). MOF-derived hollow SiOx nanoparticles wrapped in 3D porous nitrogen-doped graphene aerogel and their superior performance as the anode for lithium-ion batteries. *Nanoscale* 12 (24): 13017–13027.

53 Shao, J., Feng, J., Zhou, H., and Yuan, A. (2019). Graphene aerogel encapsulated Fe-Co oxide nanocubes derived from Prussian blue analogue as integrated anode with enhanced Li-ion storage properties. *Appl. Surf. Sci.* 471: 745–752.

54 Xie, D., Tang, W.J., Xia, X.H. et al. (2015). Integrated 3D porous C-MoS_2/nitrogen-doped graphene electrode for high capacity and prolonged stability lithium storage. *J. Power Sources* 296: 392–399.

55 Wang, J., Fang, F., Yuan, T. et al. (2017). Three-dimensional graphene/single-walled carbon nanotube aerogel anchored with SnO_2 nanoparticles for high performance lithium storage. *ACS Appl. Mater. Interfaces* 9 (4): 3544–3553.

56 Fan, L., Xiong, D., and Li, X. (2019). Enhanced lithium/sodium storage of SnO_2/graphene aerogels nanocomposites. *Mater. Chem. Phys.* 238: 121870.

57 Tang, H., Qi, X., Zhang, Z. et al. (2016). Simple self-assembly of SnS_2 entrapped graphene aerogel and its enhanced lithium storage performance. *Ceram. Int.* 42 (6): 6572–6580.

58 Wang, R., Xu, C., Sun, J., and Gao, L. (2014). Three-dimensional Fe_2O_3 nanocubes/nitrogen-doped graphene aerogels: nucleation mechanism and lithium storage properties. *Sci. Rep.* 4 (1): 1–7.

59 Qiu, B., Xing, M., and Zhang, J. (2014). Mesoporous TiO_2 nanocrystals grown in situ on graphene aerogels for high photocatalysis and lithium-ion batteries. *JACS* 136 (16): 5852–5855.

60 Zhang, H., Zhang, M., and Zheng, M. (2017). Hybrid aerogel-derived Sn–Ni alloy immobilized within porous carbon/graphene dual matrices for high-performance lithium storage. *J. Colloid Interface Sci.* 501: 267–272.

61 Shan, H., Li, X., Ciu, Y. et al. (2016). Sulfur/nitrogen dual-doped porous graphene aerogels enhancing anode performance of lithium ion batteries. *Electrochim. Acta* 205: 188–197.

62 Wang, Y., Jin, Y., Zhao, C. et al. (2018). Fe_3O_4 nanoparticle/graphene aerogel composite with enhanced lithium storage performance. *Appl. Surf. Sci.* 458: 1035–1042.

63 Zhou, D., Li, X., Ciu, Y. et al. (2017). Three-dimensional porous graphene-encapsulated CNT@ SnO_2 composite for high-performance lithium and sodium storage. *Electrochim. Acta* 230: 212–221.

64 Liu, L., Yang, X., Lv, C. et al. (2016). Seaweed-derived route to Fe_2O_3 hollow nanoparticles/N-doped graphene aerogels with high lithium ion storage performance. *ACS Appl. Mater. Interfaces* 8 (11): 7047–7053.

65 Wang, R., Xu, C., Sun, J. et al. (2014). Solvothermal-induced 3D macroscopic SnO_2/nitrogen-doped graphene aerogels for high capacity and long-life lithium storage. *ACS Appl. Mater. Interfaces* 6 (5): 3427–3436.

66 Wang, S., Wang, R., Zhao, Q. et al. (2019). Freeze-drying induced self-assembly approach for scalable constructing MoS_2/graphene hybrid aerogels for lithium-ion batteries. *J. Colloid Interface Sci.* 544: 37–45.

67 Wang, Y., Jin, Y., Duan, Y., and Jia, M. (2017). Fe_3O_4 quantum dots on 3D-framed graphene aerogel as an advanced anode material in lithium-ion batteries. *Ionics* 23 (8): 2005–2011.

68 Dong, X., Zheng, X., Deng, Y. et al. (2020). SiO_2/N-doped graphene aerogel composite anode for lithium-ion batteries. *J. Mater. Sci.* 55: 13023–13035.

69 Meng, J., Suo, Y., Li, J. et al. (2015). Nitrogen-doped graphene aerogels as anode materials for lithium-ion battery: assembly and electrochemical properties. *Mater. Lett.* 160: 392–396.

70 Wang, Y., Yu, J., Zhang, F. et al. (2017). Facile synthesis of $ZnFe_2O_4$-graphene aerogels composites as high-performance anode materials for lithium ion batteries. *Appl. Surf. Sci.* 413: 50–55.

71 Ji, J., Zhou, z., Fu, K. et al. (2020). Enhanced Li+ storage through highly hybridized networks of self-assembled SnS_2/rGO aerogels. *J. Alloys Compd.* 828: 154192.

72 Xin, H., Yang, H., Dongzhi, L. et al. (2018). Coupling Mo_2C@ C core-shell nanocrystals on 3D graphene hybrid aerogel for high-performance lithium ion battery. *Appl. Surf. Sci.* 441: 69–76.

73 Yang, M., Li, X., Yan, B. et al. (2017). Reduced graphene oxide decorated porous SnO_2 nanotubes with enhanced sodium storage. *J. Alloys Compd.* 710: 323–330.

74 Wang, Y., Jin, Y., Li, S. et al. (2018). Flower-like MoS_2 supported on three-dimensional graphene aerogels as high-performance anode materials for sodium-ion batteries. *Ionics* 24 (11): 3431–3437.

75 Chen, C., Xu, H., Zhou, T. et al. (2016). Integrated intercalation-based and interfacial sodium storage in graphene-wrapped porous $Li_4Ti_5O_{12}$ nanofibers composite aerogel. *Adv. Energy Mater.* 6 (13): 1600322.

76 Chen, W., Qi, S., Guan, L. et al. (2017). Pyrite FeS_2 microspheres anchoring on reduced graphene oxide aerogel as an enhanced electrode material for sodium-ion batteries. *J. Mater. Chem. A* 5 (11): 5332–5341.

77 Palomares, V., Serras, P., Villaluenga, I. et al. (2012). Na-ion batteries, recent advances and present challenges to become low cost energy storage systems. *Energy Environ. Sci.* 5 (3): 5884–5901.

78 Pan, H., Hu, Y.-S., and Chen, L. (2013). Room-temperature stationary sodium-ion batteries for large-scale electric energy storage. *Energy Environ. Sci.* 6 (8): 2338–2360.

79 Zhang, Y., Huang, Y., Yang, G. et al. (2017). Dispersion–assembly approach to synthesize three-dimensional graphene/polymer composite aerogel as a powerful organic cathode for rechargeable Li and Na batteries. *ACS Appl. Mater. Interfaces* 9 (18): 15549–15556.

80 Li, M., Carter, R., Cohn, A. et al. (2016). Interconnected foams of helical carbon nanofibers grown with ultrahigh yield for high capacity sodium ion battery anodes. *Carbon* 107: 109–115.

81 Fu, L., Tang, K., Song, K. et al. (2014). Nitrogen doped porous carbon fibres as anode materials for sodium ion batteries with excellent rate performance. *Nanoscale* 6 (3): 1384–1389.

82 Cao, Y., Xiao, L., Sushko, M. et al. (2012). Sodium ion insertion in hollow carbon nanowires for battery applications. *Nano Lett.* 12 (7): 3783–3787.

83 Wang, Y., Kong, D., Shi, W. et al. (2016). Ice templated free-standing hierarchically WS2/CNT-rGO aerogel for high-performance rechargeable lithium and sodium ion batteries. *Adv. Energy Mater.* 6 (21): 1601057.

84 Zhou, J., Yan, B., Yang, J. et al. (2018). A densely packed Sb_2O_3 nanosheet–graphene aerogel toward advanced sodium-ion batteries. *Nanoscale* 10 (19): 9108–9114.

85 Wang, Y., Jin, Y., Zhao, C. et al. (2017). SnO_2 quantum dots/graphene aerogel composite as high-performance anode material for sodium ion batteries. *Mater. Lett.* 191: 169–172.

86 Zhang, Y., Fan, L., Wang, P. et al. (2017). Coupled flower-like Bi_2S_3 and graphene aerogels for superior sodium storage performance. *Nanoscale* 9 (45): 17694–17698.

87 Pan, E., Jin, Y., Zhao, C. et al. (2019). Mesoporous Sn_4P_3-graphene aerogel composite as a high-performance anode in sodium ion batteries. *Appl. Surf. Sci.* 475: 12–19.

88 Li, C., Fu, Q., Zhao, K. et al. (2018). Nitrogen and phosphorous dual-doped graphene aerogel with rapid capacitive response for sodium-ion batteries. *Carbon* 139: 1117–1125.

89 Cui, J., Yao, S., Huang, J.-Q. et al. (2017). Sb-doped SnO_2/graphene-CNT aerogels for high performance Li-ion and Na-ion battery anodes. *Energy Storage Mater.* 9: 85–95.

90 Zhang, X., Liu, X.J., Wang, G., and Wang, H. (2017). Cobalt disulfide nanoparticles/graphene/carbon nanotubes aerogels with superior performance for lithium and sodium storage. *J. Colloid Interface Sci.* 505: 23–31.

91 Liang, K., Li, M., Hao, Y. et al. (2020). Reduced graphene oxide with 3D interconnected hollow channel architecture as high-performance anode for Li/Na/K-ion batteries. *Chem. Eng. J.* 394: 124956.

92 Liu, X., Ma, H., Xu, H. et al. (2020). Polypyrrole modified hierarchical porous CoS_2@RGO aerogel electrode for ultrafast sodium storage. *J. Solid State Electrochem.* 24 (1): 81–91.

93 Ma, Y., Wang, Q., Liu, L. et al. (2020). Plasma-enabled ternary SnO_2@ Sn/nitrogen-doped graphene aerogel anode for sodium-ion batteries. *ChemElectroChem* 7: 1358–1364.

94 Zhao, J., Zhang, Y.-Z., Chen, J. et al. (2020). Codoped holey graphene aerogel by selective etching for high-performance sodium-ion storage. *Adv. Energy Mater.* 10 (18): 2000099.

95 Xie, X., Chen, S., Sun, B. et al. (2015). 3D networked tin oxide/graphene aerogel with a hierarchically porous architecture for high-rate performance sodium-ion batteries. *ChemSusChem* 8 (17): 2948–2955.

96 Miao, X., Yin, R., Ge, X. et al. (2017). Ni_2P@ carbon core–shell nanoparticle-arched 3D interconnected graphene aerogel architectures as anodes for high-performance sodium-ion batteries. *Small* 13 (44): 1702138.

97 Raccichini, R., Varzi, A., Passerini, S., and Scrosati, B. (2015). The role of graphene for electrochemical energy storage. *Nat. Mater.* 14 (3): 271–279.

98 Kang, W., Deng, N., Ju, J. et al. (2016). A review of recent developments in rechargeable lithium–sulfur batteries. *Nanoscale* 8 (37): 16541–16588.

99 Yan, Y., Shi, M., Zou, Y. et al. (2019). Tunable hierarchical porous carbon aerogel/graphene composites cathode matrix for Li-S batteries. *J. Alloys Compd.* 791: 952–961.

100 Shi, H., Zhao, X., Zhong, S.-W. et al. (2019). Free-standing integrated cathode derived from 3D graphene/carbon nanotube aerogels serving as binder-free sulfur host and interlayer for ultrahigh volumetric-energy-density lithiumsulfur batteries. *Nano Energy* 60: 743–751.

101 Wang, M., Tan, S., Kan, S. et al. (2020). In-situ assembly of TiO_2 with high exposure of (001) facets on three-dimensional porous graphene aerogel for lithium-sulfur battery. *Journal of Energy Chemistry* 49: 316–322.

102 Yang, Y., Yuan, Y., Ma, G. et al. (2019). High-performance lithium– sulfur batteries fabricated from a three-dimensional porous reduced graphene oxide/La_2O_3 microboards/sulfur aerogel. *Ceram. Int.* 45 (7): 9017–9024.

103 Kang, J.-H. and Chen, J.-S. (2018). Using ethylenediamine to prepare three dimensional nitrogen-doped graphene aerogel/sulfur composite for lithium-sulfur batteries. *Diamond Relat. Mater.* 88: 222–229.

104 Gómez-Urbano, J.L., Gómez-Cálmer, J.L., Botas, C. et al. (2019). Graphene oxide-carbon nanotubes aerogels with high sulfur loadings suitable as binder-free cathodes for high performance lithiumsulfur batteries. *J. Power Sources* 412: 408–415.

105 Li, Z., Xu, R., Deng, S. et al. (2018). MnS decorated N/S codoped 3D graphene which used as cathode of the lithium-sulfur battery. *Appl. Surf. Sci.* 433: 10–15.

106 Cheng, D., Wu, P., Wang, J. et al. (2019). Synergetic pore structure optimization and nitrogen doping of 3D porous graphene for high performance lithium sulfur battery. *Carbon* 143: 869–877.

107 Ma, Q., Du, G., Guo, B. et al. (2020). Carbon-wrapped cobalt nanoparticles on graphene aerogel for solid-state room-temperature sodium-sulfur batteries. *Chem. Eng. J.* 388: 124210.

108 Enterría, M., Botas, C., Gómez-Urbano, J.L. et al. (2018). Pathways towards high performance Na–O_2 batteries: tailoring graphene aerogel cathode porosity & nanostructure. *J. Mater. Chem. A* 6 (42): 20778–20787.

109 An, Q., Li, Y., Yoo, H.D. et al. (2015). Graphene decorated vanadium oxide nanowire aerogel for long-cycle-life magnesium battery cathodes. *Nano Energy* 18: 265–272.

110 Chen, Y., Liu, S., Yuan, X. et al. (2020). rGO-CNT aerogel embedding iron phosphide nanocubes for high-performance Li-polysulfide batteries. *Carbon* 167: 446–454.

16

Theoretical Modeling of the Thermal and Mechanical Structure-Property Relationships in Aerogels

Ameya Rege and Barbara Milow

Department of Aerogels and Aerogel Composites, Institute of Materials Research, German Aerospace Center, Linder Höhe, 51147, Cologne, Germany

16.1 Introduction

Owing to the highly open-porous nanostructure of aerogels, they exhibit a unique combination of properties, such as low bulk density, low thermal conductivity, and low acoustic velocity. According to the International Union of Pure and Applied Chemistry (IUPAC) definition, an aerogel is a gel comprised of a microporous solid in which the dispersed phase is a gas. However, zeolites and microporous glass also get categorized within this definition. Two recently suggested definitions are rather more accurate [1]. The first one is based on the aerogel production process, namely, an aerogel is an open, nonfluid colloidal network or polymer network that is expanded throughout its whole volume by a gas and is formed by the removal of all swelling agents from a gel without substantial volume reduction or network compaction [2]. The second one highlights mainly the final properties: Aerogels are solids that feature very low density and high specific surface area and consist of a coherent open porous network of loosely packed, bonded particles or fibers [3]. Since the commercialization of aerogel-based products is gaining significant attention within the community, a fundamental understanding of their properties is of utmost importance. Concerning the topics considered in this book and focusing on energy storage and management, aerogel-based materials are of an importance today than like never before. Given the superinsulation properties of aerogels and aerogel composites, thermal energy management and storage is a frequently discussed subject in the literature. In 2019, an estimated 21 quadrillion BTU were consumed in the residential and commercial sectors of the United States of America. This amounted to over 28% of the total energy consumption [4]. In the European Union, it was roughly 18 quadrillion BTU in 2016 and amounted to 40% of the total energy consumption [5]. Even further, a study shows that approximately 40–50% of the total building energy consumption in China is due to the heat transfer through windows [6]. This calls for strong and urgent measures for finding green solutions toward solving the energy management problem.

The other chapters in this book discuss diverse aspects about applying aerogels and aerogel composites for energy storage and management. However, in order for this to realize, a complete understanding of the nanoscale mechanism in aerogels is important and recent studies have shown that this can only be realized when theoretical and experimental research work together. To that end, this chapter will address the theoretical aspects characterizing the thermal and

Aerogels for Energy Saving and Storage, First Edition. Edited by Meldin Mathew, Hanna J. Maria, Ange Nzihou, and Sabu Thomas.
© 2024 John Wiley & Sons, Inc. Published 2024 by John Wiley & Sons, Inc.

mechanical structure-property relationships. In the literature on aerogels, there have been very few review reports on the modeling of aerogels [7–9]. While all of them have in part discussed the structural, fractal, and mechanical properties of aerogels, none of them address the theoretical models focusing on the thermal properties of aerogels. This chapter aims to fill this gap, as recent modeling studies have shown to be useful in predicting faster solutions toward thermal energy management. The thermal conductivity (λ) is the most important parameter when interpreting the insulation performance of aerogels. The thermal conductivity is the ability of a material to conduct heat. It appears mathematically from the second law of thermodynamics, as the constant of proportionality in the equation, $Q = -\lambda\Delta T$, where Q is the heat flux and ΔT is the temperature gradient. While evaluating this property, its contribution to each mode of heat transfer, namely, convection, radiation, and conduction, is studied. Convection is defined as the heat transfer due to the macroscopic movement of the fluid. For porous materials, when the pore diameters are below 4 mm, this mode of heat transfer can be neglected [10]. Aerogels show pores below 100 nm, thus making the contribution of convection to the heat transfer negligible. The heat transfer in aerogels is thus a combination of radiation and gaseous and solid heat conduction. The theoretical models describing these effects in aerogels will be addressed in this chapter. While the thermal properties are of high importance, with increasing applications, the mechanical stability of the aerogels becomes an essential requirement. Classical aerogels are generally known to be fragile. In the past decade, several studies have focused on the reinforcement of aerogels for improving their mechanical properties [11–15]. Biopolymer aerogels, especially those from cellulose, already show relatively high strength and ductile behavior [16, 17]. Synthesizing aerogels with improved mechanical stiffness while maintaining a low thermal conductivity presents diverse challenges, as both the mechanical strength and thermal conductivity, are functions of the solid phase fraction of aerogels. This challenge is being faced currently by the aerogel community, especially with the advent of commercialization and production at the industry scale.

The chapter is organized as follows. In Section 16.2, models characterizing the different modes of heat transfer are discussed. To that end, radiative heat transfer is first described, followed by gaseous heat conduction and finally, solid heat conduction. Also discussed is the modeling concerning aerogel composites, followed by a brief review of some applications. In Section 16.3, different modeling strategies applied to model the structural and mechanical properties of aerogels are elucidated. To this end, atomistic- to meso-scale models are reviewed. In the last section, a brief outlook on the future materials development supported by a hand-in-hand progress of theoretical and experimental works is given.

16.2 Modeling the Thermal Structure-Property Relationships of Aerogels

After considering our discussion in the previous section, the effective thermal conductivity λ_{eff} in nanoporous aerogels can be calculated by summing the radiative one and the gas-solid coupled conductivities,

$$\lambda_{\text{eff}} = \lambda_{\text{rad}} + \lambda_{\text{gas–solid}},$$

where the gas-solid coupled heat conductivity $\lambda_{\text{gas}-\text{solid}}$ depends on two heat transfer modes, namely, gas and solid heat conduction. Gas heat conduction can be further considered in two forms: the thermal conduction among gas molecules only and coupled heat transfer between gas molecules and adjacent particles, such as quasi-lattice vibration. Considering the effects of the two

phases on microcosmic heat transfer, effective thermal conductivity can be decomposed into three parts in terms of physical means: contribution of radiative heat transfer λ_{rad}, which is similar to radiative thermal conductivity, contributions of solid heat conduction λ_{solid}, and gaseous heat conduction λ_{gas}. Then, λ_{eff} can be expressed as

$$\lambda_{eff} = \lambda_{rad} + \lambda_{solid} + \lambda_{gas}.$$

The different modes of heat transfer in an aerogel-like material are illustrated schematically in Figure 16.1 [18]. The solid component of the thermal conductivity shows a power-law scaling with respect to the density of the aerogels. The open-cell foam model predicts a linear scaling, but aerogels typically show

$$\lambda_{solid} \propto \rho^{t},$$

where t is between 1.7 and 2.0 [19]. This exponent has also been verified by recent atomistic modeling studies [20]. As a nanoporous material with open pores, heat transfer in aerogels is mainly contributed by the heat conduction through solid phase and gas phase at low temperatures. With the increase in the density of the aerogel, heat conduction through the solid phase increases, while that through the gaseous phase decreases. Therefore, an optimal density with minimized thermal conductivity exists.

Modeling of the thermal conductivity is of primary significance to model aerogel-based thermal energy management systems. In this section, we will look at different approaches to model the effective thermal conductivity in aerogels, followed by the effect of these modeling systems on thermal energy management and storage applications.

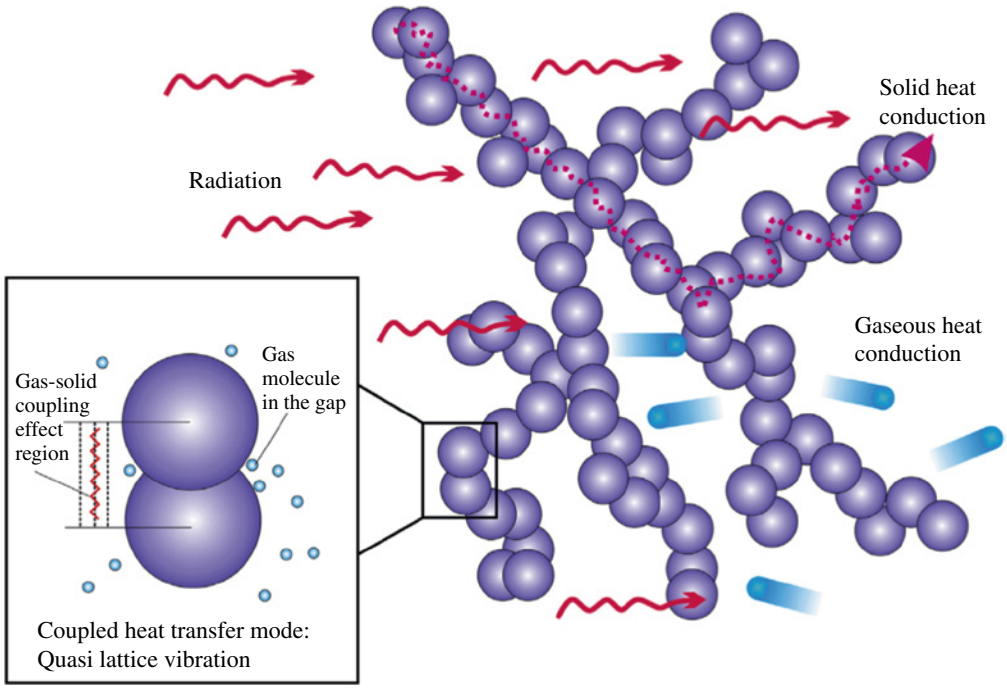


Figure 16.1 Heat transfer modes in aerogels. *Source:* Reprinted with permission from Elsevier, ref. [18].

16.2.1 Radiative Thermal Conductivity

While the contribution of the radiative component of the thermal conductivity (λ_{rad}) to the total one is of less importance at room temperature, its significance becomes much stronger at higher temperatures. For example, classical silica aerogels are almost transparent to the radiation that has a wavelength of 3–8 mm. This can lead to a rapidly rise of thermal radiation when the temperatures are high.

For high temperature thermal management solutions, aerogels are often doped with opacifiers or fibers or a combination of both. In most of the literature on modeling of aerogels, the radiative component of the effective thermal conductivity is considered while modeling aerogel composites. The radiative transfer in aerogel composites could be modeled according to the optical thickness $\tau_\lambda = k_\lambda L$ of the composite, where k_λ and L are the spectral extinction coefficient and the thickness of the aerogel matrix, respectively. For an aerogel composite with a thickness $L \approx 1.0$ cm, the optical thickness $\tau_\lambda \gg 1$ (optical thick). Thus, the radiative heat flux in aerogel composites can only travel over a short distance, and the radiative heat transfer can be evaluated by Rosseland diffusion approximation equation [21], such that λ_{rad} is given as

$$\lambda_{\text{rad}} = \frac{16\sigma n^2 T^3}{3k_r},$$

where $\sigma = 5.67 \times 10^{-8}$ $\text{Wm}^{-2}\text{K}^{-4}$ is the Stefan-Boltzmann constant, n is the refraction constant, T is the temperature, and k_r is the Rosseland mean extinction coefficient. This is a simplification of the radiative transfer equation, where the radiative energy is transformed into a diffusion relation, hence the name *diffusion approximation*. This method of expressing the radiative heat transfer was used by several authors while modeling the thermal properties of aerogel composites [22–25]. For special cases, where one has an optically thin medium, the radiation intensity is almost not attenuated along the path due to absorption or scattering. Thus, the incident intensity from the boundary is dominant and is almost unchanged along its path through the medium. For this case, simplifications to the diffuse spectral radiative heat fluxes at the boundaries are applied [23].

Thus, the heat transfer through aerogels can be modeled as a sum of the radiative heat flux in the optically thin part and that in the thick part. However, most authors directly assume aerogels as optically thick materials, and calculate λ_{rad} using the Rosseland diffusion approximation. This also is convenient, given its simple form like the Fourier law. There are certainly other methods to model the radiative thermal conductivity. Since the radiation intensity is direction-dependent, and if it is assumed to be constant within a certain angular range, the integro-differential radiative transfer equation can be simplified to a set of linear differential equations of the radiation intensity or the radiative heat flux. This is called the Schustere-Schwarschild approximation, or the two-flux method [23]. In this case, it is assumed that the energy transfer is one-dimensional (1-d), and the radiation intensity is isotropic having a constant value for all radiation intensities in the positive coordinate direction and is also isotropic with another different constant value in the negative directions. This method is suitable for the cases of optically thin mediums. This method was further extended by Chandrasekhar (cite) into a multi-flux method, also called the *discrete ordinate method*. This is a much accurate method and gives better solutions to radiation problems compared with the Rosseland diffusion approximation method and the two-flux method. A primary characteristic is that it makes no assumptions such as optically thick or optically thin, and also considers the cases with strongly anisotropic scattering. Moreover, this method if coupled with the energy equation could solve the coupled heat transfer problem. Hence, it is a powerful method for the radiation transfer problem. However, given its complexity, alternative approaches are often preferred for fast solutions.

Concerning aerogels, Zhao et al. modeled the random structure of aerogels by means of the diffusion-limited cluster-cluster aggregation (DLCA) method [26]. This method will be discussed in more detail in Section 16.3.2. The two-flux method together with finite difference were applied to solve the coupled radiative transfer equation and the energy equation. Moreover, the influences of pore and particle sizes, contact length of particles and the porosity on the effective thermal conductivity of the material were studied.

16.2.2 Gaseous Thermal Conductivity

Gaseous thermal conductivity appears due to the heat transfer from gas molecules mainly by means of collisions with each other. When gas molecules move, the molecules traveling at higher speeds collide with the low-speed ones, thus transferring energy. This process of collision results in heat conduction. In comparison to the conventional insulation materials, given that aerogels have high porosities in the micro- and mesoporous regime, the gaseous heat conduction inside an aerogel is from a geometric perspective already significantly reduced (see the schema in Figure 16.2a,b).

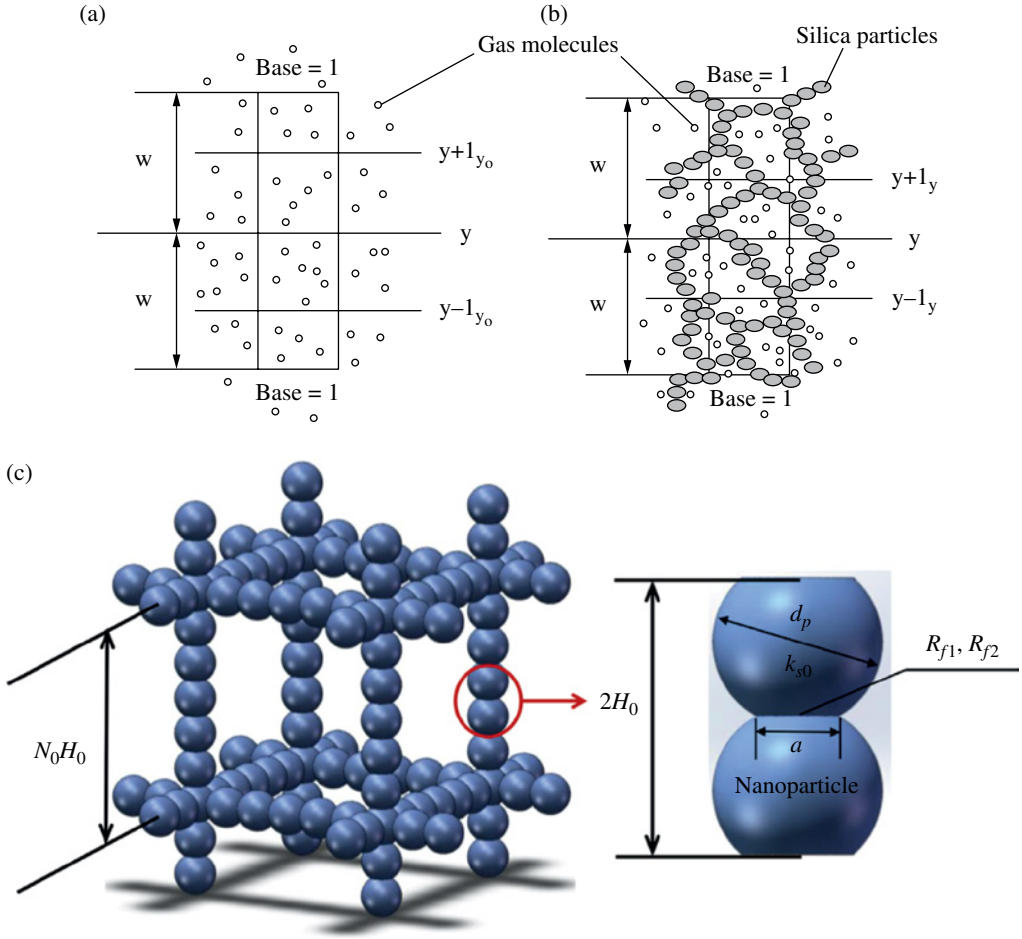


Figure 16.2 Gas molecules in (a) free space and (b) an aerogel. *Source:* Reprinted with permission from ref. [27]. (c) cubic array model of nanospheres. *Source:* Reprinted with permission from Elsevier, ref. [25].

Several studies have investigated the modeling of the gaseous thermal conductivity. One approach involves the use of the kinetic theory to describe λ_{gas} through the aerogel's nanostructure. In 1932, Kistler made use of the kinetic theory to describe λ_{gas} [28],

$$\lambda_{gas} = 0.058a\sqrt{\frac{m_g}{T}}c_{v,g}L_0\frac{D^2}{\frac{2LL_0(1-a)}{p}+aL\left(L+\frac{L_0}{p}\right)},$$

where m_g, T, $c_{v,g}$, a, L_0, D, and p denote the molecular mass, temperature, constant-volume specific heat, the accommodation coefficient, a normal mean free path of the gas at the given temperature and a pressure of 1 mmHg, the average pore diameter, and the pressure, respectively. The accommodation coefficient represents the fraction of the molecules that come to a thermal equilibrium when they strike the surface. Subsequently, $1-a$ represents the fraction of the molecules that reflect upon striking the surface.

A well-known model [29] used to calculate the effect of λ_{gas} is the one proposed by Kaganer. This is expressed as,

$$\lambda_{gas} = \frac{\lambda_{g0}}{1-2C_3K_n},$$

where λ_{g0} and K_n denote the thermal conductivity of gas under the free space and the Knudsen number, respectively. The term C_3 is further expressed as

$$C_3 = \frac{2\gamma}{\gamma+1}\frac{2-a}{a}\frac{1}{\mathrm{Pr}},$$

where γ is the adiabatic ratio of the gas. Due to the simplistic nature of the Kaganer equation and accurate predictions, it is often found in the literature used for describing λ_{gas}. One drawback of this model is that it uses an average pore size and thus, is more accurate for the aerogels that show rather concentrated pore sizes as seen from the BJH pore-size distributions. To this end, Reichenauer et al. and Bi et al. have further modified the Kaganer model to accommodate, for e.g. bimodal pore-size distributions [30, 31].

Apart from the models based on the kinetic theory, simpler empirical models have also been used to model the contribution of λ_{gas} to the total effective thermal conductivity of the aerogels. Fricke et al. used an empirically derived scaling relation to model the effect of the gaseous thermal conductivity as a function of the envelope density, $\lambda_{gas} \propto \rho_e^{-0.6}$ [32].

16.2.3 Solid Thermal Conductivity

Aerogels exhibit a nanostructured solid network that is formed by the aggregation of nanoparticles. Due to its complex nanoporous structure, heat conduction paths through the solid skeleton turn to be lengthened. Meanwhile, the characteristic length of solid skeleton at the nanoscale is similar to the phonon mean free path. Thus, the solid heat conduction through the skeleton also exhibits size effects. Heat transfer in a solid material mainly depends on the energy carriers such as phonons and electrons. Different from the gas molecules that can be moved freely, the solid molecules vibrate around their equilibrium position under the interactions of the surrounding molecules. In quantum mechanics, the vibration of the solid molecules can only be at a certain frequency, so the vibrational energy of the molecules is also discrete. The minimum vibration energy of solid molecules is called *phonon* [33]. In other words, phonon is a quantum mechanical

description of an elementary vibrational motion in which a lattice of atoms or molecules uniformly oscillates at a single frequency. Although the concept of a phonon fails in amorphous solids, some researchers continue to borrow this idea while formulating the solid thermal conductivity of amorphous solids [34]. With the aid of the concept of a phonon, the thermal conductivity of solid materials could be derived according to the kinetic theory. While silica aerogels are a kind of semi-conductor-like materials, their solid heat conduction mainly depends on phonons. According to the kinetic theory, the thermal conductivity of solid materials (λ_{solid}) is calculated as [35],

$$\lambda_{\text{solid}} = \frac{\rho c_v \upsilon_p \Lambda_p}{3},$$

where c_v, υ_p, and Λ_p represent the volume specific heat, the mean group velocity of phonons and the phonon mean free path. Λ_p is further expressed, generally, by the Matthiesen's rule [36] as a summation of the mean free path caused by the volumetric scattering, interfacial scattering between the contact particles, and boundary scattering. Liu and Bi et al. calculated λ_{solid} by this approach, by defining mathematical expressions for the individual components of Λ_p [34, 37].

Soorbaghi et al. modified and applied the classic unit cell model (Figure 16.2c) which establishes correlations between the thermal properties and structural parameters [38]. The modification was done in order to account for the phonon scattering, which otherwise is not accounted for by the classic unit cell model. The second modification was necessary, as the classic unit cell model considers fully dense sphere. This is not the case for aerogels, especially due to the presence of the so-called primary particles. The significance of this model is its true micromechanical nature. The conductivity is a function of the morphological parameters of the aerogel network.

Tang et al. obtained λ_{solid} of aerogels by measuring the sound velocity in the aerogel network, comparing the sound velocity with that in the bulk solid material, and finally scaling the bulk thermal conductivity [39]. Thus,

$$\lambda_{\text{solid}} = \lambda_0 \frac{\rho}{\rho_s} \frac{\nu}{\nu_s},$$

where, ρ_s, ν, and ν_s denote the bulk density of the aerogels, the skeletal one, the sound velocity through the aerogel, and that through the solid backbone of the aerogel material. Sound velocity measurements are also used to estimate the mechanical properties of aerogels [40]. The parameter λ_0 is the aerogel backbone thermal conductivity. This is generally assumed to be the same as the bulk thermal conductivity, thus overestimating λ_{solid}. This approach can be improved by instead using $\lambda_0 = \lambda_p$, where λ_p is the thermal conductivity of the particles in the aerogel backbone, which can be expressed using, for e.g. the Chen model [41].

Dai et al. adopted the spherical hollow cube model [42] (Figure 16.3a) to describe the nanoporous structure of the pure aerogels [22]. λ_{solid} was then calculated by means of the Fourier law. Qu et al. developed a thermal resistance network model [45] based on the Sierpinski carpet model [46] to predict the thermal insulation performance of silica aerogel doped autoclaved aerated concrete. They showed by means of model predictions that at the aerogel loading of 7 wt.%, a 30% improvement in the insulation performance could be obtained. Moreover, the compressive strength and potential durability were also increased. The predictions were verified with experimental data.

Several studies have also attempted to solve the Boltzmann transfer equation in order to model the phonon heat conduction [23]. In an alternative approach, Han et al. proposed a spherical segment structure for the aerogel particles and investigated the phonon heat transfer in silica aerogel

grains by the Lattice Boltzmann Method [47]. This was followed by Qu et al., who also used a modified Lattice Boltzmann Method to solve a 2-d heat transfer model to determine the gas–solid coupled heat conductivity in aerogels [18]. Influence of parameters such as density, ambient pressure and temperature on the thermal conductivity were also investigated.

In a rare study on the modeling of the thermal conductivity in nanofibrillar cellulose aerogels, Obori et al. used a simple open-cell model [48] and modeled λ_{solid} by calculating the thermal resistance in the cellulose filaments, in the crossbar of the cellulose filaments, due to the air trapped between the struts and the cuboid volume of air [49]. This model approach was shown to be promising of reverse engineering aerogels target dimensions for reaching minimum thermal conductivity.

16.2.4 Modeling the Thermal Conductivity of Aerogel Composites and Some Applications

In the scope of thermal management applications of aerogels, diverse approaches have been employed to model the thermal conductivity of the aerogel composites. Yang et al. proposed a theoretical model for predicting λ_{eff} of the ternary opacifier/fiber/aerogel composite [44]. In the aerogel composite, the fibers and opacifiers were assumed to be randomly distributed in the aerogel matrix. All the opacifiers and fibers were assumed to be spherical and infinitely cylindrical, respectively. They were also modeled as well-wrapped by the aerogel, as well as distributed randomly, homogeneously and independently in the aerogel matrix. The coupled conductive λ was modeled by means of the Maxwell model and the Hamilton model, while the radiative part was modeled using the Rosseland equation as discussed in Section 16.2.1. The results were shown to be in good agreement with the experimental data. Liu et al. developed an optimization method to design the geometric structures of aerogel composites with minimized thermal conductivity [25]. They showed that when the ambient temperature is lower than ~600 K, the additives with low thermal conductivity are preferred, while when it is higher than ~600 K, the additives with high extinction coefficients are needed. The Rosseland equation was used to model the radiative contribution, by further accounting for the spectral extinction coefficients of the opacifiers and fibers in the aerogel matrix. The coupled solid and gaseous conductivity was modeled using the previously discussed classic unit cell model [27]. Such an approach was also used by Soorbaghi et al. for predictive modeling of the effective thermal conductivity of silica/clay mineral nanocomposite aerogels [38]. The model showed good agreement with experimental results with a less than 10% deviation for pure and nanocomposite aerogel. Hoseini et al. proposed an analytical model to describe the thermal properties of aerogel blankets by means of modeling a unit cell consisting of a cylindrical fiber surrounded by a packed bed of aerogel particles (similar to shown in Figure 16.3c) [24]. The model accounted for all the heat transfer mechanisms making up λ_{eff} and was validated by characterizing Cryogel® Z and ThermalWrap™. The analytically predicted variation in the effective thermal conductivity as a function of temperature agreed well with the experimental data. Using the proposed model, parametric studies were performed to investigate the effect of blanket porosity and fiber thermal conductivity on the effective thermal conductivity of aerogel composites.

As discussed in previous sections, the influence of humidity on aerogel properties is of special interest [50–52]. Hoseini and Bahrami investigated the effects of humidity on the thermal insulation performance of aerogel blankets [53]. Humidity greatly affects the k-value of thermal insulation materials. In hot and humid climates, condensation can occur within the insulation material, raising its moisture content, thus leading to higher thermal conductivity due to the enhanced heat transfer by conduction and, under certain conditions, by evaporation. It could take hours for the

moisture to diffuse from the surface to its depth of an aerogel blanket placed in a humid environment, and no concentration gradient would establish inside the pores because the material would resist diffusion of humidity into the pores as well as provide a capacity to store moisture inside the pores. Thus, a zero-dimensional (0-d) resistance-capacitance circuit model was used to describe the mass transfer in an aerogel blanket porous medium.

The model predictions for λ_{eff} under different temperatures and moisture content were in good agreement with the results from experiments. Another study by Chen et al. investigated λ_{eff} for moist silica aerogels [43]. There, a fractal-intersecting sphere with inhomogeneous water film model was proposed to describe the influence of moisture in the aerogel matrix. The equivalent circuit method was then applied to derive λ_{eff}. Moreover, the influences of the nano-scale heat transfer and additives such as opacifiers and fibers were also taken into consideration. The model predictions were in good agreement with the experimental data. The numerical model showed that λ_{eff} of the low-porosity aerogels was more sensitive to change in the water content than that of the high-porosity ones.

Another application where the support of modeling studies has been used to model the heat transfer mechanism in aerogels is in glazing systems for building applications. Chen et al. presented a dynamic heat transfer model to study the applicability of aerogel-based glazing systems in various climatic conditions [54]. They measured and simulated the indoor solar heat gain and the temperatures of each glass layers. These were in good agreement. The simulations were done by applying the heat balance model [55], that accounts for 1-d heat conduction and assumes the surfaces as black bodies, and an optical model, for accounting the effects due to solar radiation. Supported by model results, and by comparing the sum of total heat loss in heating season and total heat gain in cooling season, it was concluded that the aerogel glazing systems were better suited for cold regions and hot-summer cold-winter regions. Another study by Leung et al. presented a similar study for applications in commercial buildings in Hong Kong [56]. There, two common simulation software packages, WINDOW and EnergyPlus, were applied to simulate the thermal and optical performance of aerogel glazing systems. In another study, Zheng and Zhou proposed an artificial neural network (ANN)-based machine learning (ML) model to optimize the thermal and optical performance of aerogel glazing systems [21]. The proposed ANN was found to be much faster and accurate than the traditional least squares (LSQ) curvefit methodology. The study presented an understanding of the heat transfer mechanism and solar radiation transmission of nanoporous aerogels together with an optimal design, which was shown to be significant for the promotion of green building with high energy performance.

16.3 Modeling the Mechanical Structure-Property Relationships of Aerogels

The mechanical structure-property relationships have been of interest to the aerogel community for a very long time, but a special interest in their modeling has exponentially increased in the past decade. Whenever the mechanical properties of aerogels have been discussed in the literature, their scaling relationships to their densities have been evaluated. These are similar to that of the solid thermal conductivity vs. density as discussed in Section 16.2.3. All porous materials show such scaling behavior, as their mechanical properties maximize with increasing density. The well-known scaling relations in porous materials are

$$E \propto \rho^{m},$$

$$\sigma \propto \rho^{s},$$

where E, σ, and ρ denote the Young's modulus, strength, and density of the aerogel, respectively. Considering the open-cell foam model, $m = 2$ [57]. However, for aerogel-like materials, those that show a random network connectivity, the relation is often found to be between 2 and 4 [58]. There are some exceptions, where exponents such as 1.8 have been reported [59]. This has been the case for aerogels that exhibit a foam-like appearance. Diverse attempts have been made to model the aerogel network structure and compare these relations with the experimentally obtained ones. To this end, all-atom simulations [60, 61], coarse-grained approaches [62, 63], and micro-mechanical ones [64, 65] have been exploited. In the following subsections, the simulations of aerogels using these approaches will be discussed.

16.3.1 All-Atom Simulations

An all-atom molecular dynamics-based modeling approach for silica aerogel-like materials was first proposed by means of negative pressure rupturing [66]. Fractal structures with very low density could be modeled. This approach was further extended to characterize the surface area, pore-size distributions, fractal dimensions, correlation lengths and mean particle sizes [60, 67]. The interparticle interactions were modeled based on the Vashishta potential, which includes two-body and three-body interactions [68]. Similar approaches have been used to model the structural and fractal characteristics of silica aerogels [69, 70]. In the past decade, there has been an interest in modeling the mechanical structure-property relationships of aerogels by means of MD simulations. Rivas Murillo et al. modeled aerogel simulation boxes by expanding single crystals of β-cristobalite to reach the desired density followed by a thermal treatment [71]. This process was chosen as it closely followed the diffusion-limited aggregation, which is often used to model aerogel structures and will be discussed later. Such a one-step expansion process was preferred over the gradual expansion used in the earlier approaches as described above. Here, since the atoms were initially set at distances larger than their equilibrium distances and had high kinetic energy, they diffused to farther regions in the simulation box and could potentially form any kind of structure. Apart from the characterization of their structural and fractal properties, the mechanical ones were also investigated. The simulation boxes were subjected to tension tests, where the speed of all atoms in the system was controlled by means of Langevin dynamics. The above-mentioned exponents m and s found to be 3.11 and 2.53, respectively. However, the inelastic properties such as the dissipated energy and residual deformation under cyclic loading were not investigated. Patil et al. further built up on this approach and modeled a much larger system of 192,000 atoms [61]. The model silica aerogels were subjected to large deformations under compression and tension, and the above-mentioned inelastic effects were studied in detail. In a subsequent study, the fracture properties of the aerogels, such as the fracture toughness (K_{IC}), strain energy release rate (G) and fracture strength were studied as functions of the crack length to height ratio [72]. An illustration of the notched model specimen is displayed in Figure 16.3a, with the corresponding stress-strain curves for different crack lengths shown in Figure 16.3b. In this study, systems of up to 5 million atoms were simulated, and the simulation results were compared with those from earlier experimental investigations [74]. It was found that not only E and σ, but also K_{IC} and G exhibit power-law relations with respect to the density of the aerogel. In this study, model sizes of up to 5.07 million atoms were studied. Using the Wolf BKS (van Beest, Kramer, and van Santen) potential [75], Gonçalves et al. investigated silica aerogel models with box sizes up to 7 million atoms making up a volume of up to $100^3\,\mathrm{nm}^3$ [76]. They showed that while silica aerogels belong to the large family of foams, they exhibit asymmetry in tension-compression that originates from the substantial preexisting compressive stress that ligaments are subjected to. This

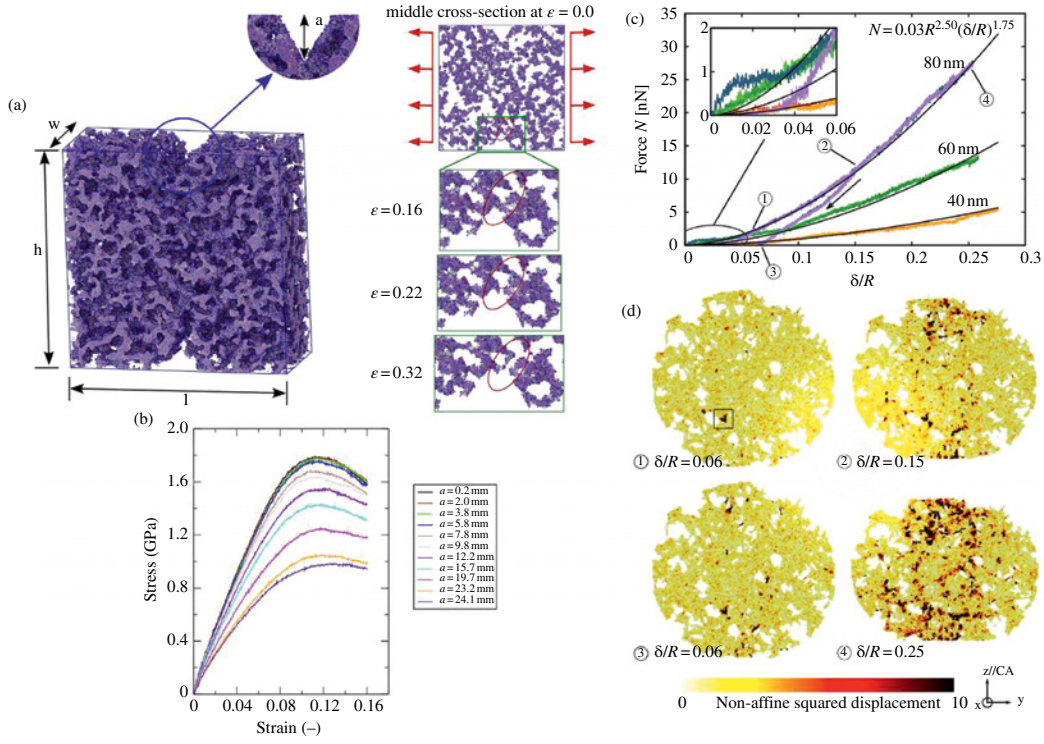


Figure 16.3 All-atom MD simulations of silica aerogels. (a) Notched 3D aerogel structure with insets showing the bond breakage under tensile loading, (b) stress-strain curves for notched silica aerogel models with varying crack lengths a (*Source:* Reprinted with permission from Elsevier, ref. [72]), (c) force-deflection curves from the compression of silica aerogel secondary particles, as simulated in MD, and (d) the visual representation of the nanocompression. *Source:* Reprinted with permission from Elsevier, ref. [73].

compressive stress in the core of ligaments arises from surface stress effects and facilitates plastic yielding of the aerogel in compression. They also investigated the pore-size distributions and compared those from the all-atom simulations with those found experimentally. In a particular case, good agreement was found. In another study, by combing MD simulations with the discrete element method (DEM), they investigated the behavior of a silica aerogel secondary particles with diameters 40–80 nm, under indentation (See Figure 16.3c,d) [73]. For low-density aerogels, the indentation force law did not scale with the square of the sphere size as in standard indentation theory but with an exponent of 2.5.

Silica aerogel composites have also been investigated by means of all-atom simulations. Patil et al. simulated the mechanical properties of glass fiber-reinforced silica aerogel composites under tension and compression [77]. In another study, they reported on the influence on the mechanical and fracture properties of aerogel composites by incorporating glass fibers, graphene sheets, and carbon nanotubes in silica aerogels [78]. The observed that the elastic modulus of the proposed glass fiber-, graphene sheet-, and carbon nanotube (CNT)-reinforced aerogel composites were 3.5, 9.5, and 11.5 times higher than that of the native silica aerogels, respectively. These results show the significance of reinforcement on the mechanical strengthening of silica aerogels. Recently, a multiscale model, supported by molecular dynamics simulations and constitute modeling, was presented to describe the multiscale behavior of fiber-reinforced silica aerogels [79].

Very recently, there has been an interest in modeling the mechanical properties of graphene aerogels by means of all-atom MD simulations. Qin et al. presented a detailed study on 3D porous graphene structures [80]. An adaptive intermolecular reactive empirical bond order (AIREBO) potential was used. The methodology was based on modeling graphene sheets and inducing porosities by inserting spherical inclusions. Porous graphene structures were shown to be 10 times stronger than steel at 4.6% of its density; however, their strength rapidly decreased with decreasing density. By modifying the method proposed in this work, Patil et al. modeled graphene aerogels and investigated their mechanical and fracture properties [81].

Thus, all-atom molecular dynamics simulations are shown to be a powerful tool in describing the mechanical structure-property relationships. With increasing availability of high-performance computing, larger aerogel models can be developed and simulated, such that the micro- and mesoporous network of the modeled aerogels can be well correlated to the experimental observations. Of special interest, would be the analysis of the pore-size distributions. These are currently estimated from the BJH model [82], which assumes cylindrical shape of the pores. If tools such as MD prove powerful enough to characterize the pore sizes at the micro- and meso-scale, it would result in significant enhancement in our understanding of the nanoporous-structure of aerogels.

16.3.2 Coarse-Grained Modeling

While all-atom simulations tend to be computationally very expensive, coarse graining appears to be a cheap alternative of simulating similar systems. The well-known diffusion-limited aggregation approach has been often discussed in the aerogel literature. Specifically, the DLCA model has been shown to mimic the sol-gel synthesis process of silica aerogels, which involves the formation of clusters by an assembly of small particles. Hasmy et al. reviewed several aggregation algorithms (exemplarily, structures generated from ballistic algorithms are shown in Figure 16.4a,b, while Figure 16.4c shows a transmission electron micrograph of a silica aerogel) and illustrated that the DLCA best interprets the structural features in silica aerogels, which was shown by correlating the shape of the experimental small angle neutron scattering (SANS) curve for large wavelength values with that as obtained from numerically characterizing the modeled aerogel structure [83, 85]. Moreover, the fractal

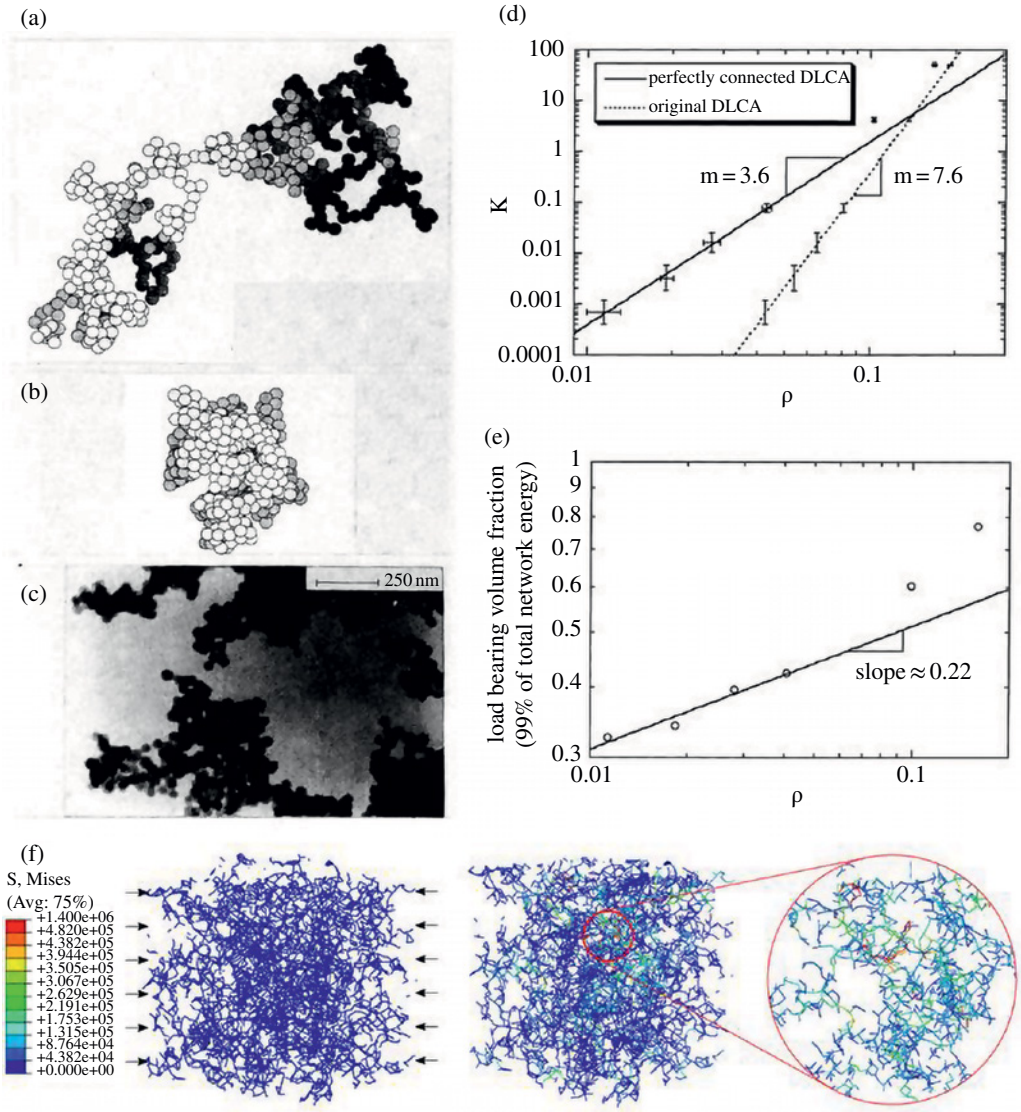


Figure 16.4 (a) and (b) Silica aerogel clusters as generated using the ballistic algorithms, (c) transmission electron microscopy image from a silica aerogel. *Source:* Reprinted with permission from ref. [83]. Copyright 1993 by the American Physical Society. (d) Bulk modulus vs. relative density plot from finite element method (FEM) simulations on DLCA aerogel structures and (e) the corresponding load-bearing volume fraction vs. relative density plot. *Source:* Reprinted with permission from Elsevier, ref. [63]. (f) Visualization of the stress distribution through the silica aerogel network showing mostly stress-free bonds along with a few load-bearing elements. *Source:* Reprinted with permission from ref. [84] Copyright (2021) American Chemical Society.

properties of aerogels, specifically the fractal dimension, were also studied. The results from these works were used as a motivation by Ma et al., who investigated the effect of dangling bonds, mass that is connected to the main backbone only by means of a single bond, on the structural and mechanical properties of silica aerogels [63]. To this end, a backbone algorithm [86] was developed to remove the dangling mass and model and simulate a perfectly connected network model of aerogels. Of a special

novelty, the DLCA modeled aerogel network was exported into a finite element program to simulate the mechanical properties. Accordingly, each particle in the model structure was exported as a rigid node, while the bonds between two particles were exported as beams. The beam theory accounts for three modes of deformation – namely, bending, stretching, and torsion. This agrees with the three modes of deformation from molecular mechanics. The aerogel representative volume element (RVE) was simulated under hydrostatic compression and the bulk modulus was characterized for different concentration of aerogel particles, thus, for their relative density. A scaling relation with an exponent 3.6 was obtained for a perfectly connected network structure (see Figure 16.4d). Of special interest, it was observed that despite the perfectly connected nature of the model, majority of the bonds were stress-free under deformation (see Figure 16.4e). Similar effects have been reported in colloidal materials [87, 88], which show the so-called backbone chain concept. A backbone chain represents the critical path that carries majority of the load in the aggregated network. Recently, experimental in-situ compression tests revealed similar observations in carbon aerogels [89]. This phenomenon in aerogels was subsequently studied by Ma et al. in their further investigations, together with the different modes of deformation affecting the stiffness in aerogels [90, 91]. Bending was shown to be the major mode of deformation, followed by torsion and tension/compression.

On similar lines, a modeling approach was recently implemented to characterize the fractal and mechanical properties in silica aerogels [84]. The effects of the morphological parameters, such as the density and particle size, on the fractal properties were investigated. The fractal properties showed a slight increase with increasing density, while they remained constant with changes to the particle size. Young's modulus was evaluated by simulating uniaxial compression of the aerogel RVEs in a finite element program. A scaling exponent of 3.61 was obtained. Of special interest, the backbone paths could be clearly visualized. Most of the bonds in the network remained stress-free (see Figure 16.4f). Although most of the above-mentioned approaches use a constant particle size, this can be easily changed, as was shown by Haard et al. [92], who modeled a log-normal distribution for the particle sizes in the model aerogel network.

In a different approach, a fiber-reinforced silica aerogel model was presented [93], where on the one hand, the silica aerogel network was modeled by means of the DLCA approach, and on the other hand, a fiber model using the embedded element technique (EET) was described. The EET model accounted for the fiber-fiber and fiber-matrix interactions. The mechanical behavior under tension was simulated using the finite element method and validated against the available experimental data from the literature. The effects of the volume fraction of fibers and the fiber curvature were analyzed. Interestingly, the primary particle diameter was shown to be significantly important parameter in the description of the mechanical properties. More specifically, aerogels with larger primary particle diameters were shown to exhibit a softer stress-strain curve, in comparison to the ones with smaller diameters.

Gelb employed a combinatorial approach by bringing hard-sphere-type coarse-graining together with Langevin dynamics to model silica aerogels with different densities and investigated the fractal and mechanical properties [62]. Such type of coarse-graining is also known as a flexible one, against the traditional hard-sphere approach. The inter-particle interactions were modeled by employing a weak nonbonding two-body potential of the shifted-center Lennard-Jones form, and a bonding potential defined by three terms, namely, a Morse-type stretching one, a bond-angle one, and a torsional displacement one. The proposed model further accounted for the damage in the network in terms of the bond breaking and bond creation. However, the proposed model underestimated the mechanical properties of the simulated aerogels.

These results were improved in their next study, where they characterized the pore-size distributions, as well as fractal and mechanical properties [94]. In this study, a larger system of up to

12,000-sol particles was modeled. The bulk modulus was shown to scale with the density with an exponent between 3.00 and 3.15. Tensile and compressive behavior of the modeled aerogels was further investigated in a subsequent paper [95]. The results from such coarse-grained simulations echoed the observations regarding the large number of stress-free paths under mechanical deformation presented in the previously described DLCA-FEM models [63, 84].

To summarize, coarse-graining has proven to be a computationally cheaper alternative to all-atom simulations, while being able to characterize properties similar to aerogel-like materials. While on the one hand the combination of hard-sphere aggregation models with FEM are likely to support investigations on the thermo-mechanical behavior of large-scale aerogel models to design particular architectures for given applications, the flexible approach on the other hand makes use of realistic inter-particle interactions, thus, making them closer to the qualities of all-atom simulations.

16.3.3 Micro-Mechanical Modeling

Constitutive models, based on either phenomenological or micro-mechanical approaches, generally describe the relationships between kinetic and kinematic quantities, for e.g. stress-strain, for a given material. Biopolymer aerogels show a foam-like appearance as the network is formed by three-dimensional interconnected fibers. Gibson and Ashby have shown that the mechanical properties of open-cellular materials are dictated by the mechanics of their pore walls, and these can be described by means of the beam theory [57]. Based on their work, Rege et al. proposed a micromechanical model based on the pore-wall kinematics to model the macroscopic mechanical behavior of cellulose aerogels [65]. Two different syntheses routes, using calcium thiocyanate and zinc chloride, respectively, were used to prepare and characterize the aerogels. The modeling approach assumed the aerogel network to be made of idealized square-shaped microcells, homogeneously distributed through the 3D network. The extended Euler-Bernoulli beam theory was used to capture the nonlinear effects [98, 99]. The model was described using the strain energy equation describing the kinematics of the pore walls (see Figure 16.5a). The different sizes of the microcells were accounted by means of the pore-size distributions. This was among the first models, to account for the pore-size distributions to model the mechanical properties of open-porous materials, thus illustrating the importance of the pore sizes. Other parameters in the model were the fiber diameter and the Young's modulus of the fibers, both of which were obtained from experimental analysis. The average diameter of the fibers (d_F) in the aerogel network is generally obtained from the Brunauer-Emmett-Teller (BET) specific surface area (S_{BET}) as [65, 100]:

$$d_F = \frac{4\varphi_s}{S_{BET}\rho_e},$$

where φ_s and ρ_e denote the solid fraction inside and the envelope density of the aerogel, respectively. The damage in the aerogel network was modeled based on the bending moment criteria for the fibers. The model showed an overall good agreement with the experimental data for different concentrations of both the aerogels. This model was further improved and extended and was shown to not only capture the mechanical properties and behavior of aerogels from cellulose but also those from pectin and k-carrageenan [101]. Recently, this modeling approach has also been applied to describe resorcinol–formaldehyde (RF) aerogels [102]. The simulated bulk properties were in very good agreement with the experimental data. In another study, the tensile behavior of

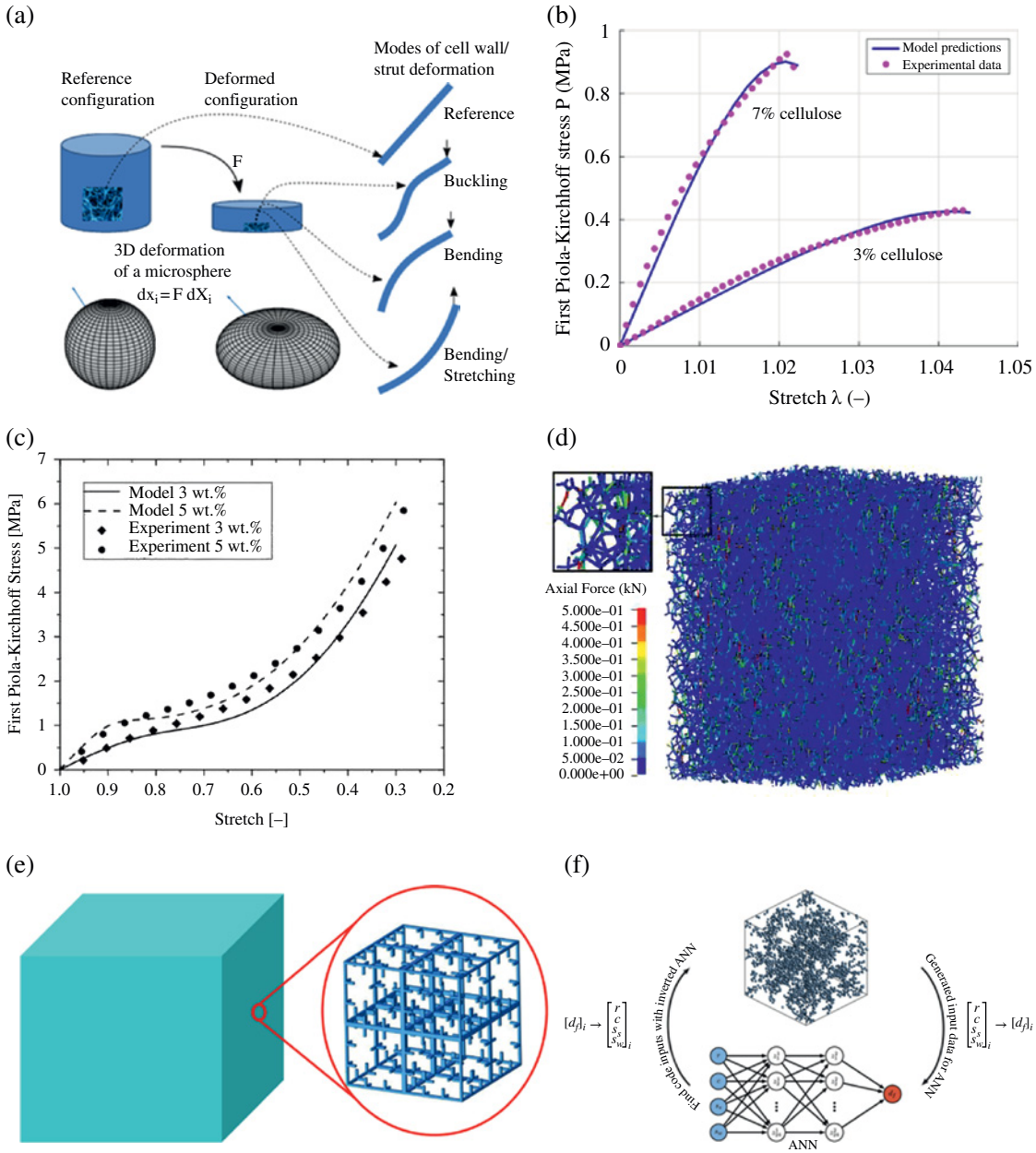


Figure 16.5 (a) Illustration of the pore-wall kinematics in aerogels. *Source:* Reprinted with permission from ref. [96]. Copyright (2021) by the American Physical Society. The predicted macroscopic stress-strain curves vs. experimental data of cellulose aerogels under (b) tension (*Source:* Reprinted with permission from ref. [96]) and (c) compression (*Source:* Reprinted with permission from ref. [97]). (d) 3D model network of κ-carrageenan aerogels in the deformed configurations. *Source:* Reprinted with permission from ref. [108]. (e) The 3D open-cell model from [64] describing the dangling bonds and their subsequent removal. *Source:* Reprinted with permission from ref. [64]. (f) The simulations of alginate aerogels from the bonded-particle-method describing the elasto-plastic material behavior. *Source:* Reprinted with permission from ref. [110].

cellulose aerogels was modeled [103]. In this work, the failure of the fibers was modeled based on the normal stress criterion, thus accounting for the bending as well as the axial stretching of the fibers. The model not only showed an overall good agreement with the experimental data, but also accurately predicted the onset of the macroscopic network failure of the aerogels (see Figure 16.5b). A more generalized form of this model, applicable to open-porous cellular materials, was recently reported [96]. However, the above-mentioned modeling approaches only accounted for the prediction of the linear-elastic range and the onset of pore collapse. Recently, it was shown that by accounting for strain energy from the collapsed pores, one can accurately describe the densification in aerogels [97]. This is illustrated in Figure 16.5c.

As with the thermal properties, there has also been a recent interest in the effect of humidity or moisture content on the mechanical behavior of biopolymer aerogels [50, 52]. The modeling approach presented in the above-mentioned works was shown to be capable of capturing the stiffening effect in alginate aerogels after being subject to wetting [51]. A theoretical assumption of decomposing the aerogel network into a swollen aerogel network and a hydrogel-like network was proposed. The model based on this ansatz was shown to be in very good agreement with the experimental data from alginate aerogels subject to different degrees of wetting. This theoretical ansatz was proven correct by a subsequent experimental characterization-based study using small-angle neutron scattering (SANS), liquid-state nuclear magnetic resonance (NMR) spectroscopy, and magic angle spinning (MAS) NMR spectroscopy, where the appearance of a clear hydrogel-like network could be observed [104]. Based on this report, a new modified modeling approach was subsequently proposed [105]. This shows the capability and flexibility of the model approach presented in [65] to be extendable to capturing the various aspects and properties of aerogels.

In another study, the pore walls were modeled as simple bars to numerically analyze the flexibility in organic aerogels [106]. They showed that the flexibility is inversely proportional to the envelope density of the aerogel and the length of the pore wall. Of course, such a simple expression can be applied to aerogels, which show a rather concentrated pore-size distribution, such that the mean pore width can be used to make interpretations of the aerogel's flexibility.

While such models have been shown to be accurate in the structure-property predictions of aerogels, a major challenge appears in describing the random pore shape of the aerogels. A recent study demonstrated the applicability of using Voronoi tessellations to model the porous fibrillar nanostructure of biopolymer aerogels [107]. In this approach, the pore-size distributions of cellulose aerogels were taken as inputs to generate 2D Voronoi tessellations adhering to these distributions. Periodic RVEs were generated, and the mechanical properties were simulated in a finite element package. The model results were qualitatively in agreement with the experimental data. A quantitative agreement could never have been obtained as the out-of-plane connectivity could not be accounted for. More recently, this approach was extended to describe the 3D network of the aerogels by combining two approaches, viz. random closed packing of polydisperse spheres and the Laguerre Voronoi tessellation [108]. The pore-size distribution and the relative density are the only required inputs to the model. Both can be obtained from experimental characterization. The modeling process is described as follows. A dense sphere pack is first generated, where the volume size distribution of the spheres adheres to the pore volume distribution of the corresponding aerogel. Voronoi tessellation is generated over the sphere pack and subsequently the spheres are removed leaving an open-porous fibrillar network. To introduce a cross-section to the fibers, the relative density is used as an input and a distribution of the fiber-diameters is obtained. The finally obtained network can be applied for investigating the mechanical or thermal properties of aerogels (see Figure 16.5d). The model was tested against the experimental data of κ-carrageenan aerogels,

and an excellent agreement was observed. It was also shown that the material response of such aerogels is isotropic. The above-mentioned modeling approach was also applied to study the influence of the pore sizes on the mechanical properties of open-porous materials in general [109]. It was concluded that while density remains a dictating factor for the mechanical properties, the pore sizes and the pore-wall morphology do have an influence as well. Such a modeling approach could in the future be used to design aerogels with network architectures better suited for tailored applications (e.g. scaffolds in tissue engineering). Furthermore, a bonded-particle-method was proposed to model the mechanical properties of alginate aerogels [110]. An elasto-plastic model was further considered within the discrete element model to characterize the damage in the aerogels. While the model could not capture the fibrillar nature of the aerogels, it was shown to be in good agreement with the mechanical response under cyclic loading of the aerogels, as well as that of the three-point bending test. Moreover, the plastic deformation and crack initiation and propagation could also be modeled (see Figure 16.5f).

With the advent of data-driven approaches, ML models are bound to play an important role in the materials development of aerogels. So far, there have not been many studies that have applied ML models for predicting or reconstructing aerogels and their properties. An ANN was recently developed to predict the fractal properties of silica aerogels based on the DLCA model parameters (see Figure 16.5(f)) [111]. An R^2 score of 0.973 could be obtained. A (guided) gradient descent-based inverse design approach was proposed to develop aerogel networks with target (fractal) properties. Such approaches of utilizing machine learning to develop fast models, either to predict the material properties or to optimize the aerogel model geometries, would enhance the digitization of the materials development, as well as provide new information for reverse engineering aerogel-like materials in the future.

16.4 Outlook

This chapter presented an overview on the developments in the theoretical investigations describing the thermal and mechanical properties of aerogels and aerogel composites. While there remains no doubt that the future of materials development would be driven by the successful combination of theoretical and experimental studies, it is important to develop physically motivated material models, such that a correlation between the model parameters and the synthesis parameters can be established. It was shown earlier that there have been several cases reported in the literature on the development of aerogels for thermal energy management applications driven by theoretical modeling. This presents a positive outlook toward achieving the same over a wide spectrum of applications.

With increasing reports on the application of aerogel-based materials for battery applications, and other electrical energy storage and management applications, there is a need to develop theoretical models that can support in a faster development of aerogels and aerogel composites for desired applications. Given the fractal or heterogeneous nature of the aerogel network, it is important to model the properties and behavior of the material at different scales, namely, from a quantum mechanical one up to a macroscopic one. It can be thus said that the future of theoretical modeling rests on the development of multiscale approaches. Also, with growing experimental and simulation data on aerogels and aerogel composites, it remains to be seen how data-driven modeling approaches, for e.g. machine learning-based models, can address the current challenges in the energy sector and drive the development of aerogels toward energy applications.

References

1 Smirnova, I. and Gurikov, P. (2017). Aerogels in chemical engineering: strategies toward tailor-made aerogels. *Annu. Rev. Chem. Biomol. Eng.* 8: 307–334.

2 Leventis, N., Sadekar, A., Chandrasekaran, N., and Sotiriou-Leventis, C. (2010). Click synthesis of monolithic silicon carbide aerogels from polyacrylonitrile-coated 3D silica networks. *Chem. Mater.* 22: 2790–2803.

3 Liebner, F., Aigner, N., Schimper, C. et al. (2012). Bacterial cellulose aerogels: from lightweight dietary food to functional materials. In: *ACS Symposium Series 1107: Functional Materials from Renewable Sources* (ed. F. Liebner and T. Rosenau), 57–74. ACS Publications.

4 US Energy Information Administration (2020). Monthly Energy Review.

5 Rousselot, M. (2018). Energy efficiency trends in buildings. *ODYSSEE-MURE Policy Brief*.

6 Feng, W., Zou, L., Gao, G. et al. (2016). Gasochromic smart window: optical and thermal properties, energy simulation and feasibility analysis. *Sol. Energy Mater. Sol. Cells* 144: 316–323.

7 Gelb, L. (2023). Simulation and modeling of aerogels using atomistic and mesoscale methods. In: *Springer Handbook of Aerogels* (ed. M.A. Aegerter, M.M. Koebel, N. Leventis, and S.A. Steiner), 273–288 Springer.

8 Rege, A. (2021). Modeling the structural, fractal and mechanical properties of aerogels. In: *Springer Handbook of Aerogels* (ed. M.A. Aegerter, M.M. Koebel, N. Leventis, and S.A. Steiner), 289–305 Springer.

9 Rege, A., Ratke, L., and Itskov, M. (2018). Chapter 8. Modelling and simulations of polysaccharide and protein based aerogels. In: *Biobased Aerogels* (ed. S. Thomas, L.A. Pothan, and R. Mavelil-Sam), 129–150. Royal Society of Chemistry.

10 Hrubesh, L.W. and Pekala, R.W. (1994). Thermal properties of organic and inorganic aerogels. *J. Mater. Res.* 9: 731–738.

11 Maleki, H., Durães, L., and Portugal, A. (2014). An overview on silica aerogels synthesis and different mechanical reinforcing strategies. *J. Non-Cryst. Solids* 385: 55–74.

12 Meador, M.A.B., Vivod, S.L., Mccorkle, L. et al. (2008). Reinforcing polymer cross-linked aerogels with carbon nanofibers. *J. Mater. Chem.* 18: 1843–1852.

13 Meador, M.A., Malow, E.J., Silva, R. et al. (2012). Mechanically strong, flexible polyimide aerogels cross-linked with aromatic triamine. *ACS Appl. Mater. Interfaces* 4: 536–544.

14 Rege, A., Voepel, P., Okumus, E. et al. (2019). Temperature-dependent stiffening and inelastic behavior of newly synthesized fiber-reinforced super flexible silica aerogels. *Materials* 12: 2878.

15 Schwan, M., Naikade, M., Raabe, D., and Ratke, L. (2015). From hard to rubber-like: mechanical properties of resorcinol–formaldehyde aerogels. *J. Mater. Sci.* 50: 5482–5493.

16 Buchtova, N., Pradille, C., Bouvard, J.-L., and Budtova, T. (2019). Mechanical properties of cellulose aerogels and cryogels. *Soft Matter* 15: 7901–7908.

17 Schestakow, M., Karadagli, I., and Ratke, L. (2016). Cellulose aerogels prepared from an aqueous zinc chloride salt hydrate melt. *Carbohydr. Polym.* 137: 642–649.

18 Qu, Z.G., Fu, Y.D., Liu, Y., and Zhou, L. (2018). Approach for predicting effective thermal conductivity of aerogel materials through a modified lattice Boltzmann method. *Appl. Therm. Eng.* 132: 730–739.

19 Lu, X., Caps, R., Fricke, J. et al. (1995). Correlation between structure and thermal conductivity of organic aerogels. *J. Non-Cryst. Solids* 188: 226–234.

20 Morthomas, J., Gonçalves, W., Perez, M. et al. (2019). A novel method to predict the thermal conductivity of nanoporous materials from atomistic simulations. *J. Non-Cryst. Solids* 516: 89–98.

21 Zheng, S. and Zhou, Y. (2019). Numerical study on the thermal and optical performances of an aerogel glazing system with the multivariable optimization using an advanced machine learning algorithm. *Adv. Theor. Simul.* 2: 1900092.

22 Dai, Y.-J., Tang, Y.-Q., Fang, W.-Z. et al. (2018). A theoretical model for the effective thermal conductivity of silica aerogel composites. *Appl. Therm. Eng.* 128: 1634–1645.

23 He, Y.-L. and Xie, T. (2015). Advances of thermal conductivity models of nanoscale silica aerogel insulation material. *Appl. Therm. Eng.* 81: 28–50.

24 Hoseini, A., Mccague, C., Andisheh-Tadbir, M., and Bahrami, M. (2016). Aerogel blankets: from mathematical modeling to material characterization and experimental analysis. *Int. J. Heat Mass Transfer* 93: 1124–1131.

25 Liu, H., Hu, M., Jiao, J., and Li, Z. (2020). Geometric optimization of aerogel composites for high temperature thermal insulation applications. *J. Non-Cryst. Solids* 547: 120306.

26 Zhao, J.-J., Duan, Y.-Y., Wang, X.-D., and Wang, B.-X. (2012). A 3-D numerical heat transfer model for silica aerogels based on the porous secondary nanoparticle aggregate structure. *J. Non-Cryst. Solids* 358: 1287–1297.

27 Zeng, S.Q., Hunt, A., and Greif, R. (1995). Transport properties of gas in silica aerogel. *J. Non-Cryst. Solids* 186: 264–270.

28 Kistler, S. (1932). The relation between heat conductivity and structure in silica aerogel. *J. Phys. Chem.* 39: 79–86.

29 Kaganer, M.G. (1969). *Thermal Insulation in Cryogenic Engineering*. Israel Program for Scientific Translations.

30 Bi, C., Tang, G.H., and Tao, W.Q. (2012). Prediction of the gaseous thermal conductivity in aerogels with non-uniform pore-size distribution. *J. Non-Cryst. Solids* 358: 3124–3128.

31 Reichenauer, G., Heinemann, U., and Ebert, H.P. (2007). Relationship between pore size and the gas pressure dependence of the gaseous thermal conductivity. *Colloids Surf., A* 300: 204–210.

32 Fricke, J., Lu, X., Wang, P. et al. (1992). Optimization of monolithic silica aerogel insulants. *Int. J. Heat Mass Transfer* 35: 2305–2309.

33 Chen, G. (2005). *Nanoscale Energy Transport and Conversion: A Parallel Treatment of Electrons, Molecules, Phonons, and Photons*. Oxford University Press.

34 Bi, C. and Tang, G.H. (2013). Effective thermal conductivity of the solid backbone of aerogel. *Int. J. Heat Mass Transfer* 64: 452–456.

35 Zhang, Z.M. (2007). *Nano/Microscale Heat Transfer*. Springer.

36 Dames, C. and Chen, G. (2004). Theoretical phonon thermal conductivity of Si/Ge superlattice nanowires. *J. Appl. Phys.* 95: 682–693.

37 Liu, Y. (2007). *Heat Transfer Mechanism and Thermal Design of Nanoporous Insulating Materials*. Beijing: School of Mechanical Engineering, University of Science and Technology Beijing.

38 Soorbaghi, F.P., Kokabi, M., and Bahramian, A.R. (2019). Predicting the effective thermal conductivity of silica/clay mineral nanocomposite aerogels. *Int. J. Heat Mass Transfer* 136: 899–910.

39 Tang, G.H., Bi, C., Zhao, Y., and Tao, W.Q. (2015). Thermal transport in nano-porous insulation of aerogel: factors, models and outlook. *Energy* 90: 701–721.

40 Groß, J., Schlief, T., and Fricke, J. (1993). Ultrasonic evaluation of elastic properties of silica aerogels. *Mater. Sci. Eng., A* 168: 235–238.

41 Chen, G. (1996). Nonlocal and nonequilibrium heat conduction in the vicinity of nanoparticles. *J. Heat Transfer* 118: 539–545.

42 Dan, D., Zhang, H., and Tao, W.-Q. (2014). Effective structure of aerogels and decomposed contributions of its thermal conductivity. *Appl. Therm. Eng.* 72: 2–9.

43 Chen, Y., Li, D., Xie, X.-Q. et al. (2020). Theoretical modeling and experimental validation for the effective thermal conductivity of moist silica aerogel. *Int. J. Heat Mass Transfer* 147: 118842.

44 Yang, J., Wu, H., Huang, G. et al. (2017). Modeling and coupling effect evaluation of thermal conductivity of ternary opacifier/fiber/aerogel composites for super-thermal insulation. *Mater. Des.* 133: 224–236.

45 Qu, M.-L., Tian, S.-Q., Fan, L.-W. et al. (2020). An experimental investigation and fractal modeling on the effective thermal conductivity of novel autoclaved aerated concrete (AAC)-based composites with silica aerogels (SA). *Appl. Therm. Eng.* 179: 115770.

46 Sierpinski, W. (1916). Sur une courbe cantorienne qui contient une image biunivoque et continue de toute courbe donnée. *CR Acad. Sci. Paris* 162: 629–632.

47 Han, Y.-F., Xia, X.-L., Tan, H.-P., and Liu, H.-D. (2013). Modeling of phonon heat transfer in spherical segment of silica aerogel grains. *Physica B* 420: 58–63.

48 Ankang, K. and Houde, H. (2013). Effective thermal conductivity of open cell polyurethane foam based on the fractal theory. *Adv. Mater. Sci. Eng.* 2013: 1–7.

49 Obori, M., Suh, D., Yamasaki, S. et al. (2019). Parametric model to analyze the components of the thermal conductivity of a cellulose-nanofibril aerogel. *Phys. Rev. Appl.* 11: 024044.

50 Antonyuk, S., Heinrich, S., Gurikov, P. et al. (2015). Influence of coating and wetting on the mechanical behaviour of highly porous cylindrical aerogel particles. *Powder Technol.* 285: 34–43.

51 Rege, A., Ratke, L., Külcü, İ.D., and Gurikov, P. (2020). Stiffening of biopolymer aerogel networks upon wetting: a model-based study. *J. Non-Cryst. Solids* 531: 119859.

52 Santos-Rosales, V., Alvarez-Rivera, G., Hillgärtner, M. et al. (2020). Stability studies of starch aerogel formulations for biomedical applications. *Biomacromolecules* 21: 5336–5344.

53 Hoseini, A. and Bahrami, M. (2017). Effects of humidity on thermal performance of aerogel insulation blankets. *J. Build. Eng.* 13: 118842 107–118842 115.

54 Chen, Y., Xiao, Y., Zheng, S. et al. (2018). Dynamic heat transfer model and applicability evaluation of aerogel glazing system in various climates of China. *Energy* 163: 1115–1124.

55 Zanghirella, F., Perino, M., and Serra, V. (2011). A numerical model to evaluate the thermal behaviour of active transparent façades. *Energy Build.* 43: 1123–1138.

56 Leung, C.K., Lu, L., Liu, Y. et al. (2020). Optimal and thermal performance analysis of aerogel glazing technology in a commercial building of Hong Kong. *Energy and Built Environment* 1: 215–223.

57 Gibson, L.J. and Ashby, M.F. (1999). *Cellular Solids: Structure and Properties*. Cambridge University Press.

58 Groß, J. and Fricke, J. (1995). Scaling of elastic properties in highly porous nanostructured aerogels. *Nanostruct. Mater.* 6: 905–908.

59 Zhao, S., Malfait, W.J., Guerrero-Alburquerque, N. et al. (2018). Biopolymer aerogels and foams: chemistry, properties, and applications. *Angew. Chem. Int. Ed.* 57: 7850–7608.

60 Nakano, A., Bi, L., Kalia, R.K., and Vashishta, P. (1993). Structural correlations in porous silica: molecular dynamics simulation on a parallel computer. *Phys. Rev. Lett.* 71: 85–88.

61 Patil, S.P., Rege, A., Sagardas et al. (2017). Mechanics of nanostructured porous silica aerogel resulting from molecular dynamics simulations. *J. Phys. Chem. B* 121: 5660–5668.

62 Gelb, L.D. (2007). Simulating silica aerogels with a coarse-grained flexible model and Langevin dynamics. *J. Phys. Chem. C* 111: 15792–15802.

63 Ma, H.-S., Roberts, A.P., Prévost, J.-H. et al. (2000). Mechanical structure-property relationship of aerogels. *J. Non-Cryst. Solids* 277: 127–141.

64 Lei, J. and Liu, Z. (2018). A novel constitutive model for the mechanical properties of silica aerogels. *J. Appl. Phys.* 124: 025102.

65 Rege, A., Schestakow, M., Karadagli, I. et al. (2016). Micro-mechanical modelling of cellulose aerogels from molten salt hydrates. *Soft Matter* 12: 7079–7088.

66 Kieffer, J. and Angell, A. (1988). Generation of fractal structures by negative pressure rupturing of SiO_2 glass. *J. Non-Cryst. Solids* 106: 336–342.

67 Nakano, A., Bi, L., Kalia, R.K., and Vashishta, P. (1994). Molecular-dynamics study of the structural correlation of porous silica with use of a parallel computer. *Phys. Rev. B: Condens. Matter* 49: 9441–9452.

68 Vashishta, P., Kalia, R.K., Rino, J.P., and Ebbsjö, I. (1990). Interaction potential for SiO_2: a molecular-dynamics study of structural correlations. *Phys. Rev. B* 41: 12197.

69 Bhattacharya, S. and Kieffer, J. (2005). Fractal dimensions of silica gels generated using reactive molecular dynamics simulations. *J. Chem. Phys.* 122: 094715.

70 Pohl, P.I., Faulon, J.-L., and Smith, D.M. (1995). Molecular dynamics computer simulations of silica aerogels. *J. Non-Cryst. Solids* 186: 349–355.

71 Rivas Murillo, J.S., Bachlechner, M.E., Campo, F.A., and Barbero, E.J. (2010). Structure and mechanical properties of silica aerogels and xerogels modeled by molecular dynamics simulation. *J. Non-Cryst. Solids* 356: 1325–1331.

72 Patil, S.P., Rege, A., Itskov, M., and Markert, B. (2018). Fracture of silica aerogels: an all-atom simulation study. *J. Non-Cryst. Solids* 498: 125–129.

73 Gonçalves, W., Amodeo, J., Morthomas, J. et al. (2018). Nanocompression of secondary particles of silica aerogel. *Scr. Mater.* 157: 157–161.

74 Phalippou, J., Woignier, T., and Rogier, R. (1989). Fracture toughness of silica aerogels. *Le Journal de Physique Colloques* 50: C4-191–C4-196.

75 Carré, A., Berthier, L., Horbach, J. et al. (2007). Amorphous silica modeled with truncated and screened Coulomb interactions: a molecular dynamics simulation study. *J. Chem. Phys.* 127: 114512.

76 Gonçalves, W., Morthomas, J., Chantrenne, P. et al. (2018). Elasticity and strength of silica aerogels: a molecular dynamics study on large volumes. *Acta Mater.* 145: 165–174.

77 Patil, S.P., Shendye, P., and Markert, B. (2020). Mechanical properties and behavior of glass fiber-reinforced silica aerogel nanocomposites: insights from all-atom simulations. *Scr. Mater.* 177: 65–68.

78 Patil, S.P., Shendye, P., and Markert, B. (2020). Molecular dynamics simulations of silica aerogel nanocomposites reinforced by glass fibers, graphene sheets and carbon nanotubes: a comparison study on mechanical properties. *Compos. Part B* 190: 107884.

79 Rege, A. and Patil, S.P. (2020). On the molecular to continuum modeling of fiber-reinforced composites. *Adv. Theor. Simul.* 3: 1900211.

80 Qin, Z., Jung, G.S., Kang, M.J., and Buehler, M.J. (2017). The mechanics and design of a lightweight three-dimensional graphene assembly. *Sci. Adv.* 3: e1601536.

81 Patil, S.P., Shendye, P., and Markert, B. (2020). Molecular investigation of mechanical properties and fracture behavior of graphene aerogel. *J. Phys. Chem. B* 124: 6132–6139.

82 Barrett, E.P., Joyner, L.G., and Halenda, P.P. (1951). The determination of pore volume and area distributions in porous substances. I. Computations from nitrogen isotherms. *J. Am. Chem. Soc.* 73: 373–380.

83 Hasmy, A., Foret, M., Pelous, J., and Jullien, R. (1993). Small-angle neutron-scattering investigation of short-range correlations in fractal aerogels: simulations and experiments. *Phys. Rev. B: Condens. Matter* 48: 9345–9353.

84 Abdusalamov, R., Scherdel, C., Itskov, M. et al. (2021). Modeling and simulation of the aggregation and the structural and mechanical properties of silica aerogels. *J. Phys. Chem. B* 125: 1944–1950.

85 Hasmy, A., Anglaret, E., Foret, M. et al. (1994). Small-angle neutron-scattering investigation of long-range correlations in silica aerogels: simulations and experiments. *Phys. Rev. B* 50: 6006–6016.

86 Herrmann, H.J., Hong, D., and Stanley, H. (1984). Backbone and elastic backbone of percolation clusters obtained by the new method of 'burning'. *J. Phys. A: Math. Gen.* 17: L261.

87 Dargazany, R., Rege, A., and Itskov, M. (2013). Elasticity of colloidal clusters with application to carbon-black aggregates in filled rubbers. In: *Constitutive Models for Rubber VIII* (ed. N. Gil-Negrete and A. Alonso), 261–266. CRC Press.

88 Dinsmore, A.D., Prasad, V., Wong, I.Y., and Weitz, D.A. (2006). Microscopic structure and elasticity of weakly aggregated colloidal gels. *Phys. Rev. Lett.* 96: 185502.

89 Rege, A., Schwan, M., Chernova, L. et al. (2020). Microstructural and mechanical characterization of carbon aerogels: an *in-situ* and digital image correlation-based analysis. *J. Non-Cryst. Solids* 529: 119568.

90 Ma, H.-S., Prévost, J.-H., Jullien, R., and Scherer, G.W. (2001). Computer simulation of mechanical structure-property. *J. Non-Cryst. Solids* 285: 216–221.

91 Ma, H.-S., Prévost, J.-H., and Scherer, G.W. (2002). Elasticity of DLCA model gels with loops. *Int. J. Solids Struct.* 39: 4605–4614.

92 Haard, T.M., Gervais, G., Nomura, R., and Halpern, W.P. (2000). The pathlength distribution of simulated aerogels. *Physica B* 284–288: 289–290.

93 Lu, Z., Yuan, Z., Liu, Q. et al. (2015). Multi-scale simulation of the tensile properties of fiber-reinforced silica aerogel composites. *Mater. Sci. Eng., A* 625: 278–287.

94 Ferreiro-Rangel, C.A. and Gelb, L.D. (2013). Investigation of the bulk modulus of silica aerogel using molecular dynamics simulations of a coarse-grained model. *J. Phys. Chem. B* 117: 7095–7105.

95 Ferreiro-Rangel, C.A. and Gelb, L.D. (2015). Computational study of uniaxial deformations in silica aerogel using a coarse-grained model. *J. Phys. Chem. B* 119: 8640–8650.

96 Rege, A., Aney, S., and Milow, B. (2021). Influence of pore-size distributions and pore-wall mechanics on the mechanical behavior of cellular solids like aerogels. *Phys. Rev. E* 103: 043001.

97 Rege, A. (2021). Constitutive modeling of the densification behavior in open-porous cellular solids. *Materials* 14: 2731.

98 Bisshopp, K. and Drucker, D. (1945). Large deflection of cantilever beams. *Q. Appl. Math.* 3: 272–275.

99 Chen, L. (2010). An integral approach for large deflection cantilever beams. *Int. J. Non-Linear Mech.* 45: 301–305.

100 Ganesan, K. and Ratke, L. (2014). Facile preparation of monolithic kappa-carrageenan aerogels. *Soft Matter* 10: 3218–3224.

101 Rege, A., Preibisch, I., Schestakow, M. et al. (2018). Correlating synthesis parameters to morphological entities: predictive modeling of biopolymer aerogels. *Materials* 11: 1670.

102 Aney, S., Schettler, J., Schwan, M. et al. (2022). Insights into the micromechanics of organic aerogels based on experimental and modeling results. *Adv. Eng. Mater.* 24: 2100095.

103 Rege, A. and Itskov, M. (2018). A microcell-based constitutive modeling of cellulose aerogels under tension. *Acta Mech.* 229: 585–593.

104 Forgacs, A., Papp, V., Paul, G. et al. (2021). Mechanism of hydration and hydration induced structural changes of calcium alginate aerogel. *ACS Appl. Mater. Interfaces* 13: 2997–3010.

105 Külcü, İ.D. and Rege, A. (2021). Physics-informed constitutive modelling of hydrated biopolymer aerogel networks. *Soft Matter* 17: 5278–5283.

106 Schwan, M., Tannert, R., and Ratke, L. (2016). New soft and spongy resorcinol–formaldehyde aerogels. *J. Supercrit. Fluids* 107: 201–208.

107 Rege, A., Hillgärtner, M., and Itskov, M. (2019). Mechanics of biopolymer aerogels based on microstructures generated from 2-d Voronoi tessellations. *J. Supercrit. Fluids* 151: 24–29.

108 Chandrasekaran, R., Hillgärtner, M., Ganesan, K. et al. (2021). Computational design of biopolymer aerogels and predictive modelling of their nanostructure and mechanical behaviour. *Sci. Rep.* 11: 10198.

109 Aney, S. and Rege, A. (2023). The effect of pore sizes on the elastic behaviour of open-porous cellular materials. *Math. Mech. Solids* 28: 1624–1634.

110 Dosta, M., Jarolin, K., and Gurikov, P. (2019). Modelling of mechanical behavior of biopolymer alginate aerogels using the bonded-particle model. *Molecules* 24: 2543.

111 Abdusalamov, R., Pandit, P., Milow, B. et al. (2021). Machine learning-based structure-property predictions in silica aerogels. *Soft Matter* 17: 7350–7358.

17

Aerogels in Energy: State of Art and New Challenges

Golnoosh Abdeali and Ahmad Reza Bahramian

Polymer Engineering Department, Faculty of Chemical Engineering, Tarbiat Modares University, P.O. Box 14115-143, Tehran, Iran

17.1 Introduction

Aerogels are three-dimensional network structures, constructed via nanoparticles connection which have drawn a great deal of research attention in recent years cause of their remarkable and unique microstructural characteristics including super low thermal conductivity (0.013 W/m·K at room temperature and atmospheric pressure), ultra-high porosity (up to 99%), and high specific surface area (up to 3,000 m^2/g), which is the main source of a wide range of potential applications [1]. Moreover, high population growth rates, combined with increasing per capita energy consumption in different countries, are causing an increase in global demand for thermal and electrical energy. Increased energy production to meet this demand is resulting in higher energy prices, increased greenhouse gases emissions, and a deterioration of environment as a result of increased fossil fuel usage. This has prompted the push for more renewable energy sources, energy consumption reductions, or both [2]. The attempts to develop systems with more efficient energy have focused on materials improvement along with unique and novel devices development with enhanced thermal and electrical characteristics. Energy performance from nanostructured, highly porous lightweight materials is particularly dependent on porous structure, which is, in turn, determined by the synthesis condition and process, type, and amount of reaction components as well as drying procedure. Consequently, energy transfer mechanism understanding, challenges, and outlooks in porous media as aerogel is pivotal for various types of materials development with energy saving approach [3, 4].

17.2 Aerogel in Thermal and Electrical Energy

17.2.1 Thermal Energy

Heat can be transferred in porous materials through three principle mechanisms of conduction, convection, and radiation(Figure 17.1). In conduction heat transfer mechanism, heat transfer is attained via electronic conduction along with phonon conduction of solid porous media matrix (k_s)

Aerogels for Energy Saving and Storage, First Edition. Edited by Meldin Mathew, Hanna J. Maria, Ange Nzihou, and Sabu Thomas.
© 2024 John Wiley & Sons, Inc. Published 2024 by John Wiley & Sons, Inc.

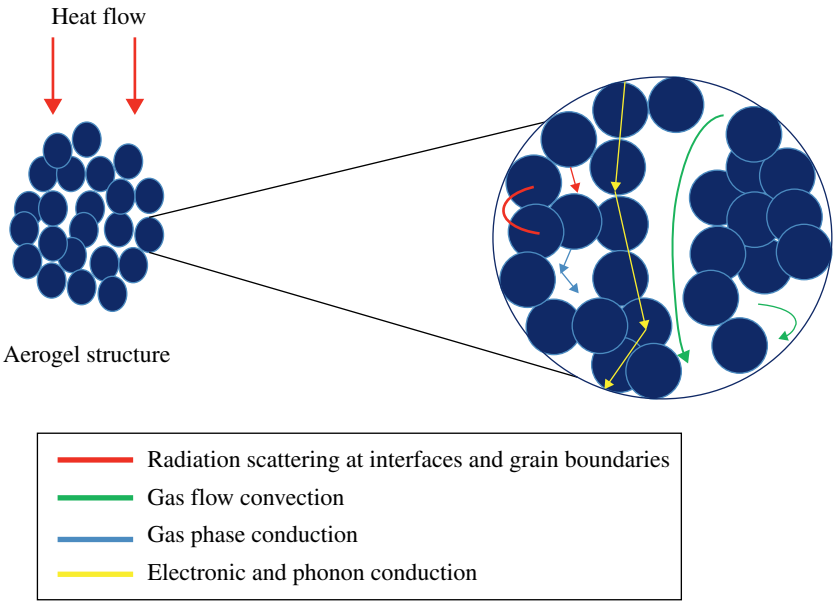


Figure 17.1 Heat transfer mechanisms in porous materials such as aerogel [5].

in addition to gas phase conduction, which takes place due to gas molecules existence in aerogel pores. Hence, thermal conductivity of gas phase (k_g) [6, 7] is estimated as follows:

$$k_g = \frac{k_g^0 V_g}{\left(1 + \beta K_n\right)} \tag{17.1}$$

which β represents energy transfer between gas molecules and aerogel solid matrix over molecules collisions (approximately 2 for aerogels) and V_g is volume fraction of voids. Furthermore, K_n, is the Knudsen number, which is determined using mean free path of gas molecules (l_g) and corresponding pore diameter (φ) [8] and is calculated via Eq. (17.2):

$$K_n = \frac{l_g}{\varphi} \tag{17.2}$$

The Knudsen effect is mainly responsible for lower thermal conductivities of porous material, including silica aerogels [9]. However, because aerogels have such a fine pore size, gas molecule suppression within pores occurs and in fact, there is no convection heat transfer in porous medias. Moreover, aerogels heat transfer by radiation is originated by scattering from grain boundaries and interfaces and is mainly persuaded by absorption and reemission in porous material. Thus, it becomes dominant primarily at high temperatures [5, 10].

17.2.2 Electrical Energy

Porous nanomaterials applicability is basically dependent on aerogel intended structure design at molecular and atomic level, which controls porosity and specific surface area and as a result, energy perspective. In addition, pores in nanometer-size can be utilized to impregnate conductive nanoparticles/ions to create multifunctional hybrids of practical and scientific interests. That is why nanoporous materials (such as graphene, carbon nanotube (CNT), carbon and conductive polymer

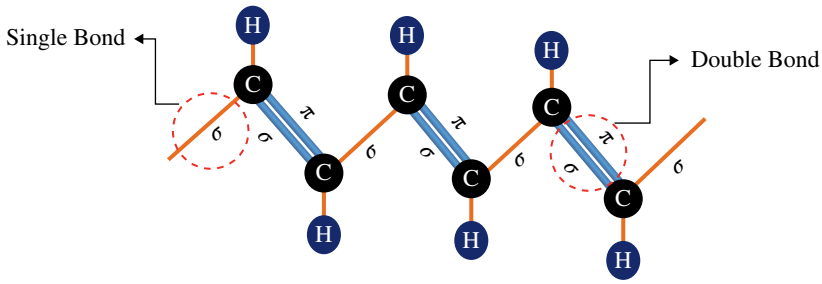


Figure 17.2 Schematic of single and double bonds in conductive structure: the backbone contains conjugated double bonds [11].

composite aerogels) are well known to be useful technologically for a wide range of electrical energy applications such as fuel cells, solar cells, batteries, supercapacitors, sensor, and optical, electronic, and magnetic devices. Aerogels electrical conductivity is as could be expected to be low because solid structure with tenuous properties provides poor conduction paths and number of charge carriers (Figure 17.2) [12]. Moreover, volume resistivity is presumed to be high for the same reason. Therefore, by adding conductive nanoparticle to aerogel microstructure, the principle mechanism in electrical energy transfer will be due to conjugated single and double bonds presence along aerogel parallel to nanoparticle skeleton. Both single and double bonds consist of a localized σ-bond, which forms a strong chemical bond. Additionally, each double bond also contains a localized π-bond, which is much weaker. The π bond between first and second carbon atoms is transferred to position between second and third carbon atoms. In turn, the π bond between the third and fourth carbon transfers to the next carbon, and so on. Consequently, electrons in double bonds move along a carbon chain and as a result, conjugated double bonds allow electric flow to induce electron transfer between medium bonds in aerogel medium, which produces large amount of electrical conductivity [11].

In addition, nano dimension and super high porosity in a porous media are also responsible for outstanding dielectric characteristics. Aerogels dielectric properties are dominated by large volume fraction of trapped gas in pores and adsorbed molecules on the abundant surfaces in high concentration. This has been verified by various measurements for dielectric properties linear change with aerogel density and large effect on aforementioned properties attributed to adsorbed water. The dielectric strength of aerogels is also expected to be a high cause of high-volume resistivity and also because of nanosized pores, which confine charge carriers to spaces that are about the same size as the mean free path for collisions. These properties show that aerogels are exceptional dielectric materials and indicate that they can be utilized for many interesting applications through further modification.

To conclude, it could be declared that aerogels are kind of 3D porous media with great intrinsic thermal properties as a result of porous structure as well as weak properties such as low electrical conductivity and dielectric properties, which could be improved by further modification using conductive structures along with aerogel microstructures to achieve high and improved electrical and thermal insulation ability [13].

17.2.3 Design and Manufacture

As depicted in Figure 17.3, aerogels can be produced via various methods (Table 17.1) and are examined in two different categories as single-component and composite aerogels. Single-component aerogels include oxide (silica and nonsilica), organic (resin and cellulose based),

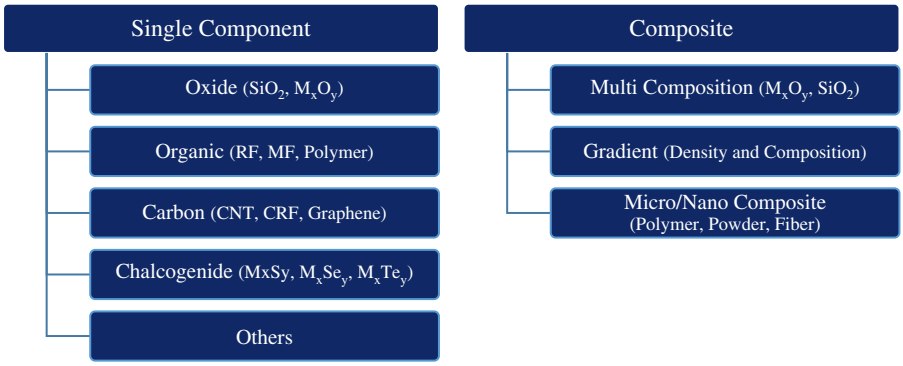


Figure 17.3 Aerogel categories as single and composite structures [14].

Table 17.1 Common procedures for aerogel production.

Aerogel fabrication method	Description
Sol-Gel	Most common technique
	Particles are cross-linked and combined with a compatible gel
	Condensation reaction
	Gelation will happen by sol pH or temperature changing [15]
Self-assembly	Large and complex structured systems synthesizing at a macroscopic level (0-D, 1-D, 2-D)
	Common for such as CdSe, CdS, ZnS, PbS, and carbonitride aerogels fabrication [16]
	Aerogel product has photophysical properties and high crystallinity
	Aerogels preparation could be done for various functional applications [17]
Emulsion	Preparation of dispersed phase by sol-gel process and emulsification in a continuous phase
	Synthesizing aerogels in microspherical form by maintaining the internal structural properties identical to that of monolithic aerogels
	Synthesizing microspherical particles of both inorganic (SiO_2) and polymeric aerogels (Starch, Alginate) [18]
	Energy conversion and drug delivery applications due to microspherical particles [19]
3-D printing	Hybrid modern technology evolved for the fabrication extremely lightweight 3D porous nanostructures
	Assembling building blocks layer by layer in accordance with structure virtual model
	Beneficial for production of composite and polymeric aerogels
	Synthesizing cellulose nanocrystal based aerogels with a dual pore structure [20]
	Diverse nanostructures fabrication such as octet cube, pyramid, and honeycomb type [21]

carbon (carbonized plastic, CNT, and graphene), chalcogenide and other aerogels (single element, carbide), while composite aerogels can be classified as multicomponent, gradient, and micro/nano aerogel [14].

Various design and manufacture process adopted for synthesizing aforementioned aerogel nanostructures, which are summarized as follows:

As previously discussed, to get deep understanding of aerogel's thermal energy applications including major aspects of thermal and electrical energy, the main focus is on synthesis of conductive (electrical view) and insulated (thermal view) aerogels and in particular carbon based ones. Generally, there are three main procedures for carbon-based aerogels production:

A) Carbonization
B) Carbothermal reduction
C) Aerogel modification using carbon-based additives

which are introduced as follows:

17.2.3.1 Carbonization Process

To induce energy (thermal, electrical) properties to fabricated aerogels, carbon aerogel must be provided through polymeric aerogel carbonization process (Figure 17.4). This procedure will be carried out after aerogel is produced by exposing fabricated aerogels to high temperatures up to 600 °C and ambient pressure in Ar gas environment or N_2 [23, 24] with main purpose of oxygen decomposition and hydrogen moieties in microstructure polymeric chain and polymeric chain replacing with carbon moieties [22].

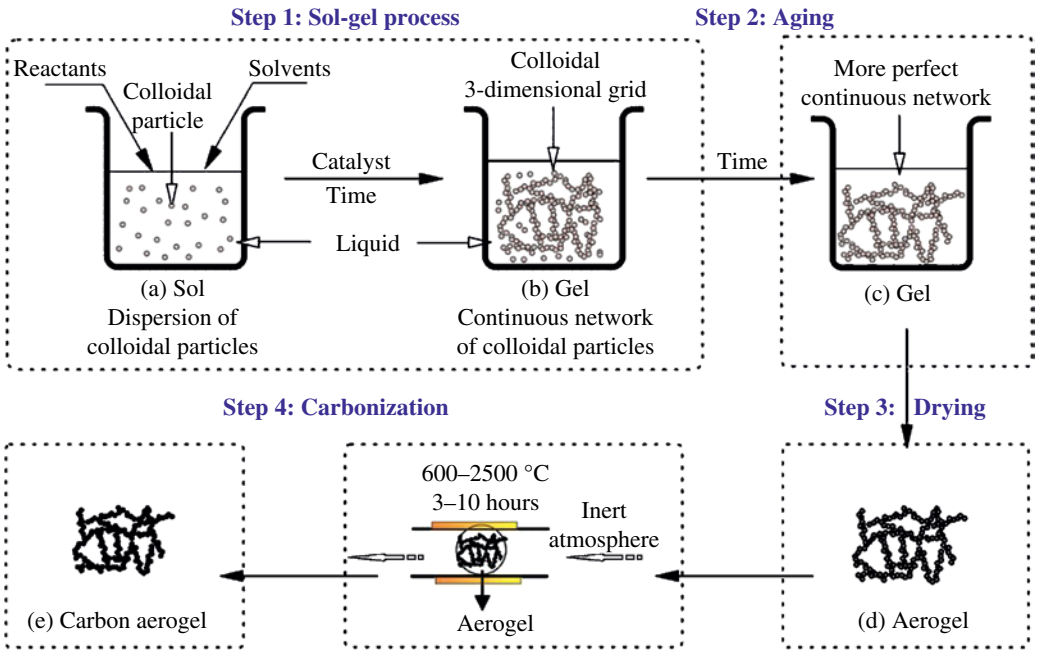


Figure 17.4 Carbonization process for polymeric aerogel [22].

17.2.3.2 Carbothermal Reduction

For particular applications, monolithic SiC composite aerogels with porous structure are considered as most adequate and advance component for presenting better physicochemical, mechanical, and thermal properties than single carbon aerogel, which are fabricated via carbonization or other type of polymeric aerogel, which could be provided by another additional procedure named silica carbothermal reduction in addition to carbon [25]. This process is executed at high temperatures; so that SiC products will have prepared in different forms such as whisker and fiber from binary precursor of carbon-silica composite. In order to produce high-porous monolithic structure, carbothermal reduction process can be used for polymer cross-linked silica aerogel as a base material, including polyacrylonitrile or RF-cross-linked silica aerogels potentially retaining textural properties as original. Carbothermal reduction process generally enhances aerogel thermal stability up to 650 °C, but a specific and crucial side effect is sharp reduction of specific surface area. Therefore, this process can be an alternative choice to produce advanced material of SiC aerogels [26, 27].

$$SiO_2 + 3C \rightarrow SiC + 2CO \tag{17.3}$$

17.2.3.3 Aerogel Modification Using Carbon-Based Additives

Carbon aerogels are a unique kind of high-surface-area materials, which generally are fabricated via sol-gel chemistry. Their high electrical conductivity and specific surface area, environmental compatibility make them promising components for many applications. As previously discussed, however, organic aerogels carbonization continues to be a common and useful technique, many procedures now use highly sp^2 hybridized carbon nanomaterials suspensions such as carbon nanotubes (CNTs), graphene, or graphene oxide in synthesis process (Figure 17.5) [28].

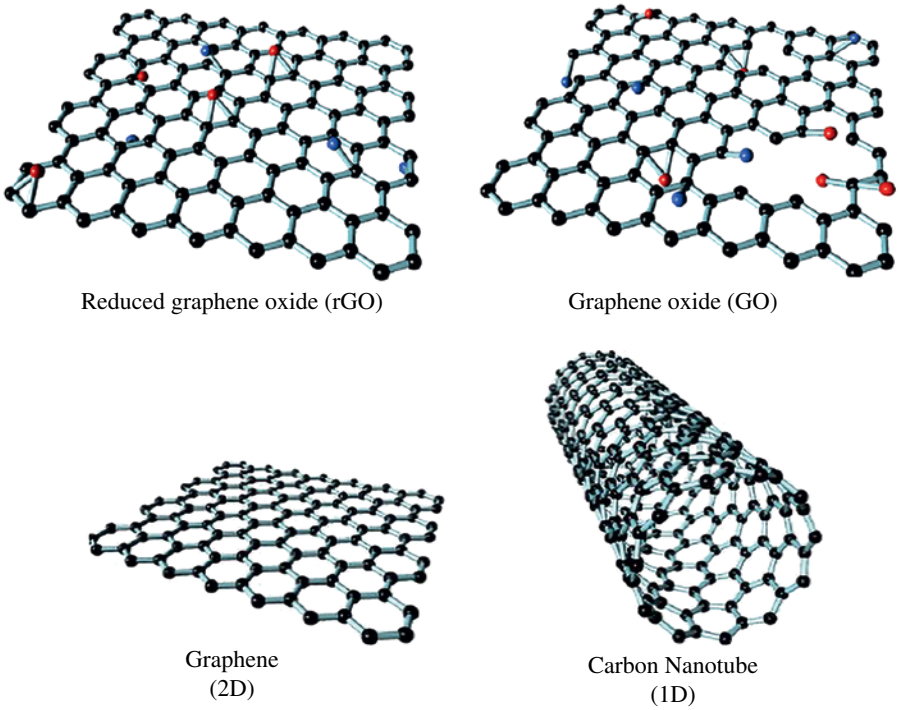


Figure 17.5 Carbon-based structures (colored part are oxide groups) [28].

These routes include freeze-drying utilization for carbon suspensions to form carbon-based aerogels, held together primarily by van der Waals forces as well as sol-gel processes that give aerogels with covalently cross-linked bonds. In the latter case, sp^2 hybridized carbon concentration in suspension and organic gel precursor can be tuned in such a way that organic particles primarily nucleate on sp^2 hybridized carbons surface. For this reason, these organic particles particularly serve to covalently cross-link sp^2 hybridized carbons with highly conductive, mechanically robust sp^2 carbon bridges after carbonization. These aerogels no longer formed of a 3D network of amorphous carbon nanoparticles, but 3D CNTs or graphene networks. Though several methods have been experimented to fabricate CNT and graphene aerogels [29, 30].

17.2.3.3.1 CNT-based Aerogels CNT aerogels were proved to be the stiffest low-density solid reported and were also extremely elastic. One of the critical features in CNT-based aerogels design is binder or "glue" selection, a which is utilized to reinforce low-density structures. These materials were assembled using covalent carbon cross-links formation between CNT bundles through organic sol-gel chemistry [31]. Organic sol chemistry involves organic precursors polymerization to form a highly cross-linked organic gel, which can then be dried and pyrolyzed (thermal treatment) to form a carbon aerogel. When the organic precursors are added to a CNTs suspension, polymerization will occur primarily on CNTs surface. Both will coat bundles and form junctions between adjacent bundles [32]. After drying and pyrolysis, organic coating and junctions will be converted to carbon and will yield CNT aerogels (Figure 17.6). The utilization of sol-gel–derived carbon to cross-link CNTs offers a good chance to enhance network architecture mechanical properties while maintaining bulk electrical conductivity. This technique could be used to prepare a new class of ultralow-density (as low as ~10 mg cm^3) nanoporous monoliths made of single-walled carbon nanotubes (SWNT) of macroscopic dimensions with unprecedented properties. These CNT aerogels could be fabricated via highly purified SWNT as tubes have a number of acid functionalization, allowing them to be readily suspended in water by sonication assistance without specific surfactants or other additives that are typically required for CNTs dispersion in aqueous media [34]. Moreover, for CNT network reinforcement, organic sol-gel could be used as a suitable process to form carbonaceous interconnections between CNTs.

With this approach, a series of monolithic SWNT-carbon aerogels with CNT content ranging from low to high wt.% (relative to the carbon binder) could be prepared. Interestingly, the densities of CNT monoliths will be decreased with CNT content increase as a consequence of smaller volumetric parts shrinkage during both supercritical drying and pyrolysis step. Furthermore, investigations have shown that using CNT in aerogel microstructures will lead to high electrical conductivity [31]. In more detail, electrical conductivity could be about three times larger for aerogels that contain 5 wt.% CNTs than for neat aerogels of same density, denoting that network struts effective conductivity, σ_{strut}, increases with increasing CNT loading [33, 35]

17.2.3.3.2 CNT-based Aerogel Composites One advantageous application of CNT aerogels is the preparation of conductive composite materials. Great effort has been concentrated on methods to disperse CNTs into target matrix medium, with moderate success. Efficient CNTs dispersion is remarkably challenging and requires specific functionalization of CNTs for several times, which can be expensive, time-consuming, complex, and not generally applicable. In contrast, ultralight and tough CNT aerogels can serve as scaffolds for the preparation of novel CNT composites. As the CNT network is already determined, aerogel can simply be impregnated through capillary

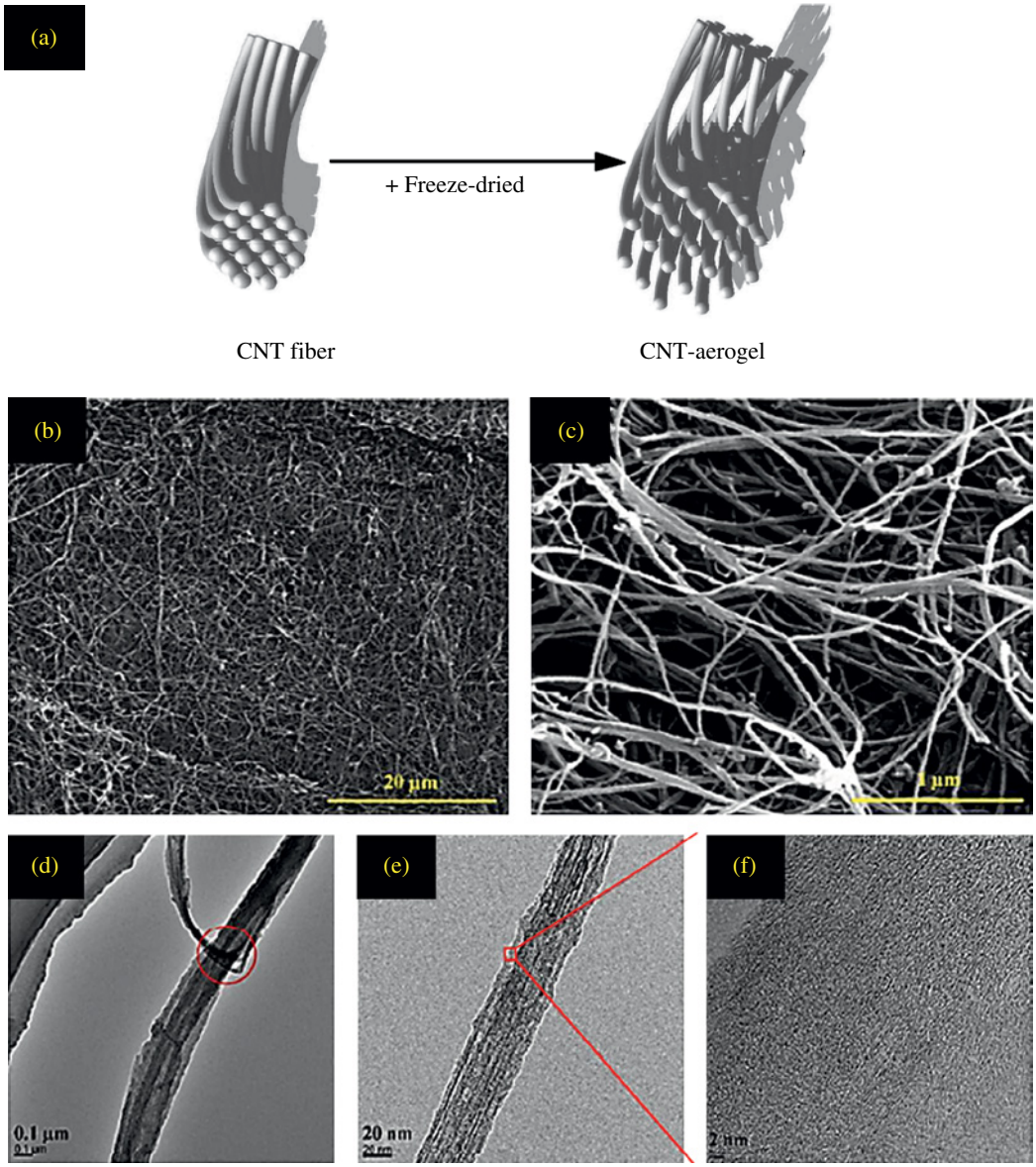


Figure 17.6 (a) Schematic of CNT-based aerogels (b, c) FESEM images of the CNT-aerogel, (d–f) TEM images of a CNT bundle in the CNT-aerogel materials [33].

technique with matrix of selection, ranging from inorganic sols to polymer melts to ceramic pastes, to develop variety of conductive CNT composites (Figure 17.7). Using CNT-aerogel composites could be useful to gain highest electrical conductivity, which is reported for a polymer/multi wall nanotube (MWNT) at low concentration of MWNT loading. This observation highlights requirement for further investigation in this area and suggests that even larger improvements in polymer composite conductivity are possible [36].

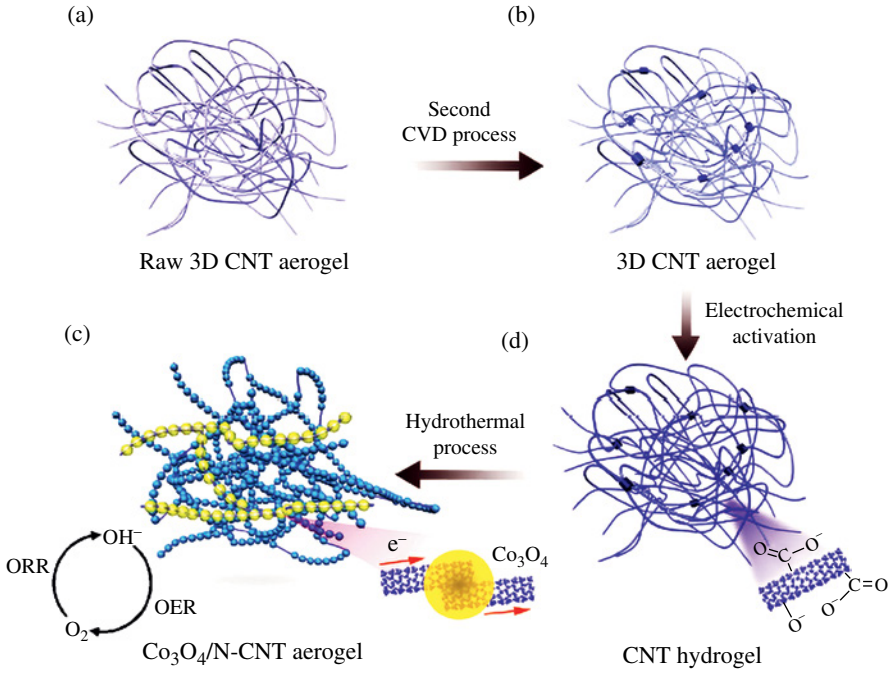


Figure 17.7 Process schematic for CNT-aerogel composite fabrication (between CNT aerogels and Co_3O_4 component) [36].

17.2.3.3.3 Graphene-based Aerogels Given comparatively cheap precursors and moderate synthesis conditions, graphene and graphene-oxide-based (GO-based) wet chemistry methodologies are simply the most common and well-known procedures to fabricate and prepare graphene aerogels. Unlike CNTs, GO is readily suspended or dissolved in aqueous solutions making it relatively easy to work with and more environmentally friendly. However, due to a high degree of oxidation present in GO structure as compared to CNTs, several reduction steps, mostly thermal or chemical, is mandatory for desired graphene-like propertie [37]. It is outstanding that graphene-based aerogel reported to be as extreme light and stabilized material. It has shown significant improvement in energy, transport, and mechanical properties compared to conventional carbon aerogels due to the primary carbon unit's crystalline nature. This kind of aerogel has different properties such as high electrical conductivity and also thermal resistance, as well as mechanical strength and adsorption capacity. Developing 3D structures with this incredible nanomaterial would further expand its significance both in applications number and in devices manufacturability. In general, former studies have relied on high stability of GO suspensions to assemble an initial macrostructure for GO, which could then have reduced thermally to yield 3D graphene microstructure network. This is a novel and unique method to produce ultra-low-density graphene aerogels with high electrical conductivities and large surface areas.

A key aspect in fabricating macro assemblies that exhibit such properties is the formation of junctions between graphene sheets that would both structurally reinforce aforementioned assembly and provide conductive interconnections between individual sheets. The presented process utilizes carbon to knit together graphene sheets into a macroscopic 3D structure. This process produces monolithic graphene architectures with low densities (approaching $10\,mg\,cm^{-3}$) and electrical conductivities more than two orders of magnitude greater than those reported for 3D

graphene assemblies formed via physical crosslinks. Besides, graphene aerogels possess surface areas on par with those reported for very high quality 2D graphene sheets. Graphene aerogel synthesis could be carried out by sol-gel polymerization of resorcinol (R) and formaldehyde (F) with sodium carbonate as a catalyst (C) in an aqueous suspension of GO (using ultrasonification) [14, 38]. The gel mixtures were formed by substituting the distilled water with a diluted suspension of graphene oxide (GO). The solution's initial pH was carefully adjusted to 6.0. Following extensive stirring at room temperature, the resulting sol was sealed in vials and subjected to a temperature of 90 °C for one week to achieve complete gelling. The polymer hydrogels were then dried using supercritical CO_2 and transformed into aerogels through heat treatment in an inert atmosphere. Also, GO could be produced by the Hummers method, which is useful for this material production. The molar ratio of aerogel sol-gel is a crucial and important variable as well as GO concentration and drying procedure, which is better to use supercritical CO_2. It should be noted that in this process, carbon junctions will be effectively incorporated into extended graphene framework. When organic precursors are added at sufficiently low concentrations to GO suspension, polymerization likely occurs at GO oxygen functionalities to form covalent interconnections between individual sheets.

To conclude, several parameters have been identified in studies which have impacted graphene aerogel structures. Among them is a specific method used during aerogel preparation. Second is precursor materials utilization, and the third one is special time and temperature for the aerogel drying stage. All mentioned parameters are seen to affect pore size and distribution as well as networking formation.

17.2.3.3.4 Graphene Aerogels from Pure Graphene Oxide Suspensions As discussed in previous section, under adequate process conditions, aqueous GO suspension gelation can proceed without traditional RF sol-gel chemistry aid. In fact, reports have demonstrated that GO suspensions can experience gelation process under several synthesis conditions, including low and high pH conditions, as well as high temperature (>150 °C- Figure 17.8) in hydrothermal methods. A significant challenge for graphene aerogel synthesis is to be able to initiate enough self-assembly and GO sheets reduction to build a mechanically robust, electrically conductive 3D network without a large degree of sheet restacking so that surface area is not compromised. A fairly suitable method for achieving this objective is to perform gelation under basic conditions that employs various functional groups, including epoxide or hydroxide, that are abundant in GO sheets serve as chemical cross-linking sites. After thermal reduction, these cross-linkers assisted for dual purpose. These sp^2 carbon bridges provide mechanical reinforcement and electrical conductivity by providing conjugated bonds, while at the same time serving as spacers, which prevent network restacking so that large surface areas can also be achieved [39].

17.2.4 Opportunities and Challenges

Aerogels in neat and composite forms are widely used in various applications. Among its tremendous performance is the lightest and most adaptable material because of its unique chemical properties to become wet gels. The basic thing that is related to all these abilities is high pore volume and high surface area. Thermal insulation is the most widely used aerogels and have been commercialized as well as other applications involving aerogel structures are electrochemistry including supercapacitors and fuel cell, materials for tissue engineering, catalysts carrier and other active agents, filling materials etc. [40, 41]. In these fields, aerogel microstructure has played a very good role – in particular, as part of the energy storage equipment itself. This is because of

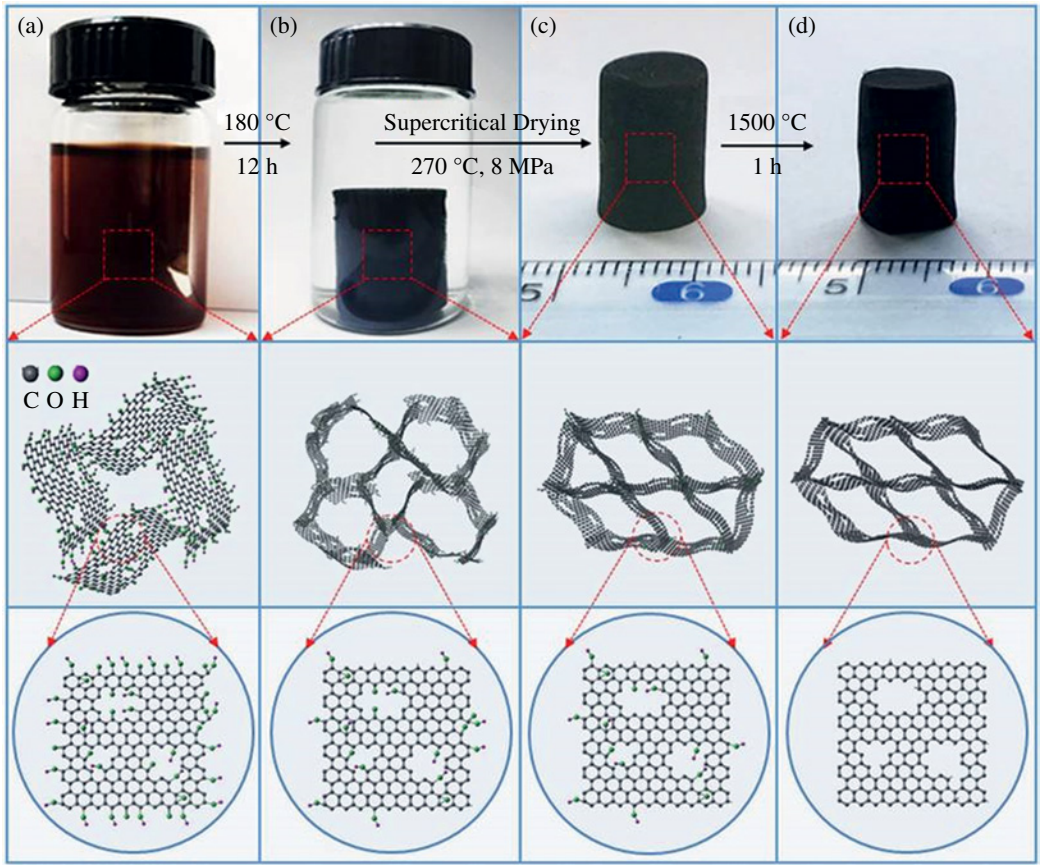


Figure 17.8 Representative of graphene based aerogel using ethanol supercritical drying and high temperature thermal reduction [39].

its special features such as high pore volume, high surface area, well-connecting formation, and flexibility [42]. Currently, some of the things seen as an opportunity for aerogel to continue to grow are as follows:

- The availability of aerogel cannot be denied, as it is accessible at both the lab scale and for large-scale production as raw materials. Aerogel is gaining increasing attention due to the abundant availability of its raw components, whether it be silica aerogel or organic aerogel. This ample supply of base materials opens up great possibilities for the expansion and exploration of aerogels. However, there are still challenges that act as barriers to aerogel production, potentially limiting its full potential from various perspectives. Scale up and aerogel production procedure [16]. Scale-up in aerogel production involves the process of increasing the production capacity from lab-scale to larger quantities. The procedure for aerogel production at scale typically begins with the selection and preparation of raw materials, such as silica or organic precursors. These materials are then mixed with solvents and additives to form a gel-like substance. The gel is subjected to supercritical drying or freeze-drying techniques to remove the solvent and create a highly porous structure. The resulting aerogel is then processed further to enhance its properties, such as surface modification or impregnation with other materials. During scale-up, careful consideration is given to optimizing the manufacturing process, ensuring consistent

quality, and addressing any challenges that arise due to increased production volumes. This involves optimizing reaction conditions, equipment selection, and developing efficient quality control measures. Scale-up in aerogel production enables the utilization of this unique material in various industries and applications, ranging from insulation and energy storage to aerospace and electronics, thereby unlocking its potential on a larger scale.

In general, the production procedures for aerogel involve three steps: gel formation, solvent exchange, and drying. Currently, the solvent exchange step, which is a common chemical technology, is only feasible at the laboratory scale, with no existing industrial-scale implementation. Additionally, maintaining the microstructure of aerogel formed after the drying step poses a crucial challenge that must be addressed for industrial-scale production of aerogels. Considering the opportunities and challenges discussed above, it is essential to take additional steps to realize the future of aerogels [3]. The following are the technology and production process gaps that need to be addressed Innovative strategies to explore the use of diverse raw materials for aerogel fabrication, taking into account factors such as availability, environmental impact, and recycling purposes. This involves investigating the potential of hybrid aerogels with different structures, including individual polymers, secondary polymers, additive materials, and their effects on the final aerogel hybrid composites. Transitioning from lab-scale to industrial-scale production, particularly for the solvent exchange technique [11].

- Controlling the characterization methods of aerogels is crucial for determining thermal conductivity, calculating pore size distribution, and evaluating mechanical properties. These comparisons provide valuable insights for different sources, benefiting both industrial and laboratory research fields. However, the current utilization of aerogel materials is restricted due to high production costs, poor mechanical properties, and health concerns related to the release of fine particles if crushed. Major challenges include the inherent mechanical brittleness of aerogels (unless supported or protected by reinforcement materials or covered with a membrane) and the time and energy-consuming fabrication process, which involves controlled aging, temperature regulation, supercritical drying, and solvent exchange. To overcome the mechanical brittleness of aerogels and expand their energy applications, hybridization with organic polymers is considered a suitable approach. It is important to note that reinforcement materials can reduce porosity and surface area.
- Aerogel modification is essential to introduce specific functional groups, and this process can be initiated during the sol-gel process either after gelation or when the aerogel is formed. This can be achieved through surface functionalization of the aerogels to regulate adsorption capacity or by applying a polymeric coating layer on the aerogel surface. Hybrid aerogels can combine the intrinsic structural properties of aerogels (high porosity and surface area) with the mechanical properties of inorganic components, enhancing their functionality.
- Designing aerogels and understanding their relationship with microstructural properties for energy storage present crucial challenges in aerogel modeling, design, and fabrication. Aerogels are known for their 3D microstructure with at least 80% porosity and 20% solid content. Achieving good electrical conductivity requires a high concentration of conductive nanoparticles such as graphene and CNT, which reduces porosity and increases the solid ratio. However, for lower thermal conductivity and higher thermal energy storage capacity (Figure 17.9), higher porosity and lower solid ratio are desirable. This creates a critical boundary for aerogel design and modeling. Therefore, when adding nanoparticles to modify the electrical and thermal energy storage properties of aerogels, careful consideration of thermal energy storage becomes crucial.

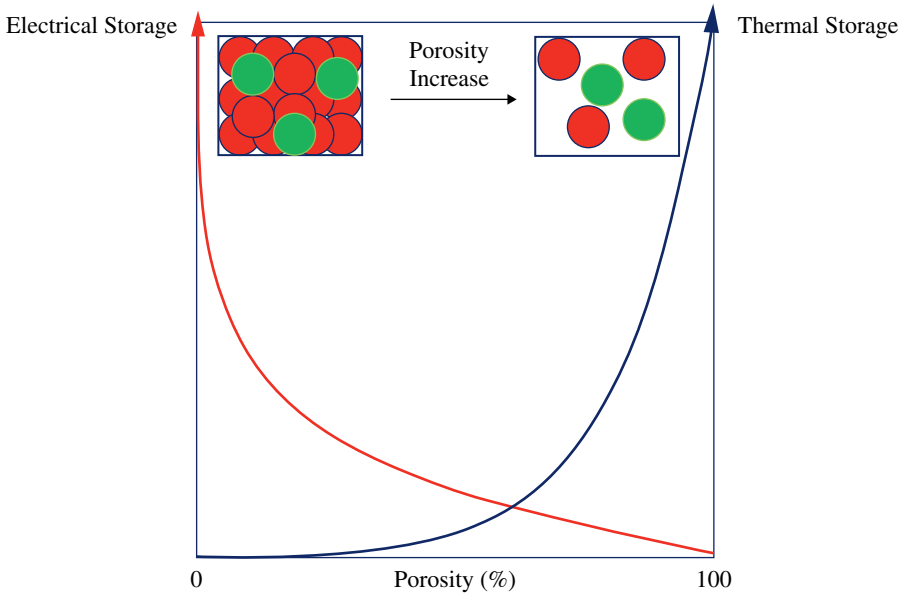


Figure 17.9 Relation between porosity and energy storage.

17.3 Methodology for Energy Performance Analysis

The aerogel-based performance strongly depends on the morphology and structure of aerogel such as carbon-based aerogels. Therefore, best designs of the developed carbon-based nanostructures in terms of surface area, pore size, pore volume, and density are essential for energy storage devices. However, some common techniques are beneficial for energy performance analysis of aerogels [43].

17.3.1 Thermal Conductivity

Density and porosity are main factors influencing the heat insulation performance of bulk materials. Generally speaking, at normal temperatures, thermal conductivity increases with mass of solid matter content in unit volume improvement [6, 44]. Thermal conductivities of aerogel samples could be recorded using hot plate disk according to ASTM C117 19. The hot plate temperature should be 60 °C for 20 minutes. Then using Eq. (17.4), the aerogel thermal conductivities can be calculated. Schematic of equipment for determining the thermal conductivity coefficient is depicted in Figure 17.9.

$$KA\frac{\left(T_H - T_C\right)}{L} = \dot{m}C_p\left(T_0 - T_i\right) \tag{17.4}$$

where, T_H is hot water temperature, T_C is cold water temperature, L, C_p is water specific heat capacity, T_0 is outlet water temperature, T_i is inlet water temperature, K is thermal conductivity, m *is* water outlet rate and A is the sample thickness [45].

17.3.2 Time-Temperature History

Time-temperature history analysis could be executed using a thermocouple type K with 0.1 °C accuracy, in which sample is prepared and cut into certain desired size (Figure 17.10 as a simple sample). After that, two thermocouples (at two symmetric locations to compare temperature results and improve results accuracy) wires should be inserted into aerogel (which should be drilled in desired dimension and should be sealed with special aerogel glue for thermocouple stability and final analysis results accuracy (Figure 17.11.)). Finally, samples should be suspended in a dryer with environment temperature of 356.85 K for time-temperature recording of 20 minutes.

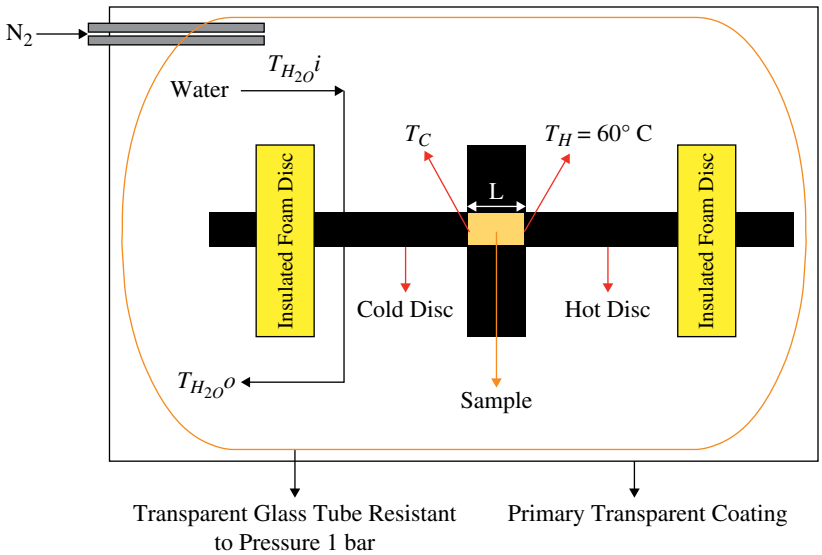


Figure 17.10 Aerogel thermal conductivity measurement equipment [45].

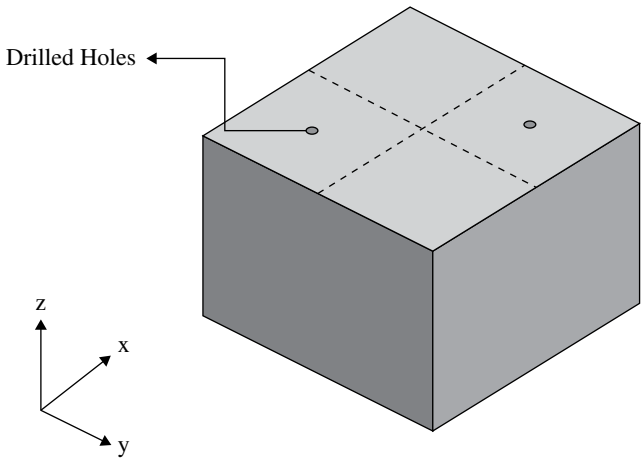


Figure 17.11 Schematic of cube like sample for time-temperature analysis [45].

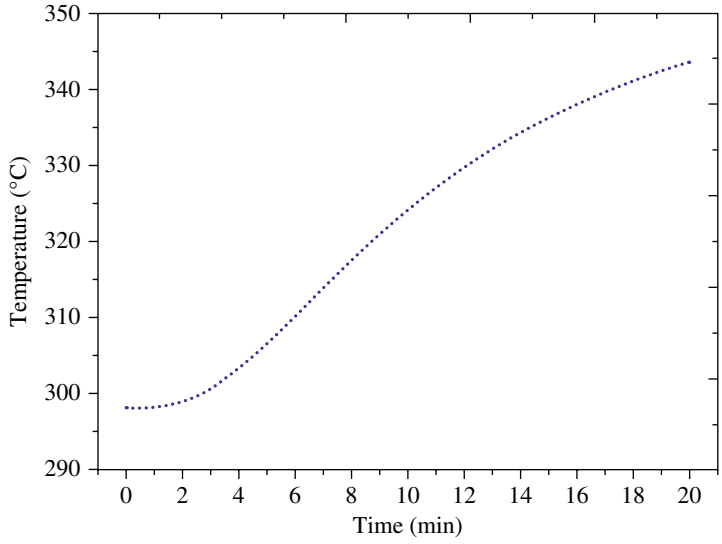


Figure 17.12 Time-temperature result of history analysis [45].

Obtained result from thermal history analysis is a time-temperature plot (Figure 17.12), which is a good representative of thermal diffusivity. In fact 1/curve slope is in relationship with thermal diffusivity, which is $\frac{k}{\rho C_p}$, the main heat transfer variable. Also, it should be noted that curve height is as a result of dryer environment temperature [45].

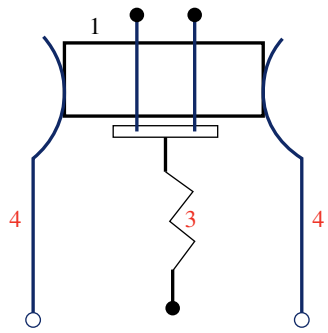


Figure 17.13 A four-point probe method (direct current) in a made cell 1: sample, 3: wires tensioning system, 4: current electrodes, bronchial clamp [46].

17.3.3 Electrical Performance

Preliminary electron conductivity of aerogels (which is 0.49 S/cm) could be carried out by a four-point probe method (direct current) in a made cell (Figure 17.13). A sample in cylindrical form should be clamped between two brass contacts of a four-contact cell. Furthermore, conductive carbon glue with a specific resistance of 3 Ohm*cm should be used. The thin tinned copper wires are useful as potential electrodes. The distance between wires (1–2 mm) is measured with an accuracy of 0.1 mm. The measurements will be carried out at ambient temperature under measuring current of 1 mA [46].

17.3.4 Potential Applications from an Energy Perspective

17.3.4.1 Potential Applications for Electrical Energy Storage

For aerogel application investigation, the main challenges of using aerogels should be pointed out because the utilization of aerogels for energy storage presents several challenges. One of the primary challenges is the inherent brittleness of aerogel materials, which can limit their practical applications without proper support or protection from reinforcement materials. Additionally, the energy-intensive and time-consuming fabrication process of aerogels, involving controlled aging,

temperature regulation, supercritical drying, and solvent exchange, can hinder their large-scale production and commercial viability. Furthermore, the high production costs associated with aerogels pose a barrier to their widespread use in energy storage applications. Poor mechanical properties and health concerns related to the release of fine particles if aerogels are crushed also need to be addressed to ensure safe and reliable deployment. Moreover, designing aerogels with optimal microstructural properties for energy storage is a complex challenge. Balancing factors such as porosity, solid ratio, thermal conductivity, and thermal energy storage capacity requires careful consideration to achieve the desired performance. Overcoming these challenges is crucial to fully unlocking the potential of aerogels for efficient and sustainable energy storage solutions.

Energy storage devices, including rechargeable batteries and supercapacitors, are vital for electric vehicles, robots, and portable devices development. Rechargeable lithium batteries are the most common electrical storage equipment due to low self-discharge rate, high energy density, and specifically long lifetime [2]. On the other hand, rechargeable sodium batteries have also been explored because sodium is more abundant than lithium in nature. Supercapacitors works with capacitive mechanisms to storage energy, which include electrical double layer capacitors resulting from Faradaic-type reactions that take place on electrode materials surface [47]. Generally, batteries have high energy densities in contrast to lower power densities. On the other hand, supercapacitors have high power densities but low energy densities. However, energy storage devices with all-in-one characteristics are desirable for industrial applications. In order to develop new types of electrode materials and batteries with great conductivity and capacity, long cycle life and outstanding rate capability are necessary. Copper and iron oxides are suitable and promising candidates as electrode materials because they are abundant and have and minimal environmental effect [48]. However, their very low electrical conductivity and capacity losses upon charging-discharging processes prevent them from being used as electrode materials. To overcome these challenges, solutions with metal nanoparticles and also hybrids with carbon such as aerogel nanomaterials for surface area and electrical conductivity improvement should be considered. Carbon aerogel is known for high purity, highly usable surface area, and high electrical conductivity material. Using this material will result in a high-capacity product that offers high energy density, very low leakage current, wide operating temperature range, and nearly infinite charge-discharge cycle life. It is also shown that the higher mass densities of the aerogels more than compensate for smaller inner surfaces (aerogels: $700\,m^2\,g^{-1}$) compared to activated carbons ($2000\,m^2\,g^{-1}$) [49, 50]. Thus, higher energy densities are possible if aerogel electrodes are utilized. A list of carbon aerogel applications as electrical energy storage are as follows:

- Carbon aerogels can be used as current collectors and scaffolds for 3D intercalaters in batteries [51].
- Carbon aerogel as functional nanomaterial can be used in hydrogen generation from water by solar energy, and electric energy from sustainable sources [52].
- Carbon aerogels as nanocatalysts can assist as electrode materials in electrocatalysis [53].
- Carbon aerogel offers substantial potential to improve desalination efficiency capacitive deionization technique. This can increase fresh water supply through capacitive desalination of brackish water and sea water [54].
- Carbon aerogel could be used as efficient material in solar-energy collectors cause of its "black" nature in infrared [55].

17.3.4.2 Potential Applications for Thermal Energy Storage

The use of aerogels for thermal insulation presents a range of challenges. One of the primary obstacles is the high production cost associated with aerogels, rendering them relatively expensive

compared to conventional insulation materials. This cost factor can limit their widespread adoption in thermal insulation applications. Additionally, aerogels are inherently brittle materials, making handling and installation more challenging. Careful support and protection are required to prevent damage during these processes. Another challenge arises from the potential health risks associated with the release of fine particles if aerogels are crushed or damaged. As a result, proper safety measures must be taken during installation and maintenance. Furthermore, maintaining long-term thermal performance poses difficulties due to factors like moisture absorption and aging. Aerogels have a porous structure that may permit moisture infiltration, compromising their insulating properties. Over time, their thermal conductivity may increase, leading to reduced effectiveness as insulators. Developing methods to enhance durability and moisture resistance while preserving optimal thermal performance remains an ongoing challenge in the field of aerogel-based thermal insulation. Addressing these challenges is vital to fully exploit the potential of aerogels as highly efficient and sustainable thermal insulation materials. Otherwise stated, thermal conductivity varies over time as a consequence of composition change in cell matrix. Ambient air in relation with external building surface temperatures in hot climates of Asia and Africa are much higher than in cold climates of such as Australia, Europe, and America. So that in aforementioned countries, temperature of 40 °C should be taken into consideration while thermal conductivities should be calculated at aging process [56]. In addition to building product specific parameter, which is thermal conductivity change, other important factors should be considered such as temperature and water absorption. Aerogels together with vacuum insulation panels are one of the new advantageous high-performance thermal and sound insulation materials in building applications. With a low thermal conductivity of $\sim 13\,\mathrm{mW\,m^{-1}\,K^{-1}}$, they show good characteristics in contrast with conventional thermal insulation materials (such as cellulose). Moreover, higher transmittances in solar spectrum are of great deal of interest for building construction sector. Another advantage of aerogels is visible transparency, which will allow their use in windows and skylights, giving engineers the opportunity of reimagining architectural answers [57]. As an example, a low thermal conductivity and also a high solar energy with good daylight transmittance of silica aerogel make it a very suitable material in highly energy efficient windows [58, 59].

17.4 Conclusions

In this report, aerogel utilization was discussed with regard to thermal insulation and electrical energy storage. Carbon aerogels (synthesized by carbonization, carbothermal reduction, and their modification with conductive nanoparticles (CNTs or graphene base)) are the most promising materials as a result of higher electrical conductivity as well as lower thermal conductivity. In addition to traditional RF-derived carbon aerogels, the methods for synthesizing graphene and CNT-based aerogels consist of roughly two procedures. Finally, after a thermal reduction, direct cross-links are converted to sp^2 carbon bridges between carbon nanomaterials network. There are several applications for aerogels that have been fabricated this way, such as batteries, hydrogen generation, supercapacitors, and building insulators as a result of adequate thermal properties, electrical conductivity, and energy storage capacity. However, using aerogels will face us with various challenges, including material availability, health issues, and transformation from lab-scale into industrial-scale production.

Acknowledgments

The authors would like to thank Tarbiat Modares University for their support during this research.

References

1 Wei, T.-Y. and Lu, S.-Y. (2011). Aerogels for energy saving and storage. In: *Energy Efficiency and Renewable Energy Through Nanotechnology* (ed. L. Zang), 873–911. Springer.

2 Ülker, Z., Sanli, D., and Erkey, C. (2014). Applications of aerogels and their composites in energy-related technologies. In: *Supercritical Fluid Technology for Energy and Environmental Applications* (ed. V. Anikeev and M. Fan), 157–180. Elsevier.

3 Alwin, S. and Sahaya Shajan, X. (2020). Aerogels: promising nanostructured materials for energy conversion and storage applications. *Mater. Renewable Sustainable Energy* 9: 1–27.

4 Polarz, S. and Smarsly, B. (2002). Nanoporous materials. *J. Nanosci. Nanotechnol.* 2 (6): 581–612.

5 Lee, J.K., Gould, G.L., and Rhine, W. (2009). Polyurea based aerogel for a high performance thermal insulation material. *J. Sol-Gel Sci. Technol.* 49 (2): 209–220.

6 Lu, X., Caps, R., Fricke, J. et al. (1995). Correlation between structure and thermal conductivity of organic aerogels. *J. Non-Cryst. Solids* 188 (3): 226–234.

7 Zhu, C.-Y. and Li, Z.-Y. (2018). Modeling of the apparent solid thermal conductivity of aerogel. *Int. J. Heat Mass Transf.* 120: 724–730.

8 Lu, X., Arduini-Schuster, M.C., Kuhn, J. et al. (1992). Thermal conductivity of monolithic organic aerogels. *Science* 255 (5047): 971–972.

9 Venkataraman, M. et al. (2016). Aerogels for thermal insulation in high-performance textiles. *Text. Prog.* 48 (2): 55–118.

10 Thapliyal, P.C. and Singh, K. (2014). Aerogels as promising thermal insulating materials: an overview. *J. Mater.* 2014 (10).

11 Smirnova, I. and Gurikov, P. (2018). Aerogel production: current status, research directions, and future opportunities. *J. Supercrit. Fluids* 134: 228–233.

12 Donthula, S. (2018). Aerogels for energy storage applications: From shape memory materials to thermites and explosives. PhD thesis. Missouri S& T. https://scholarsmine.mst.edu/cgi/viewcontent.cgi?article=3675&context=doctoral_dissertations

13 Kanamori, K. (2011). Organic–inorganic hybrid aerogels with high mechanical properties via organotrialkoxysilane-derived sol–gel process. *J. Ceram. Soc. Jpn.* 119 (1385): 16–22.

14 Korkmaz, S. and Kariper, İ.A. (2020). Graphene and graphene oxide based aerogels: synthesis, characteristics and supercapacitor applications. *J. Energy Storage* 27: 101038.

15 Lee, K.P., Begag, R., and Altiparmakov, Z. (2003). Rapid aerogel production process. HK1049295A1. Google Patents. Published May 5, 2003.

16 Shaari, N. and Kamarudin, S.K. (2019). Current status, opportunities, and challenges in fuel cell catalytic application of aerogels. *Int. J. Energy Res.* 43 (7): 2447–2467.

17 Cai, B. et al. (2018). Emerging hierarchical aerogels: self-assembly of metal and semiconductor nanocrystals. *Adv. Mater.* 30 (33): 1707518.

18 Lee, K.J. et al. (2018). Fast synthesis of spherical silica aerogel powders by emulsion polymerization from water glass. *ChemistrySelect* 3 (4): 1257–1261.

19 Baudron, V., Gurikov, P., and Smirnova, I. (2019). A continuous approach to the emulsion gelation method for the production of aerogel micro-particle. *Colloids Surf. A Physicochem. Eng. Asp.* 566: 58–69.

20 Zhang, Q. et al. (2016). 3D printing of graphene aerogels. *Small* 12 (13): 1702–1708.

21 Li, V.C.-F. et al. (2017). Direct ink write (DIW) 3D printed cellulose nanocrystal aerogel structures. *Sci. Rep.* 7 (1): 1–8.

22 Maldonado-Hódar, F.J., Moreno-Castilla, C., and Rivera-Utrilla, J. (2000). Synthesis, pore texture and surface acid–base character of TiO_2/carbon composite xerogels and aerogels and their carbonized derivatives. *Appl. Catal., A* 203 (1): 151–159.

23 Yamashita, J. et al. (2003). Organic and carbon aerogels derived from poly (vinyl chloride). *Carbon* 41 (2): 285–294.

24 Hong, P.N. et al. (2017). Carbon nanotube and graphene aerogels–the world's 3D lightest materials for environment applications: a review. *Int. J. Mater. Sci. Appl.* 6: 277–283.

25 Kong, Y. et al. (2012). Facile synthesis of resorcinol–formaldehyde/silica composite aerogels and their transformation to monolithic carbon/silica and carbon/silicon carbide composite aerogels. *J. Non-Cryst. Solids* 358 (23): 3150–3155.

26 Rousseas, M. et al. (2013). Synthesis of highly crystalline sp^2-bonded boron nitride aerogels. *ACS Nano* 7 (10): 8540–8546.

27 Meng, G. et al. (2000). Growth and characterization of nanostructured β-SiC via carbothermal reduction of SiO_2 xerogels containing carbon nanoparticles. *J. Cryst. Growth* 209 (4): 801–806.

28 Ramadan, H. et al. (2011). Synthesis and characterization of mesoporous hybrid silica-polyacrylamide aerogels and xerogels. *Silicon* 3 (2): 63–75.

29 Dinadayalane, T.C. and Leszczynski, J. (2012). Fundamental structural, electronic, and chemical properties of carbon nanostructures: graphene, fullerenes, carbon nanotubes, and their derivatives. In: *Handbook of Computational Chemistry*, 793–867. Dordrecht: Springer.

30 Zou, J. et al. (2010). Ultralight multiwalled carbon nanotube aerogel. *ACS Nano* 4 (12): 7293–7302.

31 Bryning, M.B. et al. (2007). Carbon nanotube aerogels. *Adv. Mater.* 19 (5): 661–664.

32 Abdullah, H.B. et al. (2020). Utilization of waste engine oil for carbon nanotube aerogel production using floating catalyst chemical vapor deposition. *J. Clean. Prod.* 261: 121188.

33 Li, Y. et al. (2018). A three-dimensional reticulate CNT-aerogel for a high mechanical flexibility fiber supercapacitor. *Nanoscale* 10 (19): 9360–9368.

34 Zheng, B., Li, Y., and Liu, J. (2002). CVD synthesis and purification of single-walled carbon nanotubes on aerogel-supported catalyst. *Appl. Phys. A Mater. Sci. Process.* 74 (3): 345–348.

35 Worsley, M.A., Kucheyev, S.O., Satcher, J.H. Jr. et al. (2009). Mechanically robust and electrically conductive carbon nanotube foams. *Appl. Phys. Lett.* 94 (7): 073115.

36 Zeng, S., Chen, H., Wang, H. et al. (2017). Crosslinked carbon nanotube aerogel films decorated with cobalt oxides for flexible rechargeable Zn–air batteries. *Small* 13 (29): 1700518.

37 Mao, J. et al. (2018). Graphene aerogels for efficient energy storage and conversion. *Energy Environ. Sci.* 11 (4): 772–799.

38 Wang, J. and Ellsworth, M.W. (2014). Graphene and graphene oxide aerogels. Google Patents.

39 Cheng, Y., Zhou, S., Hu, P. et al. (2017). Enhanced mechanical, thermal, and electric properties of graphene aerogels via supercritical ethanol drying and high-temperature thermal reduction. *Sci. Rep.* 7 (1): 1–11.

40 Zhao, J. et al. (2019). High-conductivity reduced-graphene-oxide/copper aerogel for energy storage. *Nano Energy* 60: 760–767.

41 Asim, N. et al. (2019). Biomass and industrial wastes as resource materials for aerogel preparation: opportunities, challenges, and research directions. *Ind. Eng. Chem. Res.* 58 (38): 17621–17645.

42 Huang, K.-J. et al. (2015). Synthesis of molybdenum disulfide/carbon aerogel composites for supercapacitors electrode material application. *J. Electroanal. Chem.* 752: 33–40.

43 Kwon, Y.C. (2013). A study on the architectural application of aerogel. *J. Civil Eng. Archit.* 7 (12): 1494.

44 Chen, Y., Li, D., Xie, X.-Q. et al. (2020). Theoretical modeling and experimental validation for the effective thermal conductivity of moist silica aerogel. *Int. J. Heat Mass Transf.* 147: 118842.

45 Abdeali, G., Bahramian, A.R., and Abdollahi, M. (2020). Scale variation enhancement on heat transfer performance of cubic-like polymeric aerogel: with regard to structural parameters. *Numer. Heat Transfer, Part A* 77 (9): 853–871.

46 Yan, M.-F., Zhang, L.-H., He, R., and Liu, Z.-F. (2015). Synthesis and characterization of carbon aerogels with different catalysts. *J. Porous. Mater.* 22 (3): 699–703.

47 Leung, C., Lu, L., Liu, Y. et al. (2020). Optical and thermal performance analysis of aerogel glazing technology in a commercial building of Hong Kong. *Energy Built Environ.* 1 (2): 215–223.

48 Wu, Z.-S., Yang, S., Sun, Y. et al. (2012). 3D nitrogen-doped graphene aerogel-supported Fe_3O_4 nanoparticles as efficient electrocatalysts for the oxygen reduction reaction. *J. Am. Chem. Soc.* 134 (22): 9082–9085.

49 Wu, D., Chen, X., Lu, S. et al. (2010). Study on synergistic effect of ordered mesoporous carbon and carbon aerogel during electrochemical charge–discharge process. *Microporous Mesoporous Mater.* 131 (1–3): 261–264.

50 Yang, I., Kim, S.-G., Kwon, S.H. et al. (2017). Relationships between pore size and charge transfer resistance of carbon aerogels for organic electric double-layer capacitor electrodes. *Electrochim. Acta* 223: 21–30.

51 Liu, M., Yang, Z., Sun, H. et al. (2016). A hybrid carbon aerogel with both aligned and interconnected pores as interlayer for high-performance lithium–sulfur batteries. *Nano Res.* 9 (12): 3735–3746.

52 Tian, X.-K., Tian, X.-K., Yang, C. et al. (2016). Active 3D Pd/graphene aerogel catalyst for hydrogen generation from the hydrolysis of ammonia-borane. *Int. J. Hydrog. Energy* 41 (34): 15225–15235.

53 Pan, J., Song, S., Li, J. et al. (2017). Solid ion transition route to 3D S–N-codoped hollow carbon nanosphere/graphene aerogel as a metal-free handheld nanocatalyst for organic reactions. *Nano Res.* 10 (10): 3486–3495.

54 Zhang, Q., Yi, G., Fu, Z. et al. (2019). Vertically aligned janus MXene-based aerogels for solar desalination with high efficiency and salt resistance. *ACS Nano* 13 (11): 13196–13207.

55 Li, Q., Zhang, Y., Wen, Z.-X., and Qiu, Y. (2020). An evacuated receiver partially insulated by a solar transparent aerogel for parabolic trough collector. *Energy Convers. Manag.* 214: 112911.

56 Baetens, R., Jelle, B.P., and Gustavsen, A. (2011). Aerogel insulation for building applications: a state-of-the-art review. *Energ. Buildings* 43 (4): 761–769.

57 Nguyen, S.T., Feng, J., Ng, S.K. et al. (2014). Advanced thermal insulation and absorption properties of recycled cellulose aerogels. *Colloids Surf. A* 445: 128–134.

58 Mandal, C., Donthula, S., Far, H.M. et al. (2019). Transparent, mechanically strong, thermally insulating cross-linked silica aerogels for energy-efficient windows. *J. Sol-Gel Sci. Technol.* 92 (1): 84–100.

59 Plawsky, J., Littman, H., and Paccione, J. (2010). Design, simulation, and performance of a draft tube spout fluid bed coating system for aerogel particles. *Powder Technol.* 199 (2): 131–138.

Index

a

aerogels 1–21, 38–57, 61–86, 90–120, 128–161, 169–189, 197–229, 237–261, 267–282, 291–319, 331–374, 386–403, 407–426, 430–440, 447–466, 473–490, 497–513
AeroShield 257, 258
air-laid paper 277
alginate 242, 269, 271, 278, 400, 415, 417, 423, 425, 488–490
alkaline fuel cells 343, 344
amorphous carbon black 340, 349, 503
anode 49–51, 53, 54, 78, 84, 184, 314–317, 343, 344, 349, 387, 390, 395, 396, 398, 399–400, 401, 402, 452, 456, 457, 461
Arabic gum 422

b

base 10, 14, 42, 54, 107, 129, 132–134, 136, 175, 177, 189, 198–200, 204, 228, 241, 295, 303, 432, 502, 507, 513
battery 20, 21, 49–53, 180, 186, 188, 189, 239, 279, 314–317, 343, 358, 401, 451, 452, 455, 457, 461, 466, 490
benzene 99, 275, 293, 294, 311, 340, 389, 390, 420
bifunctional air electrode 316
binary mixed oxides systems 142
bioanode 390
biocompatibility 104, 112, 175, 178, 242, 388, 390, 424
bio-electrochemical 390
biological 169, 279, 335, 344
biomass 4, 43, 44, 49, 177, 278, 302, 331, 335, 338, 342, 386, 388, 393, 403
borohydride 69, 344, 390
bottom-up 67, 268, 334, 448, 449

c

carbide 4, 13, 17, 20, 335, 393, 501
carbon 5, 13, 18, 20, 49, 52, 54, 56, 171, 172, 177, 184, 186, 240, 242, 332, 338, 350, 360, 373, 502, 503, 506, 512
carbonaceous 40, 42, 43, 156, 312, 315,317, 331–374, 394, 503
carbon footprint 312
catalyst 10, 41, 55, 56, 94, 99, 106–108, 159, 160, 172, 177, 186, 200, 204, 241, 257, 258, 293–298, 300, 312, 316, 331, 335, 339–341, 344, 348–350, 393, 394, 398–399, 424, 432, 506
cathode 49–52, 54, 56, 57, 78, 160, 314, 317, 343, 349, 350, 387, 390, 395, 399–400, 401, 402, 457, 460, 461
cell 43, 45, 51, 54–57, 78, 84, 85, 105, 113, 159–160, 205, 255, 258, 259, 316, 331, 342–352, 363, 388–390, 392, 394, 395, 400, 401–403, 415, 418, 420, 475, 479–480, 482, 488, 487, 506, 511, 513
cellulose 38, 40, 42, 91, 102, 105–106, 111, 139, 174, 177, 178, 200, 202, 241, 242, 244, 269–273, 275, 277, 278, 291, 299, 302, 311, 342, 373, 393, 408, 409, 411, 413, 415, 417–420, 425, 426, 435, 474, 480,488–490, 499, 513

Aerogels for Energy Saving and Storage, First Edition. Edited by Meldin Mathew, Hanna J. Maria, Ange Nzihou, and Sabu Thomas.
© 2024 John Wiley & Sons, Inc. Published 2024 by John Wiley & Sons, Inc.

chalcogenide aerogel 4, 20, 43–44, 408
characterization 48, 62, 64, 145–158, 214, 291, 340, 350, 363, 399, 411, 415, 426, 482, 489, 508
chemical vapor deposition 2, 110, 169, 172, 173, 275, 334, 388, 419, 423, 448
chitin 242, 373, 409, 420–421, 426
composite 4, 17, 18, 38–57, 61, 90–120, 142–144, 169, 177–179, 186, 189, 207, 237–261, 332, 338, 394, 407–426, 431, 452, 461, 476, 500, 503–506
condensation 40, 41, 44, 45, 92–94, 98, 130, 134–136, 142, 150, 161, 175, 200, 241, 293–295, 297, 299, 300, 305, 397, 407, 430, 432, 434, 480
conductivity 3, 11, 12, 15, 16, 18, 19, 39, 42, 48, 51–55, 61, 71, 78, 81, 84, 90, 91, 99, 102, 104–106, 108, 110–114, 117, 119, 144, 159, 160, 169, 170, 174, 178, 179, 181, 184, 186, 200, 204, 207–209, 216, 228, 239, 241–243, 245–261, 270, 275, 277–279, 291, 298, 300, 304–306, 313, 314–317, 332–335, 340, 349–351, 360, 362, 363, 373, 374, 388, 390, 392, 393, 395, 396–399, 400, 402, 403–405, 407, 417–418, 419, 423, 425, 430, 432, 434, 435–437, 439, 447, 448, 452, 473–481, 497–499, 502–506, 508–513
consumption 4, 16, 110, 183, 216, 217, 221–223, 237–239, 255–257, 260, 261, 279, 373, 449, 473, 497
coordinating ligand 129
coupling 10, 18, 175, 176, 250, 251, 401
crosslinker 99, 305, 373, 393, 420
crosslinking 42–46, 48, 71, 93, 99–102, 105–108, 112, 157, 170, 173, 174, 175, 270, 272, 273, 276, 295, 298, 299, 302, 305, 306, 311, 339, 407, 415, 417, 422–423, 432, 440
cyclic voltammetry 183, 350

d

degradation 53, 54, 160, 186, 271, 279, 307, 389, 390, 394, 418, 435
degree of crystallinity 146, 147
device 18, 38–57, 237, 243, 277, 279, 282, 331, 332, 334, 341, 342, 344, 358, 359, 373, 374, 401, 424, 448–452, 466, 497, 499, 505, 509, 512
diffusion 3, 11, 12, 14, 19, 42, 49, 53, 55, 79, 97, 138, 254, 281, 316, 343, 344, 348, 350, 363, 391, 431, 432, 476, 477, 481, 482, 484
dimethyl ether 344
dimethyl oxalate 344
dioxide 4, 13, 43, 47, 82, 137, 142, 241, 275, 296, 302, 311, 312, 318, 339, 386, 387
direct flame SOFCs 159, 160, 344
disulfide 50, 394, 400
doping 7, 53, 93, 120, 160, 175–179, 180, 183, 184, 186, 186, 254, 314–316, 396, 398, 401
drying 2, 4, 7, 10, 38, 39, 42–47, 62, 75–77, 93–95, 99, 119, 130–140, 146, 156, 169, 170, 178, 198, 199, 201–202, 216, 240, 243, 245, 257, 291, 293, 295–297, 302, 312, 335, 338–341, 388, 408, 415,417, 418, 420–426, 497, 503, 506–508

e

economy 386, 424
electrocatalyst 52, 55, 56, 75, 81, 335, 349, 387–395, 397–400, 401, 402
electrochemical 15, 20, 40, 44, 53, 54, 56, 57, 79, 81–84, 86, 144, 161, 183–186, 186, 279, 313, 314, 316, 317, 331–335, 340, 343, 349, 350, 358, 360, 363, 373, 374, 387–390, 394, 398, 401, 447–449, 451, 452, 456, 457, 460, 461, 463, 464, 466
electrochemical impedance spectroscopy (EIS) 350
electrode 18, 43, 50–54, 77, 78, 84, 86, 161, 183–186, 188, 189, 313, 314–317, 331, 332, 335, 343, 344, 348, 350, 358–363, 365, 373, 374, 388–389, 390, 392, 395, 399, 400, 401, 402, 451, 452, 456, 461, 512
electromagnetic radiation 104, 251
electrosorption 313
electrospinning 9
electrostatic 65, 96, 110, 131, 174, 179, 200, 242, 281, 399, 420, 424, 431
electrotransport 316, 392, 394, 456
energy 1–21, 38–57, 61–86, 102, 110, 128–161, 169, 170, 177–189, 197, 205, 209, 210, 216–223, 237–239, 246, 247, 255–258, 260, 276, 305–308, 313–319, 331–335, 340–343, 349, 358, 359, 363, 373, 386, 387, 430–440, 448–461, 473, 475–478, 482, 497–513

enzymatic 56, 178, 344, 391
exfoliation 334, 390, 393, 394
expanded polystyrene (EPS) 110, 111, 238
extracellular 390

f

facile 20, 110, 112, 182, 276, 300, 392, 393, 395, 397, 398, 400, 403, 415, 417, 456, 460
filter 131
frequency 15, 16, 20, 114, 214–216, 319, 396, 478, 479
fuel cells 42, 49, 54–56, 78–81, 142, 159, 331–374, 386, 387, 390, 401, 448, 499

g

gasification 334, 387
gelation 2, 43–45, 62, 65–76, 81, 86, 92, 93, 96, 99–101, 105, 107, 108, 117, 129, 130, 134–135, 139–144, 161, 170, 174, 175, 178, 179, 199, 200, 204, 240–245, 271, 294–298, 300, 302, 304, 305, 335, 340, 388, 394, 396, 431, 433–437, 440, 506, 508
Genipin 276
geometry 101, 169, 216, 222, 228, 350, 415
graphene 9–11, 18, 20, 42–44, 46, 49–56, 91, 101, 102, 105, 106, 108, 109, 111, 113–115, 117, 118, 169, 173, 175, 176, 179, 183, 184, 186, 200, 203, 242, 244, 270, 272, 273, 275–279, 314, 332–334, 338, 340–341, 360, 363, 388, 389, 389–393, 396–400, 401–403, 447–466, 482, 484, 498, 501–503, 505–508, 513
greenhouse 82, 237, 318, 342, 387, 497

h

halloysite 91, 106, 111, 411, 425
heterogeneous 23, 162, 395, 421, 490
hollow 67, 68, 79, 479, 480
homogeneous 42, 101, 108, 112, 173, 174, 175, 178, 179, 201, 331, 341, 349, 415
hydrides 84, 386
Hydroelectric 331
hydrogel 39, 56, 75, 90, 94, 179, 241, 273, 339–341, 373, 391, 393, 398–400, 411, 420, 489
hydrolysis 7, 39–41, 44, 45, 92, 93, 104, 130–134, 139, 141, 142, 144, 150, 157, 159, 161, 175, 198, 200, 241, 393, 407, 421, 430, 432
hydrothermal 44, 183, 184, 300, 341, 388–390, 391, 394, 396, 397, 399–400, 448, 449, 452, 456, 461, 466, 506
hydroxide 129, 139, 145, 186, 294, 342, 399, 411, 417, 425, 506
hydroxylamine 270, 272

i

indigo carmine 272
insulation 11, 16–18, 20, 21, 39, 48, 50, 98, 104, 105, 108, 110–112, 119, 120, 128, 158, 200, 207, 209, 214, 216, 221, 222, 227, 228, 237–261, 271, 277, 306, 308, 310, 312, 317, 322, 340, 409, 411, 415, 416, 417, 423–426, 430, 434, 435, 436, 438, 440, 474, 477, 479, 480, 504, 506, 508, 509, 512, 513
ionictransfer 349
Iron 61, 84, 129, 130, 142, 157–159, 161, 257, 279, 291, 316, 397, 410, 512
irradiation 105, 106, 181, 278, 279, 421

k

Kapok fibers-PPy aerogels 278
kinetics 52, 75, 78, 84, 186, 241, 249, 281, 294, 295, 304, 305, 312, 339, 424, 431

l

lamellar structure 410, 415, 421
lignin 302, 305, 342, 373, 409, 420, 425, 426
Li-ion 49, 50, 52, 53, 184, 239, 317, 451, 452, 454
Li-S 49–50, 317
Lithium 20, 49, 50, 84, 85, 183, 189, 314, 315, 316, 340, 448, 451–453, 455–457, 460, 461, 466, 512
luminescent 198
lyophilization 46, 47, 408

m

materials 2, 4, 40–44, 91, 96, 98, 110–112, 116–117, 119, 130, 139, 140, 142, 156, 160, 161, 207, 238, 239, 252, 269–271, 275, 277, 278, 281, 296, 314–317, 332–336, 339, 340, 342, 358, 373, 387, 388, 392, 395, 402, 407, 408, 418, 422, 431, 433, 456, 502, 503, 507
MCFCs *see* molten carbonate fuel cells (MCFCs)

mechanical 7–11, 14, 39, 42, 48, 53, 64, 76, 77, 91, 92, 98, 100–102, 104–106, 109, 112, 119, 120, 157–158, 169, 170, 176, 179–180, 186, 197, 204–207, 259, 339, 341, 414–415, 420, 423, 431, 473–490, 502, 503, 508, 512
membrane electrode assembly (MEA) 343, 344, 348, 350
Mesoporous 5, 39, 49, 50, 55, 95, 101, 141, 150, 184, 270, 334, 335, 388, 390, 430, 477, 484
metal-oxide 40, 41, 47–49
microbial fuel cells (MFCs) 344
microporosity 39, 44, 46, 53, 312
microspheres 15, 46, 71, 300
miniature 49
molten carbonate fuel cells (MCFCs) 344
monolithic 2, 10, 14–16, 46, 61, 65, 69, 75–77, 128, 130, 133, 137, 197–199, 202–211, 214, 216–219, 228, 229, 243, 257, 258, 260, 261, 269, 270, 434, 502, 503, 505
monomers 15, 42, 45, 93, 96, 98, 106, 108, 134, 201, 270, 271, 294–297, 300, 422, 431, 432
montmorillonite 91, 410, 411, 413–415, 417–420, 422, 425
MoS_2-nanosheets 278, 390–394

n

nanocarbons 391
nanocrystals 55, 91, 102, 150, 186, 393, 398, 461
nanosheets 52, 69, 71, 75, 114, 180, 183, 278, 390–394, 399, 400, 402, 424, 460
nanotube 9, 54, 75, 100, 106, 174, 176, 242, 373, 390, 392, 436, 452, 461, 482, 498, 502, 504
network 2, 9, 13, 16, 38, 39, 42–48, 52, 70, 73, 75, 76, 81, 84, 90–97, 99, 102, 105, 107, 108, 110, 112–117, 119, 128, 129, 139, 141, 142, 150, 157, 159, 169, 170, 173–176, 180, 181, 184, 186, 198, 200–202, 205, 210, 241, 269, 270, 293–299, 301, 302, 312, 313, 315, 388, 392, 398, 407, 411, 414–416, 419, 430, 432–434, 438, 448, 453, 461, 473, 478, 479, 482, 484–490, 497, 503, 505, 506, 513
nuclear 4, 5, 48, 142, 161, 239, 271, 281, 489

o

oleophilic aerogel 275
organic 4, 9, 10, 14, 15, 39, 40, 42, 43, 46, 47, 52, 67, 71, 76, 90, 91, 93, 95, 96, 98, 106–110, 128–130, 133, 139, 144, 153, 161, 169, 173, 174, 179–183, 198–200, 240–243, 252, 259, 268–275, 279, 282, 291–319, 332–334, 338, 339, 341, 342, 350, 362, 388–390, 396, 401, 408, 415, 417, 419, 421, 423, 431–437, 438, 440, 452, 489, 499, 502, 503, 506–508
oxide 2, 4, 7, 9–11, 13, 39–43, 47–49, 52, 54, 56, 61, 69, 91, 101, 108, 129, 130, 132, 139–144, 157–159, 161, 175, 184, 186, 202, 241, 242, 244, 258, 269, 270, 272, 273, 276–278, 291, 317, 333, 341, 343, 344, 351, 363, 391, 394, 399–402, 408, 410, 418, 452, 456, 460, 499, 502, 505, 506
oxyhydrogen 334, 340, 387, 388, 401

p

palygorskite 415, 417, 423
PEMFCs *see* proton exchange membrane fuel cells (PEMFCs)
phonons 11, 245, 246, 248, 437, 478, 479
Phosphoric acid fuel cells (PAFCs) 344
photoactive 307
photovoltaic 45, 334
polarization 82, 319, 389, 400
polycondensation 7, 42, 93, 94, 106, 107, 129, 199, 241, 269, 295, 297, 301, 304, 432
polyethyleneimine 409
polymer 2, 9, 10, 14, 15, 20, 38–40, 42, 43, 46, 48, 90, 120, 174, 178, 200, 239, 267–282, 299, 302, 344, 348, 349, 351, 395, 407–409, 410–412, 415–416, 418, 420–423, 425, 431–432, 438, 498, 502, 504, 506
polyvinyl alcohol (PVA) 43, 105, 139, 174, 269, 270, 273
porosity 2, 7, 12, 14, 15, 39, 44, 45, 48, 50, 53, 63, 94, 95, 99, 102, 104, 105, 110, 111, 119, 137–139, 141, 160, 161, 169, 172, 173, 175, 179, 180, 182, 183, 184, 189, 205, 238, 240, 242, 243, 248–251, 267, 269, 270, 273, 275, 277–279, 291, 297, 299, 301, 303–305, 312, 316, 317, 332,

335, 339, 342, 349, 350, 363, 373, 388, 390, 402, 407, 410, 416, 417, 430, 431, 434, 438, 448, 449, 452, 466, 477, 480, 497–499, 508, 509, 512
precipitation 65, 279
precursor 14, 38, 39, 41, 45, 52, 62, 65, 74, 77, 93, 96, 98–101, 104, 112, 130, 140, 141, 144, 145, 170, 198–200, 204, 241, 242, 244, 255, 269, 291, 299, 300, 305, 333–335, 338, 350, 389, 390, 396, 397, 400, 401, 417, 430–431, 438, 502, 503, 506
probe 63, 64, 511
properties 1–21, 48, 49, 57, 64, 93, 106, 119, 145–158, 160, 161, 204–216, 228, 242, 255, 260, 291, 293, 297, 299–305, 308, 309, 312–313, 332–335, 338, 362, 390, 408, 411–418 422, 423, 437–439, 486, 487–490, 499, 501, 505, 508
proton 39, 55, 129, 133, 134, 343, 344, 351, 390, 395–399
proton exchange membrane fuel cells (PEMFCs) 55, 348, 350
pseudocapacitors 18, 183, 184, 362
PVA *see* polyvinyl alcohol (PVA)

q

quadrupole 318

r

Rosseland mean 252, 253, 476
rubber 128, 198, 241, 271, 279, 409, 420, 423, 424

s

semiconductor 38, 49, 112, 390, 398
smectites 410, 411, 426
sol-gel 2, 4, 5, 14, 39–42, 44–46, 50, 62, 90–95, 100, 102, 107, 108, 119, 128–161, 170, 176, 179, 198, 200, 201, 240, 241, 257, 269, 270, 275, 280, 293–295, 300, 304, 308, 312, 335, 339–341, 388, 389, 390, 396, 397, 430, 434, 484, 502, 503, 506, 508
solid oxide fuel cells (SOFCs) 142, 159, 344
solvent exchange 47, 76, 95, 129, 140, 141, 143, 152, 153, 201–203, 240, 241, 245, 255, 293, 295, 296, 300, 302, 305, 340, 431, 508, 512
structure 1–3, 7, 11, 20, 45–50, 63–67, 71, 75, 94–97, 102, 105, 119, 120, 146, 201, 227, 242, 277, 293–299, 311–314, 317–319, 333–335, 340–342, 363, 373, 390, 393–395, 401, 409, 415, 418, 419, 423, 437, 473–490, 497, 499, 500, 502, 505, 506
sublimation 46, 47, 76, 77, 95, 138, 139, 202, 240, 244, 296, 339, 409, 410
substrate 20, 51, 52, 56, 57, 171–173, 181, 184, 186, 274, 277, 282, 334, 373, 389, 390, 461
supercapacitors 18, 42, 49, 53–54, 77, 86, 180, 183, 184, 189, 308, 313–315, 331–374, 448, 499, 506, 512, 513
supercritical 2, 4, 7, 10, 38, 39, 42, 45–47, 90, 94, 95, 98, 99, 101, 102, 108, 119, 128, 135, 137–139, 143, 170, 174, 176, 179, 198, 199, 201–204, 209, 229, 239–241, 243, 257, 269, 270, 275, 296, 297, 299, 302, 304, 305, 339–341, 396, 397, 408, 424, 430, 431, 433, 503, 506–508, 512
supercritical drying 7, 10, 38, 39, 42, 45–47, 90, 94, 95, 99, 101, 119, 128, 135, 137–138, 144, 170, 174, 176, 179, 198, 199, 202, 240, 241, 243, 257, 269, 270, 275, 296, 302, 304, 305, 339–341, 432, 503, 507, 508, 512
superlattice nanowire 247
synthesis 4, 7, 40, 50, 61, 62, 64–77, 85, 86, 90, 91, 96, 101, 109, 111, 128–161, 179, 185, 197–199, 202, 203, 205, 206, 210, 222, 240, 241, 268, 275, 291, 293–297, 299–305, 307, 309, 312–314, 319, 334, 335, 338–342, 350, 374, 390–392, 393, 394–395 399, 400, 408, 409–410, 416, 417, 421, 422, 430–433, 435, 438, 440, 448, 449, 461, 484, 490, 497, 501, 502, 505, 506

t

tetramethylorthosilicate (TMOS) 7, 128, 144, 175, 198–200, 204, 241, 257, 422, 430, 434
textile 271
thermal 5, 11, 48, 98, 99, 110–113, 119, 120, 178, 179, 197, 207–209, 216, 226, 229, 237–261, 277, 279, 305, 306, 317, 341, 416, 417, 422–424, 437–439, 473–490, 497–513

thermodynamics 474
thermoelectric 32, 194
thermoplastic 113
thixotropic 244, 410
titania aerogels 140–141, 146, 147, 150, 159
triazine 302

u

ultrasonic 15, 43, 271, 390
ultraviolet 48, 65
U-value 208, 209, 217, 226, 227, 257

v

vacuum 2, 18, 47, 76, 94, 95, 110, 138, 153, 170, 175, 202, 208, 209, 216, 221, 228, 238, 251, 255–257, 306, 313, 339, 410, 513
volatile 417
vulcanized natural rubber 420

w

water absorption 419, 513
wind 331, 386

x

xerogels 39, 140, 142, 144–146, 149, 150, 153, 158, 161, 198, 199, 204, 268, 280, 300–302

y

Young's modulus 7, 8, 11, 101, 103, 158, 205, 242, 306, 408, 409, 411, 415, 426, 430, 482, 486, 487

z

zeolite 424
Zn-air 52, 189, 316, 401
Zn-ion 52